SIMULATION OF COLD-FORMED STEEL STRUCTURES

by
Jiazhen Leng

A dissertation submitted to Johns Hopkins University in conformity with the requirements for the degree of Doctor of Philosophy

Baltimore, Maryland
August 2015

Abstract

Buildings framed from cold-formed steel members are becoming increasingly common. Simulation of cold-formed steel (CFS) structures in this dissertation includes seismic modeling and analysis of a two-story CFS-framed archetype building from the CFS-NEES project and shape optimization of CFS columns for maximum strength. The CFS-NEES research project is a joint effort that includes experimental and computational efforts with the objective of providing all the necessary building blocks to advance the simulation tools for seismic performance-based design evaluations of CFS-framed buildings. The simulation effort, which is a major focus of this thesis, includes the development of a wide breadth of finite element models in OpenSees of the CFS-NEES archetype building, calibration of models with full scale shaking table test results, and the exploration of the relationship between model fidelity and prediction of building response. Results indicate that high-fidelity models with consideration of structural and nonstructural components offer reasonably accurate prediction of the archetype building's seismic response in comparison with tests. Nonstructural components in design assumptions, including exterior gravity wall sheathing, interior gypsum sheathing, and partition walls have a significant contribution to the building system's lateral force resistance – and this may be captured in simulations. The performance of 3D models is considerably better than isolated 2D wall line models because of non-trivial coupling effects from the diaphragms, even though existing standards would designate the building diaphragms as flexible. Incremental dynamic analysis results of archetype models are post-processed following the procedure in FEMA P695 for performance evaluation of seismic response modification coefficients employed in design.

A companion effort on the shape optimization of CFS columns includes unconstrained and constrained search for a cross-section profile that can maximize the axial capacity with a given sheet of steel. Unconstrained optimization includes comparison between gradient-based vs. stochastic search algorithms and constrained optimization involves implementing a number of end-use and manufacturability constraints into stochastic search algorithms. A number of novel cross-section shapes with considerable capacity growth have been identified, and there is little compromise of capacity after the introduction of constraints.

The combined simulation work in this dissertation extensively explores the usage of state-of-the-art computational simulation tools in analysis and design of CFS-frame structures. Research outcomes are compared with test data, commercial products, and existing codes and specifications, and design recommendations are formulated thereafter.

Readers:
Dr. Benjamin Schafer (Ph.D. advisor)
Dr. James Guest, Dr. Shahabeddin Torabian

Preface

It is always complicated to describe a PhD candidate's mixed feeling towards the completion of his dissertation. An ignorant person can hardly be qualified for a PhD; neither does a person too quick to bear any hard work. The commencement itself is a commencement: life goes on so why not be optimistic and look forward.

Personally, I am more independent and not very gregarious. But I do know from the bottom of my heart that life is full of miracles and one should always be grateful.

I always thank my parents first for bringing me this prismatic world. You formed a cozy home and gave me love and tolerance. You always unconditionally support me when I need encouragemen but never dismiss my shortcomings. Your attitude towards life greatly shapes me into who I am. I learnt first and quite a lot from you, and I am still learning.

To Dr. Schafer: thank you for being my advisor. Thank you for setting a high standard on my research and academic performance and make me strive for it. A future scholar should be able to survive this and I am about to finish. I believe we both have great enthusiasm for research and will cooperate well by tackling similar problems from different paths.

To Dr. Guest and Dr. Buonopane: thanks for your help on my research and academic career. Not many people can have the luck of being part of two distinct research projects.

This broadens my scope and helps me prepared for future challenges. Through the process, I got more opportunities to communicate with you and emulate your research styles.

To our staff of civil engineering department: thank you all for making our small department like home. In this department, everyone is warmly welcomed and students can always find help when they need some. Your support is very important in my pursuit of PhD degree.

To my lab mates and friends: thanks for sharing your golden years with me. Our backgrounds, life styles, personal interests are diversified, but with trust and mutual respect, we stand together and form a harmonic group. I will never forget the joy and happiness with you folks, and you know my memory is not bad.

Through my life, I always feel I am lucky enough to have all these excellent people in my life so that I can have a small accomplishment with their love and help. As for the future, I cannot tell what will happen next and I have no interest in making a guess because I know am unique but not alone. Trust me, thank you and love you all!

Table of Contents

Abstract **ii**

Preface **iv**

Table of Contents **vi**

List of Figures **xii**

List of Tables **xlv**

Chapter 1 : Introduction to Cold-formed Steel Simulation **1**

1.1 Modeling CFS members using frame finite elements *6*

1.2 Modeling CFS members using finite strip method *12*

1.3 Modeling CFS members using shell finite elements *14*

1.4 Modeling of CFS-framed structures under static and dynamic loading *17*

Chapter 2 : Shape Optimization of Cold-formed Steel Columns **25**

2.1 General formulation of CFS column shape optimization problem *33*

2.1.1 Design variable formulation of unconstrained optimization problem 33

2.1.2 Design variable formulation of constrained optimization problem 34

2.1.3 Strength analysis and design optimization formulation 39

2.2 Formulation of end-use and manufacturing constraints *41*

2.2.1 End-use constraints 41

2.2.2 Manufacturing constraints 47

2.3 Solution technique and algorithms *51*

2.3.1 Algorithms for unconstrained optimization 51

2.3.2 Algorithm for constrained optimization 57

2.4 Optimization results of unconstrained optimization *64*

2.4.1 Description of the example 64

2.4.2 Optimization results of the lipped channel with long length 65

2.4.3 Optimization results of the lipped channel column with intermediate length 73

2.4.4 Summary and discussion of unconstrained optimization results 77

2.5 Optimization results of constrained optimization *79*

2.5.1 Optimization results with end-use constraints only 80

2.5.2 Optimization results with end-use and manufacturing constraints 86

2.5.3 Summary and comparison of optimization results 97

2.6 Conclusions on shape optimization of cold-formed steel columns *99*

Chapter 3 : Modeling Techniques of Cold-form Steel Framed Building with OSB and Gypsum Sheathing **103**

3.1 Description of the CFS-NEES building design and construction *104*

3.1.1 Nomenclature 104

3.1.2 CFS-NEES building design 105

3.1.3 Type I versus Type II shear wall design 112

3.1.4 CFS-NEES building construction phases 114

3.2 General note on naming convention and scope of finite element models *116*

3.3 Modeling of shear walls *120*

3.3.1 State-of-the-practice (P-) models of shear walls 120

3.3.2 State-of-the-art (A-) models of shear walls 128

3.4 Modeling of gravity system *143*

3.4.1 Modeling of gravity system at Phase 1 143

3.4.2 Modeling of gravity system at Phase 2b and above 149

3.5 Modeling of diaphragms *151*

3.6 Modeling of interior walls *155*

3.7 Distribution of seismic mass in FE models *158*

3.8 Distribution of gravity load in FE models *159*

3.9 Modeling of the chord stud connection across floors *160*

Chapter 4 : Calibration of Building Models and Comparison with Full Scale Shaking Table Tests **162**

4.1 Brief description of full scale shaking table tests of the CFS-NEES building *162*

4.2 Excitations in shaking table tests and in finite element model calibration *169*

4.2.1 Description of ground motion records in shaking table test 169

4.2.2 Description of excitation signals in time history analyses of model calibration 174

4.3 Comparison of seismic response between simulation and test in model calibration *175*

4.3.1 Description of data post-processing and output physical quantities 175

4.3.2 Phase 1 – bare structural 180

4.3.3 Phase 2a – bare structural replicate 192

4.3.4 Phase 2b – exterior sheathed structural 199

4.3.5 Phase 2c – fully sheathed structural 208

4.3.6 Phase 2d – fully sheathed structural with interior nonstructural 217

4.3.7 Phase 2e – fully sheathed structural with interior nonstructural and DensGlass 226

4.3.8 Brief summary on model calibration with shaking table tests 239

Chapter 5 : Analysis and Performance Comparison of Various Building Models 245

5.1 Review of modeling options and models in performance comparison 246

5.2 Description of analysis types in performance comparison 248

5.3 Comparison of seismic response across models at different phases 252

5.3.1 Comparison of free vibration analysis results 252

5.3.2 Comparison of static analysis results 259

5.3.3 Comparison of time history analysis results 265

5.4 Discussion and guidelines for modeling a CFS building under seismic loading 272

5.4.1 Discussion on Type I shear wall design assumption 273

5.4.2 Discussion on the role of gravity walls in lateral force resistance 278

5.4.3 Discussion on other modeling options and proposed modeling guidelines 291

Chapter 6 : Incremental Dynamic Analysis and Performance Evaluation of the Building Using FEMA P695 Procedure 300

6.1 Incremental dynamic analysis and FEMA P695 suite of far-field earthquake records 301

6.2 Overview of the archetype design and performance evaluation approach 303

6.3 Structural system information 304

6.3.1 Design requirements 304

6.3.2 Test data 304

6.4 Identification of CFS-framed archetype configuration 305

6.5 Nonlinear model development 308

6.6 Nonlinear structural analyses 311

6.7 Performance evaluation *315*

6.8 Evaluation of Ω_O using the archetype design *319*

6.9 Summary observations and discussion *320*

Chapter 7 : Conclusions and Future Work **323**

References **330**

Appdendices **351**

Appendix A : Analysis Results of State-of-the-practice, 2D, model a (P-2D-a) *351*

Appendix B : Analysis Results of State-of-the-practice, 2D, model b (P-2D-b) *373*

Appendix C : Analysis Results of State-of-the-practice, 3D, rigid-diaphragm, model a (P-3D-RD-a) *395*

Appendix D : Analysis Results of State-of-the-practice, 3D, rigid-diaphragm, model b (P-3D-RD-b) *418*

Appendix E : Analysis Results of State-of-the-art, Phase 1, 2D, model a (A1-2D-a) *441*

Appendix F : Analysis Results of State-of-the-art, Phase 1, 2D, model b (A1-2D-b) *465*

Appendix G : Analysis Results of State-of-the-art, Phase 1, 2D, model c (A1-2D-c) *487*

Appendix H : Analysis Results of State-of-the-art, Phase 1, 3D, rigid-diaphragm, model a (A1-3D-RD-a) *509*

Appendix I : Analysis Results of State-of-the-art, Phase 1, 3D, rigid-diaphragm, model b (A1-3D-RD-b) *532*

Appendix J : Analysis Results of State-of-the-art, Phase 1, 3D, rigid-diaphragm, model c (A1-3D-RD-c) *555*

Appendix K : Analysis Results of State-of-the-art, Phase 1, 3D, semirigid-diaphragm, model a (A1-3D-SD-a) *578*

Appendix L : Analysis Results of State-of-the-art, Phase 1, 3D, semirigid-diaphragm, model b (A1-3D-SD-b) *601*

Appendix M : Analysis Results of State-of-the-art, Phase 2b, 2D, model a (A2b-2D-a) *624*

Appendix N : Analysis Results of State-of-the-art, Phase 2b, 3D, rigid-diaphragm, model a (A2b-3D-RD-a) *646*

Appendix O : Analysis Results of State-of-the-art, Phase 2b, 3D, semirigid-diaphragm, model a (A2b-3D-SD-a) *669*

Appendix P : Analysis Results of State-of-the-art, Phase 2c, 2D, model a (A2c-2D-a) *692*

Appendix Q : Analysis Results of State-of-the-art, Phase 2c, 3D, rigid-diaphragm, model a (A2c-3D-RD-a) *714*

Appendix R : Analysis Results of State-of-the-art, Phase 2c, 3D, semirigid-diaphragm, model a (A2c-3D-SD-a) *737*

Appendix S : Analysis Results of State-of-the-art, Phase 2d, 3D, rigid-diaphragm, model a (A2d-3D-RD-a) *760*

Appendix T : Details on Incremental Dynamic Analysis and Performance Evaluation of A1-3D-SD-a model *784*

Appendix U : Details on Incremental Dynamic Analysis and Performance Evaluation of A2b-3D-SD-a model *801*

Appendix V : Details on Incremental Dynamic Analysis and Performance Evaluation of P-3D-RD-b model *814*

Curriculum Vita **827**

List of Figures

Figure 1-1: At left, photograph of stick-style construction for a cold-formed steel-framed hotel in Buckhead, Georgia (photo credit: Don Allen, DSi Engineering). At right, drawing of common CFS cross-sections, highlighting the two most used: zee and lipped channel _____ 3

Figure 1-2: A typical CFS member and finite element/strip models of the member ___ 12

Figure 1-3: Illustration of broad definition of reliability-based performance levels ___ 19

Figure 1-4: Illustration of the CFS-NEES building, Phase 1 and its FEM model _____ 24

Figure 2-1: Lipped channel section and design variables for unconstrained optimization34

Figure 2-2: Design variables for constrained shape optimization _____ 36

Figure 2-3: Effect of symmetry/anti-symmetry constraint on design variables _____ 42

Figure 2-4: Illustrations of end-use constraints in shape optimization_____ 46

Figure 2-5: Effect of symmetry/anti-symmetry, end-use, and manufacturing constraints on design variables _____ 50

Figure 2-6: Flow chart of simulated annealing algorithm for unconstrained shape optimization _____ 60

Figure 2-7: Flow chart of genetic algorithms for unconstrained shape optimization___ 61

Figure 2-8: Flow chart of implementation of constraints in simulated annealing for unlimited number of rollers _____ 62

Figure 2-9: Flow chart of implementation of constraints in simulated annealing for limited number of rollers _____ 63

Figure 2-10: The process from initial to optimized cross-section using steep descent method for 4.88 m (16 ft) lipped channel column _____ 66

Figure 2-11: Optimized cross-sections found by SD for 4.88 m (16 ft) columns with hat and sigma initial sections 66

Figure 2-12: Optimized cross-sections found by GA for 4.88 m (16 ft) lipped channel columns 70

Figure 2-13: Convergence curves of P_{nelite} of GA optimized designs for 4.88 m (16 ft) lipped channel column 70

Figure 2-14: Optimized cross-sections found by SA for 4.88 m (16 ft) lipped channel columns 71

Figure 2-15: Convergence curves of P_{nelite} of SA optimized designs for 4.88 m (16 ft) lipped channel column 71

Figure 2-16: Intuitive optimized cross-sections 72

Figure 2-17: Optimized sections found by SD for 4.88 m (16 ft) squashed 'S' columns 72

Figure 2-18: Optimized cross-sections found by GA for 1.22 m (4 ft) lipped channel column 76

Figure 2-19: Optimized cross-sections found by SA for 1.22 m (4 ft) lipped channel column 76

Figure 2-20: Optimized cross-sections found by SA for 0.61 m (2 ft) column with end-use constraints 81

Figure 2-21: Convergence curve of normalized P_{nelite} in search of cross-section in Figure 2-20(a) 82

Figure 2-22: Optimized cross-sections found by SA for 1.22 m (4 ft) column with end-use constraints 83

Figure 2-23: Optimized cross-sections found by SA for 4.88 m (16 ft) column with end-use constraints 84
Figure 2-24: Optimized cross-sections found by SA for 0.61 m (2 ft) column, 4 rollers 87
Figure 2-25: Optimized cross-sections found by SA for 0.61 m (2 ft) column, 6 rollers 88
Figure 2-26: Optimized cross-sections found by SA for 0.61 m (2 ft) column, 8 rollers 88
Figure 2-27: Optimized cross-sections found by SA for 0.61 m (2 ft) column, 10 rollers 88
Figure 2-28: Optimized cross-sections found by SA for 0.61 m (2 ft) column, 12 rollers 89
Figure 2-29: Convergence curve of normalized P_{nelite} in search of cross-section in Figure 2-28(a) 89
Figure 2-30: Optimized cross-sections found by SA for 1.22 m (4 ft) column, 4 rollers 91
Figure 2-31: Optimized cross-sections found by SA for 1.22 m (4 ft) column, 6 rollers 91
Figure 2-32: Optimized cross-sections found by SA for 1.22 m (4 ft) column, 8 rollers 91
Figure 2-33: Optimized cross-sections found by SA for 1.22 m (4 ft) column, 10 rollers 91
Figure 2-34: Optimized cross-sections found by SA for 1.22 m (4 ft) column, 12 rollers 92
Figure 2-35: Optimized cross-sections found by SA for 4.88 m (16 ft) column, 4 rollers 93
Figure 2-36: Optimized cross-sections found by SA for 4.88 m (16 ft) column, 6 rollers 94
Figure 2-37: Optimized cross-sections found by SA for 4.88 m (16 ft) column, 8 rollers 94
Figure 2-38: Optimized cross-sections found by SA for 4.88 m (16 ft) column, 10 rollers 94
Figure 2-39: Optimized cross-sections found by SA for 4.88 m (16 ft) column, 12 rollers 94
Figure 2-40: Nominal strength ratios between elite optimized cross-sections and lipped channel 98

Figure 3-1: Nomenclature and orientation for building specimen, as built in Phase 1_ 104
Figure 3-2: Three-Dimensional BIM model of the CFS-NEES building, Phase 1 (sheathing applied only for shear walls) 107
Figure 3-3: Exploded view of the Phase 1 building specimen, framed only with structural components (drawing by Phil Clark at Devco) 108
Figure 3-4: Gravity wall elevation drawings for Phase 1 building specimen 109
Figure 3-5: Typical shear wall framing for the Phase 1 building (chord stud fasteners are drawn staggered at 12 in. (30.48 cm) on-center but were construction in line, on the outer stud, at 6 in. (15.24 cm) on-center). 111
Figure 3-6: Drawing illustrating the two types of shear wall on the South elevation. The top drawing demonstrates the ideal anchor force distribution for Type I shear walls, or isolated shear walls. The bottom drawing provides an idealization for the hypothetical Type II, or fully-coupled shear walls 114
Figure 3-7: Phase descriptions of Phase 2 construction (Phase 2a is nominally identical to Phase 1) 115
Figure 3-8: Comparison of modeling strategies: from state-of-the-practice to state-of-the-art models 120
Figure 3-9: A typical state-of-the-practice shear wall model 123
Figure 3-10: Nonlinear models for shear wall (a) EPP (b) Pinching4 124
Figure 3-11: Pinching4 and EPP model compared with Test 12 of Liu et al. (2012), cycle numbers are numbers of displacement-based cyclic loading following the CUREE protocol 127
Figure 3-12: A typical state-of-the-art whole panel shear wall model 133

Figure 3-13: Hold down and its Pinching4 nonlinear material model of the axial response _____ 133

Figure 3-14: Implementation of Pinching4 nonlinear material model of the axial response of the hold down _____ 134

Figure 3-15: Elastic material model of the hold down's axial response _____ 134

Figure 3-16: Comparison of whole panel model, subpanel model and design drawing of South elevation _____ 140

Figure 3-17: Illustration of the deformation in a whole panel and subpanels modeled with diagonals _____ 140

Figure 3-18: A 4 ft (1.22 m) x 9 ft (2.74 m) shear wall modeled with four subpanels _ 142

Figure 3-19: Sum of subpanel shear force vs. top track deflection curve of the 4 ft (1.22 m) x 9 ft (2.74 m) shear wall _____ 142

Figure 3-20: Shear force vs. top track deflection curve of each subpanel in the 4 ft (1.22 m) x 9 ft (2.74 m) shear wall _____ 143

Figure 3-21: Elastic-perfectly-plastic uniaxial response of CFS studs under weak axis moment _____ 147

Figure 3-22: Elastic multi-linear uniaxial response of CFS gravity stud ends _____ 148

Figure 3-23: Comparison between backbone curves of a sheathed 8 ft (2.44 m) x 9 ft (2.74 m) gravity wall using fastened-based model and characterized Pinching4 truss model _____ 150

Figure 3-24: Phase 1 and Phase 2b/c model of South elevation _____ 151

Figure 3-25: Semi-rigid diaphragm FE models in OpenSees _____ 155

Figure 3-26: Interior wall FE models in OpenSees _____ 157

Figure 3-27: Architectural drawings of the test specimen, demonstrating partition wall layout 157

Figure 3-28: Shear wall tie detail from building specimen construction drawings 160

Figure 4-1: CFS-NEES Full-scale building testing at Phase 1 and Phase 2e 163

Figure 4-2: Illustration of construction milestones within Phase 2 testing, shown via cross Section views of building specimens (dashed line indicates location of cross Section) 164

Figure 4-3: Shift in long and short direction first mode period through construction phases (a – LFRS and gravity steel only, b – ext. sheathed, c – inside face of ext. sheathed w/gypsum, d – interior non-structural walls & stairs, e – exterior DensGlass sheathed) 166

Figure 4-4: Drift percent for Phase 1 building under the 100% Canoga Park ground motion 167

Figure 4-5: Shear wall anchor forces superimposed on the deformed and undeformed shapes of the building specimens at peak first story drift in the long direction 168

Figure 4-6: Canoga Park ground motions 170

Figure 4-7: Rinaldi ground motions 171

Figure 4-8: ASCE 7-10 site-specific design spectra, assuming 5% damping. T_n and T_a refer to the same quantity: the approximate natural period of vibration, per ASCE 7 172

Figure 4-9: Unscaled Canoga Park spectrum with DBE design spectrum. T_a is per ASCE 7. (from private communication with Steve Buonopane) 173

Figure 4-10: Unscaled Rinaldi spectrum with MCE design spectrum. T_a is per ASCE 7. (from private communication with Steve Buonopane) 173

Figure 4-11: Floor plan of the base level of the CFS-NEES with locations of load cells (hold downs) 178

Figure 4-12: Examples of 3D shear wall only models _____ 181

Figure 4-13: Design drawing and high-fidelity FE model of Phase 1 building _____ 182

Figure 4-14: Comparison of story drift of the building, P1S07 excitation, Phase 1___ 189

Figure 4-15: Comparison of periodogram of the building's story drift, P1S07 excitation, Phase 1 _____ 190

Figure 4-16: Comparison of load cell 5 to 8 axial forces, P1S07 excitation, Phase 1 _ 191

Figure 4-17: Comparison of simplified deformed shape and distribution of load cell forces between A1-3D-SD-a model and test, P1S07 excitation, Phase 1_____ 192

Figure 4-18: Design drawing and high-fidelity FE model of Phase 2a building _____ 193

Figure 4-19: Comparison of story drift of the building, P2aS04 excitation, Phase 2a _ 196

Figure 4-20: Comparison of periodogram of the building's story drift, P2aS04 excitation, Phase 2a _____ 197

Figure 4-21: Comparison of load cell 5 to 8 axial forces, P2aS04 excitation, Phase 2a 198

Figure 4-22: Comparison of simplified deformed shape and distribution of load cell forces between A1-3D-SD-a model and test, P2aS04 excitation, Phase 2a _____ 199

Figure 4-23: Design drawing and high-fidelity FE model of Phase 2b building _____ 200

Figure 4-24: Comparison of story drift of the building, P2bS05 excitation, Phase 2b_ 205

Figure 4-25: Comparison of periodogram of the building's story drift, P2bS05 excitation, Phase 2b _____ 206

Figure 4-26: Comparison of load cell 5 to 8 axial forces, P2bS05 excitation, Phase 2b 207

Figure 4-27: Comparison of simplified deformed shape and distribution of load cell forces between A2b-3D-SD-a model and test, P2bS05 excitation, Phase 2b_____ 208

Figure 4-28: Design drawing and high-fidelity FE model of Phase 2c building _____ 209

Figure 4-29: Comparison of story drift of the building, P2cS05 excitation, Phase 2c _ 214
Figure 4-30: Comparison of periodogram of the building's story drift, P2cS05 excitation, Phase 2c _____ 215
Figure 4-31: Comparison of load cell 5 to 8 axial forces, P2cS05 excitation, Phase 2c 216
Figure 4-32: Comparison of simplified deformed shape and distribution of load cell forces between A2c-3D-SD-a model and P2cS05 test, P2cS05 excitation, Phase 2c _ 217
Figure 4-33: Design drawing and high-fidelity FE model of Phase 2d building _____ 218
Figure 4-34: Comparison of story drift of the building, P2dS05 excitation, Phase 2d_ 223
Figure 4-35: Comparison of periodogram of the building's story drift, P2dS05 excitation, Phase 2d _____ 224
Figure 4-36: Comparison of load cell 5 to 8 axial forces, P2dS05 excitation, Phase 2d 225
Figure 4-37: Comparison of simplified deformed shape and distribution of load cell forces between A2d-3D-RD-a model and test, P2dS05 excitation, Phase 2d _____ 226
Figure 4-38: Design drawing and high-fidelity FE model of Phase 2e building _____ 227
Figure 4-39: Comparison of story drift of the building, P2eS07 excitation, Phase 2e _ 233
Figure 4-40: Comparison of story drift of the building, P2eS09 excitation, Phase 2e _ 234
Figure 4-41: Comparison of periodogram of the building's story drift, P2eS07 excitation, Phase 2e _____ 235
Figure 4-42: Comparison of periodogram of the building's story drift, P2eS09 excitation, Phase 2e _____ 236
Figure 4-43: Comparison of load cell 5 to 8 axial forces, P2eS07 excitation, Phase 2e 237
Figure 4-44: Comparison of load cell 5 to 8 axial forces, P2eS09 excitation, Phase 2e 238

Figure 4-45: Comparison of simplified deformed shape and distribution of load cell forces between A2d-3D-RD-a model and test, P2eS09 excitation, Phase 2e 239
Figure 4-46: Comparison of the first mode period in long and short direction between buildings and state-of-the-art models 241
Figure 5-1: OpenSees models of the CFS-NEES Phase 1 archetype building with their first natural periods of translational modes (the subscript indicates the order of that mode among all modes) 257
Figure 5-2: OpenSees models for building analysis at Phase 2b to Phase 2d 258
Figure 5-3: Comparison of the first mode period in long and short direction between buildings and models 259
Figure 5-4: Comparison of pushover curves in long and short direction among models at various phases 264
Figure 5-5: A1-3D-SD-a model, hysteretic plot of example shear walls at each elevation, 100% Canoga Park, 3D nonlinear analysis 270
Figure 5-6: A1-3D-SD-a model, foundation forces, 100% Canoga Park, 3D nonlinear analysis (maximum anchor/hold down base shear is 2.35 kips and max hold down tensile force is -4.63 kips) 270
Figure 5-7: Locations of load cell 5 to 8 on 2D state-of-the-art models of the CFS-NEES building 275
Figure 5-8: Comparison of nonlinear time history plots of load cell 5 to 8 axial forces among 2D models at various phases excited by 100% Canoga Park 275
Figure 5-9: Comparison of nonlinear time history plots of load cell 5 to 8 axial forces among 2D and 3D models at Phase 1 excited by 100 % Canoga Park 276

Figure 5-10: Load cell force distributions in 3D A-models at the moment of peak total base shear, excited by 100 % Canoga Park 277

Figure 5-11: Elastic stiffness breakdown between shear walls and gravity walls, 2D models (blue – shear walls, red – gravity walls) 279

Figure 5-12: Elastic stiffness breakdown between shear walls and gravity walls plus other systems, 3D models (blue – shear walls, red – gravity walls) 280

Figure 5-13: Correlation plot of area ratio vs. stiffness ratio between gravity walls and shear walls for models of Table 5-10 284

Figure 5-14: Proportion of peak base shear taken by shear walls and gravity walls, pushover analysis, 2D models (blue – shear walls, red – gravity walls) 285

Figure 5-15: Proportion of peak base shear taken by shear walls and gravity walls, pushover analysis, 3D models (blue – shear walls, red – gravity walls) 286

Figure 5-16: Correlation plot of area ratio vs. peak base shear ratio between gravity walls and shear walls for models in Table 5-13 291

Figure 6-1: Representative phase descriptions of the CFS-NEES building 306

Figure 6-2: A typical response curve of Pinching4 material 310

Figure 6-3: Monotonic static pushover curve and computation of Ω for the CFS-NEES building using A1-3D-SD-a model 312

Figure 6-4: Results of IDA to collapse for the CFS-NEES building using A1-3D-SD-a model 313

Figure 6-5: Collapse fragility curve for the CFS-NEES building using A1-3D-SD-a model 314

Figure 6-6: Monotonic static pushover curve and the illustration of δ_u and $\delta_{y,eff}$ for the CFS-NEES building using A1-3D-SD-a model 316

Figure A-1: P-2D-a model 351

Figure A-2: First two natural modes of P-2D-a model 352

Figure A-3: Pushover curve of P-2D-a model 356

Figure A-4: Pushover curve of each wall line, P-2D-a model 356

Figure A-5: P-2D-a model, base shear vector plot at the moment of peak total base shear, 100 % Canoga Park, 2D linear analysis (maximum anchor/hold down base shear is 13.48 kips) 360

Figure A-6: P-2D-a model building story drift, 100 % Canoga Park, 2D nonlinear analysis 367

Figure A-7: P-2D-a model wall line floor story drift, 100 % Canoga Park, 2D nonlinear analysis 368

Figure A-8: P-2D-a model wall line roof story drift, 100 % Canoga Park, 2D nonlinear analysis 369

Figure A-9: P-2D-a model total building base shear, 100 % Canoga Park, 2D nonlinear analysis 370

Figure A-10: P-2D-a model, load cell 5 to 8 axial forces, 100 % Canoga Park, 2D nonlinear analysis 370

Figure A-11: P-2D-a model, hysteretic plot of the building, 100 % Canoga Park, 2D nonlinear analysis 371

Figure A-12: P-2D-a model, hysteretic plot of shear walls at each elevation, 100 % Canoga Park, 2D nonlinear analysis 371

Figure A-13: P-2D-a model, field plot of peak total base shear, 100 % Canoga Park, 2D nonlinear analysis (maximum anchor/hold down base shear is 5.27 kips)_____ 372

Figure A-14: P-2D-a model, simplified illustration of corner displacements with hold down forces from load cells,100 % Canoga Park, 2D nonlinear analysis (max hold down tensile force is -11.75 kips)_____ 372

Figure B-1: P-2D-b model _____ 373

Figure B-2: First two natural modes of P-2D-b model_____ 374

Figure B-3: Pushover curve of P-2D-b model _____ 378

Figure B-4: Pushover curve of each wall line, P-2D-b model _____ 378

Figure B-5: P-2D-b model, base shear vector plot at the moment of peak total base shear, 100 % Canoga Park, 2D linear analysis (maximum anchor/hold down base shear is 13.05 kips)_____ 382

Figure B-6: P-2D-b model building story drift, 100 % Canoga Park, 2D nonlinear analysis _____ 389

Figure B-7: P-2D-b model wall line floor story drift, 100 % Canoga Park, 2D nonlinear analysis _____ 390

Figure B-8: P-2D-b model wall line roof story drift, 100 % Canoga Park, 2D nonlinear analysis _____ 391

Figure B-9: P-2D-b model total building base shear, 100 % Canoga Park, 2D nonlinear analysis (peak V_{bu} is 126.9 kips)_____ 392

Figure B-10: P-2D-b model, load cell 5 to 8 axial forces, 100 % Canoga Park, 2D nonlinear analysis _____ 392

Figure B-11: P-2D-b model, hysteretic plot of the building, 100 % Canoga Park, 2D nonlinear analysis _____ 393

Figure B-12: P-2D-b model, hysteretic plot of shear walls at each elevation, 100 % Canoga Park, 2D nonlinear analysis _____ 393

Figure B-13: P-2D-b model, field plot of peak total base shear, 100 % Canoga Park, 2D nonlinear analysis (maximum anchor/hold down base shear is 2.81 kips)_____ 394

Figure B-14: P-2D-b model, simplified illustration of corner displacements with hold down forces from load cells,100 % Canoga Park, 2D nonlinear analysis (max hold down tensile force is -8.66 kips)_____ 394

Figure C-1: P-3D-RD-a model _____ 395

Figure C-2: First two natural modes of P-3D-RD-a model _____ 396

Figure C-3: Pushover curve of P-3D-RD-a model _____ 400

Figure C-4: Pushover curve of each wall line, P-3D-RD-a model _____ 400

Figure C-5: P-3D-RD-a model, base shear vector plot at the moment of peak total base shear, 100 % Canoga Park, 3D linear analysis (maximum anchor/hold down base shear is 20.99 kips)_____ 404

Figure C-6: P-3D-RD-a model building story drift, 100 % Canoga Park, 3D nonlinear analysis _____ 412

Figure C-7: P-3D-RD-a model wall line floor story drift, 100 % Canoga Park, 3D nonlinear analysis _____ 413

Figure C-8: P-3D-RD-a model wall line roof story drift, 100 % Canoga Park, 3D nonlinear analysis _____ 414

Figure C-9: P-3D-RD-a model total building base shear, 100 % Canoga Park, 3D nonlinear analysis _____ 415

Figure C-10: P-3D-RD-a model, load cell 5 to 8 axial forces, 100 % Canoga Park, 3D nonlinear analysis _____ 415

Figure C-11: P-3D-RD-a model, hysteretic plot of the building, 100 % Canoga Park, 3D nonlinear analysis _____ 416

Figure C-12: P-3D-RD-a model, hysteretic plot of shear walls at each elevation, 100 % Canoga Park, 3D nonlinear analysis _____ 416

Figure C-13: P-3D-RD-a model, field plot of peak total base shear, 100 % Canoga Park, 3D nonlinear analysis (maximum anchor/hold down base shear is 5.22 kips)_____ 417

Figure C-14: P-3D-RD-a model, simplified illustration of corner displacements with hold down forces from load cells,100 % Canoga Park, 3D nonlinear analysis (max hold down tensile force is -14.32 kips)_____ 417

Figure D-1: P-3D-RD-b model _____ 418

Figure D-2: First two natural modes of P-3D-RD-b model _____ 419

Figure D-3: Pushover curve of P-3D-RD-b model_____ 423

Figure D-4: Pushover curve of each wall line, P-3D-RD-b model_____ 423

Figure D-5: P-3D-RD-b model, base shear vector plot at the moment of peak total base shear, 100 % Canoga Park, 3D linear analysis (maximum anchor/hold down base shear is 15.56 kips)_____ 427

Figure D-6: P-3D-RD-b model building story drift, 100 % Canoga Park, 3D nonlinear analysis _____ 435

Figure D-7: P-3D-RD-b model wall line floor story drift, 100 % Canoga Park, 3D nonlinear analysis _____ 436

Figure D-8: P-3D-RD-b model wall line roof story drift, 100 % Canoga Park, 3D nonlinear analysis _____ 437

Figure D-9: P-3D-RD-b model total building base shear, 100 % Canoga Park, 3D nonlinear analysis _____ 438

Figure D-10: P-3D-RD-b model, load cell 5 to 8 axial forces, 100 % Canoga Park, 3D nonlinear analysis _____ 438

Figure D-11: P-3D-RD-b model, hysteretic plot of the building, 100 % Canoga Park, 3D nonlinear analysis _____ 439

Figure D-12: P-3D-RD-b model, hysteretic plot of shear walls at each elevation, 100 % Canoga Park, 3D nonlinear analysis _____ 439

Figure D-13: P-3D-RD-b model, field plot of peak total base shear, 100 % Canoga Park, 3D nonlinear analysis (maximum anchor/hold down base shear is 4.74 kips)_____ 440

Figure D-14: P-3D-RD-b model, simplified illustration of corner displacements with hold down forces from load cells,100 % Canoga Park, 3D nonlinear analysis (max hold down tensile force is -10.70 kips)_____ 440

Figure E-1: A1-2D-a model _____ 441

Figure E-2: First two natural modes of A1-2D-a model_____ 442

Figure E-3: Pushover curve of A1-2D-a model _____ 447

Figure E-4: Pushover curve of each wall line, A1-2D-a model _____ 447

Figure E-5: A1-2D-a model, base shear vector plot at the moment of peak total base shear, 100 % Canoga Park, 2D linear analysis (maximum anchor/hold down base shear is 4.27 kips)_____ 452

Figure E-6: A1-2D-a model building story drift, 100 % Canoga Park, 2D nonlinear analysis _____ 459

Figure E-7: A1-2D-a model wall line floor story drift, 100 % Canoga Park, 2D nonlinear analysis _____ 460

Figure E-8: A1-2D-a model wall line roof story drift, 100 % Canoga Park, 2D nonlinear analysis _____ 461

Figure E-9: A1-2D-a model total building base shear, 100 % Canoga Park, 2D nonlinear analysis _____ 462

Figure E-10: A1-2D-a model, load cell 5 to 8 axial forces, 100 % Canoga Park, 2D nonlinear analysis _____ 462

Figure E-11: A1-2D-a model, hysteretic plot of the building, 100 % Canoga Park, 2D nonlinear analysis _____ 463

Figure E-12: A1-2D-a model, hysteretic plot of shear walls at each elevation, 100 % Canoga Park, 2D nonlinear analysis _____ 463

Figure E-13: A1-2D-a model, field plot of peak total base shear, 100 % Canoga Park, 2D nonlinear analysis (maximum anchor/hold down base shear is 2.12 kips)_____ 464

Figure E-14: A1-2D-a model, simplified illustration of corner displacements with hold down forces from load cells,100 % Canoga Park, 2D nonlinear analysis (max hold down tensile force is -5.10 kips)_____ 464

Figure F-1: A1-2D-b model _____ 465

Figure F-2: First two natural modes of A1-2D-b model 466

Figure F-3: Pushover curve of A1-2D-b model 470

Figure F-4: Pushover curve of each wall line, A1-2D-b model 470

Figure F-5: A1-2D-b model, base shear vector plot at the moment of peak total base shear, 100 % Canoga Park, 2D linear analysis (maximum anchor/hold down base shear is 3.79 kips) 474

Figure F-6: A1-2D-b model building story drift, 100 % Canoga Park, 2D nonlinear analysis 481

Figure F-7: A1-2D-b model wall line floor story drift, 100 % Canoga Park, 2D nonlinear analysis 482

Figure F-8: A1-2D-b model wall line roof story drift, 100 % Canoga Park, 2D nonlinear analysis 483

Figure F-9: A1-2D-b model total building base shear, 100 % Canoga Park, 2D nonlinear analysis 484

Figure F-10: A1-2D-b model, load cell 5 to 8 axial forces, 100 % Canoga Park, 2D nonlinear analysis 484

Figure F-11: A1-2D-b model, hysteretic plot of the building, 100 % Canoga Park, 2D nonlinear analysis 485

Figure F-12: A1-2D-b model, hysteretic plot of shear walls at each elevation, 100 % Canoga Park, 2D nonlinear analysis 485

Figure F-13: A1-2D-b model, field plot of peak total base shear, 100 % Canoga Park, 2D nonlinear analysis (maximum anchor/hold down base shear is 3.79 kips) 486

Figure F-14: A1-2D-b model, simplified illustration of corner displacements with hold down forces from load cells,100 % Canoga Park, 2D nonlinear analysis (max hold down tensile force is -5.25 kips) 486

Figure G-1: A1-2D-c model 487

Figure G-2: First two natural modes of A1-2D-c model 488

Figure G-3: Pushover curve of A1-2D-c model 492

Figure G-4: Pushover curve of each wall line, A1-2D-c model 492

Figure G-5: A1-2D-c model, base shear vector plot at the moment of peak total base shear, 100 % Canoga Park, 2D linear analysis (maximum anchor/hold down base shear is 12.03 kips) 496

Figure G-6: A1-2D-c model building story drift, 100 % Canoga Park, 2D nonlinear analysis 503

Figure G-7: A1-2D-c model wall line floor story drift, 100 % Canoga Park, 2D nonlinear analysis 504

Figure G-8: A1-2D-c model wall line roof story drift, 100 % Canoga Park, 2D nonlinear analysis 505

Figure G-9: A1-2D-c model total building base shear, 100 % Canoga Park, 2D nonlinear analysis 506

Figure G-10: A1-2D-c model, load cell 5 to 8 axial forces, 100 % Canoga Park, 2D nonlinear analysis 506

Figure G-11: A1-2D-c model, hysteretic plot of the building, 100 % Canoga Park, 2D nonlinear analysis 507

Figure G-12: A1-2D-c model, hysteretic plot of shear walls at each elevation, 100 % Canoga Park, 2D nonlinear analysis 507

Figure G-13: A1-2D-c model, field plot of peak total base shear, 100 % Canoga Park, 2D nonlinear analysis (maximum anchor/hold down base shear is 6.96 kips) 508

Figure G-14: A1-2D-c model, simplified illustration of corner displacements with hold down forces from load cells,100 % Canoga Park, 2D nonlinear analysis (max hold down tensile force is -11.36 kips) 508

Figure H-1: A1-3D-RD-a model 509

Figure H-2: First two natural modes of A1-3D-RD-a model 510

Figure H-3: Pushover curve of A1-3D-RD-a model 514

Figure H-4: Pushover curve of each wall line, A1-3D-RD-a model 514

Figure H-5: A1-3D-RD-a model, base shear vector plot at the moment of peak total base shear, 100 % Canoga Park, 3D linear analysis (maximum anchor/hold down base shear is 4.40 kips) 518

Figure H-6: A1-3D-RD-a model building story drift, 100 % Canoga Park, 3D nonlinear analysis 526

Figure H-7: A1-3D-RD-a model wall line floor story drift, 100 % Canoga Park, 3D nonlinear analysis 527

Figure H-8: A1-3D-RD-a model wall line roof story drift, 100 % Canoga Park, 3D nonlinear analysis 528

Figure H-9: A1-3D-RD-a model total building base shear, 100 % Canoga Park, 3D nonlinear analysis 529

Figure H-10: A1-3D-RD-a model, load cell 5 to 8 axial forces, 100 % Canoga Park, 3D nonlinear analysis _____ 529

Figure H-11: A1-3D-RD-a model, hysteretic plot of the building, 100 % Canoga Park, 3D nonlinear analysis _____ 530

Figure H-12: A1-3D-RD-a model, hysteretic plot of shear walls at each elevation, 100 % Canoga Park, 3D nonlinear analysis _____ 530

Figure H-13: A1-3D-RD-a model, field plot of peak total base shear, 100 % Canoga Park, 3D nonlinear analysis (maximum anchor/hold down base shear is 2.22 kips)_____ 531

Figure H-14: A1-3D-RD-a model, simplified illustration of corner displacements with hold down forces from load cells,100 % Canoga Park, 3D nonlinear analysis (max hold down tensile force is -4.78 kips)_____ 531

Figure I-1: A1-3D-RD-b model _____ 532

Figure I-2: First two natural modes of A1-3D-RD-b model_____ 533

Figure I-3: Pushover curve of A1-3D-RD-b model _____ 537

Figure I-4: Pushover curve of each wall line, A1-3D-RD-b model _____ 537

Figure I-5: A1-3D-RD-b model, base shear vector plot at the moment of peak total base shear, 100 % Canoga Park, 3D linear analysis (maximum anchor/hold down base shear is 5.88 kips)_____ 541

Figure I-6: A1-3D-RD-b model building story drift, 100 % Canoga Park, 3D nonlinear analysis _____ 549

Figure I-7: A1-3D-RD-b model wall line floor story drift, 100 % Canoga Park, 3D nonlinear analysis _____ 550

Figure I-8: A1-3D-RD-b model wall line roof story drift, 100 % Canoga Park, 3D nonlinear analysis _____ 551

Figure I-9: A1-3D-RD-b model total building base shear, 100 % Canoga Park, 3D nonlinear analysis _____ 552

Figure I-10: A1-3D-RD-b model, load cell 5 to 8 axial forces, 100 % Canoga Park, 3D nonlinear analysis _____ 552

Figure I-11: A1-3D-RD-b model, hysteretic plot of the building, 100 % Canoga Park, 3D nonlinear analysis _____ 553

Figure I-12: A1-3D-RD-b model, hysteretic plot of shear walls at each elevation, 100 % Canoga Park, 3D nonlinear analysis _____ 553

Figure I-13: A1-3D-RD-b model, field plot of peak total base shear, 100 % Canoga Park, 3D nonlinear analysis (maximum anchor/hold down base shear is 2.52 kips)_____ 554

Figure I-14: A1-3D-RD-b model, simplified illustration of corner displacements with hold down forces from load cells,100 % Canoga Park, 3D nonlinear analysis (max hold down tensile force is -4.46 kips)_____ 554

Figure J-1: A1-3D-RD-c model _____ 555

Figure J-2: First two natural modes of A1-3D-RD-c model_____ 556

Figure J-3: Pushover curve of A1-3D-RD-c model _____ 560

Figure J-4: Pushover curve of each wall line, A1-3D-RD-c model _____ 560

Figure J-5: A1-3D-RD-c model, base shear vector plot at the moment of peak total base shear, 100 % Canoga Park, 3D linear analysis (maximum anchor/hold down base shear is 14.27 kips)_____ 564

Figure J-6: A1-3D-RD-c model building story drift, 100 % Canoga Park, 3D nonlinear analysis _____ 572

Figure J-7: A1-3D-RD-c model wall line floor story drift, 100 % Canoga Park, 3D nonlinear analysis _____ 573

Figure J-8: A1-3D-RD-c model wall line roof story drift, 100 % Canoga Park, 3D nonlinear analysis _____ 574

Figure J-9: A1-3D-RD-c model total building base shear, 100 % Canoga Park, 3D nonlinear analysis _____ 575

Figure J-10: A1-3D-RD-c model, load cell 5 to 8 axial forces, 100 % Canoga Park, 3D nonlinear analysis _____ 575

Figure J-11: A1-3D-RD-c model, hysteretic plot of the building, 100 % Canoga Park, 3D nonlinear analysis _____ 576

Figure J-12: A1-3D-RD-c model, hysteretic plot of shear walls at each elevation, 100 % Canoga Park, 3D nonlinear analysis _____ 576

Figure J-13: A1-3D-RD-c model, field plot of peak total base shear, 100 % Canoga Park, 3D nonlinear analysis (maximum anchor/hold down base shear is 9.32 kips)_____ 577

Figure J-14: A1-3D-RD-c model, simplified illustration of corner displacements with hold down forces from load cells,100 % Canoga Park, 3D nonlinear analysis (max hold down tensile force is -12.99 kips)_____ 577

Figure K-1: A1-3D-SD-a model _____ 578

Figure K-2: First two natural modes of A1-3D-SD-a model _____ 579

Figure K-3: Pushover curve of A1-3D-SD-a model _____ 583

Figure K-4: Pushover curve of each wall line, A1-3D-SD-a model _____ 583

Figure K-5: A1-3D-SD-a model, base shear vector plot at the moment of peak total base shear, 100 % Canoga Park, 3D linear analysis (maximum anchor/hold down base shear is 3.89 kips) 587

Figure K-6: A1-3D-SD-a model building story drift, 100 % Canoga Park, 3D nonlinear analysis 595

Figure K-7: A1-3D-SD-a model wall line floor story drift, 100 % Canoga Park, 3D nonlinear analysis 596

Figure K-8: A1-3D-SD-a model wall line roof story drift, 100 % Canoga Park, 3D nonlinear analysis 597

Figure K-9: A1-3D-SD-a model total building base shear, 100 % Canoga Park, 3D nonlinear analysis 598

Figure K-10: A1-3D-SD-a model, load cell 5 to 8 axial forces, 100 % Canoga Park, 3D nonlinear analysis 598

Figure K-11: A1-3D-SD-a model, hysteretic plot of the building, 100 % Canoga Park, 3D nonlinear analysis 599

Figure K-12: A1-3D-SD-a model, hysteretic plot of shear walls at each elevation, 100 % Canoga Park, 3D nonlinear analysis 599

Figure K-13: A1-3D-SD-a model, field plot of peak total base shear, 100 % Canoga Park, 3D nonlinear analysis (maximum anchor/hold down base shear is 2.35 kips) 600

Figure K-14: A1-3D-SD-a model, simplified illustration of corner displacements with hold down forces from load cells,100 % Canoga Park, 3D nonlinear analysis (max hold down tensile force is -4.63 kips) 600

Figure L-1: A1-3D-SD-b model 601

Figure L-2: First two natural modes of A1-3D-SD-b model _____ 602

Figure L-3: Pushover curve of A1-3D-SD-b model _____ 606

Figure L-4: Pushover curve of each wall line, A1-3D-SD-b model _____ 606

Figure L-5: A1-3D-SD-b model, base shear vector plot at the moment of peak total base shear, 100 % Canoga Park, 3D linear analysis (maximum anchor/hold down base shear is 4.83 kips)_____ 610

Figure L-6: A1-3D-SD-b model building story drift, 100 % Canoga Park, 3D nonlinear analysis _____ 618

Figure L-7: A1-3D-SD-b model wall line floor story drift, 100 % Canoga Park, 3D nonlinear analysis _____ 619

Figure L-8: A1-3D-SD-b model wall line roof story drift, 100 % Canoga Park, 3D nonlinear analysis _____ 620

Figure L-9: A1-3D-SD-b model total building base shear, 100 % Canoga Park, 3D nonlinear analysis _____ 621

Figure L-10: A1-3D-SD-b model, load cell 5 to 8 axial forces, 100 % Canoga Park, 3D nonlinear analysis _____ 621

Figure L-11: A1-3D-SD-b model, hysteretic plot of the building, 100 % Canoga Park, 3D nonlinear analysis _____ 622

Figure L-12: A1-3D-SD-b model, hysteretic plot of shear walls at each elevation, 100 % Canoga Park, 3D nonlinear analysis _____ 622

Figure L-13: A1-3D-SD-b model, field plot of peak total base shear, 100 % Canoga Park, 3D nonlinear analysis (maximum anchor/hold down base shear is 2.49 kips)_____ 623

Figure L-14: A1-3D-SD-b model, simplified illustration of corner displacements with hold down forces from load cells,100 % Canoga Park, 3D nonlinear analysis (max hold down tensile force is -4.67 kips) 623

Figure M-1: A2b-2D-a model 624

Figure M-2: First two natural modes of A2b-2D-a model 625

Figure M-3: Pushover curve of A2b-2D-a model 629

Figure M-4: Pushover curve of each wall line, A2b-2D-a model 629

Figure M-5: A2b-2D-a model, base shear vector plot at the moment of peak total base shear, 100 % Canoga Park, 2D linear analysis (maximum anchor/hold down base shear is 5.24 kips) 633

Figure M-6: A2b-2D-a model building story drift, 100 % Canoga Park, 2D nonlinear analysis 640

Figure M-7: A2b-2D-a model wall line floor story drift, 100 % Canoga Park, 2D nonlinear analysis 641

Figure M-8: A2b-2D-a model wall line roof story drift, 100 % Canoga Park, 2D nonlinear analysis 642

Figure M-9: A2b-2D-a model total building base shear, 100 % Canoga Park, 2D nonlinear analysis 643

Figure M-10: A2b-2D-a model, load cell 5 to 8 axial forces, 100 % Canoga Park, 2D nonlinear analysis 643

Figure M-11: A2b-2D-a model, hysteretic plot of the building, 100 % Canoga Park, 2D nonlinear analysis 644

Figure M-12: A2b-2D-a model, hysteretic plot of shear walls at each elevation, 100 % Canoga Park, 2D nonlinear analysis 644

Figure M-13: A2b-2D-a model, field plot of peak total base shear, 100 % Canoga Park, 2D nonlinear analysis (maximum anchor/hold down base shear is 1.56 kips) 645

Figure M-14: A2b-2D-a model, simplified illustration of corner displacements with hold down forces from load cells,100 % Canoga Park, 2D nonlinear analysis (max hold down tensile force is -3.80 kips) 645

Figure N-1: A2b-3D-RD-a model 646

Figure N-2: First two natural modes of A2b-3D-RD-a model 647

Figure N-3: Pushover curve of A2b-3D-RD-a model 651

Figure N-4: Pushover curve of each wall line, A2b-3D-RD-a model 651

Figure N-5: A2b-3D-RD-a model, base shear vector plot at the moment of peak total base shear, 100 % Canoga Park, 3D linear analysis (maximum anchor/hold down base shear is 6.57 kips) 655

Figure N-6: A2b-3D-RD-a model building story drift, 100 % Canoga Park, 3D nonlinear analysis 663

Figure N-7: A2b-3D-RD-a model wall line floor story drift, 100 % Canoga Park, 3D nonlinear analysis 664

Figure N-8: A2b-3D-RD-a model wall line roof story drift, 100 % Canoga Park, 3D nonlinear analysis 665

Figure N-9: A2b-3D-RD-a model total building base shear, 100 % Canoga Park, 3D nonlinear analysis 666

Figure N-10: A2b-3D-RD-a model, load cell 5 to 8 axial forces, 100 % Canoga Park, 3D nonlinear analysis _____ 666

Figure N-11: A2b-3D-RD-a model, hysteretic plot of the building, 100 % Canoga Park, 3D nonlinear analysis _____ 667

Figure N-12: A2b-3D-RD-a model, hysteretic plot of shear walls at each elevation, 100 % Canoga Park, 3D nonlinear analysis _____ 667

Figure N-13: A2b-3D-RD-a model, field plot of peak total base shear, 100 % Canoga Park, 3D nonlinear analysis (maximum anchor/hold down base shear is 1.76 kips) __ 668

Figure N-14: A2b-3D-RD-a model, simplified illustration of corner displacements with hold down forces from load cells,100 % Canoga Park, 3D nonlinear analysis (max hold down tensile force is -2.76 kips)_____ 668

Figure O-1: A2b-3D-SD-a model _____ 669

Figure O-2: First two natural modes of A2b-3D-SD-a model _____ 670

Figure O-3: Pushover curve of A2b-3D-SD-a model _____ 674

Figure O-4: Pushover curve of each wall line, A2b-3D-SD-a model_____ 674

Figure O-5: A2b-3D-SD-a model, base shear vector plot at the moment of peak total base shear, 100 % Canoga Park, 3D linear analysis (maximum anchor/hold down base shear is 6.20 kips)_____ 678

Figure O-6: A2b-3D-SD-a model building story drift, 100 % Canoga Park, 3D nonlinear analysis _____ 686

Figure O-7: A2b-3D-SD-a model wall line floor story drift, 100 % Canoga Park, 3D nonlinear analysis _____ 687

Figure O-8: A2b-3D-SD-a model wall line roof story drift, 100 % Canoga Park, 3D nonlinear analysis _____ 688

Figure O-9: A2b-3D-SD-a model total building base shear, 100 % Canoga Park, 3D nonlinear analysis _____ 689

Figure O-10: A2b-3D-SD-a model, load cell 5 to 8 axial forces, 100 % Canoga Park, 3D nonlinear analysis _____ 689

Figure O-11: A2b-3D-SD-a model, hysteretic plot of the building, 100 % Canoga Park, 3D nonlinear analysis _____ 690

Figure O-12: A2b-3D-SD-a model, hysteretic plot of shear walls at each elevation, 100 % Canoga Park, 3D nonlinear analysis _____ 690

Figure O-13: A2b-3D-SD-a model, field plot of peak total base shear, 100 % Canoga Park, 3D nonlinear analysis (maximum anchor/hold down base shear is 1.61 kips) __ 691

Figure O-14: A2b-3D-SD-a model, simplified illustration of corner displacements with hold down forces from load cells,100 % Canoga Park, 3D nonlinear analysis (max hold down tensile force is -2.81 kips) _____ 691

Figure P-1: A2c-2D-a model _____ 692

Figure P-2: First two natural modes of A2c-2D-a model _____ 693

Figure P-3: Pushover curve of A2c-2D-a model _____ 697

Figure P-4: Pushover curve of each wall line, A2c-2D-a model _____ 697

Figure P-5: A2c-2D-a model, base shear vector plot at the moment of peak total base shear, 100 % Canoga Park, 2D linear analysis (maximum anchor/hold down base shear is 2.86 kips) _____ 701

Figure P-6: A2c-2D-a model building story drift, 100 % Canoga Park, 2D nonlinear analysis _____ 708

Figure P-7: A2c-2D-a model wall line floor story drift, 100 % Canoga Park, 2D nonlinear analysis _____ 709

Figure P-8: A2c-2D-a model wall line roof story drift, 100 % Canoga Park, 2D nonlinear analysis _____ 710

Figure P-9: A2c-2D-a model total building base shear, 100 % Canoga Park, 2D nonlinear analysis _____ 711

Figure P-10: A2c-2D-a model, load cell 5 to 8 axial forces, 100 % Canoga Park, 2D nonlinear analysis _____ 711

Figure P-11: A2c-2D-a model, hysteretic plot of the building, 100 % Canoga Park, 2D nonlinear analysis _____ 712

Figure P-12: A2c-2D-a model, hysteretic plot of shear walls at each elevation, 100 % Canoga Park, 2D nonlinear analysis _____ 712

Figure P-13: A2c-2D-a model, field plot of peak total base shear, 100 % Canoga Park, 2D nonlinear analysis (maximum anchor/hold down base shear is 1.54 kips)_____ 713

Figure P-14: A2c-2D-a model, simplified illustration of corner displacements with hold down forces from load cells,100 % Canoga Park, 2D nonlinear analysis (max hold down tensile force is -2.87 kips)_____ 713

Figure Q-1: A2c-3D-RD-a model_____ 714

Figure Q-2: First two natural modes of A2c-3D-RD-a model _____ 715

Figure Q-3: Pushover curve of A2c-3D-RD-a model_____ 719

Figure Q-4: Pushover curve of each wall line, A2c-3D-RD-a model_____ 719

Figure Q-5: A2c-3D-RD-a model, base shear vector plot at the moment of peak total base shear, 100 % Canoga Park, 3D linear analysis (maximum anchor/hold down base shear is 3.95 kips) 723

Figure Q-6: A2c-3D-RD-a model building story drift, 100 % Canoga Park, 3D nonlinear analysis 731

Figure Q-7: A2c-3D-RD-a model wall line floor story drift, 100 % Canoga Park, 3D nonlinear analysis 732

Figure Q-8: A2c-3D-RD-a model wall line roof story drift, 100 % Canoga Park, 3D nonlinear analysis 733

Figure Q-9: A2c-3D-RD-a model total building base shear, 100 % Canoga Park, 3D nonlinear analysis 734

Figure Q-10: A2c-3D-RD-a model, load cell 5 to 8 axial forces, 100 % Canoga Park, 3D nonlinear analysis 734

Figure Q-11: A2c-3D-RD-a model, hysteretic plot of the building, 100 % Canoga Park, 3D nonlinear analysis 735

Figure Q-12: A2c-3D-RD-a model, hysteretic plot of shear walls at each elevation, 100 % Canoga Park, 3D nonlinear analysis 735

Figure Q-13: A2c-3D-RD-a model, field plot of peak total base shear, 100 % Canoga Park, 3D nonlinear analysis (maximum anchor/hold down base shear is 1.73 kips) 736

Figure Q-14: A2c-3D-RD-a model, simplified illustration of corner displacements with hold down forces from load cells,100 % Canoga Park, 3D nonlinear analysis (max hold down tensile force is -2.65 kips) 736

Figure R-1: A2c-3D-SD-a model 737

Figure R-2: First two natural modes of A2c-3D-SD-a model _____ 738

Figure R-3: Pushover curve of A2c-3D-SD-a model _____ 742

Figure R-4: Pushover curve of each wall line, A2c-3D-SD-a model _____ 742

Figure R-5: A2c-3D-SD-a model, base shear vector plot at the moment of peak total base shear, 100 % Canoga Park, 3D linear analysis (maximum anchor/hold down base shear is 2.50 kips)_____ 746

Figure R-6: A2c-3D-SD-a model building story drift, 100 % Canoga Park, 3D nonlinear analysis _____ 754

Figure R-7: A2c-3D-SD-a model wall line floor story drift, 100 % Canoga Park, 3D nonlinear analysis _____ 755

Figure R-8: A2c-3D-SD-a model wall line roof story drift, 100 % Canoga Park, 3D nonlinear analysis _____ 756

Figure R-9: A2c-3D-SD-a model total building base shear, 100 % Canoga Park, 3D nonlinear analysis _____ 757

Figure R-10: A2c-3D-SD-a model, load cell 5 to 8 axial forces, 100 % Canoga Park, 3D nonlinear analysis _____ 757

Figure R-11: A2c-3D-SD-a model, hysteretic plot of the building, 100 % Canoga Park, 3D nonlinear analysis _____ 758

Figure R-12: A2c-3D-SD-a model, hysteretic plot of shear walls at each elevation, 100 % Canoga Park, 3D nonlinear analysis _____ 758

Figure R-13: A2c-3D-SD-a model, field plot of peak total base shear, 100 % Canoga Park, 3D nonlinear analysis (maximum anchor/hold down base shear is 1.80 kips)_____ 759

Figure R-14: A2c-3D-SD-a model, simplified illustration of corner displacements with hold down forces from load cells,100 % Canoga Park, 3D nonlinear analysis (max hold down tensile force is -1.59 kips) 759

Figure S-1: A2d-3D-RD-a model 760

Figure S-2: First two natural modes of A2d-3D-RD-a model 761

Figure S-3: Pushover curve of A2d-3D-RD-a model 765

Figure S-4: Pushover curve of each wall line, A2d-3D-RD-a model 765

Figure S-5: A2d-3D-RD-a model, base shear vector plot at the moment of peak total base shear, 100 % Canoga Park, 3D linear analysis (maximum anchor/hold down base shear is 4.74 kips) 769

Figure S-6: A2d-3D-RD-a model building story drift, 100 % Canoga Park, 3D nonlinear analysis 778

Figure S-7: A2d-3D-RD-a model wall line floor story drift, 100 % Canoga Park, 3D nonlinear analysis 779

Figure S-8: A2d-3D-RD-a model wall line roof story drift, 100 % Canoga Park, 3D nonlinear analysis 780

Figure S-9: A2d-3D-RD-a model total building base shear, 100 % Canoga Park, 3D nonlinear analysis 781

Figure S-10: A2d-3D-RD-a model, load cell 5 to 8 axial forces, 100 % Canoga Park, 3D nonlinear analysis 781

Figure S-11: A2d-3D-RD-a model, hysteretic plot of the building, 100 % Canoga Park, 3D nonlinear analysis 782

Figure S-12: A2d-3D-RD-a model, hysteretic plot of shear walls at each elevation, 100 % Canoga Park, 3D nonlinear analysis 782

Figure S-13: A2d-3D-RD-a model, field plot of peak total base shear, 100 % Canoga Park, 3D nonlinear analysis (maximum anchor/hold down base shear is 1.71 kips) 783

Figure S-14: A2d-3D-RD-a model, simplified illustration of corner displacements with hold down forces from load cells, 100 % Canoga Park, 3D nonlinear analysis (max hold down tensile force is -2.90 kips) 783

Figure T-1: IDA result of A1-3D-SD-a model 787

Figure T-2: Pushover curve of A1-3D-SD-a model 787

Figure T-3: Collapse fragility curve with two proposed collapse drift limits 795

Figure U-1: IDA result of A2b-3D-SD-a model 802

Figure U-2: Pushover curve of A2b-3D-SD-a model 805

Figure U-3: Collapse fragility curve with proposed collapse drift limits for a 4% drift limit 808

Figure V-1: IDA result of P-3D-RD-b model 815

Figure V-2: Pushover curve of P-3D-RD-b model 818

Figure V-3: Collapse fragility curve with proposed collapse drift limits for a 4% drift limit 821

List of Tables

Table 2-1: Cross sectional properties of the lipped channel, circular and optimized sections for 4.88 m (16 ft) member 73

Table 2-2: Critical and nominal loads of the lipped channel, circular and optimal sections for 1.22 m (4 ft) member 76

Table 2-3: Critical and nominal loads of C- and 'Σ'-sections normalized by P_y = 63.70 kN (14.32 kips) 85

Table 2-4: Cross-section properties of squashed 'S' sections for 4.88m (16 ft) member 85

Table 2-5: Mean value and standard deviation of axial capacity P_n of optimized sections of three column lengths, normalized by P_y = 63.70 kN (14.32 kips) 85

Table 2-6: Critical and nominal loads of C and 'Σ'–sections, normalized by P_y = 63.70 kN (14.32 kips) 89

Table 2-7: Cross-section properties of optimized sections for 4.88 m (16 ft) member 95

Table 2-8: Axial capacities of optimized cross-sections for 0.61 m (2 ft) and 1.22 m (4 ft) members evaluated as 4.88 m (16 ft) member 96

Table 2-9: Mean value and standard deviation of axial capacity P_n of optimized sections of three column lengths normalized by P_y = 63.70 kN (14.32 kips) 96

Table 2-10: Design performance comparisons of optimized cross-sections 98

Table 3-1: Definition of directions 105

Table 3-2: Building components by percentage of total wall area (Peterman 2014) for Phase 1/2a structural only building 112

Table 3-3: Modeling options of the CFS-NEES archetype building 118

Table 3-4: Parameters that characterize nonlinear materials of shear wall bracings 126

Table 3-5: Force-displacement relationship of the hold down in tension 133

Table 3-6: Uniaxial material types and properties in section aggregator of CFS studs 146

Table 3-7: Capacities of studs in the FE model 146

Table 3-8: Parameters that characterize Pinching4 materials of gravity wall bracings 150

Table 3-9: Comparison of peak lateral displacement between diaphragm models and design equation 155

Table 4-1: Maximum percent story drift across phases and ground motions 167

Table 4-2: Ground motion summary, per PEER NGA database 170

Table 4-3: Ground motion summary and levels 174

Table 4-4: Summary of load case for the calibration of a FE model 175

Table 4-5: Modeling options of the CFS-NEES archetype building in model calibration 179

Table 4-6: Damping ratio of the CFS-NEES archetype building predicted by shaking table tests at various construction phases (data from (Peterman 2014)) 180

Table 4-7: Brief comparison of 3D shear wall only models with test of Phase 1 (structural only) building 181

Table 4-8: Summary of excitations for model calibration, Phase 1 183

Table 4-9: Comparison of the first natural period between A1-3D-SD-a model and test, Phase 1 183

Table 4-10: Comparison of peak story absolute acceleration in g between A1-3D-SD-a model and test, Phase 1 184

Table 4-11: Comparison of peak story drift between A1-3D-SD-a model and test, Phase 1 185

Table 4-12: Comparison of peak hold down tensile force between A1-3D-SD-a model and test, Phase 1 _____ 188

Table 4-13: Summary of excitations for model calibration, Phase 2a _____ 193

Table 4-14: Comparison of the first natural period between A1-3D-SD-a model and test, Phase 2a _____ 194

Table 4-15: Comparison of peak story absolute acceleration in g between A1-3D-SD-a model and test, Phase 2a _____ 194

Table 4-16: Comparison of peak story drift between A1-3D-SD-a model and test, Phase 2a _____ 195

Table 4-17: Comparison of peak hold down tensile force between A1-3D-SD-a model and test, Phase 2a _____ 195

Table 4-18: Summary of excitations for model calibration, Phase 2b _____ 201

Table 4-19: Comparison of the first natural period between A2b-3D-SD-a model and test, Phase 2b _____ 201

Table 4-20: Comparison of peak story absolute acceleration in g between A2b-3D-SD-a model and test, Phase 2b _____ 202

Table 4-21: Comparison of peak story drift between A2b-3D-SD-a model and test, Phase 2b _____ 203

Table 4-22: Comparison of peak hold down tensile force between A2b-3D-SD-a model and test, Phase 2b _____ 204

Table 4-23: Summary of excitations for model calibration, Phase 2c _____ 210

Table 4-24: Comparison of the first natural period between A2c-3D-SD-a model and test, Phase 2c _____ 210

Table 4-25: Comparison of peak story absolute acceleration in g between A2c-3D-SD-a model and test, Phase 2c 211

Table 4-26: Comparison of peak story drift between A2c-3D-SD-a model and test, Phase 2c 212

Table 4-27: Comparison of peak hold down tensile force between A2c-3D-SD-a model and test, Phase 2c 213

Table 4-28: Summary of excitations for model calibration, Phase 2d 219

Table 4-29: Comparison of the first natural period between A2d-3D-RD-a model and test, Phase 2d 219

Table 4-30: Comparison of peak story absolute acceleration in g between A2d-3D-RD-a model and test, Phase 2d 220

Table 4-31: Comparison of peak story drift between A2d-3D-RD-a model and test, Phase 2d 221

Table 4-32: Comparison of peak hold down tensile force between A2d-3D-RD-a model and test, Phase 2d 222

Table 4-33: Summary of excitations for model calibration, Phase 2e 228

Table 4-34: Comparison of the first natural period between A2d-3D-RD-a model and test, Phase 2e 228

Table 4-35: Comparison of peak story absolute acceleration in g between A2d-3D-RD-a model and test, Phase 2e 229

Table 4-36: Comparison of peak story drift between A2d-3D-RD-a model and test, Phase 2e 231

Table 4-37: Comparison of peak hold down tensile force between A2d-3D-RD-a model and test, Phase 2e _____ 232

Table 5-1: Modeling options of the CFS-NEES archetype building in performance comparison _____ 248

Table 5-2: Distribution of lateral load in static analysis _____ 250

Table 5-3: Summary of excitations in time history analysis of 2D models _____ 252

Table 5-4: Summary of excitations in time history analysis of 3D models _____ 252

Table 5-5: Comparison of 3D FE models' first natural periods of lateral modes _____ 256

Table 5-6: Comparison of normalized lateral stiffness of FE models of the CFS-NEES archetype building _____ 260

Table 5-7: Comparison of normalized lateral capacity of FE models of the CFS-NEES archetype building _____ 264

Table 5-8: Building components by percent of total wall area (modified version of (Peterman 2014)) _____ 264

Table 5-9: Summary of modeling options of the CFS-NEES archetype building in performance comparison _____ 268

Table 5-10: Elastic stiffness breakdown between shear walls and gravity walls along with the normalized sheathing areas, 2D models _____ 283

Table 5-11: Elastic stiffness breakdown between shear walls and gravity walls plus other systems along with the normalized sheathing areas, 3D models _____ 283

Table 5-12: Breakdown of total peak base shear between shear walls and gravity walls in 2D models _____ 289

Table 5-13: Breakdown of total peak base shear between shear walls and gravity walls in 3D models 290

Table 5-14: Comparison of natural periods of 3D models with two stiffness options 292

Table 5-15: Comparison of natural periods of 3D models with two mass options 293

Table 5-16: Modeling guidelines for cold-formed steel framed buildings based on the CFS-NEES analysis 299

Table 6-1: Parameters for the definition of the CFS-NEES archetype building 307

Table 6-2: CFS-NEES archetype structural design properties 307

Table 6-3: Modeling options of the CFS-NEES archetype building in IDA and performance evaluation 309

Table 6-4: Summary of collapse results for the CFS-NEES building modeled by three different models 315

Table 6-5: Summary of collapse results for the CFS-NEES building modeled by three different models 319

Table A-1: Free vibration analysis results, P-2D-a model 352

Table A-2: Breakdown of peak base shear, linear static analysis, P-2D-a model 354

Table A-3: Peak building and wall line deflection, linear static analysis, P-2D-a model 354

Table A-4: Breakdown of lateral stiffness, P-2D-a model 354

Table A-5: Breakdown of peak base shear, pushover analysis, P-2D-a model 355

Table A-6: P-2D-a model peak story relative acceleration in g, linear time history analysis 358

Table A-7: P-2D-a model peak building roof drift and base shear, linear time history analysis _____ 358

Table A-8: P-2D-a model peak building story drift, linear time history analysis_____ 358

Table A-9: P-2D-a model peak building base shear, linear time history analysis ____ 359

Table A-10: P-2D-a model peak wall line story drift, linear time history analysis ___ 359

Table A-11: P-2D-a model peak wall line base shear, linear time history analysis ___ 360

Table A-12: P-2D-a model peak story relative acceleration in g, nonlinear time history analysis _____ 363

Table A-13: P-2D-a model peak building roof drift and base shear, nonlinear time history analysis _____ 363

Table A-14: P-2D-a model peak building story drift, nonlinear time history analysis_ 363

Table A-15: P-2D-a model peak building base shear, nonlinear time history analysis 364

Table A-16: P-2D-a model peak wall line story drift, nonlinear time history analysis 364

Table A-17: P-2D-a model peak wall line base shear, nonlinear time history analysis 365

Table A-18: P-2D-a model wall line base shear breakdown, nonlinear time history analysis _____ 365

Table A-19: P-2D-a model peak hold down tensile force at certain locations, nonlinear time history analysis _____ 366

Table B-1: Free vibration analysis results, P-2D-b model _____ 374

Table B-2: Breakdown of peak base shear, linear static analysis, P-2D-b model ____ 376

Table B-3: Peak building and wall line deflection, linear static analysis, P-2D-b model _____ 376

Table B-4: Breakdown of lateral stiffness, P-2D-b model _____ 376

Table B-5: Breakdown of peak base shear, pushover analysis, P-2D-b model _____ 377

Table B-6: P-2D-b model peak story relative acceleration in g, linear time history analysis _____ 380

Table B-7: P-2D-b model peak building roof drift and base shear, linear time history analysis _____ 380

Table B-8: P-2D-b model peak building story drift, linear time history analysis_____ 380

Table B-9: P-2D-b model peak building base shear, linear time history analysis ____ 381

Table B-10: P-2D-b model peak wall line story drift, linear time history analysis ___ 381

Table B-11: P-2D-b model peak wall line base shear, linear time history analysis ___ 382

Table B-12: P-2D-b model peak story relative acceleration in g, nonlinear time history analysis _____ 385

Table B-13: P-2D-b model peak building roof drift and base shear, nonlinear time history analysis _____ 385

Table B-14: P-2D-b model peak building story drift, nonlinear time history analysis_ 385

Table B-15: P-2D-b model peak building base shear, nonlinear time history analysis 386

Table B-16: P-2D-b model peak wall line story drift, nonlinear time history analysis 386

Table B-17: P-2D-b model peak wall line base shear, nonlinear time history analysis 387

Table B-18: P-2D-b model wall line base shear breakdown, nonlinear time history analysis _____ 387

Table B-19: P-2D-b model peak hold down tensile force at certain locations, nonlinear time history analysis _____ 388

Table C-1: Free vibration analysis results, P-3D-RD-a model_____ 396

Table C-2: Breakdown of peak base shear, linear static analysis, P-3D-RD-a model _ 397

Table C-3: Peak building and wall line deflection, linear static analysis, P-3D-RD-a model 398

Table C-4: Breakdown of lateral stiffness, P-3D-RD-a model 398

Table C-5: Breakdown of peak base shear, pushover analysis, P-3D-RD-a model 399

Table C-6: P-3D-RD-a model peak story relative acceleration in g, linear time history analysis 402

Table C-7: P-3D-RD-a model peak building roof drift and base shear, linear time history analysis 402

Table C-8: P-3D-RD-a model peak building story drift, linear time history analysis 403

Table C-9: P-3D-RD-a model peak building base shear, linear time history analysis 403

Table C-10: P-3D-RD-a model peak story relative acceleration in g, nonlinear time history analysis 407

Table C-11: P-3D-RD-a model peak building roof drift and base shear, nonlinear time history analysis 407

Table C-12: P-3D-RD-a model peak building story drift, nonlinear linear time history analysis 408

Table C-13: P-3D-RD-a model peak building base shear, nonlinear time history analysis 408

Table C-14: P-3D-RD-a model peak wall line story drift, nonlinear time history analysis 409

Table C-15: P-3D-RD-a model peak wall line base shear, nonlinear time history analysis 410

Table C-16: P-3D-RD-a model wall line base shear breakdown, nonlinear time history analysis _____ 411

Table C-17: P-3D-RD-a model peak hold down tensile force at certain locations, nonlinear time history analysis _____ 411

Table D-1: Free vibration analysis results, P-3D-RD-b model_____ 419

Table D-2: Breakdown of peak base shear, linear static analysis, P-3D-RD-b model _ 420

Table D-3: Peak building and wall line deflection, linear static analysis, P-3D-RD-b model_____ 421

Table D-4: Breakdown of lateral stiffness, P-3D-RD-b model _____ 421

Table D-5: Breakdown of peak base shear, pushover analysis, P-3D-RD-b model ___ 422

Table D-6: P-3D-RD-b model peak story relative acceleration in g, linear time history analysis _____ 425

Table D-7: P-3D-RD-b model peak building roof drift and base shear, linear time history analysis _____ 425

Table D-8: P-3D-RD-b model peak building story drift, linear time history analysis _ 426

Table D-9: P-3D-RD-b model peak building base shear, linear time history analysis_ 426

Table D-10: P-3D-RD-b model peak story relative acceleration in g, nonlinear time history analysis _____ 430

Table D-11: P-3D-RD-b model peak building roof drift and base shear, nonlinear time history analysis _____ 430

Table D-12: P-3D-RD-b model peak building story drift, nonlinear linear time history analysis _____ 431

Table D-13: P-3D-RD-b model peak building base shear, nonlinear time history analysis _____ 431

Table D-14: P-3D-RD-b model peak wall line story drift, nonlinear time history analysis _____ 432

Table D-15: P-3D-RD-b model peak wall line base shear, nonlinear time history analysis _____ 433

Table D-16: P-3D-RD-b model wall line base shear breakdown, nonlinear time history analysis _____ 434

Table D-17: P-3D-RD-b model peak hold down tensile force at certain locations, nonlinear time history analysis _____ 434

Table E-1: Free vibration analysis results, A1-2D-a model _____ 442

Table E-2: Breakdown of peak base shear, linear static analysis, A1-2D-a model ___ 444

Table E-3: Peak building and wall line deflection, linear static analysis, A1-2D-a model _____ 445

Table E-4: Breakdown of lateral stiffness, A1-2D-a model _____ 445

Table E-5: Breakdown of peak base shear, pushover analysis, A1-2D-a model _____ 446

Table E-6: A1-2D-a model peak story relative acceleration in g, linear time history analysis _____ 450

Table E-7: A1-2D-a model peak building roof drift and base shear, linear time history analysis _____ 450

Table E-8: A1-2D-a model peak building story drift, linear time history analysis ___ 450

Table E-9: A1-2D-a model peak building base shear, linear time history analysis ___ 451

Table E-10: A1-2D-a model peak wall line story drift, linear time history analysis __ 451

Table E-11: A1-2D-a model peak wall line base shear, linear time history analysis __ 452
Table E-12: A1-2D-a model peak story relative acceleration in g, nonlinear time history analysis _____ 455
Table E-13: A1-2D-a model peak building roof drift and base shear, nonlinear time history analysis _____ 455
Table E-14: A1-2D-a model peak building story drift, nonlinear time history analysis 455
Table E-15: A1-2D-a model peak building base shear, nonlinear time history analysis 456
Table E-16: A1-2D-a model peak wall line story drift, nonlinear time history analysis 456
Table E-17: A1-2D-a model peak wall line base shear, nonlinear time history analysis 457
Table E-18: A1-2D-a model wall line base shear breakdown, nonlinear time history analysis _____ 457
Table E-19: A1-2D-a model peak hold down tensile force at certain locations, nonlinear time history analysis _____ 458
Table F-1: Free vibration analysis results, A1-2D-b model _____ 466
Table F-2: Breakdown of peak base shear, linear static analysis, A1-2D-b model ___ 468
Table F-3: Peak building and wall line deflection, linear static analysis, A1-2D-b model _____ 468
Table F-4: Breakdown of lateral stiffness, A1-2D-b model _____ 468
Table F-5: Breakdown of peak base shear, pushover analysis, A1-2D-b model _____ 469
Table F-6: A1-2D-b model peak story relative acceleration in g, linear time history analysis _____ 472
Table F-7: A1-2D-b model peak building roof drift and base shear, linear time history analysis _____ 472

Table F-8: A1-2D-b model peak building story drift, linear time history analysis ___ 472

Table F-9: A1-2D-b model peak building base shear, linear time history analysis ___ 473

Table F-10: A1-2D-b model peak wall line story drift, linear time history analysis __ 473

Table F-11: A1-2D-b model peak wall line base shear, linear time history analysis __ 474

Table F-12: A1-2D-b model peak story relative acceleration in g, nonlinear time history analysis _____ 477

Table F-13: A1-2D-b model peak building roof drift and base shear, nonlinear time history analysis _____ 477

Table F-14: A1-2D-b model peak building story drift, nonlinear time history analysis 477

Table F-15: A1-2D-b model peak building base shear, nonlinear time history analysis 478

Table F-16: A1-2D-b model peak wall line story drift, nonlinear time history analysis 478

Table F-17: A1-2D-b model peak wall line base shear, nonlinear time history analysis 479

Table F-18: A1-2D-b model wall line base shear breakdown, nonlinear time history analysis _____ 479

Table F-19: A1-2D-b model peak hold down tensile force at certain locations, nonlinear time history analysis _____ 480

Table G-1: Free vibration analysis results, A1-2D-c model _____ 488

Table G-2: Breakdown of peak base shear, linear static analysis, A1-2D-c model ___ 490

Table G-3: Peak building and wall line deflection, linear static analysis, A1-2D-c model _____ 490

Table G-4: Breakdown of lateral stiffness, A1-2D-c model _____ 490

Table G-5: Breakdown of peak base shear, pushover analysis, A1-2D-c model _____ 491

Table G-6: A1-2D-c model peak story relative acceleration in g, linear time history analysis _____ 494

Table G-7: A1-2D-c model peak building roof drift and base shear, linear time history analysis _____ 494

Table G-8: A1-2D-c model peak building story drift, linear time history analysis ___ 494

Table G-9: A1-2D-c model peak building base shear, linear time history analysis ___ 495

Table G-10: A1-2D-c model peak wall line story drift, linear time history analysis __ 495

Table G-11: A1-2D-c model peak wall line base shear, linear time history analysis__ 496

Table G-12: A1-2D-c model peak story relative acceleration in g, nonlinear time history analysis _____ 499

Table G-13: A1-2D-c model peak building roof drift and base shear, nonlinear time history analysis _____ 499

Table G-14: A1-2D-c model peak building story drift, nonlinear time history analysis 499

Table G-15: A1-2D-c model peak building base shear, nonlinear time history analysis 500

Table G-16: A1-2D-c model peak wall line story drift, nonlinear time history analysis 500

Table G-17: A1-2D-c model peak wall line base shear, nonlinear time history analysis501

Table G-18: A1-2D-c model wall line base shear breakdown, nonlinear time history analysis _____ 501

Table G-19: A1-2D-c model peak hold down tensile force at certain locations, nonlinear time history analysis _____ 502

Table H-1: Free vibration analysis results, A1-3D-RD-a model _____ 510

Table H-2: Breakdown of peak base shear, linear static analysis, A1-3D-RD-a model 511

Table H-3: Peak building and wall line deflection, linear static analysis, A1-3D-RD-a model 512

Table H-4: Breakdown of lateral stiffness, A1-3D-RD-a model 512

Table H-5: Breakdown of peak base shear, pushover analysis, A1-3D-RD-a model 513

Table H-6: A1-3D-RD-a model peak story relative acceleration in g, linear time history analysis 516

Table H-7: A1-3D-RD-a model peak building roof drift and base shear, linear time history analysis 516

Table H-8: A1-3D-RD-a model peak building story drift, linear time history analysis 517

Table H-9: A1-3D-RD-a model peak building base shear, linear time history analysis 517

Table H-10: A1-3D-RD-a model peak story relative acceleration in g, nonlinear time history analysis 521

Table H-11: A1-3D-RD-a model peak building roof drift and base shear, nonlinear time history analysis 521

Table H-12: A1-3D-RD-a model peak building story drift, nonlinear linear time history analysis 522

Table H-13: A1-3D-RD-a model peak building base shear, nonlinear time history analysis 522

Table H-14: A1-3D-RD-a model peak wall line story drift, nonlinear time history analysis 523

Table H-15: A1-3D-RD-a model peak wall line base shear, nonlinear time history analysis 524

Table H-16: A1-3D-RD-a model wall line base shear breakdown, nonlinear time history analysis _____ 525

Table H-17: A1-3D-RD-a model peak hold down tensile force at certain locations, nonlinear time history analysis _____ 525

Table I-1: Free vibration analysis results, A1-3D-RD-b model _____ 533

Table I-2: Breakdown of peak base shear, linear static analysis, A1-3D-RD-b model 534

Table I-3: Peak building and wall line deflection, linear static analysis, A1-3D-RD-b model_____ 535

Table I-4: Breakdown of lateral stiffness, A1-3D-RD-b model _____ 535

Table I-5: Breakdown of peak base shear, pushover analysis, A1-3D-RD-b model __ 536

Table I-6: A1-3D-RD-b model peak story relative acceleration in g, linear time history analysis _____ 539

Table I-7: A1-3D-RD-b model peak building roof drift and base shear, linear time history analysis _____ 539

Table I-8: A1-3D-RD-b model peak building story drift, linear time history analysis 540

Table I-9: A1-3D-RD-b model peak building base shear, linear time history analysis 540

Table I-10: A1-3D-RD-b model peak story relative acceleration in g, nonlinear time history analysis _____ 544

Table I-11: A1-3D-RD-b model peak building roof drift and base shear, nonlinear time history analysis _____ 544

Table I-12: A1-3D-RD-b model peak building story drift, nonlinear linear time history analysis _____ 545

Table I-13: A1-3D-RD-b model peak building base shear, nonlinear time history analysis _____ 545

Table I-14: A1-3D-RD-b model peak wall line story drift, nonlinear time history analysis _____ 546

Table I-15: A1-3D-RD-b model peak wall line base shear, nonlinear time history analysis _____ 547

Table I-16: A1-3D-RD-b model wall line base shear breakdown, nonlinear time history analysis _____ 548

Table I-17: A1-3D-RD-b model peak hold down tensile force at certain locations, nonlinear time history analysis _____ 548

Table J-1: Free vibration analysis results, A1-3D-RD-c model _____ 556

Table J-2: Breakdown of peak base shear, linear static analysis, A1-3D-RD-c model 557

Table J-3: Peak building and wall line deflection, linear static analysis, A1-3D-RD-c model_____ 558

Table J-4: Breakdown of lateral stiffness, A1-3D-RD-c model _____ 558

Table J-5: Breakdown of peak base shear, pushover analysis, A1-3D-RD-c model __ 559

Table J-6: A1-3D-RD-c model peak story relative acceleration in g, linear time history analysis _____ 562

Table J-7: A1-3D-RD-c model peak building roof drift and base shear, linear time history analysis _____ 562

Table J-8: A1-3D-RD-c model peak building story drift, linear time history analysis 563

Table J-9: A1-3D-RD-c model peak building base shear, linear time history analysis 563

Table J-10: A1-3D-RD-c model peak story relative acceleration in g, nonlinear time history analysis _____ 567

Table J-11: A1-3D-RD-c model peak building roof drift and base shear, nonlinear time history analysis _____ 567

Table J-12: A1-3D-RD-c model peak building story drift, nonlinear linear time history analysis _____ 568

Table J-13: A1-3D-RD-c model peak building base shear, nonlinear time history analysis _____ 568

Table J-14: A1-3D-RD-c model peak wall line story drift, nonlinear time history analysis _____ 569

Table J-15: A1-3D-RD-c model peak wall line base shear, nonlinear time history analysis _____ 570

Table J-16: A1-3D-RD-c model wall line base shear breakdown, nonlinear time history analysis _____ 571

Table J-17: A1-3D-RD-c model peak hold down tensile force at certain locations, nonlinear time history analysis _____ 571

Table K-1: Free vibration analysis results, A1-3D-SD-a model_____ 579

Table K-2: Breakdown of peak base shear, linear static analysis, A1-3D-SD-a model 581

Table K-3: Peak building and wall line deflection, linear static analysis, A1-3D-SD-a model_____ 581

Table K-4: Breakdown of lateral stiffness, A1-3D-SD-a model _____ 581

Table K-5: Breakdown of peak base shear, pushover analysis, A1-3D-SD-a model__ 582

Table K-6: A1-3D-SD-a model peak story relative acceleration in g, linear time history analysis _____ 585

Table K-7: A1-3D-SD-a model peak building roof drift and base shear, linear time history analysis _____ 585

Table K-8: A1-3D-SD-a model peak building story drift, linear time history analysis 586

Table K-9: A1-3D-SD-a model peak building base shear, linear time history analysis 586

Table K-10: A1-3D-SD-a model peak story relative acceleration in g, nonlinear time history analysis _____ 590

Table K-11: A1-3D-SD-a model peak building roof drift and base shear, nonlinear time history analysis _____ 590

Table K-12: A1-3D-SD-a model peak building story drift, nonlinear linear time history analysis _____ 591

Table K-13: A1-3D-SD-a model peak building base shear, nonlinear time history analysis _____ 591

Table K-14: A1-3D-SD-a model peak wall line story drift, nonlinear time history analysis _____ 592

Table K-15: A1-3D-SD-a model peak wall line base shear, nonlinear time history analysis _____ 593

Table K-16: A1-3D-SD-a model wall line base shear breakdown, nonlinear time history analysis _____ 594

Table K-17: A1-3D-SD-a model peak hold down tensile force at certain locations, nonlinear time history analysis _____ 594

Table L-1: Free vibration analysis results, A1-3D-SD-b model _____ 602

Table L-2: Breakdown of peak base shear, linear static analysis, A1-3D-SD-b model 603

Table L-3: Peak building and wall line deflection, linear static analysis, A1-3D-SD-b model 604

Table L-4: Breakdown of lateral stiffness, A1-3D-SD-b model 604

Table L-5: Breakdown of peak base shear, pushover analysis, A1-3D-SD-b model 605

Table L-6: A1-3D-SD-b model peak story relative acceleration in g, linear time history analysis 608

Table L-7: A1-3D-SD-b model peak building roof drift and base shear, linear time history analysis 608

Table L-8: A1-3D-SD-b model peak building story drift, linear time history analysis 609

Table L-9: A1-3D-SD-b model peak building base shear, linear time history analysis 609

Table L-10: A1-3D-SD-b model peak story relative acceleration in g, nonlinear time history analysis 613

Table L-11: A1-3D-SD-b model peak building roof drift and base shear, nonlinear time history analysis 613

Table L-12: A1-3D-SD-b model peak building story drift, nonlinear linear time history analysis 614

Table L-13: A1-3D-SD-b model peak building base shear, nonlinear time history analysis 614

Table L-14: A1-3D-SD-b model peak wall line story drift, nonlinear time history analysis 615

Table L-15: A1-3D-SD-b model peak wall line base shear, nonlinear time history analysis 616

Table L-16: A1-3D-SD-b model wall line base shear breakdown, nonlinear time history analysis _____ 617

Table L-17: A1-3D-SD-b model peak hold down tensile force at certain locations, nonlinear time history analysis _____ 617

Table M-1: Free vibration analysis results, A2b-2D-a model _____ 625

Table M-2: Breakdown of peak base shear, linear static analysis, A2b-2D-a model__ 627

Table M-3: Peak building and wall line deflection, linear static analysis, A2b-2D-a model _____ 627

Table M-4: Breakdown of lateral stiffness, A2b-2D-a model _____ 627

Table M-5: Breakdown of peak base shear, pushover analysis, A2b-2D-a model____ 628

Table M-6: A2b-2D-a model peak story relative acceleration in g, linear time history analysis _____ 631

Table M-7: A2b-2D-a model peak building roof drift and base shear, linear time history analysis _____ 631

Table M-8: A2b-2D-a model peak building story drift, linear time history analysis __ 631

Table M-9: A2b-2D-a model peak building base shear, linear time history analysis__ 632

Table M-10: A2b-2D-a model peak wall line story drift, linear time history analysis_ 632

Table M-11: A2b-2D-a model peak wall line base shear, linear time history analysis 633

Table M-12: A2b-2D-a model peak story relative acceleration in g, nonlinear time history analysis _____ 636

Table M-13: A2b-2D-a model peak building roof drift and base shear, nonlinear time history analysis _____ 636

Table M-14: A2b-2D-a model peak building story drift, nonlinear time history analysis _____ 636

Table M-15: A2b-2D-a model peak building base shear, nonlinear time history analysis _____ 637

Table M-16: A2b-2D-a model peak wall line story drift, nonlinear time history analysis _____ 637

Table M-17: A2b-2D-a model peak wall line base shear, nonlinear time history analysis _____ 638

Table M-18: A2b-2D-a model wall line base shear breakdown, nonlinear time history analysis _____ 638

Table M-19: A2b-2D-a model peak hold down tensile force at certain locations, nonlinear time history analysis _____ 639

Table N-1: Free vibration analysis results, A2b-3D-RD-a model _____ 647

Table N-2: Breakdown of peak base shear, linear static analysis, A2b-3D-RD-a model649

Table N-3: Peak building and wall line deflection, linear static analysis, A2b-3D-RD-a model_____ 649

Table N-4: Breakdown of lateral stiffness, A2b-3D-RD-a model _____ 649

Table N-5: Breakdown of peak base shear, pushover analysis, A2b-3D-RD-a model_ 650

Table N-6: A2b-3D-RD-a model peak story relative acceleration in g, linear time history analysis _____ 653

Table N-7: A2b-3D-RD-a model peak building roof drift and base shear, linear time history analysis _____ 653

Table N-8: A2b-3D-RD-a model peak building story drift, linear time history analysis654

Table N-9: A2b-3D-RD-a model peak building base shear, linear time history analysis _____ 654

Table N-10: A2b-3D-RD-a model peak story relative acceleration in g, nonlinear time history analysis _____ 658

Table N-11: A2b-3D-RD-a model peak building roof drift and base shear, nonlinear time history analysis _____ 658

Table N-12: A2b-3D-RD-a model peak building story drift, nonlinear linear time history analysis _____ 659

Table N-13: A2b-3D-RD-a model peak building base shear, nonlinear time history analysis _____ 659

Table N-14: A2b-3D-RD-a model peak wall line story drift, nonlinear time history analysis _____ 660

Table N-15: A2b-3D-RD-a model peak wall line base shear, nonlinear time history analysis _____ 661

Table N-16: A2b-3D-RD-a model wall line base shear breakdown, nonlinear time history analysis _____ 662

Table N-17: A2b-3D-RD-a model peak hold down tensile force at certain locations, nonlinear time history analysis _____ 662

Table O-1: Free vibration analysis results, A2b-3D-SD-a model_____ 670

Table O-2: Breakdown of peak base shear, linear static analysis, A2b-3D-SD-a model 672

Table O-3: Peak building and wall line deflection, linear static analysis, A2b-3D-SD-a model_____ 672

Table O-4: Breakdown of lateral stiffness, A2b-3D-SD-a model _____ 672

Table O-5: Breakdown of peak base shear, pushover analysis, A2b-3D-SD-a model _ 673

Table O-6: A2b-3D-SD-a model peak story relative acceleration in g, linear time history analysis _____ 676

Table O-7: A2b-3D-SD-a model peak building roof drift and base shear, linear time history analysis _____ 676

Table O-8: A2b-3D-SD-a model peak building story drift, linear time history analysis 677

Table O-9: A2b-3D-SD-a model peak building base shear, linear time history analysis677

Table O-10: A2b-3D-SD-a model peak story relative acceleration in g, nonlinear time history analysis _____ 681

Table O-11: A2b-3D-SD-a model peak building roof drift and base shear, nonlinear time history analysis _____ 681

Table O-12: A2b-3D-SD-a model peak building story drift, nonlinear linear time history analysis _____ 682

Table O-13: A2b-3D-SD-a model peak building base shear, nonlinear time history analysis _____ 682

Table O-14: A2b-3D-SD-a model peak wall line story drift, nonlinear time history analysis _____ 683

Table O-15: A2b-3D-SD-a model peak wall line base shear, nonlinear time history analysis _____ 684

Table O-16: A2b-3D-SD-a model wall line base shear breakdown, nonlinear time history analysis _____ 685

Table O-17: A2b-3D-SD-a model peak hold down tensile force at certain locations, nonlinear time history analysis _____ 685

Table P-1: Free vibration analysis results, A2c-2D-a model _____ 693

Table P-2: Breakdown of peak base shear, linear static analysis, A2c-2D-a model __ 695

Table P-3: Peak building and wall line deflection, linear static analysis, A2c-2D-a model _____ 695

Table P-4: Breakdown of lateral stiffness, A2c-2D-a model _____ 695

Table P-5: Breakdown of peak base shear, pushover analysis, A2c-2D-a model ____ 696

Table P-6: A2c-2D-a model peak story relative acceleration in g, linear time history analysis _____ 699

Table P-7: A2c-2D-a model peak building roof drift and base shear, linear time history analysis _____ 699

Table P-8: A2c-2D-a model peak building story drift, linear time history analysis___ 699

Table P-9: A2c-2D-a model peak building base shear, linear time history analysis __ 700

Table P-10: A2c-2D-a model peak wall line story drift, linear time history analysis _ 700

Table P-11: A2c-2D-a model peak wall line base shear, linear time history analysis _ 701

Table P-12: A2c-2D-a model peak story relative acceleration in g, nonlinear time history analysis _____ 704

Table P-13: A2c-2D-a model peak building roof drift and base shear, nonlinear time history analysis _____ 704

Table P-14: A2c-2D-a model peak building story drift, nonlinear time history analysis704

Table P-15: A2c-2D-a model peak building base shear, nonlinear time history analysis _____ 705

Table P-16: A2c-2D-a model peak wall line story drift, nonlinear time history analysis _____ 705

Table P-17: A2c-2D-a model peak wall line base shear, nonlinear time history analysis _____ 706

Table P-18: A2c-2D-a model wall line base shear breakdown, nonlinear time history analysis _____ 706

Table P-19: A2c-2D-a model peak hold down tensile force at certain locations, nonlinear time history analysis _____ 707

Table Q-1: Free vibration analysis results, A2c-3D-RD-a model _____ 715

Table Q-2: Breakdown of peak base shear, linear static analysis, A2c-3D-RD-a model717

Table Q-3: Peak building and wall line deflection, linear static analysis, A2c-3D-RD-a model_____ 717

Table Q-4: Breakdown of lateral stiffness, A2c-3D-RD-a model _____ 717

Table Q-5: Breakdown of peak base shear, pushover analysis, A2c-3D-RD-a model_ 718

Table Q-6: A2c-3D-RD-a model peak story relative acceleration in g, linear time history analysis _____ 721

Table Q-7: A2c-3D-RD-a model peak building roof drift and base shear, linear time history analysis _____ 721

Table Q-8: A2c-3D-RD-a model peak building story drift, linear time history analysis 722

Table Q-9: A2c-3D-RD-a model peak building base shear, linear time history analysis722

Table Q-10: A2c-3D-RD-a model peak story relative acceleration in g, nonlinear time history analysis _____ 726

Table Q-11: A2c-3D-RD-a model peak building roof drift and base shear, nonlinear time history analysis _____ 726

Table Q-12: A2c-3D-RD-a model peak building story drift, nonlinear linear time history analysis _____ 727

Table Q-13: A2c-3D-RD-a model peak building base shear, nonlinear time history analysis _____ 727

Table Q-14: A2c-3D-RD-a model peak wall line story drift, nonlinear time history analysis _____ 728

Table Q-15: A2c-3D-RD-a model peak wall line base shear, nonlinear time history analysis _____ 729

Table Q-16: A2c-3D-RD-a model wall line base shear breakdown, nonlinear time history analysis _____ 730

Table Q-17: A2c-3D-RD-a model peak hold down tensile force at certain locations, nonlinear time history analysis _____ 730

Table R-1: Free vibration analysis results, A2c-3D-SD-a model _____ 738

Table R-2: Breakdown of peak base shear, linear static analysis, A2c-3D-SD-a model 740

Table R-3: Peak building and wall line deflection, linear static analysis, A2c-3D-SD-a model_____ 740

Table R-4: Breakdown of lateral stiffness, A2c-3D-SD-a model_____ 740

Table R-5: Breakdown of peak base shear, pushover analysis, A2c-3D-SD-a model _ 741

Table R-6: A2c-3D-SD-a model peak story relative acceleration in g, linear time history analysis _____ 744

Table R-7: A2c-3D-SD-a model peak building roof drift and base shear, linear time history analysis _____ 744

Table R-8: A2c-3D-SD-a model peak building story drift, linear time history analysis 745

Table R-9: A2c-3D-SD-a model peak building base shear, linear time history analysis 745

Table R-10: A2c-3D-SD-a model peak story relative acceleration in g, nonlinear time history analysis _____ 749

Table R-11: A2c-3D-SD-a model peak building roof drift and base shear, nonlinear time history analysis _____ 749

Table R-12: A2c-3D-SD-a model peak building story drift, nonlinear linear time history analysis _____ 750

Table R-13: A2c-3D-SD-a model peak building base shear, nonlinear time history analysis _____ 750

Table R-14: A2c-3D-SD-a model peak wall line story drift, nonlinear time history analysis _____ 751

Table R-15: A2c-3D-SD-a model peak wall line base shear, nonlinear time history analysis _____ 752

Table R-16: A2c-3D-SD-a model wall line base shear breakdown, nonlinear time history analysis _____ 753

Table R-17: A2c-3D-SD-a model peak hold down tensile force at certain locations, nonlinear time history analysis _____ 753

Table S-1: Free vibration analysis results, A2d-3D-RD-a model_____ 761

Table S-2: Breakdown of peak base shear, linear static analysis, A2d-3D-RD-a model 763

Table S-3: Peak building and wall line deflection, linear static analysis, A2d-3D-RD-a model_____ 763

Table S-4: Breakdown of lateral stiffness, A2d-3D-RD-a model_____ 763

Table S-5: Breakdown of peak base shear, pushover analysis, A2d-3D-RD-a model _ 764

Table S-6: A2d-3D-RD-a model peak story relative acceleration in g, linear time history analysis _____ 767

Table S-7: A2d-3D-RD-a model peak building roof drift and base shear, linear time history analysis _____ 767

Table S-8: A2d-3D-RD-a model peak building story drift, linear time history analysis 768

Table S-9: A2d-3D-RD-a model peak building base shear, linear time history analysis 768

Table S-10: A2d-3D-RD-a model peak story relative acceleration in g, nonlinear time history analysis _____ 772

Table S-11: A2d-3D-RD-a model peak building roof drift and base shear, nonlinear time history analysis _____ 773

Table S-12: A2d-3D-RD-a model peak building story drift, nonlinear linear time history analysis _____ 773

Table S-13: A2d-3D-RD-a model peak building base shear, nonlinear time history analysis _____ 774

Table S-14: A2d-3D-RD-a model peak wall line story drift, nonlinear time history analysis _____ 775

Table S-15: A2d-3D-RD-a model peak wall line base shear, nonlinear time history analysis _____ 776

Table S-16: A2d-3D-RD-a model wall line base shear breakdown, nonlinear time history analysis _____ 777

Table S-17: A2d-3D-RD-a model peak hold down tensile force at certain locations, nonlinear time history analysis _____ 777

Table T-1: Summary of calculation of overstrength and period-based ductility, A1-3D-SD-a model _____ 791

Table T-2: Modeling options of the CFS-NEES archetype building in performance comparison (the case finally used is in bold type) _____ 800

Table U-1: Summary of calculation of overstrength and period-based ductility, A2b-3D-SD-a model _____ 804

Table U-2: Modeling options of the CFS-NEES archetype building in performance comparison (the case finally used is in bold type) _____ 812

Table V-1: Summary of calculation of overstrength and period-based ductility, P-3D-RD-b model _____ 817

Table V-2: Modeling options of the CFS-NEES archetype building in performance comparison (the case finally used is in bold type) _____ 825

Chapter 1: Introduction to Cold-formed Steel Simulation

This dissertation is a comprehensive summary of my research on computational modeling and analysis of cold-formed steel (CFS) structures from 2009 to 2015. Two aspects of CFS structure simulation: shape optimization of CFS columns for maximum strength, and modeling of multi-story CFS-framed building of the CFS-NEES project for performance-based seismic design, are addressed in my research. Chapter 1 is a review of research in the general field of simulating cold-formed steel structures, including the finite element method (FEM) using frame and shell element and the finite strip method (FSM). Chapter 2 expounds the shape optimization of CFS columns: problem formulation, solution algorithms, and optimization results are presented. Chapter 3 is a description of a finite element modeling technique for CFS-framed buildings with the CFS-NEES test building used as an example. Open source software OpenSees is the simulation tool used for the building level simulation in this research. Modeling of building components, like shear walls, gravity walls and semi-rigid diaphragms, is specifically discussed in Chapter 3. Chapter 4 presents the comparison of seismic response between calibrated three-dimensional finite element models and full scale shaking table tests. Chapter 5 is a summary of simulation results for the building scale finite element models at various fidelity levels and construction phases. Performance measurements such as base shear, story drift, and hold down axial force are utilized in the comparison across models at different phases. Chapter 6 is an extensive discussion of incremental dynamic analysis results for selected building scale models of the CFS-NEES building. The relationship between excitation intensity measure and damage measure is studied. Fragility curves and

proposed drift limits are constructed to aid future improvements in the performance-based seismic design of CFS-framed buildings. Finally, Chapter 7 concludes the research findings and explores areas of future research. The detailed description and simulation results of the building scale CFS-NEES model at various phases are attached to the thesis as appendices.

Cold-formed steel (CFS) is widely used in many countries as both structural and non-structural members (Schafer 2011). Several desirable features, like high-strength to weight ratio, low shipping cost and easiness of erection, expedite the usage of CFS members as wall tracks, joists, headers, jamb studs, chord studs, field studs and others. Member cross-sections are manufactured by using roll-forming machines to bend thin steel sheet into useful shapes under room temperature. A construction site and common CFS member cross-sections are shown in Figure 1-1 (Peterman 2014). Typical section depth ranges from approximately 75 to 300 mm (3 to 12 in.) and typical thicknesses ranges from 0.478 to 0.792 mm (0.0188 to 0.0312 in.) for non-structural members and from 0.879 to 3.154 mm (0.0346 to 0.1242 in.) for structural members (Steel Framing Industry Association 2011).

Figure 1-1: At left, photograph of stick-style construction for a cold-formed steel-framed hotel in Buckhead, Georgia (photo credit: Don Allen, DSi Engineering). At right, drawing of common CFS cross-sections, highlighting the two most used: zee and lipped channel (Peterman 2014)

Computational and experimental study of structures can be categorized into three scale levels: member level, subsystem level, and system level. In terms of theoretical and computational mechanics, even at the member level, several fascinating problems of CFS structures exist.

An important geometrical feature of CFS members as a thin-walled rectilinear one that determines its structural mechanical behavior, as discussed by Slivker (Slivker 2007), is that the thickness of the member, the perimeter of the cross-section, and the member's length are substantially different in their orders of magnitude. As a result, the treatment of mechanics of thin-walled members has inherent link to beam and shell mechanics.

As an example of the unusual nature of thin-walled members consider the behavior of thin-walled members under torque. For such members under torque the primary resistance evolve from the cross-section warping (with some exceptions, see Slivker

(Slivker 2007)) and the linear relationship between the first derivative of twist angle and internal torque established by St. Venant is no longer valid. For open cross-sections, Vlasov's theory demonstrates that warping torque, which is proportional to the third derivative of twist angle, should be added to St. Venant torque. McGuire et al. (McGuire et al. 2000) provide numerical examples showing that warping torque can be dominant, especially when warping is restrained. For details of Vlasov's theory, including basic assumptions, equilibrium equations and variation formulations, see Slivker (Slivker 2007).

Also due to its combined properties of thin shells and slender bars, thin-walled members are subjected to buckling, viz. instability of equilibrium states. Moreover, there are three types of buckling modes, local, distortional and global (Schafer 2008) of primary importance. In terms of mode shapes and cross-section behavior, local buckling involves the buckling of portions of the cross-section, like plate buckling with certain boundary conditions while global buckling is a stability problem of beams and columns with no deformation of the cross-section. Distortional buckling lies in between with the buckling of webs and rotation of flanges. Also, half-wavelengths of these primary buckling modes follow an ascending order from local, to distortional to global modes.

Theoretical studies of structural stability problems can be performed from at least two perspectives (Timoshenko and Gere 2009; Slivker 2007). One is, if an equilibrium state can be recovered once a small perturbation is added. The other is, if the second derivative (or partial derivatives) of the potential energy functional is positive at a given stationary

point. However, they both require the formulation of stress and strain, force and deformation of a deformed configuration, and the critical load as the solution of an eigenvalue problem is always sought. Consequently, the second order effect or geometric nonlinearity is always paramount.

With the fast development of computers, numerical methods have become powerful tools for solving problems in structural engineering and engineering mechanics. The finite element method (FEM) (Cook et al. 2007) is the most widely studied and applied structural engineering simulation method. The structure needs to be discretized into a number of elements, and each element has a certain number of nodes. In the most commonly used displacement-based FEM, nodal degrees of freedom (DOF) are primal variables that are obtained by solving the system of linear algebraic equations of equilibrium formed into the global stiffness matrix, displacement and load vector of the discretized structure. In particular, solving stability problems and collapse analysis in FEM entails the formulation of a geometrical stiffness matrix and the implementation of iterative solvers such as Newton-Raphson method, quasi-Newton method, and/or arc-length method. Things can be more complicated when material nonlinearity is also present. Numerous classical treatises are available with focuses on various aspects of nonlinear FEM, e.g. Bathe (Bathe 2006), Crisfield (Crisfield 1991; Crisfield 1997) and Krenk (Krenk 2009). Finite element modeling and simulation of thin-walled members, given its aforementioned properties, can be tackled from multiple paths and has been one of the most intriguing problems of computational structural mechanics. The following sections will address three methods of modeling CFS members and modeling of CFS

structures. Usage of the finite strip method (FSM, is a special case of FEM) (Li and Schafer 2010) in column design optimization as a special case is presented in Chapter 2.

1.1 Modeling CFS members using frame finite elements

A frame (beam-column) element is a type of one-dimensional element in FEM. A straight CFS member (see Figure 1-2(a)) is modeled using one or several beam-column elements, each element usually has nodes at its ends (see Figure 1-2(b)). The member's cross-section is shrunk into a line represenation, so the geometrical and mechanical properties of the cross-section are represented by physical quantities calculated from sectional integration, like moment of inertia I and warping coefficient C_w. Typically, for three-dimensional problems, each node has six degrees of freedom (DOF), i.e. three translations and three rotations. However, to handle warping torsion using Vlasov's theory, the first derivative of twist angle should be added as the seventh nodal DOF. An introduction of this approach can be found in the book written by McGuire et al. (McGuire et al. 2000) for a displacement-based frame element.

In McGuire's formulation, (McGuire et al. 2000) the principle of virtual work is used to develop the variational form including internal and external virtual work. In the process, care should be taken about work conjugacy between stress and strain tensors when the deformation is large, making them different from engineering stress and small strain. The topic is covered in nonlinear continuum mechanics books, like Malvern (Malvern 1977) and Holzapfel (Holzapfel 2000). With kinematic assumptions, constitutive relationships (linear for elastic stability problems) and discretization of displacement field by shape

functions, the element tangent stiffness is developed as a summation of the linear stiffness matrix and the geometric stiffness matrix. An extension of this work to a beam with generic open sections is given by Conci (Conci and Gattass 1990; Conci and Gattass 1990). The work by Simo and Vu-Quoc (Simo and Vu-Quoc 1991) is similar, but expressed in more mathematical forms.

To solve for the equilibrium solution, the 'load' should be divided into several steps since the tangent stiffness taken at a given configuration is only accurate in a neighborhood of the configuration. The iterative formulation of updating the configuration from a solved load step to the immediate one right after can be total Lagrangian (TL) or update Lagrangian (UL). The difference is that TL always refers to the initial configuration as the reference of update while UL refers to latest updated configuration in the deformation process. For more details, see the work by Bathe (Bathe 2006), Crisfield (Crisfield 1991; Crisfield 1997) and Krenk (Krenk 2009). Within each load step, iterative methods, as mentioned above, still need to be implemented to solve the linear system using exact or approximate tangent stiffness matrices multiple times for each load increment. For example, McGuire et al. (McGuire et al. 2000) adopted UL in their formulation.

In the analysis of 3D structures with finite rotations, special measures should be taken in terms of solving nodal rotations. If the magnitude of rotation is infinitesimal, the 3D rotation can be regarded as a vector with three components, viz. a unit vector along the axis of rotation times the magnitude of rotation. In each load step, the increment of such infinitesimal rotation vector is solved and added directly to values of previous steps and

the resultant vector takes the form of compound rotation. However, for finite 3D rotation, such a vector is indeed a pseudo vector, which indicates the compound rotation of two consecutive finite rotations is not equal to the direct summation of two rotation 'vectors' (see Malvern (Malvern 1977) and Krenk (Krenk 2009)). Classical work on the properties of finite rotation is given by Argyris (Argyris 1982). Mathematical representation of finite rotation has several equivalent forms, including Rodrigues's formula, finite rotation matrix (Argyris 1982) and the quaternion method, etc (Crisfield 1997). Trigonometric functions are involved in the formulation and a singularity can exist in the extraction of the magnitude of rotation (Krenk 2009). Various researchers (Hsiao 1992; Hsiao et al. 1999; Hsiao and Lin 2000; Cardona and Geradin 1988; Crisfield and Moita 1996; Krenk 2009) have developed several ways to obtain the compound finite rotation of the member from incremental rotation of the nodes. Atluri and Cazzani (Atluri and Cazzani 1995) provided an extensive discussion on the role of finite rotation in computational solid mechanics.

A special approach called co-rotational formulation has found its successful use in development of nonlinear frame finite elements. The concept was first proposed by Argyris et al. (Argyris et al. 1982), as 'the natural approach' at that time. The idea is to consider the increment of the motion of an element as a combination of rigid body translation and rotation and local deformation modes of the member (Krenk 2009). Therefore, the rigid body motion is associated with the motion of local reference frames. The nodal DOF are separated into two parts: one contributes to rigid body motion and the second is related to deformation modes described in local co-rotated reference frame. A

welcoming feature is that the formulation of nonlinear stress, strain, internal force and displacement is simplified since it is generally assumed that large displacement and rotations are described within the rigid body motion. The developer can still introduce the desired level of nonlinearity into the formulation of deformation in the local frame (Krenk 2009). On the other hand, the DOF associated with local deformation modes should be transformed to full local nodal DOF and then to global nodal DOF before the element stiffness matrix in the global coordinate system can be generated, and variations of the local frame should be taken into account. To solve nonlinear equilibrium problems, the co-rotational formulation can be embedded in TL or UL in a flexible way.

The first trial of a co-rotational frame element formulation was given by Oran (Oran 1973; Oran 1973). Later on, a number of researchers developed their own co-rotational beam-column elements. Representatives of them include Crisfield (Crisfield 1990; Jelenić and Crisfield 1999), Conci (Conci and Gattass 1990), Hsiao (Hsiao 1992; Hsiao et al. 1999; Hsiao and Lin 2000), Battini (Battini and Pacoste 2002) and Krenk (Krenk 2009). Felippa and Haugen (Felippa and Haugen 2005) published a comprehensive report on a unified formulation of small-strain co-rotational finite elements. More recently, Auricchio (Auricchio et al. 2008), Garcia (Garcea et al. 2012) and esp. Santos (Santos et al. 2010; Santos et al. 2011; Santos 2012; Santos 2012) made further contribution by using implicit co-rotational transformations and mix-formulation on 3D beams.

Despite its relatively low computational cost, an inevitable difficulty with frame element formulation of thin-walled members in stability problems is the treatment of local and

distortional buckling. Since these two buckling modes are related to deformation of certain portions of the cross-section and only integrated physical quantities enter the stiffness matrix of a beam element, the influence of local and global buckling on the rigidity of frame element must be introduced. Hence, various frame elements mentioned above, although developed across more than three decades and differ in complexity, are capable of solving global buckling problems only, even if a close match to classical solutions has been achieved. A recent work by Zhang and Rasmussen (Zhang and Rasmussen 2013) incorporated reductions in cross-section properties for CFS I-shaped beams to address local and distortional buckling. However, their procedure requires a number of shell finite element or experimental analyses a priori before the tangent rigidities could be obtained as the ratios of the change of stress resultant to the change of generalized strain. Generalization of such procedure to beam-columns with arbitrary open cross-sections still requires a large amount of work. The search for other approaches to solve this problem within the realm of frame element is still a challenging research topic. A possible way of adding deformation modes of thin walled members into frame element formulation is the generalized beam theory (GBT) whose basic idea is to include a number of buckling modes in the formulation of frame element. An earlier effort of GBT in English dates back to Davies and Leach (Davies and Leach 1994; Davies et al. 1994); more recent advance is credit to Silvestre and Camotim (Silvestre and Camotim 2002; Silvestre and Camotim 2002; Silvestre and Camotim 2003) whose formulation can handle arbitrary orthotropic materials. Modeling of the CFS-framed building in this dissertation is performed using displacement-based frame element in OpenSees (McKenna 2011). The element adopts a conventional formulation of 6 DOF per node.

Member limit states including yielding and buckling are modeled implicitly using elastic-perfectly plastic material for each interal force component. Simlarly, Padilla-Llano characterizes member behavior under moment and axial load from test data and proposes his model using Pinching4 nonlinear material in OpenSees (Padilla-Llano 2015). Apart from these, analysts need to create models with higher resolution of section behavior, such as modeling the cross-section with finite strips or shell finite elements.

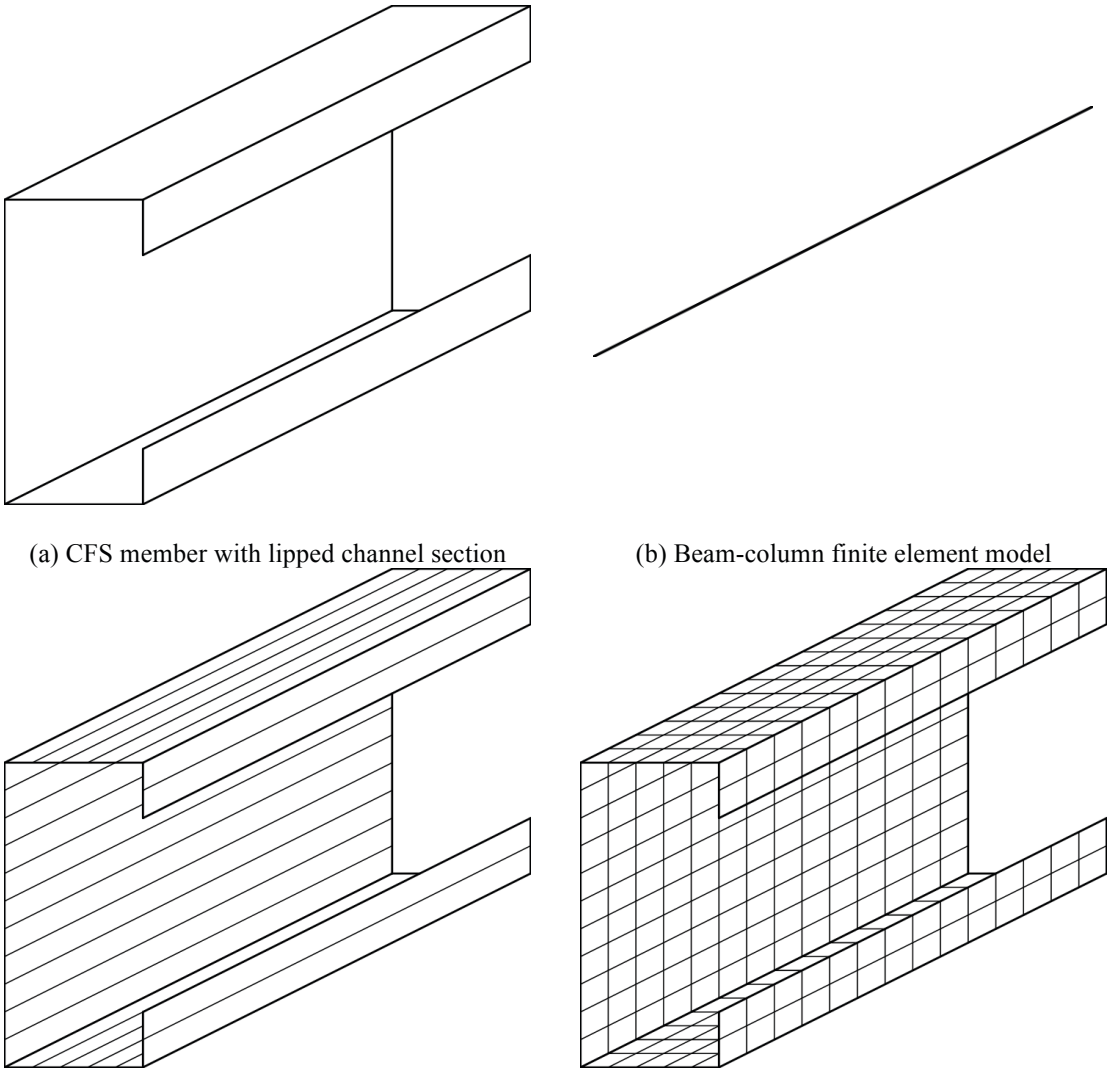

(a) CFS member with lipped channel section (b) Beam-column finite element model

(c) Finite strip model (d) Shell finite element model

Figure 1-2: A typical CFS member and finite element/strip models of the member

1.2 Modeling CFS members using finite strip method

The finite strip method (FSM) is a special version of the finite element method. As shown in Figure 1-2(c), the geometry of the member's cross-section is modeled and discretized but no further discretization in the longitudinal direction is needed. Each strip element is a long and narrow rectangle. DOF are specified at 'nodes' (strip lines) on the transverse edges and locations on the longitudinal locations of the strip. The formulation of FSM then follows the same procedure with FEM.

In terms of computational resource consumption, FSM lies between beam FEM and shell FEM in modeling CFS members. This is of great practical value, especially at an early stage of computational mechanics. The classical work by Cheung (Cheung and Tham 1997) explains the theory of FSM and its application in structural engineering with special reference to slab and box girder bridges. Even though machines are much faster than ever before, further development of FSM still shows great practical value. The work by Schafer et al. (Schafer and Ádány 2006; Li and Schafer 2010) developed the constrained finite strip method (cFSM) to more accurately determine the critical buckling load for local, distortional and global modes of a CFS member. Using three mode classification criteria, they classified deformation modes of CFS members into four categories: local, distortional, global and other (shear and transverse extension). Those criteria are formulated as a constraint matrix and then the nodal displacement vector of their finite strip element can be constructed as the multiplication between the constraint matrix and a reduced nodal displacement vector. Applying the constraint matrix in stability problems of CFS members, the critical load of specific modes can be obtained as eigenvalues in a subspace of selected modes rather than the full modal space. On the other hand, the inverse of the constraint matrix can be used to resolve a buckling mode vector into participation of various mode types, termed as 'modal identification'. The method originally works for simply-simply supported members but now it has been extended to other boundary conditions (Li and Schafer 2010; Li and Schafer 2013).

Spline finite strip method (SFSM) is another way of formulating finite strip elements. Different from trigonometric functions adopted by Schafer et al. (Schafer and Ádány 2006; Li and Schafer 2010), spline functions are used to interpolate the displacement field in longitudinal direction in SFSM. Lau and Hancock (Lau and Hancock 1986; Lau and Hancock 1989) developed their element for buckling analysis of beams, columns and plates. A recent development in SFSM and is credited to Eccher, Rasmussen and Zandonini (Eccher et al. 2008). Their element is shear deformable and is used in modeling of CFS members with perforations. Apart from solving stability problems, the element is also used in elastic nonlinear analysis of perforated thin-walled structures (Eccher et al. 2009). Furthermore, Cao and Hancock (Cao and Hancock 2012) exploited the tool to compute elastic buckling load of cold-formed channel sections in shear and provided shear buckling coefficients of the web for design.

With its increased accuracy from frame elements and less complexity than plate and shell elements, however, usage of FSM or SFSM in geometrically and materially nonlinear analysis with imperfections included (GMNIA) is not fully explored. The integration of FSM in computational software for general purposes is not frequently seen. Users may still need to use either frame elements or shell elements, or a combination of the two, to model complicated thin-walled structures in highly nonlinear problems.

1.3 Modeling CFS members using shell finite elements

Plates and shells are structural elements formed by two parallel planes/surfaces and boundaries that are able to resist transverse load. The geometry feature of plates and

shells is that the dimension in the transverse direction is at least several times smaller than dimensions in two other directions. Because the loads are generally carried in both directions, a plate/shell is considerably stiffer than a beam/arch of comparable span and thickness (Ventsel and Krauthammer 2001). The mechanics of plates and shells is more complicated than other structural elements and has been studied for centuries. The classical work by Love (Love 1888; Love 2013) first formulated the basic governing equations of thin elastic shells. Koiter verified Love's assumptions and derived a fully consistent shell theory (Koiter 1960). For more details of the theory of plates and shells, see Timoshenko and Woinowsky-Krieger (Timoshenko and Woinowsky-Krieger 1959) or a more recent text dedicated to thin plates and shells is written by Ventsel and Krauthammer (Ventsel and Krauthammer 2001). The book by Amabili (Amabili 2008) stresses nonlinear theory of plates and shells and its application in vibration and stability problems including fluid-structure interaction. Moreover, since the geometry of a shell is formed by two equidistant surfaces from its middle surface, in a rigorous description even the undeformed configuration of a shell relies on mathematical tools like tensor analysis in curvilinear coordinate systems and differential geometry. A comprehensive explanation of mathematical elasticity for plates and shells is presented by Ciarlet (Ciarlet 1988; Ciarlet 1997; Ciarlet 2000; Ciarlet 2005).

Given its intriguing mechanical properties and extensive practical use, plates and shells have been the focus of computational mechanicians since the burgeoning years of the finite element method. Numerous element formulations have been developed and archived in monographs, e.g. Zienkiewicz and Taylor (Zienkiewicz and Taylor 2005),

Chapelle and Bathe (Chapelle and Bathe 2011), and Hughes (Hughes 2000). The abovementioned co-rotational procedure has also been applied; for example, see Crisfield (Crisfield 1997).

Previous work shows that plasticity and yielding criteria, geometric imperfections, and residual stress should all be included in collapse analysis of CFS members – sometimes called a GMNIA (geometric and material nonlinear analysis on the imperfect structure) model if one follows the nomenclature of Eurocode. In addition, boundary conditions – particularly of warping displacement – should be handled carefully. Warping is important due to its significant impact on the resistance of torque. Schafer and Peköz (Schafer and Peköz 1998) measured geometric imperfections along the length of a member and quantified maxima and demonstrated a spectral representation. They modeled an idealized compression flange with modal imperfections and approximation of flexural and membrane residual stress using ABAQUS to demonstrate the impact of typical modeling assumptions. Moen et al. (Moen et al. 2008) provided an unambiguous prediction method for determination of initial residual stresses and effective plastic strains in CFS members. The method uses some simplifying structural mechanics assumptions regarding yielding, but takes into account the whole forming process including sheet coiling, uncoiling, flattening and cross-section roll-forming. Schafer, Li and Moen (Schafer et al. 2010) performed a comprehensive study on computational modeling of CFS members. The work included comparison of elastic buckling analysis results between ABAQUS shell FEM, cFSM, and theoretical solutions. In terms of collapse analysis, they considered GMNIA, performance of different shell elements,

mesh sensitivity, and impact of solvers in ABAQUS. Sensitivities of these factors and comparison between ABAQUS and ADINA were elaborated. Zeinoddini (Zeinoddini and Schafer 2012) provided a more detailed study on the simulation of geometric imperfections in CFS members. Their major focus was the utilization of random field (2D) and a new 1D modal spectra approach in characterization of imperfection and strength sensitivity to these approaches in ABAQUS shell FEM. Recently, Foroughi et al. (Foroughi et al. 2014) provided a summary and prospect of analysis and design of thin metallic shell structural members. Roughly speaking, more and more researchers and designs are in favor of GMNIA for the creation of less conservative designs as opposed to employing prescriptive codes and standards.

Apart from research needs of GMNIA on member level, relatively high computational cost limits the use of shell finite element in modeling of CFS structures. The shell FE model in Figure 1-2(d) has hundred of nodes and thousands of total DOF, a GMNIA run can sometimes take hours (or even days). With abundant data output, post processing of data can also take a great deal of time. Hence, analysts must balance between fidelity level of element types and computational cost according to their desired outcome when modeling CFS-framed structures.

1.4 Modeling of CFS-framed structures under static and dynamic loading

As mentioned in the preceding, modeling of CFS-framed structural subsystems and systems is much more complicated than modeling a single CFS member. The complexity of modeling other structural components, like sheathing panels, fasteners and hold downs,

is superimposed on the modeling of CFS members, and the interaction between these components is usually nonlinear – particular if predictions up through collapse are of interest. Despite the difficulties, there is growing interest from both academic and industrial fields in improving the fidelity of CFS structure modeling due to the switch of design methodology from limit state design to performance-based design.

Historically, the design method for CFS structures uses component level limit states design in which the internal force demands should be checked against capacities for each limit state of every member and connection. Specific limit states and internal force demands are determined by structural analysis using factored load combinations. As summarized by McGuire et al. (McGuire et al. 2000), four types of analyses are available for equilibrium problems: first-order elastic analysis, seconder-order elastic analysis, first-order inelastic analysis, and seconder-order inelastic analysis. Or the same four per Eurocode's nomenclature: linear analysis (LA), geometric nonlinear analysis (GNA), material nonlinear analysis (MNA), and geometric and material nonlinear analysis (GMNA) – which we performed on the imperfect structures becomes the aforementioned GMNIA. Second-order (geometric nonlinear) analysis includes the effects of finite deformation and inelastic analysis introduces material nonlinearity. First-order (linear) elastic analysis, being simplest one, can lead to overly conservative or unconservative designs. Today, more and more researchers and designers manage to add a certain amount of nonlinearity into the analysis for better prediction of internal forces of members.

The latest evolution in design standards, particularly for seismic design, is performance-based design. Performance-based design focuses on the performance on the system level of a given structure under certain types of loading (Yun et al. 2002). One important step with performance-based design is the characterization of the structure's performance level. The characterization is affected by uncertainties of material behavior, member size, construction process and so on. A conceptual example of the concept of performance levels for earthquake loading is illustrated in Figure 1-3.

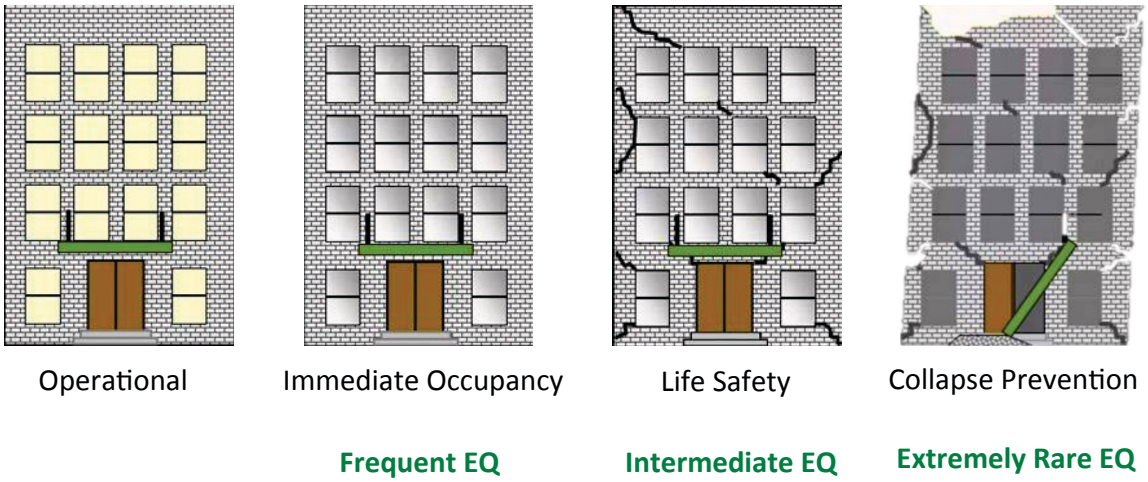

Figure 1-3: Illustration of broad definition of reliability-based performance levels (American Concrete Institute 2013)

Performance-based seismic design has been investigated in concrete and hot-rolled steel construction (Applied Technology Council 2009), and has been extended to light-framed structural systems (Landolfo et al. 2006; Filiatrault and Folz 2002; Rosowsky and Ellingwood 2002) recently. To characterize the performance level, investigations can be carried out from experimental and computational perspectives. A summary of previous experimental research and a recent study based on full scale shaking table tests of CFS-framed buildings is given by Peterman (Peterman 2014). The research presented in

chapter 3 to 7 of this dissertation is the simulation part of the George E. Brown Network for Earthquake Engineering Simulation (NEES) the project, NEESR-CR: Enabling Performance-Based Seismic Design of Multi-Story Cold-Formed Steel Structures (or CFS-NEES for short). The aim of this research is to enable the use of modern computational tools in modeling of CFS-framed buildings and to study the system level behavior under seismic loading. Together with experimental efforts, the intended research outcomes are an ability to characterize the performance of CFS-framed buildings more thoroughly and offer insights for design improvement.

Historically, research in high-fidelity computational modeling of CFS-framed structure is less reported than its experimental counterpart. Cold-formed steel design and construction is analogous to wood-framed structures in that they are both repetitively framed and share common terminology. The research conducted by van de Lindt et al. known as the NEESwood project contributed greatly to the development of performance-based seismic design criteria for wood structures. In the NEESWood simulation effort, they reviewed the modeling of wood shear walls as the major lateral force resisting system (LFRS) (van de Lindt 2004). After shaking table tests, they simulated three-dimensional seismic response of a full-scale light-frame wood building using SAPWood and compared their numerical predictions with test results (van de Lindt et al. 2010). In their models, horizontal hysteretic effect of wall elements, vertical rocking/uplift and coupled shear-bending effect are present in consideration of vertical excitation and vertical stiffness components (such as hold downs) of the test building. Furthermore, Christovasilis et al. (Christovasilis et al. 2009) performed incremental dynamic analysis

(IDA) of wood frame buildings. Their SAWS model was a degenerated planar model composed of a rigid diaphragm and a number of nonlinear spring elements representing the shear walls as condensed DOF. They ignored P-Δ effects, based on the assumptions that it is not expected to become significant until near global instability for low-rise short period wood buildings supporting light gravity loads. IDA requires a number of nonlinear history analyses of a certain structure under a group of ground motions with various scale factors (Vamvatsikos and Cornell 2002). The results of IDA are post-processed for performance evaluation and design improvement. More details are available in Chapter 6.

For CFS-framed structures, the effort of creating high-fidelity FE models started from subsystems of buildings. Leng et al. (Leng et al. 2012; Leng et al. 2013) modeled CFS-framed shear walls and oriented strand board (OSB) as elastic frame elements with nonlinear diagonal bracings and utilized a rigid diaphragm to include their interplay in a three-dimensional building model using OpenSees (McKenna 2011). Shamim and Rogers (Shamim and Rogers 2012) used a similar logic to model steel sheet shear walls, but their pattern of bracing in the shear wall models is different. Yu et al. (Yu et al. 2014) followed Leng's methodology and studied shear walls sheathed with corrugated steel sheets. Martínez-Martínez and Xu (Martínez-Martínez and Xu 2011) developed a sixteen-node shell element that accounts for the properties of the studs and sheathing and each shear wall panel was modeled by one shell element.

It can be observed that current high-fidelity FE models of CFS-framed structures still cannot computationally afford to use a large number of shell elements to model CFS

studs, tracks and sheathing panels. A trial in that direction by modeling a CFS-framed shear wall assembly using shell element of ABAQUS is reported by Bian et al. (Bian et al. 2014). Geometric and material nonlinearity is considered in a static collapse analysis and the model is still under refinement. Chatterjee et al (Chatterjee et al. 2014) modeled a CFS-framed diaphragm with OSB sheathing using ABAQUS. Joists and tracks are modeled as shell elements with reduced integration. OSB board and steel framing are isotropic and linear-elastic (in published work) and the objective is to employ the model for system reliability analysis of CFS buildings. Buonopane et al. (Buonopane et al. 2014; Buonopane et al. 2015) developed a method to model CFS-framed shear walls with fasteners as nonlinear springs and the sheathing panel as rigid diaphragms in OpenSees. The response curves of fastener elements are obtained from test results by Peterman (Peterman and Schafer 2013; Peterman et al. 2014) or similar. Bian (Bian et al. 2014; Bian et al. 2015) adopted this methodology to model shear walls with fasteners, ledger, and horizontal seams and favorably compared the results with cyclic loading tests conducted by Liu (Liu et al. 2012; Liu et al. 2014). Li et al. (Li et al. 2014) modeled the seismic behavior of a CFS-framed building in SAP2000 in comparison with their tests. They proposed a refined numerical model of shear walls similar to Bian's (Bian et al. 2014; Bian et al. 2015) and a simplified one similar to Leng's (Leng et al. 2012; Leng et al. 2013); their 3D model is a mixture of both types.

Since IDA requires a large number (at least several hundred) of nonlinear time history analyses, it is even more difficult for researchers to run this type of analysis on high-fidelity FE models. The planar SAWS model created by Christovasilis et al.

(Christovasilis et al. 2009) is simplified specifically due to the demands of IDA. Later, Christovasilis et al. (Christovasilis et al. 2014) modeled a five-story residential light-frame wood building and modeled each shear wall with nonlinear springs. They performed IDA and discussed the selection and scaling of ground motions for fragility analysis. The simulation model in this research is 3D, but the building components other than shear walls are given little attention. Dubina and his colleagues performed cold-formed steel framed wood and plaster sheathed shear wall tests (Fülöp and Dubina 2004) and developed nonlinear numerical equivalent models (phenomenological models) considering observed pinching and strength degradation from tests (Fülöp and Dubina 2004). They utilized these simulation results in the evaluation of building seismic performance and proposed full seismic design procedures (Dubina 2008). Fiorino et al. (Fiorino et al. 2012) carried out an extensive parametric nonlinear dynamic analysis performed on sheathing-braced cold-formed steel structural systems with another type of nonlinear material model that handles pinching and strength degradation. Furthermore, they evaluated the building's performance, proposed a design procedure and provided a case study. In some ways this thesis research follows a similar path to reach our insights based on the current status of seismic design of CFS structures in North America (Chapter 7). The most important difference in the approach adopted here is the explicit consideration of elements in a building beyond the shear walls that contribute to the seismic resistance – and incorporating those elements into simulation models of CFS-framed buildings.

In the following chapters, complete development of OpenSees models appropriate for CFS-framed buildings are explained. The refined model incorporates shear walls with subpanels, gravity walls and semi-rigid diaphragms (see Figure 1-4). Nonlinear behavior is characterized and included for shear walls, gravity walls, interior walls, and semi-rigid floor and roof diaphragms. CFS studs and hold downs are modeled on the basis of design equations and subsystem level tests. Mass and gravity load distribution are also refined beyond typical assumptons. Time history analysis results of calibrated models are compared with outputs of full scale shaking table tests. Simulation results across models at multiple stages are compared and sensitivities of results to modeling considerations are extracted. Preliminary guidelines for modeling seismic behavior of CFS-framed buildings are proposed thereafter. IDA analysis of 3D high-fidelity FE models helps to develop a statistical perspective of the seismic behavior of the building. Observations from research findings are concluded and intended to shed light on potential code modifications for performance-based seismic design of CFS-framed buildings.

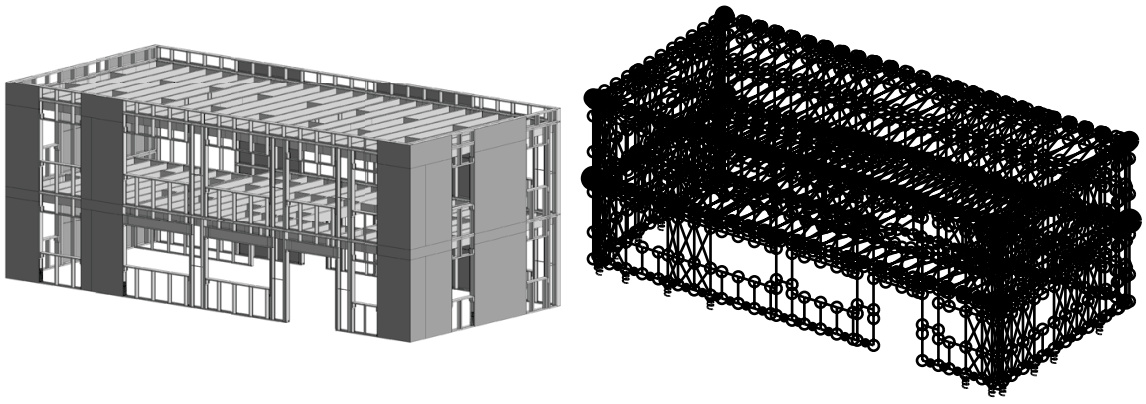

(a) CFS-NEES building, Phase 1 (b) FEM model of the CFS-NEES building, Phase 1

Figure 1-4: Illustration of the CFS-NEES building, Phase 1 and its FEM model

Chapter 2: Shape Optimization of Cold-formed Steel Columns

Shape optimization of cold-formed steel columns for maximum capacity is presented in this chapter as a special case of using the finite strip method in CFS member simulation. Structural optimization is the search for a structural design that is optimal for a certain design criterion while satisfying other criteria. It is a specific case of general optimization problems in mathematics. A well-defined optimization problem should include design variables and usually one objective function often with constraints formulated using design variables. In terms of structural optimization, objective functions in general can be the minimization of compliance, the minimization of weight or the maximization of capacity. It is customary to formulate the objective as a minimization. Multi-objective optimization problems also exist. Equality and inequality constraints developed from design, manufacturability and end-use requirements normally make constrained optimization problems more difficult to solve than unconstrained problems. Another important feature of structural optimization is that it usually requires solving equilibrium or stability problems of the structure every time the objective function needs to be evaluated. Accordingly, structural optimization problems are usually simulation-based and all methods covered in Chapter 1 can potentially be integrated into the optimization code. However, objective function evaluation can be computationally costly because of the simulation involved. The book by Arora (Arora 2004) expounds on the application of optimization theory in design problems in detail.

Typically, structural optimization incorporates dimension optimization, shape optimization, and topology optimization. The difference is that dimension optimization operates on a fixed topology by adjusting characteristic dimensions of the topology only while topology optimization has the most flexibility for developing an optimized configuration within a given domain of material - connectivity can be modified by introducing voids. Shape optimization lies in between: it requires a shape generation subroutine but may not be able to change the topology drastically. In dimension optimization, design variables are usually characteristic dimension(s) of the dictated topology and should be positive real numbers within certain bounds. For topology optimization, design variables ideally can be zero (void) or one (solid) for a given discretized domain. However, to allow the use of gradient-based method, which requires continuity and differentiability, design variables can be treated as a continuous number between zero and one in some topology optimization implementations. This treatment can also help to eliminate certain unrealistic configurations, like checkerboard patterns common in classic 2D minimum compliance topology optimization problems. A classic monograph on topology optimization is presented by Bendsøe and Sigmund (Bendsoe and Sigmund 2003). For shape optimization, design variables are parameters that can uniquely define the shape, and depend on the shape generation algorithm.

Search algorithms for optimal designs generally fall into two categories, gradient-based and stochastic search algorithms. Gradient-based algorithms have solid mathematical background in that Karush-Kuhn-Tucker (KKT) conditions are necessary conditions for local minimal solutions (under certain conditions it can also be sufficient). However,

solving the KKT conditions directly is usually cumbersome, so practical algorithms aim at decreasing the objective function value step by step instead. For unconstrained optimization, line search and trust region methods are most widely used. For more complicated constrained optimization, penalty methods and projection methods can be utilized. The duality theory can also be a powerful tool, by reformulating the primal problem in the dual space and under some conditions, the correspondent dual function is always concave and in many cases is much easier to solve. Nevertheless, all of these methods require the gradient of a certain function (typically the objective function) with respect to its variables. Closed-form expressions of the gradient are not guaranteed to exist. Further, finite difference approximations of the gradient can be computationally costly for simulation-based optimization due to the large number of required objective function evaluations, which is usually the case for structural optimization. For a theoretical background in functional analysis, see Luenberger (Luenberger 1969). For numerical optimization theory and description of algorithms, see Nocedal and Wright (Nocedal and Wright 2006).

Stochastic search algorithms are designed for problems with inherent random noise or deterministic problems solved by injected randomness. In structural optimization, these are problems with uncertainties in the design variables or problems where random perturbations are added to deterministic design variables to perform the search. Biases are introduced into the search in favor of designs offering better performance. A welcoming feature of stochastic search algorithms is that it can carry out a broad search of the design space and avoid local minima. However, there is no guarantee that an optimum solution

is found and the algorithm has to be run multiple times to give some level of confidence that the arrived solutions are robust. To handle constraints, penalties can be applied on designs that violate constraints. Also, for constraints that are difficult to formulate explicitly, a true/false check is often straightforward to form. Designs that fail the check can be penalized on their objective function values so they will be ruled out by the algorithm. In constrained optimization of this research, we treat the constraints in another way: randomly perturbed designs are checked against constraints, and only those that pass the check enter the stage of objective function evaluation. Stochastic search can be applied on one design or a population of them. Simulated annealing (SA) and genetic algorithms (GA) are popular stochastic search algorithms. A monograph devoted to stochastic search and optimization is from Spall (Spall 2003).

For design optimization of cold-formed steel structures, past research has been basically carried out on a member level, mostly columns under axial compression. Given that buckling is an important limit state for CFS members, the method used for determining nominal axial capacity, P_n, (e.g., from design specifications or from analysis, or from combinations thereof) can have a significant influence on the formulation of optimization problems. Classical design procedure adopted the long-established effective width method (American Iron and Steel Institute 2007), which requires reducing a plate under nonlinear longitudinal stress into a plate with effective width under constant stress. However, the process can be tedious and cumbersome for complicated cross-sections. The Direct Strength Method (DSM, see Appendix 1 of AISI specification (American Iron and Steel Institute 2007)) is much simpler, and requires only the critical load in local

(P_{crl}), distortional (P_{crd}), and global buckling (P_{cre}), and the load at yield (P_y). Design equations of DSM are of simple forms of elementary functions and can be coded easily into simulation-based optimization programs. In this research, the open source finite strip method software CUFSM developed by Schafer et al. (Schafer et al. 2006; Schafer 2010) was used to compute P_{crl}, P_{crd}, and P_{cre}.

Previous researchers have applied various combinations of strength evaluation criterion from design codes and search algorithms in shape optimization of CFS members. For example, in an early work from Seaburg and Salmon (Seaburg and Salmon 1971) they apply a gradient-based steepest descent method to explore the dimensions of hat sections with the effective width method by the AISI Specification (American Iron and Steel Institute 1968). Tran and Li (Tran and Li 2006) solved the optimization of a lipped channel beam using a trust-region method; various failure modes in their consideration were from the British code BS 5950-5 (British Standard Institution 1998) and Eurocode (EuroCode-3 1996). Tian and Lu (Tian and Lu 2004) performed optimization of cross-section dimensions of channel columns with and without lips utilizing sequential quadratic programming according to BS 5950-5 (British Standard Institution 1998). In terms of heuristic methods, Adeli et al. developed a computational neural network model (Adeli and Karim 1997) and applied it to the optimization of CFS beams with hat, I and Z sections (Karim and Adeli 1999) sections following AISI Allowable Strength Design (ASD) (American Iron and Steel Institute 1989) and Load and Resistance Factor Design (LRFD) specifications (American Iron and Steel Institute 1991), and space trusses with lipped channel sections (Tashakori and Adeli 2002) according to AISI ASD specification

(American Iron and Steel Institute 1996). Lu (Lu 2003) optimized Z-section dimensions under the effective width design of Eurocode 3 (EuroCode-3 1996) with CUFSM as the simulation tool. Lee et al. (Lee et al. 2005; Lee et al. 2006) modified GA to search for optimized channel cross-section dimensions of cold-formed steel columns under axial compression and beams under uniformly distributed loads. Kripka et al. (Chamberlain Pravia and Kripka 2012; Kripka and Martin 2013) published their effort using SA to optimize the dimension of a lipped channel (C-section) column following the effective width method in the AISI 2007 (American Iron and Steel Institute 2007) specification. All of these works are dimension optimization of a predetermined cross-section (i.e. adjusting web depth, flange width, lip lengths, etc.) with constraints on the member's capacity. Most of these efforts searched for minimum weight designs, except for Lu who maximized load efficiency.

Shape optimization of CFS members can be traced back to Liu et al. (Liu et al. 2004). They maximized the capacity of CFS columns by applying Bayesian classification trees as the optimizer and used DSM and CUFSM to evaluate axial capacity P_n. Kolcu et al. (Kolcu et al. 2010) combined Mindlin-Reissner finite strips and sequential quadratic programming in maximization of critical load P_{cr} of CFS members. Gilbert et al. developed 'self-shape optimization' based on floating-point type GA (Gilbert et al. 2012) and applied the algorithm in CFS columns (Gilbert et al. 2012) with CUFSM for buckling analysis. Recently, they also preliminarily introduced manufacturing rules as constraints into their algorithm (Wang et al. 2014; Wang et al. 2014). Moharrami et al. (Moharrami et al. 2014) and Gargari et al. (Gargari et al. 2013) used GA and a recent version of

CUFSM to maximize the capacity of CFS columns with consideration of general boundary conditions other than simply-simply supports. Franco et al. (Franco et al. 2014) designed a MATLAB code with GUI using shape grammar to generate cross-sections, DSM and CUFSM to evaluate capacity, and GA to optimize design of CFS columns and beams.

The work presented herein is a summary of my systematic study on shape optimization of CFS columns in search for cross-sections that can maximize the axial capacity with a given steel sheet. The research was carried out in two steps. Firstly, unconstrained optimization problem was investigated (Leng et al. 2011). For the purpose of better comparison, the same perimeter, thickness and material properties of the steel sheet with Liu et al. (Liu et al. 2004) was utilized. The cross-section is discretized by equal width finite strip elements in CUFSM. Relative turn-angles between adjacent strips form the design variable vector. All open sections are eligible for capacity evaluation of P_n; only those with self-intersection are eliminated after a true/false design check. In the process, the performance of gradient-based steepest descent method (SD), SA and GA were compared. Several novel cross-sections have been identified for intermediate length and long length columns. For 4 ft (1.22 m) columns, unsymmetrical 'Bobby pin' sections and 'circular' sections are observed to have a capacity growth of more than 140% from a commercial lipped channel section. For 16 ft (4.88 m) columns, point symmetric squashed 'S' sections have a capacity growth more than 200% while 'Bobby pin' and 'circular' sections still outperform lipped channel section by 170% and 151%. SA and

GA are capable of finding sections that perform best globally while SD is highly dependent on initial design and can only find local optimal designs.

Next, end-use and manufacturability constraints were introduced so that optimized cross-sections that are more readily fabricated and useful in practice can be explored. The first trial included the introduction of several end-use constraints. Cross-section discretization and design variable formulation are the same as unconstrained optimization, but the strip width is much smaller, representing the case of a large number of rollers in the forming process (Leng et al. 2012). The case of a limited number of rollers was taken into account later on as a reflection of fabrication cost. Design variables are reformulated to allow for variable finite strip widths. The code uses SA as the algorithm to perform stochastic search on the constrained design space. The resulting optimized cross-sections include singly symmetric 'Σ' like sections for short (2 ft, (0.61 m)) and intermediate length (4 ft, (1.22 m)) columns and point symmetric squashed 'S' like sections for long (16 ft, (4.88 m)) columns. These optimized shapes offer 50% to over 200% improvement in P_n over a reference lipped channel section (with the same amont of material), indicating that significant enhancements can be obtained through cross-section optimization without loss of manufacturability or geometric end-use requirements (Leng et al. 2013; Leng et al. 2014). The generalized optimization framework of constrained optimization of CFS columns can potentially be integrated into system optimization of cold-formed steel buildings and is a point of great interest for future work (the work by Saka et al. (Saka et al. 2015) is an example of optimizing member layout of a building framed with commercial CFS members).

2.1 General formulation of CFS column shape optimization problem

2.1.1 Design variable formulation of unconstrained optimization problem

The design objective is to maximize the capacity of a cold-formed steel column made of a fixed width coil of sheet steel. The cross-section of the column is discretized into narrow strips of equal width along the longitudinal direction (Leng et al. 2011). Cross section designs are encoded into a vector of relative turn-angles defined for every two adjacent elements. Turn-angles are locations of potential folding during the roll forming process. The design variable is defined as a vector of turn-angles

$$\boldsymbol{\theta} = \left[\theta_1, \theta_2 \cdots \theta_n\right]^T \tag{2-1}$$

where n is the number of strips in the cross-section and the width of each strip is the width of steel sheet divided by n. The turn-angle θ_i is defined as the change in angle between the axes of strips i and i-1, measured counter-clockwise (see Figure 2-1(a)[1]).

[1] All figures and tables in Chapter 2 are reprinted from the author's published journal articles. Figure 2-1, Figure 2-6, Figure 2-7, Figure 2-10 to Figure 2-19, Table 2-1 and Table 2-2 are reprinted from Thin-Walled Structures, 49(12), Leng, J., Guest, J. K., and Schafer, B. W., Shape optimization of cold-formed steel columns, 1492-1503, Copyright (2011), with permission from Elsevier. Figure 2-2 to Figure 2-5, Figure 2-8, Figure 2-9, Figure 2-20 to Figure 2-40 and Table 2-3 to Table 2-10 are reprinted from Thin-Walled Structures, 85, Leng, J., Li, Z., Guest, J. K., and Schafer, B. W., Shape optimization of cold-formed steel columns with fabrication and geometric end-use constraints, 271-290, Copyright (2014), with permission from Elsevier.

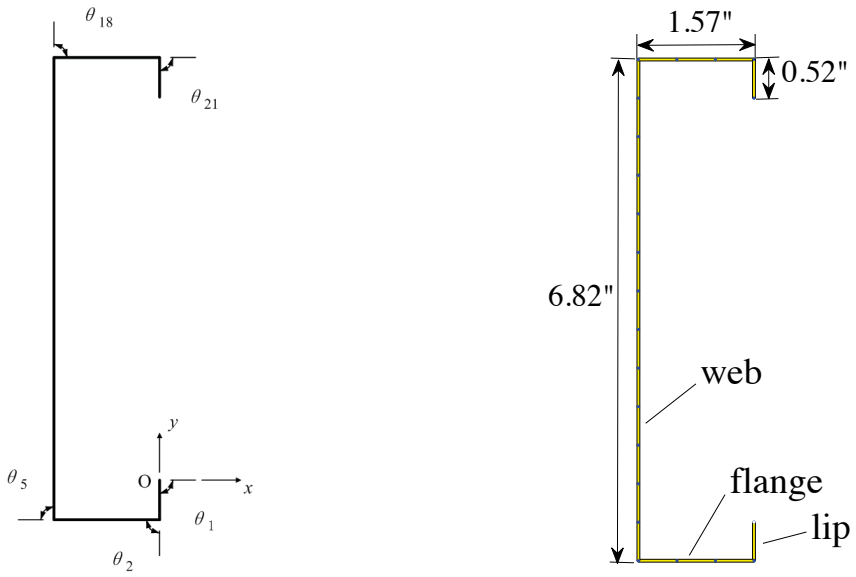

(a) Non-zero turn-angles of lipped channel section (b) Dimensions and mesh of lipped channel section

Figure 2-1: Lipped channel section and design variables for unconstrained optimization (Leng et al. 2011)

In the case of θ_1, the angle is measured from the global x-axis to the axis of the first strip. Further, θ_1 is used as a reference angle (all other angles are relative to θ_1) and thus held fixed leaving the independent design variables, denoted as $\boldsymbol{x} = \left[\theta_2, \theta_3 \cdots \theta_n\right]^T$. The only constraint in this formulation is that overlap of strips is not permitted, which is physically impossible. Every turn-angle is normalized within the interval $[-\pi, \pi)$. For a commercial lipped channel section discretized into twenty-one strips (n=21); the mesh and dimension are shown in Figure 2-1(b).

2.1.2 Design variable formulation of constrained optimization problem

At the stage of constrianed shape optimization, we introduce three sets of constraints related to end-use requirements: (i) symmetry and anti-symmetry, (ii) parallel flanges and flange, web, and lip widths, and (iii) utility pass-through; cross-sections are also required to remain open. These constraints restrict the design space and search domain of the

optimization, but reflect typical structural engineering needs in practice (Leng et al. 2013; Leng et al. 2014). Design variable formulation is addjusted to account for unique features of these constraints.

From the perspective of manufacturing, each non-zero turn-angle, or fold, requires a roller in the forming process. In unconstrained optimization, every node is a possible location of roll-forming except for the last one (total number of nodes is n+1), i.e. the maximum number of rollers n_{roll} to form a section was n. The actual number of rollers is typically less than this, as some turn-angles have zero magnitude (see Figure 2-1(a)).

In this work, we consider two cases: (1) the number of rollers is unlimited, represented by a large finite number (as in the unconstrained case), and (2) the number of rollers is constrained to an even number ranging from four to twelve (Leng et al. 2012; Leng et al. 2013; Leng et al. 2014). Similar to the formulation for unconstrained optimization, the design variable vector of a large finite number of rollers is also composed of turn-angles between equal width strips (Eqn. (2-1)) numbered in sequence from lip edge to lip edge (Figure 2-2(a)). The difference from the formulation for unconstrained optimization is that the first turn-angle, θ_1 measured with respect to x-axis, is no longer fixed as a reference angle. This change is necessary to enable consideration of straight, parallel flanges (as described later). For instance, all twenty turn-angles in Figure 2-1(a) are variables.

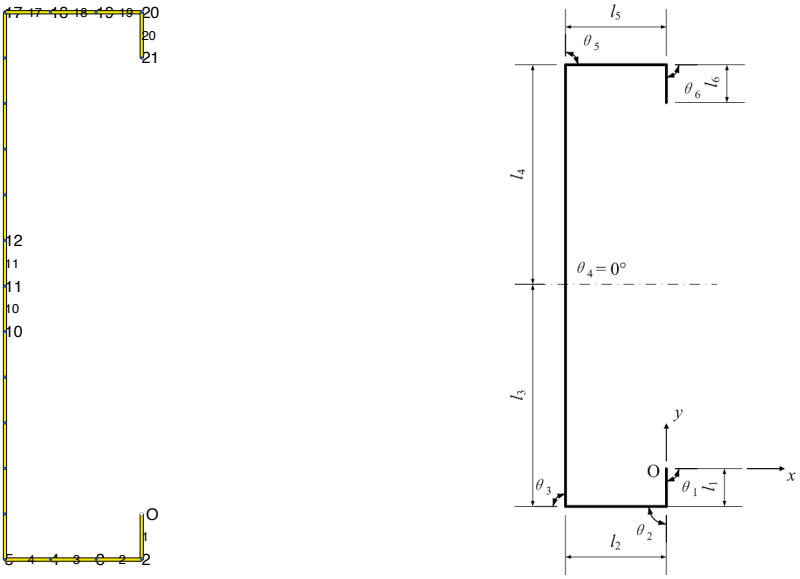

(a) End-use constraints only (b) End-use and manufacturing constraints

Figure 2-2: Design variables for constrained shape optimization (Leng et al. 2014)

To achieve the latter, a coarser discretization for the design than the analysis is adopted, with $n=n_{roll}+2$. As illustrated in Figure 2-2(b), the number of rollers is four so the design space is discretized into six finite strips (of non-uniform length). The length (cross-section width) of all strips are contained in the length vector

$$l = \left[l_1, l_2, \cdots l_n \right]^T \tag{2-2}$$

The summation of all strip widths should be equal to the given steel coil width, c, or the perimeter of the section:

$$c = \sum_{i=1}^{n} l_i \tag{2-3}$$

For the purpose of imposing end-use constraints, such as straight parallel flanges, the finite strips should be identified as belonging to the lips, flanges, or web of the cross-

section. This is achieved by identifying the number of strips in each of these components. This work also considers symmetric and anti-symmetric sections as a constraint, so the number of strips on these components for only half of the cross-section is given by

$$N = \left[n_l, n_f, n_w \right]^T \tag{2-4}$$

where n_l and n_f are the number of strips representing the lip and flange, respectively, and n_w is the number of strips representing half of the web. Note that this requires a node to be located at the midpoint of the web. Each of the entries in N must be greater than or equal to one, and their sum must equal $n/2$. The channel in Figure 2-2(a), for example, has n_l=1, n_f=3, and n_w=6.

An arbitrary strip i is identified as belonging to the set of lip strips L, the set of flange strips F, or set of web strips W in the half cross-section by the following expression:

$$\begin{aligned} &i \in L \; if \; i \le n_l \\ &i \in F \; if \; n_l + 1 \le i \le n_l + n_f \\ &i \in W \; otherwise \end{aligned} \tag{2-5}$$

The independent design variables for the constrained optimization problem are different for the two considered cases. Due to symmetry/anti-symmetry, the design variables only need to be defined on the half-section.

For the first case where the number of rollers is 'unlimited', the half cross-section is discretized into n finite strips of equal width and the independent design variable vector $\boldsymbol{x}$ is

$$\boldsymbol{x} = \left[n_l, n_f, \theta_1, \theta_2, \cdots \theta_n \right]^T \tag{2-6}$$

which we note is generally the same with the unconstrained optimization case except for the first two variables that identify the number of strips on the lip and flange.

For the second case where the number of rollers is limited to an even number n_{roll}, the half cross-section is discretized into $n=(n_{roll}/2)+1$ finite strips of variable width and the independent design variable vector $\boldsymbol{x}$ is

$$\boldsymbol{x} = \left[n_l, l_1, l_2, \cdots, l_{n-1}, \theta_1, \theta_2, \cdots \theta_n \right]^T \tag{2-7}$$

Note that n_l is the only independent variable on the number of strips, since the parallel flange constraint is achieved by using a single strip to model the flange (n_f=1), as detailed in Section (a). According to Eqn. (2-3), the sum of the widths must be equal to c and that the final strip width is computed using:

$$l_n = c/2 - \sum_{i=1}^{n-1} l_i \tag{2-8}$$

Although it appears that Eqn. (2-8) can be negative, bound constraints on the lips, flanges and web ensure that l_n remains positive (see Section (a)).

If without the restriction of symmetry and anti-symmetry, n would simply refer to the number of strips in the full cross-section and additional n_l and n_f variables are needed to account for each set of lips and flanges.

2.1.3 Strength analysis and design optimization formulation

For any eligible cross-section design, CUFSM is utilized to compute the local, distortional, and global (Euler) critical buckling loads: P_{crl}, P_{crd} and P_{cre} as the input of DSM equations (Schafer 2008) for capacity evaluation. Heuristics were used to find local minima on the signature curve of CUFSM for local and distortional modes, i.e. P_{crl} and P_{crd}. We track a reference length to determine P_{crl} and P_{crd} when distinct local optima on the signature curve for these modes are not available, as detailed in (Leng et al. 2011). In the case of constrained optimization with limited number of rollers (4 to 12), the finite strip discretization is further refined prior to the elastic buckling analysis to make sure enough accuracy is achieved. The final nominal axial strength of the column is then determined by the minimum

$$P_n = \min\left\{P_{nl}, P_{nd}, P_{ne}\right\} \tag{2-9}$$

Where P_{nl}, P_{nd}, and P_{ne} are the local, distortional, and global buckling strength as determined from DSM employing the elastic buckling loads and slenderness ratios.

Design equations of DSM are available in the AISI specifications (American Iron and Steel Institute 2007). It is customary that optimization problems are formulated as a minimization, and the objective of maximizing P_n is expressed as

$$\begin{aligned} &\min\left(-P_n\left(\boldsymbol{x}\right)\right) \\ &such\,that: g_i\left(\boldsymbol{x}\right) \le 0\ for\ i = 1,\cdots,N \end{aligned} \tag{2-10}$$

where N is the number of manufacturing constraints, expressed through constraint functions g_i. The form of constraints may vary, as detailed in the following section.

To be clear with the form of P_n as a function of P_{cr}, the DSM design equation for columns are included (Schafer 2008):

$$\begin{cases} P_{ne} = (0.658^{\lambda_c^2})P_y \ \ for\ \lambda_c \le 1.5 \\ P_{ne} = (0.877/\lambda_c^2)P_y \ \ for\ \lambda_c > 1.5 \end{cases} \tag{2-11}$$

$$\begin{cases} P_{nl} = P_{ne} \ \ for\ \lambda_l \le 0.776 \\ P_{nl} = \left[1 - 0.15\left(\dfrac{P_{crl}}{P_{ne}}\right)^{0.4}\right]\left(\dfrac{P_{crl}}{P_{ne}}\right)^{0.4} P_{ne} \ \ for\ \lambda_l > 0.776 \end{cases} \tag{2-12}$$

$$\begin{cases} P_{nd} = P_y \ \ for\ \lambda_d \le 0.561 \\ P_{nd} = \left[1 - 0.25\left(\dfrac{P_{crd}}{P_y}\right)^{0.6}\right]\left(\dfrac{P_{crd}}{P_y}\right)^{0.6} P_y \ \ for\ \lambda_d > 0.561 \end{cases} \tag{2-13}$$

where $\lambda_c = \sqrt{P_y / P_{cre}}$, $\lambda_l = \sqrt{P_{ne} / P_{crl}}$ and $\lambda_d = \sqrt{P_y / P_{crd}}$ are column slenderness, local–global slenderness and distortional slenderness and $P_y = A_g F_y$ is the squash load.

2.2 Formulation of end-use and manufacturing constraints

The end-use and manufacturing constraints appearing in Eqn. (2-10) are detailed in this section (Leng et al. 2012; Leng et al. 2013; Leng et al. 2014). We first introduce three sets of constraints related to end-use requirements: (i) symmetry and anti-symmetry, (ii) parallel flanges and flange, web, and lip widths, and (iii) utility pass-through. Cross-sections are also required to remain open as in unconstrained optimization. These constraints require that geometrical properties be feasible before the cross-section is evaluated for strength. Although the design space and search domain of the optimization is restricted, such constraints reflect typical structural engineering needs in practice. For example, constraint (ii) defines three portions of a practical cross-section (flanges, lips, and web) and restricts their lengths for installation of sheathing/covering to form a wall system. Modifications to include the limit on number of rollers as manufacturing constraints are presented subsequently. End-use and manufacturing constraints are implemented in a stochastic search (SA) algorithm, as detailed in Section 2.3.2.

2.2.1 End-use constraints

(a) Symmetry and Anti-symmetry

The first end-use constraint is the condition of symmetry/anti-symmetry as a natural consideration for many engineering applications. As mentioned above, it indicates that independent design variables in $\boldsymbol{x}$ correspond to half of the cross-section, and employing symmetry/anti-symmetry mapping can generate the remaining half of the section.

Given n strips in the half cross-section and $2n$ total strips, the mapping for anti-symmetric sections is illustrated in Figure 2-3(a) and given simply as

$$\begin{cases} \theta_{n+1} = 0 \\ \theta_{2n-i+1} = -\theta_{i+1}, for\, i = 1,2,\cdots,n-1 \end{cases} \tag{2-14}$$

For the symmetric case, the relations are slightly more complicated since the axis of symmetry should be specified first. Defining the axis of symmetry parallel to the x-axis for convenience, the relative turn-angle θ_{n+1} is calculated using the absolute turn-angle α_n defined by strip n and x-axis (counter-clockwise positive, see Figure 2-3(b)). The conversion between θ_i and α_i is trivial, since one-to-one mapping exists for any cross-section without rigid body rotation. The expression of θ_i in radians is then given by

$$\begin{cases} \theta_{n+1} = \pi - 2\alpha_n \\ \theta_{2n-i+1} = \theta_{i+1}, for\, i = 1,2,\cdots,n-1 \end{cases} \tag{2-15}$$

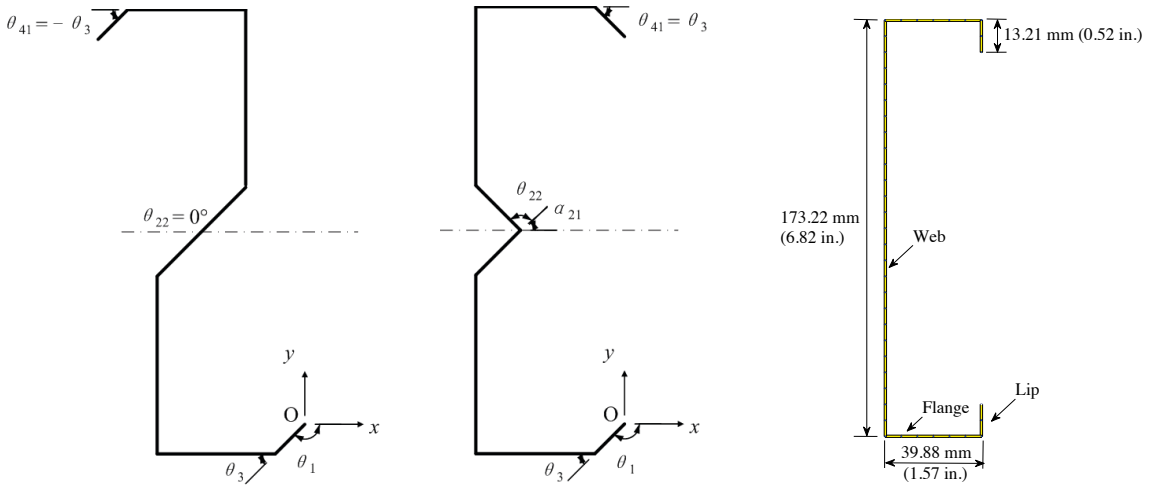

(a) Anti-symmetric section (b) Symmetric section (c) Lipped channel section

Figure 2-3: Effect of symmetry/anti-symmetry constraint on design variables (Leng et al. 2014)

In the search process of this work, candidate designs can switch between symmetric and anti-symmetric cross-sections independently to maximize the strength. One could also have the optimization algorithm dictate symmetry by adding a binary design variable to vector $\boldsymbol{x}$ whose magnitude indicates symmetry or anti-symmetry, but the selected method was adequate for our purposes. Figure 2-3(c) is the symmetric lipped channel section used as the initial design in numerical studies.

(b) Parallel flanges and dimension constraints

The second set of end-use constraints requires the existence of a pair of parallel flanges, and that these flanges be located within a minimum and maximum prescribed spacing. In addition, they should have a minimum lip width. Motivation of this constraint is wall and floor applications, where OSB or gypsum board is attached to the CFS flanges. Although the algorithm assumes an element is designated as a 'lip' when a design is generated, the optimizer has the freedom to set the lip turn-angle to zero. This would flatten the lip, essentially making it serve as an extension of the flange.

As described in Section 2.1.2, a given strip number belongs either to the set L, F, or W, defined as the set of strips composing the lip, flange, and half web, respectively. Using Eqn. (2-4) and Eqn. (2-5) and the integer variables n_l and n_f, this assignment is done and the sets of strip numbers corresponding to the lip, flange, and half web are also identified. Note also that $n_l+n_f+1\leq n$ to ensure existence of a web ($n_w\geq 1$).

The requirement of parallel flanges can then easily be achieved by setting the turn-angles of strips at nodes on the interior of flange set F to zero and employing symmetry or anti-symmetry. The x-axis of the local coordinate system is defined parallel to the flanges for convenience. It can be interpreted that two independent integer design variables n_l and n_f (Eqn. (2-4)) are introduced, and it changed n_f turn-angles from independent to dependent design variables by making the flanges flat.

With the sets defined, the width of the lip and flange can be found by multiplying the uniform strip size by the number of strips in the corresponding set. The dimension constraints are then easily applied as:

$$\begin{cases} l_l \geq l_{minl} \\ l_f \geq l_{minf} \\ d_{min} \leq d \leq d_{max} \end{cases} \tag{2-16}$$

In this work, we require each flange to be longer than l_{minf}=1 in. (2.54 mm), each lip to be longer than l_{minl}=0.5 in. (12.7 mm), and the total web depth d, the y-axis distance between flanges, to be between d_{min}=3.625 in. (92.08 mm) and d_{max}=9 in. (228.6 mm).

(c) Utility pass-through allowance

The third set of end-use constraints are developed to allow the passage of utilities. Commercial CFS products typically have perforations on the web for bridging or utilities. Two terms, the clearance and the back-fold, are helpful to address the idea. The clearance, denoted as d_c, is defined as the shortest vertical distance between any two points on the

two lips. A back-fold is a node on the web which has a smaller vertical coordinate than the previous node. There should be no back-folds within the clearance region on the web to prevent punching through multiple layers and facilitate passage through the web. A minimum allowable clearance d_{cmin} to allow passage through the open end:

$$d_c \geq d_{cmin} \tag{2-17}$$

where d_{cmin}=1.0 in. (25.4 mm) is used herein (Figure 2-4).

This constraint is difficult to formulate explicitly in the turn-angle design variables. A true/false check, however, which is all that is needed for the stochastic search optimizer, is straightforward to perform. The clearance is computed as the distance along *y*-axis between the highest point on the lower lip and the lowest point on the upper lip since the node and strip numbers related to flanges, lips and the web are identified in previous steps. The back-fold is found by comparing the *y*-coordinate of nodes on the flange.

(d) Open section

The final end-use constraint of an open section prevents the strips of the cross-section from overlapping, as required also in unconstrained optimization. This constraint is also difficult to formulate in the turn-angle and strip width design variables and so we perform a geometric check where intersecting points of line segments forming the cross-section are checked to determine if they are on the cross-section. This is also a true/false check

performed so that the randomly perturbed designs with overlapped areas are rejected before elastic buckling analysis.

(e) End-use constraint summary

In summary, design variables are mapped onto the finite strip space to achieve a symmetric (or anti-symmetric) cross-section with parallel flanges. The design variables also have to satisfy dimensional and other geometrical end-use constraints. Figure 2-4 provides an illustration of a candidate cross-section that meets all end-use constratints. These constraints define the feasible set $\boldsymbol{X}$ of design variables written in a general form in Eq (2-10). Only those purturbed designs satisfying all constraints are evaluated for its capacity and thus will be compared with current elite design in SA of constrained optimization.

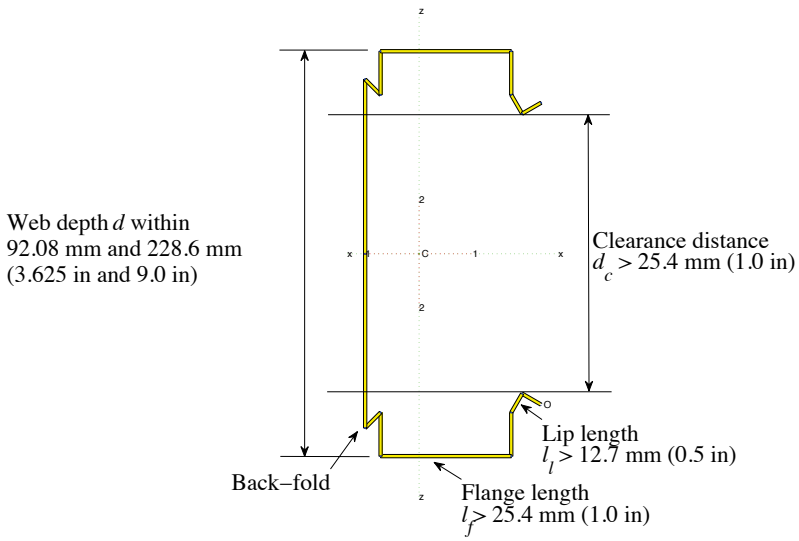

Figure 2-4: Illustrations of end-use constraints in shape optimization (Leng et al. 2014)

2.2.2 Manufacturing constraints

(a) Limiting the number of folds

The design variable formulation in Section 2.1.2 allows us to further combine end-use constraints with fabrication constraints, e.g. limiting the number of rollers (n_{roll}) and their spacing, which directly influences the number of folds and the fabrication cost of a cross-section. Herein we consider an even number of rollers between 4 and 12. Directly making use of the previous formulation as the unlimited roller case is one option, i.e. constraining the number of non-zero turn-angles to the number of rollers. However, this implies that still a large number of finite strips are required to provide freedom to locate the fold even when the number of actual rollers is smaller, which could increase the computational cost of the strength simulation (objective function evaluation) and therefore the stochastic search for an optimal solution.

As a result, the strip widths and turn-angles are considered as the independent design variables, as shown in Eqn. (2-7) in Section 2.1.2 (also Figure 2-2(b) and Figure 2-5). The half cross-section is discretized with n finite strips of different widths, with $n=(n_{roll}/2)+1$, and these strips are mapped to the lip, flange, and half web through Eqn. (2-4) and Eqn. (2-5). Ideas of symmetry/anti-symmetry and section components identification are still applicable after the change in design variable formulation, so there is little modifictiaion in the implementation of symmetry/anti-symmetry constraint and the parallel flange and section dimension constraints. There is no further difficulty in determination of nodal coordinates (i.e. strip locations), so the lip clearance, back-fold, and open section constraints are imposed as before. The realization of some dimensional

constraints is even easier given the availability of independent strip widths variables in an explicit form.

(b) Additional folding constraints

In addition to limiting the total number of rollers, a limit on the number of rollers is also imposed on the lip section. Although complex lips potentially improve local and distortional buckling (Schafer et al. 2006) resistance, too many folds in the lip increase complexity in forming and leave less design freedom for the optimization of web. The maximum number of strips defining a lip is denoted as n_{ml} and limited as follows:

$$n_{ml} = \begin{cases} 1, if\ n_{roll} = 4 \\ 2, if\ n_{roll} = 6 \\ 3, if\ n_{roll} \geq 8 \end{cases} \tag{2-18}$$

Additionally, there must be a minimum spacing between rollers to achieve a designed turn-angle. This is achieved by simply prescribing a minimum length (cross-section width) l_{min} of each strip:

$$l_{min} \leq l_i, \forall i = 1, \cdots, n \tag{2-19}$$

In this work, we use l_{min}=0.25 in. (6.35 mm).

(c) Adjustment to Symmetry and Anti-symmetry Constraint

The mapping of the half cross-section to the full cross-section is performed in a manner similar to that described in Section 2.2.1. However, we further prevent a fold from being located at the midpoint of the web and require the midpoint of the web to be perpendicular to the flange (also the *x*-axis), meaning the turn-angle at the midpoint is zero. This constraint is a requisite to prevent an odd number of total rollers for the symmetric section. It also has the practical value of offering a flat area in the web to facilitate punching holes for the passage of utilities in typical CFS studs. To make the midpoint of the web perpendicular to the flange, we adjust the turn-angle preceding the last finite strip as follows:

$$\theta_{n-1} = \begin{cases} -\pi/2, if\ n_w = 1 \\ -\pi/2 - \sum_{n_l+n_f+1}^{n-2} \theta_i, otherwise \end{cases} \tag{2-20}$$

The symmetry/anti-symmetry mapping of the relative turn-angles variables is then given by

$$\begin{cases} \theta_n = 0 \\ \theta_{2n-i} = \pm\theta_{i+1}, for\ i = 1,2,\cdots,n_{rol}/2 \end{cases} \tag{2-21}$$

where the positive sign is for symmetric sections and the negative sign is for anti-symmetric sections. Figure 2-5 illustrates these relationships. A further note is that the constraint θ_n=0 is not strictly necessary for anti-symmetric cross-sections, but maintained

for simplicity. That constraint also has a practical value since a flat area for a perforation is necessary to allow the passage of utilities in typical CFS studs.

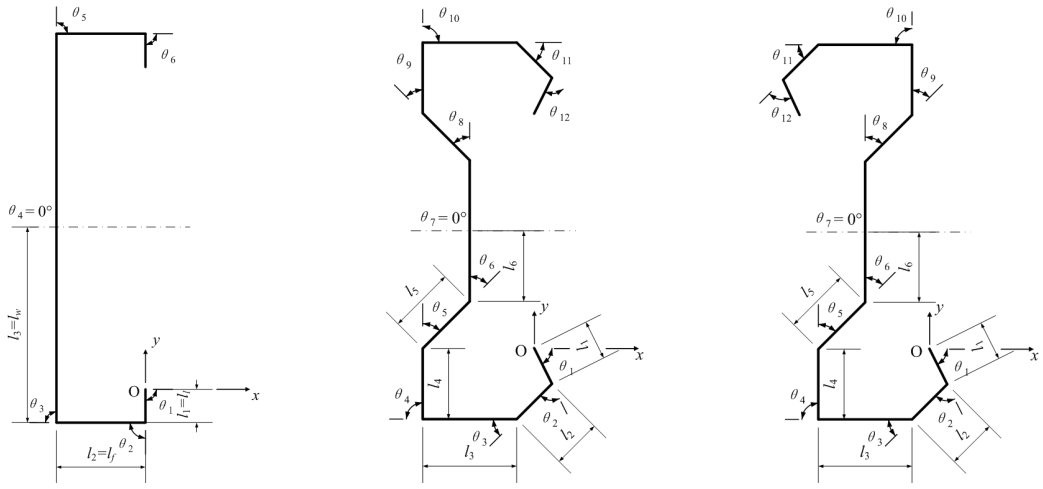

(a) Lipped channel section, 4 rollers (b) 'S' section, 10 rollers (c) Anti-symmetric section, 10 rollers

Figure 2-5: Effect of symmetry/anti-symmetry, end-use, and manufacturing constraints on design variables (Leng et al. 2014)

(d) Adjustment to parallel flange and section dimension constraints

The parallel flange constraint is achieved here by using a single strip to represent the flange (n_f=1), which is set parallel to the x-axis through the following constraint on turn-angles:

$$\theta_{n_l+1} = -\pi - \sum_{i=1}^{n_l} \theta_i \tag{2-22}$$

As the number of strips in the half web is simply n_w=n–1–n_l, the only independent integer design variable in Eqn. (2-7) is the number of strips composing the lip (n_l).

The section depth constraint of Eqn. (2-16) is computed from the *y*-coordinates of the flanges, as before. The lip and flange dimension constraints in Eqn. (2-16) are also straightforward to apply, with the widths computed as:

$$l_l = \sum_{i=1}^{n_l} l_i; l_f = l_{n_l+1} \tag{2-23}$$

2.3 Solution technique and algorithms

The capacity and efficiency of search algorithms have a significant impact on the results of optimization problems. In unconstrained optimization, we test three commonly used algorithms of two categories and compare their performance. For gradient-based algorithms, SD is chosen. For stochastic search: SA and GA were exploited; the former runs on one design and the latter operates on a population of them.

The observation from unconstrained optimization results (see Section 2.4) and the formulation of constraints initiates us to modify SA as the algorithm for constrained problems. Details about the implementation of constraints are shown in Section 2.3.2.

2.3.1 Algorithms for unconstrained optimization

(a) Gradient-based algorithm: steepest descent

SD is a simple, gradient-based optimizer that uses only first-order derivatives at the current design point to guide design. It has a well-established theoretical background and is widely used on its own and can be integrated into other algorithms as well. The iterative scheme of SD with design variables updated at an iteration *k* is as follows

$$\boldsymbol{x}^{(k+1)} = \boldsymbol{x}^{(k)} + \alpha \boldsymbol{d}^{(k)} \tag{2-24}$$

where vector $\boldsymbol{d}$ is the direction of design variable change and scalar α is a step length control parameter used to ensure improvement in the objective function. For SD, the step direction is chosen as the negative of the gradient of the function to be optimized

$$\boldsymbol{d}^{(k)} = -\nabla f\left(\boldsymbol{x}^{(k)}\right) = \nabla P_n\left(\boldsymbol{x}^{(k)}\right) \tag{2-25}$$

The gradient ∇f , formed by partial derivatives of f with respect to each component of $\boldsymbol{x}$, points in the direction in which the function $f\left(\boldsymbol{x}^{(k)}\right) = -P_n\left(\boldsymbol{x}^{(k)}\right)$ grows the fastest. Therefore taking small steps (small α) in the direction of $-\nabla f$ will always keep f decreasing (P_n increasing). When the vector norm of $-\nabla f$ is zero the necessary condition of a local minimum is satisfied and the algorithm has converged.

Given a step direction, a line search algorithm is used to identify the step size $\alpha^{(k)}$ that produces a maximum reduction of the objective function. This is equivalent to finding the optimal value of scalar α for a function of only one variable, defined as

$$\min \overline{f}\left(\alpha\right) = f\left(\boldsymbol{x}^{(k+1)}\right) = f\left(\boldsymbol{x}^{(k)} + \alpha \boldsymbol{d}^{(k)}\right) \tag{2-26}$$

The 'inaccurate line search' is used for the line search herein. The term 'inaccurate' means the target of line search is an α that does not have to make the biggest decrease of f along the given direction $\boldsymbol{d}$, see (Nocedal and Wright 2006) for additional details on line search algorithms.

In this problem, solving P_{cr} (necessary for finding P_n) involves a numerical eigenvalue solution (Schafer and Ádány 2006), and the strength formulae of DSM, which employ P_{cr} as inputs to find P_n, are not differentiable. The gradient is therefore calculated numerically using finite differences. A forward finite difference scheme is used herein:

$$\frac{\partial f}{\partial x_i} \approx -\frac{\left(P_n\left(\boldsymbol{x}+\Delta \boldsymbol{e}_i\right)-P_n\left(\boldsymbol{x}\right)\right)}{\Delta}, i=1,\cdots,20 \tag{2-27}$$

where Δ is a small number (the spacing Δ may be variable or constant; it is a constant ~0.05 herein) and $\boldsymbol{e}_i$ is a unit vector with only one nonzero component at entry i. In our case, the product between Δ and $\boldsymbol{e}_i$ serves as a perturbation on one θ_i turn-angle in $\boldsymbol{x}$. It is noted that the crossings constraint contained in Eqn. (2-10) also requires differentiation. However, the gradient-based algorithm never tended towards shapes with crossings, and thus this constraint was omitted for this algorithm and indeed the final results do not exhibit any crossings as shown in Section 2.4.2 and 2.4.3.

(b) Stochastic Search Algorithms: simulated annealing

SA and GA are also used in the unconstrained optimization. These algorithms are based on the principles of stochastic search with biases introduced into the search to favor

designs offering better performance. The elite design that offers the highest performance is monitored throughout the optimization process and the algorithm is said to converge when this design remains unchanged over a large number of iterations. As gradients are not used to guide design, stochastic search algorithms typically require a large number of analyses and must be run more than once. The robustness of optimization results can be regarded as a sign of identification of optimal solution.

SA is a mimic of the natural process of annealing in metallurgy (Kirkpatrick et al. 1983). The algorithm performs iteratively; the code generates a new candidate design by randomly perturbing the turn-angles of the current elite design. If the new design is feasible (no overlap) and offers a higher P_n, the new design becomes the elite design. A unique property of SA is that its 'hill-climbing' property allows inferior designs to be accepted in place of elite ones to expand the search space and prevent the algorithm from becoming trapped in a low quality local minimum. The probability that a suboptimal design is accepted is a function of the magnitude of performance loss and a user-selected parameter. This parameter is tightened as the optimization progresses, reducing the probability of accepting suboptimal designs. Two influential parameters of the algorithm are initial 'temperature' T_0 and the rate at which this temperature is reduced, referred to as the 'cooling rate' r. The reduction of T occurs when a certain number (k_{max}) of qualified designs have been evaluated. SA terminates after the temperature has been reduced m_{max} times. The product of k_{max} and m_{max} is the maximum number of objective function evaluations, commonly used as an indicator of algorithm efficiency. Convergence is said to occur if the elite design does not change over a large number of

iterations (n_{max}). In SA, the openness of cross-sections is realized by the false/true check on perturbed designs, i.e. perturbed designs with any overlapping will be rejected. See Spall (Spall 2003) and Arora (Arora 2004) for a more detailed discussion of SA.

Detailed description of SA in unconstrained shape optimization including a flow chart (see Figure 2-6) for the problem under study is available from (Leng et al. 2011). In the process of optimizing a lipped channel section (Figure 2-1(b)), we use $T_0 = 1$, $m_{max} = 13$ and $T_0 = 0.3$, $m_{max} = 50$ for intermediate (4 ft (1.22 m)) and long members (16 ft (4.88 m)) respectively. The number of trial designs within one temperature iteration is $k_{max} = 200$, $n_{max} = 200$ and $r = 0.5$. The maximum total number of objective function evaluation n_e of SA equals the product of k_{max} and m_{max}, which is 2600 for intermediate members and 10000 for long members.

(c) Stochastic Search Algorithms: genetic algorithms

GA are a family of popular stochastic search algorithms based on the idea of Darwin's evolution theory (Holland 1975; Golberg 1989). Rather than operate on a single design and a perturbation of that design as in SA, GA operates on a population of designs. The designs are then analyzed and ranked according to their objective function performance. The generation of a new design population includes random selection two designs (parents) and random exchange of a portion of properties of them (reproduction). Occasionally, a design is also randomly perturbed (mutation). This process is repeated until the entire new population (children) is formed. Designs with higher strengths have a

higher probability of being selected as parents, and thus the performance of the population as a whole should improve as the optimization progresses.

In our formulation of unconstrained optimization, the turn-angle vector $\boldsymbol{x}$ of a given design is rounded to a user-specified precision (e.g., three decimal places) and converted into a binary string. This is a straightforward process and facilitates exchange of information between designs. Parent selection is based on a roulette wheel algorithm and single point crossover is used to exchange turn-angle information between two parents. To handle the constraint on overlapping, the penalty method is used. If element crossing is detected in a new design ($n_{crossing}>0$), the computed strength is penalized by subtracting a large number, thereby ensuring infeasible designs will rank lower than any feasible design. The decision to use the penalty method instead of a true/false design check as in SA is that the crossover and mutation of GA can create a number of physically infeasible 'children' in the next population, so the check and regeneration process can be much longer. Also, we would like to compare different strategies of handling constraints and see their effect.

Similar to other stochastic search algorithms, GA terminates if either a maximum number of iterations is achieved (k_{max}) or convergence is detected. Convergence is said to occur if the elite design does not change over a large number of iterations (n_{max}).

A summary of the algorithm in a flow chart (see Figure 2-7) is provided in (Leng et al. 2011). In this research, the size of population is forty, $k_{\max}$ = 1000, and $n_{\max}$ =100. The

rate of crossover and mutation are 0.8 and 0.02, respectively. It is well-known that GA tend to struggle in problems requiring a large number of design variables (large dimension spaces). Turn-angles are therefore computed to one decimal point and are constrained such that $\theta_{min} = -\pi/2$ and $\theta_{max} = \pi/2$, which also prevents sharp folds in the material that may be difficult to fabricate in practice. The upper bound of number of objective function evaluation is 40000 (the product of population size with maximum number of iterations).

2.3.2 Algorithm for constrained optimization

The end-use and manufacturability constraints described in Section 2.2 include requirements on the geometry of the cross-section and restraints on its dimensions. Some of them are difficult to formulate in an explicit mathematical form and this hinders the use of gradient-based algorithm in this problem. As discussed, GA runs on a population of designs, so regeneration of randomly perturbed sections to meet feasibility can be tedious. In addition, adding punishment on a series of constraints can be complex since other research has shown that optimization results can sometimes be sensitive to penalty factors (Spall 2003). Our experience with SA in unconstrained optimization (Section 2.4) has shown that it is capable of finding optimized sections globally for intermediate and long length columns with relatively little computational cost. As a result, SA is selected as the algorithm for optimization with end-use and manufacturability constraints.

The generation of new candidate cross-section designs from random perturbations in SA has to follow the formulation of design variable vector $\boldsymbol{x}$ in Eqn. (2-6) and Eqn. (2-7). For

the unlimited roller case, the integer number of strips in the lip and web are generated and, if feasible, the turn-angles of the strips. The end-use constraints are implemented by true/false checks in the order given in Figure 2-8. For the case of a limited number of rollers, the integer number of strips in the lip is generated, followed by the widths of the strips, and if feasible, the turn-angles. All design variables are generated using a uniform distribution with minimum and maximum bounds defined by the allowable design variable magnitudes. This is shown in Figure 2-9, which is followed by the design checks on end-use constraints in Figure 2-8. If a candidate is deemed feasible, it is evaluated for capacity, P_n, using CUFSM with DSM.

Compared with the case of unconstrained optimization, short length (2 ft or 0.61 m) columns are also studied in addition to intermediate and long length columns. The governing buckling mode generally shifts from local buckling to global buckling as the unbraced length is increased. The same lipped channel cross-section as in Section 2.3.1 have been utilized as the initial design (Figure 2-2(c)). Termination conditions and algorithm efficiency measures of unconstrained optimization are kept. Like most stochastic search algorithms, parameter tuning is required for SA to perform efficiently after the addition of constraints. As Eqn. (2-6) and Eqn. (2-7) use different design variable vectors, the parameters of SA should be tuned for each case respectively. In the examples presented herein, for the 'unlimited' number of rollers case, we use k_{max} = 200, r = 0.5, and T_0 = 1.0 for all examples, and increase the maximum number of cooling iterations m_{max} to 25, 35, and 100 for the 2 ft (0.61 m), 4 ft (1.22 m), and 16 ft (4.88 m) columns, respectively. We note the maximum number of objective function evaluations is

much larger than the unconstrained case because of the increased dimension of design variables. For the case of limiting the number of rollers, which typically uses less design variables than the unlimited roller case, three parameters are adjusted slightly to $T_0 = 2.0$, $r = 0.7$, and m_{max} is 50, but these are kept constant for all column lengths.

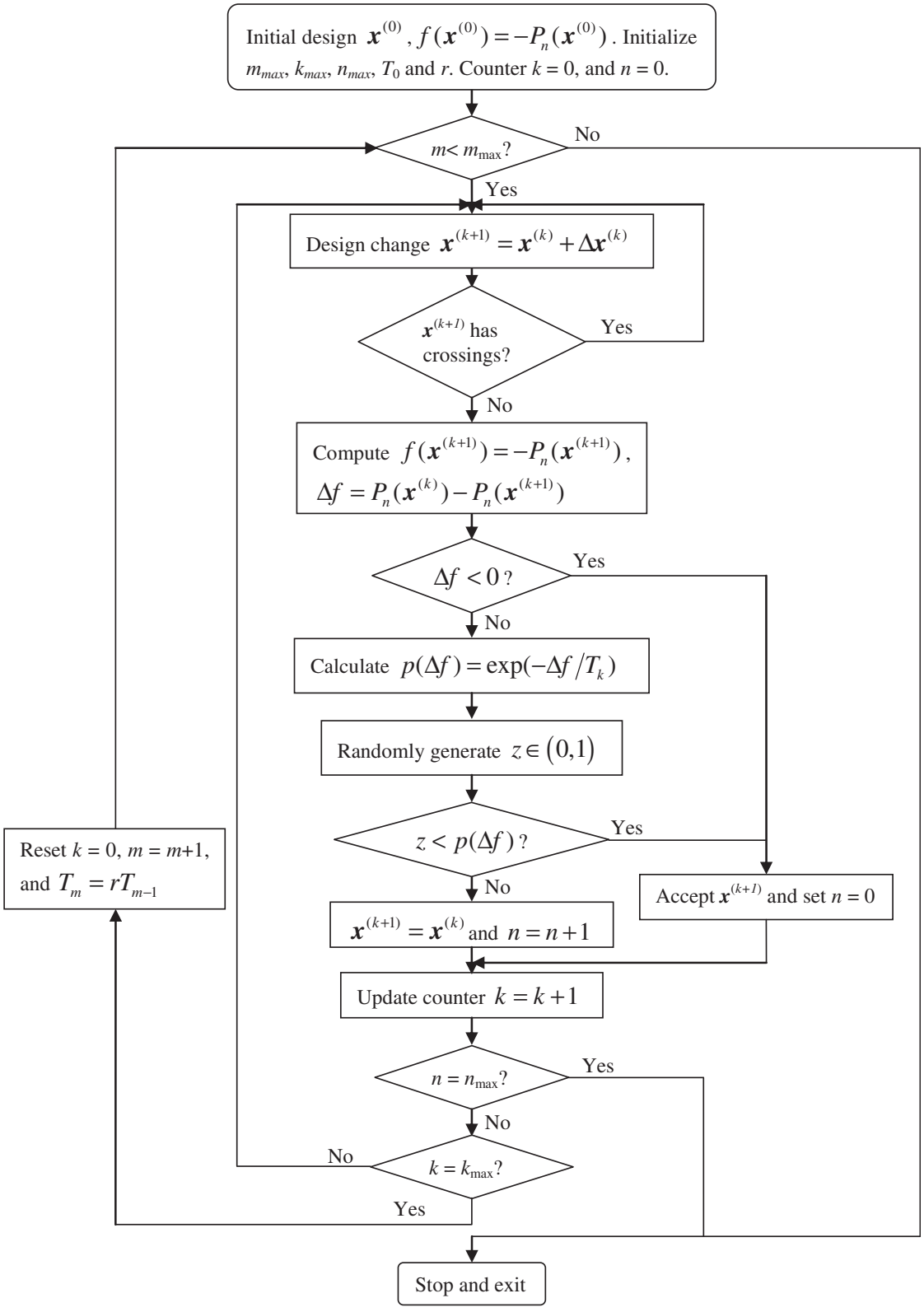

Figure 2-6: Flow chart of simulated annealing algorithm for unconstrained shape optimization (Leng et al. 2011)

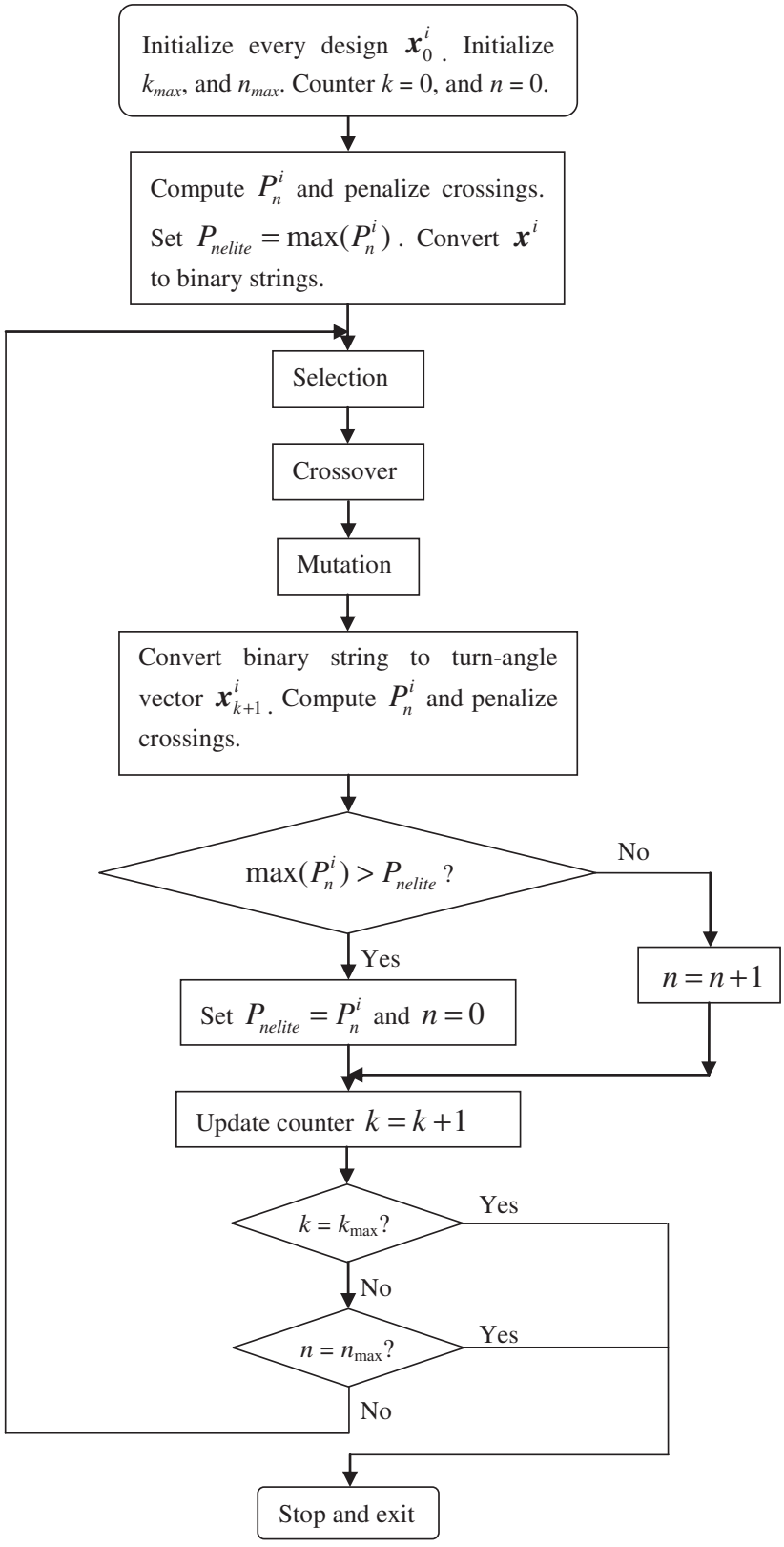

Figure 2-7: Flow chart of genetic algorithms for unconstrained shape optimization (Leng et al. 2011)

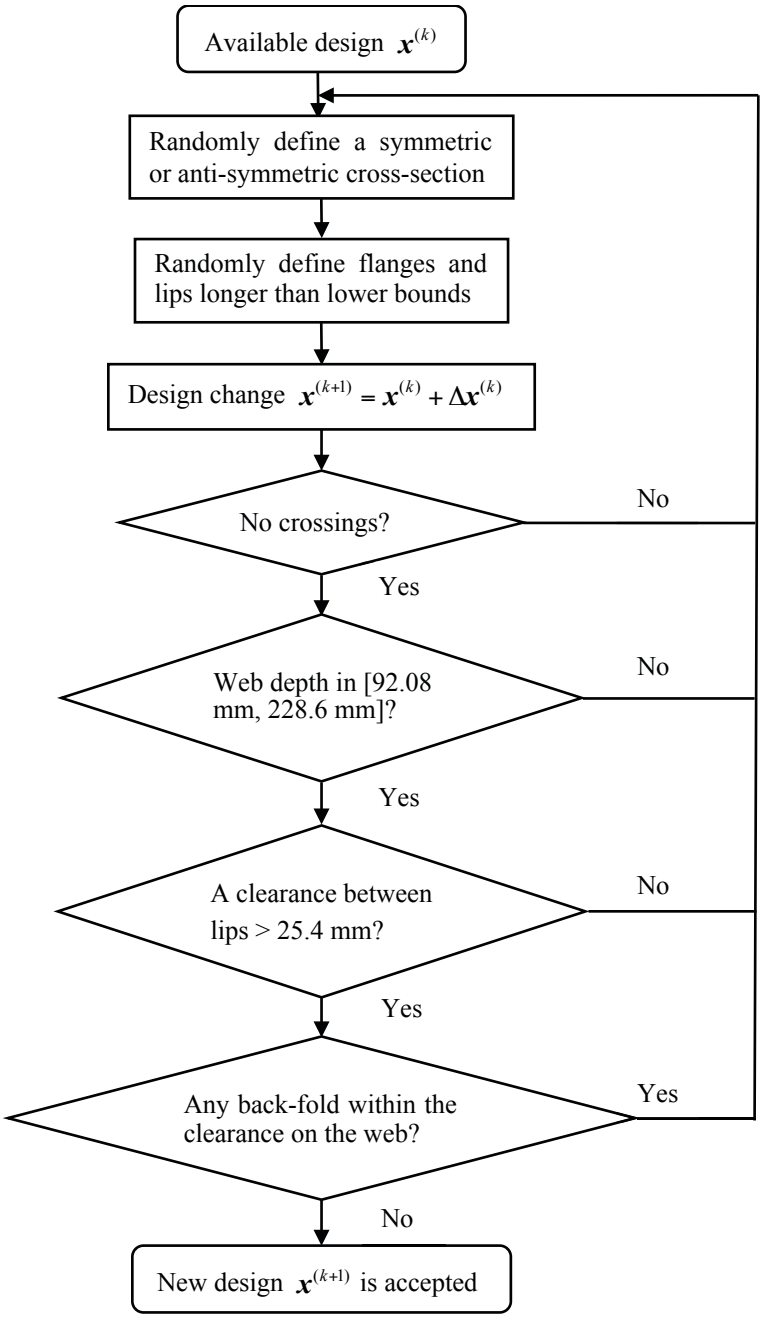

Figure 2-8: Flow chart of implementation of constraints in simulated annealing for unlimited number of rollers (Leng et al. 2014)

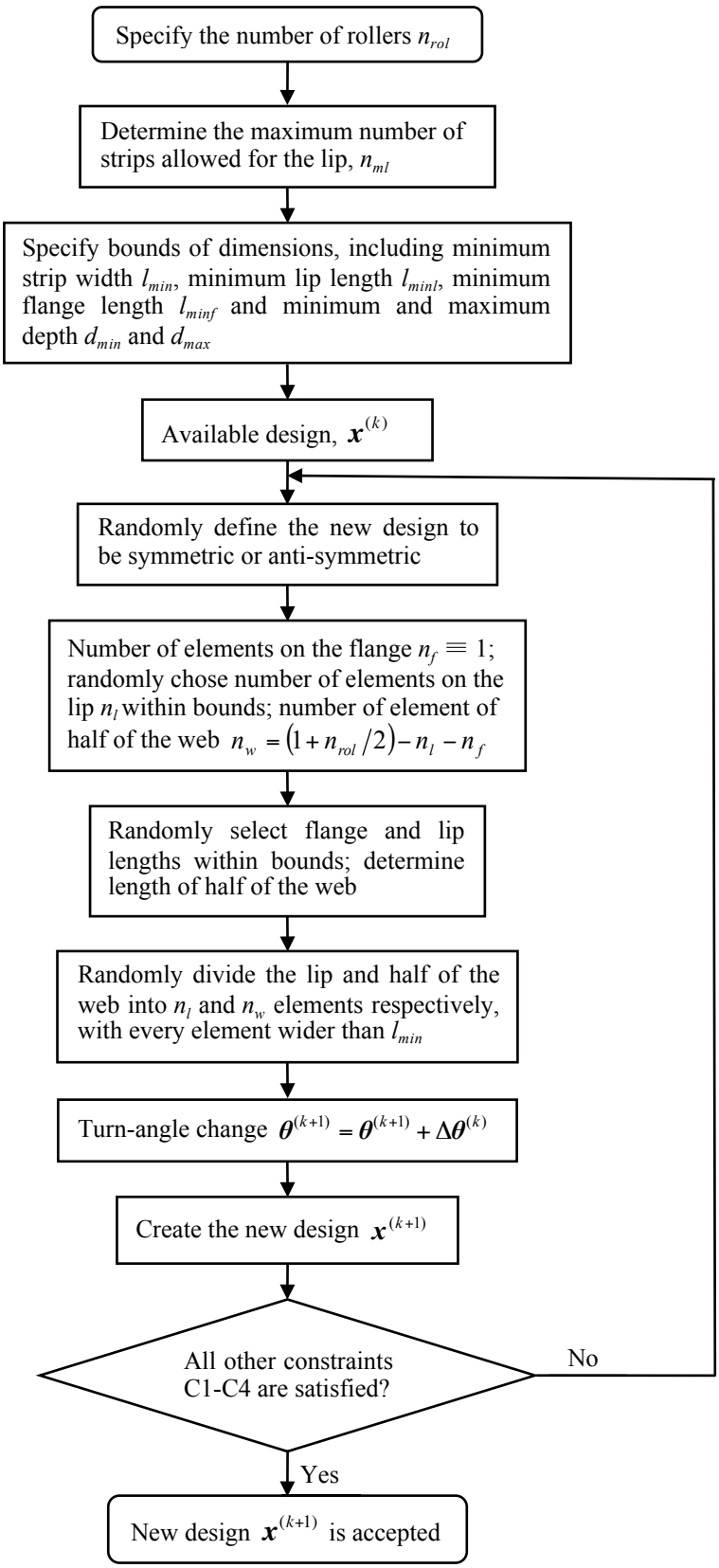

Figure 2-9: Flow chart of implementation of constraints in simulated annealing for limited number of rollers (Leng et al. 2014)

2.4 Optimization results of unconstrained optimization

2.4.1 Description of the example

An overview of optimization for a lipped channel section is shown in Figure 2-1(b). For unconstrained optimization, we investigate members with two unbraced lengths: an intermediate column of length 4 ft (1.22 m) where global, distortional, or local-global interaction may govern; and a long column of length 16 ft (4.88 m) where global buckling governs. The web depth, flange widths and lip lengths are 6.82 in. (173.33 mm), 1.57 in. (40.00 mm) and 0.52 in. (13.33 mm) in the reference column. The thickness of the steel sheet is 0.039 in. (1 mm). Young's modulus of the steel is E=30458 ksi (210,000 MPa) and the yield stress is F_y = 33 ksi (227 MPa). The dimensions of the section and material properties are chosen in the same way as Liu et al. (Liu et al. 2004) for the purpose of comparison, even though the values of E and F_y are different from 29500 ksi (203,395 MPa) and 50 ksi (345 MPa) as commonly used. The critical buckling loads computed by CUFSM are P_{crl}=2.32 kips (10.32 kN), P_{crd}=3.79 kips (16.86 kN), and P_{cre}=18.39 kips (81.79 kN) at 4 ft (1.22 m) length and P_{cre}=1.18 kips (5.23 kN) for the 16 ft (4.88 m) column. Although a column with unbraced length as long as 16 ft (4.88 m) is hardly seen in practice, it is chose to study the effect of optimization on global buckling dominated cases. The cross-section is discretized into twenty-one strips each with a width of 0.52 in. (13.33 mm) and has a total perimeter width of 11.02 in. (280 mm). The first node is fixed at the origin and the first turn-angle is fixed as $-\pi/2$.

2.4.2 Optimization results of the lipped channel with long length

(a) Results of steepest descent method

SD described above is used with a finite difference turn-angle perturbation of Δ=0.01 radian for the gradient calculations. Figure 2-10 is the evolution process from the initial lipped channel to the optimized 'circular' section. It is clear that the gradient consistently drives the cross-section to curl itself to improve the global buckling resistance and to reduce the opening between the two lips. However, the effect of steepest descent direction and line search is more local and geometry of optimized section does not change dramatically. The nominal load P_n of the optimized section is 2.47 kips (10.97 kN) compared with P_n = 1.03 kips (4.58 kN) for the lipped channel, an increase of 139%. The controlling mode is global buckling with the interaction of local buckling for both cases. To reveal the mechanism of the performance improvement, a comparison of the cross-section properties is provided in Table 2-1. The optimization process increases the warping constant C_w (increasing torsional resistance) while insuring the moment of inertia about the two principal axes I_{11} and I_{22} converge (i.e., making weak- and strong-axis buckling the same).

To further investigate the possibility of finding global optima, additional SD solutions were pursued with varied initial conditions, including a hat and sigma section. The optimized shapes found by SD are provided in Figure 2-12, but neither leads to greater strength than using the lipped channel. These unequivocally demonstrate that SD is a local optimizer dependent on initial design, and there is no guarantee of global optimality. The number of objective function evaluations, termed n_e, differs case by case, as shown

in in Table 2-1. Monitoring the iteration process further shows that the SD method tends to converge slowly as it approaches the local minima, a known property of SD (Nocedal and Wright 2006).

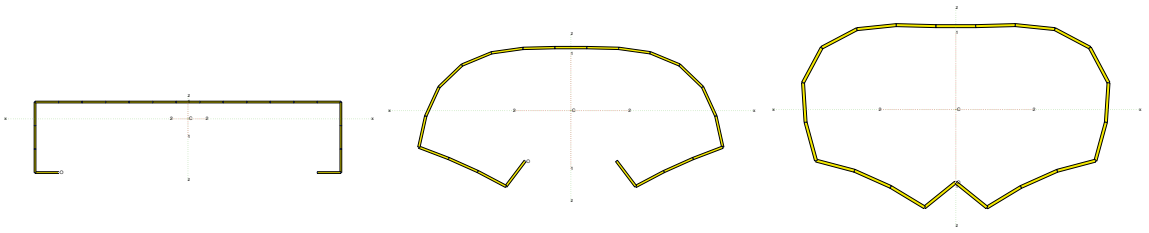

(a) Interation 1 (b) Interation 150 (c) Interation 357

Figure 2-10: The process from initial to optimized cross-section using steep descent method for 4.88 m (16 ft) lipped channel column (Leng et al. 2011)

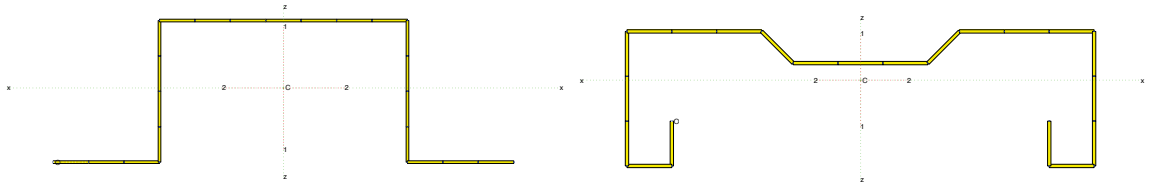

(a) Hat section, P_n = 3.56 kN (0.80 kips) (b) Sigma section, P_n = 4.66 kN (1.05 kips)

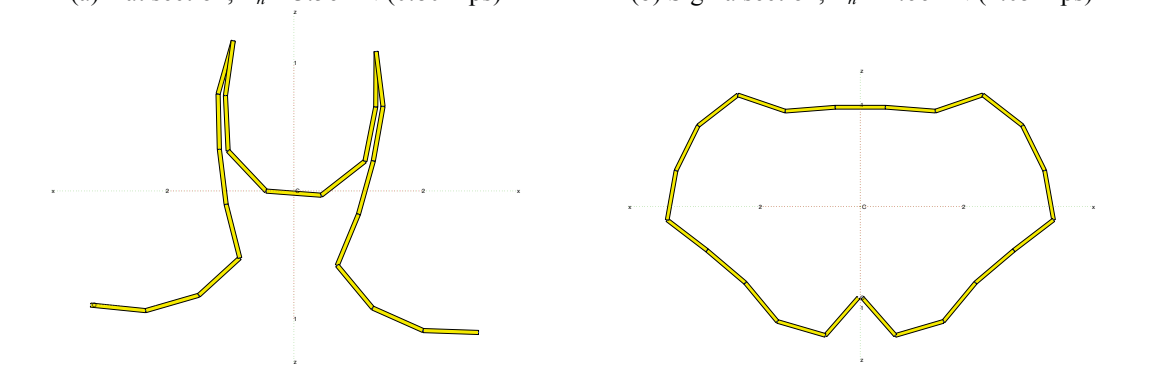

(c) SD hat, P_n = 9.36 kN (2.10 kips) (d) SD sigma, P_n = 10.63 kN (2.39 kips)

Figure 2-11: Optimized cross-sections found by SD for 4.88 m (16 ft) columns with hat and sigma initial sections (Leng et al. 2011)

(b) Results of genetic algorithms

As a stochastic search algorithm, GA needs repeated runs to check convergence and robustness of the optimized solution. Herein, GA is run ten times and the four best

optimized sections presented in Figure 2-12. The convergence curves of the elite designs are presented in Figure 2-13. The optimized shapes are highly uniform, resembling a squashed 'S' cross-section, quite distinct from the initial lipped channel and the 'circular' section from SD. GA elite designs focus on a near anti-symmetric section. Table 2-1 contains the geometric properties of these sections and reveals that (1) the I_{11} and I_{22} properties of these sections are nearly equal and (2) although the warping constant drops significantly, the distance from centroid to shear center (the eighth column in Table 2-1) is significantly reduced and approaches zero. The equation of critical axial load from classical discussion of flexural torsional buckling (Chajes 1993) can be used to give a further explanation (Leng et al. 2011). The maximum possible eigenvalues (P_{cr}) of the characteristic equation for global buckling can be found from the decoupled cases, which requires the section be bi-symmetric or point symmetric, and thus the centroid and shear center coincide, viz. the components x_0 and y_0 of their distance will be zero.

Therefore, although the moment of inertia and warping constant are not that large for GA optima (e.g., compared with the initial design, see Table 2-1), the attenuated coupling between modes from smaller x_0 and y_0 plays a crucial role in increasing the critical load and thus the nominal strength P_n in this global mode dominated case. The GA solution outperforms the cross-section found by the SD method and confirms the latter is only a locally optimal solution. However the improved search capacity of GA comes with additional computational cost. In terms of number of function evaluations n_e, each GA run took 40,000 function evaluations, as shown in Table 2-1, and multiple replications are required.

(c) Results of simulated annealing algorithm

As with GA, SA is run ten times on the lipped channel section and the best of these solutions is presented here. Unlike GA, the optimized SA shapes for the ten runs do not bear so much resemblance to one another. Generally, three types of shapes are found in the SA results, as shown in Figure 2-14. A possible reason for the optimal designs observed could be the property of SA that accepts and further explores inferior designs early in the design process, as suggested by Figure 2-15. The cross-section with the largest P_n resembles the squashed 'S' shapes observed in the GA results. The second cross-section type has a 'bobby pin' appearance, and the geometric properties in Table 2-1 show that this cross-section also has approximately the same value for I_{11} and I_{22}, and a coincidence of the centroid and shear center. However, the 'bobby pin' nominal strength P_n is 12.38 kN (2.78 kips), modestly less than the 14.17 kN (3.19 kips) of the squashed 'S' shape. The third SA elite solution is a nearly closed cross-section, resembling the unclosed 'circular' SD solution. The nominal strength of the SA solution for this third type is slightly larger (5.2%) than that of the SD solution.

The convergence curves in Figure 2-15 show that the maximum P_n of SA is 1.5% larger than GA, as illustrated by the dashed line. The diversified elite results of SA suggest that this algorithm provides a reasonably full exploration of the design space if the algorithm is run multiple times. Furthermore, this does not necessarily increase total computational cost for SA over GA, as a single SA run is generally less computationally expensive than

a single GA run according to Table 2-1, because SA operates on one single design instead of a population.

(d) Supplementary intuitive and steepest descent analysis

Motivated by the formal optimization results several additional studies are performed to validate the findings. Firstly, three 'intuitively' optimal sections were explored: an open circle and two variants of the squashed 'S' shape as shown in Figure 2-16 and summarized in Table 2-1. The open circle (Figure 2-16(a)) is motivated by the SD results for the lipped channel, but the strength of the open circle is only 72% of that of the SD result for the lipped channel (Figure 2-10(c)). The squashed 'S' shape as seen in GA results is manually cleaned up to a symmetric section with smoother variation in the turn-angles (Figure 2-16(b)) and the strength result is essentially the same from the best GA analysis. Finally, a simplified version of the 'S' shape (Figure 2-16(c)), which employs a minimum of right angle folds, is investigated. This simplified 'S' section has only 69% of the strength of the optimal squashed 'S' and demonstrates the sensitivity of the solution.

Following capacity evaluation of these intuitive explorations formal optimization using SD was again employed. Running SD on the simplified 'S' shape results (Figure 2-17(a), Table 2-1) generates a section that has strength only 5% lower than the best elite designs from GA and SA. Further, formal SD optimization of the best SA design results in the highest capacity of all observed designs: 1% greater than the SA result (Figure 2-17(b), Table 2-1).

Results presented in these sections highlight the potential role optimization can play in the discovery of new, high performance designs. The squashed 'S' section outperforms the intuitive circular section by nearly 78% and the standard lipped channel section by over 200% at the considered length of 4.88 m (16 ft).

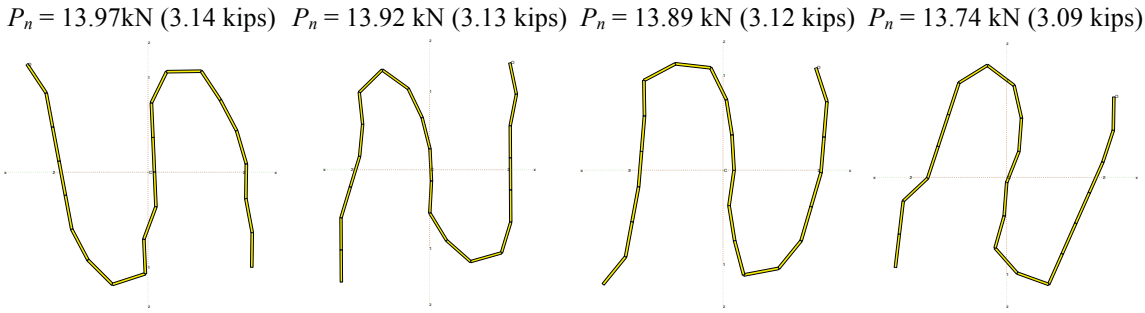

(a) GA squashed 'S' (b) GA squashed 'S' (c) GA squashed 'S' (d) GA squashed 'S'

Figure 2-12: Optimized cross-sections found by GA for 4.88 m (16 ft) lipped channel columns (Leng et al. 2011)

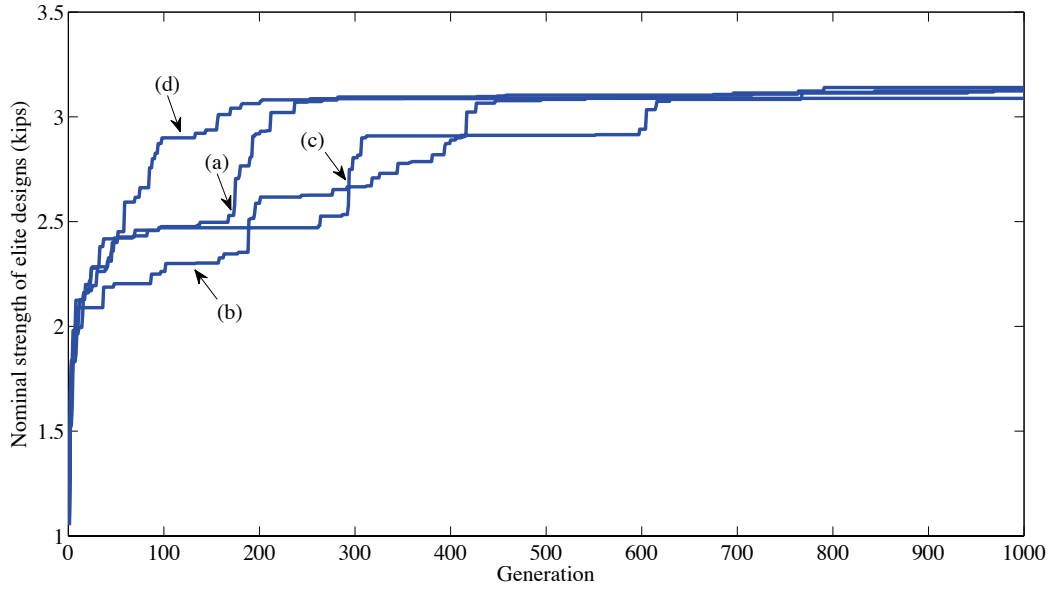

Figure 2-13: Convergence curves of P_{nelite} of GA optimized designs for 4.88 m (16 ft) lipped channel column (Leng et al. 2011)

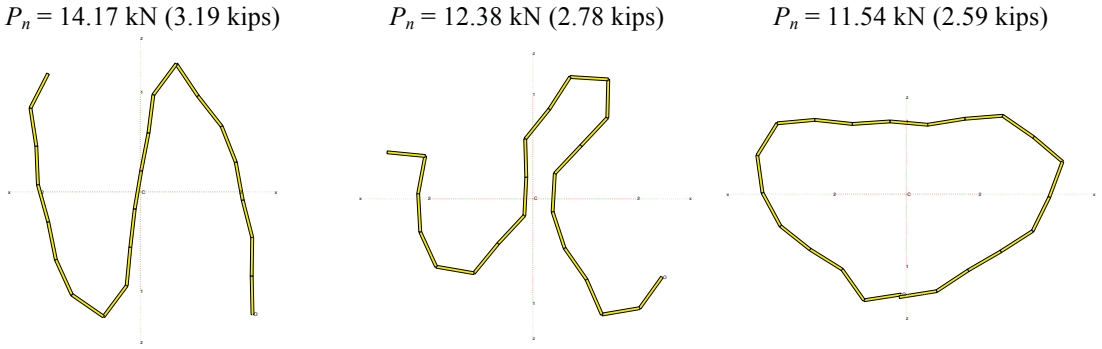

(a) SA squashed 'S' (b) SA 'bobby pin' (c) SA 'circular'

Figure 2-14: Optimized cross-sections found by SA for 4.88 m (16 ft) lipped channel columns (Leng et al. 2011)

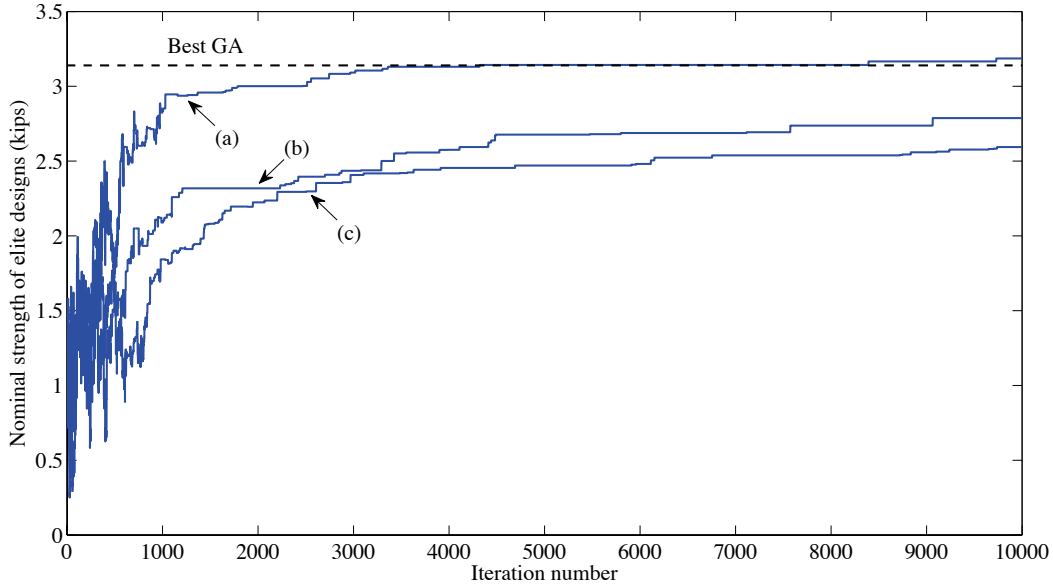

Figure 2-15: Convergence curves of P_{nelite} of SA optimized designs for 4.88 m (16 ft) lipped channel column (Leng et al. 2011)

P_n = 7.85 kN (1.77 kips)

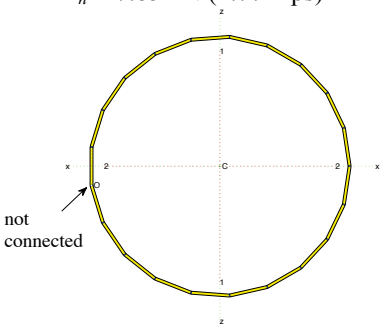

(a) Open circular

P_n = 13.70 kN (3.08 kips)

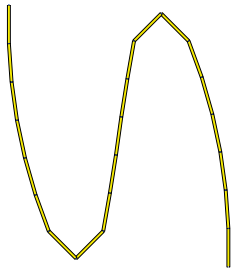

(b) Squashed ‘S’

P_n = 9.46 kN (2.13 kips)

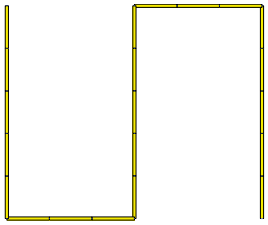

(c) Simple ‘S’

Figure 2-16: Intuitive optimized cross-sections (Leng et al. 2011)

P_n = 13.39 kN (3.01 kips)

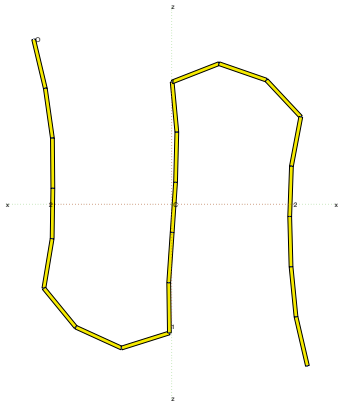

(a) SD initial section simple ‘S’

P_n = 14.33 kN (3.22 kips)

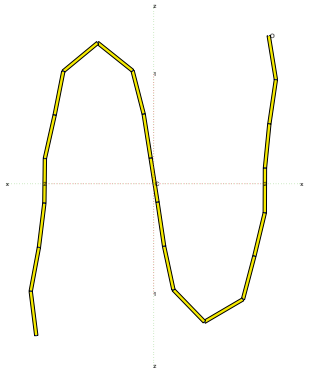

(b) SD initial section squashed ‘S’

Figure 2-17: Optimized sections found by SD for 4.88 m (16 ft) squashed ‘S’ columns (Leng et al. 2011)

Table 2-1: Cross sectional properties of the lipped channel, circular and optimized sections for 4.88 m (16 ft) member (Leng et al. 2011)

Sol'n[a]	section	n_e	Fig.	I_{11} (cm^4)	I_{22} (cm^4)	C_w (cm^6)	$\sqrt{x_0^2 + y_0^2}$ (cm)	P_n (kN)
N/A	C	1	2-1b	120.58	5.99	362.26	2.61	4.59
N/A	hat	1	2-11a	66.63	14.81	150.46	4.52	3.56
N/A	sigma	1	2-11b	80.29	6.09	331.40	2.82	4.66
N/A	open circular	1	2-16a	27.60	27.60	1403.38	8.88	7.85
N/A	squashed 'S'[b]	1	2-16b	20.65	17.98	384.28	0.00	13.70
N/A	simple 'S'[b]	1	2-16c	28.01	13.86	477.46	0.00	9.47
SD	initial: C	7434	2-10c	33.38	14.69	1194.46	6.42	10.97
SD	initial: hat	47565	2-11c	12.36	12.28	21.75	0.02	9.36
SD	initial: sigma	10878	2-11d	30.38	14.94	1103.96	6.13	10.64
SD	initial: simple 'S' [b]	14280	2-17a	17.77	17.52	385.62	0.18	13.40
SD	initial: squashed 'S'[b]	25221	2-17b	19.11	18.73	385.08	0.08	14.33
GA	squashed 'S'	40000	2-12a	20.40	18.40	411.40	0.60	13.97
GA	squashed 'S'	40000	2-12b	19.85	18.19	375.15	0.18	13.92
GA	squashed 'S'	40000	2-12c	18.69	17.98	365.48	0.58	13.90
GA	squashed 'S'	40000	2-12d	19.73	18.19	396.10	0.86	13.74
SA	squashed 'S'	10000	2-14a	19.31	18.52	385.08	0.11	14.17
SA	'bobby pin'	10000	2-14b	16.94	16.44	112.52	0.07	12.38
SA	'circular'	10000	2-14c	33.67	15.40	1135.65	5.90	11.54

a. N/A = not applicable, no optimization performed; SD = steepest descent; GA = genetic algorithms; SA = simulated annealing
b. The squashed 'S' and simple 'S' shapes are shown in Figure 9 and 10 and their explorations were motivated by the GA and SA results

2.4.3 Optimization results of the lipped channel column with intermediate length

(a) Results of steepest descent method

The lipped channel geometry of Figure 2-1(b), is again used for the initial design in the SD optimization algorithm. The optimal cross-section found closely resembles the curled channel section of Figure 2-11(c), and required about 3800 function evaluations. The capacity P_n of the final design is increased by 137% from initial, as shown in Table 2-2. The percentage of capacity growth is also quite similar to SD optimized shape for long columns.

(b) Results of genetic algorithms

Again, ten runs of the same GA code are completed to optimize the 1.22 m (4 ft) long member. The results are more diverse than in the long column. The elite designs fall into two groups, both previously identified in the SA analysis of long columns: curled channel and 'bobby pin' as shown in Figure 2-18. For the long column (Table 2-1) the bobby pin result was 13% stronger than the curled channel, but for the intermediate length column studied here (Table 2-2) the bobby pin is only 1% stronger than the curled channel – thus they provide essentially equivalent strength. The controlling mode is local bucking with global interaction.

(c) Results of simulated annealing algorithm

The SA algorithm, run with ten replications, provides essentially the same two elite designs for intermediate length columns as the GA solutions; see Figure 2-19 and here Table 2-2. From a purely elastic buckling standpoint (P_{crl}, P_{crd}, P_{cre}) the curled channel is clearly preferred over the bobby pin. However, the higher local (P_{crl}) and distortional (P_{crd}) buckling loads for the curled channel over the 'bobby pin' do not impact the strength, because even in the curled channel P_{crl} and P_{crd} are high enough to insure theses modes do not control the strength. Again, the numbers of n_e in Table 2-2 demonstrate the efficiency of SA over GA in this problem. Simple observation confirms that the optimized shapes of 4 ft (1.22 m) columns, especially those found by stochastic search algorithms, look irregular and less practical.

(d) Supplementary analysis and discussion for intermediate length column

The 'bobby pin' elite design of SA (and GA) was further explored by completing an SD optimization with the bobby pin as the initial design. The shape changed very little and strength increased by only 0.1% for this SD optimization indicating the section is a maximum of P_n.

For long columns the optimal solution was the squashed 'S' of Figure 2-12 and Figure 2-14(a) with strength about 13% higher than the bobby pin section. For intermediate columns the squashed 'S' is not observed in the elite designs. Table 2-2 provides the analysis results for the squashed 'S' at intermediate length, and the strength of a squashed 'S' is 50% lower than the bobby pin section and its growth from lipped channel is quite limited herein. As the table details, the 'S' shaped sections suffer from both local (Figure 2-16(c) simplified 'S' results) and distortional buckling problems (Figure 2-16(b) squashed 'S' results), which limit its capacity at shorter lengths.

Also note, the intuitively optimal open circular section is only 15% lower than the formal optimal designs of SD, GA, and SA (bobby pin and curled channel) – and fully 205% higher than the baseline lipped channel section if applied as a column of 4 ft (1.22 m) length.

P_n = 56.03 kN (12.60 kips)

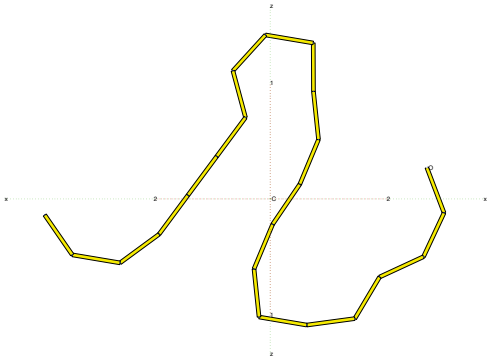

(a) GA ‘bobby pin’

P_n = 55.34 kN (12.44 kips)

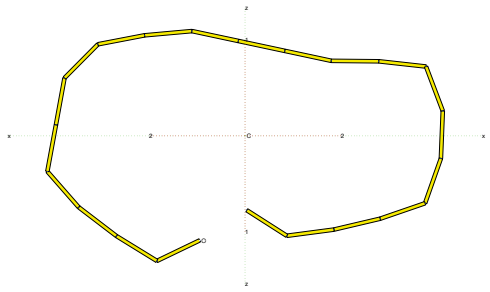

(b) GA ‘circular’

Figure 2-18: Optimized cross-sections found by GA for 1.22 m (4 ft) lipped channel column (Leng et al. 2011)

P_n = 55.98 kN (12.58 kips)

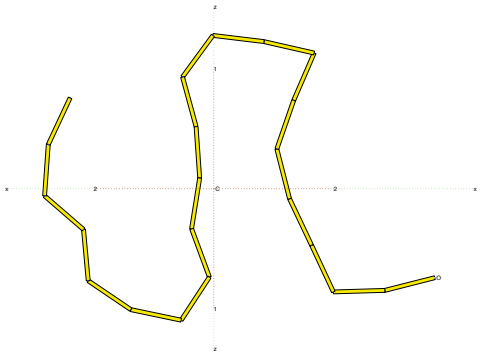

(a) SA ‘bobby pin’

P_n = 55.31 kN (12.43 kips)

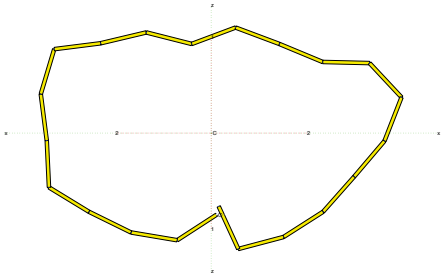

(b) SA ‘circular’

Figure 2-19: Optimized cross-sections found by SA for 1.22 m (4 ft) lipped channel column (Leng et al. 2011)

Table 2-2: Critical and nominal loads of the lipped channel, circular and optimal sections for 1.22 m (4 ft) member (Leng et al. 2011)

Sol’n[a]	section	n_e	Fig.	P_{crl} (kN)	P_{crd} (kN)	P_{cre} (kN)	P_{nl} (kN)	P_{nd} (kN)	P_{ne} (kN)	P_n (kN)
N/A	C	1	2-1b	10.32	16.86	81.79	23.19	25.46	45.99	23.19
N/A	open circular	1	2-16a	97.44	63.57	136.20	52.38	47.77	52.38	47.77
N/A	squashed ‘S’[b]	1	2-16b	26.75	17.96	231.63	39.56	26.32	56.78	26.32
N/A	simple ‘S’[b]	1	2-16c	12.29	39.41	189.03	27.82	38.81	55.33	27.82
SD	initial: C	3801	2-10c	227.48	98.21	179.79	54.93	55.83	54.93	54.93
GA	‘bobby pin’	40000	2-18a	167.12	237.67	207.73	56.03	63.71	56.03	56.03
GA	‘circular’	40000	2-18b	104.06	110.26	189.42	55.34	57.78	55.34	55.34
SA	‘bobby pin’	2600	2-19a	95.71	173.69	206.24	55.98	63.22	55.98	55.98
SA	‘circular’	2600	2-19b	230.37	243.70	188.68	55.31	63.71	55.31	55.31

a. N/A = not applicable, no optimization performed; SD = steepest descent; GA = genetic algorithms; SA = simulated annealing

b. The squashed ‘S’ and simple ‘S’ shapes are shown in Figure 9 and 10 and their explorations were motivated by the GA and SA results

2.4.4 Summary and discussion of unconstrained optimization results

Although the computational efficiency of optimization algorithms has been alluded to, it is worth noting that for both member lengths, SD with finite difference and line search normally requires thousands of analyses to identify a local optimized solution and is dependent on the initial guess. GA and SA are both able to find global optimized sections that differ significantly from the initial guess, but GA needs 40,000 analyses and SA needs 10,000 analyses at most for one run. Also, replication is needed to check the robustness of results for GA and SA. The count on objective function evaluation is a reasonable estimation of the general computational cost regardless of the logic, parameter, and convergence criteria of algorithms. In this research, running SA to identify global optimized section and using SD for a further refinement is a feasible global optimizer.

In all SD optimizations, the angle change in the design vector $\boldsymbol{x}$ is regular and corrugations (patterns of + and – θ_i changes) do not evolve. This is likely a result of using only first-order derivatives to guide design changes and the tendency of gradient-based algorithms to converge to the nearest local minimum. As observed from constrained optimization (Section 2.5), corrugation on the web is important for local and distortional buckling resistance. So it further testifies that simply using first order gradient information is not a powerful option for global optimization in shape optimization of CFS members.

As demonstrated herein, a single optimal cross-section solution for intermediate and long lengths is difficult to find. Rather, any optimized shape is a compromise against the three

buckling modes: local, distortional, and global bucking which are potentially dominate at short, intermediate, and long column lengths respectively. Nonetheless, certain classes of shapes (e.g., squashed 'S', 'bobby pin') evolve that provide more efficient solutions than classical cross-section shapes. Particularly for global buckling (squashed 'S') we may identify three general features that optimal designs drive towards: coincidence of the centroid and shear center, nearly equal moment of inertia about the two principal axes, and relatively large warping stiffness.

Even with the development of modal decomposition and identification (Schafer and Ádány 2006; Li and Schafer 2010), determination of the local and distortional buckling modes can be non-trivial, specifically for general/arbitrary sections. Heuristics are necessary, of which the most useful one is from the commentary to the Direct Strength Method in (American Iron and Steel Institute 2006), where it is suggested that employing the notion that any minima in the FSM signature curve at half-wavelength less than the perimeter length can be assumed local buckling is reasonable and conservative. Using this idea, we track a reference length to determine P_{crl} and P_{crd} when distinct local optima on the signature curve for these modes are not available, as detailed in (Leng et al. 2011).

The unconstrained optimization research provided herein demonstrates that CUFSM and DSM can be integrated into simulation-based shape optimization of CFS columns. Broadened search of the design space locates several novel cross-sections with greatly improved performance. Certain shapes amongst the optimization results, especially those found by stochastic search algorithms for intermediate length columns, are irregular so

practical use of these sections is limited. This greatly arouses the need for introduction of construction and manufacturing constraints (Section 2.2) in shape optimization. Further optimized sections with constraints, as detailed in the following section, can become potential candidates for the next generation of cold-formed steel shapes for commercial use.

2.5 Optimization results of constrained optimization

The previous section on unconstrained optimization has demonstrated the desirable features and the capability of SA algorithm as a global optimizer in shape optimization of CFS columns. In consideration of end-use and manufacturability constraints (as discussed in Section 2.2 and 2.3.2), SA is now used to design maximum strength cross-sections for CFS columns of 2 ft (0.61 m), 4 ft (1.22 m), and 16 ft (4.88 m) lengths (Leng et al. 2013; Leng et al. 2014). The same steel sheet is adopted, with the coil width c and thickness t equal to 11 in. (279.4 mm) and 0.039 in. (1 mm), respectively. Young's modulus of the steel is E=30458 ksi (210,000 MPa) and the yield stress is F_y=33 ksi (228MPa). The geometry of the initial lipped channel section also remains the same. The lip, flange and web dimensions are 0.52 in. (13.21 mm), 1.57 in. (39.88 mm), and 6.82 in. (173.22 mm), respectively, marked in Figure 2-2(c). In the unlimited roller case, the cross-section is discretized into forty-two strips (Figure 2-2(c)), each of width 0.26 in. (6.65 mm), half of the strip width in unconstrained optimization. In the second case, the number of rollers is required to be an even number between four and twelve.

The SA algorithm is run ten times, independently, for each example problem in order to verify robustness of the design algorithm. The best three performing shapes across runs are plotted, along with associated statistics thereafter.

2.5.1 Optimization results with end-use constraints only

(a) Optimization results of short length (2 ft) column

Figure 2-20 displays solutions for the three best sections found for the 2 ft (0.61 m) long columns with end-use constraints. These sections exhibit similar features, including symmetry, having relatively long complex lips at the free ends, and corrugations in the web. The results are similar to what is commonly referred to as a sigma, i.e., 'Σ'-section. Since these members are fairly short, the role of global buckling is negligible. Corrugations in the web are thus designed to reduce the flat plate width greatly and provide significant resistance to local buckling. As discussed by Schafer, Sarawit and Peköz (Schafer et al. 2006), complex stiffeners are able to provide improved ultimate strength performance over simple stiffeners. Inward angled stiffeners can provide positive rotational restraint to the attached plate for local buckling, while it can also improve elastic distortional buckling resistance moving the shear center of the stiffener/flange assembly away from the flange/lip juncture and further away from the flange/web junction.

The normalized critical buckling loads and nominal strengths related to the three buckling modes for the optimized sections and standard lipped channel section are shown in Table 2-3. It may be observed that the optimized shape increases P_n by 126% from the original

lipped channel section, a similar magnitude as unconstrained optimization result. This not only demonstrates the ability of the SA optimization algorithm to design high strength cross-sections, but also illustrates that the end-use constraints do not lead to a significant drop in column strength at this length. The optimized shapes have a nominal distortional load P_{nd} that essentially equals the squash load P_y, implying that distortional buckling does not govern strength for these shapes. Figure 2-21 plots the SA convergence for the run, resulting in the Figure 2-20(a) cross-section. The curve is typical for SA, with the fluctuation of P_n in early iterations indicating the acceptance of inferior designs to enable 'more global' search. The final optimized strength P_n is 95.6% of the maximum possible capacity P_y, as indicated by the dash line.

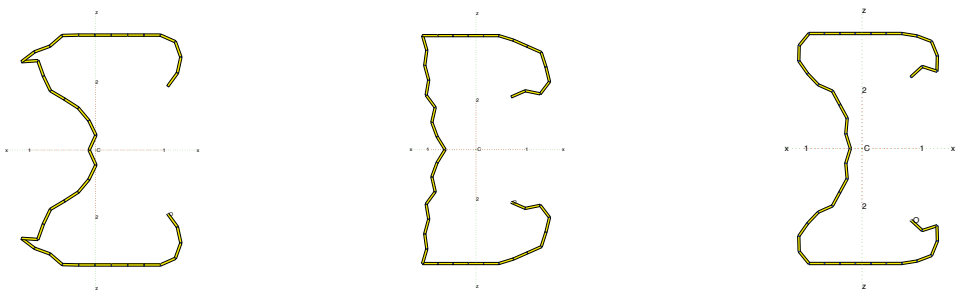

(a) P_n = 60.85 kN (13.68 kips) (b) P_n = 60.76 kN (13.66 kips) (c) P_n = 60.76 kN (13.66 kips)

Figure 2-20: Optimized cross-sections found by SA for 0.61 m (2 ft) column with end-use constraints (Leng et al. 2014)

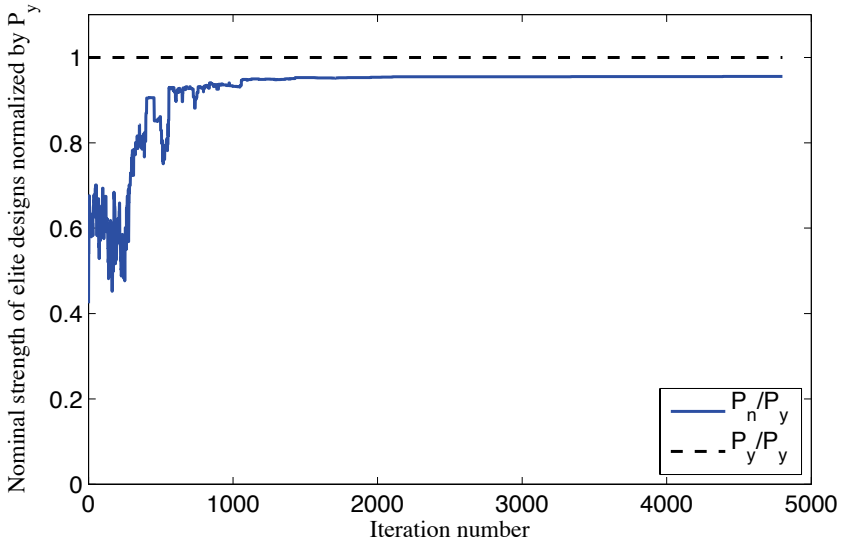

Figure 2-21: Convergence curve of normalized P_{nelite} in search of cross-section in Figure 2-20(a) (Leng et al. 2014)

(b) Optimization results of intermediate length (4 ft) column

The same procedure is repeated for 4 ft (1.22 m) long columns and the three best designs are shown in Figure 2-22. These solutions resemble the optimized 'Σ'-shapes found for the 2 ft (0.61 m) columns, and Table 2-3 confirms they have the same governing buckling/failure mode. The optimized shapes boast an increased capacity of 135% over the reference lipped channel section. It should also be noted the distance between the two free ends of the section in Figure 2-22(b) is close to 1.0 in. (25.4 mm), suggesting that the clearance constraint is near active, demonstrating that the SA algorithm is capable of approaching active constraints and finding optimized solutions in the neighborhood of them.

Previous unconstrained optimization work using unconstrained SA found the so-called 'Bobby pin' optimal section (Figure 2-19(a)), which offered a strength that is 2.9% larger

than the result found here. The 'Bobby pin', however, is impractical, most notably having a back-fold that comprised half of the web and missing parallel flanges. This loss in strength is thus quite minor when considering the significant improvement in end use.

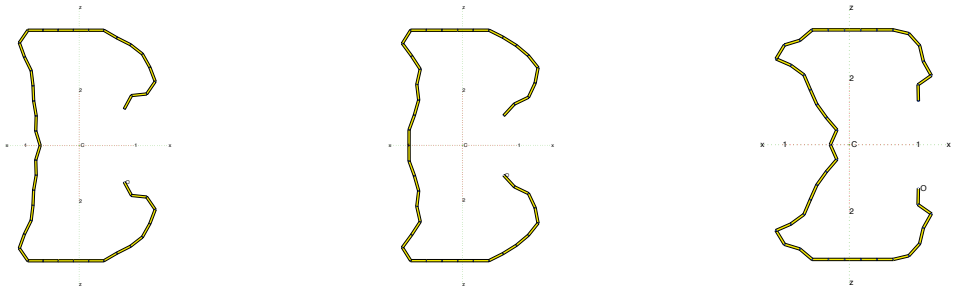

(a) P_n = 54.49 kN (12.25 kips) (b) P_n = 54.27 kN (12.20 kips) (c) P_n = 54.05 kN (12.15 kips)
Figure 2-22: Optimized cross-sections found by SA for 1.22 m (4 ft) column with end-use constraints (Leng et al. 2014)

(c) Optimization results of long length (16 ft) column

Optimized designs for the 16 ft (4.88 m) columns (Figure 2-23) are quite different than the designs for the short and intermediate length columns due to global buckling. Results from ten runs also show less uniformity of features than the previous two cases. Eight of the ten final optimized shapes are anti-symmetric, and their capacities are significantly larger than the symmetric solutions. The squashed 'S' cross-sections in Figure 2-23 closely resemble the unconstrained solutions in Section 2.4.2, the primary difference being the flat and parallel flange, which lead to a loss in strength of 7.2% below the unconstrained optimized solution. These S-sections, however, still offer significantly higher strength (187%) than the reference lipped channel Section of Figure 2-3(c). The strength reduction after adding constraints is quite acceptable, but it also shows that squashed 'S' sections are sensitive to prescribed design constraints.

Cross-sectional properties for these shapes are shown in Table 2-4. The optimized sections for global buckling include a number of key features associated with flexural-torsional buckling that can be compared with the squashed 'S' sections in unconstrained optimization. First, the final sections are point-symmetric so the shear center and centroid coincide naturally. Second, the end-use constraint of parallel flanges and the lower bound of web depth in the S-shape preclude the principal moments of inertia I_{11} and I_{22} from being equal, as was advantageously accomplished with the unconstrained optimization results. The significance of this is real: even with higher I_{11} and warping coefficient C_w, the constrained optimization section in Figure 2-23 still performs slightly worse than the previous unconstrained optimization. Finally, the optimized sections in Figure 2-23 both have lips of only two strips, indicating the minimum value allowed by lip width constraints is active in this case.

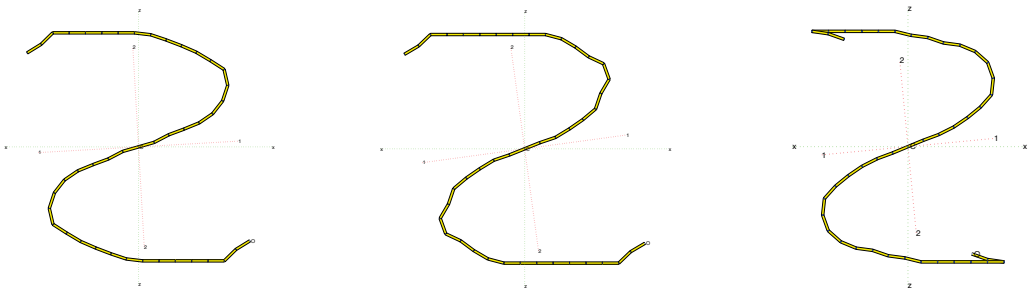

(a) P_n = 13.17 kN (2.96 kips) (b) P_n = 12.90 kN (2.90 kips) (c) P_n = 11.61 kN (2.61 kips)
Figure 2-23: Optimized cross-sections found by SA for 4.88 m (16 ft) column with end-use constraints (Leng et al. 2014)

The overall performance of SA with the proposed end-use constraints is compared in Table 2-5. The mean value and standard deviation of P_n/P_y over the ten SA runs are computed for the three considered member lengths. The small coefficient of variation (about 1%) for short and intermediate long columns suggests the algorithm yielded

solutions with similar performance properties. The coefficient of variation increases to 10.6% for the long column examples, suggesting a wider diversity of solutions. Further tuning the SA parameters could potentially reduce this diversity, since we use the same number of maximum iteration for all member lengths. However, we note that all of these solutions nearly double the capacity of the lipped channel section and that unbraced 16 ft (4.88m) columns are not typically used in practice. Indeed, the end-use constraint of parallel flanges, which allows the introduction of wall boards, serves to brace global buckling modes in practice. Overall, the presented results demonstrate the power of SA in designing cross-sections and that the end-use constraints lead to high strength cross-sections that may potentially be used in practice.

Table 2-3: Critical and nominal loads of C- and 'Σ'-sections normalized by P_y = 63.70 kN (14.32 kips) (Leng et al. 2014)

Member length	Figure	Section	P_{crl}/P_y	P_{crd}/P_y	P_{cre}/P_y	P_{nl}/P_y	P_{nd}/P_y	P_{ne}/P_y	P_n/P_y
0.61 m (2 ft)	2-3c	C	0.162	0.358	4.793	0.424	0.467	0.916	0.424
0.61 m (2 ft)	2-20a	'Σ'	2.707	3.161	9.180	0.956	1.000	0.956	0.956
0.61 m (2 ft)	2-20b	'Σ'	3.678	2.739	8.880	0.954	0.993	0.954	0.954
0.61 m (2 ft)	2-20c	'Σ'	2.260	2.975	8.841	0.954	0.999	0.954	0.954
1.22 m (4 ft)	2-3c	C	0.162	0.358	1.282	0.365	0.467	0.721	0.365
1.22 m (4 ft)	2-22a	'Σ'	3.016	3.464	2.677	0.855	1.000	0.855	0.855
1.22 m (4 ft)	2-22b	'Σ'	3.772	1.831	2.604	0.852	0.921	0.852	0.852
1.22 m (4 ft)	2-22c	'Σ'	3.398	2.807	2.547	0.849	0.995	0.849	0.849

Table 2-4: Cross-section properties of squashed 'S' sections for 4.88m (16 ft) member (Leng et al. 2014)

Section	Figure	I_{11} (cm^4)	I_{22} (cm^4)	C_w (cm^6)	$\sqrt{x_0^2 + y_0^2}$ (cm)	P_n (kN)
squashed 'S'	2-23a	37.37	16.91	655.25	0	13.15
squashed 'S'	2-23b	35.04	17.22	646.74	0	12.92
squashed 'S'	2-23c	36.60	15.20	556.78	0	11.61

Table 2-5: Mean value and standard deviation of axial capacity P_n of optimized sections of three column lengths, normalized by P_y = 63.70 kN (14.32 kips) (Leng et al. 2014)

Column length (m)	0.61	1.22	4.88
Mean value of P_n/P_y	0.951	0.841	0.178
Standard deviation of P_n/P_y	0.003	0.011	0.019
Coefficient of variation of P_n	0.003	0.013	0.106

2.5.2 Optimization results with end-use and manufacturing constraints

(a) Optimization results of short length (2 ft) column

The number of rollers has a strong influence on manufacturing cost. In this section the relationship between the number of rollers and achievable strength using the SA design algorithm with end-use constraints is explored. As in the previous section, the results are categorized by the member lengths and then by the number of rollers. For each case, the three best cross-sections resulting from the ten SA simulations are provided.

Starting from the lipped channel section in Figure 2-5(a), Figure 2-24 to Figure 2-28 show the best sections for the 2 ft (0.61 m) long column found by varying the number of rollers from four to twelve. The optimized designs are all symmetric, with increasing complexity in the lips and webs as the number of rollers is increased. When only four rollers are present, the algorithm optimizes flange, lip and web dimensions plus an adjustment of the lip angle. As shown in Figure 2-24, all shapes have shortened web and lengthened flanges and lips, with the web depth and clearance at 3.625 in. (92.08 mm) and 1.0 in. (25.4 mm), respectively, approaching their respective constraint boundaries. One can infer from the results that SA can thoroughly search the design space and the globally optimized section is fairly robust. Table 2-6 contains the critical and nominal loads for the optimized sections normalized by the squash load, and shows that the optimized section using only four rollers more than doubles the capacity against the reference lipped channel section.

Design freedom increases with increasing number of rollers, leading to optimized sections that resemble the 'Σ' shape. The simplest 'Σ' sections are those in Figure 2-25 with only one inward stiffener located at the middle of the web. A corrugated web and complex lips can be formed, and are formed, when ten or twelve rollers are applied (see Figure 2-27 and Figure 2-28). As illustrated in Table 2-6, these complex stiffeners enhance local buckling resistance, similar to end-use only results. Interestingly, Table 2-6 also indicates that the optimized result for the 2 ft (0.61 m) long column using 12 rollers and end-use constraints offers slightly larger strength than the solution of Figure 2-20(a), which considered only end-use constraints (requiring forty-one rollers). Although very similar in magnitude, this result in unexpected and suggests the SA algorithm performs well in the reduced dimension space using design variables of Eqn. (2-7).

A typical convergence curve is shown in Figure 2-29 and is similar to the convergence curve in Figure 2-21. The algorithm found the optimized design after about 3000 objective function evaluations, and the fluctuation illustrates acceptance of inferior designs at the beginning stage of search process. Finally, we note the strength of the final optimized design is only 4.3% less than the squash load (i.e., the ideal or maximum possible P_n), as indicated in the figure.

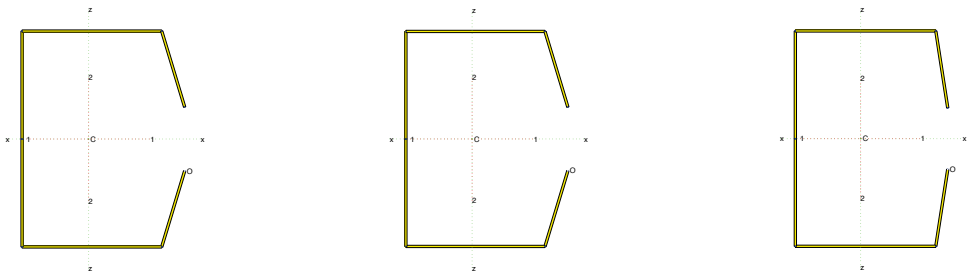

(a) P_n = 41.46 kN (9.32 kips) (b) P_n = 41.46 kN (9.32 kips) (c) P_n = 41.41 kN (9.31 kips)
Figure 2-24: Optimized cross-sections found by SA for 0.61 m (2 ft) column, 4 rollers (Leng et al. 2014)

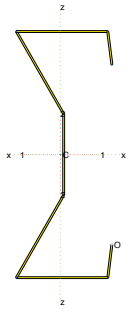

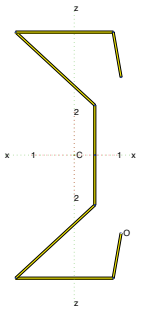

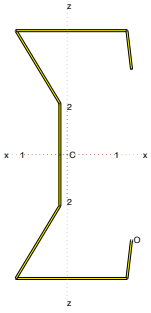

(a) P_n = 56.89 kN (12.79 kips) (b) P_n = 56.62 kN (12.73 kips) (c) P_n = 56.31 kN (12.66 kips)
Figure 2-25: Optimized cross-sections found by SA for 0.61 m (2 ft) column, 6 rollers (Leng et al. 2014)

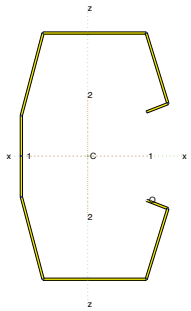

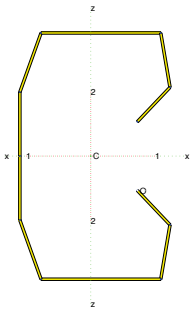

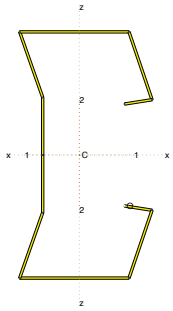

(a) P_n = 60.54 kN (13.61 kips) (b) P_n = 60.54 kN (13.61 kips) (c) P_n = 60.50 kN (13.60 kips)
Figure 2-26: Optimized cross-sections found by SA for 0.61 m (2 ft) column, 8 rollers (Leng et al. 2014)

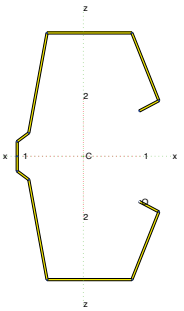

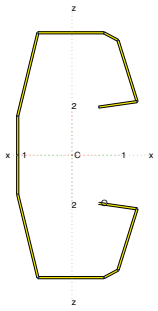

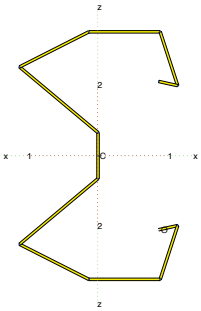

(a) P_n = 60.85 kN (13.68 kips) (b) P_n = 60.76kN (13.66 kips) (c) P_n = 60.71 kN (13.65 kips)
Figure 2-27: Optimized cross-sections found by SA for 0.61 m (2 ft) column, 10 rollers (Leng et al. 2014)

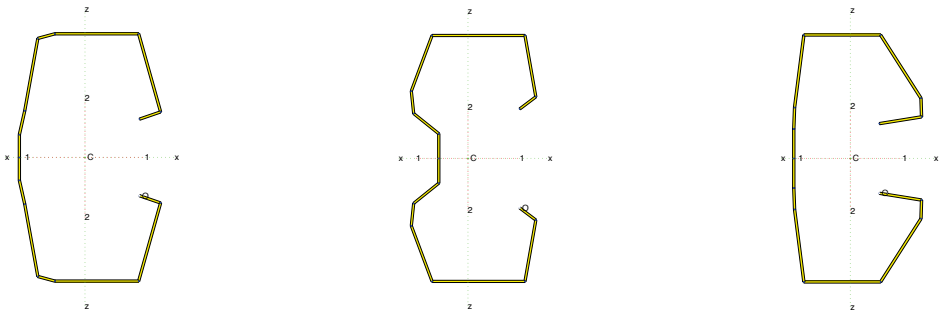

(a) P_n = 60.99 kN (13.71 kips) (b) P_n = 60.81 kN (13.67 kips) (c) P_n = 60.76 kN (13.66 kips)

Figure 2-28: Optimized cross-sections found by SA for 0.61 m (2 ft) column, 12 rollers (Leng et al. 2014)

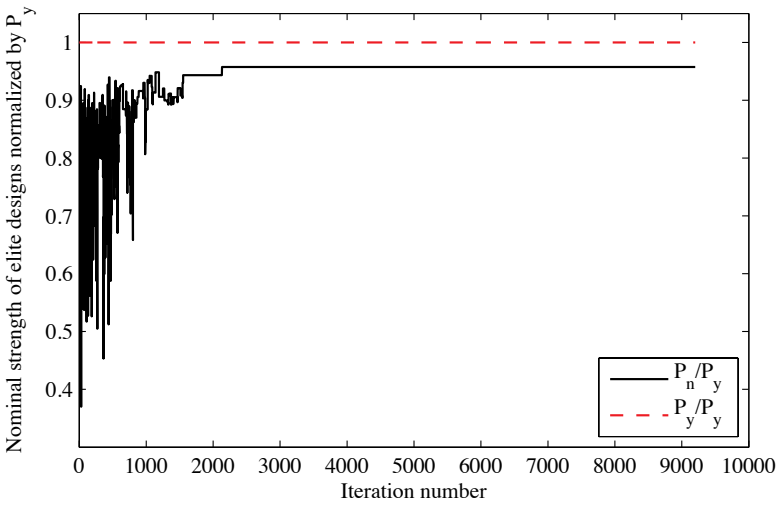

Figure 2-29: Convergence curve of normalized P_{nelite} in search of cross-section in Figure 2-28(a) (Leng et al. 2014)

Table 2-6: Critical and nominal loads of C and 'Σ'−sections, normalized by P_y = 63.70 kN (14.32 kips) (Leng et al. 2014)

Member length	Figure	Section	No. of rollers	P_{crl}/P_y	P_{crd}/P_y	P_{cre}/P_y	P_{nl}/P_y	P_{nd}/P_y	P_{ne}/P_y	P_n/P_y
0.61 m (2 ft)	2-5a	C	4	0.162	0.358	4.793	0.424	0.467	0.916	0.424
0.61 m (2 ft)	2-24a	C	4	0.503	1.505	8.138	0.651	0.869	0.950	0.651
0.61 m (2 ft)	2-25a	'Σ'	6	1.381	1.642	5.241	0.894	0.893	0.923	0.893
0.61 m (2 ft)	2-26a	'Σ'	8	2.126	2.087	9.031	0.955	0.950	0.955	0.950
0.61 m (2 ft)	2-27a	'Σ'	10	2.081	2.939	9.202	0.955	0.998	0.955	0.955
0.61 m (2 ft)	2-28a	'Σ'	12	1.669	2.264	9.591	0.957	0.966	0.957	0.957
1.22 m (4 ft)	2-5a	C	4	0.162	0.358	1.282	0.365	0.467	0.721	0.365
1.22 m (4 ft)	2-30a	C	4	0.503	1.063	2.131	0.592	0.768	0.822	0.592
1.22 m (4 ft)	2-31a	'Σ'	6	1.284	1.172	1.797	0.786	0.797	0.793	0.786
1.22 m (4 ft)	2-32a	'Σ'	8	1.448	1.802	2.338	0.836	0.917	0.836	0.836
1.22 m (4 ft)	2-33a	'Σ'	10	1.531	2.096	2.477	0.845	0.952	0.845	0.845
1.22 m (4 ft)	2-34a	'Σ'	12	1.557	1.427	2.560	0.849	0.855	0.849	0.849

(b) Optimization results of intermediate length (4 ft) column

Optimized designs for 4 ft (1.22 m) long columns using various numbers of rollers are shown in Figure 2-30 to Figure 2-34. Optimized cross-sections range from lipped channel sections with short webs and long lips when using 4 rollers to complex 'Σ'-sections when using 12 rollers. For small numbers of rollers (e.g., 4 or 6), the difference between optimized shapes for 2 ft (0.61 m) and 4 ft (1.22 m) columns is negligible. However, for 10 or 12 rollers, the algorithm focuses on changes in the lips using up to three rollers (compare Figure 2-33 and Figure 2-34), while for shorter 0.61 m (2 ft) long columns the lip is composed of two flats (two rollers) only and more folds are created in the web (See Figure 2-27 and Figure 2-28). This coincides with the observations in (Schafer et al. 2006) on the beneficial effects of complex stiffeners. Numerical results for critical loads and axial capacities of the related cross-sections are listed in Table 2-6.

Cross-sections in Figure 2-34 (12 rollers), especially Figure 2-34(a), bear a close resemblance to the section found in Figure 2-22(a) considering only end-use constraints. Both shapes are more regular and practical than the 'Bobby pin' shapes found in the unconstrained optimization (Figure 2-19(a)). Together with this improvement comes a negligible loss in strength, as the unconstrained solution had a strength of 12.60 kips (56.03 kN) compared to 12.16 kips (54.09kN) for the design of Figure 2-34(a) having end-use and manufacturing constraints.

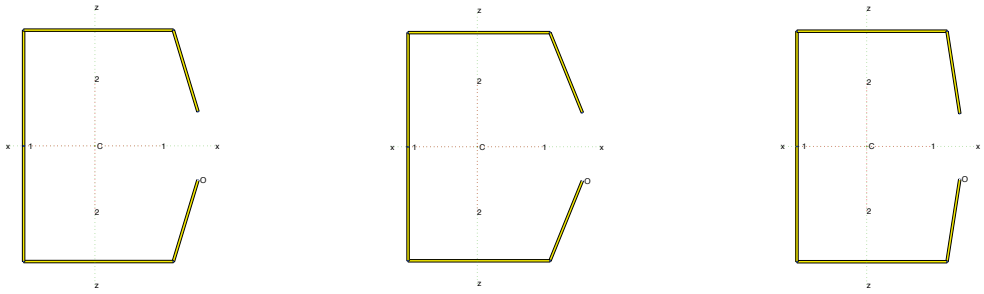

(a) P_n = 37.72 kN (8.48 kips) (b) P_n = 37.63 kN (8.46 kips) (c) P_n = 37.63 kN (8.46 kips)
Figure 2-30: Optimized cross-sections found by SA for 1.22 m (4 ft) column, 4 rollers (Leng et al. 2014)

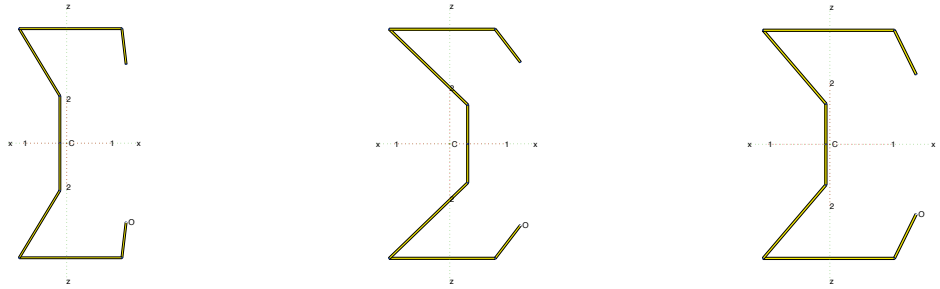

(a) P_n = 50.09 kN (11.26 kips) (b) P_n = 49.78 kN (11.19 kips) (c) P_n = 49.55 kN (11.14 kips)
Figure 2-31: Optimized cross-sections found by SA for 1.22 m (4 ft) column, 6 rollers (Leng et al. 2014)

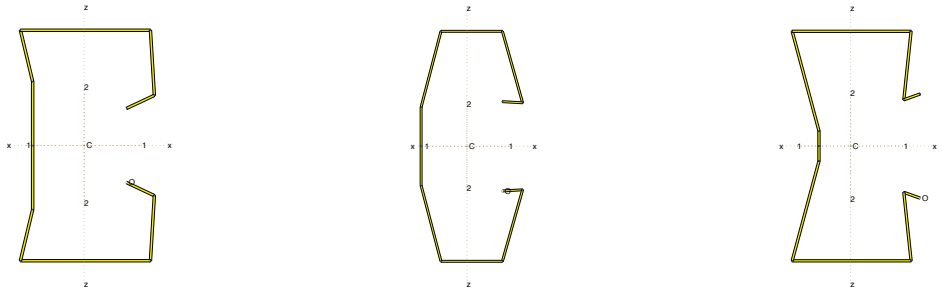

(a) P_n = 53.25 kN (11.97 kips) (b) P_n = 53.11 kN (11.94 kips) (c) P_n = 53.02 kN (11.92 kips)
Figure 2-32: Optimized cross-sections found by SA for 1.22 m (4 ft) column, 8 rollers (Leng et al. 2014)

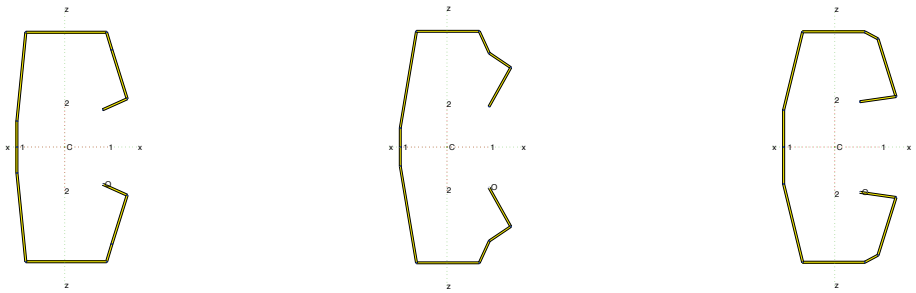

(a) P_n = 53.82 kN (12.10 kips) (b) P_n = 53.69 kN (12.07 kips) (c) P_n = 53.60 kN (12.05 kips)
Figure 2-33: Optimized cross-sections found by SA for 1.22 m (4 ft) column, 10 rollers (Leng et al. 2014)

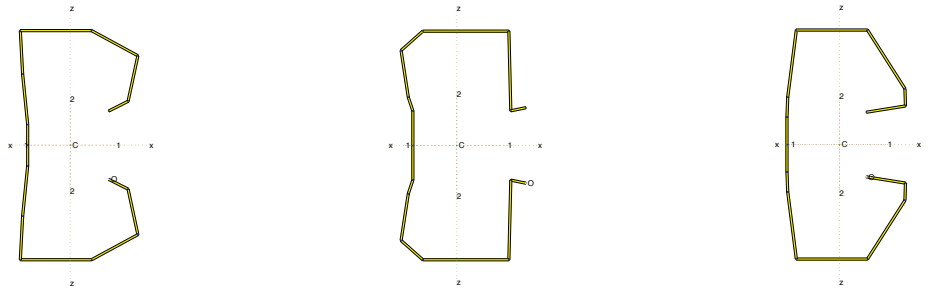

(a) P_n = 54.09 kN (12.16 kips) (b) P_n = 54.05 kN (12.15 kips) (c) P_n = 53.65 kN (12.06 kips)
Figure 2-34: Optimized cross-sections found by SA for 1.22 m (4 ft) column, 12 rollers (Leng et al. 2014)

(c) Optimization results of long length (16 ft) column

As discussed above, optimization results for 16 ft (4.88 m) long columns are significantly different from those of 2 ft (0.61 m) and 4 ft (1.22 m) long columns because of the physical nature of global flexural-torsional buckling. The optimized cross-sections are shown in Figure 2-35 through Figure 2-39, and include a mixture of symmetric and anti-symmetric sections. When only 4 rollers are permitted, the optimized results are symmetric lipped channel sections with short flanges close to the lower bound and long lips with minimum clearances and oriented at approximately 45 degrees (Figure 2-35). This is contrast to the wide flanges and short webs seen in Figure 2-24 and Figure 2-30. The anti-symmetric, squashed 'S' cross-sections found in our previous unconstrained work start to appear when considering 6 rollers and dominate the best shapes when eight or more rollers are allowed. Comparison between shapes in Figure 2-36 to Figure 2-39 to those in Figure 2-23 shows that optimized anti-symmetric sections actually prefer diagonal webs but the mid-web turn-angle constraint for hole-punching forces its midpoint to be vertical. This end-use constraint leads to a minor loss of strength, as expected.

Table 2-7 provides the cross-section properties of the optimized shapes. As seen in Section 2.5.1, end-use constraints preclude the achievement of equal moment of inertias, leading to a decrease in P_n of less than ten percent for an unlimited number of rollers (Figure 2-23(a)) and 16% for eight rollers (Figure 2-37(a)), compared with squashed 'S' without these constraints. Although this reduction of P_n is no longer negligible, the resulting cross-section is more practical and is still 165% stronger than the reference lipped channel section in Figure 2-5(a), whose P_n is only 1.03 kips (4.58 kN).

Unlike short and intermediate columns, the average increase in P_n for the long column is not particularly sensitive to the increase in the number of rollers employed, with the minimum and maximum P_n of 2.74 kips (12.19 kN) and 2.55 kips (11.34 kN), respectively. Although not expected, this maximum was found using only eight rollers, suggesting the results for ten and twelve rollers are local minima, which also suggests further tuning of SA parameters can be performed.

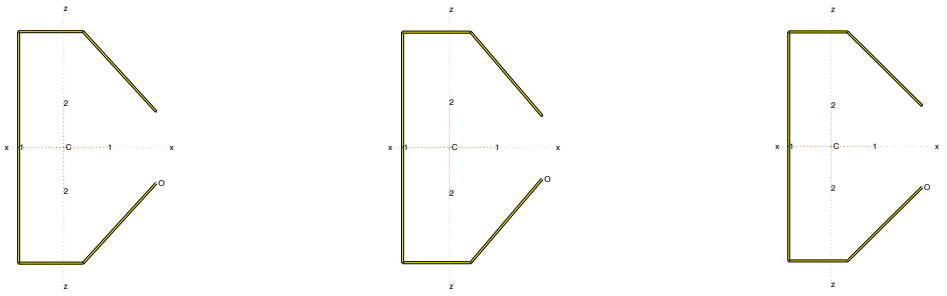

(a) P_n = 11.39 kN (2.56 kips) (b) P_n = 11.39 kN (2.56 kips) (c) P_n = 11.34 kN (2.55 kips)
Figure 2-35: Optimized cross-sections found by SA for 4.88 m (16 ft) column, 4 rollers (Leng et al. 2014)

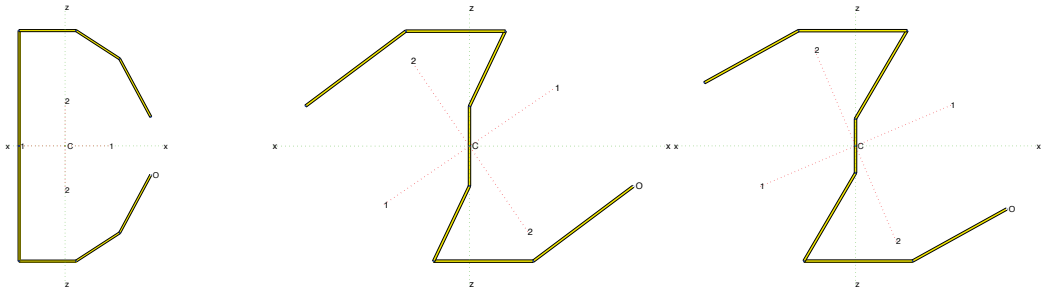

(a) P_n = 11.52 kN (2.59 kips) (b) P_n = 11.48 kN (2.58 kips) (c) P_n = 11.43 kN (2.57 kips)
Figure 2-36: Optimized cross-sections found by SA for 4.88 m (16 ft) column, 6 rollers (Leng et al. 2014)

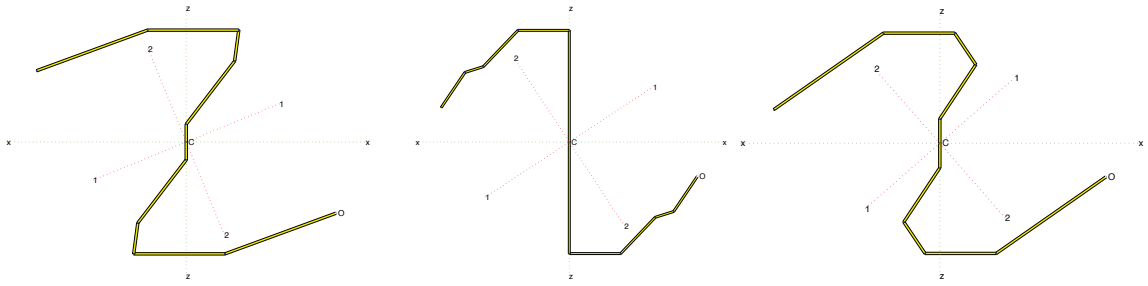

(a) P_n = 12.19 kN (2.74 kips) (b) P_n = 11.43 kN (2.57 kips) (c) P_n = 11.34 kN (2.55 kips)
Figure 2-37: Optimized cross-sections found by SA for 4.88 m (16 ft) column, 8 rollers (Leng et al. 2014)

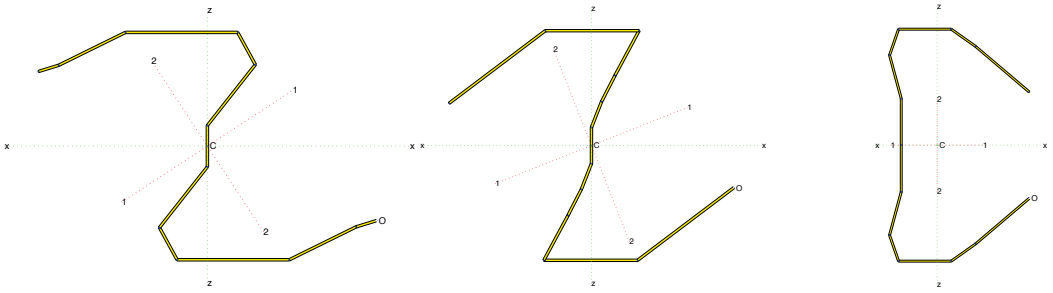

(a) P_n = 11.52 kN (2.59 kips) (b) P_n = 11.39 kN (2.56 kips) (c) P_n = 11.30 kN (2.54 kips)
Figure 2-38: Optimized cross-sections found by SA for 4.88 m (16 ft) column, 10 rollers (Leng et al. 2014)

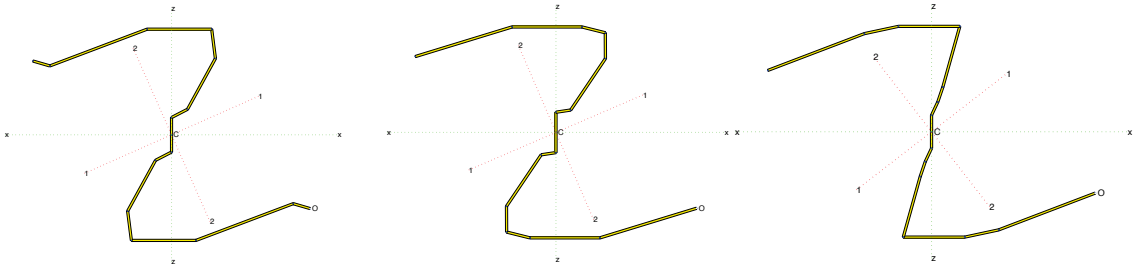

(a) P_n = 11.92 kN (2.68 kips) (b) P_n = 11.65 kN (2.62 kips) (c) P_n = 11.43 kN (2.57 kips)
Figure 2-39: Optimized cross-sections found by SA for 4.88 m (16 ft) column, 12 rollers (Leng et al. 2014)

Table 2-7: Cross-section properties of optimized sections for 4.88 m (16 ft) member (Leng et al. 2014)

Section	Figure	I_{11} (cm^4)	I_{22} (cm^4)	C_w (cm^6)	$\sqrt{x_0^2 + y_0^2}$ (cm)	P_n (kN)
C	2-35a	47.16	14.94	863.07	5.37	11.39
C	2-36a	45.95	15.07	913.83	5.46	11.52
Squashed 'S'	2-37a	41.62	15.86	557.21	0	12.19
Squashed 'S'	2-38a	49.53	15.03	653.62	0	11.52
Squashed 'S'	2-39a	42.25	15.57	583.80	0	11.92

(d) Comparison of constrained optimization results across member lengths

Unconstrained optimization has shown that it is not easy to identify a section with dominated performance for intermediate and long unbraced lengths. However, since optimized shapes for short and intermediate columns are similar herein and unbraced columns as long as 16 ft have limited practical use, it is interesting to study how the optimized cross-section for shorter lengths would perform at the long length. The optimized cross-sections in Figure 2-24 to Figure 2-28 and Figure 2-30 to Figure 2-34 are considered here as 16 ft (4.88 m) long columns and their axial capacities are evaluated and tabulated in Table 2-8. Except for the 'S' sections formed by six rollers, all of the other optimized shapes for short and intermediate length columns still perform reasonably well as long columns, rendering an increase of axial capacity of more than 77% from the reference lipped channel section of Figure 2-5(a). If the number of rollers is eight or greater, the increase is almost 100%, approaching the 140% increase achieved by the sections optimized for 16 ft (4.88 m) long columns. This suggests that the shape optimization of short and intermediate long columns could be unified and solved in one package and the results tend to have improved capacity for a wide range of physical member lengths. Further consideration of external bracing and other end-use factors for long columns is also necessary for making final conclusions on the optimized section.

The preceding results confirm that the SA algorithm is capable of identifying high strength solutions satisfying end-use and manufacturing constraints. Table 2-9 displays the mean and standard deviation of P_n for the ten SA optimized shapes at each length with various roller numbers. Similar to the first column of Table 2-5, coefficients of variation are approximately 1%, suggesting the SA algorithm is consistently producing results with similar design strengths. The coefficients of variation for the long column are the largest at 1%-3%. This; however, is much smaller than the 11% of Table 2-5, suggesting the design variable formulation for limiting the number of rollers (Eqn. (2-7)) improves robustness for this design case.

Table 2-8: Axial capacities of optimized cross-sections for 0.61 m (2 ft) and 1.22 m (4 ft) members evaluated as 4.88 m (16 ft) member (Leng et al. 2014)

Member length	Figure	Section	P_n (kN) as 4.88 m (16 ft) member	Member length	Figure	Section	P_n (kN) as 4.88 m (16 ft) member
0.61 m (2 ft)	2-24a	C	8.14	1.22 m (4 ft)	2-28a	C	8.14
0.61 m (2 ft)	2-25a	'Σ'	4.85	1.22 m (4 ft)	2-29a	'Σ'	6.41
0.61 m (2 ft)	2-26a	'Σ'	9.03	1.22 m (4 ft)	2-30a	'Σ'	9.07
0.61 m (2 ft)	2-27a	'Σ'	9.30	1.22 m (4 ft)	2-31a	'Σ'	8.94
0.61 m (2 ft)	2-28a	'Σ'	9.56	1.22 m (4 ft)	2-32a	'Σ'	9.25

Table 2-9: Mean value and standard deviation of axial capacity P_n of optimized sections of three column lengths normalized by P_y = 63.70 kN (14.32 kips) (Leng et al. 2014)

Member length	No. of rollers	4	6	8	10	12
0.61 m (2 ft)	Mean value of P_n/P_y	0.650	0.876	0.946	0.953	0.953
0.61 m (2 ft)	Standard deviation of P_n/P_y	0.001	0.010	0.003	0.001	0.002
0.61 m (2 ft)	Coefficient of variation of P_n	0.002	0.012	0.004	0.001	0.002
1.22 m (4 ft)	Mean value of P_n/P_y	0.589	0.772	0.824	0.838	0.839
1.22 m (4 ft)	Standard deviation of P_n/P_y	0.002	0.010	0.010	0.005	0.006
1.22 m (4 ft)	Coefficient of variation of P_n	0.003	0.013	0.012	0.006	0.007
4.88 m (16 ft)	Mean value of P_n/P_y	0.177	0.178	0.178	0.177	0.179
4.88 m (16 ft)	Standard deviation of P_n/P_y	0.001	0.002	0.005	0.003	0.004
4.88 m (16 ft)	Coefficient of variation of P_n	0.007	0.012	0.029	0.016	0.023

2.5.3 Summary and comparison of optimization results

To summarize, Table 2-10 contains the capacities of optimized cross-sections found by SA without constraints, with end-use constraints only (requiring forty-one rollers), and with end-use and manufacturing constraints on the number and spacing of rollers. The data is also plotted in Figure 2-40. Performance values of elite designs in the preceding figures are used. For reference, the initial design lipped channel section is also listed (whose number of P_n evaluation is one).

The key conclusions from this table and plot are that the imposition of end-use constraints leads to practical, useable cross-sections that (1) suffer a relatively minor reduction in capacity when compared to complex shapes from unconstrained optimization, and (2) offer significantly larger capacity than the initially considered lipped channel section. As for coupling the end-use constraints with manufacturing constraints limiting the number and spacing of rollers, the key conclusions are that (1) for long columns where global buckling governs, the number of rollers has little effect on the capacity, and (2) for short and intermediate length columns, a relatively large increase in capacity is achieved when increasing the number of rollers from four to six, and relatively small additional increase is achieved when increasing the number of rollers from six to twelve. As manufacturing cost is related to the number of rollers (folds), this offers guidance on the trade-off between cost and performance. Finally, we note the end-use and manufacturing constraints are achieved without significant additional cost to the SA algorithm when compared to unconstrained optimization, and could perhaps be reduced further with additional parameter tuning.

Table 2-10: Design performance comparisons of optimized cross-sections (Leng et al. 2014)

Member length	Section	Type of optimization & constraint	No. of rollers	P_n/P_y	Max No. of P_n evaluation
0.61 m (2 ft)	C	None	20	0.424	1
0.61 m (2 ft)	'Σ'	End-use constraints only	41	0.955	5000
0.61 m (2 ft)	C	End-use and manufacturability	4	0.651	10000
0.61 m (2 ft)	'Σ'	End-use and manufacturability	6	0.893	10000
0.61 m (2 ft)	'Σ'	End-use and manufacturability	8	0.950	10000
0.61 m (2 ft)	'Σ'	End-use and manufacturability	10	0.955	10000
0.61 m (2 ft)	'Σ'	End-use and manufacturability	12	0.957	10000
1.22 m (4 ft)	C	None	20	0.365	1
1.22 m (4 ft)	'Bobby pin'	Unconstrained	20	0.880	2600
1.22 m (4 ft)	'Σ'	End-use constraints only	41	0.855	7000
1.22 m (4 ft)	C	End-use and manufacturability	4	0.592	10000
1.22 m (4 ft)	'Σ'	End-use and manufacturability	6	0.786	10000
1.22 m (4 ft)	'Σ'	End-use and manufacturability	8	0.836	10000
1.22 m (4 ft)	'Σ'	End-use and manufacturability	10	0.845	10000
1.22 m (4 ft)	'Σ'	End-use and manufacturability	12	0.849	10000
4.88 m (16 ft)	C	None	20	0.072	1
4.88 m (16 ft)	Squashed 'S'	Unconstrained	20	0.223	10000
4.88 m (16 ft)	Squashed 'S'	End-use constraints only	41	0.207	20000
4.88 m (16 ft)	C	End-use and manufacturability	4	0.179	10000
4.88 m (16 ft)	C	End-use and manufacturability	6	0.181	10000
4.88 m (16 ft)	Squashed 'S'	End-use and manufacturability	8	0.191	10000
4.88 m (16 ft)	Squashed 'S'	End-use and manufacturability	10	0.181	10000
4.88 m (16 ft)	Squashed 'S'	End-use and manufacturability	12	0.187	10000

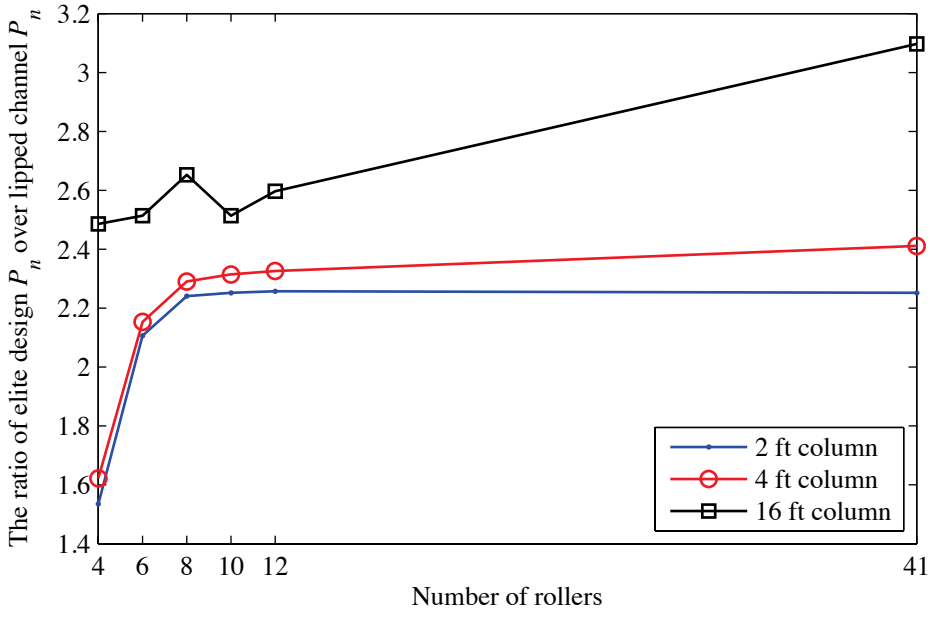

Figure 2-40: Nominal strength ratios between elite optimized cross-sections and lipped channel (Leng et al. 2014)

2.6 Conclusions on shape optimization of cold-formed steel columns

The work presented here is a systematic development of a simulation-based design optimization tool of cold-formed steel columns implemented by combining a numerical solver on cross-section stability (CUFSM), a flexible set of strength expressions (DSM) and formal optimization frameworks. The uniqueness of the developed method is the ability to explore the full design space available from roller-forming of an open cross-section given a coil of steel sheet. Constraints are taken into account step by step, from unconstrained search to incorporation of end-use constraints and manufacturability constraints for fabrication. The cross-section that maximizes the axial capacity is always sought.

For unconstrained optimization, the performance of three optimization methods are explored: steepest descent, genetic algorithms, and simulated annealing. Results indicate that the gradient-based SD provides an efficient local search, while GA and SA are stochastic search methods that provide a more general search and can identify globally optimized solutions. Among the optimized cross-sections for global buckling controlled 16 ft (4.88 m) long columns, the squashed 'S' section performs best with its distinct properties of coincident shear center and centroid, nearly equal moments of inertia about the principal axes, and relatively high warping stiffness. Capacity of the optimized section can be increased as much as 209% over standard lipped channel sections.

At intermediate length 4 ft (1.22 m) the S-shaped column still has 20% greater capacity than a standard lipped channel, but other sections (identified as the 'bobby pin', and

curled channel herein) have 140% greater capacity. These alternative sections are not as efficient in global buckling as the S-shape but greatly improve local and distortional buckling performance. The practical value of these optimized sections is reduced due to the fact that they miss shape regularity.

As a follow-up, a series of end-use and manufacturing constraints, including limits on number and spacing of roll stands where the section may be folded, are formulated and integrated in SA. The algorithm is chosen for its global search capacity and relatively low computational cost. The end constraints include symmetry and anti-symmetry; a requirement for parallel flanges for board attachments; minimum and maximum dimensions on web, flange, and lip dimensions; and depth and clearance requirements. The design variables are the turn-angles at each node of the finite strip model when only end-use constraints are considered, and the width and turn-angles of strips when end-use and manufacturing constraints are considered.

Columns with short 2 ft (0.61 m), intermediate 4 ft (1.22 m), and long 16 ft (4.88 m) unbraced lengths were studied for two formulations of the constrained optimization problem. A considerable increase of P_n was consistently achieved through the optimization, demonstrating the power of the design optimization algorithm. Optimized shapes from both formulations exhibit a number of similar features, supporting the robustness of the SA algorithm. Optimized designs for short and intermediate unbraced length columns were consistently singly-symmetric. For four rollers (four folds), only lipped channel sections with shallow webs, long flanges and lips can be formed, but P_n is

still optimized by more than 50% above the initial lipped channel section. For larger numbers of rollers (folds) 'Σ'-sections can be formed providing a further increase of P_n (more than 100% above the initial lipped channel section). For long columns, optimization with 4 rollers yields a lipped channel section with short flanges and long protruding lips. Squashed 'S' sections, found in unconstrained optimization, appear in long columns when more rollers are allowed. Numerical comparison indicates that the anti-symmetric squashed 'S' sections satisfying the end-use and manufacturing constraints are not overwhelmingly better than singly-symmetric sections. For long columns the optimized solutions all provide at least a 140% increase over the reference lipped channel section. It is also evident that increases in capacity taper off once the number of rollers approaches ten, as optimized sections with ten rollers achieve nearly the same nominal strength as sections found using forty-one equally spaced rollers.

Detailed comparison through our research from unconstrained optimization to constrained optimization shows that the formulation based on a finite number of folds lead to a reduced dimension of the design space and the total number of objective function evaluations and the machine time for each CUFSM analysis both decreased. The optimized shapes that meet the construction and manufacturing constraints have significant potential for commercial application. Of the optimized sections explored, the 'Σ'-sections developed here are currently preferred due to their ability to provide robust capacity increases across all studied limit states/unbraced lengths, yet require only minimal change in current manufacturing and construction. In the future, the shape optimization work can be extended to other CFS members like beams and beam-columns

and it can be incorporated in design optimization packages on system level of CFS structures as well.

Chapter 3: Modeling Techniques of Cold-form Steel Framed Building with OSB and Gypsum Sheathing

This chapter is the first one dedicated to the modeling and time history analysis of a two-story cold-formed steel framed building. The archetype building is central to the project funded by the U.S. National Science Foundation and AISI and formally a part of the NSF Network for Earthquake Engineering Simulation (NEES) research program under the title: Enabling Performance-Based Seismic Design of Multi-Story Cold-Formed Steel Structures, or in short CFS-NEES (Schafer 2015). In this chapter, first the design of the building will be briefly discussed, including design assumptions, major source of references for design, and the value of several important coefficients used in the design. Through the process of modeling, a series of models at various modeling fidelity levels are developed. The idea of developing these models is to study the significance of structural components and the methods to model them for nonlinear analysis. The models are frequently referred to in the current and subsequent chapters. Available and selected modeling choices and considerations are provided in Section 3.2. Later sections, from Section 3.3 to Section 3.6, provide detailed description of the modeling methodology for major structural and nonstructural components, including shear walls, gravity walls, floor and roof diaphragms, and interior walls. At the end of the chapter, Section 3.7 describes the method of assigning seismic mass to the FE models. Secition 3.8 describes the gravity load distribution in models. Section 3.9 discusses the model of the tie between shear wall chord studs across the floor.

3.1 Description of the CFS-NEES building design and construction

3.1.1 Nomenclature

The archetype CFS-NEES building (Madsen et al. 2011) is the object of the modeling and simulation detailed herein. Also, the modeling work developed herein interacts significantly with the full scale scaling shaking table tests conducted within the CFS-NEES project (Peterman 2014; Peterman et al. 2014; Peterman et al. 2014; Schafer et al. 2014; Schafer 2015). To aid comparison between models and tests the nomenclature is explained first and in general is kept the same between experimental and computational work. As the modeling work generally has followed the experimental work; consequently, the nomenclature proposed in Peterman's dissertation is adopted here (Peterman 2014).

As suggested by Peterman (Peterman 2014), Figure 3-1 documents the vocabulary and nomenclature used herein to refer to the building specimens and their orientation.

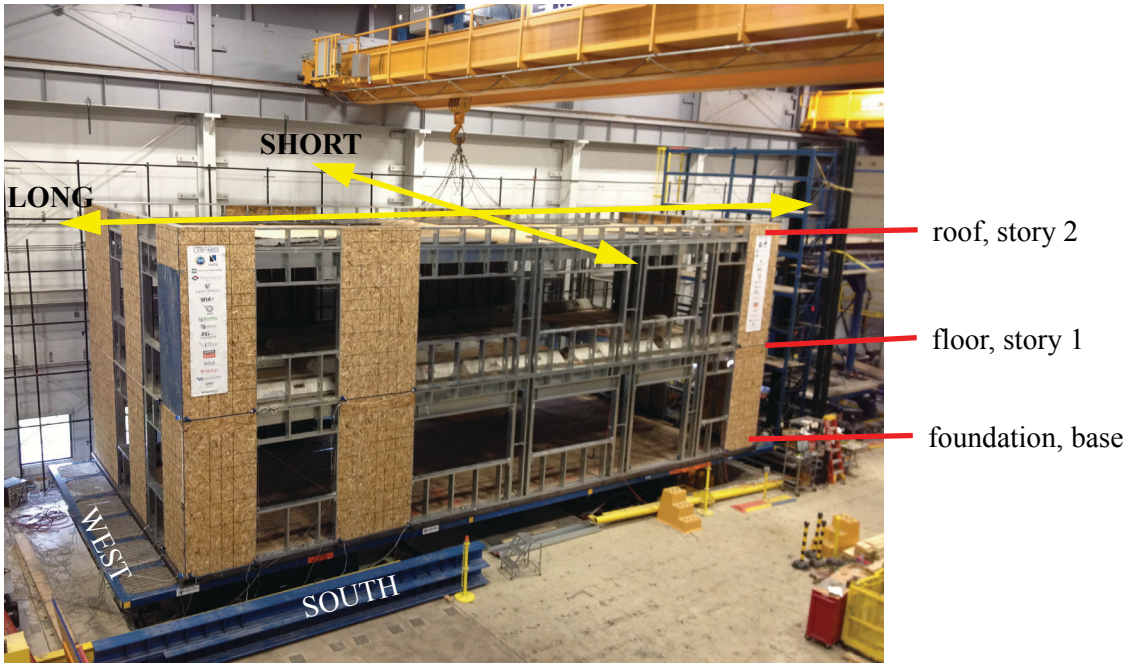

Figure 3-1: Nomenclature and orientation for building specimen, as built in Phase 1 (Peterman 2014)

In accordance with the test (Peterman 2014), the Cartesian coordinate system the building and shake table occupy will be henceforth referred to as the (long, short, and up) coordinate system. This convention is defined with respect to the building geometry. Ground motion in the long direction refers to ground motion resisted by the North and South (long) walls of the building. Ground motion in the short direction refers to ground motion resisted by the East and West (short) walls of the building. Perpendicular to the other two, the up direction is in the opposite direction of gravity. Table 3-1 summarizes the definition of directions.

Table 3-1: Definition of directions

	Motion	Resisting Walls	Displacement	Coordinate
LONG	shaking from E to W	N-S Long walls	u	x
SHORT	shaking from N to S	E-W Short walls	v	y

The lateral displacements in long and short directions are denoted by u and v respectively, and subscripts 1 and 2 are adopted for story 1 (floor level) and 2 (roof level). Thus, physical quantities, such as u_1 and v_2, are referred to frequently in later chapters. Correspondingly, coordinates in long and short directions are denoted by x and y, respectively.

3.1.2 CFS-NEES building design

The CFS-NEES building was designed by engineers from Devco Engineering with the objective of completing a state-of-the-practice archetype building. A detailed narrative of the design of the CFS-NEES building is available from Madsen et al. (Madsen et al. 2011) Design criteria, architectural concepts, calculations and design summary of structural components are included in the report. The real building was subject to full scale shaking

table tests in the Structural Engineering and Earthquake Simulation Laboratory at the University at Buffalo in the summer of 2013. Mader Construction Corporation of Alma, NY was contracted to build the structures and deconstruct them.

The building is a two-story structural system with an all-steel design for CFS-framed gravity walls and CFS-framed shear walls sheathed in oriented strand board (OSB) for the LFRS. Also, floor and roof diaphragms (as detailed in Section 3.5) are also designed with CFS-framed joists and tracks and OSB sheathings of different thickness (Figure 3-2). Gravity and lateral loads were determined per IBC (2009) which specifies ASCE 7-05 (American Society of Civil Engineers 2005) for loading. Cold-formed steel members were sized per American Iron and Steel Institute (AISI) Specifications (AISI S100, -S210, -S211) (American Iron and Steel Institute 2007; American Iron and Steel Institute 2007; American Iron and Steel Institute 2012). The LFRS was also designed using an AISI specification (AISI S213) (American Iron and Steel Institute 2009). The building was constructed in phases (as detailed later), and each single phase was tested (Peterman 2014).

The building was designed assuming a hypothetical location of 520 W. Walnut Blvd, Orange, CA, USA (latitude 33.8 degrees, longitude -117.86 degrees). Building dimensions are 50 ft (15.24 m) x 23 ft (7.01 m) in plan and 19 ft (5.79 m) in height. Designed to be a functioning office building, the building was designed with interior partition walls, windows, doorways, and staircases.

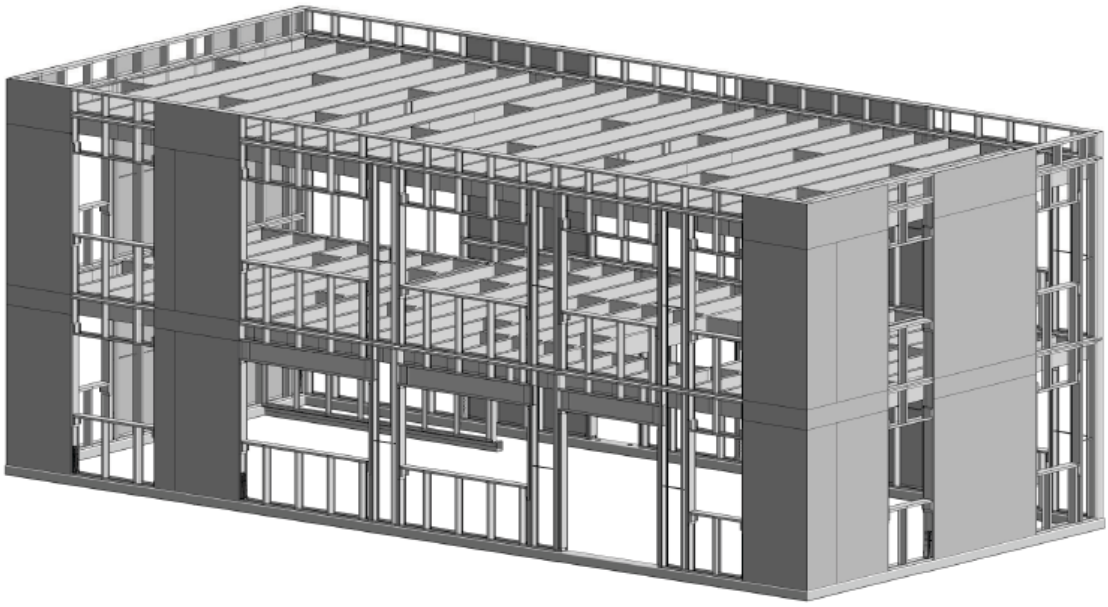

Figure 3-2: Three-Dimensional BIM model of the CFS-NEES building, Phase 1 (sheathing applied only for shear walls)

The construction of the CFS-NEES was performed at various phases. The building at Phase 1 is composed of structural components in design assumptions. Detailed description of construction phases is available at Section 3.1.4. An exploded view of the Phase 1 building structural system is shown in Figure 3-3. The floor diaphragm is unsymmetrical, with two openings for staircase framing. Additionally, the north wall contains a two-story balloon-framed wall near the northwest corner to accommodate a staircase along the wall; the rest of the building was ledger-framed. In Figure 3-3, sheathing on the floor and roof diaphragms is not shown for clarity.

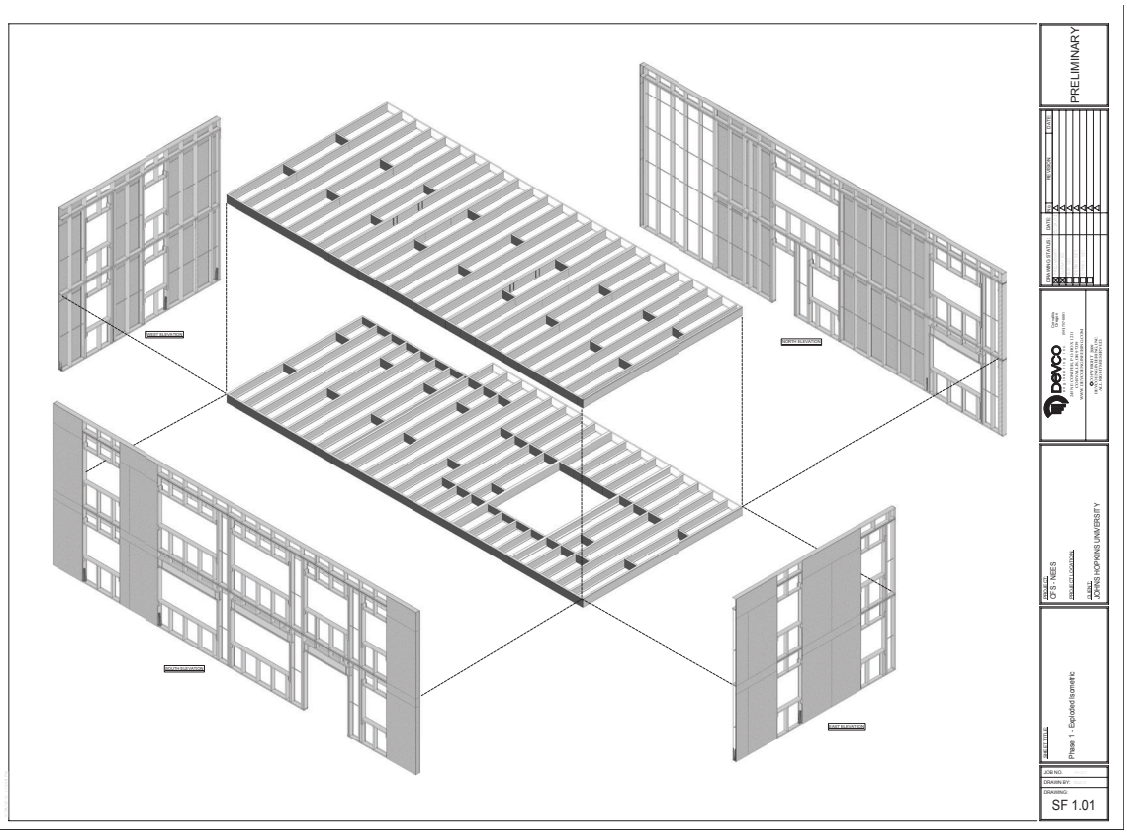

Figure 3-3: Exploded view of the Phase 1 building specimen, framed only with structural components (drawing by Phil Clark at Devco)

According to Madsen et al. (Madsen et al. 2011) the design of gravity system adopted a 'ledger framing' system rather than traditional platform framing. Typical gravity wall elevations are shown in Figure 3-4. First story gravity walls were framed with 600S162-54 studs while the second story was framed with 600S162-33 studs. All studs, including those used for shear walls, were punched with a 4 in. (10.16 cm) long by 1.5 in. (3.81 cm) wide standard oval cutout every 24 in. (60.96 cm). Ledgers are shown where the flanges of studs are screwed to the webs of diaphragm tracks and the flanges of diaphragm tracks are fastened to diaphragm joists of both levels. Also shown in the figure are details of the ballon wall in the northwest corner. At that corner, the floor joists are supported by an interior wall with studs sized as 362S162-54 at 24 in. (60.96 cm) on center. Also, the

exterior wall at that corner uses balloon framing with studs span the full 18 ft (5.49 m) height to the roof. Bridging on webs of studs is at 49 in. (124.46 cm) on center.

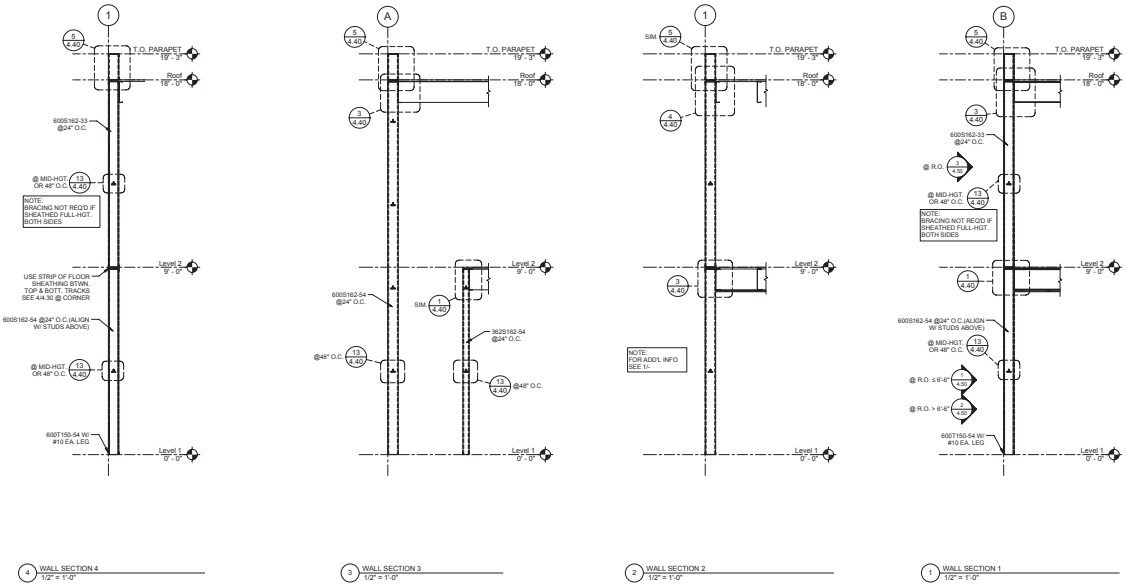

Figure 3-4: Gravity wall elevation drawings for Phase 1 building specimen

The design of the LFRS employed a base shear coefficient C_s=0.143, where C_s is determined from the response modification coefficient R=6.5, overstrength factor Ω_O=3, and deflection amplification factor C_d=4 according to ASCE 7-05 (American Society of Civil Engineers 2005) – selected based on the type of LFRS employed, shear walls with wood structural panels, and the framing type: repetitive. Typical shear wall framing details are given in Figure 3-5. In the design of this building, Type I shear walls were selected throughout (see more details in Section 3.1.3). Chord studs on both the first and second stories were framed with back-to-back 600S162-54 studs and walls were sheathed with 7/16 in. (1.11 cm) OSB sheathing. Top and bottom tracks are 54-mil (600T150-54) for shear walls on floor level, while they are 43-mil (600T150-43) on the roof level.

Shear wall ties, shown in inset drawing #2 in Figure 3-5, connect the first story chord studs to the second story chord studs. Simpson S/HDU6 hold downs anchor the shear wall chord studs to the foundation tube steel, as shown in inset drawing #3 in Figure 3-5. Data from the manufacturer were used for hold down strength and stiffness in design and finite element modeling. Shear anchors are installed to transfer shear force from shear walls on roof level to floor level and then to the foundation.

Complete drawings are available from Madsen et al. (Madsen et al. 2011). Shear walls are named following the same nomenclature as in the design narrative. The name of a shear wall is a four-character string: the story (level) number with initial L and the number of the shear wall on the wall line (with initial of North, South, East, or West). For example, the shear wall L1S2 is located on Level 1 (L1) on the South (S) wall, and is the 2nd shear wall along that wall line.

An intuitive comprehension of building components may be generated by understanding the percentage of shear walls, openings, and the amount that the building is sheathed (at least w.r.t the structural-only system). These quantities are useful in quantifying results in later discussions of results. The South wall line contains the largest percentage of openings while the West wall line contains the largest percentage of shear wall (Table 3-2).

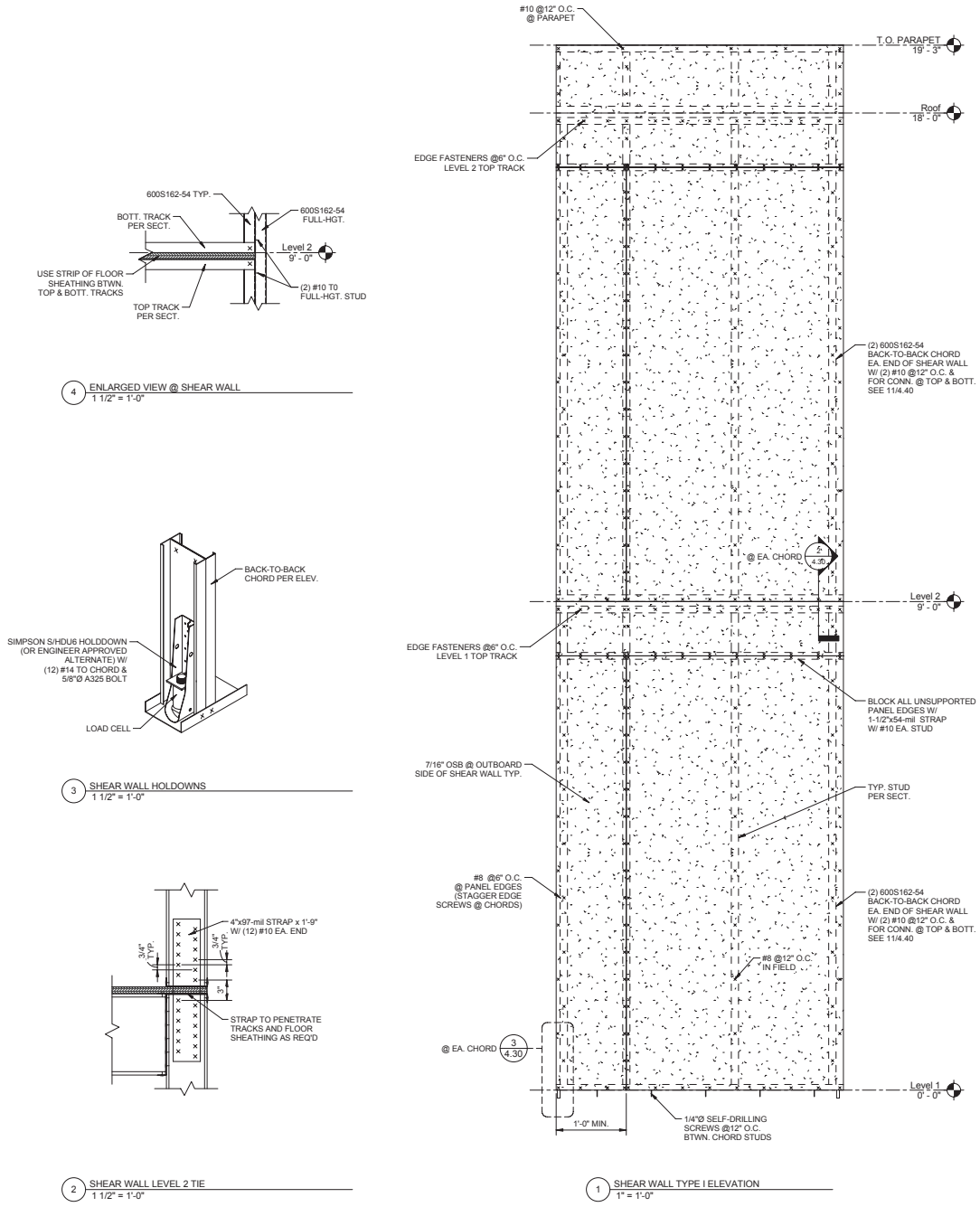

Figure 3-5: Typical shear wall framing for the Phase 1 building (chord stud fasteners are drawn staggered at 12 in. (30.48 cm) on-center but were construction in line, on the outer stud, at 6 in. (15.24 cm) on-center).

In the design of the diaphragms they were idealized as flexible according to ASCE 7-10 (American Society of Civil Engineers 2010). The floor diaphragm was framed with

1200S200-97 joists and 1200T200-97 rim tracks sheathed with 23/32 in. (1.83 cm) thick OSB sheathing. The roof diaphragm was framed with lighter sections: 1200S200-54 joists and 1200T200-68 rim tracks and the OSB sheathing was 7/16 in. (1.11 cm) thick. Diaphragm perimeter members were sized for the maximum value of drag force supplied to the shear walls and diaphragm chord forces based on a beam analogy with the chords acting as the tension and compression elements similar to beam flanges (Madsen et al. 2011). Reinforcing details of the openings on the floor diaphragm can be found in the design narrative (Madsen et al. 2011).

Table 3-2: Building components by percentage of total wall area (Peterman 2014) for Phase 1/2a structural only building

	AREA (ft^2)				PERCENT (%)		
Wall	**Shear Wall**	**Opening**	**Sheathed**	**Wall**	**Shear Wall**	**Opening**	**Sheathed**
South	243	273	685	958	25%	28%	72%
West	294	53	390	443	66%	12%	88%
North	358	129	828	957	37%	13%	87%
East	261	53	390	443	59%	12%	88%

3.1.3 Type I versus Type II shear wall design

Due to the scope of this thesis, special attention is given to the design assumptions for shear walls in current standards. The commentary to AISI S213-07 (American Iron and Steel Institute 2009) defines shear walls as either (Type I) shear walls without detailing for force transfer around openings (with hold downs installed at the ends of each wall segment) or (Type II) shear walls with detailing for force transfer around openings. As shown in Figure 3-6, the behavior of Type I shear walls in a wall line under seismic load is assumed to be isolated. Among the pair of hold downs, for an isolated shear demand it is assumed one is in compression and the other is in tension. For Type II, the coupled shear walls experience tension and compression across a wall line.

The difference of behavior between these two shear wall types is apparent. Type I shear walls are laterally decoupled (gravity walls are not designed to resist lateral forces) and the hold downs experience the same amount of tension and compression on two ends of the wall segment (for an isolated shear load), making each shear wall segment rock individually under seismic load. Type II shear walls are coupled with gravity framing and thus behave like a large wall. The hold downs of the whole wall line balance the overturning moment and a pair of them for one wall may be in tension or in compression at the same time.

Type I shear walls are specifically detailed to behave as such, while Type II are generally not—an extension from timber framing attempts to estimate the lateral resistance of a segment of wall even when it is not specifically detailed (Peterman 2014). As mentioned, the building specimens were designed to behave as Type I shear walls (Madsen et al. 2011). Seismic design coefficients were determined from ASCE 7-05 (American Society of Civil Engineers 2005) and shear walls were designed according to AISI S213 (American Iron and Steel Institute 2009). Thus, a goal of the testing and the high fidelity FE modeling presented here is to discuss/determine if the Type I designed shear walls behave like isolated walls.

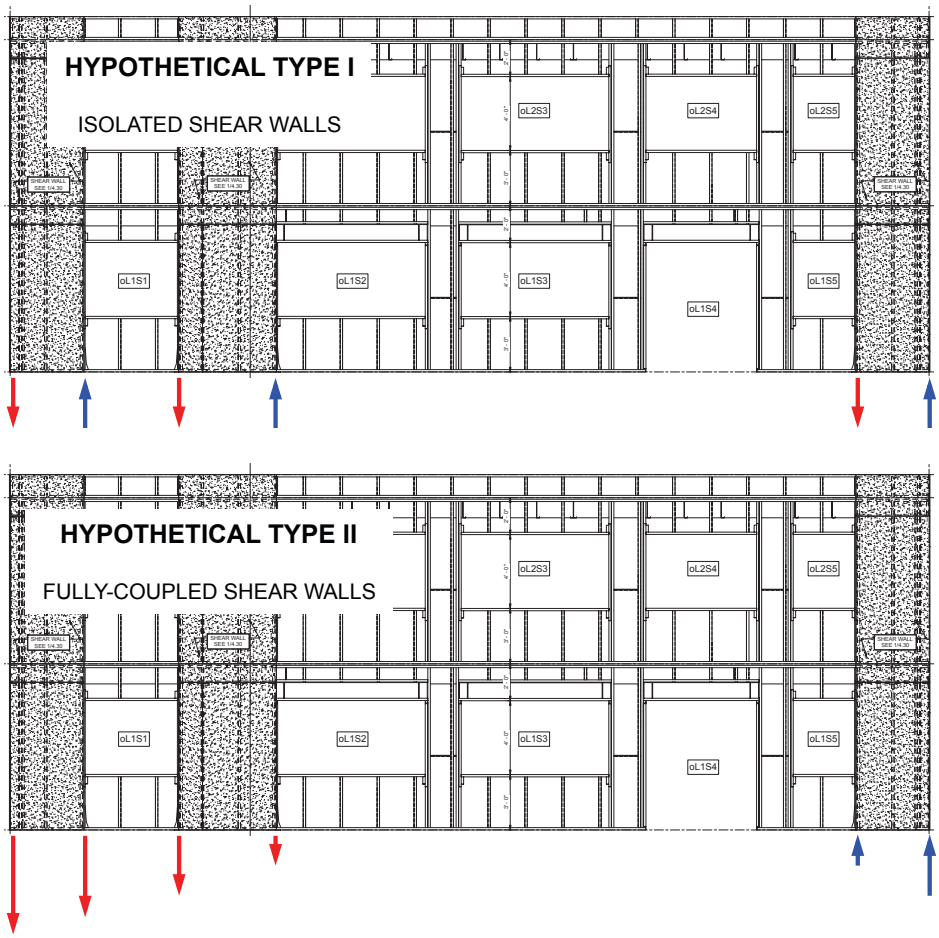

Figure 3-6: Drawing illustrating the two types of shear wall on the South elevation. The top drawing demonstrates the ideal anchor force distribution for Type I shear walls, or isolated shear walls. The bottom drawing provides an idealization for the hypothetical Type II, or fully-coupled shear walls (Peterman 2014)

Implicit in current shear wall design is that gravity framing (including window headers, door jambs and the like) has no contribution in lateral resistance. This assumption is also explored through testing and the simulations detailed herein through the results of high fidelity models, as discussed in later chapters.

3.1.4 CFS-NEES building construction phases

The CFS-NEES experimental portion involved the construction and testing of two full-scale two-story buildings (Peterman 2014). The first building, hereafter called Phase 1,

was the complete structural system and represents the engineered building system: both for lateral (OSB sheathed shear walls) and gravity loading (bare CFS frame). None of nonstructual components were included in Phase 1. The Phase 2 structure continued construction past the engineered system of Phase 1 after its deconstruction following the testing. As depicted in Figure 3-7, in Phase 2b the gravity exterior walls were externally sheathed, in Phase 2c the interior face of the exterior walls were sheathed with gypsum, in Phase 2d all the interior partition walls and staircases were installed, and finally in Phase 2e exterior DensGlass was installed (Schafer 2015). Again, the same nomenclature is referred to in this simulation work.

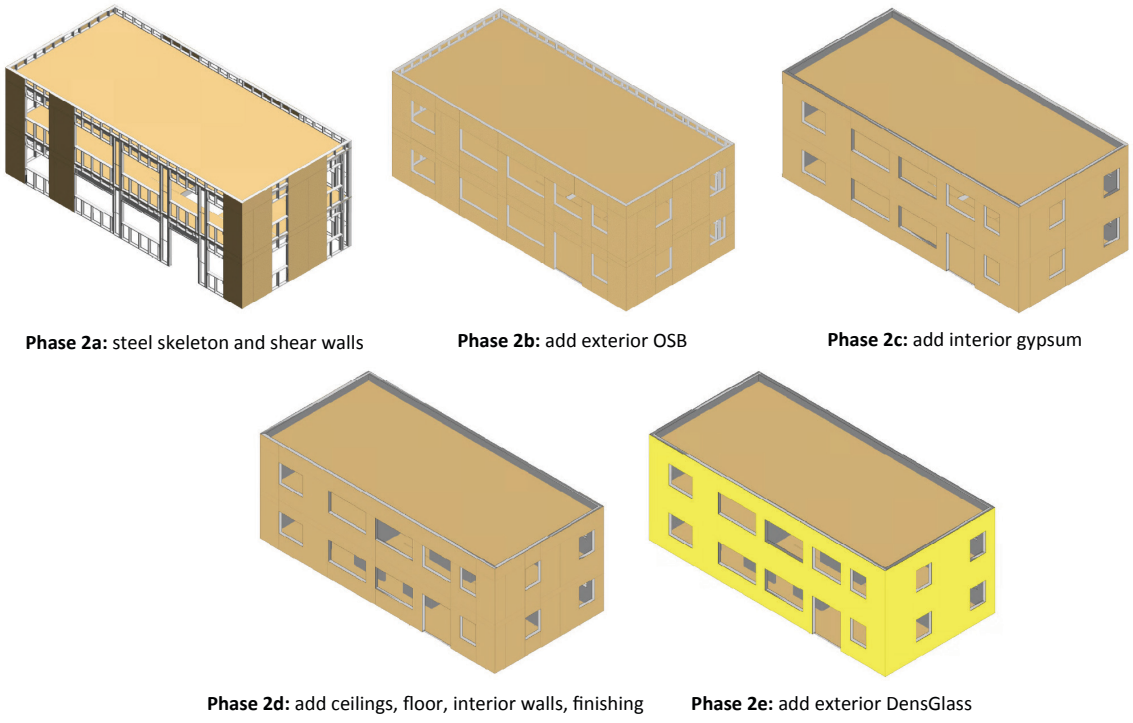

Figure 3-7: Phase descriptions of Phase 2 construction (Phase 2a is nominally identical to Phase 1) (Peterman 2014)

3.2 General note on naming convention and scope of finite element models

A series of finite element models have been created and implemented in the open source software OpenSees (McKenna 2011). OpenSees has a number of nonlinear material elements to characterize the nonlinear behavior at a member level and has been widely used in seismic analysis of both structural engineering and geotechnical engineering.

As mentioned in Chapter 1, limited efforts have been reported on the modeling of the nonlinear seismic response of CFS-framed buildings. The work herein is a summary of a series of modeling trials performed in recent years to provide an accurate nonlinear seismic model for the CFS-NEES buiding. To foster a better understanding and to explain the scope of the effort, the nomenclature for the FE models is addressed first.

Models are distinguished by two modeling stages: state-of-the-practice (P-) models and state-of-the-art (A-) models. P-models may be relatively sophisticated, but are developed based on tables and formulae in design standards and do not use specialized experimental data. A-models utilize test data in their development, may be more complicated in implementation, but generally have the potential to be more accurate. All models are assumed to match construction phases of the archetype building, so the phase number is attached. For example, A1- models are those A-models developed for Phase 1 construction.

The dimension of the models is the second segment in the nomenclature. It can be either 2D for two-dimensional or 3D for three-dimensional models. The third segment in a

model's nomenclature refers to how to model the diaphragms and is relevant for 3D models. For 3D models, we explore two options: rigid diaphragm (RD) or semi-rigid diaphragm (SD). By default, 2D models are the case of a (completely) flexible diaphragm (FD), since there is no coupling between shear walls induced by the diaphragms. A lower case letter starting from 'a' is added to uniquely mark the version of models for any other modeling considerations.

For 2D models, the initial from four directions (N, S, W or E) is added as a suffix to denote a specific wall elevation. Consequently, examples of full model names include P-2D-a-N (state-of-the-practice two-dimensional model, version 'a', North elevation) and A2a-3D-RD-a (state-of-the-art three-dimensional model with rigid diaphragms, version 'a', construction Phase 2a).

Table 3-3 below is a summary of modeling considerations and options covered in the following sections. The model space covered by Table 3-3 is extensive, but given the lack of understanding as to what level of modeling is appropriate represents an attempt to make a comprehensive exploration of the practical possibilities. The standardized outputs of each model or model set are appended at the end of the thesis. Detailed discussions on model performance, and investigation of the modeling strategies alluded to in Table 3-3 are presented in later chapters.

Table 3-3: Modeling options of the CFS-NEES archetype building

			State-of-the-practice models				State-of-the-art models										
Component	Property	Option	P-2D-a	P-2D-b	P-3D-RD-a	P-3D-RD-b	A1-2D-a	A1-2D-b	A1-2D-c	A1-3D-RD-a	A1-3D-RD-b	A1-3D-RD-c	A1-3D-SD-a	A1-3D-SD-b	A2b-2D-a	A2b-3D-RD-a	A2b-3D-SD-a
Shear wall	Stiffness	$K(0.4V_{nP})$		X		X											
		$K(V_{nP})$	X		X												
		$K(0.2V_{nA})$					X		X	X		X	X		X	X	X
		$K(0.4V_{nA})$						X			X			X			
	Capacity	V_{nA}					X	X	X	X	X	X	X	X	X	X	X
		V_{nP}	X	X	X	X											
	Backbone	EPP	X		X												
		Pinching4		X		X	X	X	X	X	X	X	X	X	X	X	X
	Panel size	Whole	X	X	X	X			X			X					
		Subpanels					X	X		X	X		X	X	X	X	X
Hold down	General	Smeared	X	X	X	X											
		Discrete					X	X	X	X	X	X	X	X	X	X	X
Shear anchors	General	Ignored	X	X	X	X											
		Included					X	X	X	X	X	X	X	X	X	X	X
Diaphragm	Stiffness	Flexible	X	X			X	X	X						X		
		Rigid			X	X				X	X	X				X	
		Semi-rigid											X	X			X
	Pinching	None	X	X	X	X	X	X	X	X	X	X			X		
		Pinching4											X	X		X	X
Gravity exterior walls	General	None	X	X	X	X			X			X					
		Frame					X	X		X	X		X	X			
		Full													X	X	X
Gypsum sheathing	General	Ignored	X	X	X	X	X	X	X	X	X	X	X	X	X	X	X
		Included															
Interior walls	General	Ignored	X	X	X	X	X	X	X	X	X	X	X	X	X	X	X
		Included															
Mass distribution	General	Corner	X	X	X	X	X	X	X			X			X		
		Stud ends								X	X		X	X		X	X

			State-of-the-art models			
Component	Property	Option	A2c-2D-a	A2c-3D-RD-a	A2c-3D-SD-a	A2d-3D-RD-a
Shear wall	Stiffness	$K(0.4V_{nP})$				
		$K(V_{nP})$				
		$K(0.2V_{nA})$	X	X	X	X
		$K(0.4V_{nA})$				
	Capacity	V_{nA}	X	X	X	X
		V_{nP}				
	Backbone	EPP				
		Pinching4	X	X	X	X
	Panel size	Whole				
		Subpanels	X	X	X	X
Hold down	General	Smeared				
		Discrete	X	X	X	X
Shear anchors	General	Ignored				
		Included	X	X	X	X
Diaphragm	Stiffness	Flexible	X			
		Rigid		X		X
		Semi-rigid			X	
	Pinching	None	X			X
		Pinching4		X	X	
Gravity exterior walls	General	None				
		Frame				
		Full	X	X	X	X
Gypsum sheathing	General	Ignored				
		Included	X	X	X	X
Interior walls	General	Ignored	X	X	X	
		Included				X
Mass distribution	General	Corner	X			
		Stud ends		X	X	X

3.3 Modeling of shear walls

The research goal of this project is to study the seismic behavior of CFS-framed buildings, so the modeling method for the shear walls is generally considered of primary importance. Two modeling strategies, state-of-the-practice (P) and state-of-the-art (A) models, are discussed respectively. Modeling options of shear wall response curves, hold downs, and shear anchors are depicted in subsections.

3.3.1 State-of-the-practice (P-) models of shear walls

State-of-the-practice models precede state-of-the-art models as trials of our basic modeling assumptions and techniques. In terms of shear walls, one major difference is that all P-models use values derived from the AISI-S213 (American Iron and Steel Institute 2009) standard to determine the peak capacity of shear walls, but A-models utilize shear wall test results by Liu et al. (Liu et al. 2012) instead. To be clear, peak shear capacity of P-models and A-models are denoted as V_{nP} and V_{nA} respectively if they appear in the same table or context requires this clarification. Key differences in modeling strategies are illustrated in Figure 3-8; and details of the actual modeling methodology follow immediately.

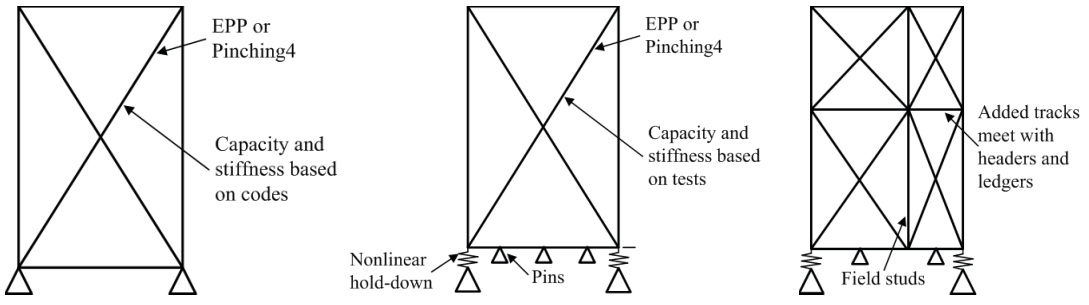

(a) State-of-the-practice (b) State-of-the-art, simplified (c) State-of-the-art, refined

Figure 3-8: Comparison of modeling strategies: from state-of-the-practice to state-of-the-art models

A typical state-of-the-practice (P-) shear wall model is shown in Figure 3-9. For the models investigated here the shear walls are treated, essentially, as a single degree of freedom: shear force V versus lateral deformation δ. However, it is desired that the models have a physical width equal to their actual width in the building and that the forces in the chord studs develop similar to the typical truss analogy. As a result, the model of the shear wall consists of nonlinear diagonal bracings and elastic frame boundary elements. In the process of development, we tried to model connections as true pins and it worked, but ultimately we decided to use rigid connections (shared nodes) since it is less complicated, had no impact at these shear wall aspect ratios, and was especially beneficial for the more complicated three-dimensional models. From a behavioral standpoint removing the pins allows bending to occur in the chord studs, which is realistic and of interest. From a practical modeling standpoint the use of coincident nodes (for modeling the pins) was not found to be compatible with rigid diaphragm modeling (which also employs multi point constraints) (Leng et al. 2012). In addition the frame action of the bending was about an order of magnitude weaker in shear than the truss action created by the diagonal struct simulating the wood-sheathed panel V-δ response.

A premise of all the models of Figure 3-8 is to condense the nonlinear response of the wall down to nonlinear response in the diagonals. The derivation of uniaxial nonlinear material model of the diagonals starts from the expression of axial force F in the diagonals using shear force V:

$$F = V/\left(2\cos\theta\right) \tag{3-1}$$

where $\cos\theta = b/\sqrt{b^2+h^2}$

Correspondingly, the stress in the diagonal (truss element) is

$$\sigma = F/A = V/\left(2A\cos\theta\right) \tag{3-2}$$

The axial strain (ε) in the diagonal is developed based on the lateral displacement of the shear wall δ from

$$\varepsilon = d/l = \delta\cos\theta/\sqrt{b^2+h^2} = \delta b/\sqrt{b^2+h^2} \tag{3-3}$$

Thus, with the preceding equations any nonlinear shear wall V-δ relationship can be expressed as a nonlinear one-dimensional σ-ε relationship for the material in the diagonals, where

$$\sigma = f\left(\varepsilon\right) \tag{3-4}$$

and function f is selected to match the desired V-δ behavior. The two material models explored for state-of-the-practice shear walls are described in the following.

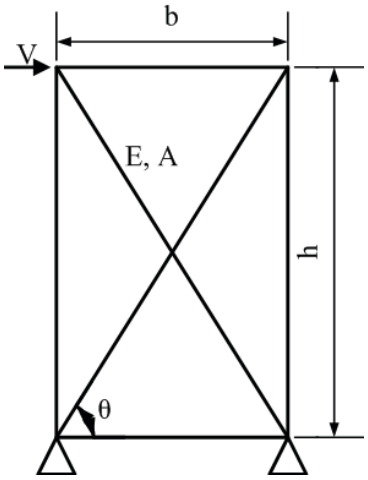

Figure 3-9: A typical state-of-the-practice shear wall model

(a) Elastic perfectly-plastic (EPP) shear wall model

The first model of uniaxial nonlinear shear wall response is the simplest elastic perfectly-plastic (EPP) model. To characterize the EPP model, only the strength and deflection up to peak are needed. Numerous variations on this model exist including the equivalent energy elastic perfectly-plastic (EEEP) model (see (Liu et al. 2012)) and others. In terms of mathematical representation, EEEP is coincident with EPP since it requires the same physical quantities to determine the response curve. However, the way to obtain the strength and deflection up to peak for EEEP entails the calculation of energy dissipation as the area of enclosed region below the backbone curve for test output, as detailed in ASTM E2126 (ASTM International 2011). Even though EEEP matches the energy dissipation of monotonic loading, it overestimates energy dissipation in the 2nd and 4th quadrants of the V-δ curve under cyclic loading (detailed comparison is given later in the same section). Our later efforts show a more complicated model is actually required to capture the behavior so it was decided that the simplest possible EPP model was only used in state-of-the-practice models: set the 'plastic' strength at the code specified

nominal strength (V_{nP}, the subscript 'P' stands for state-of-the-practice) and set the deflection (and thereby the stiffness) at the code specified deflection (δ) at the same V_{nP}; as shown in Figure 3-10(a).

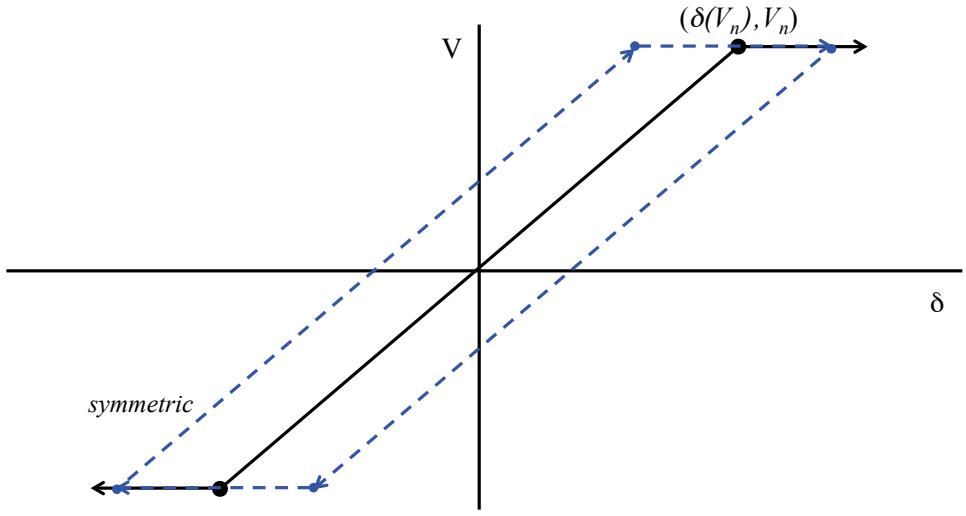

(a) EPP

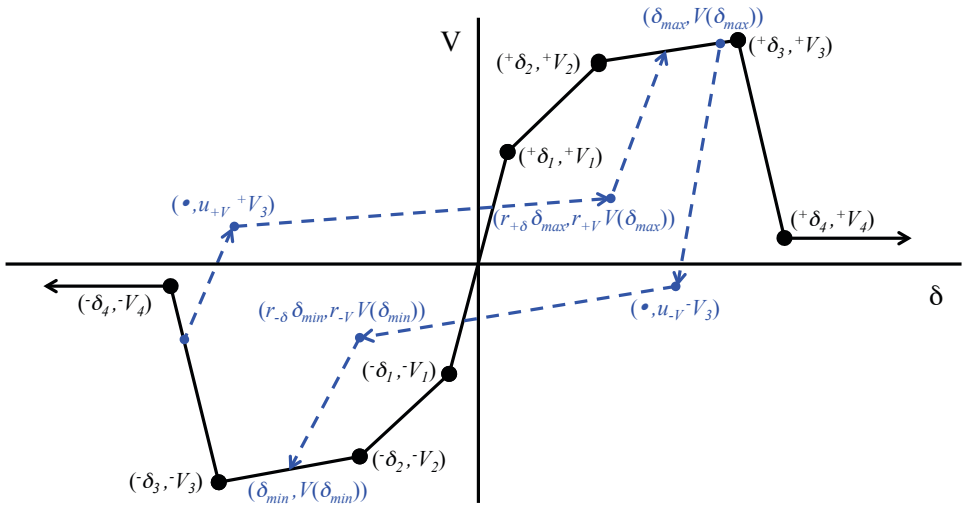

(b) Pinching4

Figure 3-10: Nonlinear models for shear wall (a) EPP (b) Pinching4

The nominal shear capacity per unit width, v_n, is found from AISI S213 (American Iron and Steel Institute 2009) and for a given wall of width b the nominal shear capacity,

$V_n=bv_n$. From Table C2.1-3 for 43 or 54 mil studs and track with 7/16 in. (1.11 cm) OSB on one-side and #8 fasteners spaced 6 in. (15.24 cm) o.c. v_n=825 plf (12.04 kN/m). (Note, this is the lower bound specified code strength and is conservatively selected for the models developed here; further, this value must be reduced for walls with aspect ratios greater than 2:1). The deflection of the shear wall at v_n is provided by Equation C2.1-1 of AISI S213:

$$\delta\left(v_n\right)=\frac{2v_nh^3}{3E_sA_cb}+\omega_1\omega_2\frac{v_nh}{\rho Gt_{sheathing}}+\omega_1^{5/4}\omega_2\omega_3\omega_4\left(\frac{v_n}{\beta}\right)^2+\frac{h}{b}\delta_{v_n} \tag{3-5}$$

All variables are defined in AISI S213; briefly, the first term accounts for chord stud bending, the second term is from shear in the sheathing, the third term is empirically fit to test data (and accounts for the bulk of δ) and the final term is based on deformation at the hold downs (Leng et al. 2012). After the determination of the shear wall's V-δ backbone curve of EPP, the EPP material properties (σ-ε relationship) for the diagonal trusses in Figure 3-9 are calculated using Eqn. (3-1) to (3-3). Parameters are summarized in Table 3-4.

(b) Pinching4 hysteretic shear wall model

The Pinching4 material (Lowes and Altoontash 2003) in OpenSees is a far more realistic characterization of the shear wall behavior with a multipoint backbone curve, pinching effect, and degradation. The backbone curves of positive and negative branches are defined by four points, and the response can be reduced as a function of the maximum (+) or minimum (–) force or displacement experienced in a cycle as illustrated in Figure 3-10

(b). The parameters of Pinching4 material are obtained by fitting of dissipated energy of shear walls tested under CUREE cyclic load protocol, as detailed in the paper by Liu et al. (Liu et al. 2012).

As illustrated in Figure 3-10(b) the first three points in the backbone curve of Pinching4 are set to ($\delta(0.4V_n)$,$0.4V_n$), ($\delta(0.8V_n)$,$0.8V_n$), and ($\delta(1.0V_n)$,$1.0V_n$) and provide the pre-peak envelope as specified by AISI S213 for state-of-the-practice models. Initially (Leng et al. 2012), the last (fourth) point on the backbone curve and the pinching parameters are selected as the average of Test 4 and Test 14 from (Liu et al. 2012). However, full scale shaking table test results showed that the post peak drop of shear wall capacities is not very steep, so a 'best case scenario' approach was taken and the fourth point on the backbone curve was set as ($1.534\delta(1.0V_n)$, $0.395V_n$) from Liu's test. Following the same logic, the pinching parameters of reloading and unloading are also selected as r_s=0.33, r_V=0.02, and u_V=0.0 (see Figure 3-10(b)). The V-δ curve is converted into material properties for the diagonals in Figure 3-9 as described above for EPP. Parameters are also summarized in Table 3-4. Note, Pinching4 is also the nonlinear material model for state-of-the-art shear wall models, as discussed in Section 3.3.2.

Table 3-4: Parameters that characterize nonlinear materials of shear wall bracings

Material name	Model type	v_n (plf)	$\delta/\delta(1.0V_n)$				
EPP	P-model	825	1.0				
Material name	Model type	v_n (plf)	$\delta_4/\delta(1.0V_n)$	V_4/V_n	r_s	r_V	u_V
Pinching4	P-model	825	1.534	0.395	0.33	0.02	0.0
	A-model	1013*	1.534	0.395	0.33	0.02	0.0

*: The capacity v_n for Pinching4 in A-models is determined from test, see Section 3.3.2

The developed EPP and Pinching4 models are compared to Test 12 of the shear wall tests of Liu et al. (2012) in Figure 3-11. The single story 8 ft (2.44 m) x 9 ft OSB (2.74 m) sheathed shear walls have the same details as the CFS-NEES building and are tested to the CUREE protocol (Leng et al. 2012).

In addition to showing the entire hysteretic response specific cyclic test loops are also provided in Figure 3-11, including pre-peak loops 10, 26, 29, 32, and 35, the cyclic loop with maximum force: loop 38, and post-peak degraded loops: 39 (at 75% of the maximum deflection at peak load, loop 28) and 41 (at 150% of the maximum deflection at peak load).

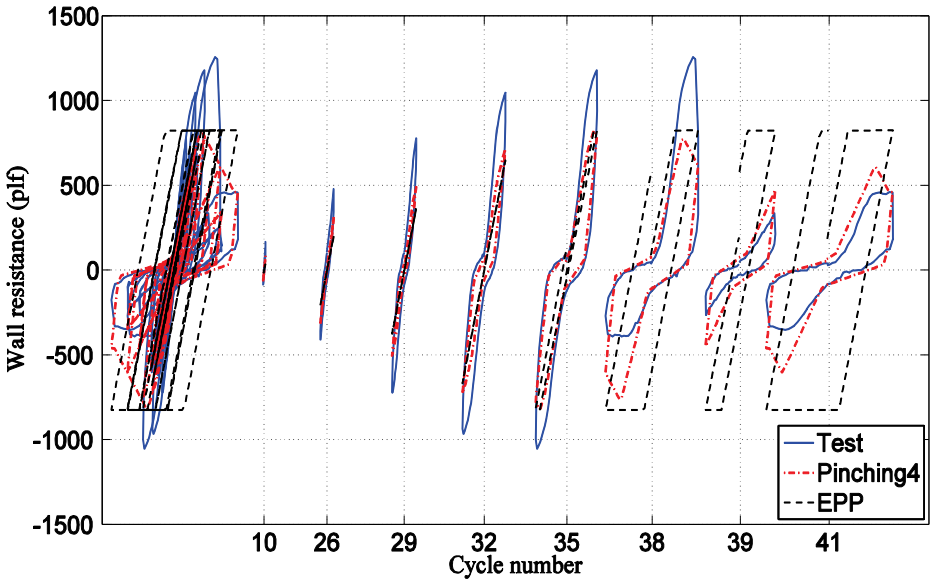

Figure 3-11: Pinching4 and EPP model compared with Test 12 of Liu et al. (2012), cycle numbers are numbers of displacement-based cyclic loading following the CUREE protocol

Several observations are available regarding EPP and Pinching4 shear wall response models. First, the selected maximum capacity from AISI S213 (825 plf or 12.04 kN/m)

for the EPP and Pinching4 model is conservative when compared to the tests - capacities based on shear wall tests are adopted in state-of-the-art models (see next subsection). Second, initial stiffness in the Pinching4 model is greater than the EPP model due to the use of deflection (δ) at lower force levels in the first branch of the Pinching4 model for the P-models - and this is definitely much closer to the test than the EPP model, which uses the code specified V_n-δ and the first δ branch is at 100% of peak instead of 40% of peak of the Pinching4 model. Note the use of 40% stiffness values is consistent with service force levels traditionally at V_n/2.5. Third, the EPP model ignores pinching in the hysteretic behavior, near and past peak this assumption is untenable, as the actual response is severely pinched. As a result, EPP model over-estimates the energy dissipation to a fairly large extent. (Note, as discussed in (Liu et al. 2012) equivalent energy elastic-plastic models sometimes refereed to as EEEP models have the same drawback as the traditional EEP model in that they only match the energy of the backbone curve and ignore pinching, which is the dominant effect in the hysteretic response). EPP models (or EEEP models) are only appropriate for monotonic pushover. Given these observations, EPP and Pinching4 model of the shear walls are examined in the stage of P-models, but only Pinching4 model is used in more complicated and more accurate state-of-the-art (A-) models.

3.3.2 State-of-the-art (A-) models of shear walls

State-of-the-art (A-) models are more accurate than P-models in several ways and are therefore the major focus of this research. The basic approach of modeling a shear wall panels as diagonals, as seen in the P-models is kept, and further developed herein. There

are two variants of the A-model: the simpler one models the whole panel with two diagonals (as in the P-models); the other one divides the sheathing into subpanels and each subpanel is modeled with two diagonals (see Figure 3-8). The subpanel model is developed to account for the incorporation of gravity system in the structure, otherwise there is only force transfer possibilities at the top and bottom of the wall, while in reality any location a member frames in to the shear wall can potentially transfer forces to/from the shear wall.

(a) Whole panel A-model

A typical state-of-the-art 'whole panel' shear wall model is shown in Figure 3-12. A noticeable difference between A-models and P-models (Figure 3-8) is that hold downs are modeled explicitly in A-models. (Note in P-models the influence of hold downs is smeared into the code specified deflection expression, term 4 in Equation (3-5)) In the A-models only the Pinching4 material model is used to represent the shear wall response, but the capacities are determined by using test data.

For A-models, the shear wall capacity, termed as V_{nA} in order to distinguish from V_{nP} for P-models, is based on the testing of Liu et al. (Liu et al. 2012), as opposed to the codified values of AISI S213 (Leng et al. 2013). From Liu et al. (Liu et al. 2012), test 4 and 14 were selected. The test 4 shear wall dimensions are 4 ft (1.22 m) x 9 ft (2.74 m) and Test 14, 8 ft (2.44 m) x 9 ft (2.74 m), both with horizontal panel seams at 8 ft (1.22 m) up and OSB sheathing on one side only. The average shear capacity of the wall is v_n=1013 plf (14.78 kN/m) and this is used uniformly for other shear walls, i.e., $V_n = v_n b$. The capacity

from test is 23% larger than 825 plf (12.04 kN/m) with aspect ratio adjustment from AISI S213 that was previously used in P-models.

Other parameters for the Pinching4 model were arrived at by matching equivalent energy dissipation against shear wall test results by Liu et al. (2012) as done before for the P-models. The schematic plot in Figure 3-10(b) is still explanatory, but we set the first point on the backbone curve to ($\delta(0.2V_n)$, $0.2V_n$) for some A-models since shear wall test response curves bend at a force level lower than $0.4V_n$ and we would like to take this effect into account. So the linear stiffness of shear walls can be $K(0.2V_n)$ or $K(0.4V_n)$ when it refers to a specific A-model. The second and the third point on the backbone curve are set to ($\delta(0.8V_n)$, $0.8V_n$), and ($\delta(1.0V_n)$, $1.0V_n$). Same with P-models, the fourth point on the backbone curve was set as ($1.534\delta(1.0V_n)$, $0.395V_n$) from Liu's test. The pinching parameters of reloading and unloading are r_s=0.33, r_V=0.02, and u_V=0.0.

The hold down is a connector that ties the chord stud to the foundation (Figure 3-12). The overturning moment induced by lateral forces in the shear wall are balanced by axial forces in the hold down. Since the hold down is modeled explicitly, the shear wall lateral deflection induced by hold down extension (δ_h) must be subtracted from total measured horizontal deflection (δ_t) of the shear wall. The axial force in the hold down due to the overturning moment from lateral force V is Vh/b under the assumptions of the simplified truss analogy. The axial extension of the hold down d_h at this force level is computed using the nonlinear material model for the hold down (as detailed in the next paragraph). The induced lateral displacement from hold down's extension is then calculated using

geometric relationship as $\delta_h = d_h/\cot\theta = hd_h/b$. Thus the deflection δ used in Eq (3-3) is $\delta = \delta_t - \delta_h$. For shear walls with 4 ft (1.22 m) and 8 ft (2.44 m) width, this is done directly since V and δ_t are available from test, and δ_h is available from d_h after V is given. For other shear walls, δ_t at the force level V is unknown. The calculation of δ is carried out by interpolation of δ of 4 ft (1.22 m) and 8 ft (2.44 m) wide walls to other widths.

(b) Modeling of hold downs in A-model

The Simpson S/HDU6 hold down (Figure 3-13(a)) is specified for the CFS-NEES building and was also utilized in the shear wall tests of Liu et al. (Liu et al. 2012). Tension tests of the hold down itself are available with stiffness at ASD and LRFD force levels as well as ultimate capacity (Simpson Strong-Tie Company Inc. 2013). These values are used to determine the tension stiffness of the hold down as provided in Table 3-5. At ultimate the hold down is assumed plastic. (Due to the application of overstrength factor Ω_o force levels in design the shear panel itself will fail well before the hold down). In compression the hold down is in bearing and an infinite (numerically high) axial stiffness is employed. A simplified nonlinear model of the hold down is thus created as shown in the load displacement curve of Figure 3-13 (b), this curve can also be captured in the Pinchin4 model and is thus employed.

The implementation of nonlinear hold down axial response is not straightforward. The response curve of Figure 3-13(b) can be implemented into a zerolength spring element in OpenSees with Pinching4 uniaxial material. However, our practice shows that the large difference between the linear stiffness under tension and compression can sometimes lead

to dubious simulation results. Instead, we used the idea of parallel springs, as shown in Figure 3-14(a). Two zerolength spring elements in parallel, each one with its own response curve, are used together to model one hold down. One spring uses Pinching4 material (Figure 3-14(b)) that has the same tensile response with Figure 3-13(b), but the compressive stiffness is the same with tensile. The other spring uses Elastic-Perfectly-Plastic Gap (EPP Gap) material (Figure 3-14(c)) with the gap close to zero and a very large stiffness in compression. The superimposed response of Figure 3-14(b) and Figure 3-14(c) makes no difference with Figure 3-13(b) and was found to more reliably work in our simulations.

In elasitc analysis, hold downs have to be modeled by elastic spring elements, which does not allow different stiffness in tenson and compression. Simply using the hold down's stiffness in tension from test data (Table 3-5) for linear hold down models is conservative so an equivalent stiffness must be provided for linear hold down models. We look at the rocking of hold downs in an isoloated shear wall. A pair of hold downs, if modeled as two elastic springs, has axial displacement $\pm d_h$ each and the induced lateral displacement of the pair is $2\delta_h=2d_h/\cot\theta=2hd_h/b$. Given that Pinching4 hold down models are rigid in compression, the stiffness of elastic hold down models must be twice the tensile stiffness of the Pinching4 hold down model so that the pair of elastic hold downs makes the same amount of induced lateral displacement with the pair of Pinching4 hold downs. The response curve of elastic hold down models is illustrated in Figure 3-15. It should be noted that the derivation above assumes the foundation is rigid; however, bottom tracks of the CFS-NEES building on the base level is fastened to the HSS

6x6x3/8 in. steel tubes through hold downs and the tubes are connected to the shaking table's frame. Deformation in the tubes under vertical load from the building is real but idealized as zero (assumed rigid foundation) in our FE models, since it cannot be measured during testing.

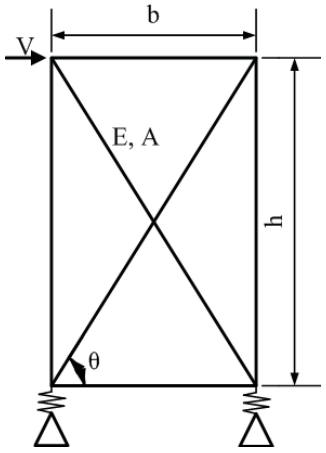

Figure 3-12: A typical state-of-the-art whole panel shear wall model

Table 3-5: Force-displacement relationship of the hold down in tension

Tension Load (lbf)	**Deflection** (in.)	**Stiffness** (lbf/in.)
6125	0.108	56712.96
9785	0.234	29047.62
15005		

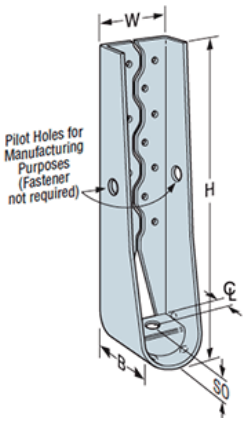

(a) Hold down (Simpson Strong-Tie, 2013)

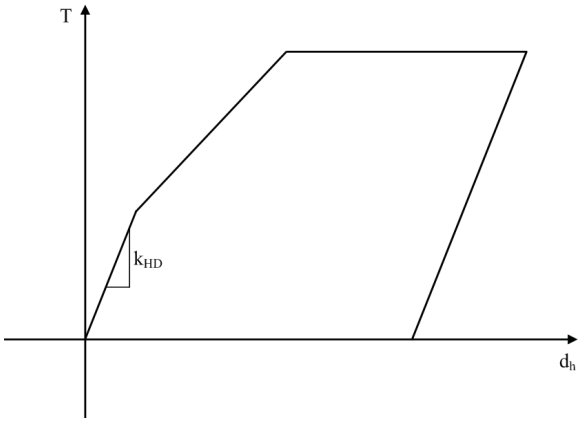

(b) Axial load-displacement Pinching4 model

Figure 3-13: Hold down and its Pinching4 nonlinear material model of the axial response

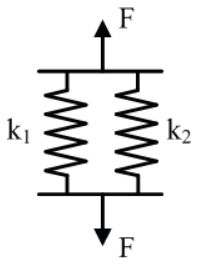

(a) Modeling hold down as two parallel springs in inelastic analysis

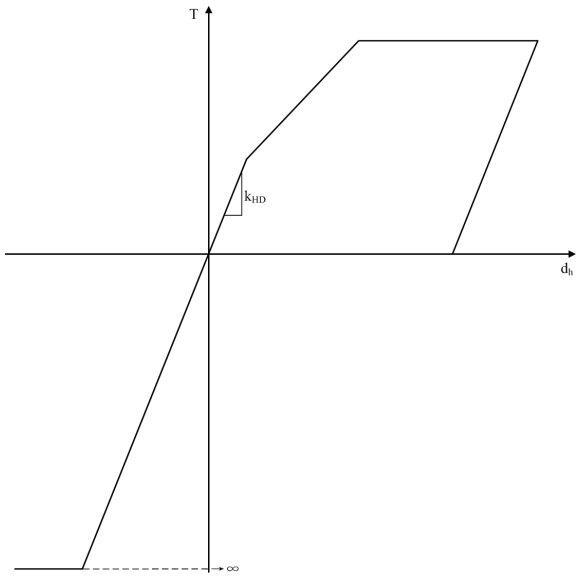

(b) Pingching4, tension branch

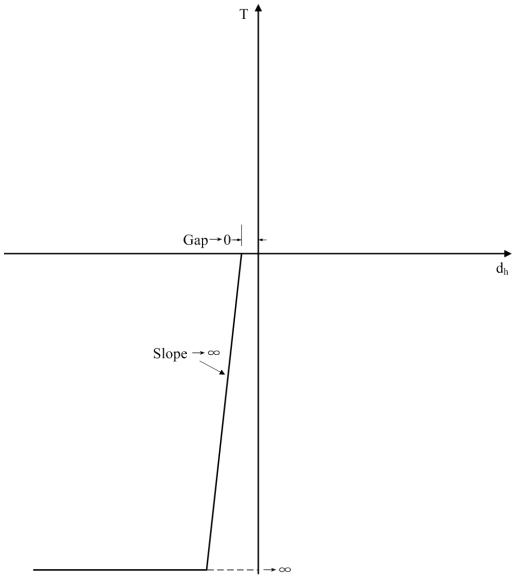

(c) EPP Gap, compression branch

Figure 3-14: Implementation of Pinching4 nonlinear material model of the axial response of the hold down

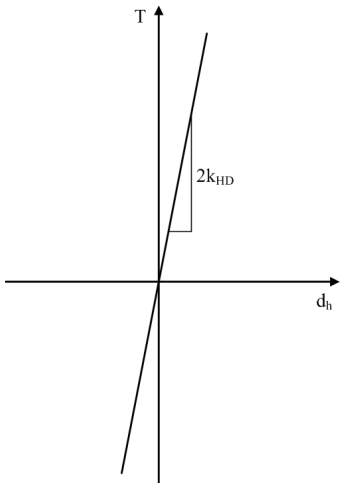

Figure 3-15: Elastic material model of the hold down's axial response

(c) Modeling of shear anchors in A-model

In addition to hold downs, shear anchors connect the bottom track to the foundation (every 12 in. (30.48 cm) o.c.). In current models, these anchors are modeled as pin supports (see Figure 3-8(b) and Figure 3-8(c)). These supports have high shear stiffness since they engage the axial stiffness of the bottom track. Thus, they are effective in removing shear. However, these shear anchors are assumed to have a low uplift stiffness (even when fully pinned) since they engage the weak-axis bending of the bottom track (Leng et al. 2013). Further, these pin supports also exist at the gravity wall locations. More details on gravity walls can be found in Section 3.4.

(d) Subpanel A-model

The idea of further dividing the sheathing of a wall into subpanels was initiated from our comparison of whole panel A-model simulation results to shaking table test results of the Phase 1 building (as elaborated in later chapters). The major structural component missing in the whole panel A-models is the ledger track (1200T200-97 at floor level and 1200T200-68 at roof level) and the gravity system (bare CFS framing at Phase 1). To accommodate these components, the whole sheathing panel of the shear wall should be divided into subpanels while other modeling options for hold downs, shear anchors and nodal connections remain the same. It should be noted that in real constructions there are vertical and horizontal seams where several pieces of sheathing meet. The subdivision of panel in our modeling does not follow the seams of realistic shear walls in our test. Instead our panels follow locations where external framing occur. Field studs are

included to make subdivisions horizontally; window tracks are extended and joists and ledger tracks are modeled at their centerlines (6 in. (15.24 cm) below the diaphragm plane) so the panel is subdivided vertically. Each subpanel is modeled with two diagonals. An example of the South elevation is available in Figure 3-16. The subpanel model in Figure 3-16(b) appears much more complicated than the whole panel model in Figure 3-16(a). The total number of diagonals is about tens times larger after subdivision. However, the subpanel looks much closer to the design drawing in Figure 3-16(c) after the incorporation of ledger track and gravity steel framing and its performance also matches well with the test as a natural result (detailed discussions available in Chapter 4 and 5).

To determine the Pinching4 parameters for the subpanel diagonals, the basic approach using equilibrium and geometric relations in Eqn. (3-1) to Eqn. (3-4) can be followed. Namely, the axial stress and strain of a diagonal in a subpanel should also be a nonlinear function

$$\sigma_p = f\left(\varepsilon_p\right) \tag{3-6}$$

where the subscript ‘p’ stands for ‘subpanel’. The physical quantities of the whole panel are denoted by the subscript ‘0’.

Two assumptions still need to be addressed before formulating the stress and strain of a diagonal in a subpanel using total shear force and lateral displacement. Firstly, the panel is uniform and no localization exists. This assumption ensures that even though a

subpanel may be quite small but it is still at the same length scale level with the whole panel. Secondly, the deformation of the panel is pure shear, so the deformed shape is a parallelogram. The assumption is arguable since the framing is modeled with fixed connection so bending of studs contributes to the lateral displacement additionally. However, in our research, the lateral deflection of the top track under static or dynamic load is normally less than 2% of the height of the wall. Within a piece of subpanel, the curved stud due to internal moment can still be regarded as a slanted straight line. In addition, nonlinear response is also introduced in CFS studs (as detailed in subsequent pages) of the subpanel models. An immediate outcome of these assumptions is that any subpanel has the same shear strain (change of right angle) with the whole one, as illustrated in Figure 3-17.

These equilibrium and geometric relationships mentioned above are then valid for any subpanel of shear walls, but with the subscript 'p'

$$F_p = V_p / \left(2\cos\theta_p\right) \tag{3-7}$$

$$\sigma_p = F_p / A_p = V_p / \left(2A_p \cos\theta_p\right) \tag{3-8}$$

$$d_p = \delta_p \cos\theta_p \tag{3-9}$$

$$\varepsilon_p = d_p / l_p = \delta_p \cos\theta_p / \sqrt{b_p^2 + h_p^2} = \delta_p b_p / \left(b_p^2 + h_p^2\right) \tag{3-10}$$

where $l_p = \sqrt{b_p^2 + h_p^2}$ and $\cos\theta_p = b_p / l_p$

Guaranteed by two assumptions, shear force and lateral displacement of a subpanel are given by

$$V_p = Vb_p / b_0 \tag{3-11}$$

$$\delta_p = \delta h_p / h_0 \tag{3-12}$$

Substituting Eqn. (3-11) and Eqn. (3-12) into Eqn. (3-8) and Eqn. (3-10) and using Eqn. (3-2) and Eqn. (3-3) of whole panels yield

$$\sigma_p = \sigma_0 \frac{A_0}{A_p} \frac{\cos\theta_0}{\cos\theta_p} \frac{b_p}{b_0} = \sigma_0 \frac{A_0}{A_p} \frac{b_0/l_0}{b_p/l_p} \frac{b_p}{b_0} = \sigma_0 \frac{A_0}{A_p} \frac{l_p}{l_0} \tag{3-13}$$

$$\varepsilon_p = \varepsilon_0 \frac{\cos\theta_p}{\cos\theta_0} \frac{l_0}{l_p} \frac{h_p}{h_0} = \varepsilon_0 \frac{b_p/l_p}{b_0/l_0} \frac{l_0}{l_p} \frac{h_p}{h_0} = \varepsilon_0 \frac{b_p}{b_0} \frac{h_p}{h_0} \frac{l_0^2}{l_p^2} \tag{3-14}$$

If the truss cross-section area is the same, i.e. A_0=A_p, then the expression of σ_p is simplified as

$$\sigma_p = \sigma_0 \frac{l_p}{l_0} \tag{3-15}$$

Eqn. (3-15) indicates that σ_p is always smaller than σ_0.

Taking the ratio of Eqn. (3-13) and Eqn. (3-14) yields

$$\frac{\sigma_p}{\varepsilon_p} = \frac{A_0}{A_p}\frac{l_p^3}{l_0^3}\frac{b_0}{b_p}\frac{h_0}{h_p}\frac{\sigma_0}{\varepsilon_0} \tag{3-16}$$

Once again, the backbone curve of Pinching4 is defined by four points in the stress-strain space. As a result, (σ_p, ε_p) must be clearly specified at each point. The strain ε_p, as shown in Eqn. (3-14), is determined using geometrical properties of deformed and undeformed configurations and the scale factor of $\varepsilon_p/\varepsilon_0$ is explicitly dependent on the geometry of subpanel. Thus, each subpanel needs its own backbone curve points.

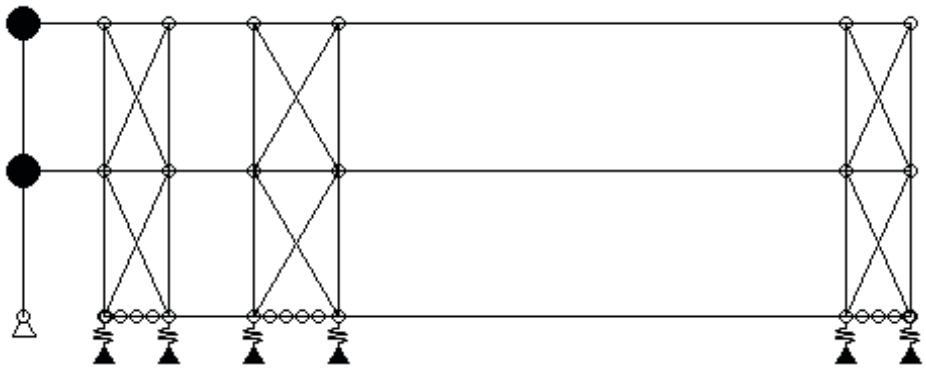

(a) Whole panel model

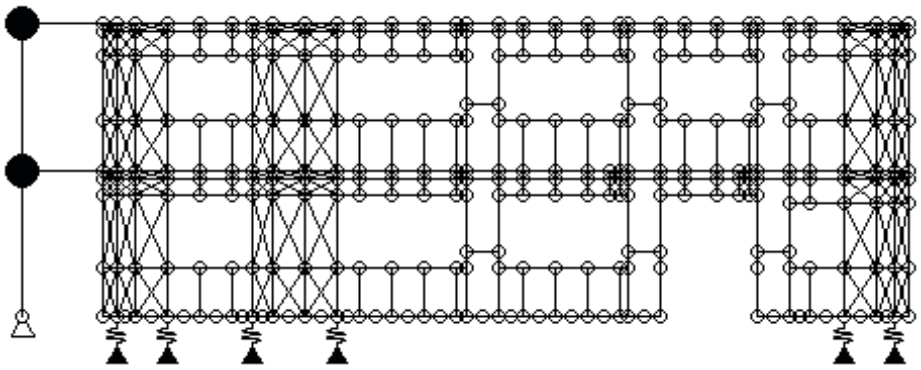

(b) Subpanel shear wall model with gravity framing included

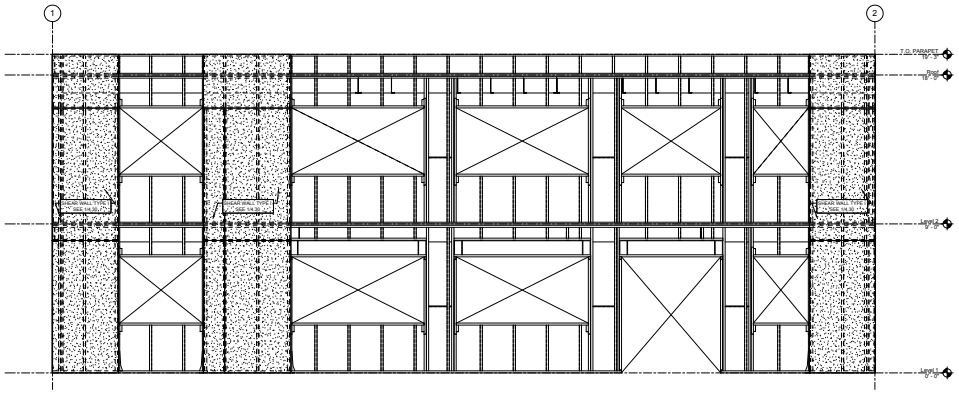

(c) Design drawing

Figure 3-16: Comparison of whole panel model, subpanel model and design drawing of South elevation

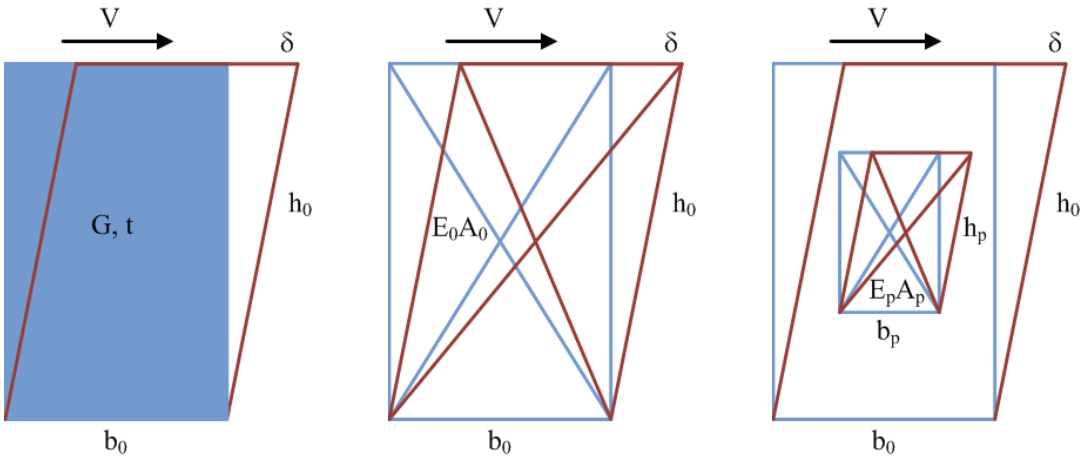

Figure 3-17: Illustration of the deformation in a whole panel and subpanels modeled with diagonals

To convert backbone points of the whole panel model to subpanel models, the modeler needs to use Eqn. (3-13) and Eqn. (3-14) to convert every point (σ_0, ε_0) on the whole panel model's backbone curve to (σ_p, ε_p) for each subpanel. In this research, we took A_0=A_p=1.0 and used Eqn. (3-15) instead of Eqn. (3-13).

To validate this important idea of modeling shear walls with diagonals representing subpanels, a 4 ft (1.22 m) x 9 ft (2.74 m) shear wall is modeled with four subpanels (see

Figure 3-18). Cyclic displacement control loading is applied on the top track, and horizontal component of every diagonal bracing's axial force is recorded. The summation of horizontal force in diagonals equals shear force in the subpanels. A whole panel model with only two diagonals of the same wall is also created and the same analysis is performed.

A comparison of the shear-deflection response between the whole panel model and the subpanel model is presented in Figure 3-19. The same amount of shear force is transferred from top track to subpanels on the upper level (subpanel 3 and 4) and then to the lower level (subpanel 1 and 2). The shear-deflection curve shows that the summed shear force of lower level subpanels is exactly the same with whole panel model. Upper subpanels also match whole panel's behavior quite well until the peak on the backbone curve. The post-peak behavior of upper subpanels indicate that the elastic stiffness of boundary steel members plays a certain limited role, as a consequence of rigid connections between bracing and frame members. Nevertheless, this discrepancy does not change the fact that failure initiates in the subpanel once the post-peak behavior starts to manifest. Subplots of individual subpanel's response in Figure 3-20 further support this observation. These results confirm that the idea and method of modeling shear walls with subpanels can realize the designated backbone curve and pinching effect and align with gravity systems.

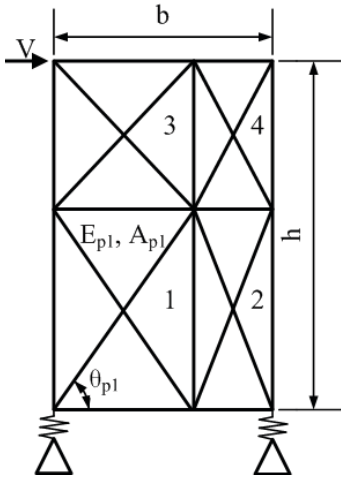

Figure 3-18: A 4 ft (1.22 m) x 9 ft (2.74 m) shear wall modeled with four subpanels

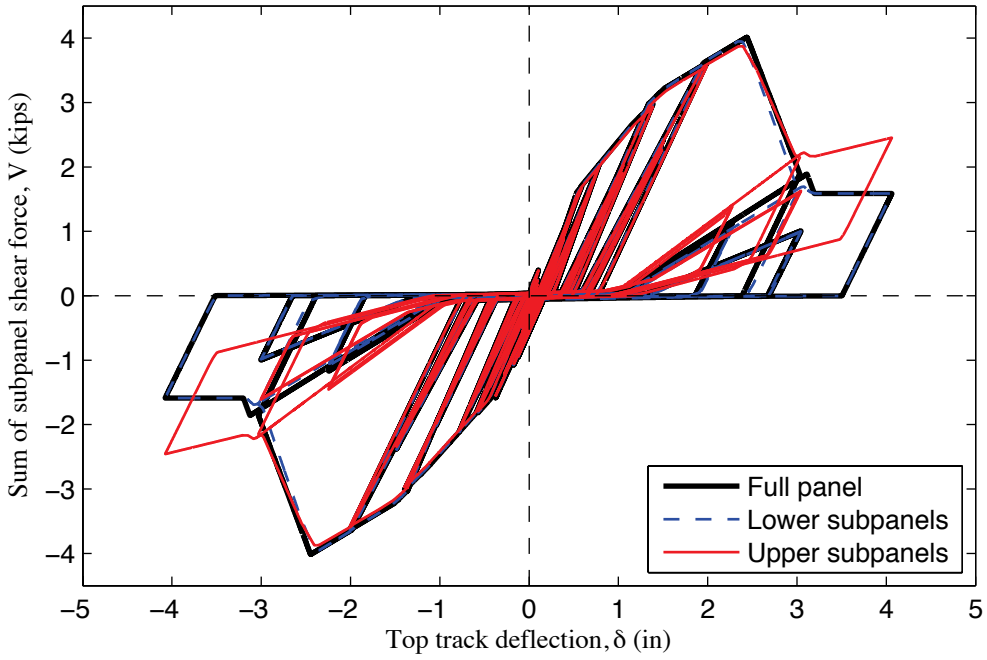

Figure 3-19: Sum of subpanel shear force vs. top track deflection curve of the 4 ft (1.22 m) x 9 ft (2.74 m) shear wall

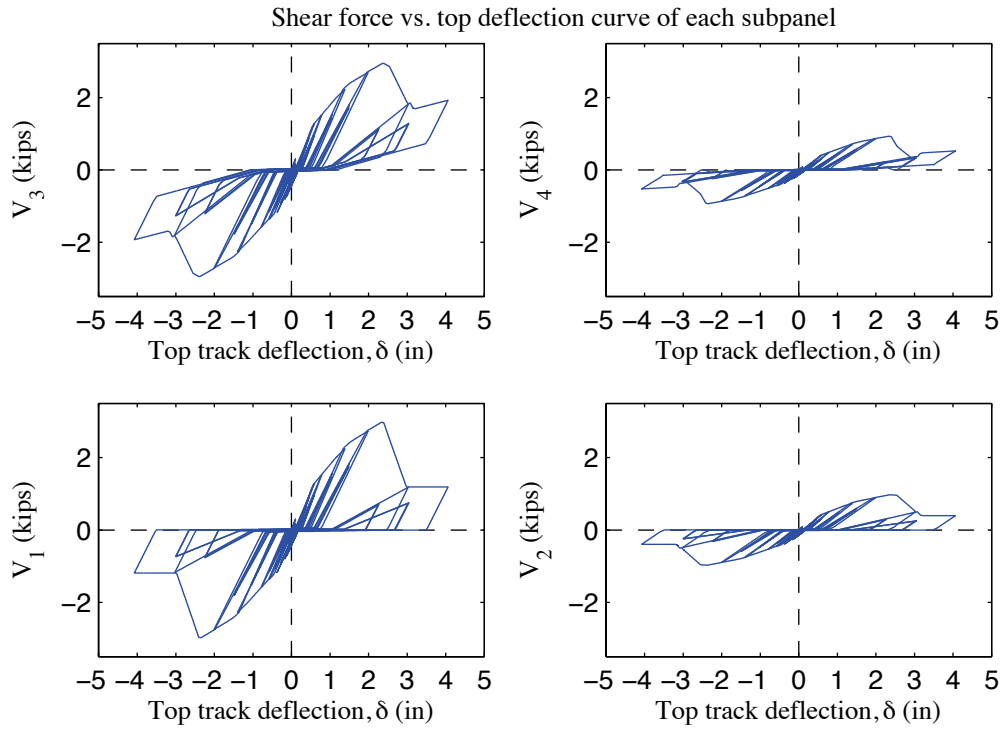

Figure 3-20: Shear force vs. top track deflection curve of each subpanel in the 4 ft (1.22 m) x 9 ft (2.74 m) shear wall

3.4 Modeling of gravity system

3.4.1 Modeling of gravity system at Phase 1

The gravity system of the CFS-NEES building is designed as all-steel. As a result, steel framing without sheathing is the structural component of first interest. As mentioned in Chapter 1, Phase 1 and 2a of the archetype (CFS-NEES) building has structural components only, so bare steel framing of gravity systems as seen in Figure 3-5 and Figure 3-16 are taken into account in the OpenSees FE models accordingly.

As a consequence of the subpanel modeling method, nonlinear material models are necessary for CFS studs. If the steel is modeled as linear elastic members, the building model would have a remaining CFS frame stiffness after failure of the shear walls with

unduly large stiffness - Figure 3-19 and Figure 3-20 support this observation. However, nonlinear material models for cold-formed beam-column elements itself is a research topic still under investigation. The difficulty includes the failure modes controlled by buckling including local, distortional and global modes. Also the lack of symmetry (most common lipped channels are mono-symmetric) results in different response of minor and major axis bending and complicated coupling between the member's internal forces and moments. Some available research work focus more on the response of CFS members under pure strong axis bending. Ayhan and Schafer (Ayhan and Schafer 2012) characterized the moment-rotation (M-θ) curve of a number of CFS sections under strong axis bending following the definition of ASCE/SEI 41 (American Society of Civil Engineers 2007). Padilla-Llano et al. (Padilla-Llano et al. 2014) performed strong axis bending test of CFS beams with various cross-sections and characterized their response as Pinching4 materials, available in both moment-rotation and moment-curvature (M-κ) forms for concentrated and distributive models respectively. The procedure is also extended to Pinching4 material characterization of CFS columns and is summarized in his dissertation (Padilla-Llano 2015).

A practical concern is that CFS-framing is only one structural component of the building, but the design of CFS-framing requires a large number (compared to hot-rolled steel structures) of CFS members be used. We therefore prefer not to introduce, again, nonlinear uniaxial materials as complicated as Pinching4 in the frame elements (although this is what recent work by Padilla-Llano pursues). Besides, due to the number of different cross-sections tested, some conversion would still be needed before these

models could be adopted for cross-sections in our research. Therefore, we make a tradeoff between accuracy and efficiency by using the simplest EPP material models for uniaxial response of CFS studs in our A-models with gravity framing and subpanel diagonals of shear walls.

To achieve this goal, uniaxial materials are defined specifically for the response of studs under axial force (P), strong/weak axis bending moment (M_z/M_y) and torque (T). Hence, for each stud section, four uniaxial materials should be defined. Then, a special type of element called 'section aggregator' in OpenSees combines these uniaxial materials together for a given section, so members with the certain section can resist force and moments in 3D analysis.

Table 3-6 lists uniaxial material types and properties used in the section aggregator of CFS studs. The axial force and two bending moment responses are all EPP. Compressive force and bending moment can cause buckling failure, so capacities P_n, M_{ny} and M_{nz} are computed using critical buckling load P_{cr}, M_{cry}, M_{crz} available from CFSEI technical note G103-11 (Li and Schafer 2011) and the Direct Strength Method (Appendix 1, AISI S100-12). Global buckling mode is considered as fully braced (inelastic bending reserve not allowed), and distortional buckling only counts for Phase 1 and 2a models of the building since gravity framings are not covered with sheathing. OpenSees frame elements in this research are defined in a certain way that moment about local y-axis is always weak axis bending and moment about local z-axis coincides with strong axis bending. The technical note also indicates that for minor axis bending, the value of M_{cry} differs when flange lips

are in compression instead of tension. So there are two values of M_{ny} for as peak capacities in positive and negative branches of EPP. Tensile force does not lead to buckling, so positive peak force $T_n=F_yA_g$, viz. the squashed load of the section. Quantities F_y and A_g are yielding stress and gross cross-section area respectively. As an example of EPP uniaxial material used in studs, the response curve of weak axis bending moment is plotted in Figure 3-21. With this approach we insure that no framing element can develop forces beyond their expected code limit state strength (in axial, bending, or torsion).

Table 3-6: Uniaxial material types and properties in section aggregator of CFS studs

Load type	**Material type**	**Stiffness**	**Peak capacity**
Axial force, P	EPP	EA	T_n (+), P_n (-)
Strong axis moment, M_z	EPP	EI_z	M_{nz}
Weak axis moment, M_y	EPP	EI_y	M_{nyt} (+), M_{nyc} (-)
Torque, T	Elastic	GJ	∞

Table 3-7: Capacities of studs in the FE model

	Phase 1 or Phase 2a				
	P_n (kip)	T_n (kip)	M_{nyt} (kip-in)	M_{nyc} (kip-in)	M_{nz} (kip-in)
600S162-54	14.72	27.80	6.11	7.45	42.15
600S162-33	5.04	11.35	2.13	3.09	16.00
362S162-54	16.32	21.10	7.08	7.10	23.62
	Phase 2b to 2e				
	P_n (kip)	T_n (kip)	M_{nyt} (kip-in)	M_{nyc} (kip-in)	M_{nz} (kip-in)
600S162-54	14.72	27.80	6.11	7.45	46.57
600S162-33	5.04	11.35	2.13	3.16	16.00
362S162-54	16.32	21.10	7.08	7.10	24.10

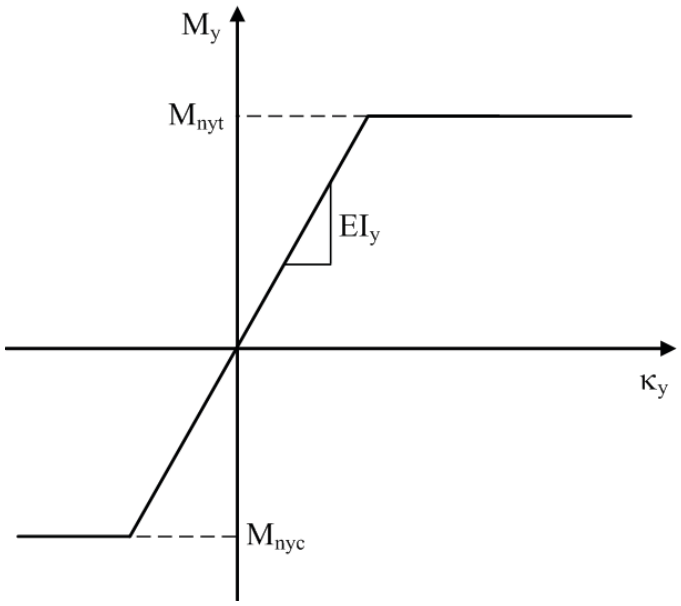

Figure 3-21: Elastic-perfectly-plastic uniaxial response of CFS studs under weak axis moment

Besides, the models by Ayhan and Schafer (Ayhan and Schafer 2012) and Padilla-Llano et al. (Padilla-Llano et al. 2014) are uniaxial response only. The section aggregator in OpenSees works on diagonal terms of element stiffness matrix only and it is a superposition of each single uniaxial response, so it can not generate any interaction. Missing moment-axial force interaction can be problematic and less conservative in member design. However, a posteriori design checks on studs of our 3D A-models in pushover analysis shows that failures of studs are mostly axial force or single axis bending dominated. Further study and design improvement on interaction in P-M-M space is beyond the scope of this research and is recommended for future work.

Another important consideration in the models of the gravity system is the load path of vertical loads. Lateral load is transferred to the foundation through the hold downs. However, there are no specific connectors that are supposed to transfer vertical load to the foundation. The ends of gravity frame members are screwed to bottom tracks on the

base level. This connection bears against the foundation and has limited deformation under compression. However, the connection can be pulled above and create a small gap when tensile axial load is applied since discrete shear anchors (every 12 in. (30.48 cm) o.c.) connect the bottom track to the foundation and these anchors have a low uplift stiffness in series with the track. So the ends of studs of the gravity systems have an axial stiffness that is very large in compression but very small in tension. The axial response curve in Figure 3-22 is realized by elastic multi-linear uniaxial material attached to zerolength spring elements in OpenSees. The material is linear in that it has no energy dissipation under cyclic loading, but it has greatly different stiffness in tension and compression.

Shear anchors with the same 12 in. (30.48 cm) spacing on bottom tracks are also modeled as pins. Consequently, gravity system can also resist lateral load. The effect is quantified and addressed in detail in Chapter 5.

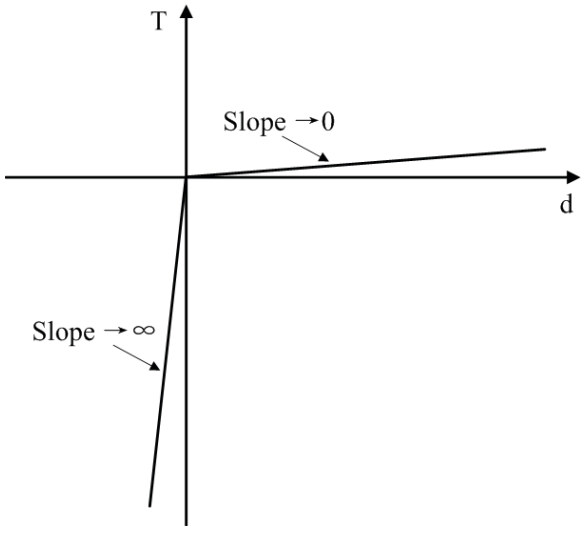

Figure 3-22: Elastic multi-linear uniaxial response of CFS gravity stud ends

3.4.2 Modeling of gravity system at Phase 2b and above

When it refers to the archetype CFS-NEES building in Phase 2b and beyond, gravity walls are built with CFS framing and sheathed by OSB and in later phases gypsum boards. The sheathing type for the gravity walls is the same as with shear walls, but the spacing of fasteners is different. So far, little is known about the lateral resistance of sheathed gravity walls in CFS-framed buildings. Consequently, this effect is not included in current version of design standards. A viable way to estimate the stiffness and backbone curve of sheathed gravity walls is to make use of Buonopane and Bian's (Buonopane et al. 2014; Buonopane et al. 2015; Bian et al. 2014; Bian et al. 2015) OpenSees models of sheathed gravity walls with nonlinear fastener elements developed using Peterman's (Peterman and Schafer 2013) test results. Since our purpose is to develop a reasonable estimation of gravity walls' lateral resistance and integrate it into wall line and building models for seismic performance evaluation, not all variables in Buonopane and Bian's research are considered herein. An 8 ft (2.44 m) by 9 ft (2.74 m) gravity wall with the same sheathing and steel framing as the real building is modeled using Buonopane and Bian's approach and its backbone curve of its lateral response is obtained from pushover analysis (see Figure 3-23). The backbone curve is then characterized as Pinching4 material in the same way as the shear walls (see Section 3.3.2). Due to the shortage of research data and for simplicity, parameters of the pinching effect are kept the same with the tested shear walls (see Table 3-8). Figure 3-23 also shows the post-peak drop on the backbone curve of characterized Pinching4 material. The sheathing panel is further discretized into subpanels, as discussed above (see Section 3.3.2). Both OSB and gypsum sheathings are considered, as gypsum sheathing is applied in Phase 2c

and above (see Figure 3-7 for design drawing and Figure 3-24 for comparison between gravity wall models with and without sheathing).

Table 3-8: Parameters that characterize Pinching4 materials of gravity wall bracings

	v_n (plf)	$\delta_4/\delta(1.0V_n)$	V_4/V_n	r_s	r_V	u_V
OSB	809.8	1.534	0.395	0.33	0.02	0.0
Gypsum	284.6	1.534	0.395	0.33	0.02	0.0

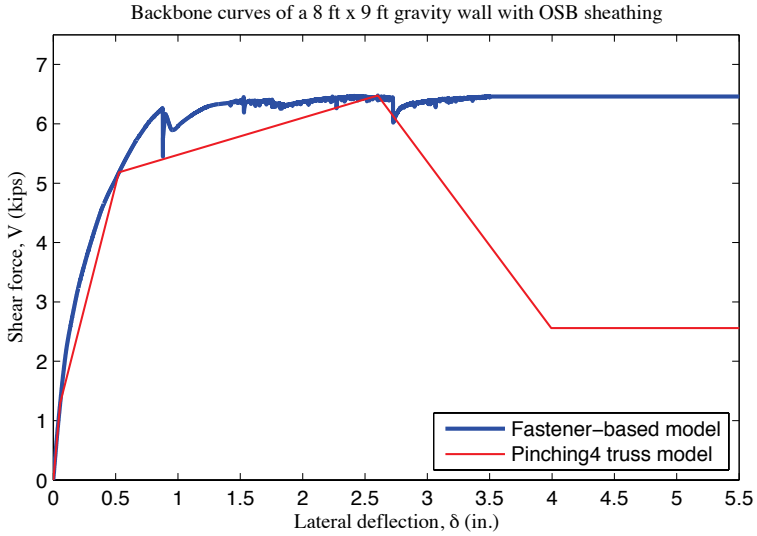

(a) Backbone curves of a 8 ft (2.44 m) x 9 ft (2.74 m) gravity wall with OSB sheathing

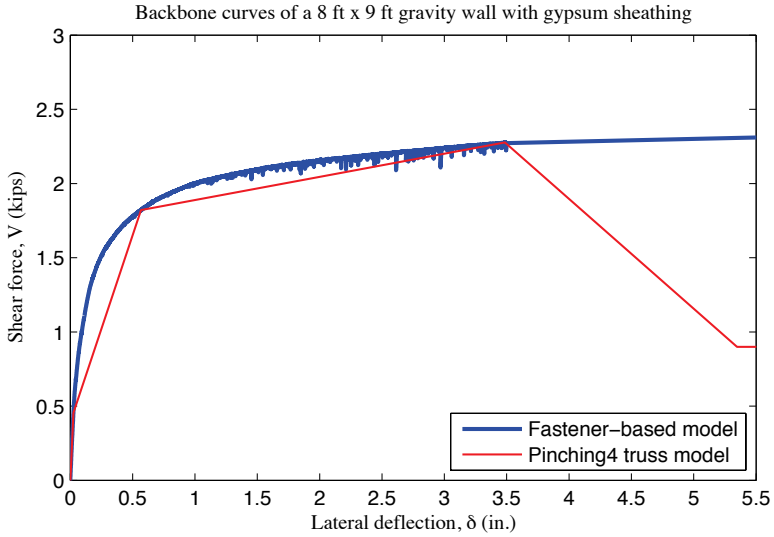

(b) Backbone curves of a 8 ft (2.44 m) x 9 ft (2.74 m) gravity wall with gypsum sheathing

Figure 3-23: Comparison between backbone curves of a sheathed 8 ft (2.44 m) x 9 ft (2.74 m) gravity wall using fastened-based model and characterized Pinching4 truss model

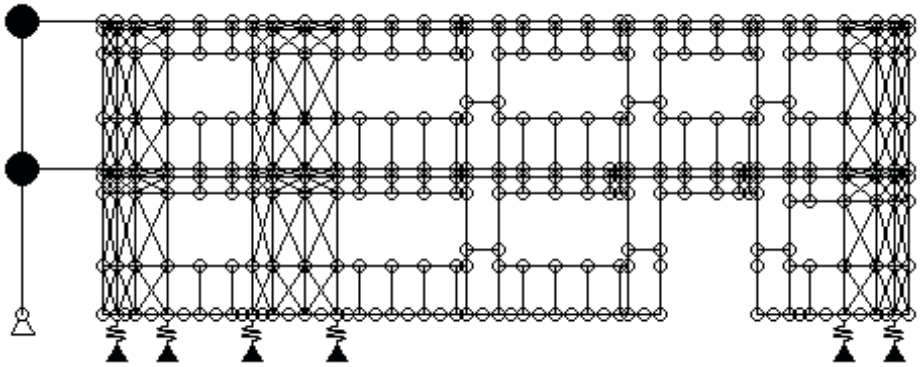

(a) Phase 1 model

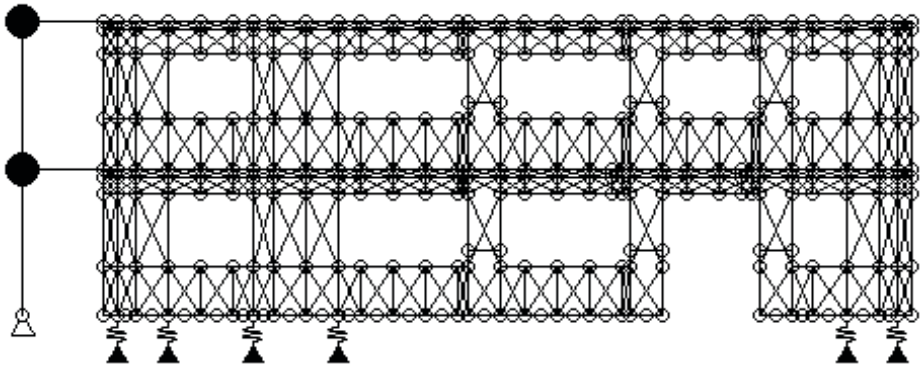

(b) Phase 2b/c model with additional trusses modeling sheathing of gravity walls

Figure 3-24: Phase 1 and Phase 2b/c model of South elevation

3.5 Modeling of diaphragms

Basic modeling options for diaphragms include rigid, flexible (no stiffness) and semi-rigid diaphragms. Among the three, rigid diaphragms are directly realized by a built-in element of OpenSees. The rigid diaphragm element requires a master-slave relationship of nodes in the same plane. Lateral displacement in two directions and rotation about the vertical axis is defined at the master node. Flexible diaphragm behavior indicates that the facing elevations are completely decoupled so two-dimensional analysis of each elevation

can be applied instead. The remaining choice of semi-rigid diaphragm and its implementation is addressed thereafter.

The importance of modeling semi-rigid diaphragms has been reported in the full scale shaking table test and our modeling trials. The stiffness of diaphragms contributes greatly to the overall stiffness of 3D models and it determines the extent of coupling between shear walls. Peterman (Peterman 2014) compared shaking table test results to the definition of flexible diaphragms in ASCE 7 (American Society of Civil Engineers 2010) and the design assumption of the archetype building and concluded that considering the diaphragm as semi-rigid is most consistent with observations.

The semi-rigid diaphragm models of floor and roof levels are shown in Figure 3-25. Compared with the exploded view of design drawing in Figure 3-3, those models correctly capture the out-to-out dimensions of real diaphragms and include openings on the floor level. The basic modeling approach of semi-rigid diaphragms is similar to modeling shear walls with subpanels, and these models are intended to work together to provide more accurate results. Steel members in Figure 3-25 include joists, ledger tracks, blocking, straps and top tracks of shear walls on the boundary. Among those members, joists, ledger tracks and blockings are positioned 6 in. (15.24 cm) below the actual the diaphragm plane (at their centroid) since the web depth of joists and ledger tracks is 12 in. (30.48 cm). Blocking is not continuous in design drawings (Madsen et al. 2011), but we extend them to allow subdivision of the sheathing panel into subpanels. Nodes that are 6 in. (15.24 cm) apart vertically are connected using two-node link and rigid link elements

of OpenSees. The linked nodes have the same translations but their three rotation DOFs are weakly coupled by the spring stiffness (0.01 kip·in/rad) of two-node link elements. These links considers the connection stiffness between very deep CFS joists and ledger tracks and sheathing panels fastened to them from above.

The subpanels enclosed by joists, tracks and extended straps are modeled using diagonals. However, unlike modeling of shear walls, test data are not available in this research for us to characterize the Pinching4 parameters of each diagonal in diaphragm subpanels. Consequently, we have to utilize our knowledge from shear wall models to make a reasonable estimation of diaphragm stiffness and approximate its nonlinear behavior. More accurate insight into the behavior of diaphragm itself is left to future research.

After a trial-and-error process, the backbone curve and Pinching4 parameters of our full panel A-model of 12 ft (3.66 m) x 9 ft (2.74 m) shear wall was chosen. The process of conversion from full panel to subpanel models, as described in Section 3.3.2(b), was taken so that all diagonals on the roof (Figure 3-25 (b)) were characterized.

The sheathing of floor level is 23/32 in. (1.83 cm) and is thicker than 7/16 in. (1.11 cm) sheathing of roof level and shear walls. To account for the increase of stiffness, we resorted to Table 9 of American Plywood Association (now APA—The Engineered Wood Association) panel design specification (APA—The Engineered Wood Association 2012). According to that table, we find the panel rigidity through the thickness $G_v t_v$ of 23/32 in. (directly from the table) and 7/16 in. sheathing (by interpolation of 3/8 in. and

15/32 in. thickness) and take their ratio 1.53 as the stiffness magnification factor. So diagonals of the floor diaphragm can be characterized by the same procedure using parameters of the roof diaphragm.

The design criterion we compared the response of our diaphragm model with was Eqn. D2.1-1 in AISI S213 for the deflection of diaphragms, which takes a similar form the deflection equation of shear walls:

$$\delta(v) = \frac{0.052vL^3}{E_s A_c b} + \omega_1\omega_2 \frac{vL}{\rho G t_{sheathing}} + \omega_1^{5/4}\omega_2(\alpha)\left(\frac{v}{\beta}\right)^2 + \frac{\sum_{j=1}^{n}\Delta_{ci}x_i}{2b} \qquad (3\text{-}17)$$

Two facing sides our diaphragm model were pinned and the in plane lateral load (design base shear form the design narrative (Madsen et al. 2011)) was applied on one free side and peak lateral displacement δ was recorded and compared with the prediction of Eqn. (3-17) for unblocked diaphragms.

As shown in Table 3-9, the lateral displacement of the developed semi-rigid diaphragm models in an approximated and heuristic way still compares reasonably well with Eqn. (3-17). The numbers are of the same order, and the maximum discrepancy is about 60% of the equation value. Therefore, those semi-rigid diaphragm models are integrated in high fidelity state-of-the-art models. Rigid and flexible diaphragm results bound the behavior and the semi-rigid models provide a best current model approximation of actual response.

Table 3-9: Comparison of peak lateral displacement between diaphragm models and design equation

Level	**Direction of load**	**δ of FE model** (in.)	**δ of Eqn.** (3-17) (in.)
Floor	Short	0.110	0.178
Floor	Long	0.031	0.033
Roof	Short	0.075	0.192
Roof	Long	0.024	0.037

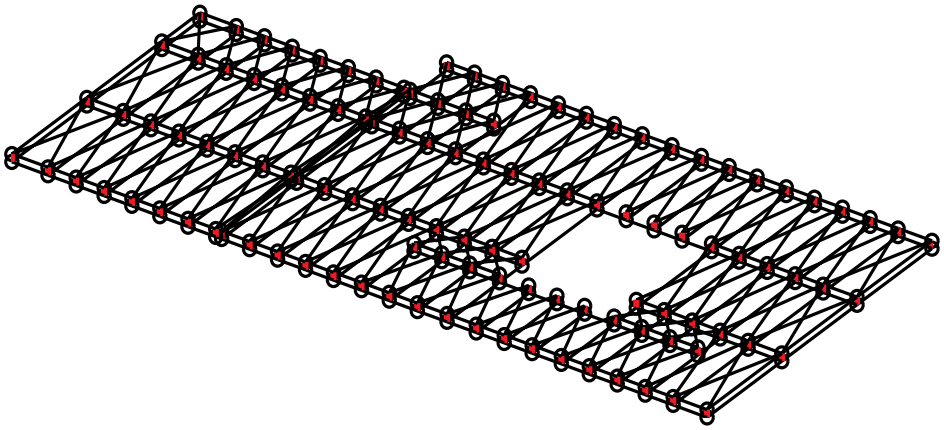

(a) Floor diaphragm

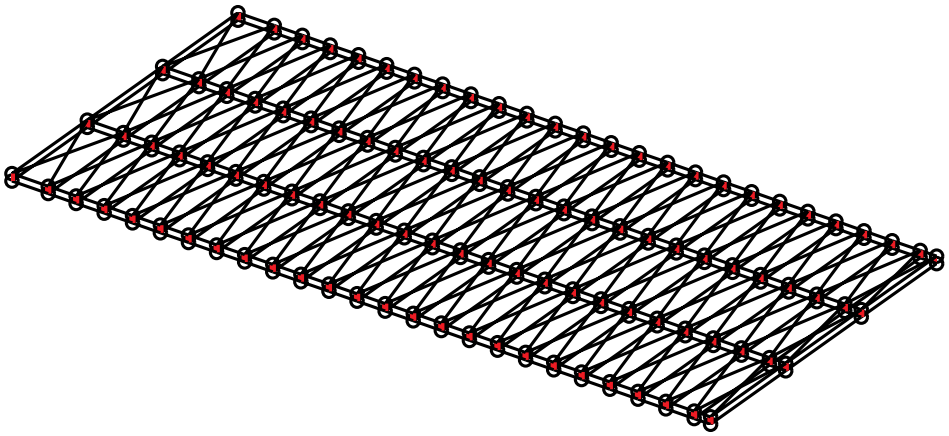

(b) Roof diaphragm

Figure 3-25: Semi-rigid diaphragm FE models in OpenSees

3.6 Modeling of interior walls

Interior walls are installed in Phase 2d and present as well in Phase 2e of the archetype CS-NEES building. Typically considered as nonstructural, they still potentially provide

additional support to exterior walls and contribute to the lateral resistance of the building. In the CFS-NEES building, interior walls are framed with nonstructural drywall studs studs and sheathed with gypsum boards. Since little is known about its role as a supportive part in the LFRS, some assumptions and simplifications are needed before model development. In this research, the gravity wall model with gypsum sheathing mentioned in Section 3.4 is adopted to make an estimation of interior wall's lateral behavior (see Table 3-8) and 362S162-54 studs are used (structural studs that overstimates drywall stud stiffness). The same backbone curve is utilized in the repeated procedure of Pinching4 material characterization of interior wall panels.

The resulting OpenSees model of interior walls is illustrated in Figure 3-26. For simplicity, each wall is modeled as two nonlinear diagonals. For interior walls on the floor level, the boundary condition of stud end bearing is set at stud end nodes (see Figure 3-26(a)). No lateral constraints are applied, which indicates that interior walls cannot resist base shear itself, but they provide additional stiffness to the building and support exterior walls wherever they meet (see Figure 3-27).

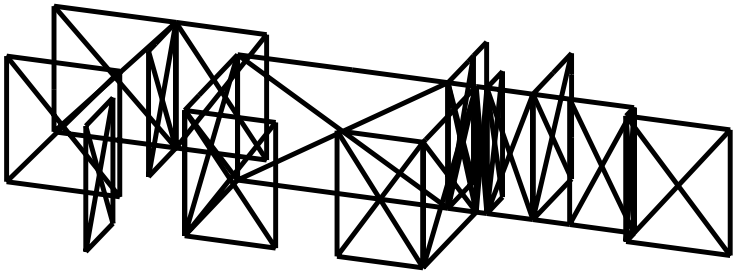

(a) Interior walls on floor level

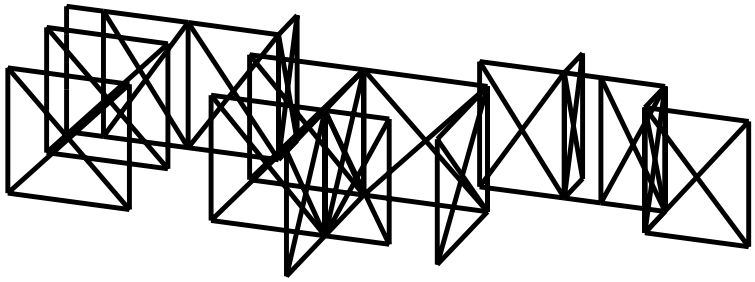

(b) Interior walls on roof level

Figure 3-26: Interior wall FE models in OpenSees

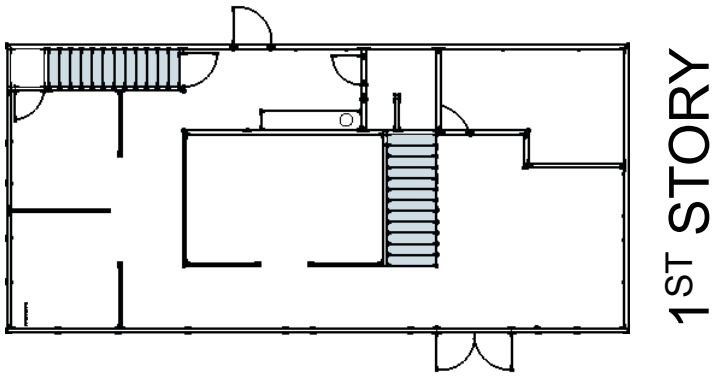

(a) Interior walls on floor level

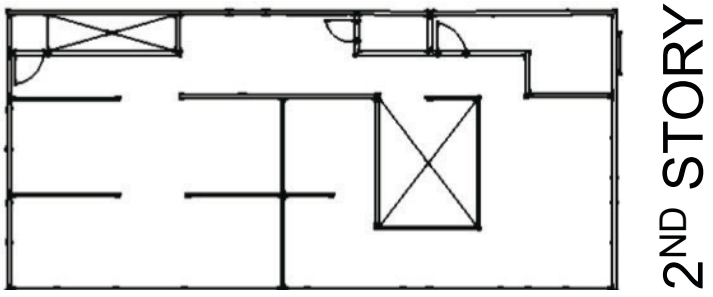

(b) Interior walls on roof level

Figure 3-27: Architectural drawings of the test specimen, demonstrating partition wall layout (Peterman 2014)

3.7 Distribution of seismic mass in FE models

Total seismic mass of the building is documented in the design narrative (Madsen et al. 2011). At each construction phase, supplemental mass is added to the archetype building to make sure total mass meet the design requirement. The value of supplemental mass at each phase and its breakdown are tabulated in Peterman's thesis (Peterman 2014).

In FE models of the archetype building, total seismic mass is set to the value from the design narrative (seismic weight is 77.5 kips; see (Madsen et al. 2011)) for P-models or the actual mass of the constructed building for A-models. As pointed out by Peterman (Peterman 2014), "the achieved supplemental mass is about 10% less than ideal but given the joist capacities and required layout of the masses, this was deemed acceptable." So same 10% difference in the seismic mass exist between P-models and A-models. From the perspective of seismic mass modeling, lumped mass is adopted. The distribution of lumped mass determines the mass matrix and can significantly affect the inertia of the building and its seismic response. Several approaches were explored for mass modeling from simplified P-models to complicated A-models.

For all 2D models, total seismic mass of the building is equally distributed to two facing elevations along the direction of the load. On a specific wall line, the mass is assigned solely to the node on the leaning column for floor and roof level respectively.

For 3D state-of-the-practice models, seismic mass of a building level is equally distributed to four corner nodes on the rigid diaphragm. The mass distribution of 3D state-of-the-art models is much closer to reality. The structural mass is equally distributed to corner nodes, and the supplemental mass is distributed to nodes on tracks where the diaphragm plane meets Northern or Southern wall line. The idea stems from the fact that additional concrete blocks and steel plates are placed on diaphragms and joists go from South elevation to North elevation. As a result, each joist is assumed to distribute the supplement weight to its end nodes. Note, openings on the floor diaphragm is modeled only in the semi-rigid diaphragm model, so there is a small difference in supplemental mass distribution between rigid diaphragm models and semi-rigid diaphragm models at the same construction phase. This distributed mass is applied to all 3D A-models, with the only exception of A1-3D-RD-c model, which is as a simplified approximation.

3.8 Distribution of gravity load in FE models

Gravity load of the building should be added separately since seismic mass is only related to the mass matrix in the FE formulation. The weight applied in the FE models of this research is proportional to seismic mass defined in Section 3.7 by the factor of g (acceleration of gravity). Consequently, refined lumping of seismic mass to corners and studs ends creates a more realistic gravity load distribution while large concentrated gravity load corresponds with lumped mass in the diaphragm corners only. Gravity load pattern is related to the distribution of vertical reactions among hold downs and stud ends and the effect will be expounded in Chapter 4 and Chapter 5.

3.9 Modeling of the chord stud connection across floors

In the CFS-NEES building the chord studs of the shear walls on the floor level and the roof level are connected via a cold-formed strap directly through the floor and track, fastened to the webs of the shear wall chord studs. It is installed through the floor sheathing, requiring holes to be cut in the sheathing after the floor system is installed (Peterman 2014). Peterman (Peterman 2014) further studied the behavior of the shear wall tie showing that the ties regularly experience 10% of the yield force.

In FE models of the CFS-NEES building, the tie is modeled as a fixed connection for the consideration of simplicity. This idealization overstimates the connection stiffness of the tie and it forms a direct load path of gravity load from top floor to the foundation. The error introduced by this modeling idealization may need to be quatified in the future.

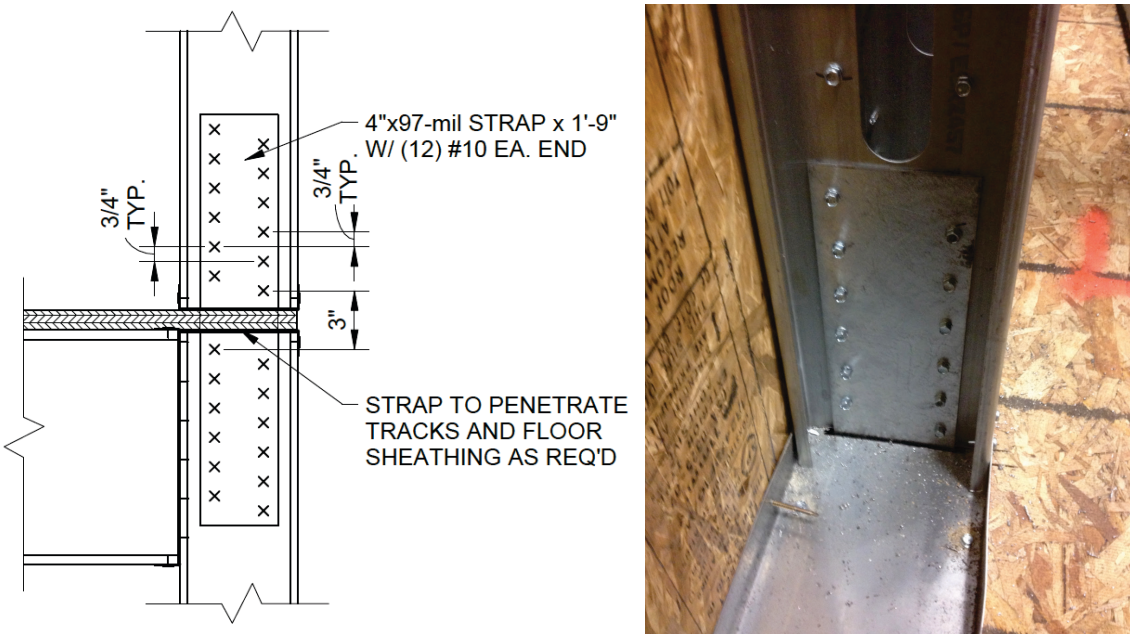

Figure 3-28: Shear wall tie detail from building specimen construction drawings (Peterman 2014)

Illustrations and verbal description of all nineteen types of FE models are appended to the main body of the thesis (Appendix A to Appendix S). The developed models are subjected to static and dynamic loading at multiple scale levels. Original and post-processed results are documented and discussed in subsequent chapters and appendices.

Chapter 4: Calibration of Building Models and Comparison with Full Scale Shaking Table Tests

This chapter covers the calibration/validation of high-fidelity OpenSees finite element models using full scale shaking table test results. High-fidelity models incorporate most design features of the archetype building in each construction phase. Accordingly, the calibration is carried out at each construction phase. Typical physical quantities that depict the building's response under seismic load, including natural period, nodal acceleration, story drift, axial force in the hold down, are recorded and compared between simulation and test. It can be observed that high-fidelity FE models' performance matches reasonably well with the testing at each construction phase. Section 4.1 briefly summarizes the setup and results of full scale shaking table test of the CFS-NEES project, a joint experimental and computational effort with the objective of advancing the simulation tools necessary for seismic performance-based design evaluations of cold-formed steel framed buildings (Schafer 2015). Section 4.2 describes the ground motion in the shaking table tests and in the time history analysis of the FE model. The terminology and methodology of computing the output physical quantities precedes the simulation results in Section 4.3. The chapter concludes with observations from simulation-test comparisons of each phase, as detailed in Section 4.3.

4.1 Brief description of full scale shaking table tests of the CFS-NEES building

Full scale shaking table test of the CFS-NEES building were performed in the summer of 2013 (Peterman et al. 2014; Peterman et al. 2014; Peterman 2014) at the University at

Buffalo's (UB) Structural Engineering and Earthquake Simulation Laboratory. The archetype building, as described in Chapter 1, was built following each design phase and was subjected to various scale levels of the specified ground motion excitation.

The first building was set up following design Phase 1 (Figure 4-1(a)). A significant amount of supplemental mass was added, over 4 times the building's self-weight (Peterman 2014), to meet code specified gravity load levels (Madsen et al. 2011; American Society of Civil Engineers 2005). The building was tested up to three-axis 100% Canoga Park excitation record of 1994 Northridge earthquake. At 100% scale the excitation meets the design spectrum and is essentially equal to a Design Basis Earthquake (DBE) per U.S. standards (Madsen et al. 2011; American Society of Civil Engineers 2005). Further details on excitation selection and scaling are addressed in Peterman's dissertation (Peterman 2014) and are briefly summarized in the next section for the sake of introducing inputs for the time history analysis.

(a) Phase 1 or 2a building (b) Phase 2e completed building

Figure 4-1: CFS-NEES Full-scale building testing at Phase 1 and Phase 2e (Schafer 2015)

The Phase 1 building was demolished after 100% Canoga Park testing and the Phase 2 building was built on the shaking tables according to the same specifications. The Phase 2 building repeated all details of Phase 1 and was finished with all exterior and interior, structural and non-structural components.

As depicted in Figure 4-2, Phase 2a is a replica of Phase 1 with structural system only; in Phase 2b gravity walls were sheathed with OSB panels; in Phase 2c gypsum sheathing was added to interior face of all gravity and shear walls; in Phase 2d all interior partition walls and staircases and ceilings were installed; finally in Phase 2e (also see Figure 4-1(b)) exterior weather-proofing DensGlass was installed. Through its construction phases, total mass of Phase 2 building was held constant while supplemental mass was adjusted.

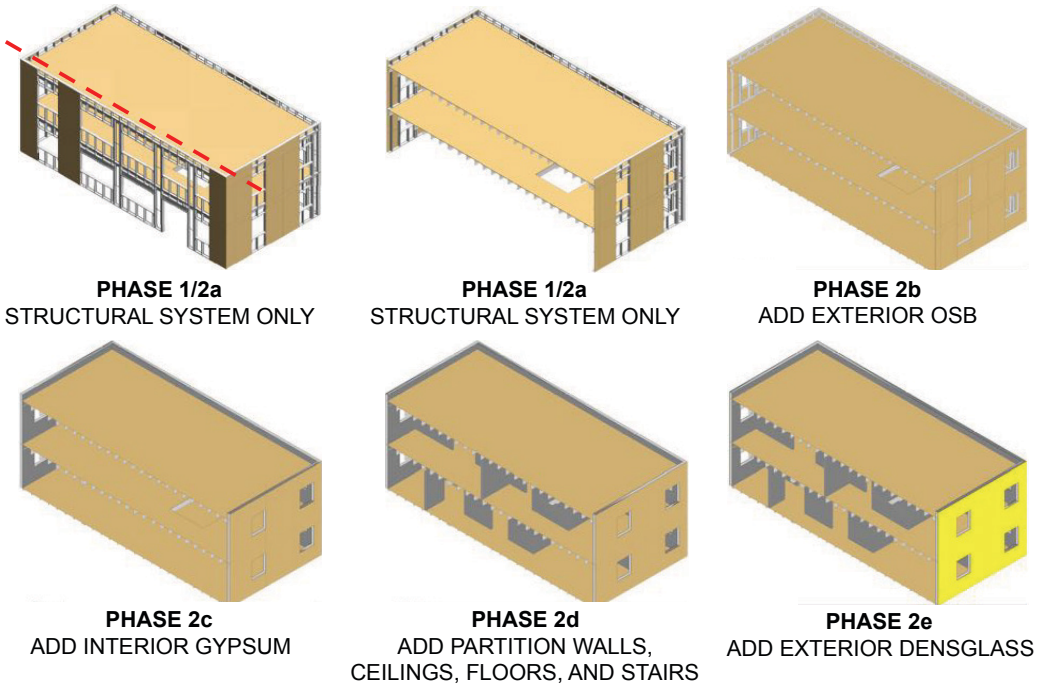

Figure 4-2: Illustration of construction milestones within Phase 2 testing, shown via cross Section views of building specimens (dashed line indicates location of cross Section) (Schafer 2015)

The test plan of the Phase 2 building include 16% Canoga Park excitation for Phase 2a, 44% Canoga Park for Phase 2b – 2d, and 100% Canoga Park at Phase 2e. Finally Phase 2e was also excited with 16% and then 100% near-field Rinaldi record of the 1994 Northridge earthquake. Testing was conducted for uniaxial excitations, in-plane excitations, and excitations included vertical motions. White noise tests for system identiiction were also conducted at all testing levels. For this building, the ground motion of 100% Rinaldi is consistent with the Maximum Considered Earthquake (MCE) per U.S. standards (Madsen et al. 2011; American Society of Civil Engineers 2005).

A major observation from tests is that the stiffness, damping and response of the building are significantly altered by the non-structural systems (Schafer 2015). Natural period is an indicator of the building's stiffness given fixed seismic mass. Figure 4-3 demonstrates the decrease of first two natural periods (translation modes in long and short direction) determined from 0.1 g white-noise system identification tests through Phase 2 construction. Given a fixed mass, the decrease of first natural period in the long direction from 0.32 s to 0.15 indicates the lateral stiffness of the building in that direction increases by about 450%. Similar comparison for the short direction shows a stiffness increase of 190%. As for damping of the structure, system identification reveals that the damping is about 4% prior to Phase 1 testing, and 9% prior to Phase 2e testing. Subsequent to the 100% Canoga Park record, damping is measured at 18% on the Phase 1 building, and subsequent to the 100% Rinaldi record, damping is measured at 15% on the Phase 2e building (Schafer 2015).

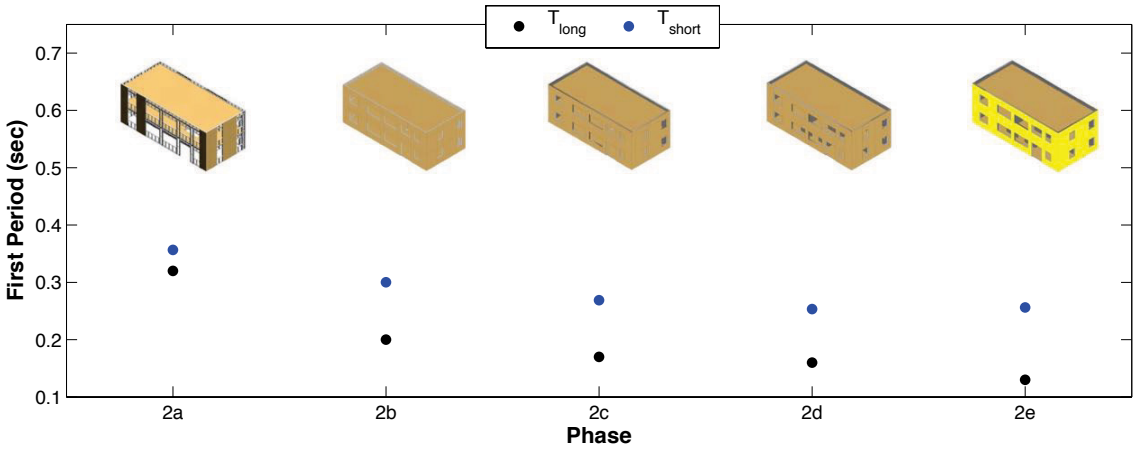

Figure 4-3: Shift in long and short direction first mode period through construction phases (a – LFRS and gravity steel only, b – ext. sheathed, c – inside face of ext. sheathed w/gypsum, d – interior non-structural walls & stairs, e – exterior DensGlass sheathed) (Schafer 2015)

Key recorded output from the tests include story/building drifts, load cell axial forces in hold downs, and acceleration amplification factors (Peterman 2014). Story drifts of the Phase 1 building during the 100% Canoga Park excitation in the long (u) and short (v) direction for floor and roof level (story 1 and 2, denoted by subscript 1 and 2) of story height, h, are plotted in Figure 4-4. Peak story drift is 1.18%, recorded at floor level in the long direction. Table 4-1 provides peak story drift from Phase 1 to Phase 2e. The maximum of recorded story drift across phases is 1.18% of Phase 1 building under 100% Canoga Park ground motion. This is somewhat surprising since 100% Rinaldi excitation has a peak ground acceleration of 0.83 g vs. 0.42 g of Canoga Park, but the experienced peak story drift of Phase 2e building is only 0.72% (Schafer 2015). On the other hand, this also indicates non-structural components actually provide a significant amount of lateral stiffness.

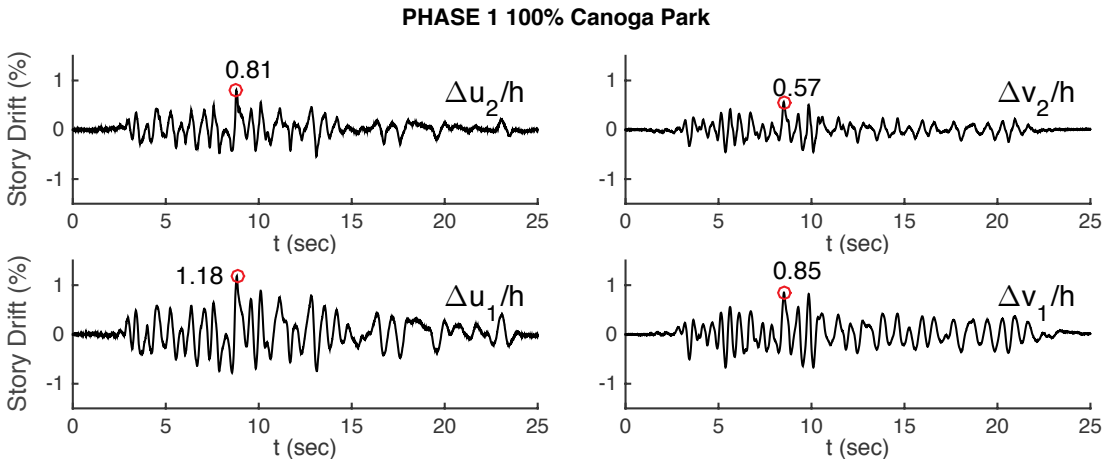

Figure 4-4: Drift percent for Phase 1 building under the 100% Canoga Park ground motion (Schafer 2015)

Table 4-1: Maximum percent story drift across phases and ground motions (Schafer 2015)

		LONG		SHORT	
Phase	**Ground Motion**	**$\Delta u_1/h$**	**$\Delta u_2/h$**	**$\Delta v_1/h$**	**$\Delta v_2/h$**
-	-	%	%	%	%
1	44% Canoga Park	0.55	0.38	0.36	0.29
2b	44% Canoga Park	0.19	0.29	0.11	0.21
2c	44% Canoga Park	0.12	-0.12	0.11	0.17
2d	44% Canoga Park	0.11	-0.19	0.08	-0.15
2e	44% Canoga Park	0.08	-0.20	0.06	-0.14
1	100% Canoga Park	1.18	0.81	0.85	0.56
2e	100% Canoga Park	0.25	-0.48	0.16	-0.32
2e	16% Rinaldi	0.11	0.07	-0.16	0.11
2e	100% Rinaldi	0.67	-0.72	0.45	0.49

Axial forces in the hold downs that fasten the end of a shear wall's chord studs to foundations is recorded as the force in pre-compressed load cells. Output of these sensors helps to understand the way the building, especially the shear wall system, carries the seismic demands. Figure 4-5 is a summary of the reconstructed deformed shape of the building using measured displacement at corners along with hold down axial force at the moment of peak drift during testing (Schafer 2015). According to the figure, the building's response is complex even at a relative low level of excitation (44% Canoga Park) and at every construction phase, exhibits a coupled system behavior. Note, the load cell can read tension and a small amount of compression (only up to the amount of pre-

tension on the anchor rods) therefore tension may be read based on magnitude (length of the bar), and compression is essentially only an indicator of compression, not its magnitude. The building is designed as a series of independent shear walls and assuming a flexible diaphragm. Under these assumptions each shear wall should experience force couples of tension and compression. However, the actual response is more tied to the overall motion of the building (in three dimensions) and significant amount of coupling amongst shear walls is observed (Schafer 2015). Comparison of 100% Canoga Park in the Phase 1 and Phase 2e response in the lower left of Figure 4-5 provides further evidence that the engineered system (Phase 1) and the actual building (Phase 2e) do not respond the same.

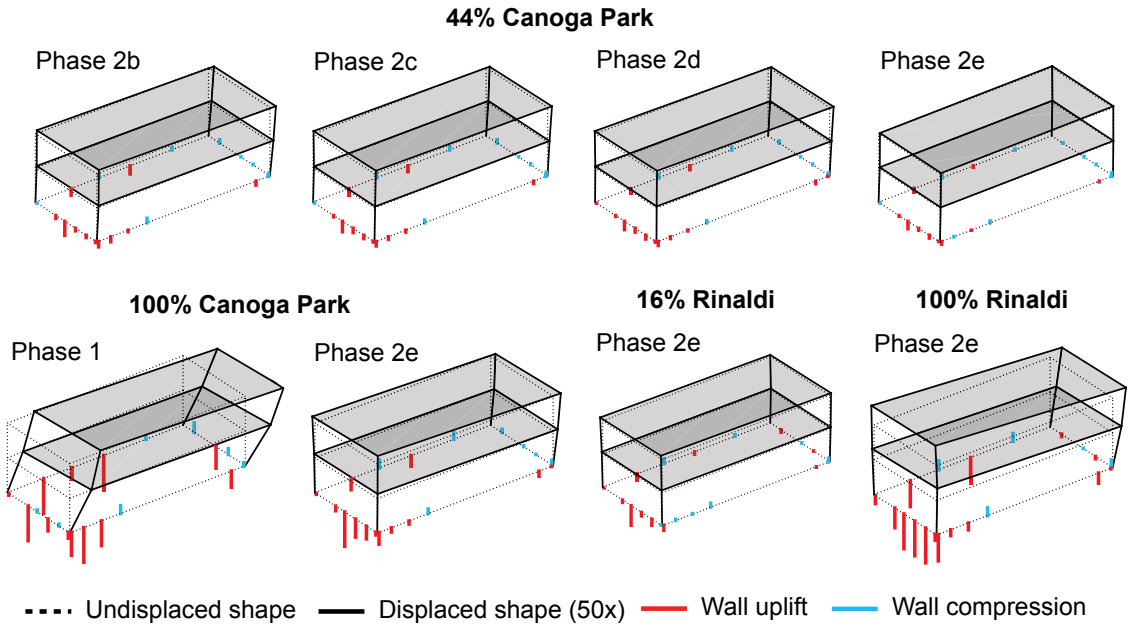

Figure 4-5: Shear wall anchor forces superimposed on the deformed and undeformed shapes of the building specimens at peak first story drift in the long direction (Schafer 2015)

Phase 1 and Phase 2e buildings remained intact and returned to upright configuration after three-axis excitations of DBE or MCE, respectively. Visual examination after test

could not identify noticeable structural damage and the only damage of the Phase 2e building after 100% MCE excitation occurred in the interior non-structural walls – largely confined to corners and near openings. As pointed out by Schafer (Schafer 2015), "this full scale testing provides a first examination of the full system effect for buildings framed from cold-formed steel and it is significant: the building is stiffer and stronger than engineering designs suggest; the building responds as a system, not as a set of uncoupled shear walls; and the gravity system contributes to the lateral response." Details of test setup, instrumentation, data post-processing and conclusion are available in Peterman's thesis (Peterman 2014). For published work on the CFS-NEES full scale shaking table test, see (Peterman et al. 2014; Peterman et al. 2014; Schafer et al. 2014; Schafer 2015).

4.2 Excitations in shaking table tests and in finite element model calibration

4.2.1 Description of ground motion records in shaking table test

Two sets of ground motions from the 1994 Northridge earthquake were selected as excitations in the CFS-NEES project: (1) Canoga Park, Topanga Canyon Road, USC 90053, and (2) Rinaldi Receiving Station, DWP 77. The Rinaldi record is also part (record no. 9) of the near-field suite of ground motions for FEMA P695 (FEMA 2009). Table 4-2 provides basic information about the Canoga Park and Rinaldi records (Peterman 2014). Figure 4-6 is a plot of three components of the Canoga Park record. Figure 4-7 is a plot of three components of the Rinaldi record. Peak ground accelerations are marked with circles (Peterman 2014). Those records have also been used in the

CUREE/Caltech wood-frame project (Krawinkler et al. 2001) and the NEESWood project (Filiatrault et al. 2009).

Table 4-2: Ground motion summary, per PEER NGA database (Peterman 2014)

	Canoga Park	**Rinaldi**
Peer Rec. No.	NGA 0959	NGA1063
File name, dir. 1	CNP106	RRS228
File name, dir. 2	CNP196	RRS318
File name, vertical	CNP-UP	RRS-UP
Latitude	34.212	34.281
Longitude	-118.606	-118.478
Epicentral distance (km)	4.85	10.91
Distance to site (km)	83	78
PGA, dir. 1 (g)	0.3558	0.8252
PGA, dir. 2 (g)	0.4203	0.4865
PGA, vertical (g)	0.4888	0.8343
Time step (s)	0.01	0.01

source: PEER NGA Database at <http://peer.berkeley.edu/nga/index.html>

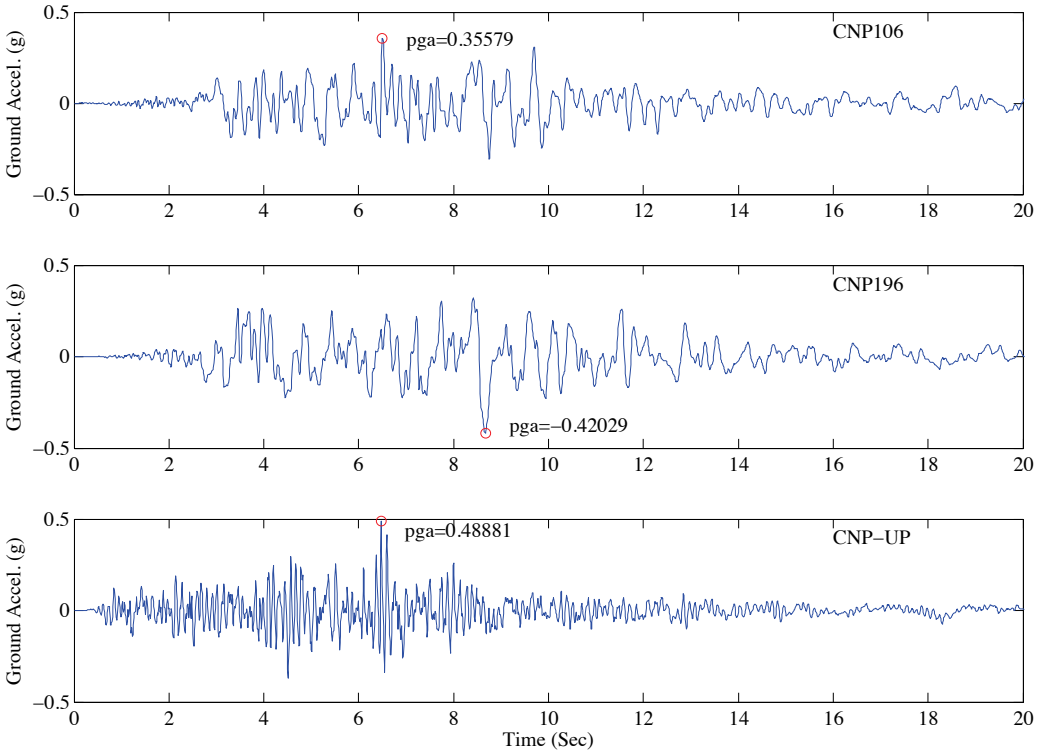

Figure 4-6: Canoga Park ground motions (Peterman 2014)

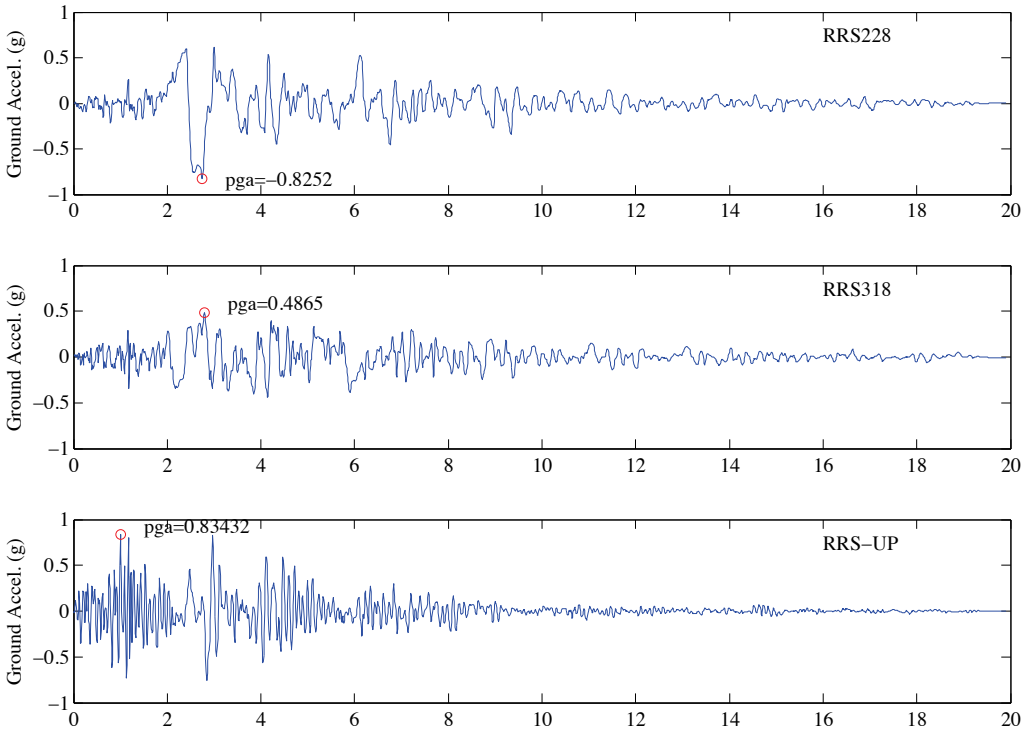

Figure 4-7: Rinaldi ground motions (Peterman 2014)

Following the design of the CFS-NEES archetype building (Madsen et al. 2011), the elastic and inelastic (R=6.5) design spectra, as well as the estimated fundamental period based on Eqn. 12.8-7 of ASCE 7-10 is plotted in Figure 4-8 (Peterman 2014).

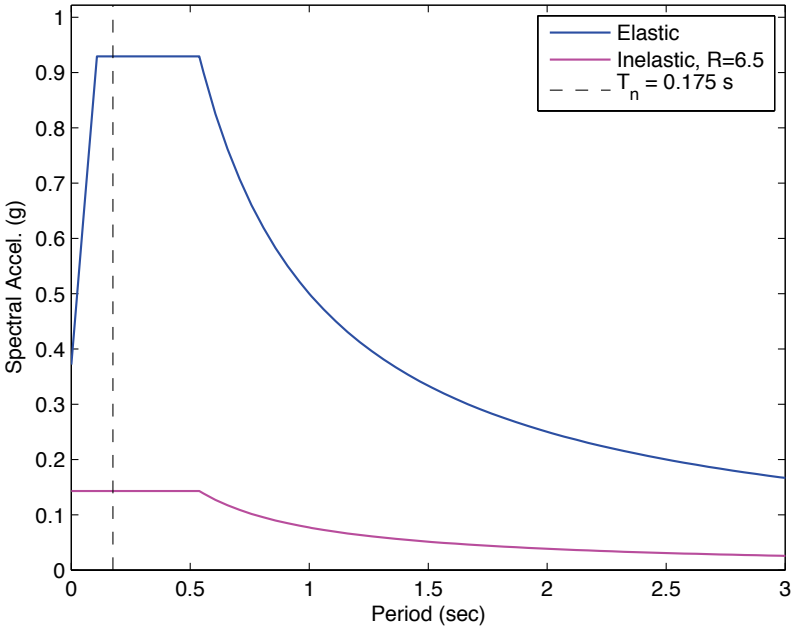

Figure 4-8: ASCE 7-10 site-specific design spectra, assuming 5% damping. T_n and T_a refer to the same quantity: the approximate natural period of vibration, per ASCE 7 (Peterman 2014)

As discussed by Krawinkler et al. (Krawinkler et al. 2001), far-field ground motion records can be linearly scaled such that the spectral acceleration matches the design spectrum near the estimated fundamental period. However, for the CFS-NEES archetype building, the spectral acceleration near the estimated fundamental period is very close to the design spectrum and the spectral acceleration scale factor is less than 1.05. Consequently, the Canoga Park record was used unscaled as our DBE. Krawinkler et al. (Krawinkler et al. 2001) also recommends that near fault records such as Rinaldi should not be scaled, thus the Rinaldi motion was left unscaled. Response spectra of CNP and RRS are plotted together with the design spectrum in Figure 4-9 and Figure 4-10.

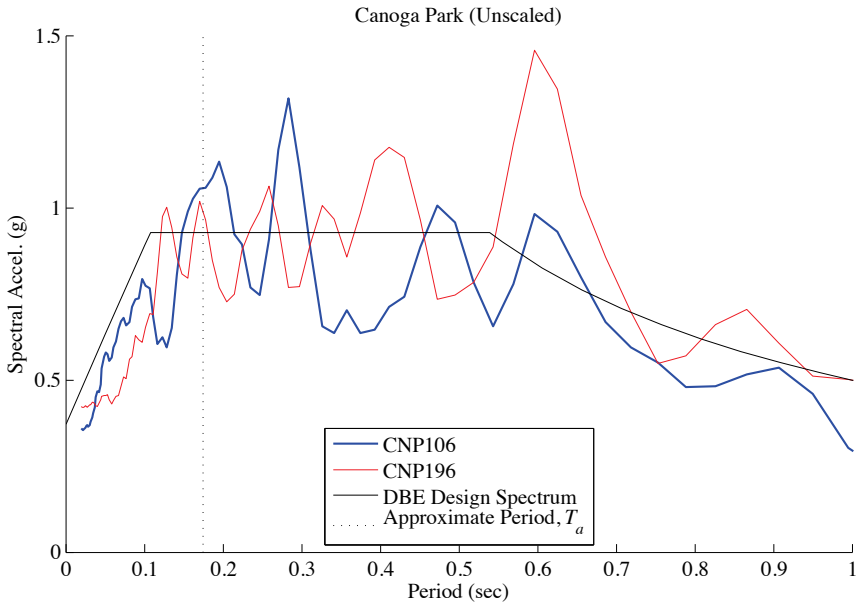

Figure 4-9: Unscaled Canoga Park spectrum with DBE design spectrum. T_a is per ASCE 7. (from private communication with Steve Buonopane) (Peterman 2014)

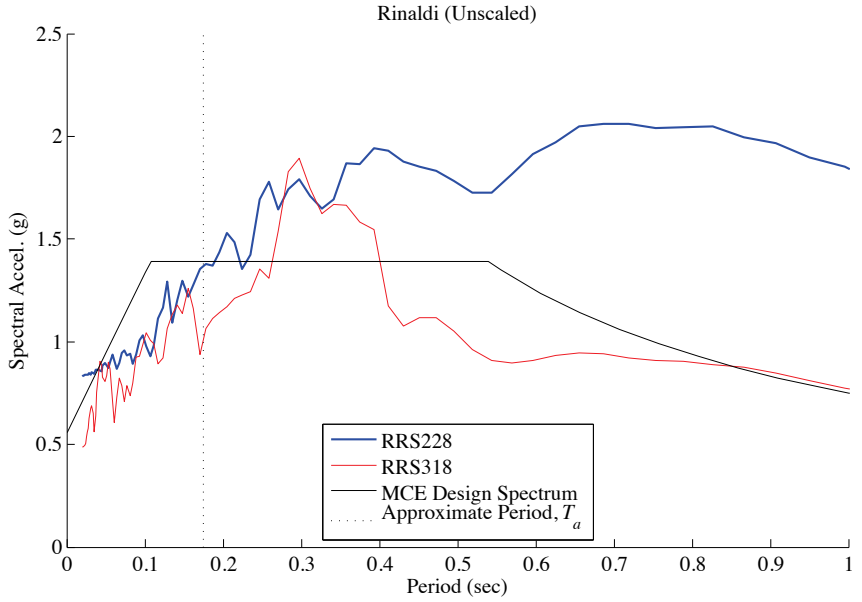

Figure 4-10: Unscaled Rinaldi spectrum with MCE design spectrum. T_a is per ASCE 7. (from private communication with Steve Buonopane) (Peterman 2014)

In consideration of various ground motion hazard levels (probability of occurrence in a 50 year time span), four scaled versions of the Canoga Park ground motion were employed for low level testing. The peak ground acceleration (PGA, in the unit of g) for

each scale level, along with corresponding hazard levels, are listed in Table 4-3. Scale factors, commonly referred to as a percent of the full-scale ground motion, are rounded to the nearest percent for use in testing.

Table 4-3: Ground motion summary and levels (Peterman 2014)

Level	Ground Motion	Hazard Level	Scale Factor	PGA EW	PGA NS	PGA vertical
1	Canoga Park	99.9% / 50 yr	0.1564	0.0657	0.0556	0.0764
2	Canoga Park	50% / 50 yr	0.436	0.1833	0.1551	0.2131
3	Canoga Park	20% / 50 yr	0.7184	0.3019	0.2556	0.3512
4	Canoga Park (DBE)	10% / 50 yr	1	0.4203	0.3558	0.4888
5	Rinaldi (MCE)	2% / 50 yr	n/a	0.8252	0.4865	0.8343

4.2.2 Description of excitation signals in time history analyses of model calibration

Similar to the shaking table tests, comparison between simulation results and test outputs is performed at each construction phase of the archetype building (as detailed in next section). High fidelity models that capture most design features of the archetype building (see Table 3-3 in Chapter 3) are selected at each construction phase and are excited with the recorded acceleration experienced by the real building during testing at the same phase. The usage of recorded building acceleration is justified by the fact that the experienced acceleration is different from the targeted acceleration 'loaded' into actuators to excite the structure. Moreover, as depicted in Peterman's thesis (Peterman 2014), the difference between actual excitation signal and the desired signal of the original ground motion is minimized but still inevitable due to the tuning of the shake table. Consequently, PGA of the building's experienced acceleration can deviate noticeably from original record. An extreme case is observed in Phase 2e building under 100% Rinaldi excitation. The resulted vertical PGA of the building is 1.27 g, 55% larger than 0.82 g of the original signal (Schafer 2015).

Tests of the archetype building across phases follow the same general pattern: white noise tests always proceed and follow seismic tests. White noise tests are acceleration-controlled flat random noise with a frequency band of 0.5-50 Hz (Peterman 2014). As mentioned above, white noise tests are used for system identification of the building's natural periods and damping ratios. Natural periods/frequencies are directly available from free vibration analysis; however the damping ratio is set as 5% for all time history analyses of FE models (see more details in next section). The white noise excitation is not included in load cases for the time history analyses for our purpose of comparing models' performance with tests. Comparable to the testing plan at each phase, load cases are tabulated in Table 4-4 for a selected phase as an example. Note: this is simply a skeleton load case table, and does not reflect simulations as-conducted for each phase. Exact load case tables are produced in the next section.

Table 4-4: Summary of load case for the calibration of a FE model

Ground Motion	Direction	Scale Level
Seismic, case 1	1D: long	CNP 16%
Seismic, case 2	1D: short	CNP 16%
Seismic, case 3	2D: long, short	CNP 16%
Seismic, case 4	3D: long, short	CNP 16%
Seismic, case 5	3D: long, short	CNP 44%
Seismic, case 6	3D: long, short	CNP 100%

4.3 Comparison of seismic response between simulation and test in model calibration

4.3.1 Description of data post-processing and output physical quantities

Comparison of response variables between the simulation/high-fidelity FE models and the shake table tests is performed at each construction phase of the building. This section outlines the assumptions and calculations made in determining these response parameters. Ideally, output physical quantities at every node and element in the simulation model can

be recorded, so the calculation of the building's performance metrics can be done in a more complete way in the simulation as opposed to the testing where channel, instrumentation, and other physical issues limit the amount of output data from a test.

Natural periods/frequencies are directly available from free vibration (eigenvalue) analysis and are compared to system identification results from white-noise test at each phase. Eigenvectors from OpenSees analysis are also recorded and plotted in MATLAB, so that analysts can identify every mode shape.

Nodal acceleration, displacement and element forces are immediate outputs of time history analysis and can be post-processed to determine story drifts, peak story acceleration and hold down axial forces. Peak story drift is calculated as the peak value of inter-story lateral displacement of floor and roof level (story 1 and story 2) in the long/short direction over story height. Story drifts are calculated at every corner node and the average drift of four corners on the same level is taken as the building's story drift. A wall line's story drift is different in that it is the average drift of two corner nodes on the same level of the same elevation. Peak absolute accelerations of the story are taken as mean values of absolute accelerations on four corners in long, short and vertical directions. Note that in Peteman's thesis (Peterman 2014), the peak acceleration amplification factor defined as peak absolute value of the building's peak corner accelerations devided by the mean of peak absolute values of the shaking table's corner accelerations was adopted. Among graphical comparisons are time history plots of story drifts and axial forces of selected hold downs for each phase in following subsections.

The periodogram of story drifts offers a comparison in the frequency domain. The distribution of hold down axial force in a specific model at a certain time is also provided. Since a load cell can record the axial force in a hold down while the hold down is in tension only during testing, any comparison on peak hold down force between models and tests in this thesis are with respect to tensile force only. Also, load cells are tightened before applying the excitation in a test, the static tensioning force is removed in tables and figures of this thesis. Similarly, predicted axial force in a hold down from OpenSees models is zeroed by removing the static force from gravity load everywhere in this thesis. Also, to be consistent with the sign convention of tests (see Section 2.2.6 and Section 3.4.2 of (Peterman 2014)) negative sign symbolizes tensile force in hold downs.

As described in Chapter 3, in most A-models the hold downs are modeled with two nonlinear spring elements in parallel. The summation of recorded element force in these two springs equals the axial force in a hold down. The locations of all twenty hold downs are shown in Figure 4-11, and load cell 5, 6, 7 and 8 (see (Peterman 2014)) are selected for the purpose of comparison between simulation and test. These two hold down pairs belong to shear wall L1S1 on the South elevation and L1W1 on the West elevation. These shear walls are the weakest ones on the wall line, and they meet at the southeast edge, so they tend to be predicted to fail first because of lower capacities of the walls and the complicated coupling effect of the building as a whole and the corner in particular. Time history plots of hold down forces and tabulated peak values are presented for each phase.

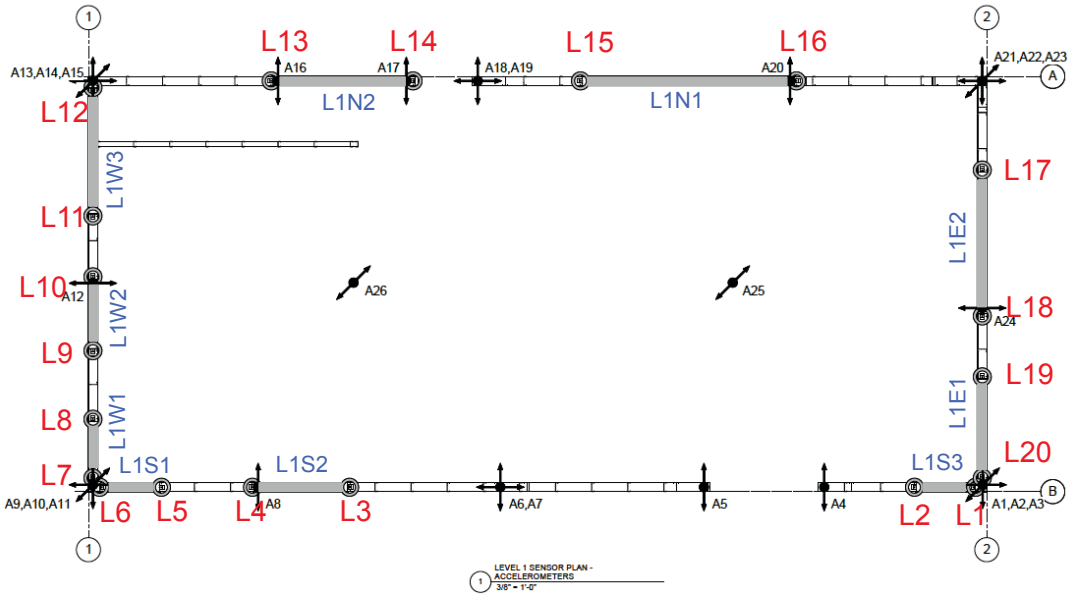

Figure 4-11: Floor plan of the base level of the CFS-NEES with locations of load cells (hold downs) (Peterman 2014)

High fidelity OpenSees FE models (A1-3D-SD-a, A2b-3D-SD-a, A2c-3D-SD-a and A2d-3D-RD-a) are selected for comparison with the tests as these models have the most features of the real building. Table 4-5 is an excerpt from the general table of modeling options (Table 3-3 in Chapter 3) that only highlights models used in the calibration/validation process covered in this section. All time history analyses are second-order inelastic (i.e. materal and geometric nonlinear), with Rayleigh damping ratio set to 5%. Summarized damping ratio from test data is tabulated in Table 4-6. The damping in time history analyses is close to pre-test damping, but much less than damping of the building after shaking table tests with real ground motions; however, the value of 5% is chosen to keep it uniform across phases and to match it with specifications and the design spectrum. Also, FEMA P-750 (Building Seismic Safety Council 2009), the National Earthquake Hazards Reduction Program (NEHRP) Recommended Provisions (2009) suggests that inherent damping shall not be greater than 5% unless

supported by test data at or close to the deformation level of the effective yield displacement of the seismic-force- resisting system. The impact of damping ratio on the model's history response will be expounded in Chapter 5.

Since the excitations of analyses in this section are the building's experienced acceleration at corresponding phases, the time step of analyses equals the sampling period of the test, which is 1/256=0.00390625 seconds (sampling frequency is 256 Hz). PGAs of excitations are given below in summary tables of each phase.

Table 4-5: Modeling options of the CFS-NEES archetype building in model calibration

			State of the Art			
			Phase 1/2a	Phase 2b	Phase 2c	Phase 2d/2e
Component	Property	Option	A1-3D-SD-a	A2b-3D-SD-a	A2c-3D-SD-a	A2d-3D-RD-a
Shear wall	Stiffness	$K(0.4V_{nP})$				
		$K(V_{nP})$				
		$K(0.2V_{nA})$	X	X	X	X
		$K(0.4V_{nA})$				
	Capacity	V_{nA}	X	X	X	X
		V_{nP}				
	Backbone	EPP				
		Pinching4	X	X	X	X
	Panel size	Whole				
		Subpanels	X	X	X	X
Hold down	General	Smeared				
		Discrete	X	X	X	X
Shear anchors	General	Ignored				
		Included	X	X	X	X
Diaphragm	Stiffness	Flexible				
		Rigid				X
		Semi-rigid	X	X	X	
	Pinching	None				X
		Pinching4	X	X	X	
Gravity exterior walls	General	None				
		Frame	X			
		Full		X	X	X
Gypsum sheathing	General	Ignored	X	X		
		Included			X	X
Interior walls	General	Ignored	X	X	X	
		Included				X
Mass distribution	General	Corner				
		Stud ends	X	X	X	X

Table 4-6: Damping ratio of the CFS-NEES archetype building predicted by shaking table tests at various construction phases (data from (Peterman 2014))

		Damping	
		LONG	SHORT
Phase	**Ground Motion**	**ζ_1 (%)**	**ζ_1 (%)**
1	white noise	3.75	4.00
1	CNP 100%	18.00	19.00
2a	white noise	4.25	4.00
2a	CNP 16%	6.00	5.25
2b	white noise	6.50	5.25
2b	CNP 44%	7.50	10.00
2c	white noise	8.00	10.00
2c	CNP 44%	8.00	11.00
2d	white noise	8.00	11.00
2d	CNP 44%	9.50	11.00
2e	white noise	8.00	10.00
2e	CNP 100%	11.50	14.00
2e	CNP 100%	15.00	16.00

4.3.2 Phase 1 – bare structural

The modeling effort for the CFS-NEES archetype started with the simple idea, close to P-models (Figure 4-12 (a)) (Leng et al. 2012) of Table 3-3, on the basis of code specified stiffness and capacity. Shear wall backbone curves were characterized after the completion of shear wall tests and the modified model became the earliest A-models (Figure 4-12 (b)) (Leng et al. 2013). These models' LFRS were shear walls only and their predicted behavior was much more flexible than the building's response in shaking table tests. Careful investigations into the test data suggested that the idealization of modeling shear walls as the only LRFS was very conservative, so it was necessary to include the gravity system and other nonstructual components in the later A-models in order to achieve high-fidelty. A brief comparison is presented in Table 4-7 showing the incapability of the shear wall only models. Detailed discussion of model performance is available in Chapter 5.

Table 4-7: Brief comparison of 3D shear wall only models with test of Phase 1 (structural only) building

Data source	First natural period, T_1 (s)	Peak story drift, CNP 100% (%)	Peak hold down tensile force, CNP 100% (kip)
P-3D-RD-b model	0.66	5.09	14.1
A1-3D-RD-c model	0.45	3.17	14.7
Phase 1 building test	0.36	1.18	9.8

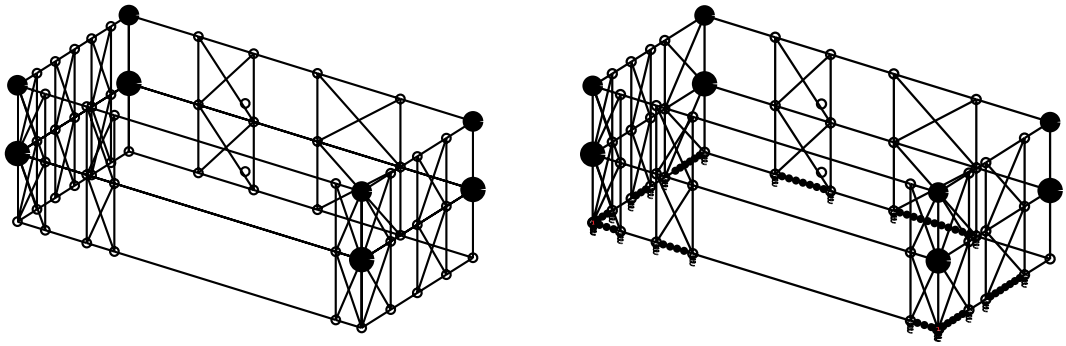

(a) P-3D-RD-b model (b) A1-3D-RD-c model

Figure 4-12: Examples of 3D shear wall only models

In this subsection and the next five ones, the response of high fidelty models at each construction phase will be compared with shaking table test results of the archetype building at the same phase. For Phase 1, the selected high fidelity model is A1-3D-SD-a. Figure 4-13 is a comparison between the design drawing of the Phase 1 building and A1-3D-SD-a model. The model captures the geometry and material properties of steel framing members and sheathing panels of shear walls on four perimeter wall lines. The model also employs semi-rigid diaphragms modeled as subpanels.

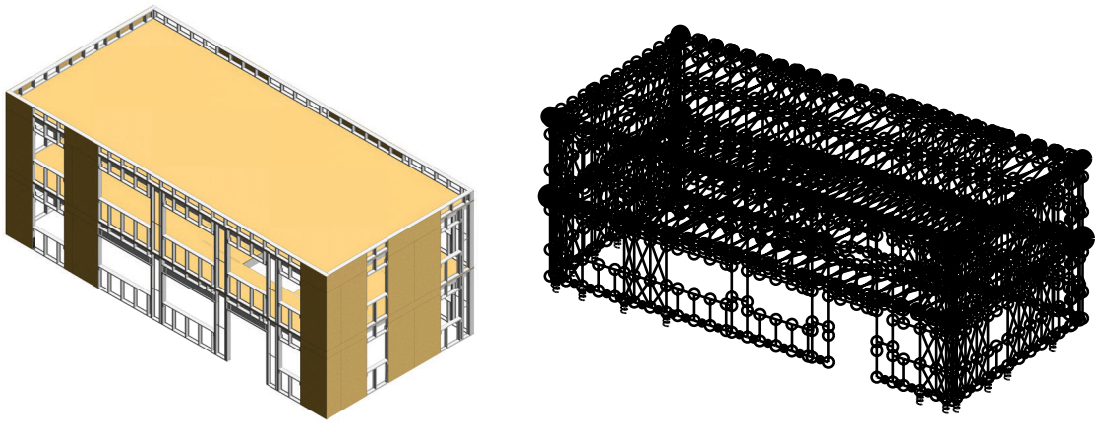

(a) Isometric design drawing (b) FE model (A1-3D-SD-a)

Figure 4-13: Design drawing and high-fidelity FE model of Phase 1 building

Table 4-8 is a summary of excitations in the validation of the Phase 1 model. The 'Record PGA' column of Table 4-8 is the peak ground acceleration of the original ground motion record in the unit of g. 'Excitation PGA' is the peak ground acceleration of the excitation used in time history analyses, which is the acceleration experienced by the building during testing. That is, excitations measured in the test were used in the models where the objective was to compare directly with testing. The 'Excitation PGA' on the right half of the table is ~20% larger than 'Record PGA' on the left. Note, the name of excitations is in accordance with test names in (Peterman 2014), excitation names that are skipped indicate that the corresponding tests were not performed. To be clear with the nomenclature, excitation names on the left will be frequently referred to in this chapter when results of a certain simulation need to be addressed. In this series the largest scale of excitation is P1S07 that corresponds to 100% Canoga Park ground motion in three axes, which is also consistent with the DBE-level for the CFS-NEES archetype building.

Table 4-8: Summary of excitations for model calibration, Phase 1

Excitation Name	Ground Motion	Record PGA long (g)	Record PGA short (g)	Record PGA up (g)	Excitation PGA long (g)	Excitation PGA short (g)	Excitation PGA up (g)
P1S01	CNP 16%	0.0657	0	0	0.0830	0	0
P1S02	CNP 16%	0	0.0556	0	0	0.0614	0
P1S03	CNP 16%	0.0657	0.0556	0	0.0822	0.0616	0
P1S04	CNP 16%	0.0657	0.0556	0.0764	0.0828	0.0692	0.0987
P1S05	CNP 44%	0.1833	0.1551	0.2131	0.2029	0.2029	0.2645
P1S07	CNP 100%	0.4204	0.3558	0.4888	0.5858	0.4782	0.5223

Table 4-9 provides the first natural period of the translational modes in the long and short direction. The first natural period is larger in the short direction, as observed from both tests and simulations. Although the model is modestly stiffer than the building as predicted by system identification of white-noise tests, the match between test and model periods is reasonable (i.e. the difference is less than 10%). This indicates that the model successfully incorporates multiple sources of lateral stiffness, including shear walls, and all gravity framing, and as appropriate the diaphragms.

Table 4-9: Comparison of the first natural period between A1-3D-SD-a model and test, Phase 1

LONG		SHORT	
T_1 (s), Test	T_1 (s), Model	T_1 (s), Test	T_1 (s), Model
0.32	0.30	0.36	0.32

Table 4-10 provides the comparison of peak story absolute acceleration between A1-3D-SD-a model and test. At higher excitation levels (P1S05 and P1S07), the difference between the model and the test is less than 30% in the long direction, but it can be ~100% in the vertical direction. At lower excitation levels (P1S01 to P1S04) the difference between model and test can be 0.06g in the long direction of P1S02 excitation. However, long direction is unloaded under P1S02, and the peak value of story acceleration is small (less than 0.1 g) so it can be susceptible to random noise. In general the match of peak story acceleration, as the second order time derivative of displacement, is not quite

accurate, but acceptable. Further examination of the error in the long, short and vertical directions shows that the matching of peak story absolute acceleration is worse in the vertical component, which suggests the modeling of the vertical load path, although not the first and foremost focus of this research, should be scrutinized and has a large potential for further improvement.

Table 4-10: Comparison of peak story absolute acceleration in g between A1-3D-SD-a model and test, Phase 1

LONG					
Excitation Name	**Ground Motion**	**Floor, Test**	**Floor, Model**	**Roof, Test**	**Roof, Model**
P1S01	CNP 16%[1]	0.142	0.170	0.177	0.179
P1S02	CNP 16%[2]	0.018	0.062	0.014	0.075
P1S03	CNP 16%[3]	0.145	0.167	0.184	0.215
P1S04	CNP 16%	0.146	0.178	0.189	0.198
P1S05	CNP 44%	0.368	0.422	0.631	0.506
P1S07	CNP 100%	1.280	0.787	1.834	1.116
SHORT					
Excitation Name	**Ground Motion**	**Floor, Test**	**Floor, Model**	**Roof, Test**	**Roof, Model**
P1S01	CNP 16%[1]	0.015	0.210	0.014	0.212
P1S02	CNP 16%[2]	0.085	0.224	0.125	0.228
P1S03	CNP 16%[3]	0.085	0.215	0.128	0.278
P1S04	CNP 16%	0.089	0.193	0.134	0.238
P1S05	CNP 44%	0.274	0.487	0.399	0.683
P1S07	CNP 100%	0.592	0.763	0.995	0.91
UP					
Excitation Name	**Ground Motion**	**Floor, Test**	**Floor, Model**	**Roof, Test**	**Roof, Model**
P1S01	CNP 16%[1]	-	0.035	0.014	0.047
P1S02	CNP 16%[2]	-	0.088	0.011	0.082
P1S03	CNP 16%[3]	-	0.086	0.016	0.089
P1S04	CNP 16%	-	0.213	0.098	0.194
P1S05	CNP 44%	-	0.462	0.270	0.601
P1S07	CNP 100%	-	1.306	0.552	1.201

[1]long direction only [2]short direction only [3]long and short directions only

Peak story drifts calculated using test and simulation data of A1-3D-SD-a model are summarized in Table 4-11. At lower excitation scale levels (P1S01 to P1S05) when nonlinearity in the structure is not significant, peak drifts in the model/simualtion is close to the test results. At P1S07 (corresponds to DBE level, 100% Canoga Park excitation),

the model (conservatively) over-predicts the magnitude of first story peak drift by 40% in the long direction, and 3% in the short direction. Another common observation among the results is that the model's peak drift on the roof level is always smaller than the tested building in both long and short direction, suggesting that walls or diaphragm on that level (in the simulaiton) is modestly stiffer than reality.

Time history plots of the story drifts with P1S07 are provided in Figure 4-14. Despite the difference in peak values (Table 4-11), the model's response is in phase with the building and the magnitude does not deviate greatly. Figure 4-15 further shows that the predicted drift from A1-3D-SD-a model has the same power spectral density with test outputs. Table 4-11, Figure 4-14 and Figure 4-15 demonstrate that the model is capable of predicting the lateral deflection and story drift of Phase 1 building to acceptable accuracy.

Table 4-11: Comparison of peak story drift between A1-3D-SD-a model and test, Phase 1

LONG					
Excitation Name	**Ground Motion**	**$\Delta u_1/h$ (%) Test**	**$\Delta u_1/h$ (%) Model**	**$\Delta u_2/h$ (%) Test**	**$\Delta u_2/h$ (%) Model**
P1S01	CNP 16%[1]	0.12	0.10	0.11	0.03
P1S02	CNP 16%[2]	0.01	0.04	0.01	0.01
P1S03	CNP 16%[3]	0.14	0.11	0.10	0.04
P1S04	CNP 16%	0.16	0.11	0.11	0.04
P1S05	CNP 44%	0.55	0.47	0.38	0.13
P1S07	CNP 100%	1.18	1.66	0.81	-0.55
SHORT					
Excitation Name	**Ground Motion**	**$\Delta v_1/h$ (%) Test**	**$\Delta v_1/h$ (%) Model**	**$\Delta v_2/h$ (%) Test**	**$\Delta v_2/h$ (%) Model**
P1S01	CNP 16%[1]	0.01	-0.02	0.02	0.01
P1S02	CNP 16%[2]	0.10	0.08	0.08	0.04
P1S03	CNP 16%[3]	0.10	0.08	0.08	0.04
P1S04	CNP 16%	0.10	0.08	0.09	0.05
P1S05	CNP 44%	0.36	0.27	0.29	-0.11
P1S07	CNP 100%	0.85	0.88	0.56	0.34

[1]long direction only [2]short direction only [3]long and short directions only

Table 4-12 along with Figure 4-16 offers a comparison on the axial force in the load cells of hold downs. As mentioned in Section 4.3.1, only tensile (negative) forces in hold downs are tabulated. At low excitation levels, e.g. P1S01 to P1S04 that correspond to 16% CNP, peak axial force amongst all hold downs of the model is larger than the test values (77% larger for P1S01, less than 50% larger for P1S02 to P1S04). At higher excitation levels (P1S05 and P1S07), the peak tensile force in hold downs is underestimated by A1-3D-SD-a model and it can be 45% lower than test P1S07. Investigation on the specific load cells under P1S07 excitation that corresponds to 100% CNP, as shown in Figure 4-16, demonstrates that the model underestimates the peak tensile force in load cell No. 8 (see the sensor plan in Figure 4-11) by 44%. Apart from this load cell, the behavior of load cell No. 5 to No. 7 matches closely with the test results. Also shown in Figure 4-16 are some sharp impulses of the recorded compressive hold down axial force from the simulation. With the author's effort to tune the hold down model to mimic its greatly different behavior under tensile and compressive force (Section 3.3.2), numerical difficulties do appear at times in nonlinear analyses even after careful selection of controlling parameters for the numerical integration algorithms. In addition, the model simplifies the corner of the building in locations, such as load cell 6 and 7, see the construction drawing for details.

Figure 4-17 juxtaposes simplified deformed shapes of the building and the model at the same time (see (Peterman 2014) for details on generating simplified deformed shape of the diaphragms from the testing), together with hold down load cell forces. Note, for the plot of the test results, blue bars only indicate that those hold downs are in compression

but has nothing to do with the magnitude of the force since load cell measurement cannot record compressive forces for anything other than small force levels accurately. The model's deflection is smaller on the roof level than the floor level and is less than the measurement from the test. As discussed in Section 3.9, the model has a direct vertical load path due to the fixed connection between chord studs at floor and roof levels. This idealization overestimates the connection stiffness of the shear wall tie in reality. Hold down force distribution after the removal of gravity load (Figure 4-17(b) and Figure 4-17 (c)) of the model does not closely match the real test, showing that the vertical load path in the model may need to be further revised in the future. A possible effect that can be included in further refined models, as discussed in Section 3.3.2, is the stiffness of the HSS steel tube that is the foundation of the CFS-NEES building. Compressive (blue) spikes in Figure 4-17(d) indicate that the compressive bearing at stud ends modeled by multilinear spring elements can sometimes generate very large forces. Iteration history of the analysis is recorded, and at moments of large compressive bearing force, convergence of the nonlinear analysis usually meets difficulties: the algorithm has to reduce the load step or try other convergence criteria. Spring elements that have highly unsymmetric response in tension and compression, including hold downs and stud end bearings, can be modified further to improve the model's gravity load path and speed up convergence of the iteration.

Table 4-12: Comparison of peak hold down tensile force between A1-3D-SD-a model and test, Phase 1

Excitation Name	Ground Motion	Peak F (kip) Test	t @ peak F (s) Test	Peak F (kip) Model	t @ peak F (s) Model
P1S01	CNP 16%[1]	-0.97	8.75	-1.72	10.51
P1S02	CNP 16%[2]	-1.28	5.54	-1.33	10.19
P1S03	CNP 16%[3]	-1.27	5.52	-1.81	11.92
P1S04	CNP 16%	-1.32	5.97	-1.87	11.91
P1S05	CNP 44%	-4.85	8.79	-3.27	9.73
P1S07	CNP 100%	-9.78	8.79	-5.37	8.78

[1]long direction only [2]short direction only [3]long and short directions only

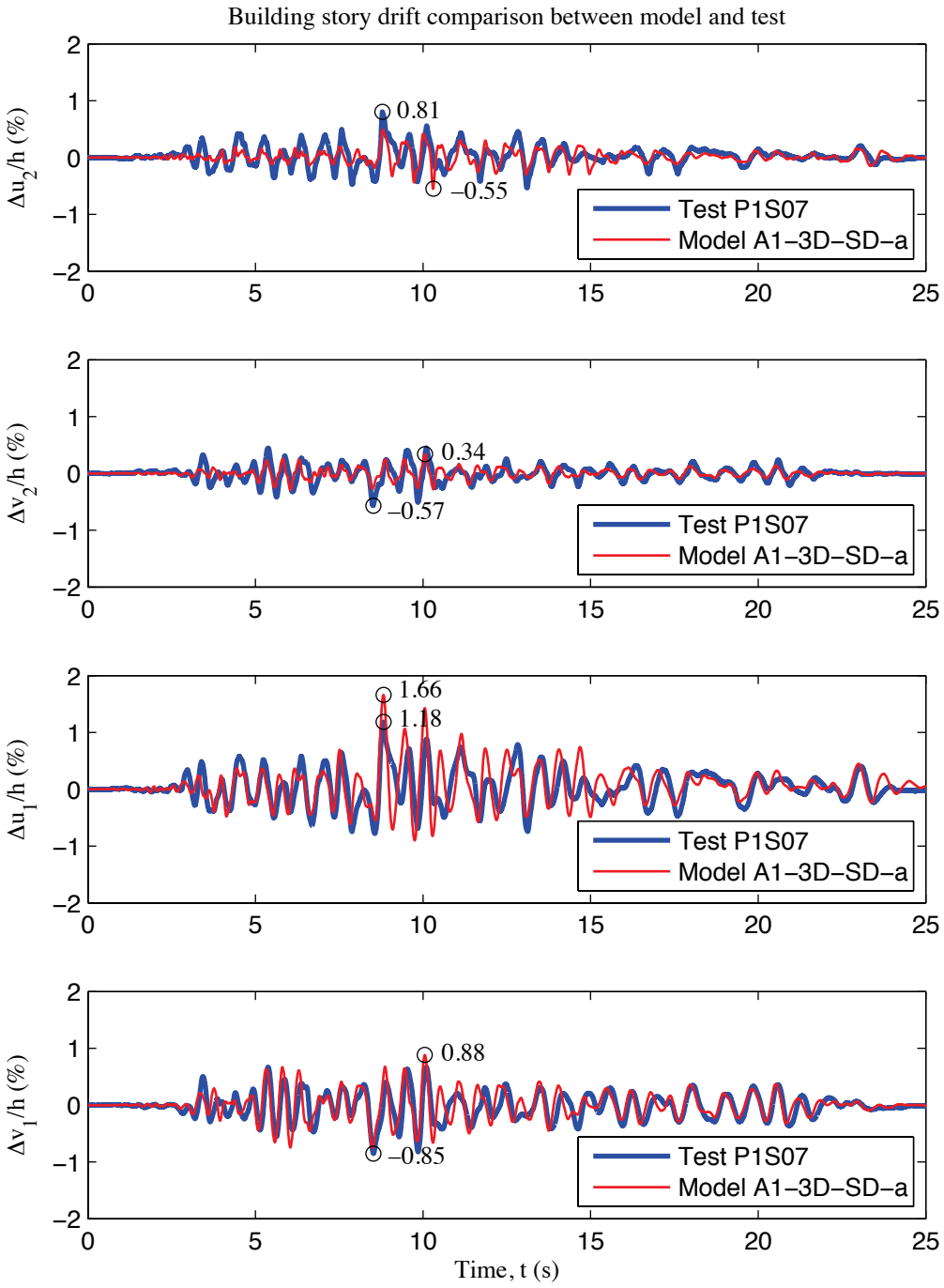

Figure 4-14: Comparison of story drift of the building, P1S07 excitation, Phase 1

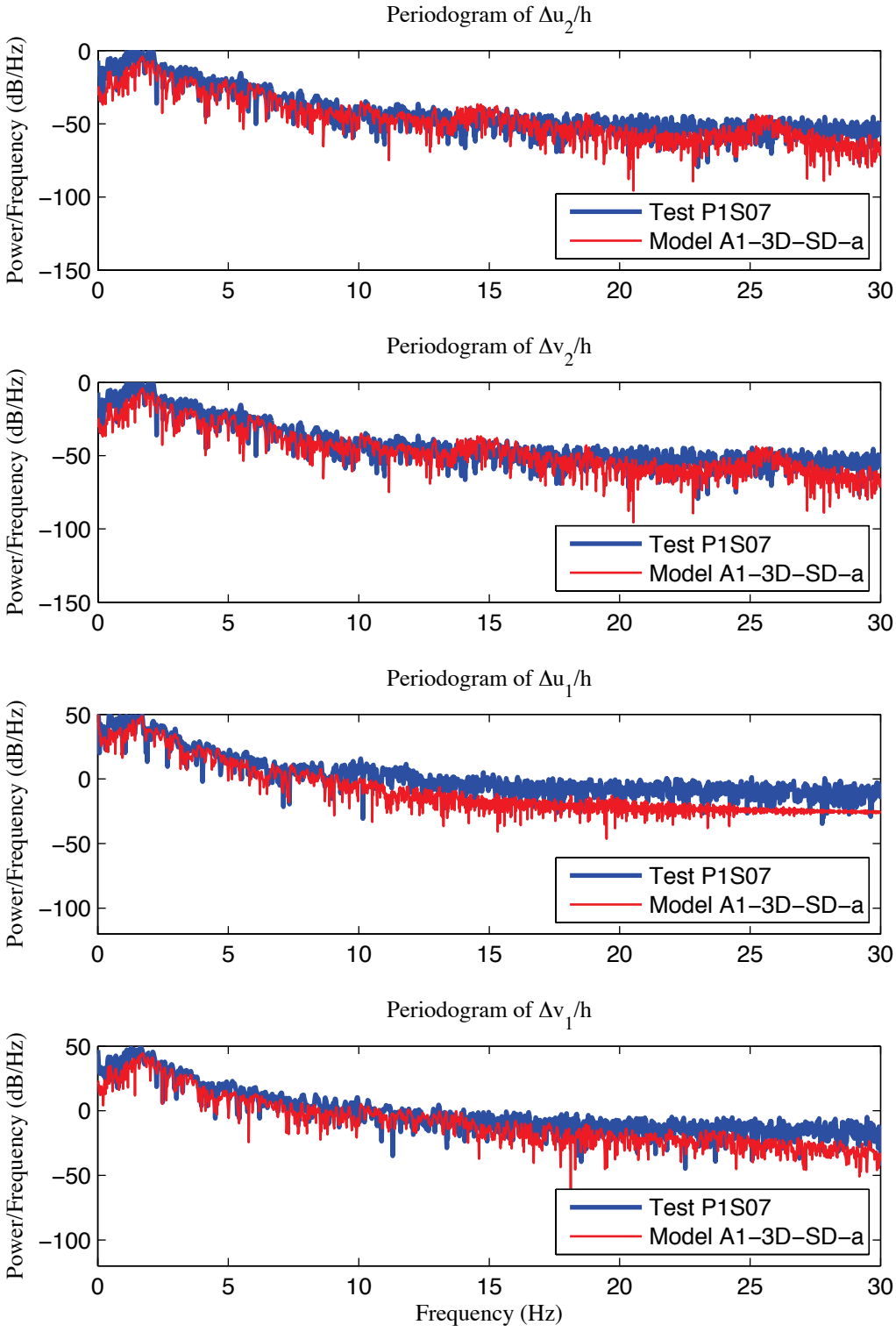

Figure 4-15: Comparison of periodogram of the building's story drift, P1S07 excitation, Phase 1

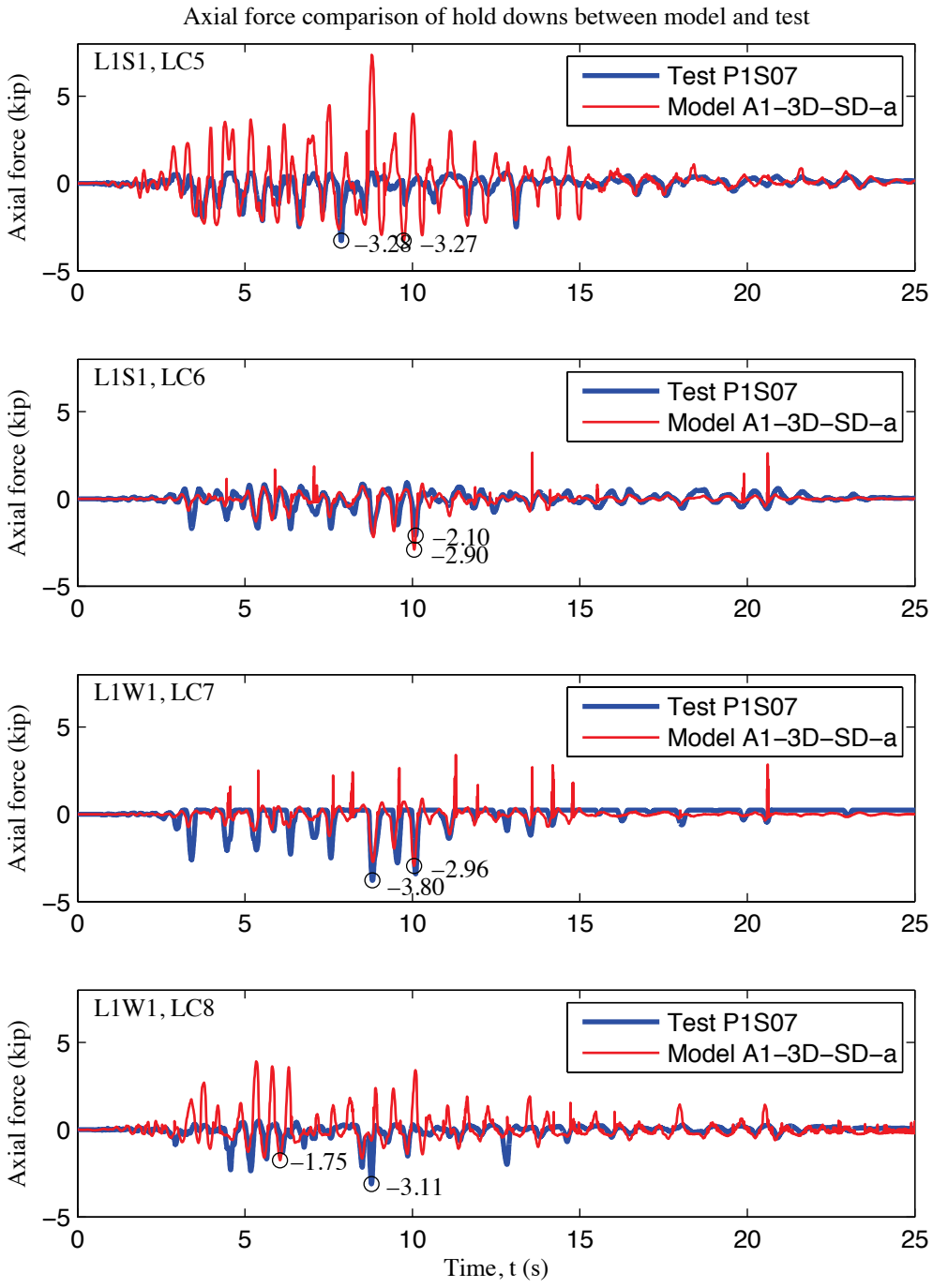

Figure 4-16: Comparison of load cell 5 to 8 axial forces, P1S07 excitation, Phase 1

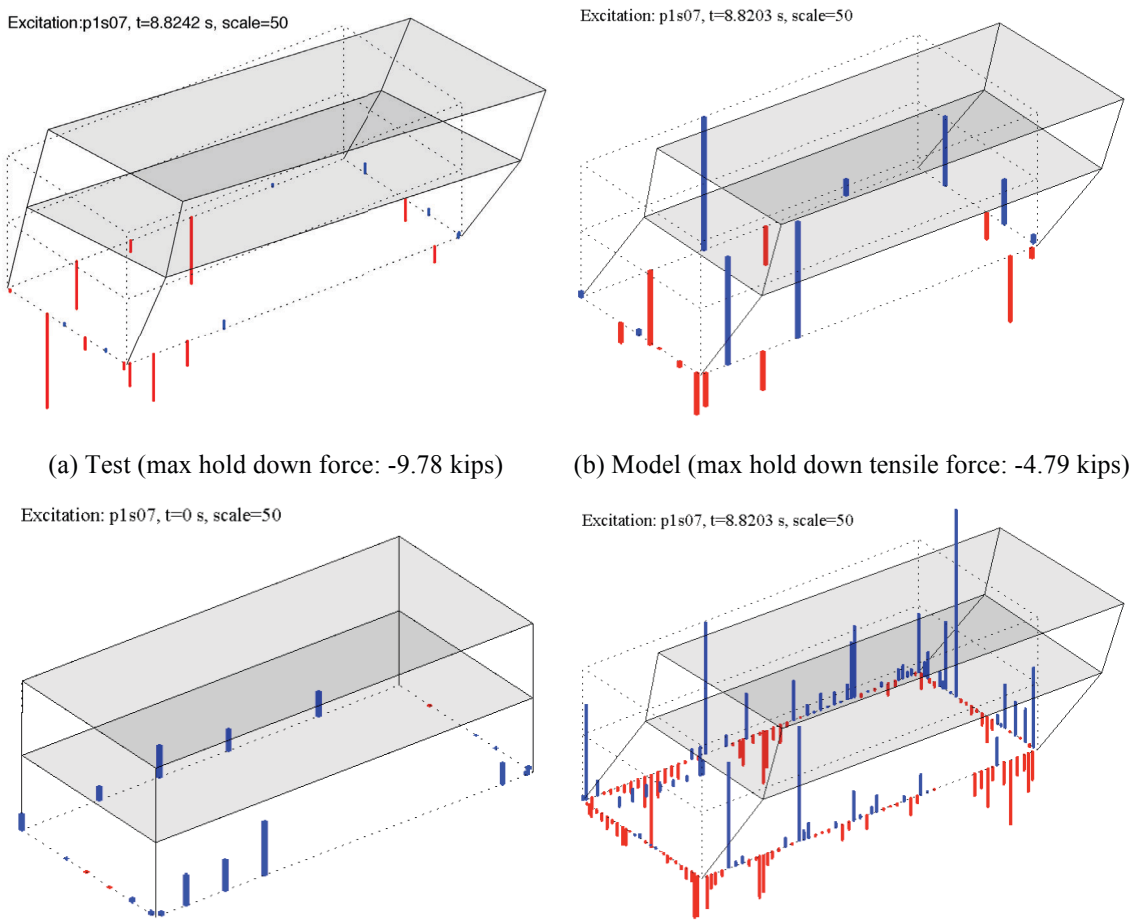

(a) Test (max hold down force: -9.78 kips)

(b) Model (max hold down tensile force: -4.79 kips)

(c) Model (gravity load only)

(d) Model (bearing force also plotted)

Figure 4-17: Comparison of simplified deformed shape and distribution of load cell forces between A1-3D-SD-a model and test, P1S07 excitation, Phase 1

4.3.3 Phase 2a – bare structural replicate

Phase 1 building was demolished after being tested under 100% Canoga Park excitation. The reconstructed building at Phase 2a is a replica of Phase 1. As a result, there is little difference between these two buildings and the same A1-3D-SD-a model used in comparison with Phase 1 test results (Section 4.3.2) is adopted again for performance comparison with tests at Phase 2a.

Table 4-13 is a summary of excitations in model validation at Phase 2a. In this phase, the ground motion in testing (P2aS01 to P2aS04) only reaches 16% of the CNP record at its maximum. PGA experienced by the building used as excitations in time history analayses in Phase 2a is very close to numbers in Table 4-8 of Phase 1.

Table 4-13: Summary of excitations for model calibration, Phase 2a

Excitation Name	Ground Motion	Record PGA long (g)	Record PGA short (g)	Record PGA up (g)	Excitation PGA long (g)	Excitation PGA short (g)	Excitation PGA up (g)
P2aS01	CNP 16%	0.0657	0	0	0.0829	0	0
P2aS02	CNP 16%	0	0.0556	0	0	0.0628	0
P2aS03	CNP 16%	0.0657	0.0556	0	0.0825	0.0627	0
P2aS04	CNP 16%	0.0657	0.0556	0.0764	0.0851	0.0667	0.0772

The building's design drawing and the FE model in Figure 4-18 are identical with Figure 4-13 for Phase 1 building. The first natural periods in Table 4-14 also indicate that there is hardly any difference in terms of the building's mass and stiffness between Phase 1 and Phase 2a, so A1-3D-SD-a model's natural periods are still quite close to test predictions.

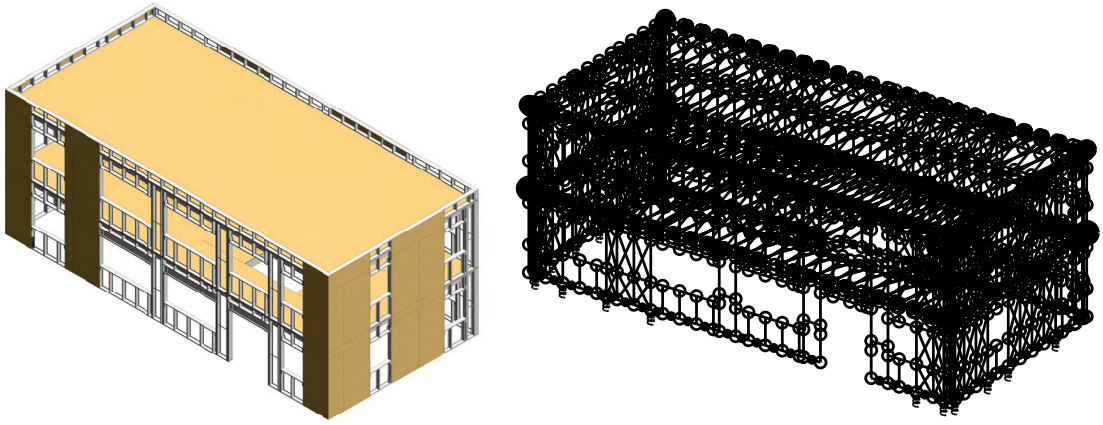

(a) Isometric design drawing (b) FE model (A1-3D-SD-a)

Figure 4-18: Design drawing and high-fidelity FE model of Phase 2a building

Table 4-14: Comparison of the first natural period between A1-3D-SD-a model and test, Phase 2a

LONG		SHORT	
T_1 (s), Test	**T_1 (s), Model**	**T_1 (s), Test**	**T_1 (s), Model**
0.32	0.30	0.36	0.32

Table 4-15 is the comparison of peak story acceleration. As before (Table 4-10), peak story acceleration of the model is not the same as the test, and larger differences are in the short and vertical directions (~0.1g).

Table 4-15: Comparison of peak story absolute acceleration in g between A1-3D-SD-a model and test, Phase 2a

LONG					
Excitation Name	**Ground Motion**	**Floor, Test**	**Floor, Model**	**Roof, Test**	**Roof, Model**
P2aS01	CNP 16%[1]	0.128	0.178	0.178	0.184
P2aS02	CNP 16%[2]	0.023	0.058	0.012	0.077
P2aS03	CNP 16%[3]	0.130	0.171	0.185	0.206
P2aS04	CNP 16%	0.119	0.177	0.200	0.207
SHORT					
Excitation Name	**Ground Motion**	**Floor, Test**	**Floor, Model**	**Roof, Test**	**Roof, Model**
P2aS01	CNP 16%[1]	0.017	0.216	0.012	0.228
P2aS02	CNP 16%[2]	0.077	0.194	0.12	0.23
P2aS03	CNP 16%[3]	0.082	0.202	0.124	0.231
P2aS04	CNP 16%	0.079	0.189	0.131	0.222
UP					
Excitation Name	**Ground Motion**	**Floor, Test**	**Floor, Model**	**Roof, Test**	**Roof, Model**
P2aS01	CNP 16%[1]	-	0.061	0.011	0.074
P2aS02	CNP 16%[2]	-	0.107	0.011	0.115
P2aS03	CNP 16%[3]	-	0.112	0.017	0.099
P2aS04	CNP 16%	-	0.124	0.077	0.133

[1]long direction only [2]short direction only [3]long and short directions only

Table 4-16 and Figure 4-19 are developed for story drift comparison. As with Phase 1, the model's story drift matches reasonably well with test data, especially for the floor level. The model is stiffer on the roof level in comparison with testing. Figure 4-20 further shows that the predicted drift from A1-3D-SD-a model has the same power spectral density with test outputs for frequency lower than 15 Hz. For higher frequencies, the match is not very close.

Table 4-16: Comparison of peak story drift between A1-3D-SD-a model and test, Phase 2a

LONG					
Excitation Name	**Ground Motion**	**$\Delta u_1/h$ (%) Test**	**$\Delta u_1/h$ (%) Model**	**$\Delta u_2/h$ (%) Test**	**$\Delta u_2/h$ (%) Model**
P2aS01	CNP 16%[1]	0.13	0.10	0.12	0.03
P2aS02	CNP 16%[2]	-0.01	0.04	-0.01	0.01
P2aS03	CNP 16%[3]	0.14	0.11	0.11	0.04
P2aS04	CNP 16%	0.14	0.11	0.12	0.04
SHORT					
Excitation Name	**Ground Motion**	**$\Delta v_1/h$ (%) Test**	**$\Delta v_1/h$ (%) Model**	**$\Delta v_2/h$ (%) Test**	**$\Delta v_2/h$ (%) Model**
P2aS01	CNP 16%[1]	-0.02	-0.02	0.02	-0.01
P2aS02	CNP 16%[2]	0.10	0.08	0.08	0.05
P2aS03	CNP 16%[3]	0.10	0.08	-0.09	0.04
P2aS04	CNP 16%	0.10	0.08	0.09	0.04

[1]long direction only [2]short direction only [3]long and short directions only

Table 4-17, Figure 4-21, and Figure 4-22 are related to comparisons of the axial forces in hold downs. The same trend as in Phase 1 is found here: the model over predicts peak axial forces in the hold downs at excitation levels not exceed 16% CNP (P2aS01 to P2aS04). As for specific hold downs, the discrepancy of the axial force in load cell No. 5 (shear wall S1) and No. 7 (shear wall W1) is non-trivial between the model and test; however, the difference is less for other load cells (No. 6 to No. 8), as shown in Figure 4-21. Figure 4-22 is different from Figure 4-17 due to the difference in scale factors (P2aS04 corresponds to 16% instead of 100% of CNP), but it once again demonstrates that the model's second story drift is less compared with the test and the vertical load path may need to be revised, as discussed in Section 4.3.2.

Table 4-17: Comparison of peak hold down tensile force between A1-3D-SD-a model and test, Phase 2a

Excitation Name	**Ground Motion**	**Peak F (kip) Test**	**t @ peak F (s) Test**	**Peak F (kip) Model**	**t @ peak F (s) Model**
P2aS01	CNP 16%[1]	-0.65	8.73	-1.81	10.48
P2aS02	CNP 16%[2]	-0.77	6.00	-1.33	10.52
P2aS03	CNP 16%[3]	-0.98	5.99	-1.87	12.2
P2aS04	CNP 16%	-1.24	5.97	-1.94	9.72

[1]long direction only [2]short direction only [3]long and short directions only

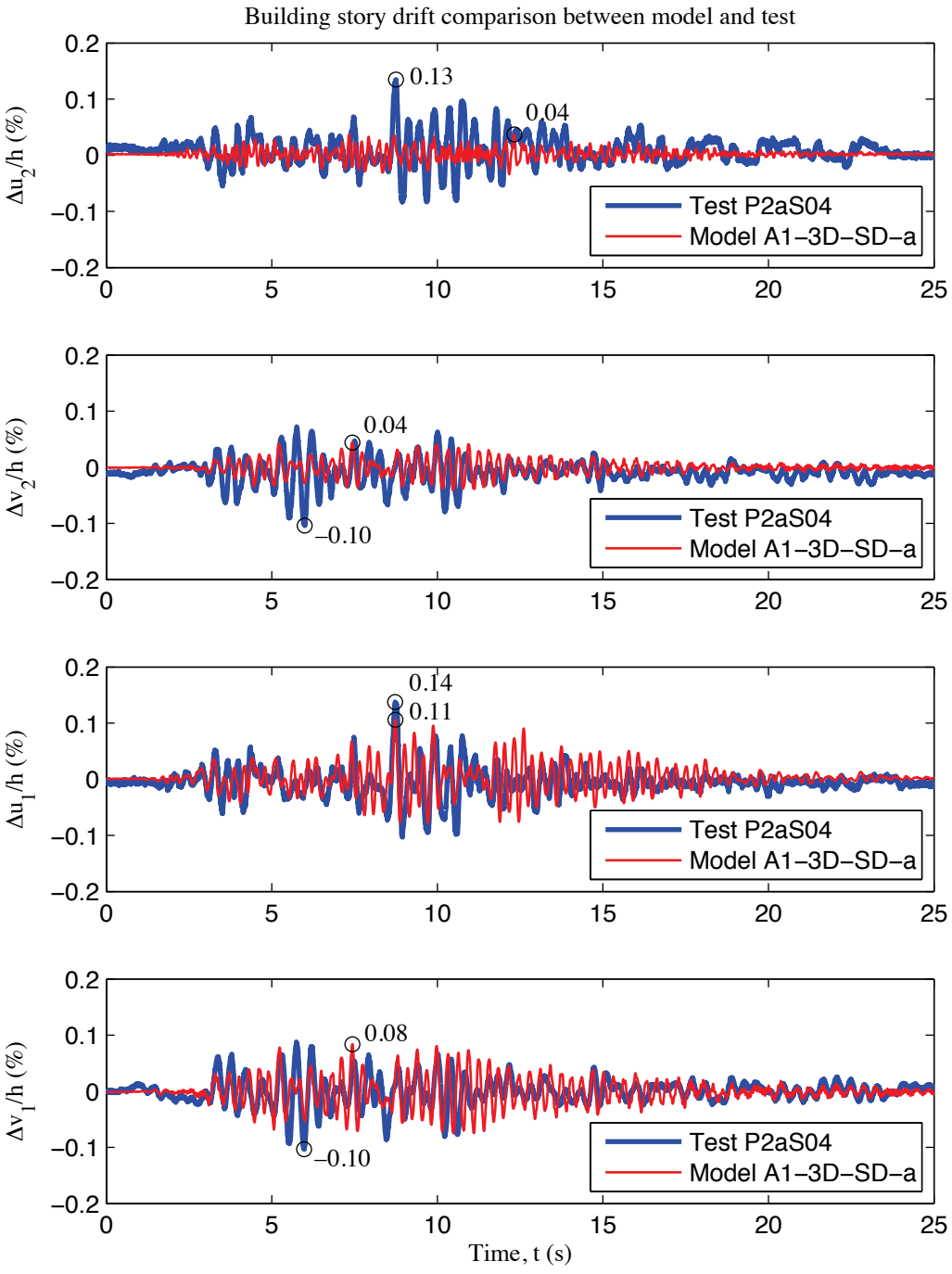

Figure 4-19: Comparison of story drift of the building, P2aS04 excitation, Phase 2a

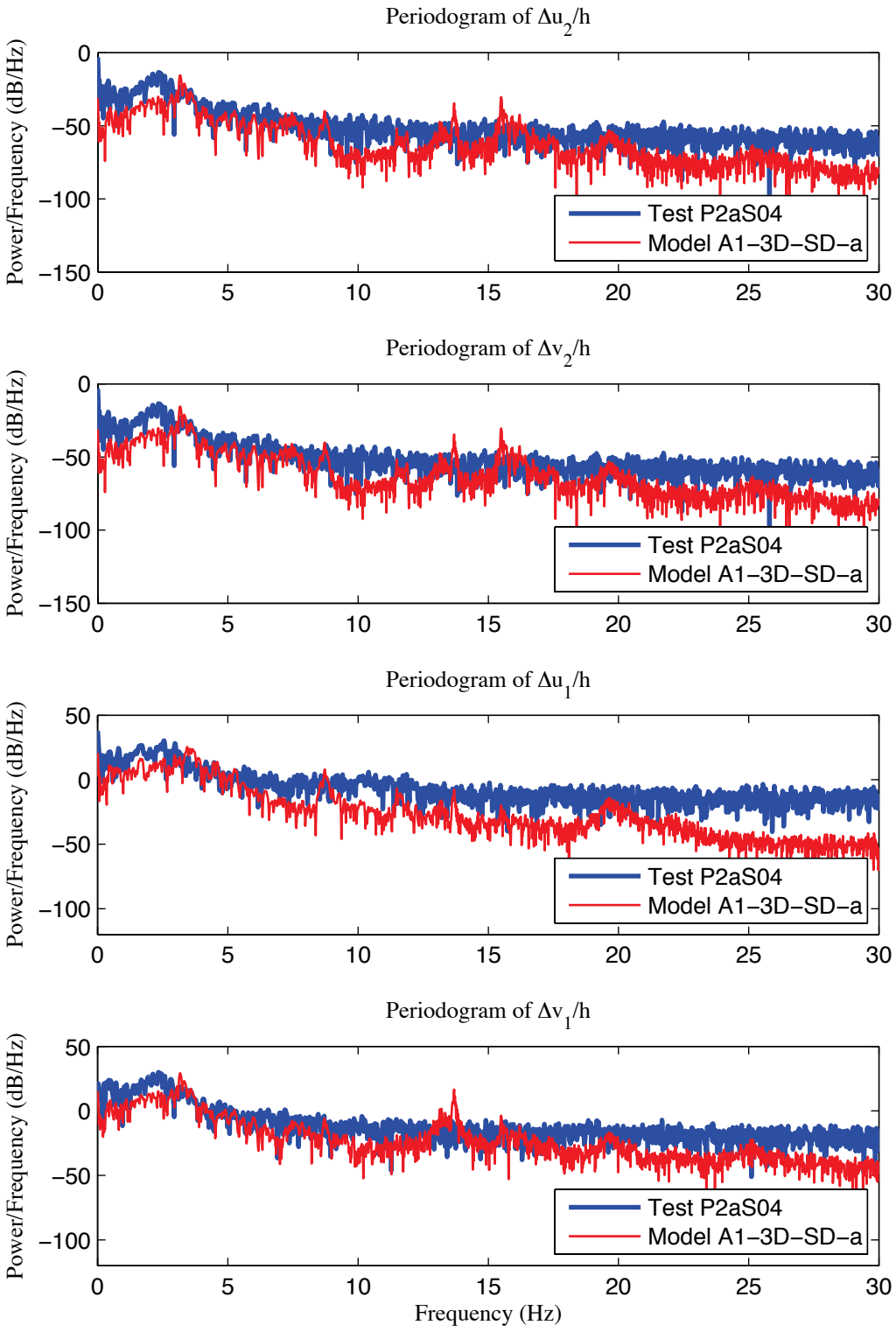

Figure 4-20: Comparison of periodogram of the building's story drift, P2aS04 excitation, Phase 2a

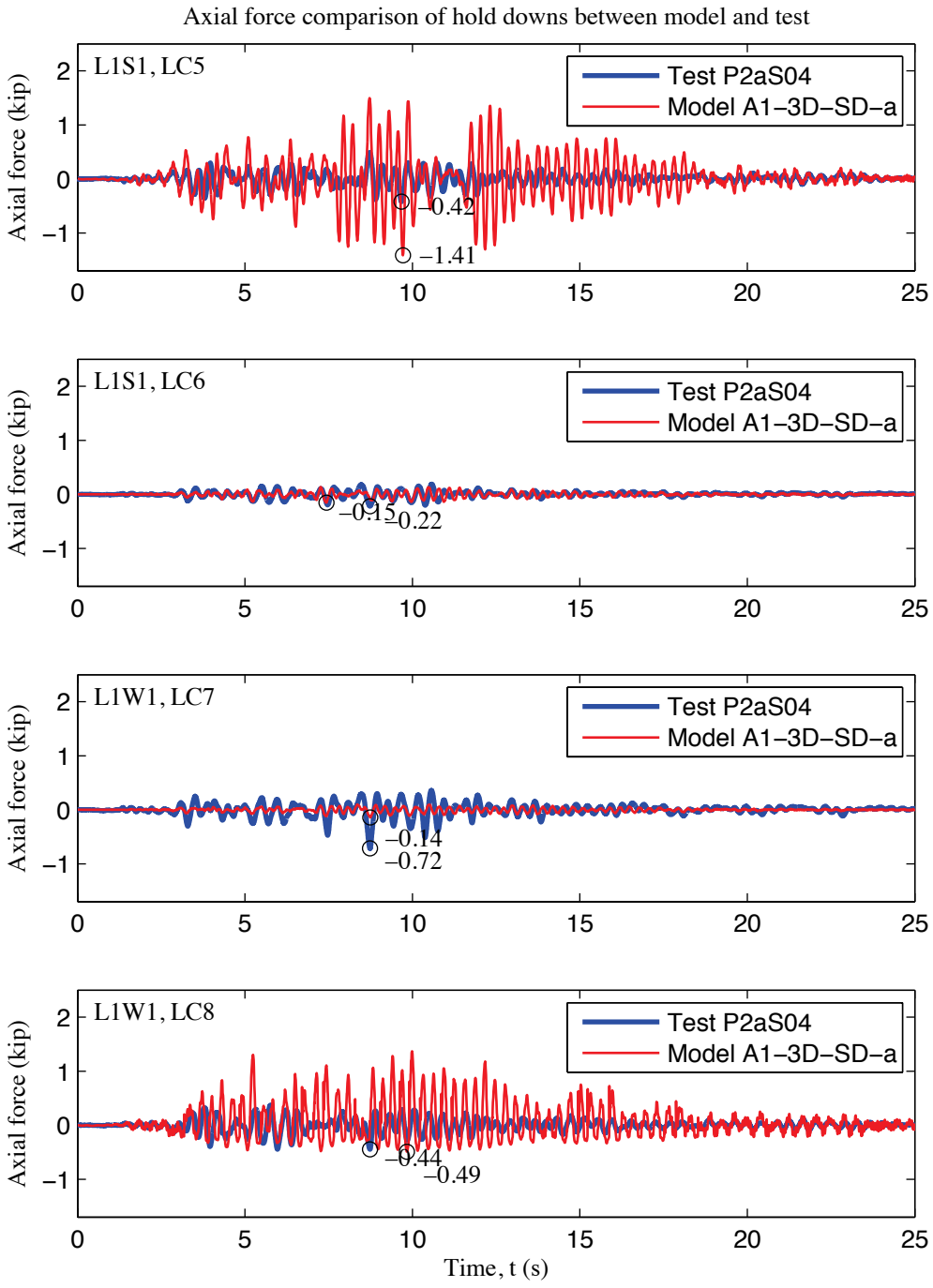

Figure 4-21: Comparison of load cell 5 to 8 axial forces, P2aS04 excitation, Phase 2a

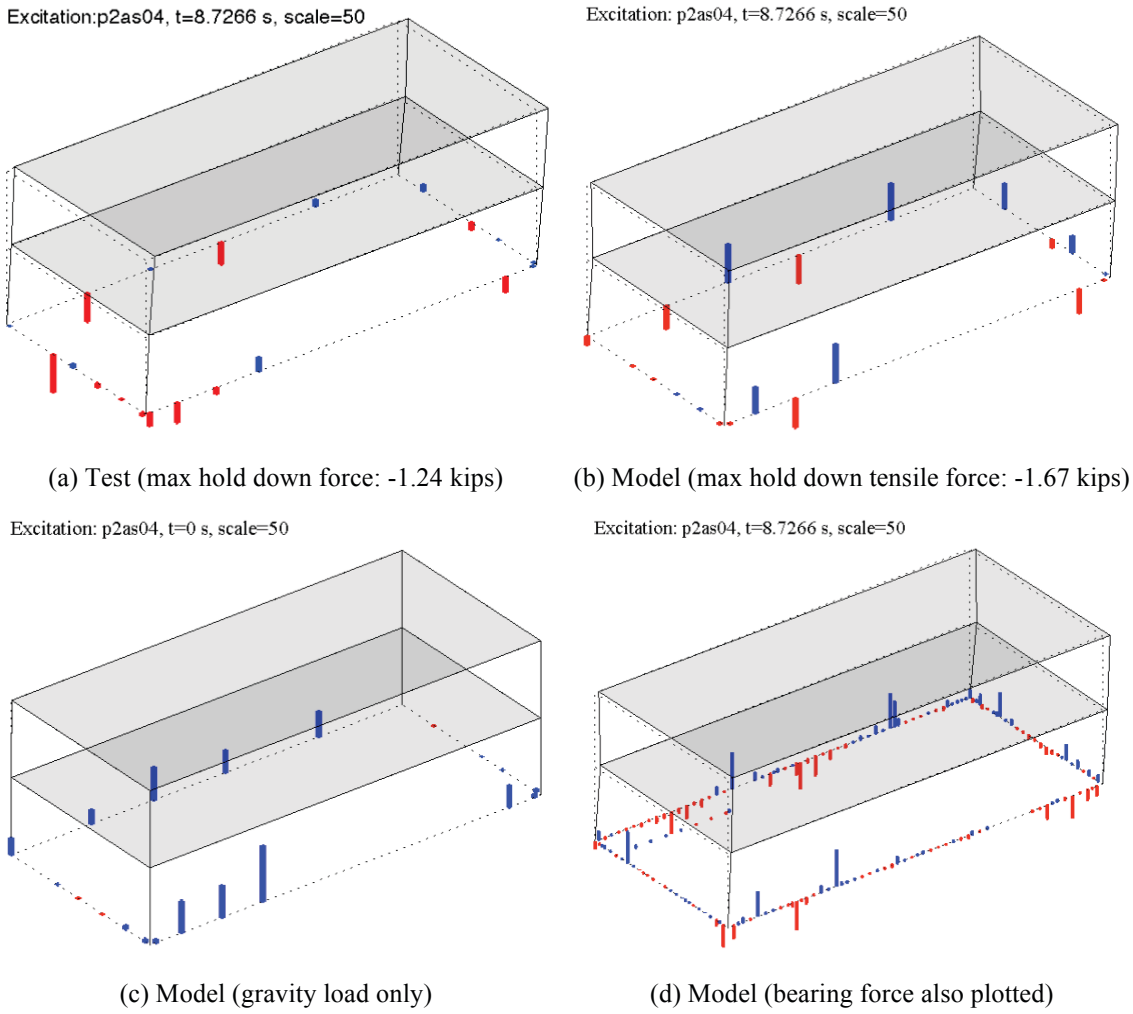

(a) Test (max hold down force: -1.24 kips)

(b) Model (max hold down tensile force: -1.67 kips)

(c) Model (gravity load only)

(d) Model (bearing force also plotted)

Figure 4-22: Comparison of simplified deformed shape and distribution of load cell forces between A1-3D-SD-a model and test, P2aS04 excitation, Phase 2a

4.3.4 Phase 2b – exterior sheathed structural

Phase 2b is the first construction phase that steps forward from Phase 1/2a by adding OSB sheathing to the exterior gravity framing, making all the wall lines covered except openings for doors and windows. Although sheathing of gravity walls is regarded as non-structural in design standards, tests have shown that this additional amount of sheathing contributes significantly to the lateral stiffness and capacity of the building. The state-of-the-art (A-) FE models developed for this phase are expected to be able to reflect the role played by the added sheathing in time history analysis. Figure 4-23 compares the building

and its FE model (A2b-3D-SD-a) graphically. The tested building is fully sheathed by OSB panels, and nonlinear diagonal bracings are added correspondingly in the FE model. Subpanel properties of the additional bracings are characterized from fastener-based OpenSees models, as discussed in Section 3.4, Chapter 3.

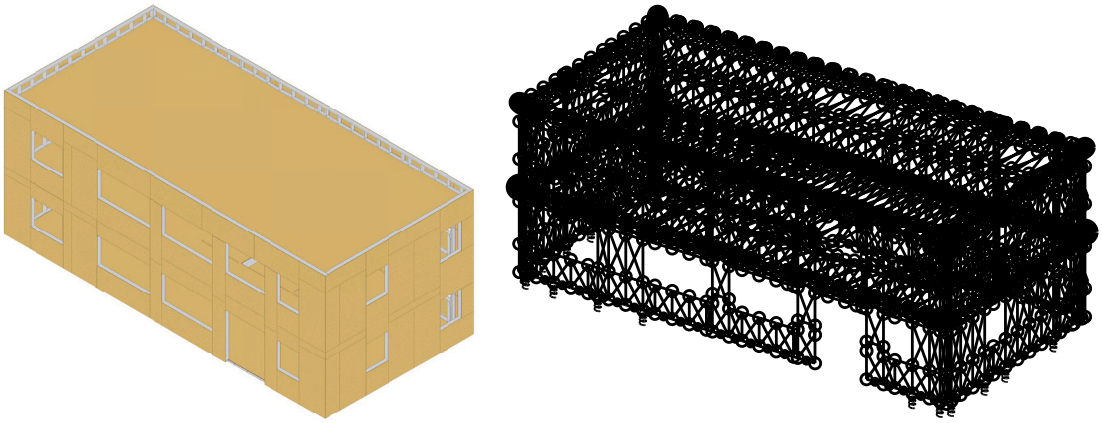

(a) Isometric design drawing (b) FE model (A2b-3D-SD-a)

Figure 4-23: Design drawing and high-fidelity FE model of Phase 2b building

Table 4-18 summarizes PGA of the ground motion records and excitations actually applied in testing. The actual excitations applied in testing are used for the time history analysis conducted here. As discussed in Section 4.3.2 for Phase 1, the acceleration input on the tested building is a little larger than originally recorded. In Phase 2b testing, the strongest excitation tested (or modeled) is P2bS05 which corresponds to 44% CNP in three-axes.

Table 4-18: Summary of excitations for model calibration, Phase 2b

Excitation Name	Ground Motion	Record PGA long (g)	Record PGA short (g)	Record PGA up (g)	Excitation PGA long (g)	Excitation PGA short (g)	Excitation PGA up (g)
P2bS01	CNP 16%	0.0657	0	0	0.0845	0	0
P2bS02	CNP 16%	0	0.0556	0	0	0.0606	0
P2bS03	CNP 16%	0.0657	0.0556	0	0.0868	0.0601	0
P2bS04	CNP 16%	0.0657	0.0556	0.0764	0.0881	0.0567	0.0866
P2bS05	CNP 44%	0.1833	0.1551	0.2131	0.2341	0.2122	0.2612

The first natural periods in the long and short direction for the tested and simulated building are tabulated in Table 4-19. The developed model is a little stiffer in the short direction and a bit more flexible in long direction, but the difference is less than 10% in both directions. Even though the way chosen to characterize the gravity sheathing stiffness from the fastener-based models is somewhat heuristic (see Section 3.4 in Chapter 3), comparison with test suggests that our method is feasible and can render a reliable prediction of the linear stiffness of Phase 2b building without calibration; i.e., the fastener-based stiffness results are used directly no additional model calibration is performed.

Table 4-19: Comparison of the first natural period between A2b-3D-SD-a model and test, Phase 2b

LONG		SHORT	
T_1 (s), Test	T_1 (s), Model	T_1 (s), Test	T_1 (s), Model
0.20	0.22	0.30	0.28

As with previous models, the comparison of peak story absolute acceleration in Table 4-20 demonstrates that the model amplifies the model's predicted story acclerations are larger than test outputs. At lower excitation levels that correspond to 16% CNP (P2bS01 to P2bS04), the difference can be as much as ~0.9g in the short direction. At P2bS05 (corresponds to 44% CNP), the error can be 250% in the vertical direction (~0.4g).

Modifying the vertical load paths is thought to be helpful for making a better match (as discussed in Section 4.3.2 for Phase 1), but it is still open for further discussion.

Table 4-20: Comparison of peak story absolute acceleration in g between A2b-3D-SD-a model and test, Phase 2b

LONG					
Excitation Name	**Ground Motion**	**Floor, Test**	**Floor, Model**	**Roof, Test**	**Roof, Model**
P2bS01	CNP 16%[1]	0.106	0.431	0.133	0.398
P2bS02	CNP 16%[2]	0.014	0.374	0.013	0.263
P2bS03	CNP 16%[3]	0.116	0.454	0.144	0.370
P2bS04	CNP 16%	0.117	0.440	0.143	0.501
P2bS05	CNP 44%	0.325	0.501	0.385	0.588
SHORT					
Excitation Name	**Ground Motion**	**Floor, Test**	**Floor, Model**	**Roof, Test**	**Roof, Model**
P2bS01	CNP 16%[1]	0.015	0.626	0.016	0.924
P2bS02	CNP 16%[2]	0.079	0.630	0.119	0.884
P2bS03	CNP 16%[3]	0.089	0.689	0.124	0.733
P2bS04	CNP 16%	0.088	0.636	0.119	0.629
P2bS05	CNP 44%	0.231	0.603	0.344	0.659
UP					
Excitation Name	**Ground Motion**	**Floor, Test**	**Floor, Model**	**Roof, Test**	**Roof, Model**
P2bS01	CNP 16%[1]	-	0.310	0.007	0.266
P2bS02	CNP 16%[2]	-	0.694	0.005	0.617
P2bS03	CNP 16%[3]	-	0.916	0.010	0.775
P2bS04	CNP 16%	-	0.681	0.090	0.596
P2bS05	CNP 44%	-	0.738	0.269	0.677

[1]long direction only [2]short direction only [3]long and short directions only

Peak story drifts of floor or roof level from test and simulation are listed in Table 4-21. In terms of magnitude, the difference between the test and simulation is acceptable for both levels and in both directions with the only exception being 0.21% test drift vs. 0.11% simulation drift for the short direction peak roof drift under P2bS05 excitation (corresponds to 44% CNP) – all other values have less than 30 % error. Further details are available from the comparative time history plots in Figure 4-24. Story drifts from the simulation matches well with test results all the way through the loading history: responses of the model and the building are in phase and the difference in magnitude is

generally minor. Figure 4-25 further shows that the predicted drift from A2b-3D-SD-a model has the same power spectral density with test outputs for frequency lower than 20 Hz. For higher frequencies, the match is not very close in long direction of the floor level.

Table 4-21: Comparison of peak story drift between A2b-3D-SD-a model and test, Phase 2b

LONG					
Excitation Name	**Ground Motion**	**$\Delta u_1/h$ (%) Test**	**$\Delta u_1/h$ (%) Model**	**$\Delta u_2/h$ (%) Test**	**$\Delta u_2/h$ (%) Model**
P2bS01	CNP 16%[1]	0.04	0.10	-0.04	0.05
P2bS02	CNP 16%[2]	-0.01	-0.02	-0.01	0.03
P2bS03	CNP 16%[3]	0.05	0.10	-0.05	-0.05
P2bS04	CNP 16%	0.06	0.10	-0.05	0.06
P2bS05	CNP 44%	0.19	0.19	0.11	-0.08
SHORT					
Excitation Name	**Ground Motion**	**$\Delta v_1/h$ (%) Test**	**$\Delta v_1/h$ (%) Model**	**$\Delta v_2/h$ (%) Test**	**$\Delta v_2/h$ (%) Model**
P2bS01	CNP 16%[1]	-0.03	-0.03	-0.01	0.03
P2bS02	CNP 16%[2]	-0.08	0.12	-0.06	-0.05
P2bS03	CNP 16%[3]	-0.06	0.09	-0.05	0.06
P2bS04	CNP 16%	-0.06	0.11	-0.05	0.05
P2bS05	CNP 44%	0.29	0.28	0.21	0.11

[1]long direction only [2]short direction only [3]long and short directions only

Comparisons of hold down axial forces, as detailed in Table 4-22, Figure 4-26 and Figure 4-27, reflects a different trend as seen in previous phases. Peak hold down axial force is always underestimated by the model, and the difference is as high as 43% at P2cS05 excitation (corresponds to 44% CNP). Among hold downs near southwest corner, load cell No. 5 and No. 7 are most underestimated by the model (45% less in Figure 4-26). The compressive spikes in Figure 4-26 shows the large stiffness of hold downs in compression can cause numerical difficulties, as observed in the output of iteration history. The illustrations of deformed shape and load cell force distribution in Figure 4-27 suggest that the model has almost the same deflection with the real building at this specific time step (t=8.73 s). The load cell force distribution is still different in the simulation, and the difference of the peak hold down tensile force is about 57% (3.39

kips vs. 1.43 kips) at the selected time. Large compressive force in bearing is again observed in A2b-3D-SD-a model response under P2cS05 excitation (Figure 4-27 (d)), indicating difficulties in covergence of the model vertical load path.

Table 4-22: Comparison of peak hold down tensile force between A2b-3D-SD-a model and test, Phase 2b

Excitation Name	Ground Motion	Peak F (kip) Test	t @ peak F (s) Test	Peak F (kip) Model	t @ peak F (s) Model
P2bS01	CNP 16%[1]	-1.84	7.02	-1.76	13.64
P2bS02	CNP 16%[2]	-1.93	10.55	-1.27	9.82
P2bS03	CNP 16%[3]	-1.94	8.68	-1.69	8.54
P2bS04	CNP 16%	-1.91	6.99	-1.62	8.02
P2bS05	CNP 44%	-3.39	5.07	-1.93	11.86

[1]long direction only [2]short direction only [3]long and short directions only

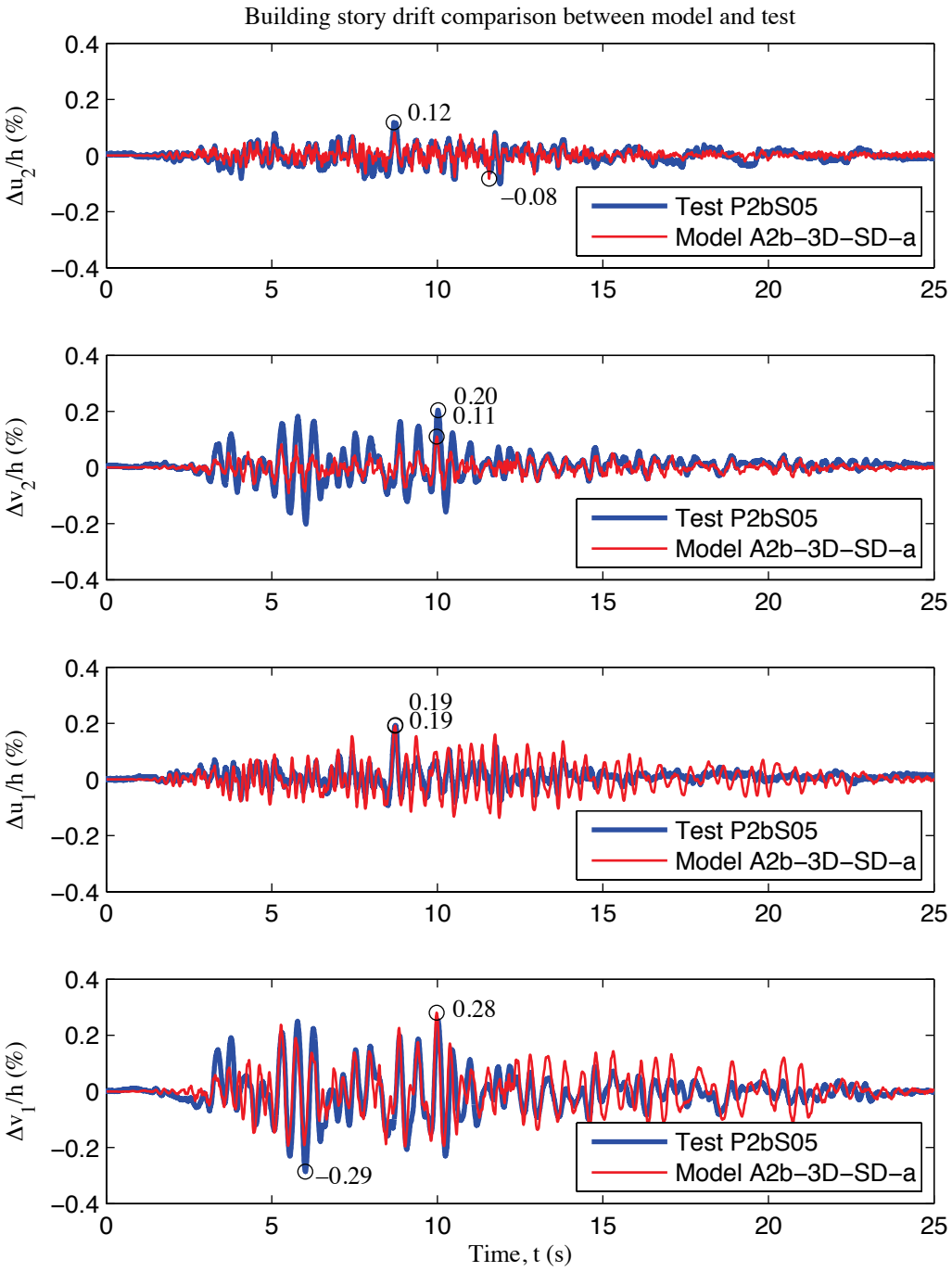

Figure 4-24: Comparison of story drift of the building, P2bS05 excitation, Phase 2b

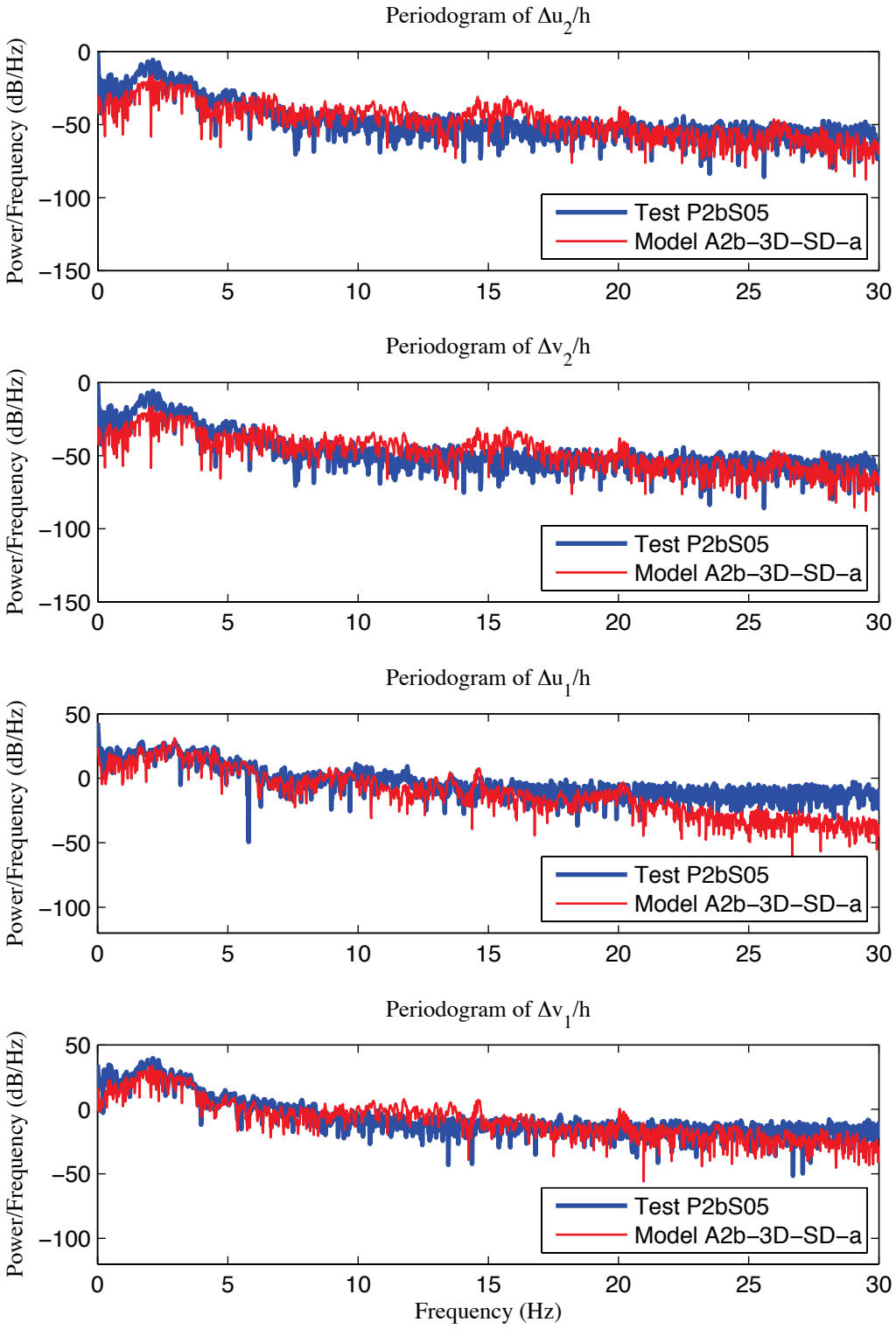

Figure 4-25: Comparison of periodogram of the building's story drift, P2bS05 excitation, Phase 2b

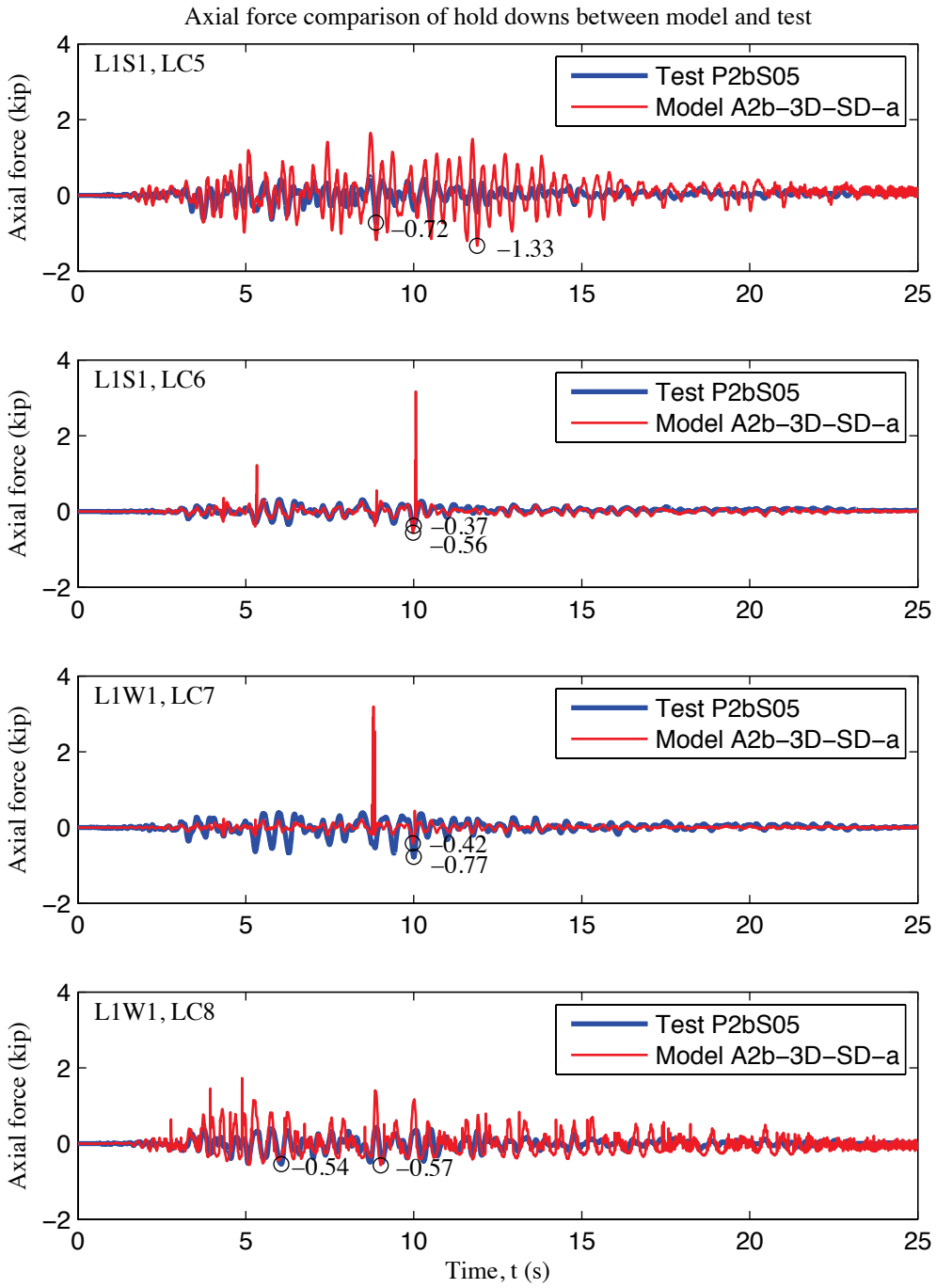

Figure 4-26: Comparison of load cell 5 to 8 axial forces, P2bS05 excitation, Phase 2b

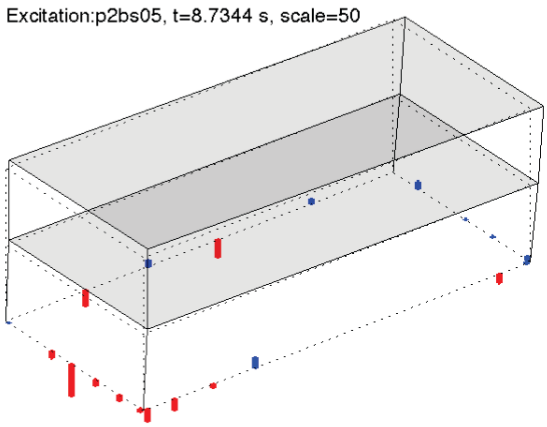

(a) Test (max hold down force: -3.39 kips)

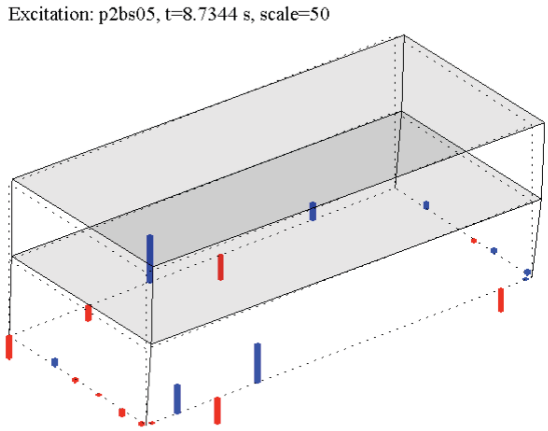

(b) Model (max hold down tensile force: -1.43 kips)

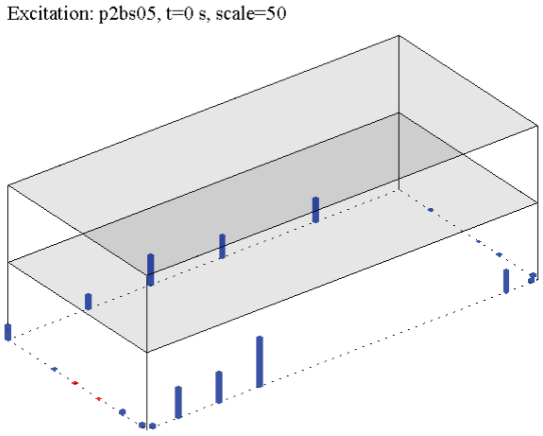

(c) Model (gravity load only)

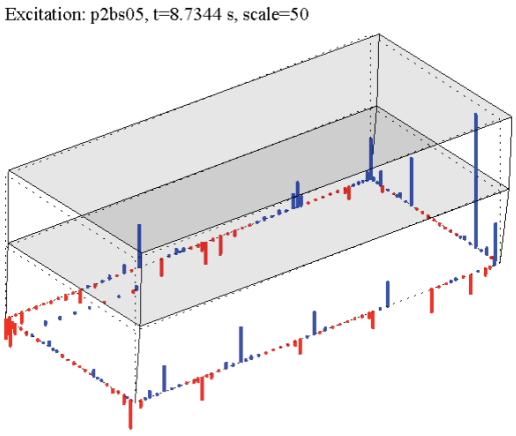

(d) Model (bearing force also plotted)

Figure 4-27: Comparison of simplified deformed shape and distribution of load cell forces between A2b-3D-SD-a model and test, P2bS05 excitation, Phase 2b

4.3.5 Phase 2c – fully sheathed structural

The archetype building evolves to Phase 2c by adding gypsum sheathings to the interior side of the shear walls and gravity walls. Accordingly, the response of gypsum sheathing is characterized using the same method (OpenSees fastener-based models for determination of nonlinear bracing elements, see Section 3.4.2) and is converted to nonlinear response models in the subpanel bracings. The number of bracings is doubled in the FE model from Phase 2c. Comparison between the appearance of the Phase 2c building and its FE simulation model is given in Figure 4-28. It is not easy to distinguish

the drawing of the Phase 2c building from Phase 2b, since gypsum sheathing is installed inside of the OSB sheathing, but on the exterior walls only. There is no difference in the appearance of the FE model between Phase 2b and Phase 2c, because the bracing modeling of the gypsum and OSB panels are coincident. Investigations reveal how much additional stiffness and capacity interior gypsum sheathing can provide in spite of being significantly weaker than OSB sheathing.

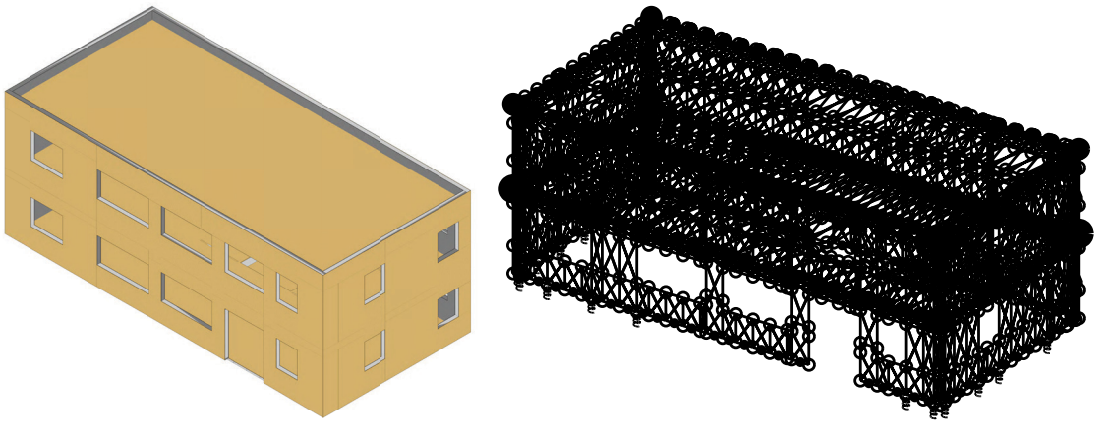

(a) Isometric design drawing (b) FE model (A2c-3D-SD-a)

Figure 4-28: Design drawing and high-fidelity FE model of Phase 2c building

PGAs of excitations are summarized in Table 4-23. Same with Phase 2b, the building was tested up to 44% of Canoga Park ground motion. The natural periods of the first modes in the long and the short directions are presented in Table 4-24. The model's first natural period is almost the same (5 % error) with the real building in the long direction, but 15% shorter in the short direction. The results show that the model successfully realizes the increased stiffness by adding interior gypsum sheathings, but perhaps is a bit over-stiff in the short direction.

Table 4-23: Summary of excitations for model calibration, Phase 2c

Excitation Name	Ground Motion	Record PGA long (g)	Record PGA short (g)	Record PGA up (g)	Excitation PGA long (g)	Excitation PGA short (g)	Excitation PGA up (g)
P2cS01	CNP 16%	0.0657	0	0	0.0834	0	0
P2cS02	CNP 16%	0	0.0556	0	0	0.0626	0
P2cS03	CNP 16%	0.0657	0.0556	0	0.0865	0.0639	0
P2cS04	CNP 16%	0.0657	0.0556	0.0764	0.0851	0.0611	0.0877
P2cS05	CNP 44%	0.1833	0.1551	0.2131	0.2286	0.1954	0.2459

Table 4-24: Comparison of the first natural period between A2c-3D-SD-a model and test, Phase 2c

LONG		SHORT	
T_1 (s), Test	**T_1 (s), Model**	**T_1 (s), Test**	**T_1 (s), Model**
0.17	0.18	0.27	0.23

The comparison of peak story absolute acceleration in Table 4-25 once again demonstrates that the model amplifies the match of peak acceleration between model and test is not quite accurate. The difference is smaller in the long direction, but it can still be ~0.3g. At the excitation of P2cS05 (corresponds to 44% CNP), the difference of peak story acceleration is as much as 240% (~0.6g) in the vertical direction. Possible modification of the vertical load path in the model, like including the stiffness of the foundation steel tube, modifying the link between chord studs at two levels and adjusting the compressive stiffness of hold downs and bearings would be applied in the future.

Table 4-25: Comparison of peak story absolute acceleration in g between A2c-3D-SD-a model and test, Phase 2c

LONG					
Excitation Name	**Ground Motion**	**Floor, Test**	**Floor, Model**	**Roof, Test**	**Roof, Model**
P2cS01	CNP 16%[1]	0.102	0.448	0.129	0.374
P2cS02	CNP 16%[2]	0.008	0.508	0.010	0.360
P2cS03	CNP 16%[3]	0.106	0.485	0.136	0.404
P2cS04	CNP 16%	0.103	0.473	0.132	0.385
P2cS05	CNP 44%	0.329	0.628	0.392	0.703
SHORT					
Excitation Name	**Ground Motion**	**Floor, Test**	**Floor, Model**	**Roof, Test**	**Roof, Model**
P2cS01	CNP 16%[1]	0.010	0.611	0.013	0.599
P2cS02	CNP 16%[2]	0.082	0.765	0.123	0.599
P2cS03	CNP 16%[3]	0.087	0.653	0.125	0.584
P2cS04	CNP 16%	0.082	0.556	0.119	0.561
P2cS05	CNP 44%	0.227	0.654	0.339	0.638
UP					
Excitation Name	**Ground Motion**	**Floor, Test**	**Floor, Model**	**Roof, Test**	**Roof, Model**
P2cS01	CNP 16%[1]	-	0.400	0.010	0.440
P2cS02	CNP 16%[2]	-	0.263	0.007	0.263
P2cS03	CNP 16%[3]	-	0.817	0.014	0.743
P2cS04	CNP 16%	-	0.621	0.091	0.588
P2cS05	CNP 44%	-	0.924	0.254	0.866

[1]long direction only [2]short direction only [3]long and short directions only

Story drifts in the long and short directions are tabulated and compared in Table 4-26. At Phase 2c, a desirable agreement of story drifts is achieved for every excitation that corresponds to 16% Canoga Park excitation (P2cS01 to P2cS04). When the excitation is increased to P2cS05 that corresponds to 44% CNP in three-axis, the model is stiffer than the test on the roof level by 47% in the short direction (0.17% vs. 0.09%); other than this case, the model still gives an acceptable prediction of story drifts under that load (< 40%). As shown in Figure 4-29, the magnitude of computed story drift on the roof level is smaller than the test, especially before about 12 seconds of the time history; but, the phase of the drift matches well with the tests and the floor level drifts also agrees with the test results. Figure 4-30 further shows that the predicted drift from A2c-3D-SD-a model has the same power spectral density with test output, expect for some minor difference

above 20 Hz. The model is regarded as capable of representing lateral deflections and drifts of the building at this phase.

Table 4-26: Comparison of peak story drift between A2c-3D-SD-a model and test, Phase 2c

LONG					
Excitation Name	**Ground Motion**	**$\Delta u_1/h$ (%) Test**	**$\Delta u_1/h$ (%) Model**	**$\Delta u_2/h$ (%) Test**	**$\Delta u_2/h$ (%) Model**
P2cS01	CNP 16%[1]	0.04	-0.04	0.03	0.04
P2cS02	CNP 16%[2]	0.01	-0.02	-0.01	0.04
P2cS03	CNP 16%[3]	0.04	-0.04	-0.04	-0.04
P2cS04	CNP 16%	0.04	-0.05	-0.04	-0.03
P2cS05	CNP 44%	0.12	0.17	0.11	0.08
SHORT					
Excitation Name	**Ground Motion**	**$\Delta v_1/h$ (%) Test**	**$\Delta v_1/h$ (%) Model**	**$\Delta v_2/h$ (%) Test**	**$\Delta v_2/h$ (%) Model**
P2cS01	CNP 16%[1]	-0.02	0.03	-0.01	-0.02
P2cS02	CNP 16%[2]	-0.07	-0.05	-0.05	-0.03
P2cS03	CNP 16%[3]	-0.07	-0.07	-0.05	-0.04
P2cS04	CNP 16%	-0.06	-0.07	-0.05	-0.03
P2cS05	CNP 44%	-0.22	0.21	0.17	-0.09

[1]long direction only [2]short direction only [3]long and short directions only

Table 4-27 provides peak forces in the hold downs and the time during the response when this occurs. Peak hold down tensile forces from the simulation do not compare well with the tests. At lower excitations (P2cS01 to P2cS04), peak hold hown forces are overestimated by 300%; however, peak values from tests are very small (~0.25 kips (1.11 kN)). At P2cS05 excitation that corresponds to 44% CNP, the overestimation drops to 58%. Figure 4-31 provides the response time history of selected hold downs (load cell No. 5 to No. 8). The axial force of load cell No. 5 is always over-predicted by the model. For other load cells, the matching is not as bad though errors and at the peak value persist. The matching is actually quite good in load cell No. 6. At time steps of 5.0, 8.7 and 10.0 seconds (or thereabouts) there are sharp increases of the compressive force magnitude in the hold down predicted by the model. This is a numerical difficulty caused by the hold down's nonlinear, unsymmetric response model, making it hard for the algorithm to

converge (as seen in the iteration history). Figure 4-32 illustrates and compares the deformed shapes of the building and the model together with the distribution of hold down axial forces at a specified time. The model's distribution and peak value of hold down forces does not match well with the test; the explanation on possible reason, as detailed in Section 4.3.2 still applies. However, the deformed shape indicates the floor story drift of the model is close to the test value, and the model's roof story drift is smaller than the test.

Table 4-27: Comparison of peak hold down tensile force between A2c-3D-SD-a model and test, Phase 2c

Excitation Name	Ground Motion	Peak F (kip) Test	t @ peak F (s) Test	Peak F (kip) Model	t @ peak F (s) Model
P2cS01	CNP 16%[1]	-0.23	8.68	-1.26	8.45
P2cS02	CNP 16%[2]	0.25	10.00	-0.99	8.34
P2cS03	CNP 16%[3]	-0.24	10.00	-1.12	4.58
P2cS04	CNP 16%	-0.24	5.20	-1.35	8.43
P2cS05	CNP 44%	-1.19	5.05	-1.90	5.04

[1]long direction only [2]short direction only [3]long and short directions only

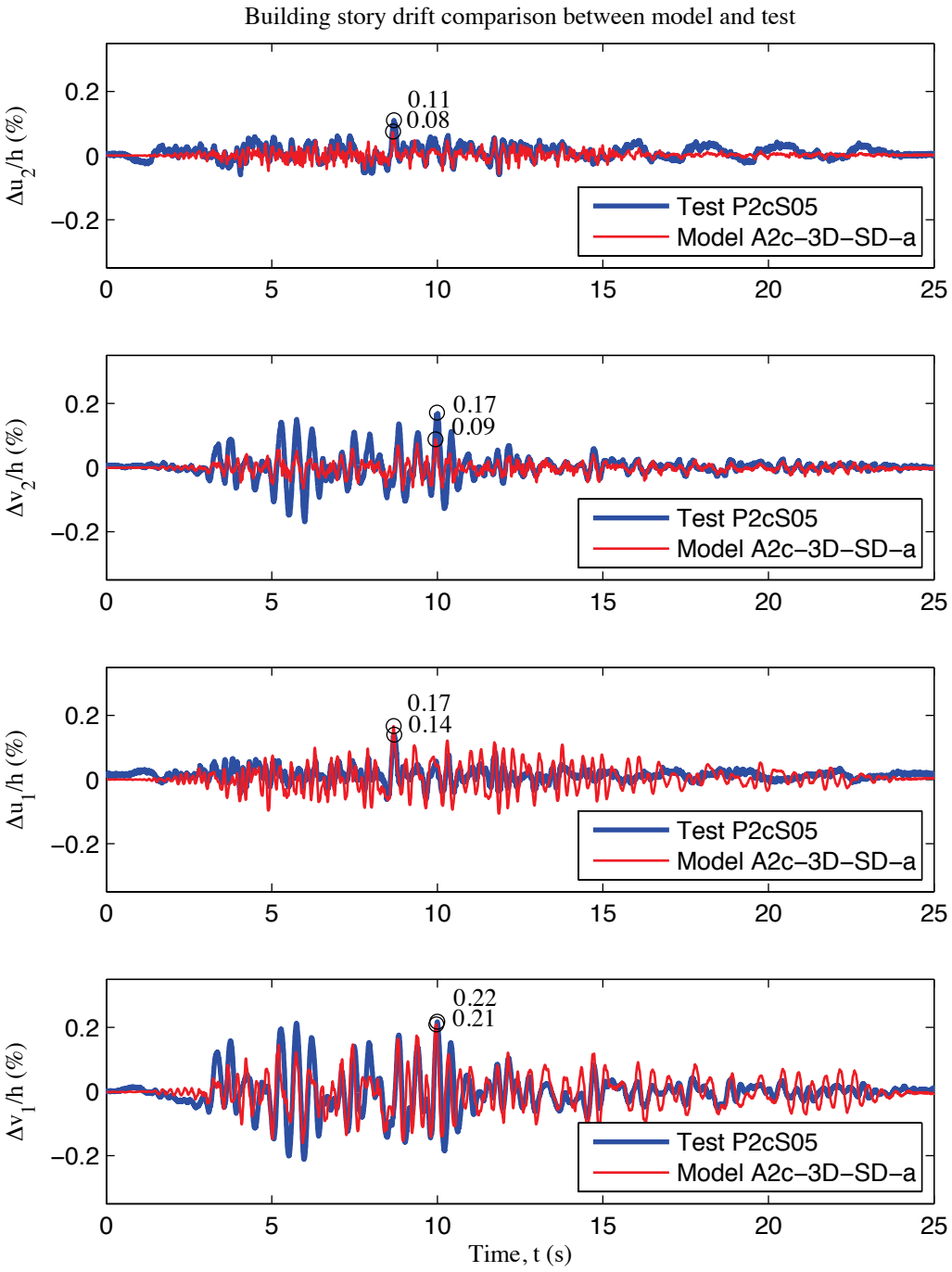

Figure 4-29: Comparison of story drift of the building, P2cS05 excitation, Phase 2c

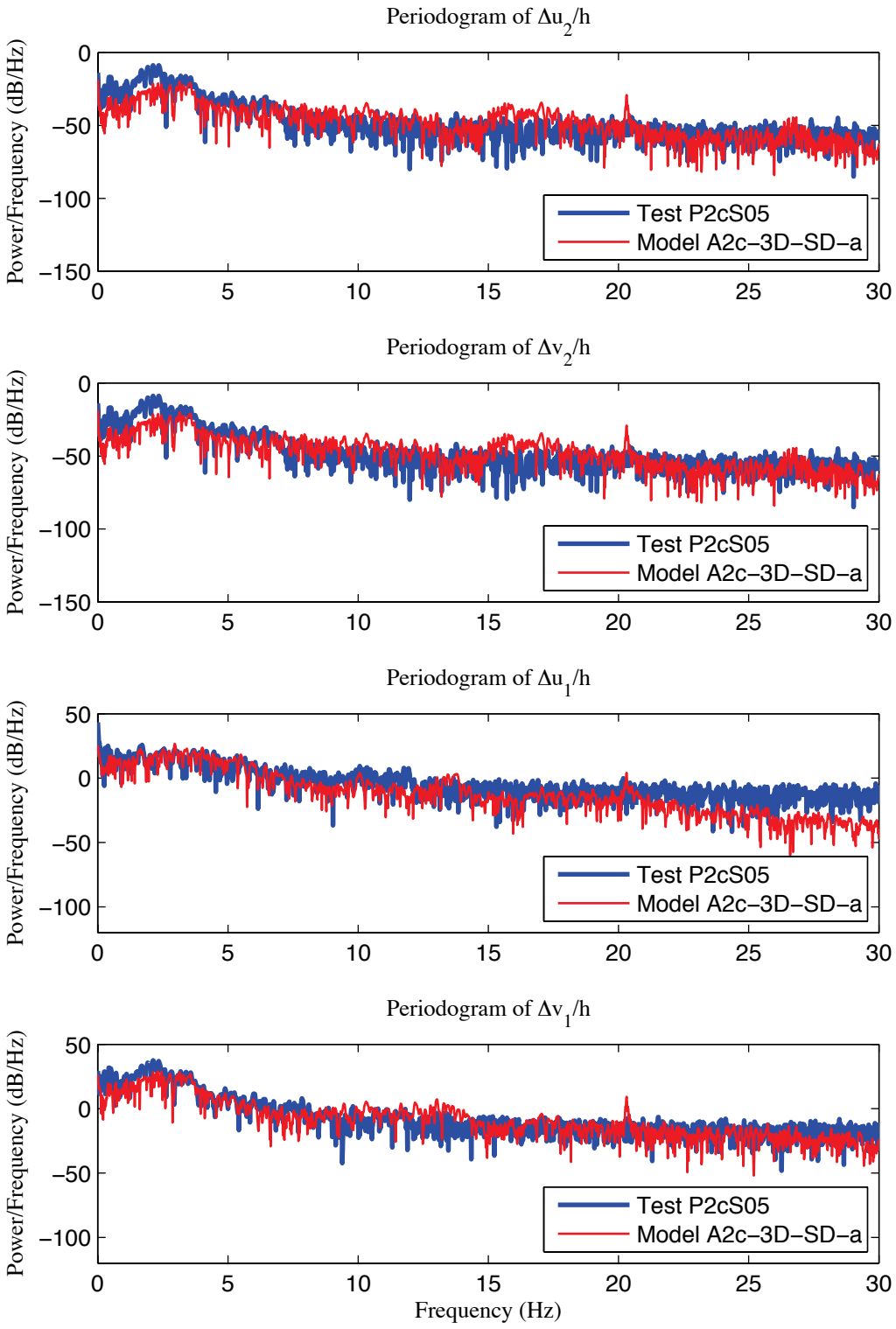

Figure 4-30: Comparison of periodogram of the building's story drift, P2cS05 excitation, Phase 2c

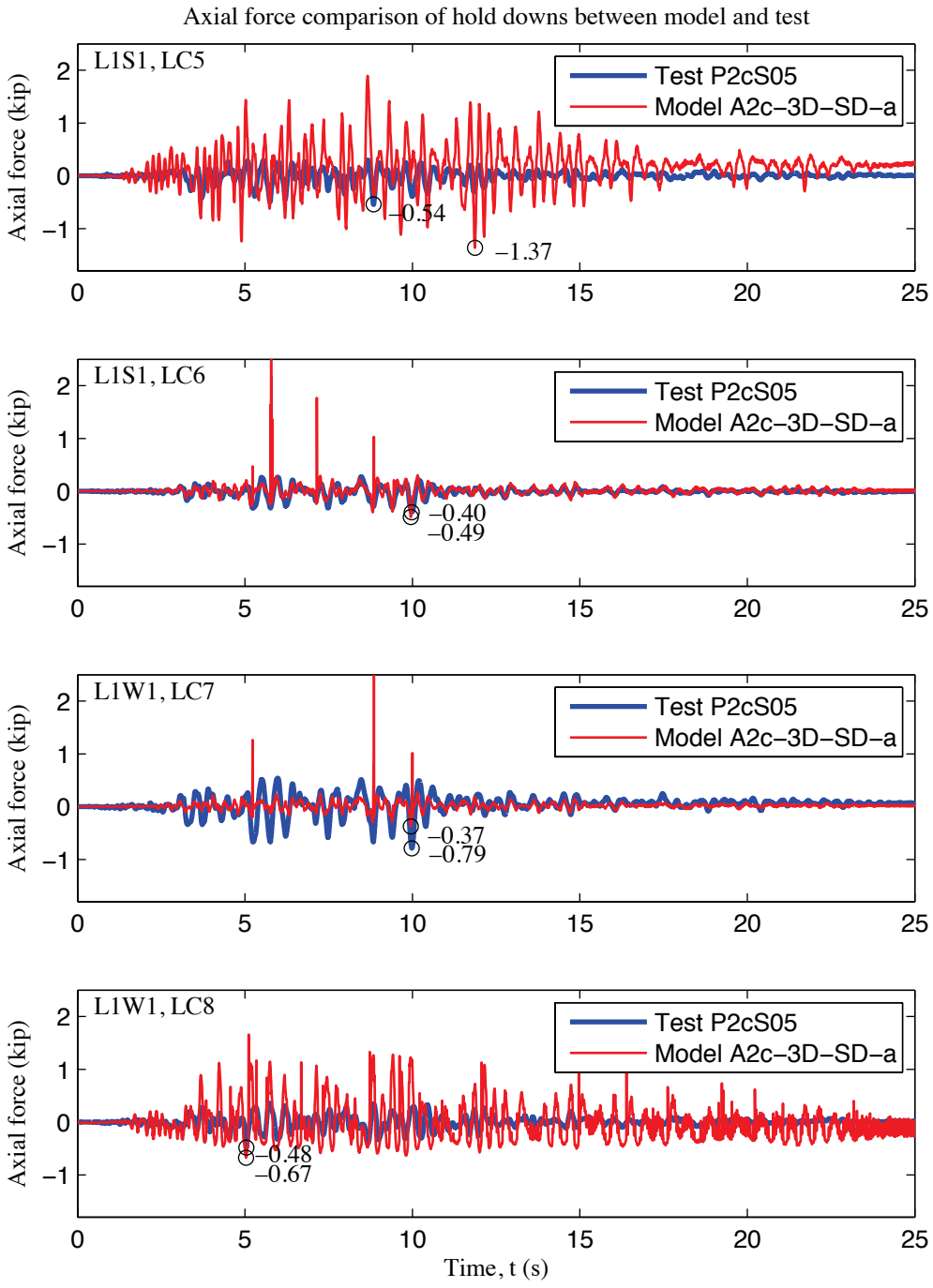

Figure 4-31: Comparison of load cell 5 to 8 axial forces, P2cS05 excitation, Phase 2c

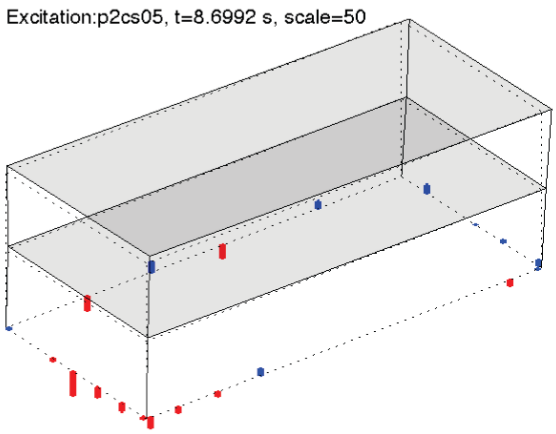

(a) Test (max hold down force: -1.19 kips)

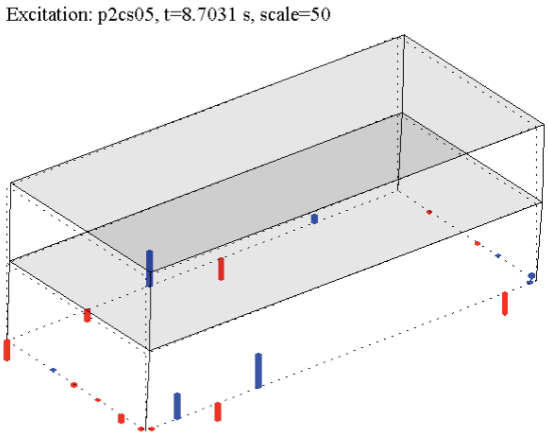

(b) Model (max hold down tensile force: -1.17 kips)

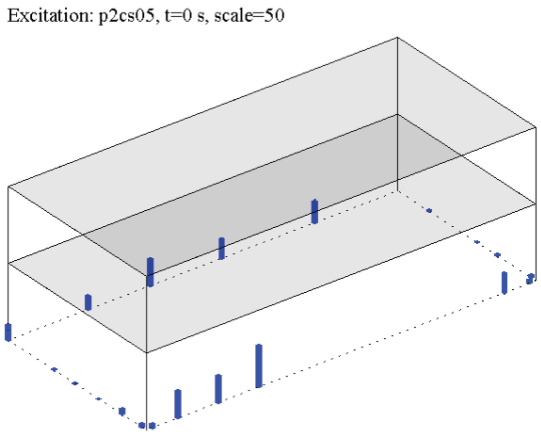

(c) Model (gravity load only)

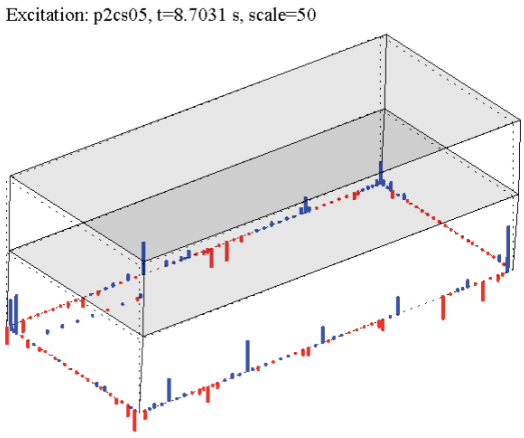

(d) Model (bearing force also plotted)

Figure 4-32: Comparison of simplified deformed shape and distribution of load cell forces between A2c-3D-SD-a model and P2cS05 test, P2cS05 excitation, Phase 2c

4.3.6 Phase 2d – fully sheathed structural with interior nonstructural

The archetype building at Phase 2d has interior nonstructural partition walls and stairs and ceilings in addition to fully sheathed exterior walls with OSB and gypsum panels realized in Phase 2c. The interior walls can be seen through the window and door openings in the design drawing (Figure 4-33(a)). Similar to the modeling of the shear wall and gravity walls, the partition walls are modeled with bracings, but the sheathing is not discretized into subpanels. The characterized properties of gypsum sheathings at Phase 2c are employed again. Note that we use structural studs instead of dry wall studs

for interior walls and are modestly unconservative, as explained in Section 3.6. Rigid diaphragm is the only option of diaphragm since the mesh of subpanels of diaphragms does not always meet the locations of interior walls. Also, note that the addition of ceilings further stiffens the diaphragms. This could be included, in spirit, similar to the wall modeling but was not done here for convenience as the diaphragm subpanels would have had to be redone again to match the interior framing. Staircases are also missing in A2d-3D-RD-a of Phase 2d; their possible role in multi-story coupling of response is left for future work. The resulting FE model is shown in Figure 4-33(b). Designers believe that the role of interior partition walls in lateral force resistance is trivial, but this needs to be quantified by test measurements and simulation data.

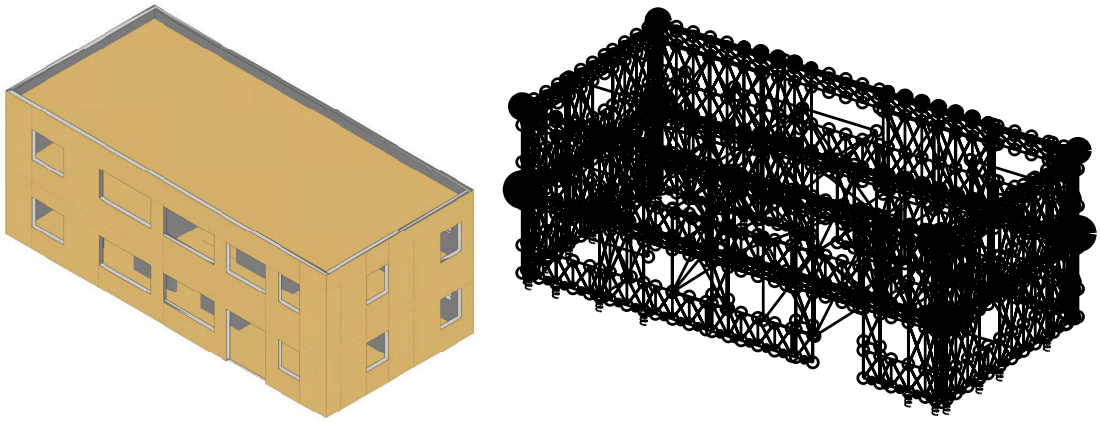

(a) Isometric design drawing (b) FE model (A2d-3D-RD-a)

Figure 4-33: Design drawing and high-fidelity FE model of Phase 2d building

Table 4-28 summarizes the PGA of excitations applied in tests and simulations at this phase. Same with every other phase, the accelarations experienced by the building, as shown in the right half of the table, are actual excitations of the model. The strongest excitation (P2dS05) corresponds to 44% CNP, same with Phase 2b and Phase 2c. The

first natural period in the long and short direction is listed in Table 4-29. The model's first natural period is quite accurate in long direction (6% error) and is 88% of the building's period in the short direction. Although a little stiffer in short direction, the model's stiffness is regarded as 'close' to the real building in general. Adding interior walls to models, as realized in A2d-3D-RD-b, makes the predicted natural periods reduce by ~5%, in comparison to A2c-3D-SD-a model in Section 4.3.5. Similar amount of natural period reduction (~7%) is seen for the CFS-NEES building from Phase 2c to Phase 2d.

Table 4-28: Summary of excitations for model calibration, Phase 2d

Excitation Name	Ground Motion	Record PGA long (g)	Record PGA short (g)	Record PGA up (g)	Excitation PGA long (g)	Excitation PGA short (g)	Excitation PGA up (g)
P2dS01	CNP 16%	0.0657	0	0	0.0848	0	0
P2dS02	CNP 16%	0	0.0556	0	0	0.0589	0
P2dS03	CNP 16%	0.0657	0.0556	0	0.0876	0.0599	0
P2dS04	CNP 16%	0.0657	0.0556	0.0764	0.0845	0.0602	0.0916
P2dS05	CNP 44%	0.1833	0.1551	0.2131	0.2388	0.1760	0.2749

Table 4-29: Comparison of the first natural period between A2d-3D-RD-a model and test, Phase 2d

LONG		SHORT	
T_1 (s), Test	T_1 (s), Model	T_1 (s), Test	T_1 (s), Model
0.16	0.17	0.25	0.22

The comparison of peak story absolute acceleration, as shown in Table 4-30, is still not very satisfying. The error can be as much as 100% in loaded directions (~0.1g) for excitation P2dS01 to P2dS04 (all correspond to 16% CNP). Under the excitation of P2dS05 (corresponds to 44% CNP), the predicted acceleration from A2d-3D-RD-a model in vertical direction of the roof is ten times larger than test (3.27 g vs. 0.284 g). This very large error peak acceleration, together with observation on hold down and bearing force distribution (as shown below), suggest the convergence was very difficult at certain

moments of the time history analysis in the vertical direction. Possible modifications of the model's vertical load path, as expounded in Section 4.3.2, would be applied in the future.

Table 4-30: Comparison of peak story absolute acceleration in g between A2d-3D-RD-a model and test, Phase 2d

LONG					
Excitation Name	**Ground Motion**	**Floor, Test**	**Floor, Model**	**Roof, Test**	**Roof, Model**
P2dS01	CNP 16%[1]	0.103	0.252	0.141	0.253
P2dS02	CNP 16%[2]	0.009	0.204	0.007	0.180
P2dS03	CNP 16%[3]	0.108	0.274	0.140	0.251
P2dS04	CNP 16%	0.108	0.251	0.139	0.241
P2dS05	CNP 44%	0.314	0.416	0.392	0.491
SHORT					
Excitation Name	**Ground Motion**	**Floor, Test**	**Floor, Model**	**Roof, Test**	**Roof, Model**
P2dS01	CNP 16%[1]	0.008	0.048	0.013	0.053
P2dS02	CNP 16%[2]	0.091	0.136	0.126	0.169
P2dS03	CNP 16%[3]	0.090	0.162	0.129	0.161
P2dS04	CNP 16%	0.087	0.17	0.123	0.170
P2dS05	CNP 44%	0.202	0.443	0.35	0.486
UP					
Excitation Name	**Ground Motion**	**Floor, Test**	**Floor, Model**	**Roof, Test**	**Roof, Model**
P2dS01	CNP 16%[1]	-	0.087	0.012	0.127
P2dS02	CNP 16%[2]	-	0.080	0.007	0.115
P2dS03	CNP 16%[3]	-	0.080	0.012	0.123
P2dS04	CNP 16%	-	0.109	0.094	0.166
P2dS05	CNP 44%	-	3.541	0.284	3.27

[1]long direction only [2]short direction only [3]long and short directions only

Comparison of the story drift remains encouraging. As shown in Table 4-31 and Figure 4-34, peak story drift in the model is similar to the building at lower excitation scales (~0.02% difference for P2dS01 to P2dS04 excitation (corresponds to 16% CNP)) . At P2dS05 excitation (corresponds to 44% CNP), the floor peak drift matches with tests well (less than 20% error), and the difference in peak roof story drift is less than 33% between the model and the test. Through the time history of the P2dS05 excitation, the model's story drift is in phase with the test output. Figure 4-35 further shows that the predicted

drift from A2d-3D-SD-a model has the same power spectral density with test outputs for frequency lower than 15 Hz. These results demonstrates that the model's selected mass distribution and lateral stiffness as derived from all the model elements is generally accurate, thus model predicted lateral response is deemed reliable at least to the scale level of 44% CNP (i.e. 44% of DBE level, represented by P2dS05 excitation).

Table 4-31: Comparison of peak story drift between A2d-3D-RD-a model and test, Phase 2d

LONG					
Excitation Name	**Ground Motion**	**$\Delta u_1/h$ (%) Test**	**$\Delta u_1/h$ (%) Model**	**$\Delta u_2/h$ (%) Test**	**$\Delta u_2/h$ (%) Model**
P2dS01	CNP 16%[1]	0.04	-0.03	-0.04	-0.02
P2dS02	CNP 16%[2]	0.01	0.01	-0.01	0.01
P2dS03	CNP 16%[3]	0.04	-0.03	-0.04	-0.02
P2dS04	CNP 16%	0.03	-0.03	-0.03	-0.02
P2dS05	CNP 44%	0.11	0.10	0.08	0.05
SHORT					
Excitation Name	**Ground Motion**	**$\Delta v_1/h$ (%) Test**	**$\Delta v_1/h$ (%) Model**	**$\Delta v_2/h$ (%) Test**	**$\Delta v_2/h$ (%) Model**
P2dS01	CNP 16%[1]	-0.02	-0.01	-0.01	-0.01
P2dS02	CNP 16%[2]	-0.08	-0.05	-0.05	-0.02
P2dS03	CNP 16%[3]	-0.08	-0.05	-0.04	-0.02
P2dS04	CNP 16%	-0.08	-0.05	-0.05	-0.02
P2dS05	CNP 44%	-0.19	0.23	-0.15	0.10

[1]long direction only [2]short direction only [3]long and short directions only

The peak values and response time histories for axial forces in the hold downs, as shown in Table 4-32, Figure 4-36 and Figure 4-37, follow the same trend as seen in Phase 2c (Table 4-27). The model always overestimates peak load cell force to a non-trivial extent, and the distribution of hold down forces at the base level is different from the building in the test. At P2dS05 excitation (corresponds to 44% CNP), this overestimation of peak load cell force is still 280% (1.7 kips (7.56 kN)) after the removal of axial force due to static gravity load. Large compressive force in bearing is again observed in A2b-3D-SD-a model's response under P2dS05 excitation (Figure 4-37(d)), indicating difficulties in covergence of the model in vertical load path (large vertical acceleration in Table 4-30

and the iteration history also support this observation). Note that load cell No. 8 even has a small (less than 0.2 kips (0.89 kN)) residual axial tensile force at the end of P2dS05 excitation. The proposed modification of the model's vertical load path (see Section 4.3.2) would be implemented in the future.

Table 4-32: Comparison of peak hold down tensile force between A2d-3D-RD-a model and test, Phase 2d

Excitation Name	Ground Motion	Peak F (kip) Test	t @ peak F (s) Test	Peak F (kip) Model	t @ peak F (s) Model
P2dS01	CNP 16%[1]	-0.01	4.06	-1.06	4.2
P2dS02	CNP 16%[2]	-0.03	9.98	-1.15	7.22
P2dS03	CNP 16%[3]	-0.03	9.41	-1.13	7.24
P2dS04	CNP 16%	-0.03	7.47	-1.12	7.22
P2dS05	CNP 44%	-0.61	5.07	-2.34	8.59

[1]long direction only [2]short direction only [3]long and short directions only

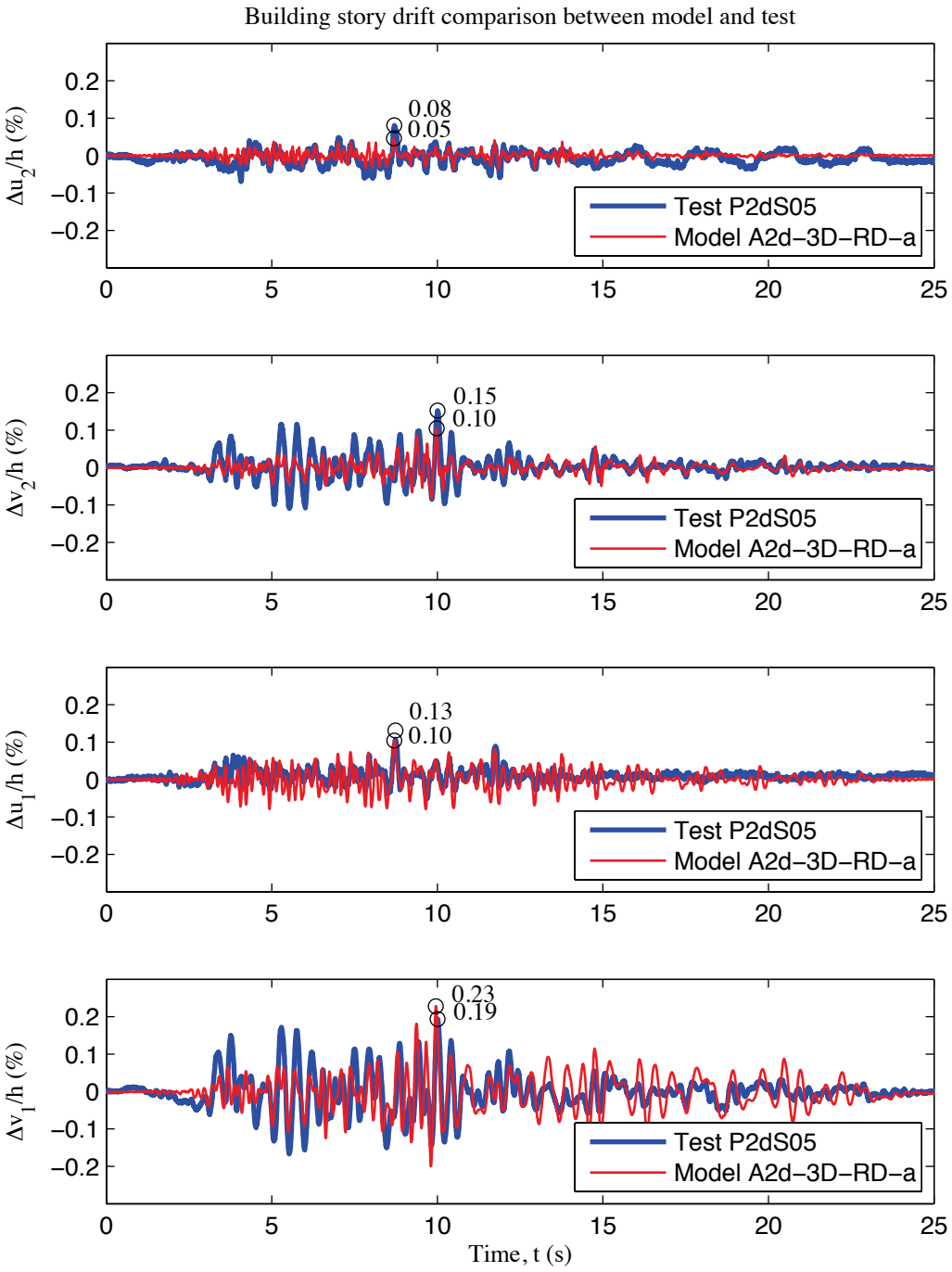

Figure 4-34: Comparison of story drift of the building, P2dS05 excitation, Phase 2d

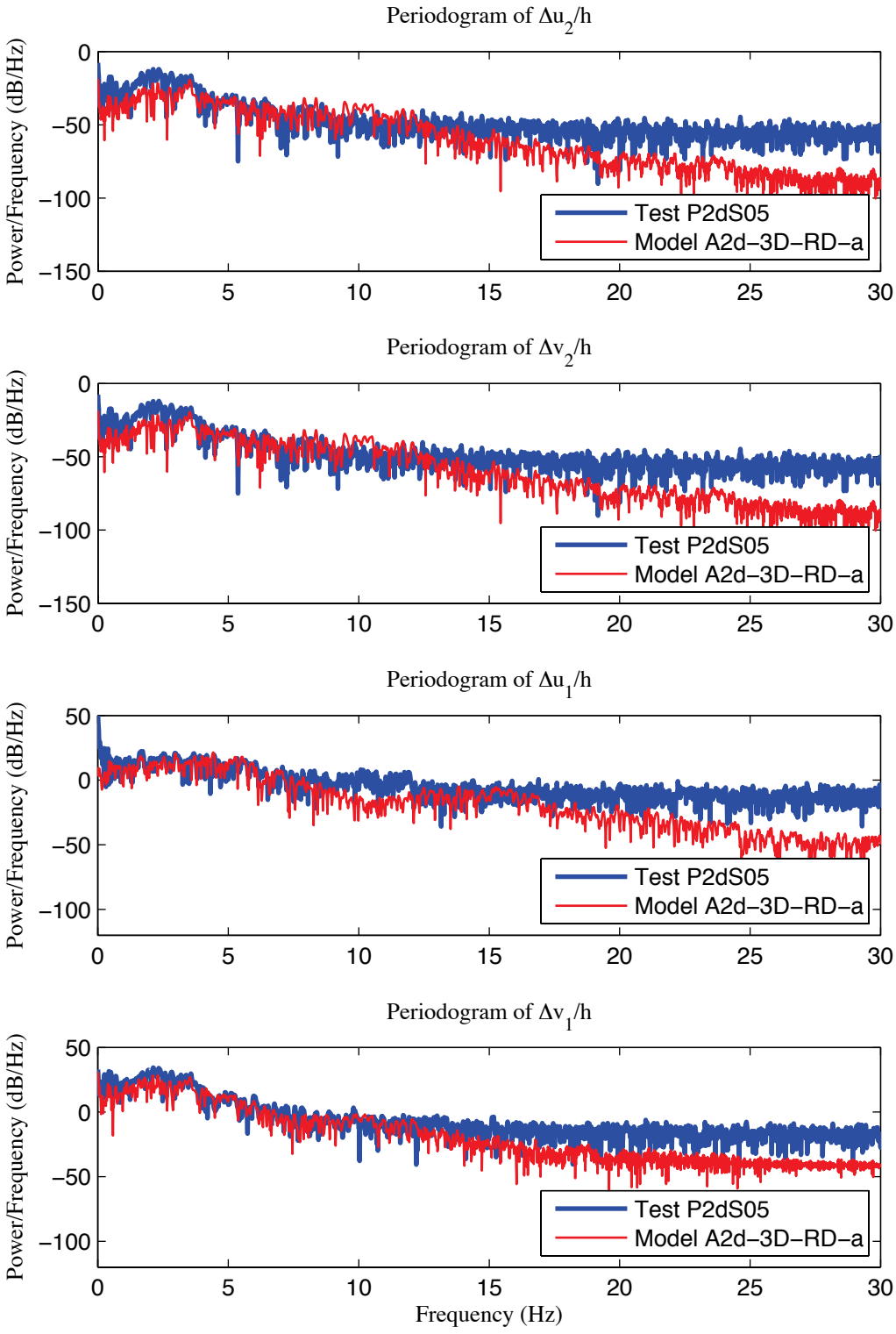

Figure 4-35: Comparison of periodogram of the building's story drift, P2dS05 excitation, Phase 2d

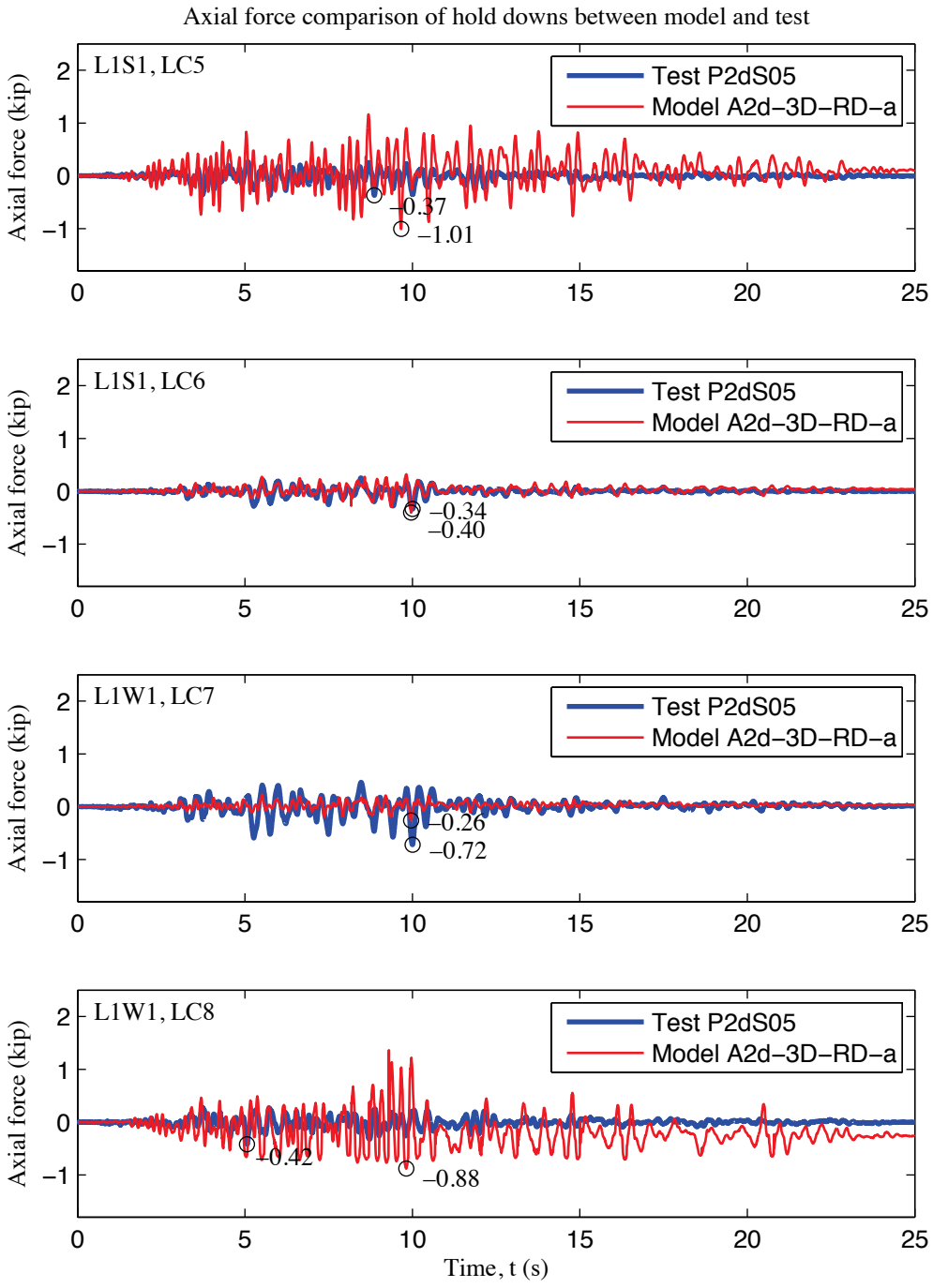

Figure 4-36: Comparison of load cell 5 to 8 axial forces, P2dS05 excitation, Phase 2d

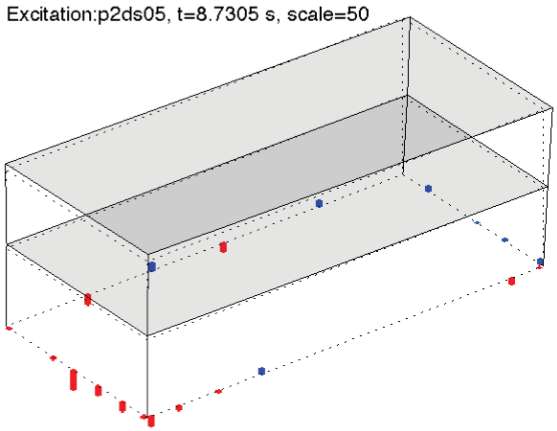

(a) Test (max hold down force: -0.61 kips)

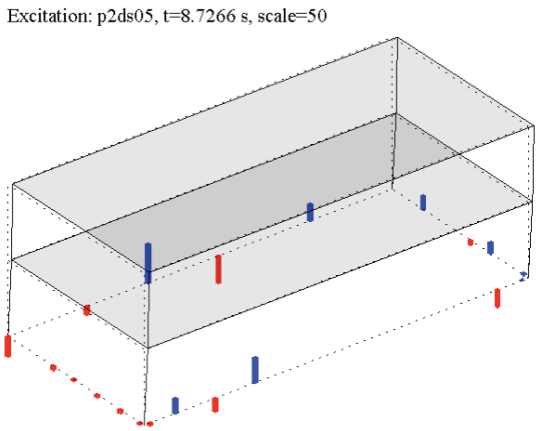

(b) Model (max hold down tensile force: -1.55 kips)

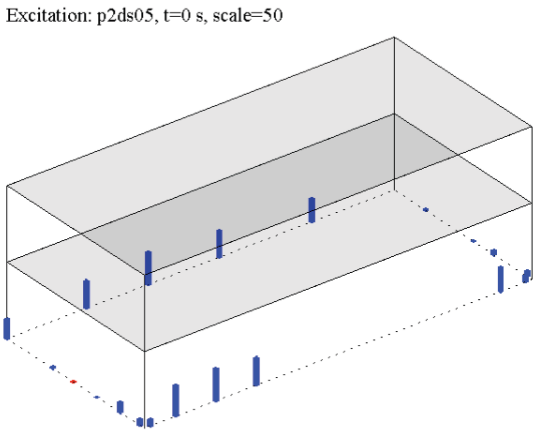

(c) Model (gravity load only)

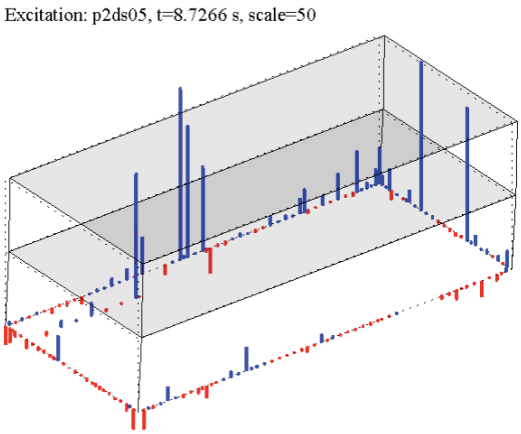

(d) Model (bearing force also plotted)

Figure 4-37: Comparison of simplified deformed shape and distribution of load cell forces between A2d-3D-RD-a model and test, P2dS05 excitation, Phase 2d

4.3.7 Phase 2e – fully sheathed structural with interior nonstructural and DensGlass

The Phase 2e building is the final phase, and the building is as complete as the testing explored. The final addition from the Phase 2d building to the Phase 2e building includes waterproof DensGlass on the façade as shown in Figure 4-38(a). From a modeling perspective, the DensGlass was not taken into account. However, the author believes that the shift of the building's lateral response from Phase 2d to Phase 2e is minimial and it is thus worth comparing Phase 2d models (i.e. A2d-3D-RD-a) with the Phase 2e building to

see the closeness of lateral response between the most complicated model and the complete building. The A2d-3D-RD-a model is plotted again in Figure 4-38(b).

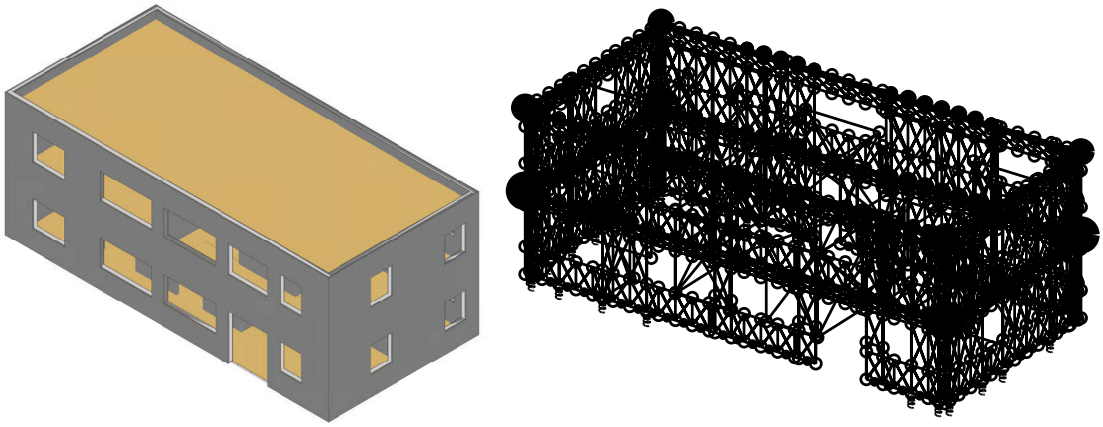

(a) Isometric design drawing (b) FE model (A2d-3D-RD-a)

Figure 4-38: Design drawing and high-fidelity FE model of Phase 2e building

Table 4-33 lists PGAs of the original ground motions and excitations used in the time history analyses based on actual experienced excitations in the tests. The Phase 2e building is tested with the most ground motions, including excitations correspond to Canoga Park at 16%, 44% and 100% and Rinaldi at 16% and 100%. The excitation (in Table 4-33) is the experienced acceleration of the building in the shaking table test, with the only exception of P2eS09. As reported by Peterman (Peterman 2014), the facility over shot the ground motion by about 0.2 g in the vertical direction. Indeed, the PGA of experienced vertical ground motion of the building is 1.03 g, much greater the original record. Experienced PGA in the long direction is also about 0.2 g larger than original. However, the analysis of A2d-3D-RD-a model always suffered from numerical difficulties (i.e. convergence test failed at about 5.0 seconds) despite the author's best

effort. Hence, the original signal of 100% RRS was used instead to excite A2d-3D-RD-a model. This is documented in the last row of Table 4-33.

Table 4-33: Summary of excitations for model calibration, Phase 2e

Excitation Name	Ground Motion	Record PGA long (g)	Record PGA short (g)	Record PGA up (g)	Excitation PGA long (g)	Excitation PGA short (g)	Excitation PGA up (g)
P2eS01	CNP 16%	0.0657	0	0	0.0841	0	0
P2eS02	CNP 16%	0	0.0556	0	0	0.0510	0
P2eS03	CNP 16%	0.0657	0.0556	0	0.0839	0.0500	0
P2eS04	CNP 16%	0.0657	0.0556	0.0764	0.0892	0.0604	0.0709
P2eS05	CNP 44%	0.1833	0.1551	0.2131	0.2565	0.1642	0.2068
P2eS07	CNP 100%	0.4204	0.3558	0.4888	0.6002	0.3509	0.4501
P2eS08	RRS 16%	0.1650	0.0973	0.1669	0.1679	0.0869	0.1956
P2eS09*	RRS 100%	0.8252	0.4865	0.8343	0.8252	0.4865	0.8343

*: The original ground motion was adopted in time history analysis.

Table 4-34 reports the natural periods of the first translational mode in the long and short direction. Although the FE model is not updated from Phase 2d, the model's natural periods are still close to those of the complete Phase 2e building: the error is 13% (flexible) in long direction and 16% (stiff) in short direction. This comparison supports the author's speculation that the change of lateral stiffness from Phase 2d to Phase 2e is small that it is justifiable to use the A2d-3D-RD-a model in the performance comparison of Phase 2e. Note that DensGlass indeed has a role by reducing the T_1 of the CFS-NEES building by 6% in the long direction and increasing T_1 by 4% in the short direction.

Table 4-34: Comparison of the first natural period between A2d-3D-RD-a model and test, Phase 2e

LONG		SHORT	
T_1 (s), Test	T_1 (s), Model	T_1 (s), Test	T_1 (s), Model
0.15	0.17	0.26	0.22

The comparison of peak story absolute acceleration in Table 4-35 shows the match is generally acceptable (error always less than 100%) from P2eS01 to P2eS07 excitations (corresponds to 16% CNP to 100% CNP) with the only exception of the vertical

acceleration under P2eS07 (corresponds to 100% CNP (DBE), ten times over-predicted by the model). Under the strongest excition of P2eS09 (corresponds to 100% RRS (MCE)), the predicted acceleration by A2d-3D-RD-a model differs greatly from test data and it is even 73 times larger in the vertical direction. Unduely large acceleration in the vertical direction, as discussed in previous sections, is a sign of convergence problem in hold downs and compressive bearing elements modeling the building's veritical load path.

Table 4-35: Comparison of peak story absolute acceleration in g between A2d-3D-RD-a model and test, Phase 2e

LONG					
Excitation Name	**Ground Motion**	**Floor, Test**	**Floor, Model**	**Roof, Test**	**Roof, Model**
P2eS01	CNP 16%[1]	0.104	0.230	0.141	0.243
P2eS02	CNP 16%[2]	0.006	0.205	0.007	0.192
P2eS03	CNP 16%[3]	0.104	0.244	0.139	0.234
P2eS04	CNP 16%	0.104	0.281	0.134	0.260
P2eS05	CNP 44%	0.294	0.428	0.373	0.477
P2eS07	CNP 100%	0.816	0.984	0.965	0.988
P2eS08	RRS 16%	0.252	0.302	0.325	0.363
P2eS09	RRS 100%	1.646	3.59	1.923	5.196
SHORT					
Excitation Name	**Ground Motion**	**Floor, Test**	**Floor, Model**	**Roof, Test**	**Roof, Model**
P2eS01	CNP 16%[1]	0.008	0.044	0.008	0.047
P2eS02	CNP 16%[2]	0.093	0.125	0.136	0.147
P2eS03	CNP 16%[3]	0.093	0.134	0.137	0.149
P2eS04	CNP 16%	0.089	0.126	0.13	0.15
P2eS05	CNP 44%	0.211	0.361	0.361	0.467
P2eS07	CNP 100%	0.503	0.462	0.863	0.717
P2eS08	RRS 16%	0.133	0.227	0.178	0.263
P2eS09	RRS 100%	0.734	7.08	1.063	13.156
UP					
Excitation Name	**Ground Motion**	**Floor, Test**	**Floor, Model**	**Roof, Test**	**Roof, Model**
P2eS01	CNP 16%[1]	-	0.044	0.01	0.047
P2eS02	CNP 16%[2]	-	0.026	0.006	0.030
P2eS03	CNP 16%[3]	-	0.052	0.011	0.085
P2eS04	CNP 16%	-	0.134	0.098	0.190
P2eS05	CNP 44%	-	0.643	0.288	0.568
P2eS07	CNP 100%	-	6.951	0.645	7.008
P2eS08	RRS 16%	-	0.559	0.241	0.483
P2eS09	RRS 100%	-	73.851	1.299	73.007

[1]long direction only [2]short direction only [3]long and short directions only

Comparison of story drift is presented in Table 4-36, Figure 4-39 and Figure 4-40. Even though the model misses features of the Phase 2e building, its peak lateral drifts are still comparable to the test results. The magnitudes of peak story drift are almost equal between test and simulation (less than 40% error) up to the P2eS05 (corresponds to 44% CNP) excitation. However, when the excitation reaches P2eS07 (corresponds to 100% CNP), the error in the magnitude of peak story drift can be as much as 68% (over-predicted) in the long direction at the floor level (0.27%, test vs. 0.42%, model). However, time history plots in Figure 4-39 indicate that the model's story drifts are still in phase with tests and the discrepancy in magnitude is most noticeable at the time of peak drift. For P2eS09 excitation that corresponds to 100% RRS excitation, the same key observations remain valid. Figure 4-41 and Figure 4-42 are periodogram of story drift under P2eS07 and P2eS09 excitation respectively. These figures show that predicted story drifts have the same power spectral density with test outputs at least up to 15 Hz. The model developed for Phase 2d may be used to predict to lateral drift response of the complete Phase 2e building under strong ground motions. Both test and simulation results confirm that the complete CFS-NEES building should survive the MCE without significant damage since its peak story drift is less than 1% and the building returns to an upright position (no residual drift) after the ground motion (see Figure 4-40).

Table 4-36: Comparison of peak story drift between A2d-3D-RD-a model and test, Phase 2e

LONG					
Excitation Name	**Ground Motion**	**$\Delta u_1/h$ (%) Test**	**$\Delta u_1/h$ (%) Model**	**$\Delta u_2/h$ (%) Test**	**$\Delta u_2/h$ (%) Model**
P2eS01	CNP 16%[1]	0.04	0.03	0.04	-0.02
P2eS02	CNP 16%[2]	0.01	-0.01	-0.01	0.01
P2eS03	CNP 16%[3]	0.04	-0.03	0.03	-0.02
P2eS04	CNP 16%	0.04	-0.03	-0.03	0.02
P2eS05	CNP 44%	0.08	-0.09	0.06	0.04
P2eS07	CNP 100%	0.25	0.42	0.16	0.14
P2eS08	RRS 16%	0.11	0.06	0.07	0.03
P2eS09	RRS 100%	0.67	0.84	0.45	-0.34
SHORT					
Excitation Name	**Ground Motion**	**$\Delta v_1/h$ (%) Test**	**$\Delta v_1/h$ (%) Model**	**$\Delta v_2/h$ (%) Test**	**$\Delta v_2/h$ (%) Model**
P2eS01	CNP 16%[1]	-0.01	-0.01	-0.01	-0.01
P2eS02	CNP 16%[2]	-0.07	-0.04	-0.05	-0.02
P2eS03	CNP 16%[3]	-0.06	-0.05	-0.05	-0.02
P2eS04	CNP 16%	-0.06	-0.04	-0.05	-0.02
P2eS05	CNP 44%	-0.20	-0.16	-0.14	0.08
P2eS07	CNP 100%	-0.48	0.37	-0.32	0.19
P2eS08	RRS 16%	-0.16	-0.09	0.11	0.04
P2eS09	RRS 100%	-0.72	0.99	0.49	0.52

[1]long direction only [2]short direction only [3]long and short directions only

Table 4-37, Figure 4-43, Figure 4-44 and Figure 4-45 compare the axial force in the hold downs between the building and the model. Among all load cases corresponds to 16% CNP (P2eS01 to P2eS04) in Phase 2e, peak hold-forces predicted by the model are always much larger than the test (see Table 4-37). However, these excitations are not strong and the axial forces in load cells recorded during testing are very small. For P2eS05 (corresponds to 44% CNP) and P2eS08 (corresponds to 16% RRS) excitations, the difference is still ~300% (~1.5 kips (6.67 kN) overestimation by the model). For two strongest excitations (P2eS07 and P2eS09), the model's predicted peak load cell forces makes much closer matches to test values. The difference is less than 11%. Time history plots (Figure 4-43 and Figure 4-44) show that the match of axial force in load cell 5 is always worse than others in the southwest corner. A sharp change of load cell force in compression appears for the 100% CNP and it is more apparent under the 100% RRS

excitation. The phenomenon is frequently linked with difficulties of convergence during the analysis. Figure 4-45 again shows that the model cannot match the building's distribution of hold down forces. Very high blue bars in Figure 4-45(d) indicates that at t=4.63 s, the compressive bearing force is singularly high near the northwest corner. Highly unsymmetric behavior in tension and compression of hold downs and bearings can lead to unduely large forces in these elements.

Table 4-37: Comparison of peak hold down tensile force between A2d-3D-RD-a model and test, Phase 2e

Excitation Name	Ground Motion	Peak F (kip) Test	t @ peak F (s) Test	Peak F (kip) Model	t @ peak F (s) Model
P2eS01	CNP 16%[1]	-0.08	8.66	-1.04	4.21
P2eS02	CNP 16%[2]	-0.03	9.96	-1.14	7.22
P2eS03	CNP 16%[3]	-0.03	9.97	-1.14	7.00
P2eS04	CNP 16%	-0.02	9.98	-1.12	6.81
P2eS05	CNP 44%	-0.50	5.07	-2.01	4.04
P2eS07	CNP 100%	-3.43	5.04	-3.06	8.68
P2eS08	RRS 16%	-0.47	4.56	-1.89	5.03
P2eS09	RRS 100%	-7.63	6.33	-6.97	4.43

[1]long direction only [2]short direction only [3]long and short directions only

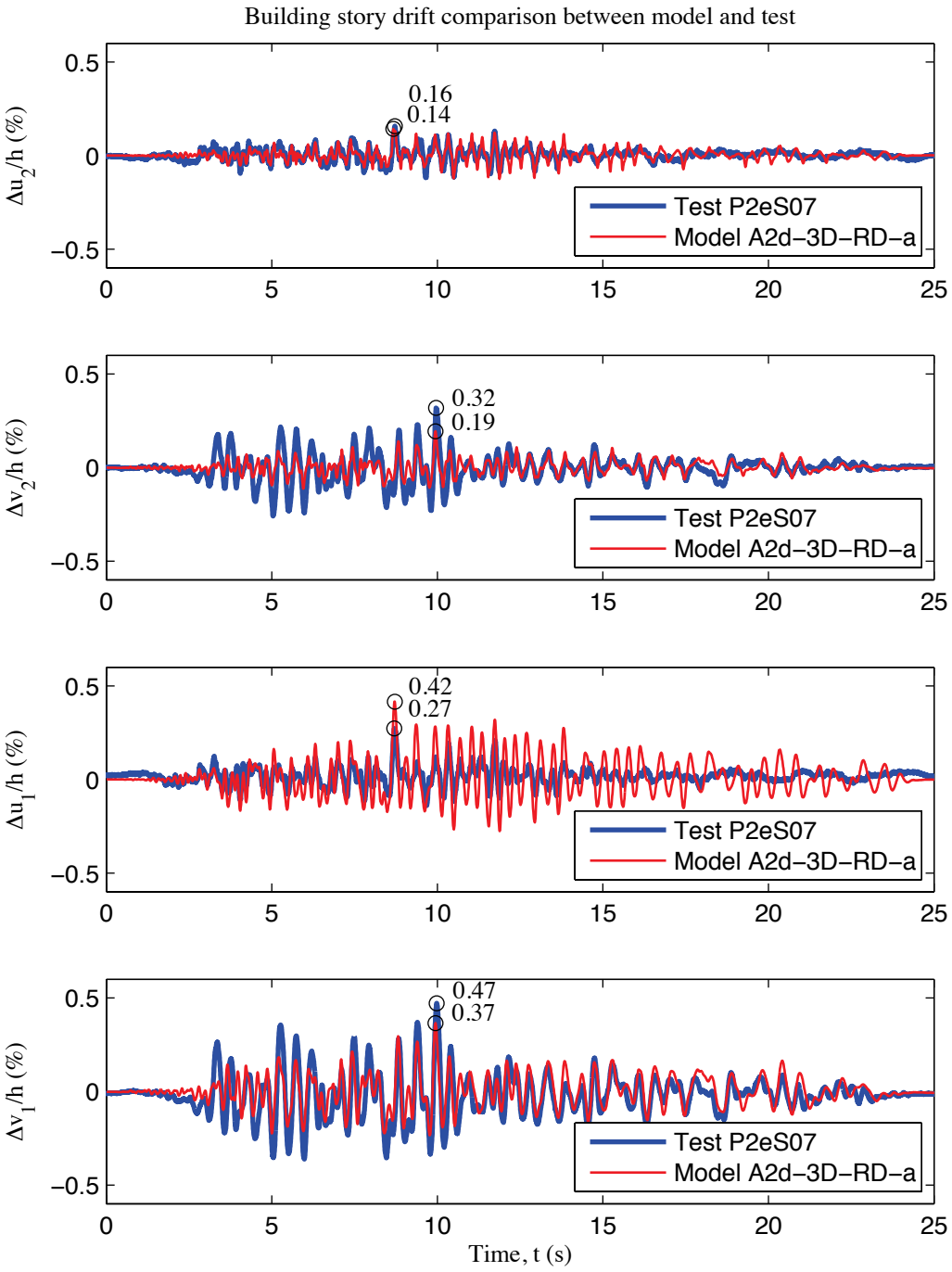

Figure 4-39: Comparison of story drift of the building, P2eS07 excitation, Phase 2e

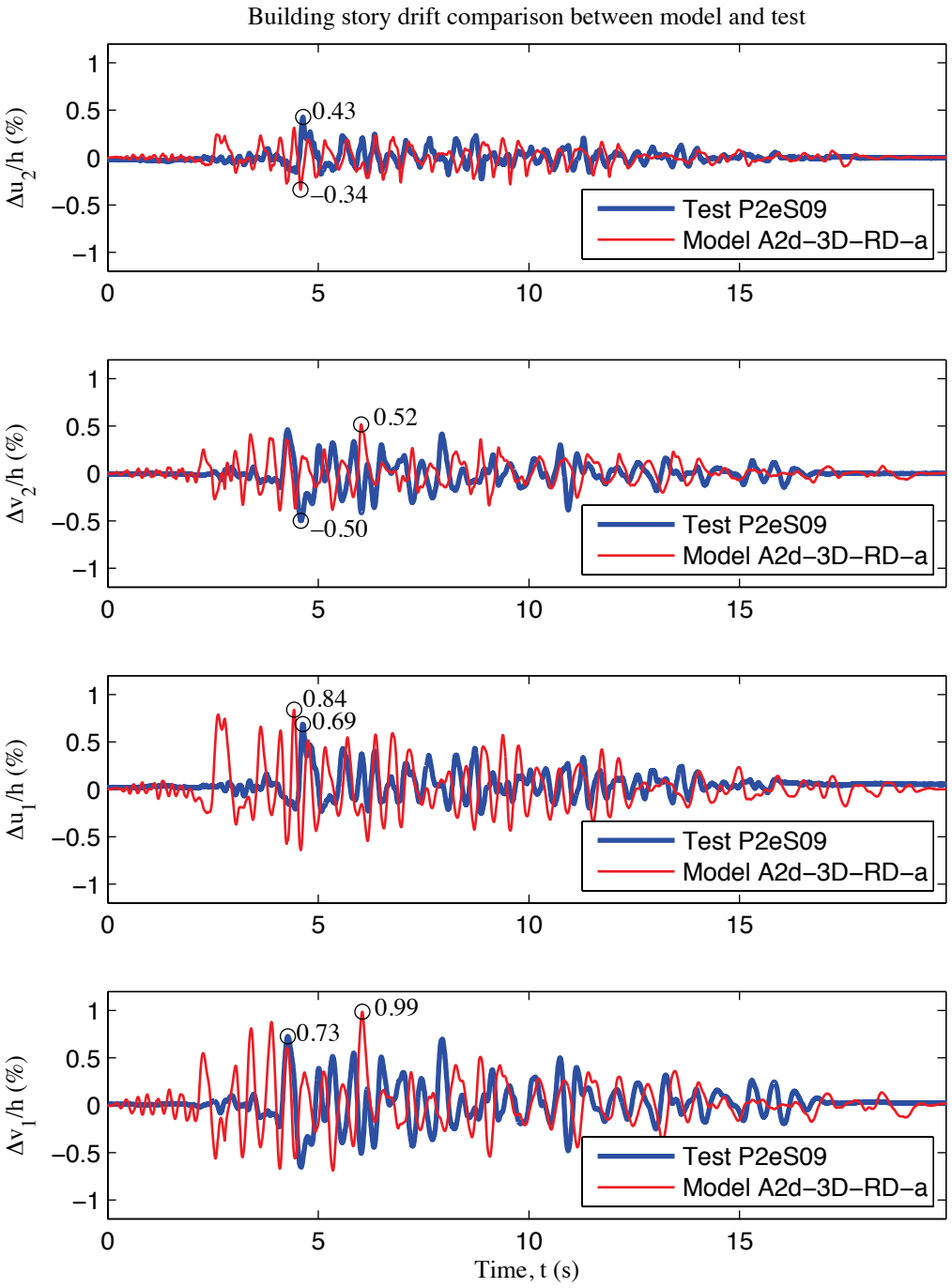

Figure 4-40: Comparison of story drift of the building, P2eS09 excitation, Phase 2e

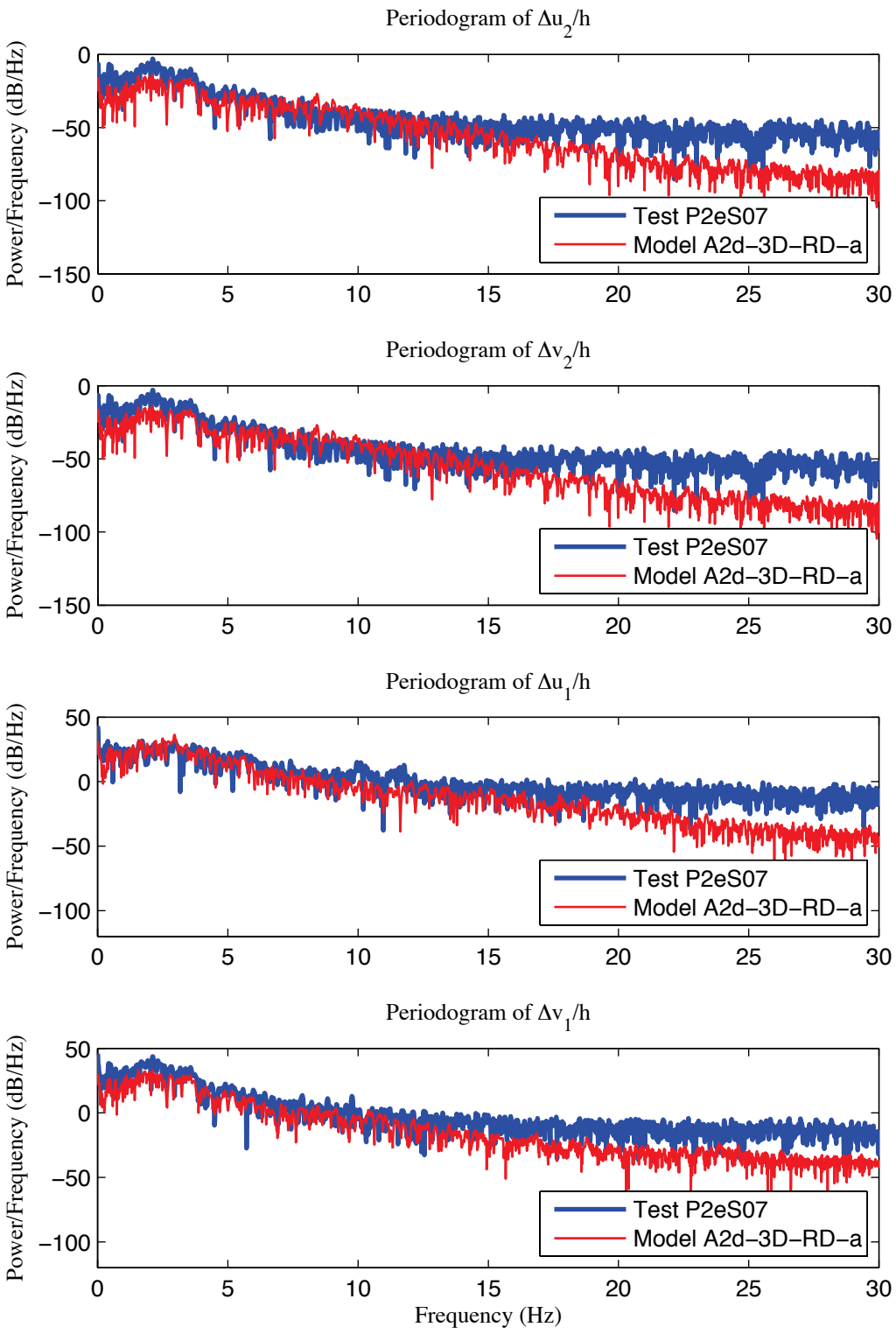

Figure 4-41: Comparison of periodogram of the building's story drift, P2eS07 excitation, Phase 2e

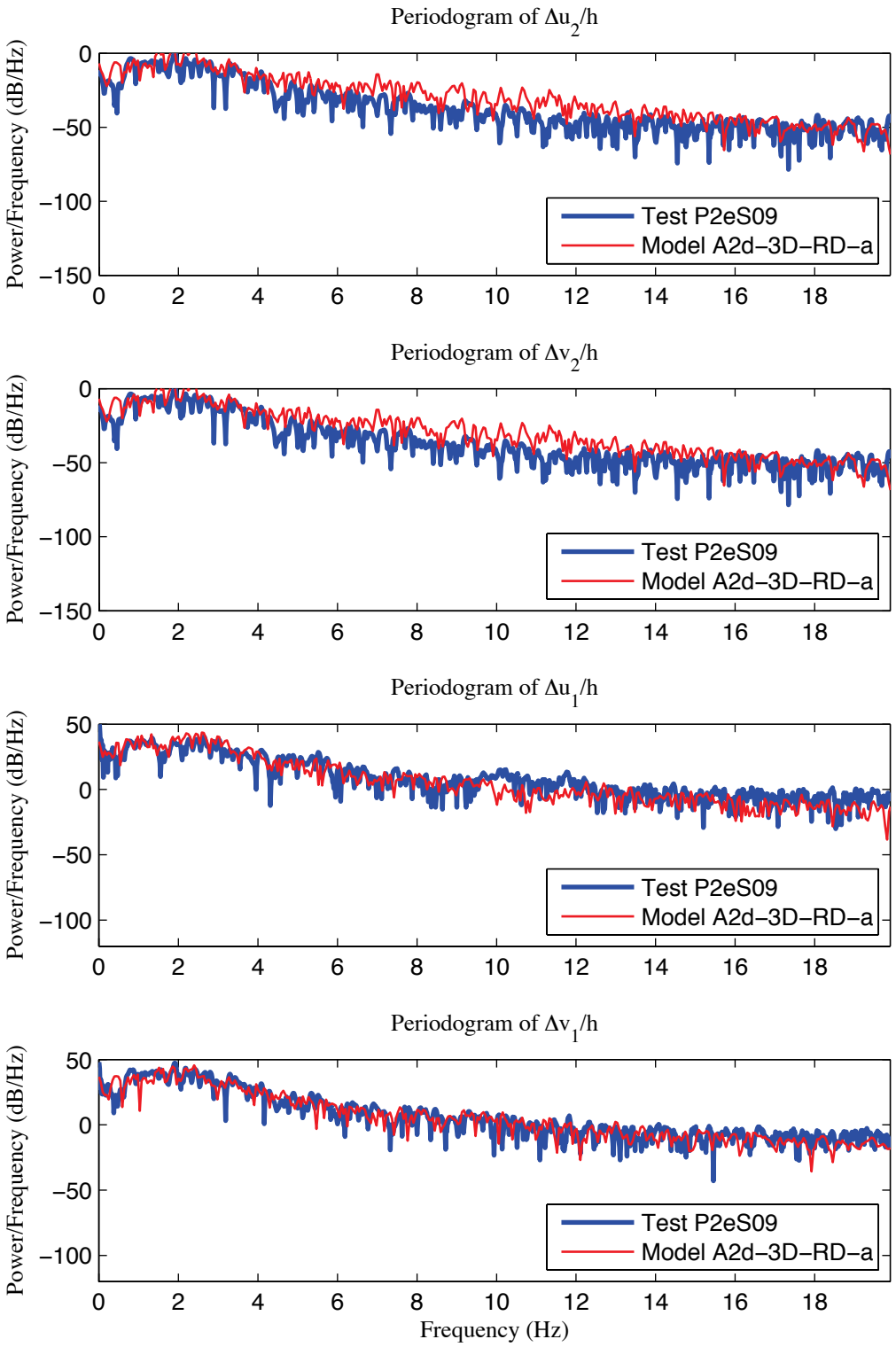

Figure 4-42: Comparison of periodogram of the building's story drift, P2eS09 excitation, Phase 2e

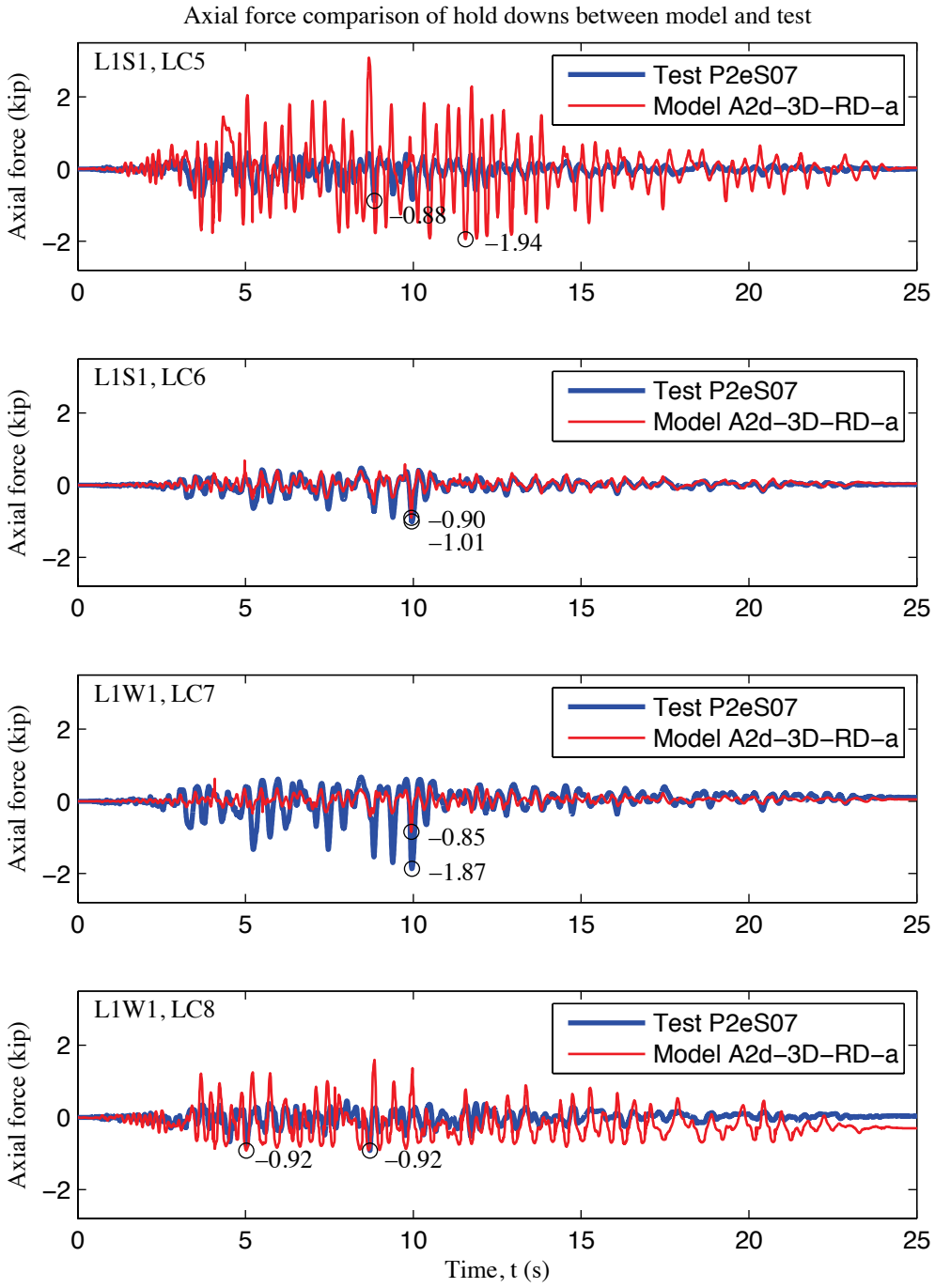

Figure 4-43: Comparison of load cell 5 to 8 axial forces, P2eS07 excitation, Phase 2e

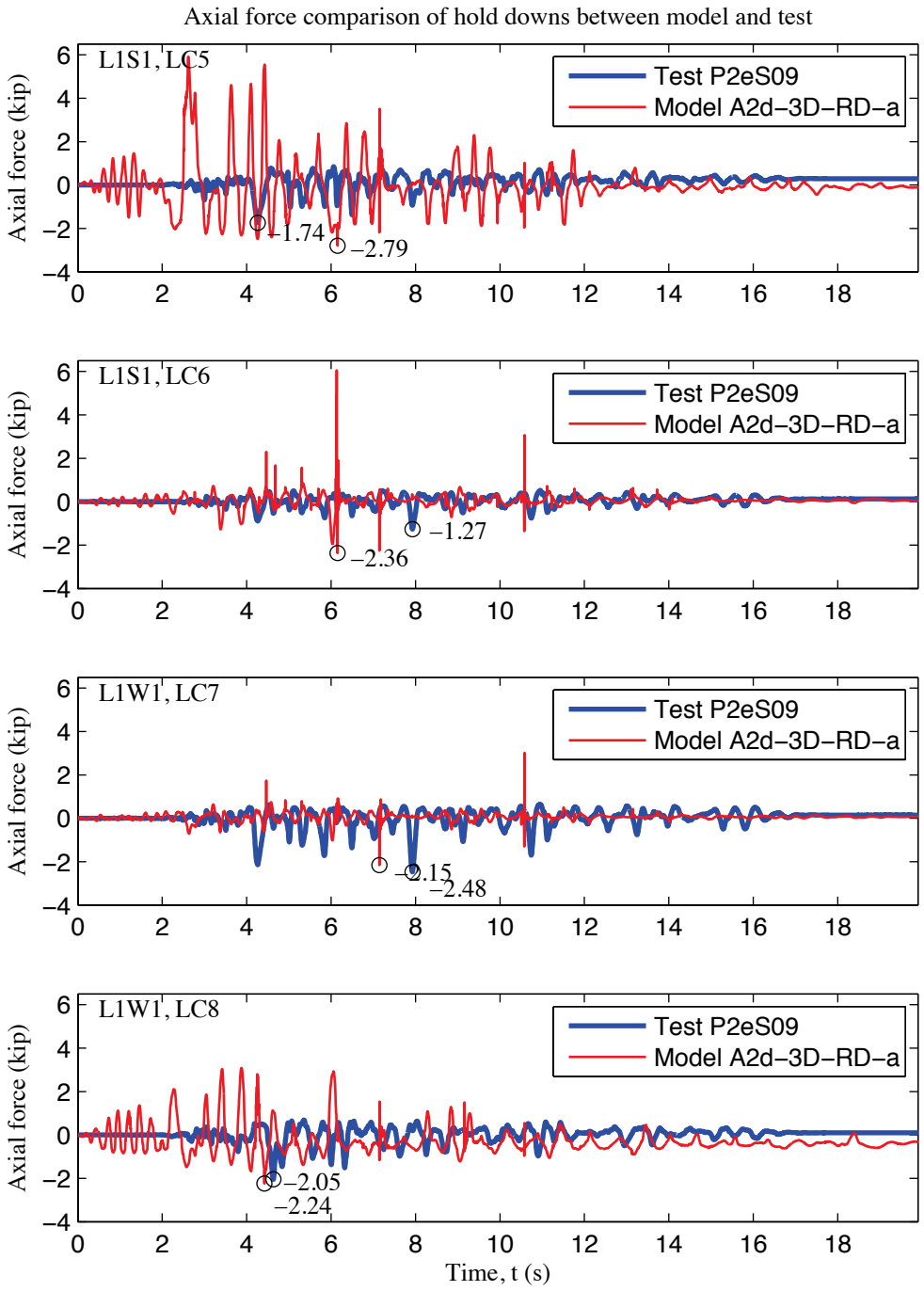

Figure 4-44: Comparison of load cell 5 to 8 axial forces, P2eS09 excitation, Phase 2e

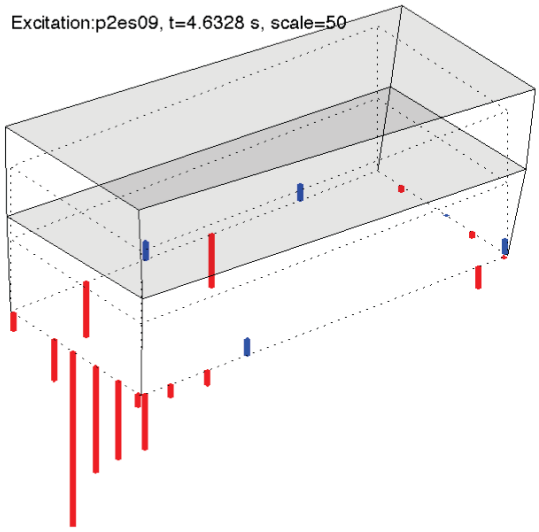

(a) Test (max hold down force: -7.63 kips)

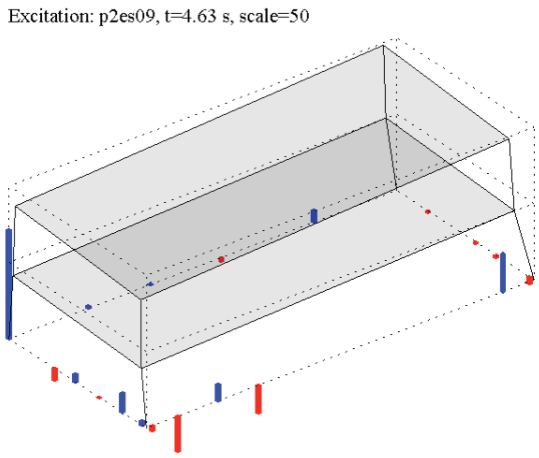

(b) Model (max hold down tensile force: -2.00 kips)

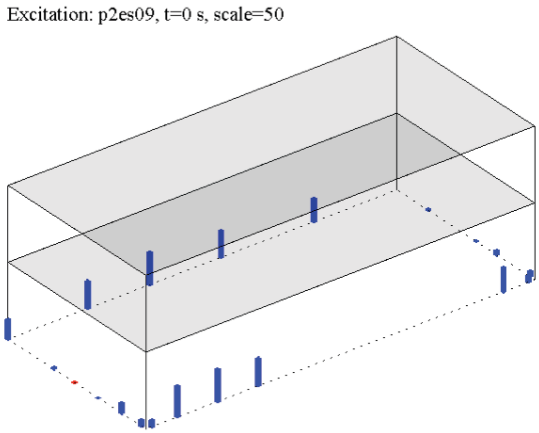

(c) Model (gravity load only)

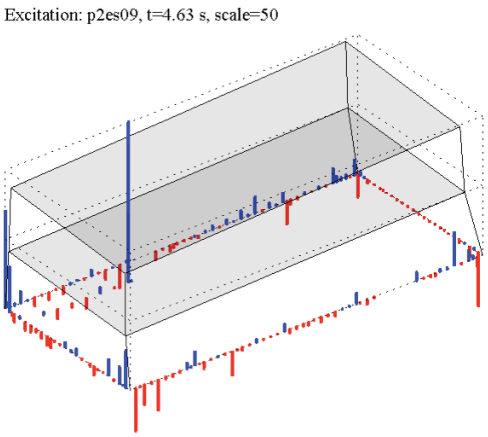

(d) Model (bearing force also plotted)

Figure 4-45: Comparison of simplified deformed shape and distribution of load cell forces between A2d-3D-RD-a model and test, P2eS09 excitation, Phase 2e

4.3.8 Brief summary on model calibration with shaking table tests

High fidelity finite element models of the CFS-NEES building are subjected to free vibration and nonlinear time history analyses and the results are compared with tests to examine the performance of the FE models. Comparison at each construction phase from Phase 1 to Phase 2e is addressed in previous subsections. Common observations are briefly summarized below.

Figure 4-46 plots the first natural periods in the long and short direction obtained from test and predicted by models at each phase. It is proposed that the model's natural periods match sufficiently well with those of the real building, at every phase, inclusive of the fact that the building's natural periods reduce almost by half from Phase 1 to Phase 2d and 2e. Given a fixed seismic mass, such a significant change implies the lateral stiffness of the building at Phase 2d or 2e is almost four times of the stiffness of the Phase 1 building that has structural components only. Our modeling procedure takes structural and nonstructural components into account, successfully estimates the lateral stiffness of each of them and incorporates these components step by step in mechanistically realistic fashion at each construction phase. The adequacy of such a methodology is demonstrated in the work herein.

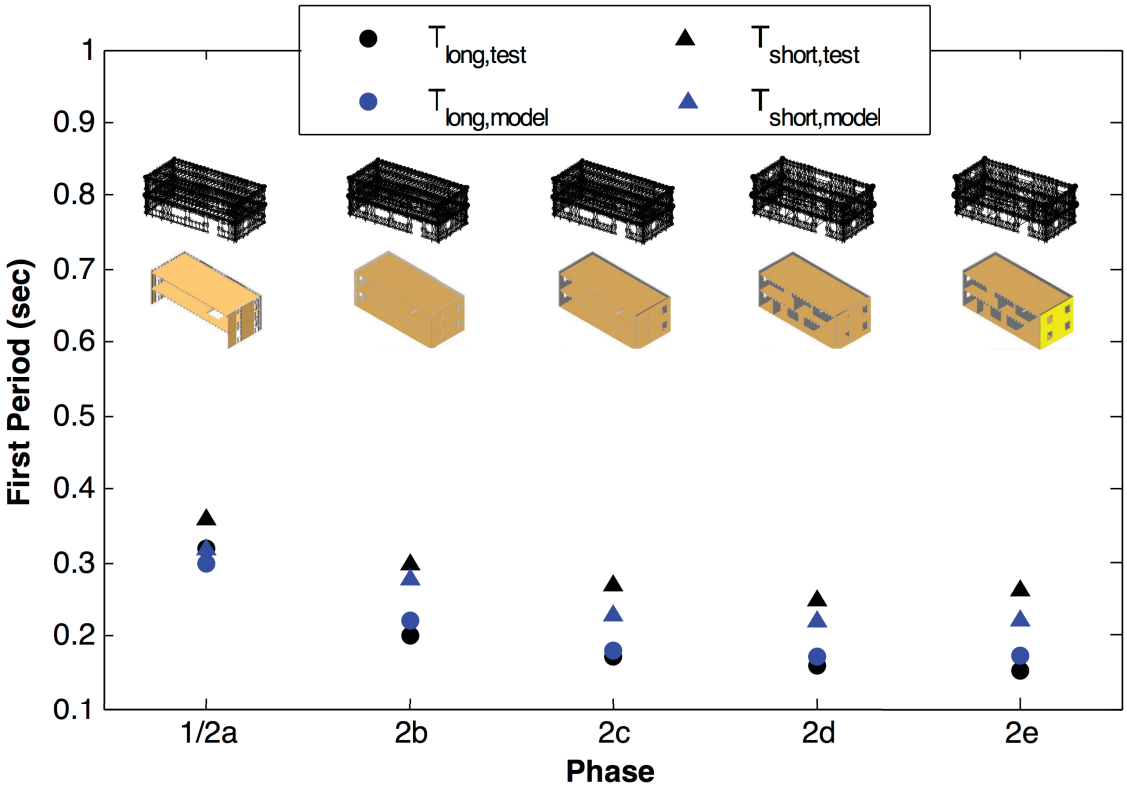

Figure 4-46: Comparison of the first mode period in long and short direction between buildings and state-of-the-art models

Three types of physical quantities, including story drifts, axial forces in hold downs, and peak story acceleration, are selected as performance metrics in simulation vs. test comparison of the nonlinear time-history analysis results. Among the three output quantities, the predicted story drift of the building is consistently the most accurate and matches best with the test results. Peak story drifts are closer to test data at lower excitation levels (16%, sometimes up to 44%) while the difference can be as much as 40% at high excitation levels. However, time history plots show that the model's story drift is always in phase with the response of the tested building. The magnitude of the model's story drift response does not deviate significantly from the tested building all the way through the response history, but may just fail to match the peak value at times. To be

more specific, the model's floor level drift matches better to corresponding tests than roof level drift. Roof level of the model behaves more rigidly compared to the real building at Phase 1, but the difference is mitigated as more nonstructural components are added at later phases. According to Section 3.9, the models ignore the flexibilty introduced by the CFS strap that ties chord studs across two stories and can have larger stiffness for the roof level. In general, the mass, stiffness and predicted drift of the high fidelity FE model is reliable across construction phases.

Predicted peak tensile axial forces in the hold downs (after the removal of static forces from gravity load) are overly large (can be more than 500% larger than tests), however the maginitude difference is less than 1.5 kips (6.67 kN) for almost every model at lowest excitations that corresponds to 16% CNP. When the excitaion is comparable to 44% CNP, A1-3D-SD-a model for Phase 1/2a starts to underestimate the peak hold down force and the percentage of overstimation from models at Phase 2c, 2d and 2e drops to ~300% (1.3 kips (5.78 kN) in magnitude). For excitations as strong as 100% CNP or even 100% RRS, A1-3D-SD-a model underestimate 50% of the peak force from test, while A2d-3D-RD-a model matches reasonably well with tests by only 11% of underestimation. Model A2b-3D-SD-a is the only exception to these observations, which always underestimates peak tensile axial forces in the hold downs. Time history plots of four selected hold downs near the southwest corner show that the axial force in one of them is always overestimated more significantly than others. At a given moment in the time history analysis, the distribution of hold down forces from the simulation cannot accurately match the distribution of the test data. Sharp increase in the magnitude of compressive

axial force of a specific hold down or stud end bearing is an outcome of difficulties in updating the axial force since the nonlinear response curve of the hold down or the compressive bearing is highly unsymmetric, as seen in the system output of iteration history. It is worth noting the potential shortcoming of only using peak values to measure the performance of models. However, more importantly, further consideration is needed on modeling of the gravity load path, so that the load cell hold down forces can match more accurately with the test data. Proposed modifications include accurate models of the shear wall tie between two stories and the incorporation of the stiffness of HSS steel tubes as the CFS-NEES building's foundation.

The match of peak story absolute acceleration between model and test is less accurate. The match is best in the long direction of both floor and roof level, with the difference less than 100% for various excitations and models across all phases. The worst match is in the vertical direction; models tend to overestimate the peak vertical acceleration and the difference can sometimes be more than 500%. The large error in vertical acceleration can be associated with difficulties in convergence of the iterative solver, since system outputs of iteration history and plots of load cell and bearing axial forces show that failure of convergence usually coincides with unduly large vertical accelerations and large compressive forces in hold downs and stud end bearings. Consequently, modifying gravity load path would be able to reduce the error in predicted peak vertical acceleration.

Comparison of models across phases reveals an interesting phenomenon: the performance of models at Phase 2b and above, with nonstructural components modeled simply using

heuristic methods, matches with the corresponding tested buildings as well as, sometimes even better, than Phase 1. A tentative explanation from a modeler's perspective is that the building and FE model at Phase 1 both have large areas of bare steel framing and thus there is a very large difference in stiffness and capacity between the shear wall system and the gravity framing. Ideally, the lateral capacity and stiffness of gravity framing is assumed to be zero. However, the separation of lateral system vs. gravity system is only a conceptual model accepted by engineers at the stage of preliminary design for simplicity. The capacity and stiffness of sheathed gravity walls is non-trivial and they significantly improve the lateral resistance of the whole building. On the other hand, load paths of lateral and vertical loads in CFS-framed structures should be continuous and these load paths are mixed to a certain extent in reality. Once the gravity framing is covered by sheathing, the stiffness and capacity of gravity walls are much closer to shear walls so the interplay between subsystems in the building is much more harmonic.

It is worth mentioning that all comparisons in this chapter can be augmented to include more and even all types of models developed so far to extensively investigate the sensitivity of simulation analysis to modeling options. The above discussion can be enriched and supported by further details. The next chapter, Chapter 5, is specially developed for this task.

Chapter 5: Analysis and Performance Comparison of Various Building Models

This chapter is an extensive discussion on seismic performance of finite element models for the CFS-NEES building at various modeling fidelity levels. Response of typical models from different types of analyses, and under multiple load cases, are collected and summarized. Sensitivity of the response with respect to modeling options is explored through straightforward comparisons. Section 5.1 introduces the finite element models employed for performance comparison and reviews the modeling options. Section 5.2 describes the types of analysis and load cases in the comparison of performance. Section 5.3 details the comparison of the models' seismic response, including their natural periods, lateral capacity, peak story drifts, and hold down load cell forces. Finally, Section 5.4 provides further discussion on common features observed in the models' performance vs. design assumptions. This section also explores the relationship between model fidelity and prediction of building response.

5.1 Review of modeling options and models in performance comparison

The CFS-NEES full-scale building modeling effort has two major goals (Schafer 2015): "(1) to provide a model than can meaningfully predict the CFS-NEES building response in order to better understand the behavior of the building and use the model to examine response against a full suite of seismic excitations, and (2) to evaluate what level of model fidelity is necessary for engineers and researchers modeling buildings with cold-formed steel framing." Four high-fidelity models, out of all nineteen types, are excited with shaking table test signals and their predictions of story drifts, hold down (load cell) forces, and peak story absolute acceleration have been compared with test data in Chapter 4. Validation confirmed the models' capability and laid the foundation for extensive comparisons that are directly related to major research goals in this chapter.

A complete comparison of all nineteen types of models, covering all fidelity levels and modeling options (see Table 3-3 in Chapter 3) would be too exhaustive. Model description and post-processed simulation results of all models are appended to the main body of this thesis as Appendix A to S. However, a subspace of the models can be selected to reflect major options and considerations in the modeling effort. Table 5-1 is a truncated model tree that includes ten types of models whose performance will be discussed in detail. Selected models ranges from 2D to 3D, from state-of-the-practice models (P-models) to state-of-the-art models (A-models), and include various construction phases.

The P-models use shear wall stiffness and strength based on codes and standards, i.e. AISI S213 (American Iron and Steel Institute 2009), and ignore the lateral contribution from all elements except shear walls (Schafer 2015) (see Figure 5-1(a) as an example of 3D P-model, as discussed in Section 3.3.1 and Section 3.5). The adopted nonlinear hysteretic model for P-models can be EPP or Pinching4. The development of the A-model is aligned with the construction of the CFS-NEES archetype building. Stiffness and strength in the A-models are based on direct testing (Liu et al. 2012) or higher-fidelity surrogate models (Bian et al. 2015). Gravity steel framing is explicitly modeled in most A-models, and an example of the resulting models is provided in Figure 5-1(b). A-models also explore the impact of the diaphragm stiffness on the response. Other related modeling techniques have been elaborated in Chapter 3. Comparison between the response of other models in the full model tree (Table 3-3) and models in Table 5-1 will be alluded to, especially in Section 5.4, to discover the relationship between model fidelity and predicted building response as necessary.

Table 5-1: Modeling options of the CFS-NEES archetype building in performance comparison

			State of the Practice		State of the Art							
					Phase 1/2a			Phase 2b		Phase 2c		2d
Component	Property	Option	P-2D-b	P-3D-RD-b	A1-2D-a	A1-3D-RD-a	A1-3D-SD-a	A2b-3D-RD-a	A2b-3D-SD-a	A2c-3D-RD-a	A2c-3D-SD-a	A2d-3D-RD-a
Shear wall	Stiffness	$K(0.4V_{nP})$	X	X								
		$K(V_{nP})$										
		$K(0.2V_{nA})$			X	X	X	X	X	X	X	X
		$K(0.4V_{nA})$										
	Capacity	V_{nA}			X	X	X	X	X	X	X	X
		V_{nP}	X	X								
	Backbone	EPP										
		Pinching4	X	X	X	X	X	X	X	X	X	X
	Panel size	Whole	X	X								
		Subpanels			X	X	X	X	X	X	X	X
Hold down	General	Smeared	X	X								
		Discrete			X	X	X	X	X	X	X	X
Shear anchors	General	Ignored	X	X								
		Included			X	X	X	X	X	X	X	X
Diaphragm	Stiffness	Flexible	X		X							
		Rigid		X		X		X		X		X
		Semi-rigid					X		X		X	
	Pinching	None	X	X	X	X						X
		Pinching4					X	X	X	X	X	
Gravity exterior walls	General	None	X	X								
		Frame			X	X	X					
		Full						X	X	X	X	X
Gypsum sheathing	General	Ignored	X	X	X	X	X	X	X			
		Included								X	X	X
Interior walls	General	Ignored	X	X	X	X	X	X	X	X	X	
		Included										X
Mass distribution	General	Corner	X	X	X							
		Stud ends				X	X	X	X	X	X	X

5.2 Description of analysis types in performance comparison

For the purpose of performance comparison, same types of analyses have been performed for all models. Analysis types include free vibration (eigenvalue), linear static, nonlinear static (pushover) and linear/nonlinear time history. Loading conditions and deliverables of these analyses are summarized before the presentation of simulation results.

Free vibration analysis is performed to determine a model's natural periods or natural frequencies. For 3D models, natural periods/frequencies of the first six modes are recorded. These can cover the first two of the translational modes in the long and short directions as well as torsional modes about the vertical axis and may in reality be coupled across all these direcitons. For the 2D models, the possible deformation modes are much simpler, so only the first two modes are recorded - both of which are lateral modes. Also, corresponding eigenvectors are stored for plots of the (vibration) modes shapes. In the appendices, the first two mode shapes are always plotted. Another usage of the natural frequencies is the formulation of the Rayleigh damping matrix in the time history analysis.

Linear and nonlinear static (pushover) analyses are performed after eigenvalue (free vibration) analysis. A major goal of linear static analysis, being the simplest and cheapest one, is to determine the linear stiffness of the model. Any type of nonlinearity is missing in this analysis, making it the least expensive computationally – and typically the only model used in many designs. Of course, the cost is that its prediction of response tends to be less reliable without empirical correction. The linear static results can also be used as benchmarks for comparison with pushover analysis as well. The selected lateral load of the linear static analysis is the archetype building's equivalent lateral force with a total design base shear (as documented in (Madsen et al. 2011)) of 11,061 lbf (49.2 kN), and whose magnitude and distribution is determined per ASCE 7-10 (American Society of Civil Engineers 2010). The gravity load is the weight of mass at specific locations, and has a total of 77585 lbf (345.1 kN) (Madsen et al. 2011) for all models consistent with the

design and testing. The distribution of gravity and lateral load between two levels is documented in Table 5-2.

Table 5-2: Distribution of lateral load in static analysis

Level	Weight,W (lbf)	Lateral force, F (lbf)
Roof	32451	6524
Floor	45134	4537

Pushover analysis is the most complicated form of static analysis. From a pushover analysis, the nonlinear response of the building's base shear vs. lateral drift/deflection can be determined along with the building's lateral capacity and corresponding roof drift (roof displacement u_2 or v_2 divided by full height 2h). Pushover analysis offers an insight into the structure's full design behavior, at least from a static perspective. Available nonlinear response models of structural and nonstructural components are applied, and P-Δ effects are included. As for its implementation in OpenSees, material models such as EPP and Pinching4 are adopted to handle material nonlineairty, and the corotational transformation is utilized to handle the P-Δ effect, i.e. geometric nonlinearity. Since the backbone curve of the Pinching4 material has a post-peak drop, loading in the pushover analysis is set as displacement control. The displacement control in OpenSees requires a nominal lateral load and the targeted displacement is met by scaling the load. Equivalent lateral force of the design base shear in Table 5-2 is applied again in pushover analysis. There is no modification of gravity load from the linear analysis.

Linear and nonlinear time history analysis can generate the model's response of drift/displacement, element force, and nodal acceleration by exciting from one, two or three axes. Differences between linear and nonlinear time history analysis are the

application of linear vs. nonlinear material model, and inclusion of the P-Δ effect. Material and geometrical nonlinearity modify the form of the stiffness matrix while the mass matrix is determined by the distribution of lumped mass. The damping matrix in the equations of motion takes the form of Rayleigh damping by using the first two natural frequencies (McKenna 2011) and a 5% damping ratio. Test data suggest the damping ratio in reality could be larger, especially after the initiation of nonlinear response at higher excitation levels. However, the value of 5% is still chosen to keep it uniform for all cases and matches the development of the response spectrum. Nonetheless sensitivity to this assumption could be considered in the future.

As detailed in Chapter 4, unscaled far-field Canoga Park (CNP) and near-field Rinaldi (RRS) ground motion records from the Northridge earthquake in 1994 are taken as representative of a DBE-level and a MCE-level excitation of the archetype building due to the close match between their response spectra and the design spectrum at the approximate fundamental period of the building. The original ground motions and reduced scale factors are applied in extensive time history analyses (as in the testing). Multi-axial excitation is also implemented in the 3D analysis models. Information regarding the excitations is tabulated in Table 5-3 and Table 5-4 for 2D and 3D models respectively. The amount of output data from the time history analysis is abundant, to simplify oftentimes peak response values are identified through post-processing and are compared among different excitation levels and models at different construction phases. Only a fraction of the post-processed output data are addressed in this chapter, more complete results are included in the appendices.

Table 5-3: Summary of excitations in time history analysis of 2D models

Excitation Name	Ground Motion	PGA long (g)	PGA short (g)
EQ_2D_1axis_1	CNP 16%	0.067	0.057
EQ_2D_1axis_2	CNP 44%	0.185	0.157
EQ_2D_1axis_3	CNP 100%	0.420	0.356
EQ_2D_1axis_4	RRS 16%	0.132	0.078
EQ_2D_1axis_5	RRS 44%	0.363	0.214
EQ_2D_1axis_6	RRS 100%	0.825	0.486

Table 5-4: Summary of excitations in time history analysis of 3D models

Excitation Name	Ground Motion	PGA long (g)	PGA short (g)	PGA up (g)
EQ_3D_3axis_1	CNP 16%	0.067	0.057	0.078
EQ_3D_3axis_2	CNP 44%	0.185	0.157	0.215
EQ_3D_1axis_1	CNP 100%	0.420	0	0
EQ_3D_1axis_2	CNP 100%	0	0.356	0
EQ_3D_2axis_1	CNP 100%	0.420	0.356	0
EQ_3D_3axis_3	CNP 100%	0.420	0.356	0.489
EQ_3D_3axis_4	RRS 16%	0.132	0.078	0.134
EQ_3D_3axis_5	RRS 44%	0.363	0.214	0.367
EQ_3D_3axis_6	RRS 100%	0.825	0.487	0.834

5.3 Comparison of seismic response across models at different phases

5.3.1 Comparison of free vibration analysis results

Free vibration analysis provides a certain number of natural periods/frequencies and vibration mode shapes. Given a fixed seismic mass (although its distribution changes at different phases), natural periods are directly related to lateral stiffness of the FE model.

As discussed in Chapter 4, A-models with sophistication for modeling gravity framing and sheathing of the gravity walls create generally desirable predictions for natural periods/frequencies in comparison with tests. An examination of the broader modeling scope reveals sources of lateral stiffness in CFS-framed buildings and proper ways of modeling these sources.

Figure 5-1 presents the appearance of several FE models, from a simpler 3D P-model to 2D and 3D A-models of the Phase 1 building. The first natural period in the translational mode is listed below Figure 5-1. A-models in Figure 5-1(c) and Figure 5-1(d) offer much better prediction of the first natural period T_1 in the short direction to the test value of 0.36 s than models in Figure 5-1(a) and Figure 5-1(b). Predicted T_1 in the long direction by A-models in Figure 5-1(c) and Figure 5-1(d) are also very close to reality (see Appendix H and Appendix K). A key feature of these more detailed models is the inclusion of the full-length ledger, or carrier track, and the header members above openings in the long directions and diaphragm joists in the short direction. The ledger, with much wider flanges and higher depth than other members, links shear wall and gravity framing together laterally and significantly increases the building's lateral stiffness as a system. Once the modeling of ledger and gravity framing is properly handled, the only difference of diaphragm modeling (rigid vs. semi-rigid) between these two models (A1-3D-RD-a with rigid diaphrams and A1-3D-SD-a with semi-rigid diaphragms) does not have a major impact on the result of free vibration analysis (difference in T_1 less than 3%).

The natural period of the same mode predicted by the simplest 3D model, P-3D-RD-b (Figure 5-1(a)), is twice that of the high-fidelity models (A1-3D-RD-a and A1-3D-SD-a). This is an increase of the model stiffness by almost 400%. Clearly, the P-3D-RD-b model misses the ledgers and gravity framing – but design ignores the impact of these factors too. In addition, consistent with design, the stiffness of the shear walls is calculated using the shear force and deflection at 40% of the shear walls' capacity in a typical P-model.

The simplest A-model, A1-3D-RD-c, is shown in Figure 5-1(b) - being the single A-model that employs shear walls as the only LFRS, A1-3D-RD-c is closest to the 3D P-models. However, the total mass of A1-3D-RD-c is 92% of P-models (seismic weight 77.5 kips (344.7 kN) as designed, see (Madsen et al. 2011))), since the value has been adjusted after measuring the real building (the realized mass in Phase 1 building, also see Section 3.7). The initial stiffness in A1-3D-RD-c is performed at 20% of the shear walls' capacity, making it closer to the real elastic stiffness of the building (as opposed to 40% in the P-models). Shear anchors on the bottom tracks of the shear walls are modeled as well in the A-model. The combined effect makes the natural period drop from 0.66 s of P-3D-RD-b model to 0.45 s. Then, the inclusion of ledger and gravity framing, even unsheathed, again doubles the lateral stiffness of the model from A1-3D-RD-c to A1-3D-RD-a model. Another interesting observation is that the first natural period will be a torsional mode if the ledgers and gravity framing are missing in the 3D models (e.g. P-3D-RD-b and A1-3D-RD-c models in Figure 5-1), and this further demonstrates the importance of the inclusion of these two structural components.

Figure 5-1(e) to Figure 5-1(h) are high-fidelity 2D models of four wall lines at Phase 1. The modeling of diaphragm has no role in these 2D models. The 2D models may be viewed as the case of flexible diaphragms in which the behavior of wall lines are totally decoupled. However, natural periods of individual wall lines can deviate greatly from the building's periods since the distributions of shear walls and gravity walls (bare framing in Phase 1) are not uniform in the building. The first natural period of the North elevation is only 58% of the South elevation due to the large difference in the area of shear walls,

even though their spans are identical (49.75 ft (15.2 m)). Note that the shear walls are not uniformly the same length or uniformly placed along the wall lines; neither is the gravity framing. The result is the center of stiffness and center of mass are not aligned. Therefore, the diaphragm potentially matters in the response. The absence of the stiffness of diaphragms itself and the interplay between walls lines in 2D models is another source of the discrepancy in natural periods between 2D and 3D models.

Modeling the Phase 2 response of building is more involved than Phase 1. Figure 5-2 provides a graphical depiction of the additional complexity that must be introduced into the model – including the additional lateral stiffness from OSB sheathed gravity walls (note additional diagonal truss elements in comparison with Figure 5-1(c) and Figure 5-1(d)) in Phase 2b and interior gypsum sheathing of whole wall lines in Phase 2c (Schafer 2015). Stiffness and backbone curves of these additions are developed from fastener-based models, as detailed in Chapter 3. The most advanced model (A2d-3D-RD-a) also includes internal partition walls sheathed by gypsum boards from both sides. The first natural periods of the 3D models are tabulated in Table 5-5. As shown in the table, the addition of non-structural components to high-fidelity models in Phase 1 can increase the lateral stiffness by about 300% and thus reduce the natural periods by 40%. The large increase of lateral stiffness from the shear wall only models (i.e., A1-3D-RD-c) suggests "the engineering assumption of separation in response between shear walls and gravity walls is false, even for the bare structural system (Schafer 2015)."

Close match between natural periods of the high-fidelity models and the archetype building at various construction phases, as shown in Chapter 4, has confirmed our consideration on the important but previously overlooked role of gravity systems and non-structural components in lateral force resistance and validated our method to predict their lateral stiffness. Figure 5-3 is an augmented graphical comparison of natural periods between simulation and test, with the P-3D-RD-b model included (labeled as 'Phase 0' on the horizontal axis). The figure intuitively presents the drastic increase of lateral stiffness between models at different phases, and shows how much the state-of-practice model, based on design standards and engineering assumptions, deviates from advanced models and reality. Even though the author did not model DensGlass installed to the building only at Phase 2e or staircases at Phase 2d, the natural periods of the most advanced A2d-3D-RD-a model (0.17 s, long direction and 0.22 s, short direction) are comparable to test predictions of the complete building (0.15 s, long direction and 0.26 s, short direction).

Table 5-5: Comparison of 3D FE models' first natural periods of lateral modes

Model	P-3D-RD-b	A1-3D-RD-a	A1-3D-SD-a	A2b-3D-RD-a	A2b-3D-SD-a	A2c-3D-RD-a	A2c-3D-SD-a	A2d-3D-RD-a
T_1, long (s)	0.50	0.29	0.30	0.21	0.22	0.17	0.18	0.17
T_1, short (s)	0.66	0.33	0.32	0.28	0.28	0.23	0.23	0.22

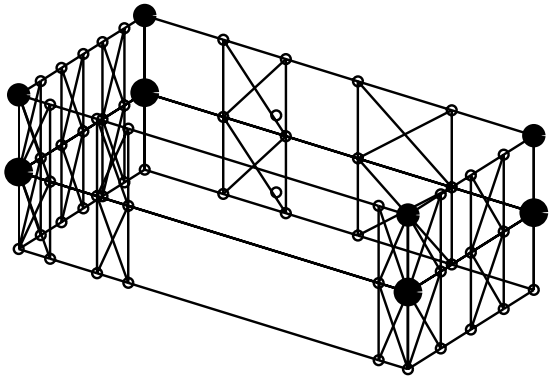

(a) Shear wall only, P-3D-RD-b
T_2 = 0.66 s, short

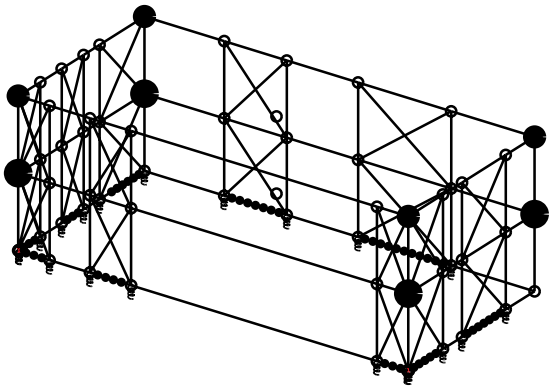

(b) Shear wall only, A1-3D-RD-c
T_2 = 0.45 s, short

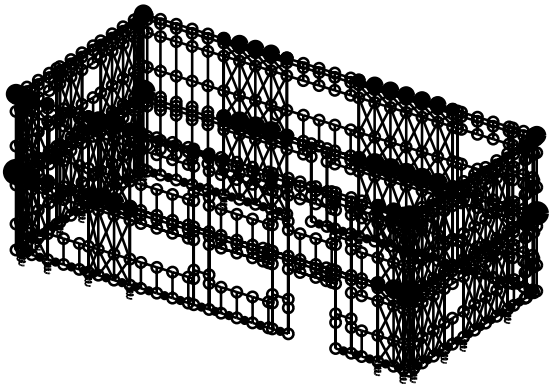

(c) Shear wall with gravity framing, A1-3D-RD-a
T_1 = 0.33 s, short

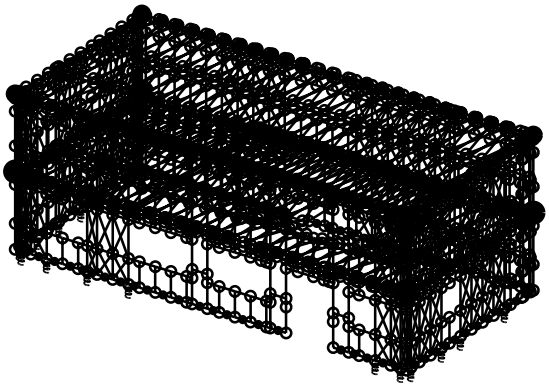

(d) Shear wall with gravity framing, A1-3D-SD-a
T_1 = 0.32 s, short

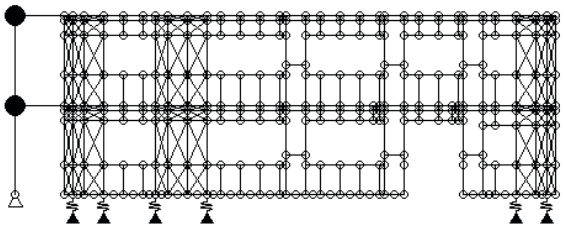

(e) South elevation, A1-2D-a
T_1 = 0.43 s

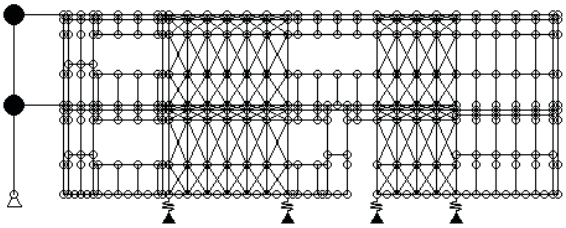

(f) North elevation, A1-2D-a
T_1 = 0.25 s

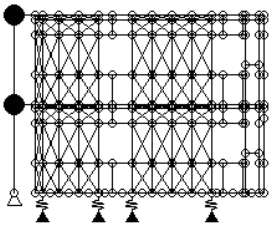

(g) East elevation, A1-2D-a
T_1 = 0.34 s

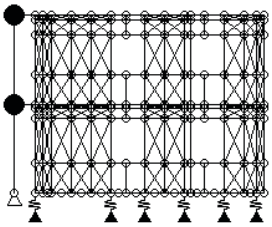

(h) West elevation, A1-2D-a
T_1 = 0.36 s

Figure 5-1: OpenSees models of the CFS-NEES Phase 1 archetype building with their first natural periods of translational modes (the subscript indicates the order of that mode among all modes)

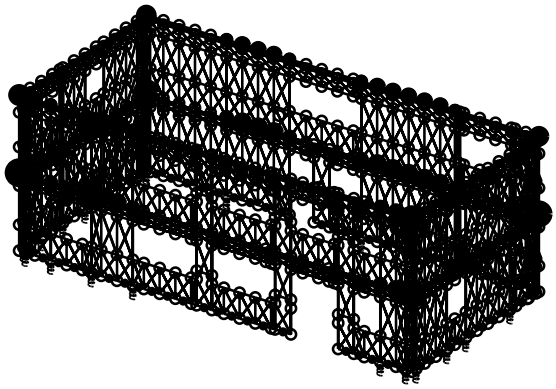

(a) A2b-3D-RD-a & A2c-3D-RD-a

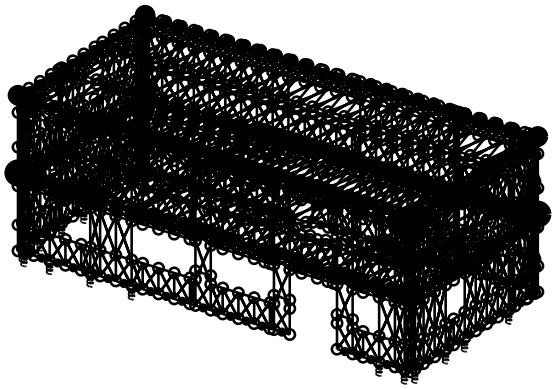

(b) A2b-3D-SD-a & A2c-3D-SD-a

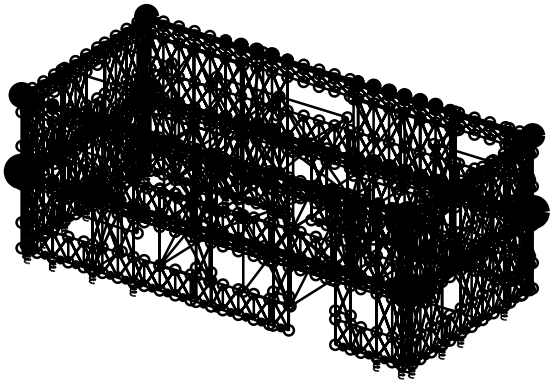

(c) A2d-3D-RD-a

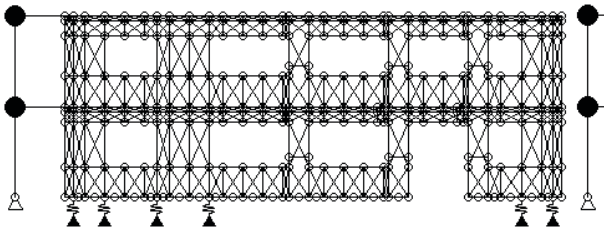

(d) South elevation, A2b-2D-a & A2c-2D-a

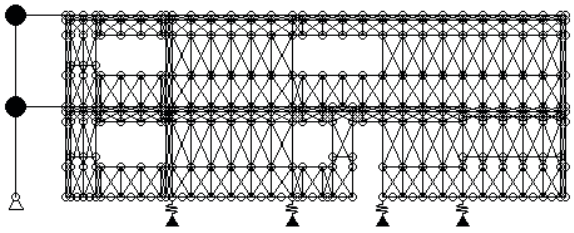

(e) North elevation, A2b-2D-a & A2c-2D-a

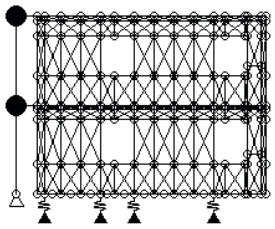

(f) West elevation, A2b-2D-a & A2c-2D-a

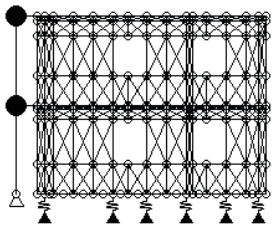

(g) East elevation, A2b-2D-a & A2c-2D-a

Figure 5-2: OpenSees models for building analysis at Phase 2b to Phase 2d

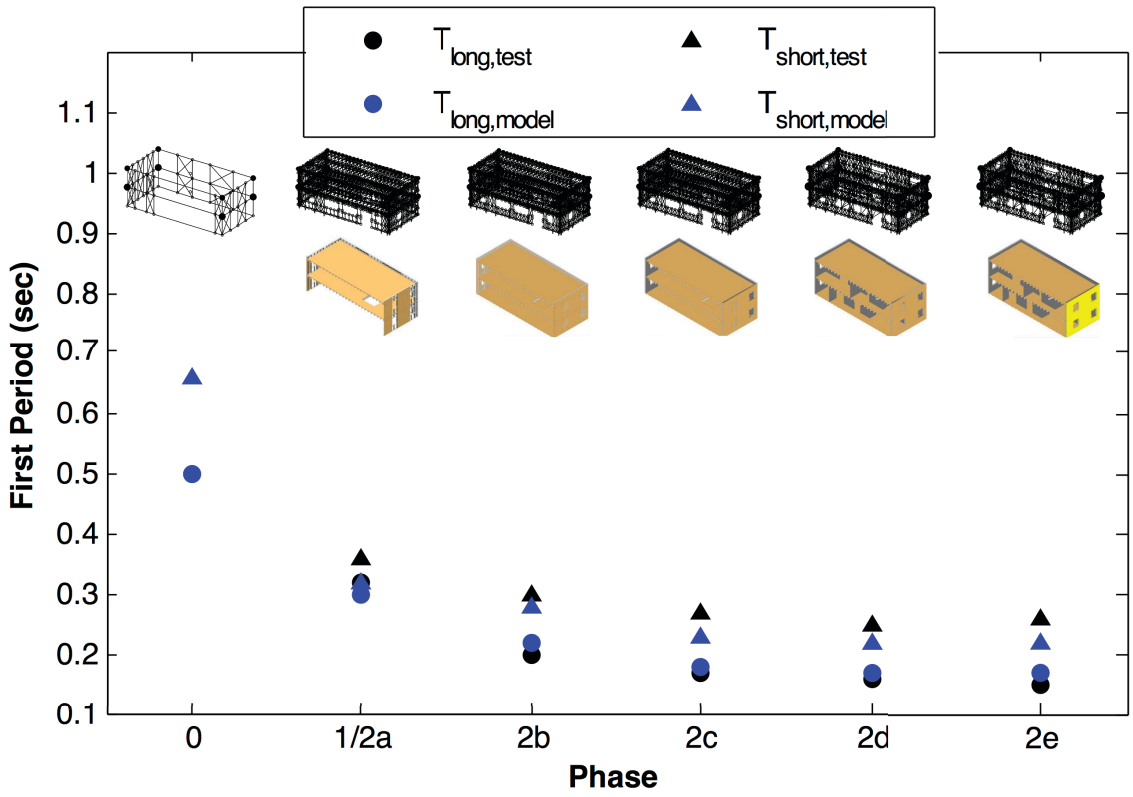

Figure 5-3: Comparison of the first mode period in long and short direction between buildings and models

5.3.2 Comparison of static analysis results

Linear static analysis is simple but can create an estimation of the model's lateral stiffness. In this research, the lateral stiffness is estimated by calculating the slope of the straight line of total base shear vs. roof center deflection in the long and short direction. The calculated lateral stiffness is tabulated in Table 5-6. For 2D models, the stiffness of stiffer wall lines in the long and short directions (North and East wall lines) is picked up and filled in the table. Note that the stiffness of wall lines changes as the construction proceeds, so North wall line is about 87% to 200% stiffer than South wall line and East wall line is about 7% to 20% stiffer than West wall line at various phases.

This table confirms our observation from free vibration analysis results in the previous subsection by quantitatively presenting the increase of lateral stiffness from P-models to A-models with additional complexity at each construction phase. Similar to the prediction above, 3D A-models at Phase 1 with ledgers and bare gravity steel framing are already 400% stiffer than 3D P-models. The stiffness of the A2d-3D-RD-a model with the most nonstructural features is about three times larger than the Phase 1 A-model and is thirteen times larger than P-3D-RD-b model. The table also explicitly shows that 2D models are weaker than 3D models for the aforementioned reasons and the discrepancy of stiffness between rigid diaphragm and semi-rigid diaphragm models is quite small. In other words, the stiffness of semi-rigid diaphragms in 3D models is large, presumably close to the effect of rigid diaphragms.

Table 5-6: Comparison of normalized lateral stiffness of FE models of the CFS-NEES archetype building*

Option	P-2D-b[1]	P-3D-RD-b	A1-2D-a[1]	A1-3D-RD-a	A1-3D-SD-a	A2b-3D-RD-a	A2b-3D-SD-a	A2c-3D-RD-a	A2c-3D-SD-a	A2d-3D-RD-a
Stiffness, long	0.21	0.26	0.69	1.00	1.00	1.93	1.93	3.01	2.96	3.39
Stiffness, short	0.11	0.17	0.38	0.88	1.00	1.21	1.34	1.93	1.74	2.26

1: The stiffer wall line long/short direction is chosen: North for long direction and East short direction
*: Lateral stiffness of A1-3D-SD-a model is 72.2 k/in in the long direction, and 63.3 k/in in the short direction.

Nonlinear static analysis results, i.e., pushover curves in the long and short direction of the various models, as shown in the appendices for each model, are collected and presented together in Figure 5-4. The model's name and the loading direction is attached at the end of each curve. Since wall lines are independent in 2D analyses, the summed base shear of two facing wall lines at the same deflection level is used in the plot, similar to the analogy of parallel springs. Pushover curves of various models in same direction

(long and short respectively) are grouped together and presented in Figure 5-4(b) and Figure 5-4(c) for clarity.

The figure is quite informative in that it provides the nonlinear shear-deflection response of each model; peak capacity, stiffness, and drift level of failure can be compared graphically among all models. Clearly, the building's capacity increases significantly from P-models to A1-models because of the adoption of test-based shear wall capacity instead of code-based capacity. The capacity of bare steel gravity framing also has its contribution. Note that the studs are modeled with EPP material, but considering their design buckling strength in A1-models and above (see Section 3.4). The building's capacity keeps increasing as additional sheathing and partition walls are introduced. At the end of the model tree, A2d-3D-RD-a model's lateral capacity is close to five times the capacity of simplest P-3D-RD-b model.

To be more direct, the capacities of the models in Figure 5-4 are tabulated in Table 5-7. The amount of capacity increase between phases is then calculated. The capacity of the most advanced A2d-3D-RD model is 4.83 times that of the capacity of the P-3D-RD-b model in the long direction, and 4.16 times in short direction. Apparently, the amount of capacity growth is different in the two directions. The most significant growth is found after the introduction of exterior OSB sheathing on gravity walls in the Phase 2b models. This increase can be as much as 54% (rigid diaphragm) or 47% (semi-rigid diaphragm) from Phase 1 models in the long direction. As shown in Table 5-8, the area of gravity wall sheathing is 50% and 47% of the total area in the North and South elevation and that

area is 1.35 and 1.88 times of the shear wall sheathing area respectively. The large percentage of gravity sheathing helps to explain this considerable growth in capacity. For the short direction, the capacity increase from Phase 1 to Phase 2b is about 15% due to the fact the gravity sheathing is only about 1/3 of the shear wall sheathing for the East and West elevations. The capacity growth from Phase 2b to Phase 2c is about 20% for all models since the total area of sheathing doubles from Phase 2b to Phase 2c, but with much weaker gypsum board than OSB. The additional amount of interior partition walls in Phase 2d not only contributes to the lateral stiffness, but is predicted to increase the lateral capacity by about 20% as well.

Comparison of capacities can also be done between models with different diaphragm options. All other factors being the same, rigid diaphragm model capacity is less than 10% smaller than semi-rigid diaphragm models in the long direction, and about 20% smaller in the short direction. The figure and the table also indicates that the capacity of a 2D model (i.e., flexible diaphragm option) is less than any 3D model at the same phase since the interplay between wall lines is missing in 2D models and 2D analysis, and thus the weakest wall line controls.

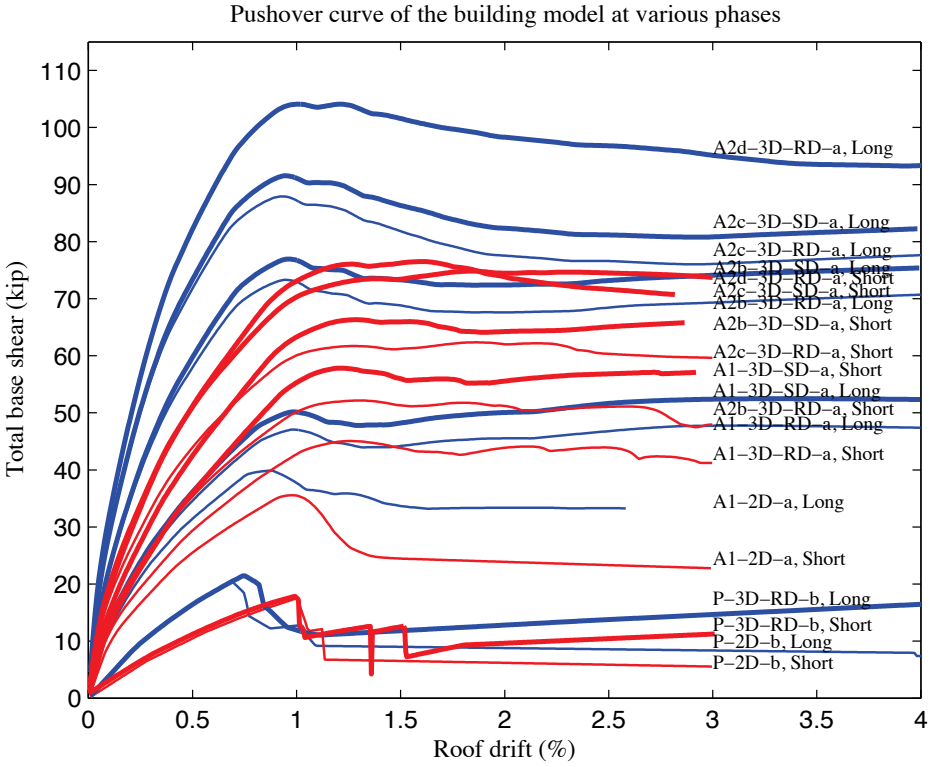

(a) Long and short directions

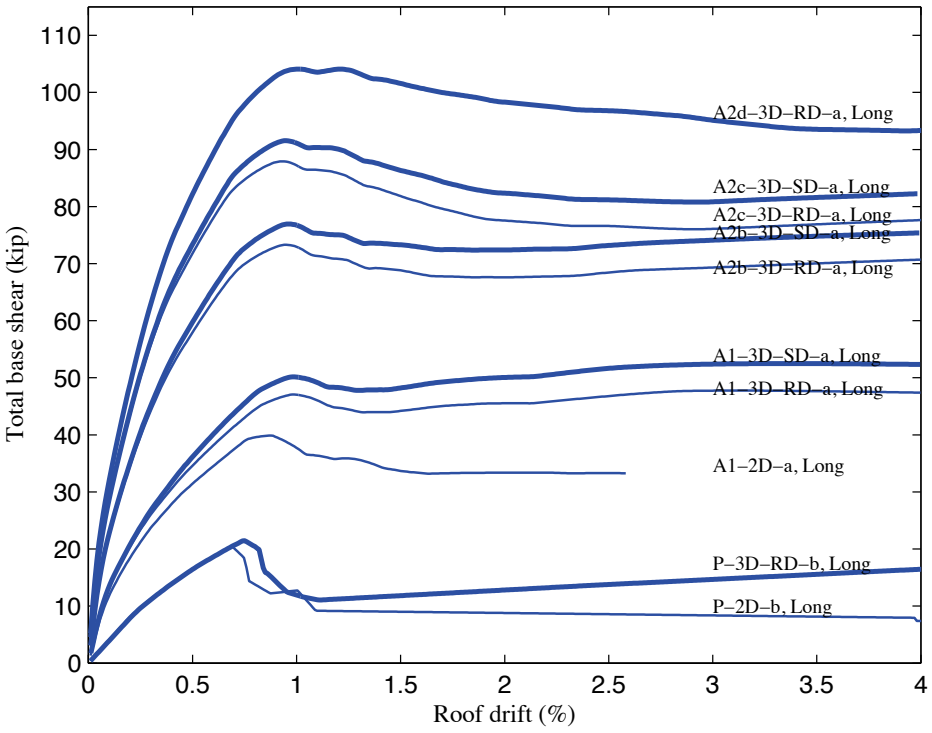

(b) Long direction

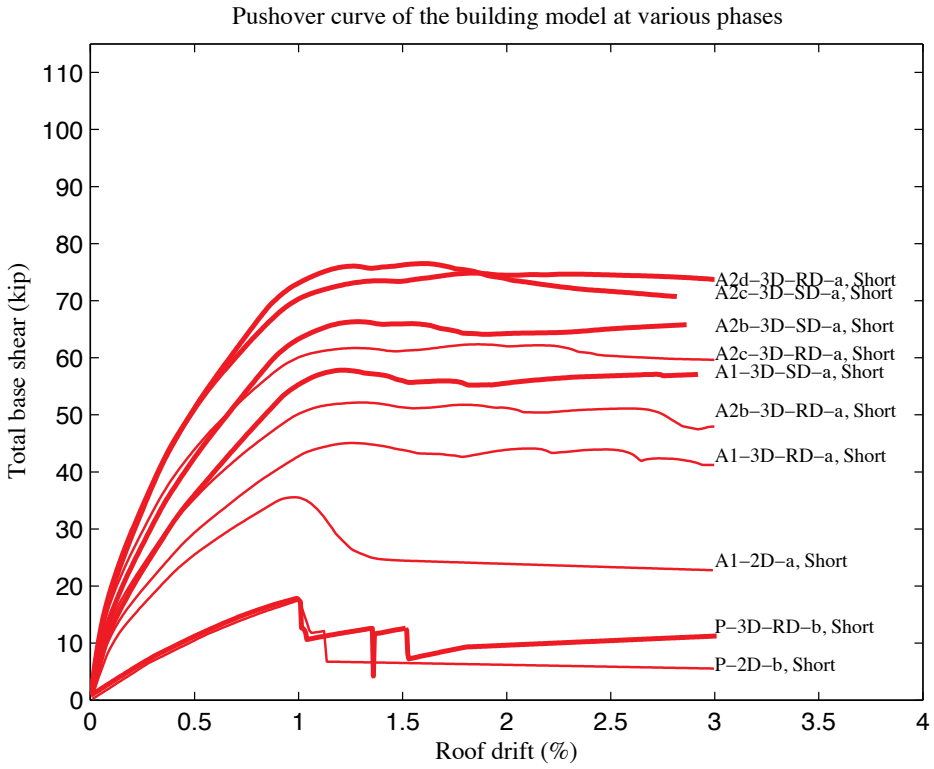

(c) Short direction

Figure 5-4: Comparison of pushover curves in long and short direction among models at various phases

Table 5-7: Comparison of normalized lateral capacity of FE models of the CFS-NEES archetype building*

Option	P-2D-b	P-3D-RD-b	A1-2D-a	A1-3D-RD-a	A1-3D-SD-a	A2b-3D-RD-a	A2b-3D-SD-a	A2c-3D-RD-a	A2c-3D-SD-a	A2d-3D-RD-a
Capacity, long	0.39	0.41	0.76	0.91	1.00	1.40	1.47	1.68	1.74	1.98
Capacity, short	0.30	0.31	0.62	0.78	1.00	0.90	1.15	1.08	1.32	1.29

*: Lateral capacity of A1-3D-SD-a model is 52.5 kips/in the long direction, and 57.8 kips/in the short direction.

Table 5-8: Building components by percent of total wall area (modified version of (Peterman 2014))

	AREA (ft^2)					PERCENT (%)			
Wall	**Total**	**Opening**	**Sheathed**	**Shear Wall**	**Gravity Wall**	**Opening**	**Sheathed**	**Shear Wall**	**Gravity Wall**
South	958	273	685	243	442	28%	72%	25%	47%
West	443	53	390	294	96	12%	88%	66%	22%
North	957	129	828	358	470	13%	87%	37%	50%
East	443	53	390	261	129	12%	88%	59%	29%

Analysts can also identify the roof drift level at peak capacity from pushover curves in Figure 5-4. In the long direction, the predicted roof drift is less than 1%, but it gets close to 1% once the gravity framing is modeled in Phase 1 and it gets even closer after more sheathing and other nonstructural components are included in later phases. Similar trends are also seen in the short direction, but the drift level at peak capacity is a bit larger than 1% for Phase 1 models and it is about 1.5% for Phase 2d model. The shape of a pushover curve is also of great interest. Pushover curves of the P-models have a clear post-peak drop of the building's lateral capacity as defined in the backbone curve of the Pinching4 material since shear walls are the only LFRS in those models. However, as additional elements added are capable of sustaining lateral loads starting from the A1-models, the post-peak drop is alleviated and the pushover curves of A1-3D-RD-a and A1-3D-SD-a models are much flattened. Once more sheathing is added as in Phase 2b, etc., the pushover curves more closely resemble the backbone curve of the Pinching4 material models since all sheathings (OSB on shear walls, OSB on gravity walls, gypsum on all walls and interior partitions, etc.) are characterized by Pinching4 material with the same amount of post-peak drop on their backbone curves.

5.3.3 Comparison of time history analysis results

With the excitations in Table 5-3 and Table 5-4, hundreds of linear and nonlinear time history analyses of developed models have been performed. Appendices A to S provide full details of post-processed results including peak story acceleration relative to the ground, story drift, base shear, and hold down axial forces. A condensed version of the results is presented in Table 5-9. Simulation results generated from 100% 3-axis Canoga

Park excitation (i.e. at a DBE-level) for Phase 1 and 100% 3-axis Rinaldi excitation (i.e. at an MCE-level) for Phase 2e are tabulated and compared among models described in Table 5-1. In the table, hysteretic models are equivalent to Pinching4 models; elastic models use the first slope of the Pinching4 backbone as the elastic stiffness and are designed for linear time history analysis.

The upper half of Table 5-9 focuses on the comparison between the models' prediction and actual response of the Phase 1 building tested with Canoga Park excitation. The experimental response under 100% CNP (DBE-level) is summarized, along with experimental response predictions that are scaled from lower-level elastic tests (see first three rows in Table 5-9). Although the Phase 1 building returns to straight and has little visible damage (see (Peterman 2014) for more details) after 100% CNP (DBE-level) ground motion, it does experience inelastic deformations – approximately 25% increased drift and foundation forces. None of the P-models in row 4 to 7 give meaningful prediction of the tested building's response. The elastic P-models have a grossly under-predicted stiffness, which for this model results in higher displacements, and the hysteretic P-models (Pinching4 with capacity and stiffness based on AISI S213 (American Iron and Steel Institute 2009)) over-predict the drifts and forces by about 200% to 400% (Schafer 2015). The state-of-the-art (A-) models have approximately the correct initial stiffness (see previous sections for comparison of natural periods and elastic stiffness) and thus the elastic model response is similar to the response of scaled lower-level elastic tests in terms of peak load cell (hold down) force, but the peak story drift is underestimated. The value of a 3D model is exhibited in the prediction of the hold down

forces – the 2D model over predicts the foundation demands. In general the elastic A-model is inadequate for safe prediction of the response of Phase 1 building because of the nonlinear behavior observed in tests. ("Obviously, seismic response modification coefficients are used to correct such analyses when used in design; here the interest is in basic model performance (Schafer 2015).") The nonlinear A-models, utilizing calibrated Pinching4 shear wall models and the complete gravity framing system, perform reasonably well. The 2D A-models over-predict drift by ~50% at maximum and the 3D A-models by about ±30% if the diaphragm is properly modeled. Foundation forces are under-predicted by 45%. The underestimation of the hold down forces indicates that there may be other vertical load paths in the real structure that do not exist in the model. In particular, compression bearing paths from contact at the ends of all studs deserves further consideration. The drift of the floor level in the short direction is consistently underestimated. "In general, the state-of-the-art A-models can reasonably represent the observed behavior in the Phase I testing (Schafer 2015)."

Table 5-9: Summary of modeling options of the CFS-NEES archetype building in performance comparison

Model Building Phase	Model State-of-	Model Type	Dim.	Floor, Roof Diaph.	Drift, long $\Delta u_1/h$ (%)	Drift, long $\Delta u_2/h$ (%)	Drift, short $\Delta v_1/h$ (%)	Drift, short $\Delta v_2/h$ (%)	Hold down F_{HD} (kips)	Base shear $V_{b\text{-}long}$ (kips)	Base shear $V_{b\text{-}short}$ (kips)	$\frac{\lvert\Delta u_1\rvert_m}{\lvert\Delta u_1\rvert_t}$	$\frac{\lvert\Delta u_2\rvert_m}{\lvert\Delta u_2\rvert_t}$	$\frac{\lvert\Delta v_1\rvert_m}{\lvert\Delta v_1\rvert_t}$	$\frac{\lvert\Delta v_2\rvert_m}{\lvert\Delta v_2\rvert_t}$	$\frac{F_{HDm}}{F_{HDt}}$	ID[1]
Phase 1/2a Building response, Canoga Park 100%, 3 directions, DBE level																	
Experiment at 100% Canoga Park					1.18	0.81	0.85	0.56	9.8	-	-	**1.00**	**1.00**	**1.00**	**1.00**	**1.00**	P1S07
Experiment Scaled from Elastic					1.00	0.69	0.62	0.56	8.3	-	-	0.85	0.85	0.73	1.00	0.84	P1S04/0.16
Experiment Scaled from Elastic					0.88	0.75	0.62	0.56	7.8	-	-	0.75	0.93	0.73	1.00	0.79	P2aS04/0.16
1/2a	Practice	Elastic	2D	-	1.70	1.64	1.61	1.75	35.9	59.4	40.8	1.44	2.02	1.89	3.12	3.66	P-2D-b
1/2a	Practice	Elastic	3D	Rigid	1.83	1.68	2.03	-2.16	66.6	69.3	57.7	1.55	2.08	2.39	3.85	6.80	P-3D-RD-b
1/2a	Practice	Hyster.	2D	-	-3.96	-0.65	-4.39	-1.23	11.7	127	28.9	3.36	0.80	5.17	2.19	1.19	P-2D-b
1/2a	Practice	Hyster.	3D	Rigid	5.09	-0.78	-3.57	1.45	14.1	21.0	16.6	4.31	0.96	4.20	2.58	1.44	P-3D-RD-b
1/2a	Art	Elastic	2D	-	0.69	-0.45	-0.51	0.34	16.0	52.1	46.3	0.59	0.56	0.60	0.61	1.63	A1-2D-a
1/2a	Art	Elastic	3D	Rigid	-0.44	-0.31	-0.51	-0.35	9.3	53.9	51.7	0.38	0.38	0.60	0.63	0.95	A1-3D-RD-a
1/2a	Art	Elastic	3D	Semi.	-0.53	-0.21	0.53	0.30	8.1	48.8	58.1	0.45	0.26	0.63	0.54	0.83	A1-3D-SD-a
1/2a	Art	Hyster.	2D	-	1.81	0.52	1.26	-0.59	6.5	51.9	37.0	1.53	0.64	1.48	1.06	0.66	A1-2D-a
1/2a	Art	Hyster.	3D	Rigid	1.40	-0.69	1.15	0.68	5.5	46.4	39.1	1.19	0.86	1.36	1.21	0.56	A1-3D-RD-a
1/2a	Art	Hyster.	3D	Semi.	1.41	-0.53	0.90	0.33	5.0	51.5	41.5	1.19	0.66	1.06	0.59	0.51	A1-3D-SD-a
Phase 2e Building response, Rinaldi 100%, 3 directions, MCE level																	
Experiment at 100% Rinaldi					0.67	0.45	0.72	0.99	7.6	-	-	**1.00**	**1.00**	**1.00**	**1.00**	**1.00**	P2eS09
Experiment Scaled from Elastic					0.69	0.44	1.00	0.69	2.9	-	-	1.03	0.98	1.39	0.70	0.39	P2eS08/0.16
1/2a	Practice	Elastic	2D	-	4.56	-4.18	-2.82	2.56	92.0	107	63.5	6.80	9.28	3.91	2.59	12.1	P-2D-b
1/2a	Practice	Elastic	3D	Rigid	3.17	-3.09	-3.12	-3.13	68.3	126	67.9	4.73	6.88	4.34	3.16	8.99	P-3D-RD-b
1/2a	Practice	Hyster.	2D	-	Analysis failed*									∞		∞	P-2D-b
1/2a	Practice	Hyster.	3D	Rigid	12.14	9.14	-10.7	-3.96	17.3	21.9	18.6	18.1	20.3	14.9	4.00	2.28	P-3D-RD-b
1/2a	Art	Elastic	2D	-	1.14	0.75	1.34	0.88	24.7	92.2	119	1.71	1.66	1.85	0.89	3.25	A1-2D-a
1/2a	Art	Elastic	3D	Rigid	0.91	-0.62	1.17	0.72	25.6	117	117	1.36	1.39	1.63	0.73	3.37	A1-3D-RD-a
1/2a	Art	Hyster.	2D	-	Analysis failed*									∞		∞	A1-2D-a
1/2a	Art	Hyster.	3D	Rigid	Analysis failed*									∞		∞	A1-3D-RD-a
2b	Art	Hyster.	3D	Rigid	1.85	-0.41	-1.01	-0.56	7.8	73.6	42.4	2.76	0.90	1.40	0.57	1.03	A2b-3D-RD-a
2c	Art	Hyster.	3D	Rigid	1.07	-0.37	1.04	0.57	6.9	84.0	53.2	1.59	0.83	1.45	0.58	0.91	A2c-3D-RD-a
2d	Art	Hyster.	3D	Rigid	0.84	-0.34	0.99	0.52	7.0	86.8	61.9	1.25	0.76	1.37	0.52	0.92	A2d-3D-RD-a
1/2a	Art	Hyster.	3D	Semi.	7.30	0.67	-1.19	-0.44	6.5	52.6	48.4	10.9	1.48	1.65	0.44	0.86	A1-3D-SD-a
2b	Art	Hyster.	3D	Semi.	1.64	0.33	1.20	0.38	7.4	77.1	53.5	2.45	0.74	1.66	0.38	0.97	A2b-3D-SD-a
2c	Art	Hyster.	3D	Semi.	1.01	0.25	1.16	0.37	6.9	85.1	64.0	1.51	0.55	1.61	0.37	0.91	A2c-3D-SD-a
2d	Art	Hyster.	3D	Semi.	Model not completed at this time												A2d-3D-SD-a

1: Experimental ID from (Peterman 2014) and Model ID from Table 3-3 in Chapter 3

*: Displacements increase without bound during analysis

A benefit of having reasonable model confidence in the Phase 1 (state-of-the-art) modeling is that additional analyses can be performed and more response quantities are available from the model. For example, the predicted performance of selected shear walls during the 100% Canoga Park excitation is provided in Figure 5-5. “In addition to demonstrating that the modeling of the shear wall into multiple panels (note the many diagonal truss elements in the shear wall of Figure 5-1(c) and (d) vs. Figure 5-1(a) and (b)) is working correctly, the results also indicate how much and which shear walls provide energy dissipation (Schafer 2015).” In addition, as provided in Figure 5-6, the foundation forces and the manner in which the base shear and compression/uplift is carried can be investigated in detail. The distribution of base shear at the time when peak total base shear is recorded is provided in Figure 5-6(a) and highlights the three-dimensional nature of the response, in that the base shear force vectors in the hold downs and anchors are not aligned with the direction of the wall line, and they are not in the same direction even within a single wall. Figure 5-6(b) strengthens this impression from anther perspective, the vertical load path of the building is involved, and the assumption that a pair of hold downs of a shear wall forms a force couple is unrealistic. However, comparison with tests (see Chapter 4) indicates the models still need further refinement in order to exhibit the same amount of coupling in the shear wall response observed in the tests.

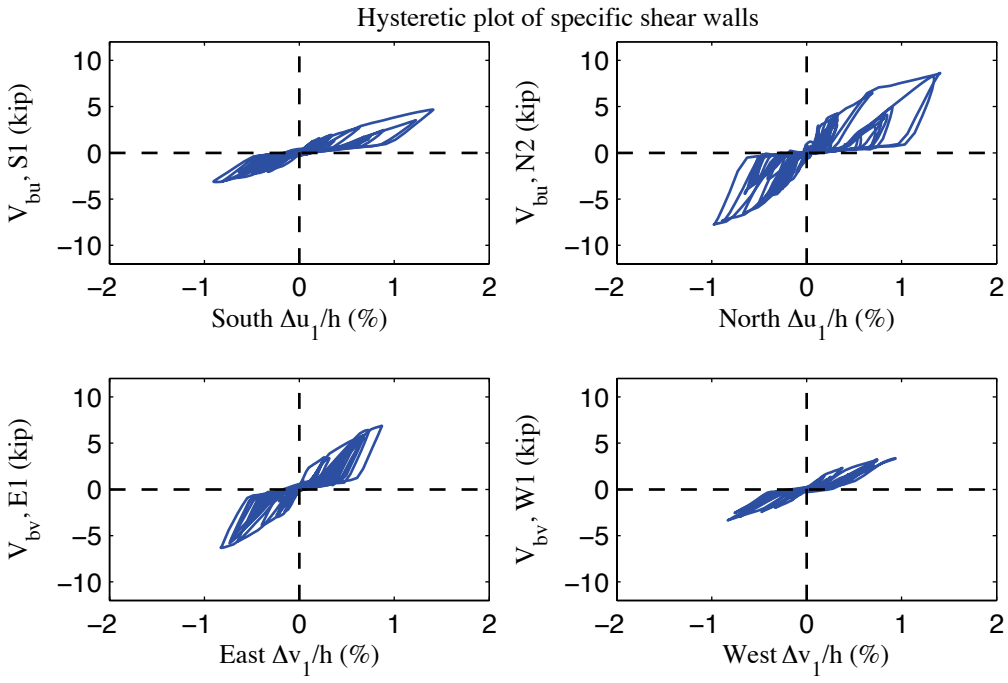

Figure 5-5: A1-3D-SD-a model, hysteretic plot of example shear walls at each elevation, 100% Canoga Park, 3D nonlinear analysis

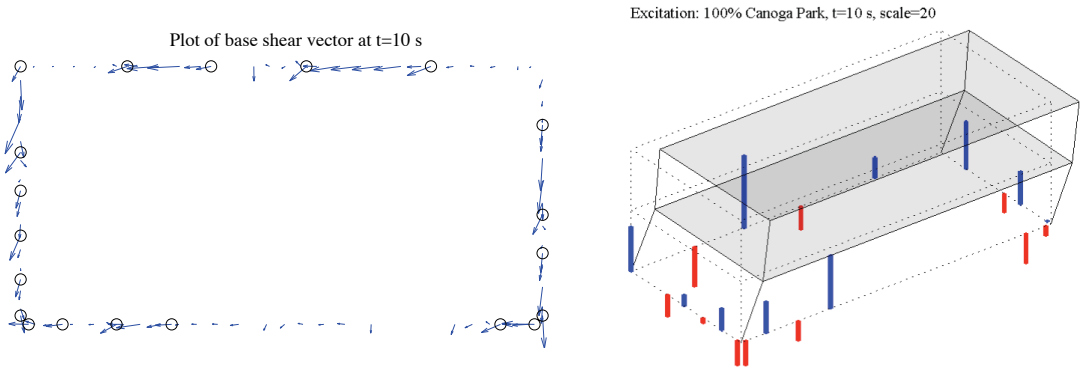

(a) in-plane (shear) force (b) out-of-plane (vertical) force

Figure 5-6: A1-3D-SD-a model, foundation forces, 100% Canoga Park, 3D nonlinear analysis (maximum anchor/hold down base shear is 2.35 kips and max hold down tensile force is -4.63 kips)

Elastic and nonlinear time history response of the OpenSees models essentially consistent with Phase 2e testing at an excitation of 100% Rinaldi is provided in the lower half of Table 5-9. The standard state-of-the-practice assumption that only the shear walls contribute in the lateral system, i.e. Figure 5-1(a), is grossly conservative (Schafer 2015).

"Essentially all of the state-of-the-practice (P-) models predict failure of the building due to the excessive drift. That is, for a building that experienced no residual drift and only minor damage under an earthquake excitation consistent with the MCE level, even fairly robust P-models predict building collapse (Schafer 2015)."

The state-of-the-art (A-) models are better, although improvements would still be beneficial. If the engineer chooses to model the full structural system as assumed in common practice – i.e. shear walls and gravity framing, but ignores all additional phases of construction then this leads to the A1 or Phase 1/2a models (Figure 5-1(c) and Figure 5-1(d)). These A1-models are more accurate than P-models, as confirmed by the comparison of response under DBE-level excitation, but not accurate enough to reasonably predict the observed behavior of the Phase 2e building under MCE-level excitation (Schafer 2015). Inelastic time history analyses for A1 (structural-only) models, whether 2D or 3D, predict excessive drift and collapse of the building, while the recorded peak story drift of the actual building is less than 1%. Once gravity sheathing and other non-structural components are added to model, the model prediction starts to converge toward the real building's response. "A conclusion to be drawn from this is that, in addition to the gravity walls, fire protection, exterior finish, and interior partitions also play a critical role in positively contributing to the observed, successful, lateral performance of the CFS-NEES building (Schafer 2015)."

The state-of-the-art model that includes construction through Phase 2d (A2d-3D-RD-a, Figure 5-2(c)) successfully predicts that the building will survive the Rinaldi 100%

excitation and that story drifts in both the long and the short directions will be less than 1%. The model over-predicts (by 37%) floor level drift but under-predicts roof level drift (by 48%) and hold down forces (by 8%). Compared with the 45% underestimation of peak hold down force from Phase 1 model, the match of hold down force improves since the modeling of gravity walls' sheathing starts at Phase 2b. Additional analyses are discussed in the appendences, and Incremental Dynamic Analysis of this model is covered in the next chapter.

5.4 Discussion and guidelines for modeling a CFS building under seismic loading

It is convenient and useful for engineers to employ a series of assumptions to simply the design process so a preliminary design can be created with less time consumed on modeling and analysis but one that is still able to represent the behavior of the as-built building at a reliable fidelity level. One important goal of the CFS-NEES project, with all its extensive experimental and computational efforts, is to examine the validity of state-of-the-practice design assumptions by state-of-the-art test and modeling outcomes and propose possible improvements for the ultimate goal of a more credible and more efficient design for CFS-framed buildings.

A top-down description of assumptions in CFS-framed buildings starts with the separation between structural and nonstructural systems. Engineers have less control over nonstructural systems and nonstructural additions to structural systems, including OSB sheathing of gravity walls, interior gypsum sheathing for fire protection, interior partition walls, staircases, DensGlass covering, etc. The structural system can be further

categorized as the lateral or gravity systems for the two major load types and little coupling is assumed to be existent between these load paths, particularly for the lateral system. Note, that the LFRS involves shear walls with structural sheathing (OSB herein); however, the structural gravity system is composed of bare (steel only) CFS framing. Further, shear walls in the lateral system are commonly assumed as Type I shear walls in design, assuming each shear wall works individually so the pair of hold downs at the end of chord studs form a force couple to balance the overturning moment from a lateral shear.

From a modeler and/or analyst perspective, these assumptions are evaluated in bottom-up order using simulation data of the various models developed. The assumption of Type I shear wall behavior is examined first, followed by a discussion of the role of gravity walls in lateral force resistance and general modeling insights are presented at the end of the section.

5.4.1 Discussion on Type I shear wall design assumption

The Type I shear wall design assumption states that shear walls are considered totally decoupled, with no consideration of gravity framing and/or window headers etc. in the lateral resistance. The assumption is tested by an examination of its key behavior – i.e. the hold downs are assumed to experience the same amount of tension and compression on two ends of the wall segment.

Hold downs (or load cells in the tests) 5 to 8 are selected and their axial forces are recorded in every nonlinear time history analysis. Locations of those hold downs/load cells are marked in 2D models of the South and West elevations as shown in Figure 5-7. Time history plots of these load cell/hold downs axial forces in two pairs are provided in Figure 5-8. As mentioned in Section 4.3.1, hold down forces due to static gravity load is removed before plotting and the same sign convention with Peterman (Peterman 2014) (negative value for tensile force in the hold down) is adopted. In Figure 5-8(a), for Phase 1/2a the two hold down pairs comprising a shear wall only model (A1-2D-c-S and A1-2D-c-W) follow the Type I shear wall assumption reasonably well, especially load cell 7 and 8 (The model, see Figure 5-7(b) has little choice as the model enforces that the shear walls are decoupled). However, once the gravity system is introduced, even the bare gravity steel framing, the behavior of the hold down pairs on a shear wall does not meet/follow the Type I shear wall assumption – see Figure 5-8(b). As more nonstructural sheathing is added, the difference becomes even more noticeable – see Figure 5-8(c) and Figure 5-8(d). For 2D models, the Type I shear wall assumption is valid only when the gravity system is completely absent in the model.

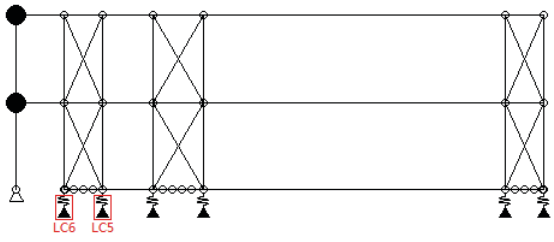

(a) South elevation, A1-2D-c

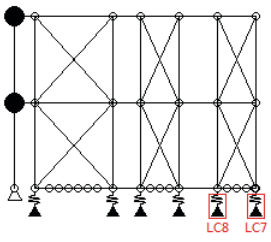

(b) West elevation, A1-2D-c

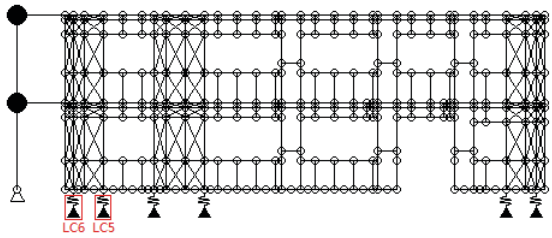

(c) South elevation, A1-2D-a

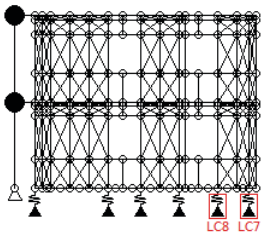

(d) West elevation, A1-2D-a

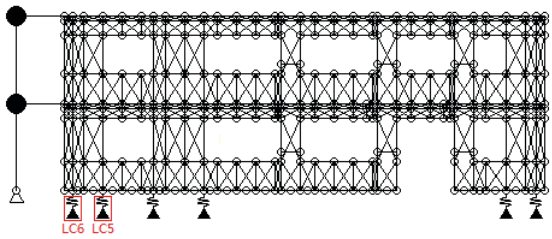

(e) South elevation, A2b-2D-a & A2c-2D-a

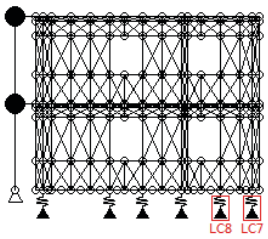

(f) West elevation, A2b-2D-a & A2c-2D-a

Figure 5-7: Locations of load cell 5 to 8 on 2D state-of-the-art models of the CFS-NEES building

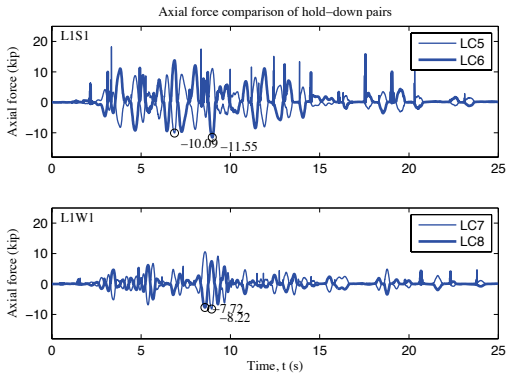

(a) A1-2D-c, Phase 1, shear wall only

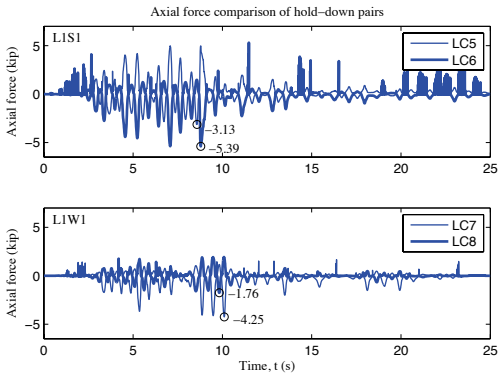

(b) A1-2D-a, Phase 1, shear wall and gravity framing

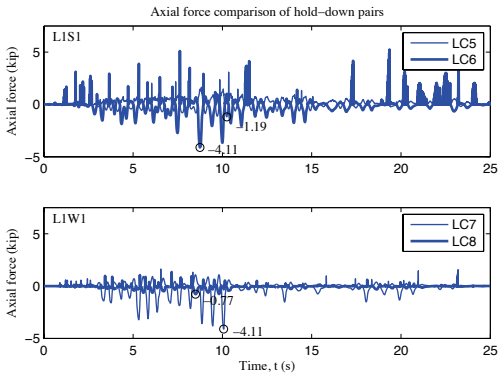

(c) A2b-2D-a, Phase 2b, shear wall and gravity wall

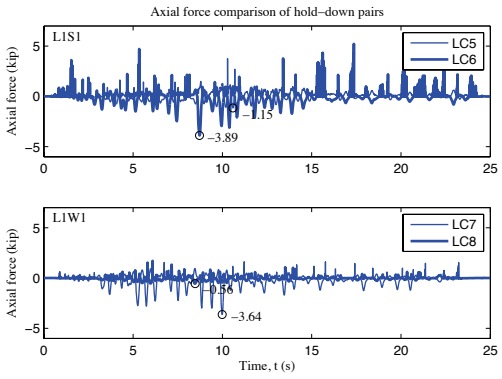

(d) A2c-2D-a, Phase 2c, shear wall and gravity wall

Figure 5-8: Comparison of nonlinear time history plots of load cell 5 to 8 axial forces among 2D models at various phases excited by 100% Canoga Park

The same investigation of hold down forces can be carried out between 2D and 3D models in Phase 1, as illustrated in Figure 5-9 (static forces in hold downs from gravity also removed). The observation with 3D models is, even for the shear wall only A1-3D-RD-c model (as shown in Figure 5-1(b)), the recorded behavior of specified hold down pairs fails the Type I assumption because of the coupling between shear walls induced by the diaphragms (see Figure 5-9(b)). Hold down/load cells in the 3D models with the details of the gravity framing (Figure 5-1(c) and (d)) do not meet the Type I assumption either (see Figure 5-9(c) and (d)), due to the even more complicated 3D coupling between shear walls and the gravity system.

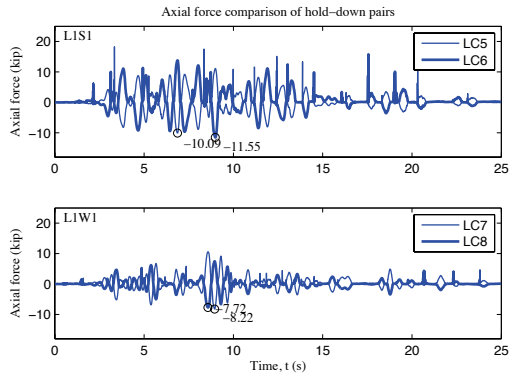

(a) A1-2D-c, 2D, shear wall only

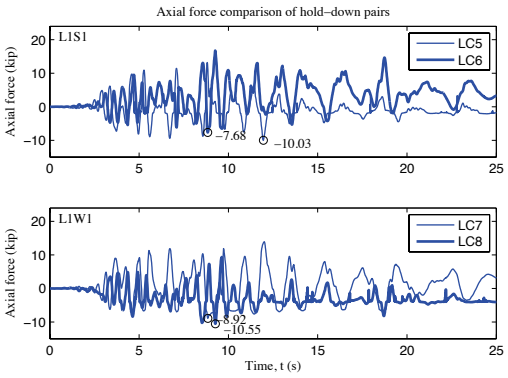

(b) A1-3D-RD-c, 3D, shear wall only

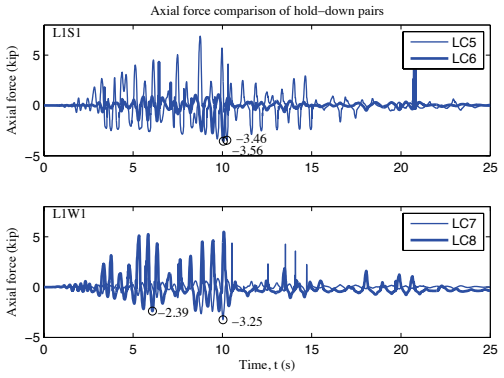

(c) A1-3D-RD-a, 3D, shear wall and gravity framing

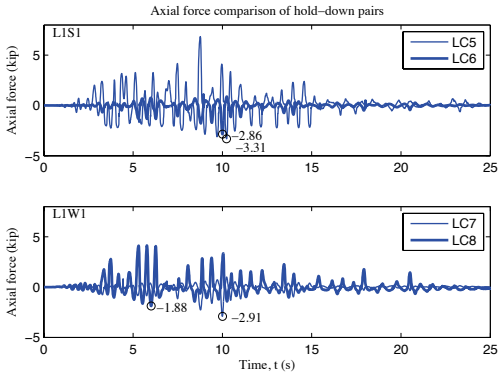

(d) A1-3D-SD-a, 3D, shear wall and gravity framing

Figure 5-9: Comparison of nonlinear time history plots of load cell 5 to 8 axial forces among 2D and 3D models at Phase 1 excited by 100 % Canoga Park

Figure 5-10 offers a comparison of the distribution of hold down load cell force among the 3D models at various construction phases. The subfigures are plotted at the time of peak total base shear. The distribution of force is complex, and 3D models do not meet Type I assumption, even the simplest A1-3D-RD-c model (note the pair of hold down simultaneously in compression at southeast corner ind Figure 5-10(a)). As the model becomes more complicated, greater coupling between the shear walls and the gravity walls in the same or in different walls makes the load cell force distribution largely follow more complex behavior. All of these comparisons lead to a clear conclusion: the assumption of a Type I shear wall is ideal and it only works when there is no coupling between the lateral and gravity system nor 3D coupling between wall lines. This conclusion further supports proper modeling of the gravity system and diaphragms for prediction of building performance.

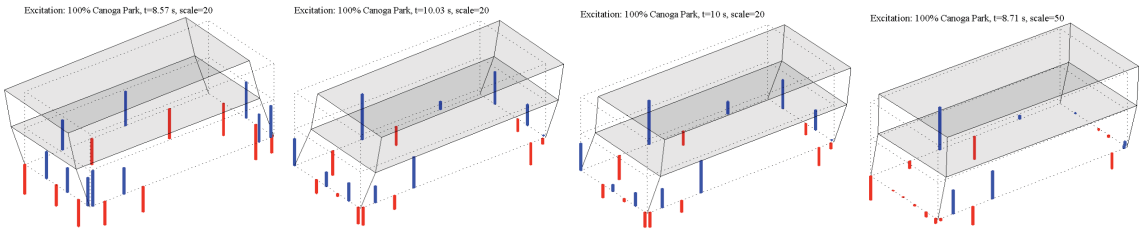

(a) A1-3D-RD-c (b) A1-3D-RD-a (c) A1-3D-SD-a (d) A2b-3D-RD-a

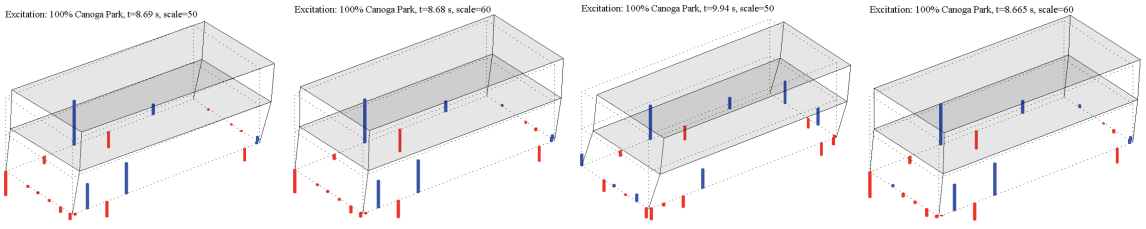

(e) A2b-3D-SD-a (f) A2c-3D-RD-a (g) A2c-3D-SD-a (h) A2d-3D-RD-a

Figure 5-10: Load cell force distributions in 3D A-models at the moment of peak total base shear, excited by 100 % Canoga Park

5.4.2 Discussion on the role of gravity walls in lateral force resistance

Performance comparisons of models vs. tests and across models in Chapter 4 and previous sections of Chapter 5 confirm the author's observation that separation in response between shear walls and gravity walls is a false engineering assumption, even for the structural-only system (Schafer 2015). Moreover, the exterior OSB sheathing of the gravity walls and interior gypsum sheathing of all wall lines, although taken as nonstructural, actually can significantly increase the building's stiffness and capacity. Further, nonstructural details make non-trivial contributions to response. This effect has been quantified in Section 5.3, and the focus here in this subsection is to identify the exact amount of contributions from lateral and gravity systems to a selected metric of the building's performance.

In linear static analysis, the stiffness of the shear wall elements can be set close to zero, so the stiffness of the resulted model is the lateral stiffness of the gravity system only (for 3D models the stiffness of diaphragms and partition walls also counts). Therefore, the stiffness of the lateral system only is determined by subtracting the stiffness of the gravity system from total stiffness. The breakdown of lateral stiffness between shear walls and from the gravity system is provided in Figure 5-11 and Figure 5-12 as bar plots for four elevations (2D models) or long and short directions (3D models). Clearly, the stiffness from the gravity system starts to appear even after the introduction of the bare gravity system in A-models at Phase 1. After the gravity walls are covered by sheathing (Phase 2b), the proportion of the gravity system's lateral stiffness keeps a relatively stable level. The impact of the gravity system on lateral stiffness also differs significantly between

wall lines or elevations, depending at least in part on the ratio of shear wall area over gravity wall area. For example, the largest portion of gravity wall stiffness is observed in the 2D model of the South elevation at Phase 2b, which is about 50%. However, the maximum for the West elevation is only about 15%. In terms of the composition of lateral stiffness, South and North elevations are largely different, but East and West elevations are similar. Diaphragm options in 3D, i.e. rigid vs. semi-rigid, can affect the proportion of shear wall's stiffness to a certain extent in short direction (11.7% difference between A1-3D-RD-a and A1-3D-SD-a), but only a little in long direction (4.1% difference between A2c-3D-RD-a and A2c-3D-SD-a).

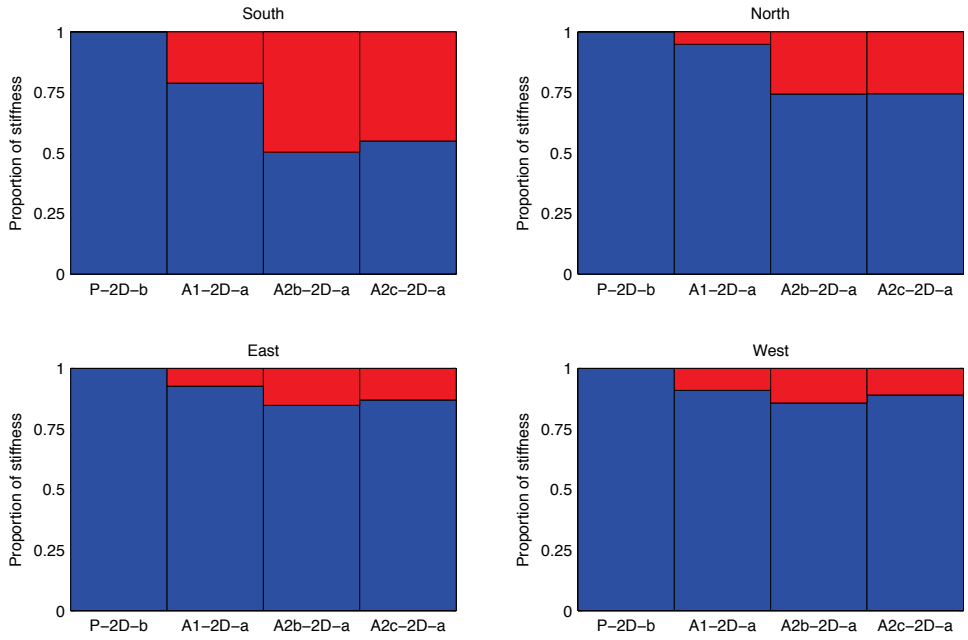

Figure 5-11: Elastic stiffness breakdown between shear walls and gravity walls, 2D models (blue – shear walls, red – gravity walls)

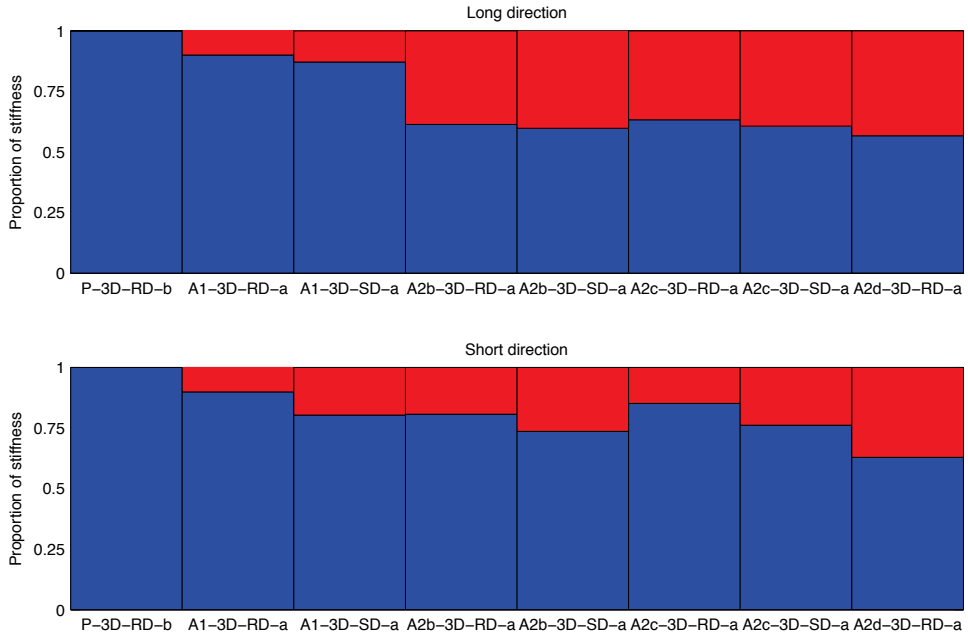

Figure 5-12: Elastic stiffness breakdown between shear walls and gravity walls plus other systems, 3D models (blue – shear walls, red – gravity walls)

The comparison can be enriched by introducing the normalized area of the shear walls and gravity walls as a reference. The percentage of stiffness in Figure 5-11 and Figure 5-12, along with areas of shear wall and gravity walls normalized by the total area of the elevation is tabulated in Table 5-10 and Table 5-11 for 2D and 3D models respectively. The areas in these two tables are calculated from FE models, but are close to the tested buildings (see Table 5-8). Note, that the area of gravity wall refers to the area of sheathing so bare gravity steel framing still counts as zero area for Phase 1/2a; however, the stiffness it provides is not zero, as shown above. For the South elevation, even the bare gravity framing can offer as much as 21% of the wall line's lateral stiffness. It is worth mentioning that using shared nodes to model connections in CFS framing is the most conservative option and should offer the upper bound of frame's stiffness, but close match to test results in terms of natural periods suggests the connection does have a

certain amount stiffness. This topic would be a piece of interesting future work for experimentalists and modelers.

In the South and North elevations the area of gravity sheathing accounts for almost half of the total area. In particular, for the South elevation the sheathing area of the gravity walls is 1.56 times that of the area of the shear wall sheathing. The sheathing type is identical for the shear and gravity walls, differences exist in the fastener spacing and boundary conditions (hold downs). However, with such a large amount of sheathing area, it is not a surprise perhaps that the gravity wall can account for 45% of the total lateral stiffness of the South wall line. Similar cases are found for East and West elevations. The amount gravity sheathing is small (about 20% of total area) and the vertical distribution of the gravity sheathing is not continuous because of the window openings (see Figure 5-7(d) and Figure 5-7(f)). Even so, the gravity sheathing still modifies the load path of the lateral loads by transferring a share of lateral force to shear anchors on the bottom tracks below window openings. This effect is definitely non-trivial: twenty percent of the total wall area as gravity wall, even with discontinuous sheathing, can still contribute to 15% of the provided lateral stiffness in the wall line. Figure 5-13 further shows the correlation between the area ratio A_{GW}/A_{SW} and the stiffness ratio k_{GW}/k_{SW} for four wall lines (data from Table 5-10). The area ratio A_{GW}/A_{SW} are the same for Phase 2b and 2c, and the stiffness ratio k_{GW}/k_{SW} are also very similar for these two phases, indicating there is some correlation between them. The area ratio A_{GW}/A_{SW} differ among wall lines due to their difference in configuration; more data points from models or tests can help to propose an estimation of k_{GW}/k_{SW} once A_{GW}/A_{SW} of a wall line is determined.

If the breakdown of stiffness in 2D models (Table 5-10) is compared to 3D models (Table 5-11), the role of the diaphragm models in linear static analysis can be discovered - this is done most easily in the short direction. The East and West wall lines have similar layout, capacity, stiffness and breakdown between shear walls and gravity walls in 2D. However, in 3D models, the lateral stiffness contribution of the diaphragms is lumped with the gravity walls' stiffness, so the summed stiffness takes a larger share than it does with East or West wall line alone and this effect is more significant with semi-rigid diaphragms. In the long direction, since the difference in terms of lateral force resistance between the South and North elevation is quite large, the interplay induced by the diaphragms makes the 3D models' stiffness breakdown a median value of two wall lines. For example, in Phase 2d, the stiffness of the interior partition walls is taken into the 'gravity systems' making its proportion even larger. It is possible, and indeed would be beneficial, if future work can more precisely determine the stiffness of diaphragms in CFS-framed buildings through experiments and analyses.

Table 5-10: Elastic stiffness breakdown between shear walls and gravity walls along with the normalized sheathing areas, 2D models

	SOUTH		**NORTH**		**EAST**		**WEST**	
Stiffness	SW k_u (%)	GW k_u (%)	SW k_u (%)	GW k_u (%)	SW k_v (%)	GW k_v (%)	SW k_v (%)	GW k_v (%)
P-2D-b	100.0	0.0	100.0	0.0	100.0	0.0	100.0	0.0
A1-2D-a	78.8	21.2	94.8	5.2	92.6	7.4	90.9	9.1
A2b-2D-a	50.3	49.7	74.3	25.7	84.7	15.3	85.7	14.3
A2c-2D-a	54.9	45.1	74.4	25.6	86.9	13.1	89.0	11.0
Area	A_{SW} (%)	A_{GW} (%)	A_{SW} (%)	A_{GW} (%)	A_{SW} (%)	A_{GW} (%)	A_{SW} (%)	A_{GW} (%)
P-2D-b	27	0	40	0	63	0	68	0
A1-2D-a	27	0	40	0	63	0	68	0
A2b-2D-a A2c-2D-a	27	42	40	45	63	24	68	18

Table 5-11: Elastic stiffness breakdown between shear walls and gravity walls plus other systems along with the normalized sheathing areas, 3D models

	LONG		**SHORT**	
Stiffness	SW k_u (%)	GW & others k_u (%)	SW k_v (%)	GW & others k_v (%)
P-3D-RD-b	100.0	0.0	100.0	0.0
A1-3D-RD-a	90.0	10.0	89.9	10.1
A1-3D-SD-a	87.1	12.9	80.3	19.7
A2b-3D-RD-a	61.4	38.6	80.7	19.3
A2b-3D-SD-a	59.8	41.2	73.6	26.4
A2c-3D-RD-a	63.3	36.7	85.1	14.9
A2c-3D-SD-a	60.7	39.3	76.1	23.9
A2d-3D-RD-a	56.7	43.3	62.9	37.1
Area	A_{SW} (%)	A_{GW} (%)	A_{SW} (%)	A_{GW} (%)
P-3D-RD-b	33	0	65	0
A1-3D models	33	0	65	0
A2b-3D and above models	33	44	65	21

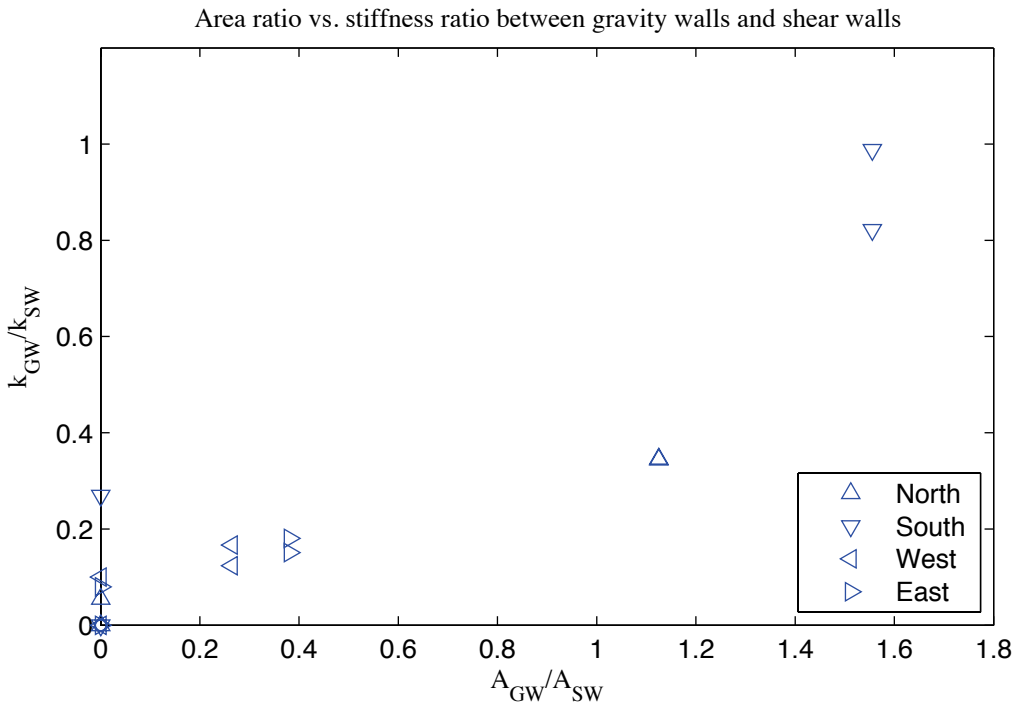

Figure 5-13: Correlation plot of area ratio vs. stiffness ratio between gravity walls and shear walls for models of Table 5-10

Similar to stiffness, the breakdown in capacities of the building and wall lines can also be determined. The total base shear of a wall line or the building is the summation of the horizontal reaction forces from the hold downs and shear anchors. The base shear of a specific shear wall or gravity wall can be determined by summing the reaction of fasteners that are attached to the specified wall; hold downs are always associated with shear walls. The method works for both static and time history analyses.

The breakdown of peak capacity from pushover analysis is illustrated as bar plots in Figure 5-14 and Figure 5-15 for selected 2D and 3D models. The trends in the breakdown of lateral capacities is apparent: they depend on the amount of gravity system in the wall line. The lateral capacity contribution to the total from the gravity system can be as much as 25% even in Phase 1 (steel framing only). In the South elevation where there is the

greatest percentage of sheathed gravity walls these gravity systems provide more than 60% of the wall line capacity in Phase 2b and 2c. Again, the situation is different in the short direction East and West elevations, but the conclusion is manifest: the gravity systems' contribution to lateral stiffness and capacity in CFS-framing is significant, and sometimes even comparable to the shear walls themselves (the only lateral system in design assumptions). The diaphragms, appropriately, do not have a significant impact on the breakdown of lateral wall line capacity, as evidenced by the bar plots where wall lines in 3D models are close to the 2D models at the same construction phase.

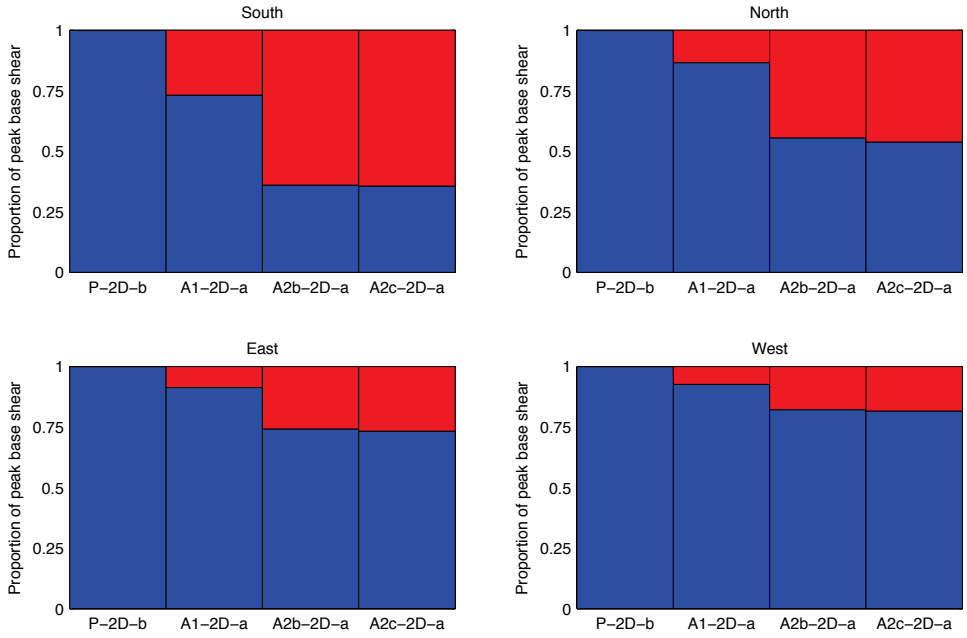

Figure 5-14: Proportion of peak base shear taken by shear walls and gravity walls, pushover analysis, 2D models (blue – shear walls, red – gravity walls)

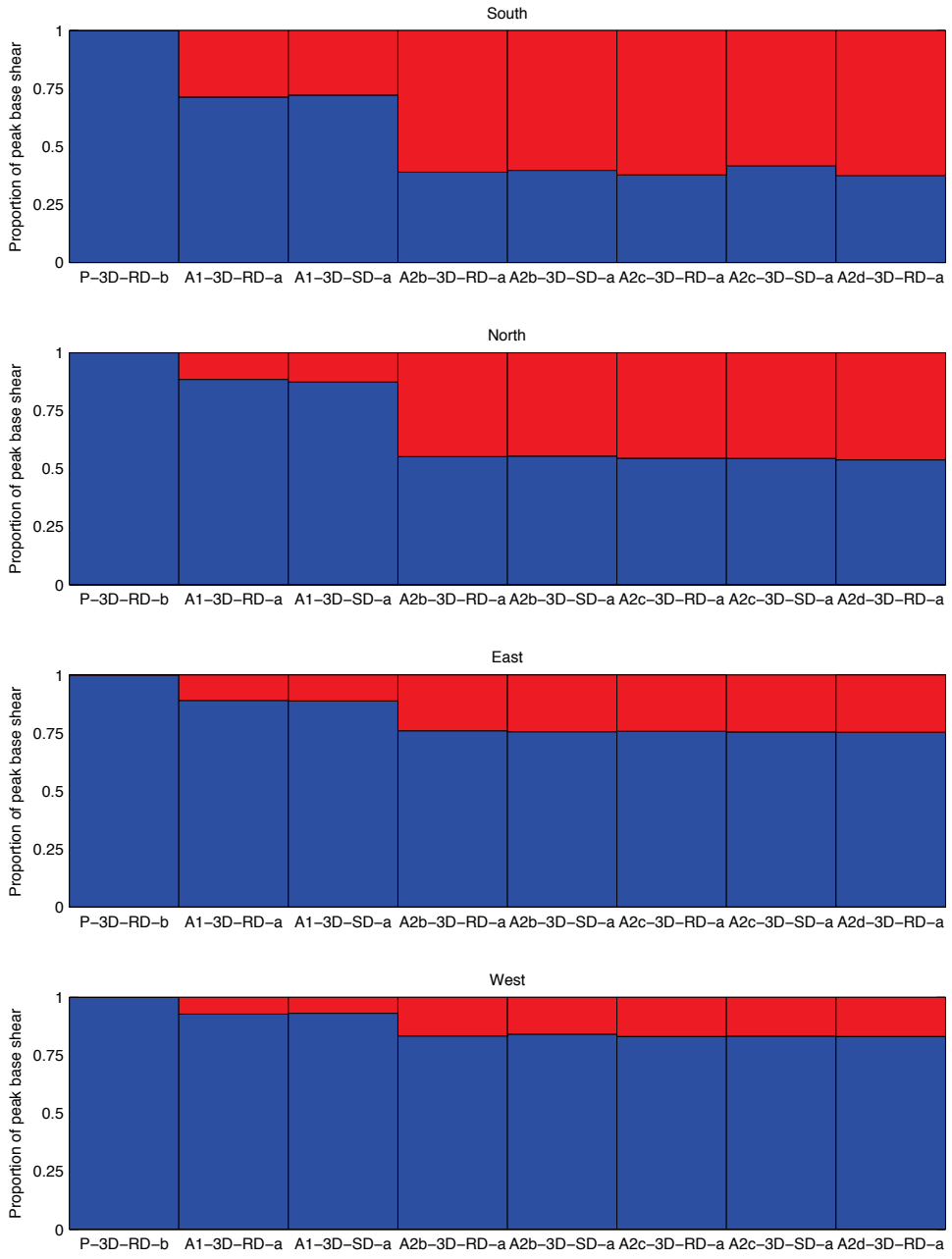

Figure 5-15: Proportion of peak base shear taken by shear walls and gravity walls, pushover analysis, 3D models (blue – shear walls, red – gravity walls)

The breakdown of peak dynamic base shear from nonlinear time history analysis is performed in the same way as performed for pushover analysis (with some additional care regarding direction) and the results are tabulated in Table 5-12 and Table 5-13 for 2D and 3D models. There is no 2D models for Phase 2d, since there is no modification to the exterior wall lines of the CFS-NEES buidling from Phase 2c to Phase 2d. Excitations for this investigation include 16% and 100% Canoga Park excitation and 100% Rinaldi excitation. The breakdown of the pushover peak capacity is placed on top of the dynamic peak base shear breakdowns as a reference. Once stronger excitation is applied (e.g. 100% CNP), the breakdown of peak dynamic base shear is very close to the breakdown of peak pushover capacity and there is little difference between the 2D and 3D models. However, the behavior of A1-models (i.e. Phase 1 structural-only models) is different from A-models simuating the later construction phases. Under lower level of excitation (16% CNP) when the behavior remains linear, the shear wall systems in the 2D and 3D A1-models take a larger amount of base shear than they do when the response becomes nonlinear under stronger excitations. However, for A-models of later construction phases, the breakdown of peak dynamic base shear changes little, as the excitation gets stronger. A possible explanation of this phenomenon is developed regarding the layout of the A-models across the construction phases. Only the A1-models have bare gravity framing, so the stiffness and backbone response curve of the shear walls and gravity systems are very different. Note, that the OSB sheathing of shear walls is modeled with Pinching4 material so its backbone curve has four segments, but studs (in the A1 models) are modeled with EPP so the tangent of its backbone curve does not change before yielding. At various excitation levels, the tangent stiffness ratio between shear walls and the bare steel

framing changes so the breakdown of peak dynamic base shear changes accordingly. For models at Phase 2b and above, gravity walls and shear walls are both sheathed and their nonlinear response models are characterized in the same way so tabulated results suggest that shear walls and gravity walls of these models are generally at the same region of their Pinching4 backbone curves despite the scaling of excitation. (This suggests their response is essentially drift controlled as an entire wall line experiences nearly the same drift at any instant in time.) Closer examination of this phenomenon would require more detailed test measurement of shear walls response. Improved models with details of the gravity framing may help too. For example, compression bearing paths from contact at the ends of all studs deserves further consideration. Also, the stiffness and capacity of shear anchors can be added explicitly into the model once a reasonable estimation is available. Similar to Figure 5-13, Figure 5-16 is generated to illustrate the correlation between the area ratio A_{GW}/A_{SW} and the peak base shear ratio V_{bGW}/V_{bSW} for four wall lines (data from Table 5-13). The area ratio A_{GW}/A_{SW} holds constant for each wall line from A2b-3D-RD-a model to A2d-3D-RD-a model. The the peak base shear ratio V_{bGW}/V_{bSW} varies very little between Phase 2b, Phase 2c and Phase 2d models despite analysis types and excitation levels, indicating there is some correlation between them. The area ratio A_{GW}/A_{SW} differs between wall lines due to their difference in configuration; more data points from models or tests can help to propose an estimation of V_{bGW}/V_{bSW} once the A_{GW}/A_{SW} of a wall line is determined.

Table 5-12: Breakdown of total peak base shear between shear walls and gravity walls in 2D models

Pushover								
	SOUTH		**NORTH**		**EAST**		**WEST**	
	SW V_{bu} (%)	GW V_{bu} (%)	SW V_{bu} (%)	GW V_{bu} (%)	SW V_{bv} (%)	GW V_{bv} (%)	SW V_{bv} (%)	GW V_{bv} (%)
P-2D-b	100.0	0.0	100.0	0.0	100.0	0.0	100.0	0.0
A1-2D-a	73.2	26.8	86.6	13.4	91.3	8.7	92.6	7.4
A2b-2D-a	36.0	64.0	55.5	44.5	74.2	25.8	82.2	17.8
A2c-2D-a	35.6	64.4	53.8	46.2	73.3	26.7	81.6	18.4
Canoga Park 16%, 1 direction								
	SOUTH		**NORTH**		**EAST**		**WEST**	
	SW V_{bu} (%)	GW V_{bu} (%)	SW V_{bu} (%)	GW V_{bu} (%)	SW V_{bv} (%)	GW V_{bv} (%)	SW V_{bv} (%)	GW V_{bv} (%)
P-2D-b	100.0	0.0	100.0	0.0	100.0	0.0	100.0	0.0
A1-2D-a	83.4	16.6	96.2	3.8	96.9	3.1	97.3	2.7
A2b-2D-a	31.5	68.5	63.4	36.6	75.5	24.5	82.3	17.7
A2c-2D-a	34.0	66.0	60.2	39.8	71.2	28.8	81.1	18.9
Canoga Park 100%, 1 direction, DBE level								
	SOUTH		**NORTH**		**EAST**		**WEST**	
	SW V_{bu} (%)	GW V_{bu} (%)	SW V_{bu} (%)	GW V_{bu} (%)	SW V_{bv} (%)	GW V_{bv} (%)	SW V_{bv} (%)	GW V_{bv} (%)
P-2D-b	100.0	0.0	100.0	0.0	100.0	0.0	100.0	0.0
A1-2D-a	73.8	26.2	86.8	13.2	88.5	11.5	93.2	6.8
A2b-2D-a	36.4	63.6	55.9	44.1	74.2	25.8	82.3	17.7
A2c-2D-a	36.4	63.6	56.1	43.9	70.7	29.3	80.2	19.8
Rinaldi 100%, 1 direction, MCE level								
	SOUTH		**NORTH**		**EAST**		**WEST**	
	SW V_{bu} (%)	GW V_{bu} (%)	SW V_{bu} (%)	GW V_{bu} (%)	SW V_{bv} (%)	GW V_{bv} (%)	SW V_{bv} (%)	GW V_{bv} (%)
P-2D-b*	N/A	N/A	N/A	N/A	N/A	N/A	N/A	N/A
A1-2D-a*	N/A	N/A	N/A	N/A	N/A	N/A	N/A	N/A
A2b-2D-a	36.5	63.5	55.5	44.5	74.1	25.9	82.1	17.9
A2c-2D-a	35.7	64.3	53.8	46.2	73.8	26.2	81.7	18.3

*: Displacement increase without bound during analysis

Table 5-13: Breakdown of total peak base shear between shear walls and gravity walls in 3D models

	SOUTH		NORTH		EAST		WEST	
Pushover								
	SW V_{bu} (%)	GW V_{bu} (%)	SW V_{bu} (%)	GW V_{bu} (%)	SW V_{bv} (%)	GW V_{bv} (%)	SW V_{bv} (%)	GW V_{bv} (%)
P-3D-RD-b	100.0	0.0	100.0	0.0	100.0	0.0	100.0	0.0
A1-3D-RD-a	71.3	28.7	88.5	11.5	89.0	11.0	92.7	7.3
A1-3D-SD-a	72.1	27.9	87.4	12.6	88.8	11.2	93.1	6.9
A2b-3D-RD-a	38.9	61.1	55.2	44.8	75.9	24.1	83.3	16.7
A2b-3D-SD-a	39.7	60.3	55.4	44.6	75.5	24.5	84.1	15.9
A2c-3D-RD-a	37.7	62.3	54.5	45.5	75.7	24.3	83.1	16.9
A2c-3D-SD-a	41.6	58.4	54.4	45.6	75.4	24.6	83.2	16.8
A2d-3D-RD-a	37.4	62.6	53.8	46.2	75.3	24.7	83.1	16.9
Canoga Park 16%, 3 directions								
	SOUTH		**NORTH**		**EAST**		**WEST**	
	SW V_{bu} (%)	GW V_{bu} (%)	SW V_{bu} (%)	GW V_{bu} (%)	SW V_{bv} (%)	GW V_{bv} (%)	SW V_{bv} (%)	GW V_{bv} (%)
P-3D-RD-b	100.0	0.0	100.0	0.0	100.0	0.0	100.0	0.0
A1-3D-RD-a	88.9	11.1	96.9	3.1	95.4	4.6	97.0	3.0
A1-3D-SD-a	88.2	11.8	96.7	3.3	96.9	3.1	97.2	2.8
A2b-3D-RD-a	37.6	62.4	63.8	36.2	77.8	22.2	84.1	15.9
A2b-3D-SD-a	39.2	60.8	62.6	37.4	78.8	21.2	84.1	15.9
A2c-3D-RD-a	39.4	60.6	59.6	40.4	71.1	28.9	81.2	18.8
A2c-3D-SD-a	39.9	60.1	59.3	40.7	74.1	25.9	82.4	17.6
A2d-3D-RD-a	39.2	60.8	57.5	42.5	69.5	30.5	82.1	17.9
Canoga Park 100%, 3 directions, DBE level								
	SOUTH		**NORTH**		**EAST**		**WEST**	
	SW V_{bu} (%)	GW V_{bu} (%)	SW V_{bu} (%)	GW V_{bu} (%)	SW V_{bv} (%)	GW V_{bv} (%)	SW V_{bv} (%)	GW V_{bv} (%)
P-3D-RD-b	100.0	0.0	100.0	0.0	100.0	0.0	100.0	0.0
A1-3D-RD-a	74.9	25.1	88.2	11.8	89.5	10.5	93.2	6.8
A1-3D-SD-a	75.6	24.4	87.7	12.3	91.3	8.7	93.2	6.8
A2b-3D-RD-a	39.1	60.9	55.7	44.3	73.7	26.3	83.3	16.7
A2b-3D-SD-a	39.8	60.2	55.1	44.9	73.3	26.7	82.4	17.6
A2c-3D-RD-a	41.2	58.8	55.0	45.0	72.4	27.6	81.7	18.3
A2c-3D-SD-a	41.6	58.4	54.8	45.2	72.0	28.0	80.9	19.1
A2d-3D-RD-a	41.4	58.6	55.6	44.4	72.9	27.1	81.2	18.8
Rinaldi 100%, 3 directions, MCE level								
	SOUTH		**NORTH**		**EAST**		**WEST**	
	SW V_{bu} (%)	GW V_{bu} (%)	SW V_{bu} (%)	GW V_{bu} (%)	SW V_{bv} (%)	GW V_{bv} (%)	SW V_{bv} (%)	GW V_{bv} (%)
P-3D-RD-b	100.0	0.0	100.0	0.0	100.0	0.0	100.0	0.0
A1-3D-RD-a*	N/A	N/A	N/A	N/A	N/A	N/A	N/A	N/A
A1-3D-SD-a	70.8	29.2	89.7	10.3	87.8	12.2	93.9	6.1
A2b-3D-RD-a	40.9	59.1	55.8	44.2	72.4	27.6	81.4	18.6
A2b-3D-SD-a	41.7	58.3	55.4	44.6	73.6	26.4	84.2	15.8
A2c-3D-RD-a	40.1	59.9	53.9	46.1	73.8	26.2	83.3	16.7
A2c-3D-SD-a	40.5	59.5	54.0	46.0	73.7	26.3	83.6	16.4
A2d-3D-RD-a	41.0	59.0	54.0	46.0	74.1	25.9	83.2	16.8

*: Displacement increase without bound during analysis

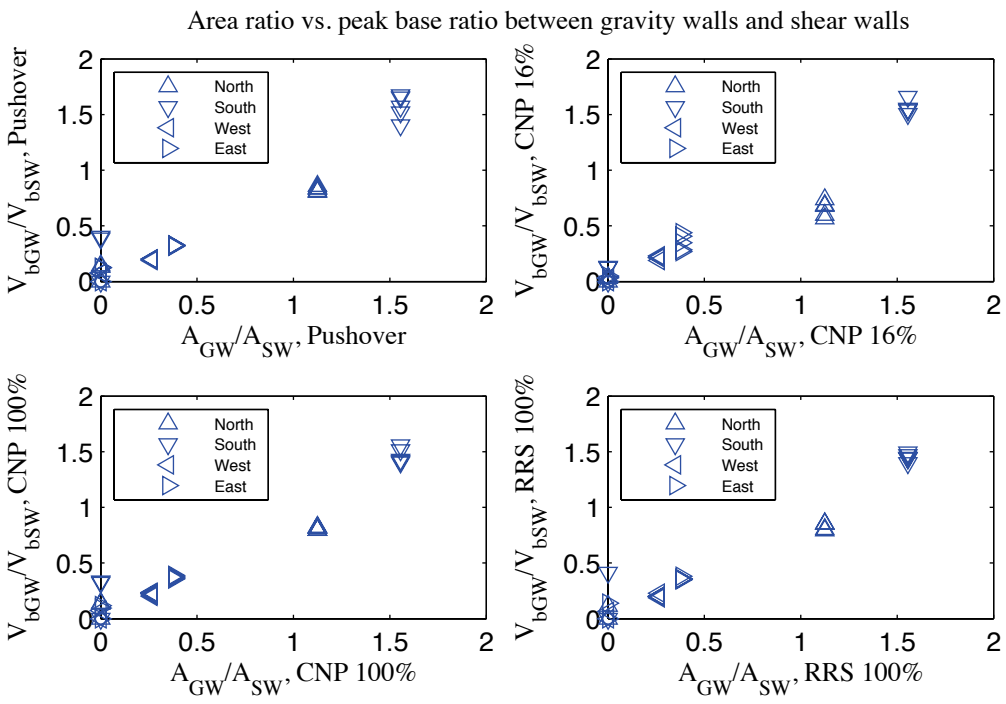

Figure 5-16: Correlation plot of area ratio vs. peak base shear ratio between gravity walls and shear walls for models in Table 5-13

5.4.3 Discussion on other modeling options and proposed modeling guidelines

The role of other nonstructural components and other options in modeling is discussed in this section. A summary of these discussions are presented at the end of this chapter.

(a) Determination of elastic stiffness of shear wall elements

The stiffness of a structural element is generally calculated as the secant slope between the origin and specific point on the actual load-deformation curve. The limit of the secant slope converges to the tangent slope as a general rule of calculus, and this effect is non-trivial herein according to previous comparison on the model's natural periods and stiffness. To further demonstrate this effect, every other detail of A1-3D-RD-a and A1-3D-SD-a models is duplicated in new models expect the elastic stiffness. New models, termed as A1-3D-RD-b and A1-3D-SD-b used the load and deflection of ($\delta(0.4V_n)$,

$0.4V_n$) on shear walls backbone curve for stiffness determination instead of ($\delta(0.2V_n)$, $0.2V_n$).

These 40% stiffness A1-models' first natural periods from free vibration analysis are available in Table 5-14. With the same mass distribution and diaphragm option, the difference in natural periods indicates the secant stiffness of shear walls determined from ($\delta(0.2V_n)$, $0.2V_n$) is about 40% larger than that determined from ($\delta(0.4V_n)$, $0.4V_n$). Comparison with the real building's periods has shown the stiffness from ($\delta(0.2V_n)$, $0.2V_n$) is meaningfully closer to the reality. Consequently, the secant stiffness of building components should be taken using points on the backbone curve that are closer to the origin and great care should be taken with initial stiffness.

Table 5-14: Comparison of natural periods of 3D models with two stiffness options

Model name	**A1-3D-RD-a**	**A1-3D-RD-b**	**A1-3D-SD-a**	**A1-3D-SD-b**
Stiffness option	$K(0.2V_{nA})$	$K(0.4V_{nA})$	$K(0.2V_{nA})$	$K(0.4V_{nA})$
T_{long} (s)	0.33	0.39	0.32	0.37
T_{short} (s)	0.29	0.35	0.30	0.35

(b) Mass distribution: corner mass vs. stud-end mass

The amount of mass and its distribution is another factor that determines the model's natural periods. Typically, less attention is paid to the mass distribution as long as the total amount is correct and it is easy and fairly natural to lump the mass equally to corner nodes. However, in the process of modeling the Phase 1 building with semi-rigid diaphragms, it is found that the distribution of nodal mass does have a significant impact on the model performance and predictions.

Table 5-15 compares natural periods predicted by A1-3D-RD-a and A1-3D-SD-a models and those predicted by modified models with mass lumped only at the four corners (similar to the lumped mass in model A1-3D-RD-c in Figure 5-1 (b)). This modification of mass distribution does not make a big difference for rigid diaphragm model (A1-3D-RD-a) results, but drastically changes the first natural period of the semi-rigid diaphragm model (A1-3D-SD-a). The semi-rigid diaphragm on the floor level has an opening in the northwest corner for staircases (see Chapter 3) and the North wall line is not sheathed at that corner in Phase 1 (see Figure 5-1(f)) so the lateral stiffness is low locally. The vibration mode shape of modified A1-3D-SD-a model also shows large local deformations in the corner. Recorded drift from time history analysis is also much larger at the corner than other locations. The configuration of the CFS-NEES building at Phase 1 requires that seismic mass should be lumped to stud ends for A1-3D-SD-a model and it becomes the only feasible option.

Table 5-15: Comparison of natural periods of 3D models with two mass options

Model name	**A1-3D-RD-a**	**A1-3D-RD-a, modified**	**A1-3D-SD-a**	**A1-3D-SD-a, modified**
Mass option	Stud ends	Corners	Stud ends	Corners
T_1 (s)	0.33	0.34	0.32	0.42
T_2 (s)	0.29	0.32	0.30	0.33
T_3 (s)	0.23	0.27	0.23	0.30

(c) The effect diaphragm modeling

Peterman has observed that the stiffness of the diaphragms in the tested CFS-NEES building are large enough such that the design assumption of a flexible diaphragm is not valid (Peterman 2014). Three modeling options of the diaphragm: rigid, semi-rigid and flexible, are taken into account and their effects having been covered previously, are summarized here.

In terms of lateral stiffness of the building, free vibration analysis results indicate that the difference between the discrepancy of stiffness between rigid diaphragm and semi-rigid diaphragm models is relatively small. In the long direction, stiffness of rigid and semi-rigid diaphragm models at the same phase is almost the same and the difference of stiffness is about 10% in short direction. Comparison of peak capacity from pushover analysis shows that the rigid diaphragm model's capacity is 10% smaller than the semi-rigid diaphragm models in the long direction, and about 20% smaller in the short direction. Note, typically one might consider a rigid diaphragm stronger, but here rigid referes to the in-plane stiffness only and the two diaphragms are modeled quite differentlty. The semi-rigid diaphragm models the structural CFS member and connections to the walls while the rigid diaphragm uses a simiple multi-point constraint to enforce the in-plane rigidity (See Section 3.5 for further discussion on the modeling differences). From the perspective of dynamic analysis, the predicted peak drifts and peak hold down load cell tensile forces (after the removal of static force from gravity) from rigid diaphragm and semi-rigid diaphragm models are close, generally with less than 25% difference (See Table 5-9). The effect of a rigid or semi-rigid diaphragm on the breakdown of stiffness and capacity, between lateral and gravity systems, is also similar. All these comparisons lead to a conclusion that the performance of the semi-rigid models (see Chapter 3 Section 3.5 for its full description) developed for the CFS-NEES building is essentially similar to the rigid diaphragms - and far different from flexible diaphragms. Note, the rigid diaphragm is a simple built-in element in OpenSees, but the semi-rigid option requires tens of CFS members and hundreds of truss elements for diaphragm

sheathings. Also note, ASCE 7-10 (American Society of Civil Engineers 2010) as pointed out in Madsen (Madsen et al. 2011) specifies the specific diaphragms under study are flexible – clearly once again design assumptions and our best estimation of reality diverge.

As a side note, the author tried to model 3D models with real flexible diaphragms, viz. no diaphragms in 3D models. However, the model fails in P-Δ analysis because of large local deformation at certain places. Analysis of the 2D models is equivalent to the effect of flexible diaphragm since the coupling between wall lines is zero.

(d) Dimensionality of models: 2D vs. 3D

Two-dimensional models of the building ignore the 3D coupling effect from diaphragms, and comparisons in previous sections have confirmed this observation. Simply summing up contributions from wall lines cannot accurately represent the building's performance. One reason for the lateral capacity of 3D models being larger than the summation of capacities of the wall lines in the loading direction is that other wall lines still contribute to the capacity (i.e. all foundation forces are not in the plane of the wall). Selecting the maximum or minimum of a given response metric of the four elevations is not a desirable option either. For example, the stiffness of the building is always larger than any single wall line in the same direction.

The possible danger of missing interplay between wall lines introduced by diaphragms can be exacerbated if the stiffness and capacity of two facing wall lines are quite different,

as seen in the long direction of the CFS-NEES model/building. As an example, predicted peak story drifts under 100% Rinaldi ground motion by the South and North elevation models at Phase 2c are 5.54% and 0.93% (see Appendix P). However, after the introduction of rigid or semi-rigid diaphragms (see Appendices Q and R), peak story drifts of South and North elevations drop greatly and get very close (1.11% vs. 1.10% or 1.16% vs. 0.97%) to test results. A peak story drift of over 5% in the South elevation as predicted by 2D models indicates failure, but the 3D effect from the diaphragms makes the peak drift drop by 400% to a safe level of 1.1%. Apparently, using the worst case from 2D analysis can greatly underestimate the real structure's performance and may be unduly conservative.

Despite the limitations, two-dimensional models are computationally much cheaper than three-dimensional models. For example, take the nonlinear time history analysis with 100% Canoga Park excitation: if the high-fidelity 2D model of the South elevation at Phase 1 is analyzed, it takes 44 seconds; if the 2D model of the South elevation at Phase 2c is run the computational time increases to 58 seconds on the same platform; for the 3D A1-3D-SD-a model, analysis under the same excitation takes 48 minutes (about 60 times of 2D analysis). Worse, for the A2c-3D-SD-a model, the machine time soars to 400 minutes, which is tens of A1-3D-SD-a's model time and four hundred times the 2D models. Consequently, if the performance difference between 2D models and 3D models can be predicted a priori, it is still worth modeling all four elevations in 2D and analyzing them for the sake of efficiency. It also suggests reduced order models, especially in 3D,

that can reasonably predict the response but simpler than current high-fidelity models are still desirable.

For 3D models, the excitation can be applied in one, two or three-axis. Here the effect of uniaxial vs. multi-axial excitation is compared (see Table 5-4 for standard excitations in 3D analyses). For every 3D model developed, 100% Canoga Park excitation is applied from the long or short direction individually, from two lateral directions, and from all three directions. Standard output quantities, including peak story acceleration relative to the ground, peak drift, peak base shear, and peak hold down/load cell force are tabulated in the appendices. Uniaxial time history analysis shows that the building's response in the direction perpendicular to the loading is non-zero due to the 3D coupling effect of the diaphragms, but it is much smaller than the loading direction. If multi-axial excitation is applied, the resulted response is not the same with the superposition of uniaxial response in long and short directions. However, for every model, adding the vertical ground motion simultaneously with lateral components provides little change of response from the case of two-axis excitation (the preceding is consistent with testing). The results are summarized in Table X-6 to Table X-8 and Table X-10 to Table X-16 in appendix chapters (where X is an appropriate appendix) for 3D models described in Table 3-3. Lack of dependence on vertical motion is in agreement with the comment on rejecting vertical ground motion component in the far-field ground motion suite in Section 6.2.2 of FEMA P695 (Applied Technology Council 2009): it says "The record sets do not include the vertical component of ground motion since this direction of earthquake shaking is not

considered of primary importance for collapse evaluation, and is not required by the Methodology for nonlinear dynamic analysis."

(e) Preference on modeling options

As a conclusion of extensive comparisons and discussions above, suggested modeling options for cold-formed steel framed buildings are summarized below in Table 5-16. Possible improvements and future work are briefly mentioned, and they will be presented in the final chapter of the dissertation.

Table 5-16: Modeling guidelines for cold-formed steel framed buildings based on the CFS-NEES analysis

Property	Suggested modeling option
Shear walls' stiffness	The stiffness is nonlinear and accurate models may require accurate shear wall stiffness at low exciation levels. In our models initial stiffness determined at ($\delta(0.2V_n)$, $0.2V_n$) provide useful and adequate.
Shear walls' capacity	Code-based capacities may be less than expected shear wall capacities, even for the isolated shear wall, and this should be accounted for. In our modeling utilizing capacity determined from shear wall tests with the actual construction details brought the models much closer to reality and were preferred.
Shear walls' backbone	Pinching4 or other nonlinear hysteretic models that have degradation and pinching effect should be applied. Although sensitivity exists in the output due to hysteretic model assumptions for CFS-framed wood sheathed shear walls the essential necessity is the inclusion of the pinching effect.
Hold down	Inclusion of hold down flexibility is necessary, but one must also consider the large difference in tension and compression stiffness in the model and consider how bearing end conditions are handled.
Shear anchors	Important for modeling of lateral load path, but pull-through stiffness and capacity (and reliability) should be further explored.
Diaphragms	Even for wood sheathed CFS-framed floors flexible diaphragm assumptions seems unrealistic and excessively conservative; unless investigation the diaphragm in specific the difference between rigid and semi-rigid diaphragms is not excessive; therefore modeling diaphragms as rigid is simpler and a better initial assumption. Additional work is needed, but surrogate fastener-based models as detailed in Chapter 3 for shear walls show promise for providing needed model inputs.
Gravity walls' framing	Lateral resistance and contribution of graviety wall framing should be included. Foundation load paths, such as bearing paths from contact at the ends of studs needs further consideration.
Gravity walls' sheathing	The impact of any sheathing on gravity walls needs to be considered in the lateral wall resistance. Surrogate fastener-based models as detailed in Chapter 3 are adequate for this purpose.
Gypsum sheathings	Gypsum sheathing also contributes to stiffness and strength; though good reasons may exist for ignoring its contribution in final design it should be assessed as the contribution can alter the expected building performance. Surrogate fastener-based models as detailed in Chapter 3 are adequate for this purpose.
Interior walls	The impact of interior partition walls may depend on their configuration. Inclusion greatly increases model complexity. Surrogate fastener-based models as detailed in Chapter 3 are adequate for this purpose.
Mass distribution	Distributed mass should be used to more accurately model gravity effects and vertical load distributions in the model; however, lumped corner mass models perform adequately in most cases.

Chapter 6: Incremental Dynamic Analysis and Performance Evaluation of the Building Using FEMA P695 Procedure

This chapter provides a discussion on a specific application of time history analysis – Incremental Dynamic Analysis (IDA) and performance evaluation using IDA results for the CFS-NEES building. The idea of IDA and the excitation in our case study – the far-field ground motion record set of FEMA P695 are briefly introduced in Section 6.1. Section 6.2 briefly overviews the design and performance evaluation approach of the CFS-NEES building. Section 6.3 reports the structural system information and uncertainties in design requirements and test data. Section 6.4 is the identification of the CFS-framed archetype building. Description of the CFS-NEES building is provided with tables of key design factors. Section 6.5 summarizes the nonlinear structural model development of Chapter 3 and proposes necessary factors related to uncertainties in the models. Section 6.6 is a summary of the nonlinear structural analysis, including pushover analysis and IDA. The fragility curve developed from the empirical cumulative distribution function of the collapse probability estimated using IDA results is also provided. Section 6.7 is the performance evaluation of the response modification factor R for the archetype building. Section 6.8 is the evaluation of the overstrength factor Ω_O. The chapter concludes with further discussion and tentative suggestions on design improvements in Section 6.9.

6.1 Incremental dynamic analysis and FEMA P695 suite of far-field earthquake records

Incremental Dynamic Analysis (IDA), as proposed by Vamvatsikos and Cornell (Vamvatsikos and Cornell 2002; Vamvatsikos and Cornell 2002; Vamvatsikos and Cornell 2004), may be conceptualized as a dynamic extension of pushover analysis. Under linearly scaled earthquake excitations with a monotonic scalable intensity measure (IM), response quantities of the structure are recorded as the damage measure (DM), and the overall building response of DM vs. IM can be summarized. Story drift is a typical DM and the spectral acceleration of the first natural period of the structure is a typical IM. Multiple ground motions are employed to account for record-to-record difference in the ground motion signals (Vamvatsikos and Cornell 2004). Output from an IDA enables analysts to propose criterion for collapse prevention based on deformation measures and use statistics of the various excitations to evaluate the overall performance of a lateral force resisting system or building type. A detailed procedure is provided in the FEMA P695 report (Applied Technology Council 2009). IDA and the nonlinear time history analysis that it requires is an enabling tool towards performance-based seismic design as it provides a probabilistic assessment of building damage (performance) as a function of input excitation (Leng et al. 2013). The kernel of performance evaluation, as detailed in Chapter 7 of FEMA P695 (Applied Technology Council 2009), is the check of adjusted collapse margin ratio (*ACMR*) vs. accepted collapse margin ratio to see if the modeled archetype structure is robust enough to survive a suite of earthquakes in consideration of a series of uncertainties.

IDA is a collection of a number of nonlinear time history analyses of the modeled archetype structure. The ground motion record is linearly scaled (IM is also linearly scaled) and the structural model is analyzed until a designated DM limit for collapse is reached. To avoid bias, a specified set of ground motion records should be utilized as excitations. A well-documented and recommended set is the far-field ground motion record set of FEMA P695 (Applied Technology Council 2009). The set includes twenty-two component pairs of horizontal ground motions from sites located greater than or equal to 10 km from fault rupture. The vertical component of the ground motion is ignored (by the FEMA P695 method) since it is not considered of primary importance for collapse evaluation. The ground motion record sets each include a sufficient number of records to permit evaluation of record-to-record (*RTR*) variability. The document also specifies use of the far-field record set for collapse evaluation of index archetypes designed for Seismic Design Category (SDC) B, C or D criteria (Applied Technology Council 2009). Our building was designed for SDC D, according to site class and values of S_{DS} and S_{D1} in (Madsen et al. 2011) with reference to Table 11.6-1 and Table 11.6-2 of ASCE/SEI 7-10 (American Society of Civil Engineers 2010). FEMA P695 also includes a near-field record set, but it is only for supplemental information and is used in special studies to evaluate potential differences in the *CMR* for SDC E structures. Details about the selection and more properties of ground motions in far-field and near-field sets can be found in Appendix A of FEMA P695 (Applied Technology Council 2009).

In this research, the procedure of IDA has been applied to state-of-the-art A1-3D-SD-a model of the CFS-NEES building at construction Phase 1 with assumed structural

components only, A2b-3D-SD-a model that corresponds to Phase 2b building with additional OSB sheathing of gravity walls, and the simplified state-of-the-practice P-3D-RD-b model. Nonlinear analyses results and the performance evaluation are detailed in Appendices T, U and V. Section 6.2 to Section 6.7 below are based on Chapter 3 to Chapter 5 and these appendices. Comparison of IDA and performance evaluation results of the same CFS-NEES archetype building models demonstrates that the CFS-framed building designed by current codes and standards satisfies the seismic demand with a large safety margin. Summary observations also indicate that only high-fidelity models that incorporate details of both structural and nonstructural components can provide meaningful predictions of the building's behavior for performance evaluation.

6.2 Overview of the archetype design and performance evaluation approach

CFS-framed system design requirements of ASCE/SEI 7-10 are used as the framework. Following the procedure in FEMA P695 (Applied Technology Council 2009), an archetype (the CFS-NEES building) is developed; nonlinear OpenSees FE models are developed to simulate structural collapse; models are analyzed to predict the collapse capacities the archetype design, and *ACMR*, is evaluated and compared to acceptance criteria.

In examples of FEMA P695, seismic performance factors are determined by iteration until the acceptance criteria of the Methodology are met. The IDA and performance evaluation herein are performed for the CFS-NEES building designed with the current value of R = 6.5 as required by ASCE/SEI 7-10 for CFS-framed structures. We did not

develop a trial design with an initial of value of R other than 6.5 and there was no design modification after the performance evaluation. The overstrength factor Ω_O is 3.0 for the archetype design, as also required by ASCE/SEI 7-10.

6.3 Structural system information

6.3.1 Design requirements

This example utilizes design requirements for engineered CFS-framed buildings included in ASCE/SEI 7-10 (American Society of Civil Engineers 2010), in place of the requirements that would need to be developed for a newly proposed system. For the purpose of assessing uncertainty, the ASCE/SEI 7-10 design requirements are categorized as (B) Good since they represent many years of development, include lessons learned from a number of major earthquakes and can render safe designs of CFS-framed system. However, it is not rated as (A) Superior not for intentional conservativeness, but due to the fact that more recent experimental and computational research efforts should be included to make future designs not only safe but more efficient (see Table 3-1 of FEMA P695 (Applied Technology Council 2009)). The uncertainty of design requirements (β_{DR} per FEMA P695 terminology) will be used in the determination of accepted collapse margin ratio in performance evaluation of the archetype design.

6.3.2 Test data

This example relies on existing published sheathing-to-framing connection test data and sheathed shear wall assembly test data. Specifically, this example relies on information developed during the NSF funded CFS-NEES Project (Schafer 2015; Peterman and

Schafer 2013; Peterman 2014), and data provided directly by CFS stud (Steel Framing Industry Association 2011) and anchor industry (Simpson Strong-Tie Company Inc. 2013).

The quality of the test data is an important consideration when quantifying the uncertainty in the overall collapse assessment process. Test data of sheathing-to-framing connections and isolated shear walls were used by the authors to calibrate and validate the numerical model; these include monotonic and cyclic tests which take into account a number of factors including the sheathing type (OSB vs. gypsum), shear wall width (aspect ratio), spacing of fasteners and location of seams. Loading protocols were continued to deformations large enough for the capping strength to be observed, which allows better calibration of models for structural collapse assessment. Nevertheless, some uncertainties still exist with these test data sets. Most importantly, the stiffness, capacity and system behavior of ledger framing between CFS joists to ledger tracks and of CFS-framed diaphragms with sheathing are not available from tests. Therefore, for the purpose of assessing uncertainty, this test data set is categorized as (B) Good (see Table 3-2 of FEMA P695 (Applied Technology Council 2009)). The uncertainty of test data (β_{TD} per FEMA P695 terminilogy) will be used in the determination of accepted collapse margin ratio in performance evaluation of the archetype design.

6.4 Identification of CFS-framed archetype configuration

In this research, only one archetype building, the CFS-NEES building was designed as apposed to performance groups composed of multiple archetypes in the examples of

FEMA P695 (Applied Technology Council 2009). Figure 6-1 shows the configurations of two construction phases of the CFS-NEES archetype building. The first configuration is representative of the CFS-NEES building at Phase 1 with structural components only (OSB sheathed shear walls and bare CFS framing of the gravity system), while the second configuration is associated with the complete building at Phase 2e with all nonstructural components installed (Models investigated herein for IDA analysis only cover up through Phase 2b).

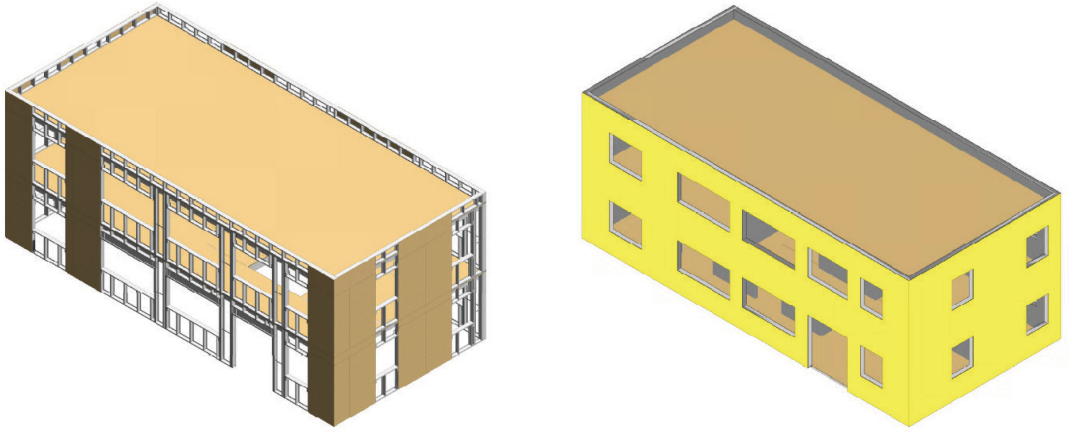

(a) Phase 1, structural components only (b) Phase 2e, complete with all components

Figure 6-1: Representative phase descriptions of the CFS-NEES building

Table 6-1 lists the value of design parameters considered for the development of 3D FE models of the CFS-NEES building. Only one archetype design is developed. High-fidelity OpenSees models include shear wall models based on test data and nonstructural components such as OSB exterior sheathing of gravity walls. Models of gypsum interior sheathing and interior partition walls have been investigated, but are not evaluated per FEMAP695 at this time. General modeling options and their implementation are

explained in Chapter 3. Models used in IDA and performance evaluation will be discussed in the next section.

Table 6-1: Parameters for the definition of the CFS-NEES archetype building

Parameter	Value
Number of stories	2
Occupancy Categories	II
Seismic Design Categories (SDC)	D
Story height	9 ft (2.74 m)
Interior and exterior nonstructural components	Considered

As mentioned above, the CFS-NEES building is the only archetype in performance evaluation of the research, so there is only one performance group and it is composed of the CFS-NEES archetype only. Table 6-1 is therefore also the description of design variables among performance groups since there are no other ones.

Table 6-2 reports the properties of the archetype building. Seismic demands are based on the ground motion intensities of ASCE/SEI 7-10 (American Society of Civil Engineers 2010) with SDC D. According to ASCE/SEI 7-10: S_{DS} = 0.927 g and S_{D1} = 0.5 g. The MCE ground motion spectral response accelerations, S_{MT}, = 1.39 g. The periods reported in Table 6-2 are the fundamental period of the archetypes based on Section 12.8.2 of ASCE/SEI 7-10 ($T = C_u T_a$) with a lower bound limit of 0.25 sec. Details on the design of the archetype is available from the design report (Madsen et al. 2011).

Table 6-2: CFS-NEES archetype structural design properties

		Key Archetype Design Parameters					
Arch. ID	No. of stories	Building Configuration	Seismic Design Criteria				$S_{MT}(T)$ (g)
			SDC	*T* (sec)	T_a (sec)	*V*/*W* (g)	
1	2	Commercial	D	0.25	0.175	0.143	1.39

6.5 Nonlinear model development

Even though there is only one archetype in this research, nonlinear FE models are developed at various fidelity levels and for the CFS-NEES building at various construction phases. Modeling options and their implementation are discussed in Chapter 3. Table 3-3 summarizes modeling options of each FE model, and Table 6-3 below is an excerpt of that table for the three IDA models selected.

Among the three IDA models, the simplest one is state-of-the-practice P-3D-RD-b model. This model only employs shear walls and rigid diaphragm, and a shear wall with OSB sheathing is modeled as a whole piece by two nonlinear truss elements using Pinching4 materials on the basis of AISI S213 (American Iron and Steel Institute 2009). The second model is the state-of-the-art A1-3D-SD-a model, and it is a high-fidelity model of the CFS-NEES building at Phase 1 with subpanel models of shear walls, CFS gravity framing and semi-rigid diaphragms. The Pinching4 material employed in this model is characterized from tests for shear walls and it is also applied to diaphragms.The third model: A2b-3D-SD-a is developed for the Phase 2b building with additional models for OSB sheathing of gravity walls. Note, A2b-3D-SD-a model is not the most complicated model for the CFS-NEES building. Models for Phase 2c and Phase 2d are also developed but are not run for IDA due to the limit of time and computational resource and remain for future work.

Pinching4 material (Lowes and Altoontash 2003) is the nonlinear material model used widely in this research to model sheathed elements (shear walls, gravity walls and semi-

rigid diaphragms) under lateral load for its capability of modeling the pinching effect and strength degradation. The general way to incorporate the Pinching4 model is to convert the shear-deflection response of the wall or the diaphragm into nonlinear Pinching4 material employed in the axial stress-strain relationship of diagonal truss elements simultating sheathing. The source of shear-deflection response curves can be test data or estimation from standards and codes. A schematic drawing of the Pinching4 response is given below (see Figure 6-2). Detailed discussion on Pinching4 models in this research can be found in Section 3.3, including characterized parameters of Pinching4 in Table 3-4.

Table 6-3: Modeling options of the CFS-NEES archetype building in IDA and performance evaluation

			State of the Practice	State of the Art	
				Phase 1/2a	Phase 2b
Component	Property	Option	P-3D-RD-b	A1-3D-SD-a	A2b-3D-SD-a
Shear wall	Stiffness	$K(0.4V_{nP})$	X		
		$K(V_{nP})$			
		$K(0.2V_{nA})$		X	X
		$K(0.4V_{nA})$			
	Capacity	V_{nA}		X	X
		V_{nP}	X		
	Backbone	EPP			
		Pinching4	X	X	X
	Panel size	Whole	X		
		Subpanels		X	X
Hold-down	General	Smeared	X		
		Discrete		X	X
Shear anchors	General	Ignored	X		
		Included		X	X
Diaphragm	Stiffness	Flexible			
		Rigid	X		
		Semi-rigid		X	X
	Pinching	None	X		
		Pinching4		X	X
Gravity exterior walls	General	None	X		
		Frame		X	
		Full			X
Gypsum sheathing	General	Ignored	X	X	X
		Included			
Interior walls	General	Ignored	X	X	X
		Included			
Mass distribution	General	Corner	X		
		Stud ends		X	X

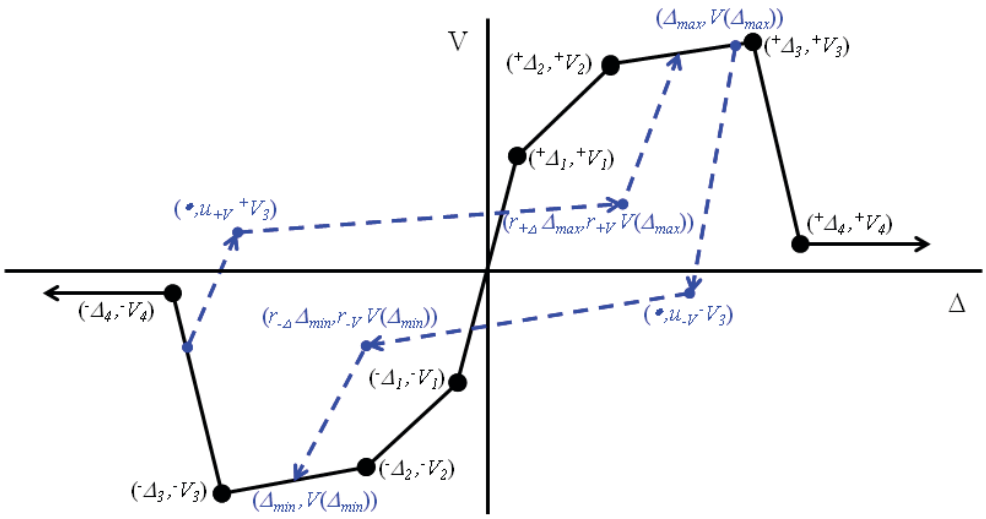

Figure 6-2: A typical response curve of Pinching4 material

Model uncertainty for performance evaluation is documented in Section 5.7 of FEMA P695 (Applied Technology Council 2009). Three models with various fidelity levels are selected for IDA. The A2b-3D-SD-a model incorporates details of all structural components, and the OSB sheathing of gravity walls, a nonstructural component that greatly contributes to the LFRS of the building (see Chapter 5 for model performance comparisons). Failure modes related to collapse are modeled and the model's response matches well with the test data, so the A2b-3D-SD-a model uncertainty level is categorized as (A) Superior (see Table 5-3 of FEMA P695 (Applied Technology Council 2009)). The A1-3D-SD-a model, although it models the Phase 1 building reasonably well (see Chapter 4), is rated as (B) Good since the nonstructural components are missing and they were shown to impact the results in the testing. P-3D-RD-b, being the most complicated state-of-the-practice model (Table 3-3), still overwhelmingly underestimates the building's stiffness and capacity (Chapter 5) due to the absence of gravity and nonstructural system. Hence, P-3D-RD-b model's uncertainty level is considered (D) Poor despite the relative sophistication when compared with current engineering practice.

These characterizations are used to establish the uncertainty of modeling parameter (β_{MDL} per FEMA P695 terminilogy) and will be used in the determination of the accepted collapse margin ratio in performance evaluation of the archetype design per FEMA P695.

6.6 Nonlinear structural analyses

To compute the system overstrength, Ω, and to help verify the structural model, monotonic static pushover analysis is used with a load pattern equal to the vertical distribution of the design base shear (Madsen et al. 2011). Figure 6-3 shows an example of the pushover curve for the A1-3D-SD-a model in the long direction (other model results may be found in Appendices T - V). For the CFS-NEES building, the design LRFD seismic coefficient is V/W = 0.143. Capping (the onset of negative stiffness) occurs for a seismic coefficient of 0.677 and at a roof drift ratio of 3.33. Therefore, Ω is calculated to be 4.74 for this archetype model.

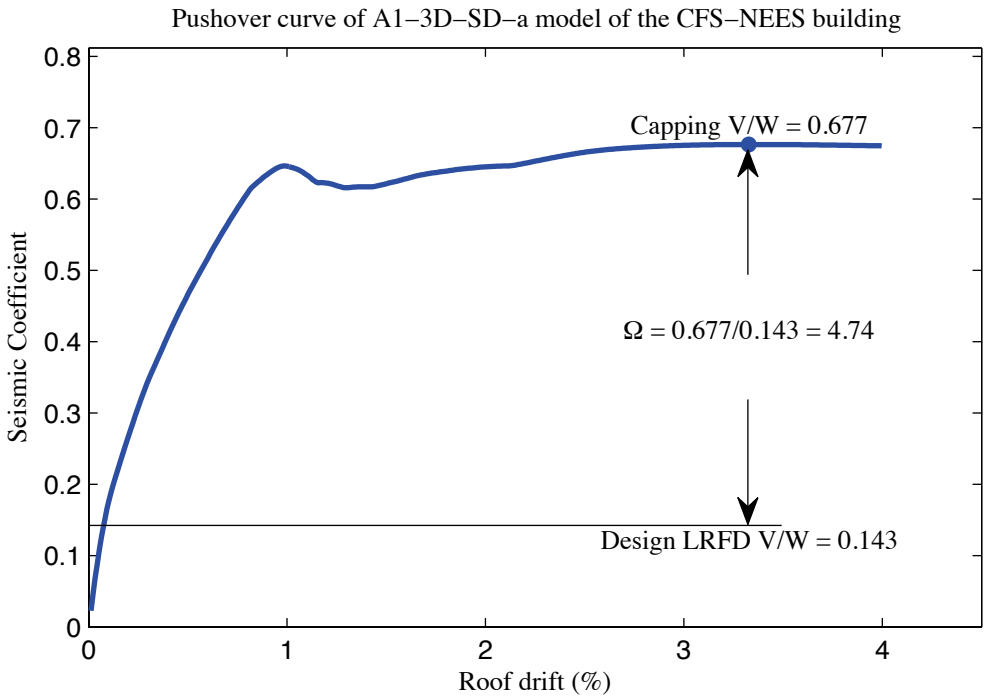

Figure 6-3: Monotonic static pushover curve and computation of Ω for the CFS-NEES building using A1-3D-SD-a model

To compute the collapse capacity of the CFS-NEES archetype design, the incremental dynamic analysis (IDA) approach is used with the far-field record set and ground motion scaling method specified in Section 6.2 of FEMA P695 (Applied Technology Council 2009). The intensity of the ground motion causing collapse of the A1-3D-SD-a model of the CFS-NEES archetype building is defined as the point on the intensity-drift IDA curve having a peak story drift exceeding a drift criterion of 4% (see Figure 6-4 below). This collapse story drift limit was selected based on shear wall tests by Liu et al. (Liu et al. 2012). Isolated shear walls utilizing the same details as the CFS-NEES building shear walls took up to 4% before collapse.

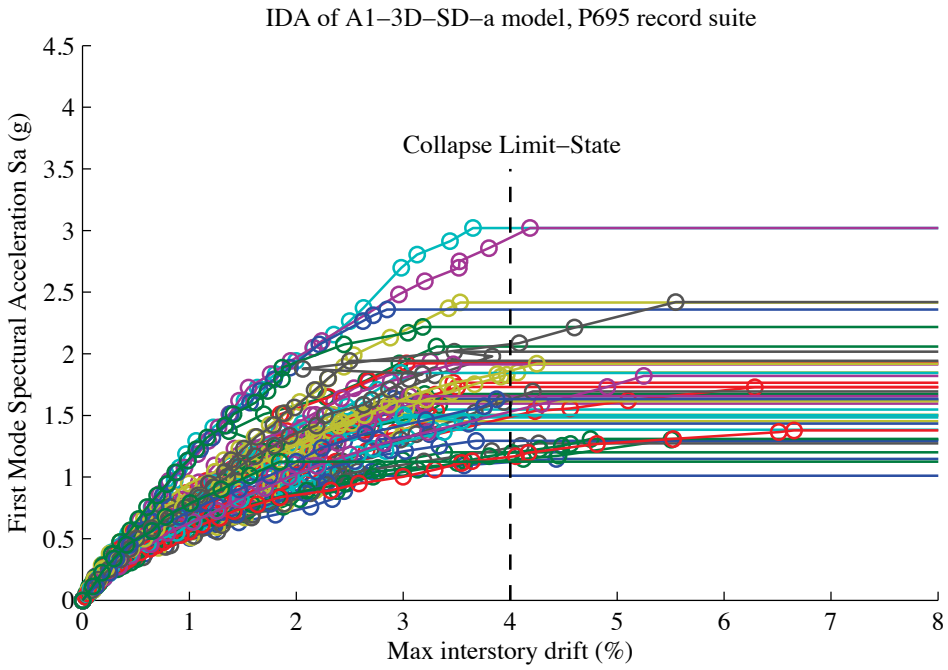

Figure 6-4: Results of IDA to collapse for the CFS-NEES building using A1-3D-SD-a model

Figure 6-4 and Figure 6-5 illustrate how the IDA method is used to compute the collapse margin ratio, *CMR*, for the CFS-NEES building. The spectral acceleration at collapse is computed for each of the 44 ground motions of the far-field set. The collapse fragility curve can then be constructed from the IDA plots, as shown in Figure 6-5. The collapse level earthquake spectral acceleration (spectral acceleration causing collapse in 50% of the analyses) is $\hat{S}_{CT}$ = 1.69 g for the CFS-NEES building modeled by the A1-3D-SD-a model. The collapse margin ratio, *CMR*, of 1.39 is then computed as the ratio of $\hat{S}_{CT}$ and the MCE spectral acceleration value at T = 0.175 sec, which is S_{MT} =1.39 g for this building and site class D and then multiplied by a factor of 1.2 for 3D models. The amplification factor should be applied to *CMR* obtained from 3D IDA results according to Section 6.4.5 of FEMA P695 (Applied Technology Council 2009), "because ground motions records are applied in pairs in three-dimensional nonlinear dynamic analyses,

collapse behavior of each index archetype model resulting from each ground motion component is coupled."

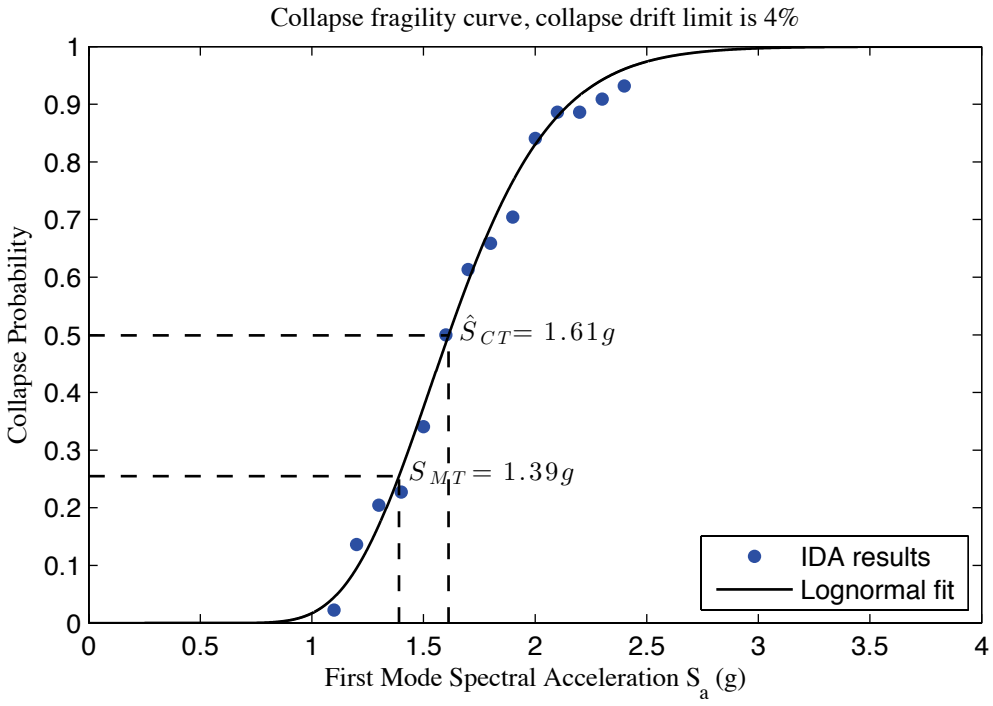

Figure 6-5: Collapse fragility curve for the CFS-NEES building using A1-3D-SD-a model

Static pushover analysis and IDA have been performed for P-3D-RD-b, A1-3D-SD-a and A2b-3D-RD-a model of the same CFS-NEES archetype building and the results are summarized in Table 6-4. The results show that the predicted Ω factor and *CMR* of the CFS-NEES building high fidelity models (A1-3D-SD-a and A2b-3D-RD-a) are much larger than those predicted by the P-3D-RD-b model. The P-3D-RD-b model due to its simplification of eliminating the gravity system and nonstructural system significantly underestimates the archetype building's stiffness and capacity. The predicted *CMR* is even less than 1, indicating there is no safety margin for the CFS-NEES building under seismic loading - despite test results showing that the CFS-NEES building can even

survive MCE excitations with little to no damage. This observation, along with model vs. test comparison in Chapter 4 and Chapter 5 confirms the incapability and unreliability of the state-of-the-practice models. On the other hand, adding OSB sheathing of the gravity walls from the A1-3D-SD-a model to the A2b-3D-SD-a model increases Ω and the *CMR* by 30% and 45% respectively, indicating the traditionally believed 'nonstructural' components in CFS-framed building design actually contributes significantly to lateral force resistance of the building. Nonstructural components that are absent in the A2b-3D-SD-a model, such as gypsum sheathing, interior walls, staircases and DensGlass, will yield an even larger *CMR* once included (Chapter 5 provides insights on the Ω for these models, but IDA analysis has not been performed).

Table 6-4: Summary of collapse results for the CFS-NEES building modeled by three different models

Arch. ID	Model Name	Design Configuration		Pushover and IDA Results			
		No. of stories	Building Configuration	Static Ω	$S_{MT}(T)$ (g)	$\hat{S}_{CT}(T)$ (g)	*CMR*
1	A2b-3D-SD-a	2	Commercial	6.48	1.39	2.33	2.01
1	A1-3D-SD-a	2	Commercial	4.99	1.39	1.61	1.39
1	P-3D-RD-a	2	Commercial	1.78	1.39	0.48	0.41

6.7 Performance evaluation

Collapse margin ratios computed above do not account for the unique spectral shape of rare ground motions. According to Section 7.2 of FEMA P695 (Applied Technology Council 2009), spectral shape adjustment factors, *SSF*, must be applied to the *CMR* results to account for spectral shape effects. In accordance with Section 7.2.2 of FEMA P695, the *SSF* can be computed for each archetype based on the SDC and the archetypes' period-based ductility, μ_T, obtained from the pushover curve. Figure 6-6 shows an example of calculating μ_T from the pushover curve for the A1-3D-SD-a model of the

CFS-NEES building. The period-based ductility, μ_T, of 7.59 is then computed as the ratio of the ultimate roof displacement δ_u, to the equivalent yield roof displacement $\delta_{y,eff}$. For 3D models, the mean value of μ_T along the two directions should be taken, per FEMA P695. Calculation details are presented in Appendices T - V.

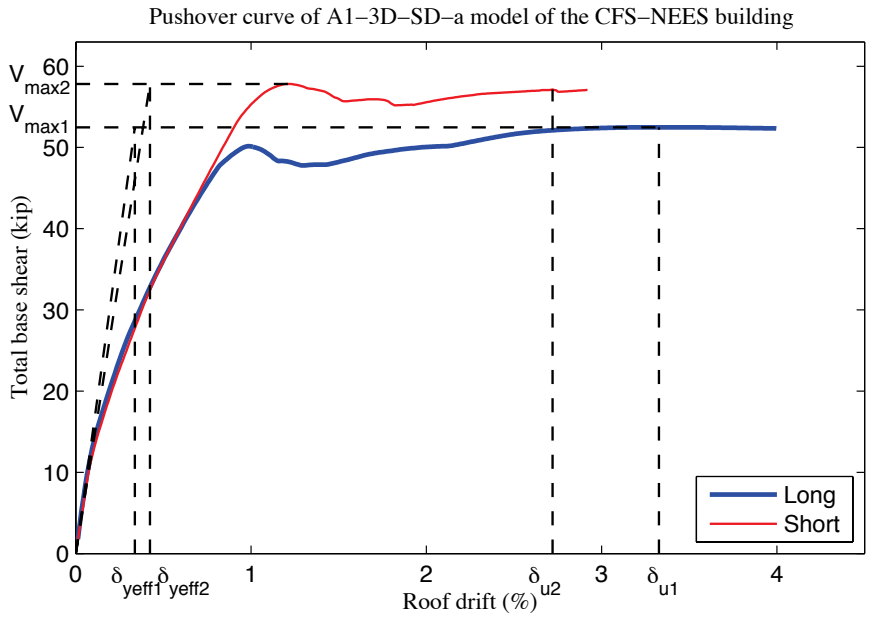

Figure 6-6: Monotonic static pushover curve and the illustration of δ_u and $\delta_{y,eff}$ for the CFS-NEES building using A1-3D-SD-a model

SSF, as reported in Section 7.2 of FEMA P695 (Applied Technology Council 2009), are considerably different between SDC D_{max} and other SDC. The CFS-NEES archetype building was not intentionally designed using the spectral acceleration of SDC D_{max}, but its S_{DS} (0.927 g) and S_{D1} (0.5 g) (Madsen et al. 2011) allow us to approximately regard its SDC as D_{max} since these number are close to S_{DS} (1.0 g) and S_{D1} (0.6 g) of SDC D_{max}, as shown in Table 5-1a and Table 5-1b of FEMA P695. Therefore, Table 7-1b for SDC D_{max} in FEMA P695 can be used to determine *SSF*. (Note the design spectral accelerations are

also much closer to D_{max} than D_{min}.) The adjusted collapse margin ratio, *ACMR*, is then computed for each model of the CFS-NEES building as the multiple of the *SSF* and *CMR*.

Finally, the evaluation of the Response Modification Coefficient *R*, is performed by checking adjusted collapse margin ratio against accepted collapse margin ratio. As per FEMA P695 (Applied Technology Council 2009), acceptable performance is achieved when, for each performance group, adjusted collapse margin ratios, *ACMR*, for each index archetype meet the following two criteria:

1. The average value of the adjusted collapse margin ratio for each performance group exceeds $ACMR_{10\%}$

$$\overline{ACMR_i} \geq ACMR_{10\%} \tag{6-1}$$

2. Individual values of adjusted collapse margin ratio for each index archetype within a performance group exceeds

$$ACMR_i \geq ACMR_{20\%} \tag{6-2}$$

where $ACMR_{10\%}$ and $ACMR_{20\%}$ are dependent on total system collapse uncertainty β_{TOT}. Also, note we are evaluating only one archetype model, so *i* is just one and the second criterion of $ACMR_{20\%}$ is adopted.

The determination of acceptable collapse margin ratio requires characterization of uncertainties including Record-to-Record Uncertainty (*RTR*), Design Requirements Uncertainty (*DR*), Test Data Uncertainty (*TD*) and Modeling Uncertainty (*MDL*) before calculating β_{TOT}.

According to Section 7.3 of FEMA P695 (Applied Technology Council 2009), a fixed value of $\beta_{RTR} = 0.40$ is assumed in the performance evaluation of systems with significant period elongation (i.e., period-based ductility, $\mu_T \geq 3$). Most systems, even those with limited ductile capacity, have significant period elongation before collapse, and are appropriately evaluated using this value.

The rating of *DR*, *TD* and *MDL* are specifically discussed in Chapter 3 and Chapter 5 of FEMA P695 and have been selected in Section 6.3 and Section 6.5. If four component random variables (*RTR*, *DR*, *TD*, and *MDL*) are assumed to be statistically independent, the lognormal standard deviation parameter, β_{TOT}, describing the total collapse uncertainty, is given by Eqn. (7-5) in FEMA P695 (Applied Technology Council 2009)

$$\beta_{TOT} = \sqrt{\beta_{RTR}^2 + \beta_{DR}^2 + \beta_{TD}^2 + \beta_{MDL}^2} \tag{6-3}$$

For $\beta_{RTR} = 0.40$, the value of total system collapse uncertainty β_{TOT} is tabulated in Table 7-2a to Table 7-2d in FEMA P695 (Applied Technology Council 2009) with respect to *DR*, *TD*, and *MDL*. With the rating of *DR*, *TD* and *MDL* in Section 6.3 and Section 6.5, β_{TOT} is determined for each model and used in the determination of $ACMR_{10\%}$ and

$ACMR_{20\%}$. For the three models: P-3D-RD-b, A1-3D-SD-a, A2b-3D-SD-a β_{TOT} is 0.700 0.525, and 0.500 respectively.

Table 6-5 lists the resulting adjusted collapse margin ratios for the CFS-NEES archetype building. Performance evaluation of three models of the CFS-NEES building shows that Phase 1 of the building with structural components only (A1-3D-SD-a model) is capable of passing the acceptance check. Adding OSB gravity wall sheathing to the model (A2b-3D-SD-a) leads to an even larger *ACMR*, indicating that CFS-framed buildings designed by current codes and standard are safe under seismic load but the design may be inefficient. This evaluation also confirms that state-of-the-practice models can lead to the wrong conclusion on the performance of CFS-framed building's under seismic load.

Table 6-5: Summary of collapse results for the CFS-NEES building modeled by three different models

Model Name	Design Configuration		Computed Overstrength and Collapse Margin Parameters						Acceptance Check
	No. of stories	Building Configuration	Static Ω	*CMR*	μ_T	*SSF*	*ACMR*	Accept. *ACMR*	Pass/Fail
A2b-3D-SD-a	2	Commercial	6.48	2.01	8.5	1.33	2.67	1.52	Pass
A1-3D-SD-a	2	Commercial	4.99	1.39	7.6	1.33	1.85	1.56	Pass
P-3D-SD-a	2	Commercial	1.78	0.41	1.2	1.06	0.43	1.80	Fail

6.8 Evaluation of Ω_O using the archetype design

The evaluation of the overstrength factor Ω_O, requires a comparison between the average value of archetype overstrength, Ω calculated for each performance group, to the system overstrength factor Ω_O used in design. As mentioned in Section 7.6 of FEMA P695, "Ω_O should not be taken as less than the largest average value of calculated archetype overstrength, Ω, from any performance group." Also Ω_O need not exceed 1.5 times the response modification coefficient, *R*. A practical limit on the value of Ω_O is about 3.0.

For our models of the CFS-NEES building in Table 6-5, the computed Ω from the high-fidelity models are 4.99 (Phase 1) and 6.48 (Phase 2b), 66% and 116% larger than Ω_O = 3.0 taken in the design process (Ω from P-3D-RD-b model is ignored, See Appendix V). However, FEMA P695 also points out that "example applications show that values of archetype overstrength, Ω, can be as large as Ω = 6.0 for certain configurations, and are highly variable." As a result, caution and scrutiny is needed before drawing any deterministic conclusion from the evaluation of Ω_O. Again, the results are from models of one single archetype; performance evaluation of more archetype designs is needed in the future.

6.9 Summary observations and discussion

This chapter shows that the design of the CFS-NEES building using current seismic provisions from ASCE/SEI 7-10 (with R = 6.5) provides an acceptable level of collapse safety. IDA of high-fidelity 3D models of the CFS-NEES building further shows that current design passes the performance evaluation even with structural components only, and the additional lateral force resistance from nonstructural components significantly increases the collapse margin ratio. The complete building with every design detail will have a large safety margin for collapse, but it also suggests material usage following current design procedure is inefficient. The comparison of performance evaluation results also demonstrates that state-of-the-practice models are incapable of reasonably predicting the behavior of CFS-framed buildings under seismic load. Pushover analyses of high-fidelity 3D models suggest the overstrength factor Ω of the CFS-NEES archetype

building is larger than Ω_O =3.0 taken in the design process. These observations, together with those from simulation results in Chapter 4 and Chapter 5 and shaking table test data of the archetype building (Peterman 2014), suggests that current codes and standards for CFS-framed buildings are conservative and the completed building is significantly stiffer and stronger than the designer's prediction.

Since the building designed by current codes and specifications is 'too stiff' and 'too strong', it is possible to reduce the seismic design criteria to some extent so that future designs will use materials more efficiently. Design base shear V is the crucial load level in seismic design with the nonlinear behavior and energy dissipation capacity of the real structure taken care of by the response modification factor R. Consequently, the design base shear will be reduced if R becomes larger, since $V = C_s W$ and $C_s = S_{MT}/(1.5R)$. Lower demand from further reduced design base shear will render less conservative designs. Combined with the observation that predicted Ω of the archetype building is larger than current Ω_O, a tentative design modification would be reducing overall seismic demand but increasing the demand of force-controlled members, like chord studs in the shear wall system. These reductions would need to be tied to some engineering assurance of the lateral performance of systems currently not designed for lateral load: e.g. gravity walls and interior walls.

It is important to note that the performance evaluation of R and Ω_O herein is performed for only one archetype design modeled in different ways. A complete performance evaluation of the current value of R and Ω_O requires groups of archetype designs of the

same type of structure with various design demand and configuration be developed (see FEMA P695 (Applied Technology Council 2009)). Conclusive observation of the structural type's performance and solid suggestion on code modification can only be generalized after the evaluation of all performance groups. This is an important future work of the current research.

Chapter 7: Conclusions and Future Work

In this dissertation, research findings from two projects: shape optimization of CFS columns; and modeling, analysis, and performance evaluation of a two-story CFS-framed building have been presented under the general topic of simulation of cold-formed steel structures.

Shape optimization of CFS columns includes performance comparison of gradient-based vs. stochastic search algorithms for unconstrained search of a cross-section profile that maximizes axial capacity with fixed perimeter and thickness - and integrates a series of end-use and manufacturability constraints in the stochastic search algorithms for the same objective. Major conclusions of this project are:

- Unconstrained shape optimization of CFS columns has identified several novel but irregular cross-section profiles that can at least double the capacity of commercial lipped channel sections. Stochastic search algorithms, including genetic algorithms and simulated annealing, are capable of finding global optima but require multiple replications. A gradient-based algorithm is a local optimizer dependent on initial guess, but can be used in further improvement of global search results.
- A number of end-use and manufacturability constraints have been successfully added in the simulated annealing algorithm to allow constrained search of optimized cross-section profiles of CFS columns with significantly increased and

greater applicability for engineering constructions. Detailed investigations on limiting the number of rollers in the forming process and shifting the unbraced length from short to long have identified a family of promising cross-section shapes for the next generation of commercial products.

Simulation of the CFS-NEES building involves modeling of the archetype building at multiple construction phases with various fidelity levels, calibration of developed models with experimental data of full scale shaking table tests, investigation of the sensitivity of the predicted response with respect to modeling options, and performance evaluation of the archetype building based on pushover and Incremental Dynamic Analysis results. Major conclusions of this project are:

- Full-scale, high fidelity, finite element models provide reasonable prediction of an archetype building's seismic response and have shown the importance of simulation in quantification of the roles of individual systems of the building, and their interactions, and in performance evaluation of the archetype building.
- An archetype building designed by the current design approach are predicted to survive design basis and maximum considered earthquakes with minimal damage due in part to their much larger stiffness and capacity beyond design assumptions derived from previously underestimated contributions of gravity walls and nonstructural components and complicated interactions between subsystems.

- The gravity system, even with bare unsheathed framing, helps to increase the building's lateral force resistance significantly; sheathed gravity walls can transfer a considerable amount of lateral load, sometimes comparable to shear walls.
- The design assumption of isolated shear wall behavior (Type I) is overly idealized, coupled behavior (Type II) is initiated with even minimal addition of gravity systems, as shown even in two-dimensional modeling and analysis of wall lines.
- Interior gypsum sheathing of shear walls and gravity walls also contribute notably to the LFRS of the studied archetype building.
- Interior partition walls support exterior wall lines, provide additional coupling to the floor and roof diaphragms, increase diaphragm rigidity, and also increase lateral stiffness and capacity.
- Weatherproofing (DensGlass) exterior covering also strengthens the LFRS, but not as significantly as other nonstructural components and was ignored in modeling herein.
- The semi-rigid diaphragm in the archetype building plays an important role in lateral force resistance in that it couples wall lines and create three-dimensional interaction in addition to its own stiffness and capacity. The coupled system behavior can not be reliably predicted by an isolated wall line analysis or a linear combination of same.
- Performance evaluation of the response modification factor, R, and overstrength factor, Ω_o, for the CFS-NEES building modeled at three different fidelity levels shows the current design procedure can render safe designs if lateral resistance of

the gravity walls is included and it generally motivates improvement in the design codes for less conservative and more efficient designs in the future.

In general, a successful research not only answers a number of questions in the field, but proposes some or even more illuminating questions about the future as well.

Despite the success with shape optimization of CFS compressive members, optimization algorithms have been applied less in improvement of the layout and configuration of CFS systems. Dimension and shape optimization are available tools, but once topology optimization is implemented in the design of CFS members and systems, a larger space of improved design will become manifest. A smaller, but still useful point current shape optimization of CFS columns per se is imperfect; the radii of rollers are not considered in current formulation.

The research presented here on modeling and analysis of the CFS-NEES building is extensive, but not yet complete. First, high-fidelity models developed so far are not perfect. In particular, the vertical load path, especially the compressive bearing behavior at stud ends needs further consideration and improvement. The pull-through stiffness and capacity of shear anchors should also be further investigated. Bending stiffness of the foundation HSS steel tube could be taken into account in further refined models. The stiffness of the shear wall tie between chord studs at two levels also has an impact on the vertical load path.

The quantification of the role of semi-rigid diaphragms should proceed further. Current models are developed based on code provisions; specific tests on diaphragm systems can foster the understanding of diaphragm behavior greatly and provide information for more accurate state-of-the-art modeling of diaphragms.

The damping ratio is conservatively set to 5% in all time history analyses on the basis of the adoption of 5% damping in codes and standards and recommended provisions. The actual value of damping as identified in the CFS-NEES building after shaking table tests can be over 10%. The discrepancy in damping is thought to have an impact on the model's dynamical response. Observations from further exploration on the effect of damping ratio would be insightful.

In terms of simulation output, the lateral displacement of corner nodes at window and door openings should be recorded so that shear strain at those corners can be back calculated and compared with test. Strain at certain nodes should also be output, such as locations of shear wall ties that connect the first story shear walls to the second story. The simulation work in this dissertation is still a first trial of high-fidelity modeling and large-scale nonlinear analysis of real buildings in the realm of CFS structures. The work of the author and successors should be curated and form a database for further discussion and inquisition, since the idea of 'virtual test' and 'big data' has been around for a while and preliminary achievement has been reported by researchers in related fields.

Apparently, the interaction between components in CFS structures is complex, so corresponding high-fidelity FE models are complicated, but needed for better predictions of the building's performance. Even though the author has studied the sensitivity of simulation results with respect to modeling options and offered modeling guidelines, it seems impractical for engineers to create similar models of this type for everyday use. To enhance the applicability of modeling techniques in this research, further work is needed in the development of simplified models from high-fidelity ones currently available. Tradeoff between fidelity and practicality is expected, and this process requires a combination of mechanical concept and engineering intuition and dialogues between analysts and designers.

Two decisive factors for seismic design of structures using current design methods, R and Ω_O, have been evaluated following the procedure of FEMA P695. Although interesting findings regarding the design of the CFS-NEES building have been achieved from this effort, many more archetypes and their FE models should be analyzed and evaluated to form a conclusive judgment. Examples in Chapter 9 of FEMA P695 (Applied Technology Council 2009) all involve a number of archetypes with perturbation on important design considerations. This future work is somewhat related to previous one: extensive performance evaluation of archetype buildings is possible only if FE models with enough fidelity-levels can be generated without much effort or even automatically.

On the other hand, the exploration of modeling fidelity is still not complete. The complicated interaction in CFS-framed building can be understood from smaller scales.

Fastener-based models can help greatly for the understanding of load paths in sheathed walls between steel frame elements and sheathing pieces through local nonlinear behavior of fasteners. The limit state of stud buckling is modeled implicitly in current models as an approximation; however a much better way to model this would be a beam-element that allows the computation of global, even local and distortional buckling critical loads. Connection stiffness between CFS studs and tracks and the strap that ties chord studs across the floor is finite, semi-rigid models of these connections should be developed.

Some nonstructural components in the CFS-NEES building are still absent in the model. Staircases installed at Phase 2d is currently missing, but their possible role in multi-story coupling of response needs to be explored. Ceilings in the CFS-NEES building at Phase 2d can further contribute to the lateral stiffness and capacity of semi-rigid diaphragms. The weatherproofing DensGlass on the exterior façade can alter the mass distribution and can offer additional stiffness if the seam locations of DensGlass and OSB sheathing do not meet or if the DensGlass is attached all the way through the OSB to the steel. Effects of these modeling options could be investigated using refined models in the future.

All works presented above serves the author's ultimate goal: to maximize the usage of computational tools in the analysis and design of CFS structures for the creation of future designs with better performance in a more efficient way.

References

Adeli, H., and Karim, A. (1997). "Neural network model for optimization of cold-formed steel beams." *J.Struct.Eng.,* 123(11), 1535-1543.

Amabili, M. (2008). *Nonlinear vibrations and stability of shells and plates.* Cambridge University Press, New York, NY.

American Concrete Institute. (2013). "Performance-Based Seismic Design of Tall Building: A World View." https://www.youtube.com/watch?v=V72vQVXkI5w (5/13, 2013).

American Iron and Steel Institute. (2012). *North American standard for cold-formed steel framing – wall stud design, 2007 edition with supplement 1.* American Iron and Steel Institute, Washington, DC.

American Iron and Steel Institute. (2009). *North American standard for cold-formed steel framing - lateral design 2007 edition with supplement no. 1 and commentary.* American Iron and Steel Institute, Washington, DC.

American Iron and Steel Institute. (2008). *Cold-Formed Steel Design Manual.* American Iron and Steel Institute, Washington, DC.

American Iron and Steel Institute. (2007). *North American specification for the design of cold-formed steel structural members, 2007 edition.* American Iron and Steel Institute, Washington, DC.

American Iron and Steel Institute. (2007). *North American specification for the design of cold-formed steel structural members, 2007 edition with supplement 2.* American Iron and Steel Institute, Washington, DC.

American Iron and Steel Institute. (2007). *North American standard for cold-formed steel framing - floor and roof system design, 2007 edition.* American Iron and Steel Institute, Washington, DC.

American Iron and Steel Institute. (2007). *North American standard for cold-formed steel framing - general provisions, 2007 edition.* American Iron and Steel Institute, Washington, DC.

American Iron and Steel Institute. (2006). *Direct strength method (DSM) design guide.* American Iron and Steel Institute, Washington, DC.

American Iron and Steel Institute. (1996). *AISI specification for the design of cold-formed steel structural members.* American Iron and Steel Institute, Washington, DC.

American Iron and Steel Institute. (1991). *AISI Load and resistance factor design specification for cold-formed steel structural members.* American Iron and Steel InstituteAmerican Iron and Steel Institute, Washington, DC.

American Iron and Steel Institute. (1989). *AISI specification for the design of cold-formed steel structural members.* American Iron and Steel Institute, Washington, DC.

American Iron and Steel Institute. (1968). *AISI specification for the design of cold-formed steel structural members.* American Iron and Steel Institute, Washington, DC.

American Iron and Steel Institute. *North American standard for cold-formed steel framing - wall stud design, 2007 edition.* American Iron and Steel Institute, Washington, DC.

American Society of Civil Engineers. (2010). *Minimum design loads for buildings and other structures.* American Society of Civil Engineers, Reston, VA.

American Society of Civil Engineers. (2007). *Seismic rehabilitation of existing buildings.* American Society of Civil Engineers, Reston, VA.

American Society of Civil Engineers. (2005). *Minimum design loads for buildings and other structures.* American Society of Civil Engineers, Reston, VA.

APA—The Engineered Wood Association. (2012). *Panel design specification*. APA—The Engineered Wood Association, Tacoma, Washington.

Applied Technology Council. (2009). "Quantification of building seismic performance factors." *Rep. No. FEMA P695,* Applied Technology Council, Redwood City, CA.

Argyris, J., Boni, B., Hindenlang, U., and Kleiber, M. (1982). "Finite element analysis of two-and three-dimensional elasto-plastic frames—the natural approach." *Comput.Methods Appl.Mech.Eng.,* 35(2), 221-248.

Argyris, J. (1982). "An excursion into large rotations." *Comput.Methods Appl.Mech.Eng.,* 32(1), 85-155.

Arora, J. S. (2004). *Introduction to optimum design.* Academic Press, Waltham, MA.

ASCE/SEI Seismic Rehabilitation Standards Committee. (2007). *Seismic Rehabilitation of Existing Buildings (ASCE/SEI 41-06)*. American Society of Civil Engineers, Reston, VA.

ASTM International. (2011). "Standard Test Methods for Cyclic (Reversed) Load Test for Shear Resistance of Vertical Elements of the Lateral Force Resisting Systems for Buildings." ASTM International, West Conshohocken, PA.

Atluri, S. N., and Cazzani, A. (1995). "Rotations in computational solid mechanics." *Archives of Computational Methods in Engineering,* 2(1), 49-138.

Auricchio, F., Carotenuto, P., and Reali, A. (2008). "On the geometrically exact beam model: A consistent, effective and simple derivation from three-dimensional finite-elasticity." *Int.J.Solids Structures,* 45(17), 4766-4781.

Ayhan, D., and Schafer, B. W. (2012). "Moment-rotation characterization of cold-formed steel beams." *Rep. No. CFS-NEES-RR02,* Johns Hopkins University, Baltimore, MD.

Baker, J. W. (2015). "Efficient analytical fragility function fitting using dynamic structural analysis." *Earthquake Spectra,* 31(1), 579-599.

Baker, J. W., and Cornell, C. A. (2006). "Which spectral acceleration are you using?" *Earthquake Spectra,* 22(2), 293-312.

Bathe, K. (2006). *Finite element procedures.* Prentice Hall, Upper Saddle River, NJ.

Battini, J., and Pacoste, C. (2002). "Co-rotational beam elements with warping effects in instability problems." *Comput.Methods Appl.Mech.Eng.,* 191(17), 1755-1789.

Bendsoe, M. P., and Sigmund, O. (2003). *Topology optimization: theory, methods and applications.* Springer-Verlag, Berlin, Germany.

Bian, G., Buonopane, S. G., Ngo, H., and Schafer, B. W. (2014). "Fastener-based computational models with application to cold-formed steel shear walls." *Proceedings of the 22nd International Specialty Conference on Cold-Formed Steel Structures,* 825-840, St. Louis, MO.

Bian, G., Padilla-Llano, D. A., Leng, J., Buonopane, S. G., Moen, C. D., and Schafer, B. W. (2015). "OpenSees modeling of cold formed steel framed wall system." *Proceedings of 8th International Conference on Behavior of Steel Structures in Seismic Areas,* Shanghai, China.

British Standard Institution. (1998). *structural use of steel in building: part 5: code of practice for design of cold formed sections.* British Standard Institution, London, UK.

Building Seismic Safety Council. (2009). "NEHRP recommended seismic provisions for new buildings and other structures." *Rep. No. FEMA P750,* Building Seismic Safety Council, Washington, DC.

Buonopane, S. G., Bian, G., Tun, T. H., and Schafer, B. W. (2015). "Computationally efficient fastener-based models of cold-formed steel shear walls with wood sheathing." *Journal of Constructional Steel Research,* 110 137-148.

Buonopane, S. G., Tun, T. H., and Schafer, B. W. (2014). "Fastener-based computational models for prediction of seismic behavior of CFS shear walls." *Proceedings of the 10th National Conference in Earthquake Engineering,* Anchorage, AK.

Cao, H. P., and Hancock, G. J. (2012). "Elastic buckling of cold-formed channel sections in shear." *Thin-Walled Structures,* 61 22-26.

Cardona, A., and Geradin, M. (1988). "A beam finite element non‐linear theory with finite rotations." *Int J Numer Methods Eng,* 26(11), 2403-2438.

Chajes, A. (1993). *Principles of structural stability theory.* Waveland Press, Prospect Heights, IL.

Chamberlain Pravia, Z. M., and Kripka, M. (2012). "Cross section optimization using simulated annealing of cold-formed steel channel columns." *Proceedings of the Annual Stability Conference Structural Stability Research Council,* Grapevine, TX.

Chapelle, D., and Bathe, K. (2011). *The finite element analysis of shells-fundamentals.* Springer-Verlag, Berlin, Germany.

Chatterjee, A., Xiang, Y., Moen, C. D., Arwade, S. R., and Schafer, B. W. (2014). "Towards quantifying beneficial system effects in cold-formed steel wood-sheathed floor diaphragms." *Proceedings of the 22nd International Specialty Conference on Cold-Formed Steel Structures,* 903-917, St. Louis, MO.

Cheung, Y. K., and Tham, L. G. (1997). *The finite strip method.* CRC Press, Boca Raton, FL.

Christovasilis, I. P., Cimellaro, G. P., Barani, S., and Foti, S. (2014). "On the selection and scaling of ground motions for fragility analysis of structures." *Proceedings of 2nd European Conference on Earthquake Engineering and Seismology,* Istanbul, Turkey.

Christovasilis, I. P., Filiatrault, A., Constantinou, M. C., and Wanitkorkul, A. (2009). "Incremental dynamic analysis of woodframe buildings." *Earthquake Eng.Struct.Dyn.,* 38(4), 477-496.

Ciarlet, P. G. (2005). *An introduction to differential geometry with applications to elasticity.* Springer, Dordrecht, Netherlands.

Ciarlet, P. G. (2000). *Mathematical elasticity, volume three: theory of shells.* Elsevier Science Publishers B.V., Amsterdam, Netherlands.

Ciarlet, P. G. (1997). *Mathematical elasticity, volume two: theory of plates.* Elsevier Science Publishers B.V., Amsterdam, Netherlands.

Ciarlet, P. G. (1988). *Mathematical elasticity, volume one: three-dimensional elasticity.* Elsevier Science Publishers B.V., Amsterdam, Netherlands.

Conci, A., and Gattass, M. (1990). "Natural approach for geometric non‐linear analysis of thin‐walled frames." *Int J Numer Methods Eng,* 30(2), 207-231.

Conci, A., and Gattass, M. (1990). "Natural approach for thin‐walled beam‐columns with elastic‐plasticity." *Int J Numer Methods Eng,* 29(8), 1653-1679.

Cook, R. D., Malkus, D. S., Plesha, M. E., and Witt, R. J. (2007). *Concepts and applications of finite element analysis.* John Wiley & Sons, Hoboken, NJ.

Crisfield, M. A. (1997). *Nonlinear finite element analysis of solids and structures. Volume 2: Advanced topics.* John Wiley & Sons, New York, NY.

Crisfield, M. A. (1991). *Nonlinear finite element analysis of solids and structures. Volume 1: Essentials.* John Wiley & Sons, New York, NY.

Crisfield, M. A. (1990). "A consistent co-rotational formulation for non-linear, three-dimensional, beam-elements." *Comput.Methods Appl.Mech.Eng.,* 81(2), 131-150.

Crisfield, M. A., and Moita, G. F. (1996). "A unified co-rotational framework for solids, shells and beams." *Int.J.Solids Structures,* 33(20), 2969-2992.

Davies, J., and Leach, P. (1994). "First-order generalised beam theory." *Journal of Constructional Steel Research,* 31(2), 187-220.

Davies, J., Leach, P., and Heinz, D. (1994). "Second-order generalised beam theory." *Journal of Constructional Steel Research,* 31(2), 221-241.

Dubina, D. (2008). "Behavior and performance of cold-formed steel-framed houses under seismic action." *Journal of Constructional Steel Research,* 64(7), 896-913.

Eccher, G., Rasmussen, K. J. R., and Zandonini, R. (2009). "Geometric nonlinear isoparametric spline finite strip analysis of perforated thin-walled structures." *Thin-Walled Structures,* 47(2), 219-232.

Eccher, G., Rasmussen, K. J. R., and Zandonini, R. (2008). "Elastic buckling analysis of perforated thin-walled structures by the isoparametric spline finite strip method." *Thin-Walled Structures,* 46(2), 165-191.

EuroCode-3. (1996). *Design of steel structures, part1.3: general rules for cold formed thin gauge members and sheeting.* British Standard Institution, London UK.

Felippa, C. A., and Haugen, B. (2005). "A unified formulation of small-strain corotational finite elements: I. Theory." *Comput.Methods Appl.Mech.Eng.,* 194(21), 2285-2335.

Filiatrault, A., and Folz, B. (2002). "Performance-based seismic design of wood framed buildings." *J.Struct.Eng.,* 128(1), 39-47.

Fiorino, L., Iuorio, O., and Landolfo, R. (2012). "Seismic analysis of sheathing-braced cold-formed steel structures." *Eng.Struct.,* 34 538-547.

Foroughi, H., Moen, C. D., Myers, A., Tootkaboni, M., Vieira, L., and Schafer, B. (2014). "Analysis and design of thin metallic shell structural members–current practice and future research needs." *Proceedings of the Annual Stability Conference Structural Stability Research Council,* Toronto, Canada.

Franco, J. M. S., Duarte, J. P., Batista, E. d. M., and Landesmann, A. (2014). "Shape Grammar of steel cold-formed sections based on manufacturing rules." *Thin-Walled Structures,* 79 218-232.

Fülöp, L. A., and Dubina, D. (2004). "Performance of wall-stud cold-formed shear panels under monotonic and cyclic loading: Part I: Experimental research." *Thin-Walled Structures,* 42(2), 321-338.

Fülöp, L. A., and Dubina, D. (2004). "Performance of wall-stud cold-formed shear panels under monotonic and cyclic loading: Part II: Numerical modelling and performance analysis." *Thin-Walled Structures,* 42(2), 339-349.

Garcea, G., Madeo, A., and Casciaro, R. (2012). "The implicit corotational method and its use in the derivation of nonlinear structural models for beams and plates." *Journal of Mechanics of Materials and Structures,* 7(6), 509-538.

Gargari, M., Louhghalam, A., and Tootkaboni, M. (2013). "Optimal Cross Sections for Cold Formed Steel Members under Compression." *Proceedings of 10th World Congress on Structural and Multidisciplinary Optimization,* Orlando, FL.

Gilbert, B. P., Savoyat, T. J. M., and Teh, L. H. (2012). "Self-shape optimisation application: Optimisation of cold-formed steel columns." *Thin-Walled Structures,* 60 173-184.

Gilbert, B. P., Teh, L. H., and Guan, H. (2012). "Self-shape optimisation principles: Optimisation of section capacity for thin-walled profiles." *Thin-Walled Structures,* 60 194-204.

Golberg, D. E. (1989). *Genetic algorithms in search, optimization, and machine learning.* Addison-Wesley Publishing Company, Boston, MA.

Holland, J. H. (1975). *Adaptation in natural and artificial systems: an introductory analysis with applications to biology, control, and artificial intelligence.* University of Michigan Press, Ann Arbor, MI.

Holzapfel, G. A. (2000). *Nonlinear solid mechanics: a continuum approach for engineering.* John Wiley & Sons, Hoboken, NJ.

Hsiao, K. M. (1992). "Corotational total Lagrangian formulation for three-dimensional beamelement." *Aiaa j.,* 30(3), 797-804.

Hsiao, K. M., Lin, J. Y., and Lin, W. Y. (1999). "A consistent co-rotational finite element formulation for geometrically nonlinear dynamic analysis of 3-D beams." *Comput.Methods Appl.Mech.Eng.,* 169(1), 1-18.

Hsiao, K. M., and Lin, W. Y. (2000). "A co-rotational formulation for thin-walled beams with monosymmetric open section." *Comput.Methods Appl.Mech.Eng.,* 190(8), 1163-1185.

Hughes, T. J. R. (2000). *The finite element method: linear static and dynamic finite element analysis.* Dover Publications, Mineola, NY.

Ibarra, L. F., and Krawinkler, H. (2005). "Global collapse of frame structures under seismic excitations." *Rep. No. 2005/06,* Pacific Earthquake Engineering Research Center, Berkeley, CA.

Jelenić, G., and Crisfield, M. A. (1999). "Geometrically exact 3D beam theory: implementation of a strain-invariant finite element for statics and dynamics." *Comput.Methods Appl.Mech.Eng.,* 171(1), 141-171.

Karim, A., and Adeli, H. (1999). "Global optimum design of cold-formed steel hat-shape beams." *Thin-Walled Structures,* 35(4), 275-288.

Kirkpatrick, S., Gelatt, C. D., and Vecchi, M. P. (1983). "Optimization by simulated annealing." *Science,* 220(4598), 671-680.

Koiter, W. T. (1960). "A consistent first approximation in the general theory of thin elastic shells." *Theory of Thin Elastic Shells,* 12-33.

Kolcu, F., Ekmekyapar, T., and Özakça, M. (2010). "Linear buckling optimization and post-buckling behavior of optimized cold formed steel members." *Scientific Research and Essays,* 5(14), 1916-1924.

Krenk, S. (2009). *Non-linear Modeling and Analysis of Solids and Structures*. Cambridge University Press, Cambridge, England.

Kripka, M., and Martin, Z. (2013). "Cold-formed steel channel columns optimization with simulated annealing method." *Structural Engineering and Mechanics,* 48(3), 383-394.

Landolfo, R., Fiorino, L., and Corte, G. D. (2006). "Seismic behavior of sheathed cold-formed structures: physical tests." *J.Struct.Eng.,* 132(4), 570-581.

Lau, S. C. W., and Hancock, G. J. (1989). "Inelastic buckling analyses of beams, columns and plates using the spline finite strip method." *Thin-Walled Structures,* 7(3), 213-238.

Lau, S. C. W., and Hancock, G. J. (1986). "Buckling of thin flat-walled structures by a spline finite strip method." *Thin-Walled Structures,* 4(4), 269-294.

Lee, J., Kim, S., Park, H., and Woo, B. (2005). "Optimum design of cold-formed steel channel beams using micro Genetic Algorithm." *Eng.Struct.,* 27(1), 17-24.

Lee, J., Kim, S., and Seon Park, H. (2006). "Optimum design of cold-formed steel columns by using micro genetic algorithms." *Thin-Walled Structures,* 44(9), 952-960.

Leng, J., Guest, J. K., and Schafer, B. W. (2011). "Shape optimization of cold-formed steel columns." *Thin-Walled Structures,* 49(12), 1492-1503.

Leng, J., Li, Z., Guest, J. K., and Schafer, B. W. (2013). "Shape optimization of cold-formed steel columns with manufacturing constraints and limited number of rollers."

Proceedings of the Annual Stability Conference-Structural Stability Research Council, St. Louis, MO.

Leng, J., Li, Z., Guest, J. K., and Schafer, B. W. (2012). "Constrained shape optimization of cold-formed steel columns." *Proceedings of 21st International Specialty Conference on Cold-Formed Steel Structures,* St. Louis, MO.

Leng, J., Li, Z., Guest, J. K., and Schafer, B. W. (2014). "Shape optimization of cold-formed steel columns with fabrication and geometric end-use constraints." *Thin-Walled Structures,* 85 271-290.

Leng, J., Schafer, B. W., and Buonopane, S. G. (2012). "Seismic Computational Analysis of CFS-NEES Building." *Proceedings of 21st International Specialty Conference on Cold-Formed Steel Structures,* 801-820, St. Louis, MO.

Leng, J., Schafer, B. W., and Buonopane, S. G. (2013). "Modeling the seismic response of cold-formed steel framed buildings: model development for the CFS-NEES building." *Proceedings of the Annual Stability Conference-Structural Stability Research Council,* St. Louis, MO.

Li, Y., Ma, R., and Shen, Z. (2014). "Numerical simulation on dynamic behavior of a cold-formed steel framing building test model." *Proceedings of 22nd International Specialty Conference on Cold-Formed Steel Structures,* 873-885, St. Louis, MO.

Li, Z., and Schafer, B. W. (2013). "Constrained finite strip method for thin-walled members with general end boundary conditions." *Journal of Engineering Mechanics,* 139(11), 1566-1576.

Li, Z., and Schafer, B. W. (2011). "Tabulated local and distortional elastic buckling solutions for standard shapes." *Rep. No. TN-G103-11,* Cold-formed steel engineers institute, Washington, DC.

Li, Z., and Schafer, B. W. (2010). "Application of the finite strip method in cold-formed steel member design." *Journal of Constructional Steel Research,* 66(8), 971-980.

Li, Z., Hanna, M., Ádány, S., and Schafer, B. (2011). "Impact of basis, orthogonalization, and normalization on the constrained Finite Strip Method for stability solutions of open thin-walled members." *Thin-Walled Structures,* 49(9), 1108-1122.

Liu, H., Igusa, T., and Schafer, B. (2004). "Knowledge-based global optimization of cold-formed steel columns." *Thin-Walled Structures,* 42(6), 785-801.

Liu, P., Peterman, K. D., Yu, C., and Schafer, B. W. (2012). "Characterization of cold-formed steel shear wall behavior under cyclic loading for the CFS-NEES building." *Proceedings of 21st International Specialty Conference on Cold-Formed Steel Structures,* 703-722, St. Louis, MO.

Liu, P., Peterman, K. D., and Schafer, B. W. (2014). "Impact of construction details on OSB-sheathed cold-formed steel framed shear walls." *Journal of Constructional Steel Research,* 101 114-123.

Love, A. E. H. (1888). "The small free vibrations and deformation of a thin elastic shell." *Philosophical Transactions of the Royal Society of London,* 179 491-546.

Love, A. E. H. (2013). *A treatise on the mathematical theory of elasticity.* Cambridge University Press, Cambridge, England.

Lowes, L. N., and Altoontash, A. (2003). "Modeling reinforced-concrete beam-column joints subjected to cyclic loading." *Journal of Structural Engineering,* 129(12), 1686-1697.

Lu, W. (2003). *Optimum design of cold-formed steel purlins using genetic algorithms.* Helsinki University of Technology, Helsinki, Finland.

Luenberger, D. G. (1969). *Optimization by vector space methods.* John Wiley & Sons, New York, NY.

Madsen, R. L., Nakata, N., and Schafer, B. W. (2011). "CFS-NEES building structural design narrative." *Rep. No. CFS-NEES-RR01,* Johns Hopkins University, Baltimore, MD.

Malvern, L. E. (1977). *Introduction to the mechanics of a continuous medium.* Prentice Hall, Upper Saddle River, NJ.

Martínez-Martínez, J., and Xu, L. (2011). "Simplified nonlinear finite element analysis of buildings with CFS shear wall panels." *Journal of Constructional Steel Research,* 67(4), 565-575.

McGuire, W., Gallagher, R. H., and Ziemian, R. D. (2000). *Matrix structural analysis.* John Wiley and Sons, Hoboken, NJ.

McKenna, F. e. a. (2011). "Open system for earthquake engineering simulation (OpenSees)." Pacific Earthquake Engineering Research Center, Berkeley, CA.

Moen, C. D., Igusa, T., and Schafer, B. W. (2008). "Prediction of residual stresses and strains in cold-formed steel members." *Thin-Walled Structures,* 46(11), 1274-1289.

Moharrami, M., Louhghalam, A., and Tootkaboni, M. (2014). "Optimal folding of cold formed steel cross sections under compression." *Thin-Walled Structures,* 76 145-156.

Nocedal, J., and Wright, S. (2006). *Numerical optimization.* Springer, New York.

Oran, C. (1973). "Tangent stiffness in plane frames." *Journal of the Structural Division,* 99(6), 973-985.

Oran, C. (1973). "Tangent stiffness in space frames." *Journal of the Structural Division,* 99(6), 987-1001.

Padilla-Llano, D. A. (2015). "A Framework for Cyclic Simulation of Thin-Walled Cold-Formed Steel Members in Structural Systems." .

Padilla-Llano, D. A., Moen, C. D., and Eatherton, M. R. (2014). "Cyclic flexural hysteretic models for cold-formed steel seismic simulation." *Proceedings of European Conference on Steel and Composite Structures,* Naples, Italy.

Peterman, K. D. (2014). "Behavior of full-scale cold-formed steel buildings under seismic excitations." Doctoral dissertation. Johns Hopkins University, Baltimore, MD.

Peterman, K. D., Madsen, R. L., and Schafer, B. W. (2014). "Experimental seismic behavior of the CFS-NEES building: system-level performance of a full-scale two-story light steel framed building." *Proceedings of 22nd International Specialty Conference on Cold-Formed Steel Structures,* 887-901, St. Louis, MO.

Peterman, K. D., Nakata, N., and Schafer, B. W. (2014). "Hysteretic characterization of cold-formed steel stud-to-sheathing connections." *Journal of Constructional Steel Research,* 101 254-264.

Peterman, K. D., and Schafer, B. W. (2013). "Hysteretic shear response of fasteners connecting sheathing to cold-formed steel studs." *Rep. No. CFS-NEES-RR04,* Johns Hopkins University, Baltimore, MD.

Peterman, K. D., Stehman, M. J. J., Buonopane, S. G., Nakata, N., Madsen, R. L., and Schafer, B. W. (2014). "Stability behavior of full-scale cold-formed steel buildings under

seismic excitations." *Proceedings of the Annual Stability Conference-Structural Stability Research Council,* Toronto, Canada.

Rosowsky, D. V., and Ellingwood, B. R. (2002). "Performance-based engineering of wood frame housing: fragility analysis methodology." *J.Struct.Eng.,* 128(1), 32-38.

Saka, M., Carbas, S., Aydogdu, I., Akin, A., and Geem, Z. (2015). "Comparative Study on Recent Metaheuristic Algorithms in Design Optimization of Cold-Formed Steel Structures." *Engineering and Applied Sciences Optimization,* N. Lagaros, and M. Papadrakakis, eds., Springer International Publishing, Cham, Switzerland, 145-173.

Santos, H. (2012). "A complementary-energy based criterion for the stability analysis of geometrically exact framed structures." *Comput.Struct.,* 106 196-203.

Santos, H. (2012). "Variationally consistent force-based finite element method for the geometrically non-linear analysis of Euler–Bernoulli framed structures." *Finite Elements Anal.Des.,* 53 24-36.

Santos, H., Pimenta, P., and Almeida, J. (2011). "A hybrid-mixed finite element formulation for the geometrically exact analysis of three-dimensional framed structures." *Comput.Mech.,* 48(5), 591-613.

Santos, H., Pimenta, P., and Moitinho de Almeida, J. (2010). "Hybrid and multi-field variational principles for geometrically exact three-dimensional beams." *Int.J.Non-Linear Mech.,* 45(8), 809-820.

Schafer, B. W. (2015). "Seismic response and engineering of cold-formed steel framed buildings." *Proceedings of 8th International Conference on Advances in Steel Structures,* Lisbon, Portugal.

Schafer, B. W. (2011). "Cold‐formed steel structures around the world." *Steel Construction,* 4(3), 141-149.

Schafer, B. W. (2010). "User's manual and tutorials of CUFSM 3.12." Johns Hopkins University, Baltimore, MD.

Schafer, B. W. (2008). "Review: the direct strength method of cold-formed steel member design." *Journal of Constructional Steel Research,* 64(7), 766-778.

Schafer, B. W., and Ádány, S. (2006). "Buckling analysis of cold-formed steel members using CUFSM: conventional and constrained finite strip methods." *Proceedings of 18th International Specialty Conference on Cold-Formed Steel Structures,* 39-54, Orlando, FL.

Schafer, B. W., Ayhan, D., Leng, J., Liu, P., Padilla-Llano, D. A., Peterman, K. D., Stehman, M., Buonopane, S. G., Eatherton, M. R., and Madsen, R. L. (2014). "The CFS-NEES effort: Advancing Cold-Formed Steel Earthquake Engineering." *Proceedings of the 10th National Conference in Earthquake Engineering,* Anchorage AK.

Schafer, B. W., Li, Z., and Moen, C. D. (2010). "Computational modeling of cold-formed steel." *Thin-Walled Structures,* 48(10), 752-762.

Schafer, B. W., and Peköz, T. (1998). "Computational modeling of cold-formed steel: characterizing geometric imperfections and residual stresses." *Journal of Constructional Steel Research,* 47(3), 193-210.

Schafer, B. W., Sarawit, A., and Peköz, T. (2006). "Complex edge stiffeners for thin-walled members." *J.Struct.Eng.,* 132(2), 212-226.

Seaburg, P. A., and Salmon, C. G. (1971). "Minimum weight design of light gage steel members." *Journal of the Structural Division,* 97(1), 203-222.

SEAOC Seismology Committee. (2008). "A brief guide to seismic design factors." *Structure Magazine,* 30-32.

Shamim, I., and Rogers, C. A. (2012). "Numerical Modeling and Calibration of CFS Framed Shear Walls under Dynamic Loading." *Proceedings of 21st International Specialty Conference on Cold-Formed Steel Structures,* 687-701, St. Louis, MO.

Silvestre, N., and Camotim, D. (2003). "Nonlinear generalized beam theory for cold-formed steel members." *International Journal of Structural Stability and Dynamics,* 3(04), 461-490.

Silvestre, N., and Camotim, D. (2002). "First-order generalised beam theory for arbitrary orthotropic materials." *Thin-Walled Structures,* 40(9), 755-789.

Silvestre, N., and Camotim, D. (2002). "Second-order generalised beam theory for arbitrary orthotropic materials." *Thin-Walled Structures,* 40(9), 791-820.

Simo, J. C., and Vu-Quoc, L. (1991). "A geometrically-exact rod model incorporating shear and torsion-warping deformation." *Int.J.Solids Structures,* 27(3), 371-393.

Simpson Strong-Tie Company Inc. (2013). "Load table of S/HDU Holdowns." Simpson Strong-Tie Company Inc., Baltimore, MD.

Slivker, V. (2007). *Mechanics of structural elements: theory and applications.* Springer, Berlin, Germany.

Spall, J. C. (2003). *Introduction to stochastic search and optimization: estimation, simulation, and control.* John Wiley and Sons, Hoboken, NJ.

Steel Framing Industry Association. (2011). "Technical guide for cold-formed steel framing products." SFIA, Falls Church, VA.

Tashakori, A., and Adeli, H. (2002). "Optimum design of cold-formed steel space structures using neural dynamics model." *Journal of Constructional Steel Research,* 58(12), 1545-1566.

Tian, Y., and Lu, T. (2004). "Minimum weight of cold-formed steel sections under compression." *Thin-Walled Structures,* 42(4), 515-532.

Timoshenko, S. P., and Gere, J. M. (2009). *Theory of elastic stability.* Dover Publications, Mineola, NY.

Timoshenko, S. P., and Woinowsky-Krieger, S. (1959). *Theory of plates and shells.* McGraw-Hill, New York, NY.

Tran, T., and Li, L. (2006). "Global optimization of cold-formed steel channel sections." *Thin-Walled Structures,* 44(4), 399-406.

Vamvatsikos, D., and Cornell, C. A. (2002). "Incremental dynamic analysis." *Earthquake Engineering & Structural Dynamics,* 31(3), 491-514.

Vamvatsikos, D., and Cornell, C. A. (2004). "Applied incremental dynamic analysis." *Earthquake Spectra,* 20(2), 523-553.

Vamvatsikos, D., and Cornell, C. A. (2002). "The incremental dynamic analysis and its application to performance-based earthquake engineering." *Proceedings of the 12th European Conference on Earthquake Engineering,* London, UK.

van de Lindt, J. W. (2004). "Evolution of wood shear wall testing, modeling, and reliability analysis: bibliography." *Practice Periodical on Structural Design and Construction,* 9(1), 44-53.

van de Lindt, J. W., Pei, S., Liu, H., and Filiatrault, A. (2010). "Three-dimensional seismic response of a full-scale light-frame wood building: numerical study." *Journal of Structural Engineering,* 136(1), 56-65.

Ventsel, E., and Krauthammer, T. (2001). *Thin plates and shells: theory, analysis, and applications.* CRC Press, Boca Raton, FL.

Wang, B., Gilbert, B. P., Molinier, A. M., Guan, H., and Teh, L. H. (2014). "Shape optimisation of cold-formed steel profiles with manufacturing constraints - Part I: Algorithm." *Proceedings of 22nd International Specialty Conference on Cold-Formed Steel Structures,* 21-36, St. Louis, MO.

Wang, B., Gilbert, B. P., Molinier, A. M., Guan, H., and Teh, L. H. (2014). "Shape optimisation of cold-formed steel profiles with manufacturing constraints - Part II: Applications." *Proceedings of 22nd International Specialty Conference on Cold-Formed Steel Structures,* 37-50, St. Louis, MO.

Yu, C., Yu, G., and Wang, J. (2014). "Innovative cold-formed steel framed shear wall sheathed with corrugated steel sheets: experiments and dynamic analysis." *Proceedings of 22nd International Specialty Conference on Cold-Formed Steel Structures,* 775-792, St. Louis, MO.

Yun, S., Hamburger, R. O., Cornell, C. A., and Foutch, D. A. (2002). "Seismic performance evaluation for steel moment frames." *J.Struct.Eng.,* 128(4), 534-545.

Zeinoddini, V. M., and Schafer, B. W. (2012). "Simulation of geometric imperfections in cold-formed steel members using spectral representation approach." *Thin-Walled Structures,* 60 105-117.

Zhang, X., and Rasmussen, K. (2013). "Analysis of locally/distortionally buckled beams." *Proceedings of the Annual Stability Conference Structural Stability Research Council,* St. Louis, MO.

Zienkiewicz, O. C., and Taylor, R. L. (2005). *The finite element method for solid and structural mechanics.* Butterworth-heinemann, Oxford, England.

Appdendices

Appendix A: Analysis Results of State-of-the-practice, 2D, model a (P-2D-a)

A.1 Model description

This set of state-of-the-practice 2D models features bracing models of whole shear wall panels, smeared models of hold downs into shear walls as pinned supports and rigid leaning columns. Interplay between different wall lines is not allowed in 2D models, representing the effect of flexible diaphragms. Seismic mass is lumped at leaning column nodes. The lateral displacement and shear wall capacity ($\delta(V_{nP})$, V_{nP}) from AISI-213 standard is utilized to determine the stiffness of elastic material and the turning point on the backbone curve of elastic-perfectly plastic (EPP) material of shear wall bracing. Figure A-1 (a) to (d) illustrate OpenSees models of South, North, East and West elevations. Simulation results are presented and discussed in later sections. Definitions of output physical quantities and explanation of post-process method can be found in Appendix E.

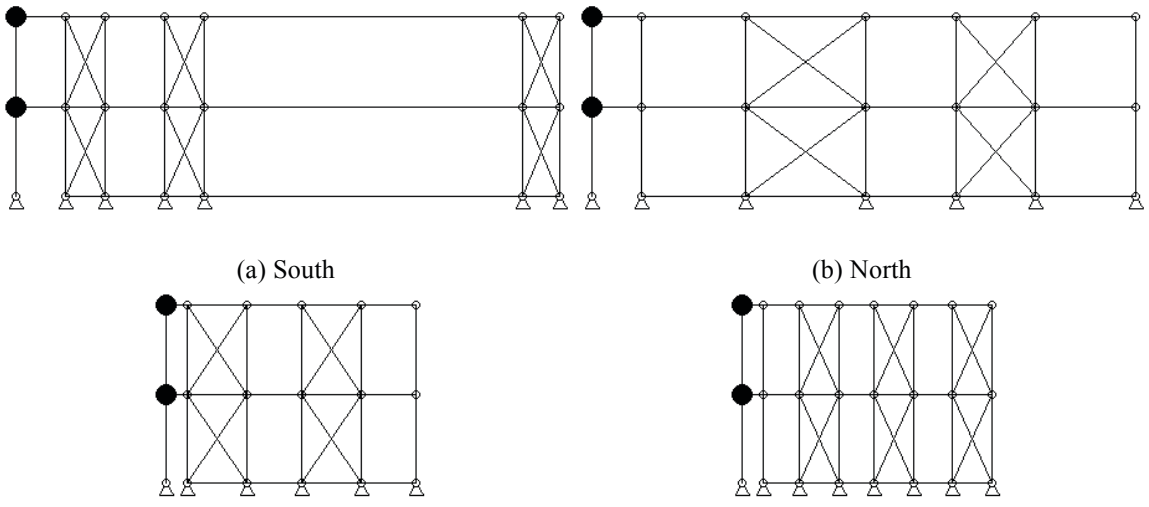

(a) South (b) North

(c) East (d) West

Figure A-1: P-2D-a model

A.2 Free vibration analysis results

Free vibration analysis is performed for each elevation model. Values of first two natural periods are tabulated (Table A-1). Figure A-2 shows corresponding mode shapes.

Table A-1: Free vibration analysis results, P-2D-a model

Elevation	1st natural period (s)	2nd natural period (s)
South	0.926	0.399
North	0.568	0.272
East	0.834	0.363
West	0.908	0.393

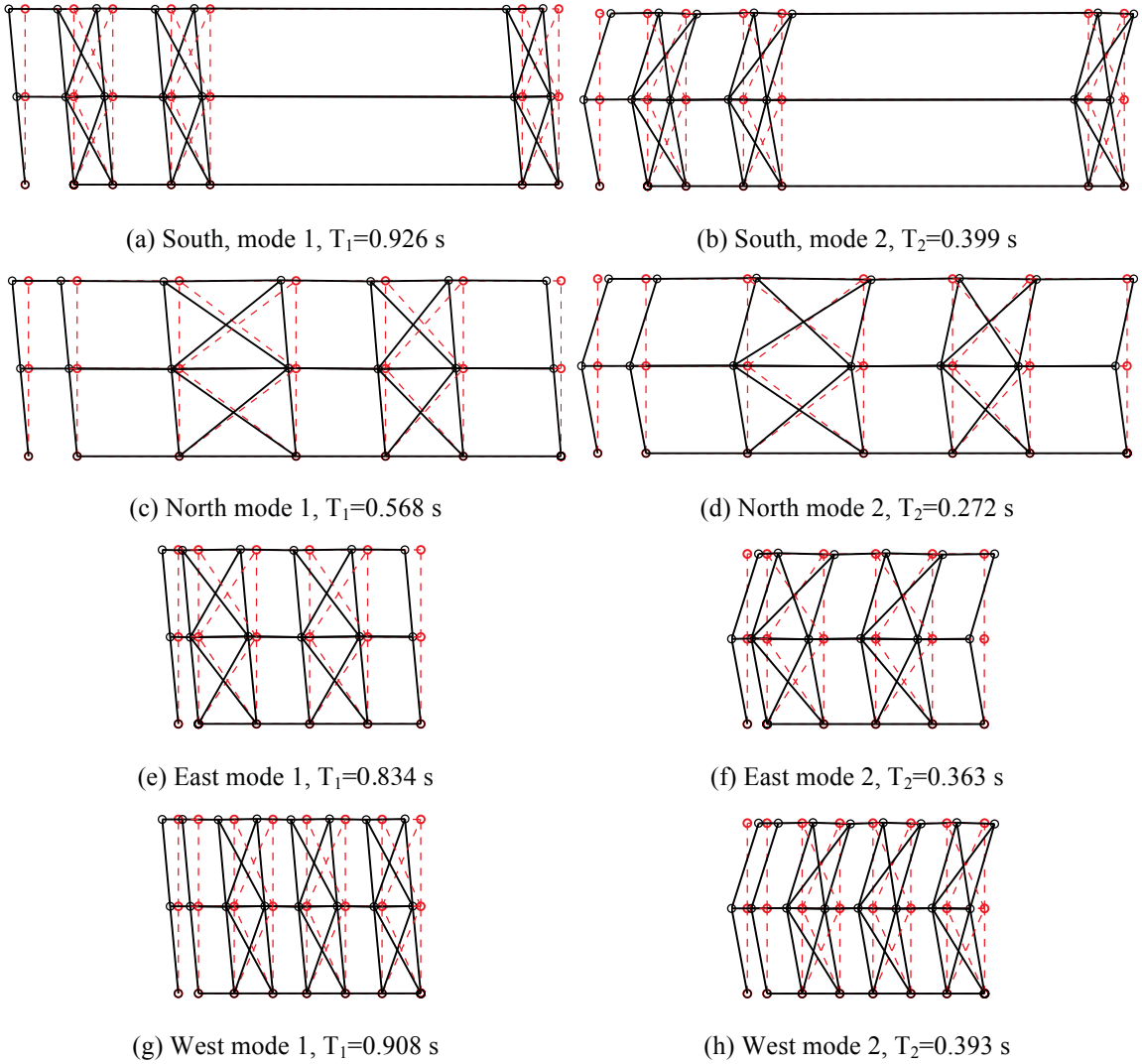

(a) South, mode 1, T_1=0.926 s

(b) South, mode 2, T_2=0.399 s

(c) North mode 1, T_1=0.568 s

(d) North mode 2, T_2=0.272 s

(e) East mode 1, T_1=0.834 s

(f) East mode 2, T_2=0.363 s

(g) West mode 1, T_1=0.908 s

(h) West mode 2, T_2=0.393 s

Figure A-2: First two natural modes of P-2D-a model

A.3 Linear static analysis results

Linear static analysis is performed on each wall line. The total lateral load on that wall line is one half of the design base shear. The vertical distribution of lateral load follows the distribution of equivalent lateral load in the design narrative(Madsen et al. 2011)

Although each wall line is analyzed independently, to make a better summary and to make better comparisons with 3D models, results of individual wall lines are post-processed to reconstruct physical quantities of the whole building behavior, such as building displacements/drifts and total building base shear.

Table A-2 summarizes the breakdown of peak total base shear among four elevations. As shown in the table, each of two facing wall lines take 5.5 kips of base shear, and wall lines perpendicular to the loading direction take zero base shear as a natural result of 2D analysis.

Table A-3 shows peak building and wall line deflections. Practicing engineers can linearly upscale these data and develop an estimate of the building's performance at a certain lateral force level. In 2D analysis, only wall lines along the loading direction have displacements in the loading direction.

Table A-4 is an evaluation of the each wall line's lateral stiffness of long and short direction and its breakdown among shear walls (SW) and other systems. Since gravity

walls (GW) are not modeled in state-of-the-practice models, all base shear goes to shear walls.

Table A-2: Breakdown of peak base shear, linear static analysis, P-2D-a model

Load direction	**LONG**				
Elevation	**South V_b**	**North V_b**	**East V_b**	**West V_b**	**Peak V_b**
kips	5.5	5.5	0.0	0.0	11.1
%	50.0	50.0	0.0	0.0	100.0
Load direction	**SHORT**				
Elevation	**South V_b**	**North V_b**	**East V_b**	**West V_b**	**Peak V_b**
kips	0.0	0.0	5.5	5.5	11.1
%	0.0	0.0	50.0	50.0	100.0

Table A-3: Peak building and wall line deflection, linear static analysis, P-2D-a model

Load direction	**LONG**							
Deflection (in.)	**u_1**	**u_2**	**v_1**	**v_2**	**Δu_1**	**Δu_2**	**Δv_1**	**Δv_2**
Building	0.574	1.132	0.000	0.000	0.574	0.558	0.000	0.000
South	0.842	1.657	0.000	0.000	0.842	0.816	0.000	0.000
North	0.306	0.606	0.000	0.000	0.306	0.301	0.000	0.000
East	-	-	-	-	-	-	-	-
West	-	-	-	-	-	-	-	-
Load direction	**SHORT**							
Deflection (in.)	**u_1**	**u_2**	**v_1**	**v_2**	**Δu_1**	**Δu_2**	**Δv_1**	**Δv_2**
Building	0.000	0.000	0.752	1.476	0.000	0.000	0.752	0.724
South	-	-	-	-	-	-	-	-
North	-	-	-	-	-	-	-	-
East	0.000	0.000	0.688	1.353	0.000	0.000	0.688	0.665
West	0.000	0.000	0.816	1.599	0.000	0.000	0.816	0.783

Table A-4: Breakdown of lateral stiffness, P-2D-a model

SOUTH			**NORTH**		
Shear wall k_u (%)	**Gravity wall k_u (%)**	**k_u (kip/in)**	**Shear wall k_v (%)**	**Gravity wall k_v (%)**	**k_v (kip/in)**
100.0	0.0	3.3	100.0	0.0	9.1
EAST			**WEST**		
Shear wall k_u (%)	**Gravity wall k_u (%)**	**k_u (kip/in)**	**Shear wall k_v (%)**	**Gravity wall k_v (%)**	**k_v (kip/in)**
100.0	0.0	4.1	100.0	0.0	3.5

A.4 Nonlinear static (pushover) analysis results

Table A-5 is created following the same logic with Table A-2, but the analysis type is nonlinear static (pushover). Pushover curves of the building and each wall line are presented in Figure A-3 and Figure A-4.

These tables and figures indicate that the wall lines do not reach their peak capacity at exactly the same drift level. Accordingly, total capacity of the building reconstructed using 2D results is no greater than the sum of wall line capacities in the load direction. This observation is more apparent in long direction. The missing of diaphragm stiffness and induced interplay of wall lines can make a significant difference between 2D analysis and real 3D analysis.

Table A-5: Breakdown of peak base shear, pushover analysis, P-2D-a model

Load direction	**LONG**				
Elevation	**South V_b**	**North V_b**	**East V_b**	**West V_b**	**Peak V_b**
kips	10.4	18.1	0.0	0.0	24.3
%	42.7	74.5	0.0	0.0	100.0
Load direction	**SHORT**				
Elevation	**South V_b**	**North V_b**	**East V_b**	**West V_b**	**Peak V_b**
kips	0.0	0.0	10.7	10.1	18.2
%	0.0	0.0	59.0	55.6	100.0

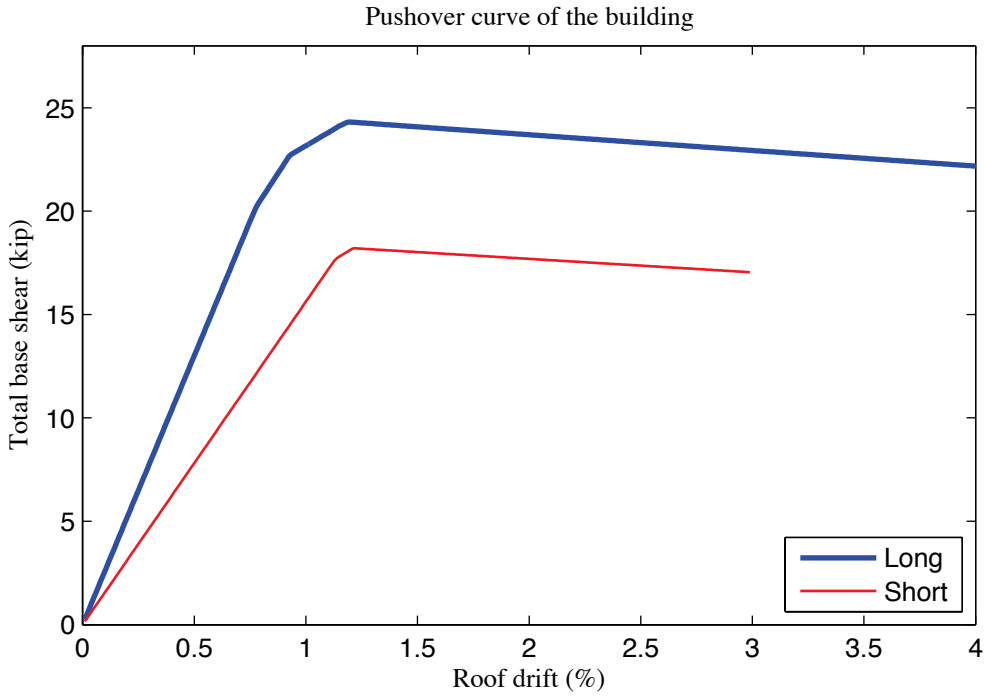

Figure A-3: Pushover curve of P-2D-a model

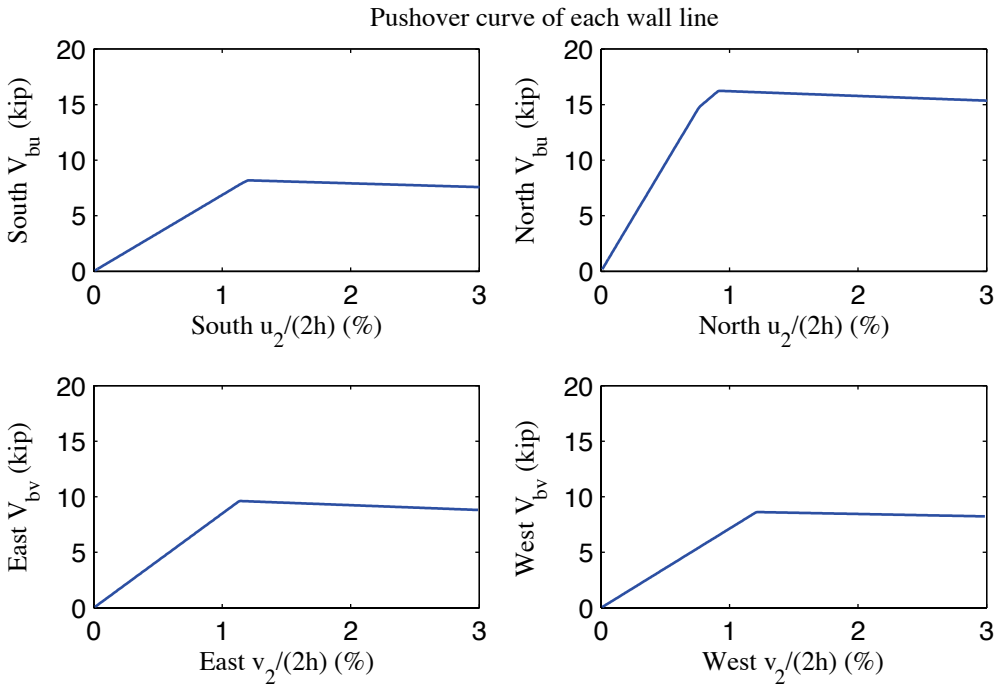

Figure A-4: Pushover curve of each wall line, P-2D-a model

A.5 Linear time history analysis results

Linear time history analysis is performed on 2D models under Canoga Park and Rinaldi ground motion records of Northridge earthquake in 1994. We considered three scale levels (16%, 44% and 100%) and single axis excitation is applied in the lateral direction of a single wall line.

Table A-6 to Table A-9 demonstrate the reconstructed linear elastic performance of the building under designated ground motions. Table A-6 shows peak story relative accelerations in the unit of g. Table A-7 and Table A-8 report peak roof drift and story drift of the building and the corresponding time step (t_*) and the base shear at that time. Note that the base shear at the time of peak roof drift may not be the peak total building base shear in that direction (see Table A-9).

The response of each wall line is available directly from 2D analysis results, so peak story drift and peak base shear of each wall line are listed in Table A-10 and Table A-11.

Wall lines behave linearly since peak drift and peak base shear appear at the same time when the ground motion is linearly scaled. Figure A-5 is a vector plot of the peak total resultant base shear of the building under 100% Canoga Park excitation. Since four dynamical analyses in 2D should be performed separately in order to create the plot, base shear vectors are always in-line with the wall. Comparison with nonlinear analysis results of the same excitation provides insightful observations on the building's response and requirements on modeling fidelity and analysis type.

Table A-6: P-2D-a model peak story relative acceleration in g, linear time history analysis

Load Case	Ground Motion	LONG			SHORT		
		a_g	Floor a	Roof a	a_g	Floor a	Roof a
EQ_2D_1axis_1	CNP 16%	0.067	0.110	0.164	0.057	0.092	0.122
EQ_2D_1axis_2	CNP 44%	0.185	0.303	0.452	0.157	0.252	0.334
EQ_2D_1axis_3	CNP 100%	0.420	0.688	1.027	0.356	0.572	0.760
EQ_2D_1axis_4	RRS 16%	0.132	0.189	0.317	0.078	0.197	0.218
EQ_2D_1axis_5	RRS 44%	0.363	0.519	0.870	0.214	0.543	0.598
EQ_2D_1axis_6	RRS 100%	0.825	1.179	1.978	0.486	1.234	1.360

Table A-7: P-2D-a model peak building roof drift and base shear, linear time history analysis

Load Case	Ground Motion	LONG			SHORT		
		$u_2/(2h)$ (%)	t_* (s)	V_b @ t_* (kips)	$v_2/(2h)$ (%)	t_* (s)	V_b @ t_* (kips)
EQ_2D_1axis_1	CNP 16%	-0.349	7.84	9.3	0.365	9.05	5.4
EQ_2D_1axis_2	CNP 44%	-0.959	7.84	25.6	1.003	9.05	15.0
EQ_2D_1axis_3	CNP 100%	-2.180	7.84	58.1	2.279	9.05	34.0
EQ_2D_1axis_4	RRS 16%	0.943	3.85	16.9	-0.583	2.90	11.4
EQ_2D_1axis_5	RRS 44%	2.593	3.85	46.5	-1.604	2.90	31.5
EQ_2D_1axis_6	RRS 100%	5.893	3.85	105.7	-3.645	2.90	71.5

Table A-8: P-2D-a model peak building story drift, linear time history analysis

Load Case	Ground Motion	LONG				SHORT			
		$\Delta u_1/h$ (%)	t_* (s)	$\Delta u_2/h$ (%)	t_* (s)	$\Delta v_1/h$ (%)	t_* (s)	$\Delta v_2/h$ (%)	t_* (s)
EQ_2D_1 axis_1	CNP 16%	-0.376	7.82	-0.333	7.86	-0.351	8.66	0.382	9.05
EQ_2D_1 axis_2	CNP 44%	-1.033	7.82	-0.915	7.86	-0.964	8.66	1.049	9.05
EQ_2D_1 axis_3	CNP 100%	-2.349	7.82	-2.079	7.86	-2.192	8.66	2.385	9.05
EQ_2D_1 axis_4	RRS 16%	0.955	3.85	0.931	3.86	-0.712	2.89	0.597	3.26
EQ_2D_1 axis_5	RRS 44%	2.626	3.85	2.561	3.86	-1.958	2.89	1.642	3.26
EQ_2D_1 axis_6	RRS 100%	5.967	3.85	5.820	3.86	-4.450	2.89	3.732	3.26

Table A-9: P-2D-a model peak building base shear, linear time history analysis

		LONG		SHORT		RESULTANT	
Load Case	**Ground Motion**	**Peak V_{bu} (kip)**	**t @ peak V_{bu} (s)**	**Peak V_{bv} (kip)**	**t @ peak V_{bv} (s)**	**Peak V_b (kip)**	**t @ peak V_b (s)**
EQ_2D_1 axis_1	CNP 16%	9.5	7.82	5.5	8.66	9.5	7.82
EQ_2D_1 axis_2	CNP 44%	26.0	7.82	15.0	8.66	26.2	7.82
EQ_2D_1 axis_3	CNP 100%	59.1	7.82	34.1	8.66	59.5	7.82
EQ_2D_1 axis_4	RRS 16%	17.0	2.80	11.5	2.89	19.2	2.82
EQ_2D_1 axis_5	RRS 44%	46.8	2.80	31.6	2.89	52.8	2.82
EQ_2D_1 axis_6	RRS 100%	106.4	2.80	71.9	2.89	120.1	2.82

Table A-10: P-2D-a model peak wall line story drift, linear time history analysis

LONG		**SOUTH**				**NORTH**			
Load Case	**Ground Motion**	**$\Delta u_1/h$ (%)**	**t_* (s)**	**$\Delta u_2/h$ (%)**	**t_* (s)**	**$\Delta u_1/h$ (%)**	**t_* (s)**	**$\Delta u_2/h$ (%)**	**t_* (s)**
EQ_2D_1axis_1	CNP 16%	0.501	9.10	0.531	8.99	0.396	8.75	0.370	10.28
EQ_2D_1axis_2	CNP 44%	1.377	9.10	1.460	8.99	1.090	8.75	1.019	10.28
EQ_2D_1axis_3	CNP 100%	3.130	9.10	3.317	8.99	2.477	8.75	2.315	10.28
EQ_2D_1axis_4	RRS 16%	1.674	3.83	1.606	3.86	0.533	2.75	0.565	2.74
EQ_2D_1axis_5	RRS 44%	4.602	3.83	4.416	3.86	1.466	2.75	1.555	2.74
EQ_2D_1axis_6	RRS 100%	10.460	3.83	10.037	3.86	3.333	2.75	3.533	2.74
SHORT		**EAST**				**WEST**			
Load Case	**Ground Motion**	**$\Delta v_1/h$ (%)**	**t_* (s)**	**$\Delta v_2/h$ (%)**	**t_* (s)**	**$\Delta v_1/h$ (%)**	**t_* (s)**	**$\Delta v_2/h$ (%)**	**t_* (s)**
EQ_2D_1axis_1	CNP 16%	0.327	8.98	0.335	9.03	0.457	8.67	0.457	8.67
EQ_2D_1axis_2	CNP 44%	0.899	8.98	0.921	9.03	1.257	8.67	1.258	8.67
EQ_2D_1axis_3	CNP 100%	2.043	8.98	2.094	9.03	2.858	8.67	2.858	8.67
EQ_2D_1axis_4	RRS 16%	0.682	2.88	0.761	4.53	0.772	2.91	0.712	6.05
EQ_2D_1axis_5	RRS 44%	1.876	2.88	2.092	4.53	2.123	2.91	1.958	6.05
EQ_2D_1axis_6	RRS 100%	4.265	2.88	4.756	4.53	4.824	2.91	4.451	6.05

Table A-11: P-2D-a model peak wall line base shear, linear time history analysis

LONG		SOUTH		NORTH		% of Peak V_{bu}	
Load Case	**Ground Motion**	**Peak V_{bu} (kips)**	**t @ peak V_{bu} (s)**	**Peak V_{bu} (kips)**	**t @ peak V_{bu} (s)**	**South**	**North**
EQ_2D_1axis_1	CNP 16%	3.6	9.10	7.4	8.75	31.9	68.1
EQ_2D_1axis_2	CNP 44%	9.8	9.10	20.5	8.75	31.9	68.1
EQ_2D_1axis_3	CNP 100%	22.2	9.10	46.5	8.75	31.9	68.1
EQ_2D_1axis_4	RRS 16%	11.8	3.83	10.1	2.75	44.5	55.5
EQ_2D_1axis_5	RRS 44%	32.4	3.83	27.8	2.75	44.5	55.5
EQ_2D_1axis_6	RRS 100%	73.5	3.83	63.1	2.75	44.5	55.5
SHORT		**EAST**		**WEST**		**% of Peak V_{bv}**	
Load Case	**Ground Motion**	**Peak V_{bv} (kips)**	**t @ peak V_{bv} (s)**	**Peak V_{bv} (kips)**	**t @ peak V_{bv} (s)**	**East**	**West**
EQ_2D_1axis_1	CNP 16%	2.8	8.98	3.3	8.67	39.4	60.6
EQ_2D_1axis_2	CNP 44%	7.8	8.98	9.1	8.67	39.4	60.6
EQ_2D_1axis_3	CNP 100%	17.6	8.98	20.8	8.67	39.4	60.6
EQ_2D_1axis_4	RRS 16%	5.9	2.88	5.7	2.91	51.2	48.8
EQ_2D_1axis_5	RRS 44%	16.4	2.88	15.6	2.91	51.2	48.8
EQ_2D_1axis_6	RRS 100%	37.2	2.88	35.5	2.91	51.2	48.8

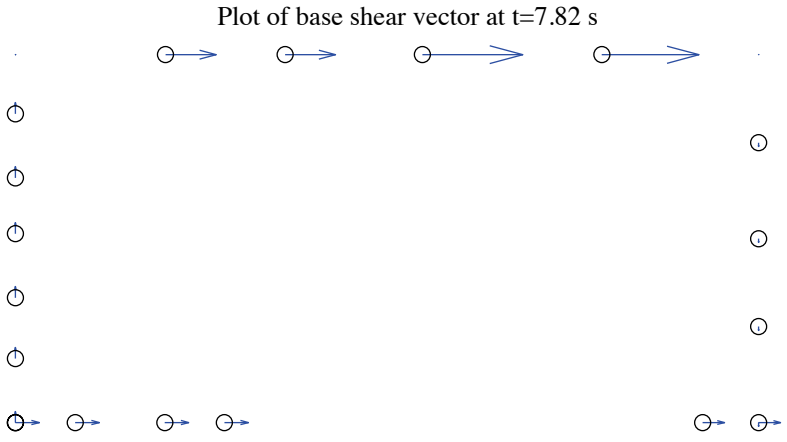

Figure A-5: P-2D-a model, base shear vector plot at the moment of peak total base shear, 100 % Canoga Park, 2D linear analysis (maximum anchor/hold down base shear is 13.48 kips)

A.6 Nonlinear time history analysis results

Same ground motions are applied to the model with material and geometrical nonlinearity. Table A-12 to Table A-17 are replicas of Table A-6 to Table A-11, but for nonlinear time history analyses. Since this analysis type is most complicated and closest to reality and experiments, behavior of wall lines and smeared hold downs are further studied. Table A-18 expands the breakdown of each wall line's peak base shear between shear walls, gravity walls and other systems. Table A-19 is peak value of hold down tensile force of two selected pairs. Hold down 5 and 6 are on shear wall L1S1, South elevation and hold down 7 and 8 are on shear wall L1W1, West elevation. These shear walls have lowest capacities compared with others on the same wall line and they meet at the southwest edge of the building.

Time history plots in this section include plots of story drifts of the building and each wall line (Figure A-6 to Figure A-8), total building base shear in long and short direction (Figure A-9) and axial forces of hold downs in (Figure A-10). Hysteretic plots in Figure A-11 and Figure A-12 are helpful for visual examination of nonlinear base shear-drift relationship of the building and the weakest shear wall on each wall line. In comparison with linear time history analysis, vector plot of peak total base shear is illustrated in Figure A-13. Figure A-14 presents a simplified deformed shape of the building (see (Peterman 2014) for details of the method) and axial force of all twenty hold downs at the moment of peak total base shear. The same sign convention with tests is adopted. Red bars indicate tensile (negative) force and blue ones are for compressive (positive) force.

Hysteretic behavior is seen in the building and typical shear walls under design-based earthquake (100% Canoga Park excitation in one axis, see Figure A-11 and Figure A-12). However, behaviors of individual wall lines differ significantly. The linear stiffness of South wall line is much smaller than North wall line (Table A-4), and has larger peak story drift in linear time history analysis (Table A-10). However, when the response turns into nonlinear, the floor story drift of South wall line can be much smaller than North wall line, as shown in the row of 100% Canoga Park in Table A-16. Wall line model of this type is expected to fail under 100% Canoga Park excitation since permanent drift can be seen in Figure A-7 and Figure A-8. Hysteretic response curves also imply that EPP material model tends to over estimate the energy dissipation of walls since pinching effect is missing.

The reconstructed peak building story drift in long direction is 1.96% (Table A-14), much less than the peak value of North wall line. The worst-case scenario from 2D analysis can greatly overestimate the nonlinear response of the whole building and yield conservative observation. Table A-18 implies that peak resultant base shear is taken all by shear walls, and Figure A-13 shows that base shear vectors in anchors and hold downs align with wall lines due to the limit of 2D modeling and analysis. Table A-19, Figure A-10 and Figure A-14 demonstrate that axial forces of hold downs in a pair have almost the same magnitude but opposite signs, matching the assumption of Type I shear walls. This also suggests that the design assumption is valid when there is no gravity or other system in the wall line, and no coupling between wall lines is included.

The near-field Rinaldi record is much stronger in terms of peak ground acceleration, especially in the long direction. When loaded at 100%, peak story drifts of South and North elevation both exceed 10%. Peak story drift in short direction exceeds 7%, also large enough to cause failure.

Table A-12: P-2D-a model peak story relative acceleration in g, nonlinear time history analysis

		LONG			SHORT		
Load Case	**Ground Motion**	**a_g**	**Floor a**	**Roof a**	**a_g**	**Floor a**	**Roof a**
EQ_2D_1axis_1	CNP 16%	0.067	0.131	0.216	0.057	0.125	0.150
EQ_2D_1axis_2	CNP 44%	0.185	0.353	0.456	0.157	0.361	0.410
EQ_2D_1axis_3	CNP 100%	0.420	0.686	0.706	0.356	0.523	0.611
EQ_2D_1axis_4	RRS 16%	0.132	0.259	0.429	0.078	0.252	0.306
EQ_2D_1axis_5	RRS 44%	0.363	0.428	0.531	0.214	0.413	0.501
EQ_2D_1axis_6	RRS 100%	0.825	1.128	1.445	0.486	0.660	0.934

Table A-13: P-2D-a model peak building roof drift and base shear, nonlinear time history analysis

		LONG			SHORT		
Load Case	**Ground Motion**	**$u_2/(2h)$ (%)**	**t_* (s)**	**V_b @ t_* (kips)**	**$v_2/(2h)$ (%)**	**t_* (s)**	**V_b @ t_* (kips)**
EQ_2D_1axis_1	CNP 16%	-0.428	7.85	10.4	-0.394	8.65	4.9
EQ_2D_1axis_2	CNP 44%	-1.039	7.86	24.0	-0.979	8.66	12.9
EQ_2D_1axis_3	CNP 100%	1.640	10.09	21.0	-2.138	8.68	25.3
EQ_2D_1axis_4	RRS 16%	0.782	2.85	14.9	-0.598	2.91	11.8
EQ_2D_1axis_5	RRS 44%	3.103	6.93	18.5	-1.614	2.91	26.0
EQ_2D_1axis_6	RRS 100%	5.257	9.12	17.7	-4.328	5.48	4.8

Table A-14: P-2D-a model peak building story drift, nonlinear time history analysis

		LONG				SHORT			
Load Case	**Ground Motion**	**$\Delta u_1/h$ (%)**	**t_* (s)**	**$\Delta u_2/h$ (%)**	**t_* (s)**	**$\Delta v_1/h$ (%)**	**t_* (s)**	**$\Delta v_2/h$ (%)**	**t_* (s)**
EQ_2D_1 axis_1	CNP 16%	-0.427	7.84	-0.434	7.86	0.391	9.04	-0.476	8.62
EQ_2D_1 axis_2	CNP 44%	-1.068	7.84	-1.028	7.88	-0.921	8.68	-1.049	8.65
EQ_2D_1 axis_3	CNP 100%	1.960	6.43	1.466	8.99	-3.061	8.74	-1.610	8.63
EQ_2D_1 axis_4	RRS 16%	0.805	2.84	0.787	3.89	-0.744	2.89	-0.639	4.59
EQ_2D_1 axis_5	RRS 44%	5.624	6.90	1.031	2.84	-2.179	2.92	-1.465	4.61
EQ_2D_1 axis_6	RRS 100%	9.673	16.10	1.348	9.11	-7.792	5.62	1.952	2.47

Table A-15: P-2D-a model peak building base shear, nonlinear time history analysis

		LONG		SHORT		RESULTANT	
Load Case	**Ground Motion**	**Peak V_{bu} (kip)**	**t @ peak V_{bu} (s)**	**Peak V_{bv} (kip)**	**t @ peak V_{bv} (s)**	**Peak V_b (kip)**	**t @ peak V_b (s)**
EQ_2D_1 axis_1	CNP 16%	10.6	7.84	6.1	9.03	10.6	7.84
EQ_2D_1 axis_2	CNP 44%	24.9	7.79	15.2	9.00	25.2	7.79
EQ_2D_1 axis_3	CNP 100%	45.0	10.00	34.8	8.62	45.2	10.00
EQ_2D_1 axis_4	RRS 16%	17.9	2.81	11.8	2.90	20.1	2.81
EQ_2D_1 axis_5	RRS 44%	105.3	2.92	29.3	2.85	108.3	2.92
EQ_2D_1 axis_6	RRS 100%	168.9	2.91	90.5	2.94	178.7	2.91

Table A-16: P-2D-a model peak wall line story drift, nonlinear time history analysis

LONG		**SOUTH**				**NORTH**			
Load Case	**Ground Motion**	**$\Delta u_1/h$ (%)**	**t_* (s)**	**$\Delta u_2/h$ (%)**	**t_* (s)**	**$\Delta u_1/h$ (%)**	**t_* (s)**	**$\Delta u_2/h$ (%)**	**t_* (s)**
EQ_2D_1axis_1	CNP 16%	0.570	11.17	0.613	11.60	0.457	8.75	0.407	8.78
EQ_2D_1axis_2	CNP 44%	1.302	7.37	1.349	6.90	1.216	8.81	0.992	8.77
EQ_2D_1axis_3	CNP 100%	1.999	6.49	2.939	9.00	3.129	10.09	1.201	7.58
EQ_2D_1axis_4	RRS 16%	1.572	3.44	1.506	2.91	0.545	2.75	0.574	2.73
EQ_2D_1axis_5	RRS 44%	8.587	6.89	1.992	2.87	3.244	2.86	1.226	2.70
EQ_2D_1axis_6	RRS 100%	10.554	16.11	2.080	3.57	10.800	4.40	1.790	2.74
SHORT		**EAST**				**WEST**			
Load Case	**Ground Motion**	**$\Delta v_1/h$ (%)**	**t_* (s)**	**$\Delta v_2/h$ (%)**	**t_* (s)**	**$\Delta v_1/h$ (%)**	**t_* (s)**	**$\Delta v_2/h$ (%)**	**t_* (s)**
EQ_2D_1axis_1	CNP 16%	0.437	8.98	0.463	9.36	0.521	8.74	0.552	8.65
EQ_2D_1axis_2	CNP 44%	0.983	9.00	1.017	8.61	1.157	8.71	1.262	8.69
EQ_2D_1axis_3	CNP 100%	3.007	8.72	1.607	8.59	3.245	8.77	1.926	5.49
EQ_2D_1axis_4	RRS 16%	0.742	2.88	0.767	4.55	0.772	2.91	0.712	6.05
EQ_2D_1axis_5	RRS 44%	2.365	5.47	1.293	4.57	2.123	2.91	1.958	6.05
EQ_2D_1axis_6	RRS 100%	7.284	5.59	1.921	2.46	8.440	5.65	2.221	3.57

Table A-17: P-2D-a model peak wall line base shear, nonlinear time history analysis

LONG		SOUTH		NORTH		% of Peak V_{bu}	
Load Case	**Ground Motion**	**Peak V_{bu} (kips)**	**t @ peak V_{bu} (s)**	**Peak V_{bu} (kips)**	**t @ peak V_{bu} (s)**	**South**	**North**
EQ_2D_1axis_1	CNP 16%	4.1	11.17	8.6	8.75	30.9	71.7
EQ_2D_1axis_2	CNP 44%	8.7	7.37	16.7	8.81	31.5	62.3
EQ_2D_1axis_3	CNP 100%	8.8	6.49	17.0	10.09	14.4	37.0
EQ_2D_1axis_4	RRS 16%	8.7	3.45	10.3	2.75	44.0	52.0
EQ_2D_1axis_5	RRS 44%	10.3	6.89	17.0	2.86	9.0	9.9
EQ_2D_1axis_6	RRS 100%	10.8	16.11	18.4	4.39	5.1	10.7
SHORT		**EAST**		**WEST**		**% of Peak V_{bv}**	
Load Case	**Ground Motion**	**Peak V_{bv} (kips)**	**t @ peak V_{bv} (s)**	**Peak V_{bv} (kips)**	**t @ peak V_{bv} (s)**	**East**	**West**
EQ_2D_1axis_1	CNP 16%	3.8	8.98	3.8	8.74	56.0	47.2
EQ_2D_1axis_2	CNP 44%	8.5	9.00	8.4	8.71	55.9	30.6
EQ_2D_1axis_3	CNP 100%	10.4	8.72	9.7	8.77	29.6	26.8
EQ_2D_1axis_4	RRS 16%	6.5	2.88	5.7	2.91	54.1	48.0
EQ_2D_1axis_5	RRS 44%	10.3	5.47	15.6	2.91	34.8	46.2
EQ_2D_1axis_6	RRS 100%	11.2	5.59	11.2	5.65	12.1	11.4

Table A-18: P-2D-a model wall line base shear breakdown, nonlinear time history analysis

LONG		SOUTH			NORTH		
Load Case	**Ground Motion**	**Peak V_{bu} (kips)**	**SW V_{bu} (%)**	**GW V_{bu} (%)**	**Peak V_{bu} (kips)**	**SW V_{bu} (%)**	**GW V_{bu} (%)**
EQ_2D_1axis_1	CNP 16%	4.1	100.0	0.0	8.6	100.0	0.0
EQ_2D_1axis_2	CNP 44%	8.7	100.0	0.0	16.7	100.0	0.0
EQ_2D_1axis_3	CNP 100%	8.8	100.0	0.0	17.0	100.0	0.0
EQ_2D_1axis_4	RRS 16%	8.7	100.0	0.0	10.3	100.0	0.0
EQ_2D_1axis_5	RRS 44%	10.3	100.0	0.0	17.0	100.0	0.0
EQ_2D_1axis_6	RRS 100%	10.8	100.0	0.0	18.4	100.0	0.0
SHORT		**EAST**			**WEST**		
Load Case	**Ground Motion**	**Peak V_{bv} (kips)**	**SW V_{bv} (%)**	**GW V_{bu} (%)**	**Peak V_{bv} (kips)**	**SW V_{bv} (%)**	**GW V_{bv} (%)**
EQ_2D_1axis_1	CNP 16%	3.8	100.0	0.0	3.8	100.0	0.0
EQ_2D_1axis_2	CNP 44%	8.5	100.0	0.0	8.4	100.0	0.0
EQ_2D_1axis_3	CNP 100%	10.4	100.0	0.0	9.7	100.0	0.0
EQ_2D_1axis_4	RRS 16%	6.5	100.0	0.0	5.7	100.0	0.0
EQ_2D_1axis_5	RRS 44%	10.3	100.0	0.0	15.6	100.0	0.0
EQ_2D_1axis_6	RRS 100%	11.2	100.0	0.0	11.2	100.0	0.0

Table A-19: P-2D-a model peak hold down tensile force at certain locations, nonlinear time history analysis

		L1S1, LC5		L1S1, LC6		L1W1, LC7		L1W1, LC8	
Load Case	**Ground Motion**	**Peak F (kips)**	**t @ peak F (s)**	**Peak F (kips)**	**t @ peak F (s)**	**Peak F (kips)**	**t @ peak F (s)**	**Peak F (kips)**	**t @ peak F (s)**
EQ_2D_1axis_1	CNP 16%	-4.28	7.87	-4.38	7.32	-4.23	8.71	-3.75	9.14
EQ_2D_1axis_2	CNP 44%	-10.88	6.88	-11.08	7.30	-10.14	8.70	-8.69	9.12
EQ_2D_1axis_3	CNP 100%	-12.71	7.96	-13.18	9.02	-13.03	8.68	-11.95	5.47
EQ_2D_1axis_4	RRS 16%	-10.88	3.39	-11.75	2.92	-5.92	2.93	-6.04	6.15
EQ_2D_1axis_5	RRS 44%	-10.16	3.52	-13.73	2.87	-10.74	2.85	-10.78	6.14
EQ_2D_1axis_6	RRS 100%	-12.93	3.56	-14.22	3.91	-13.81	5.47	-13.05	2.48

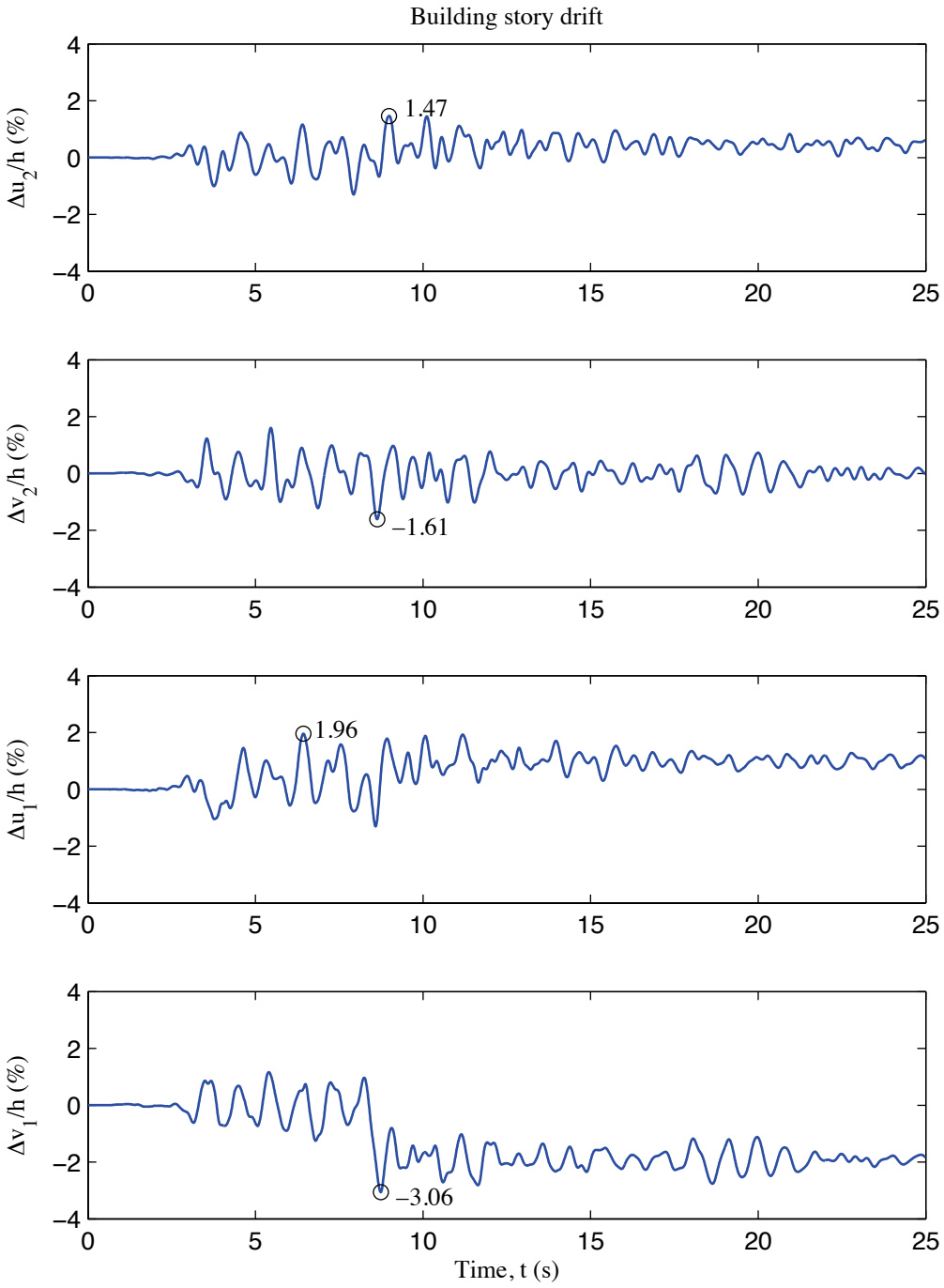

Figure A-6: P-2D-a model building story drift, 100 % Canoga Park, 2D nonlinear analysis

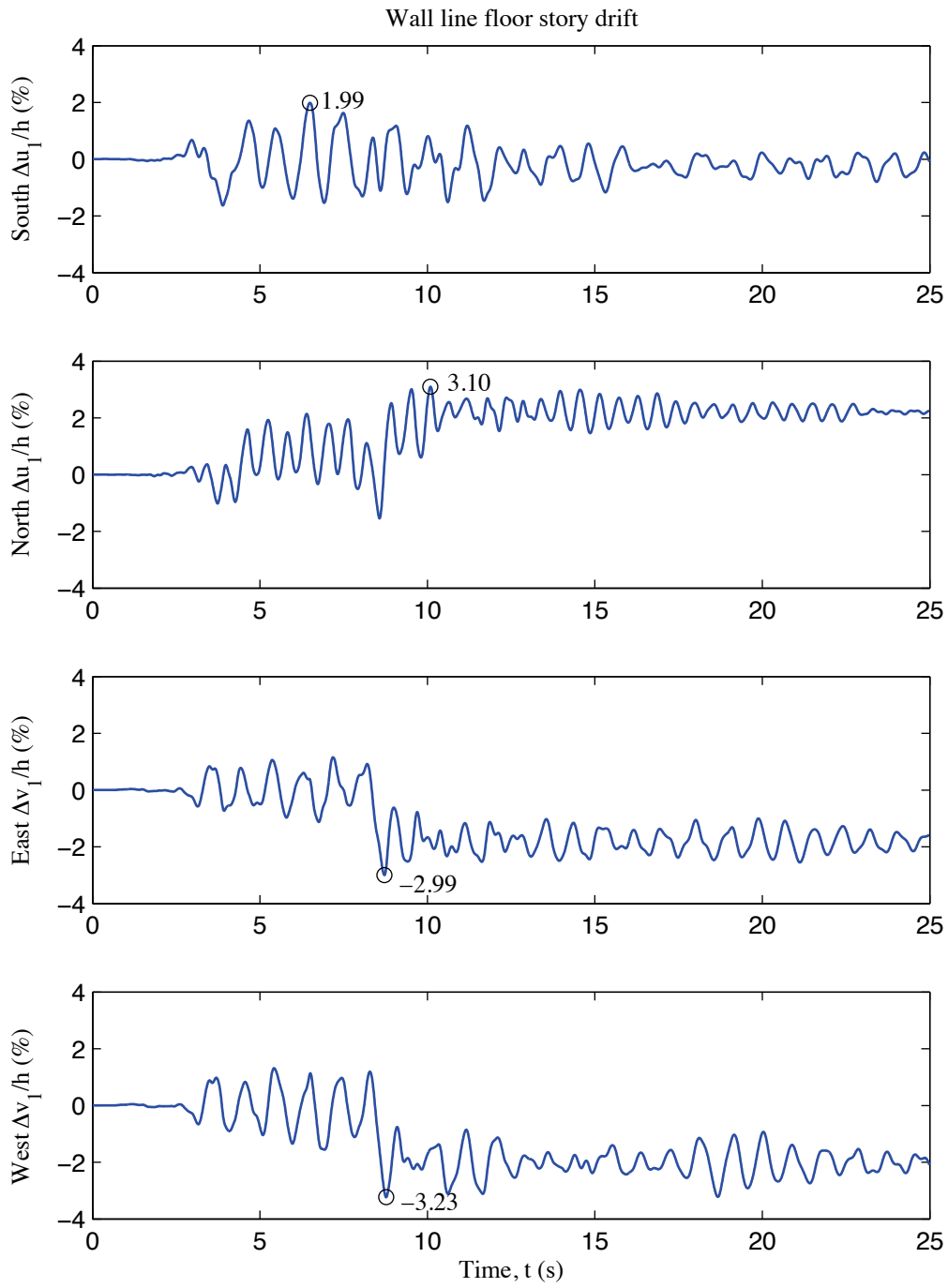

Figure A-7: P-2D-a model wall line floor story drift, 100 % Canoga Park, 2D nonlinear analysis

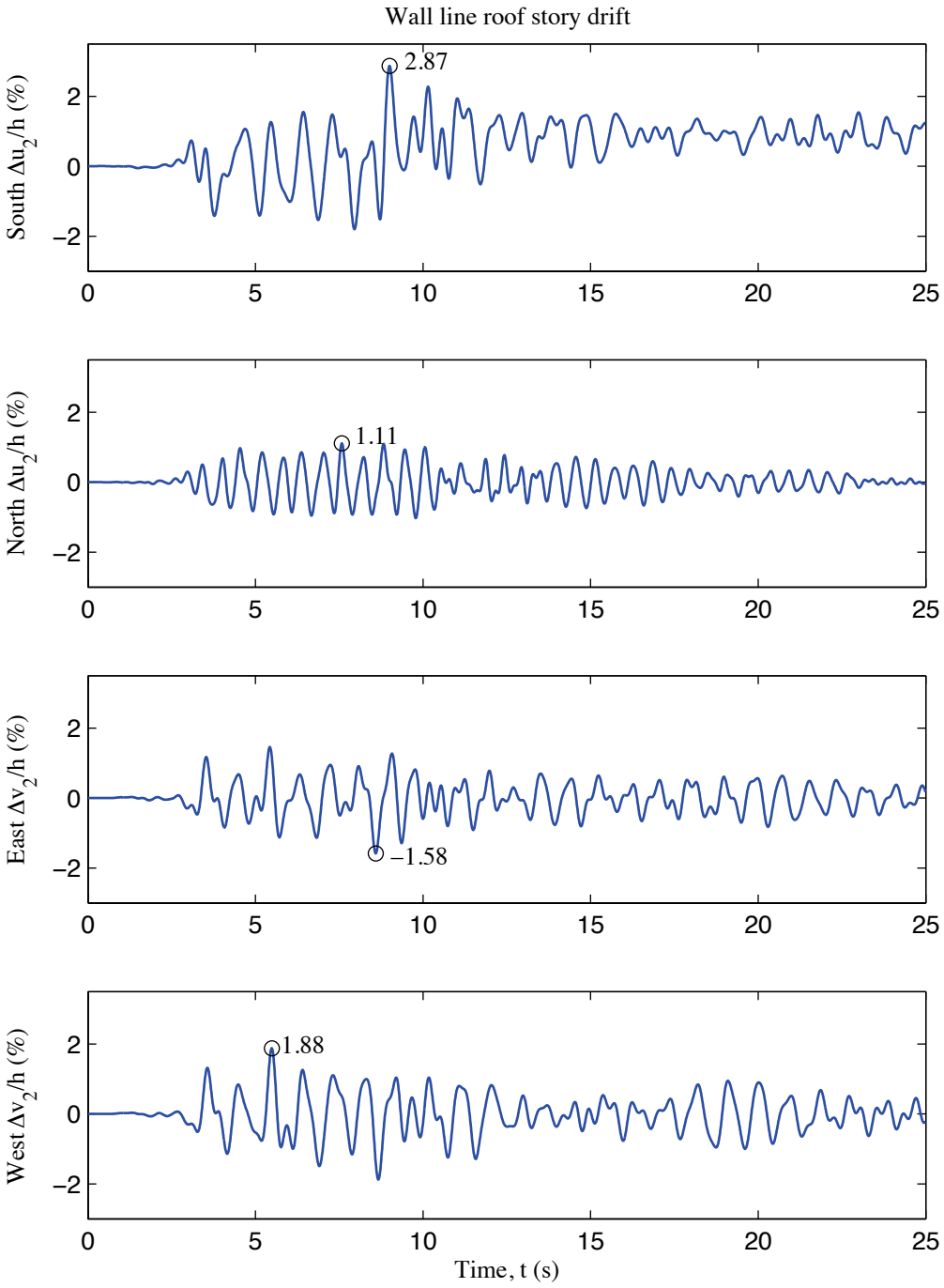

Figure A-8: P-2D-a model wall line roof story drift, 100 % Canoga Park, 2D nonlinear analysis

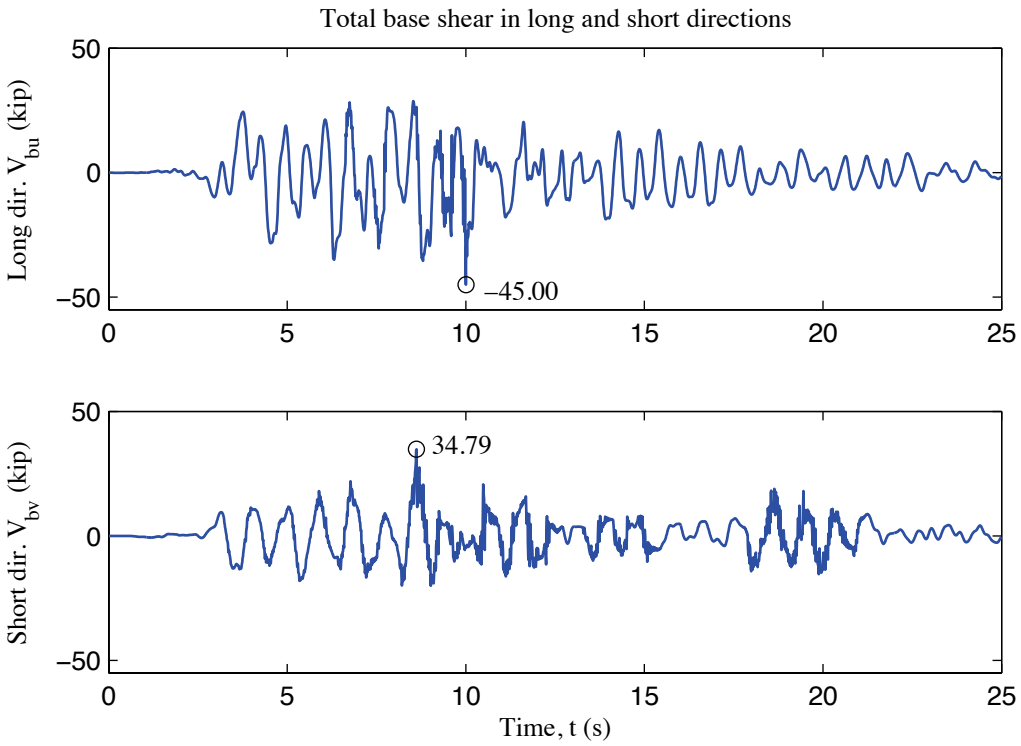

Figure A-9: P-2D-a model total building base shear, 100 % Canoga Park, 2D nonlinear analysis

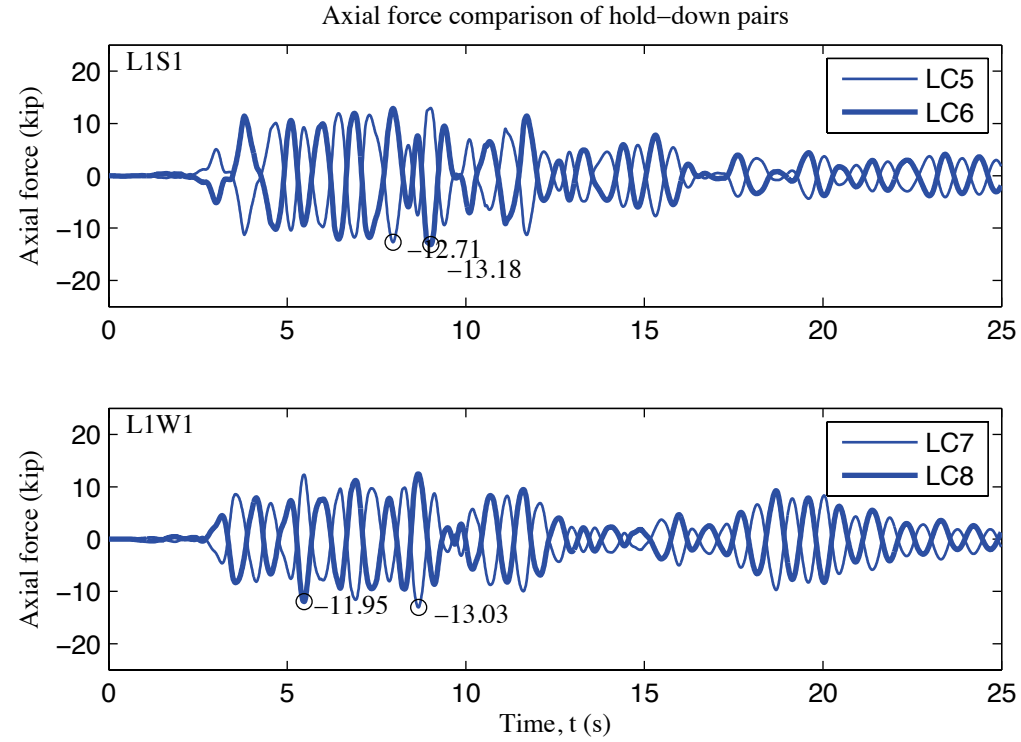

Figure A-10: P-2D-a model, load cell 5 to 8 axial forces, 100 % Canoga Park, 2D nonlinear analysis

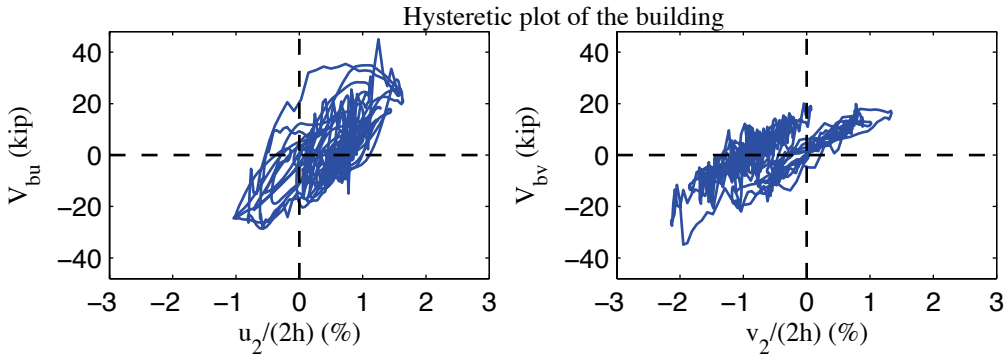

Figure A-11: P-2D-a model, hysteretic plot of the building, 100 % Canoga Park, 2D nonlinear analysis

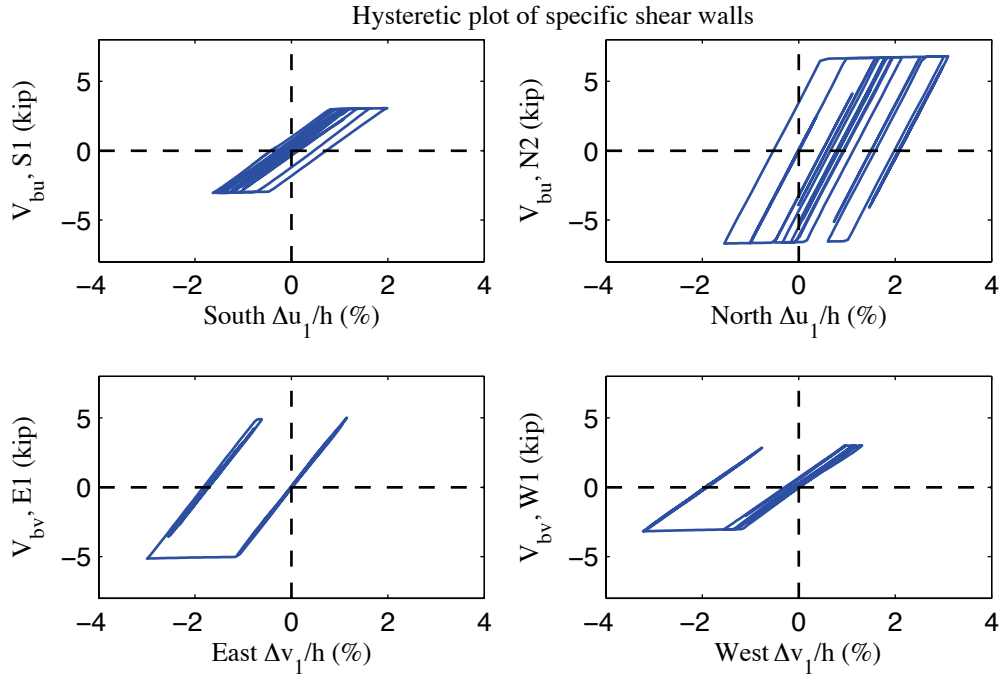

Figure A-12: P-2D-a model, hysteretic plot of shear walls at each elevation, 100 % Canoga Park, 2D nonlinear analysis

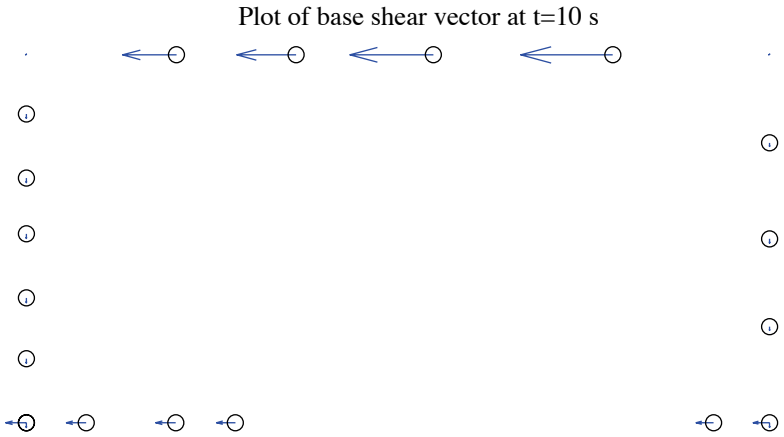

Figure A-13: P-2D-a model, field plot of peak total base shear, 100 % Canoga Park, 2D nonlinear analysis (maximum anchor/hold down base shear is 5.27 kips)

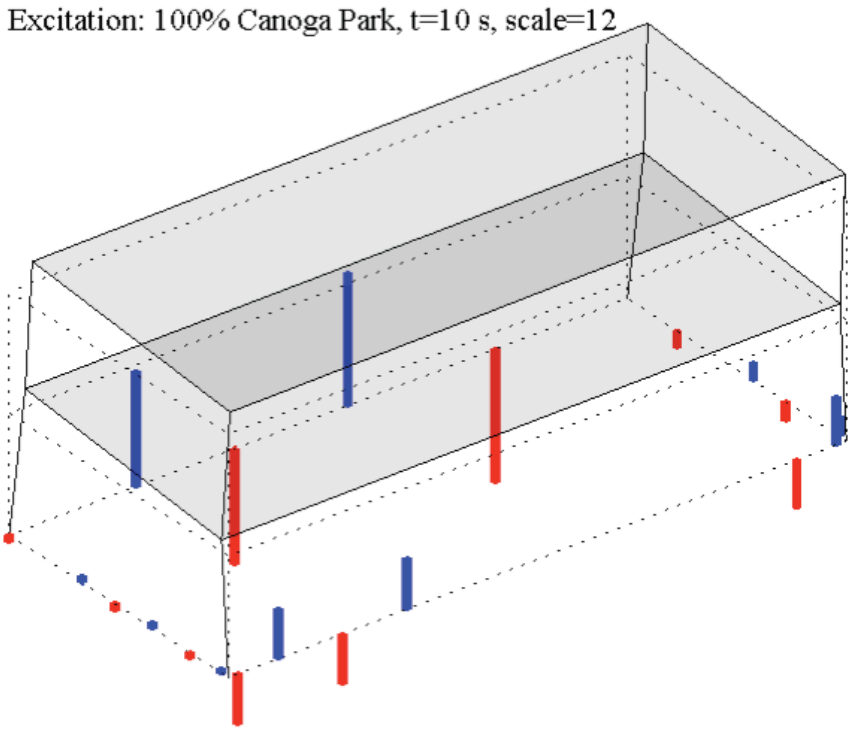

Figure A-14: P-2D-a model, simplified illustration of corner displacements with hold down forces from load cells,100 % Canoga Park, 2D nonlinear analysis (max hold down tensile force is -11.75 kips)

Appendix B: Analysis Results of State-of-the-practice, 2D, model b (P-2D-b)

B.1 Model description

This set of state-of-the-practice 2D models features bracing models of whole shear wall panels, smeared models of hold downs into shear walls as pinned supports and rigid leaning columns. Interplay between different wall lines is not allowed in 2D models, representing the effect of flexible diaphragms. Seismic mass is lumped at leaning column nodes. The lateral displacement and shear wall capacity ($\delta(0.4V_{nP})$, $0.4V_{nP}$) from AISI-213 standard is utilized to determine the stiffness of elastic material and the first point on the backbone curve of Pinching4 material of shear wall bracing. Figure B-1 (a) to (d) illustrate OpenSees models of South, North, East and West elevations. Simulation results are presented and discussed in later sections. Definitions of output physical quantities and explanation of post-process method can be found in Appendix E.

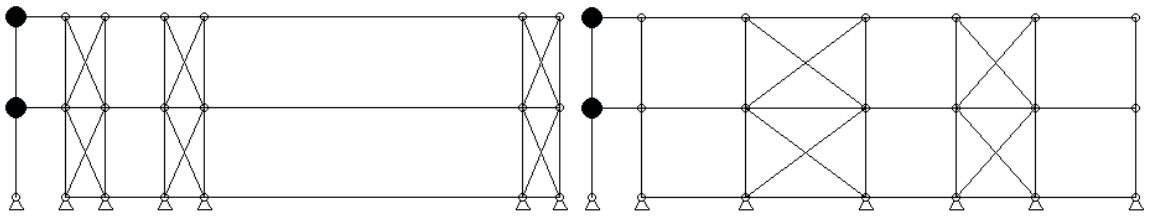

(a) South

(b) North

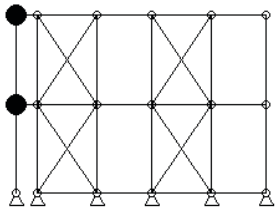

(c) East

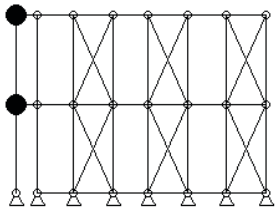

(d) West

Figure B-1: P-2D-b model

B.2 Free vibration analysis results

Free vibration analysis is performed for each elevation model. Values of first two natural periods are tabulated (Table B-1). Figure B-2 shows corresponding mode shapes.

Table B-1: Free vibration analysis results, P-2D-b model

Elevation	1st natural period (s)	2nd natural period (s)
South	0.823	0.350
North	0.443	0.220
East	0.654	0.278
West	0.805	0.344

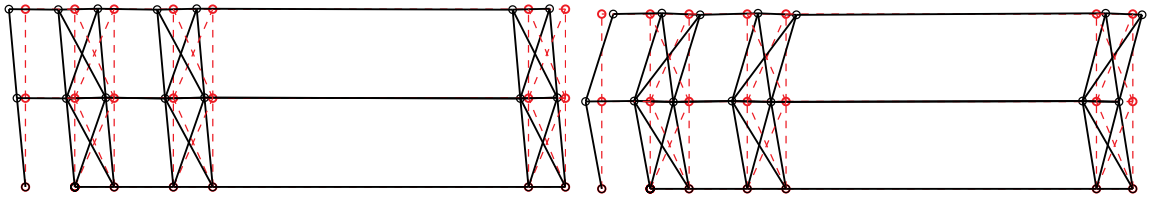

(a) South, mode 1, T_1=0.823 s (b) South, mode 2, T_2=0.350 s

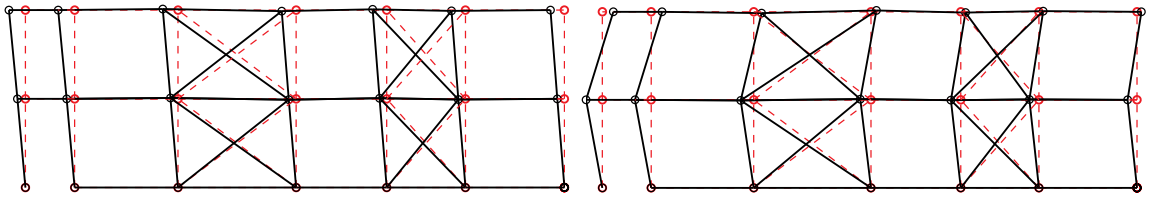

(c) North mode 1, T_1=0.443 s (d) North mode 2, T_2=0.220 s

(e) East mode 1, T_1=0.654 s (f) East mode 2, T_2=0.278 s

(g) West mode 1, T_1=0.805 s (h) West mode 2, T_2=0.344 s

Figure B-2: First two natural modes of P-2D-b model

B.3 Linear static analysis results

Linear static analysis is performed on each wall line. The total lateral load on that wall line is one half of the design base shear. The vertical distribution of lateral load follows the distribution of equivalent lateral load in the design narrative(Madsen et al. 2011)

Although each wall line is analyzed independently, to make a better summary and to make better comparisons with 3D models, results of individual wall lines are post-processed to reconstruct physical quantities of the whole building behavior, such as building displacements/drifts and total building base shear.

Table B-2 summarizes the breakdown of peak total base shear among four elevations. As shown in the table, each of two facing wall lines take 5.5 kips of base shear, and wall lines perpendicular to the loading direction take zero base shear as a natural result of 2D analysis.

Table B-3 shows peak building and wall line deflections. Practicing engineers can linearly upscale these data and develop an estimate of the building's performance at a certain lateral force level. In 2D analysis, only wall lines along the loading direction have displacements in the loading direction.

Table B-4 is an evaluation of the each wall line's lateral stiffness of long and short direction and its breakdown among shear walls (SW) and other systems. Since gravity walls (GW) are not modeled in state-of-the-practice models, all base shear goes to shear

walls. Pinching4 material renders a larger linear stiffness than elastic-perfectly plastic material, which is closer to the initial tangent stiffness.

Table B-2: Breakdown of peak base shear, linear static analysis, P-2D-b model

Load direction	**LONG**				
Elevation	**South V_b**	**North V_b**	**East V_b**	**West V_b**	**Peak V_b**
kips	5.5	5.5	0.0	0.0	11.1
%	50.0	50.0	0.0	0.0	100.0
Load direction	**SHORT**				
Elevation	**South V_b**	**North V_b**	**East V_b**	**West V_b**	**Peak V_b**
kips	0.0	0.0	5.5	5.5	11.1
%	0.0	0.0	50.0	50.0	100.0

Table B-3: Peak building and wall line deflection, linear static analysis, P-2D-b model

Load direction	**LONG**							
Deflection (in.)	**u_1**	**u_2**	**v_1**	**v_2**	**Δu_1**	**Δu_2**	**Δv_1**	**Δv_2**
Building	0.424	0.830	0.000	0.000	0.424	0.406	0.000	0.000
South	0.668	1.300	0.000	0.000	0.668	0.632	0.000	0.000
North	0.180	0.360	0.000	0.000	0.180	0.180	0.000	0.000
East	-	-	-	-	-	-	-	-
West	-	-	-	-	-	-	-	-
Load direction	**SHORT**							
Deflection (in.)	**u_1**	**u_2**	**v_1**	**v_2**	**Δu_1**	**Δu_2**	**Δv_1**	**Δv_2**
Building	0.000	0.000	0.532	1.039	0.000	0.000	0.532	0.507
South	-	-	-	-	-	-	-	-
North	-	-	-	-	-	-	-	-
East	0.000	0.000	0.419	0.828	0.000	0.000	0.419	0.409
West	0.000	0.000	0.645	1.250	0.000	0.000	0.645	0.605

Table B-4: Breakdown of lateral stiffness, P-2D-b model

SOUTH			**NORTH**		
Shear wall k_u (%)	**Gravity wall k_u (%)**	**k_u (kip/in)**	**Shear wall k_v (%)**	**Gravity wall k_v (%)**	**k_v (kip/in)**
100.0	0.0	4.3	100.0	0.0	15.4
EAST			**WEST**		
Shear wall k_u (%)	**Gravity wall k_u (%)**	**k_u (kip/in)**	**Shear wall k_v (%)**	**Gravity wall k_v (%)**	**k_v (kip/in)**
100.0	0.0	6.7	100.0	0.0	4.4

B.4 Nonlinear static (pushover) analysis results

Table B-5 is created following the same logic with Table B-2, but the analysis type is nonlinear static (pushover). Pushover curves of the building and each wall line are presented in Figure B-3 and Figure B-4.

These tables and figures indicate that the wall lines do not reach their peak capacity at exactly the same drift level. Accordingly, total capacity of the building reconstructed using 2D results is no greater than the sum of wall line capacities in the load direction. This observation is more apparent in long direction. There is a sharp drop on the pushover backbone curve, since controlling parameters of pinching effect are determined under the worst-case scenario of our tests. The missing of diaphragm stiffness and induced interplay of wall lines can make a significant difference between 2D analysis and real 3D analysis.

Table B-5: Breakdown of peak base shear, pushover analysis, P-2D-b model

Load direction	**LONG**				
Elevation	**South V_b**	**North V_b**	**East V_b**	**West V_b**	**Peak V_b**
kips	7.1	15.5	0.0	0.0	20.4
%	34.7	76.1	0.0	0.0	100.0
Load direction	**SHORT**				
Elevation	**South V_b**	**North V_b**	**East V_b**	**West V_b**	**Peak V_b**
kips	0.0	0.0	10.0	9.1	17.5
%	0.0	0.0	57.4	51.9	100.0

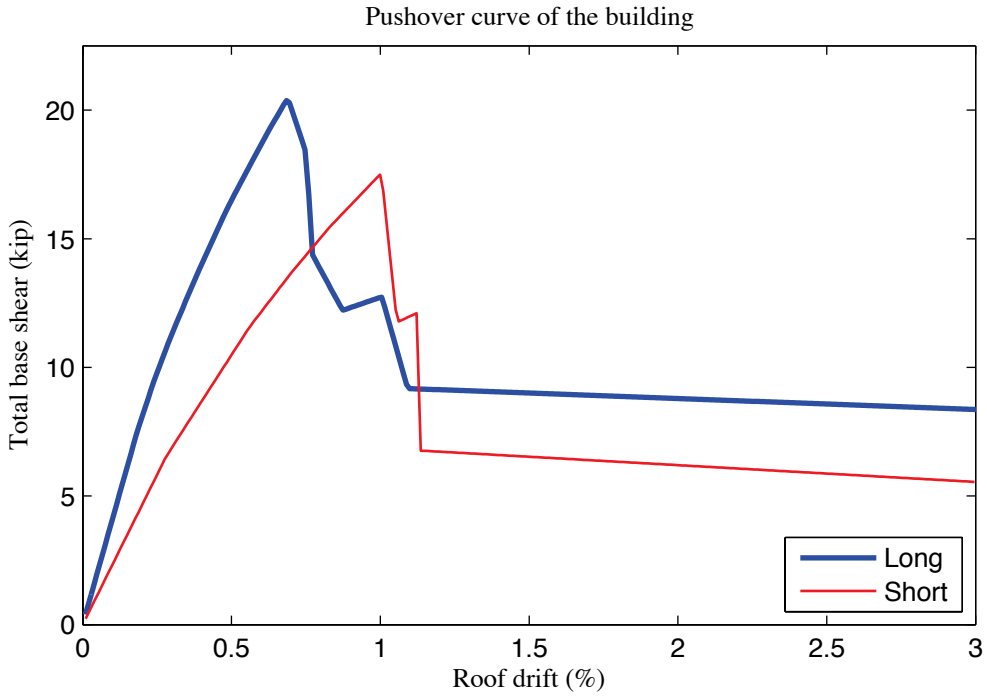

Figure B-3: Pushover curve of P-2D-b model

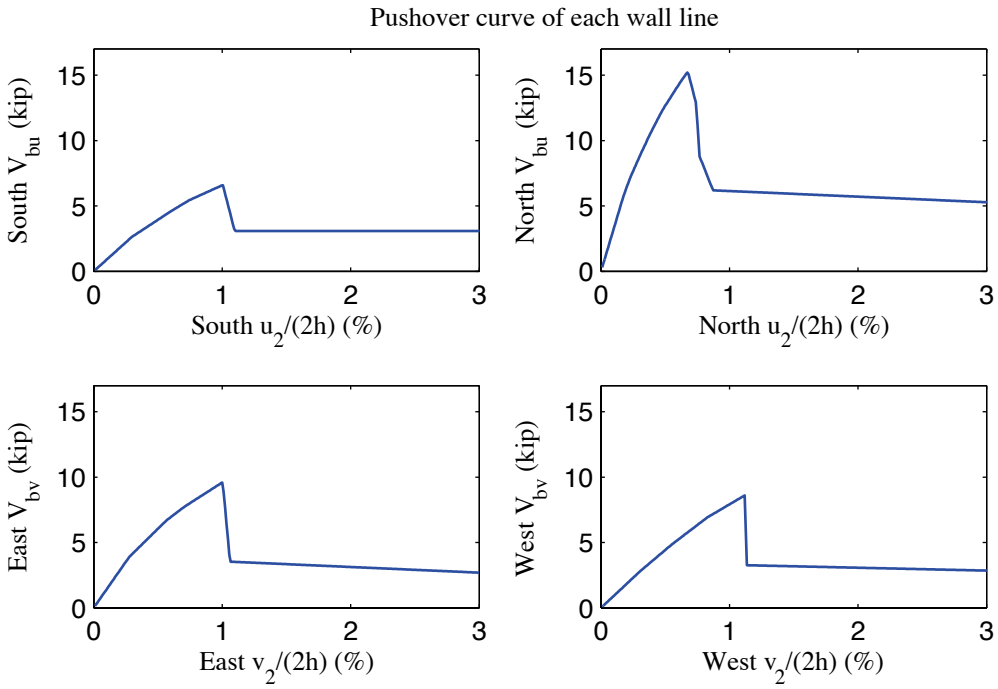

Figure B-4: Pushover curve of each wall line, P-2D-b model

B.5 Linear time history analysis results

Linear time history analysis is performed on 2D models under Canoga Park and Rinaldi ground motion records of Northridge earthquake in 1994. We considered three scale levels (16%, 44% and 100%) and single axis excitation is applied in the lateral direction of a single wall line.

Table B-6 to Table B-9 demonstrate the reconstructed linear elastic performance of the building under designated ground motions. Table B-6 shows peak story relative accelerations in the unit of g. Table B-7 and Table B-8 report peak roof drift and story drift of the building and the corresponding time step (t_*) and the base shear at that time. Note that the base shear at the time of peak roof drift may not be the peak total building base shear in that direction (see Table B-9).

The response of each wall line is available directly from 2D analysis results, so peak story drift and peak base shear of each wall line are listed in Table B-10 and Table B-11.

Wall lines behave linearly since peak drift and peak base shear appear at the same time when the ground motion is linearly scaled. Figure B-5 is a vector plot of the peak total resultant base shear of the building under 100% Canoga Park excitation. Since four dynamical analyses in 2D should be performed separately in order to create the plot, base shear vectors are always in-line with the wall. Comparison with nonlinear analysis results of the same excitation provides insightful observations on the building's response and requirements on modeling fidelity and analysis type.

Table B-6: P-2D-b model peak story relative acceleration in g, linear time history analysis

Load Case	Ground Motion	LONG			SHORT		
		a_g	Floor a	Roof a	a_g	Floor a	Roof a
EQ_2D_1axis_1	CNP 16%	0.067	0.092	0.144	0.057	0.104	0.166
EQ_2D_1axis_2	CNP 44%	0.185	0.252	0.396	0.157	0.285	0.456
EQ_2D_1axis_3	CNP 100%	0.420	0.573	0.900	0.356	0.649	1.037
EQ_2D_1axis_4	RRS 16%	0.132	0.161	0.310	0.078	0.125	0.214
EQ_2D_1axis_5	RRS 44%	0.363	0.442	0.852	0.214	0.344	0.588
EQ_2D_1axis_6	RRS 100%	0.825	1.006	1.937	0.486	0.781	1.336

Table B-7: P-2D-b model peak building roof drift and base shear, linear time history analysis

Load Case	Ground Motion	LONG			SHORT		
		$u_2/(2h)$ (%)	t_* (s)	V_b @ t_* (kips)	$v_2/(2h)$ (%)	t_* (s)	V_b @ t_* (kips)
EQ_2D_1axis_1	CNP 16%	0.261	8.84	8.1	0.252	8.95	5.0
EQ_2D_1axis_2	CNP 44%	0.717	8.84	22.3	0.693	8.95	13.7
EQ_2D_1axis_3	CNP 100%	1.630	8.84	50.7	1.576	8.95	31.1
EQ_2D_1axis_4	RRS 16%	-0.667	3.29	12.3	-0.391	2.79	10.1
EQ_2D_1axis_5	RRS 44%	-1.833	3.29	33.8	-1.075	2.79	27.9
EQ_2D_1axis_6	RRS 100%	-4.166	3.29	76.8	-2.442	2.79	63.4

Table B-8: P-2D-b model peak building story drift, linear time history analysis

Load Case	Ground Motion	LONG				SHORT			
		$\Delta u_1/h$ (%)	t_* (s)	$\Delta u_2/h$ (%)	t_* (s)	$\Delta v_1/h$ (%)	t_* (s)	$\Delta v_2/h$ (%)	t_* (s)
EQ_2D_1 axis_1	CNP 16%	0.272	8.82	0.262	8.86	0.258	9.62	0.279	8.95
EQ_2D_1 axis_2	CNP 44%	0.749	8.82	0.721	8.86	0.708	9.62	0.768	8.95
EQ_2D_1 axis_3	CNP 100%	1.701	8.82	1.639	8.86	1.610	9.62	1.746	8.95
EQ_2D_1 axis_4	RRS 16%	0.729	3.70	-0.668	3.30	-0.450	2.82	0.410	3.17
EQ_2D_1 axis_5	RRS 44%	2.004	3.70	-1.838	3.30	-1.239	2.82	1.127	3.17
EQ_2D_1 axis_6	RRS 100%	4.555	3.70	-4.176	3.30	-2.816	2.82	2.561	3.17

Table B-9: P-2D-b model peak building base shear, linear time history analysis

		LONG		SHORT		RESULTANT	
Load Case	**Ground Motion**	**Peak V_{bu} (kip)**	**t @ peak V_{bu} (s)**	**Peak V_{bv} (kip)**	**t @ peak V_{bv} (s)**	**Peak V_b (kip)**	**t @ peak V_b (s)**
EQ_2D_1 axis_1	CNP 16%	9.5	8.80	6.5	9.61	9.9	8.81
EQ_2D_1 axis_2	CNP 44%	26.1	8.80	17.9	9.61	27.2	8.81
EQ_2D_1 axis_3	CNP 100%	59.4	8.80	40.8	9.61	61.7	8.81
EQ_2D_1 axis_4	RRS 16%	17.1	3.69	10.2	2.80	18.8	2.75
EQ_2D_1 axis_5	RRS 44%	47.0	3.69	27.9	2.80	51.6	2.75
EQ_2D_1 axis_6	RRS 100%	106.9	3.69	63.5	2.80	117.4	2.75

Table B-10: P-2D-b model peak wall line story drift, linear time history analysis

LONG		**SOUTH**				**NORTH**			
Load Case	**Ground Motion**	**$\Delta u_1/h$ (%)**	**t_* (s)**	**$\Delta u_2/h$ (%)**	**t_* (s)**	**$\Delta u_1/h$ (%)**	**t_* (s)**	**$\Delta u_2/h$ (%)**	**t_* (s)**
EQ_2D_1axis_1	CNP 16%	0.475	9.29	0.479	8.92	0.211	8.78	0.200	9.01
EQ_2D_1axis_2	CNP 44%	1.307	9.29	1.316	8.92	0.581	8.78	0.551	9.01
EQ_2D_1axis_3	CNP 100%	2.970	9.29	2.991	8.92	1.320	8.78	1.251	9.01
EQ_2D_1axis_4	RRS 16%	1.339	3.27	1.356	3.29	0.340	2.68	0.344	2.70
EQ_2D_1axis_5	RRS 44%	3.682	3.27	3.729	3.29	0.935	2.68	0.945	2.70
EQ_2D_1axis_6	RRS 100%	8.369	3.27	8.475	3.29	2.125	2.68	2.148	2.70
SHORT		**EAST**				**WEST**			
Load Case	**Ground Motion**	**$\Delta v_1/h$ (%)**	**t_* (s)**	**$\Delta v_2/h$ (%)**	**t_* (s)**	**$\Delta v_1/h$ (%)**	**t_* (s)**	**$\Delta v_2/h$ (%)**	**t_* (s)**
EQ_2D_1axis_1	CNP 16%	0.405	10.18	0.471	9.89	0.299	9.34	0.368	9.01
EQ_2D_1axis_2	CNP 44%	1.113	10.18	1.296	9.89	0.824	9.34	1.012	9.01
EQ_2D_1axis_3	CNP 100%	2.530	10.18	2.946	9.89	1.872	9.34	2.299	9.01
EQ_2D_1axis_4	RRS 16%	0.410	2.73	0.408	3.12	0.630	2.86	0.596	3.21
EQ_2D_1axis_5	RRS 44%	1.128	2.73	1.121	3.12	1.731	2.86	1.639	3.21
EQ_2D_1axis_6	RRS 100%	2.564	2.73	2.549	3.12	3.935	2.86	3.726	3.21

Table B-11: P-2D-b model peak wall line base shear, linear time history analysis

LONG		SOUTH		NORTH		% of Peak V_{bu}	
Load Case	**Ground Motion**	**Peak V_{bu} (kips)**	**t @ peak V_{bu} (s)**	**Peak V_{bu} (kips)**	**t @ peak V_{bu} (s)**	**South**	**North**
EQ_2D_1axis_1	CNP 16%	4.2	9.29	6.6	8.78	32.7	67.3
EQ_2D_1axis_2	CNP 44%	11.6	9.29	18.1	8.78	32.7	67.3
EQ_2D_1axis_3	CNP 100%	26.4	9.29	41.1	8.78	32.7	67.3
EQ_2D_1axis_4	RRS 16%	11.8	3.27	10.6	2.68	68.1	31.9
EQ_2D_1axis_5	RRS 44%	32.4	3.27	29.3	2.68	68.1	31.9
EQ_2D_1axis_6	RRS 100%	73.7	3.27	66.5	2.68	68.1	31.9
SHORT		**EAST**		**WEST**		**% of Peak V_{bv}**	
Load Case	**Ground Motion**	**Peak V_{bv} (kips)**	**t @ peak V_{bv} (s)**	**Peak V_{bv} (kips)**	**t @ peak V_{bv} (s)**	**East**	**West**
EQ_2D_1axis_1	CNP 16%	5.8	10.18	2.8	9.34	74.5	25.5
EQ_2D_1axis_2	CNP 44%	16.0	10.18	7.6	9.34	74.5	25.5
EQ_2D_1axis_3	CNP 100%	36.4	10.18	17.3	9.34	74.5	25.5
EQ_2D_1axis_4	RRS 16%	5.8	2.73	5.8	2.86	49.1	50.9
EQ_2D_1axis_5	RRS 44%	16.0	2.73	16.1	2.86	49.1	50.9
EQ_2D_1axis_6	RRS 100%	36.4	2.73	36.5	2.86	49.1	50.9

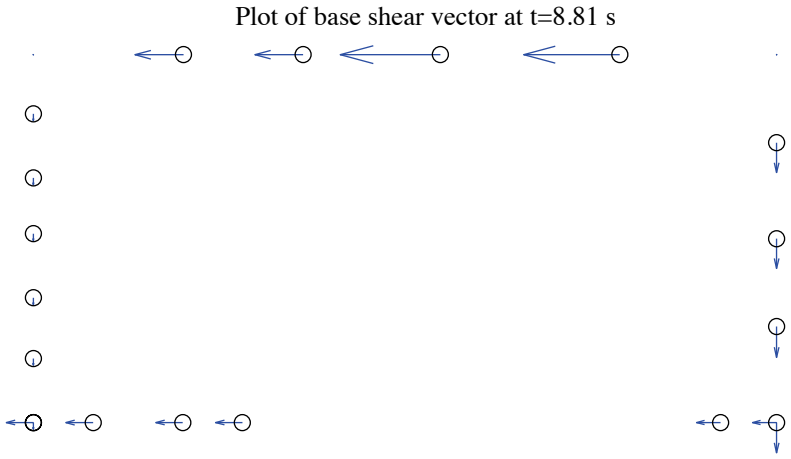

Figure B-5: P-2D-b model, base shear vector plot at the moment of peak total base shear, 100 % Canoga Park, 2D linear analysis (maximum anchor/hold down base shear is 13.05 kips)

B.6 Nonlinear time history analysis results

Same ground motions are applied to the model with material and geometrical nonlinearity. Table B-12 to Table B-17 are replicas of Table B-6 to Table B-11, but for nonlinear time history analyses. Since this analysis type is most complicated and closest to reality and experiments, behavior of wall lines and smeared hold downs are further studied. Table B-18 expands the breakdown of each wall line's peak base shear between shear walls, gravity walls and other systems. Table B-19 is peak value of hold down tensile force of two selected pairs. Hold down 5 and 6 are on shear wall L1S1, South elevation and hold down 7 and 8 are on shear wall L1W1, West elevation. These shear walls have lowest capacities compared with others on the same wall line and they meet at the southwest edge of the building.

Time history plots in this section include plots of story drifts of the building and each wall line (Figure B-6 to Figure B-8), total building base shear in long and short direction (Figure B-9) and axial forces of hold downs in (Figure B-10). Hysteretic plots in Figure B-11 and Figure B-12 are helpful for visual examination of nonlinear base shear-drift relationship of the building and the weakest shear wall on each wall line. In comparison with linear time history analysis, vector plot of peak total base shear is illustrated in Figure B-13. Figure B-14 presents a simplified deformed shape of the building (see (Peterman 2014) for details of the method) and axial force of all twenty hold downs at the moment of peak total base shear. The same sign convention with tests is adopted. Red bars indicate tensile (negative) force and blue ones are for compressive (positive) force.

Hysteretic behavior is seen in the building and typical shear walls under design-based earthquake (100% Canoga Park excitation in one axis, see Figure B-11 and Figure B-12). Results also imply that when loaded by 100% Canoga Park ground motion, all wall lines fail since peak drifts are all over 4% (Table B-16) and the response curves of typical shear walls go very far into the post-peak region of Pinching4 material backbone. Permanent drift is also seen in time history plots (Figure B-7). All those figures and table also suggest magnitudes of response measures differ between four wall lines.

The reconstructed peak building story drift in long direction is 3.96% (Table B-14), much less than the peak value of South wall line. The worst-case scenario from 2D analysis can greatly overestimate the nonlinear response of the whole building and yield conservative observation. Table B-18 implies that peak resultant base shear is taken all by shear walls, and Figure B-13 shows that base shear vectors in anchors and hold downs align with wall lines due to the limit of 2D modeling and analysis. Table B-19, Figure B-10 and Figure B-14 demonstrate that axial forces of hold downs in a pair have almost the same magnitude but opposite signs, matching the assumption of Type I shear walls. This also suggests that the design assumption is valid when there is no gravity or other system in the wall line, and no coupling between wall lines is included. It is mentioning that peak total base shear of the building in long direction (see Figure B-9) is incredibly larger than the sum of shear wall capacities. The reason is that supports of leaning columns can take a large amount of base shear when shear walls fail so the analysis process can still proceed, but failure actually happens on the structure.

The near-field Rinaldi record is much stronger in terms of peak ground acceleration, especially in the long direction. When loaded at 100%, analyses of North and South elevation both fail. Wall line drifts go to infinity after about 5 seconds.

Table B-12: P-2D-b model peak story relative acceleration in g, nonlinear time history analysis

		LONG			SHORT		
Load Case	**Ground Motion**	**a_g**	**Floor a**	**Roof a**	**a_g**	**Floor a**	**Roof a**
EQ_2D_1axis_1	CNP 16%	0.067	0.177	0.174	0.057	0.158	0.162
EQ_2D_1axis_2	CNP 44%	0.185	0.652	1.333	0.157	0.262	0.388
EQ_2D_1axis_3	CNP 100%	0.420	0.886	0.893	0.356	0.444	0.585
EQ_2D_1axis_4	RRS 16%	0.132	0.355	0.449	0.078	0.190	0.292
EQ_2D_1axis_5	RRS 44%	0.363	1.038	0.645	0.214	0.367	0.531
EQ_2D_1axis_6	RRS 100%	N/A	N/A	N/A	N/A	N/A	N/A

Table B-13: P-2D-b model peak building roof drift and base shear, nonlinear time history analysis

		LONG			SHORT		
Load Case	**Ground Motion**	**$u_2/(2h)$ (%)**	**t_* (s)**	**V_b @ t_* (kips)**	**$v_2/(2h)$ (%)**	**t_* (s)**	**V_b @ t_* (kips)**
EQ_2D_1axis_1	CNP 16%	0.215	7.15	4.3	0.264	8.95	4.3
EQ_2D_1axis_2	CNP 44%	-0.638	8.53	11.4	0.692	8.99	12.8
EQ_2D_1axis_3	CNP 100%	-2.226	8.61	67.8	-2.370	9.27	5.5
EQ_2D_1axis_4	RRS 16%	0.628	2.86	6.5	-0.421	2.82	10.6
EQ_2D_1axis_5	RRS 44%	2.849	3.11	13.9	-2.120	5.60	8.0
EQ_2D_1axis_6	RRS 100%	N/A	N/A	N/A	N/A	N/A	N/A

Table B-14: P-2D-b model peak building story drift, nonlinear time history analysis

		LONG				SHORT			
Load Case	**Ground Motion**	**$\Delta u_1/h$ (%)**	**t_* (s)**	**$\Delta u_2/h$ (%)**	**t_* (s)**	**$\Delta v_1/h$ (%)**	**t_* (s)**	**$\Delta v_2/h$ (%)**	**t_* (s)**
EQ_2D_1 axis_1	CNP 16%	0.277	7.18	-0.248	8.61	0.319	9.65	0.304	8.96
EQ_2D_1 axis_2	CNP 44%	-1.200	8.53	0.460	9.26	0.710	8.97	-1.200	8.53
EQ_2D_1 axis_3	CNP 100%	-3.964	8.64	-0.648	8.55	-4.393	9.28	1.226	5.44
EQ_2D_1 axis_4	RRS 16%	0.990	3.04	0.479	2.83	-0.523	2.83	0.433	3.18
EQ_2D_1 axis_5	RRS 44%	5.633	3.12	0.439	2.95	-3.923	5.73	0.975	6.53
EQ_2D_1 axis_6	RRS 100%	N/A	N/A	N/A	N/A	N/A	N/A	N/A	N/A

Table B-15: P-2D-b model peak building base shear, nonlinear time history analysis

		LONG		SHORT		RESULTANT	
Load Case	**Ground Motion**	**Peak V_{bu} (kip)**	**t @ peak V_{bu} (s)**	**Peak V_{bv} (kip)**	**t @ peak V_{bv} (s)**	**Peak V_b (kip)**	**t @ peak V_b (s)**
EQ_2D_1 axis_1	CNP 16%	6.9	7.74	7.1	9.64	8.0	8.83
EQ_2D_1 axis_2	CNP 44%	18.6	7.85	12.8	8.99	18.6	7.85
EQ_2D_1 axis_3	CNP 100%	126.9	8.54	28.9	8.66	127.6	8.54
EQ_2D_1 axis_4	RRS 16%	15.5	2.81	10.6	2.82	18.8	2.81
EQ_2D_1 axis_5	RRS 44%	69.9	2.96	20.9	6.41	72.1	2.96
EQ_2D_1 axis_6	RRS 100%	N/A	N/A	N/A	N/A	N/A	N/A

Table B-16: P-2D-b model peak wall line story drift, nonlinear time history analysis

LONG		**SOUTH**				**NORTH**			
Load Case	**Ground Motion**	**$\Delta u_1/h$ (%)**	**t_* (s)**	**$\Delta u_2/h$ (%)**	**t_* (s)**	**$\Delta u_1/h$ (%)**	**t_* (s)**	**$\Delta u_2/h$ (%)**	**t_* (s)**
EQ_2D_1axis_1	CNP 16%	0.615	9.01	0.452	9.40	0.239	8.79	0.213	9.02
EQ_2D_1axis_2	CNP 44%	2.176	8.58	0.800	6.47	0.890	10.03	0.581	8.79
EQ_2D_1axis_3	CNP 100%	7.570	8.69	0.951	7.80	5.588	9.56	0.663	6.93
EQ_2D_1axis_4	RRS 16%	2.184	3.03	0.937	2.86	0.422	2.72	0.296	2.69
EQ_2D_1axis_5	RRS 44%	6.284	3.20	0.474	2.39	5.543	3.04	0.649	2.67
EQ_2D_1axis_6	RRS 100%	N/A	N/A	N/A	N/A	N/A	N/A	N/A	N/A
SHORT		**EAST**				**WEST**			
Load Case	**Ground Motion**	**$\Delta v_1/h$ (%)**	**t_* (s)**	**$\Delta v_2/h$ (%)**	**t_* (s)**	**$\Delta v_1/h$ (%)**	**t_* (s)**	**$\Delta v_2/h$ (%)**	**t_* (s)**
EQ_2D_1axis_1	CNP 16%	0.407	10.24	0.435	8.93	0.347	8.94	0.395	9.05
EQ_2D_1axis_2	CNP 44%	0.794	9.66	0.627	8.97	0.897	9.01	0.935	8.61
EQ_2D_1axis_3	CNP 100%	4.972	9.27	1.071	8.56	4.098	8.89	1.467	5.44
EQ_2D_1axis_4	RRS 16%	0.501	2.76	0.384	3.14	0.630	2.86	0.596	3.21
EQ_2D_1axis_5	RRS 44%	3.155	5.71	1.188	6.48	4.718	5.74	1.342	6.59
EQ_2D_1axis_6	RRS 100%	N/A	N/A	N/A	N/A	N/A	N/A	N/A	N/A

Table B-17: P-2D-b model peak wall line base shear, nonlinear time history analysis

LONG		SOUTH		NORTH		% of Peak V_{bu}	
Load Case	**Ground Motion**	**Peak V_{bu} (kips)**	**t @ peak V_{bu} (s)**	**Peak V_{bu} (kips)**	**t @ peak V_{bu} (s)**	**South**	**North**
EQ_2D_1axis_1	CNP 16%	4.5	9.01	6.9	8.79	29.4	72.6
EQ_2D_1axis_2	CNP 44%	7.0	9.08	15.5	8.76	25.7	58.3
EQ_2D_1axis_3	CNP 100%	7.0	4.85	15.5	3.61	4.2	8.0
EQ_2D_1axis_4	RRS 16%	7.0	2.81	10.1	2.72	44.8	35.3
EQ_2D_1axis_5	RRS 44%	7.0	2.31	15.3	2.63	6.5	10.6
EQ_2D_1axis_6	RRS 100%	N/A	N/A	N/A	N/A	N/A	N/A
SHORT		**EAST**		**WEST**		**% of Peak V_{bv}**	
Load Case	**Ground Motion**	**Peak V_{bv} (kips)**	**t @ peak V_{bv} (s)**	**Peak V_{bv} (kips)**	**t @ peak V_{bv} (s)**	**East**	**West**
EQ_2D_1axis_1	CNP 16%	5.1	10.24	3.2	8.94	67.7	35.5
EQ_2D_1axis_2	CNP 44%	8.0	9.66	7.3	9.01	40.3	57.2
EQ_2D_1axis_3	CNP 100%	9.9	8.49	8.9	8.24	15.6	14.2
EQ_2D_1axis_4	RRS 16%	5.7	2.77	5.8	2.86	49.1	52.3
EQ_2D_1axis_5	RRS 44%	10.0	6.37	9.1	2.78	41.7	39.6
EQ_2D_1axis_6	RRS 100%	N/A	N/A	N/A	N/A	N/A	N/A

Table B-18: P-2D-b model wall line base shear breakdown, nonlinear time history analysis

LONG		SOUTH			NORTH		
Load Case	**Ground Motion**	**Peak V_{bu} (kips)**	**SW V_{bu} (%)**	**GW V_{bu} (%)**	**Peak V_{bu} (kips)**	**SW V_{bu} (%)**	**GW V_{bu} (%)**
EQ_2D_1axis_1	CNP 16%	4.5	100.0	0.0	6.9	100.0	0.0
EQ_2D_1axis_2	CNP 44%	7.0	100.0	0.0	15.5	100.0	0.0
EQ_2D_1axis_3	CNP 100%	7.0	100.0	0.0	15.5	100.0	0.0
EQ_2D_1axis_4	RRS 16%	7.0	100.0	0.0	10.1	100.0	0.0
EQ_2D_1axis_5	RRS 44%	7.0	100.0	0.0	15.3	100.0	0.0
EQ_2D_1axis_6	RRS 100%	N/A	N/A	N/A	N/A	N/A	N/A
SHORT		**EAST**			**WEST**		
Load Case	**Ground Motion**	**Peak V_{bv} (kips)**	**SW V_{bv} (%)**	**GW V_{bu} (%)**	**Peak V_{bv} (kips)**	**SW V_{bv} (%)**	**GW V_{bv} (%)**
EQ_2D_1axis_1	CNP 16%	5.1	100.0	0.0	3.2	100.0	0.0
EQ_2D_1axis_2	CNP 44%	8.0	100.0	0.0	7.3	100.0	0.0
EQ_2D_1axis_3	CNP 100%	9.9	100.0	0.0	8.9	100.0	0.0
EQ_2D_1axis_4	RRS 16%	5.7	100.0	0.0	5.8	100.0	0.0
EQ_2D_1axis_5	RRS 44%	10.0	100.0	0.0	9.1	100.0	0.0
EQ_2D_1axis_6	RRS 100%	N/A	N/A	N/A	N/A	N/A	N/A

Table B-19: P-2D-b model peak hold down tensile force at certain locations, nonlinear time history analysis

		L1S1, LC5		L1S1, LC6		L1W1, LC7		L1W1, LC8	
Load Case	**Ground Motion**	**Peak F (kips)**	**t @ peak F (s)**	**Peak F (kips)**	**t @ peak F (s)**	**Peak F (kips)**	**t @ peak F (s)**	**Peak F (kips)**	**t @ peak F (s)**
EQ_2D_1axis_1	CNP 16%	-4.10	6.76	-4.86	7.19	-3.29	9.00	-3.00	9.36
EQ_2D_1axis_2	CNP 44%	-9.24	6.85	-8.85	6.44	-8.52	9.03	-8.03	8.63
EQ_2D_1axis_3	CNP 100%	-9.69	3.74	-8.66	4.92	-11.74	5.43	-10.73	6.85
EQ_2D_1axis_4	RRS 16%	-6.49	3.62	-10.04	2.82	-4.90	3.29	-5.83	2.89
EQ_2D_1axis_5	RRS 44%	-8.16	2.32	-7.44	2.84	-9.21	6.54	-9.92	2.78
EQ_2D_1axis_6	RRS 100%	N/A	N/A	N/A	N/A	N/A	N/A	N/A	N/A

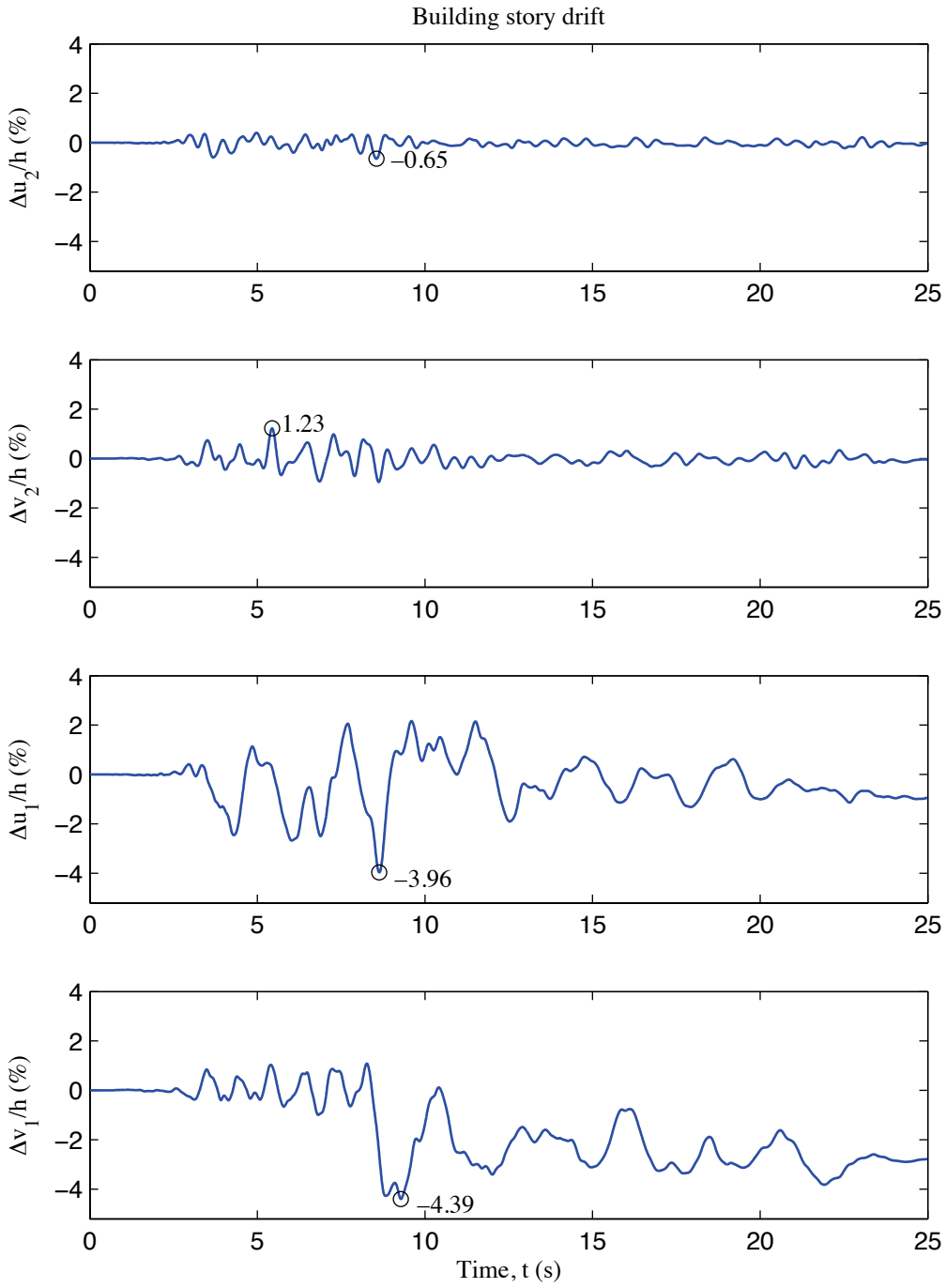

Figure B-6: P-2D-b model building story drift, 100 % Canoga Park, 2D nonlinear analysis

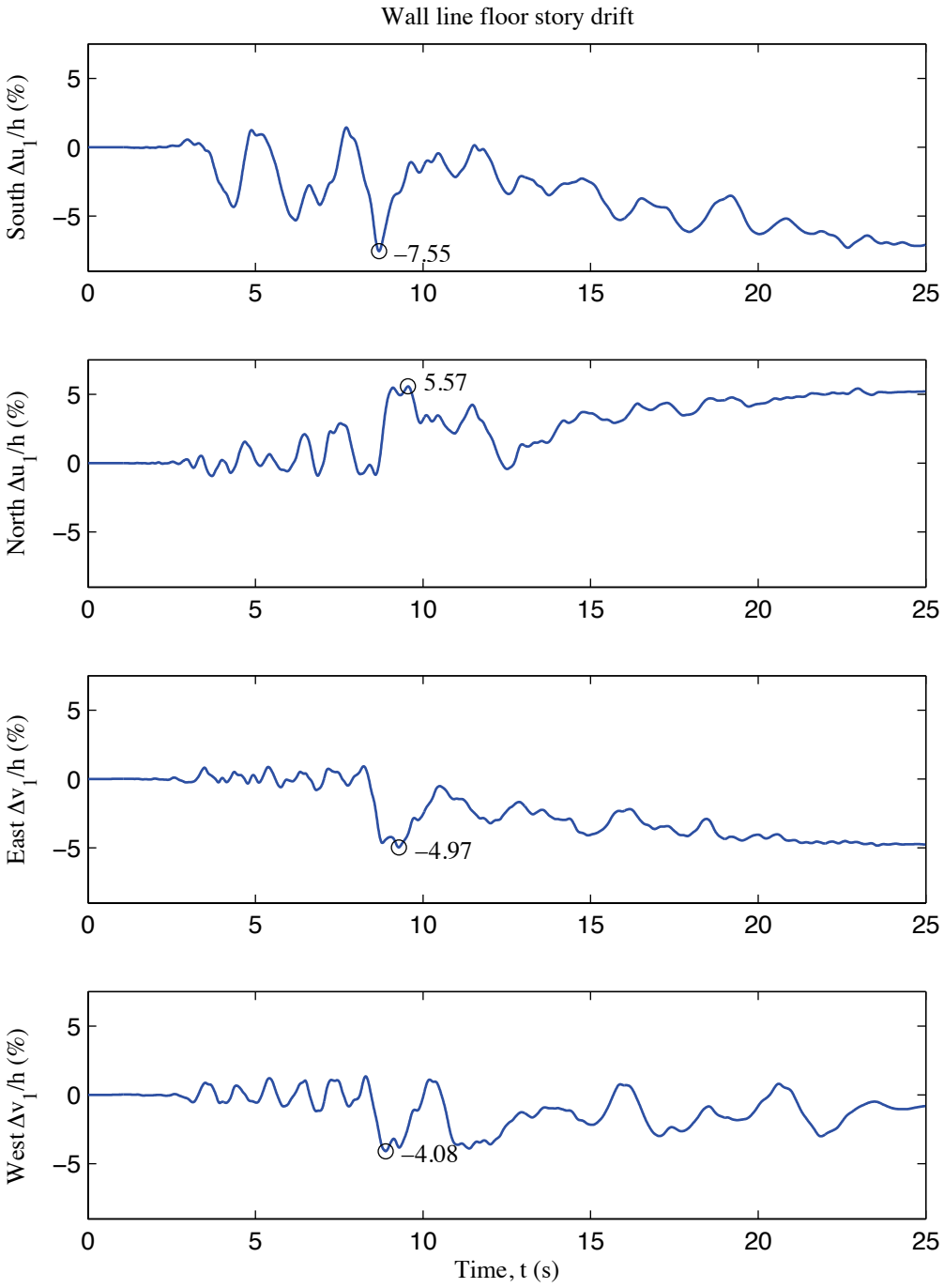

Figure B-7: P-2D-b model wall line floor story drift, 100 % Canoga Park, 2D nonlinear analysis

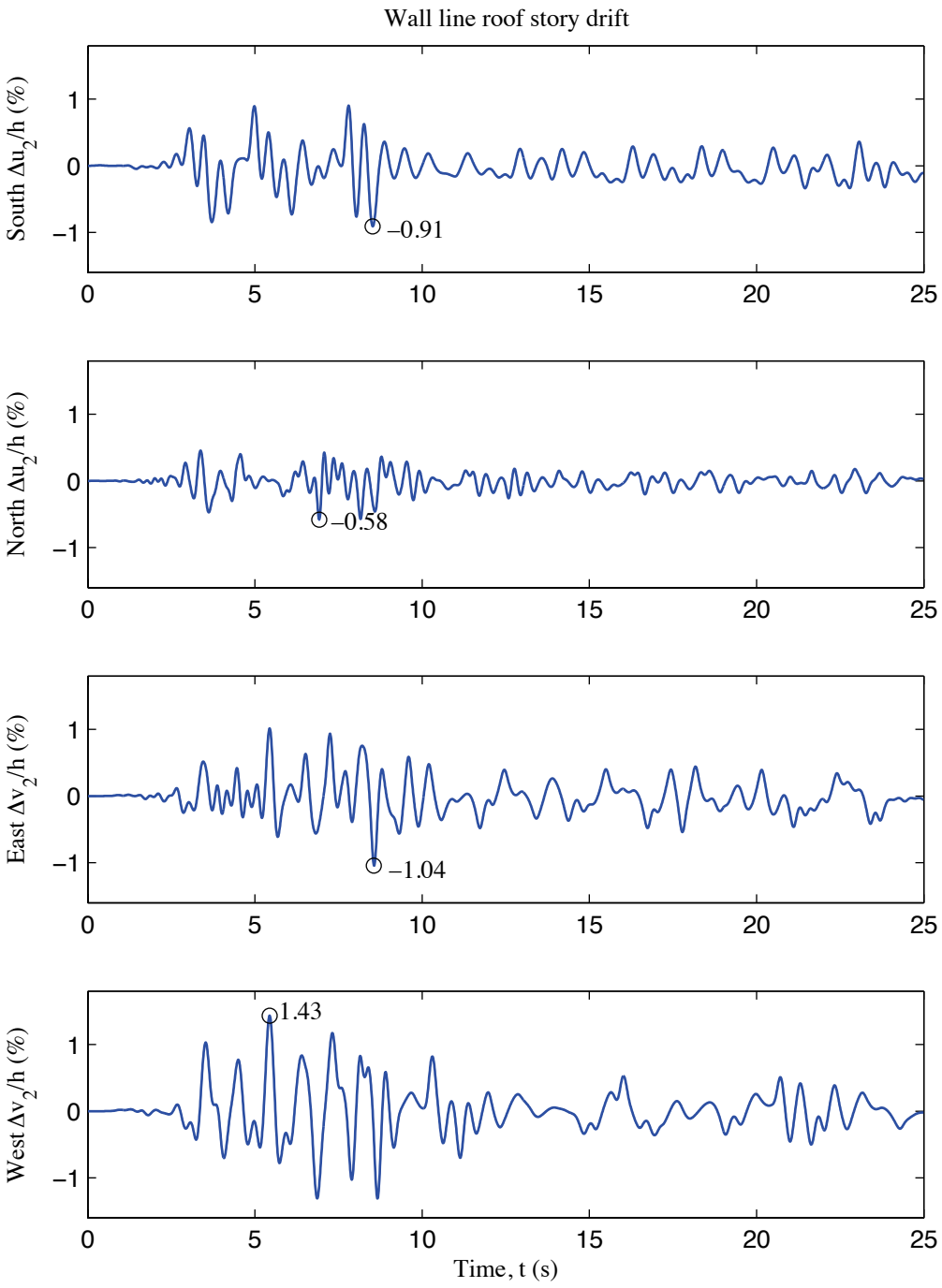

Figure B-8: P-2D-b model wall line roof story drift, 100 % Canoga Park, 2D nonlinear analysis

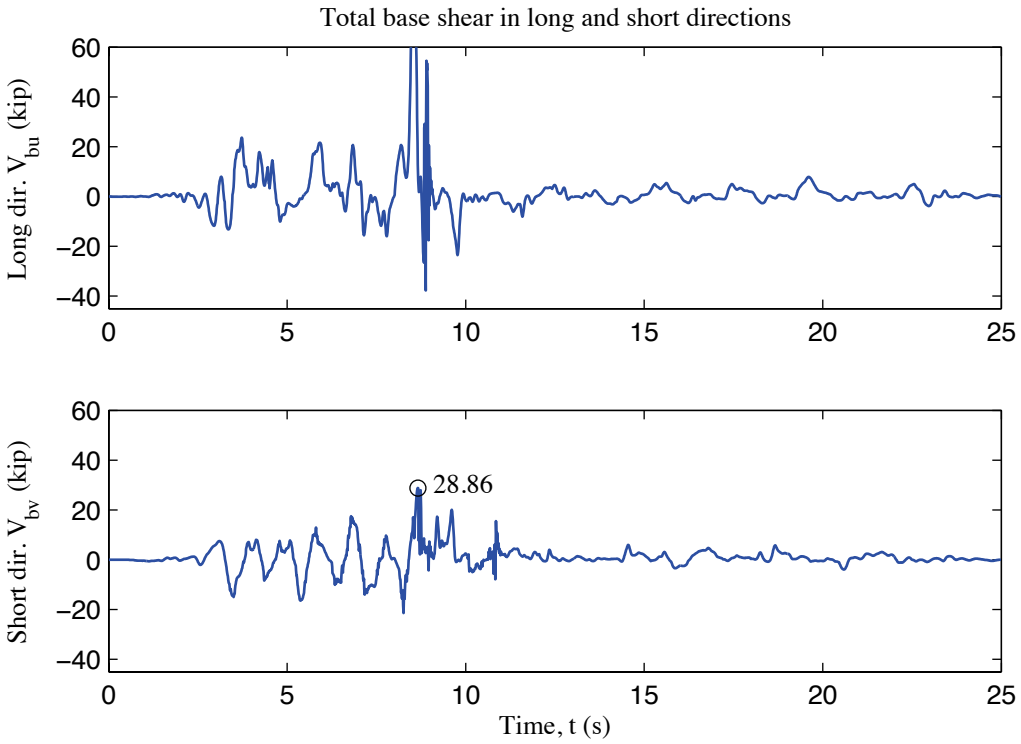

Figure B-9: P-2D-b model total building base shear, 100 % Canoga Park, 2D nonlinear analysis (peak V_{bu} is 126.9 kips)

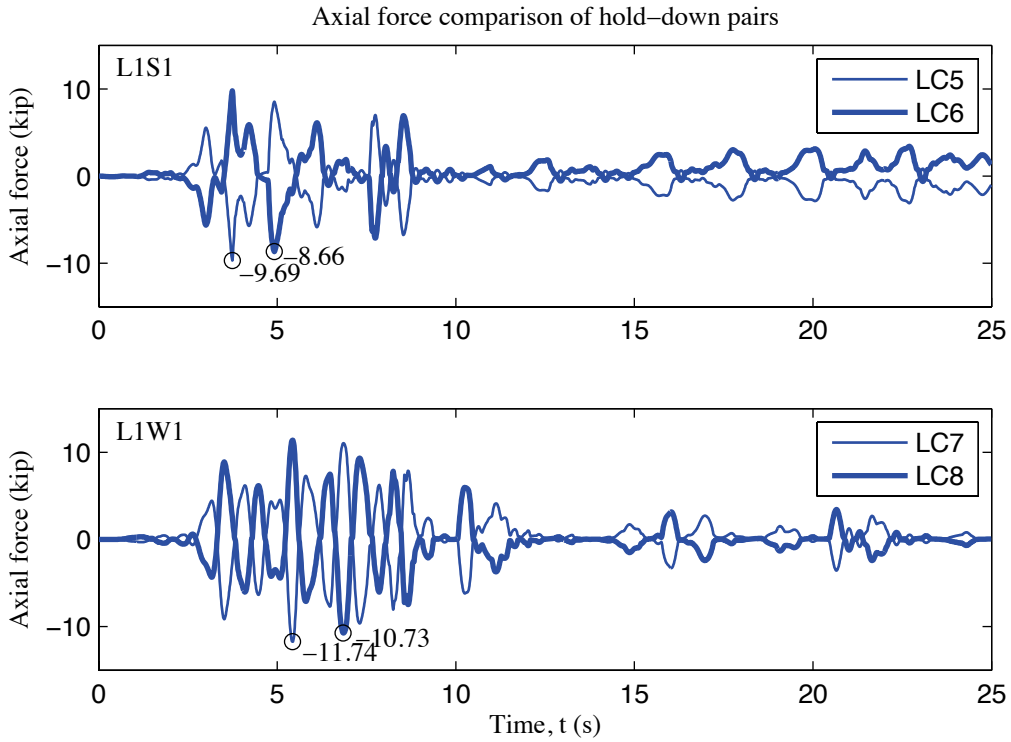

Figure B-10: P-2D-b model, load cell 5 to 8 axial forces, 100 % Canoga Park, 2D nonlinear analysis

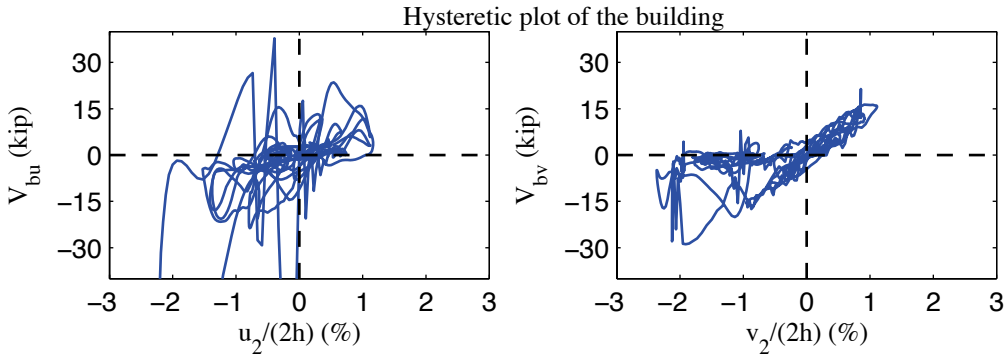

Figure B-11: P-2D-b model, hysteretic plot of the building, 100 % Canoga Park, 2D nonlinear analysis

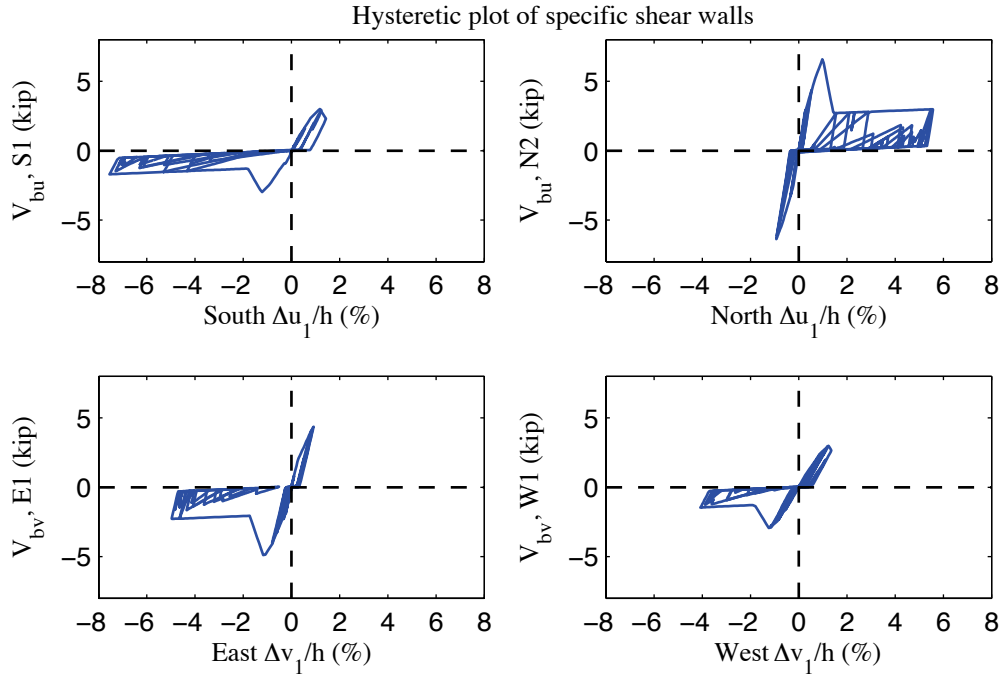

Figure B-12: P-2D-b model, hysteretic plot of shear walls at each elevation, 100 % Canoga Park, 2D nonlinear analysis

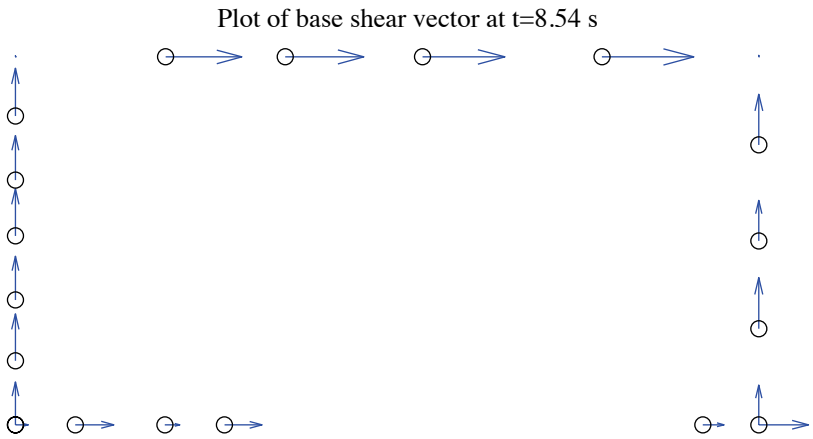

Figure B-13: P-2D-b model, field plot of peak total base shear, 100 % Canoga Park, 2D nonlinear analysis (maximum anchor/hold down base shear is 2.81 kips)

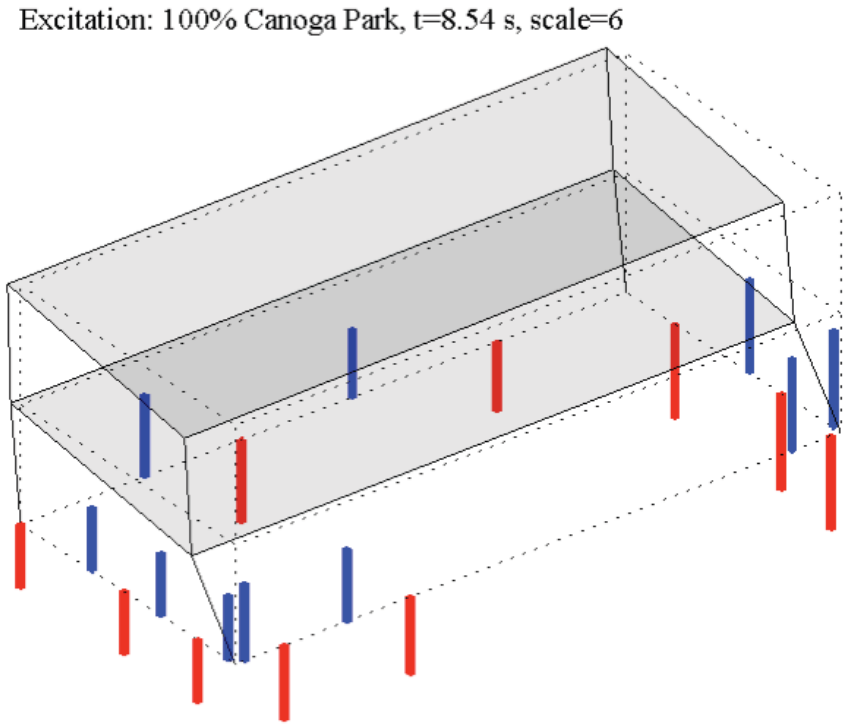

Figure B-14: P-2D-b model, simplified illustration of corner displacements with hold down forces from load cells,100 % Canoga Park, 2D nonlinear analysis (max hold down tensile force is -8.66 kips)

Appendix C: Analysis Results of State-of-the-practice, 3D, rigid-diaphragm, model a (P-3D-RD-a)

C.1 Model description

This state-of-the-practice 3D model features bracing models of whole shear wall panels, smeared models of hold downs into shear walls as pinned supports, and rigid diaphragms. Seismic mass is equally distributed to four corners. The lateral displacement and shear wall capacity ($\delta(V_{nP})$, V_{nP}) from AISI-213 standard is utilized to determine the stiffness of elastic material and the turning point on the backbone curve of elastic-perfectly plastic (EPP) material of shear wall bracing. Figure C-1 is the 3D drawing of the building model with all members and diagonal bracings of sheathing panels. Simulation results are presented and discussed in later sections. Definitions of output physical quantities and explanation of post-process method can be found in Appendix K.

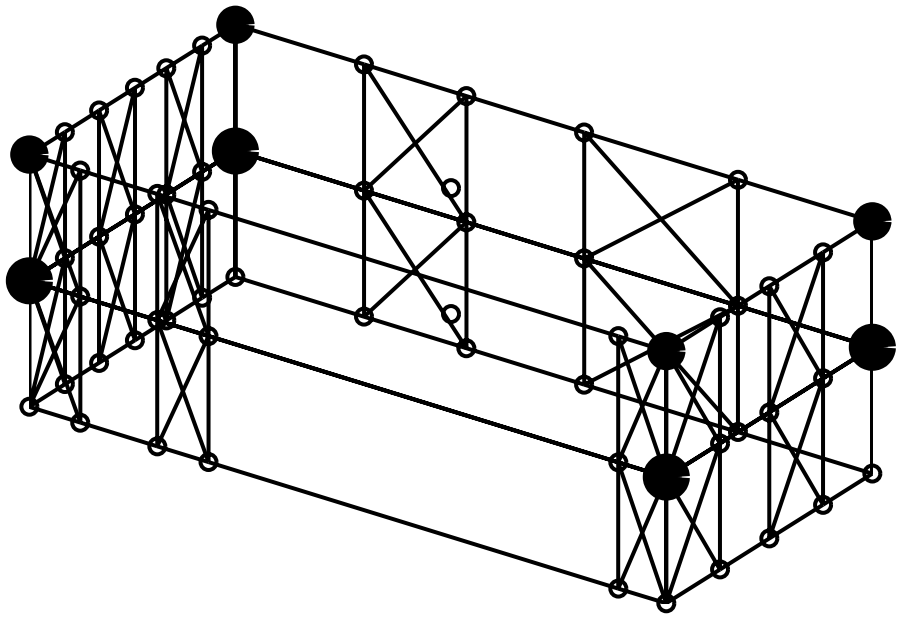

Figure C-1: P-3D-RD-a model

C.2 Free vibration analysis results

Free vibration analysis results are presented in Table C-1 and Figure C-2. Torsional stiffness is smaller than lateral stiffness in the short direction and lateral stiffness in the long direction and the largest. The observation holds for the first and the second mode, as indicated by Table C-1.

Table C-1: Free vibration analysis results, P-3D-RD-a model

Mode number	**Natural period (s)**	**Mode description**
1	0.893	Torsion, 1st
2	0.833	Short, 1st
3	0.637	Long, 1st
4	0.353	Torsion, 2nd
5	0.333	Short, 2nd
6	0.262	Long, 2nd

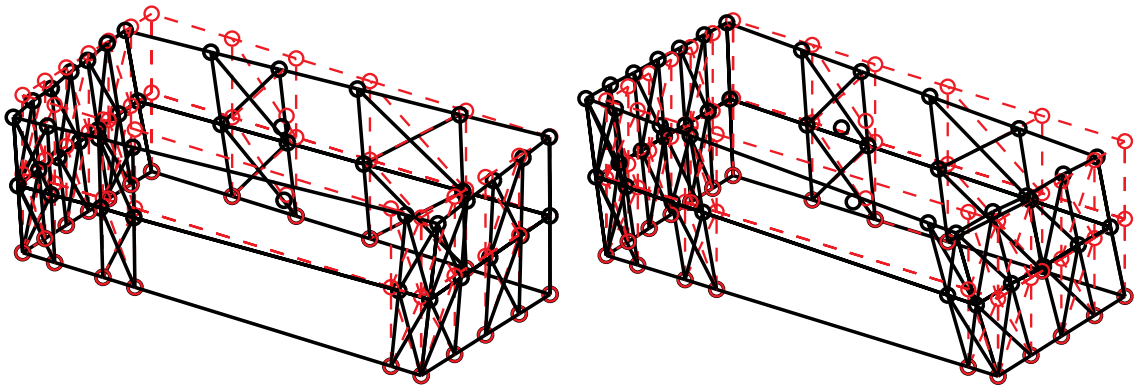

(a) Mode 1, T_1=0.893 s (b) Mode 2, T_2=0.833 s

Figure C-2: First two natural modes of P-3D-RD-a model

C.3 Linear static analysis results

Table C-2 to Table C-4 present linear static analysis results. The lateral load is the equivalent lateral force available from the design narrative (Madsen et al. 2011), applied equally at four corners. Two separate analyses were performed with the loading at long or short direction.

Table C-2 summarizes the breakdown of peak total base shear among four elevations. Due to the interplay of asymmetrical LFRS, wall lines perpendicular to the loading direction still take a very small portion of base shear.

Table C-3 shows peak building and wall line deflections. Practicing engineers can linearly upscale these data and develop an estimate of the building's performance at a certain lateral force level.

Table C-4 is an evaluation of the building's lateral stiffness of long and short direction and its breakdown among shear walls (SW) and other systems. Since gravity walls (GW) are not modeled in state-of-the-practice models, all base shear goes to shear walls.

Table C-2: Breakdown of peak base shear, linear static analysis, P-3D-RD-a model

Load direction	**LONG**				
Elevation	**South V_b**	**North V_b**	**East V_b**	**West V_b**	**Peak V_b**
kips	3.5	7.5	0.0	0.0	11.1
%	31.7	68.2	0.0	0.1	100.0
Load direction	**SHORT**				
Elevation	**South V_b**	**North V_b**	**East V_b**	**West V_b**	**Peak V_b**
kips	0.0	0.0	5.6	5.4	11.1
%	0.2	0.2	50.7	48.9	100.0

Table C-3: Peak building and wall line deflection, linear static analysis, P-3D-RD-a model

Load direction	**LONG**							
Deflection (in.)	u_1	u_2	v_1	v_2	Δu_1	Δu_2	Δv_1	Δv_2
Building	0.465	0.913	-0.034	-0.094	0.465	0.448	-0.034	-0.059
South	0.521	1.019	-0.034	-0.094	0.521	0.498	-0.034	-0.059
North	0.409	0.807	-0.034	-0.094	0.409	0.397	-0.034	-0.059
East	0.465	0.913	0.086	0.136	0.465	0.448	0.086	0.050
West	0.465	0.913	-0.155	-0.323	0.465	0.448	-0.155	-0.168
Load direction	**SHORT**							
Deflection (in.)	u_1	u_2	v_1	v_2	Δu_1	Δu_2	Δv_1	Δv_2
Building	-0.010	-0.020	0.713	1.370	-0.010	-0.009	0.713	0.656
South	-0.032	-0.062	0.713	1.370	-0.032	-0.030	0.713	0.656
North	0.012	0.023	0.713	1.370	0.012	0.011	0.713	0.656
East	-0.010	-0.020	0.666	1.278	-0.010	-0.009	0.666	0.612
West	-0.010	-0.020	0.761	1.462	-0.010	-0.009	0.761	0.701

Table C-4: Breakdown of lateral stiffness, P-3D-RD-a model

LONG			**SHORT**		
Shear wall k_u (%)	**Gravity wall k_u (%)**	**k_u (kip/in)**	**Shear wall k_v (%)**	**Gravity wall k_v (%)**	**k_v (kip/in)**
100.0	0.0	12.1	100.0	0.0	7.7

C.4 Nonlinear static (pushover) analysis results

Table C-5 is created following the same logic with Table C-2, but the analysis type is nonlinear static (pushover). Pushover curves of the building and each wall line are presented in Figure C-3 and Figure C-4.

Clearly, the interaction between wall lines is much more significant when material and geometrical nonlinearity is included. These tables and figures indicate that the wall lines do not reach their peak capacity at exactly the same drift level and wall lines perpendicular to the load can take a nontrivial amount of base shear. Accordingly, total capacity of the building is larger than the sum of wall line capacities in the load direction. Total capacity of the building in the short direction is smaller than the long direction.

Table C-5: Breakdown of peak base shear, pushover analysis, P-3D-RD-a model

Load direction	**LONG**				
Elevation	**South V_b**	**North V_b**	**East V_b**	**West V_b**	**Peak V_b**
kips	8.8	16.3	1.6	3.2	29.7
%	29.5	55.0	5.2	10.7	100.0
Load direction	**SHORT**				
Elevation	**South V_b**	**North V_b**	**East V_b**	**West V_b**	**Peak V_b**
kips	1.8	1.9	9.7	9.2	22.5
%	8.0	8.4	43.3	40.8	100.0

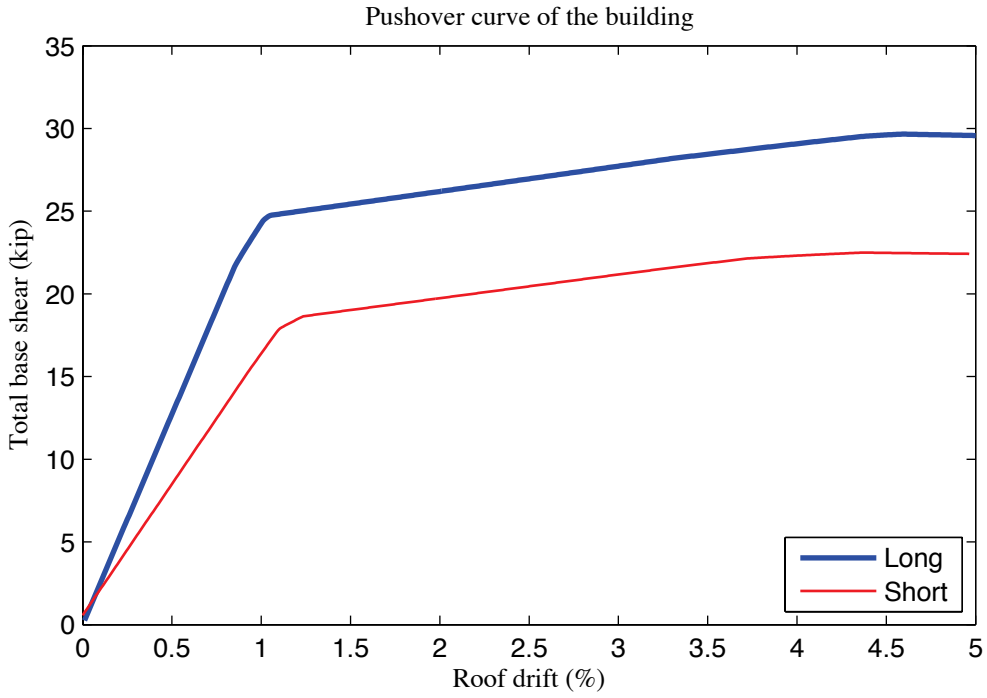

Figure C-3: Pushover curve of P-3D-RD-a model

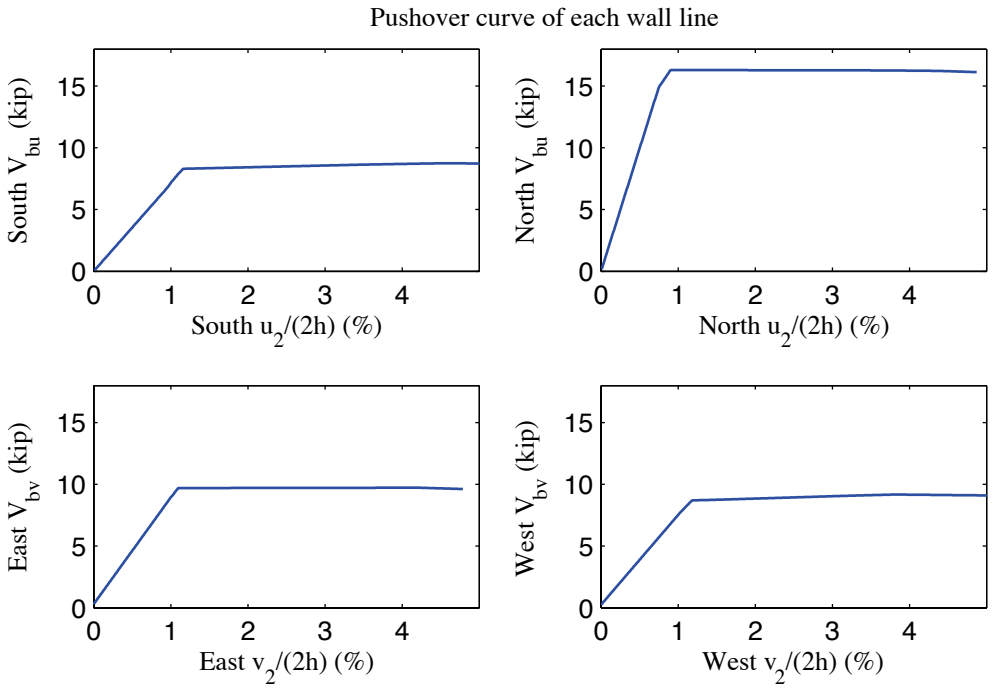

Figure C-4: Pushover curve of each wall line, P-3D-RD-a model

C.5 Linear time history analysis results

Linear time history analysis is performed on the model under Canoga Park and Rinaldi ground motion records of Northridge earthquake in 1994. We considered three scale levels (16%, 44% and 100%) and loadings in one, two and three axes.

Table C-6 to Table C-9 demonstrate the building's linear elastic performance under designated ground motions. Table C-6 shows peak story relative accelerations in the unit of g. Table C-7 and Table C-8 report peak roof drift and story drift of the building and the corresponding time step (t_*) and the base shear at that time. Note that the base shear at the time of peak roof drift may not be the peak total building base shear in that direction (see Table C-9).

The building behaves linearly since peak drift and peak base shear appear at the same time when the ground motion is linearly scaled. Figure C-5 is a vector plot of the peak total resultant base shear of the building under three axial, 100% Canoga Park excitation. The directions of arrows imply that base shear taken by shear walls does not necessarily follow the direction of wall lines due to the effect of 3D coupling. Comparison with nonlinear analysis results of the same excitation provides insightful observations on the building's response and requirements on modeling fidelity and analysis type.

Table C-6: P-3D-RD-a model peak story relative acceleration in g, linear time history analysis

		LONG			SHORT			UP		
Load Case	**Ground Motion**	**a_g**	**Floor a**	**Roof a**	**a_g**	**Floor a**	**Roof a**	**a_g**	**Floor a**	**Roof a**
EQ_3D_3axis_1	CNP 16%	0.067	0.168	0.303	0.057	0.100	0.132	0.078	0.001	0.001
EQ_3D_3axis_2	CNP 44%	0.185	0.461	0.834	0.157	0.274	0.363	0.215	0.002	0.003
EQ_3D_1axis_1	CNP 100%	0.420	1.060	1.905	0	0.162	0.263	0	0.002	0.002
EQ_3D_1axis_2	CNP 100%	0	0.107	0.161	0.356	0.624	0.885	0	0.005	0.007
EQ_3D_2axis_1	CNP 100%	0.420	1.048	1.896	0.356	0.623	0.825	0	0.004	0.007
EQ_3D_3axis_3	CNP 100%	0.420	1.048	1.896	0.356	0.623	0.825	0.489	0.004	0.007
EQ_3D_3axis_4	RRS 16%	0.132	0.227	0.366	0.078	0.176	0.232	0.133	0.001	0.001
EQ_3D_3axis_5	RRS 44%	0.363	0.624	1.006	0.214	0.483	0.637	0.367	0.003	0.004
EQ_3D_3axis_6	RRS 100%	0.825	1.418	2.286	0.486	1.097	1.448	0.834	0.007	0.009

Table C-7: P-3D-RD-a model peak building roof drift and base shear, linear time history analysis

		LONG			SHORT		
Load Case	**Ground Motion**	**u_2/(2h) (%)**	**t_* (s)**	**V_b @ t_* (kips)**	**v_2/(2h) (%)**	**t_* (s)**	**V_b @ t_* (kips)**
EQ_3D_3axis_1	CNP 16%	-0.507	9.24	13.2	-0.336	9.39	4.6
EQ_3D_3axis_2	CNP 44%	-1.396	9.24	36.2	0.918	9.00	12.9
EQ_3D_1axis_1	CNP 100%	3.044	8.91	86.3	-0.776	10.05	12.4
EQ_3D_1axis_2	CNP 100%	0.487	10.48	9.5	2.411	9.02	34.1
EQ_3D_2axis_1	CNP 100%	-3.172	9.24	82.3	2.129	9.00	29.4
EQ_3D_3axis_3	CNP 100%	-3.172	9.24	82.3	2.129	9.00	29.4
EQ_3D_3axis_4	RRS 16%	0.826	2.80	23.5	-0.652	2.91	10.5
EQ_3D_3axis_5	RRS 44%	2.270	2.80	64.7	-1.733	2.91	28.8
EQ_3D_3axis_6	RRS 100%	5.159	2.80	147.0	-3.895	2.91	65.4

Table C-8: P-3D-RD-a model peak building story drift, linear time history analysis

		LONG				SHORT			
Load Case	**Ground Motion**	**$\Delta u_1/h$ (%)**	**t_* (s)**	**$\Delta u_2/h$ (%)**	**t_* (s)**	**$\Delta v_1/h$ (%)**	**t_* (s)**	**$\Delta v_2/h$ (%)**	**t_* (s)**
EQ_3D_3axis_1	CNP 16%	0.512	8.92	-0.517	9.23	-0.332	8.63	-0.381	9.41
EQ_3D_3axis_2	CNP 44%	1.407	8.92	-1.421	9.23	-0.873	8.63	1.035	8.99
EQ_3D_1axis_1	CNP 100%	3.186	8.93	3.095	10.14	-0.798	10.86	-0.820	10.05
EQ_3D_1axis_2	CNP 100%	0.532	10.50	-0.470	10.11	-2.395	8.64	2.669	9.01
EQ_3D_2axis_1	CNP 100%	3.198	8.92	-3.229	9.23	-1.956	8.63	2.411	8.99
EQ_3D_3axis_3	CNP 100%	3.198	8.92	-3.229	9.23	-1.956	8.63	2.411	8.99
EQ_3D_3axis_4	RRS 16%	0.883	2.81	0.780	2.78	-0.710	2.88	-0.648	2.95
EQ_3D_3axis_5	RRS 44%	2.429	2.81	2.144	2.78	-1.913	2.88	-1.701	2.95
EQ_3D_3axis_6	RRS 100%	5.521	2.81	4.872	2.78	-4.319	2.88	-3.808	2.95

Table C-9: P-3D-RD-a model peak building base shear, linear time history analysis

		LONG		SHORT		RESULTANT	
Load Case	**Ground Motion**	**Peak V_{bu} (kip)**	**t @ peak V_{bu} (s)**	**Peak V_{bv} (kip)**	**t @ peak V_{bv} (s)**	**Peak V_b (kip)**	**t @ peak V_b (s)**
EQ_3D_3axis_1	CNP 16%	14.0	9.54	5.1	9.06	14.6	8.92
EQ_3D_3axis_2	CNP 44%	38.6	9.54	13.9	9.06	40.1	8.92
EQ_3D_1axis_1	CNP 100%	88.3	9.85	14.8	10.44	88.3	9.85
EQ_3D_1axis_2	CNP 100%	9.6	10.50	38.8	8.64	38.9	8.64
EQ_3D_2axis_1	CNP 100%	87.7	9.54	31.7	9.06	91.2	8.92
EQ_3D_3axis_3	CNP 100%	87.7	9.54	31.7	9.06	91.2	8.92
EQ_3D_3axis_4	RRS 16%	23.6	2.81	11.1	2.87	25.4	2.81
EQ_3D_3axis_5	RRS 44%	64.8	2.81	30.4	2.87	69.9	2.81
EQ_3D_3axis_6	RRS 100%	147.2	2.81	69.2	2.87	158.8	2.81

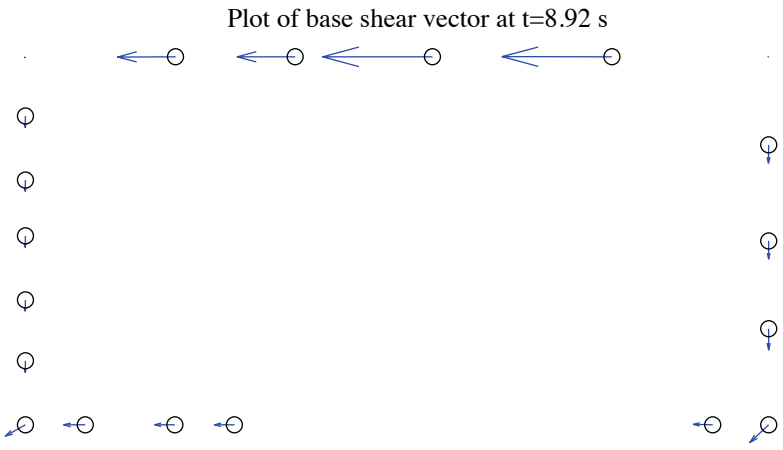

Figure C-5: P-3D-RD-a model, base shear vector plot at the moment of peak total base shear, 100 % Canoga Park, 3D linear analysis (maximum anchor/hold down base shear is 20.99 kips)

C.6 Nonlinear time history analysis results

Same ground motions are applied to the model with material and geometrical nonlinearity. Table C-10 to Table C-13 are replicas of Table C-6 to Table C-9, but for nonlinear time history analyses. Since this analysis type is most complicated and closest to reality and experiments, behavior of wall lines and hold downs are further studied. Table C-14 is the table of peak wall line story drifts and corresponding time steps. Table C-15 is designed for peak base shear of each wall line and the last two columns of the table are percentages of base shear of two facing wall lines in the same direction when the total base shear in that direction takes peak value. Table C-16 expands the breakdown of each wall line's peak base shear between shear walls, gravity walls and other systems. Table C-17 is peak value of hold down tensile force of two selected pairs. Hold down 5 and 6 are on shear wall L1S1, South elevation and hold down 7 and 8 are on shear wall L1W1, West elevation. These shear walls have lowest capacities compared with others on the same wall line and they meet at the southwest edge of the building, so interacted nonlinear behavior is expected to appear. Since hold downs are smeared to shear wall stud ends, hold down 6 and 7 are combined together in 3D model as one single pinned support.

Time history plots in this section include plots of story drifts of the building and each wall line (Figure C-6 to Figure C-8), total building base shear in long and short direction (Figure C-9) and axial forces of hold downs in Table C-17 (Figure C-10). Hysteretic plots in Figure C-11 and Figure C-12 are helpful for visual examination of nonlinear base shear-drift relationship of the building and the weakest shear wall on each wall line. In comparison with linear time history analysis, vector plot of peak total base shear is

illustrated in Figure C-13. Figure C-14 presents a simplified deformed shape of the building (see (Peterman 2014) for details of the method) and axial force of all twenty hold downs at the moment of peak total base shear. The same sign convention with tests is adopted. Red bars indicate tensile (negative) force and blue ones are for compressive (positive) force.

Hysteretic behavior is seen in the building and typical shear walls under design-based earthquake (100% Canoga Park excitation in 3 axes, see Figure C-11 and Figure C-12). The response curves shows that peak capacities of the building has been reached, and they also imply that EPP material model tends to over estimate the energy dissipation of walls since pinching effect and strength degradation are missing. Max peak story drifts among wall lines is about 3% (Table C-12), and larger deflection is seen in the short direction. Figure C-13 clearly shows that base shear vectors in anchors and hold downs do not align with wall lines. Since load cells 6 and 7 are combined, it is not easy to use Table C-17 and Figure C-10 to examine Type I shear wall design assumption for this case. However, at the moment of the peak base shear, the pair of hold downs in South elevation at southeast corner is in compression (Figure C-14), which still challenges the assumption.

The near-field Rinaldi record is much stronger in terms of peak ground acceleration, especially in the long direction. When loaded at 100%, both directions are believed to be destroyed with peak story drift larger than 11% and 5.5%. Such a large drift level is a sign of structural failure.

Table C-10: P-3D-RD-a model peak story relative acceleration in g, nonlinear time history analysis

		LONG			SHORT			UP		
Load Case	**Ground Motion**	**a_g**	**Floor a**	**Roof a**	**a_g**	**Floor a**	**Roof a**	**a_g**	**Floor a**	**Roof a**
EQ_3D_3axis_1	CNP 16%	0.067	0.129	0.204	0.057	0.093	0.126	0.078	0.018	0.025
EQ_3D_3axis_2	CNP 44%	0.185	0.347	0.555	0.157	0.287	0.398	0.215	0.067	0.085
EQ_3D_1axis_1	CNP 100%	0.420	0.581	0.814	0	0.058	0.083	0	0.043	0.040
EQ_3D_1axis_2	CNP 100%	0	0.284	0.293	0.356	0.623	0.582	0	0.091	0.154
EQ_3D_2axis_1	CNP 100%	0.420	0.641	0.818	0.356	0.665	0.619	0	0.121	0.170
EQ_3D_3axis_3	CNP 100%	0.420	0.641	0.818	0.356	0.665	0.619	0.489	0.121	0.170
EQ_3D_3axis_4	RRS 16%	0.132	0.187	0.305	0.078	0.144	0.218	0.133	0.045	0.060
EQ_3D_3axis_5	RRS 44%	0.363	0.527	0.726	0.214	0.324	0.462	0.367	0.082	0.095
EQ_3D_3axis_6	RRS 100%	0.825	1.086	1.173	0.486	0.662	0.880	0.834	0.292	0.296

Table C-11: P-3D-RD-a model peak building roof drift and base shear, nonlinear time history analysis

		LONG			SHORT		
Load Case	**Ground Motion**	**u_2/(2h) (%)**	**t_* (s)**	**V_b @ t_* (kips)**	**v_2/(2h) (%)**	**t_* (s)**	**V_b @ t_* (kips)**
EQ_3D_3axis_1	CNP 16%	0.419	8.89	10.5	-0.361	8.61	5.5
EQ_3D_3axis_2	CNP 44%	0.390	21.46	2.5	-1.794	8.67	19.9
EQ_3D_1axis_1	CNP 100%	1.593	9.56	22.2	-0.311	8.37	4.2
EQ_3D_1axis_2	CNP 100%	0.390	21.46	2.5	-1.794	8.67	19.9
EQ_3D_2axis_1	CNP 100%	1.721	9.57	23.4	-2.172	8.66	20.1
EQ_3D_3axis_3	CNP 100%	1.721	9.57	23.4	-2.172	8.66	20.1
EQ_3D_3axis_4	RRS 16%	0.803	2.81	21.6	-0.637	2.91	9.7
EQ_3D_3axis_5	RRS 44%	3.206	2.98	22.7	-1.755	2.93	17.2
EQ_3D_3axis_6	RRS 100%	6.972	3.10	24.0	-3.674	3.04	18.3

Table C-12: P-3D-RD-a model peak building story drift, nonlinear linear time history analysis

		LONG				SHORT			
Load Case	**Ground Motion**	**$\Delta u_1/h$ (%)**	**t_* (s)**	**$\Delta u_2/h$ (%)**	**t_* (s)**	**$\Delta v_1/h$ (%)**	**t_* (s)**	**$\Delta v_2/h$ (%)**	**t_* (s)**
EQ_3D_3 axis_1	CNP 16%	0.421	8.91	0.422	8.88	-0.391	8.64	-0.363	8.57
EQ_3D_3 axis_2	CNP 44%	0.465	17.80	0.634	24.12	-2.715	8.72	-1.595	8.57
EQ_3D_1 axis_1	CNP 100%	2.394	8.98	1.242	8.87	-0.307	7.49	-0.320	9.31
EQ_3D_1 axis_2	CNP 100%	0.465	17.80	0.634	24.12	-2.715	8.72	-1.595	8.57
EQ_3D_2 axis_1	CNP 100%	2.550	8.98	1.296	8.87	-3.332	8.72	-1.787	8.58
EQ_3D_3 axis_3	CNP 100%	2.550	8.98	1.296	8.87	-3.332	8.72	-1.787	8.58
EQ_3D_3 axis_4	RRS 16%	0.862	2.82	0.745	2.80	-0.681	2.89	-0.630	2.95
EQ_3D_3 axis_5	RRS 44%	5.311	2.95	1.365	2.75	-2.223	2.94	-1.308	2.91
EQ_3D_3 axis_6	RRS 100%	11.178	3.06	3.709	4.52	-5.746	3.18	-1.999	5.44

Table C-13: P-3D-RD-a model peak building base shear, nonlinear time history analysis

		LONG		SHORT		RESULTANT	
Load Case	**Ground Motion**	**Peak V_{bu} (kip)**	**t @ peak V_{bu} (s)**	**Peak V_{bv} (kip)**	**t @ peak V_{bv} (s)**	**Peak V_b (kip)**	**t @ peak V_b (s)**
EQ_3D_3axis_1	CNP 16%	10.6	8.91	5.8	8.64	11.3	8.91
EQ_3D_3axis_2	CNP 44%	9.7	21.96	20.3	8.70	20.3	8.70
EQ_3D_1axis_1	CNP 100%	26.3	8.97	4.9	9.73	26.4	8.97
EQ_3D_1axis_2	CNP 100%	9.7	21.96	20.3	8.70	20.3	8.70
EQ_3D_2axis_1	CNP 100%	26.5	8.98	21.1	8.72	31.8	8.62
EQ_3D_3axis_3	CNP 100%	26.5	8.98	21.1	8.72	31.8	8.62
EQ_3D_3axis_4	RRS 16%	21.6	2.81	10.0	2.88	23.2	2.82
EQ_3D_3axis_5	RRS 44%	29.0	2.91	19.1	2.87	34.6	2.89
EQ_3D_3axis_6	RRS 100%	33.4	3.00	22.6	2.94	39.9	2.94

Table C-14: P-3D-RD-a model peak wall line story drift, nonlinear time history analysis

LONG		SOUTH				NORTH			
Load Case	**Ground Motion**	**$\Delta u_1/h$ (%)**	**t_* (s)**	**$\Delta u_2/h$ (%)**	**t_* (s)**	**$\Delta u_1/h$ (%)**	**t_* (s)**	**$\Delta u_2/h$ (%)**	**t_* (s)**
EQ_3D_3axis_1	CNP 16%	0.458	8.90	0.464	8.89	0.383	8.91	0.384	8.87
EQ_3D_3axis_2	CNP 44%	0.773	8.85	0.900	24.11	0.299	17.41	0.375	24.13
EQ_3D_1axis_1	CNP 100%	2.413	9.00	1.251	6.77	2.543	9.56	1.299	8.86
EQ_3D_1axis_2	CNP 100%	0.773	8.85	0.900	24.11	0.299	17.41	0.375	24.13
EQ_3D_2axis_1	CNP 100%	2.675	8.99	1.414	8.88	2.521	9.55	1.209	8.86
EQ_3D_3axis_3	CNP 100%	2.675	8.99	1.414	8.88	2.521	9.55	1.209	8.86
EQ_3D_3axis_4	RRS 16%	0.931	2.83	0.797	2.82	0.814	2.80	0.724	3.14
EQ_3D_3axis_5	RRS 44%	5.805	2.97	1.446	2.77	4.937	2.92	1.323	2.74
EQ_3D_3axis_6	RRS 100%	11.351	3.07	3.729	5.82	11.046	3.04	3.831	4.52
SHORT		**EAST**				**WEST**			
Load Case	**Ground Motion**	**$\Delta v_1/h$ (%)**	**t_* (s)**	**$\Delta v_2/h$ (%)**	**t_* (s)**	**$\Delta v_1/h$ (%)**	**t_* (s)**	**$\Delta v_2/h$ (%)**	**t_* (s)**
EQ_3D_3axis_1	CNP 16%	0.475	9.40	0.545	9.41	0.429	8.66	0.369	8.62
EQ_3D_3axis_2	CNP 44%	2.514	8.69	1.818	8.53	3.092	8.75	1.803	8.63
EQ_3D_1axis_1	CNP 100%	0.722	7.66	0.732	9.43	0.976	7.35	0.884	7.35
EQ_3D_1axis_2	CNP 100%	2.514	8.69	1.818	8.53	3.092	8.75	1.803	8.63
EQ_3D_2axis_1	CNP 100%	3.190	8.72	1.727	8.58	3.475	8.72	1.847	8.58
EQ_3D_3axis_3	CNP 100%	3.190	8.72	1.727	8.58	3.475	8.72	1.847	8.58
EQ_3D_3axis_4	RRS 16%	0.448	2.82	0.336	3.16	1.252	3.40	1.013	2.98
EQ_3D_3axis_5	RRS 44%	1.670	2.87	1.255	4.48	3.448	3.01	1.783	2.88
EQ_3D_3axis_6	RRS 100%	5.921	2.97	2.147	4.51	6.311	3.17	2.308	3.26

Table C-15: P-3D-RD-a model peak wall line base shear, nonlinear time history analysis

LONG		SOUTH		NORTH		% of Peak V_{bu}	
Load Case	**Ground Motion**	**Peak V_{bu} (kips)**	**t @ peak V_{bu} (s)**	**Peak V_{bu} (kips)**	**t @ peak V_{bu} (s)**	**South**	**North**
EQ_3D_3axis_1	CNP 16%	3.2	8.91	7.5	8.91	29.8	70.4
EQ_3D_3axis_2	CNP 44%	5.7	8.85	6.2	17.41	50.3	46.1
EQ_3D_1axis_1	CNP 100%	8.6	9.00	16.4	8.97	32.5	62.4
EQ_3D_1axis_2	CNP 100%	5.7	8.85	6.2	17.41	50.3	46.1
EQ_3D_2axis_1	CNP 100%	9.0	8.99	16.4	8.98	33.9	61.9
EQ_3D_3axis_3	CNP 100%	9.0	8.99	16.4	8.98	33.9	61.9
EQ_3D_3axis_4	RRS 16%	6.4	2.83	15.3	2.80	28.9	70.3
EQ_3D_3axis_5	RRS 44%	8.2	2.69	16.5	3.32	26.6	56.5
EQ_3D_3axis_6	RRS 100%	9.9	2.49	17.1	3.46	21.9	48.0
SHORT		**EAST**		**WEST**		**% of Peak V_{bv}**	
Load Case	**Ground Motion**	**Peak V_{bv} (kips)**	**t @ peak V_{bv} (s)**	**Peak V_{bv} (kips)**	**t @ peak V_{bv} (s)**	**East**	**West**
EQ_3D_3axis_1	CNP 16%	3.8	9.39	2.9	8.66	49.8	49.3
EQ_3D_3axis_2	CNP 44%	9.9	8.88	9.2	8.75	48.4	44.4
EQ_3D_1axis_1	CNP 100%	6.1	7.30	6.8	7.35	51.9	46.4
EQ_3D_1axis_2	CNP 100%	9.9	8.88	9.2	8.75	48.4	44.4
EQ_3D_2axis_1	CNP 100%	9.9	6.66	9.2	8.73	46.4	43.4
EQ_3D_3axis_3	CNP 100%	9.9	6.66	9.2	8.73	46.4	43.4
EQ_3D_3axis_4	RRS 16%	3.6	2.82	8.7	3.40	30.6	68.7
EQ_3D_3axis_5	RRS 44%	9.7	3.96	9.3	3.01	50.6	46.5
EQ_3D_3axis_6	RRS 100%	10.1	4.36	9.6	3.08	43.2	41.8

Table C-16: P-3D-RD-a model wall line base shear breakdown, nonlinear time history analysis

LONG		SOUTH			NORTH		
Load Case	**Ground Motion**	**Peak V_{bu} (kips)**	**SW V_{bu} (%)**	**GW V_{bu} (%)**	**Peak V_{bu} (kips)**	**SW V_{bu} (%)**	**GW V_{bu} (%)**
EQ_3D_3axis_1	CNP 16%	3.2	100.0	0.0	7.5	100.0	0.0
EQ_3D_3axis_2	CNP 44%	5.7	100.0	0.0	6.2	100.0	0.0
EQ_3D_1axis_1	CNP 100%	8.6	100.0	0.0	16.4	100.0	0.0
EQ_3D_1axis_2	CNP 100%	5.7	100.0	0.0	6.2	100.0	0.0
EQ_3D_2axis_1	CNP 100%	9.0	100.0	0.0	16.4	100.0	0.0
EQ_3D_3axis_3	CNP 100%	9.0	100.0	0.0	16.4	100.0	0.0
EQ_3D_3axis_4	RRS 16%	6.4	100.0	0.0	15.3	100.0	0.0
EQ_3D_3axis_5	RRS 44%	8.2	100.0	0.0	16.5	100.0	0.0
EQ_3D_3axis_6	RRS 100%	9.9	100.0	0.0	17.1	100.0	0.0
SHORT		**EAST**			**WEST**		
Load Case	**Ground Motion**	**Peak V_{bv} (kips)**	**SW V_{bv} (%)**	**GW V_{bu} (%)**	**Peak V_{bv} (kips)**	**SW V_{bv} (%)**	**GW V_{bv} (%)**
EQ_3D_3axis_1	CNP 16%	3.8	100.0	0.0	2.9	100.0	0.0
EQ_3D_3axis_2	CNP 44%	9.9	100.0	0.0	9.2	100.0	0.0
EQ_3D_1axis_1	CNP 100%	6.1	100.0	0.0	6.8	100.0	0.0
EQ_3D_1axis_2	CNP 100%	9.9	100.0	0.0	9.2	100.0	0.0
EQ_3D_2axis_1	CNP 100%	9.9	100.0	0.0	9.2	100.0	0.0
EQ_3D_3axis_3	CNP 100%	9.9	100.0	0.0	9.2	100.0	0.0
EQ_3D_3axis_4	RRS 16%	3.6	100.0	0.0	8.7	100.0	0.0
EQ_3D_3axis_5	RRS 44%	9.7	100.0	0.0	9.3	100.0	0.0
EQ_3D_3axis_6	RRS 100%	10.1	100.0	0.0	9.6	100.0	0.0

Table C-17: P-3D-RD-a model peak hold down tensile force at certain locations, nonlinear time history analysis

		L1S1, LC5		L1S1 and L1W1, LC6+LC7		L1W1, LC8	
Load Case	**Ground Motion**	**Peak F (kips)**	**t @ peak F (s)**	**Peak F (kips)**	**t @ peak F (s)**	**Peak F (kips)**	**t @ peak F (s)**
EQ_3D_3axis_1	CNP 16%	-3.65	9.26	-5.40	8.94	-2.08	9.03
EQ_3D_3axis_2	CNP 44%	-9.42	9.27	-14.72	8.96	-6.48	9.04
EQ_3D_1axis_1	CNP 100%	-11.49	6.77	-14.71	8.85	-5.85	6.93
EQ_3D_1axis_2	CNP 100%	-5.77	21.88	-11.16	5.41	-12.30	5.45
EQ_3D_2axis_1	CNP 100%	-10.94	6.76	-19.20	5.37	-10.60	5.40
EQ_3D_3axis_3	CNP 100%	-10.94	6.76	-19.20	5.37	-10.60	5.40
EQ_3D_3axis_4	RRS 16%	-6.20	3.22	-8.51	3.44	-9.64	3.41
EQ_3D_3axis_5	RRS 44%	-10.35	2.48	-7.96	2.68	-10.17	3.43
EQ_3D_3axis_6	RRS 100%	-12.35	2.54	-15.66	5.94	-13.32	2.44

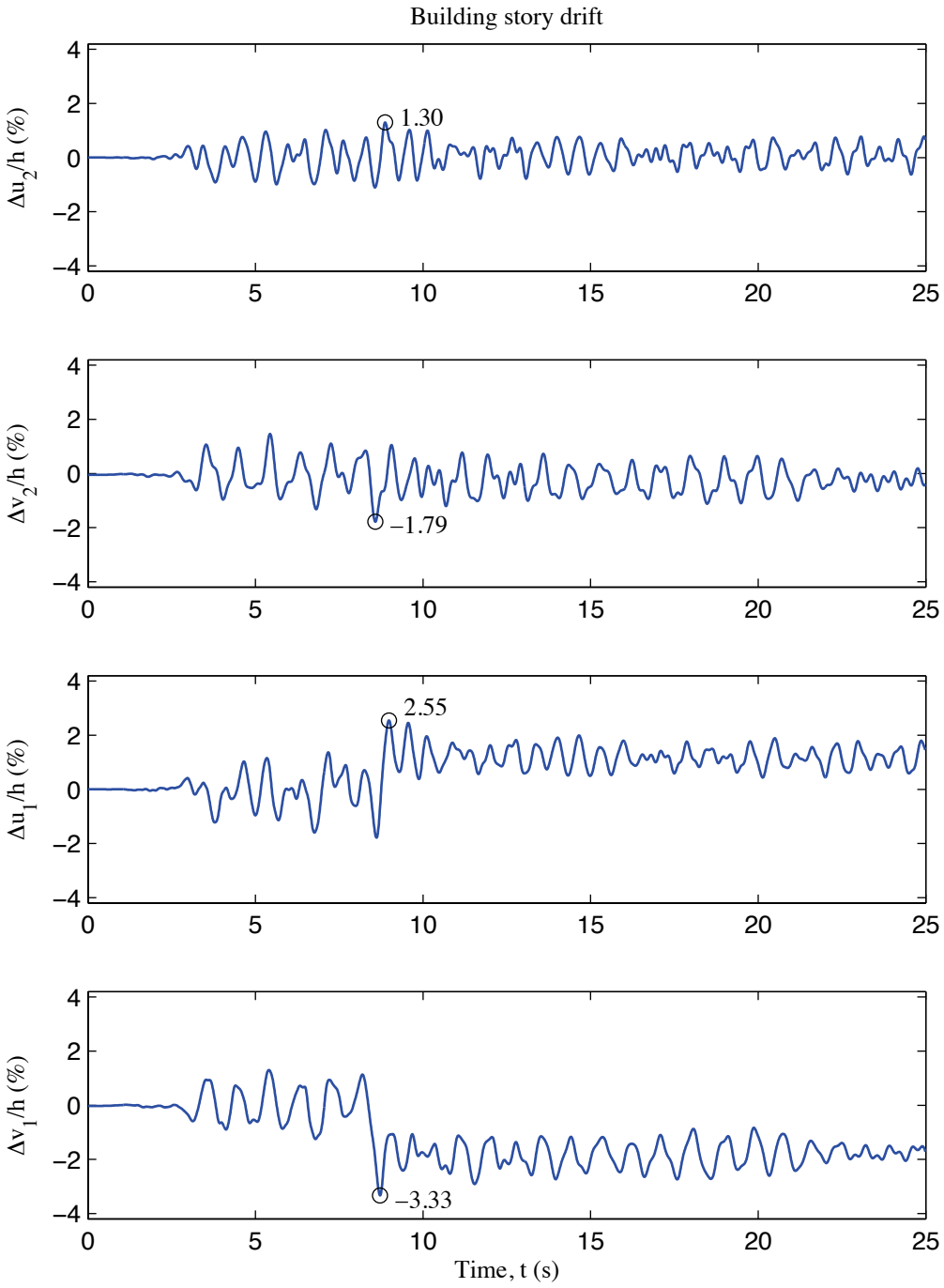

Figure C-6: P-3D-RD-a model building story drift, 100 % Canoga Park, 3D nonlinear analysis

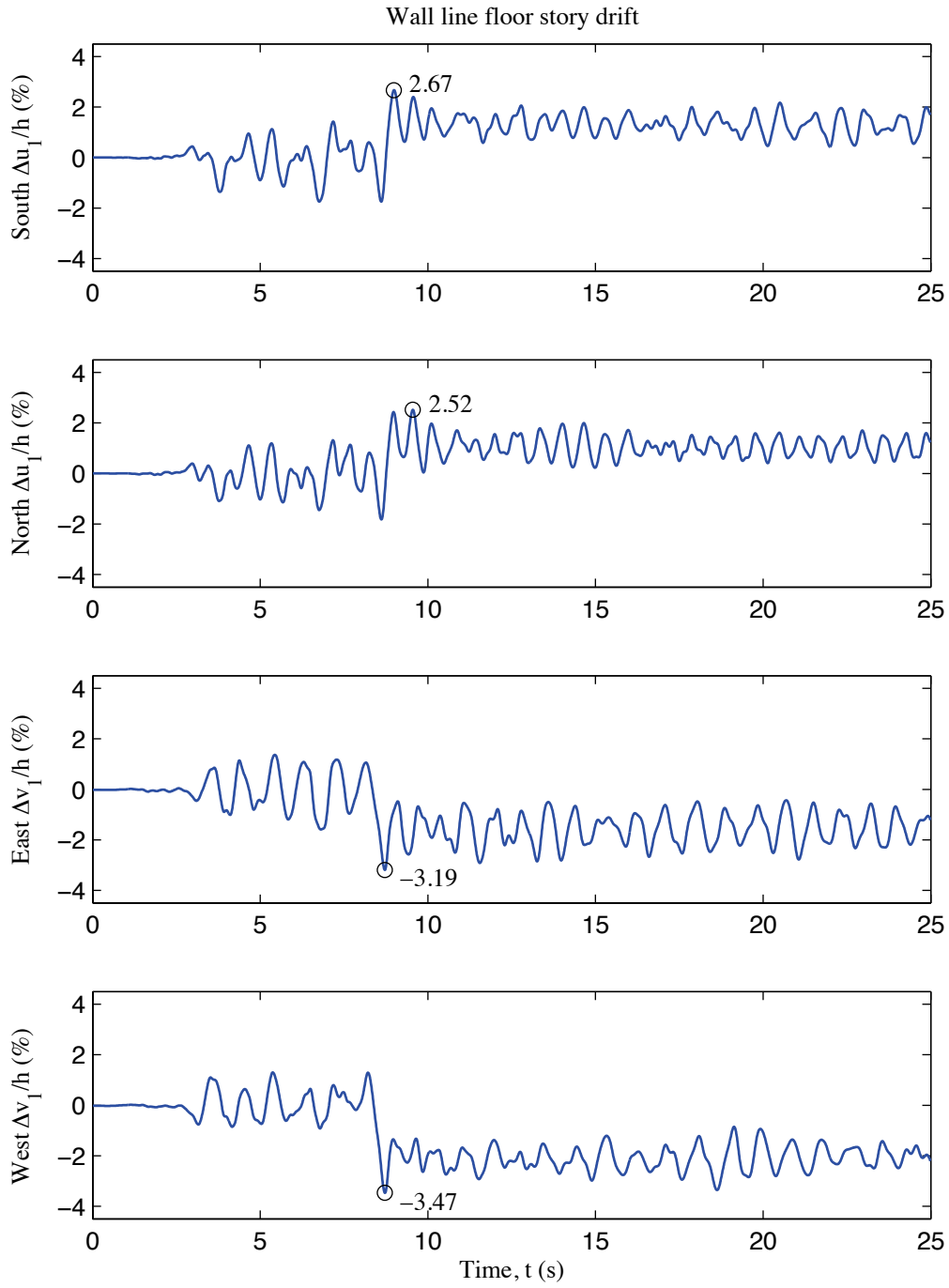

Figure C-7: P-3D-RD-a model wall line floor story drift, 100 % Canoga Park, 3D nonlinear analysis

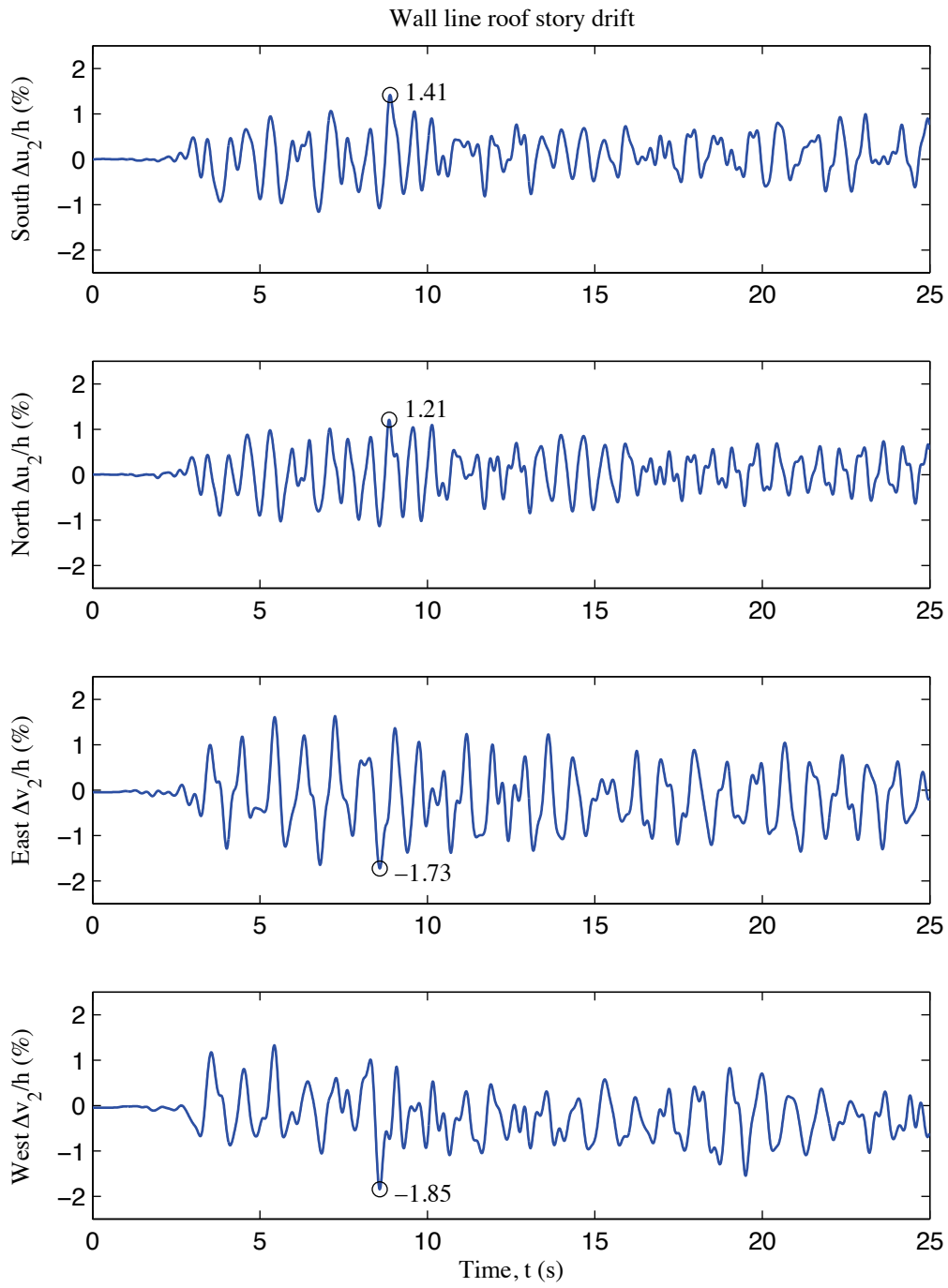

Figure C-8: P-3D-RD-a model wall line roof story drift, 100 % Canoga Park, 3D nonlinear analysis

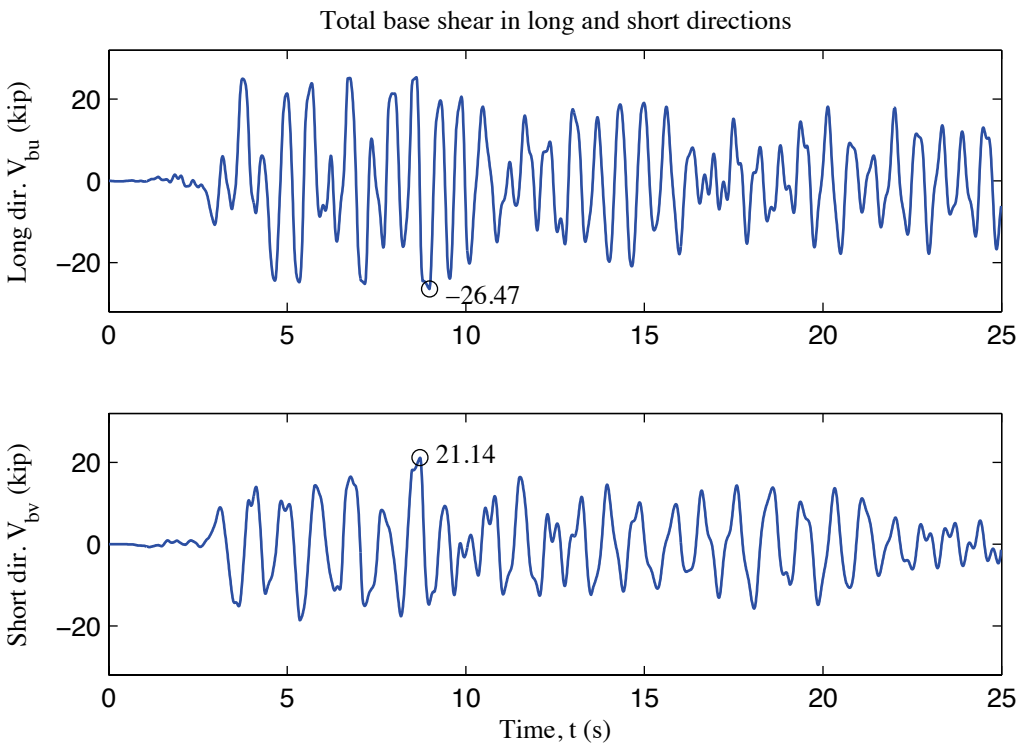

Figure C-9: P-3D-RD-a model total building base shear, 100 % Canoga Park, 3D nonlinear analysis

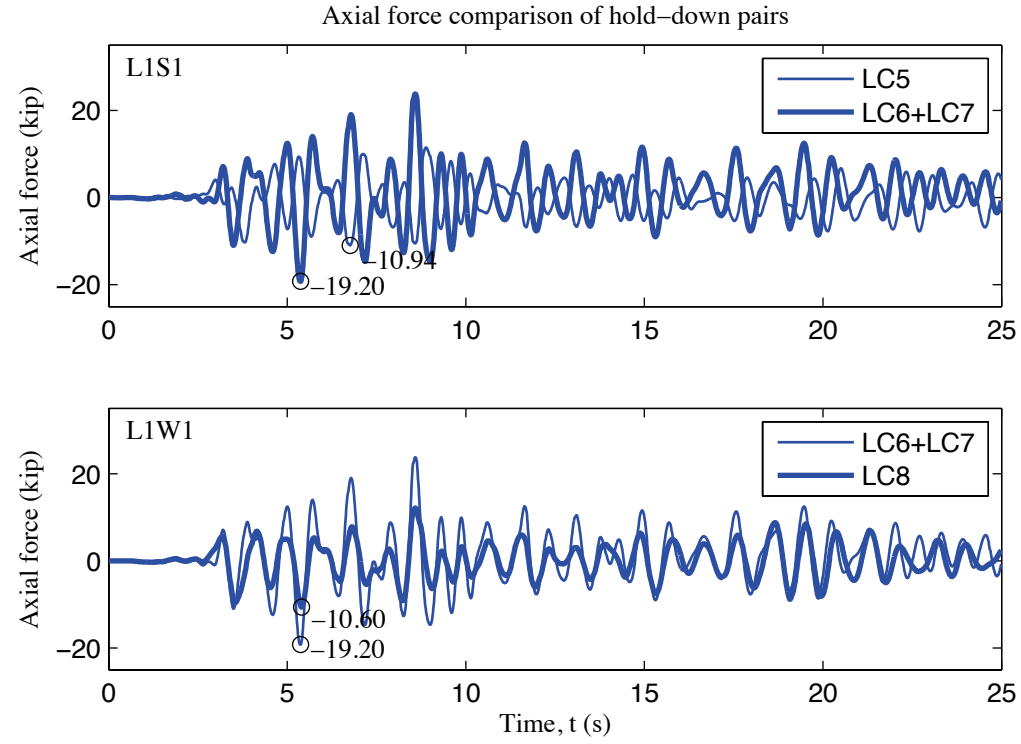

Figure C-10: P-3D-RD-a model, load cell 5 to 8 axial forces, 100 % Canoga Park, 3D nonlinear analysis

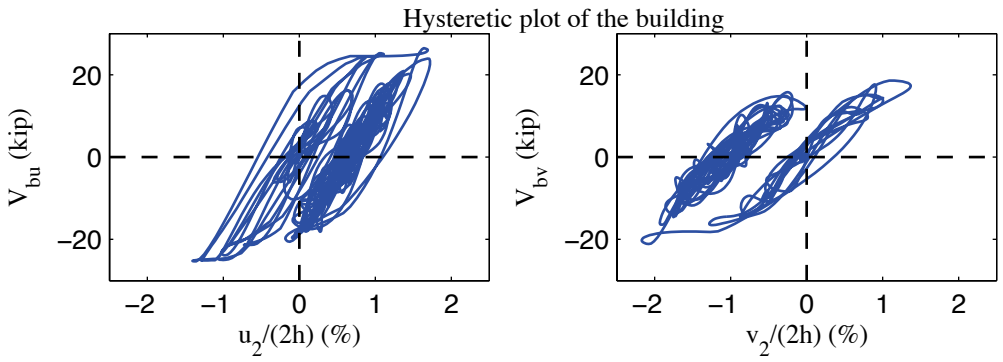

Figure C-11: P-3D-RD-a model, hysteretic plot of the building, 100 % Canoga Park, 3D nonlinear analysis

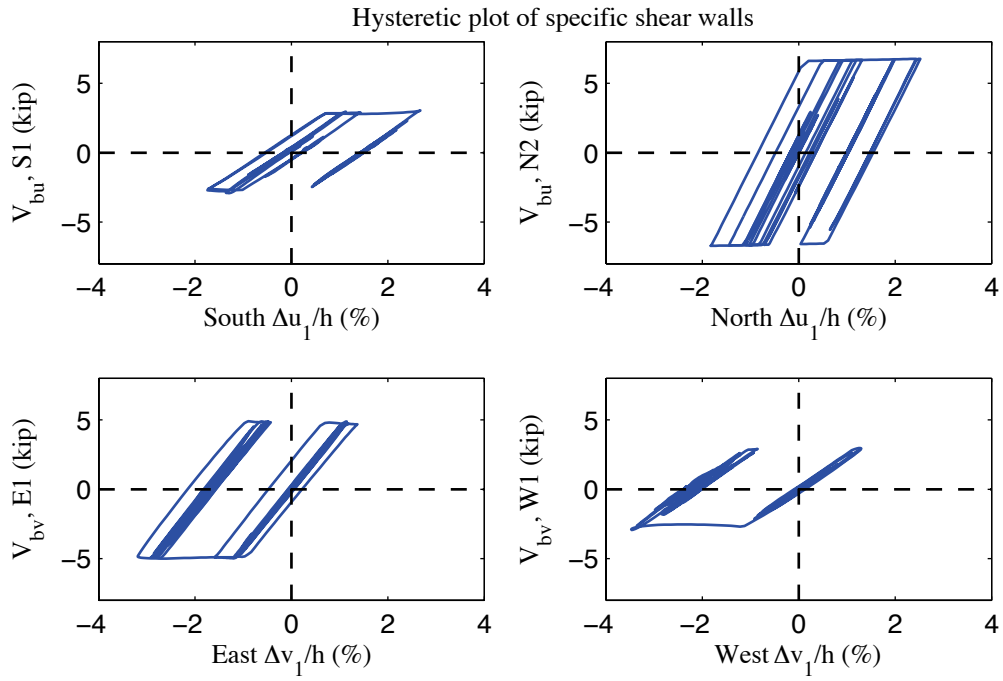

Figure C-12: P-3D-RD-a model, hysteretic plot of shear walls at each elevation, 100 % Canoga Park, 3D nonlinear analysis

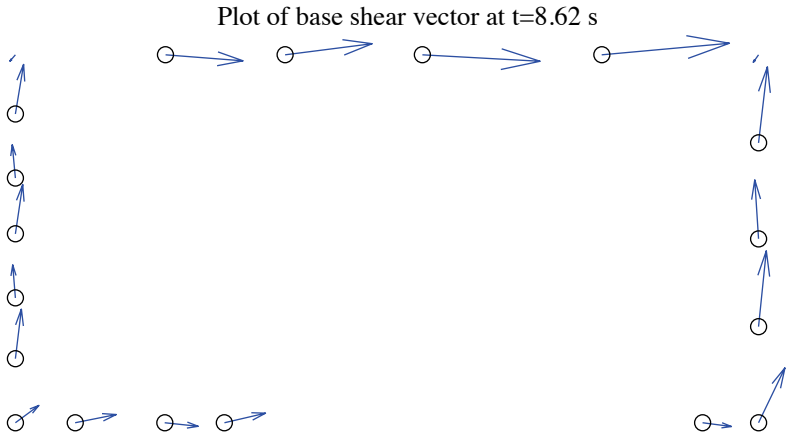

Figure C-13: P-3D-RD-a model, field plot of peak total base shear, 100 % Canoga Park, 3D nonlinear analysis (maximum anchor/hold down base shear is 5.22 kips)

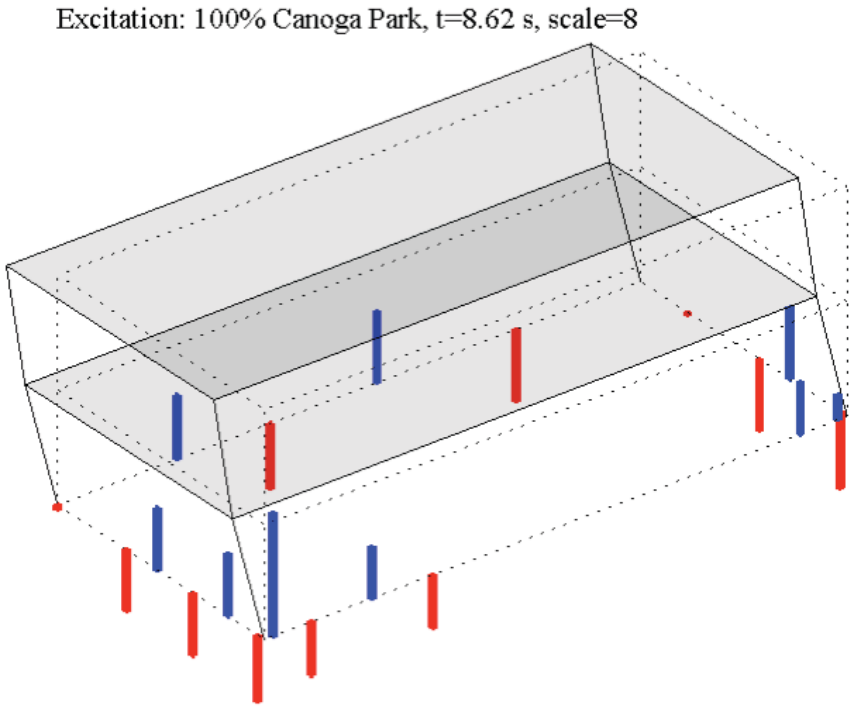

Figure C-14: P-3D-RD-a model, simplified illustration of corner displacements with hold down forces from load cells,100 % Canoga Park, 3D nonlinear analysis (max hold down tensile force is -14.32 kips)

Appendix D: Analysis Results of State-of-the-practice, 3D, rigid-diaphragm, model b (P-3D-RD-b)

D.1 Model description

This state-of-the-practice 3D model features bracing models of whole shear wall panels, smeared models of hold downs into shear walls as pinned supports, and rigid diaphragms. Seismic mass is equally distributed to four corners. The lateral displacement and shear wall capacity ($\delta(0.4V_{nP})$, $0.4V_{nP}$) from AISI-213 standard is utilized to determine the stiffness of elastic material and the first point on the backbone curve of Pinching4 material of shear wall bracing. Figure D-1 is the 3D drawing of the building model with all members and diagonal bracings of sheathing panels. Simulation results are presented and discussed in later sections. Definitions of output physical quantities and explanation of post-process method can be found in Appendix K.

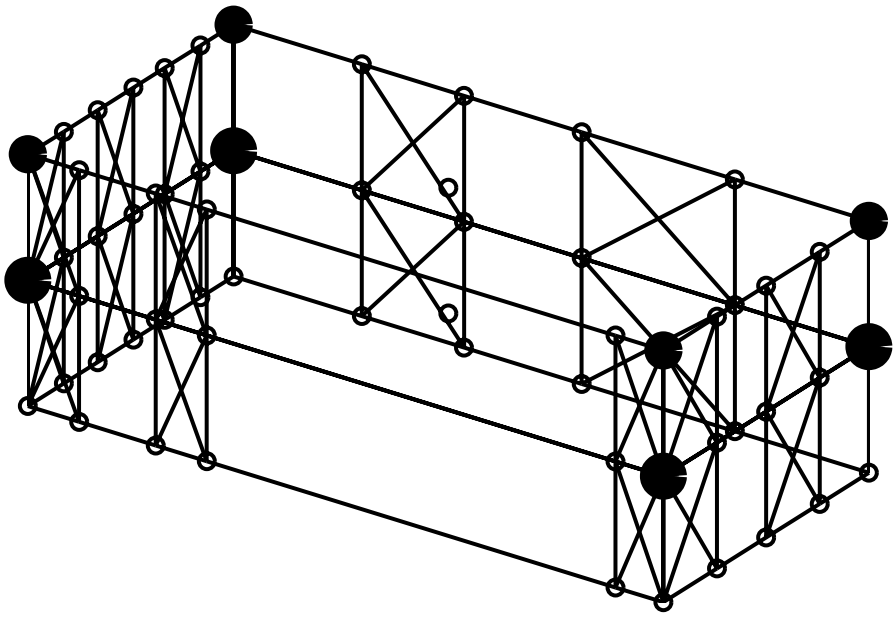

Figure D-1: P-3D-RD-b model

D.2 Free vibration analysis results

Free vibration analysis results are presented in Table D-1 and Figure D-2. Torsional stiffness is smaller than lateral stiffness in the short direction and lateral stiffness in the long direction and the largest. The observation holds for the first and the second mode, as indicated by Table D-1.

Table D-1: Free vibration analysis results, P-3D-RD-b model

Mode number	Natural period (s)	Mode description
1	0.789	Torsion, 1st
2	0.660	Short, 1st
3	0.497	Long, 1st
4	0.309	Torsion, 2nd
5	0.265	Short, 2nd
6	0.203	Long, 2nd

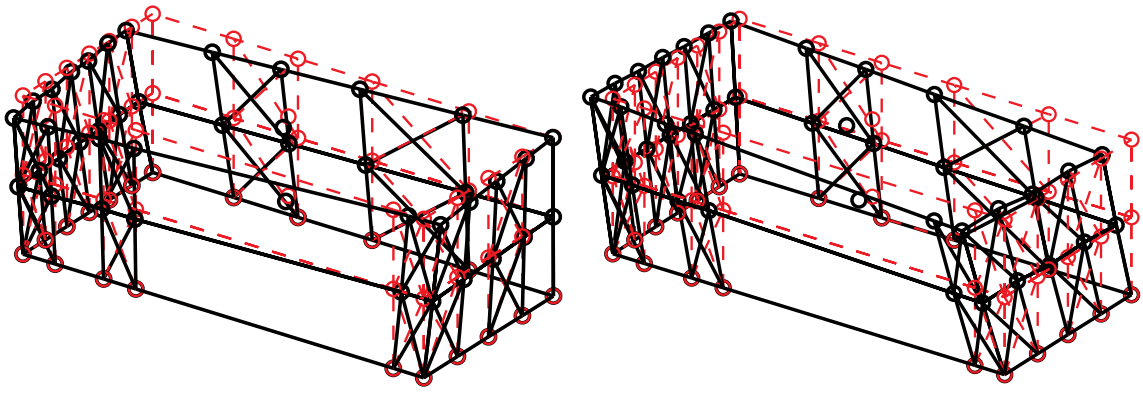

(a) Mode 1, T_1=0.789 s (b) Mode 2, T_2=0.660 s

Figure D-2: First two natural modes of P-3D-RD-b model

D.3 Linear static analysis results

Table D-2 to Table D-4 present linear static analysis results. The lateral load is the equivalent lateral force available from the design narrative (Madsen et al. 2011), applied equally at four corners. Two separate analyses were performed with the loading at long or short direction.

Table D-2 summarizes the breakdown of peak total base shear among four elevations. Due to the interplay of asymmetrical LFRS, wall lines perpendicular to the loading direction still take a very small portion of base shear.

Table D-3 shows peak building and wall line deflections. Practicing engineers can linearly upscale these data and develop an estimate of the building's performance at a certain lateral force level.

Table D-4 is an evaluation of the building's lateral stiffness of long and short direction and its breakdown among shear walls (SW) and other systems. Since gravity walls (GW) are not modeled in state-of-the-practice models, all base shear goes to shear walls.

Table D-2: Breakdown of peak base shear, linear static analysis, P-3D-RD-b model

Load direction	**LONG**				
Elevation	**South V_b**	**North V_b**	**East V_b**	**West V_b**	**Peak V_b**
kips	3.0	8.0	0.0	0.0	11.1
%	27.2	72.7	0.0	0.1	100.0
Load direction	**SHORT**				
Elevation	**South V_b**	**North V_b**	**East V_b**	**West V_b**	**Peak V_b**
1.0	0.0	0.0	5.8	5.3	11.1
9.1	0.2	0.2	52.1	47.5	100.0

Table D-3: Peak building and wall line deflection, linear static analysis, P-3D-RD-b model

Load direction	**LONG**							
Deflection (in.)	u_1	u_2	v_1	v_2	Δu_1	Δu_2	Δv_1	Δv_2
Building	0.303	0.592	-0.047	-0.118	0.303	0.289	-0.047	-0.071
South	0.352	0.683	-0.047	-0.118	0.352	0.331	-0.047	-0.071
North	0.254	0.500	-0.047	-0.118	0.254	0.246	-0.047	-0.071
East	0.303	0.592	0.059	0.080	0.303	0.289	0.059	-0.052
West	0.303	0.592	-0.153	-0.316	0.303	0.289	-0.153	-0.163
Load direction	**SHORT**							
Deflection (in.)	u_1	u_2	v_1	v_2	Δu_1	Δu_2	Δv_1	Δv_2
Building	-0.023	-0.043	0.492	0.928	-0.023	-0.020	0.492	0.436
South	-0.063	-0.119	0.492	0.928	-0.063	-0.056	0.492	0.436
North	0.017	0.032	0.492	0.928	0.017	0.015	0.492	0.436
East	-0.023	-0.043	0.406	0.765	-0.023	-0.020	0.406	0.359
West	-0.023	-0.043	0.578	1.091	-0.023	-0.020	0.578	0.512

Table D-4: Breakdown of lateral stiffness, P-3D-RD-b model

LONG			**SHORT**		
Shear wall k_u (%)	**Gravity wall k_u (%)**	**k_u (kip/in)**	**Shear wall k_v (%)**	**Gravity wall k_v (%)**	**k_v (kip/in)**
100.0	0.0	18.7	100.0	0.0	11.0

D.4 Nonlinear static (pushover) analysis results

Table D-5 is created following the same logic with Table D-2, but the analysis type is nonlinear static (pushover). Pushover curves of the building and each wall line are presented in Figure D-3 and Figure D-4. There is a sharp drop on the pushover backbone curve, since controlling parameters of pinching effect are determined under the worst-case scenario of our tests. This brittle post-peak response can cause some numerical difficulties, as shown in pushover plots.

Clearly, the interaction between wall lines is much more significant when material and geometrical nonlinearity is included. These tables and figures indicate that the wall lines do not reach their peak capacity at exactly the same drift level and wall lines perpendicular to the load can take a nontrivial amount of base shear. Total capacity of the building in the short direction is smaller than the long direction.

Table D-5: Breakdown of peak base shear, pushover analysis, P-3D-RD-b model

Load direction	**LONG**				
Elevation	**South V_b**	**North V_b**	**East V_b**	**West V_b**	**Peak V_b**
kips	6.6	15.4	2.3	4.3	21.5
%	30.5	71.6	10.7	20.1	100.0
Load direction	**SHORT**				
Elevation	**South V_b**	**North V_b**	**East V_b**	**West V_b**	**Peak V_b**
kips	1.6	1.7	9.2	8.5	17.8
%	9.1	9.8	51.5	47.5	100.0

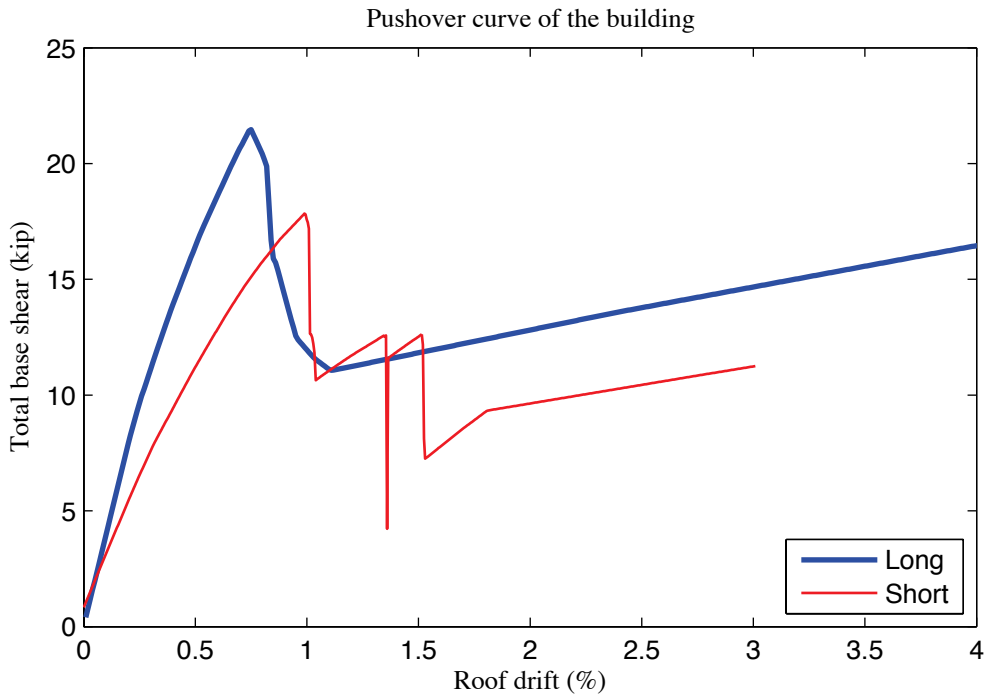

Figure D-3: Pushover curve of P-3D-RD-b model

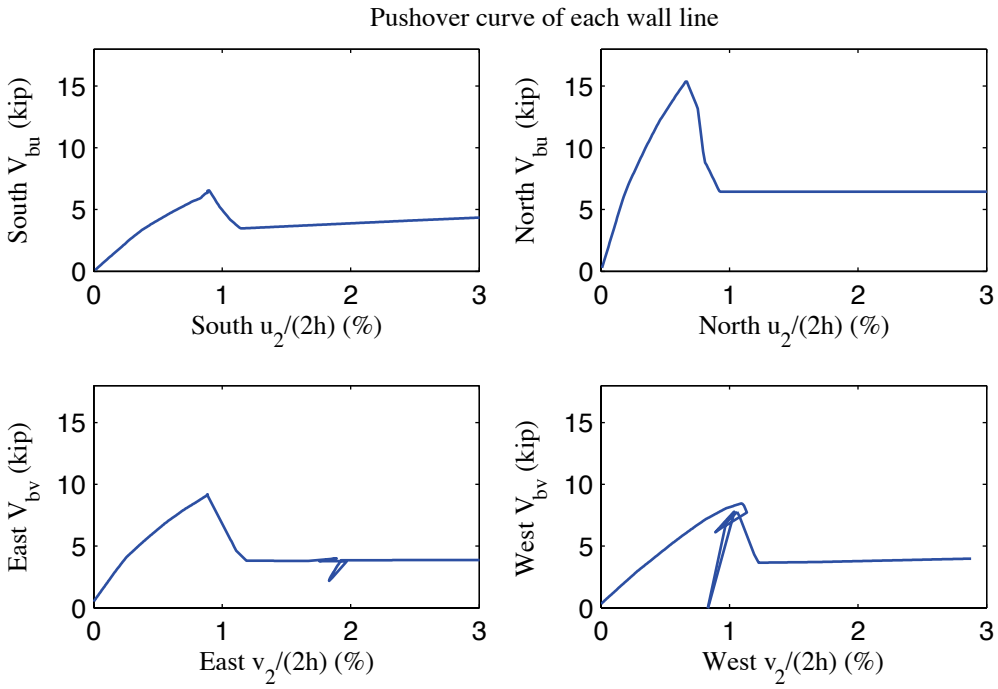

Figure D-4: Pushover curve of each wall line, P-3D-RD-b model

D.5 Linear time history analysis results

Linear time history analysis is performed on the model under Canoga Park and Rinaldi ground motion records of Northridge earthquake in 1994. We considered three scale levels (16%, 44% and 100%) and loadings in one, two and three axes.

Table D-6 to Table D-9 demonstrate the building's linear elastic performance under designated ground motions. Table D-6 shows peak story relative accelerations in the unit of g. Table D-7 and Table D-8 report peak roof drift and story drift of the building and the corresponding time step (t_*) and the base shear at that time. Note that the base shear at the time of peak roof drift may not be the peak total building base shear in that direction (see Table D-9).

The building behaves linearly since peak drift and peak base shear appear at the same time when the ground motion is linearly scaled. Figure D-5 is a vector plot of the peak total resultant base shear of the building under three axial, 100% Canoga Park excitation. The directions of arrows imply that base shear taken by shear walls does not necessarily follow the direction of wall lines due to the effect of 3D coupling. Comparison with nonlinear analysis results of the same excitation provides insightful observations on the building's response and requirements on modeling fidelity and analysis type.

Table D-6: P-3D-RD-b model peak story relative acceleration in g, linear time history analysis

		LONG			SHORT			UP		
Load Case	**Ground Motion**	**a_g**	**Floor a**	**Roof a**	**a_g**	**Floor a**	**Roof a**	**a_g**	**Floor a**	**Roof a**
EQ_3D_3axis_1	CNP 16%	0.067	0.104	0.197	0.057	0.106	0.229	0.078	0.002	0.003
EQ_3D_3axis_2	CNP 44%	0.185	0.286	0.543	0.157	0.292	0.629	0.215	0.006	0.008
EQ_3D_1axis_1	CNP 100%	0.420	0.657	1.310	0	0.261	0.450	0	0.004	0.006
EQ_3D_1axis_2	CNP 100%	0	0.327	0.456	0.356	0.625	1.143	0	0.010	0.014
EQ_3D_2axis_1	CNP 100%	0.420	0.650	1.234	0.356	0.664	1.430	0	0.013	0.018
EQ_3D_3axis_3	CNP 100%	0.420	0.650	1.234	0.356	0.664	1.430	0.489	0.013	0.018
EQ_3D_3axis_4	RRS 16%	0.132	0.239	0.413	0.078	0.124	0.228	0.133	0.002	0.002
EQ_3D_3axis_5	RRS 44%	0.363	0.659	1.134	0.214	0.341	0.626	0.367	0.004	0.006
EQ_3D_3axis_6	RRS 100%	0.825	1.497	2.578	0.486	0.774	1.424	0.834	0.010	0.014

Table D-7: P-3D-RD-b model peak building roof drift and base shear, linear time history analysis

		LONG			SHORT		
Load Case	**Ground Motion**	**$u_2/(2h)$ (%)**	**t_* (s)**	**V_b @ t_* (kips)**	**$v_2/(2h)$ (%)**	**t_* (s)**	**V_b @ t_* (kips)**
EQ_3D_3axis_1	CNP 16%	0.280	10.90	11.0	-0.341	9.89	7.9
EQ_3D_3axis_2	CNP 44%	0.769	10.90	30.1	-0.877	9.89	21.6
EQ_3D_1axis_1	CNP 100%	-1.283	11.67	53.5	-0.861	10.47	24.3
EQ_3D_1axis_2	CNP 100%	-0.755	10.49	21.3	-1.679	9.29	34.7
EQ_3D_2axis_1	CNP 100%	1.748	10.90	68.5	-1.949	9.89	49.1
EQ_3D_3axis_3	CNP 100%	1.748	10.90	68.5	-1.949	9.89	49.1
EQ_3D_3axis_4	RRS 16%	-0.495	4.01	18.0	-0.517	4.47	8.9
EQ_3D_3axis_5	RRS 44%	-1.361	4.01	49.5	-1.360	4.47	24.5
EQ_3D_3axis_6	RRS 100%	-3.093	4.01	112.5	-3.048	4.47	55.6

Table D-8: P-3D-RD-b model peak building story drift, linear time history analysis

		LONG				SHORT			
Load Case	**Ground Motion**	**$\Delta u_1/h$ (%)**	**t_* (s)**	**$\Delta u_2/h$ (%)**	**t_* (s)**	**$\Delta v_1/h$ (%)**	**t_* (s)**	**$\Delta v_2/h$ (%)**	**t_* (s)**
EQ_3D_3axis_1	CNP 16%	0.293	10.91	0.269	10.89	-0.324	10.51	-0.385	9.89
EQ_3D_3axis_2	CNP 44%	0.805	10.91	0.739	10.89	0.880	9.59	-0.975	9.89
EQ_3D_1axis_1	CNP 100%	-1.294	13.10	-1.348	11.67	-0.890	10.46	-0.840	10.48
EQ_3D_1axis_2	CNP 100%	0.889	10.16	-0.824	9.85	1.804	9.62	-1.820	9.30
EQ_3D_2axis_1	CNP 100%	1.829	10.91	1.681	10.89	2.028	9.59	-2.155	9.89
EQ_3D_3axis_3	CNP 100%	1.829	10.91	1.681	10.89	2.028	9.59	-2.155	9.89
EQ_3D_3axis_4	RRS 16%	0.507	2.77	-0.495	4.01	-0.518	5.30	-0.541	4.48
EQ_3D_3axis_5	RRS 44%	1.394	2.77	-1.361	4.01	-1.387	5.30	-1.404	4.48
EQ_3D_3axis_6	RRS 100%	3.169	2.77	-3.094	4.01	-3.123	5.30	-3.131	4.48

Table D-9: P-3D-RD-b model peak building base shear, linear time history analysis

		LONG		SHORT		RESULTANT	
Load Case	**Ground Motion**	**Peak V_{bu} (kip)**	**t @ peak V_{bu} (s)**	**Peak V_{bv} (kip)**	**t @ peak V_{bv} (s)**	**Peak V_b (kip)**	**t @ peak V_b (s)**
EQ_3D_3axis_1	CNP 16%	11.1	10.91	9.2	9.58	12.9	10.90
EQ_3D_3axis_2	CNP 44%	30.5	10.91	25.4	9.58	35.6	10.90
EQ_3D_1axis_1	CNP 100%	56.7	10.66	24.3	10.46	56.9	10.66
EQ_3D_1axis_2	CNP 100%	24.3	10.16	45.8	9.60	48.4	9.60
EQ_3D_2axis_1	CNP 100%	69.3	10.91	57.7	9.58	80.9	10.90
EQ_3D_3axis_3	CNP 100%	69.3	10.91	57.7	9.58	80.9	10.90
EQ_3D_3axis_4	RRS 16%	20.2	2.75	10.9	5.30	22.3	2.75
EQ_3D_3axis_5	RRS 44%	55.5	2.75	29.9	5.30	61.3	2.75
EQ_3D_3axis_6	RRS 100%	126.1	2.75	67.9	5.30	139.2	2.75

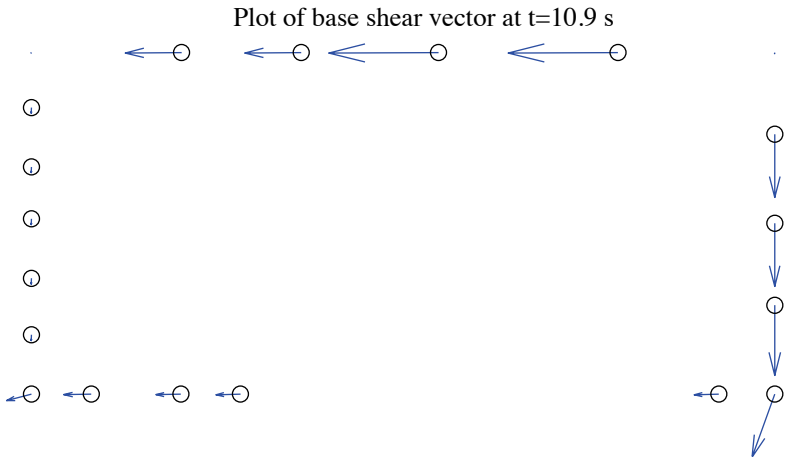

Figure D-5: P-3D-RD-b model, base shear vector plot at the moment of peak total base shear, 100 % Canoga Park, 3D linear analysis (maximum anchor/hold down base shear is 15.56 kips)

D.6 Nonlinear time history analysis results

Same ground motions are applied to the model with material and geometrical nonlinearity. Table D-10 to Table D-13 are replicas of Table D-6 to Table D-9, but for nonlinear time history analyses. Since this analysis type is most complicated and closest to reality and experiments, behavior of wall lines and hold downs are further studied. Table D-14 is the table of peak wall line story drifts and corresponding time steps. Table D-15 is designed for peak base shear of each wall line and the last two columns of the table are percentages of base shear of two facing wall lines in the same direction when the total base shear in that direction takes peak value. Table D-16 expands the breakdown of each wall line's peak base shear between shear walls, gravity walls and other systems. Table D-17 is peak value of hold down tensile force of two selected pairs. Hold down 5 and 6 are on shear wall L1S1, South elevation and hold down 7 and 8 are on shear wall L1W1, West elevation. These shear walls have lowest capacities compared with others on the same wall line and they meet at the southwest edge of the building, so interacted nonlinear behavior is expected to appear. Since hold downs are smeared to shear wall stud ends, hold down 6 and 7 are combined together in 3D model as one single pinned support.

Time history plots in this section include plots of story drifts of the building and each wall line (Figure D-6 to Figure D-8), total building base shear in long and short direction (Figure D-9) and axial forces of hold downs in Table D-17 (Figure D-10). Hysteretic plots in Figure D-11 and Figure D-12 are helpful for visual examination of nonlinear base shear-drift relationship of the building and the weakest shear wall on each wall line. In comparison with linear time history analysis, vector plot of peak total base shear is

illustrated in Figure D-13. Figure D-14 presents a simplified deformed shape of the building (see (Peterman 2014) for details of the method) and axial force of all twenty hold downs at the moment of peak total base shear. The same sign convention with tests is adopted. Red bars indicate tensile (negative) force and blue ones are for compressive (positive) force.

Hysteretic behavior is seen in the building and typical shear walls under design-based earthquake (100% Canoga Park excitation in 3 axes, see Figure D-11 and Figure D-12). Results also imply that when loaded by 100% Canoga Park ground motion, all wall lines fail in tension or in compression since peak drifts are all over 3.2% (Table D-14) and the response curves of typical shear walls go very far into the post-peak region of Pinching4 material backbone. Figure D-13 clearly shows that base shear vectors in anchors and hold downs do not align with wall lines. Since load cells 6 and 7 are combined, it is not easy to use Table D-17 and Figure D-10 to examine Type I shear wall design assumption for this case. However, at the moment of the peak base shear, the pair of hold downs in West elevation at southwest corner is in compression (Figure D-14), which still challenges the assumption.

The near-field Rinaldi record is much stronger in terms of peak ground acceleration, especially in the long direction. When loaded at 100%, both directions are believed to be destroyed with peak story drift larger than 12% and 10%. Such a large drift level is a sign of structural failure.

Table D-10: P-3D-RD-b model peak story relative acceleration in g, nonlinear time history analysis

		LONG			SHORT			UP		
Load Case	**Ground Motion**	**a_g**	**Floor a**	**Roof a**	**a_g**	**Floor a**	**Roof a**	**a_g**	**Floor a**	**Roof a**
EQ_3D_3axis_1	CNP 16%	0.067	0.145	0.161	0.057	0.123	0.161	0.078	0.037	0.058
EQ_3D_3axis_2	CNP 44%	0.185	0.461	0.495	0.157	0.297	0.381	0.215	0.087	0.141
EQ_3D_1axis_1	CNP 100%	0.420	0.491	0.587	0	0.104	0.110	0	0.049	0.066
EQ_3D_1axis_2	CNP 100%	0	0.325	0.279	0.356	0.538	0.697	0	0.109	0.142
EQ_3D_2axis_1	CNP 100%	0.420	0.467	0.697	0.356	0.596	0.666	0	0.148	0.199
EQ_3D_3axis_3	CNP 100%	0.420	0.467	0.697	0.356	0.596	0.666	0.489	0.148	0.199
EQ_3D_3axis_4	RRS 16%	0.132	0.248	0.242	0.078	0.175	0.188	0.133	0.053	0.059
EQ_3D_3axis_5	RRS 44%	0.363	0.576	0.678	0.214	0.309	0.469	0.367	0.166	0.184
EQ_3D_3axis_6	RRS 100%	0.825	0.922	1.139	0.486	0.655	0.745	0.834	0.524	0.586

Table D-11: P-3D-RD-b model peak building roof drift and base shear, nonlinear time history analysis

		LONG			SHORT		
Load Case	**Ground Motion**	**u_2/(2h) (%)**	**t_* (s)**	**V_b @ t_* (kips)**	**v_2/(2h) (%)**	**t_* (s)**	**V_b @ t_* (kips)**
EQ_3D_3axis_1	CNP 16%	-0.212	10.69	7.5	-0.280	9.30	5.2
EQ_3D_3axis_2	CNP 44%	0.799	8.91	19.1	-0.799	8.66	11.7
EQ_3D_1axis_1	CNP 100%	2.810	9.20	14.5	-0.191	6.57	3.3
EQ_3D_1axis_2	CNP 100%	-0.189	8.52	0.9	-1.811	8.76	9.8
EQ_3D_2axis_1	CNP 100%	2.866	9.22	14.0	-2.103	8.77	9.5
EQ_3D_3axis_3	CNP 100%	2.866	9.22	14.0	-2.103	8.77	9.5
EQ_3D_3axis_4	RRS 16%	0.473	2.81	16.1	-0.445	2.84	8.2
EQ_3D_3axis_5	RRS 44%	4.003	3.04	16.1	1.737	6.40	9.4
EQ_3D_3axis_6	RRS 100%	9.876	6.03	4.8	-6.971	5.94	8.6

Table D-12: P-3D-RD-b model peak building story drift, nonlinear linear time history analysis

		LONG				SHORT			
Load Case	**Ground Motion**	**$\Delta u_1/h$ (%)**	**t_* (s)**	**$\Delta u_2/h$ (%)**	**t_* (s)**	**$\Delta v_1/h$ (%)**	**t_* (s)**	**$\Delta v_2/h$ (%)**	**t_* (s)**
EQ_3D_3 axis_1	CNP 16%	-0.221	10.66	-0.218	10.71	-0.318	8.60	-0.301	9.32
EQ_3D_3 axis_2	CNP 44%	1.005	8.93	-0.644	11.71	0.961	9.03	-0.856	8.69
EQ_3D_1 axis_1	CNP 100%	5.023	9.20	0.704	9.07	-0.190	5.16	-0.230	5.88
EQ_3D_1 axis_2	CNP 100%	-0.272	10.76	-0.310	13.99	-3.115	8.77	1.360	5.43
EQ_3D_2 axis_1	CNP 100%	5.089	9.21	-0.781	8.63	-3.571	8.75	1.445	5.44
EQ_3D_3 axis_3	CNP 100%	5.089	9.21	-0.781	8.63	-3.571	8.75	1.445	5.44
EQ_3D_3 axis_4	RRS 16%	0.608	2.80	0.351	2.84	-0.504	2.84	-0.385	2.83
EQ_3D_3 axis_5	RRS 44%	7.114	3.07	1.063	2.98	2.970	6.50	1.238	6.33
EQ_3D_3 axis_6	RRS 100%	12.136	3.18	9.138	6.06	-10.730	5.90	-3.959	6.07

Table D-13: P-3D-RD-b model peak building base shear, nonlinear time history analysis

		LONG		SHORT		RESULTANT	
Load Case	**Ground Motion**	**Peak V_{bu} (kip)**	**t @ peak V_{bu} (s)**	**Peak V_{bv} (kip)**	**t @ peak V_{bv} (s)**	**Peak V_b (kip)**	**t @ peak V_b (s)**
EQ_3D_3axis_1	CNP 16%	7.8	10.67	6.9	8.60	8.6	10.66
EQ_3D_3axis_2	CNP 44%	21.2	7.09	16.4	8.58	22.8	7.13
EQ_3D_1axis_1	CNP 100%	20.7	4.52	4.7	5.17	20.9	4.52
EQ_3D_1axis_2	CNP 100%	9.9	8.92	16.7	6.78	17.8	9.67
EQ_3D_2axis_1	CNP 100%	21.0	3.65	16.6	6.75	22.5	3.65
EQ_3D_3axis_3	CNP 100%	21.0	3.65	16.6	6.75	22.5	3.65
EQ_3D_3axis_4	RRS 16%	17.2	2.78	8.8	2.78	19.4	2.78
EQ_3D_3axis_5	RRS 44%	20.5	2.47	15.6	2.74	24.6	2.46
EQ_3D_3axis_6	RRS 100%	21.9	2.13	18.6	2.83	26.0	2.13

Table D-14: P-3D-RD-b model peak wall line story drift, nonlinear time history analysis

LONG		SOUTH				NORTH			
Load Case	**Ground Motion**	**$\Delta u_1/h$ (%)**	**t_* (s)**	**$\Delta u_2/h$ (%)**	**t_* (s)**	**$\Delta u_1/h$ (%)**	**t_* (s)**	**$\Delta u_2/h$ (%)**	**t_* (s)**
EQ_3D_3axis_1	CNP 16%	0.285	10.65	0.255	10.71	0.177	10.22	0.188	4.46
EQ_3D_3axis_2	CNP 44%	1.046	8.95	0.691	11.25	1.106	9.58	0.710	9.28
EQ_3D_1axis_1	CNP 100%	5.077	9.20	0.799	9.09	4.972	9.19	0.636	9.05
EQ_3D_1axis_2	CNP 100%	0.434	8.59	0.450	7.43	0.220	11.54	0.318	13.66
EQ_3D_2axis_1	CNP 100%	4.765	9.40	0.984	8.62	5.445	9.21	0.745	9.07
EQ_3D_3axis_3	CNP 100%	4.765	9.40	0.984	8.62	5.445	9.21	0.745	9.07
EQ_3D_3axis_4	RRS 16%	0.741	2.83	0.471	2.85	0.516	2.77	0.323	2.69
EQ_3D_3axis_5	RRS 44%	7.658	3.07	1.239	3.18	6.571	3.06	1.070	2.98
EQ_3D_3axis_6	RRS 100%	12.212	3.18	10.357	6.09	12.066	3.17	8.768	4.64
SHORT		**EAST**				**WEST**			
Load Case	**Ground Motion**	**$\Delta v_1/h$ (%)**	**t_* (s)**	**$\Delta v_2/h$ (%)**	**t_* (s)**	**$\Delta v_1/h$ (%)**	**t_* (s)**	**$\Delta v_2/h$ (%)**	**t_* (s)**
EQ_3D_3axis_1	CNP 16%	0.488	9.61	0.434	9.29	0.307	8.62	0.297	21.00
EQ_3D_3axis_2	CNP 44%	1.296	9.05	0.939	8.70	0.793	19.92	0.990	21.29
EQ_3D_1axis_1	CNP 100%	0.304	5.19	0.352	5.88	0.315	7.40	0.401	6.56
EQ_3D_1axis_2	CNP 100%	3.294	8.75	1.450	8.60	3.013	8.79	1.558	5.44
EQ_3D_2axis_1	CNP 100%	3.916	8.76	1.736	8.59	3.241	8.74	1.634	5.43
EQ_3D_3axis_3	CNP 100%	3.916	8.76	1.736	8.59	3.241	8.74	1.634	5.43
EQ_3D_3axis_4	RRS 16%	0.361	2.72	0.373	3.30	0.950	2.89	0.719	2.94
EQ_3D_3axis_5	RRS 44%	2.346	5.76	1.411	6.32	4.301	6.54	1.533	3.87
EQ_3D_3axis_6	RRS 100%	13.031	5.90	1.997	7.10	8.440	5.89	6.641	6.10

Table D-15: P-3D-RD-b model peak wall line base shear, nonlinear time history analysis

LONG		SOUTH		NORTH		% of Peak V_{bu}	
Load Case	**Ground Motion**	**Peak V_{bu} (kips)**	**t @ peak V_{bu} (s)**	**Peak V_{bu} (kips)**	**t @ peak V_{bu} (s)**	**South**	**North**
EQ_3D_3axis_1	CNP 16%	2.4	11.01	6.0	10.22	28.7	70.9
EQ_3D_3axis_2	CNP 44%	6.5	8.95	15.5	5.55	25.9	72.3
EQ_3D_1axis_1	CNP 100%	6.7	3.74	15.4	4.52	23.2	74.6
EQ_3D_1axis_2	CNP 100%	3.2	7.54	7.4	11.54	30.5	66.1
EQ_3D_2axis_1	CNP 100%	6.8	3.69	15.2	4.55	27.2	71.6
EQ_3D_3axis_3	CNP 100%	6.8	3.69	15.2	4.55	27.2	71.6
EQ_3D_3axis_4	RRS 16%	5.1	2.83	12.2	2.77	27.8	70.5
EQ_3D_3axis_5	RRS 44%	6.8	6.64	15.4	3.59	29.6	69.3
EQ_3D_3axis_6	RRS 100%	6.6	2.17	15.3	2.13	26.8	70.0
SHORT		**EAST**		**WEST**		**% of Peak V_{bv}**	
Load Case	**Ground Motion**	**Peak V_{bv} (kips)**	**t @ peak V_{bv} (s)**	**Peak V_{bv} (kips)**	**t @ peak V_{bv} (s)**	**East**	**West**
EQ_3D_3axis_1	CNP 16%	5.7	9.61	2.7	8.61	60.6	38.2
EQ_3D_3axis_2	CNP 44%	9.6	8.59	7.1	19.92	58.1	39.1
EQ_3D_1axis_1	CNP 100%	4.4	4.81	2.8	7.40	83.2	14.3
EQ_3D_1axis_2	CNP 100%	9.5	8.55	8.6	6.79	48.6	50.3
EQ_3D_2axis_1	CNP 100%	9.6	8.24	8.8	9.58	46.4	51.3
EQ_3D_3axis_3	CNP 100%	9.6	8.24	8.8	9.58	46.4	51.3
EQ_3D_3axis_4	RRS 16%	4.4	2.72	7.4	2.89	38.6	60.9
EQ_3D_3axis_5	RRS 44%	9.5	2.72	8.5	2.78	54.0	44.5
EQ_3D_3axis_6	RRS 100%	9.5	2.11	8.5	2.33	48.1	45.3

Table D-16: P-3D-RD-b model wall line base shear breakdown, nonlinear time history analysis

LONG		SOUTH			NORTH		
Load Case	**Ground Motion**	**Peak V_{bu} (kips)**	**SW V_{bu} (%)**	**GW V_{bu} (%)**	**Peak V_{bu} (kips)**	**SW V_{bu} (%)**	**GW V_{bu} (%)**
EQ_3D_3axis_1	CNP 16%	2.4	100.0	0.0	6.0	100.0	0.0
EQ_3D_3axis_2	CNP 44%	6.5	100.0	0.0	15.5	100.0	0.0
EQ_3D_1axis_1	CNP 100%	6.7	100.0	0.0	15.4	100.0	0.0
EQ_3D_1axis_2	CNP 100%	3.2	100.0	0.0	7.4	100.0	0.0
EQ_3D_2axis_1	CNP 100%	6.8	100.0	0.0	15.2	100.0	0.0
EQ_3D_3axis_3	CNP 100%	6.8	100.0	0.0	15.2	100.0	0.0
EQ_3D_3axis_4	RRS 16%	5.1	100.0	0.0	12.2	100.0	0.0
EQ_3D_3axis_5	RRS 44%	6.8	100.0	0.0	15.4	100.0	0.0
EQ_3D_3axis_6	RRS 100%	6.6	100.0	0.0	15.3	100.0	0.0
SHORT		**EAST**			**WEST**		
Load Case	**Ground Motion**	**Peak V_{bv} (kips)**	**SW V_{bv} (%)**	**GW V_{bu} (%)**	**Peak V_{bv} (kips)**	**SW V_{bv} (%)**	**GW V_{bv} (%)**
EQ_3D_3axis_1	CNP 16%	5.7	100.0	0.0	2.7	100.0	0.0
EQ_3D_3axis_2	CNP 44%	9.6	100.0	0.0	7.1	100.0	0.0
EQ_3D_1axis_1	CNP 100%	4.4	100.0	0.0	2.8	100.0	0.0
EQ_3D_1axis_2	CNP 100%	9.5	100.0	0.0	8.6	100.0	0.0
EQ_3D_2axis_1	CNP 100%	9.6	100.0	0.0	8.8	100.0	0.0
EQ_3D_3axis_3	CNP 100%	9.6	100.0	0.0	8.8	100.0	0.0
EQ_3D_3axis_4	RRS 16%	4.4	100.0	0.0	7.4	100.0	0.0
EQ_3D_3axis_5	RRS 44%	9.5	100.0	0.0	8.5	100.0	0.0
EQ_3D_3axis_6	RRS 100%	9.5	100.0	0.0	8.5	100.0	0.0

Table D-17: P-3D-RD-b model peak hold down tensile force at certain locations, nonlinear time history analysis

		L1S1, LC5		L1S1 and L1W1, LC6+LC7		L1W1, LC8	
Load Case	**Ground Motion**	**Peak F (kips)**	**t @ peak F (s)**	**Peak F (kips)**	**t @ peak F (s)**	**Peak F (kips)**	**t @ peak F (s)**
EQ_3D_3axis_1	CNP 16%	-2.91	10.68	-3.15	8.88	-1.97	9.01
EQ_3D_3axis_2	CNP 44%	-7.27	6.81	-13.47	8.95	-5.75	8.98
EQ_3D_1axis_1	CNP 100%	-8.77	3.75	-7.53	4.58	-2.49	7.00
EQ_3D_1axis_2	CNP 100%	-4.09	8.53	-8.24	3.49	-11.29	5.42
EQ_3D_2axis_1	CNP 100%	-9.35	3.70	-11.55	3.45	-11.86	5.42
EQ_3D_3axis_3	CNP 100%	-9.35	3.70	-11.55	3.45	-11.86	5.42
EQ_3D_3axis_4	RRS 16%	-5.79	3.25	-4.70	6.02	-7.62	3.34
EQ_3D_3axis_5	RRS 44%	-10.44	3.76	-5.94	6.36	-10.62	3.84
EQ_3D_3axis_6	RRS 100%	-10.33	2.56	-11.87	4.03	-9.58	2.34

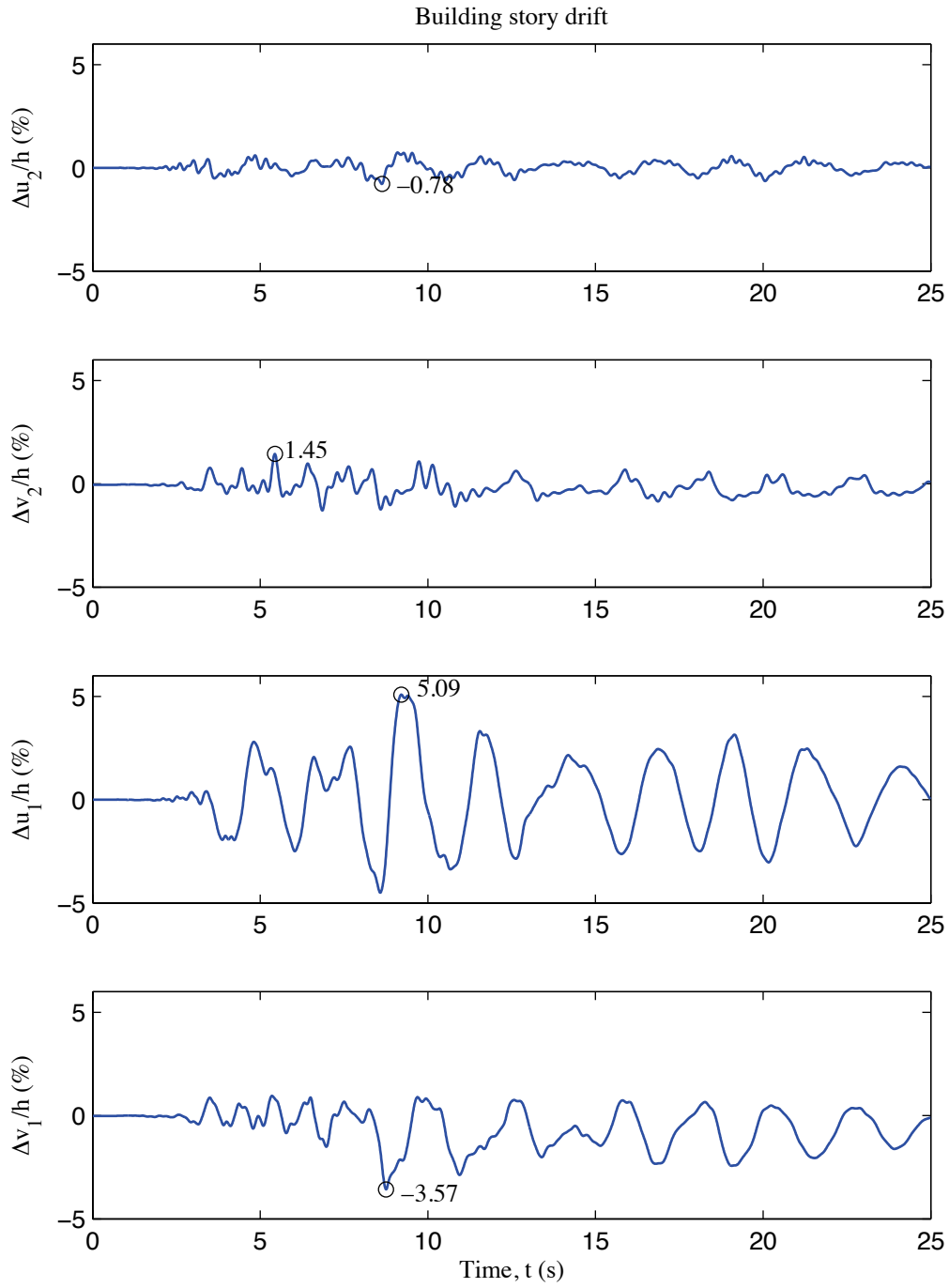

Figure D-6: P-3D-RD-b model building story drift, 100 % Canoga Park, 3D nonlinear analysis

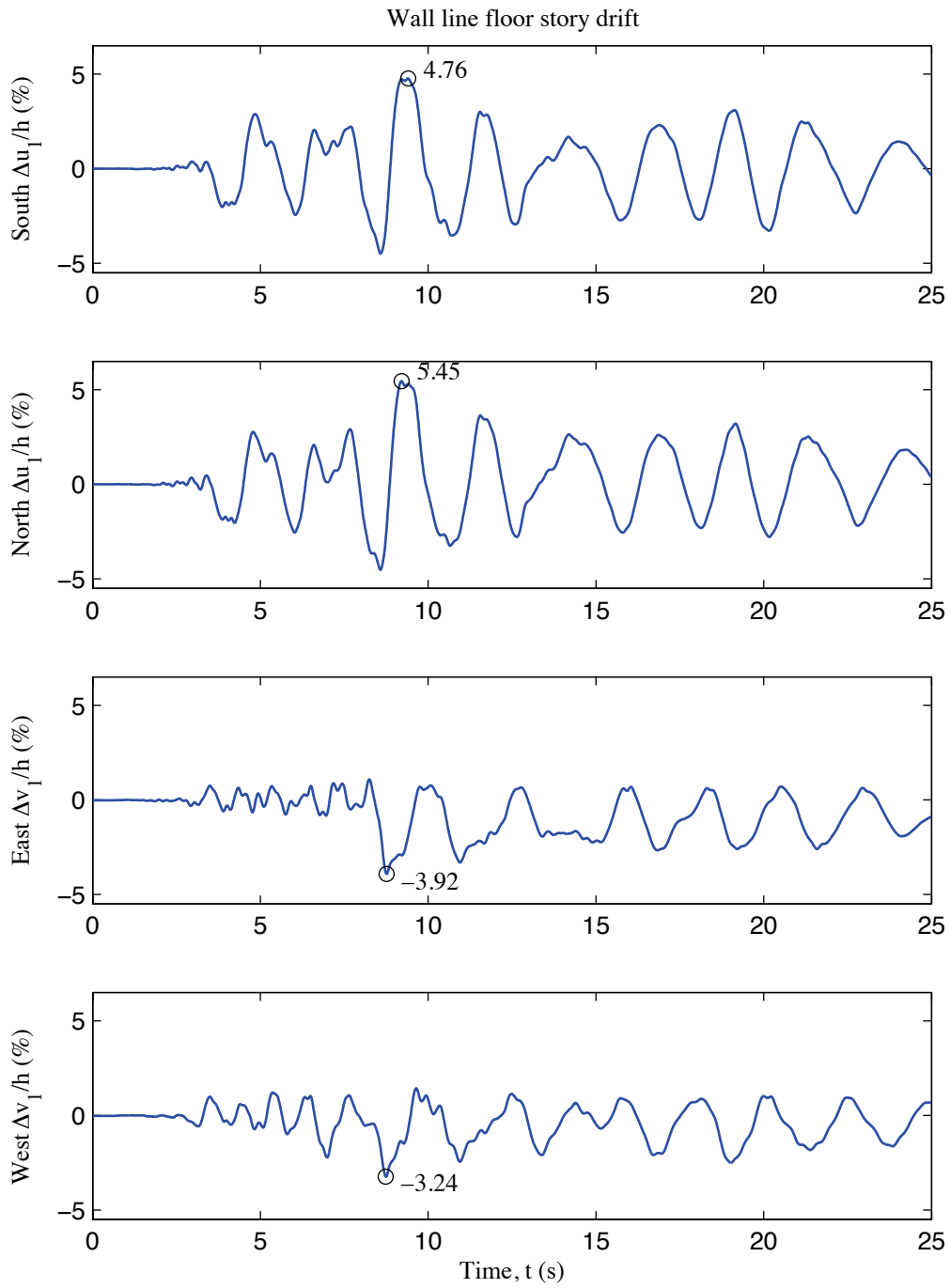

Figure D-7: P-3D-RD-b model wall line floor story drift, 100 % Canoga Park, 3D nonlinear analysis

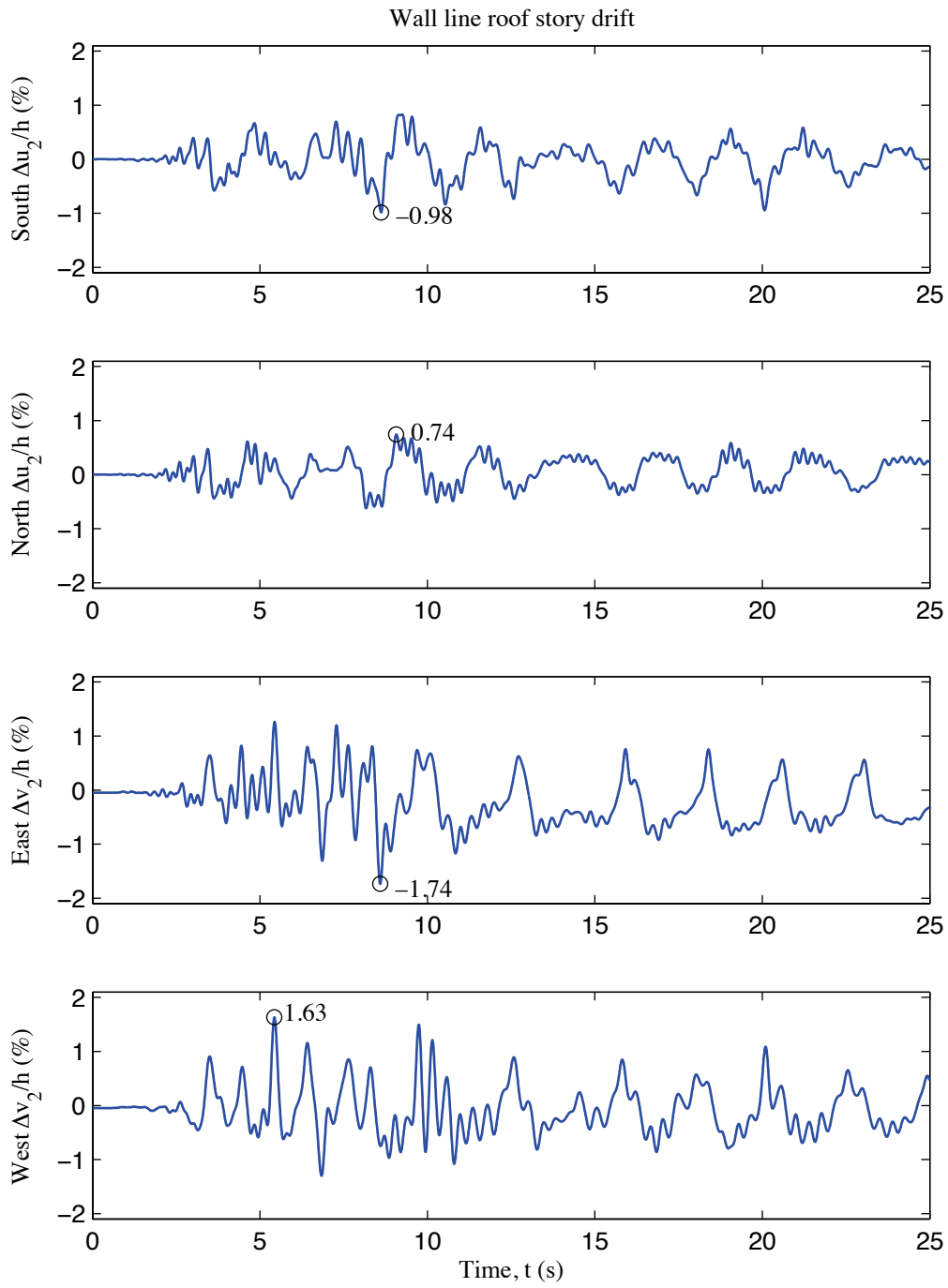

Figure D-8: P-3D-RD-b model wall line roof story drift, 100 % Canoga Park, 3D nonlinear analysis

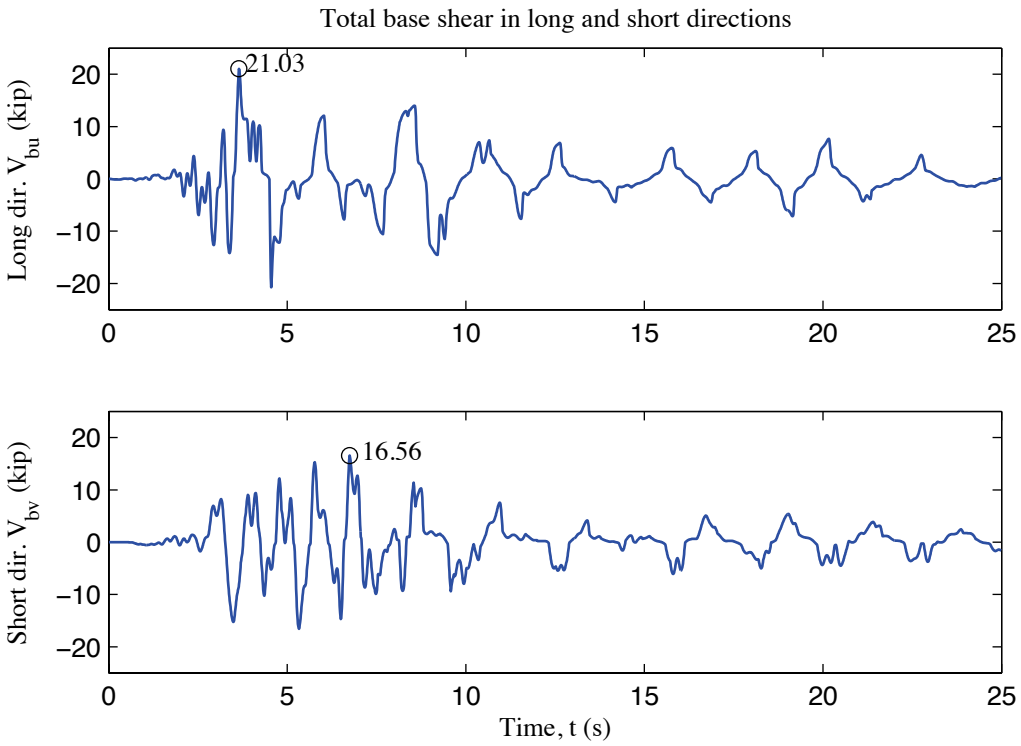

Figure D-9: P-3D-RD-b model total building base shear, 100 % Canoga Park, 3D nonlinear analysis

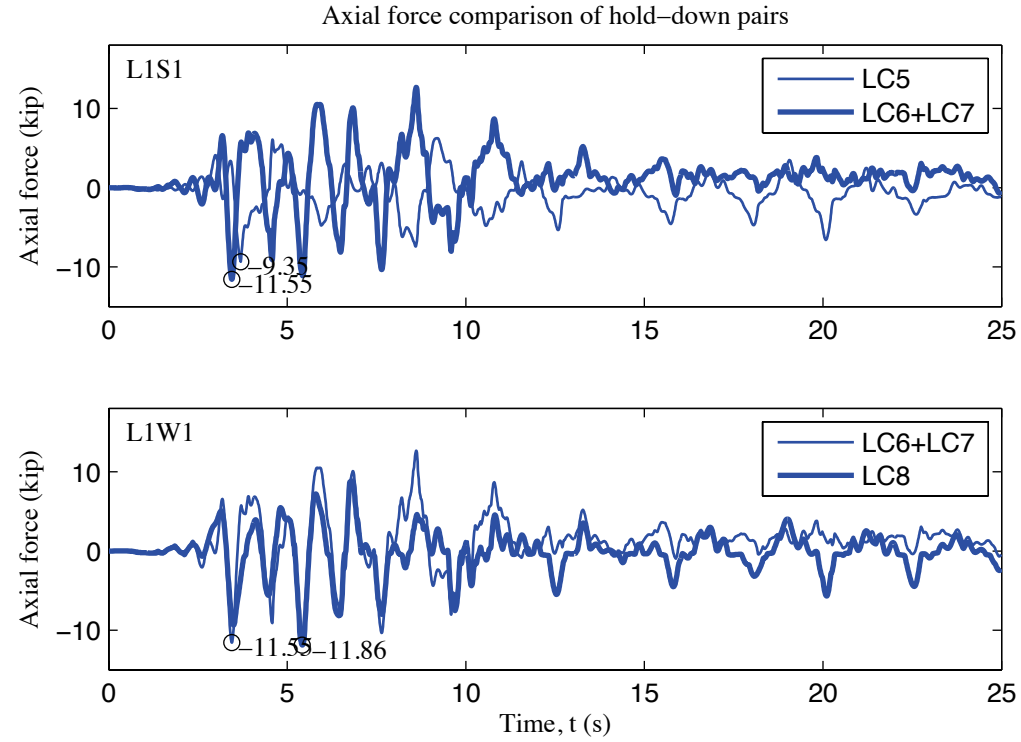

Figure D-10: P-3D-RD-b model, load cell 5 to 8 axial forces, 100 % Canoga Park, 3D nonlinear analysis

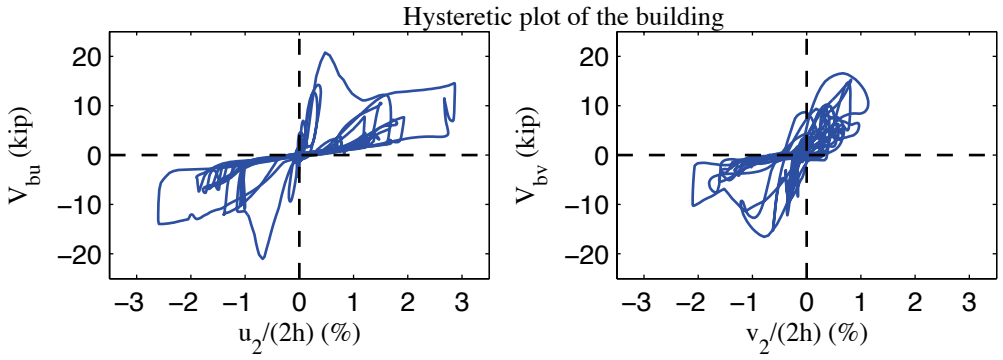

Figure D-11: P-3D-RD-b model, hysteretic plot of the building, 100 % Canoga Park, 3D nonlinear analysis

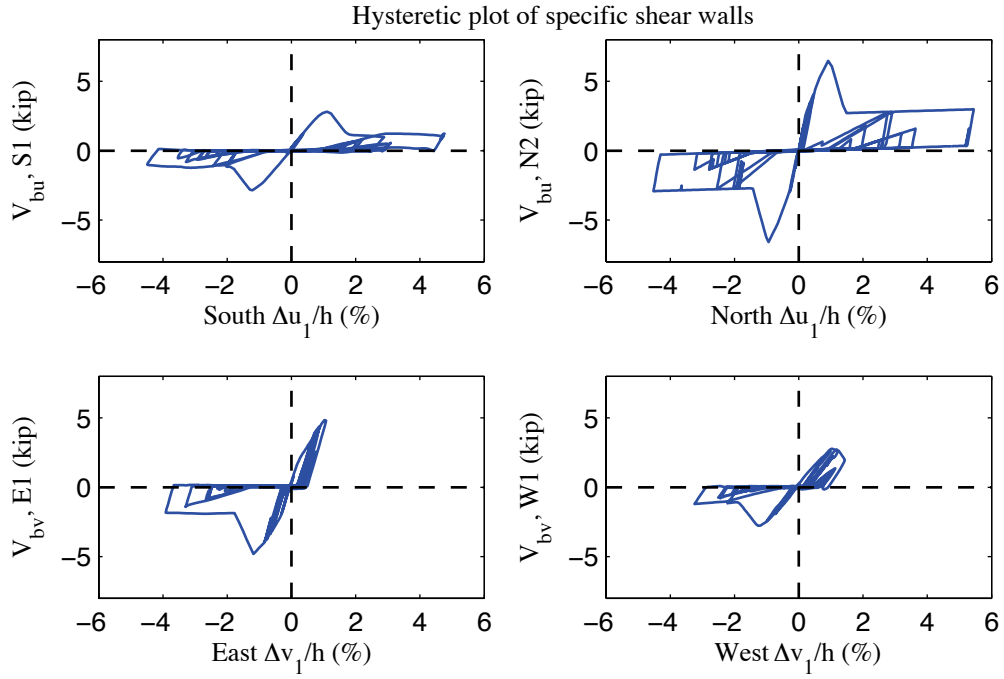

Figure D-12: P-3D-RD-b model, hysteretic plot of shear walls at each elevation, 100 % Canoga Park, 3D nonlinear analysis

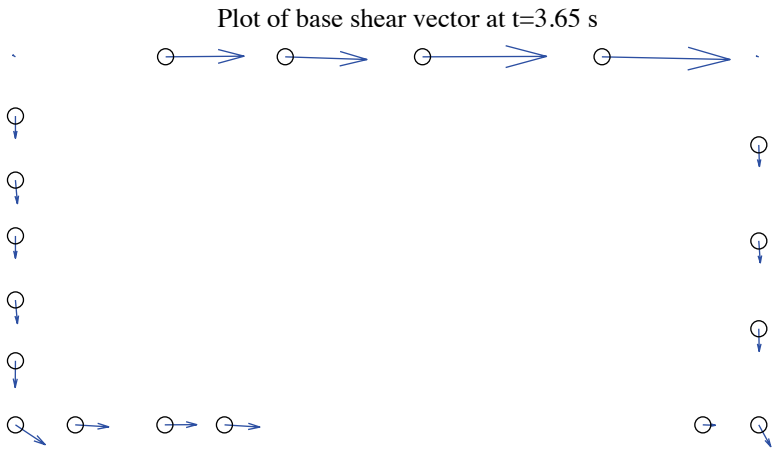

Figure D-13: P-3D-RD-b model, field plot of peak total base shear, 100 % Canoga Park, 3D nonlinear analysis (maximum anchor/hold down base shear is 4.74 kips)

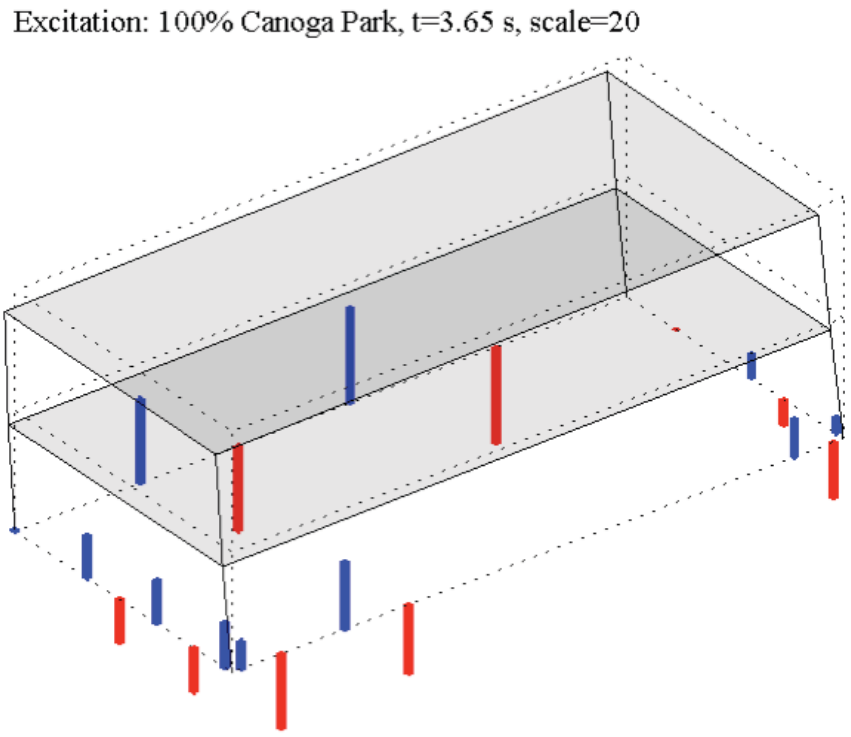

Figure D-14: P-3D-RD-b model, simplified illustration of corner displacements with hold down forces from load cells,100 % Canoga Park, 3D nonlinear analysis (max hold down tensile force is -10.70 kips)

Appendix E: Analysis Results of State-of-the-art, Phase 1, 2D, model a (A1-2D-a)

E.1 Model description

This set of state-of-the-art 2D models features subpanel bracing models of shear walls, explicit models of hold downs, bare steel framing of gravity walls, and rigid leaning columns. Interplay between different wall lines is not allowed in 2D models, representing the effect of flexible diaphragms. Seismic mass is lumped at leaning column nodes. The lateral displacement and shear wall capacity ($\delta(0.2V_{nA})$, $0.2V_{nA}$) from test is utilized to determine the stiffness of elastic material and the first point on the backbone curve of Pinching4 material of shear wall bracing. Figure E-1 (a) to (d) illustrate OpenSees models of South, North, East and West elevations.

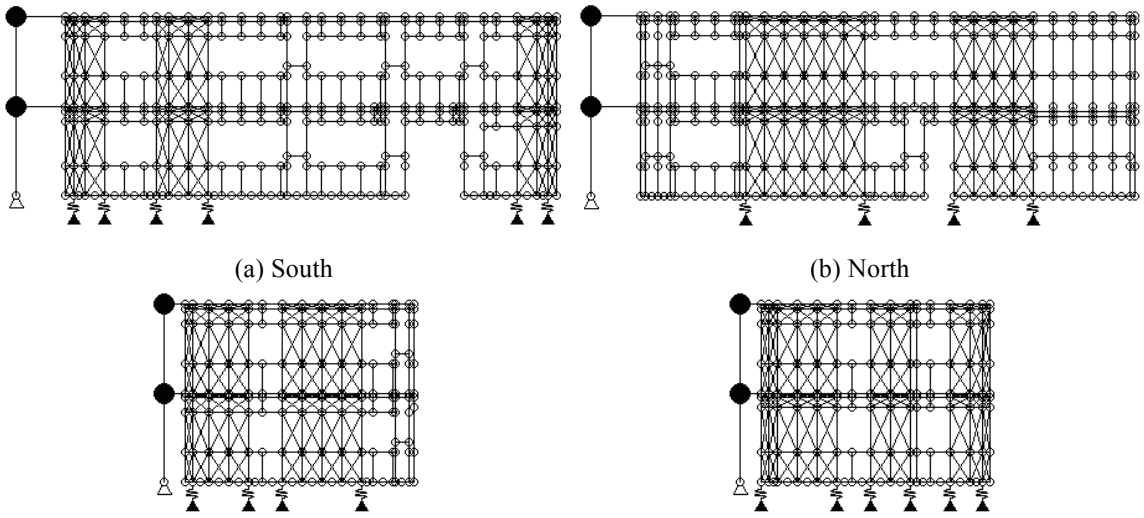

(a) South (b) North

(c) East (d) West

Figure E-1: A1-2D-a model

E.2 Free vibration analysis results

Free vibration analysis is performed for each wall line model. Values of first two natural periods are tabulated (Table E-1). Figure E-2 shows corresponding mode shapes.

Table E-1: Free vibration analysis results, A1-2D-a model

Elevation	1st natural period (s)	2nd natural period (s)
South	0.432	0.162
North	0.254	0.116
East	0.344	0.131
West	0.358	0.136

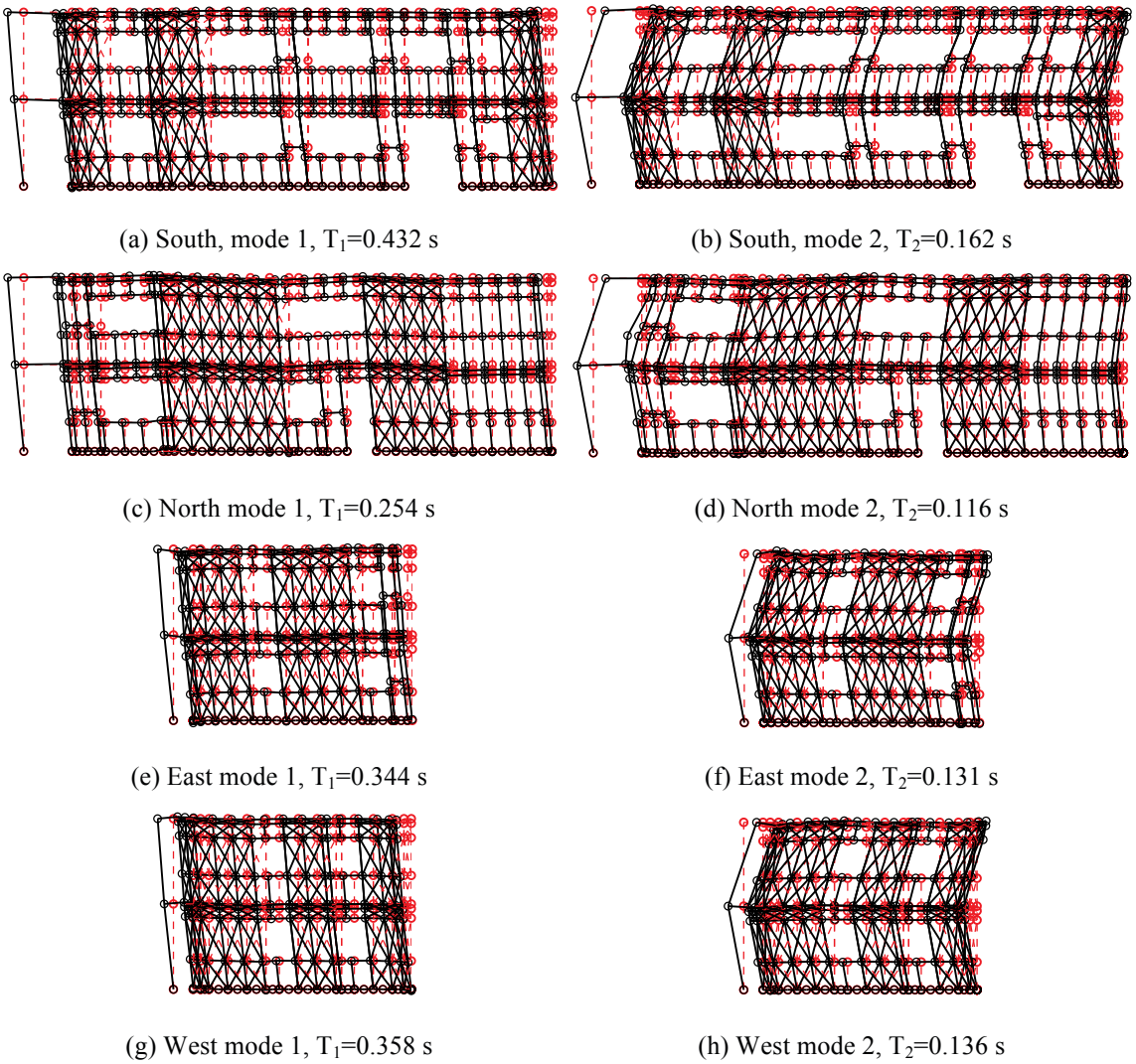

(a) South, mode 1, T_1=0.432 s (b) South, mode 2, T_2=0.162 s

(c) North mode 1, T_1=0.254 s (d) North mode 2, T_2=0.116 s

(e) East mode 1, T_1=0.344 s (f) East mode 2, T_2=0.131 s

(g) West mode 1, T_1=0.358 s (h) West mode 2, T_2=0.136 s

Figure E-2: First two natural modes of A1-2D-a model

E.3 Linear static analysis results

Linear static analysis is performed on each wall line. The total lateral load on that wall line is one half of the design base shear. The vertical distribution of lateral load follows the distribution of equivalent lateral load in the design narrative (Madsen et al. 2011).

Although each wall line is analyzed independently, to make a better summary and to make better comparisons with 3D models, results of individual wall lines are post-processed to reconstruct physical quantities of the whole building behavior, such as building displacements/drifts and total building base shear.

Table E-2 summarizes the breakdown of peak total base shear among four elevations. Two facing wall lines are loaded in the same direction, so the summed base shear of these two wall lines represent the building's total base shear in that direction. As shown in the table, each of two facing wall lines take 5.5 kips of base shear, and wall lines perpendicular to the loading direction take zero base shear as a natural result of 2D analysis.

Table E-3 shows peak building and wall line deflections. Displacements of corner nodes at floor and roof levels are recorded from OpenSees analysis. The average displacement of two corners on the same level of the same wall line is taken as the wall line displacement and the building displacement is the average of four corners. Peak absolute values are taken and the negative sign is kept if it exists. The displacement in long direction is denoted as 'u' and 'v' is for short direction displacement. Subscripts 1 and 2

indicate floor and roof level. The displacement outputs of OpenSees are relative to the ground, so inter-story displacement $\mathbf{\Delta u_1}$ and $\mathbf{\Delta v_1}$ are equal to $\mathbf{u_1}$ and $\mathbf{v_1}$ respectively. For roof level, $\mathbf{\Delta u_2 = u_2 - u_1}$ and $\mathbf{\Delta v_2 = v_2 - v_1}$. Practicing engineers can linearly upscale these data and develop an estimate of the building's performance at a certain lateral force level. In 2D analysis, only wall lines along the loading direction have displacements in the loading direction. Wall lines perpendicular to the static loading is regarded as no deformation under that load.

Table E-4 is an evaluation of the each wall line's lateral stiffness of long and short direction and its breakdown among shear walls (SW) and other systems. The lateral stiffness is calculated as the slope of the total base shear of the wall line vs. its lateral deflection curve (a straight line herein). In addition, we run two more analyses with the stiffness of shear walls set to a number close to zero so the lateral stiffness of gravity walls (GW) and other systems is computed in the same way. Interestingly, the bare CFS framing still accounts for 5.2% (North) to 21.2% (South) total lateral stiffness in this case. This also indicates that behaviors of individual wall lines can vary significantly since they have very different stiffness and breakdown of lateral force and gravity systems.

Table E-2: Breakdown of peak base shear, linear static analysis, A1-2D-a model

Load direction	**LONG**				
Elevation	**South V_b**	**North V_b**	**East V_b**	**West V_b**	**Peak V_b**
kips	5.5	5.5	0.0	0.0	11.1
%	50.0	50.0	0.0	0.0	100.0
Load direction	**SHORT**				
Elevation	**South V_b**	**North V_b**	**East V_b**	**West V_b**	**Peak V_b**
kips	0.0	0.0	5.5	5.5	11.1
%	0.0	0.0	50.0	50.0	100.0

Table E-3: Peak building and wall line deflection, linear static analysis, A1-2D-a model

Load direction	**LONG**							
Deflection (in.)	**u_1**	**u_2**	**v_1**	**v_2**	**Δu_1**	**Δu_2**	**Δv_1**	**Δv_2**
Building	0.133	0.233	0.000	0.000	0.133	0.100	0.000	0.000
South	0.205	0.355	0.000	0.000	0.205	0.150	0.000	0.000
North	0.062	0.111	0.000	0.000	0.062	0.049	0.000	0.000
East	-	-	-	-	-	-	-	-
West	-	-	-	-	-	-	-	-
Load direction	**SHORT**							
Deflection (in.)	**u_1**	**u_2**	**v_1**	**v_2**	**Δu_1**	**Δu_2**	**Δv_1**	**Δv_2**
Building	0.000	0.000	0.135	0.234	0.000	0.000	0.135	0.099
South	-	-	-	-	-	-	-	-
North	-	-	-	-	-	-	-	-
East	0.000	0.000	0.131	0.227	0.000	0.000	0.131	0.097
West	0.000	0.000	0.140	0.240	0.000	0.000	0.140	0.101

Table E-4: Breakdown of lateral stiffness, A1-2D-a model

SOUTH			**NORTH**		
Shear wall k_u (%)	**Gravity wall k_u (%)**	**k_u (kip/in)**	**Shear wall k_v (%)**	**Gravity wall k_v (%)**	**k_v (kip/in)**
78.8	21.2	15.6	94.8	5.2	49.8
EAST			**WEST**		
Shear wall k_u (%)	**Gravity wall k_u (%)**	**k_u (kip/in)**	**Shear wall k_v (%)**	**Gravity wall k_v (%)**	**k_v (kip/in)**
92.6	7.4	24.3	90.9	9.1	23.0

E.4 Nonlinear static (pushover) analysis results

Table E-5 is created following the same logic with Table E-2, but the analysis type is nonlinear static (pushover). Pushover curves of the building and each wall line are presented in Figure E-3 and Figure E-4. The horizontal coordinate is building roof drift, which is the building's roof deflection divided by the building's full height (2h), also twice of the story height. Models in 2D all have a rigid leaning column pinned to the ground, so the base shear in that pinned support (normally quite small) is taken into total base shear of wall lines and the building.

These tables and figures indicate that the wall lines do not reach their peak capacity at exactly the same drift level. Accordingly, total capacity of the building reconstructed using 2D results is no greater than the sum of wall line capacities in the load direction. This observation is more apparent in long direction. The missing of diaphragm stiffness and induced interplay of wall lines can make a significant difference between 2D analysis and real 3D analysis.

Table E-5: Breakdown of peak base shear, pushover analysis, A1-2D-a model

Load direction	**LONG**				
Elevation	**South V_b**	**North V_b**	**East V_b**	**West V_b**	**Peak V_b**
kips	19.9	24.6	0.0	0.0	39.9
%	49.9	61.6	0.0	0.0	100.0
Load direction	**SHORT**				
Elevation	**South V_b**	**North V_b**	**East V_b**	**West V_b**	**Peak V_b**
kips	0.0	0.0	17.4	19.3	35.6
%	0.0	0.0	49.0	54.4	100.0

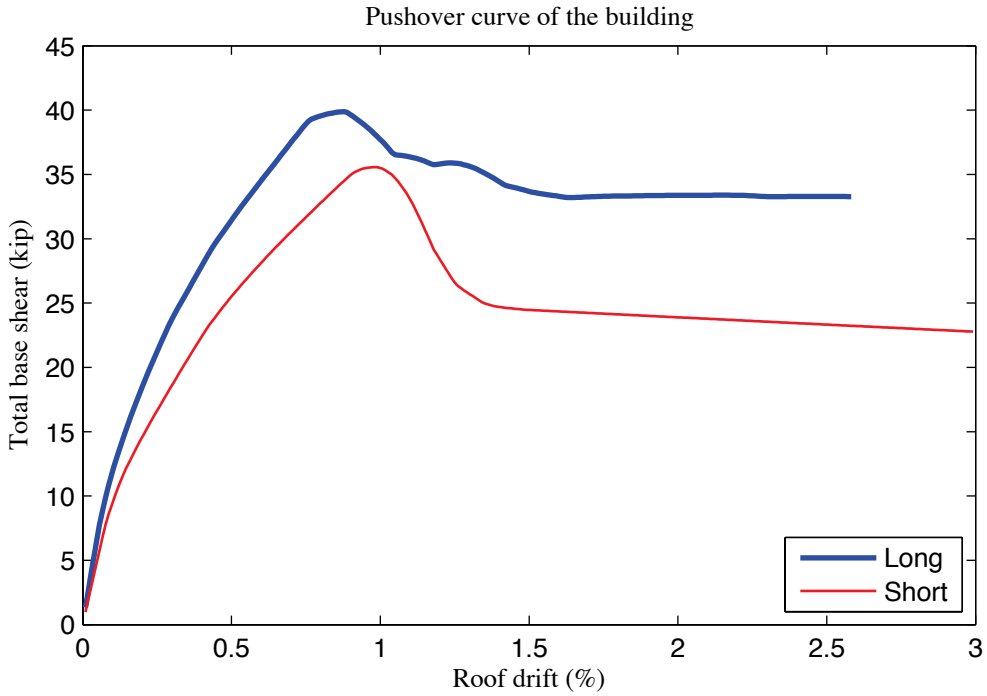

Figure E-3: Pushover curve of A1-2D-a model

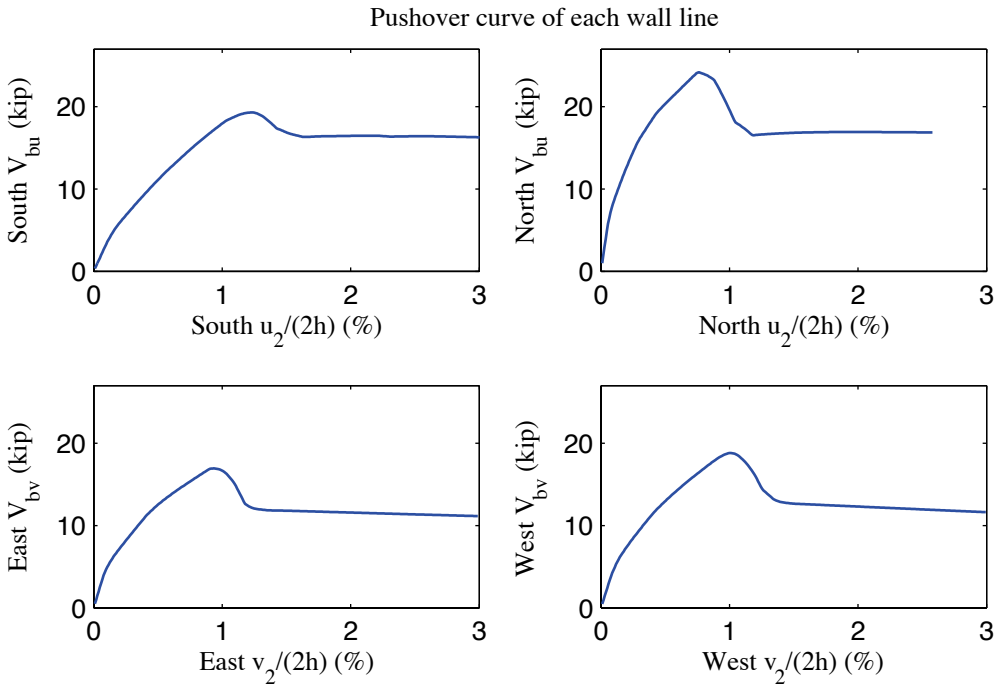

Figure E-4: Pushover curve of each wall line, A1-2D-a model

E.5 Linear time history analysis results

Linear time history analysis is performed on 2D models under Canoga Park and Rinaldi ground motion records of Northridge earthquake in 1994. Details about the ground motion itself and the way we select them are addressed in Chapter 4 and Chapter 5. We considered three scale levels (16%, 44% and 100%) and single axis excitation is applied in the lateral direction of a single wall line. Four uniaxial time history analyses are performed on each wall line individually for one given scale factor, and two facing wall lines are loaded by the same ground motion record. The summary table of time history load cases is also available in Chapter 5 (see Table 5-3 of Chapter 5).

Table E-6 to Table E-9 demonstrate the reconstructed linear elastic performance of the building under designated ground motions. Table E-6 shows peak story relative accelerations in the unit of g. Table E-7 and Table E-8 report peak roof drift and story drift of the building and the corresponding time step (t_*) and the base shear at that time. Note that the base shear at the time of peak roof drift may not be the peak total building base shear in that direction (see Table E-9).

The response of each wall line is available directly from 2D analysis results, so peak story drift and peak base shear of each wall line are listed in Table E-10 and Table E-11. The last two columns of Table E-11 are percentages of base shear of two facing wall lines in the same direction when the total base shear in that direction takes peak value. The sum of these two percentages is exactly 100% since there is no coupling between wall lines 2D analysis and there is no base shear at the support of the leaning column in first

order analysis. It must be noted that base shear at the support of the leaning column is actually not taken into account when it refers to peak wall line base shear in Table E-11 because leaning columns are fictional members.

Wall lines behave linearly since peak drift and peak base shear appear at the same time when the ground motion is linearly scaled. Figure E-5 is a vector plot of the peak total resultant base shear of the building under 100% Canoga Park excitation. Since four dynamical analyses in 2D should be performed separately in order to create the plot, base shear vectors are always in-line with the wall. Comparison with nonlinear analysis results of the same excitation provides insightful observations on the building's response and requirements on modeling fidelity and analysis type.

Table E-6: A1-2D-a model peak story relative acceleration in g, linear time history analysis

Load Case	Ground Motion	LONG			SHORT		
		a_g	Floor a	Roof a	a_g	Floor a	Roof a
EQ_2D_1axis_1	CNP 16%	0.067	0.079	0.126	0.057	0.096	0.149
EQ_2D_1axis_2	CNP 44%	0.185	0.225	0.354	0.157	0.291	0.464
EQ_2D_1axis_3	CNP 100%	0.420	0.511	0.808	0.356	0.565	0.911
EQ_2D_1axis_4	RRS 16%	0.132	0.127	0.210	0.078	0.214	0.344
EQ_2D_1axis_5	RRS 44%	0.363	0.348	0.576	0.214	0.546	0.947
EQ_2D_1axis_6	RRS 100%	0.825	0.792	1.311	0.486	1.246	2.135

Table E-7: A1-2D-a model peak building roof drift and base shear, linear time history analysis

Load Case	Ground Motion	LONG			SHORT		
		$u_2/(2h)$ (%)	t_* (s)	V_b @ t_* (kips)	$v_2/(2h)$ (%)	t_* (s)	V_b @ t_* (kips)
EQ_2D_1axis_1	CNP 16%	0.091	8.74	6.6	-0.067	10.50	7.3
EQ_2D_1axis_2	CNP 44%	0.250	8.74	18.1	-0.184	10.50	20.0
EQ_2D_1axis_3	CNP 100%	0.569	8.74	41.2	-0.419	10.50	45.6
EQ_2D_1axis_4	RRS 16%	0.151	2.65	12.8	0.176	3.37	18.9
EQ_2D_1axis_5	RRS 44%	0.415	2.65	35.3	0.485	3.37	51.9
EQ_2D_1axis_6	RRS 100%	0.943	2.65	80.1	1.103	3.37	118.1

Table E-8: A1-2D-a model peak building story drift, linear time history analysis

Load Case	Ground Motion	LONG				SHORT			
		$\Delta u_1/h$ (%)	t_* (s)	$\Delta u_2/h$ (%)	t_* (s)	$\Delta v_1/h$ (%)	t_* (s)	$\Delta v_2/h$ (%)	t_* (s)
EQ_2D_1 axis_1	CNP 16%	0.111	8.74	-0.072	10.61	-0.082	10.51	0.055	8.84
EQ_2D_1 axis_2	CNP 44%	0.304	8.74	-0.199	10.61	-0.224	10.51	0.151	8.84
EQ_2D_1 axis_3	CNP 100%	0.691	8.74	-0.453	10.61	-0.510	10.51	0.343	8.84
EQ_2D_1 axis_4	RRS 16%	0.183	2.66	0.119	2.65	0.214	3.36	0.141	3.37
EQ_2D_1 axis_5	RRS 44%	0.504	2.66	0.328	2.65	0.587	3.36	0.387	3.37
EQ_2D_1 axis_6	RRS 100%	1.144	2.66	0.746	2.65	1.335	3.36	0.880	3.37

Table E-9: A1-2D-a model peak building base shear, linear time history analysis

		LONG		SHORT		RESULTANT	
Load Case	**Ground Motion**	**Peak V_{bu} (kip)**	**t @ peak V_{bu} (s)**	**Peak V_{bv} (kip)**	**t @ peak V_{bv} (s)**	**Peak V_b (kip)**	**t @ peak V_b (s)**
EQ_2D_1 axis_1	CNP 16%	8.3	8.69	7.4	10.51	9.5	9.00
EQ_2D_1 axis_2	CNP 44%	22.9	8.69	20.4	10.51	26.0	9.00
EQ_2D_1 axis_3	CNP 100%	52.1	8.69	46.3	10.51	59.2	9.00
EQ_2D_1 axis_4	RRS 16%	14.7	2.61	19.1	3.36	19.3	3.36
EQ_2D_1 axis_5	RRS 44%	40.6	2.61	52.4	3.36	52.9	3.36
EQ_2D_1 axis_6	RRS 100%	92.2	2.61	119.1	3.36	120.3	3.36

Table E-10: A1-2D-a model peak wall line story drift, linear time history analysis

LONG		**SOUTH**				**NORTH**			
Load Case	**Ground Motion**	**$\Delta u_1/h$ (%)**	**t_* (s)**	**$\Delta u_2/h$ (%)**	**t_* (s)**	**$\Delta u_1/h$ (%)**	**t_* (s)**	**$\Delta u_2/h$ (%)**	**t_* (s)**
EQ_2D_1axis_1	CNP 16%	0.234	8.76	0.156	8.76	0.061	8.65	0.047	8.65
EQ_2D_1axis_2	CNP 44%	0.643	8.76	0.430	8.76	0.169	8.65	0.130	8.65
EQ_2D_1axis_3	CNP 100%	1.462	8.76	0.977	8.76	0.384	8.65	0.296	8.65
EQ_2D_1axis_4	RRS 16%	0.371	2.68	0.237	2.67	0.110	4.34	0.079	4.48
EQ_2D_1axis_5	RRS 44%	1.020	2.68	0.653	2.67	0.303	4.34	0.217	4.48
EQ_2D_1axis_6	RRS 100%	2.318	2.68	1.484	2.67	0.689	4.34	0.493	4.48
SHORT		**EAST**				**WEST**			
Load Case	**Ground Motion**	**$\Delta v_1/h$ (%)**	**t_* (s)**	**$\Delta v_2/h$ (%)**	**t_* (s)**	**$\Delta v_1/h$ (%)**	**t_* (s)**	**$\Delta v_2/h$ (%)**	**t_* (s)**
EQ_2D_1axis_1	CNP 16%	0.090	8.82	0.058	8.84	0.096	8.38	0.065	10.50
EQ_2D_1axis_2	CNP 44%	0.247	8.82	0.159	8.84	0.265	8.38	0.179	10.50
EQ_2D_1axis_3	CNP 100%	0.561	8.82	0.362	8.84	0.603	8.38	0.407	10.50
EQ_2D_1axis_4	RRS 16%	0.211	3.35	0.141	3.36	0.233	3.37	0.158	3.39
EQ_2D_1axis_5	RRS 44%	0.580	3.35	0.388	3.36	0.641	3.37	0.435	3.39
EQ_2D_1axis_6	RRS 100%	1.318	3.35	0.883	3.36	1.457	3.37	0.989	3.39

Table E-11: A1-2D-a model peak wall line base shear, linear time history analysis

LONG		SOUTH		NORTH		% of Peak V_{bu}	
Load Case	**Ground Motion**	**Peak V_{bu} (kips)**	**t @ peak V_{bu} (s)**	**Peak V_{bu} (kips)**	**t @ peak V_{bu} (s)**	**South**	**North**
EQ_2D_1axis_1	CNP 16%	6.7	8.76	5.6	8.65	50.2	49.8
EQ_2D_1axis_2	CNP 44%	18.5	8.76	15.3	8.65	50.2	49.8
EQ_2D_1axis_3	CNP 100%	42.0	8.76	34.8	8.65	50.2	49.8
EQ_2D_1axis_4	RRS 16%	10.7	2.68	9.9	4.34	48.2	51.8
EQ_2D_1axis_5	RRS 44%	29.4	2.68	27.2	4.34	48.2	51.8
EQ_2D_1axis_6	RRS 100%	66.7	2.68	61.9	4.34	48.2	51.8
SHORT		**EAST**		**WEST**		**% of Peak V_{bv}**	
Load Case	**Ground Motion**	**Peak V_{bv} (kips)**	**t @ peak V_{bv} (s)**	**Peak V_{bv} (kips)**	**t @ peak V_{bv} (s)**	**East**	**West**
EQ_2D_1axis_1	CNP 16%	4.0	8.82	4.0	8.38	45.9	54.1
EQ_2D_1axis_2	CNP 44%	11.1	8.82	11.1	8.38	45.9	54.1
EQ_2D_1axis_3	CNP 100%	25.1	8.82	25.3	8.38	45.9	54.1
EQ_2D_1axis_4	RRS 16%	9.4	3.35	9.9	3.37	49.1	50.9
EQ_2D_1axis_5	RRS 44%	25.9	3.35	27.2	3.37	49.1	50.9
EQ_2D_1axis_6	RRS 100%	58.8	3.35	61.8	3.37	49.1	50.9

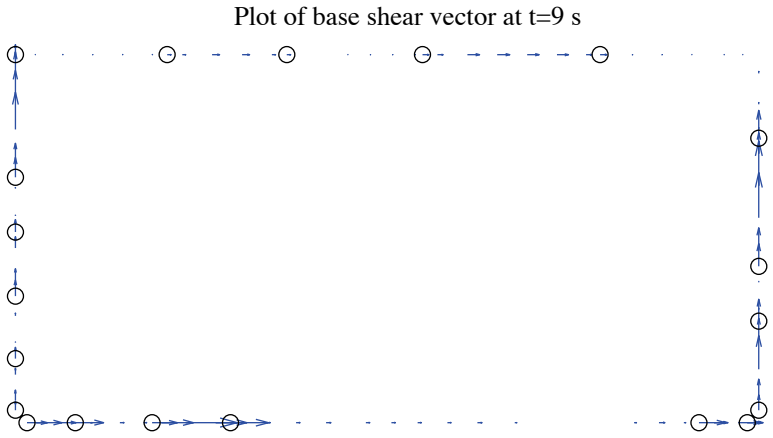

Figure E-5: A1-2D-a model, base shear vector plot at the moment of peak total base shear, 100 % Canoga Park, 2D linear analysis (maximum anchor/hold down base shear is 4.27 kips)

E.6 Nonlinear time history analysis results

Same ground motions are applied to the model with material and geometrical nonlinearity. Table E-12 to Table E-17 are replicas of Table E-6 to Table E-11, but for nonlinear time history analyses. Since this analysis type is most complicated and closest to reality and experiments, behavior of wall lines and hold downs are further studied. Table E-18 expands the breakdown of each wall line's peak base shear between shear walls, gravity walls and other systems. Table E-19 is peak value of hold down tensile force of two selected pairs. Hold down 5 and 6 are on shear wall L1S1, South elevation and hold down 7 and 8 are on shear wall L1W1, West elevation. These shear walls have lowest capacities compared with others on the same wall line and they meet at the southwest edge of the building.

Time history plots in this section include plots of story drifts of the building and each wall line (Figure E-6 to Figure E-8), total building base shear in long and short direction (Figure E-9) and axial forces of hold downs in Table E-19 (Figure E-10). Hysteretic plots in Figure E-11 and Figure E-12 are helpful for visual examination of nonlinear base shear-drift relationship of the building and the weakest shear wall on each wall line. In comparison with linear time history analysis, vector plot of peak total base shear is illustrated in Figure E-13. Figure E-14 presents a simplified deformed shape of the building (see (Peterman 2014) for details of the method) and axial force of all twenty hold downs at the moment of peak total base shear. The same sign convention with tests is adopted. Red bars indicate tensile (negative) force and blue ones are for compressive (positive) force.

Hysteretic behavior is seen in the building and typical shear walls under design-based earthquake (100% Canoga Park excitation in one axis, see Figure E-11 and Figure E-12). However, behaviors of individual wall lines differ significantly. South wall line reaches 3.3% peak floor story drift and the backbone of response curve goes into the post peak deeply but peak story drifts of all other wall lines are less than 1.5% (Table E-16). The reconstructed peak building story drift is 1.81% (Table E-14), still much less than the peak value of South wall line. The worst-case scenario from 2D analysis can greatly overestimate the nonlinear response of the whole building and yield conservative observation. Figure E-13 shows that peak resultant base shear is largely taken by shear walls, and that base shear vectors in anchors and hold downs align with wall lines due to the limit of 2D modeling and analysis. Table E-19, Figure E-10 and Figure E-14 demonstrate that hold downs in a pair do not experience the same amount of force with opposite signs even in 2D analysis, an evidence that supports Type II shear wall behavior despite Type I design assumption.

The near-field Rinaldi record is much stronger in terms of peak ground acceleration, especially in the long direction. When loaded at 100%, North elevation fails at 2.86 seconds. At that moment, wall line floor story drift is 7.8%, a drift level that will make a real wall line fail. Table E-18 reveals that as nonlinearity increases, the portion of base shear taken by gravity wall and other system grows significantly, from 2.7% to 6.8% on West elevation at minimum and from 16.6% to 26.5% on South elevation at maximum.

Table E-12: A1-2D-a model peak story relative acceleration in g, nonlinear time history analysis

Load Case	Ground Motion	LONG			SHORT		
		a_g	Floor a	Roof a	a_g	Floor a	Roof a
EQ_2D_1axis_1	CNP 16%	0.067	0.121	0.155	0.057	0.110	0.182
EQ_2D_1axis_2	CNP 44%	0.185	0.654	0.520	0.157	0.336	0.458
EQ_2D_1axis_3	CNP 100%	0.420	0.982	0.788	0.356	0.675	0.995
EQ_2D_1axis_4	RRS 16%	0.132	0.300	0.225	0.078	0.366	0.386
EQ_2D_1axis_5	RRS 44%	0.363	0.830	1.276	0.214	0.524	0.529
EQ_2D_1axis_6	RRS 100%	0.825	N/A	N/A	0.487	N/A	N/A

Table E-13: A1-2D-a model peak building roof drift and base shear, nonlinear time history analysis

Load Case	Ground Motion	LONG			SHORT		
		$u_2/(2h)$ (%)	t_* (s)	V_b @ t_* (kips)	$v_2/(2h)$ (%)	t_* (s)	V_b @ t_* (kips)
EQ_2D_1axis_1	CNP 16%	0.092	8.75	5.3	-0.072	10.51	8.0
EQ_2D_1axis_2	CNP 44%	0.364	8.78	13.7	0.286	10.00	18.0
EQ_2D_1axis_3	CNP 100%	1.108	8.84	11.1	0.875	10.12	32.1
EQ_2D_1axis_4	RRS 16%	0.169	2.69	9.7	0.169	3.42	13.2
EQ_2D_1axis_5	RRS 44%	0.753	2.80	24.4	0.349	6.10	20.3
EQ_2D_1axis_6	RRS 100%	N/A	N/A	N/A	N/A	N/A	N/A

Table E-14: A1-2D-a model peak building story drift, nonlinear time history analysis

Load Case	Ground Motion	LONG				SHORT			
		$\Delta u_1/h$ (%)	t_* (s)	$\Delta u_2/h$ (%)	t_* (s)	$\Delta v_1/h$ (%)	t_* (s)	$\Delta v_2/h$ (%)	t_* (s)
EQ_2D_1 axis_1	CNP 16%	0.120	8.77	0.065	8.74	-0.093	10.52	0.057	9.97
EQ_2D_1 axis_2	CNP 44%	0.453	10.02	0.282	8.78	0.376	10.00	0.195	9.40
EQ_2D_1 axis_3	CNP 100%	1.808	8.88	0.519	8.81	1.257	10.10	-0.594	9.85
EQ_2D_1 axis_4	RRS 16%	0.255	2.72	0.109	2.65	0.234	3.41	0.130	6.07
EQ_2D_1 axis_5	RRS 44%	1.200	2.80	-0.366	3.17	0.457	6.10	0.241	6.10
EQ_2D_1 axis_6	RRS 100%	N/A	N/A	N/A	N/A	N/A	N/A	N/A	N/A

Table E-15: A1-2D-a model peak building base shear, nonlinear time history analysis

		LONG		SHORT		RESULTANT	
Load Case	**Ground Motion**	**Peak V_{bu} (kip)**	**t @ peak V_{bu} (s)**	**Peak V_{bv} (kip)**	**t @ peak V_{bv} (s)**	**Peak V_b (kip)**	**t @ peak V_b (s)**
EQ_2D_1 axis_1	CNP 16%	8.1	8.69	8.0	10.52	9.2	9.01
EQ_2D_1 axis_2	CNP 44%	22.2	8.72	18.0	10.01	23.1	10.01
EQ_2D_1 axis_3	CNP 100%	51.9	8.77	37.0	10.09	52.3	8.77
EQ_2D_1 axis_4	RRS 16%	13.7	2.61	13.7	3.40	13.9	2.82
EQ_2D_1 axis_5	RRS 44%	45.2	2.65	20.5	2.57	45.8	2.65
EQ_2D_1 axis_6	RRS 100%	N/A	N/A	N/A	N/A	N/A	N/A

Table E-16: A1-2D-a model peak wall line story drift, nonlinear time history analysis

LONG		**SOUTH**				**NORTH**			
Load Case	**Ground Motion**	**$\Delta u_1/h$ (%)**	**t_* (s)**	**$\Delta u_2/h$ (%)**	**t_* (s)**	**$\Delta u_1/h$ (%)**	**t_* (s)**	**$\Delta u_2/h$ (%)**	**t_* (s)**
EQ_2D_1axis_1	CNP 16%	0.264	8.77	0.138	8.75	0.062	8.65	0.048	8.65
EQ_2D_1axis_2	CNP 44%	0.840	10.02	0.559	8.78	0.260	11.77	0.122	9.64
EQ_2D_1axis_3	CNP 100%	3.271	8.91	0.903	8.82	1.179	8.76	0.355	10.26
EQ_2D_1axis_4	RRS 16%	0.485	2.72	0.196	2.66	0.138	4.37	0.070	6.16
EQ_2D_1axis_5	RRS 44%	1.927	2.80	0.659	3.19	0.664	2.66	0.220	3.99
EQ_2D_1axis_6	RRS 100%	N/A	N/A	N/A	N/A	N/A	N/A	N/A	N/A
SHORT		**EAST**				**WEST**			
Load Case	**Ground Motion**	**$\Delta v_1/h$ (%)**	**t_* (s)**	**$\Delta v_2/h$ (%)**	**t_* (s)**	**$\Delta v_1/h$ (%)**	**t_* (s)**	**$\Delta v_2/h$ (%)**	**t_* (s)**
EQ_2D_1axis_1	CNP 16%	0.096	8.82	0.059	8.97	0.121	10.53	0.073	9.97
EQ_2D_1axis_2	CNP 44%	0.341	10.00	0.189	10.00	0.423	10.01	0.238	9.41
EQ_2D_1axis_3	CNP 100%	1.203	10.11	0.595	9.85	1.349	10.09	0.642	9.84
EQ_2D_1axis_4	RRS 16%	0.230	3.40	0.142	3.86	0.250	3.42	0.155	3.89
EQ_2D_1axis_5	RRS 44%	0.465	6.10	0.270	6.10	0.473	2.58	0.233	2.59
EQ_2D_1axis_6	RRS 100%	N/A	N/A	N/A	N/A	N/A	N/A	N/A	N/A

Table E-17: A1-2D-a model peak wall line base shear, nonlinear time history analysis

LONG		SOUTH		NORTH		% of Peak V_{bu}	
Load Case	**Ground Motion**	**Peak V_{bu} (kips)**	**t @ peak V_{bu} (s)**	**Peak V_{bu} (kips)**	**t @ peak V_{bu} (s)**	**South**	**North**
EQ_2D_1axis_1	CNP 16%	6.1	8.78	5.5	8.65	48.7	51.8
EQ_2D_1axis_2	CNP 44%	13.5	8.81	12.0	11.77	51.0	45.8
EQ_2D_1axis_3	CNP 100%	20.0	8.77	24.7	8.74	38.5	47.2
EQ_2D_1axis_4	RRS 16%	9.2	2.72	8.5	4.37	42.1	57.4
EQ_2D_1axis_5	RRS 44%	20.1	2.72	20.0	2.66	35.0	44.3
EQ_2D_1axis_6	RRS 100%	N/A	N/A	N/A	N/A	N/A	N/A
SHORT		**EAST**		**WEST**		**% of Peak V_{bv}**	
Load Case	**Ground Motion**	**Peak V_{bv} (kips)**	**t @ peak V_{bv} (s)**	**Peak V_{bv} (kips)**	**t @ peak V_{bv} (s)**	**East**	**West**
EQ_2D_1axis_1	CNP 16%	4.2	8.82	4.6	10.53	43.7	57.2
EQ_2D_1axis_2	CNP 44%	8.4	10.00	9.9	10.01	46.2	55.2
EQ_2D_1axis_3	CNP 100%	17.2	9.84	19.2	10.07	46.0	51.8
EQ_2D_1axis_4	RRS 16%	6.7	3.40	7.3	3.42	48.9	52.3
EQ_2D_1axis_5	RRS 44%	10.4	2.58	10.5	6.10	50.7	50.9
EQ_2D_1axis_6	RRS 100%	N/A	N/A	N/A	N/A	N/A	N/A

Table E-18: A1-2D-a model wall line base shear breakdown, nonlinear time history analysis

LONG		SOUTH			NORTH		
Load Case	**Ground Motion**	**Peak V_{bu} (kips)**	**SW V_{bu} (%)**	**GW V_{bu} (%)**	**Peak V_{bu} (kips)**	**SW V_{bu} (%)**	**GW V_{bu} (%)**
EQ_2D_1axis_1	CNP 16%	6.1	83.4	16.6	5.5	96.2	3.8
EQ_2D_1axis_2	CNP 44%	13.5	76.2	23.8	12.0	92.9	7.1
EQ_2D_1axis_3	CNP 100%	20.0	73.8	26.2	24.7	86.8	13.2
EQ_2D_1axis_4	RRS 16%	9.2	79.7	20.3	8.5	94.8	5.2
EQ_2D_1axis_5	RRS 44%	20.1	73.5	26.5	20.0	90.3	9.7
EQ_2D_1axis_6	RRS 100%	N/A	N/A	N/A	N/A	N/A	N/A
SHORT		**EAST**			**WEST**		
Load Case	**Ground Motion**	**Peak V_{bv} (kips)**	**SW V_{bv} (%)**	**GW V_{bu} (%)**	**Peak V_{bv} (kips)**	**SW V_{bv} (%)**	**GW V_{bv} (%)**
EQ_2D_1axis_1	CNP 16%	4.2	96.9	3.1	4.6	97.3	2.7
EQ_2D_1axis_2	CNP 44%	8.4	94.5	5.5	9.9	94.9	5.1
EQ_2D_1axis_3	CNP 100%	17.2	88.5	11.5	19.2	93.2	6.8
EQ_2D_1axis_4	RRS 16%	6.7	95.4	4.6	7.3	95.8	4.2
EQ_2D_1axis_5	RRS 44%	10.4	92.5	7.5	10.5	94.6	5.4
EQ_2D_1axis_6	RRS 100%	N/A	N/A	N/A	N/A	N/A	N/A

Table E-19: A1-2D-a model peak hold down tensile force at certain locations, nonlinear time history analysis

		L1S1, LC5		L1S1, LC6		L1W1, LC7		L1W1, LC8	
Load Case	**Ground Motion**	**Peak F (kips)**	**t @ peak F (s)**	**Peak F (kips)**	**t @ peak F (s)**	**Peak F (kips)**	**t @ peak F (s)**	**Peak F (kips)**	**t @ peak F (s)**
EQ_2D_1axis_1	CNP 16%	-0.77	9.01	-1.52	8.77	-0.64	9.97	-0.37	10.53
EQ_2D_1axis_2	CNP 44%	-1.89	9.73	-3.89	8.79	-2.02	10.01	-0.79	10.25
EQ_2D_1axis_3	CNP 100%	-3.13	8.58	-5.39	8.79	-4.25	10.10	-1.76	9.83
EQ_2D_1axis_4	RRS 16%	-0.87	3.06	-2.12	2.70	-1.31	3.42	-0.58	3.23
EQ_2D_1axis_5	RRS 44%	-2.70	3.17	-5.35	2.74	-2.13	6.10	-0.97	2.58
EQ_2D_1axis_6	RRS 100%	N/A	N/A	N/A	N/A	N/A	N/A	N/A	N/A

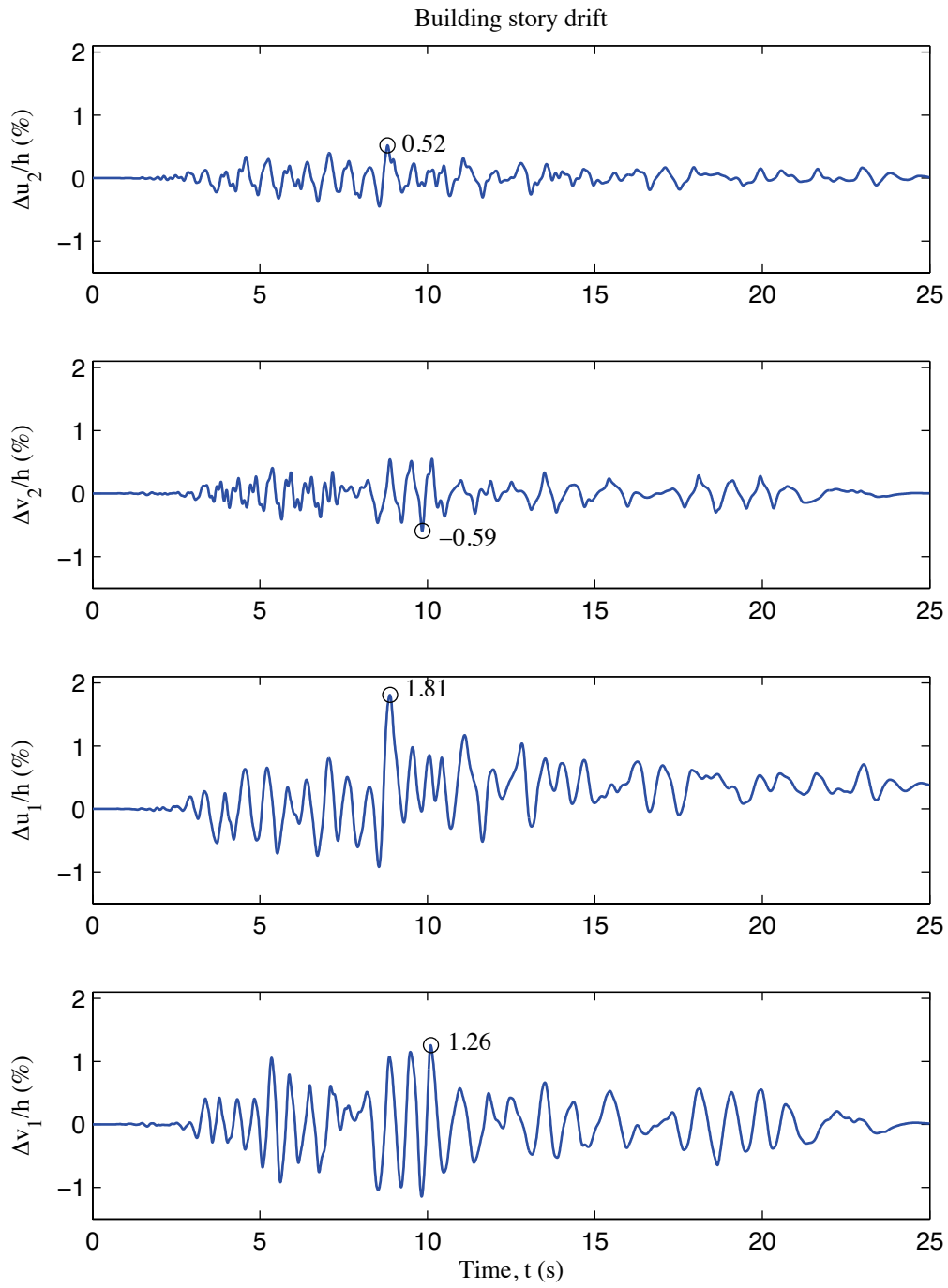

Figure E-6: A1-2D-a model building story drift, 100 % Canoga Park, 2D nonlinear analysis

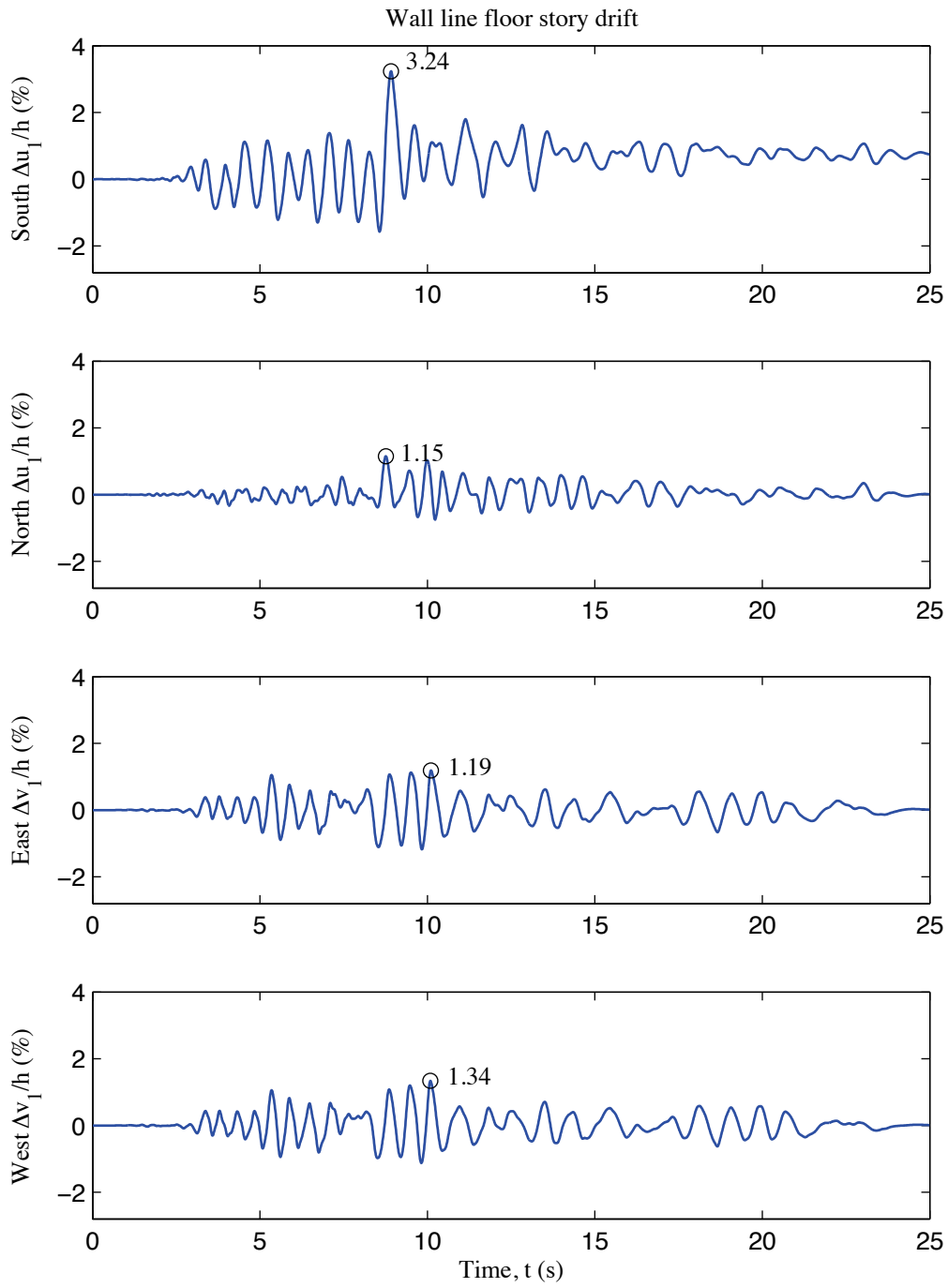

Figure E-7: A1-2D-a model wall line floor story drift, 100 % Canoga Park, 2D nonlinear analysis

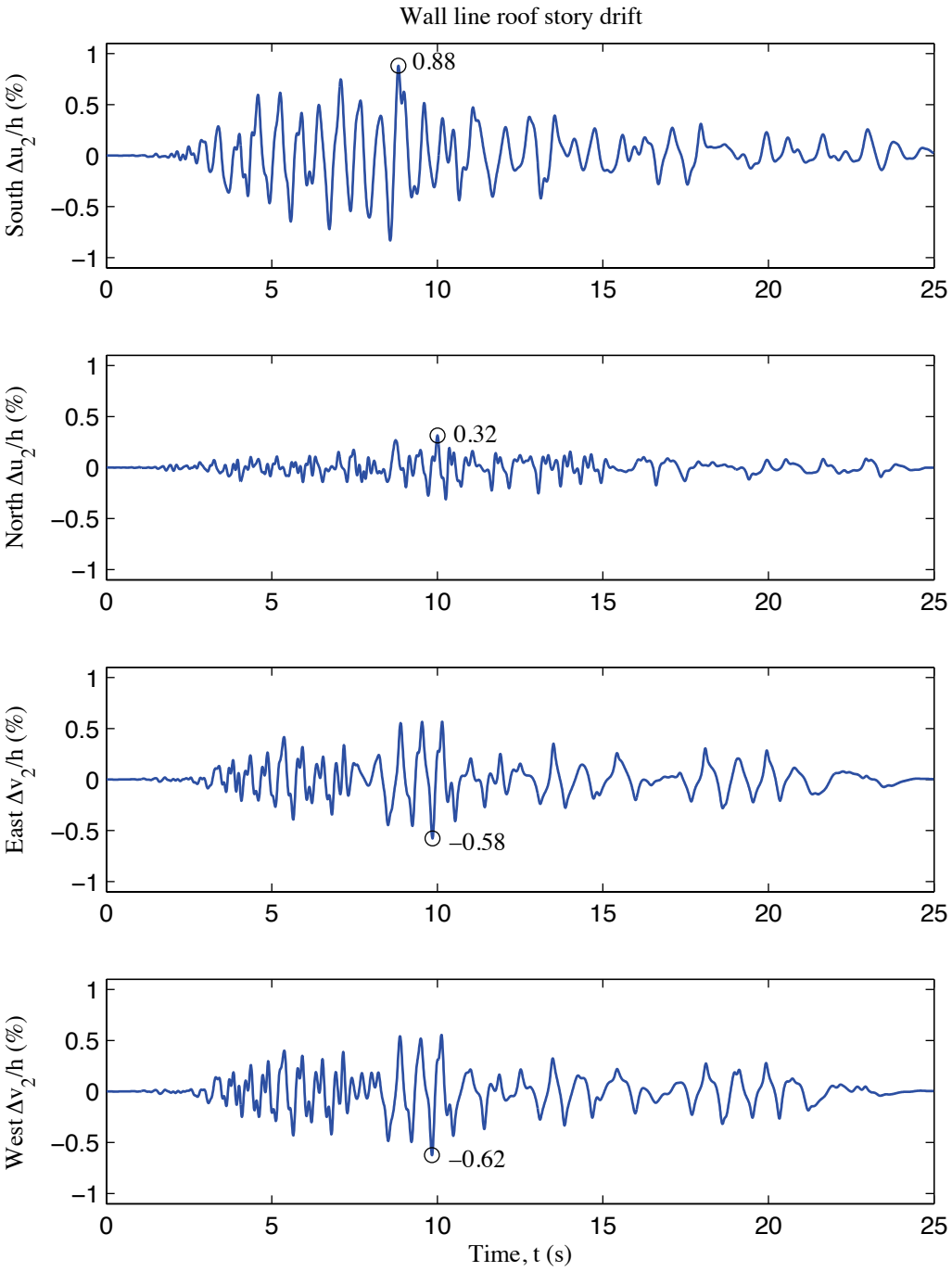

Figure E-8: A1-2D-a model wall line roof story drift, 100 % Canoga Park, 2D nonlinear analysis

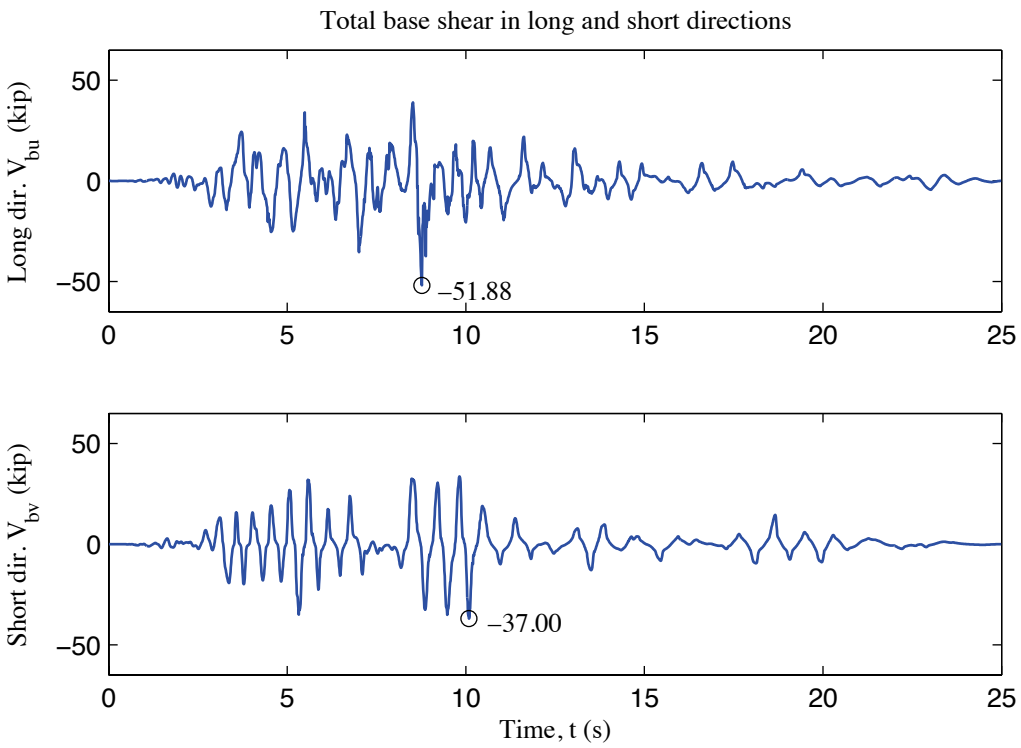

Figure E-9: A1-2D-a model total building base shear, 100 % Canoga Park, 2D nonlinear analysis

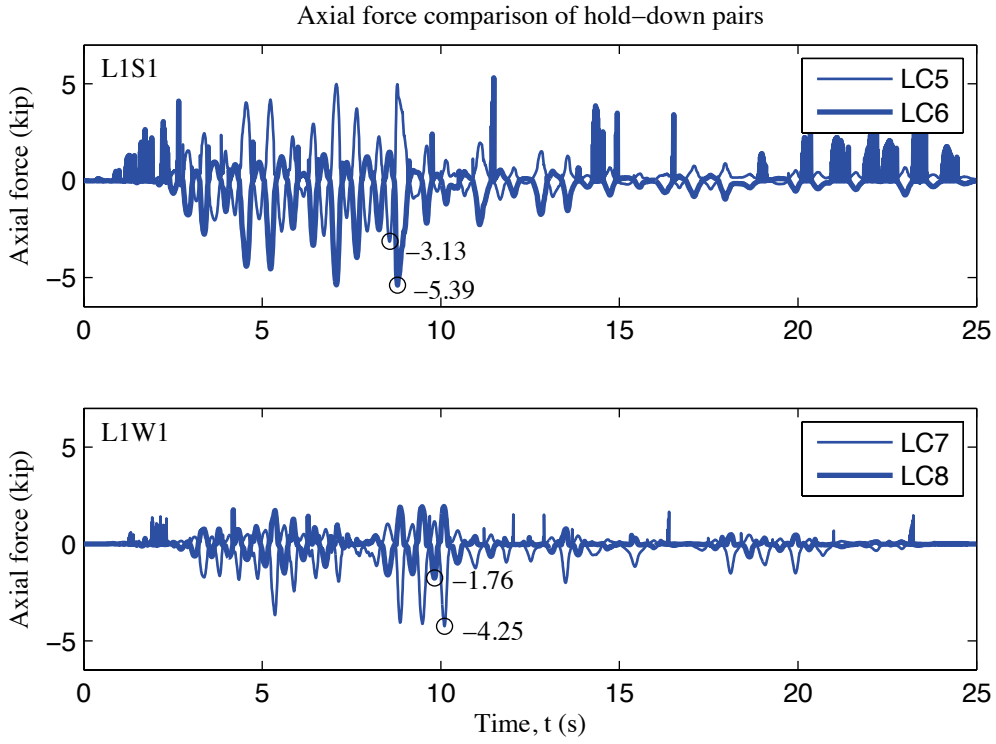

Figure E-10: A1-2D-a model, load cell 5 to 8 axial forces, 100 % Canoga Park, 2D nonlinear analysis

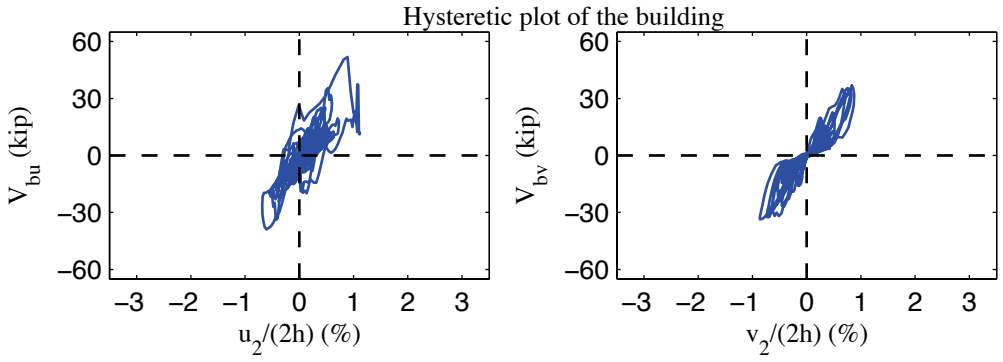

Figure E-11: A1-2D-a model, hysteretic plot of the building, 100 % Canoga Park, 2D nonlinear analysis

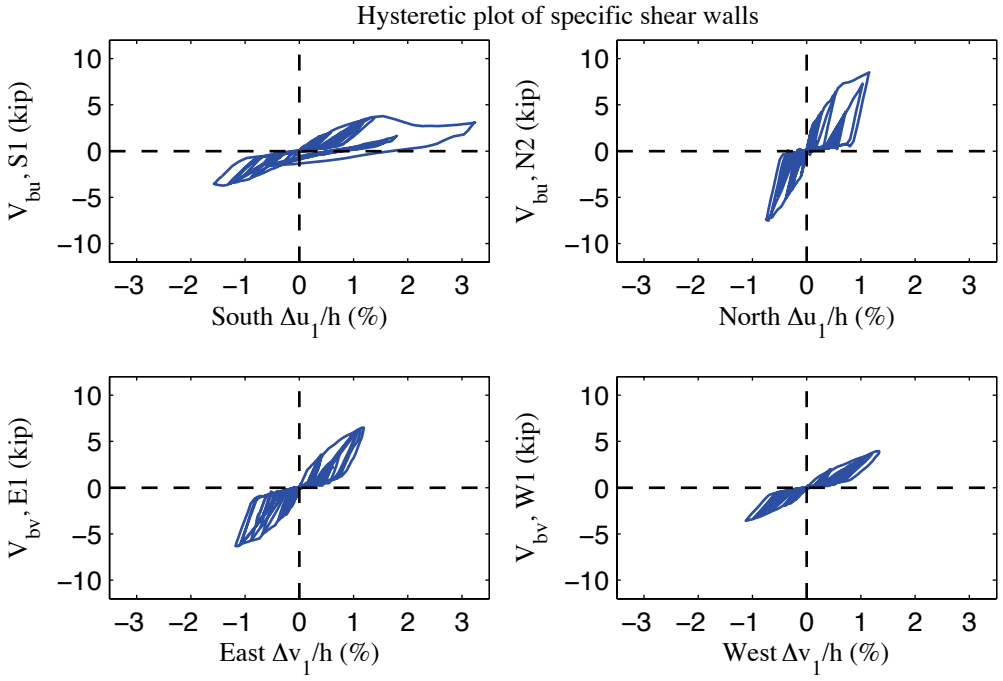

Figure E-12: A1-2D-a model, hysteretic plot of shear walls at each elevation, 100 % Canoga Park, 2D nonlinear analysis

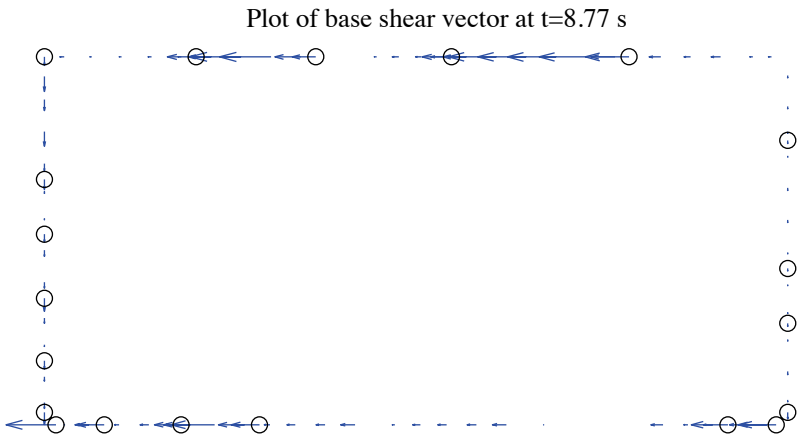

Figure E-13: A1-2D-a model, field plot of peak total base shear, 100 % Canoga Park, 2D nonlinear analysis (maximum anchor/hold down base shear is 2.12 kips)

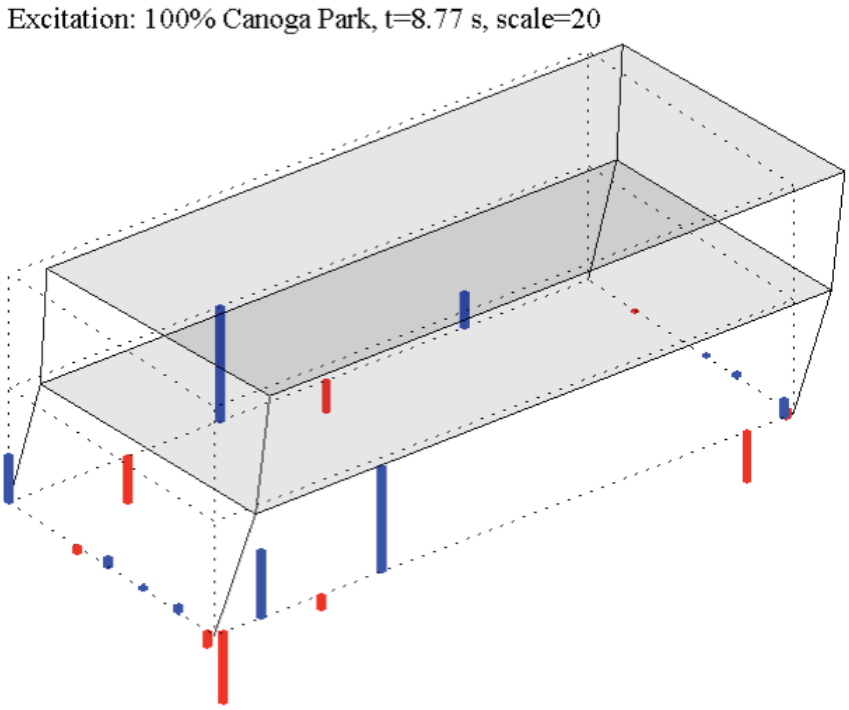

Figure E-14: A1-2D-a model, simplified illustration of corner displacements with hold down forces from load cells,100 % Canoga Park, 2D nonlinear analysis (max hold down tensile force is -5.10 kips)

Appendix F: Analysis Results of State-of-the-art, Phase 1, 2D, model b (A1-2D-b)

F.1 Model description

This set of state-of-the-art 2D models features subpanel bracing models of shear walls, explicit models of hold downs, bare steel framing of gravity walls, and rigid leaning columns. Interplay between different wall lines is not allowed in 2D models, representing the effect of flexible diaphragms. Seismic mass is lumped at leaning column nodes. The lateral displacement and shear wall capacity ($\delta(0.4V_{nA})$, $0.4V_{nA}$) from test is utilized to determine the stiffness of elastic material and the first point on the backbone curve of Pinching4 material of shear wall bracing. Figure F-1 (a) to (d) illustrate OpenSees models of South, North, East and West elevations. Simulation results are presented and discussed in later sections. Definitions of output physical quantities and explanation of post-process method can be found in Appendix E.

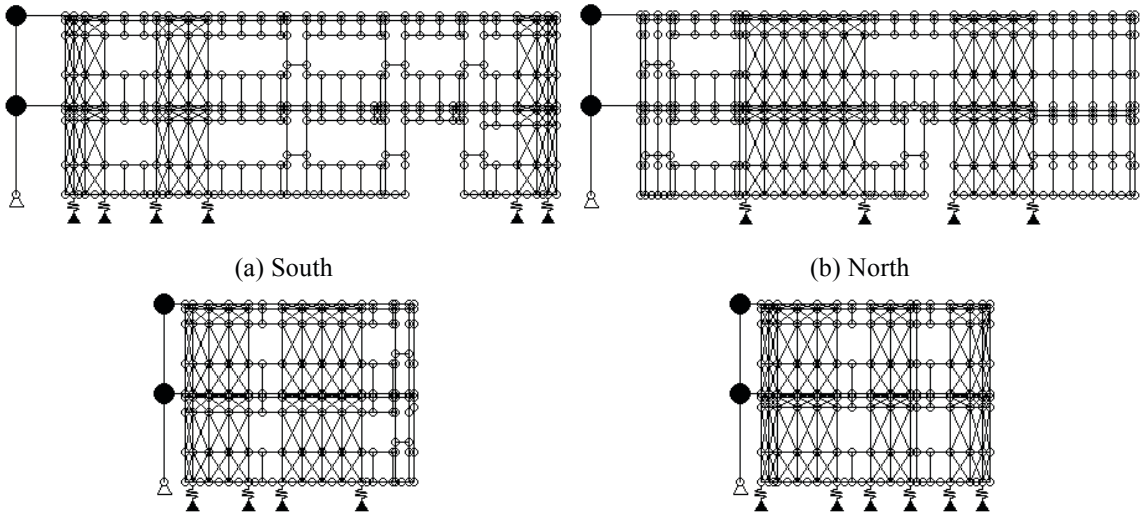

(a) South (b) North

(c) East (d) West

Figure F-1: A1-2D-b model

F.2 Free vibration analysis results

Free vibration analysis is performed for each wall line model. Values of first two natural periods are tabulated (Table F-1). Figure F-2 shows corresponding mode shapes.

Table F-1: Free vibration analysis results, A1-2D-b model

Elevation	1st natural period (s)	2nd natural period (s)
South	0.479	0.183
North	0.306	0.138
East	0.406	0.158
West	0.416	0.161

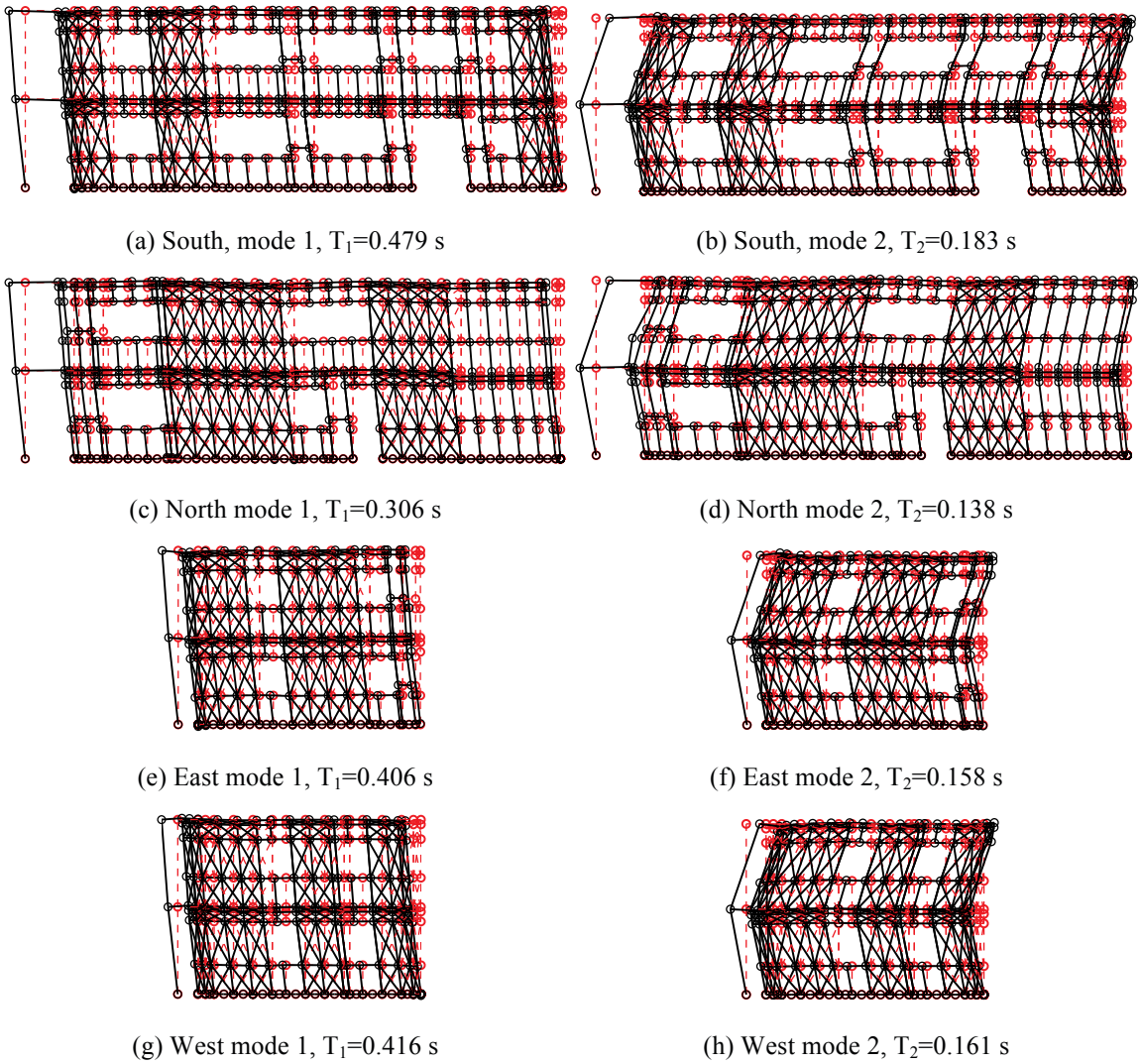

(a) South, mode 1, T_1=0.479 s (b) South, mode 2, T_2=0.183 s

(c) North mode 1, T_1=0.306 s (d) North mode 2, T_2=0.138 s

(e) East mode 1, T_1=0.406 s (f) East mode 2, T_2=0.158 s

(g) West mode 1, T_1=0.416 s (h) West mode 2, T_2=0.161 s

Figure F-2: First two natural modes of A1-2D-b model

F.3 Linear static analysis results

Linear static analysis is performed on each wall line. The total lateral load on that wall line is one half of the design base shear. The vertical distribution of lateral load follows the distribution of equivalent lateral load in the design narrative (Madsen et al. 2011).

Although each wall line is analyzed independently, to make a better summary and to make better comparisons with 3D models, results of individual wall lines are post-processed to reconstruct physical quantities of the whole building behavior, such as building displacements/drifts and total building base shear.

Table F-2 summarizes the breakdown of peak total base shear among four elevations. As shown in the table, each of two facing wall lines take 5.5 kips of base shear, and wall lines perpendicular to the loading direction take zero base shear as a natural result of 2D analysis.

Table F-3 shows peak building and wall line deflections. Practicing engineers can linearly upscale these data and develop an estimate of the building's performance at a certain lateral force level. In 2D analysis, only wall lines along the loading direction have displacements in the loading direction.

Table F-4 is an evaluation of the each wall line's lateral stiffness of long and short direction and its breakdown among shear walls (SW) and other systems. Interestingly, the bare CFS framing still accounts for 8.0% (North) to 26.2% (South) total lateral stiffness

in this case. This also indicates that behaviors of individual wall lines can vary significantly since they have very different stiffness and breakdown of lateral force and gravity systems.

Table F-2: Breakdown of peak base shear, linear static analysis, A1-2D-b model

Load direction	**LONG**				
Elevation	**South V_b**	**North V_b**	**East V_b**	**West V_b**	**Peak V_b**
kips	5.5	5.5	0.0	0.0	11.1
%	50.0	50.0	0.0	0.0	100.0
Load direction	**SHORT**				
Elevation	**South V_b**	**North V_b**	**East V_b**	**West V_b**	**Peak V_b**
kips	0.0	0.0	5.5	5.5	11.1
%	0.0	0.0	50.0	50.0	100.0

Table F-3: Peak building and wall line deflection, linear static analysis, A1-2D-b model

Load direction	**LONG**							
Deflection (in.)	**u_1**	**u_2**	**v_1**	**v_2**	**Δu_1**	**Δu_2**	**Δv_1**	**Δv_2**
Building	0.178	0.305	0.000	0.000	0.178	0.127	0.000	0.000
South	0.258	0.439	0.000	0.000	0.258	0.181	0.000	0.000
North	0.099	0.171	0.000	0.000	0.099	0.072	0.000	0.000
East	-	-	-	-	-	-	-	-
West	-	-	-	-	-	-	-	-
Load direction	**SHORT**							
Deflection (in.)	**u_1**	**u_2**	**v_1**	**v_2**	**Δu_1**	**Δu_2**	**Δv_1**	**Δv_2**
Building	0.000	0.000	0.192	0.326	0.000	0.000	0.192	0.134
South	-	-	-	-	-	-	-	-
North	-	-	-	-	-	-	-	-
East	0.000	0.000	0.189	0.321	0.000	0.000	0.189	0.132
West	0.000	0.000	0.196	0.331	0.000	0.000	0.196	0.135

Table F-4: Breakdown of lateral stiffness, A1-2D-b model

SOUTH			**NORTH**		
Shear wall k_u (%)	**Gravity wall k_u (%)**	**k_u (kip/in)**	**Shear wall k_v (%)**	**Gravity wall k_v (%)**	**k_v (kip/in)**
73.8	26.2	12.6	92.0	8.0	32.3
EAST			**WEST**		
Shear wall k_u (%)	**Gravity wall k_u (%)**	**k_u (kip/in)**	**Shear wall k_v (%)**	**Gravity wall k_v (%)**	**k_v (kip/in)**
89.5	10.5	17.2	87.4	12.6	16.7

F.4 Nonlinear static (pushover) analysis results

Table F-5 is created following the same logic with Table F-2, but the analysis type is nonlinear static (pushover). Pushover curves of the building and each wall line are presented in Figure F-3 and Figure F-4.

These tables and figures indicate that the wall lines do not reach their peak capacity at exactly the same drift level. Accordingly, total capacity of the building reconstructed using 2D results is no greater than the sum of wall line capacities in the load direction. This observation is more apparent in long direction. The missing of diaphragm stiffness and induced interplay of wall lines can make a significant difference between 2D analysis and real 3D analysis.

Table F-5: Breakdown of peak base shear, pushover analysis, A1-2D-b model

Load direction	**LONG**				
Elevation	**South V_b**	**North V_b**	**East V_b**	**West V_b**	**Peak V_b**
kips	19.9	24.6	0.0	0.0	39.9
%	49.9	61.7	0.0	0.0	100.0
Load direction	**SHORT**				
Elevation	**South V_b**	**North V_b**	**East V_b**	**West V_b**	**Peak V_b**
kips	0.0	0.0	17.4	19.3	35.6
%	0.0	0.0	49.0	54.3	100.0

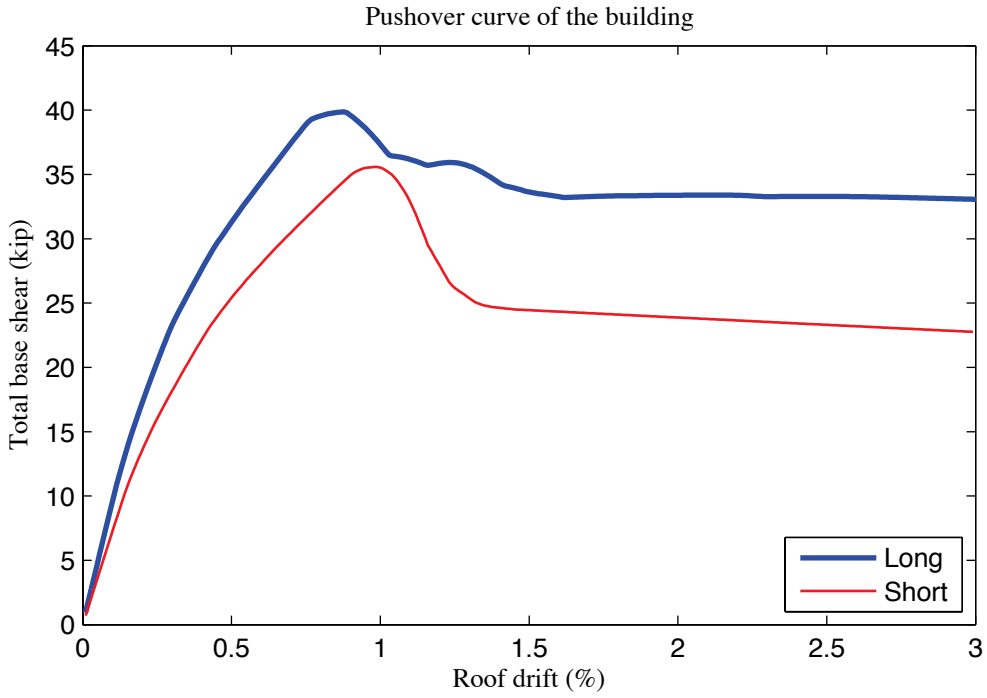

Figure F-3: Pushover curve of A1-2D-b model

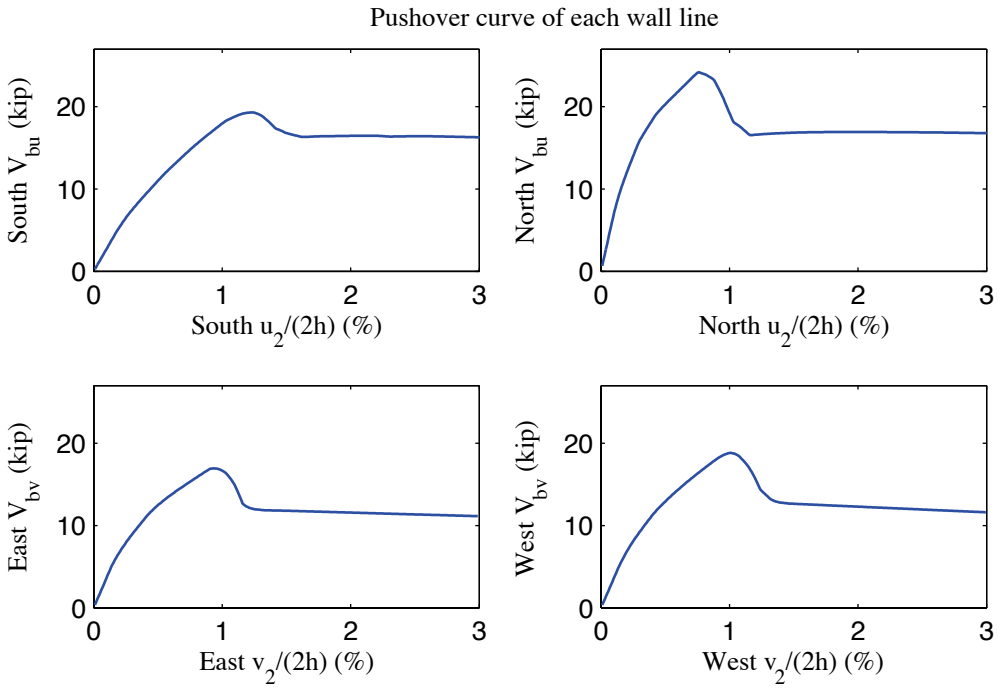

Figure F-4: Pushover curve of each wall line, A1-2D-b model

F.5 Linear time history analysis results

Linear time history analysis is performed on 2D models under Canoga Park and Rinaldi ground motion records of Northridge earthquake in 1994. We considered three scale levels (16%, 44% and 100%) and single axis excitation is applied in the lateral direction of a single wall line.

Table F-6 to Table F-9 demonstrate the reconstructed linear elastic performance of the building under designated ground motions. Table F-6 shows peak story relative accelerations in the unit of g. Table F-7 and Table F-8 report peak roof drift and story drift of the building and the corresponding time step (t_*) and the base shear at that time. Note that the base shear at the time of peak roof drift may not be the peak total building base shear in that direction (see Table F-9).

The response of each wall line is available directly from 2D analysis results, so peak story drift and peak base shear of each wall line are listed in Table F-10 and Table F-11.

Wall lines behave linearly since peak drift and peak base shear appear at the same time when the ground motion is linearly scaled. Figure F-5 is a vector plot of the peak total resultant base shear of the building under 100% Canoga Park excitation. Since four dynamical analyses in 2D should be performed separately in order to create the plot, base shear vectors are always in-line with the wall. Comparison with nonlinear analysis results of the same excitation provides insightful observations on the building's response and requirements on modeling fidelity and analysis type.

Table F-6: A1-2D-b model peak story relative acceleration in g, linear time history analysis

Load Case	Ground Motion	LONG			SHORT		
		a_g	Floor a	Roof a	a_g	Floor a	Roof a
EQ_2D_1axis_1	CNP 16%	0.067	0.096	0.117	0.057	0.100	0.175
EQ_2D_1axis_2	CNP 44%	0.185	0.218	0.327	0.157	0.264	0.462
EQ_2D_1axis_3	CNP 100%	0.420	0.496	0.745	0.356	0.595	1.050
EQ_2D_1axis_4	RRS 16%	0.132	0.154	0.255	0.078	0.238	0.355
EQ_2D_1axis_5	RRS 44%	0.363	0.414	0.693	0.214	0.657	0.970
EQ_2D_1axis_6	RRS 100%	0.825	0.935	1.582	0.486	1.494	2.210

Table F-7: A1-2D-b model peak building roof drift and base shear, linear time history analysis

Load Case	Ground Motion	LONG			SHORT		
		$u_2/(2h)$ (%)	t_* (s)	V_b @ t_* (kips)	$v_2/(2h)$ (%)	t_* (s)	V_b @ t_* (kips)
EQ_2D_1axis_1	CNP 16%	-0.081	7.82	6.2	-0.104	5.95	8.0
EQ_2D_1axis_2	CNP 44%	-0.223	7.82	17.0	-0.286	5.95	21.9
EQ_2D_1axis_3	CNP 100%	-0.507	7.82	38.7	-0.649	5.95	49.8
EQ_2D_1axis_4	RRS 16%	0.210	2.67	16.4	-0.206	4.44	16.8
EQ_2D_1axis_5	RRS 44%	0.578	2.67	45.2	-0.568	4.44	46.1
EQ_2D_1axis_6	RRS 100%	1.315	2.67	102.8	-1.290	4.44	104.9

Table F-8: A1-2D-b model peak building story drift, linear time history analysis

Load Case	Ground Motion	LONG				SHORT			
		$\Delta u_1/h$ (%)	t_* (s)	$\Delta u_2/h$ (%)	t_* (s)	$\Delta v_1/h$ (%)	t_* (s)	$\Delta v_2/h$ (%)	t_* (s)
EQ_2D_1 axis_1	CNP 16%	-0.102	7.81	-0.065	13.00	-0.126	5.94	0.084	5.72
EQ_2D_1 axis_2	CNP 44%	-0.281	7.81	-0.179	13.00	-0.347	5.94	0.232	5.72
EQ_2D_1 axis_3	CNP 100%	-0.638	7.81	-0.406	13.00	-0.789	5.94	0.526	5.72
EQ_2D_1 axis_4	RRS 16%	0.259	2.67	0.162	2.67	-0.260	4.44	0.174	4.26
EQ_2D_1 axis_5	RRS 44%	0.712	2.67	0.445	2.67	-0.715	4.44	0.477	4.26
EQ_2D_1 axis_6	RRS 100%	1.619	2.67	1.010	2.67	-1.625	4.44	1.086	4.26

Table F-9: A1-2D-b model peak building base shear, linear time history analysis

		LONG		SHORT		RESULTANT	
Load Case	**Ground Motion**	**Peak V_{bu} (kip)**	**t @ peak V_{bu} (s)**	**Peak V_{bv} (kip)**	**t @ peak V_{bv} (s)**	**Peak V_b (kip)**	**t @ peak V_b (s)**
EQ_2D_1 axis_1	CNP 16%	6.2	7.81	8.1	5.94	8.6	5.94
EQ_2D_1 axis_2	CNP 44%	17.1	7.81	22.2	5.94	23.8	5.94
EQ_2D_1 axis_3	CNP 100%	38.8	7.81	50.4	5.94	54.1	5.94
EQ_2D_1 axis_4	RRS 16%	17.4	2.64	16.8	4.44	17.5	2.64
EQ_2D_1 axis_5	RRS 44%	47.9	2.64	46.1	4.44	48.1	2.64
EQ_2D_1 axis_6	RRS 100%	108.8	2.64	104.9	4.44	109.3	2.64

Table F-10: A1-2D-b model peak wall line story drift, linear time history analysis

LONG		**SOUTH**				**NORTH**			
Load Case	**Ground Motion**	**$\Delta u_1/h$ (%)**	**t_* (s)**	**$\Delta u_2/h$ (%)**	**t_* (s)**	**$\Delta u_1/h$ (%)**	**t_* (s)**	**$\Delta u_2/h$ (%)**	**t_* (s)**
EQ_2D_1axis_1	CNP 16%	0.181	13.00	0.124	10.65	0.078	8.68	0.053	4.07
EQ_2D_1axis_2	CNP 44%	0.498	13.00	0.340	10.65	0.215	8.68	0.145	4.07
EQ_2D_1axis_3	CNP 100%	1.132	13.00	0.774	10.65	0.487	8.68	0.330	4.07
EQ_2D_1axis_4	RRS 16%	0.449	2.71	0.274	2.69	0.176	2.62	0.124	4.55
EQ_2D_1axis_5	RRS 44%	1.235	2.71	0.755	2.69	0.484	2.62	0.340	4.55
EQ_2D_1axis_6	RRS 100%	2.808	2.71	1.715	2.69	1.101	2.62	0.773	4.55
SHORT		**EAST**				**WEST**			
Load Case	**Ground Motion**	**$\Delta v_1/h$ (%)**	**t_* (s)**	**$\Delta v_2/h$ (%)**	**t_* (s)**	**$\Delta v_1/h$ (%)**	**t_* (s)**	**$\Delta v_2/h$ (%)**	**t_* (s)**
EQ_2D_1axis_1	CNP 16%	0.124	5.93	0.086	5.71	0.135	5.95	0.096	5.97
EQ_2D_1axis_2	CNP 44%	0.340	5.93	0.236	5.71	0.372	5.95	0.263	5.97
EQ_2D_1axis_3	CNP 100%	0.773	5.93	0.537	5.71	0.845	5.95	0.598	5.97
EQ_2D_1axis_4	RRS 16%	0.290	4.43	0.194	4.26	0.247	4.45	0.170	4.27
EQ_2D_1axis_5	RRS 44%	0.799	4.43	0.535	4.26	0.679	4.45	0.469	4.27
EQ_2D_1axis_6	RRS 100%	1.817	4.43	1.216	4.26	1.543	4.45	1.065	4.27

Table F-11: A1-2D-b model peak wall line base shear, linear time history analysis

LONG		SOUTH		NORTH		% of Peak V_{bu}	
Load Case	**Ground Motion**	**Peak V_{bu} (kips)**	**t @ peak V_{bu} (s)**	**Peak V_{bu} (kips)**	**t @ peak V_{bu} (s)**	**South**	**North**
EQ_2D_1axis_1	CNP 16%	4.2	13.00	4.5	8.68	63.2	36.8
EQ_2D_1axis_2	CNP 44%	11.5	13.00	12.3	8.68	63.2	36.8
EQ_2D_1axis_3	CNP 100%	26.1	13.00	28.0	8.68	63.2	36.8
EQ_2D_1axis_4	RRS 16%	10.3	2.71	10.1	2.62	44.7	55.3
EQ_2D_1axis_5	RRS 44%	28.3	2.71	27.8	2.62	44.6	55.4
EQ_2D_1axis_6	RRS 100%	64.4	2.71	63.2	2.62	44.6	55.4
SHORT		**EAST**		**WEST**		**% of Peak V_{bv}**	
Load Case	**Ground Motion**	**Peak V_{bv} (kips)**	**t @ peak V_{bv} (s)**	**Peak V_{bv} (kips)**	**t @ peak V_{bv} (s)**	**East**	**West**
EQ_2D_1axis_1	CNP 16%	4.1	5.93	4.1	5.95	49.9	50.1
EQ_2D_1axis_2	CNP 44%	11.2	5.93	11.2	5.95	49.9	50.1
EQ_2D_1axis_3	CNP 100%	25.4	5.93	25.4	5.95	50.0	50.0
EQ_2D_1axis_4	RRS 16%	9.5	4.43	7.4	4.45	56.3	43.7
EQ_2D_1axis_5	RRS 44%	26.3	4.43	20.5	4.45	56.3	43.7
EQ_2D_1axis_6	RRS 100%	59.7	4.43	46.5	4.45	56.4	43.6

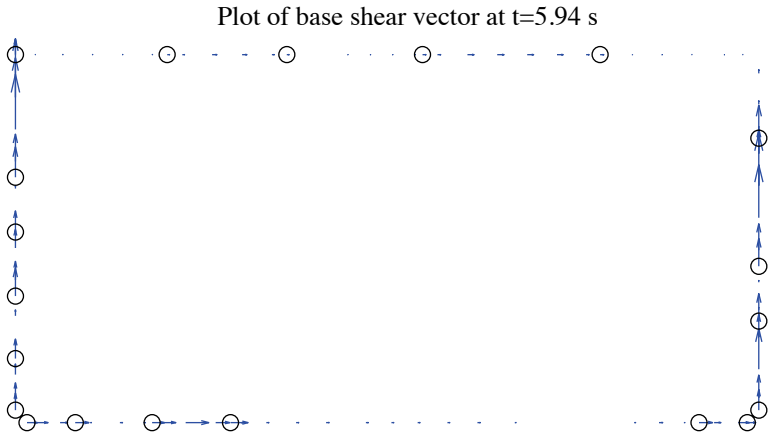

Figure F-5: A1-2D-b model, base shear vector plot at the moment of peak total base shear, 100 % Canoga Park, 2D linear analysis (maximum anchor/hold down base shear is 3.79 kips)

F.6 Nonlinear time history analysis results

Same ground motions are applied to the model with material and geometrical nonlinearity. Table F-12 to Table F-17 are replicas of Table F-6 to Table F-11, but for nonlinear time history analyses. Since this analysis type is most complicated and closest to reality and experiments, behavior of wall lines and smeared hold downs are further studied. Table F-18 expands the breakdown of each wall line's peak base shear between shear walls, gravity walls and other systems. Table F-19 is peak value of hold down tensile force of two selected pairs. Hold down 5 and 6 are on shear wall L1S1, South elevation and hold down 7 and 8 are on shear wall L1W1, West elevation. These shear walls have lowest capacities compared with others on the same wall line and they meet at the southwest edge of the building.

Time history plots in this section include plots of story drifts of the building and each wall line (Figure F-6 to Figure F-8), total building base shear in long and short direction (Figure F-9) and axial forces of hold downs in (Figure F-10). Hysteretic plots in Figure F-11 and Figure F-12 are helpful for visual examination of nonlinear base shear-drift relationship of the building and the weakest shear wall on each wall line. In comparison with linear time history analysis, vector plot of peak total base shear is illustrated in Figure F-13. Figure F-14 presents a simplified deformed shape of the building (see (Peterman 2014) for details of the method) and axial force of all twenty hold downs at the moment of peak total base shear. The same sign convention with tests is adopted. Red bars indicate tensile (negative) force and blue ones are for compressive (positive) force.

Hysteretic behavior is seen in the building and typical shear walls under design-based earthquake (100% Canoga Park excitation in one axis, see Figure F-11 and Figure F-12). However, behaviors of individual wall lines differ significantly. South wall line reaches 3.3% peak floor story drift and the backbone of response curve goes into the post peak deeply but peak story drifts of all other wall lines are less than 1.6% (Table F-16). The reconstructed peak building story drift is 1.82% (Table F-14), still much less than the peak value of South wall line. The worst-case scenario from 2D analysis can greatly overestimate the nonlinear response of the whole building and yield conservative observation. Figure F-13 shows that peak resultant base shear is largely taken by shear walls, and that base shear vectors in anchors and hold downs align with wall lines due to the limit of 2D modeling and analysis. Table F-19, Figure F-10 and Figure F-14 demonstrate that hold downs in a pair do not experience the same amount of force with opposite signs even in 2D analysis, an evidence that supports Type II shear wall behavior despite Type I design assumption.

The near-field Rinaldi record is much stronger in terms of peak ground acceleration, especially in the long direction. When loaded at 100%, North elevation fails at 2.84 seconds. At that moment, wall line floor story drift is 7.6%, a drift level that will make a real wall line fail. Table F-18 reveals that as nonlinearity increases, the portion of base shear taken by gravity wall and other system grows significantly, from 3.6% to 6.6% on West elevation at minimum and from 19.2% to 26.5% on South elevation at maximum.

Table F-12: A1-2D-b model peak story relative acceleration in g, nonlinear time history analysis

Load Case	Ground Motion	LONG			SHORT		
		a_g	Floor a	Roof a	a_g	Floor a	Roof a
EQ_2D_1axis_1	CNP 16%	0.067	0.106	0.148	0.057	0.132	0.188
EQ_2D_1axis_2	CNP 44%	0.185	0.597	0.442	0.157	0.364	0.447
EQ_2D_1axis_3	CNP 100%	0.420	1.093	1.011	0.356	0.800	1.075
EQ_2D_1axis_4	RRS 16%	0.132	0.241	0.294	0.078	0.236	0.316
EQ_2D_1axis_5	RRS 44%	0.363	1.021	0.982	0.214	0.438	0.578
EQ_2D_1axis_6	RRS 100%	0.825	N/A	N/A	0.487	N/A	N/A

Table F-13: A1-2D-b model peak building roof drift and base shear, nonlinear time history analysis

Load Case	Ground Motion	LONG			SHORT		
		$u_2/(2h)$ (%)	t_* (s)	V_b @ t_* (kips)	$v_2/(2h)$ (%)	t_* (s)	V_b @ t_* (kips)
EQ_2D_1axis_1	CNP 16%	-0.086	13.01	5.2	-0.114	5.95	8.2
EQ_2D_1axis_2	CNP 44%	0.378	8.76	19.3	-0.330	6.00	19.4
EQ_2D_1axis_3	CNP 100%	1.097	8.84	7.9	-1.030	9.85	34.5
EQ_2D_1axis_4	RRS 16%	0.216	2.67	15.8	0.203	6.01	14.8
EQ_2D_1axis_5	RRS 44%	0.777	2.74	31.3	-0.428	2.58	25.0
EQ_2D_1axis_6	RRS 100%	N/A	N/A	N/A	N/A	N/A	N/A

Table F-14: A1-2D-b model peak building story drift, nonlinear time history analysis

Load Case	Ground Motion	LONG				SHORT			
		$\Delta u_1/h$ (%)	t_* (s)	$\Delta u_2/h$ (%)	t_* (s)	$\Delta v_1/h$ (%)	t_* (s)	$\Delta v_2/h$ (%)	t_* (s)
EQ_2D_1 axis_1	CNP 16%	-0.103	13.01	-0.068	13.01	-0.132	5.94	-0.097	5.96
EQ_2D_1 axis_2	CNP 44%	0.488	9.98	0.298	8.77	0.437	10.00	-0.239	6.01
EQ_2D_1 axis_3	CNP 100%	1.822	8.88	-0.467	8.57	1.481	10.12	-0.682	9.85
EQ_2D_1 axis_4	RRS 16%	0.283	2.68	0.153	2.66	0.279	6.00	-0.141	4.09
EQ_2D_1 axis_5	RRS 44%	1.240	2.80	0.406	2.72	-0.617	2.58	0.300	6.10
EQ_2D_1 axis_6	RRS 100%	N/A	N/A	N/A	N/A	N/A	N/A	N/A	N/A

Table F-15: A1-2D-b model peak building base shear, nonlinear time history analysis

		LONG		SHORT		RESULTANT	
Load Case	**Ground Motion**	**Peak V_{bu} (kip)**	**t @ peak V_{bu} (s)**	**Peak V_{bv} (kip)**	**t @ peak V_{bv} (s)**	**Peak V_b (kip)**	**t @ peak V_b (s)**
EQ_2D_1 axis_1	CNP 16%	6.2	12.32	8.3	5.94	8.8	5.94
EQ_2D_1 axis_2	CNP 44%	25.4	8.71	19.9	5.97	25.9	10.22
EQ_2D_1 axis_3	CNP 100%	53.1	8.78	39.5	9.45	57.5	8.79
EQ_2D_1 axis_4	RRS 16%	16.7	2.64	14.9	6.00	16.8	2.64
EQ_2D_1 axis_5	RRS 44%	48.2	2.67	25.3	2.57	48.9	2.67
EQ_2D_1 axis_6	RRS 100%	N/A	N/A	N/A	N/A	N/A	N/A

Table F-16: A1-2D-b model peak wall line story drift, nonlinear time history analysis

LONG		**SOUTH**				**NORTH**			
Load Case	**Ground Motion**	**$\Delta u_1/h$ (%)**	**t_* (s)**	**$\Delta u_2/h$ (%)**	**t_* (s)**	**$\Delta u_1/h$ (%)**	**t_* (s)**	**$\Delta u_2/h$ (%)**	**t_* (s)**
EQ_2D_1axis_1	CNP 16%	0.197	13.02	0.136	10.66	0.078	8.68	0.055	4.07
EQ_2D_1axis_2	CNP 44%	0.878	9.99	0.583	8.78	0.370	11.77	0.190	10.53
EQ_2D_1axis_3	CNP 100%	3.313	8.93	0.819	8.58	1.334	8.77	0.445	10.26
EQ_2D_1axis_4	RRS 16%	0.519	2.73	0.253	2.68	0.187	2.63	0.121	4.56
EQ_2D_1axis_5	RRS 44%	2.015	2.81	0.703	3.20	0.767	2.67	0.313	6.86
EQ_2D_1axis_6	RRS 100%	N/A	N/A	N/A	N/A	N/A	N/A	N/A	N/A
SHORT		**EAST**				**WEST**			
Load Case	**Ground Motion**	**$\Delta v_1/h$ (%)**	**t_* (s)**	**$\Delta v_2/h$ (%)**	**t_* (s)**	**$\Delta v_1/h$ (%)**	**t_* (s)**	**$\Delta v_2/h$ (%)**	**t_* (s)**
EQ_2D_1axis_1	CNP 16%	0.133	5.94	0.092	5.71	0.137	10.19	0.116	8.46
EQ_2D_1axis_2	CNP 44%	0.447	10.01	0.251	10.02	0.439	10.00	0.263	6.00
EQ_2D_1axis_3	CNP 100%	1.486	9.52	0.681	9.86	1.631	10.11	0.740	9.85
EQ_2D_1axis_4	RRS 16%	0.298	6.00	0.153	6.05	0.270	5.99	0.156	4.09
EQ_2D_1axis_5	RRS 44%	0.617	2.58	0.314	6.09	0.635	2.58	0.327	6.11
EQ_2D_1axis_6	RRS 100%	N/A	N/A	N/A	N/A	N/A	N/A	N/A	N/A

Table F-17: A1-2D-b model peak wall line base shear, nonlinear time history analysis

LONG		SOUTH		NORTH		% of Peak V_{bu}	
Load Case	**Ground Motion**	**Peak V_{bu} (kips)**	**t @ peak V_{bu} (s)**	**Peak V_{bu} (kips)**	**t @ peak V_{bu} (s)**	**South**	**North**
EQ_2D_1axis_1	CNP 16%	4.5	13.02	4.5	8.68	57.0	44.2
EQ_2D_1axis_2	CNP 44%	14.1	9.99	15.0	11.78	44.1	53.6
EQ_2D_1axis_3	CNP 100%	20.1	8.79	24.9	8.72	36.9	43.6
EQ_2D_1axis_4	RRS 16%	9.7	2.73	9.7	2.63	42.6	57.5
EQ_2D_1axis_5	RRS 44%	20.1	2.72	21.0	2.67	37.2	43.6
EQ_2D_1axis_6	RRS 100%	N/A	N/A	N/A	N/A	N/A	N/A
SHORT		**EAST**		**WEST**		**% of Peak V_{bv}**	
Load Case	**Ground Motion**	**Peak V_{bv} (kips)**	**t @ peak V_{bv} (s)**	**Peak V_{bv} (kips)**	**t @ peak V_{bv} (s)**	**East**	**West**
EQ_2D_1axis_1	CNP 16%	4.3	5.94	4.2	9.96	52.4	48.7
EQ_2D_1axis_2	CNP 44%	10.4	5.99	10.2	10.00	51.2	49.3
EQ_2D_1axis_3	CNP 100%	17.9	9.21	19.8	10.07	35.3	49.4
EQ_2D_1axis_4	RRS 16%	7.7	6.01	7.4	6.00	51.6	49.7
EQ_2D_1axis_5	RRS 44%	12.8	2.58	12.7	2.58	50.2	49.8
EQ_2D_1axis_6	RRS 100%	N/A	N/A	N/A	N/A	N/A	N/A

Table F-18: A1-2D-b model wall line base shear breakdown, nonlinear time history analysis

LONG		SOUTH			NORTH		
Load Case	**Ground Motion**	**Peak V_{bu} (kips)**	**SW V_{bu} (%)**	**GW V_{bu} (%)**	**Peak V_{bu} (kips)**	**SW V_{bu} (%)**	**GW V_{bu} (%)**
EQ_2D_1axis_1	CNP 16%	4.5	80.8	19.2	4.5	94.4	5.6
EQ_2D_1axis_2	CNP 44%	14.1	76.3	23.7	15.0	91.5	8.5
EQ_2D_1axis_3	CNP 100%	20.1	73.7	26.3	24.9	86.7	13.3
EQ_2D_1axis_4	RRS 16%	9.7	79.2	20.8	9.7	93.6	6.4
EQ_2D_1axis_5	RRS 44%	20.1	73.5	26.5	21.0	89.8	10.2
EQ_2D_1axis_6	RRS 100%	N/A	N/A	N/A	N/A	N/A	N/A
SHORT		**EAST**			**WEST**		
Load Case	**Ground Motion**	**Peak V_{bv} (kips)**	**SW V_{bv} (%)**	**GW V_{bu} (%)**	**Peak V_{bv} (kips)**	**SW V_{bv} (%)**	**GW V_{bv} (%)**
EQ_2D_1axis_1	CNP 16%	4.3	95.1	4.9	4.2	96.4	3.6
EQ_2D_1axis_2	CNP 44%	10.4	92.4	7.6	10.2	95.0	5.0
EQ_2D_1axis_3	CNP 100%	17.9	88.9	11.1	19.8	93.4	6.6
EQ_2D_1axis_4	RRS 16%	7.7	94.9	5.1	7.4	95.6	4.4
EQ_2D_1axis_5	RRS 44%	12.8	91.9	8.1	12.7	95.2	4.8
EQ_2D_1axis_6	RRS 100%	N/A	N/A	N/A	N/A	N/A	N/A

Table F-19: A1-2D-b model peak hold down tensile force at certain locations, nonlinear time history analysis

		L1S1, LC5		L1S1, LC6		L1W1, LC7		L1W1, LC8	
Load Case	**Ground Motion**	**Peak F (kips)**	**t @ peak F (s)**	**Peak F (kips)**	**t @ peak F (s)**	**Peak F (kips)**	**t @ peak F (s)**	**Peak F (kips)**	**t @ peak F (s)**
EQ_2D_1axis_1	CNP 16%	-0.66	13.02	-1.01	13.26	-0.68	5.73	-0.35	5.96
EQ_2D_1axis_2	CNP 44%	-1.88	9.71	-3.75	8.79	-1.92	10.01	-0.91	5.99
EQ_2D_1axis_3	CNP 100%	-3.02	6.73	-5.67	7.08	-4.59	9.49	-1.97	9.83
EQ_2D_1axis_4	RRS 16%	-1.00	3.05	-2.33	2.71	-1.32	6.00	-0.58	4.10
EQ_2D_1axis_5	RRS 44%	-2.74	3.18	-5.39	2.72	-2.11	6.11	-1.09	2.59
EQ_2D_1axis_6	RRS 100%	N/A	N/A	N/A	N/A	N/A	N/A	N/A	N/A

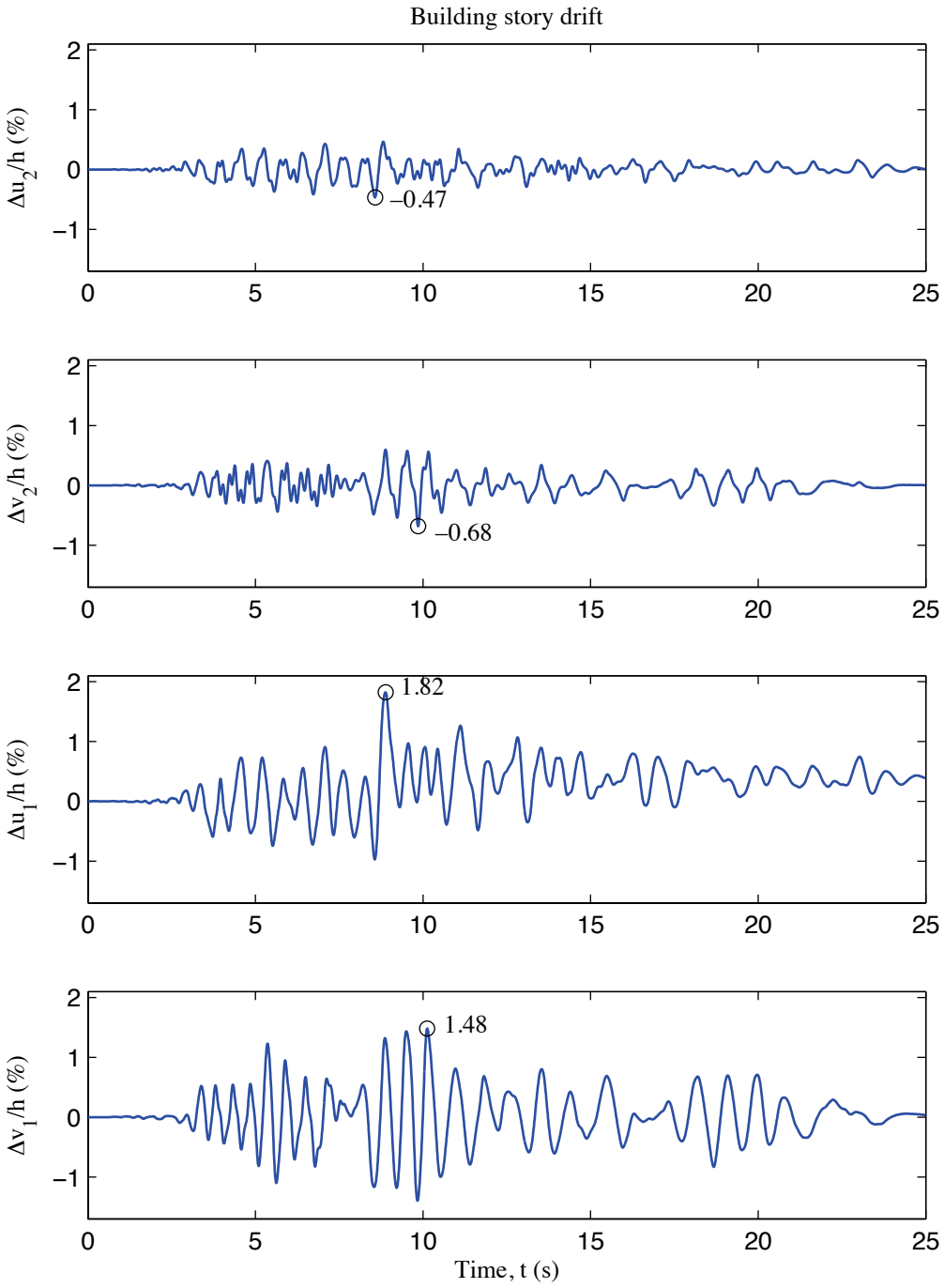

Figure F-6: A1-2D-b model building story drift, 100 % Canoga Park, 2D nonlinear analysis

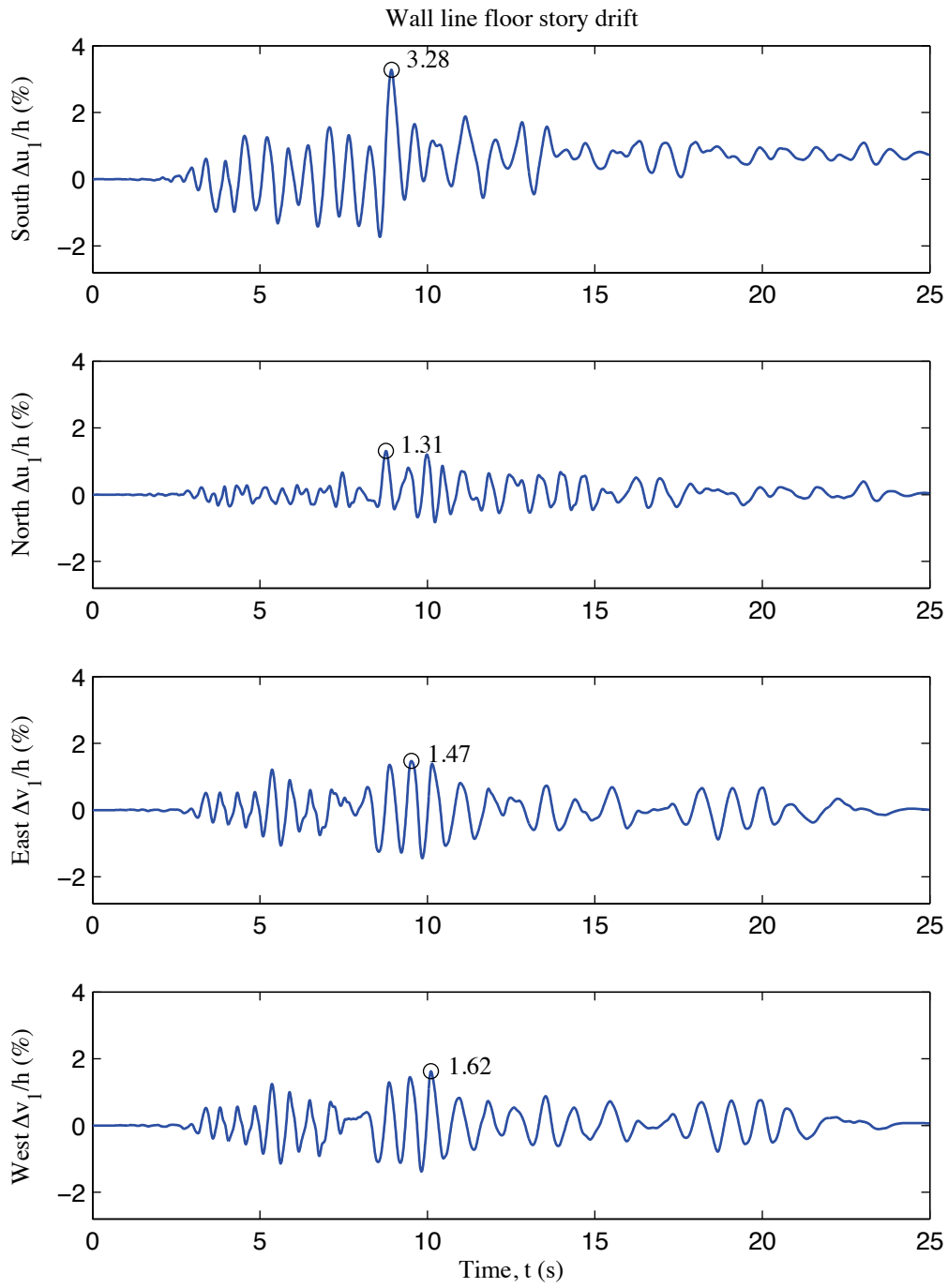

Figure F-7: A1-2D-b model wall line floor story drift, 100 % Canoga Park, 2D nonlinear analysis

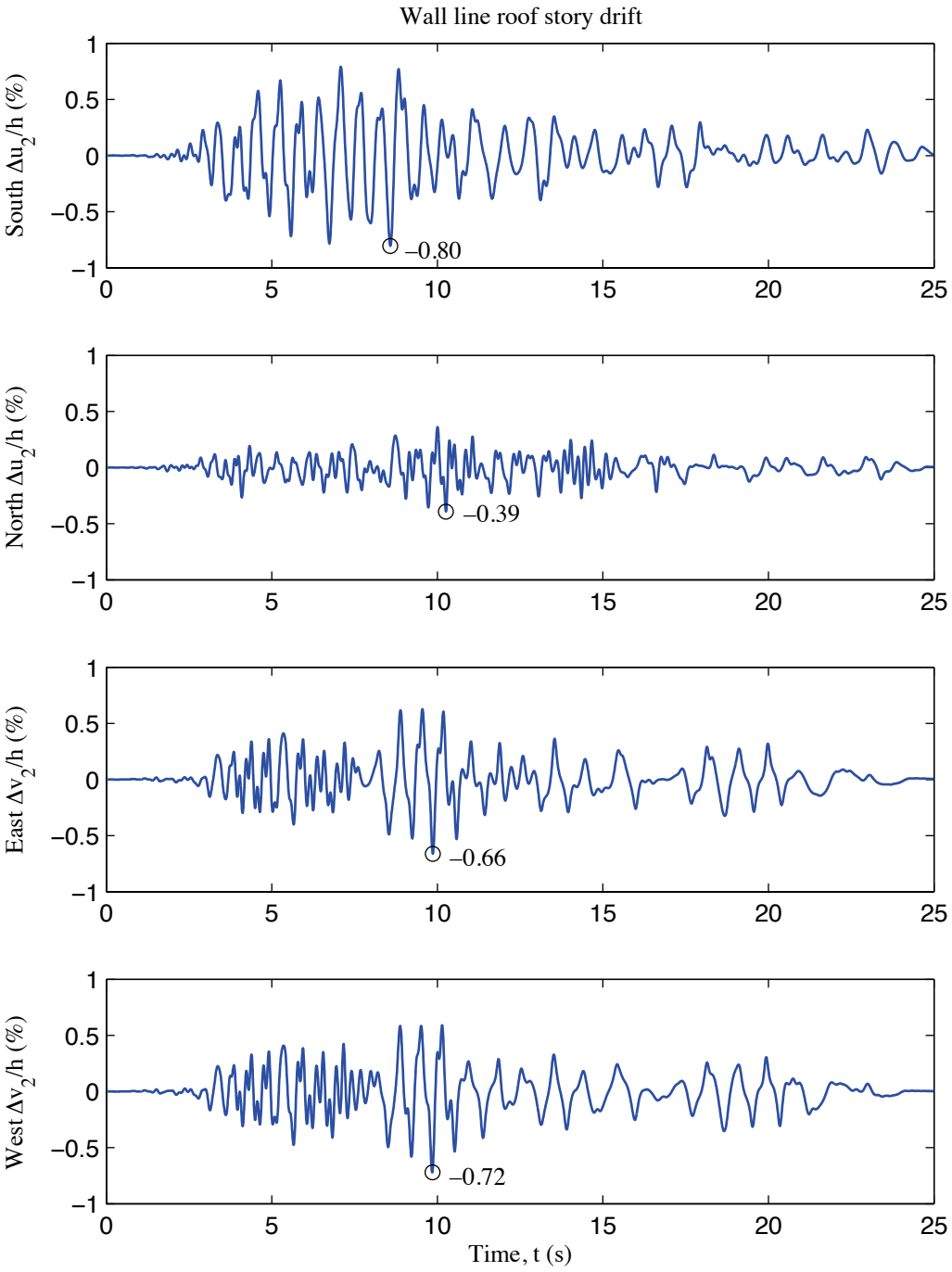

Figure F-8: A1-2D-b model wall line roof story drift, 100 % Canoga Park, 2D nonlinear analysis

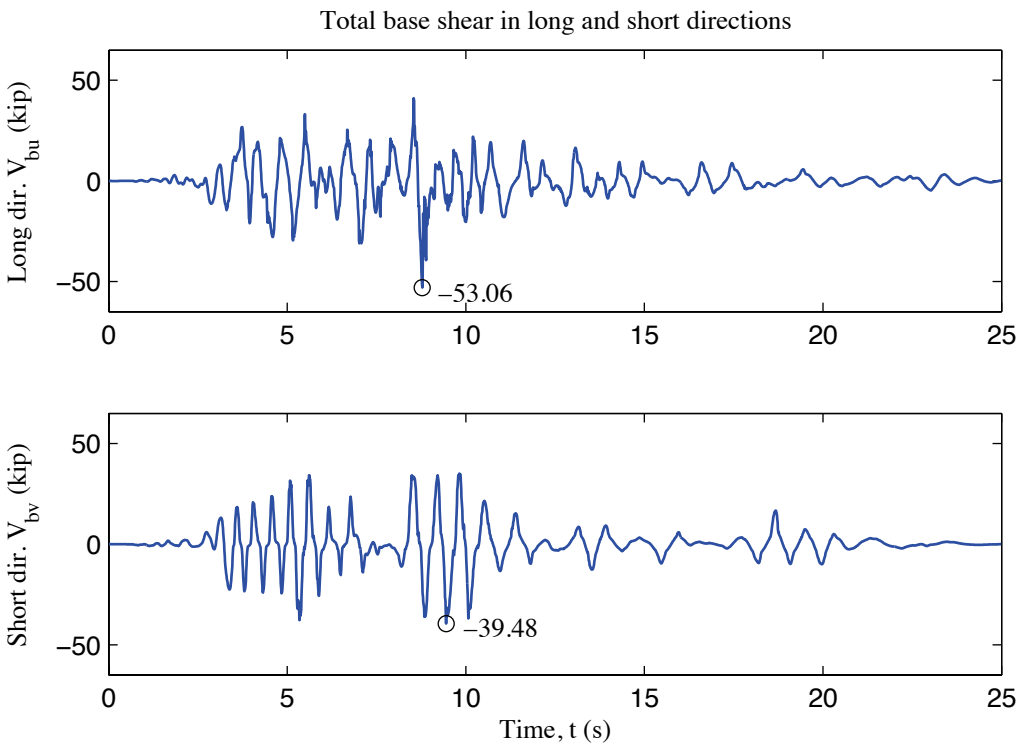

Figure F-9: A1-2D-b model total building base shear, 100 % Canoga Park, 2D nonlinear analysis

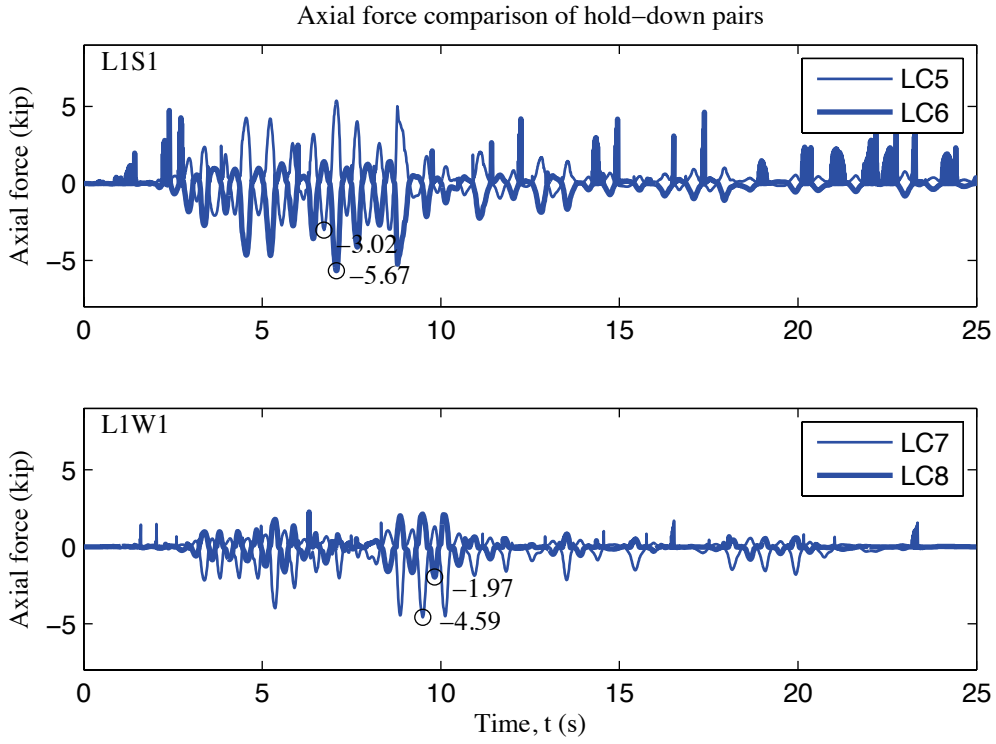

Figure F-10: A1-2D-b model, load cell 5 to 8 axial forces, 100 % Canoga Park, 2D nonlinear analysis

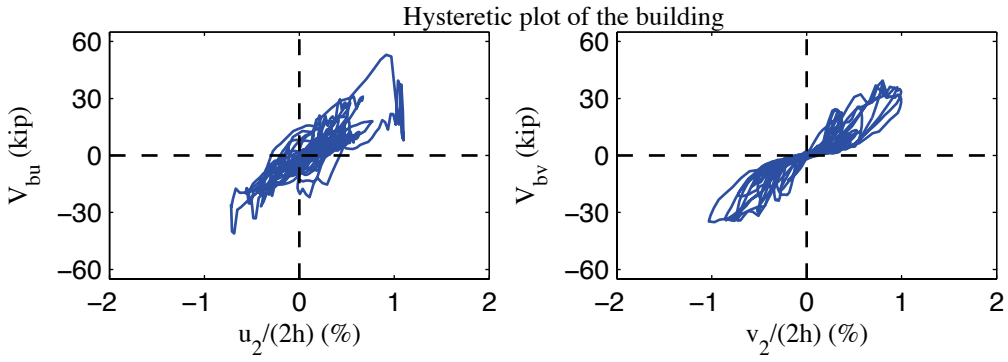

Figure F-11: A1-2D-b model, hysteretic plot of the building, 100 % Canoga Park, 2D nonlinear analysis

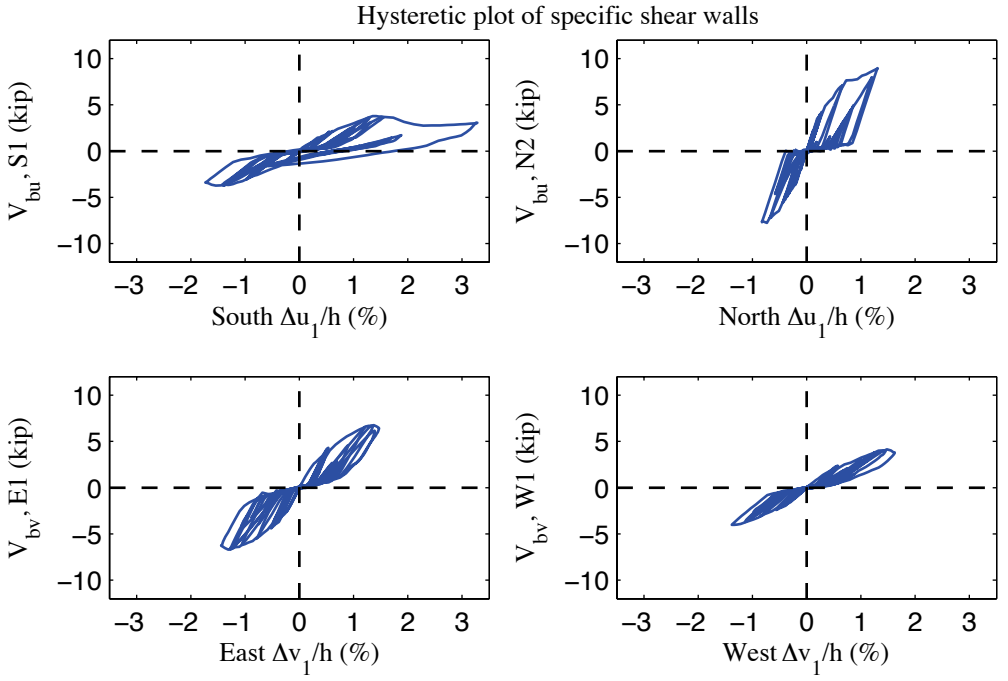

Figure F-12: A1-2D-b model, hysteretic plot of shear walls at each elevation, 100 % Canoga Park, 2D nonlinear analysis

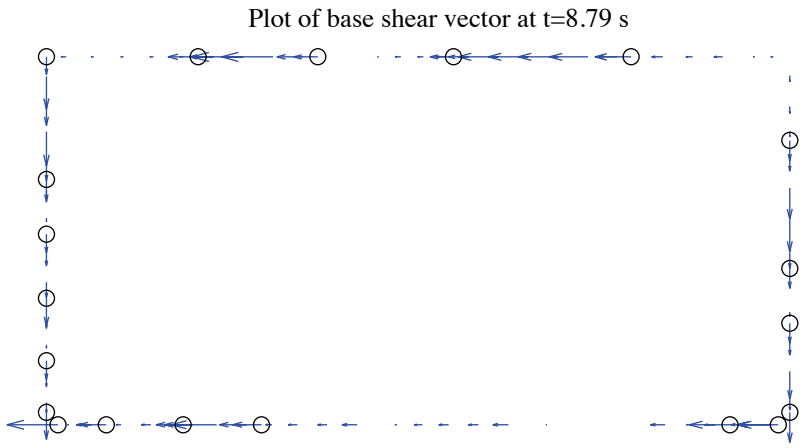

Figure F-13: A1-2D-b model, field plot of peak total base shear, 100 % Canoga Park, 2D nonlinear analysis (maximum anchor/hold down base shear is 3.79 kips)

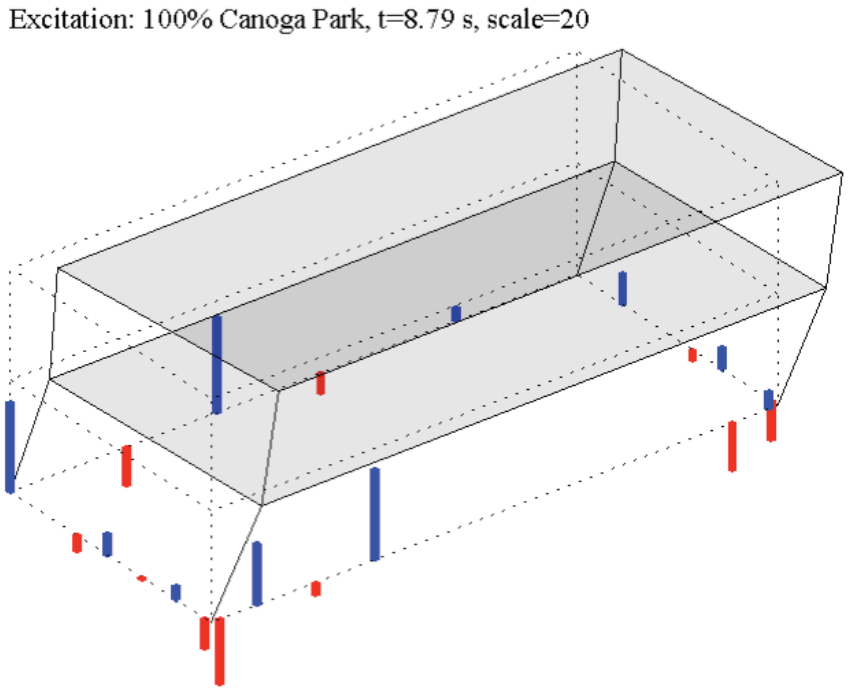

Figure F-14: A1-2D-b model, simplified illustration of corner displacements with hold down forces from load cells,100 % Canoga Park, 2D nonlinear analysis (max hold down tensile force is -5.25 kips)

Appendix G: Analysis Results of State-of-the-art, Phase 1, 2D, model c (A1-2D-c)

G.1 Model description

This set of state-of-the-art 2D models features bracing models of whole shear wall panels, explicit models of hold downs, and rigid leaning columns. Shear anchors are modeled as pin supports on bottom tracks of shear walls only. Interplay between different elevations is not allowed in 2D models, representing the effect of flexible diaphragms. Seismic mass is lumped at leaning column nodes. The lateral displacement and shear wall capacity ($\delta(0.2V_{nA}),0.2V_{nA}$) from test is utilized to determine the stiffness of elastic material and the first point on the backbone curve of Pinching4 material of shear wall bracing. Figure G-1 (a) to (d) illustrate OpenSees models of South, North, East and West elevations. Simulation results are presented and discussed in later sections. Definitions of output physical quantities and explanation of post-process method can be found in Appendix E.

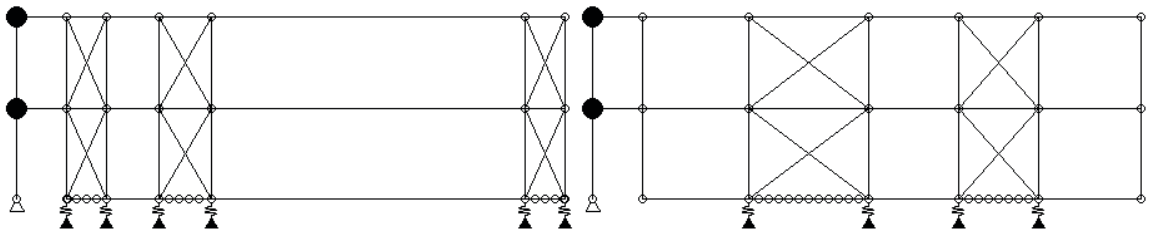

(a) South

(b) North

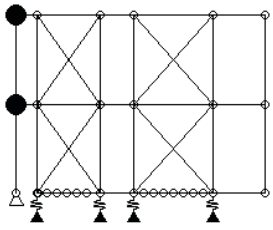

(c) East

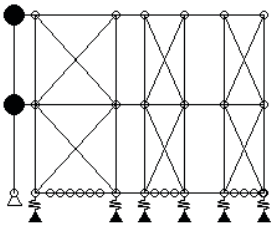

(d) West

Figure G-1: A1-2D-c model

G.2 Free vibration analysis results

Free vibration analysis is performed for each elevation model. Values of first two natural periods are tabulated (Table G-1). Figure G-2 shows corresponding mode shapes.

Table G-1: Free vibration analysis results, A1-2D-c model

Elevation	1st natural period (s)	2nd natural period (s)
South	0.649	0.195
North	0.355	0.157
East	0.480	0.150
West	0.492	0.150

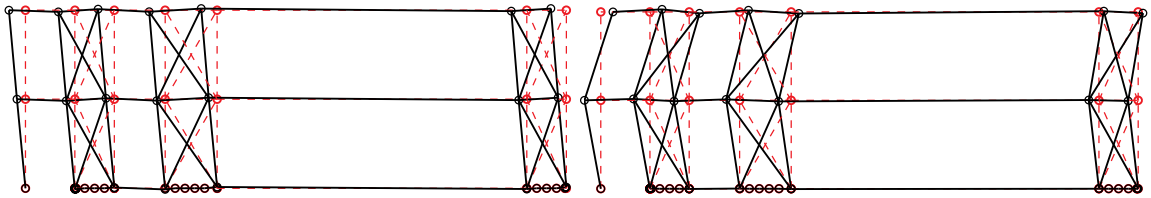

(a) South, mode 1, T_1=0.649 s (b) South, mode 2, T_2=0.195 s

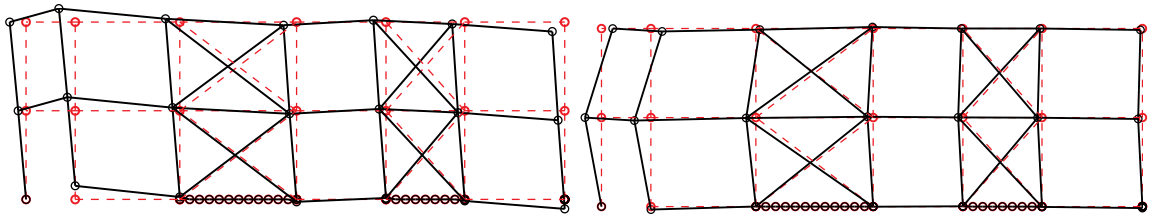

(c) North mode 1, T_1=0.355 s (d) North mode 2, T_2=0.157 s

(e) East mode 1, T_1=0.480 s (f) East mode 2, T_2=0.150 s

(g) West mode 1, T_1=0.492 s (h) West mode 2, T_2=0.150 s

Figure G-2: First two natural modes of A1-2D-c model

G.3 Linear static analysis results

Linear static analysis is performed on each wall line. The total lateral load on that wall line is one half of the design base shear. The vertical distribution of lateral load follows the distribution of equivalent lateral load in the design narrative (Madsen et al. 2011).

Although each wall line is analyzed independently, to make a better summary and to make better comparisons with 3D models, results of individual wall lines are post-processed to reconstruct physical quantities of the whole building behavior, such as building displacements/drifts and total building base shear.

Table G-2 summarizes the breakdown of peak total base shear among four elevations. As shown in the table, each of two facing wall lines take 5.5 kips of base shear, and wall lines perpendicular to the loading direction take zero base shear as a natural result of 2D analysis.

Table G-3 shows peak building and wall line deflections. Practicing engineers can linearly upscale these data and develop an estimate of the building's performance at a certain lateral force level. In 2D analysis, only wall lines along the loading direction have displacements in the loading direction.

Table G-4 is an evaluation of the each wall line's lateral stiffness of long and short direction and its breakdown among shear walls (SW) and other systems. Since gravity

walls (GW) are not modeled in this state-of-the-art model, all base shear goes to shear walls.

Table G-2: Breakdown of peak base shear, linear static analysis, A1-2D-c model

Load direction	**LONG**				
Elevation	**South V_b**	**North V_b**	**East V_b**	**West V_b**	**Peak V_b**
kips	5.5	5.5	0.0	0.0	11.1
%	50.0	50.0	0.0	0.0	100.0
Load direction	**SHORT**				
Elevation	**South V_b**	**North V_b**	**East V_b**	**West V_b**	**Peak V_b**
kips	0.0	0.0	5.5	5.5	11.1
%	0.0	0.0	50.0	50.0	100.0

Table G-3: Peak building and wall line deflection, linear static analysis, A1-2D-c model

Load direction	**LONG**							
Deflection (in.)	**u_1**	**u_2**	**v_1**	**v_2**	**Δu_1**	**Δu_2**	**Δv_1**	**Δv_2**
Building	0.289	0.557	0.000	0.000	0.289	0.268	0.000	0.000
South	0.455	0.873	0.000	0.000	0.455	0.418	0.000	0.000
North	0.122	0.241	0.000	0.000	0.122	0.119	0.000	0.000
East	-	-	-	-	-	-	-	-
West	-	-	-	-	-	-	-	-
Load direction	**SHORT**							
Deflection (in.)	**u_1**	**u_2**	**v_1**	**v_2**	**Δu_1**	**Δu_2**	**Δv_1**	**Δv_2**
Building	0.000	0.000	0.256	0.492	0.000	0.000	0.256	0.236
South	-	-	-	-	-	-	-	-
North	-	-	-	-	-	-	-	-
East	0.000	0.000	0.249	0.478	0.000	0.000	0.249	0.229
West	0.000	0.000	0.263	0.505	0.000	0.000	0.263	0.242

Table G-4: Breakdown of lateral stiffness, A1-2D-c model

SOUTH			**NORTH**		
Shear wall k_u (%)	**Gravity wall k_u (%)**	**k_u (kip/in)**	**Shear wall k_v (%)**	**Gravity wall k_v (%)**	**k_v (kip/in)**
100.0	0.0	6.3	100.0	0.0	22.9
EAST			**WEST**		
Shear wall k_u (%)	**Gravity wall k_u (%)**	**k_u (kip/in)**	**Shear wall k_v (%)**	**Gravity wall k_v (%)**	**k_v (kip/in)**
100.0	0.0	11.6	100.0	0.0	10.9

G.4 Nonlinear static (pushover) analysis results

Table G-5 is created following the same logic with Table G-2, but the analysis type is nonlinear static (pushover). Pushover curves of the building and each wall line are presented in Figure G-3 and Figure G-4.

These tables and figures indicate that the wall lines do not reach their peak capacity at exactly the same drift level. Accordingly, total capacity of the building reconstructed using 2D results is no greater than the sum of wall line capacities in the load direction. This observation is more apparent in long direction. The missing of diaphragm stiffness and induced interplay of wall lines can make a significant difference between 2D analysis and real 3D analysis.

Table G-5: Breakdown of peak base shear, pushover analysis, A1-2D-c model

Load direction	**LONG**				
Elevation	**South V_b**	**North V_b**	**East V_b**	**West V_b**	**Peak V_b**
kips	12.9	20.0	0.0	0.0	29.0
%	44.4	69.0	0.0	0.0	100.0
Load direction	**SHORT**				
Elevation	**South V_b**	**North V_b**	**East V_b**	**West V_b**	**Peak V_b**
kips	0.0	0.0	14.5	15.5	28.4
%	0.0	0.0	50.9	54.5	100.0

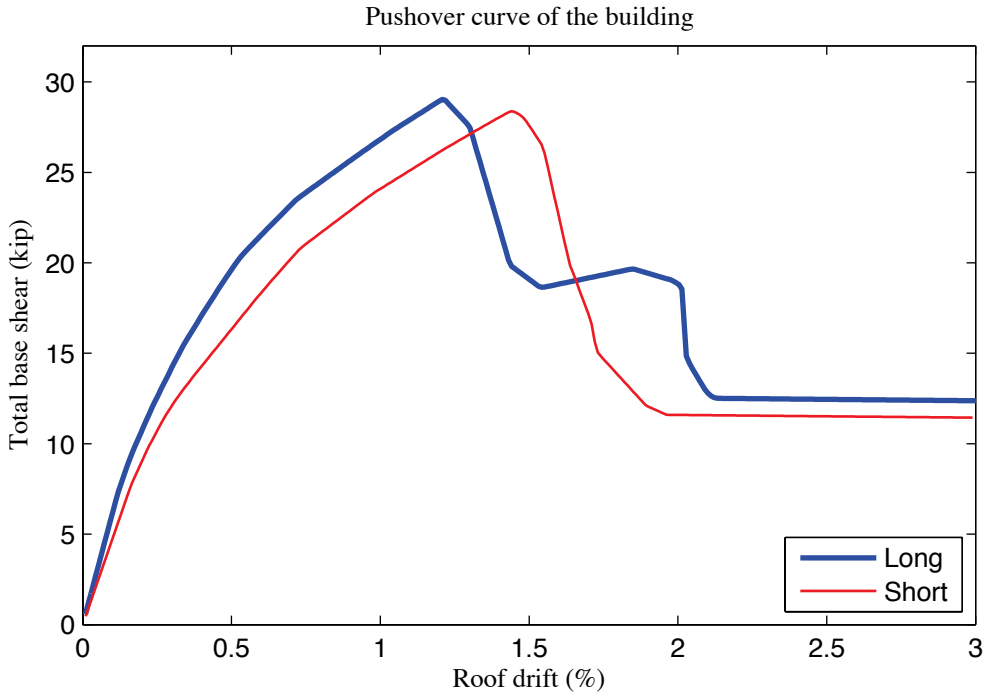

Figure G-3: Pushover curve of A1-2D-c model

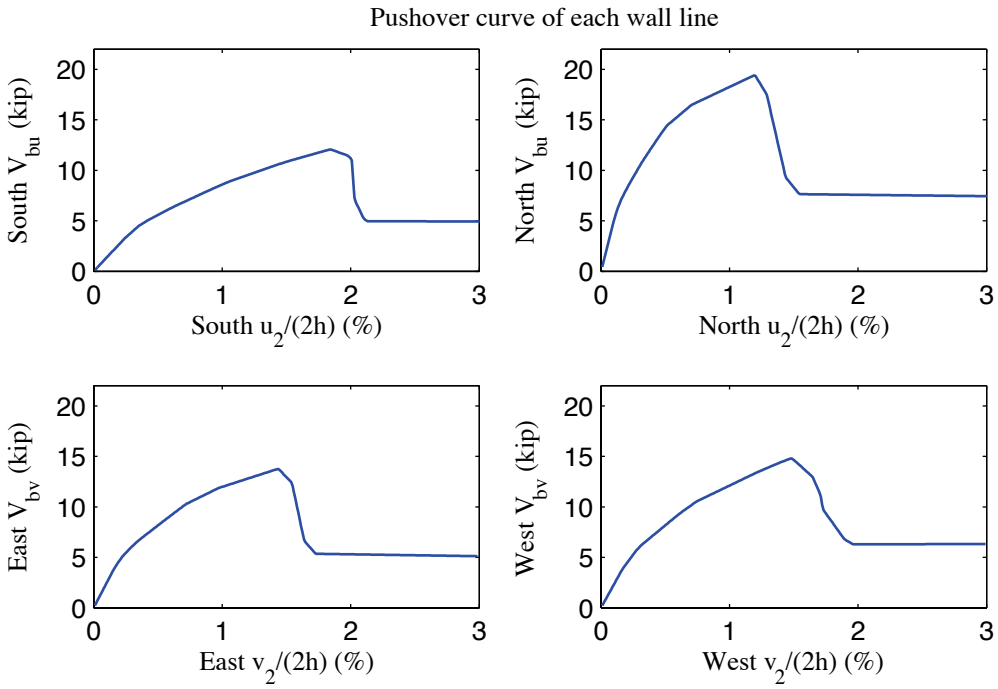

Figure G-4: Pushover curve of each wall line, A1-2D-c model

G.5 Linear time history analysis results

Linear time history analysis is performed on 2D models under Canoga Park and Rinaldi ground motion records of Northridge earthquake in 1994. We considered three scale levels (16%, 44% and 100%) and single axis excitation is applied in the lateral direction of a single wall line.

Table G-6 to Table G-9 demonstrate the reconstructed linear elastic performance of the building under designated ground motions. Table G-6 shows peak story relative accelerations in the unit of g. Table G-7 and Table G-8 report peak roof drift and story drift of the building and the corresponding time step (t_*) and the base shear at that time. Note that the base shear at the time of peak roof drift may not be the peak total building base shear in that direction (see Table G-9).

The response of each wall line is available directly from 2D analysis results, so peak story drift and peak base shear of each wall line are listed in Table G-10 and Table G-11.

Wall lines behave linearly since peak drift and peak base shear appear at the same time when the ground motion is linearly scaled. Figure G-5 is a vector plot of the peak total resultant base shear of the building under 100% Canoga Park excitation. Since four dynamical analyses in 2D should be performed separately in order to create the plot, base shear vectors are always in-line with the wall. Comparison with nonlinear analysis results of the same excitation provides insightful observations on the building's response and requirements on modeling fidelity and analysis type.

Table G-6: A1-2D-c model peak story relative acceleration in g, linear time history analysis

Load Case	Ground Motion	LONG			SHORT		
		a_g	Floor a	Roof a	a_g	Floor a	Roof a
EQ_2D_1axis_1	CNP 16%	0.067	0.076	0.160	0.057	0.131	0.219
EQ_2D_1axis_2	CNP 44%	0.185	0.208	0.439	0.157	0.360	0.603
EQ_2D_1axis_3	CNP 100%	0.420	0.502	0.999	0.356	0.818	1.357
EQ_2D_1axis_4	RRS 16%	0.132	0.127	0.260	0.078	0.131	0.257
EQ_2D_1axis_5	RRS 44%	0.363	0.349	0.715	0.214	0.361	0.705
EQ_2D_1axis_6	RRS 100%	0.825	0.789	1.622	0.486	0.817	1.603

Table G-7: A1-2D-c model peak building roof drift and base shear, linear time history analysis

Load Case	Ground Motion	LONG			SHORT		
		$u_2/(2h)$ (%)	t_* (s)	V_b @ t_* (kips)	$v_2/(2h)$ (%)	t_* (s)	V_b @ t_* (kips)
EQ_2D_1axis_1	CNP 16%	-0.209	9.23	7.2	-0.227	6.05	11.2
EQ_2D_1axis_2	CNP 44%	-0.575	9.23	19.9	-0.624	6.05	30.7
EQ_2D_1axis_3	CNP 100%	-1.306	9.23	45.2	-1.417	6.05	69.5
EQ_2D_1axis_4	RRS 16%	-0.441	3.15	15.0	-0.234	2.60	11.5
EQ_2D_1axis_5	RRS 44%	-1.213	3.15	41.2	-0.644	2.60	31.6
EQ_2D_1axis_6	RRS 100%	-2.746	3.15	93.4	-1.462	2.60	71.4

Table G-8: A1-2D-c model peak building story drift, linear time history analysis

Load Case	Ground Motion	LONG				SHORT			
		$\Delta u_1/h$ (%)	t_* (s)	$\Delta u_2/h$ (%)	t_* (s)	$\Delta v_1/h$ (%)	t_* (s)	$\Delta v_2/h$ (%)	t_* (s)
EQ_2D_1 axis_1	CNP 16%	-0.216	9.23	-0.203	9.24	-0.238	6.05	-0.216	6.05
EQ_2D_1 axis_2	CNP 44%	-0.595	9.23	-0.557	9.24	-0.654	6.05	-0.595	6.05
EQ_2D_1 axis_3	CNP 100%	-1.352	9.23	-1.267	9.24	-1.487	6.05	-1.347	6.05
EQ_2D_1 axis_4	RRS 16%	-0.453	3.14	-0.430	3.15	-0.245	2.60	-0.223	2.60
EQ_2D_1 axis_5	RRS 44%	-1.246	3.14	-1.182	3.15	-0.673	2.60	-0.614	2.60
EQ_2D_1 axis_6	RRS 100%	-2.817	3.14	-2.678	3.15	-1.533	2.61	-1.392	2.60

Table G-9: A1-2D-c model peak building base shear, linear time history analysis

		LONG		SHORT		RESULTANT	
Load Case	**Ground Motion**	**Peak V_{bu} (kip)**	**t @ peak V_{bu} (s)**	**Peak V_{bv} (kip)**	**t @ peak V_{bv} (s)**	**Peak V_b (kip)**	**t @ peak V_b (s)**
EQ_2D_1 axis_1	CNP 16%	7.3	9.24	11.2	6.30	11.3	6.05
EQ_2D_1 axis_2	CNP 44%	20.0	9.24	30.8	6.30	31.2	6.05
EQ_2D_1 axis_3	CNP 100%	45.4	9.24	69.7	6.30	70.6	6.05
EQ_2D_1 axis_4	RRS 16%	15.0	3.15	11.6	2.61	16.9	2.65
EQ_2D_1 axis_5	RRS 44%	41.2	3.15	31.8	2.61	46.5	2.65
EQ_2D_1 axis_6	RRS 100%	93.4	3.15	71.9	2.61	105.7	2.65

Table G-10: A1-2D-c model peak wall line story drift, linear time history analysis

LONG		**SOUTH**				**NORTH**			
Load Case	**Ground Motion**	**$\Delta u_1/h$ (%)**	**t_* (s)**	**$\Delta u_2/h$ (%)**	**t_* (s)**	**$\Delta u_1/h$ (%)**	**t_* (s)**	**$\Delta u_2/h$ (%)**	**t_* (s)**
EQ_2D_1axis_1	CNP 16%	0.461	9.84	0.430	9.85	0.106	11.95	0.117	11.94
EQ_2D_1axis_2	CNP 44%	1.267	9.84	1.183	9.85	0.290	11.95	0.323	11.94
EQ_2D_1axis_3	CNP 100%	2.870	9.84	2.656	9.85	0.660	11.95	0.734	11.94
EQ_2D_1axis_4	RRS 16%	0.831	3.14	0.806	3.15	0.231	4.60	0.258	4.59
EQ_2D_1axis_5	RRS 44%	2.286	3.14	2.216	3.15	0.635	4.60	0.710	4.59
EQ_2D_1axis_6	RRS 100%	5.196	2.79	5.019	3.15	1.444	4.60	1.613	4.59
SHORT		**EAST**				**WEST**			
Load Case	**Ground Motion**	**$\Delta v_1/h$ (%)**	**t_* (s)**	**$\Delta v_2/h$ (%)**	**t_* (s)**	**$\Delta v_1/h$ (%)**	**t_* (s)**	**$\Delta v_2/h$ (%)**	**t_* (s)**
EQ_2D_1axis_1	CNP 16%	0.242	6.04	0.227	6.04	0.247	6.06	0.228	6.06
EQ_2D_1axis_2	CNP 44%	0.666	6.04	0.625	6.04	0.680	6.06	0.627	6.06
EQ_2D_1axis_3	CNP 100%	1.512	6.04	1.414	6.04	1.546	6.06	1.426	6.06
EQ_2D_1axis_4	RRS 16%	0.248	2.60	0.232	2.59	0.253	2.61	0.233	2.60
EQ_2D_1axis_5	RRS 44%	0.681	2.60	0.638	2.59	0.696	2.61	0.641	2.60
EQ_2D_1axis_6	RRS 100%	1.551	2.60	1.448	2.59	1.581	2.61	1.457	2.60

Table G-11: A1-2D-c model peak wall line base shear, linear time history analysis

LONG		SOUTH		NORTH		% of Peak V_{bu}	
Load Case	**Ground Motion**	**Peak V_{bu} (kips)**	**t @ peak V_{bu} (s)**	**Peak V_{bu} (kips)**	**t @ peak V_{bu} (s)**	**South**	**North**
EQ_2D_1axis_1	CNP 16%	6.0	9.83	4.8	11.95	68.4	31.6
EQ_2D_1axis_2	CNP 44%	16.4	9.83	13.1	11.95	68.4	31.6
EQ_2D_1axis_3	CNP 100%	36.5	9.83	29.7	11.95	68.4	31.6
EQ_2D_1axis_4	RRS 16%	11.1	2.78	10.4	4.60	69.8	30.2
EQ_2D_1axis_5	RRS 44%	30.6	2.78	28.6	4.60	69.8	30.2
EQ_2D_1axis_6	RRS 100%	69.4	2.78	65.0	4.60	69.8	30.2
SHORT		**EAST**		**WEST**		**% of Peak V_{bv}**	
Load Case	**Ground Motion**	**Peak V_{bv} (kips)**	**t @ peak V_{bv} (s)**	**Peak V_{bv} (kips)**	**t @ peak V_{bv} (s)**	**East**	**West**
EQ_2D_1axis_1	CNP 16%	5.7	6.29	5.6	6.31	50.2	49.8
EQ_2D_1axis_2	CNP 44%	15.8	6.29	15.4	6.31	50.2	49.8
EQ_2D_1axis_3	CNP 100%	35.3	6.04	34.9	6.31	50.0	50.0
EQ_2D_1axis_4	RRS 16%	5.9	2.60	5.7	2.61	50.6	49.4
EQ_2D_1axis_5	RRS 44%	16.1	2.60	15.7	2.61	50.6	49.4
EQ_2D_1axis_6	RRS 100%	36.2	2.61	35.7	2.61	50.4	49.6

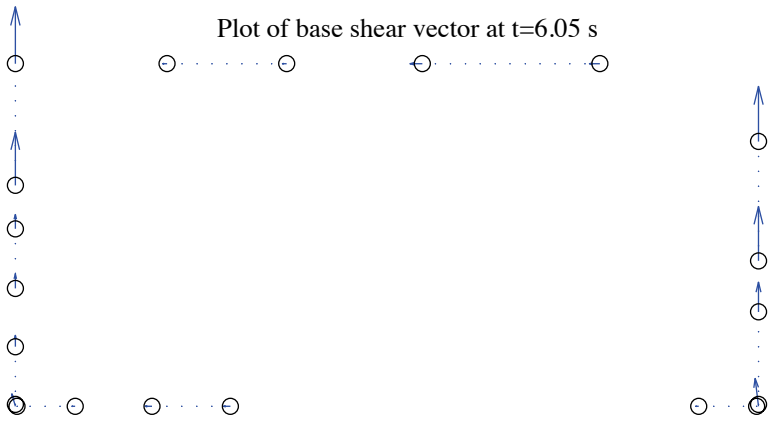

Figure G-5: A1-2D-c model, base shear vector plot at the moment of peak total base shear, 100 % Canoga Park, 2D linear analysis (maximum anchor/hold down base shear is 12.03 kips)

G.6 Nonlinear time history analysis results

Same ground motions are applied to the model with material and geometrical nonlinearity. Table G-12 to Table G-17 are replicas of Table G-6 to Table G-11, but for nonlinear time history analyses. Since this analysis type is most complicated and closest to reality and experiments, behavior of wall lines and smeared hold downs are further studied. Table G-18 expands the breakdown of each wall line's peak base shear between shear walls, gravity walls and other systems. Table G-19 is peak value of hold down tensile force of two selected pairs. Hold down 5 and 6 are on shear wall L1S1, South elevation and hold down 7 and 8 are on shear wall L1W1, West elevation. These shear walls have lowest capacities compared with others on the same wall line and they meet at the southwest edge of the building.

Time history plots in this section include plots of story drifts of the building and each wall line (Figure G-6 to Figure G-8), total building base shear in long and short direction (Figure G-9) and axial forces of hold downs in (Figure G-10). Hysteretic plots in Figure G-11 and Figure G-12 are helpful for visual examination of nonlinear base shear-drift relationship of the building and the weakest shear wall on each wall line. In comparison with linear time history analysis, vector plot of peak total base shear is illustrated in Figure G-13. Figure G-14 presents a simplified deformed shape of the building (see(Peterman 2014) for details of the method) and axial force of all twenty hold downs at the moment of peak total base shear. The same sign convention with tests is adopted. Red bars indicate tensile (negative) force and blue ones are for compressive (positive) force.

Hysteretic behavior is seen in the building and typical shear walls under design-based earthquake (100% Canoga Park excitation in one axis, see Figure G-11 and Figure G-12). However, behaviors of individual wall lines differ significantly. North wall line reaches 2.8% peak floor story drift and the backbone of response curve goes into the post peak deeply but peak story drifts of South wall lines, whose linear stiffness is much lower, is only 2.3%. The reconstructed peak building story drift is 2.5% in long direction and 1.5% in short direction (Table G-14). Under this excitation, the peak drift of worst-case scenario in 2D analysis is comparable to reconstructed peak building story drift. As shown in Figure G-7 floor drifts of facing wall lines are somewhat in phase, but the observation does not hold well for roof drift in Figure G-8. Table G-18 implies that peak resultant base shear is taken all by shear walls, and Figure G-13 shows that base shear vectors in anchors and hold downs align with wall lines due to the limit of 2D modeling and analysis. Table G-19, Figure G-10 and Figure G-14 demonstrate that axial forces of hold downs in a pair have almost the same magnitude but opposite signs, matching the assumption of Type I shear walls. This also suggests that the design assumption is valid when there is no gravity or other system in the wall line, and no coupling between wall lines is included.

The near-field Rinaldi record is much stronger in terms of peak ground acceleration, especially in the long direction. When loaded at 100%, peak story drifts of South and North elevation both exceed 14%. Peak story drift in short direction exceeds 6%, also large enough to cause failure. It is mentioning that peak total base shear of the building in

long direction (see the last row of Table G-15) is incredibly larger than the sum of shear wall capacities. The reason is that supports of leaning columns can take a large amount of base shear when shear walls fail so the analysis process may still proceed, but failure actually happens on the structure.

Table G-12: A1-2D-c model peak story relative acceleration in g, nonlinear time history analysis

Load Case	Ground Motion	LONG			SHORT		
		a_g	Floor a	Roof a	a_g	Floor a	Roof a
EQ_2D_1axis_1	CNP 16%	0.067	0.362	0.407	0.057	0.244	0.271
EQ_2D_1axis_2	CNP 44%	0.185	2.229	5.161	0.157	1.104	1.488
EQ_2D_1axis_3	CNP 100%	0.420	1.773	1.575	0.356	0.800	0.997
EQ_2D_1axis_4	RRS 16%	0.132	0.422	0.545	0.078	0.355	0.237
EQ_2D_1axis_5	RRS 44%	0.363	1.312	1.312	0.214	0.539	0.775
EQ_2D_1axis_6	RRS 100%	0.825	3.751	2.404	0.486	1.671	0.868

Table G-13: A1-2D-c model peak building roof drift and base shear, nonlinear time history analysis

Load Case	Ground Motion	LONG			SHORT		
		$u_2/(2h)$ (%)	t_* (s)	V_b @ t_* (kips)	$v_2/(2h)$ (%)	t_* (s)	V_b @ t_* (kips)
EQ_2D_1axis_1	CNP 16%	-0.187	9.25	6.3	-0.210	6.08	9.1
EQ_2D_1axis_2	CNP 44%	0.484	8.85	9.7	-0.570	9.85	14.8
EQ_2D_1axis_3	CNP 100%	1.614	8.98	17.2	-1.013	8.60	25.9
EQ_2D_1axis_4	RRS 16%	0.439	2.85	9.0	-0.233	2.60	10.1
EQ_2D_1axis_5	RRS 44%	1.858	3.03	1.3	-0.613	2.72	19.4
EQ_2D_1axis_6	RRS 100%	8.368	3.17	12.4	3.605	6.71	15.2

Table G-14: A1-2D-c model peak building story drift, nonlinear time history analysis

Load Case	Ground Motion	LONG				SHORT			
		$\Delta u_1/h$ (%)	t_* (s)	$\Delta u_2/h$ (%)	t_* (s)	$\Delta v_1/h$ (%)	t_* (s)	$\Delta v_2/h$ (%)	t_* (s)
EQ_2D_1 axis_1	CNP 16%	-0.199	9.24	-0.179	9.26	-0.232	6.07	-0.204	6.61
EQ_2D_1 axis_2	CNP 44%	0.622	8.86	0.370	7.16	0.668	10.13	-0.541	9.86
EQ_2D_1 axis_3	CNP 100%	2.480	8.96	0.786	9.00	-1.381	8.62	-0.727	8.55
EQ_2D_1 axis_4	RRS 16%	0.604	2.83	-0.313	3.30	-0.260	2.62	-0.215	2.59
EQ_2D_1 axis_5	RRS 44%	3.500	2.99	0.825	2.81	-0.806	2.70	0.459	6.12
EQ_2D_1 axis_6	RRS 100%	16.129	3.18	-0.700	2.40	6.676	6.69	0.767	3.88

Table G-15: A1-2D-c model peak building base shear, nonlinear time history analysis

		LONG		SHORT		RESULTANT	
Load Case	**Ground Motion**	**Peak V_{bu} (kip)**	**t @ peak V_{bu} (s)**	**Peak V_{bv} (kip)**	**t @ peak V_{bv} (s)**	**Peak V_b (kip)**	**t @ peak V_b (s)**
EQ_2D_1 axis_1	CNP 16%	6.4	9.24	9.8	6.05	10.2	6.05
EQ_2D_1 axis_2	CNP 44%	18.4	8.78	17.9	8.83	22.3	8.83
EQ_2D_1 axis_3	CNP 100%	32.2	8.92	26.6	8.90	40.2	8.92
EQ_2D_1 axis_4	RRS 16%	13.6	2.68	10.6	2.63	16.4	2.65
EQ_2D_1 axis_5	RRS 44%	97.9	2.98	20.6	2.63	97.9	2.98
EQ_2D_1 axis_6	RRS 100%	381.6	3.42	67.8	5.95	381.8	3.42

Table G-16: A1-2D-c model peak wall line story drift, nonlinear time history analysis

LONG		**SOUTH**				**NORTH**			
Load Case	**Ground Motion**	**$\Delta u_1/h$ (%)**	**t_* (s)**	**$\Delta u_2/h$ (%)**	**t_* (s)**	**$\Delta u_1/h$ (%)**	**t_* (s)**	**$\Delta u_2/h$ (%)**	**t_* (s)**
EQ_2D_1axis_1	CNP 16%	0.401	9.54	0.371	9.59	0.107	11.95	0.120	11.94
EQ_2D_1axis_2	CNP 44%	1.118	8.93	0.815	8.93	0.604	8.76	0.363	10.03
EQ_2D_1axis_3	CNP 100%	2.256	8.98	1.351	9.01	2.843	8.93	0.625	8.57
EQ_2D_1axis_4	RRS 16%	1.167	2.84	0.691	3.30	0.247	2.66	0.183	2.62
EQ_2D_1axis_5	RRS 44%	6.754	3.05	1.323	2.82	1.521	2.77	0.649	3.19
EQ_2D_1axis_6	RRS 100%	14.125	3.23	1.054	2.40	18.744	5.87	0.591	2.68
SHORT		**EAST**				**WEST**			
Load Case	**Ground Motion**	**$\Delta v_1/h$ (%)**	**t_* (s)**	**$\Delta v_2/h$ (%)**	**t_* (s)**	**$\Delta v_1/h$ (%)**	**t_* (s)**	**$\Delta v_2/h$ (%)**	**t_* (s)**
EQ_2D_1axis_1	CNP 16%	0.237	6.05	0.231	6.33	0.240	6.07	0.244	6.63
EQ_2D_1axis_2	CNP 44%	0.650	9.51	0.572	9.86	0.710	10.12	0.573	9.85
EQ_2D_1axis_3	CNP 100%	1.415	8.62	0.761	8.54	1.380	8.62	0.814	9.70
EQ_2D_1axis_4	RRS 16%	0.262	2.62	0.227	2.59	0.269	2.63	0.226	2.59
EQ_2D_1axis_5	RRS 44%	0.796	2.69	0.478	6.12	0.837	2.70	0.485	6.12
EQ_2D_1axis_6	RRS 100%	7.916	6.79	0.866	2.83	5.856	6.54	1.026	6.33

Table G-17: A1-2D-c model peak wall line base shear, nonlinear time history analysis

LONG		SOUTH		NORTH		% of Peak V_{bu}	
Load Case	**Ground Motion**	**Peak V_{bu} (kips)**	**t @ peak V_{bu} (s)**	**Peak V_{bu} (kips)**	**t @ peak V_{bu} (s)**	**South**	**North**
EQ_2D_1axis_1	CNP 16%	4.9	9.84	4.8	11.95	65.8	36.5
EQ_2D_1axis_2	CNP 44%	8.4	8.93	14.0	8.76	16.3	71.1
EQ_2D_1axis_3	CNP 100%	12.8	8.96	19.8	8.78	38.4	26.9
EQ_2D_1axis_4	RRS 16%	9.2	2.83	8.3	2.66	38.1	58.6
EQ_2D_1axis_5	RRS 44%	12.8	2.77	19.1	2.77	7.5	0.1
EQ_2D_1axis_6	RRS 100%	13.2	2.33	19.7	2.65	1.2	1.2
SHORT		**EAST**		**WEST**		**% of Peak V_{bv}**	
Load Case	**Ground Motion**	**Peak V_{bv} (kips)**	**t @ peak V_{bv} (s)**	**Peak V_{bv} (kips)**	**t @ peak V_{bv} (s)**	**East**	**West**
EQ_2D_1axis_1	CNP 16%	5.2	6.04	5.0	6.06	51.1	50.3
EQ_2D_1axis_2	CNP 44%	9.0	9.49	9.5	10.11	47.9	47.0
EQ_2D_1axis_3	CNP 100%	13.2	8.62	13.4	8.62	44.6	46.8
EQ_2D_1axis_4	RRS 16%	5.4	2.63	5.4	2.64	51.2	50.5
EQ_2D_1axis_5	RRS 44%	10.3	2.67	10.6	2.70	47.7	46.5
EQ_2D_1axis_6	RRS 100%	12.7	2.34	15.6	2.71	2.1	2.2

Table G-18: A1-2D-c model wall line base shear breakdown, nonlinear time history analysis

LONG		SOUTH			NORTH		
Load Case	**Ground Motion**	**Peak V_{bu} (kips)**	**SW V_{bu} (%)**	**GW V_{bu} (%)**	**Peak V_{bu} (kips)**	**SW V_{bu} (%)**	**GW V_{bu} (%)**
EQ_2D_1axis_1	CNP 16%	4.9	100.0	0.0	4.8	100.0	0.0
EQ_2D_1axis_2	CNP 44%	8.4	100.0	0.0	14.0	100.0	0.0
EQ_2D_1axis_3	CNP 100%	12.8	100.0	0.0	19.8	100.0	0.0
EQ_2D_1axis_4	RRS 16%	9.2	100.0	0.0	8.3	100.0	0.0
EQ_2D_1axis_5	RRS 44%	12.8	100.0	0.0	19.1	100.0	0.0
EQ_2D_1axis_6	RRS 100%	13.2	100.0	0.0	19.7	100.0	0.0
SHORT		**EAST**			**WEST**		
Load Case	**Ground Motion**	**Peak V_{bv} (kips)**	**SW V_{bv} (%)**	**GW V_{bu} (%)**	**Peak V_{bv} (kips)**	**SW V_{bv} (%)**	**GW V_{bv} (%)**
EQ_2D_1axis_1	CNP 16%	5.2	100.0	0.0	5.0	100.0	0.0
EQ_2D_1axis_2	CNP 44%	9.0	100.0	0.0	9.5	100.0	0.0
EQ_2D_1axis_3	CNP 100%	13.2	100.0	0.0	13.4	100.0	0.0
EQ_2D_1axis_4	RRS 16%	5.4	100.0	0.0	5.4	100.0	0.0
EQ_2D_1axis_5	RRS 44%	10.3	100.0	0.0	10.6	100.0	0.0
EQ_2D_1axis_6	RRS 100%	12.7	100.0	0.0	15.6	100.0	0.0

Table G-19: A1-2D-c model peak hold down tensile force at certain locations, nonlinear time history analysis

		L1S1, LC5		L1S1, LC6		L1W1, LC7		L1W1, LC8	
Load Case	**Ground Motion**	**Peak F (kips)**	**t @ peak F (s)**	**Peak F (kips)**	**t @ peak F (s)**	**Peak F (kips)**	**t @ peak F (s)**	**Peak F (kips)**	**t @ peak F (s)**
EQ_2D_1axis_1	CNP 16%	-3.74	9.25	-4.16	9.57	-2.47	5.85	-2.39	6.10
EQ_2D_1axis_2	CNP 44%	-6.45	9.34	-8.06	8.94	-6.00	10.14	-5.79	9.84
EQ_2D_1axis_3	CNP 100%	-10.09	6.87	-11.55	8.99	-8.22	8.95	-7.72	8.57
EQ_2D_1axis_4	RRS 16%	-6.39	3.28	-7.34	2.85	-2.63	6.12	-2.65	2.61
EQ_2D_1axis_5	RRS 44%	-8.03	2.49	-12.58	2.79	-5.33	6.13	-5.49	2.71
EQ_2D_1axis_6	RRS 100%	-10.12	2.35	-9.10	3.18	-10.10	3.87	-9.61	2.76

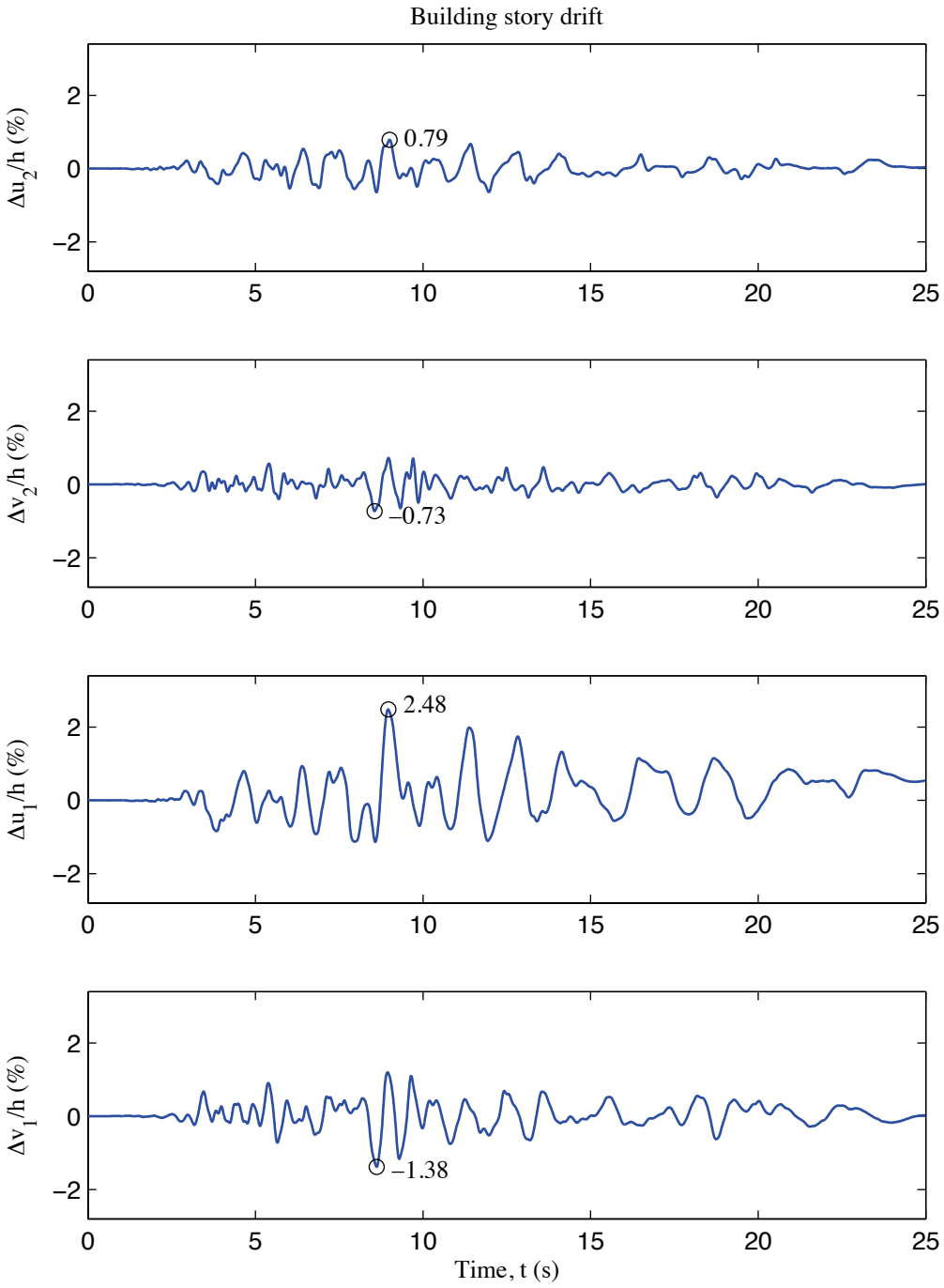

Figure G-6: A1-2D-c model building story drift, 100 % Canoga Park, 2D nonlinear analysis

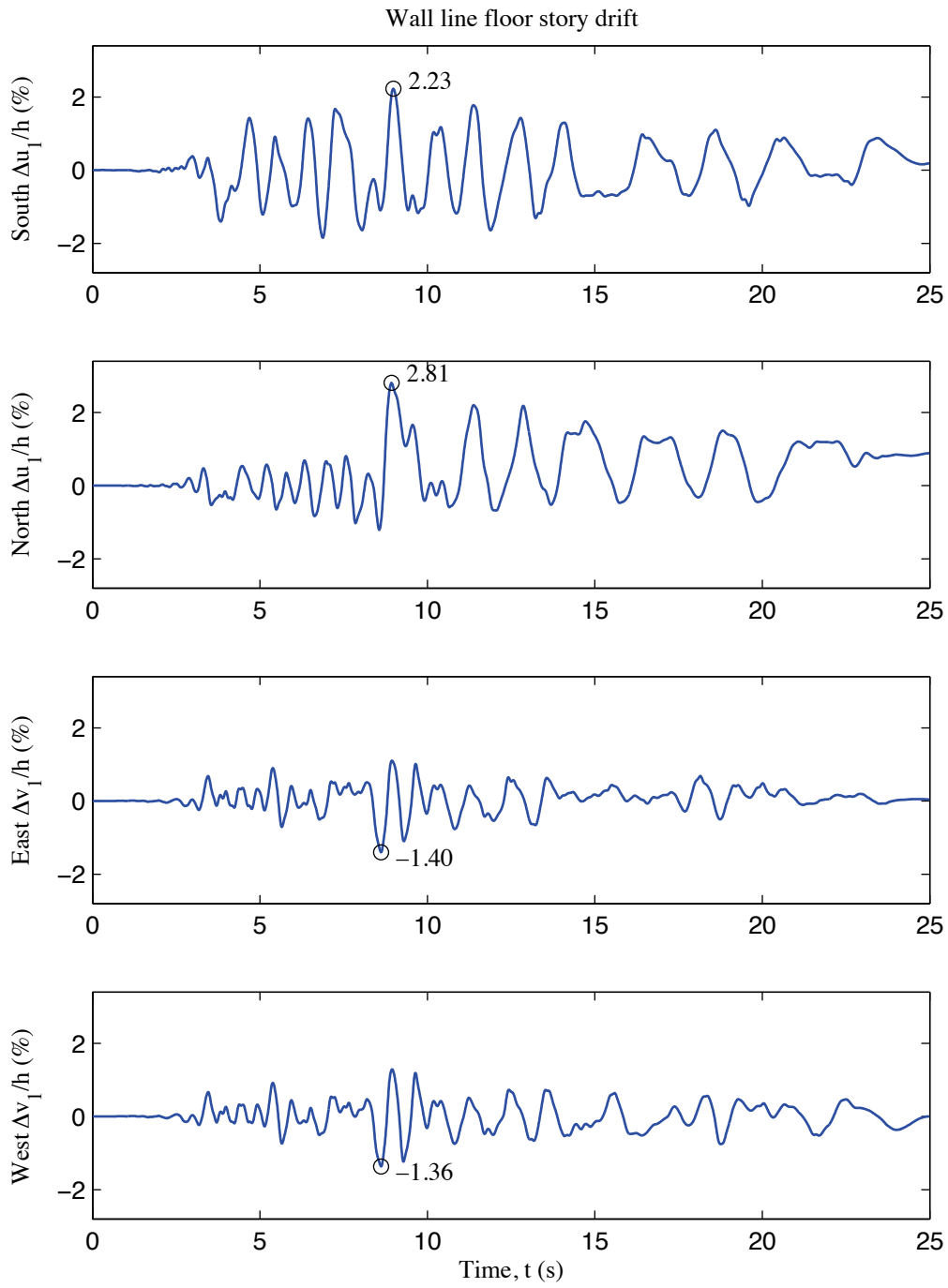

Figure G-7: A1-2D-c model wall line floor story drift, 100 % Canoga Park, 2D nonlinear analysis

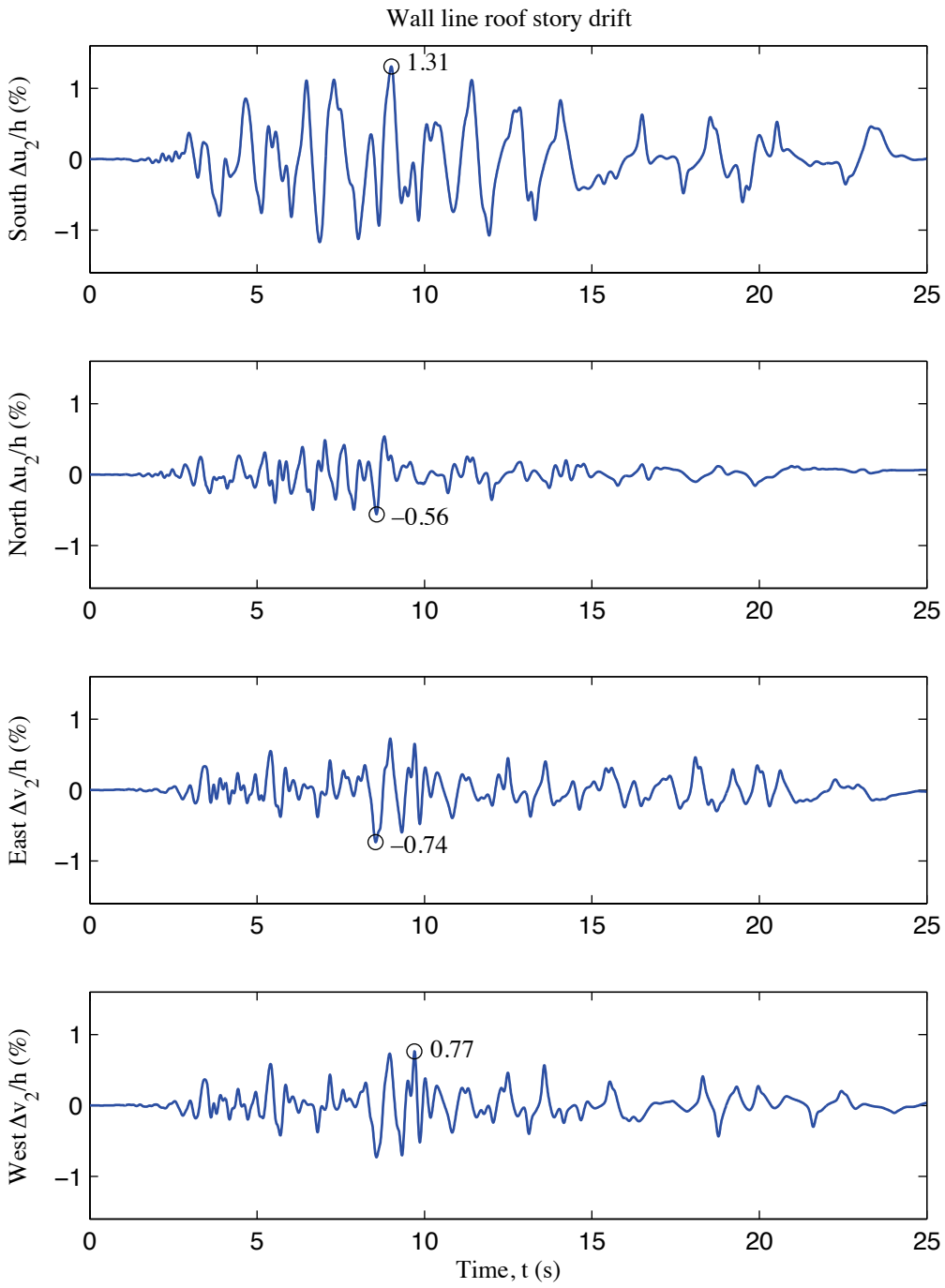

Figure G-8: A1-2D-c model wall line roof story drift, 100 % Canoga Park, 2D nonlinear analysis

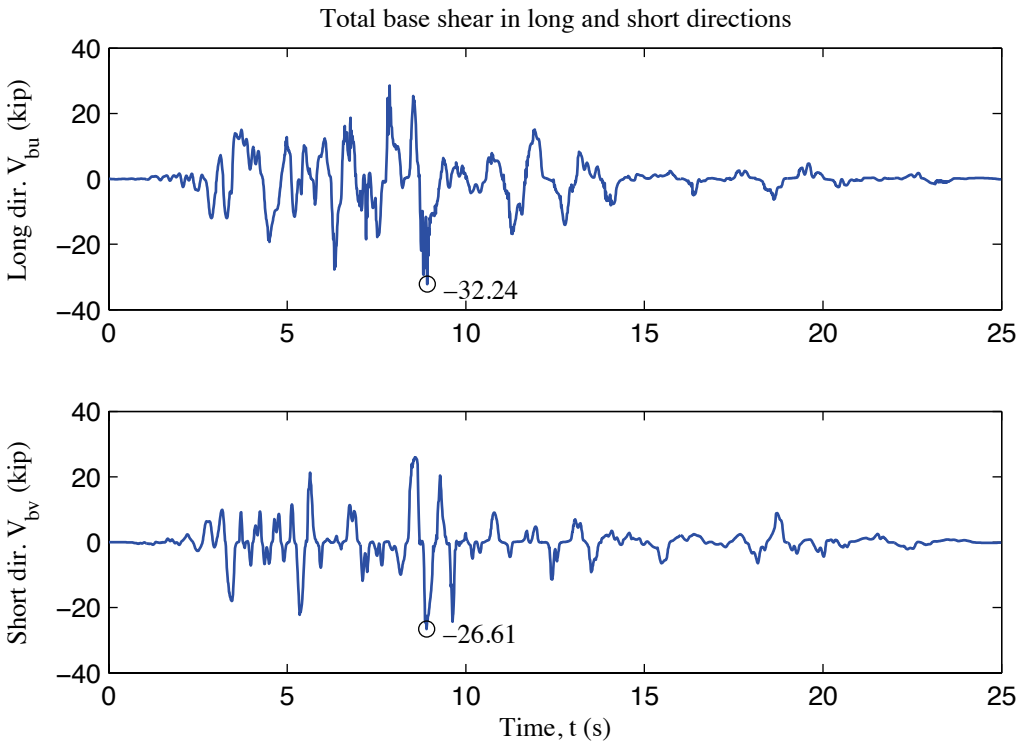

Figure G-9: A1-2D-c model total building base shear, 100 % Canoga Park, 2D nonlinear analysis

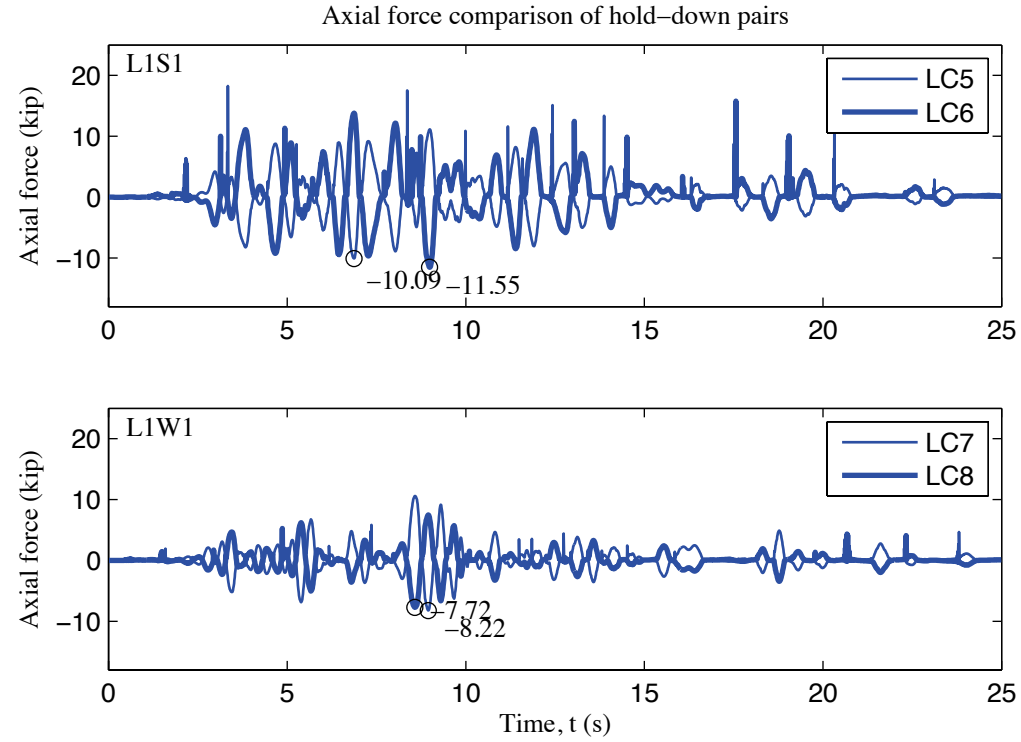

Figure G-10: A1-2D-c model, load cell 5 to 8 axial forces, 100 % Canoga Park, 2D nonlinear analysis

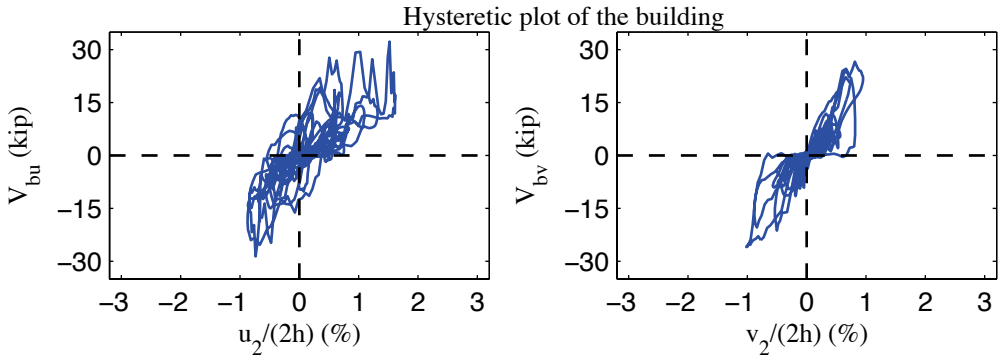

Figure G-11: A1-2D-c model, hysteretic plot of the building, 100 % Canoga Park, 2D nonlinear analysis

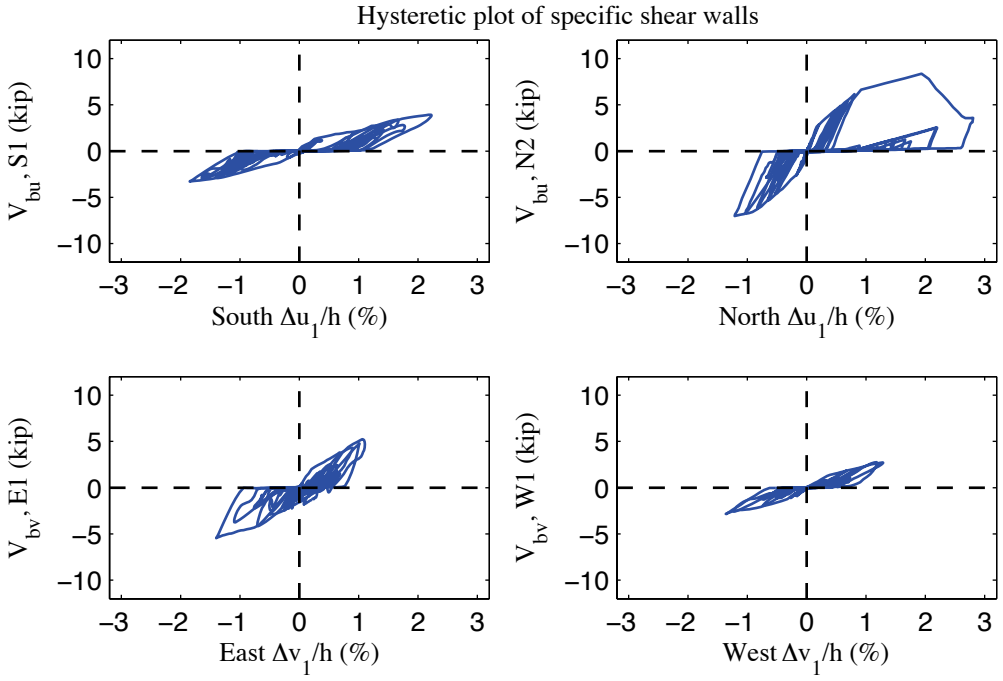

Figure G-12: A1-2D-c model, hysteretic plot of shear walls at each elevation, 100 % Canoga Park, 2D nonlinear analysis

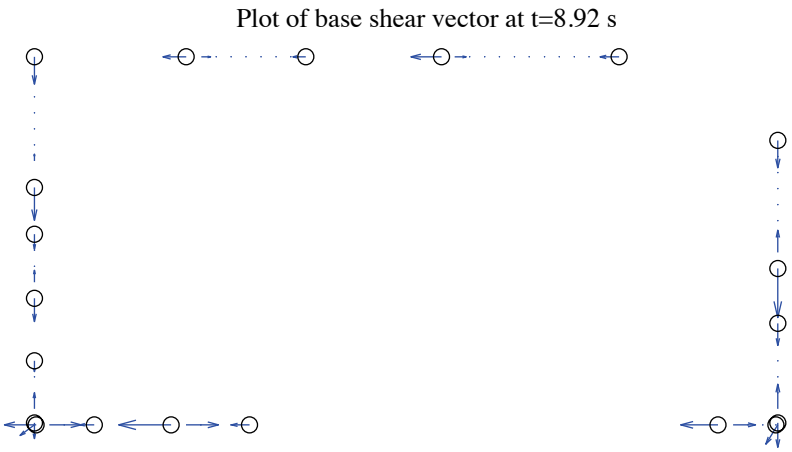

Figure G-13: A1-2D-c model, field plot of peak total base shear, 100 % Canoga Park, 2D nonlinear analysis (maximum anchor/hold down base shear is 6.96 kips)

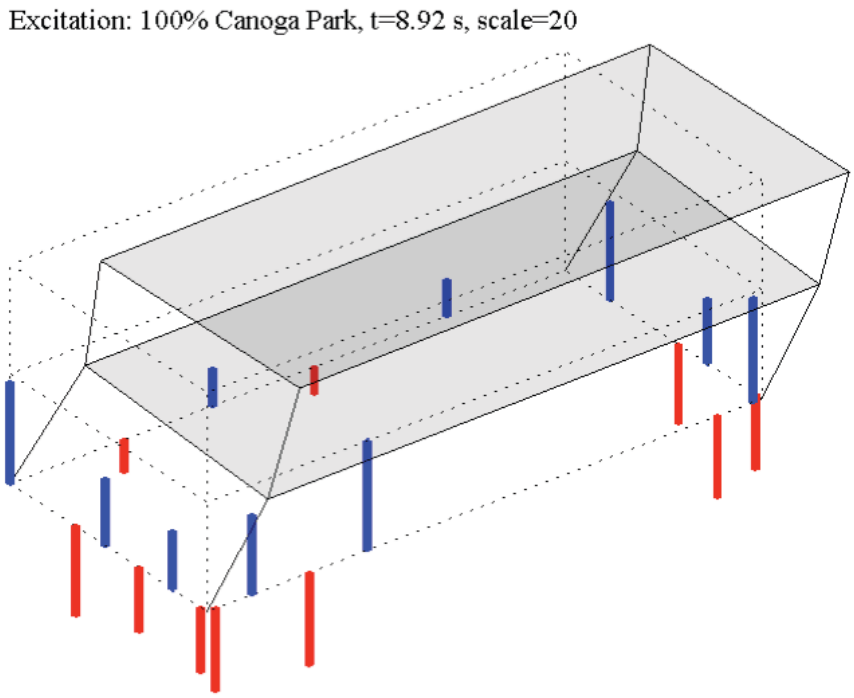

Figure G-14: A1-2D-c model, simplified illustration of corner displacements with hold down forces from load cells,100 % Canoga Park, 2D nonlinear analysis (max hold down tensile force is -11.36 kips)

Appendix H: Analysis Results of State-of-the-art, Phase 1, 3D, rigid-diaphragm, model a (A1-3D-RD-a)

H.1 Model description

This state-of-the-art 3D model features subpanel bracing models of shear walls, explicit models of hold downs, bare steel framing of gravity walls, and rigid diaphragms. Seismic mass is distributed to corners and stud ends. The lateral displacement and shear wall capacity ($\delta(0.2V_{nA})$, $0.2V_{nA}$) from test is utilized to determine the stiffness of elastic material and the first point on the backbone curve of Pinching4 material of shear wall bracing. Figure H-1 is the 3D drawing of the building model with all members and diagonal bracings of sheathing panels. Definitions of output physical quantities and explanation of post-process method can be found in Appendix K.

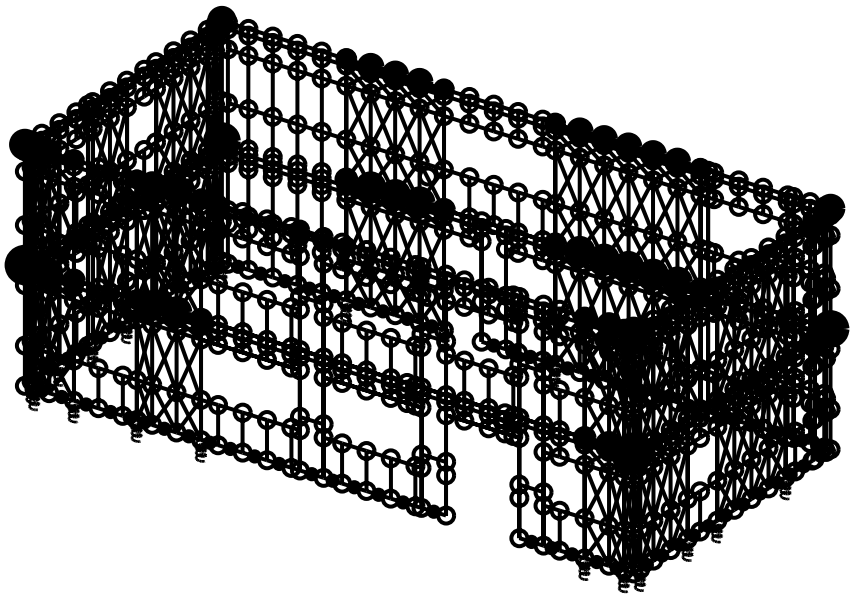

Figure H-1: A1-3D-RD-a model

H.2 Free vibration analysis results

Free vibration analysis results are presented in Table H-1 and Figure H-2. Lateral stiffness in the short direction is smaller than lateral stiffness in the long direction and torsional stiffness is the largest. The observation holds for the first and the second mode, as indicated by Table H-1.

Table H-1: Free vibration analysis results, A1-3D-RD-a model

Mode number	Natural period (s)	Mode description
1	0.329	Short, 1st
2	0.292	Long, 1st
3	0.234	Torsion, 1st
4	0.115	Short, 2nd
5	0.102	Long, 2nd
6	0.083	Torsion, 2nd

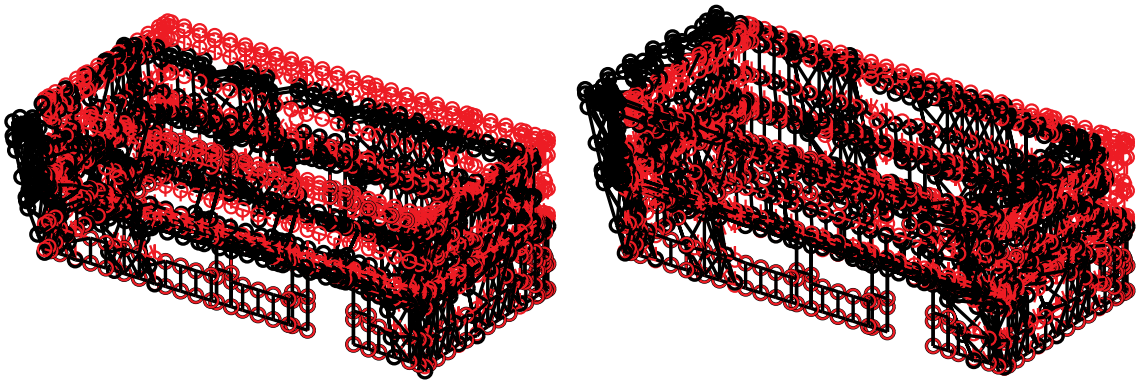

(a) Mode 1, T_1=0.329 s (b) Mode 2, T_2=0.292 s

Figure H-2: First two natural modes of A1-3D-RD-a model

H.3 Linear static analysis results

Table H-2 to Table H-4 present linear static analysis results. The lateral load is the equivalent lateral force available from the design narrative (Madsen et al. 2011), applied equally at four corners. Two separate analyses were performed with the loading at long or short direction.

Table H-2 summarizes the breakdown of peak total base shear among four elevations. Due to the interplay of asymmetrical LFRS, wall lines perpendicular to the loading direction still take a very small portion of base shear.

Table H-3 shows peak building and wall line deflections. Practicing engineers can linearly upscale these data and develop an estimate of the building's performance at a certain lateral force level.

Table H-4 is an evaluation of the building's lateral stiffness of long and short direction and its breakdown among shear walls (SW) and other systems. Interestingly, the bare CFS framing still accounts for 10% total lateral stiffness in this case.

Table H-2: Breakdown of peak base shear, linear static analysis, A1-3D-RD-a model

Load direction	**LONG**				
Elevation	**South V_b**	**North V_b**	**East V_b**	**West V_b**	**Peak V_b**
kips	3.1	7.9	0.0	0.1	11.1
%	27.7	71.3	0.3	0.8	100.0
Load direction	**SHORT**				
Elevation	**South V_b**	**North V_b**	**East V_b**	**West V_b**	**Peak V_b**
kips	0.1	0.1	5.5	5.3	11.1
%	0.9	0.8	50.0	48.3	100.0

Table H-3: Peak building and wall line deflection, linear static analysis, A1-3D-RD-a model

Load direction	**LONG**							
Deflection (in.)	u_1	u_2	v_1	v_2	Δu_1	Δu_2	Δv_1	Δv_2
Building	0.088	0.150	-0.004	-0.009	0.088	0.062	-0.004	-0.005
South	0.097	0.165	-0.004	-0.009	0.097	0.067	-0.004	-0.005
North	0.079	0.136	-0.004	-0.009	0.079	0.057	-0.004	-0.005
East	0.088	0.150	0.015	0.022	0.088	0.062	0.015	0.007
West	0.088	0.150	-0.024	-0.040	0.088	0.062	-0.024	-0.016
Load direction	**SHORT**							
Deflection (in.)	u_1	u_2	v_1	v_2	Δu_1	Δu_2	Δv_1	Δv_2
Building	-0.003	-0.007	0.114	0.193	-0.003	-0.003	0.114	0.079
South	-0.006	-0.013	0.114	0.193	-0.006	-0.006	0.114	0.079
North	-0.001	-0.002	0.114	0.193	-0.001	-0.001	0.114	0.079
East	-0.003	-0.007	0.107	0.180	-0.003	-0.003	0.107	0.072
West	-0.003	-0.007	0.121	0.206	-0.003	-0.003	0.121	0.085

Table H-4: Breakdown of lateral stiffness, A1-3D-RD-a model

LONG			**SHORT**		
Shear wall k_u (%)	**Gravity wall k_u (%)**	**k_u (kip/in)**	**Shear wall k_v (%)**	**Gravity wall k_v (%)**	**k_v (kip/in)**
90.0	10.0	72.2	89.9	10.1	55.6

H.4 Nonlinear static (pushover) analysis results

Table H-5 is created following the same logic with Table H-2, but the analysis type is nonlinear static (pushover). Pushover curves of the building and each wall line are presented Figure H-3 in and Figure H-4.

Clearly, the interaction between wall lines is much more significant when material and geometrical nonlinearity is included. These tables and figures indicate that the wall lines do not reach their peak capacity at exactly the same drift level and wall lines perpendicular to the load can take a nontrivial amount of base shear. Total capacity of the building in the short direction is smaller than the long direction.

Table H-5: Breakdown of peak base shear, pushover analysis, A1-3D-RD-a model

Load direction	**LONG**				
Elevation	**South V_b**	**North V_b**	**East V_b**	**West V_b**	**Peak V_b**
kips	24.4	23.9	4.3	5.4	47.8
%	51.1	50.1	9.1	11.3	100.0
Load direction	**SHORT**				
Elevation	**South V_b**	**North V_b**	**East V_b**	**West V_b**	**Peak V_b**
kips	5.4	4.1	20.3	22.3	45.1
%	12.0	9.1	45.2	49.4	100.0

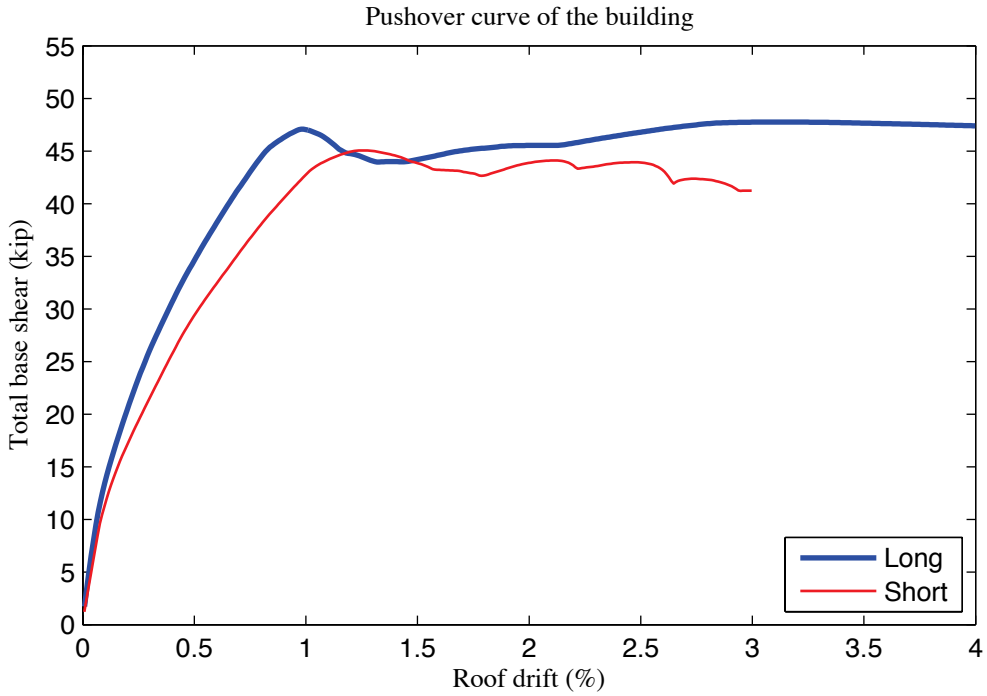

Figure H-3: Pushover curve of A1-3D-RD-a model

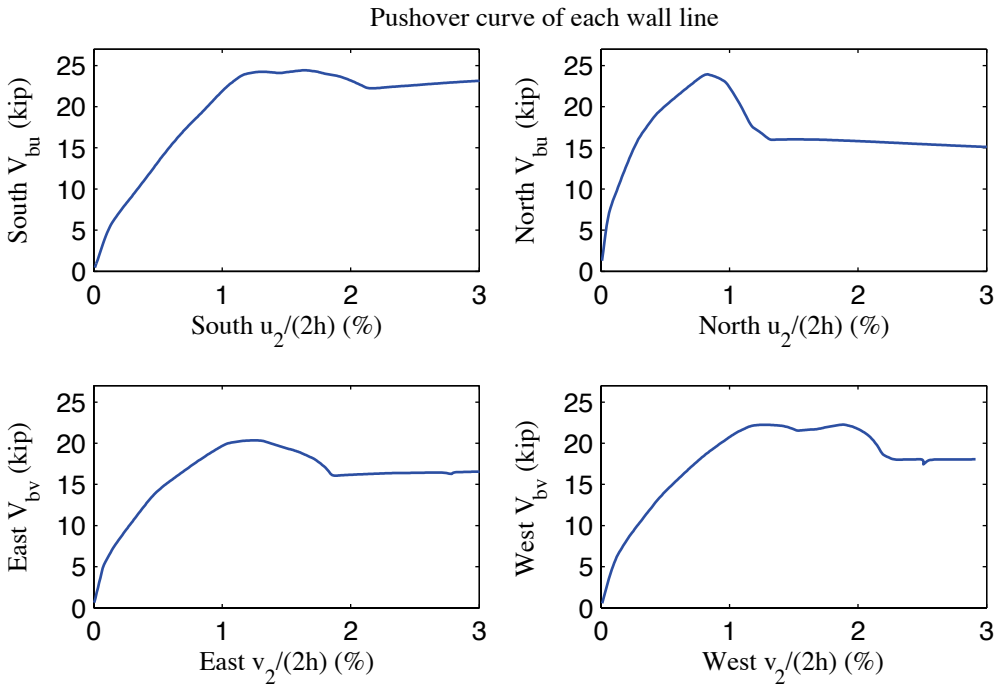

Figure H-4: Pushover curve of each wall line, A1-3D-RD-a model

H.5 Linear time history analysis results

Linear time history analysis is performed on the model under Canoga Park and Rinaldi ground motion records of Northridge earthquake in 1994. We considered three scale levels (16%, 44% and 100%) and loadings in one, two and three axes.

Table H-6 to Table H-9 demonstrate the building's linear elastic performance under designated ground motions. Table H-6 shows peak story relative accelerations in the unit of g. Table H-7 and Table H-8 report peak roof drift and story drift of the building and the corresponding time step (t_*) and the base shear at that time. Note that the base shear at the time of peak roof drift may not be the peak total building base shear in that direction (see Table H-9).

The building behaves linearly since peak drift and peak base shear appear at the same time when the ground motion is linearly scaled. Figure H-5 is a vector plot of the peak total resultant base shear of the building under three axial, 100% Canoga Park excitation. The directions of arrows imply that base shear taken by shear walls and gravity systems does not necessarily follow the direction of wall lines due to the effect of 3D coupling. Comparison with nonlinear analysis results of the same excitation provides insightful observations on the building's response and requirements on modeling fidelity and analysis type.

Table H-6: A1-3D-RD-a model peak story relative acceleration in g, linear time history analysis

		LONG			SHORT			UP		
Load Case	**Ground Motion**	**a_g**	**Floor a**	**Roof a**	**a_g**	**Floor a**	**Roof a**	**a_g**	**Floor a**	**Roof a**
EQ_3D_3axis_1	CNP 16%	0.067	0.104	0.175	0.057	0.117	0.174	0.078	0.117	0.112
EQ_3D_3axis_2	CNP 44%	0.185	0.278	0.460	0.157	0.309	0.467	0.215	0.241	0.231
EQ_3D_1axis_1	CNP 100%	0.420	0.539	0.892	0	0.136	0.218	0	0.220	0.204
EQ_3D_1axis_2	CNP 100%	0	0.236	0.359	0.356	0.735	1.044	0	0.679	0.650
EQ_3D_2axis_1	CNP 100%	0.420	0.625	1.049	0.356	0.677	1.037	0	0.629	0.592
EQ_3D_3axis_3	CNP 100%	0.420	0.625	1.049	0.356	0.677	1.037	0.489	0.629	0.592
EQ_3D_3axis_4	RRS 16%	0.132	0.195	0.313	0.078	0.229	0.357	0.133	0.189	0.179
EQ_3D_3axis_5	RRS 44%	0.363	0.536	0.847	0.214	0.605	0.924	0.367	0.441	0.414
EQ_3D_3axis_6	RRS 100%	0.825	1.199	1.915	0.486	1.356	2.033	0.834	1.999	1.900

Table H-7: A1-3D-RD-a model peak building roof drift and base shear, linear time history analysis

		LONG			SHORT		
Load Case	**Ground Motion**	**$u_2/(2h)$ (%)**	**t_* (s)**	**V_b @ t_* (kips)**	**$v_2/(2h)$ (%)**	**t_* (s)**	**V_b @ t_* (kips)**
EQ_3D_3axis_1	CNP 16%	-0.064	11.87	9.6	-0.075	10.47	8.8
EQ_3D_3axis_2	CNP 44%	-0.173	11.88	25.5	-0.199	10.48	23.5
EQ_3D_1axis_1	CNP 100%	-0.338	11.88	49.9	-0.071	12.69	8.6
EQ_3D_1axis_2	CNP 100%	0.140	10.17	19.4	-0.457	10.48	53.1
EQ_3D_2axis_1	CNP 100%	-0.374	11.88	53.9	-0.433	10.48	50.7
EQ_3D_3axis_3	CNP 100%	-0.374	11.88	53.9	-0.433	10.48	50.7
EQ_3D_3axis_4	RRS 16%	-0.121	4.54	16.7	0.148	4.55	17.9
EQ_3D_3axis_5	RRS 44%	-0.330	4.54	44.1	0.412	3.34	51.9
EQ_3D_3axis_6	RRS 100%	-0.755	4.54	99.8	0.944	3.34	117.1

Table H-8: A1-3D-RD-a model peak building story drift, linear time history analysis

		LONG				SHORT			
Load Case	**Ground Motion**	**$\Delta u_1/h$ (%)**	**t_* (s)**	**$\Delta u_2/h$ (%)**	**t_* (s)**	**$\Delta v_1/h$ (%)**	**t_* (s)**	**$\Delta v_2/h$ (%)**	**t_* (s)**
EQ_3D_3axis_1	CNP 16%	-0.076	11.87	-0.052	11.87	-0.088	10.47	-0.062	10.47
EQ_3D_3axis_2	CNP 44%	-0.206	11.88	-0.140	11.88	-0.235	10.48	-0.163	10.48
EQ_3D_1axis_1	CNP 100%	-0.400	11.88	-0.276	11.87	-0.083	8.34	-0.060	12.69
EQ_3D_1axis_2	CNP 100%	0.169	10.17	-0.111	10.03	-0.546	10.49	-0.370	10.48
EQ_3D_2axis_1	CNP 100%	-0.443	11.88	-0.305	11.88	-0.511	10.48	-0.354	10.48
EQ_3D_3axis_3	CNP 100%	-0.443	11.88	-0.305	11.88	-0.511	10.48	-0.354	10.48
EQ_3D_3axis_4	RRS 16%	-0.145	4.54	-0.097	4.55	0.183	3.34	-0.118	4.39
EQ_3D_3axis_5	RRS 44%	-0.393	4.54	-0.271	4.55	0.513	3.34	0.312	3.35
EQ_3D_3axis_6	RRS 100%	0.909	2.60	-0.624	4.55	1.170	3.34	0.723	3.35

Table H-9: A1-3D-RD-a model peak building base shear, linear time history analysis

		LONG		SHORT		RESULTANT	
Load Case	**Ground Motion**	**Peak V_{bu} (kip)**	**t @ peak V_{bu} (s)**	**Peak V_{bv} (kip)**	**t @ peak V_{bv} (s)**	**Peak V_b (kip)**	**t @ peak V_b (s)**
EQ_3D_3axis_1	CNP 16%	9.6	11.87	8.9	7.43	10.7	10.48
EQ_3D_3axis_2	CNP 44%	25.5	11.88	23.7	7.43	28.1	10.49
EQ_3D_1axis_1	CNP 100%	49.9	11.88	9.5	8.34	50.0	11.88
EQ_3D_1axis_2	CNP 100%	19.4	10.17	55.1	7.44	55.5	7.44
EQ_3D_2axis_1	CNP 100%	53.9	11.88	51.7	7.43	58.9	7.42
EQ_3D_3axis_3	CNP 100%	53.9	11.88	51.7	7.43	58.9	7.42
EQ_3D_3axis_4	RRS 16%	17.7	2.60	19.0	3.34	24.1	4.54
EQ_3D_3axis_5	RRS 44%	49.7	2.60	51.9	3.34	62.0	4.55
EQ_3D_3axis_6	RRS 100%	117.0	2.60	117.1	3.34	136.9	4.55

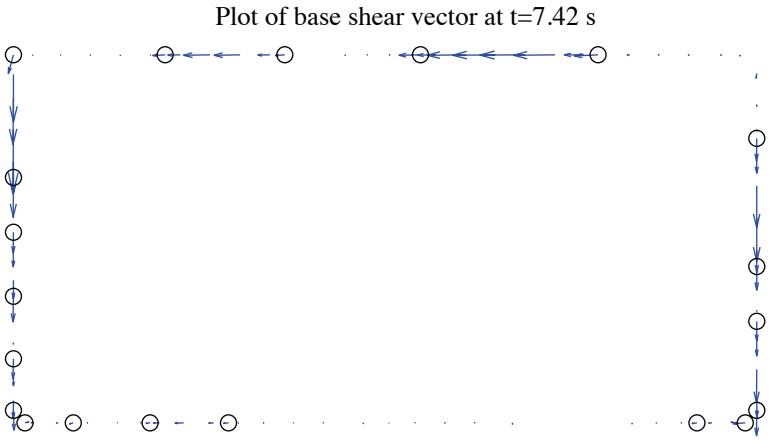

Figure H-5: A1-3D-RD-a model, base shear vector plot at the moment of peak total base shear, 100 % Canoga Park, 3D linear analysis (maximum anchor/hold down base shear is 4.40 kips)

H.6 Nonlinear time history analysis results

Same ground motions are applied to the model with material and geometrical nonlinearity. Table H-10 to Table H-13 are replicas of Table H-6 to Table H-9, but for nonlinear time history analyses. Since this analysis type is most complicated and closest to reality and experiments, behavior of wall lines and hold downs are further studied. Table H-14 is the table of peak wall line story drifts and corresponding time steps. Table H-15 is designed for peak base shear of each wall line and the last two columns of the table are percentages of base shear of two facing wall lines in the same direction when the total base shear in that direction takes peak value. Table H-16 expands the breakdown of each wall line's peak base shear between shear walls, gravity walls and other systems. Table H-17 is peak value of hold down tensile force of two selected pairs. Hold down 5 and 6 are on shear wall L1S1, South elevation and hold down 7 and 8 are on shear wall L1W1, West elevation. These shear walls have lowest capacities compared with others on the same wall line and they meet at the southwest edge of the building, so interacted nonlinear behavior is expected to appear.

Time history plots in this section include plots of story drifts of the building and each wall line (Figure H-6 to Figure H-8), total building base shear in long and short direction (Figure H-9) and axial forces of hold downs in Table H-17 (Figure H-10). Hysteretic plots in Figure H-11 and Figure H-12 are helpful for visual examination of nonlinear base shear-drift relationship of the building and the weakest shear wall on each wall line. In comparison with linear time history analysis, vector plot of peak total base shear is illustrated in Figure H-13. Figure H-14 presents a simplified deformed shape of the

building (see (Peterman 2014) for details of the method) and axial force of all twenty hold downs at the moment of peak total base shear. The same sign convention with tests is adopted. Red bars indicate tensile (negative) force and blue ones are for compressive (positive) force.

Hysteretic behavior is seen in the building and typical shear walls under design-based earthquake (100% Canoga Park excitation in 3 axes, see Figure H-11 and Figure H-12). However, the backbones of response curves hardly reach the post-peak range. Peak story drifts are not greater than 1.0% (Table H-12), and larger deflection is seen in the long direction. Peak wall line drifts are smaller than 1.6% (Table H-14), with the maximum found in West elevation. Figure H-13 clearly shows that base shear vectors in anchors and hold downs do not align with wall lines and they can change directions even within a single piece of wall, a sign of localized behavior. Table H-17, Figure H-10 and Figure H-14 demonstrate that hold downs in a pair do not experience the same amount of force with opposite signs, an evidence that supports Type II shear wall behavior despite Type I design assumption.

The near-field Rinaldi record is much stronger in terms of peak ground acceleration, especially in the long direction. Analysis fails when loaded with 100% Rinaldi ground motion. The response goes to infinity at 2.56 s, the moment of peak ground acceleration. Table H-16 reveals that as nonlinearity increases, the portion of base shear taken by gravity wall and other system grows significantly, from 2.1% to 6.8% on West elevation at minimum and from 11.1% to 25.1% on South elevation at maximum.

Table H-10: A1-3D-RD-a model peak story relative acceleration in g, nonlinear time history analysis

		LONG			SHORT			UP		
Load Case	**Ground Motion**	**a_g**	**Floor a**	**Roof a**	**a_g**	**Floor a**	**Roof a**	**a_g**	**Floor a**	**Roof a**
EQ_3D_3axis_1	CNP 16%	0.067	0.131	0.177	0.057	0.151	0.186	0.078	0.108	0.108
EQ_3D_3axis_2	CNP 44%	0.185	0.344	0.460	0.157	0.276	0.339	0.215	0.686	0.630
EQ_3D_1axis_1	CNP 100%	0.420	0.782	1.326	0	0.062	0.062	0	0.111	0.101
EQ_3D_1axis_2	CNP 100%	0	0.207	0.177	0.356	0.606	0.955	0	1.154	1.108
EQ_3D_2axis_1	CNP 100%	0.420	0.746	1.310	0.356	0.576	0.895	0	1.377	1.251
EQ_3D_3axis_3	CNP 100%	0.420	0.743	1.314	0.356	0.576	0.897	0.489	1.184	1.076
EQ_3D_3axis_4	RRS 16%	0.132	0.231	0.300	0.078	0.237	0.236	0.133	0.122	0.117
EQ_3D_3axis_5	RRS 44%	0.363	0.486	0.702	0.214	0.418	0.656	0.367	0.709	0.750
EQ_3D_3axis_6	RRS 100%	N/A	N/A	N/A	N/A	N/A	N/A	N/A	N/A	N/A

Table H-11: A1-3D-RD-a model peak building roof drift and base shear, nonlinear time history analysis

		LONG			SHORT		
Load Case	**Ground Motion**	**u_2/(2h) (%)**	**t_* (s)**	**V_b @ t_* (kips)**	**v_2/(2h) (%)**	**t_* (s)**	**V_b @ t_* (kips)**
EQ_3D_3axis_1	CNP 16%	0.057	8.71	9.9	0.064	8.81	7.9
EQ_3D_3axis_2	CNP 44%	-0.277	10.56	24.3	0.252	10.00	18.6
EQ_3D_1axis_1	CNP 100%	0.934	8.78	47.5	-0.018	7.13	1.1
EQ_3D_1axis_2	CNP 100%	-0.040	5.29	3.5	0.918	10.06	39.5
EQ_3D_2axis_1	CNP 100%	0.947	8.78	46.5	0.913	10.06	38.8
EQ_3D_3axis_3	CNP 100%	0.950	8.78	46.4	0.911	10.06	38.6
EQ_3D_3axis_4	RRS 16%	0.126	4.41	13.9	0.122	3.37	12.7
EQ_3D_3axis_5	RRS 44%	0.635	2.69	41.1	0.413	3.93	25.3
EQ_3D_3axis_6	RRS 100%	N/A	N/A	N/A	N/A	N/A	N/A

Table H-12: A1-3D-RD-a model peak building story drift, nonlinear linear time history analysis

		LONG				SHORT			
Load Case	**Ground Motion**	**$\Delta u_1/h$ (%)**	**t_* (s)**	**$\Delta u_2/h$ (%)**	**t_* (s)**	**$\Delta v_1/h$ (%)**	**t_* (s)**	**$\Delta v_2/h$ (%)**	**t_* (s)**
EQ_3D_3 axis_1	CNP 16%	0.078	8.70	-0.044	7.82	-0.082	8.32	-0.053	5.03
EQ_3D_3 axis_2	CNP 44%	-0.366	10.55	-0.192	10.56	0.318	10.01	0.189	10.00
EQ_3D_1 axis_1	CNP 100%	1.407	8.78	-0.730	10.27	-0.019	7.44	-0.022	7.13
EQ_3D_1 axis_2	CNP 100%	0.054	8.54	-0.042	10.07	1.144	10.07	0.718	10.04
EQ_3D_2 axis_1	CNP 100%	1.395	8.79	-0.697	10.27	1.156	10.07	0.680	10.06
EQ_3D_3 axis_3	CNP 100%	1.402	8.79	-0.694	10.27	1.154	10.07	0.678	10.05
EQ_3D_3 axis_4	RRS 16%	0.176	4.40	0.084	4.42	0.165	3.36	-0.083	4.80
EQ_3D_3 axis_5	RRS 44%	0.917	2.69	0.354	2.69	0.516	3.93	0.311	3.94
EQ_3D_3 axis_6	RRS 100%	N/A	N/A	N/A	N/A	N/A	N/A	N/A	N/A

Table H-13: A1-3D-RD-a model peak building base shear, nonlinear time history analysis

		LONG		SHORT		RESULTANT	
Load Case	**Ground Motion**	**Peak V_{bu} (kip)**	**t @ peak V_{bu} (s)**	**Peak V_{bv} (kip)**	**t @ peak V_{bv} (s)**	**Peak V_b (kip)**	**t @ peak V_b (s)**
EQ_3D_3axis_1	CNP 16%	9.9	8.71	7.9	8.32	10.3	7.79
EQ_3D_3axis_2	CNP 44%	25.0	8.73	18.6	10.01	26.0	8.73
EQ_3D_1axis_1	CNP 100%	47.5	8.75	2.1	7.25	47.5	8.75
EQ_3D_1axis_2	CNP 100%	5.2	5.13	40.0	10.07	40.0	10.07
EQ_3D_2axis_1	CNP 100%	46.5	8.78	38.9	10.05	57.7	10.03
EQ_3D_3axis_3	CNP 100%	46.4	8.78	39.1	10.05	57.7	10.03
EQ_3D_3axis_4	RRS 16%	15.1	4.39	13.0	3.36	18.5	4.39
EQ_3D_3axis_5	RRS 44%	41.1	2.69	25.3	3.93	41.1	2.69
EQ_3D_3axis_6	RRS 100%	N/A	N/A	N/A	N/A	N/A	N/A

Table H-14: A1-3D-RD-a model peak wall line story drift, nonlinear time history analysis

LONG		SOUTH				NORTH			
Load Case	**Ground Motion**	**$\Delta u_1/h$ (%)**	**t_* (s)**	**$\Delta u_2/h$ (%)**	**t_* (s)**	**$\Delta u_1/h$ (%)**	**t_* (s)**	**$\Delta u_2/h$ (%)**	**t_* (s)**
EQ_3D_3axis_1	CNP 16%	0.097	8.70	0.056	7.82	0.063	11.87	0.037	9.31
EQ_3D_3axis_2	CNP 44%	0.374	10.55	0.191	10.56	0.382	8.72	0.193	10.56
EQ_3D_1axis_1	CNP 100%	1.385	8.78	0.723	10.27	1.428	8.78	0.736	10.27
EQ_3D_1axis_2	CNP 100%	0.121	8.53	0.086	10.07	0.030	5.02	0.043	22.61
EQ_3D_2axis_1	CNP 100%	1.343	8.79	0.719	10.27	1.470	10.03	0.678	10.28
EQ_3D_3axis_3	CNP 100%	1.348	8.79	0.716	10.27	1.477	10.03	0.673	10.28
EQ_3D_3axis_4	RRS 16%	0.221	4.40	0.111	4.42	0.145	2.63	0.069	6.74
EQ_3D_3axis_5	RRS 44%	0.928	2.69	0.372	2.68	0.905	2.69	0.342	2.70
EQ_3D_3axis_6	RRS 100%	N/A	N/A	N/A	N/A	N/A	N/A	N/A	N/A
SHORT		**EAST**				**WEST**			
Load Case	**Ground Motion**	**$\Delta v_1/h$ (%)**	**t_* (s)**	**$\Delta v_2/h$ (%)**	**t_* (s)**	**$\Delta v_1/h$ (%)**	**t_* (s)**	**$\Delta v_2/h$ (%)**	**t_* (s)**
EQ_3D_3axis_1	CNP 16%	0.101	8.33	0.061	8.35	0.125	8.82	0.084	5.22
EQ_3D_3axis_2	CNP 44%	0.276	10.00	0.178	8.80	0.368	10.02	0.228	10.00
EQ_3D_1axis_1	CNP 100%	0.081	8.83	0.048	8.88	0.061	8.85	0.040	8.89
EQ_3D_1axis_2	CNP 100%	1.062	10.06	0.645	10.04	1.232	10.07	0.803	10.05
EQ_3D_2axis_1	CNP 100%	0.869	8.51	0.562	10.04	1.578	10.09	0.806	10.06
EQ_3D_3axis_3	CNP 100%	0.867	8.51	0.561	10.04	1.577	10.09	0.804	10.06
EQ_3D_3axis_4	RRS 16%	0.115	3.17	0.072	3.15	0.257	4.57	0.134	4.43
EQ_3D_3axis_5	RRS 44%	0.428	6.07	0.307	3.94	0.618	3.93	0.328	3.92
EQ_3D_3axis_6	RRS 100%	N/A	N/A	N/A	N/A	N/A	N/A	N/A	N/A

Table H-15: A1-3D-RD-a model peak wall line base shear, nonlinear time history analysis

LONG		SOUTH		NORTH		% of Peak V_{bu}	
Load Case	**Ground Motion**	**Peak V_{bu} (kips)**	**t @ peak V_{bu} (s)**	**Peak V_{bu} (kips)**	**t @ peak V_{bu} (s)**	**South**	**North**
EQ_3D_3axis_1	CNP 16%	3.7	8.70	6.1	11.88	37.3	61.3
EQ_3D_3axis_2	CNP 44%	8.8	10.55	16.0	8.72	33.5	63.2
EQ_3D_1axis_1	CNP 100%	22.0	8.78	24.1	8.72	44.6	49.3
EQ_3D_1axis_2	CNP 100%	4.1	8.53	3.5	4.89	51.5	46.9
EQ_3D_2axis_1	CNP 100%	21.7	8.79	24.4	8.73	46.7	47.0
EQ_3D_3axis_3	CNP 100%	21.8	8.79	24.4	8.73	46.9	46.7
EQ_3D_3axis_4	RRS 16%	6.5	4.40	9.4	2.63	42.0	55.8
EQ_3D_3axis_5	RRS 44%	16.9	2.68	22.3	2.69	41.0	54.2
EQ_3D_3axis_6	RRS 100%	N/A	N/A	N/A	N/A	N/A	N/A
SHORT		**EAST**		**WEST**		**% of Peak V_{bv}**	
Load Case	**Ground Motion**	**Peak V_{bv} (kips)**	**t @ peak V_{bv} (s)**	**Peak V_{bv} (kips)**	**t @ peak V_{bv} (s)**	**East**	**West**
EQ_3D_3axis_1	CNP 16%	4.9	8.34	5.5	8.82	59.8	37.8
EQ_3D_3axis_2	CNP 44%	8.5	10.00	9.9	10.03	44.8	52.5
EQ_3D_1axis_1	CNP 100%	3.7	8.83	3.2	8.85	77.2	17.2
EQ_3D_1axis_2	CNP 100%	17.9	10.07	20.4	10.08	44.7	50.7
EQ_3D_2axis_1	CNP 100%	16.5	8.52	22.4	10.09	40.7	55.5
EQ_3D_3axis_3	CNP 100%	16.5	8.51	22.4	10.09	40.7	55.4
EQ_3D_3axis_4	RRS 16%	5.2	3.17	8.2	4.58	36.5	60.9
EQ_3D_3axis_5	RRS 44%	11.0	6.07	13.9	3.93	41.8	55.1
EQ_3D_3axis_6	RRS 100%	N/A	N/A	N/A	N/A	N/A	N/A

Table H-16: A1-3D-RD-a model wall line base shear breakdown, nonlinear time history analysis

LONG		SOUTH			NORTH		
Load Case	**Ground Motion**	**Peak V_{bu} (kips)**	**SW V_{bu} (%)**	**GW V_{bu} (%)**	**Peak V_{bu} (kips)**	**SW V_{bu} (%)**	**GW V_{bu} (%)**
EQ_3D_3axis_1	CNP 16%	3.7	88.9	11.1	6.1	96.9	3.1
EQ_3D_3axis_2	CNP 44%	8.8	81.6	18.4	16.0	92.7	7.3
EQ_3D_1axis_1	CNP 100%	22.0	74.9	25.1	24.1	88.3	11.7
EQ_3D_1axis_2	CNP 100%	4.1	88.4	11.6	3.5	97.4	2.6
EQ_3D_2axis_1	CNP 100%	21.7	74.9	25.1	24.4	88.2	11.8
EQ_3D_3axis_3	CNP 100%	21.8	74.9	25.1	24.4	88.2	11.8
EQ_3D_3axis_4	RRS 16%	6.5	86.2	13.8	9.4	95.4	4.6
EQ_3D_3axis_5	RRS 44%	16.9	77.2	22.8	22.3	89.7	10.3
EQ_3D_3axis_6	RRS 100%	N/A	N/A	N/A	N/A	N/A	N/A
SHORT		**EAST**			**WEST**		
Load Case	**Ground Motion**	**Peak V_{bv} (kips)**	**SW V_{bv} (%)**	**GW V_{bu} (%)**	**Peak V_{bv} (kips)**	**SW V_{bv} (%)**	**GW V_{bv} (%)**
EQ_3D_3axis_1	CNP 16%	4.9	95.4	4.6	5.5	97.0	3.0
EQ_3D_3axis_2	CNP 44%	8.5	93.9	6.1	9.9	95.4	4.6
EQ_3D_1axis_1	CNP 100%	3.7	95.1	4.9	3.2	97.4	2.6
EQ_3D_1axis_2	CNP 100%	17.9	89.7	10.3	20.4	93.2	6.8
EQ_3D_2axis_1	CNP 100%	16.5	89.6	10.4	22.4	93.2	6.8
EQ_3D_3axis_3	CNP 100%	16.5	89.5	10.5	22.4	93.2	6.8
EQ_3D_3axis_4	RRS 16%	5.2	95.0	5.0	8.2	96.1	3.9
EQ_3D_3axis_5	RRS 44%	11.0	92.9	7.1	13.9	94.4	5.6
EQ_3D_3axis_6	RRS 100%	N/A	N/A	N/A	N/A	N/A	N/A

Table H-17: A1-3D-RD-a model peak hold down tensile force at certain locations, nonlinear time history analysis

		L1S1, LC5		L1S1, LC6		L1W1, LC7		L1W1, LC8	
Load Case	**Ground Motion**	**Peak F (kips)**	**t @ peak F (s)**	**Peak F (kips)**	**t @ peak F (s)**	**Peak F (kips)**	**t @ peak F (s)**	**Peak F (kips)**	**t @ peak F (s)**
EQ_3D_3axis_1	CNP 16%	-1.35	12.15	-0.15	7.44	-0.11	8.75	-0.68	8.98
EQ_3D_3axis_2	CNP 44%	-2.53	10.55	-0.67	9.97	-0.59	9.97	-1.11	8.48
EQ_3D_1axis_1	CNP 100%	-3.54	10.26	-1.02	8.77	-1.87	8.77	-0.93	8.75
EQ_3D_1axis_2	CNP 100%	-2.48	10.06	-1.88	10.06	-0.96	10.05	-2.39	8.48
EQ_3D_2axis_1	CNP 100%	-3.44	10.25	-3.54	10.04	-3.24	10.03	-2.39	9.81
EQ_3D_3axis_3	CNP 100%	-3.46	10.25	-3.56	10.05	-3.25	10.03	-2.39	6.08
EQ_3D_3axis_4	RRS 16%	-2.21	4.58	-0.23	3.37	-0.19	2.63	-1.04	4.41
EQ_3D_3axis_5	RRS 44%	-2.89	6.16	-0.90	3.91	-1.28	2.70	-1.33	2.57
EQ_3D_3axis_6	RRS 100%	N/A	N/A	N/A	N/A	N/A	N/A	N/A	N/A

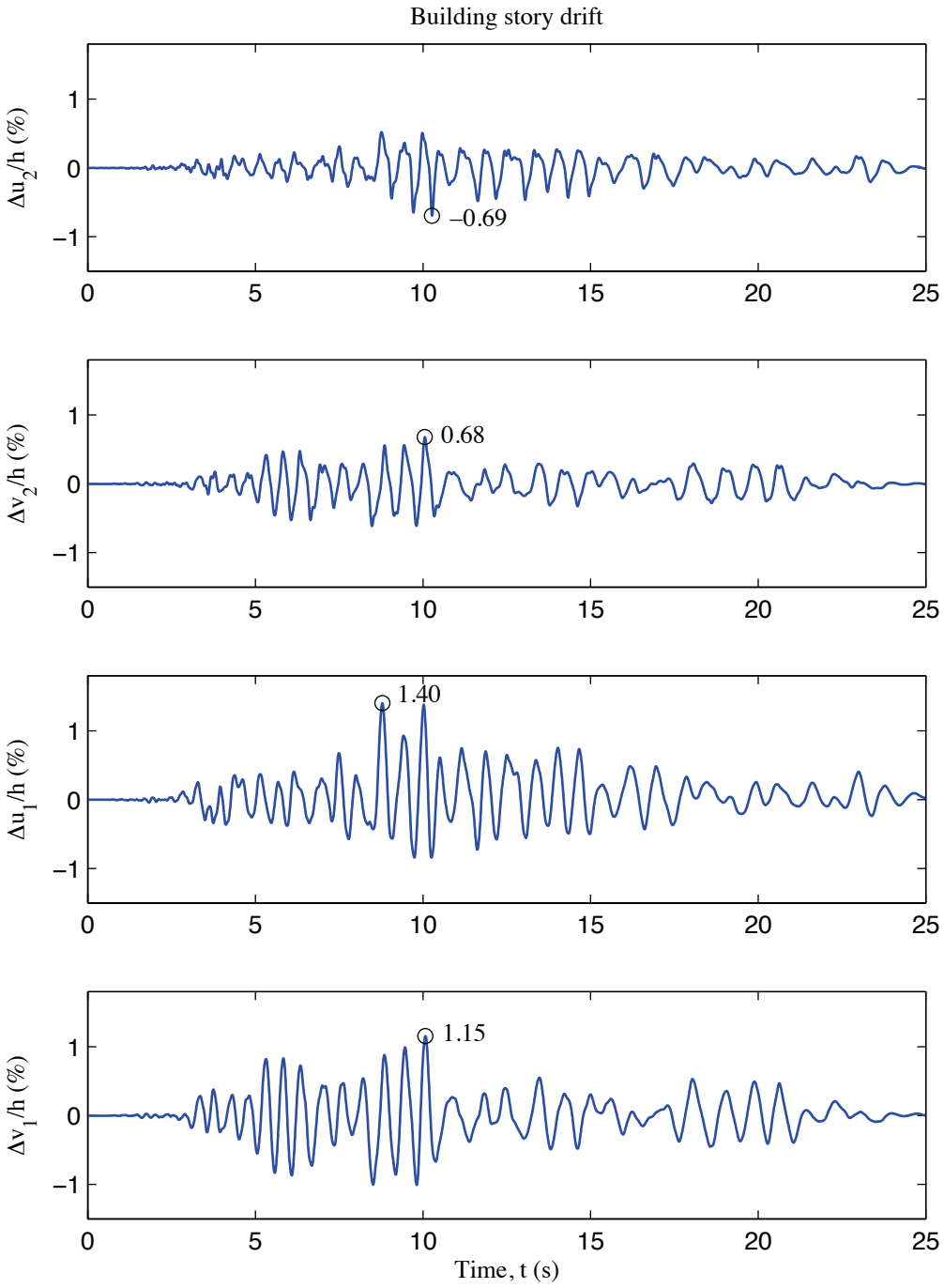

Figure H-6: A1-3D-RD-a model building story drift, 100 % Canoga Park, 3D nonlinear analysis

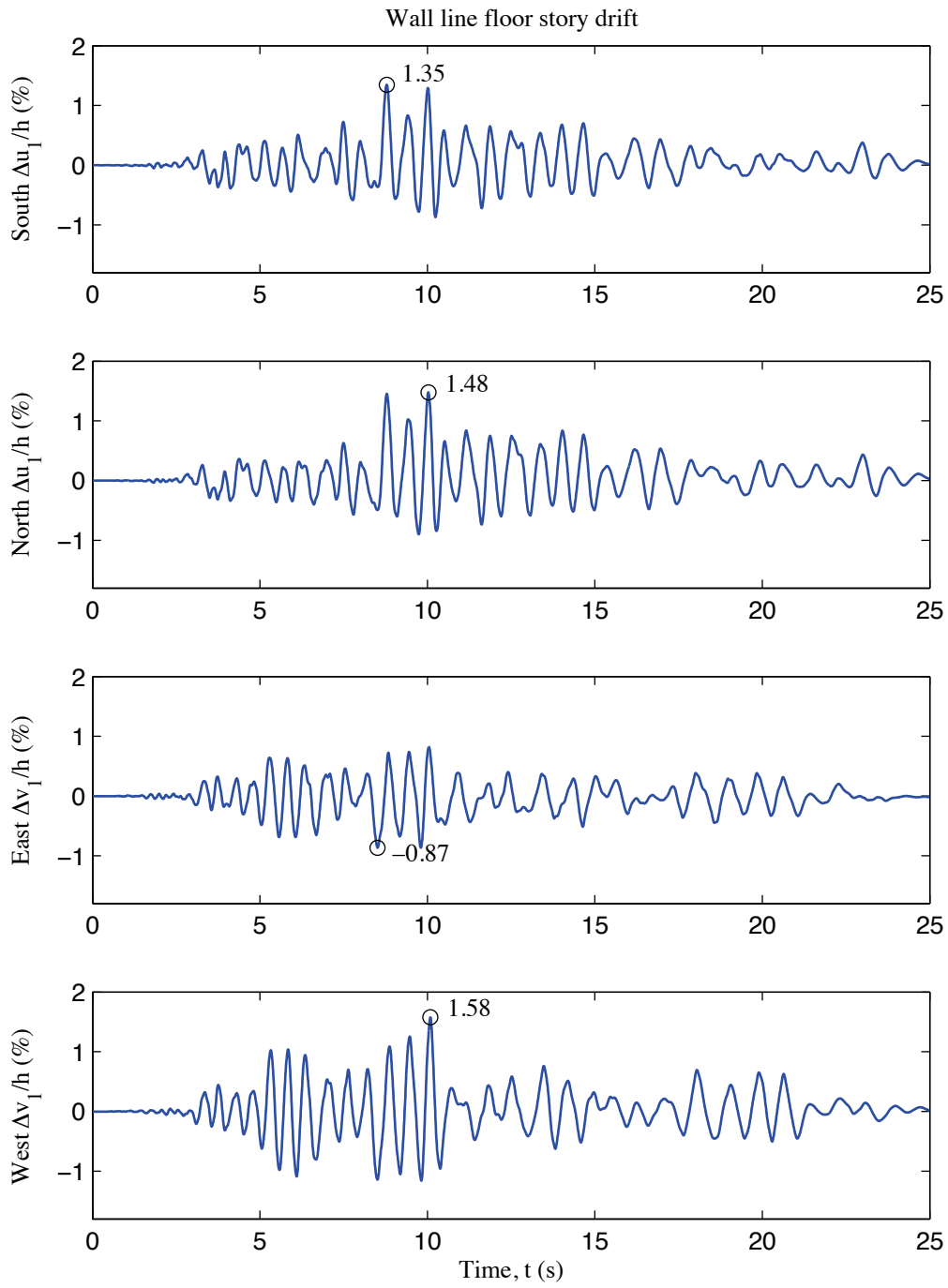

Figure H-7: A1-3D-RD-a model wall line floor story drift, 100 % Canoga Park, 3D nonlinear analysis

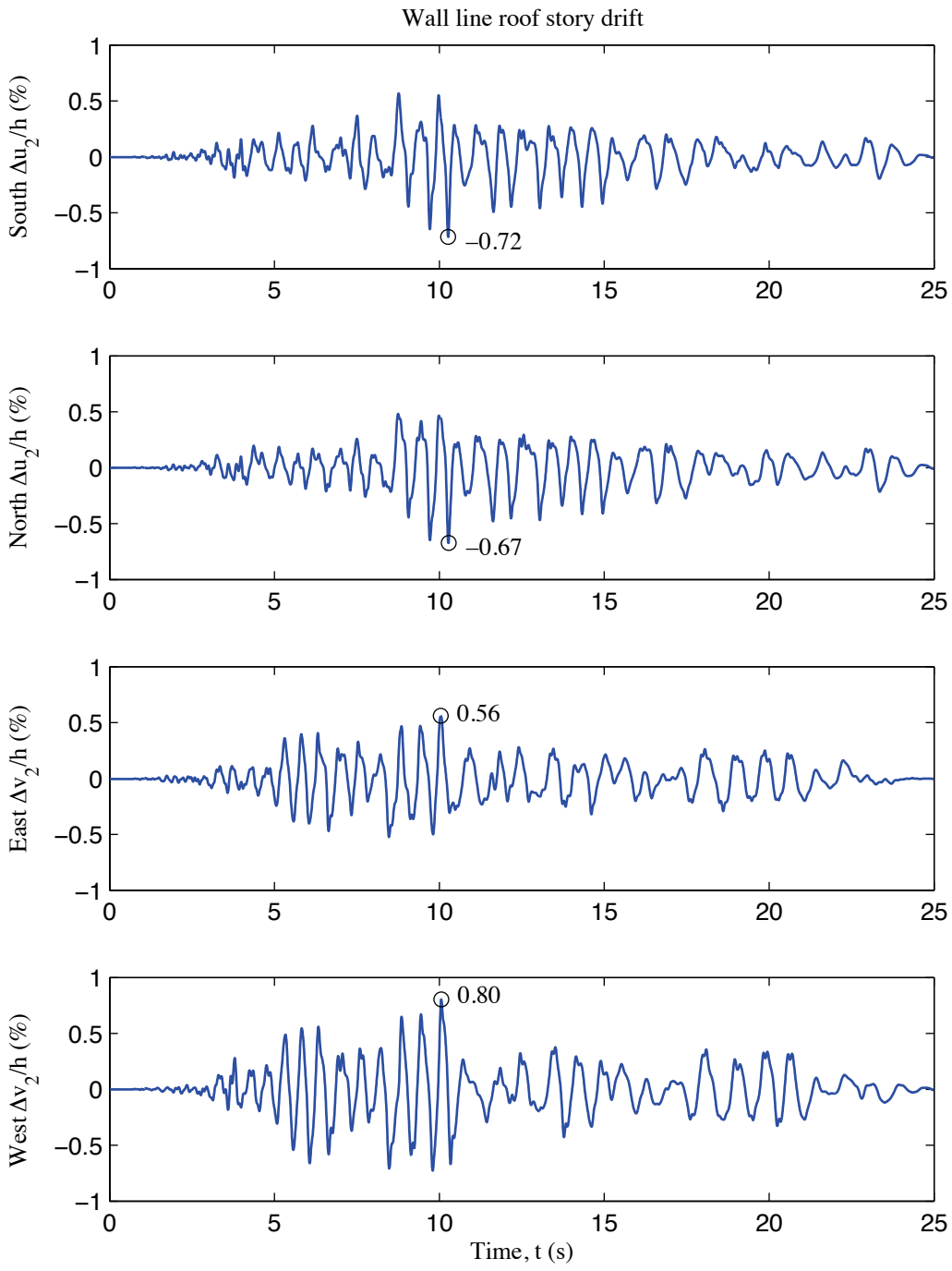

Figure H-8: A1-3D-RD-a model wall line roof story drift, 100 % Canoga Park, 3D nonlinear analysis

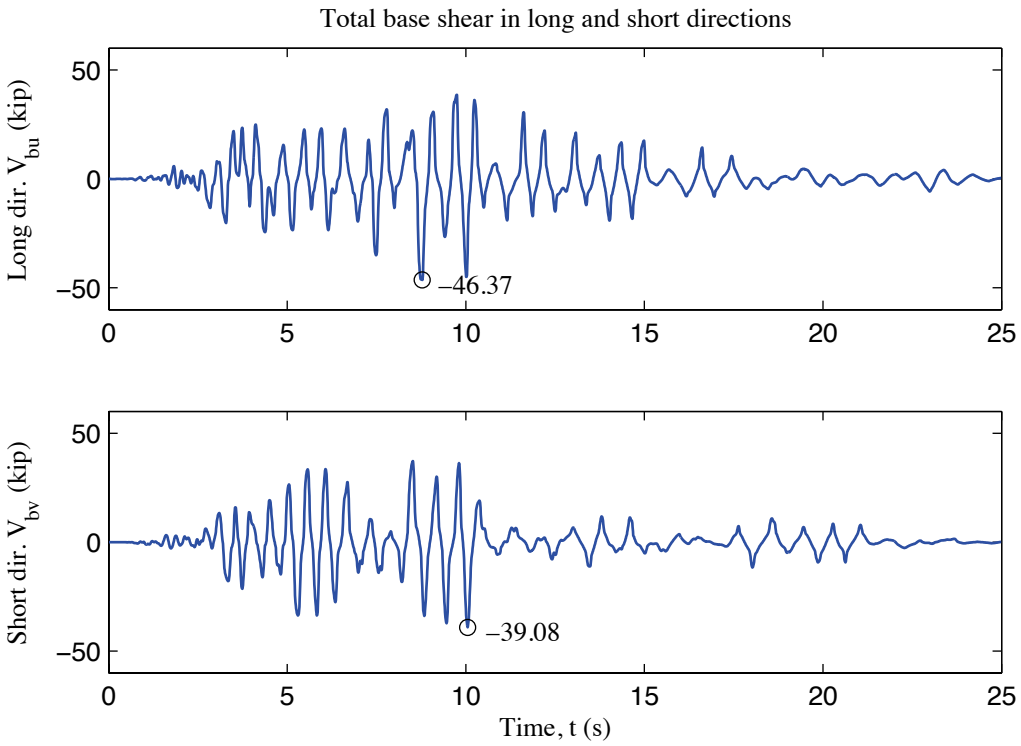

Figure H-9: A1-3D-RD-a model total building base shear, 100 % Canoga Park, 3D nonlinear analysis

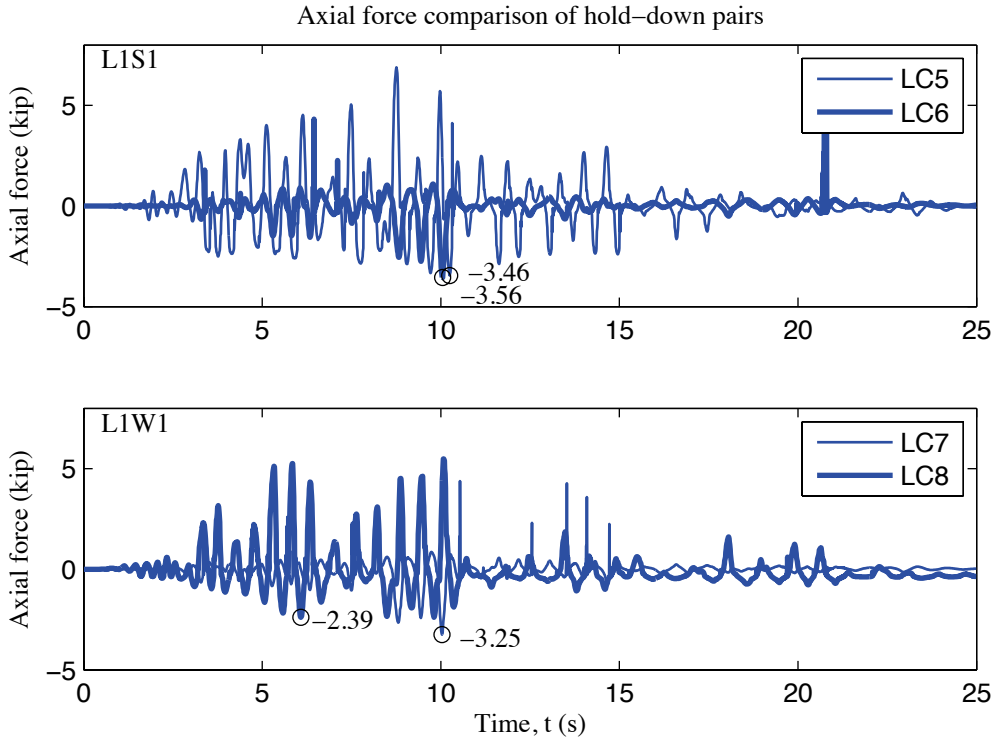

Figure H-10: A1-3D-RD-a model, load cell 5 to 8 axial forces, 100 % Canoga Park, 3D nonlinear analysis

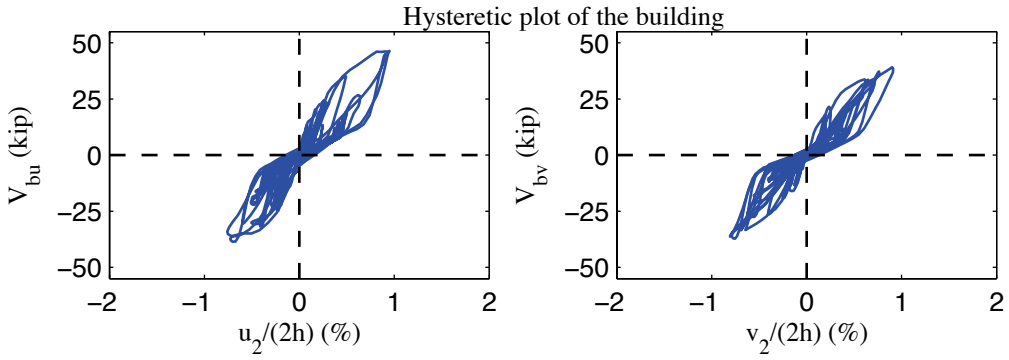

Figure H-11: A1-3D-RD-a model, hysteretic plot of the building, 100 % Canoga Park, 3D nonlinear analysis

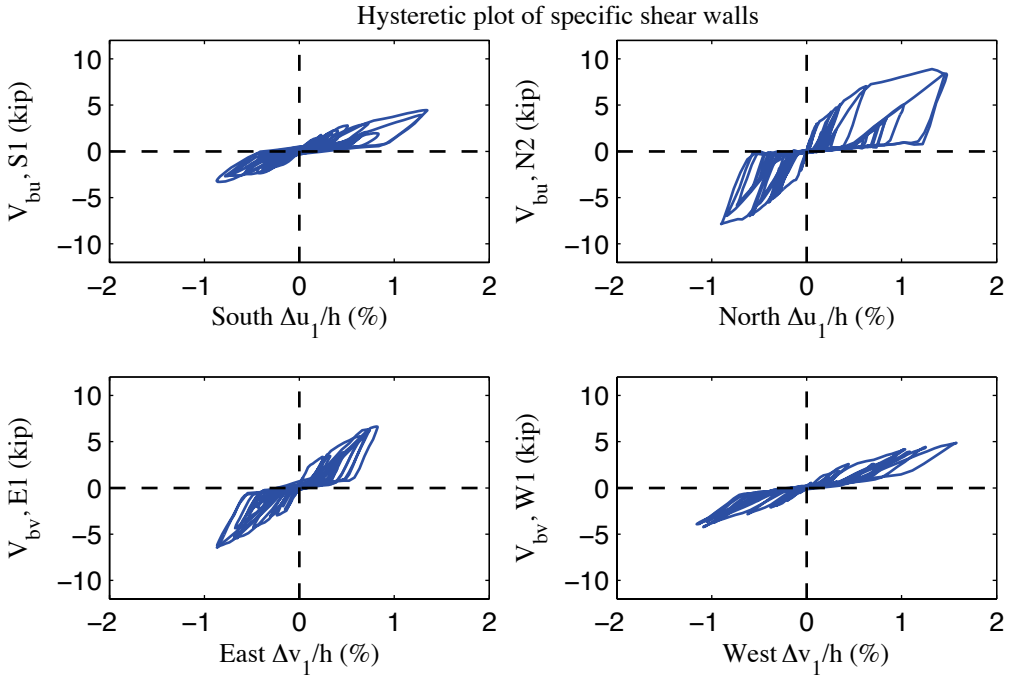

Figure H-12: A1-3D-RD-a model, hysteretic plot of shear walls at each elevation, 100 % Canoga Park, 3D nonlinear analysis

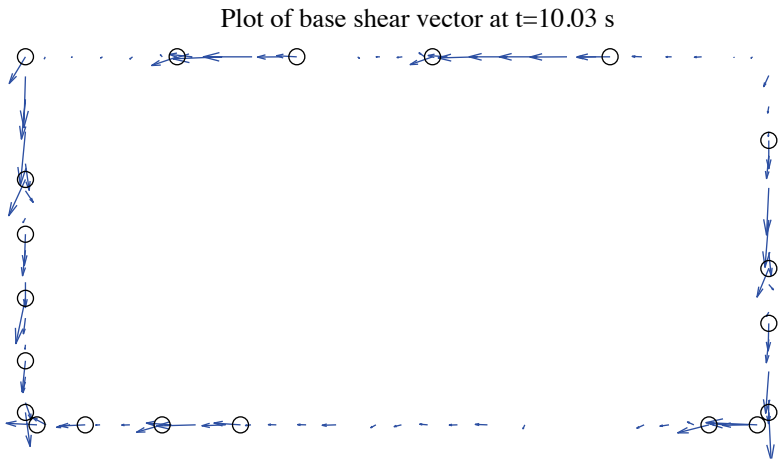

Figure H-13: A1-3D-RD-a model, field plot of peak total base shear, 100 % Canoga Park, 3D nonlinear analysis (maximum anchor/hold down base shear is 2.22 kips)

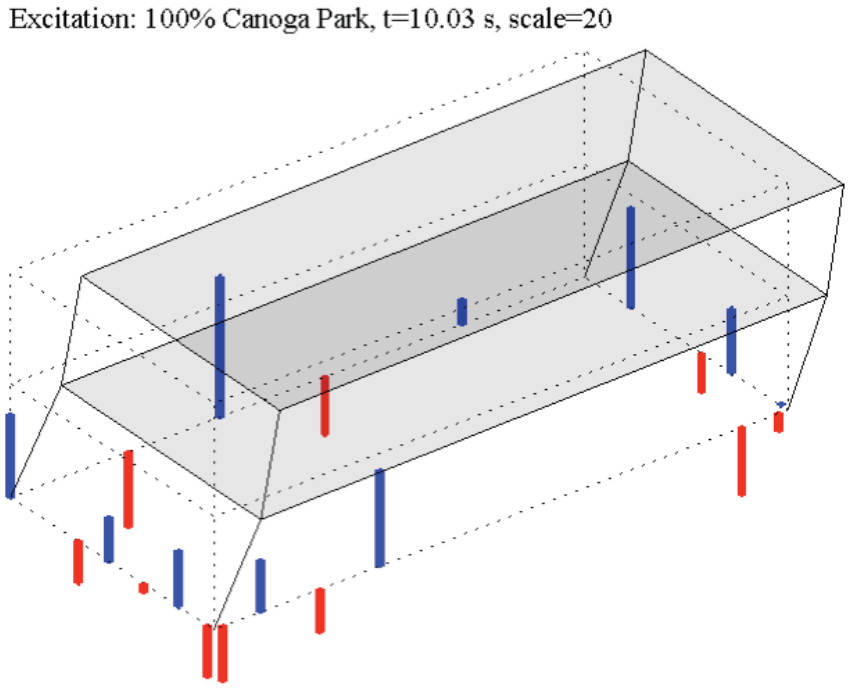

Figure H-14: A1-3D-RD-a model, simplified illustration of corner displacements with hold down forces from load cells,100 % Canoga Park, 3D nonlinear analysis (max hold down tensile force is -4.78 kips)

Appendix I: Analysis Results of State-of-the-art, Phase 1, 3D, rigid-diaphragm, model b (A1-3D-RD-b)

I.1 Model description

This state-of-the-art 3D model features subpanel bracing models of shear walls, explicit models of hold downs, bare steel framing of gravity walls, and rigid diaphragms. Seismic mass is distributed to corners and stud ends. The lateral displacement and shear wall capacity ($\delta(0.4V_{nA})$, $0.4V_{nA}$) from test is utilized to determine the stiffness of elastic material and the first point on the backbone curve of Pinching4 material of shear wall bracing. Figure I-1 is the 3D drawing of the building model with all members and diagonal bracings of sheathing panels. Definitions of output physical quantities and explanation of post-process method can be found in Appendix K.

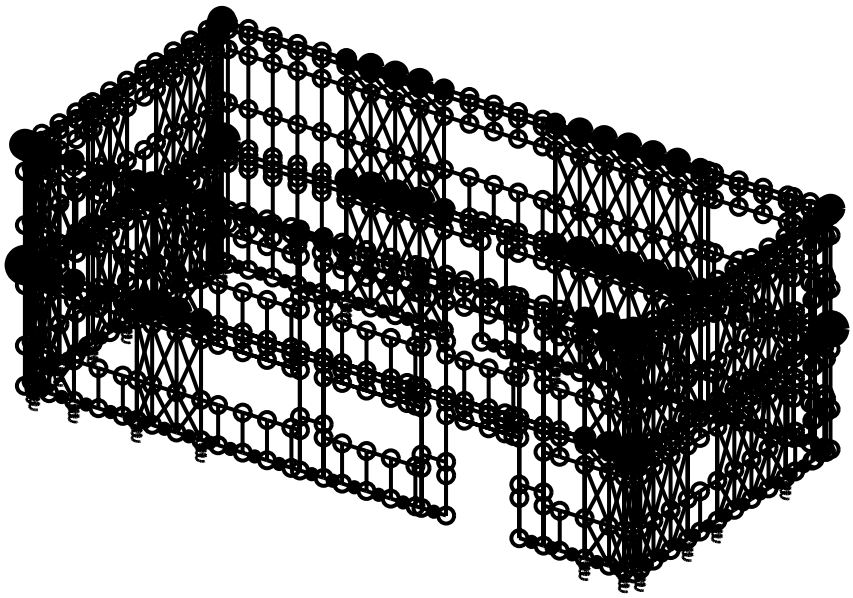

Figure I-1: A1-3D-RD-b model

I.2 Free vibration analysis results

Free vibration analysis results are presented in Table I-1 and Figure I-2. Lateral stiffness in the short direction is smaller than lateral stiffness in the long direction and torsional stiffness is the largest. The observation holds for the first and the second mode, as indicated by Table I-1.

Table I-1: Free vibration analysis results, A1-3D-RD-b model

Mode number	Natural period (s)	Mode description
1	0.386	Short, 1st
2	0.347	Long, 1st
3	0.280	Torsion, 1st
4	0.137	Short, 2nd
5	0.126	Long, 2nd
6	0.104	Torsion, 2nd

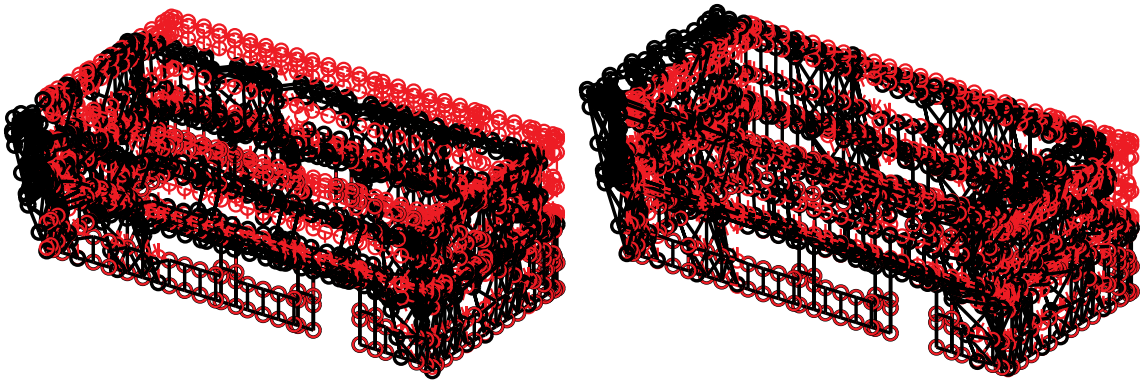

(a) Mode 1, T_1=0.386 s (b) Mode 2, T_2=0.347 s

Figure I-2: First two natural modes of A1-3D-RD-b model

I.3 Linear static analysis results

Table I-2 to Table I-4 present linear static analysis results. The lateral load is the equivalent lateral force available from the design narrative (Madsen et al. 2011), applied equally at four corners. Two separate analyses were performed with the loading at long or short direction.

Table I-2 summarizes the breakdown of peak total base shear among four elevations. Due to the interplay of asymmetrical LFRS, wall lines perpendicular to the loading direction still take a very small portion of base shear.

Table I-3 shows peak building and wall line deflections. Practicing engineers can linearly upscale these data and develop an estimate of the building's performance at a certain lateral force level.

Table I-4 is an evaluation of the building's lateral stiffness of long and short direction and its breakdown among shear walls (SW) and other systems. Interestingly, the bare CFS framing still accounts for 14% total lateral stiffness in this case.

Table I-2: Breakdown of peak base shear, linear static analysis, A1-3D-RD-b model

Load direction	**LONG**				
Elevation	**South V_b**	**North V_b**	**East V_b**	**West V_b**	**Peak V_b**
kips	3.6	7.3	0.0	0.1	11.1
%	32.2	66.1	0.5	1.2	100.0
Load direction	**SHORT**				
Elevation	**South V_b**	**North V_b**	**East V_b**	**West V_b**	**Peak V_b**
kips	0.1	0.1	5.5	5.3	11.1
%	1.2	1.3	49.3	48.2	100.0

Table I-3: Peak building and wall line deflection, linear static analysis, A1-3D-RD-b model

Load direction	**LONG**							
Deflection (in.)	u_1	u_2	v_1	v_2	Δu_1	Δu_2	Δv_1	Δv_2
Building	0.134	0.226	-0.005	-0.010	0.134	0.091	-0.005	-0.005
South	0.144	0.242	-0.005	-0.010	0.144	0.098	-0.005	-0.005
North	0.124	0.209	-0.005	-0.010	0.124	0.085	-0.005	-0.005
East	0.134	0.226	0.017	0.025	0.134	0.091	0.017	0.008
West	0.134	0.226	-0.027	-0.046	0.134	0.091	-0.027	-0.019
Load direction	**SHORT**							
Deflection (in.)	u_1	u_2	v_1	v_2	Δu_1	Δu_2	Δv_1	Δv_2
Building	-0.003	-0.006	0.164	0.275	-0.003	-0.003	0.164	0.111
South	-0.006	-0.012	0.164	0.275	-0.006	-0.006	0.164	0.111
North	-0.001	-0.001	0.164	0.275	-0.001	-0.001	0.164	0.111
East	-0.003	-0.006	0.157	0.263	-0.003	-0.003	0.157	0.105
West	-0.003	-0.006	0.170	0.288	-0.003	-0.003	0.170	0.117

Table I-4: Breakdown of lateral stiffness, A1-3D-RD-b model

LONG			**SHORT**		
Shear wall k_u (%)	**Gravity wall k_u (%)**	**k_u (kip/in)**	**Shear wall k_v (%)**	**Gravity wall k_v (%)**	**k_v (kip/in)**
85.2	14.8	48.6	85.7	14.3	39.2

I.4 Nonlinear static (pushover) analysis results

Table I-5 is created following the same logic with Table I-2, but the analysis type is nonlinear static (pushover). Pushover curves of the building and each wall line are presented Figure I-3 in and Figure I-4.

Clearly, the interaction between wall lines is much more significant when material and geometrical nonlinearity is included. These tables and figures indicate that the wall lines do not reach their peak capacity at exactly the same drift level and wall lines perpendicular to the load can take a nontrivial amount of base shear. Total capacity of the building in the short direction is smaller than the long direction.

Table I-5: Breakdown of peak base shear, pushover analysis, A1-3D-RD-b model

Load direction	**LONG**				
Elevation	**South V_b**	**North V_b**	**East V_b**	**West V_b**	**Peak V_b**
kips	24.4	23.9	4.3	5.4	47.7
%	51.1	50.1	9.1	11.3	100.0
Load direction	**SHORT**				
Elevation	**South V_b**	**North V_b**	**East V_b**	**West V_b**	**Peak V_b**
kips	5.4	4.1	20.3	22.2	45.0
%	11.9	9.1	45.2	49.4	100.0

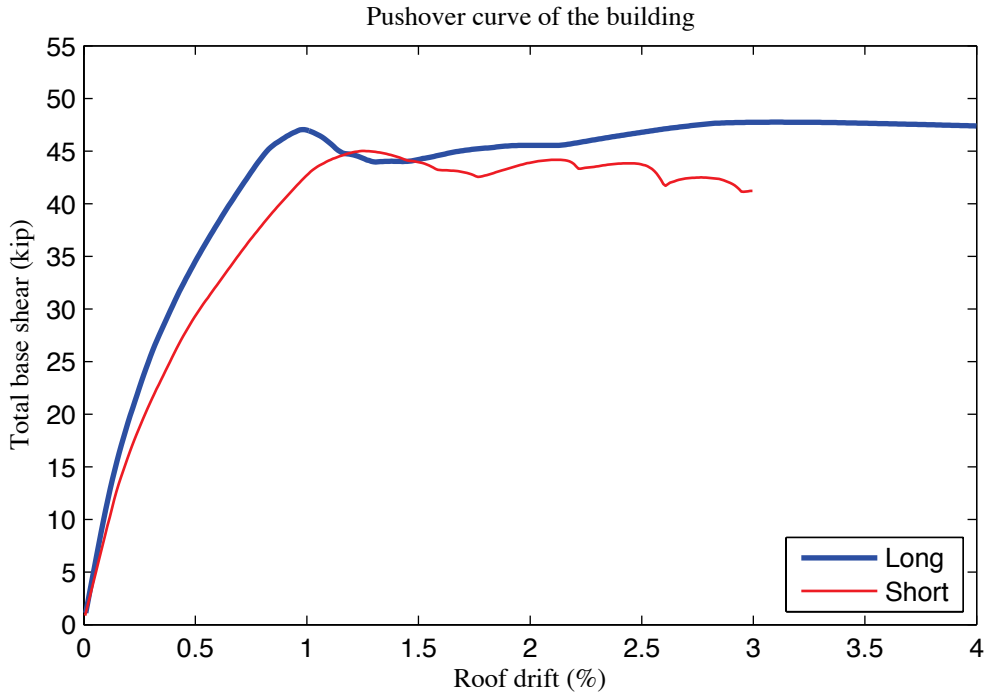

Figure I-3: Pushover curve of A1-3D-RD-b model

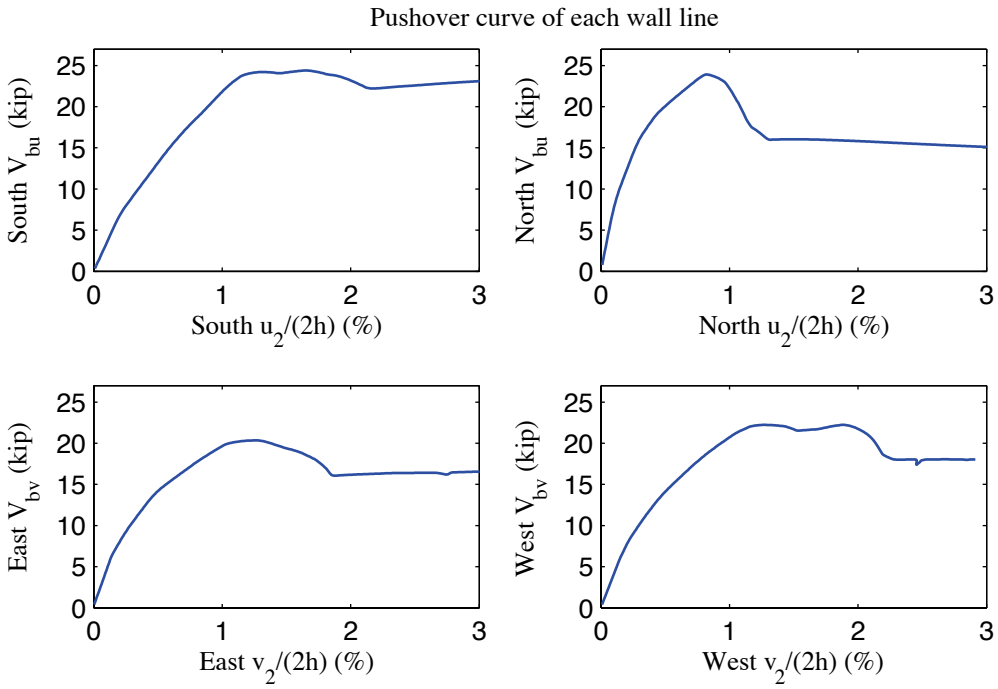

Figure I-4: Pushover curve of each wall line, A1-3D-RD-b model

I.5 Linear time history analysis results

Linear time history analysis is performed on the model under Canoga Park and Rinaldi ground motion records of Northridge earthquake in 1994. We considered three scale levels (16%, 44% and 100%) and loadings in one, two and three axes.

Table I-6 to Table I-9 demonstrate the building's linear elastic performance under designated ground motions. Table I-6 shows peak story relative accelerations in the unit of g. Table I-7 and Table I-8 report peak roof drift and story drift of the building and the corresponding time step (t_*) and the base shear at that time. Note that the base shear at the time of peak roof drift may not be the peak total building base shear in that direction (see Table I-9).

The building behaves linearly since peak drift and peak base shear appear at the same time when the ground motion is linearly scaled. Figure I-5 is a vector plot of the peak total resultant base shear of the building under three axial, 100% Canoga Park excitation. The directions of arrows imply that base shear taken by shear walls and gravity systems does not necessarily follow the direction of wall lines due to the effect of 3D coupling. Comparison with nonlinear analysis results of the same excitation provides insightful observations on the building's response and requirements on modeling fidelity and analysis type.

Table I-6: A1-3D-RD-b model peak story relative acceleration in g, linear time history analysis

		LONG			SHORT			UP		
Load Case	**Ground Motion**	**a_g**	**Floor a**	**Roof a**	**a_g**	**Floor a**	**Roof a**	**a_g**	**Floor a**	**Roof a**
EQ_3D_3axis_1	CNP 16%	0.067	0.151	0.252	0.057	0.104	0.164	0.078	0.066	0.073
EQ_3D_3axis_2	CNP 44%	0.185	0.421	0.700	0.157	0.282	0.441	0.215	0.158	0.136
EQ_3D_1axis_1	CNP 100%	0.420	0.916	1.545	0	0.164	0.252	0	0.217	0.204
EQ_3D_1axis_2	CNP 100%	0	0.095	0.129	0.356	0.575	0.957	0	0.508	0.464
EQ_3D_2axis_1	CNP 100%	0.420	0.947	1.597	0.356	0.625	0.979	0	0.432	0.421
EQ_3D_3axis_3	CNP 100%	0.420	0.947	1.597	0.356	0.625	0.979	0.489	0.432	0.421
EQ_3D_3axis_4	RRS 16%	0.132	0.226	0.324	0.078	0.267	0.417	0.133	0.182	0.160
EQ_3D_3axis_5	RRS 44%	0.363	0.648	0.922	0.214	0.738	1.128	0.367	0.505	0.470
EQ_3D_3axis_6	RRS 100%	0.825	1.541	2.169	0.486	1.675	2.536	0.834	1.535	1.428

Table I-7: A1-3D-RD-b model peak building roof drift and base shear, linear time history analysis

		LONG			SHORT		
Load Case	**Ground Motion**	**$u_2/(2h)$ (%)**	**t_* (s)**	**V_b @ t_* (kips)**	**$v_2/(2h)$ (%)**	**t_* (s)**	**V_b @ t_* (kips)**
EQ_3D_3axis_1	CNP 16%	-0.130	11.90	13.6	-0.092	10.56	8.2
EQ_3D_3axis_2	CNP 44%	-0.365	11.90	37.6	-0.246	10.56	22.0
EQ_3D_1axis_1	CNP 100%	-0.806	11.91	82.9	-0.133	12.23	12.4
EQ_3D_1axis_2	CNP 100%	0.067	11.32	6.5	-0.547	8.45	44.8
EQ_3D_2axis_1	CNP 100%	-0.842	11.91	85.5	-0.549	5.46	46.2
EQ_3D_3axis_3	CNP 100%	-0.842	11.91	85.5	-0.549	5.46	46.2
EQ_3D_3axis_4	RRS 16%	-0.183	4.56	19.0	-0.238	4.40	20.6
EQ_3D_3axis_5	RRS 44%	-0.539	4.57	54.7	-0.658	4.40	56.7
EQ_3D_3axis_6	RRS 100%	-1.283	4.57	129.0	-1.498	4.41	127.7

Table I-8: A1-3D-RD-b model peak building story drift, linear time history analysis

		LONG				SHORT			
Load Case	**Ground Motion**	**$\Delta u_1/h$ (%)**	**t_* (s)**	**$\Delta u_2/h$ (%)**	**t_* (s)**	**$\Delta v_1/h$ (%)**	**t_* (s)**	**$\Delta v_2/h$ (%)**	**t_* (s)**
EQ_3D_3axis_1	CNP 16%	-0.158	11.90	-0.102	11.90	-0.114	10.55	-0.072	8.45
EQ_3D_3axis_2	CNP 44%	-0.443	11.90	-0.288	11.90	-0.305	10.56	-0.192	8.45
EQ_3D_1axis_1	CNP 100%	-0.971	11.91	-0.641	11.91	-0.163	12.23	-0.105	12.57
EQ_3D_1axis_2	CNP 100%	0.082	11.32	0.060	8.47	-0.652	8.44	-0.448	8.45
EQ_3D_2axis_1	CNP 100%	-1.016	11.91	-0.668	11.91	-0.680	10.56	-0.439	5.46
EQ_3D_3axis_3	CNP 100%	-1.016	11.91	-0.668	11.91	-0.680	10.56	-0.439	5.46
EQ_3D_3axis_4	RRS 16%	-0.229	4.57	-0.139	4.56	-0.295	4.40	0.181	4.57
EQ_3D_3axis_5	RRS 44%	-0.669	4.57	-0.408	4.57	-0.816	4.40	-0.505	4.41
EQ_3D_3axis_6	RRS 100%	-1.588	4.57	-0.978	4.57	-1.855	4.40	-1.158	4.41

Table I-9: A1-3D-RD-b model peak building base shear, linear time history analysis

		LONG		SHORT		RESULTANT	
Load Case	**Ground Motion**	**Peak V_{bu} (kip)**	**t @ peak V_{bu} (s)**	**Peak V_{bv} (kip)**	**t @ peak V_{bv} (s)**	**Peak V_b (kip)**	**t @ peak V_b (s)**
EQ_3D_3axis_1	CNP 16%	13.6	11.90	8.2	10.55	13.6	11.90
EQ_3D_3axis_2	CNP 44%	37.6	11.90	22.0	10.56	37.6	11.90
EQ_3D_1axis_1	CNP 100%	82.9	11.91	12.8	12.40	83.3	11.91
EQ_3D_1axis_2	CNP 100%	6.9	9.16	45.7	5.24	45.7	5.24
EQ_3D_2axis_1	CNP 100%	85.5	11.91	49.0	10.56	85.5	11.91
EQ_3D_3axis_3	CNP 100%	85.5	11.91	49.0	10.56	85.5	11.91
EQ_3D_3axis_4	RRS 16%	19.0	4.57	20.6	4.40	27.4	4.39
EQ_3D_3axis_5	RRS 44%	54.7	4.57	56.7	4.40	77.4	4.40
EQ_3D_3axis_6	RRS 100%	129.0	4.57	128.7	4.40	179.5	4.40

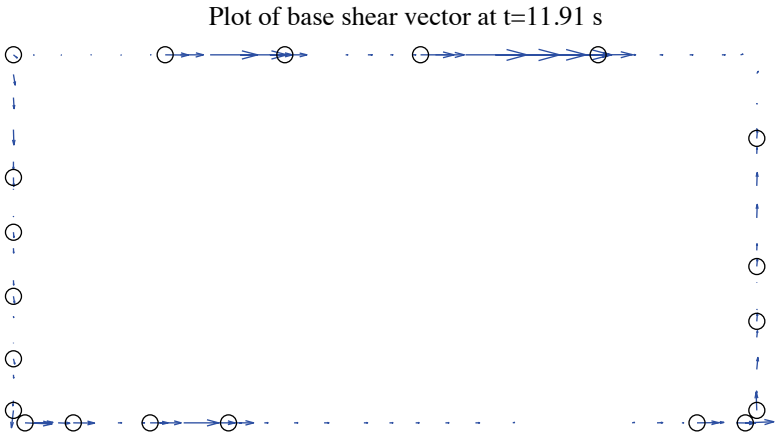

Figure I-5: A1-3D-RD-b model, base shear vector plot at the moment of peak total base shear, 100 % Canoga Park, 3D linear analysis (maximum anchor/hold down base shear is 5.88 kips)

I.6 Nonlinear time history analysis results

Same ground motions are applied to the model with material and geometrical nonlinearity. Table I-10 to Table I-13 are replicas of Table I-6 to Table I-9, but for nonlinear time history analyses. Since this analysis type is most complicated and closest to reality and experiments, behavior of wall lines and hold downs are further studied. Table I-14 is the table of peak wall line story drifts and corresponding time steps. Table I-15 is designed for peak base shear of each wall line and the last two columns of the table are percentages of base shear of two facing wall lines in the same direction when the total base shear in that direction takes peak value. Table I-16 expands the breakdown of each wall line's peak base shear between shear walls, gravity walls and other systems. Table I-17 is peak value of hold down tensile force of two selected pairs. Hold down 5 and 6 are on shear wall L1S1, South elevation and hold down 7 and 8 are on shear wall L1W1, West elevation. These shear walls have lowest capacities compared with others on the same wall line and they meet at the southwest edge of the building, so interacted nonlinear behavior is expected to appear.

Time history plots in this section include plots of story drifts of the building and each wall line (Figure I-6 to Figure I-8), total building base shear in long and short direction (Figure I-9) and axial forces of hold downs in Table I-17 (Figure I-10). Hysteretic plots in Figure I-11 and Figure I-12 are helpful for visual examination of nonlinear base shear-drift relationship of the building and the weakest shear wall on each wall line. In comparison with linear time history analysis, vector plot of peak total base shear is illustrated in Figure I-13. Figure I-14 presents a simplified deformed shape of the

building (see (Peterman 2014) for details of the method) and axial force of all twenty hold downs at the moment of peak total base shear. The same sign convention with tests is adopted. Red bars indicate tensile (negative) force and blue ones are for compressive (positive) force.

Hysteretic behavior is seen in the building and typical shear walls under design-based earthquake (100% Canoga Park excitation in 3 axes, see Figure I-11 and Figure I-12). However, wall lines behave differently. Backbones of response curves of shear walls on North and West wall lines reach the post-peak range. Peak story drifts of the building are not greater than 1.7% (Table I-12), and larger deflection is seen in the long direction. Peak wall line drifts are smaller than 2.2% (Table I-14), with the maximum found in West elevation. Figure I-13 clearly shows that base shear vectors in anchors and hold downs do not align with wall lines and they can change directions even within a single piece of wall, a sign of localized behavior. Table I-17, Figure I-10 and Figure I-14 demonstrate that hold downs in a pair do not experience the same amount of force with opposite signs, an evidence that supports Type II shear wall behavior despite Type I design assumption.

The near-field Rinaldi record is much stronger in terms of peak ground acceleration, especially in the long direction. Analysis fails when loaded with 100% Rinaldi ground motion. The response goes to infinity at 2.56 s, the moment of peak ground acceleration. Table I-16 reveals that as nonlinearity increases, the portion of base shear taken by

gravity wall and other system grows significantly, from 3.1% to 7.2% on West elevation at minimum and from 15.1% to 25.4% on South elevation at maximum.

Table I-10: A1-3D-RD-b model peak story relative acceleration in g, nonlinear time history analysis

		LONG			SHORT			UP		
Load Case	**Ground Motion**	**a_g**	**Floor a**	**Roof a**	**a_g**	**Floor a**	**Roof a**	**a_g**	**Floor a**	**Roof a**
EQ_3D_3axis_1	CNP 16%	0.067	0.137	0.200	0.057	0.101	0.170	0.078	0.091	0.078
EQ_3D_3axis_2	CNP 44%	0.185	0.553	0.651	0.157	0.391	0.440	0.215	1.095	0.965
EQ_3D_1axis_1	CNP 100%	0.420	0.778	1.318	0	0.043	0.056	0	0.161	0.142
EQ_3D_1axis_2	CNP 100%	0	0.394	0.350	0.356	0.676	0.949	0	1.042	0.952
EQ_3D_2axis_1	CNP 100%	0.420	0.700	1.155	0.356	0.616	0.914	0	1.586	1.474
EQ_3D_3axis_3	CNP 100%	0.420	0.698	1.142	0.356	0.616	0.916	0.489	1.598	1.485
EQ_3D_3axis_4	RRS 16%	0.132	0.240	0.311	0.078	0.249	0.281	0.133	0.193	0.178
EQ_3D_3axis_5	RRS 44%	0.363	0.758	0.851	0.214	0.525	0.606	0.367	0.497	0.495
EQ_3D_3axis_6	RRS 100%	N/A	N/A	N/A	N/A	N/A	N/A	N/A	N/A	N/A

Table I-11: A1-3D-RD-b model peak building roof drift and base shear, nonlinear time history analysis

		LONG			SHORT		
Load Case	**Ground Motion**	**$u_2/(2h)$ (%)**	**t_* (s)**	**V_b @ t_* (kips)**	**$v_2/(2h)$ (%)**	**t_* (s)**	**V_b @ t_* (kips)**
EQ_3D_3axis_1	CNP 16%	0.105	8.71	11.4	-0.101	8.45	8.2
EQ_3D_3axis_2	CNP 44%	-0.397	10.59	29.6	-0.325	5.98	20.2
EQ_3D_1axis_1	CNP 100%	1.063	10.01	44.8	-0.030	4.45	1.8
EQ_3D_1axis_2	CNP 100%	-0.053	9.48	2.1	1.147	10.07	44.8
EQ_3D_2axis_1	CNP 100%	1.075	10.01	43.8	1.094	10.07	37.4
EQ_3D_3axis_3	CNP 100%	1.075	10.01	43.8	1.095	10.07	37.4
EQ_3D_3axis_4	RRS 16%	0.166	4.41	17.5	-0.186	4.42	14.8
EQ_3D_3axis_5	RRS 44%	0.627	2.68	42.2	0.429	6.08	27.1
EQ_3D_3axis_6	RRS 100%	N/A	N/A	N/A	N/A	N/A	N/A

Table I-12: A1-3D-RD-b model peak building story drift, nonlinear linear time history analysis

		LONG				SHORT			
Load Case	**Ground Motion**	**$\Delta u_1/h$ (%)**	**t_* (s)**	**$\Delta u_2/h$ (%)**	**t_* (s)**	**$\Delta v_1/h$ (%)**	**t_* (s)**	**$\Delta v_2/h$ (%)**	**t_* (s)**
EQ_3D_3 axis_1	CNP 16%	-0.130	11.89	0.086	8.70	-0.120	8.44	-0.086	8.46
EQ_3D_3 axis_2	CNP 44%	-0.542	10.57	-0.282	10.60	-0.415	5.96	-0.269	6.00
EQ_3D_1 axis_1	CNP 100%	1.685	10.02	-0.749	10.28	-0.037	4.81	-0.028	4.45
EQ_3D_1 axis_2	CNP 100%	-0.077	8.77	0.108	24.45	1.474	10.08	0.829	10.06
EQ_3D_2 axis_1	CNP 100%	1.680	10.03	-0.686	9.72	1.452	10.08	0.750	10.06
EQ_3D_3 axis_3	CNP 100%	1.681	10.03	-0.686	9.72	1.453	10.09	0.749	10.06
EQ_3D_3 axis_4	RRS 16%	0.222	4.40	0.117	4.43	-0.246	4.42	-0.136	5.26
EQ_3D_3 axis_5	RRS 44%	0.949	2.69	0.388	6.88	0.580	6.07	0.299	6.10
EQ_3D_3 axis_6	RRS 100%	N/A	N/A	N/A	N/A	N/A	N/A	N/A	N/A

Table I-13: A1-3D-RD-b model peak building base shear, nonlinear time history analysis

		LONG		SHORT		RESULTANT	
Load Case	**Ground Motion**	**Peak V_{bu} (kip)**	**t @ peak V_{bu} (s)**	**Peak V_{bv} (kip)**	**t @ peak V_{bv} (s)**	**Peak V_b (kip)**	**t @ peak V_b (s)**
EQ_3D_3axis_1	CNP 16%	11.9	8.73	8.4	8.44	12.7	10.53
EQ_3D_3axis_2	CNP 44%	31.2	10.57	22.0	5.95	31.2	10.57
EQ_3D_1axis_1	CNP 100%	48.0	8.73	2.5	4.82	48.0	8.73
EQ_3D_1axis_2	CNP 100%	6.8	22.20	44.8	10.07	44.8	10.07
EQ_3D_2axis_1	CNP 100%	46.5	8.73	41.6	10.04	59.0	10.04
EQ_3D_3axis_3	CNP 100%	46.5	8.73	41.5	10.04	58.9	10.04
EQ_3D_3axis_4	RRS 16%	17.6	4.40	14.8	4.42	22.7	4.41
EQ_3D_3axis_5	RRS 44%	42.3	2.69	27.7	6.06	42.3	2.68
EQ_3D_3axis_6	RRS 100%	N/A	N/A	N/A	N/A	N/A	N/A

Table I-14: A1-3D-RD-b model peak wall line story drift, nonlinear time history analysis

LONG		SOUTH				NORTH			
Load Case	**Ground Motion**	**$\Delta u_1/h$ (%)**	**t_* (s)**	**$\Delta u_2/h$ (%)**	**t_* (s)**	**$\Delta u_1/h$ (%)**	**t_* (s)**	**$\Delta u_2/h$ (%)**	**t_* (s)**
EQ_3D_3axis_1	CNP 16%	0.148	11.89	0.088	8.70	0.121	8.73	0.085	8.70
EQ_3D_3axis_2	CNP 44%	0.588	10.57	0.298	10.60	0.526	8.72	0.266	10.60
EQ_3D_1axis_1	CNP 100%	1.620	10.02	0.745	10.28	1.750	10.02	0.753	10.28
EQ_3D_1axis_2	CNP 100%	0.162	8.55	0.106	22.20	0.071	22.20	0.126	22.07
EQ_3D_2axis_1	CNP 100%	1.532	10.02	0.716	10.28	1.854	10.04	0.693	9.72
EQ_3D_3axis_3	CNP 100%	1.533	10.02	0.711	10.27	1.856	10.04	0.693	9.72
EQ_3D_3axis_4	RRS 16%	0.261	4.41	0.141	4.43	0.188	4.40	0.099	2.61
EQ_3D_3axis_5	RRS 44%	0.978	2.68	0.405	6.88	0.923	2.69	0.371	6.88
EQ_3D_3axis_6	RRS 100%	N/A	N/A	N/A	N/A	N/A	N/A	N/A	N/A
SHORT		**EAST**				**WEST**			
Load Case	**Ground Motion**	**$\Delta v_1/h$ (%)**	**t_* (s)**	**$\Delta v_2/h$ (%)**	**t_* (s)**	**$\Delta v_1/h$ (%)**	**t_* (s)**	**$\Delta v_2/h$ (%)**	**t_* (s)**
EQ_3D_3axis_1	CNP 16%	0.137	10.55	0.090	8.48	0.128	8.42	0.097	8.45
EQ_3D_3axis_2	CNP 44%	0.370	8.39	0.277	8.44	0.480	5.96	0.370	6.00
EQ_3D_1axis_1	CNP 100%	0.173	10.04	0.074	8.91	0.137	10.07	0.062	8.92
EQ_3D_1axis_2	CNP 100%	1.364	10.07	0.754	10.06	1.593	10.08	0.905	10.06
EQ_3D_2axis_1	CNP 100%	1.038	8.51	0.619	10.06	2.225	10.11	0.885	10.07
EQ_3D_3axis_3	CNP 100%	1.037	8.51	0.618	10.06	2.230	10.11	0.886	10.07
EQ_3D_3axis_4	RRS 16%	0.185	5.24	0.126	5.26	0.347	4.43	0.183	4.45
EQ_3D_3axis_5	RRS 44%	0.451	6.06	0.241	3.96	0.713	6.08	0.393	6.11
EQ_3D_3axis_6	RRS 100%	N/A	N/A	N/A	N/A	N/A	N/A	N/A	N/A

Table I-15: A1-3D-RD-b model peak wall line base shear, nonlinear time history analysis

LONG		SOUTH		NORTH		% of Peak V_{bu}	
Load Case	**Ground Motion**	**Peak V_{bu} (kips)**	**t @ peak V_{bu} (s)**	**Peak V_{bu} (kips)**	**t @ peak V_{bu} (s)**	**South**	**North**
EQ_3D_3axis_1	CNP 16%	4.3	11.89	7.7	8.73	33.1	65.0
EQ_3D_3axis_2	CNP 44%	12.3	10.57	18.4	8.72	39.4	57.2
EQ_3D_1axis_1	CNP 100%	23.5	10.02	24.1	8.72	44.9	48.8
EQ_3D_1axis_2	CNP 100%	4.4	8.56	4.8	23.75	21.5	70.6
EQ_3D_2axis_1	CNP 100%	23.3	8.80	24.5	8.72	42.8	51.7
EQ_3D_3axis_3	CNP 100%	23.3	8.80	24.5	8.72	42.8	51.5
EQ_3D_3axis_4	RRS 16%	7.0	4.59	10.4	4.39	38.9	59.0
EQ_3D_3axis_5	RRS 44%	17.6	2.68	22.4	2.69	41.6	53.1
EQ_3D_3axis_6	RRS 100%	N/A	N/A	N/A	N/A	N/A	N/A
SHORT		**EAST**		**WEST**		**% of Peak V_{bv}**	
Load Case	**Ground Motion**	**Peak V_{bv} (kips)**	**t @ peak V_{bv} (s)**	**Peak V_{bv} (kips)**	**t @ peak V_{bv} (s)**	**East**	**West**
EQ_3D_3axis_1	CNP 16%	4.9	10.56	4.4	8.42	49.0	49.3
EQ_3D_3axis_2	CNP 44%	10.1	8.39	11.6	5.96	42.9	52.8
EQ_3D_1axis_1	CNP 100%	5.3	10.04	4.9	10.08	78.0	20.6
EQ_3D_1axis_2	CNP 100%	20.0	10.07	22.3	10.07	44.7	49.8
EQ_3D_2axis_1	CNP 100%	17.9	8.51	23.1	10.04	39.7	55.6
EQ_3D_3axis_3	CNP 100%	17.9	8.51	23.1	10.04	39.7	55.6
EQ_3D_3axis_4	RRS 16%	6.4	5.24	9.4	4.43	34.1	63.0
EQ_3D_3axis_5	RRS 44%	11.4	6.06	15.1	6.08	41.1	54.1
EQ_3D_3axis_6	RRS 100%	N/A	N/A	N/A	N/A	N/A	N/A

Table I-16: A1-3D-RD-b model wall line base shear breakdown, nonlinear time history analysis

LONG		SOUTH			NORTH		
Load Case	**Ground Motion**	**Peak V_{bu} (kips)**	**SW V_{bu} (%)**	**GW V_{bu} (%)**	**Peak V_{bu} (kips)**	**SW V_{bu} (%)**	**GW V_{bu} (%)**
EQ_3D_3axis_1	CNP 16%	4.3	84.9	15.1	7.7	95.2	4.8
EQ_3D_3axis_2	CNP 44%	12.3	79.1	20.9	18.4	92.5	7.5
EQ_3D_1axis_1	CNP 100%	23.5	74.6	25.4	24.1	89.1	10.9
EQ_3D_1axis_2	CNP 100%	4.4	84.9	15.1	4.8	95.5	4.5
EQ_3D_2axis_1	CNP 100%	23.3	74.6	25.4	24.5	88.1	11.9
EQ_3D_3axis_3	CNP 100%	23.3	74.6	25.4	24.5	88.2	11.8
EQ_3D_3axis_4	RRS 16%	7.0	84.5	15.5	10.4	94.7	5.3
EQ_3D_3axis_5	RRS 44%	17.6	77.1	22.9	22.4	89.8	10.2
EQ_3D_3axis_6	RRS 100%	N/A	N/A	N/A	N/A	N/A	N/A
SHORT		**EAST**			**WEST**		
Load Case	**Ground Motion**	**Peak V_{bv} (kips)**	**SW V_{bv} (%)**	**GW V_{bu} (%)**	**Peak V_{bv} (kips)**	**SW V_{bv} (%)**	**GW V_{bv} (%)**
EQ_3D_3axis_1	CNP 16%	4.9	93.9	6.1	4.4	96.9	3.1
EQ_3D_3axis_2	CNP 44%	10.1	92.2	7.8	11.6	95.6	4.4
EQ_3D_1axis_1	CNP 100%	5.3	93.4	6.6	4.9	96.4	3.6
EQ_3D_1axis_2	CNP 100%	20.0	88.9	11.1	22.3	92.9	7.1
EQ_3D_2axis_1	CNP 100%	17.9	88.4	11.6	23.1	92.8	7.2
EQ_3D_3axis_3	CNP 100%	17.9	88.3	11.7	23.1	92.8	7.2
EQ_3D_3axis_4	RRS 16%	6.4	93.6	6.4	9.4	96.1	3.9
EQ_3D_3axis_5	RRS 44%	11.4	92.8	7.2	15.1	94.2	5.8
EQ_3D_3axis_6	RRS 100%	N/A	N/A	N/A	N/A	N/A	N/A

Table I-17: A1-3D-RD-b model peak hold down tensile force at certain locations, nonlinear time history analysis

		L1S1, LC5		L1S1, LC6		L1W1, LC7		L1W1, LC8	
Load Case	**Ground Motion**	**Peak F (kips)**	**t @ peak F (s)**	**Peak F (kips)**	**t @ peak F (s)**	**Peak F (kips)**	**t @ peak F (s)**	**Peak F (kips)**	**t @ peak F (s)**
EQ_3D_3axis_1	CNP 16%	-1.71	11.89	-0.17	10.36	-0.18	9.39	-0.55	8.44
EQ_3D_3axis_2	CNP 44%	-2.80	10.58	-0.95	9.97	-0.96	9.97	-1.32	5.99
EQ_3D_1axis_1	CNP 100%	-3.72	10.27	-1.25	10.02	-2.13	10.01	-0.95	8.77
EQ_3D_1axis_2	CNP 100%	-2.55	10.08	-2.46	10.06	-1.33	10.06	-2.67	8.49
EQ_3D_2axis_1	CNP 100%	-3.82	10.26	-4.36	10.05	-3.94	10.04	-2.66	9.81
EQ_3D_3axis_3	CNP 100%	-3.81	10.25	-4.37	10.05	-3.93	10.04	-2.67	9.81
EQ_3D_3axis_4	RRS 16%	-2.30	4.59	-0.28	3.41	-0.23	2.66	-1.13	4.43
EQ_3D_3axis_5	RRS 44%	-3.07	6.17	-0.78	6.07	-1.27	2.70	-1.54	2.58
EQ_3D_3axis_6	RRS 100%	N/A	N/A	N/A	N/A	N/A	N/A	N/A	N/A

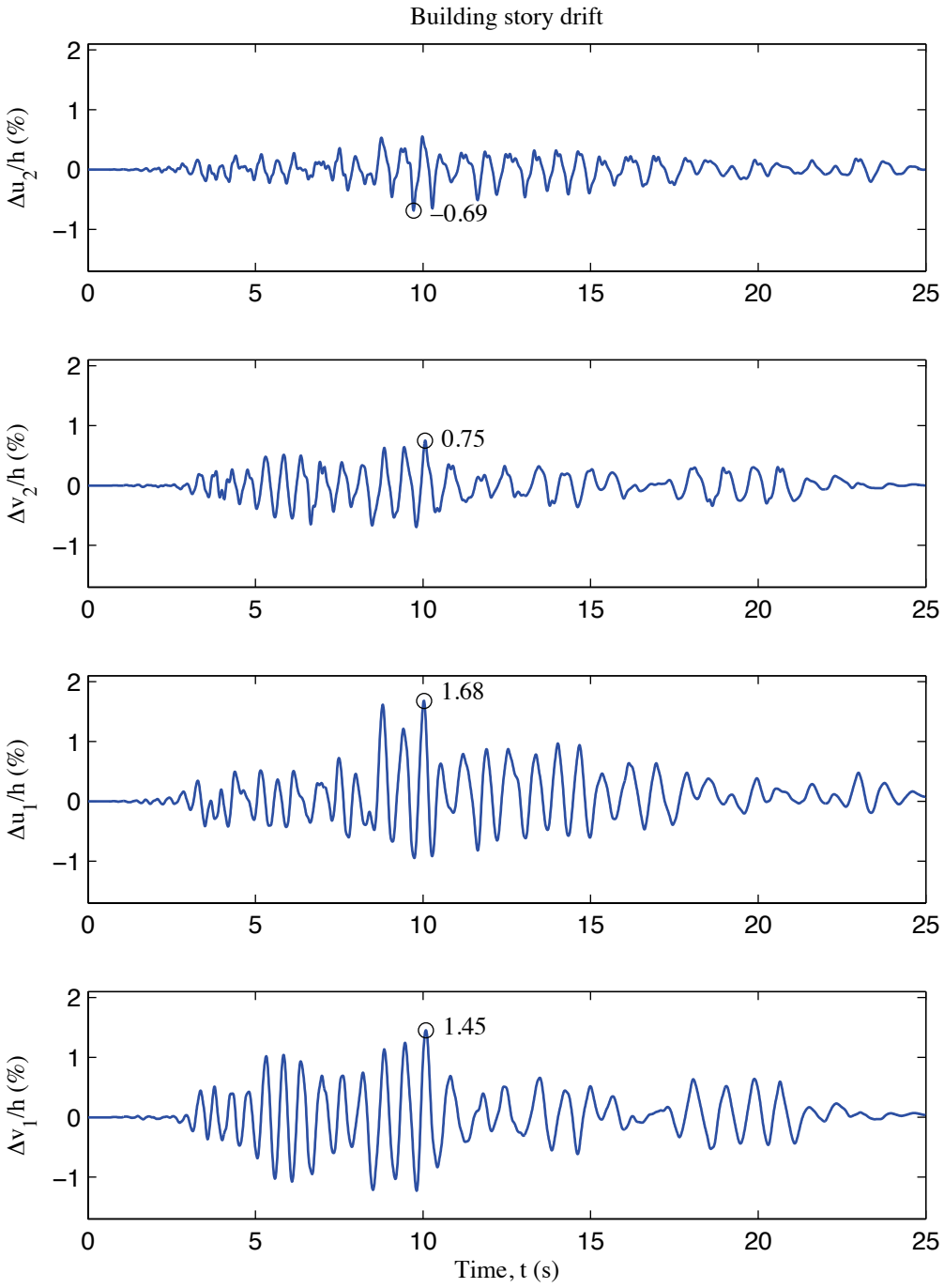

Figure I-6: A1-3D-RD-b model building story drift, 100 % Canoga Park, 3D nonlinear analysis

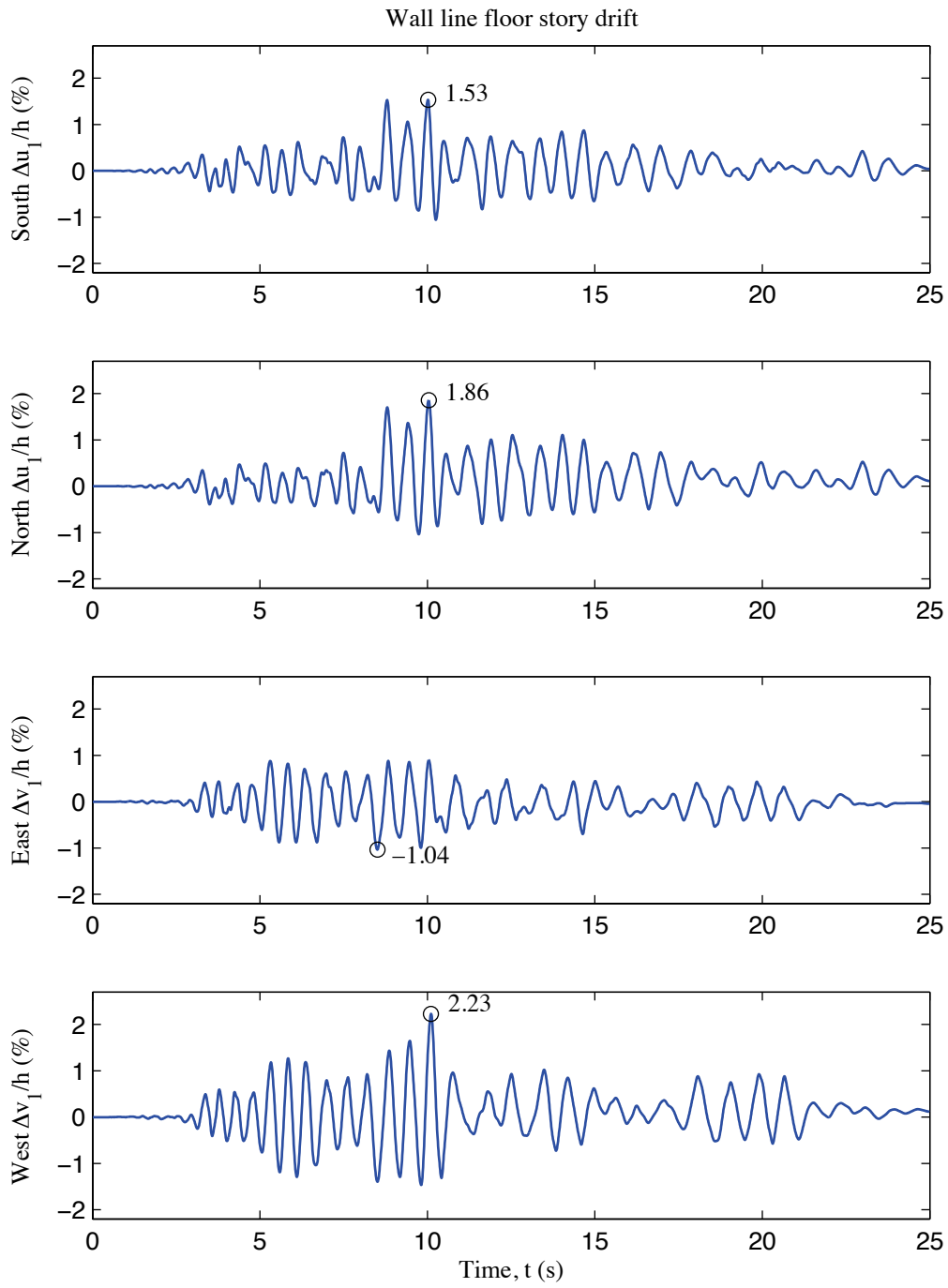

Figure I-7: A1-3D-RD-b model wall line floor story drift, 100 % Canoga Park, 3D nonlinear analysis

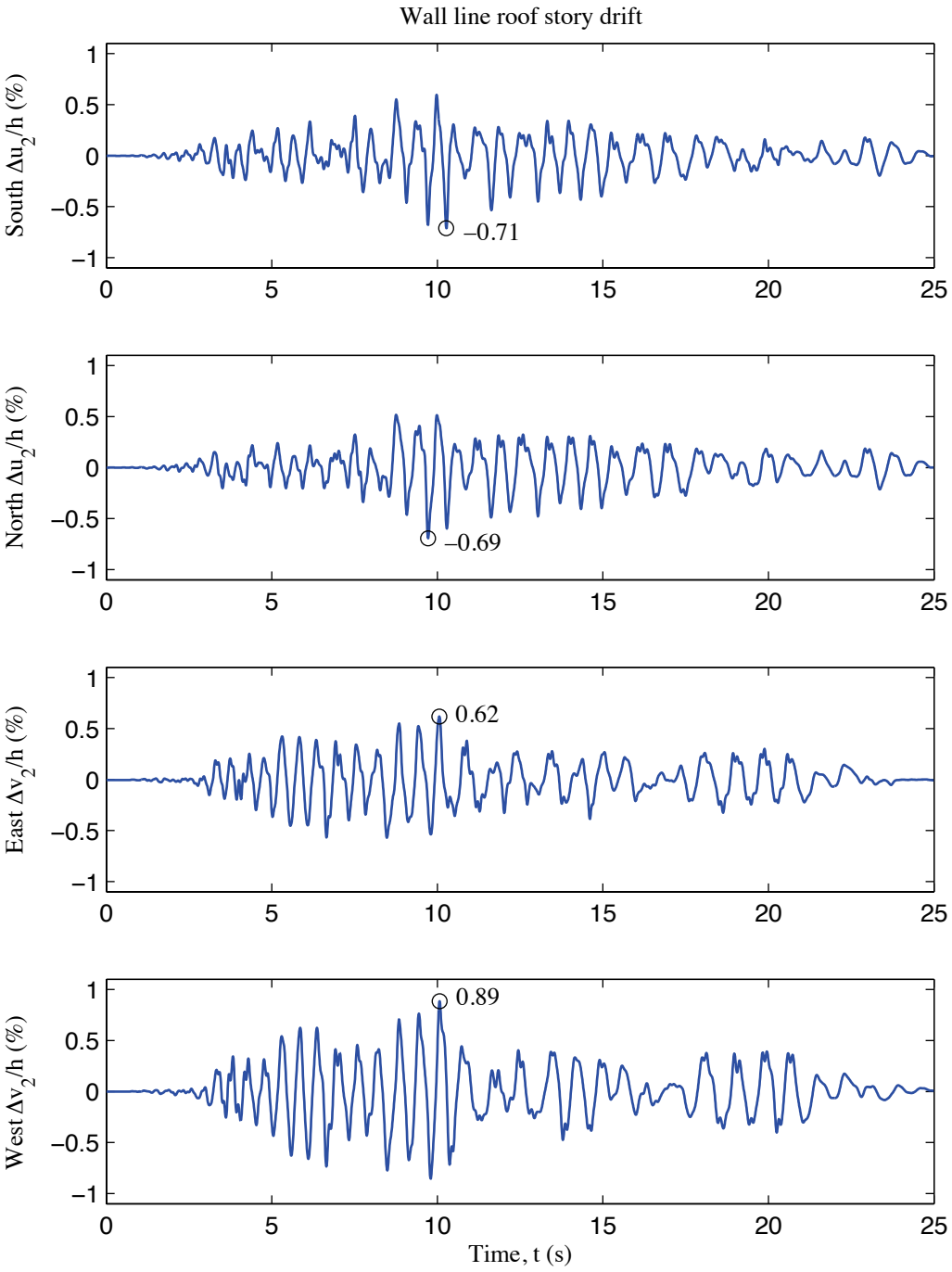

Figure I-8: A1-3D-RD-b model wall line roof story drift, 100 % Canoga Park, 3D nonlinear analysis

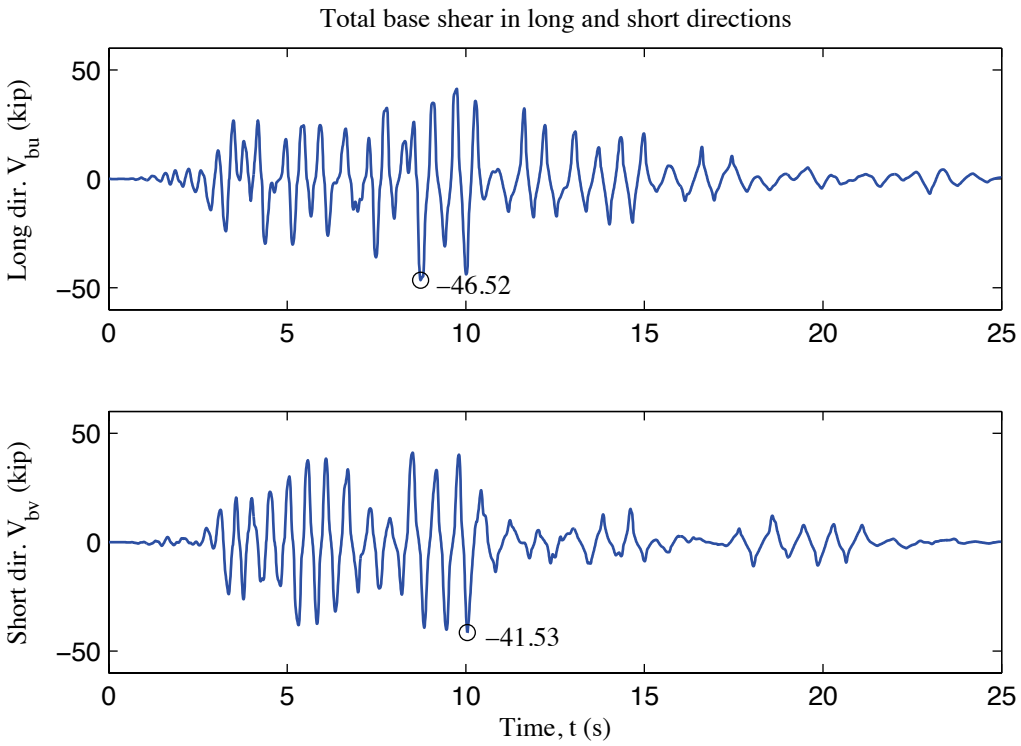

Figure I-9: A1-3D-RD-b model total building base shear, 100 % Canoga Park, 3D nonlinear analysis

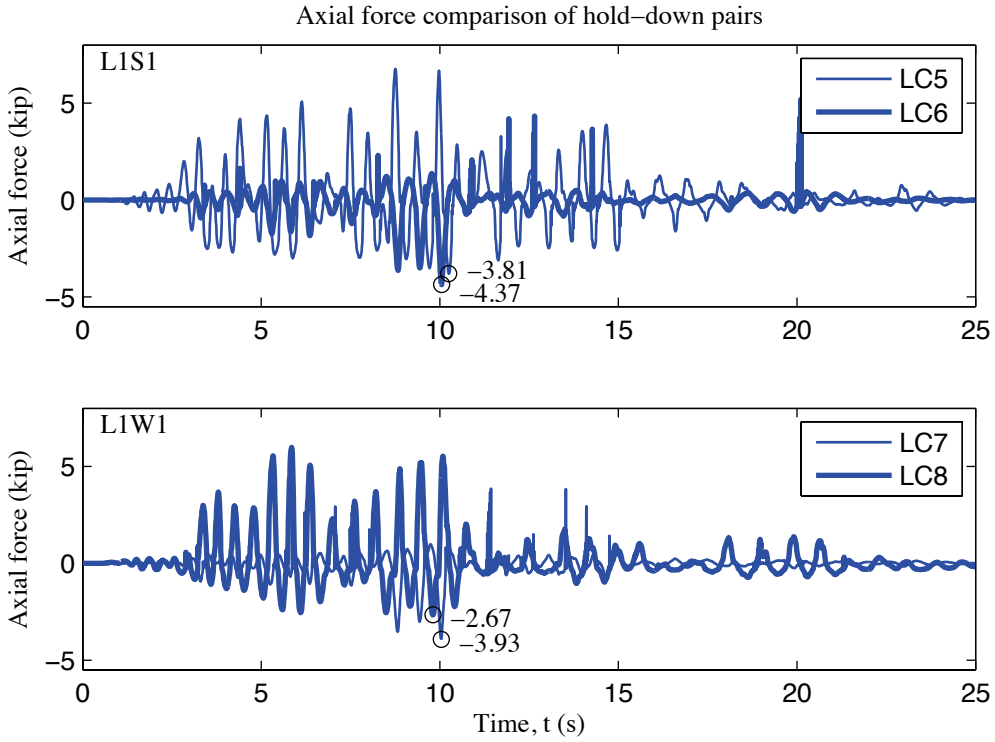

Figure I-10: A1-3D-RD-b model, load cell 5 to 8 axial forces, 100 % Canoga Park, 3D nonlinear analysis

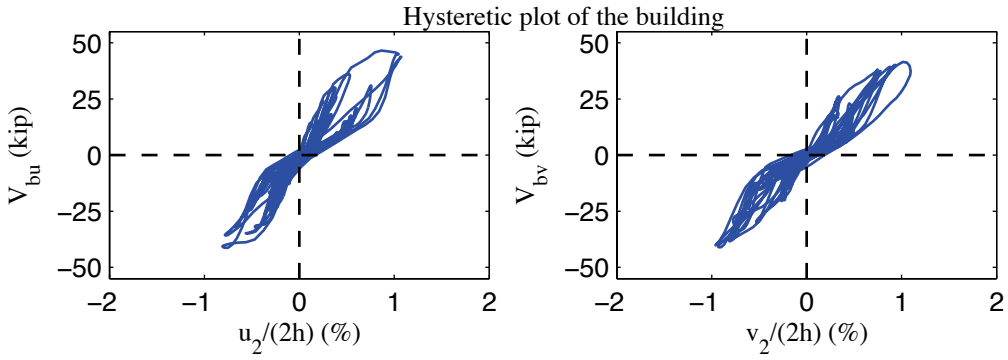

Figure I-11: A1-3D-RD-b model, hysteretic plot of the building, 100 % Canoga Park, 3D nonlinear analysis

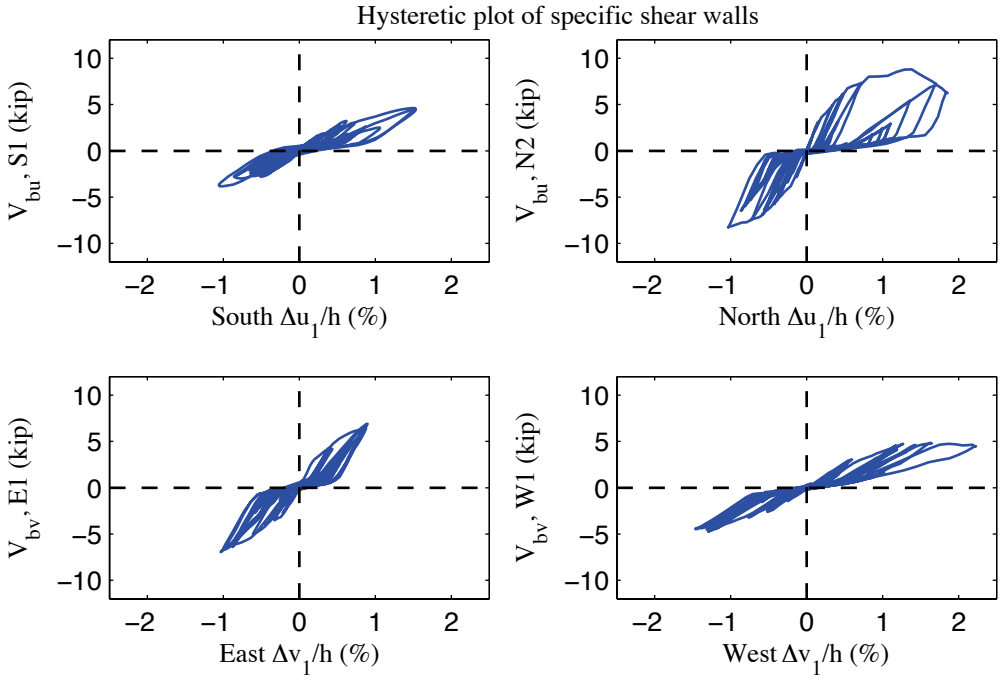

Figure I-12: A1-3D-RD-b model, hysteretic plot of shear walls at each elevation, 100 % Canoga Park, 3D nonlinear analysis

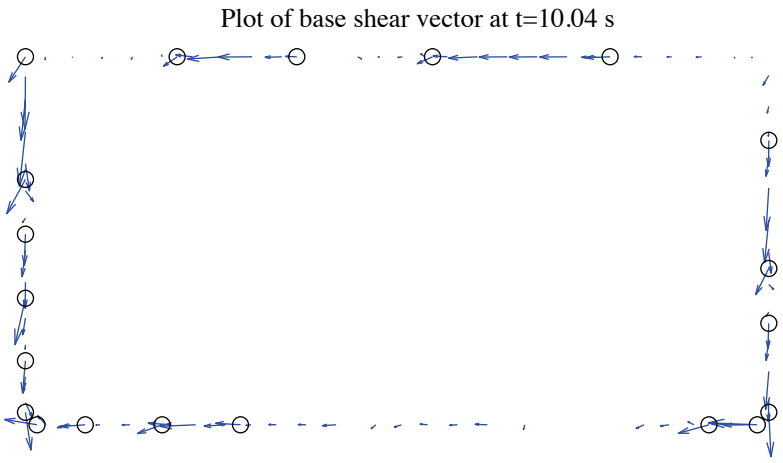

Figure I-13: A1-3D-RD-b model, field plot of peak total base shear, 100 % Canoga Park, 3D nonlinear analysis (maximum anchor/hold down base shear is 2.52 kips)

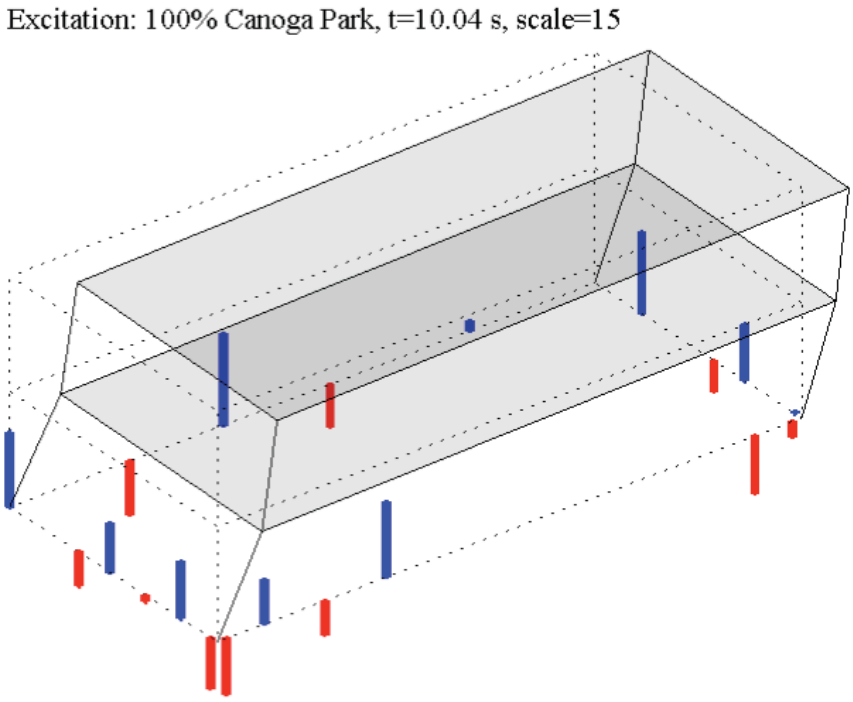

Figure I-14: A1-3D-RD-b model, simplified illustration of corner displacements with hold down forces from load cells,100 % Canoga Park, 3D nonlinear analysis (max hold down tensile force is -4.46 kips)

Appendix J: Analysis Results of State-of-the-art, Phase 1, 3D, rigid-diaphragm, model c (A1-3D-RD-c)

J.1 Model description

This state-of-the-art 3D model features bracing models of whole shear wall panels, explicit models of hold downs and rigid diaphragms. Shear anchors are modeled as pin supports on bottom tracks of shear walls only. Seismic mass is equally distributed to four corners. The lateral displacement and shear wall capacity ($\delta(0.2V_{nA})$, $0.2V_{nA}$) from test is utilized to determine the stiffness of elastic material and the first point on the backbone curve of Pinching4 material of shear wall bracing. Figure J-1 is the 3D drawing of the building model with all members and diagonal bracings of sheathing panels. Definitions of output physical quantities and explanation of post-process method can be found in Appendix K.

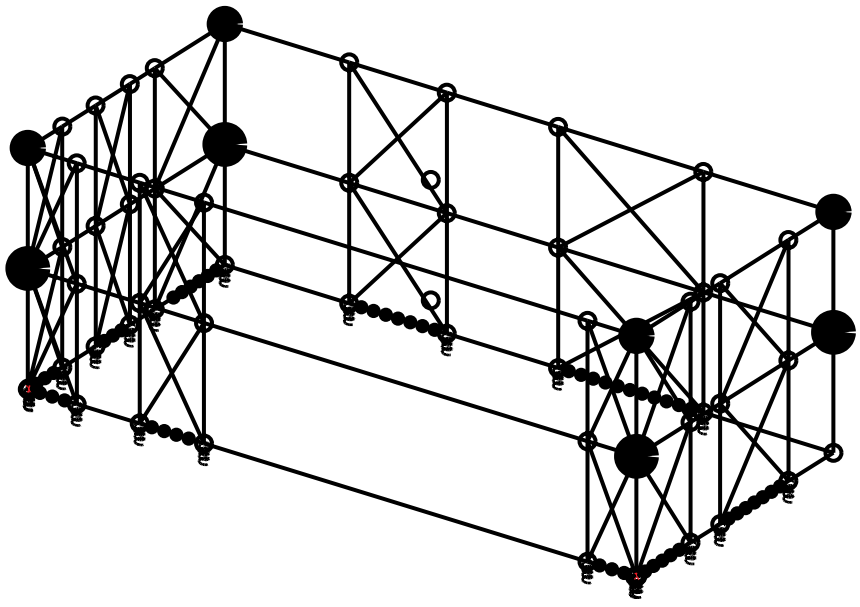

Figure J-1: A1-3D-RD-c model

J.2 Free vibration analysis results

Free vibration analysis results are presented in Table J-1 and Figure J-2. Torsional stiffness is smaller than lateral stiffness in the short direction and lateral stiffness in the long direction and the largest. The observation holds for the first and the second mode, as indicated by Table J-1.

Table J-1: Free vibration analysis results, A1-3D-RD-c model

Mode number	**Natural period (s)**	**Mode description**
1	0.482	Torsion, 1st
2	0.447	Short, 1st
3	0.378	Long, 1st
4	0.138	Torsion, 2nd
5	0.126	Short, 2nd
6	0.102	Long, 2nd

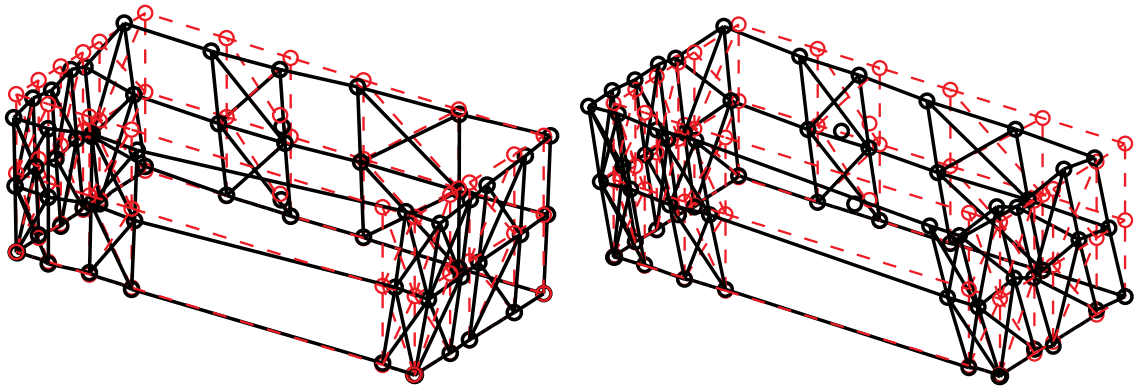

(a) Mode 1, T_1=0.482 s (b) Mode 2, T_2=0.447 s

Figure J-2: First two natural modes of A1-3D-RD-c model

J.3 Linear static analysis results

Table J-2 to Table J-4 present linear static analysis results. The lateral load is the equivalent lateral force available from the design narrative (Madsen et al. 2011), applied equally at four corners. Two separate analyses were performed with the loading at long or short direction.

Table J-2 summarizes the breakdown of peak total base shear among four elevations. Due to the interplay of asymmetrical LFRS, wall lines perpendicular to the loading direction still take a very small portion of base shear.

Table J-3 shows peak building and wall line deflections. Practicing engineers can linearly upscale these data and develop an estimate of the building's performance at a certain lateral force level.

Table J-4 is an evaluation of the building's lateral stiffness of long and short direction and its breakdown among shear walls (SW) and other systems. Since gravity walls (GW) are not modeled in this state-of-the-art model, all base shear goes to shear walls.

Table J-2: Breakdown of peak base shear, linear static analysis, A1-3D-RD-c model

Load direction	**LONG**				
Elevation	**South V_b**	**North V_b**	**East V_b**	**West V_b**	**Peak V_b**
kips	2.4	8.6	0.0	0.0	11.1
%	22.0	77.5	0.1	0.3	100.0
Load direction	**SHORT**				
Elevation	**South V_b**	**North V_b**	**East V_b**	**West V_b**	**Peak V_b**
kips	0.0	0.0	5.8	5.2	11.1
%	0.1	0.1	52.5	47.4	100.0

Table J-3: Peak building and wall line deflection, linear static analysis, A1-3D-RD-c model

Load direction	**LONG**							
Deflection (in.)	**u_1**	**u_2**	**v_1**	**v_2**	**Δu_1**	**Δu_2**	**Δv_1**	**Δv_2**
Building	0.175	0.324	0.024	0.062	0.175	0.149	0.024	0.037
South	0.164	0.289	0.024	0.062	0.164	0.125	0.024	0.037
North	0.186	0.360	0.024	0.062	0.186	0.174	0.024	0.037
East	0.175	0.324	-0.037	-0.084	0.175	0.149	-0.037	-0.047
West	0.175	0.324	0.086	0.208	0.175	0.149	0.086	0.122
Load direction	**SHORT**							
Deflection (in.)	**u_1**	**u_2**	**v_1**	**v_2**	**Δu_1**	**Δu_2**	**Δv_1**	**Δv_2**
Building	-0.017	-0.040	0.258	0.505	-0.017	-0.023	0.258	0.247
South	-0.052	-0.121	0.258	0.505	-0.052	-0.069	0.258	0.247
North	0.018	0.041	0.258	0.505	0.018	0.023	0.258	0.247
East	-0.017	-0.040	0.182	0.329	-0.017	-0.023	0.182	0.147
West	-0.017	-0.040	0.334	0.680	-0.017	-0.023	0.334	0.346

Table J-4: Breakdown of lateral stiffness, A1-3D-RD-c model

LONG			**SHORT**		
Shear wall k_u (%)	**Gravity wall k_u (%)**	**k_u (kip/in)**	**Shear wall k_v (%)**	**Gravity wall k_v (%)**	**k_v (kip/in)**
100.0	0.0	31.2	100.0	0.0	25.0

J.4 Nonlinear static (pushover) analysis results

Table J-5 is created following the same logic with Table J-2, but the analysis type is nonlinear static (pushover). Pushover curves of the building and each wall line are presented Figure J-3 in and Figure J-4.

Clearly, the interaction between wall lines is much more significant when material and geometrical nonlinearity is included. These tables and figures indicate that the wall lines do not reach their peak capacity at exactly the same drift level and wall lines perpendicular to the load can take a nontrivial amount of base shear. Total capacity of the building in the short direction is smaller than the long direction.

Table J-5: Breakdown of peak base shear, pushover analysis, A1-3D-RD-c model

Load direction	**LONG**				
Elevation	**South V_b**	**North V_b**	**East V_b**	**West V_b**	**Peak V_b**
kips	12.8	19.7	4.1	5.6	33.2
%	38.7	59.3	12.4	16.9	100.0
Load direction	**SHORT**				
Elevation	**South V_b**	**North V_b**	**East V_b**	**West V_b**	**Peak V_b**
kips	3.5	3.6	14.2	15.7	30.4
%	11.6	11.7	46.7	51.6	100.0

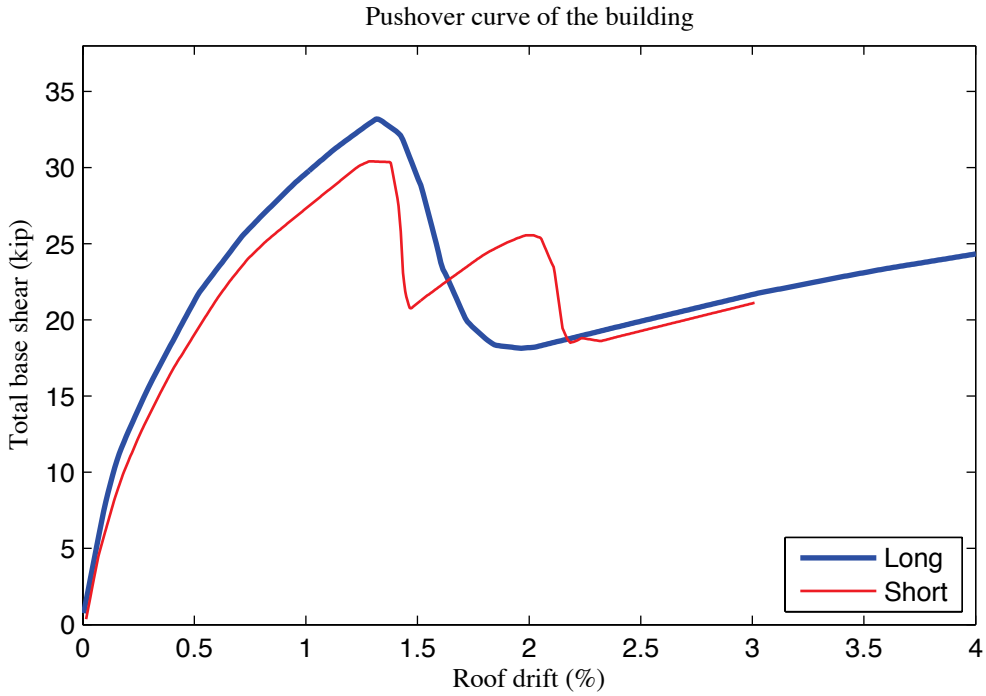

Figure J-3: Pushover curve of A1-3D-RD-c model

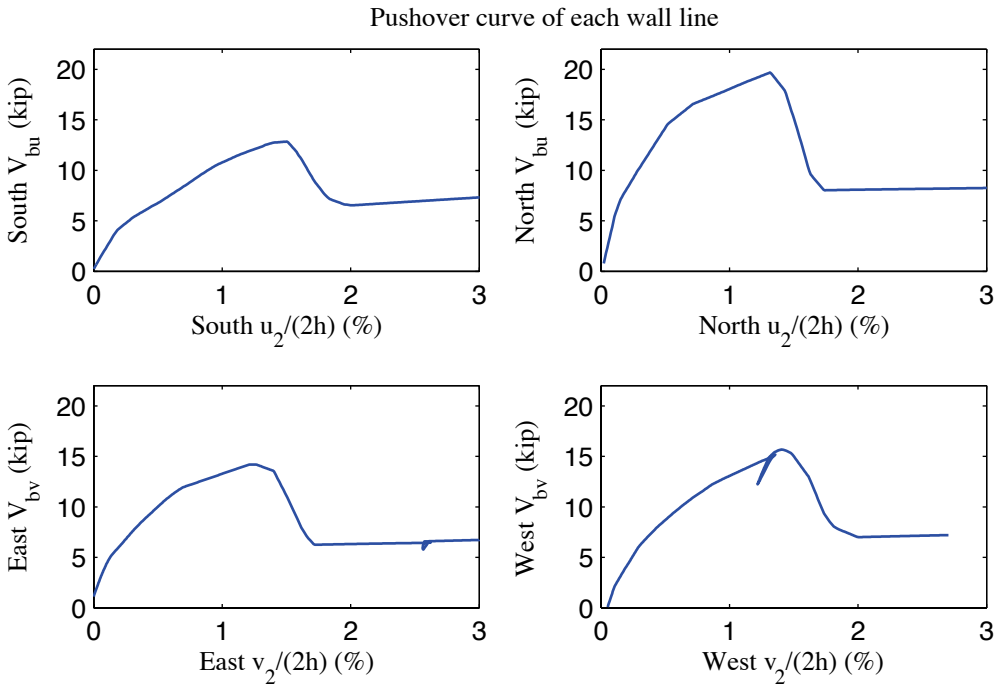

Figure J-4: Pushover curve of each wall line, A1-3D-RD-c model

J.5 Linear time history analysis results

Linear time history analysis is performed on the model under Canoga Park and Rinaldi ground motion records of Northridge earthquake in 1994. We considered three scale levels (16%, 44% and 100%) and loadings in one, two and three axes.

Table J-6 to Table J-9 demonstrate the building's linear elastic performance under designated ground motions. Table J-6 shows peak story relative accelerations in the unit of g. Table J-7 and Table J-8 report peak roof drift and story drift of the building and the corresponding time step (t_*) and the base shear at that time. Note that the base shear at the time of peak roof drift may not be the peak total building base shear in that direction (see Table J-9).

The building behaves linearly since peak drift and peak base shear appear at the same time when the ground motion is linearly scaled. Figure J-5 is a vector plot of the peak total resultant base shear of the building under three axial, 100% Canoga Park excitation. The directions of arrows imply that base shear taken by shear walls does not necessarily follow the direction of wall lines due to the effect of 3D coupling. Comparison with nonlinear analysis results of the same excitation provides insightful observations on the building's response and requirements on modeling fidelity and analysis type.

Table J-6: A1-3D-RD-c model peak story relative acceleration in g, linear time history analysis

		LONG			SHORT			UP		
Load Case	**Ground Motion**	**a_g**	**Floor a**	**Roof a**	**a_g**	**Floor a**	**Roof a**	**a_g**	**Floor a**	**Roof a**
EQ_3D_3axis_1	CNP 16%	0.067	0.112	0.236	0.057	0.107	0.222	0.078	0.006	0.007
EQ_3D_3axis_2	CNP 44%	0.185	0.307	0.648	0.157	0.294	0.610	0.215	0.015	0.018
EQ_3D_1axis_1	CNP 100%	0.420	0.668	1.417	0	0.181	0.343	0	0.037	0.042
EQ_3D_1axis_2	CNP 100%	0	0.237	0.420	0.356	0.678	1.258	0	0.086	0.089
EQ_3D_2axis_1	CNP 100%	0.420	0.699	1.484	0.356	0.664	1.237	0	0.209	0.204
EQ_3D_3axis_3	CNP 100%	0.420	0.699	1.484	0.356	0.664	1.237	0.489	0.209	0.204
EQ_3D_3axis_4	RRS 16%	0.132	0.218	0.351	0.078	0.148	0.236	0.133	0.013	0.014
EQ_3D_3axis_5	RRS 44%	0.363	0.599	0.965	0.214	0.407	0.649	0.367	0.035	0.039
EQ_3D_3axis_6	RRS 100%	0.825	1.363	2.194	0.486	0.945	1.468	0.834	0.278	0.276

Table J-7: A1-3D-RD-c model peak building roof drift and base shear, linear time history analysis

		LONG			SHORT		
Load Case	**Ground Motion**	**$u_2/(2h)$ (%)**	**t_* (s)**	**V_b @ t_* (kips)**	**$v_2/(2h)$ (%)**	**t_* (s)**	**V_b @ t_* (kips)**
EQ_3D_3axis_1	CNP 16%	-0.150	11.62	9.1	0.196	6.22	9.3
EQ_3D_3axis_2	CNP 44%	-0.385	11.62	25.1	0.485	6.22	25.5
EQ_3D_1axis_1	CNP 100%	-0.858	11.63	56.3	0.357	13.57	16.6
EQ_3D_1axis_2	CNP 100%	-0.412	6.82	20.9	-1.142	6.00	62.4
EQ_3D_2axis_1	CNP 100%	0.883	11.80	59.5	-1.083	5.99	59.0
EQ_3D_3axis_3	CNP 100%	0.883	11.80	59.5	-1.083	5.99	59.0
EQ_3D_3axis_4	RRS 16%	0.285	2.67	20.7	0.220	6.03	10.2
EQ_3D_3axis_5	RRS 44%	0.809	2.67	56.9	-0.587	2.58	35.1
EQ_3D_3axis_6	RRS 100%	1.850	2.67	129.5	-1.375	2.58	78.9

Table J-8: A1-3D-RD-c model peak building story drift, linear time history analysis

		LONG				SHORT			
Load Case	**Ground Motion**	**$\Delta u_1/h$ (%)**	**t_* (s)**	**$\Delta u_2/h$ (%)**	**t_* (s)**	**$\Delta v_1/h$ (%)**	**t_* (s)**	**$\Delta v_2/h$ (%)**	**t_* (s)**
EQ_3D_3axis_1	CNP 16%	-0.155	11.62	-0.144	11.62	0.202	6.23	0.190	8.84
EQ_3D_3axis_2	CNP 44%	0.417	7.49	-0.368	11.62	0.510	6.23	0.463	8.84
EQ_3D_1axis_1	CNP 100%	-0.895	11.62	-0.824	11.63	0.369	13.58	0.346	13.57
EQ_3D_1axis_2	CNP 100%	-0.436	6.82	-0.388	6.82	-1.211	6.00	-1.072	6.00
EQ_3D_2axis_1	CNP 100%	0.926	11.81	0.842	11.80	-1.150	5.99	-1.016	5.99
EQ_3D_3axis_3	CNP 100%	0.926	11.81	0.842	11.80	-1.150	5.99	-1.016	5.99
EQ_3D_3axis_4	RRS 16%	0.311	2.67	0.259	2.67	0.227	6.03	0.213	6.02
EQ_3D_3axis_5	RRS 44%	0.878	2.67	0.740	2.67	-0.641	2.58	-0.536	2.57
EQ_3D_3axis_6	RRS 100%	2.006	2.67	1.694	2.67	-1.518	2.58	-1.238	2.57

Table J-9: A1-3D-RD-c model peak building base shear, linear time history analysis

		LONG		SHORT		RESULTANT	
Load Case	**Ground Motion**	**Peak V_{bu} (kip)**	**t @ peak V_{bu} (s)**	**Peak V_{bv} (kip)**	**t @ peak V_{bv} (s)**	**Peak V_b (kip)**	**t @ peak V_b (s)**
EQ_3D_3axis_1	CNP 16%	9.9	7.49	9.7	5.99	11.1	7.49
EQ_3D_3axis_2	CNP 44%	27.2	7.49	26.5	5.99	30.6	7.49
EQ_3D_1axis_1	CNP 100%	61.8	8.71	17.1	13.11	61.9	8.71
EQ_3D_1axis_2	CNP 100%	20.9	6.82	62.4	6.00	62.4	6.00
EQ_3D_2axis_1	CNP 100%	60.9	12.00	59.0	5.98	65.0	7.49
EQ_3D_3axis_3	CNP 100%	60.9	12.00	59.0	5.98	65.0	7.49
EQ_3D_3axis_4	RRS 16%	20.9	2.66	12.8	2.58	21.9	2.64
EQ_3D_3axis_5	RRS 44%	57.5	2.66	35.1	2.58	60.3	2.64
EQ_3D_3axis_6	RRS 100%	130.9	2.66	78.9	2.58	136.7	2.64

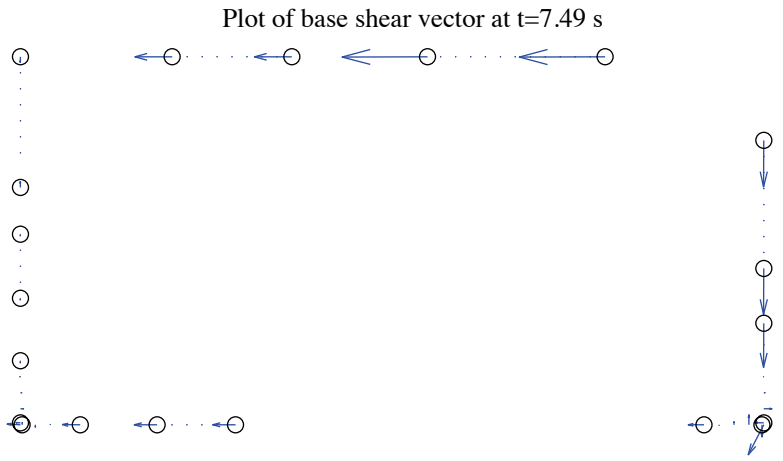

Figure J-5: A1-3D-RD-c model, base shear vector plot at the moment of peak total base shear, 100 % Canoga Park, 3D linear analysis (maximum anchor/hold down base shear is 14.27 kips)

J.6 Nonlinear time history analysis results

Same ground motions are applied to the model with material and geometrical nonlinearity. Table J-10 to Table J-13 are replicas of Table J-6 to Table J-9, but for nonlinear time history analyses. Since this analysis type is most complicated and closest to reality and experiments, behavior of wall lines and hold downs are further studied. Table J-14 is the table of peak wall line story drifts and corresponding time steps. Table J-15 is designed for peak base shear of each wall line and the last two columns of the table are percentages of base shear of two facing wall lines in the same direction when the total base shear in that direction takes peak value. Table J-16 expands the breakdown of each wall line's peak base shear between shear walls, gravity walls and other systems. Table J-17 is peak value of hold down tensile force of two selected pairs. Hold down 5 and 6 are on shear wall L1S1, South elevation and hold down 7 and 8 are on shear wall L1W1, West elevation. These shear walls have lowest capacities compared with others on the same wall line and they meet at the southwest edge of the building, so interacted nonlinear behavior is expected to appear.

Time history plots in this section include plots of story drifts of the building and each wall line (Figure J-6 to Figure J-8), total building base shear in long and short direction (Figure J-9) and axial forces of hold downs in Table J-17 (Figure J-10). Hysteretic plots in Figure J-11 and Figure J-12 are helpful for visual examination of nonlinear base shear-drift relationship of the building and the weakest shear wall on each wall line. In comparison with linear time history analysis, vector plot of peak total base shear is illustrated in Figure J-13. presents a simplified deformed shape of the building (see

(Peterman 2014) for details of the method) and axial force of all twenty hold downs at the moment of peak total base shear. The same sign convention with tests is adopted. Red bars indicate tensile (negative) force and blue ones are for compressive (positive) force.

Hysteretic behavior is seen in the building and typical shear walls under design-based earthquake (100% Canoga Park excitation in 3 axes, see Figure J-11 and Figure J-12). Results also imply that when loaded by 100% Canoga Park ground motion, South and North wall lines fail in tension or in compression since peak drifts are both over 3% (Table J-14) and the response curves of typical shear walls enter the post-peak region of Pinching4 material backbone. Figure J-13 clearly shows that base shear vectors in anchors and hold downs do not align with wall lines and they can change directions even within a single piece of wall, a sign of localized behavior. Table J-17, Figure J-10 and Figure J-14 demonstrate that hold downs in a pair do not experience the same amount of force with opposite signs, an evidence that supports Type II shear wall behavior despite Type I design assumption.

The near-field Rinaldi record is much stronger in terms of peak ground acceleration, especially in the long direction. When loaded at 100%, both directions are believed to be destroyed with peak story drift larger than 14% and 4.5%. Such a large drift level is a sign of structural failure.

Table J-10: A1-3D-RD-c model peak story relative acceleration in g, nonlinear time history analysis

		LONG			SHORT			UP		
Load Case	**Ground Motion**	**a_g**	**Floor a**	**Roof a**	**a_g**	**Floor a**	**Roof a**	**a_g**	**Floor a**	**Roof a**
EQ_3D_3axis_1	CNP 16%	0.067	0.144	0.209	0.057	0.120	0.157	0.078	0.145	0.173
EQ_3D_3axis_2	CNP 44%	0.185	0.293	0.394	0.157	0.278	0.457	0.215	0.231	0.260
EQ_3D_1axis_1	CNP 100%	0.420	0.574	0.840	0	0.114	0.085	0	0.260	0.291
EQ_3D_1axis_2	CNP 100%	0	0.129	0.104	0.356	0.540	0.837	0	0.369	0.470
EQ_3D_2axis_1	CNP 100%	0.420	0.557	0.779	0.356	0.482	0.646	0	0.556	0.674
EQ_3D_3axis_3	CNP 100%	0.420	0.557	0.779	0.356	0.482	0.646	0.489	0.556	0.674
EQ_3D_3axis_4	RRS 16%	0.132	0.200	0.263	0.078	0.181	0.274	0.133	0.213	0.221
EQ_3D_3axis_5	RRS 44%	0.363	0.533	0.902	0.214	0.331	0.402	0.367	0.514	0.577
EQ_3D_3axis_6	RRS 100%	0.825	1.534	1.199	0.486	0.617	0.799	0.834	0.886	1.102

Table J-11: A1-3D-RD-c model peak building roof drift and base shear, nonlinear time history analysis

		LONG			SHORT		
Load Case	**Ground Motion**	**u_2/(2h) (%)**	**t_* (s)**	**V_b @ t_* (kips)**	**v_2/(2h) (%)**	**t_* (s)**	**V_b @ t_* (kips)**
EQ_3D_3axis_1	CNP 16%	0.122	8.75	9.9	0.107	5.73	5.9
EQ_3D_3axis_2	CNP 44%	0.542	8.80	22.5	-0.448	9.83	12.4
EQ_3D_1axis_1	CNP 100%	2.243	8.98	13.5	0.029	9.58	0.2
EQ_3D_1axis_2	CNP 100%	-0.033	13.30	1.6	0.991	9.64	25.8
EQ_3D_2axis_1	CNP 100%	1.977	8.97	10.6	-1.036	8.59	27.2
EQ_3D_3axis_3	CNP 100%	1.977	8.97	10.6	-1.036	8.59	27.2
EQ_3D_3axis_4	RRS 16%	0.274	2.70	15.5	0.167	6.04	8.9
EQ_3D_3axis_5	RRS 44%	1.543	2.86	22.9	-0.539	2.65	17.6
EQ_3D_3axis_6	RRS 100%	12.164	3.20	7.1	3.087	6.42	19.0

Table J-12: A1-3D-RD-c model peak building story drift, nonlinear linear time history analysis

		LONG				SHORT			
Load Case	**Ground Motion**	**$\Delta u_1/h$ (%)**	**t_* (s)**	**$\Delta u_2/h$ (%)**	**t_* (s)**	**$\Delta v_1/h$ (%)**	**t_* (s)**	**$\Delta v_2/h$ (%)**	**t_* (s)**
EQ_3D_3 axis_1	CNP 16%	0.150	8.75	-0.112	11.63	-0.126	5.97	0.118	5.72
EQ_3D_3 axis_2	CNP 44%	0.686	8.80	0.398	8.80	-0.500	9.82	-0.401	9.84
EQ_3D_1 axis_1	CNP 100%	3.567	8.95	1.110	8.83	-0.035	18.59	0.053	9.58
EQ_3D_1 axis_2	CNP 100%	-0.039	10.89	-0.052	13.30	-1.331	8.61	0.788	9.65
EQ_3D_2 axis_1	CNP 100%	3.166	8.95	1.087	8.84	-1.371	8.62	-0.784	8.56
EQ_3D_3 axis_3	CNP 100%	3.166	8.95	1.087	8.84	-1.371	8.62	-0.784	8.56
EQ_3D_3 axis_4	RRS 16%	0.364	2.69	0.186	2.71	-0.179	2.56	0.163	6.05
EQ_3D_3 axis_5	RRS 44%	2.467	2.86	-0.941	6.29	-0.661	2.62	-0.432	2.66
EQ_3D_3 axis_6	RRS 100%	14.564	2.99	13.982	3.23	4.679	6.46	1.647	6.22

Table J-13: A1-3D-RD-c model peak building base shear, nonlinear time history analysis

		LONG		SHORT		RESULTANT	
Load Case	**Ground Motion**	**Peak V_{bu} (kip)**	**t @ peak V_{bu} (s)**	**Peak V_{bv} (kip)**	**t @ peak V_{bv} (s)**	**Peak V_b (kip)**	**t @ peak V_b (s)**
EQ_3D_3axis_1	CNP 16%	9.9	8.75	7.7	5.97	11.0	8.75
EQ_3D_3axis_2	CNP 44%	22.5	8.79	15.9	9.49	26.1	8.81
EQ_3D_1axis_1	CNP 100%	33.2	8.78	2.8	9.21	33.2	8.78
EQ_3D_1axis_2	CNP 100%	3.0	13.36	27.7	8.60	27.7	8.60
EQ_3D_2axis_1	CNP 100%	32.0	8.78	27.2	8.59	37.3	8.57
EQ_3D_3axis_3	CNP 100%	32.0	8.78	27.2	8.59	37.3	8.57
EQ_3D_3axis_4	RRS 16%	16.2	2.68	9.2	2.55	16.2	2.68
EQ_3D_3axis_5	RRS 44%	33.4	2.73	19.9	2.61	37.0	2.72
EQ_3D_3axis_6	RRS 100%	35.9	2.94	30.5	2.37	44.4	2.41

Table J-14: A1-3D-RD-c model peak wall line story drift, nonlinear time history analysis

LONG		SOUTH				NORTH			
Load Case	**Ground Motion**	**$\Delta u_1/h$ (%)**	**t_* (s)**	**$\Delta u_2/h$ (%)**	**t_* (s)**	**$\Delta u_1/h$ (%)**	**t_* (s)**	**$\Delta u_2/h$ (%)**	**t_* (s)**
EQ_3D_3axis_1	CNP 16%	0.171	8.76	0.131	11.62	0.136	8.73	0.115	8.72
EQ_3D_3axis_2	CNP 44%	0.767	8.82	0.424	8.80	0.631	10.00	0.410	10.03
EQ_3D_1axis_1	CNP 100%	3.575	8.95	1.128	8.83	3.565	8.96	1.093	8.83
EQ_3D_1axis_2	CNP 100%	0.097	10.15	0.093	13.30	0.030	10.82	0.044	21.23
EQ_3D_2axis_1	CNP 100%	3.252	8.96	1.091	8.84	3.095	8.93	1.089	8.83
EQ_3D_3axis_3	CNP 100%	3.252	8.96	1.091	8.84	3.095	8.93	1.089	8.83
EQ_3D_3axis_4	RRS 16%	0.378	2.71	0.178	2.72	0.360	2.68	0.194	2.70
EQ_3D_3axis_5	RRS 44%	2.468	2.86	0.979	6.29	2.466	2.86	0.903	6.29
EQ_3D_3axis_6	RRS 100%	14.509	2.99	14.047	3.23	14.622	3.00	13.917	3.23
SHORT		**EAST**				**WEST**			
Load Case	**Ground Motion**	**$\Delta v_1/h$ (%)**	**t_* (s)**	**$\Delta v_2/h$ (%)**	**t_* (s)**	**$\Delta v_1/h$ (%)**	**t_* (s)**	**$\Delta v_2/h$ (%)**	**t_* (s)**
EQ_3D_3axis_1	CNP 16%	0.183	9.02	0.199	9.04	0.145	9.43	0.147	7.86
EQ_3D_3axis_2	CNP 44%	0.841	10.16	0.733	9.85	0.363	9.99	0.372	10.03
EQ_3D_1axis_1	CNP 100%	0.224	3.70	0.189	3.66	0.194	3.68	0.188	5.63
EQ_3D_1axis_2	CNP 100%	1.355	8.61	0.828	9.30	1.312	8.60	0.856	9.64
EQ_3D_2axis_1	CNP 100%	1.560	8.63	1.018	8.57	1.267	8.58	0.892	9.64
EQ_3D_3axis_3	CNP 100%	1.560	8.63	1.018	8.57	1.267	8.58	0.892	9.64
EQ_3D_3axis_4	RRS 16%	0.248	2.55	0.217	2.57	0.208	6.00	0.210	6.04
EQ_3D_3axis_5	RRS 44%	0.773	2.62	0.476	2.65	0.605	6.12	0.502	6.10
EQ_3D_3axis_6	RRS 100%	4.575	2.96	1.241	6.21	5.101	6.46	2.063	6.23

Table J-15: A1-3D-RD-c model peak wall line base shear, nonlinear time history analysis

LONG		SOUTH		NORTH		% of Peak V_{bu}	
Load Case	**Ground Motion**	**Peak V_{bu} (kips)**	**t @ peak V_{bu} (s)**	**Peak V_{bu} (kips)**	**t @ peak V_{bu} (s)**	**South**	**North**
EQ_3D_3axis_1	CNP 16%	3.5	8.76	6.5	8.75	34.6	64.8
EQ_3D_3axis_2	CNP 44%	7.9	8.82	14.7	9.99	33.6	65.0
EQ_3D_1axis_1	CNP 100%	12.7	8.80	19.6	8.78	37.2	59.0
EQ_3D_1axis_2	CNP 100%	2.2	10.16	2.8	14.31	46.4	51.7
EQ_3D_2axis_1	CNP 100%	12.9	8.84	19.6	8.78	35.2	61.1
EQ_3D_3axis_3	CNP 100%	12.9	8.84	19.6	8.78	35.2	61.1
EQ_3D_3axis_4	RRS 16%	5.5	2.71	10.6	2.68	32.8	65.7
EQ_3D_3axis_5	RRS 44%	12.7	2.78	19.6	2.73	36.5	58.7
EQ_3D_3axis_6	RRS 100%	13.5	2.44	19.7	2.44	21.8	24.4
SHORT		**EAST**		**WEST**		**% of Peak V_{bv}**	
Load Case	**Ground Motion**	**Peak V_{bv} (kips)**	**t @ peak V_{bv} (s)**	**Peak V_{bv} (kips)**	**t @ peak V_{bv} (s)**	**East**	**West**
EQ_3D_3axis_1	CNP 16%	5.1	10.87	4.2	8.45	47.9	51.0
EQ_3D_3axis_2	CNP 44%	11.9	10.16	7.1	5.56	71.5	26.5
EQ_3D_1axis_1	CNP 100%	5.2	3.71	4.3	3.67	3.4	93.7
EQ_3D_1axis_2	CNP 100%	12.9	9.63	13.7	8.60	46.4	49.4
EQ_3D_2axis_1	CNP 100%	13.9	8.96	13.2	8.59	47.6	48.7
EQ_3D_3axis_3	CNP 100%	13.9	8.96	13.2	8.59	47.6	48.7
EQ_3D_3axis_4	RRS 16%	5.2	3.88	4.5	5.99	54.1	44.7
EQ_3D_3axis_5	RRS 44%	9.8	2.61	9.6	2.61	49.0	48.4
EQ_3D_3axis_6	RRS 100%	14.4	6.14	15.4	2.36	44.0	50.4

Table J-16: A1-3D-RD-c model wall line base shear breakdown, nonlinear time history analysis

LONG		SOUTH			NORTH		
Load Case	**Ground Motion**	**Peak V_{bu} (kips)**	**SW V_{bu} (%)**	**GW V_{bu} (%)**	**Peak V_{bu} (kips)**	**SW V_{bu} (%)**	**GW V_{bu} (%)**
EQ_3D_3axis_1	CNP 16%	3.5	100.0	0.0	6.5	100.0	0.0
EQ_3D_3axis_2	CNP 44%	7.9	100.0	0.0	14.7	100.0	0.0
EQ_3D_1axis_1	CNP 100%	12.7	100.0	0.0	19.6	100.0	0.0
EQ_3D_1axis_2	CNP 100%	2.2	100.0	0.0	2.8	100.0	0.0
EQ_3D_2axis_1	CNP 100%	12.9	100.0	0.0	19.6	100.0	0.0
EQ_3D_3axis_3	CNP 100%	12.9	100.0	0.0	19.6	100.0	0.0
EQ_3D_3axis_4	RRS 16%	5.5	100.0	0.0	10.6	100.0	0.0
EQ_3D_3axis_5	RRS 44%	12.7	100.0	0.0	19.6	100.0	0.0
EQ_3D_3axis_6	RRS 100%	13.5	100.0	0.0	19.7	100.0	0.0
SHORT		**EAST**			**WEST**		
Load Case	**Ground Motion**	**Peak V_{bv} (kips)**	**SW V_{bv} (%)**	**GW V_{bu} (%)**	**Peak V_{bv} (kips)**	**SW V_{bv} (%)**	**GW V_{bv} (%)**
EQ_3D_3axis_1	CNP 16%	5.1	100.0	0.0	4.2	100.0	0.0
EQ_3D_3axis_2	CNP 44%	11.9	100.0	0.0	7.1	100.0	0.0
EQ_3D_1axis_1	CNP 100%	5.2	100.0	0.0	4.3	100.0	0.0
EQ_3D_1axis_2	CNP 100%	12.9	100.0	0.0	13.7	100.0	0.0
EQ_3D_2axis_1	CNP 100%	13.9	100.0	0.0	13.2	100.0	0.0
EQ_3D_3axis_3	CNP 100%	13.9	100.0	0.0	13.2	100.0	0.0
EQ_3D_3axis_4	RRS 16%	5.2	100.0	0.0	4.5	100.0	0.0
EQ_3D_3axis_5	RRS 44%	9.8	100.0	0.0	9.6	100.0	0.0
EQ_3D_3axis_6	RRS 100%	14.4	100.0	0.0	15.4	100.0	0.0

Table J-17: A1-3D-RD-c model peak hold down tensile force at certain locations, nonlinear time history analysis

		L1S1, LC5		L1S1, LC6		L1W1, LC7		L1W1, LC8	
Load Case	**Ground Motion**	**Peak F (kips)**	**t @ peak F (s)**	**Peak F (kips)**	**t @ peak F (s)**	**Peak F (kips)**	**t @ peak F (s)**	**Peak F (kips)**	**t @ peak F (s)**
EQ_3D_3axis_1	CNP 16%	-2.55	9.00	-1.20	6.18	-2.33	8.75	-4.16	8.44
EQ_3D_3axis_2	CNP 44%	-5.48	9.77	-2.43	10.03	-6.28	8.82	-6.25	5.57
EQ_3D_1axis_1	CNP 100%	-10.13	6.73	-2.70	8.79	-8.05	8.95	-4.97	8.91
EQ_3D_1axis_2	CNP 100%	-2.32	8.88	-6.36	9.63	-2.20	9.64	-11.12	8.55
EQ_3D_2axis_1	CNP 100%	-10.03	11.96	-7.68	8.84	-8.92	8.85	-10.55	9.27
EQ_3D_3axis_3	CNP 100%	-10.03	11.96	-7.68	8.84	-8.92	8.85	-10.55	9.27
EQ_3D_3axis_4	RRS 16%	-3.54	3.06	-1.29	6.00	-3.84	2.70	-4.30	9.05
EQ_3D_3axis_5	RRS 44%	-10.04	3.31	-5.67	6.15	-7.49	2.85	-8.58	2.68
EQ_3D_3axis_6	RRS 100%	-12.11	2.47	-8.37	3.58	-15.31	2.99	-15.39	2.76

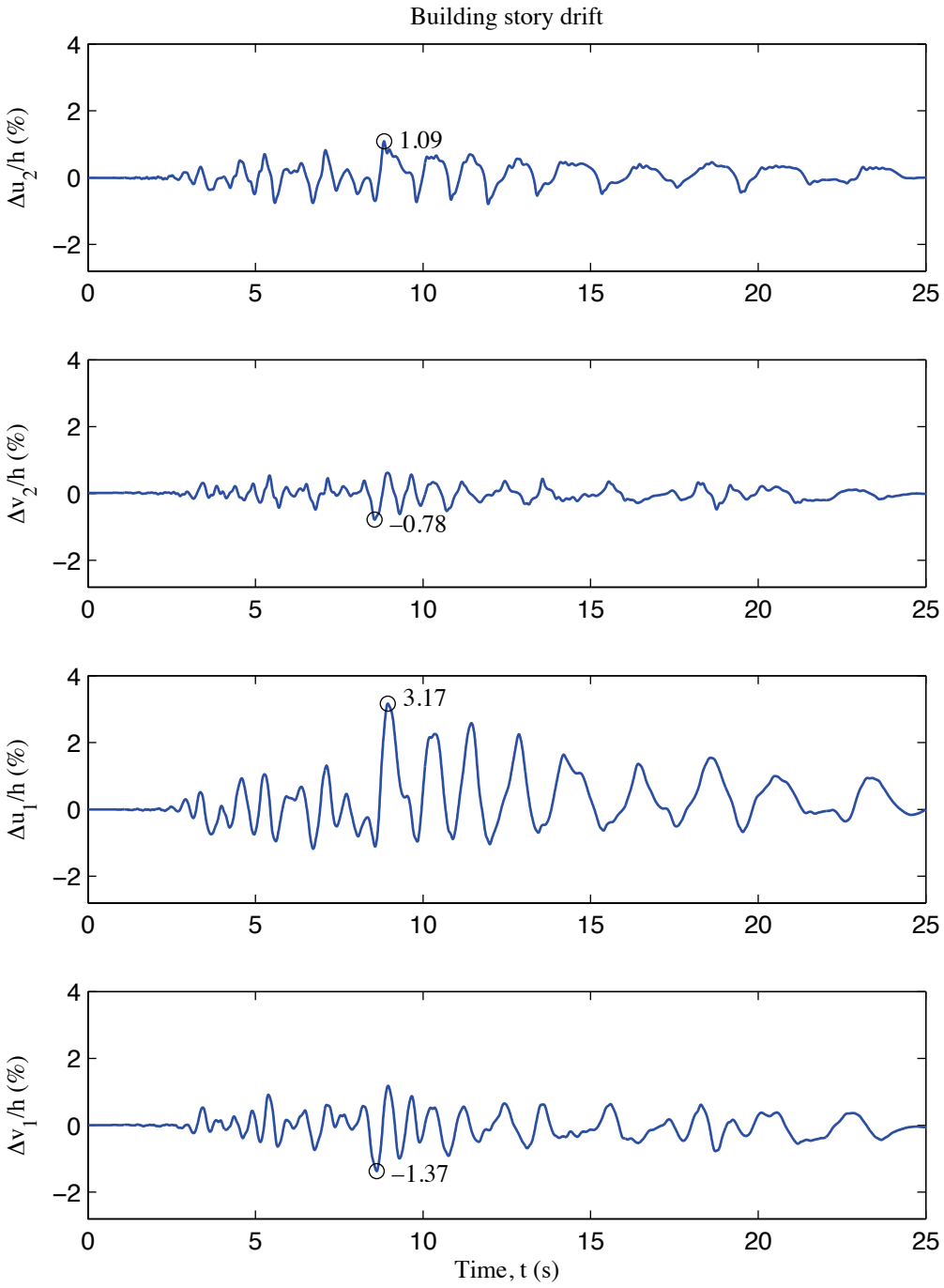

Figure J-6: A1-3D-RD-c model building story drift, 100 % Canoga Park, 3D nonlinear analysis

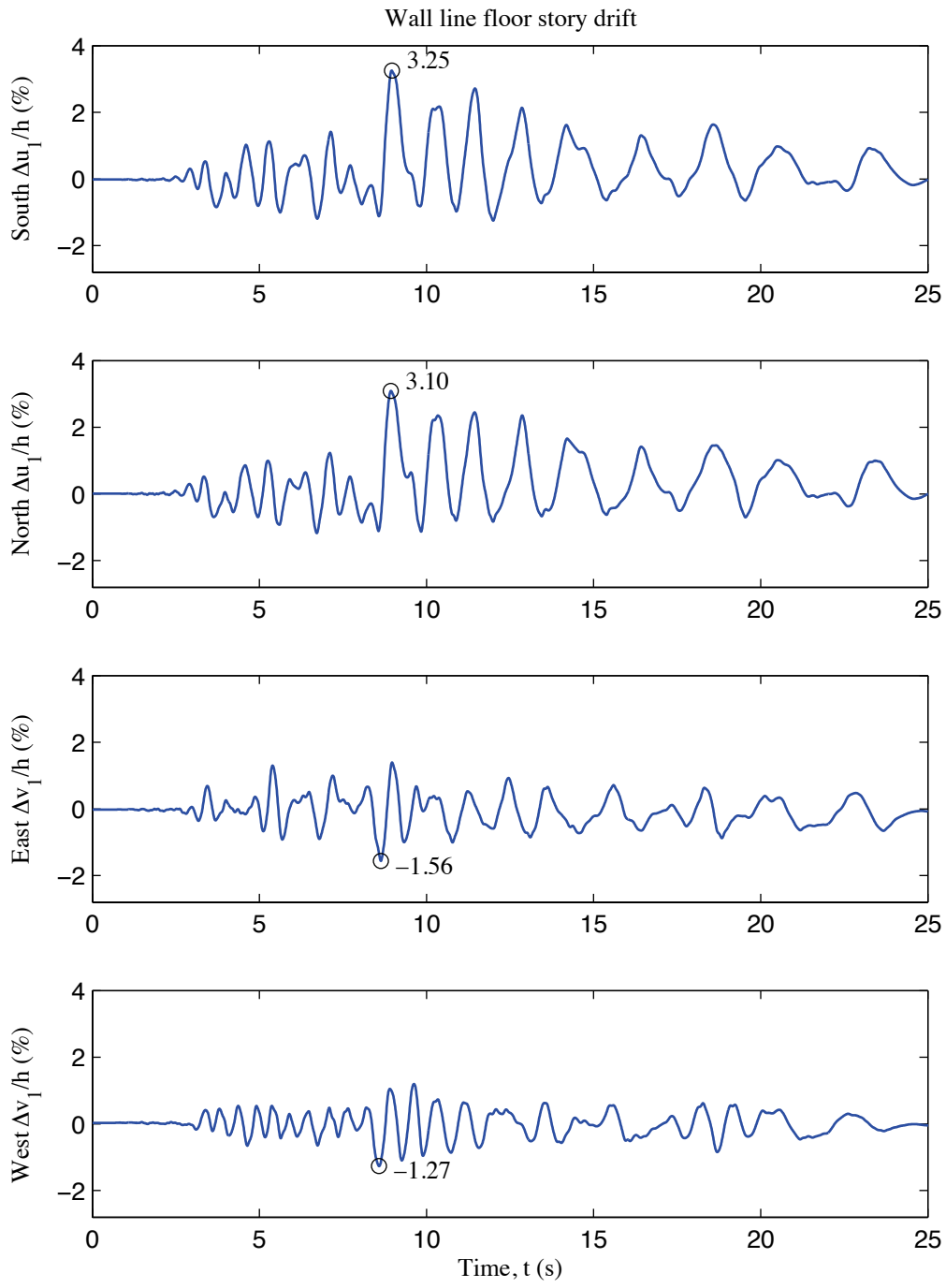

Figure J-7: A1-3D-RD-c model wall line floor story drift, 100 % Canoga Park, 3D nonlinear analysis

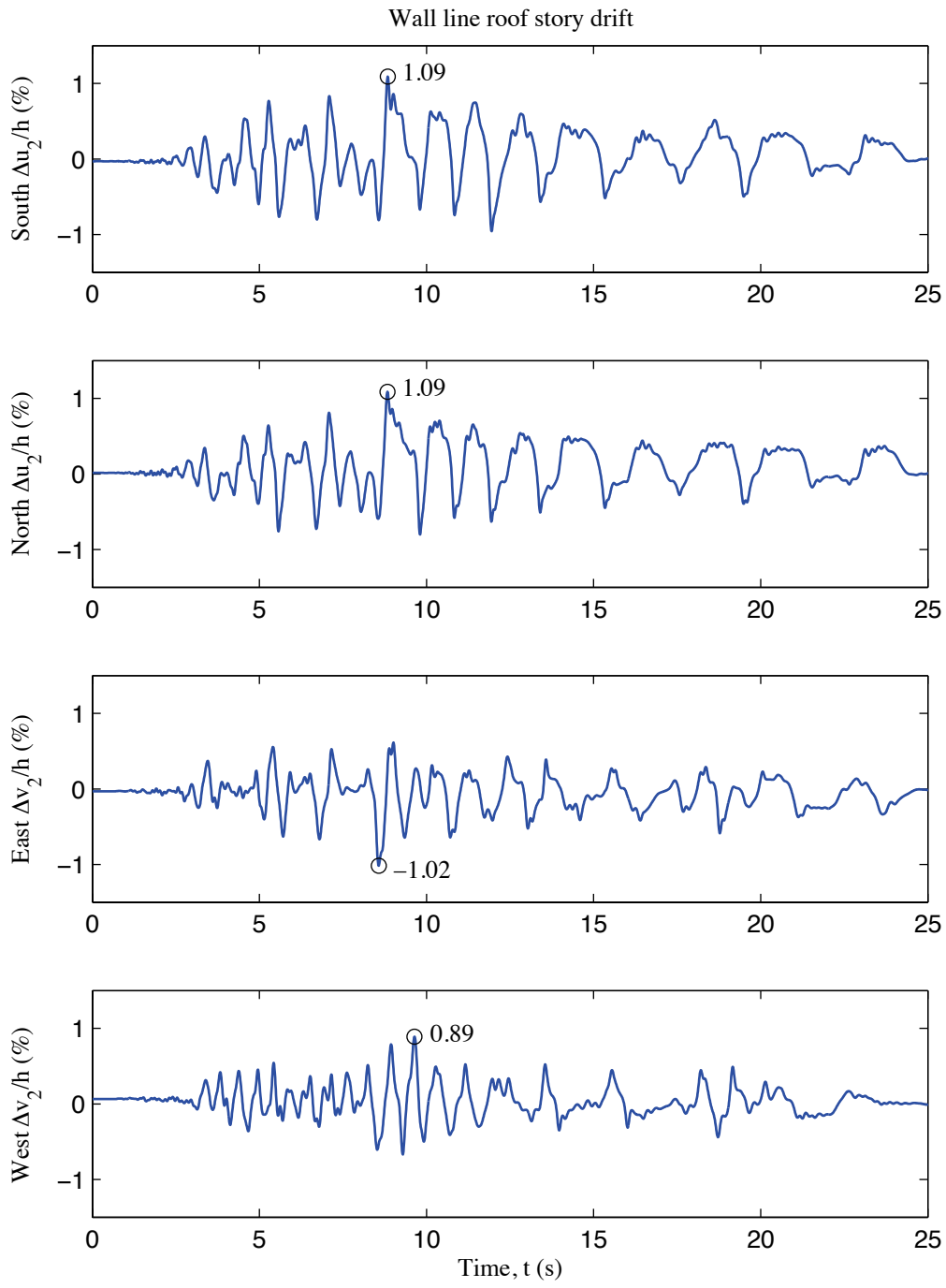

Figure J-8: A1-3D-RD-c model wall line roof story drift, 100 % Canoga Park, 3D nonlinear analysis

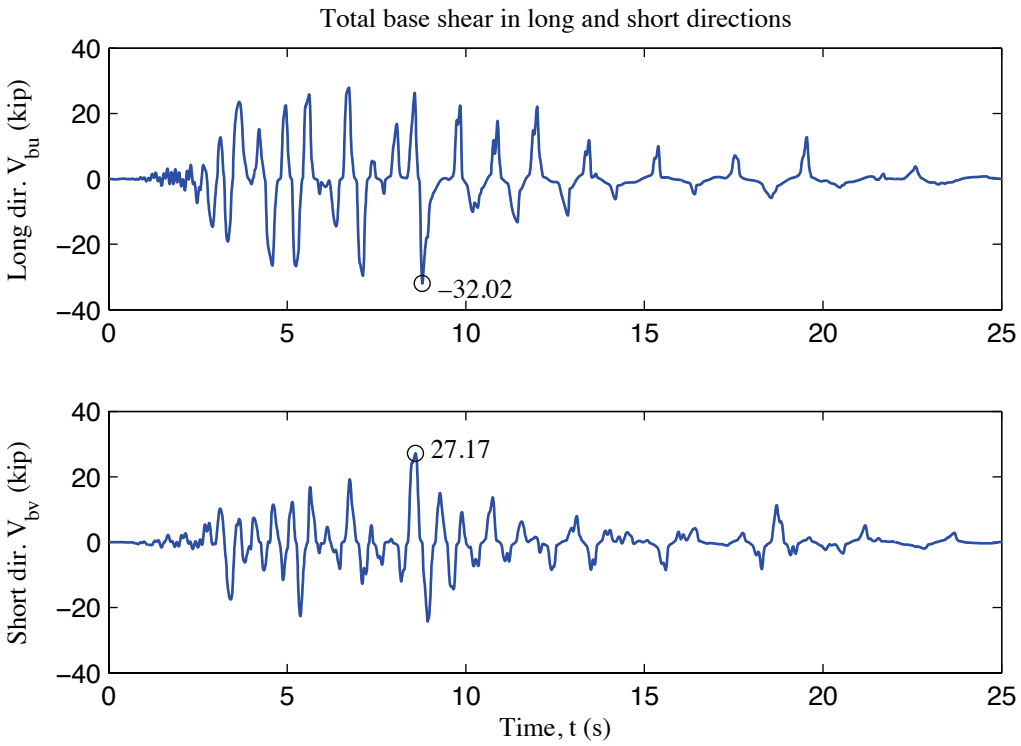

Figure J-9: A1-3D-RD-c model total building base shear, 100 % Canoga Park, 3D nonlinear analysis

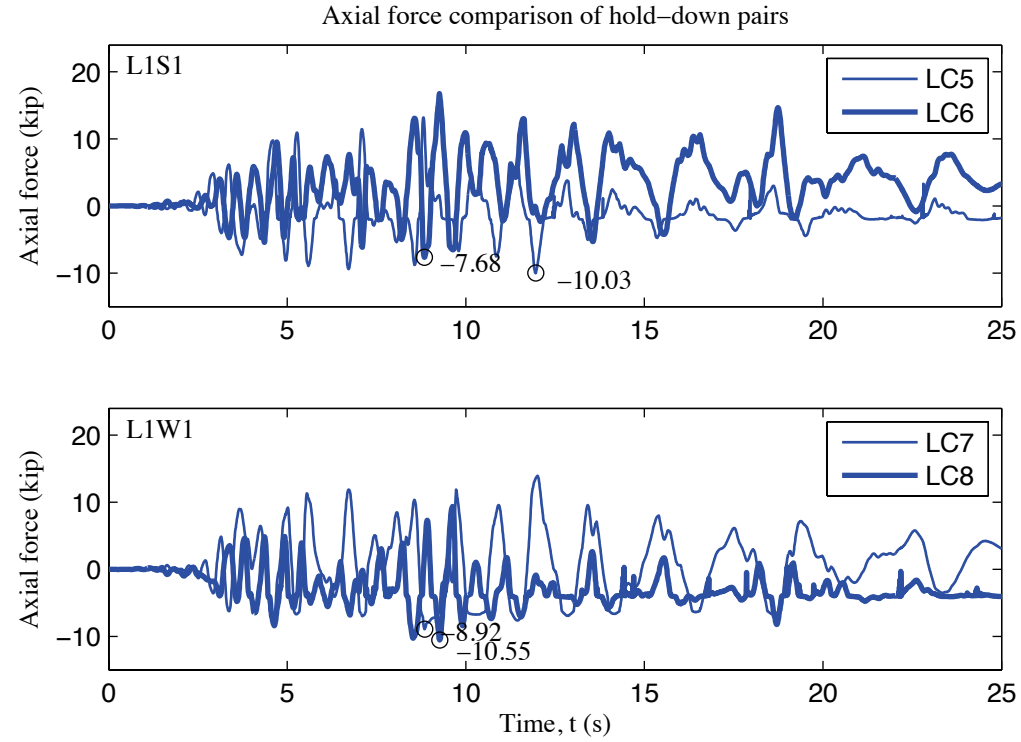

Figure J-10: A1-3D-RD-c model, load cell 5 to 8 axial forces, 100 % Canoga Park, 3D nonlinear analysis

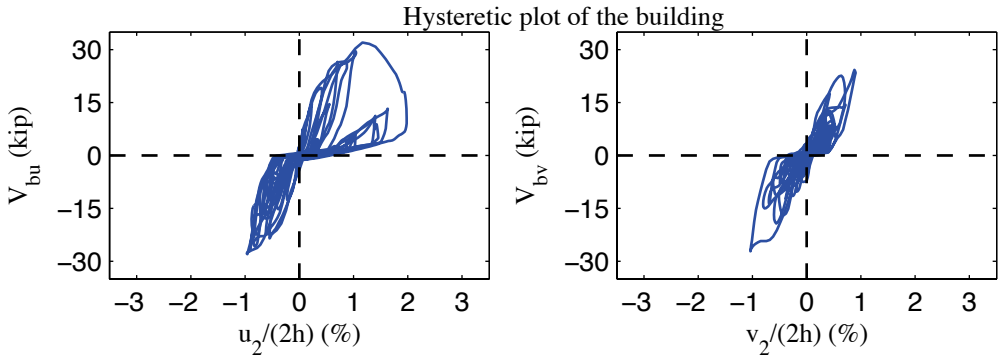

Figure J-11: A1-3D-RD-c model, hysteretic plot of the building, 100 % Canoga Park, 3D nonlinear analysis

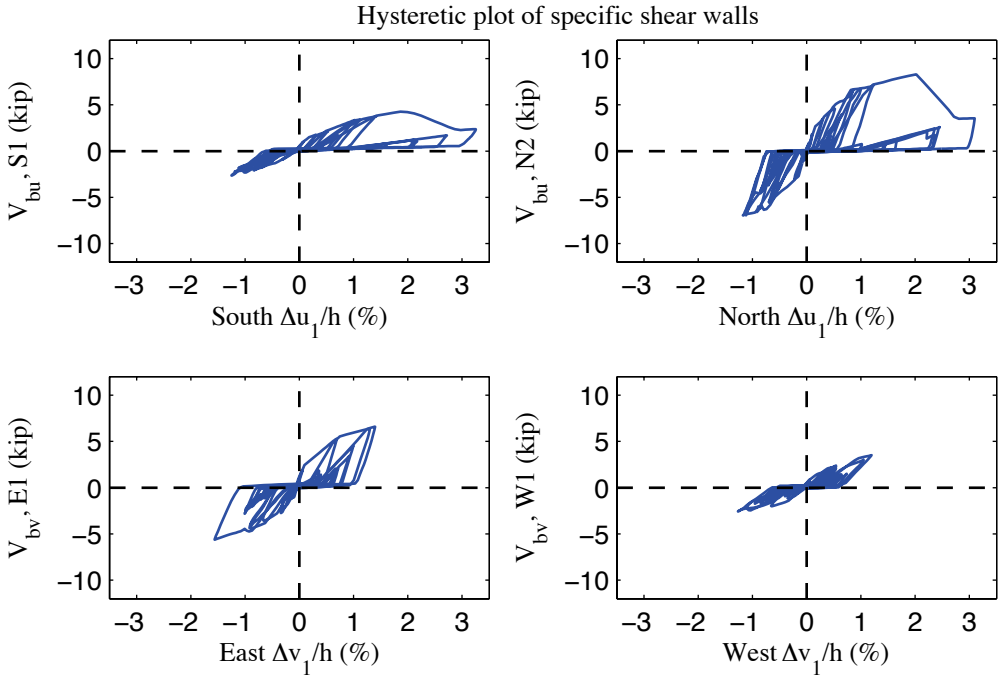

Figure J-12: A1-3D-RD-c model, hysteretic plot of shear walls at each elevation, 100 % Canoga Park, 3D nonlinear analysis

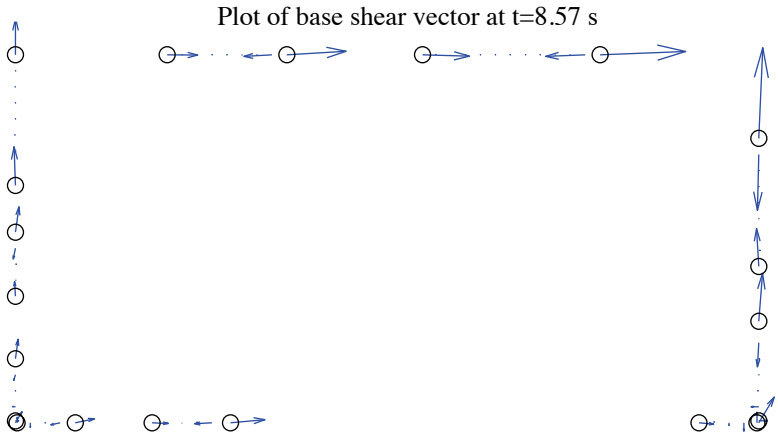

Figure J-13: A1-3D-RD-c model, field plot of peak total base shear, 100 % Canoga Park, 3D nonlinear analysis (maximum anchor/hold down base shear is 9.32 kips)

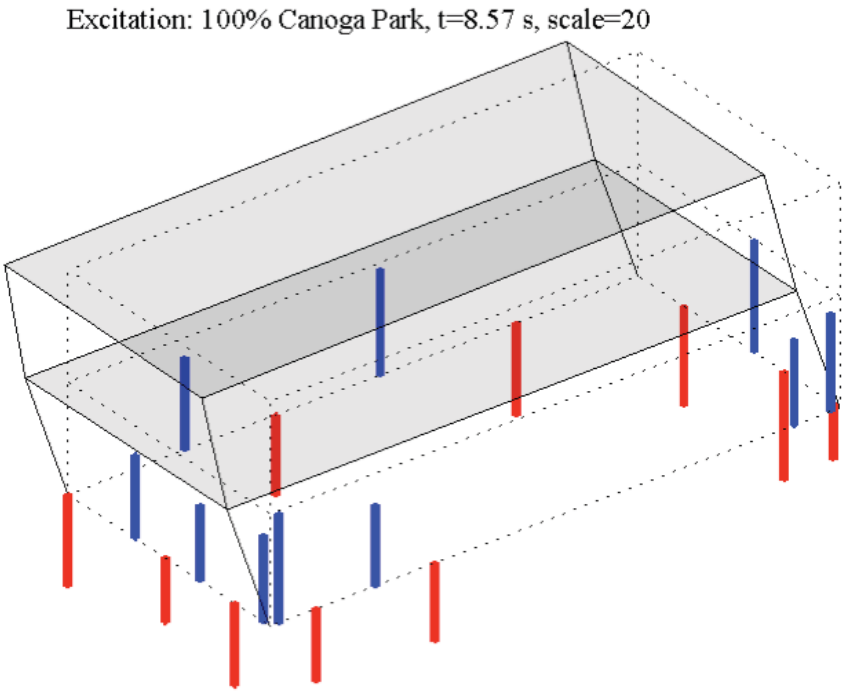

Figure J-14: A1-3D-RD-c model, simplified illustration of corner displacements with hold down forces from load cells,100 % Canoga Park, 3D nonlinear analysis (max hold down tensile force is -12.99 kips)

Appendix K: Analysis Results of State-of-the-art, Phase 1, 3D, semirigid-diaphragm, model a (A1-3D-SD-a)

K.1 Model description

This state-of-the-art 3D model features subpanel bracing models of shear walls, explicit models of hold downs, bare steel framing of gravity walls, and semi-rigid diaphragms modeled by subpanel bracings. Seismic mass is distributed to corners and stud ends. The lateral displacement and shear wall capacity ($\delta(0.2V_{nA})$, $0.2V_{nA}$) from test is utilized to determine the stiffness of elastic material and the first point on the backbone curve of Pinching4 material of shear wall bracing. Figure K-1 is the 3D drawing of the building model with all members and diagonal bracings of sheathing panels.

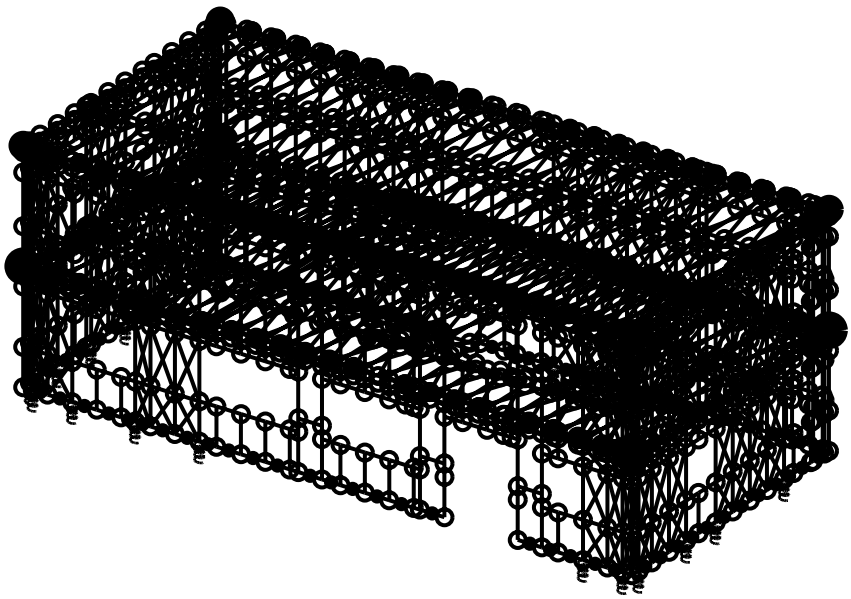

Figure K-1: A1-3D-SD-a model

K.2 Free vibration analysis results

Free vibration analysis results are presented in Table K-1 and Figure K-2. Lateral stiffness in the short direction is smaller than lateral stiffness in the long direction and torsional stiffness is the largest. The observation holds for the first and the second mode, as indicated by Table K-1.

Table K-1: Free vibration analysis results, A1-3D-SD-a model

Mode number	Natural period (s)	Mode description
1	0.321	Short, 1st
2	0.295	Long, 1st
3	0.229	Torsion, 1st
4	0.195	Short, 2nd
5	0.132	Long, 2nd
6	0.110	Torsion, 2nd

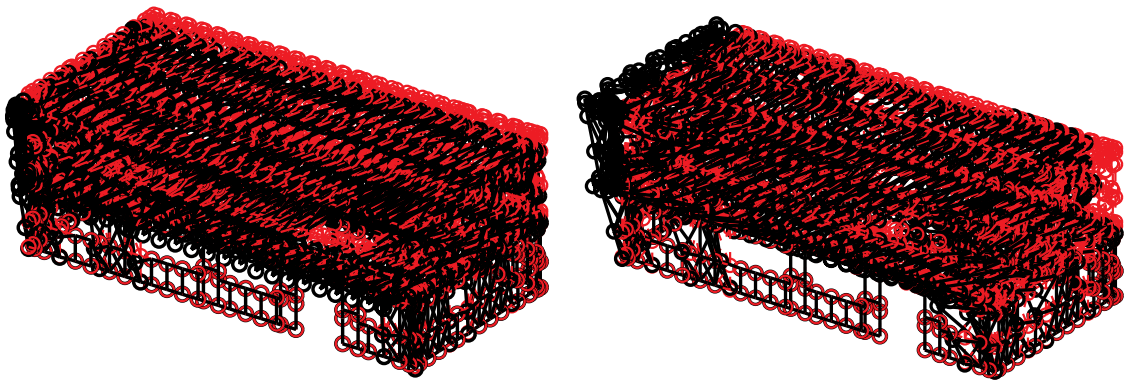

(a) Mode 1, T_1=0.321 s (b) Mode 2, T_2=0.295 s

Figure K-2: First two natural modes of A1-3D-SD-a model

K.3 Linear static analysis results

Table K-2 to Table K-4 present linear static analysis results. The lateral load is the equivalent lateral force available from the design narrative (Madsen et al. 2011), applied equally at four corners. Two separate analyses were performed with the loading at long or short direction.

Table K-2 summarizes the breakdown of peak total base shear among four elevations. Due to the interplay of asymmetrical LFRS, wall lines perpendicular to the loading direction still take a small portion of base shear.

Table K-3 shows peak building and wall line deflections. Displacements of corner nodes at floor and roof levels are recorded from OpenSees analysis. The average displacement of two corners on the same level of the same wall line is taken as the wall line displacement and the building displacement is the average of four corners. Peak absolute values are taken and the negative sign is kept if it exists. The displacement in long direction is denoted as 'u' and 'v' is for short direction displacement. Subscripts 1 and 2 indicate floor and roof level. The displacement outputs of OpenSees are relative to the ground, so inter-story displacement $\mathbf{\Delta u_1}$ and $\mathbf{\Delta v_1}$ are equal to $\mathbf{u_1}$ and $\mathbf{v_1}$ respectively. For roof level, $\mathbf{\Delta u_2 = u_2 - u_1}$ and $\mathbf{\Delta v_2 = v_2 - v_1}$. Practicing engineers can linearly upscale these data and develop an estimate of the building's performance at a certain lateral force level.

Table K-4 is an evaluation of the building's lateral stiffness of long and short direction and its breakdown among shear walls (SW) and other systems. The lateral stiffness is

calculated as the slope of the total base shear vs. building lateral deflection curve (a straight line herein). In addition, we run two more analyses with the stiffness of shear walls set to a number close to zero so the lateral stiffness of gravity walls (GW) and other systems is computed in the same way. Interestingly, the bare CFS framing still accounts for 10% to 20% total lateral stiffness in this case.

Table K-2: Breakdown of peak base shear, linear static analysis, A1-3D-SD-a model

Load direction	**LONG**				
Elevation	**South V_b**	**North V_b**	**East V_b**	**West V_b**	**Peak V_b**
kips	3.2	7.6	0.1	0.3	11.1
%	28.6	68.3	0.8	2.3	100.0
Load direction	**SHORT**				
Elevation	**South V_b**	**North V_b**	**East V_b**	**West V_b**	**Peak V_b**
kips	0.4	0.6	5.2	4.9	11.1
%	3.5	5.7	46.6	44.2	100.0

Table K-3: Peak building and wall line deflection, linear static analysis, A1-3D-SD-a model

Load direction	**LONG**							
Deflection (in.)	**u_1**	**u_2**	**v_1**	**v_2**	**Δu_1**	**Δu_2**	**Δv_1**	**Δv_2**
Building	0.100	0.159	-0.002	-0.003	0.100	0.059	-0.002	-0.002
South	0.103	0.176	-0.002	-0.005	0.103	0.072	-0.002	-0.002
North	0.096	0.142	-0.001	-0.002	0.096	0.045	-0.001	-0.001
East	0.092	0.158	0.015	0.022	0.092	0.066	0.015	0.007
West	0.108	0.159	-0.018	-0.029	0.108	0.052	-0.018	-0.011
Load direction	**SHORT**							
Deflection (in.)	**u_1**	**u_2**	**v_1**	**v_2**	**Δu_1**	**Δu_2**	**Δv_1**	**Δv_2**
Building	0.002	0.006	0.106	0.174	0.002	0.003	0.106	0.068
South	-0.003	0.005	0.106	0.173	-0.003	0.003	0.106	0.067
North	0.003	0.007	0.106	0.175	0.003	0.007	0.106	0.069
East	0.002	0.005	0.099	0.158	0.002	0.003	0.099	0.058
West	-0.003	0.006	0.112	0.190	-0.003	0.005	0.112	0.078

Table K-4: Breakdown of lateral stiffness, A1-3D-SD-a model

LONG			**SHORT**		
Shear wall k_u (%)	**Gravity wall k_u (%)**	**k_u (kip/in)**	**Shear wall k_v (%)**	**Gravity wall k_v (%)**	**k_v (kip/in)**
87.1	12.9	72.2	80.3	19.7	63.3

K.4 Nonlinear static (pushover) analysis results

Table K-5 is created following the same logic with Table K-2, but the analysis type is nonlinear static (pushover). Pushover curves of the building and each wall line are presented in Figure K-3 and Figure K-4. The horizontal coordinate is building roof drift, which is the building's roof deflection divided by the building's full height (2h), also twice of the story height.

Clearly, the interaction between wall lines is much more significant when material and geometrical nonlinearity is included. These tables and figures indicate that the wall lines do not reach their peak capacity at exactly the same drift level and wall lines perpendicular to the load can take a nontrivial amount of base shear. Accordingly, total capacity of the building is larger than the sum of wall line capacities in the load direction. Furthermore, total capacity of the building in the short direction is larger than the long direction; however, total capacity of wall lines in the short direction is smaller compared with long direction wall lines.

Table K-5: Breakdown of peak base shear, pushover analysis, A1-3D-SD-a model

Load direction	**LONG**				
Elevation	**South V_b**	**North V_b**	**East V_b**	**West V_b**	**Peak V_b**
kips	24.2	24.0	5.7	7.7	52.5
%	46.1	45.7	10.8	14.6	100.0
Load direction	**SHORT**				
Elevation	**South V_b**	**North V_b**	**East V_b**	**West V_b**	**Peak V_b**
kips	10.4	10.0	20.7	23.2	57.8
%	17.9	17.2	35.8	40.1	100.0

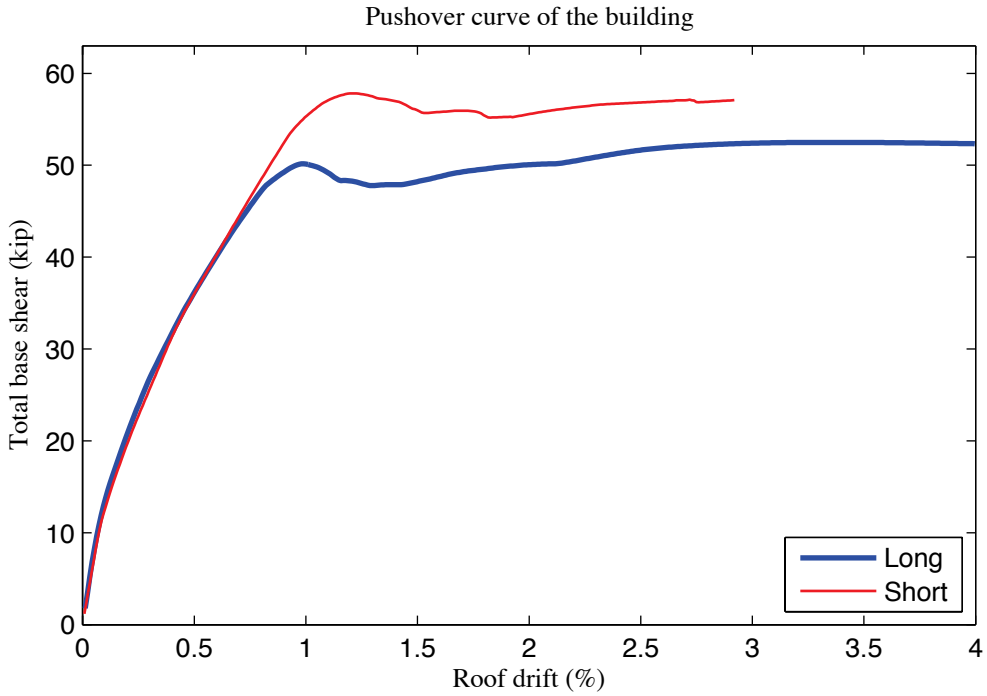

Figure K-3: Pushover curve of A1-3D-SD-a model

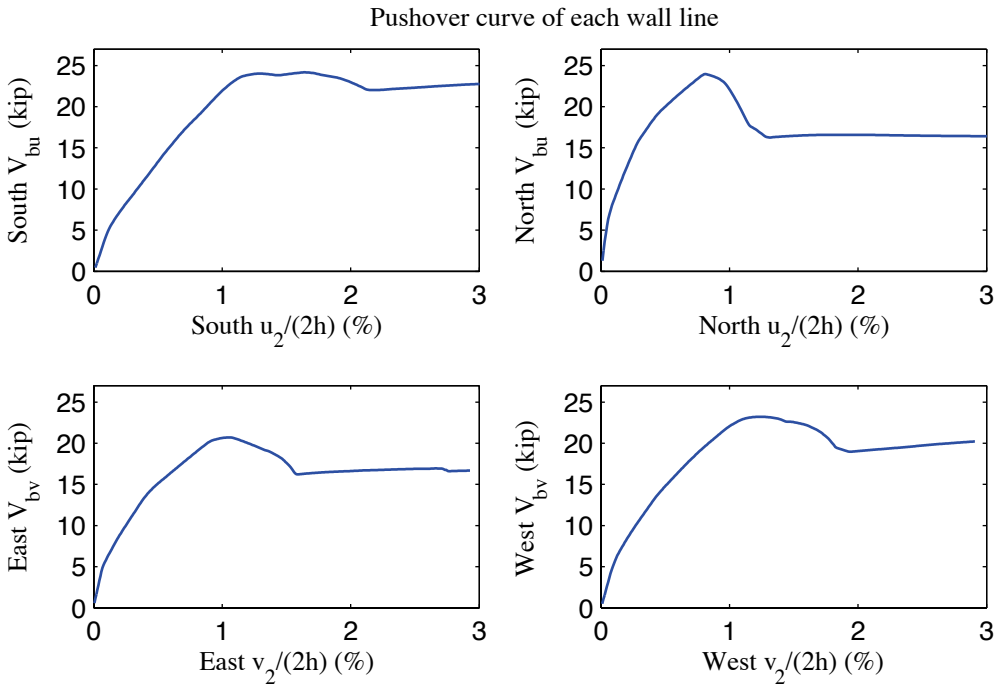

Figure K-4: Pushover curve of each wall line, A1-3D-SD-a model

K.5 Linear time history analysis results

Linear time history analysis is performed on the model under Canoga Park and Rinaldi ground motion records of Northridge earthquake in 1994. Details about the ground motion itself and the way we select them are addressed in Chapter 4 and Chapter 5. We considered three scale levels (16%, 44% and 100%) and loadings in one, two and three axes. The summary table of time history load cases is also available in Chapter 5 (see Table 5-4 in Chapter 5).

Table K-6 to Table K-9 demonstrate the building's linear elastic performance under designated ground motions. Table K-6 shows peak story relative accelerations in the unit of g. Table K-7 and Table K-8 report peak roof drift and story drift of the building and the corresponding time step (t_*) and the base shear at that time. Note that the base shear at the time of peak roof drift may not be the peak total building base shear in that direction (see Table K-9).

The building behaves linearly since peak drift and peak base shear appear at the same time when the ground motion is linearly scaled. Figure K-5 is a vector plot of the peak total resultant base shear of the building under three axial, 100% Canoga Park excitation. The directions of arrows imply that base shear taken by shear walls and gravity systems does not necessarily follow the direction of wall lines due to the effect of 3D coupling. Comparison with nonlinear analysis results of the same excitation provides insightful observations on the building's response and requirements on modeling fidelity and analysis type.

Table K-6: A1-3D-SD-a model peak story relative acceleration in g, linear time history analysis

		LONG			SHORT			UP		
Load Case	**Ground Motion**	**a_g**	**Floor a**	**Roof a**	**a_g**	**Floor a**	**Roof a**	**a_g**	**Floor a**	**Roof a**
EQ_3D_3axis_1	CNP 16%	0.067	0.107	0.139	0.057	0.106	0.149	0.078	0.083	0.072
EQ_3D_3axis_2	CNP 44%	0.185	0.301	0.385	0.157	0.295	0.419	0.215	0.237	0.209
EQ_3D_1axis_1	CNP 100%	0.420	0.550	0.762	0	0.115	0.153	0	0.184	0.163
EQ_3D_1axis_2	CNP 100%	0	0.314	0.418	0.356	0.670	0.997	0	0.706	0.641
EQ_3D_2axis_1	CNP 100%	0.420	0.691	0.907	0.356	0.680	0.972	0	0.588	0.529
EQ_3D_3axis_3	CNP 100%	0.420	0.691	0.912	0.356	0.679	0.976	0.489	0.561	0.503
EQ_3D_3axis_4	RRS 16%	0.132	0.230	0.314	0.078	0.233	0.351	0.133	0.236	0.222
EQ_3D_3axis_5	RRS 44%	0.363	0.628	0.883	0.214	0.630	0.928	0.367	0.524	0.480
EQ_3D_3axis_6	RRS 100%	0.825	1.455	2.053	0.486	1.398	2.046	0.834	1.730	1.558

Table K-7: A1-3D-SD-a model peak building roof drift and base shear, linear time history analysis

		LONG			SHORT		
Load Case	**Ground Motion**	**$u_2/(2h)$ (%)**	**t_* (s)**	**V_b @ t_* (kips)**	**$v_2/(2h)$ (%)**	**t_* (s)**	**V_b @ t_* (kips)**
EQ_3D_3axis_1	CNP 16%	0.053	12.31	7.6	0.067	9.95	9.5
EQ_3D_3axis_2	CNP 44%	0.143	12.31	20.6	0.184	9.96	25.8
EQ_3D_1axis_1	CNP 100%	0.286	8.70	45.9	-0.056	12.70	8.3
EQ_3D_1axis_2	CNP 100%	0.160	10.18	22.9	0.458	9.96	63.6
EQ_3D_2axis_1	CNP 100%	-0.330	11.88	48.8	0.420	9.96	58.6
EQ_3D_3axis_3	CNP 100%	-0.331	11.88	48.8	0.418	9.96	58.1
EQ_3D_3axis_4	RRS 16%	-0.121	4.55	17.7	0.150	4.54	20.1
EQ_3D_3axis_5	RRS 44%	-0.350	4.55	48.9	0.396	4.54	52.2
EQ_3D_3axis_6	RRS 100%	-0.823	4.55	113.2	0.872	4.54	114.1

Table K-8: A1-3D-SD-a model peak building story drift, linear time history analysis

		LONG				SHORT			
Load Case	**Ground Motion**	**$\Delta u_1/h$ (%)**	**t_* (s)**	**$\Delta u_2/h$ (%)**	**t_* (s)**	**$\Delta v_1/h$ (%)**	**t_* (s)**	**$\Delta v_2/h$ (%)**	**t_* (s)**
EQ_3D_3axis_1	CNP 16%	0.083	12.59	0.034	12.30	0.086	9.95	0.048	9.95
EQ_3D_3axis_2	CNP 44%	-0.225	11.87	0.091	12.30	0.235	9.96	0.133	9.96
EQ_3D_1axis_1	CNP 100%	-0.419	11.88	0.180	8.69	-0.073	12.70	-0.040	12.70
EQ_3D_1axis_2	CNP 100%	-0.244	10.33	0.084	10.17	0.583	9.96	0.333	9.96
EQ_3D_2axis_1	CNP 100%	-0.527	11.87	-0.211	12.17	0.536	9.96	0.304	9.96
EQ_3D_3axis_3	CNP 100%	-0.527	11.87	-0.211	12.17	0.533	9.96	0.303	9.96
EQ_3D_3axis_4	RRS 16%	-0.180	4.54	0.070	4.70	0.190	4.54	0.111	4.54
EQ_3D_3axis_5	RRS 44%	-0.508	4.54	-0.202	4.56	0.499	4.54	0.293	4.54
EQ_3D_3axis_6	RRS 100%	-1.187	4.54	-0.480	4.56	1.103	4.55	0.647	4.54

Table K-9: A1-3D-SD-a model peak building base shear, linear time history analysis

		LONG		SHORT		RESULTANT	
Load Case	**Ground Motion**	**Peak V_{bu} (kip)**	**t @ peak V_{bu} (s)**	**Peak V_{bv} (kip)**	**t @ peak V_{bv} (s)**	**Peak V_b (kip)**	**t @ peak V_b (s)**
EQ_3D_3axis_1	CNP 16%	8.4	8.72	9.5	9.95	10.4	7.40
EQ_3D_3axis_2	CNP 44%	21.4	8.72	25.8	9.96	28.3	7.41
EQ_3D_1axis_1	CNP 100%	45.9	8.71	8.9	8.20	45.9	8.70
EQ_3D_1axis_2	CNP 100%	22.9	10.18	63.6	9.96	63.7	9.96
EQ_3D_2axis_1	CNP 100%	48.8	11.88	58.6	9.96	64.7	7.41
EQ_3D_3axis_3	CNP 100%	48.8	11.88	58.1	9.96	64.5	7.41
EQ_3D_3axis_4	RRS 16%	18.6	2.60	20.1	4.54	26.9	4.54
EQ_3D_3axis_5	RRS 44%	52.2	2.60	52.4	4.55	71.7	4.55
EQ_3D_3axis_6	RRS 100%	121.3	2.60	115.4	4.55	161.6	4.55

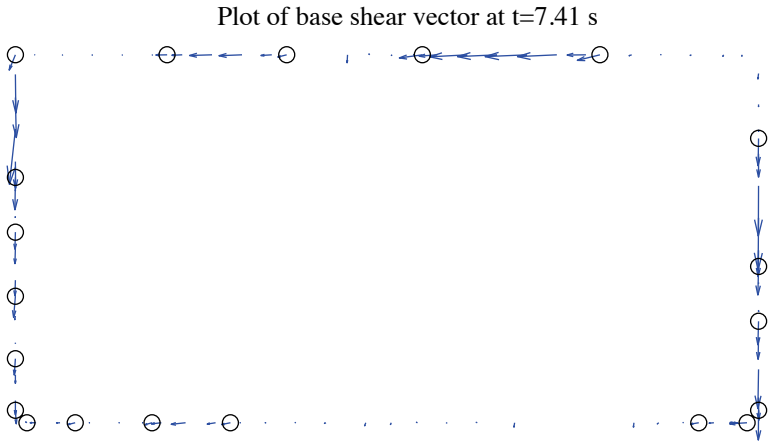

Figure K-5: A1-3D-SD-a model, base shear vector plot at the moment of peak total base shear, 100 % Canoga Park, 3D linear analysis (maximum anchor/hold down base shear is 3.89 kips)

K.6 Nonlinear time history analysis results

Same ground motions are applied to the model with material and geometrical nonlinearity. Table K-10 to Table K-13 are replicas of Table K-6 to Table K-9, but for nonlinear time history analyses. Since this analysis type is most complicated and closest to reality and experiments, behavior of wall lines and hold downs are further studied. Table K-14 is the table of peak wall line story drifts and corresponding time steps. Table K-15 is designed for peak base shear of each wall line and the last two columns of the table are percentages of base shear of two facing wall lines in the same direction when the total base shear in that direction takes peak value. The base shear is summed up for each wall, each wall line and the building step by step. Table K-16 expands the breakdown of each wall line's peak base shear between shear walls, gravity walls and other systems. Table K-17 is peak value of hold down tensile force of two selected pairs. Hold down 5 and 6 are on shear wall L1S1, South elevation and hold down 7 and 8 are on shear wall L1W1, West elevation. These shear walls have lowest capacities compared with others on the same wall line and they meet at the southwest edge of the building, so interacted nonlinear behavior is expected to appear.

Time history plots in this section include plots of story drifts of the building and each wall line (Figure K-6 to Figure K-8), total building base shear in long and short direction (Figure K-9) and axial forces of hold downs in Table K-17 (Figure K-10). Hysteretic plots in Figure K-11 and Figure K-12 are helpful for visual examination of nonlinear base shear-drift relationship of the building and the weakest shear wall on each wall line. In comparison with linear time history analysis, vector plot of peak total base shear is

illustrated in Figure K-13. Figure K-14 presents a simplified deformed shape of the building (see (Peterman 2014) for details of the method) and axial force of all twenty hold downs at the moment of peak total base shear. The same sign convention with tests is adopted. Red bars indicate tensile (negative) force and blue ones are for compressive (positive) force.

Hysteretic behavior is seen in the building and typical shear walls under design-based earthquake (100% Canoga Park excitation in 3 axes, see Figure K-11 and Figure K-12). However, the backbones of response curves do not reach the post-peak range. Peak story drifts are not greater than 1.5% (Table K-12), and larger deflection is seen in the long direction. Peak wall line drifts are smaller than 1.5% (Table K-14), with the maximum found in North elevation. Figure K-13 clearly shows that base shear vectors in anchors and hold downs do not align with wall lines and they can change directions even within a single piece of wall, a sign of localized behavior. Table K-17, Figure K-10 and Figure K-14 demonstrate that hold downs in a pair do not experience the same amount of force with opposite signs, an evidence that supports Type II shear wall behavior despite Type I design assumption.

The near-field Rinaldi record is much stronger in terms of peak ground acceleration, especially in the long direction. When loaded at 100%, the long direction is believed to be destroyed with peak story drift larger than 7%. Table K-16 reveals that as nonlinearity increases, the portion of base shear taken by gravity wall and other system grows

significantly, from 2.1% to 6.3% on West elevation at minimum and from 11.8% to 29.2% on South elevation at maximum.

Table K-10: A1-3D-SD-a model peak story relative acceleration in g, nonlinear time history analysis

		LONG			SHORT			UP		
Load Case	**Ground Motion**	**a_g**	**Floor a**	**Roof a**	**a_g**	**Floor a**	**Roof a**	**a_g**	**Floor a**	**Roof a**
EQ_3D_3axis_1	CNP 16%	0.067	0.143	0.171	0.057	0.140	0.188	0.078	0.092	0.076
EQ_3D_3axis_2	CNP 44%	0.185	0.331	0.406	0.157	0.258	0.344	0.215	0.205	0.198
EQ_3D_1axis_1	CNP 100%	0.420	0.758	1.296	0	0.259	0.208	0	0.906	0.818
EQ_3D_1axis_2	CNP 100%	0	0.102	0.104	0.356	0.523	0.815	0	0.391	0.354
EQ_3D_2axis_1	CNP 100%	0.420	0.655	1.279	0.356	0.525	0.741	0	0.240	0.211
EQ_3D_3axis_3	CNP 100%	0.420	0.654	1.274	0.356	0.522	0.743	0.489	0.239	0.224
EQ_3D_3axis_4	RRS 16%	0.132	0.196	0.242	0.078	0.181	0.236	0.133	0.150	0.125
EQ_3D_3axis_5	RRS 44%	0.363	0.626	0.686	0.214	0.538	0.583	0.367	0.332	0.259
EQ_3D_3axis_6	RRS 100%	0.825	0.852	1.039	0.486	0.683	0.957	0.834	0.396	0.378

Table K-11: A1-3D-SD-a model peak building roof drift and base shear, nonlinear time history analysis

		LONG			SHORT		
Load Case	**Ground Motion**	**$u_2/(2h)$ (%)**	**t_* (s)**	**V_b @ t_* (kips)**	**$v_2/(2h)$ (%)**	**t_* (s)**	**V_b @ t_* (kips)**
EQ_3D_3axis_1	CNP 16%	0.059	8.71	9.9	0.065	7.43	9.2
EQ_3D_3axis_2	CNP 44%	0.219	8.72	23.3	-0.155	8.43	16.8
EQ_3D_1axis_1	CNP 100%	0.935	8.77	55.4	-0.020	8.78	2.5
EQ_3D_1axis_2	CNP 100%	0.029	4.59	2.5	0.596	10.01	41.4
EQ_3D_2axis_1	CNP 100%	0.896	8.77	51.6	0.611	10.01	41.4
EQ_3D_3axis_3	CNP 100%	0.896	8.77	51.5	0.618	10.01	41.5
EQ_3D_3axis_4	RRS 16%	0.111	4.41	13.2	0.107	3.35	13.4
EQ_3D_3axis_5	RRS 44%	0.578	2.68	41.8	0.363	6.06	29.2
EQ_3D_3axis_6	RRS 100%	3.914	2.90	51.0	-0.815	2.59	47.2

Table K-12: A1-3D-SD-a model peak building story drift, nonlinear linear time history analysis

		LONG				SHORT			
Load Case	**Ground Motion**	**$\Delta u_1/h$ (%)**	**t_* (s)**	**$\Delta u_2/h$ (%)**	**t_* (s)**	**$\Delta v_1/h$ (%)**	**t_* (s)**	**$\Delta v_2/h$ (%)**	**t_* (s)**
EQ_3D_3 axis_1	CNP 16%	0.094	8.72	0.035	7.33	0.084	7.43	0.046	7.42
EQ_3D_3 axis_2	CNP 44%	0.356	8.72	-0.109	10.56	-0.231	10.56	0.085	9.98
EQ_3D_1 axis_1	CNP 100%	1.473	8.77	-0.564	10.25	-0.027	7.11	-0.019	7.14
EQ_3D_1 axis_2	CNP 100%	-0.048	5.26	0.034	4.58	0.881	10.01	-0.315	6.01
EQ_3D_2 axis_1	CNP 100%	1.408	8.77	-0.536	10.24	0.894	10.01	0.329	10.01
EQ_3D_3 axis_3	CNP 100%	1.406	8.77	-0.534	10.24	0.903	10.01	0.333	10.01
EQ_3D_3 axis_4	RRS 16%	0.179	2.61	-0.057	4.58	0.153	3.35	-0.065	3.17
EQ_3D_3 axis_5	RRS 44%	0.904	2.67	0.266	2.70	0.533	6.05	0.198	6.07
EQ_3D_3 axis_6	RRS 100%	7.302	2.89	0.666	2.77	-1.189	2.59	-0.440	2.59

Table K-13: A1-3D-SD-a model peak building base shear, nonlinear time history analysis

		LONG		SHORT		RESULTANT	
Load Case	**Ground Motion**	**Peak V_{bu} (kip)**	**t @ peak V_{bu} (s)**	**Peak V_{bv} (kip)**	**t @ peak V_{bv} (s)**	**Peak V_b (kip)**	**t @ peak V_b (s)**
EQ_3D_3axis_1	CNP 16%	9.9	8.71	9.2	7.43	10.5	8.72
EQ_3D_3axis_2	CNP 44%	23.3	8.72	16.8	8.43	27.4	10.54
EQ_3D_1axis_1	CNP 100%	58.7	8.76	3.2	9.07	58.7	8.76
EQ_3D_1axis_2	CNP 100%	5.0	4.88	41.4	10.01	41.4	10.01
EQ_3D_2axis_1	CNP 100%	51.6	8.77	41.4	10.01	62.1	10.00
EQ_3D_3axis_3	CNP 100%	51.5	8.77	41.5	10.01	62.2	10.00
EQ_3D_3axis_4	RRS 16%	15.1	2.61	13.4	3.35	16.5	4.57
EQ_3D_3axis_5	RRS 44%	41.8	2.67	29.8	6.05	41.8	2.68
EQ_3D_3axis_6	RRS 100%	52.6	2.61	48.4	2.58	68.6	2.60

Table K-14: A1-3D-SD-a model peak wall line story drift, nonlinear time history analysis

LONG		SOUTH				NORTH			
Load Case	**Ground Motion**	**$\Delta u_1/h$ (%)**	**t_* (s)**	**$\Delta u_2/h$ (%)**	**t_* (s)**	**$\Delta u_1/h$ (%)**	**t_* (s)**	**$\Delta u_2/h$ (%)**	**t_* (s)**
EQ_3D_3axis_1	CNP 16%	0.095	9.86	0.057	12.16	0.142	8.74	0.089	7.52
EQ_3D_3axis_2	CNP 44%	0.381	8.73	0.161	10.56	0.416	8.70	0.117	10.56
EQ_3D_1axis_1	CNP 100%	1.417	8.77	0.619	10.24	1.637	8.77	0.558	10.25
EQ_3D_1axis_2	CNP 100%	0.078	10.24	0.056	6.03	0.087	5.26	0.066	5.25
EQ_3D_2axis_1	CNP 100%	1.419	8.77	0.585	10.24	1.518	8.76	0.570	10.24
EQ_3D_3axis_3	CNP 100%	1.416	8.77	0.582	10.24	1.518	8.76	0.570	10.24
EQ_3D_3axis_4	RRS 16%	0.202	4.41	0.098	4.42	0.259	2.61	0.068	7.20
EQ_3D_3axis_5	RRS 44%	0.909	2.68	0.310	2.70	1.018	2.66	0.308	2.69
EQ_3D_3axis_6	RRS 100%	7.179	2.90	0.731	2.80	7.598	2.88	0.836	2.74
SHORT		**EAST**				**WEST**			
Load Case	**Ground Motion**	**$\Delta v_1/h$ (%)**	**t_* (s)**	**$\Delta v_2/h$ (%)**	**t_* (s)**	**$\Delta v_1/h$ (%)**	**t_* (s)**	**$\Delta v_2/h$ (%)**	**t_* (s)**
EQ_3D_3axis_1	CNP 16%	0.076	10.80	0.045	10.77	0.109	5.22	0.064	9.97
EQ_3D_3axis_2	CNP 44%	0.270	10.55	0.096	10.56	0.239	10.00	0.124	9.98
EQ_3D_1axis_1	CNP 100%	0.097	9.32	0.074	9.20	0.078	9.77	0.060	7.62
EQ_3D_1axis_2	CNP 100%	0.808	10.00	0.266	10.00	0.959	10.01	0.367	6.01
EQ_3D_2axis_1	CNP 100%	0.869	10.01	0.327	10.00	0.922	10.01	0.350	10.02
EQ_3D_3axis_3	CNP 100%	0.871	10.01	0.327	10.00	0.939	10.01	0.358	10.02
EQ_3D_3axis_4	RRS 16%	0.099	3.15	0.055	3.16	0.228	3.36	0.093	3.34
EQ_3D_3axis_5	RRS 44%	0.453	6.05	0.171	3.41	0.614	6.05	0.247	6.07
EQ_3D_3axis_6	RRS 100%	1.027	2.57	0.321	2.59	1.404	2.61	0.560	2.59

Table K-15: A1-3D-SD-a model peak wall line base shear, nonlinear time history analysis

LONG		SOUTH		NORTH		% of Peak V_{bu}	
Load Case	**Ground Motion**	**Peak V_{bu} (kips)**	**t @ peak V_{bu} (s)**	**Peak V_{bu} (kips)**	**t @ peak V_{bu} (s)**	**South**	**North**
EQ_3D_3axis_1	CNP 16%	3.7	11.88	6.1	8.71	35.0	61.4
EQ_3D_3axis_2	CNP 44%	9.0	8.74	13.0	8.71	38.1	55.4
EQ_3D_1axis_1	CNP 100%	23.9	8.76	26.6	8.76	40.7	45.3
EQ_3D_1axis_2	CNP 100%	2.4	10.07	3.3	4.88	29.5	66.7
EQ_3D_2axis_1	CNP 100%	22.3	8.77	24.0	8.72	43.1	45.1
EQ_3D_3axis_3	CNP 100%	22.2	8.77	24.0	8.72	43.1	45.1
EQ_3D_3axis_4	RRS 16%	6.2	4.56	8.9	2.62	36.1	59.0
EQ_3D_3axis_5	RRS 44%	16.7	2.67	21.2	2.68	39.9	50.8
EQ_3D_3axis_6	RRS 100%	23.9	2.66	23.5	2.60	43.3	42.6
SHORT		**EAST**		**WEST**		**% of Peak V_{bv}**	
Load Case	**Ground Motion**	**Peak V_{bv} (kips)**	**t @ peak V_{bv} (s)**	**Peak V_{bv} (kips)**	**t @ peak V_{bv} (s)**	**East**	**West**
EQ_3D_3axis_1	CNP 16%	4.2	7.43	5.0	5.22	46.0	46.4
EQ_3D_3axis_2	CNP 44%	8.4	10.56	7.8	10.00	44.2	44.9
EQ_3D_1axis_1	CNP 100%	5.1	9.09	4.2	9.77	146.1	52.2
EQ_3D_1axis_2	CNP 100%	15.9	10.00	18.2	10.01	38.3	43.9
EQ_3D_2axis_1	CNP 100%	16.6	10.01	17.4	10.01	40.1	42.2
EQ_3D_3axis_3	CNP 100%	16.6	10.01	17.6	10.01	40.0	42.5
EQ_3D_3axis_4	RRS 16%	4.9	3.15	7.7	4.57	34.2	56.5
EQ_3D_3axis_5	RRS 44%	11.3	3.88	14.2	6.05	37.6	47.6
EQ_3D_3axis_6	RRS 100%	17.6	2.57	22.2	2.60	35.3	45.2

Table K-16: A1-3D-SD-a model wall line base shear breakdown, nonlinear time history analysis

LONG		SOUTH			NORTH		
Load Case	**Ground Motion**	**Peak V_{bu} (kips)**	**SW V_{bu} (%)**	**GW V_{bu} (%)**	**Peak V_{bu} (kips)**	**SW V_{bu} (%)**	**GW V_{bu} (%)**
EQ_3D_3axis_1	CNP 16%	3.7	88.2	11.8	6.1	96.7	3.3
EQ_3D_3axis_2	CNP 44%	9.0	82.7	17.3	13.0	92.9	7.1
EQ_3D_1axis_1	CNP 100%	23.9	76.9	23.1	26.6	88.1	11.9
EQ_3D_1axis_2	CNP 100%	2.4	87.5	12.5	3.3	97.2	2.8
EQ_3D_2axis_1	CNP 100%	22.3	75.6	24.4	24.0	87.7	12.3
EQ_3D_3axis_3	CNP 100%	22.2	75.6	24.4	24.0	87.7	12.3
EQ_3D_3axis_4	RRS 16%	6.2	86.3	13.7	8.9	95.1	4.9
EQ_3D_3axis_5	RRS 44%	16.7	77.9	22.1	21.2	89.7	10.3
EQ_3D_3axis_6	RRS 100%	23.9	70.8	29.2	23.5	89.7	10.3
SHORT		**EAST**			**WEST**		
Load Case	**Ground Motion**	**Peak V_{bv} (kips)**	**SW V_{bv} (%)**	**GW V_{bu} (%)**	**Peak V_{bv} (kips)**	**SW V_{bv} (%)**	**GW V_{bv} (%)**
EQ_3D_3axis_1	CNP 16%	4.2	96.9	3.1	5.0	97.2	2.8
EQ_3D_3axis_2	CNP 44%	8.4	92.9	7.1	7.8	96.1	3.9
EQ_3D_1axis_1	CNP 100%	5.1	95.9	4.1	4.2	97.9	2.1
EQ_3D_1axis_2	CNP 100%	15.9	90.9	9.1	18.2	93.7	6.3
EQ_3D_2axis_1	CNP 100%	16.6	91.3	8.7	17.4	93.2	6.8
EQ_3D_3axis_3	CNP 100%	16.6	91.3	8.7	17.6	93.2	6.8
EQ_3D_3axis_4	RRS 16%	4.9	95.4	4.6	7.7	96.4	3.6
EQ_3D_3axis_5	RRS 44%	11.3	92.7	7.3	14.2	94.7	5.3
EQ_3D_3axis_6	RRS 100%	17.6	87.8	12.2	22.2	93.9	6.1

Table K-17: A1-3D-SD-a model peak hold down tensile force at certain locations, nonlinear time history analysis

		L1S1, LC5		L1S1, LC6		L1W1, LC7		L1W1, LC8	
Load Case	**Ground Motion**	**Peak F (kips)**	**t @ peak F (s)**	**Peak F (kips)**	**t @ peak F (s)**	**Peak F (kips)**	**t @ peak F (s)**	**Peak F (kips)**	**t @ peak F (s)**
EQ_3D_3axis_1	CNP 16%	-1.50	12.17	-0.15	7.41	-0.13	8.73	-0.49	7.27
EQ_3D_3axis_2	CNP 44%	-2.17	10.54	-0.48	10.36	-0.54	10.36	-0.88	8.43
EQ_3D_1axis_1	CNP 100%	-3.46	10.25	-1.07	8.77	-1.90	8.77	-1.00	8.73
EQ_3D_1axis_2	CNP 100%	-2.10	10.01	-1.50	10.00	-0.78	10.00	-2.00	6.00
EQ_3D_2axis_1	CNP 100%	-3.32	10.23	-2.84	10.00	-2.90	10.00	-1.87	6.01
EQ_3D_3axis_3	CNP 100%	-3.31	10.23	-2.86	10.00	-2.91	10.00	-1.88	6.01
EQ_3D_3axis_4	RRS 16%	-2.02	4.57	-0.23	3.34	-0.21	2.63	-0.87	4.41
EQ_3D_3axis_5	RRS 44%	-2.59	3.97	-0.99	3.89	-1.43	2.69	-1.38	4.11
EQ_3D_3axis_6	RRS 100%	-3.39	2.37	-1.89	3.97	-2.13	2.80	-2.83	2.60

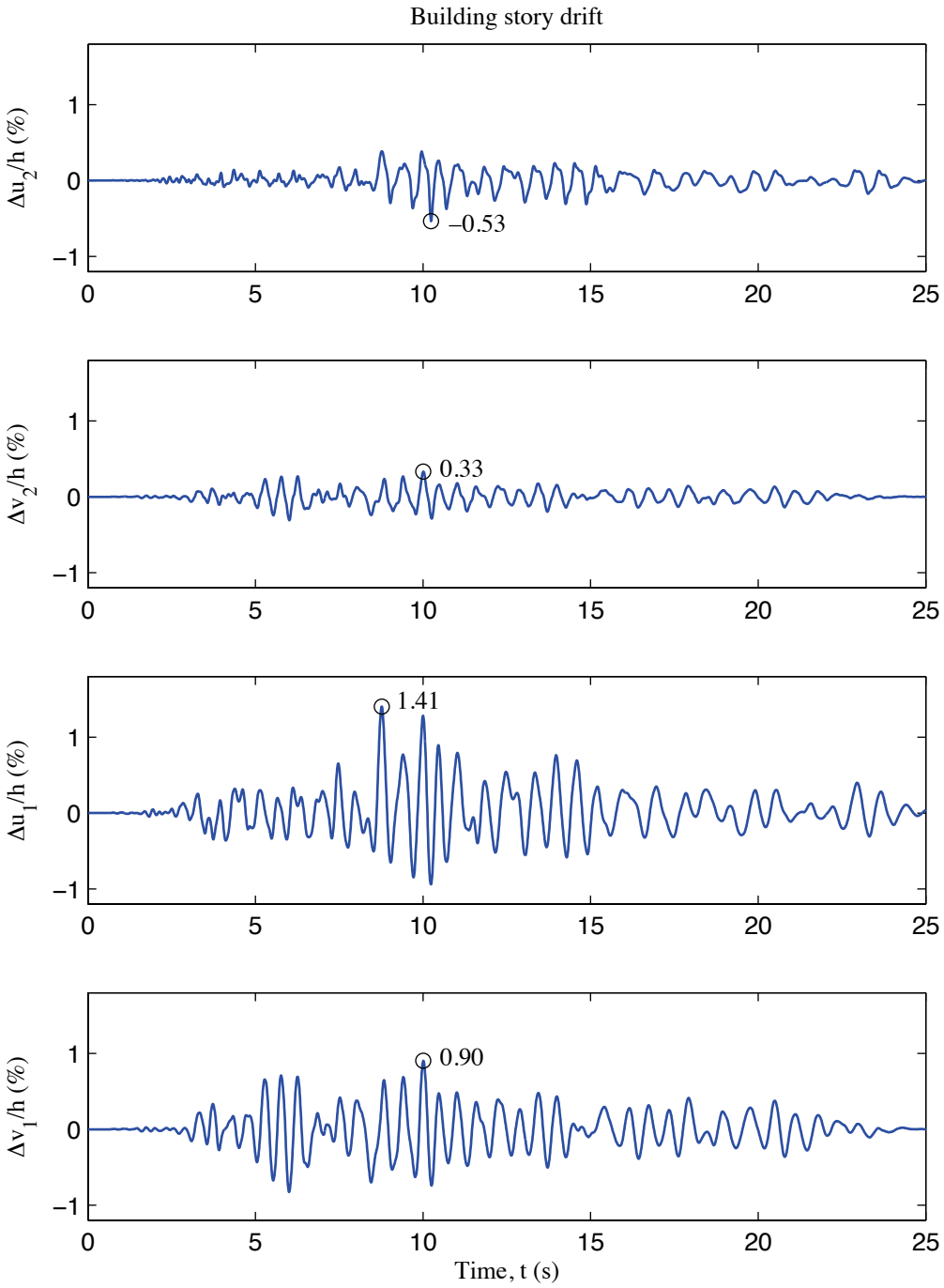

Figure K-6: A1-3D-SD-a model building story drift, 100 % Canoga Park, 3D nonlinear analysis

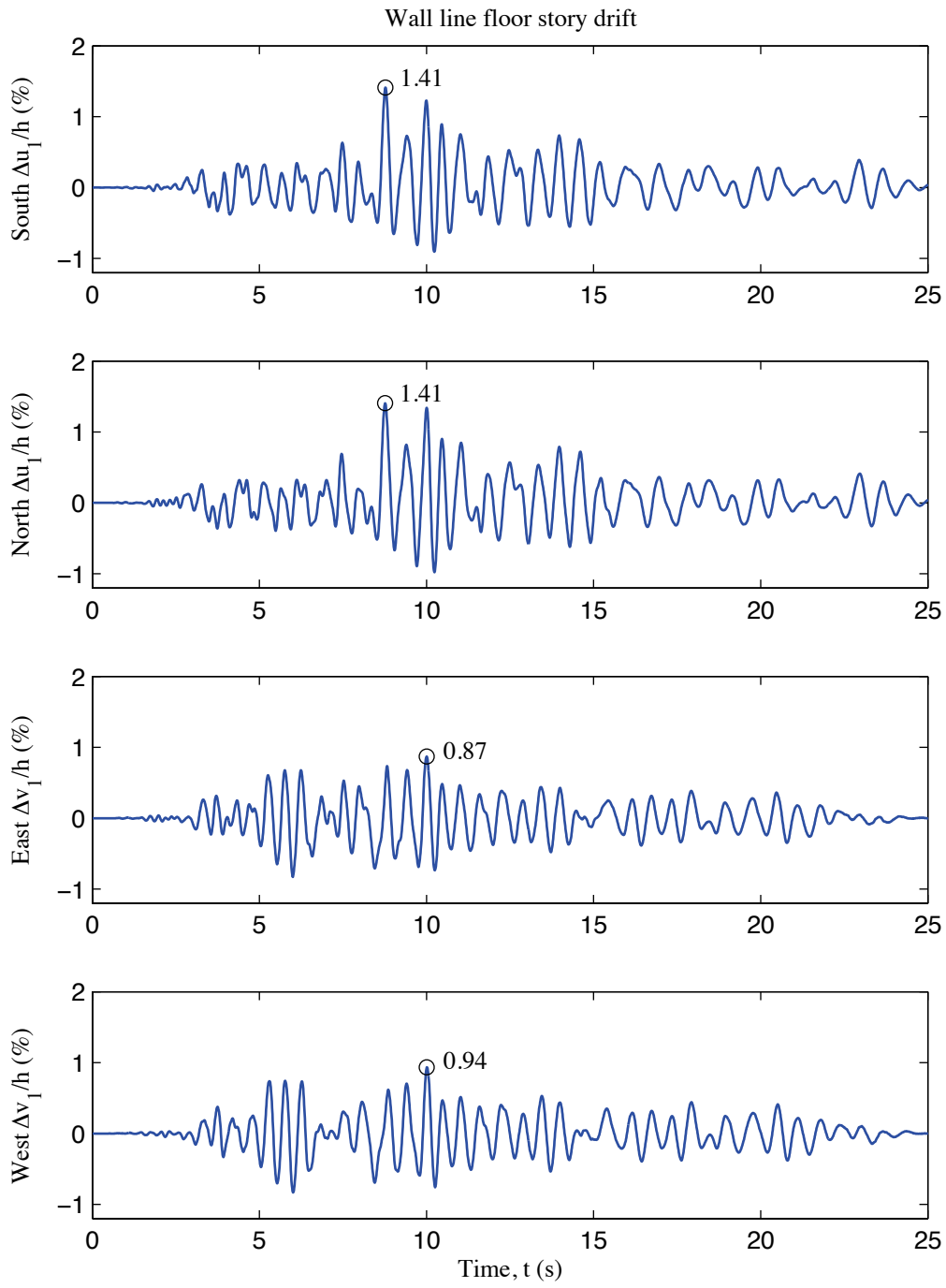

Figure K-7: A1-3D-SD-a model wall line floor story drift, 100 % Canoga Park, 3D nonlinear analysis

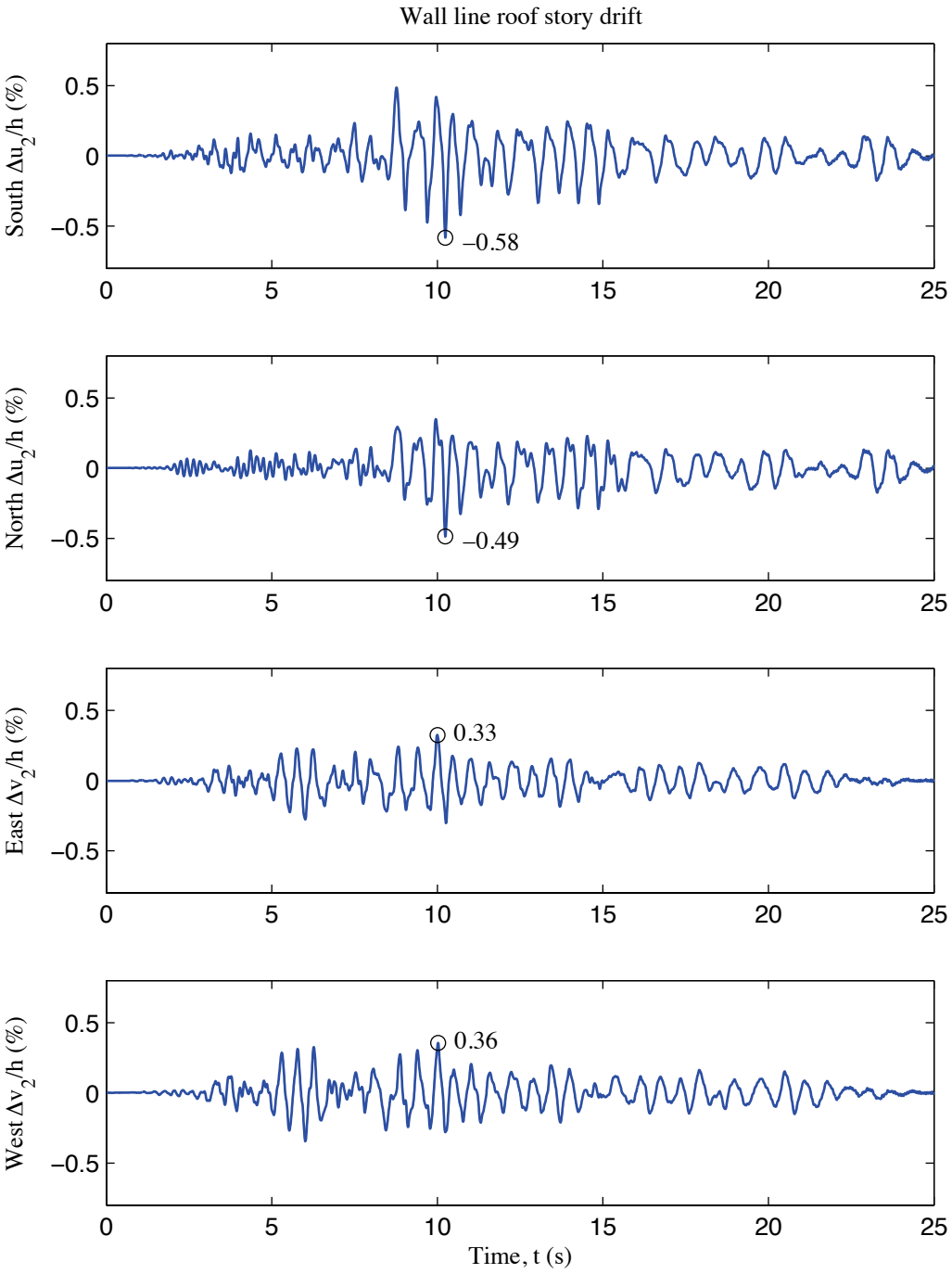

Figure K-8: A1-3D-SD-a model wall line roof story drift, 100 % Canoga Park, 3D nonlinear analysis

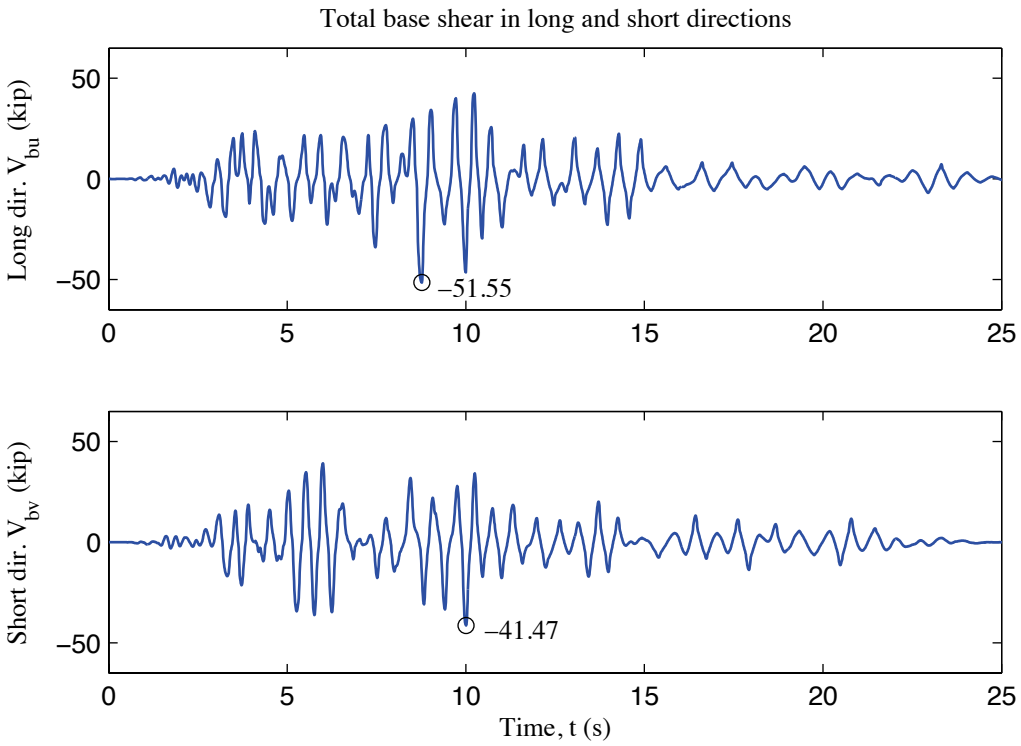

Figure K-9: A1-3D-SD-a model total building base shear, 100 % Canoga Park, 3D nonlinear analysis

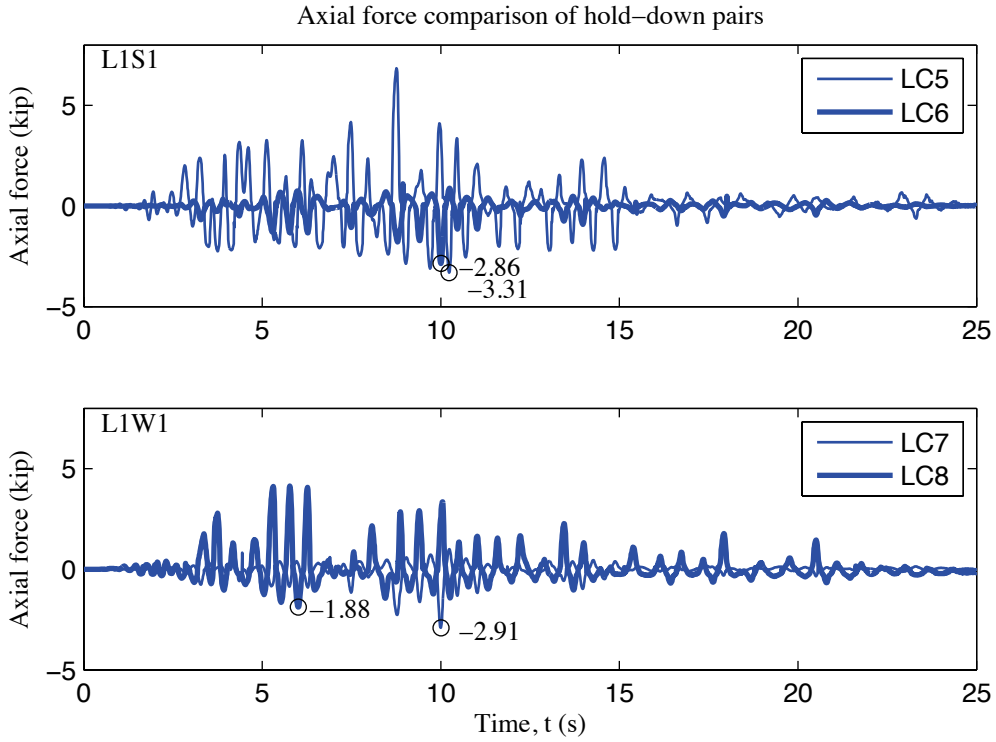

Figure K-10: A1-3D-SD-a model, load cell 5 to 8 axial forces, 100 % Canoga Park, 3D nonlinear analysis

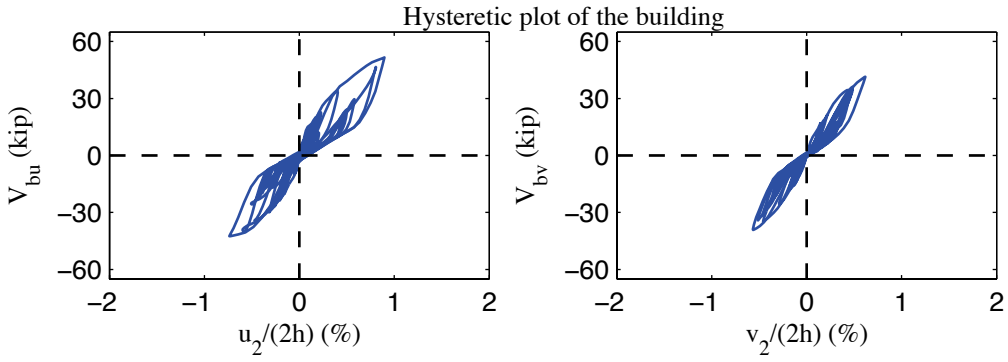

Figure K-11: A1-3D-SD-a model, hysteretic plot of the building, 100 % Canoga Park, 3D nonlinear analysis

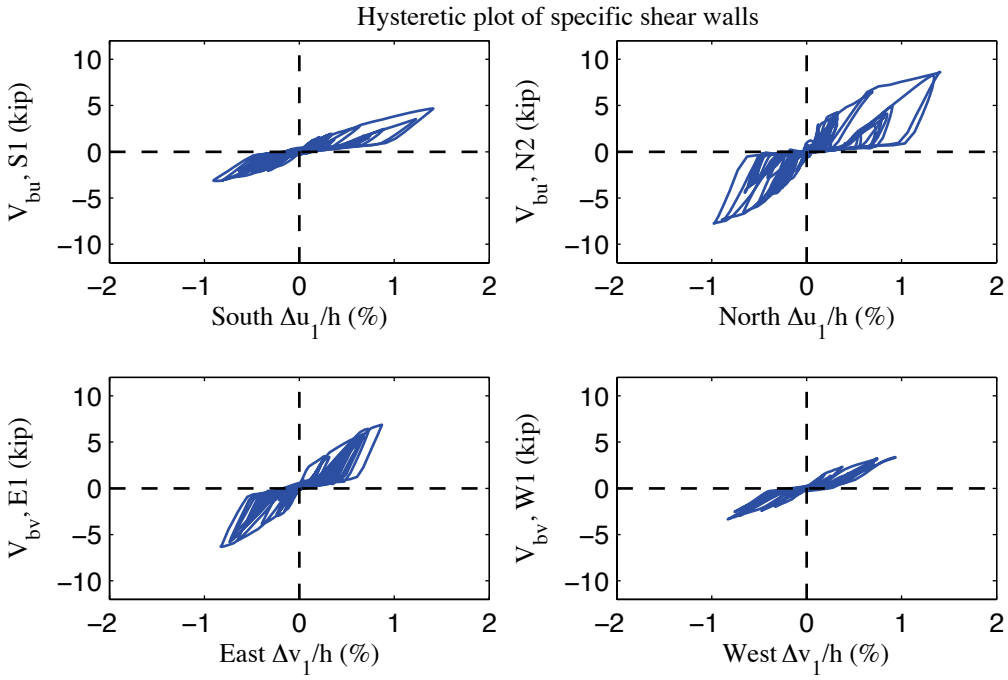

Figure K-12: A1-3D-SD-a model, hysteretic plot of shear walls at each elevation, 100 % Canoga Park, 3D nonlinear analysis

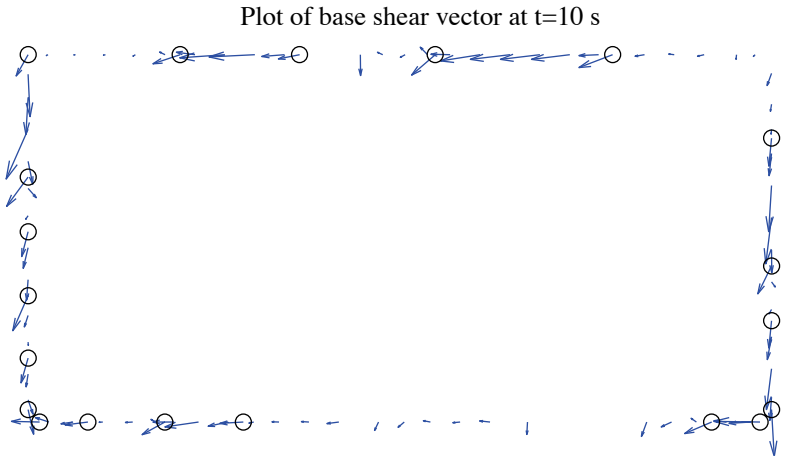

Figure K-13: A1-3D-SD-a model, field plot of peak total base shear, 100 % Canoga Park, 3D nonlinear analysis (maximum anchor/hold down base shear is 2.35 kips)

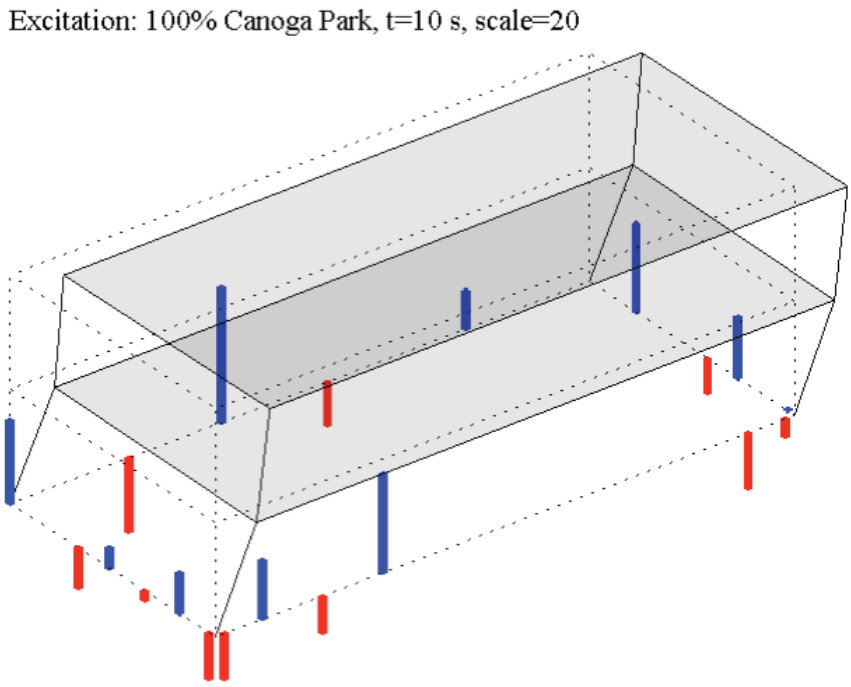

Figure K-14: A1-3D-SD-a model, simplified illustration of corner displacements with hold down forces from load cells,100 % Canoga Park, 3D nonlinear analysis (max hold down tensile force is -4.63 kips)

Appendix L: Analysis Results of State-of-the-art, Phase 1, 3D, semirigid-diaphragm, model b (A1-3D-SD-b)

L.1 Model description

This state-of-the-art 3D model features subpanel bracing models of shear walls, explicit models of hold downs, bare steel framing of gravity walls, and semi-rigid diaphragms modeled by subpanel bracings. Seismic mass is distributed to corners and stud ends. The lateral displacement and shear wall capacity ($\delta(0.4V_{nA})$, $0.4V_{nA}$) from test is utilized to determine the stiffness of elastic material and the first point on the backbone curve of Pinching4 material of shear wall bracing. Figure L-1 is the 3D drawing of the building model with all members and diagonal bracings of sheathing panels. Definitions of output physical quantities and explanation of post-process method can be found in Appendix K.

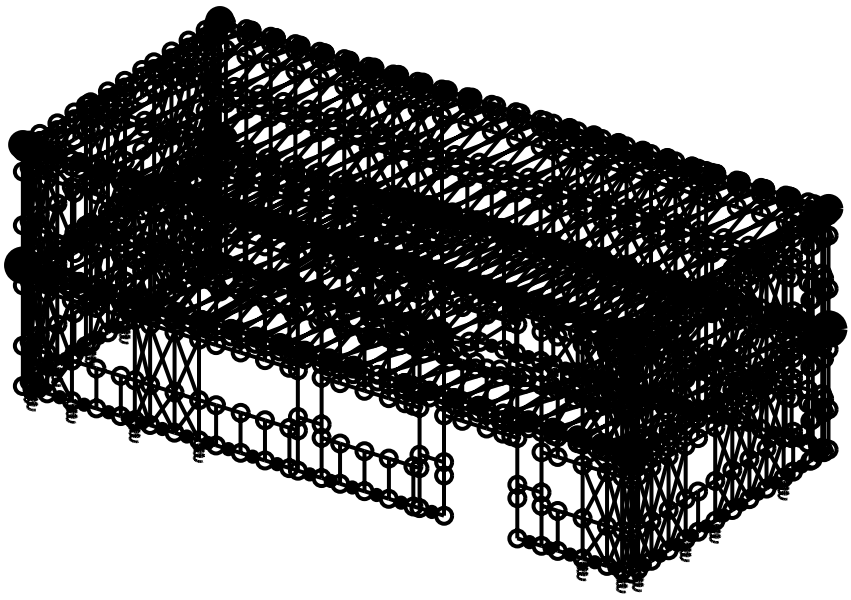

Figure L-1: A1-3D-SD-b model

L.2 Free vibration analysis results

Free vibration analysis results are presented in Table L-1 and Figure L-2. Lateral stiffness in the short direction is smaller than lateral stiffness in the long direction and torsional stiffness is the largest. The observation holds for the first and the second mode, as indicated by Table L-1.

Table L-1: Free vibration analysis results, A1-3D-SD-b model

Mode number	**Natural period (s)**	**Mode description**
1	0.367	Short, 1st
2	0.345	Long, 1st
3	0.267	Torsion, 1st
4	0.200	Short, 2nd
5	0.143	Long, 2nd
6	0.128	Torsion, 2nd

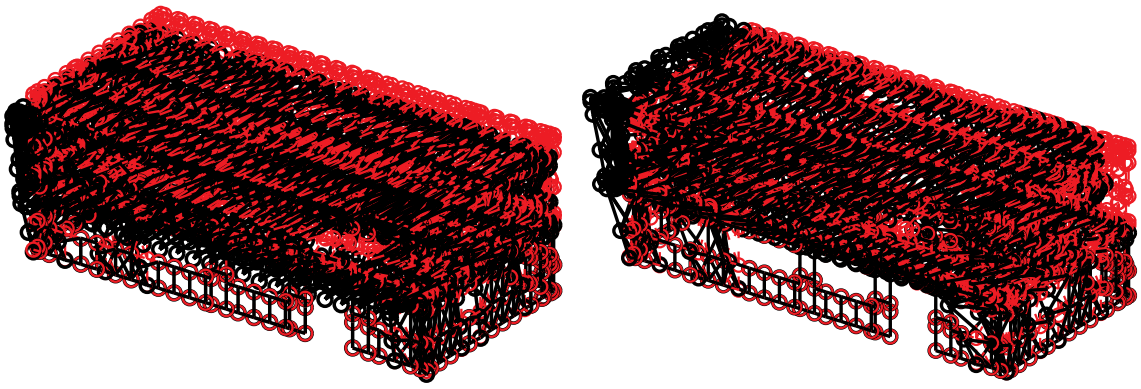

(a) Mode 1, T_1=0.367 s (b) Mode 2, T_2=0.345 s

Figure L-2: First two natural modes of A1-3D-SD-b model

L.3 Linear static analysis results

Table L-2 to Table L-4 present linear static analysis results. The lateral load is the equivalent lateral force available from the design narrative (Madsen et al. 2011), applied equally at four corners. Two separate analyses were performed with the loading at long or short direction.

Table L-2 summarizes the breakdown of peak total base shear among four elevations. Due to the interplay of asymmetrical LFRS, wall lines perpendicular to the loading direction still take a very small portion of base shear.

Table L-3 shows peak building and wall line deflections. Practicing engineers can linearly upscale these data and develop an estimate of the building's performance at a certain lateral force level.

Table L-4 is an evaluation of the building's lateral stiffness of long and short direction and its breakdown among shear walls (SW) and other systems. Interestingly, the bare CFS framing still accounts for 19% to 26% total lateral stiffness in this case.

Table L-2: Breakdown of peak base shear, linear static analysis, A1-3D-SD-b model

Load direction	**LONG**				
Elevation	**South V_b**	**North V_b**	**East V_b**	**West V_b**	**Peak V_b**
kips	3.6	7.0	0.1	0.4	11.1
%	32.2	63.2	1.3	3.2	100.0
Load direction	**SHORT**				
Elevation	**South V_b**	**North V_b**	**East V_b**	**West V_b**	**Peak V_b**
kips	0.5	0.8	4.9	4.8	11.1
%	4.7	7.3	44.6	43.4	100.0

Table L-3: Peak building and wall line deflection, linear static analysis, A1-3D-SD-b model

Load direction	**LONG**							
Deflection (in.)	u_1	u_2	v_1	v_2	Δu_1	Δu_2	Δv_1	Δv_2
Building	0.143	0.228	-0.002	-0.004	0.143	0.085	-0.002	-0.002
South	0.147	0.245	-0.003	-0.005	0.147	0.098	-0.003	-0.002
North	0.139	0.210	-0.001	-0.003	0.139	0.071	-0.001	-0.002
East	0.135	0.227	0.017	0.025	0.135	0.092	0.017	0.008
West	0.151	0.228	-0.020	-0.032	0.151	0.077	-0.020	-0.012
Load direction	**SHORT**							
Deflection (in.)	u_1	u_2	v_1	v_2	Δu_1	Δu_2	Δv_1	Δv_2
Building	0.003	0.006	0.148	0.236	0.003	0.003	0.148	0.089
South	-0.003	0.005	0.147	0.235	-0.003	0.003	0.147	0.088
North	0.003	0.009	0.148	0.237	0.003	0.008	0.148	0.089
East	0.003	0.006	0.141	0.219	0.003	0.003	0.141	0.077
West	0.003	0.006	0.154	0.254	0.003	0.005	0.154	0.100

Table L-4: Breakdown of lateral stiffness, A1-3D-SD-b model

LONG			**SHORT**		
Shear wall k_u (%)	**Gravity wall k_u (%)**	**k_u (kip/in)**	**Shear wall k_v (%)**	**Gravity wall k_v (%)**	**k_v (kip/in)**
81.4	18.6	50.0	73.2	26.8	46.6

L.4 Nonlinear static (pushover) analysis results

Table L-5 is created following the same logic with Table L-2, but the analysis type is nonlinear static (pushover). Pushover curves of the building and each wall line are presented Figure L-3 in and Figure L-4.

Clearly, the interaction between wall lines is much more significant when material and geometrical nonlinearity is included. These tables and figures indicate that the wall lines do not reach their peak capacity at exactly the same drift level and wall lines perpendicular to the load can take a nontrivial amount of base shear. Accordingly, total capacity of the building is larger than the sum of wall line capacities in the load direction. Furthermore, total capacity of the building in the short direction is larger than the long direction; however, total capacity of wall lines in the short direction is smaller compared with long direction wall lines.

Table L-5: Breakdown of peak base shear, pushover analysis, A1-3D-SD-b model

Load direction	**LONG**				
Elevation	**South V_b**	**North V_b**	**East V_b**	**West V_b**	**Peak V_b**
kips	24.1	24.0	5.7	7.7	52.5
%	46.0	45.6	10.8	14.7	100.0
Load direction	**SHORT**				
Elevation	**South V_b**	**North V_b**	**East V_b**	**West V_b**	**Peak V_b**
kips	10.4	10.0	20.7	23.2	57.7
%	18.0	17.2	35.9	40.2	100.0

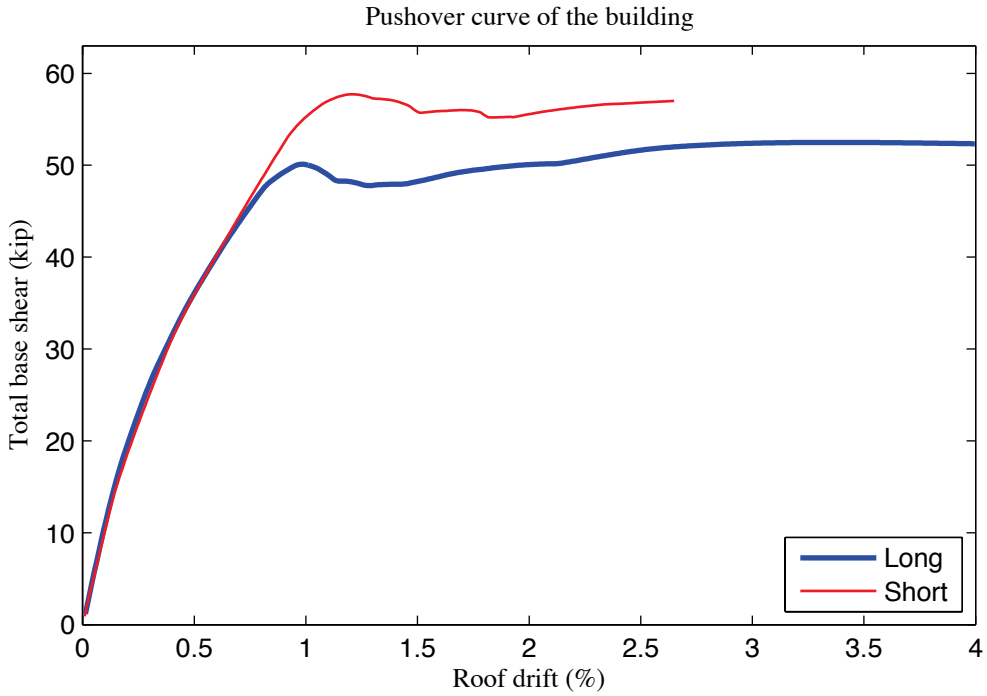

Figure L-3: Pushover curve of A1-3D-SD-b model

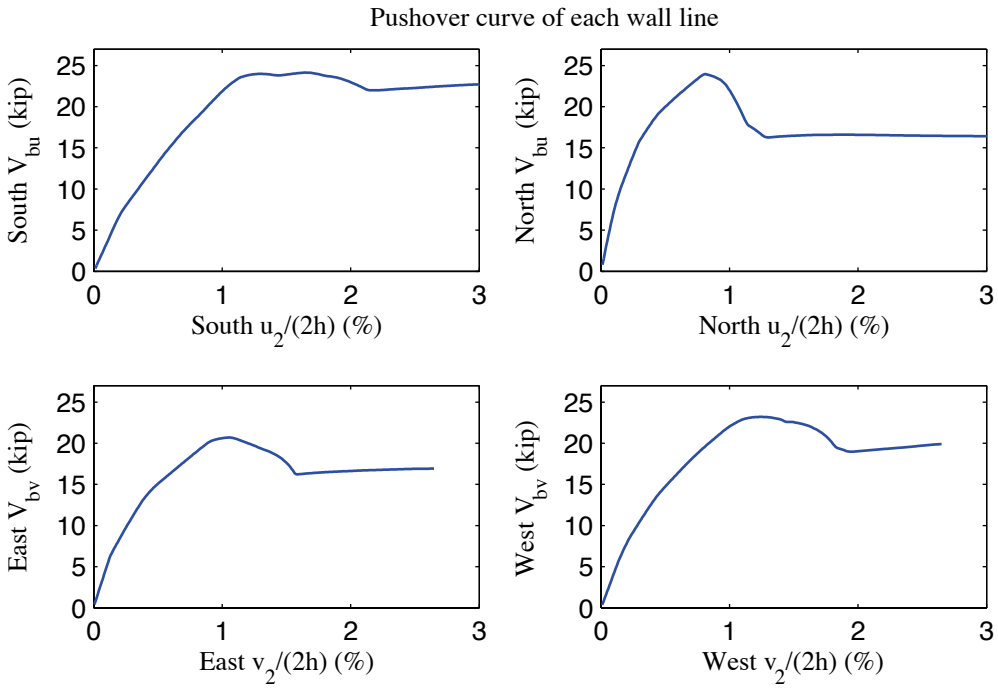

Figure L-4: Pushover curve of each wall line, A1-3D-SD-b model

L.5 Linear time history analysis results

Linear time history analysis is performed on the model under Canoga Park and Rinaldi ground motion records of Northridge earthquake in 1994. We considered three scale levels (16%, 44% and 100%) and loadings in one, two and three axes.

Table L-6 to Table L-9 demonstrate the building's linear elastic performance under designated ground motions. Table L-6 shows peak story relative accelerations in the unit of g. Table L-7 and Table L-8 report peak roof drift and story drift of the building and the corresponding time step (t_*) and the base shear at that time. Note that the base shear at the time of peak roof drift may not be the peak total building base shear in that direction (see Table L-9).

The building behaves linearly since peak drift and peak base shear appear at the same time when the ground motion is linearly scaled. Figure L-5 is a vector plot of the peak total resultant base shear of the building under three axial, 100% Canoga Park excitation. The directions of arrows imply that base shear taken by shear walls and gravity systems does not necessarily follow the direction of wall lines due to the effect of 3D coupling. Comparison with nonlinear analysis results of the same excitation provides insightful observations on the building's response and requirements on modeling fidelity and analysis type.

Table L-6: A1-3D-SD-b model peak story relative acceleration in g, linear time history analysis

		LONG			SHORT			UP		
Load Case	**Ground Motion**	**a_g**	**Floor a**	**Roof a**	**a_g**	**Floor a**	**Roof a**	**a_g**	**Floor a**	**Roof a**
EQ_3D_3axis_1	CNP 16%	0.067	0.162	0.218	0.057	0.115	0.177	0.078	0.064	0.080
EQ_3D_3axis_2	CNP 44%	0.185	0.444	0.599	0.157	0.316	0.480	0.215	0.249	0.233
EQ_3D_1axis_1	CNP 100%	0.420	1.007	1.375	0	0.189	0.286	0	0.199	0.191
EQ_3D_1axis_2	CNP 100%	0	0.148	0.215	0.356	0.619	0.927	0	0.537	0.473
EQ_3D_2axis_1	CNP 100%	0.420	0.991	1.357	0.356	0.711	1.065	0	0.543	0.525
EQ_3D_3axis_3	CNP 100%	0.420	0.995	1.361	0.356	0.710	1.057	0.489	0.644	0.588
EQ_3D_3axis_4	RRS 16%	0.132	0.254	0.336	0.078	0.198	0.314	0.133	0.143	0.141
EQ_3D_3axis_5	RRS 44%	0.363	0.737	0.962	0.214	0.531	0.861	0.367	0.454	0.403
EQ_3D_3axis_6	RRS 100%	0.825	1.738	2.256	0.486	1.202	1.943	0.834	1.436	1.310

Table L-7: A1-3D-SD-b model peak building roof drift and base shear, linear time history analysis

		LONG			SHORT		
Load Case	**Ground Motion**	**$u_2/(2h)$ (%)**	**t_* (s)**	**V_b @ t_* (kips)**	**$v_2/(2h)$ (%)**	**t_* (s)**	**V_b @ t_* (kips)**
EQ_3D_3axis_1	CNP 16%	-0.109	11.90	12.5	-0.098	10.53	10.5
EQ_3D_3axis_2	CNP 44%	-0.309	11.90	34.2	-0.266	10.53	28.5
EQ_3D_1axis_1	CNP 100%	-0.716	11.91	77.1	-0.147	12.55	16.2
EQ_3D_1axis_2	CNP 100%	0.105	11.28	10.8	-0.538	10.53	56.3
EQ_3D_2axis_1	CNP 100%	-0.715	11.91	77.4	-0.594	10.53	63.3
EQ_3D_3axis_3	CNP 100%	-0.718	11.91	77.7	-0.595	10.54	63.8
EQ_3D_3axis_4	RRS 16%	-0.173	4.56	19.0	0.182	3.39	18.9
EQ_3D_3axis_5	RRS 44%	-0.517	4.56	54.7	0.502	3.39	51.6
EQ_3D_3axis_6	RRS 100%	-1.233	4.57	129.6	1.144	3.39	117.1

Table L-8: A1-3D-SD-b model peak building story drift, linear time history analysis

		LONG				SHORT			
Load Case	**Ground Motion**	**$\Delta u_1/h$ (%)**	**t_* (s)**	**$\Delta u_2/h$ (%)**	**t_* (s)**	**$\Delta v_1/h$ (%)**	**t_* (s)**	**$\Delta v_2/h$ (%)**	**t_* (s)**
EQ_3D_3axis_1	CNP 16%	-0.158	11.90	0.061	11.73	-0.130	10.53	-0.065	10.52
EQ_3D_3axis_2	CNP 44%	-0.445	11.90	-0.174	11.90	-0.355	10.53	-0.178	10.53
EQ_3D_1axis_1	CNP 100%	-1.028	11.91	-0.404	11.91	0.196	12.38	-0.100	12.55
EQ_3D_1axis_2	CNP 100%	0.155	11.29	0.063	9.12	-0.715	10.53	-0.361	10.53
EQ_3D_2axis_1	CNP 100%	-1.019	11.91	-0.411	11.91	-0.794	10.54	-0.398	10.53
EQ_3D_3axis_3	CNP 100%	-1.024	11.91	-0.413	11.91	-0.795	10.54	-0.397	10.53
EQ_3D_3axis_4	RRS 16%	-0.253	4.56	0.104	4.73	0.240	3.39	0.124	3.39
EQ_3D_3axis_5	RRS 44%	-0.751	4.56	0.306	4.74	0.660	3.39	0.345	3.40
EQ_3D_3axis_6	RRS 100%	-1.780	4.57	0.727	4.74	1.504	3.39	0.791	3.40

Table L-9: A1-3D-SD-b model peak building base shear, linear time history analysis

		LONG		SHORT		RESULTANT	
Load Case	**Ground Motion**	**Peak V_{bu} (kip)**	**t @ peak V_{bu} (s)**	**Peak V_{bv} (kip)**	**t @ peak V_{bv} (s)**	**Peak V_b (kip)**	**t @ peak V_b (s)**
EQ_3D_3axis_1	CNP 16%	12.5	11.90	10.5	10.53	13.5	10.53
EQ_3D_3axis_2	CNP 44%	34.2	11.90	28.6	10.54	36.8	11.91
EQ_3D_1axis_1	CNP 100%	77.1	11.91	16.5	12.38	77.8	11.91
EQ_3D_1axis_2	CNP 100%	11.1	8.97	56.3	10.53	56.5	10.53
EQ_3D_2axis_1	CNP 100%	77.4	11.91	64.0	10.54	83.4	11.92
EQ_3D_3axis_3	CNP 100%	77.7	11.91	63.8	10.54	83.2	11.92
EQ_3D_3axis_4	RRS 16%	19.0	4.56	18.9	3.39	23.6	4.56
EQ_3D_3axis_5	RRS 44%	54.9	4.39	51.6	3.39	68.0	4.56
EQ_3D_3axis_6	RRS 100%	129.6	4.57	117.1	3.39	158.6	4.56

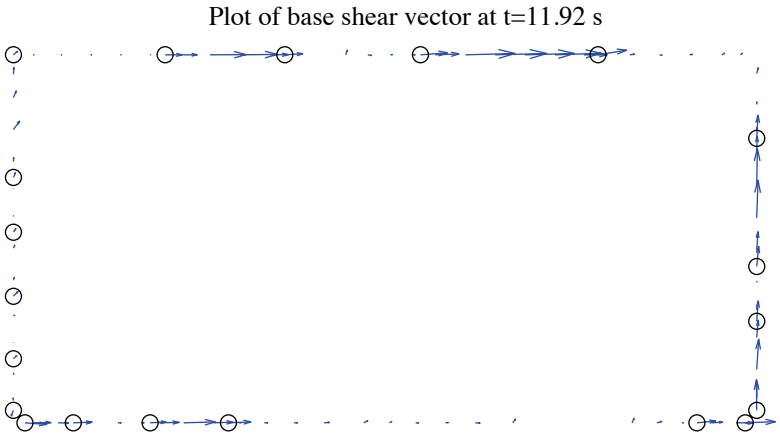

Figure L-5: A1-3D-SD-b model, base shear vector plot at the moment of peak total base shear, 100 % Canoga Park, 3D linear analysis (maximum anchor/hold down base shear is 4.83 kips)

L.6 Nonlinear time history analysis results

Same ground motions are applied to the model with material and geometrical nonlinearity. Table L-10 to Table L-13 are replicas of Table L-6 to Table L-9, but for nonlinear time history analyses. Since this analysis type is most complicated and closest to reality and experiments, behavior of wall lines and hold downs are further studied. Table L-14 is the table of peak wall line story drifts and corresponding time steps. Table L-15 is designed for peak base shear of each wall line and the last two columns of the table are percentages of base shear of two facing wall lines in the same direction when the total base shear in that direction takes peak value. Table L-16 expands the breakdown of each wall line's peak base shear between shear walls, gravity walls and other systems. Table L-17 is peak value of hold down tensile force of two selected pairs. Hold down 5 and 6 are on shear wall L1S1, South elevation and hold down 7 and 8 are on shear wall L1W1, West elevation. These shear walls have lowest capacities compared with others on the same wall line and they meet at the southwest edge of the building, so interacted nonlinear behavior is expected to appear.

Time history plots in this section include plots of story drifts of the building and each wall line (Figure L-6 to Figure L-8), total building base shear in long and short direction (Figure L-9) and axial forces of hold downs in Table L-17 (Figure L-10). Hysteretic plots in Figure L-11 and Figure L-12 are helpful for visual examination of nonlinear base shear-drift relationship of the building and the weakest shear wall on each wall line. In comparison with linear time history analysis, vector plot of peak total base shear is illustrated in Figure L-13. Figure L-14 presents a simplified deformed shape of the

building (see (Peterman 2014) for details of the method) and axial force of all twenty hold downs at the moment of peak total base shear. The same sign convention with tests is adopted. Red bars indicate tensile (negative) force and blue ones are for compressive (positive) force.

Hysteretic behavior is seen in the building and typical shear walls under design-based earthquake (100% Canoga Park excitation in 3 axes, see Figure L-11 and Figure L-12). Results also imply that when loaded by 100% Canoga Park ground motion, South and However, the backbones of response curves do not reach the post-peak range. Peak story drifts are not greater than 1.6% (Table L-12), and larger deflection is seen in the long direction. Peak wall line drifts are smaller than 1.7% (Table L-14), with the maximum found in North elevation. Figure L-13 clearly shows that base shear vectors in anchors and hold downs do not align with wall lines and they can change directions even within a single piece of wall, a sign of localized behavior. Table L-17, Figure L-10 and Figure L-14 demonstrate that hold downs in a pair do not experience the same amount of force with opposite signs, an evidence that supports Type II shear wall behavior despite Type I design assumption.

The near-field Rinaldi record is much stronger in terms of peak ground acceleration, especially in the long direction. When loaded at 100%, the long direction is believed to be destroyed with peak story drift larger than 7%. Table L-16 reveals that as nonlinearity increases, the portion of base shear taken by gravity wall and other system grows

significantly, from 3.6% to 7.0% on West elevation at minimum and from 14.7% to 24.6% on South elevation at maximum.

Table L-10: A1-3D-SD-b model peak story relative acceleration in g, nonlinear time history analysis

		LONG			SHORT			UP		
Load Case	**Ground Motion**	**a_g**	**Floor a**	**Roof a**	**a_g**	**Floor a**	**Roof a**	**a_g**	**Floor a**	**Roof a**
EQ_3D_3axis_1	CNP 16%	0.067	0.148	0.192	0.057	0.131	0.187	0.078	0.044	0.043
EQ_3D_3axis_2	CNP 44%	0.185	0.357	0.390	0.157	0.255	0.338	0.215	0.106	0.099
EQ_3D_1axis_1	CNP 100%	0.420	0.667	1.265	0	0.081	0.078	0	0.244	0.229
EQ_3D_1axis_2	CNP 100%	0	0.160	0.117	0.356	0.911	1.040	0	1.447	1.294
EQ_3D_2axis_1	CNP 100%	0.420	0.639	1.270	0.356	0.585	0.765	0	0.293	0.269
EQ_3D_3axis_3	CNP 100%	0.420	0.639	1.269	0.356	0.597	0.759	0.489	0.294	0.299
EQ_3D_3axis_4	RRS 16%	0.132	0.242	0.274	0.078	0.206	0.291	0.133	0.138	0.117
EQ_3D_3axis_5	RRS 44%	0.363	0.743	0.891	0.214	0.603	0.742	0.367	0.940	0.734
EQ_3D_3axis_6	RRS 100%	0.825	10.990	15.237	0.486	3.301	4.479	0.834	10.841	10.226

Table L-11: A1-3D-SD-b model peak building roof drift and base shear, nonlinear time history analysis

		LONG			SHORT		
Load Case	**Ground Motion**	**$u_2/(2h)$ (%)**	**t_* (s)**	**V_b @ t_* (kips)**	**$v_2/(2h)$ (%)**	**t_* (s)**	**V_b @ t_* (kips)**
EQ_3D_3axis_1	CNP 16%	0.103	8.72	11.8	-0.098	10.53	10.5
EQ_3D_3axis_2	CNP 44%	0.249	8.73	23.9	-0.193	10.56	18.5
EQ_3D_1axis_1	CNP 100%	1.002	8.77	51.0	-0.031	4.78	3.3
EQ_3D_1axis_2	CNP 100%	0.052	10.30	3.6	-0.678	6.01	43.7
EQ_3D_2axis_1	CNP 100%	1.010	8.78	51.1	0.637	10.01	41.8
EQ_3D_3axis_3	CNP 100%	1.010	8.78	51.0	0.643	10.01	41.9
EQ_3D_3axis_4	RRS 16%	0.158	4.40	17.5	0.162	3.39	16.2
EQ_3D_3axis_5	RRS 44%	0.576	2.67	42.3	0.423	3.91	32.1
EQ_3D_3axis_6	RRS 100%	3.977	2.90	52.3	-0.840	2.58	49.7

Table L-12: A1-3D-SD-b model peak building story drift, nonlinear linear time history analysis

		LONG				SHORT			
Load Case	**Ground Motion**	**$\Delta u_1/h$ (%)**	**t_* (s)**	**$\Delta u_2/h$ (%)**	**t_* (s)**	**$\Delta v_1/h$ (%)**	**t_* (s)**	**$\Delta v_2/h$ (%)**	**t_* (s)**
EQ_3D_3 axis_1	CNP 16%	0.151	8.71	0.056	8.72	-0.131	10.53	-0.066	10.52
EQ_3D_3 axis_2	CNP 44%	0.376	8.73	-0.127	10.56	-0.276	10.56	-0.112	10.55
EQ_3D_1 axis_1	CNP 100%	1.577	8.78	-0.543	10.24	-0.043	4.42	0.026	7.79
EQ_3D_1 axis_2	CNP 100%	0.080	10.30	0.034	4.30	-0.980	6.00	-0.391	6.02
EQ_3D_2 axis_1	CNP 100%	1.607	8.78	-0.536	10.25	0.921	10.00	0.353	10.01
EQ_3D_3 axis_3	CNP 100%	1.606	8.78	-0.537	10.25	0.929	10.01	0.356	10.01
EQ_3D_3 axis_4	RRS 16%	0.246	4.40	0.078	4.76	0.220	3.39	0.105	3.40
EQ_3D_3 axis_5	RRS 44%	0.910	2.67	0.278	4.18	0.611	3.90	0.244	3.92
EQ_3D_3 axis_6	RRS 100%	7.461	2.90	0.681	2.79	-1.252	2.58	-0.429	2.59

Table L-13: A1-3D-SD-b model peak building base shear, nonlinear time history analysis

		LONG		SHORT		RESULTANT	
Load Case	**Ground Motion**	**Peak V_{bu} (kip)**	**t @ peak V_{bu} (s)**	**Peak V_{bv} (kip)**	**t @ peak V_{bv} (s)**	**Peak V_b (kip)**	**t @ peak V_b (s)**
EQ_3D_3axis_1	CNP 16%	11.8	8.72	10.5	10.53	13.9	10.53
EQ_3D_3axis_2	CNP 44%	24.0	8.74	18.5	10.56	29.2	10.54
EQ_3D_1axis_1	CNP 100%	51.9	8.75	3.5	4.61	51.9	8.75
EQ_3D_1axis_2	CNP 100%	5.9	4.65	44.0	10.00	44.0	10.00
EQ_3D_2axis_1	CNP 100%	51.3	8.74	42.2	10.00	63.2	10.00
EQ_3D_3axis_3	CNP 100%	51.3	8.74	42.2	10.00	63.1	10.00
EQ_3D_3axis_4	RRS 16%	17.5	4.40	16.2	3.39	22.5	4.40
EQ_3D_3axis_5	RRS 44%	42.3	2.67	32.3	3.90	42.6	3.92
EQ_3D_3axis_6	RRS 100%	64.3	2.64	96.3	3.64	98.5	3.64

Table L-14: A1-3D-SD-b model peak wall line story drift, nonlinear time history analysis

LONG		SOUTH				NORTH			
Load Case	**Ground Motion**	**$\Delta u_1/h$ (%)**	**t_* (s)**	**$\Delta u_2/h$ (%)**	**t_* (s)**	**$\Delta u_1/h$ (%)**	**t_* (s)**	**$\Delta u_2/h$ (%)**	**t_* (s)**
EQ_3D_3axis_1	CNP 16%	0.151	8.73	0.084	8.71	0.205	8.70	0.069	8.70
EQ_3D_3axis_2	CNP 44%	0.374	8.74	0.182	10.56	0.467	8.72	0.154	8.72
EQ_3D_1axis_1	CNP 100%	1.546	8.77	0.623	10.24	1.703	8.77	0.550	10.24
EQ_3D_1axis_2	CNP 100%	0.133	10.28	0.085	6.06	0.098	4.53	0.064	8.46
EQ_3D_2axis_1	CNP 100%	1.616	8.78	0.581	10.24	1.720	8.76	0.584	10.25
EQ_3D_3axis_3	CNP 100%	1.613	8.78	0.580	10.24	1.721	8.76	0.587	10.25
EQ_3D_3axis_4	RRS 16%	0.266	4.58	0.131	4.58	0.302	4.39	0.092	2.63
EQ_3D_3axis_5	RRS 44%	0.916	2.67	0.379	4.18	0.998	2.66	0.298	2.68
EQ_3D_3axis_6	RRS 100%	7.305	2.90	0.767	2.81	7.775	2.89	0.811	2.75
SHORT		**EAST**				**WEST**			
Load Case	**Ground Motion**	**$\Delta v_1/h$ (%)**	**t_* (s)**	**$\Delta v_2/h$ (%)**	**t_* (s)**	**$\Delta v_1/h$ (%)**	**t_* (s)**	**$\Delta v_2/h$ (%)**	**t_* (s)**
EQ_3D_3axis_1	CNP 16%	0.174	10.53	0.090	10.52	0.149	9.98	0.082	9.98
EQ_3D_3axis_2	CNP 44%	0.343	10.56	0.155	10.57	0.243	10.00	0.137	9.99
EQ_3D_1axis_1	CNP 100%	0.107	6.63	0.062	10.25	0.112	8.89	0.075	8.75
EQ_3D_1axis_2	CNP 100%	0.860	10.00	0.311	9.99	1.131	6.00	0.473	6.02
EQ_3D_2axis_1	CNP 100%	0.872	6.00	0.345	9.99	1.015	10.01	0.406	6.02
EQ_3D_3axis_3	CNP 100%	0.871	6.00	0.346	9.99	1.031	10.01	0.412	6.02
EQ_3D_3axis_4	RRS 16%	0.179	3.19	0.092	3.20	0.312	4.59	0.152	4.59
EQ_3D_3axis_5	RRS 44%	0.476	4.09	0.204	6.10	0.763	3.90	0.308	3.93
EQ_3D_3axis_6	RRS 100%	1.085	2.58	0.362	4.11	1.454	2.60	0.551	2.60

Table L-15: A1-3D-SD-b model peak wall line base shear, nonlinear time history analysis

LONG		SOUTH		NORTH		% of Peak V_{bu}	
Load Case	**Ground Motion**	**Peak V_{bu} (kips)**	**t @ peak V_{bu} (s)**	**Peak V_{bu} (kips)**	**t @ peak V_{bu} (s)**	**South**	**North**
EQ_3D_3axis_1	CNP 16%	4.2	8.73	7.0	8.71	35.7	59.4
EQ_3D_3axis_2	CNP 44%	8.9	8.74	13.7	8.73	37.1	56.6
EQ_3D_1axis_1	CNP 100%	23.0	8.77	24.2	8.72	43.8	43.6
EQ_3D_1axis_2	CNP 100%	3.5	10.50	4.4	4.65	20.2	74.4
EQ_3D_2axis_1	CNP 100%	23.6	8.78	24.2	10.24	43.5	44.0
EQ_3D_3axis_3	CNP 100%	23.6	8.78	24.3	10.24	43.5	44.0
EQ_3D_3axis_4	RRS 16%	7.1	4.59	9.7	2.63	39.3	54.9
EQ_3D_3axis_5	RRS 44%	16.8	2.67	21.4	2.67	39.9	50.7
EQ_3D_3axis_6	RRS 100%	28.0	2.64	24.3	2.60	43.5	34.3
SHORT		**EAST**		**WEST**		**% of Peak V_{bv}**	
Load Case	**Ground Motion**	**Peak V_{bv} (kips)**	**t @ peak V_{bv} (s)**	**Peak V_{bv} (kips)**	**t @ peak V_{bv} (s)**	**East**	**West**
EQ_3D_3axis_1	CNP 16%	6.3	10.53	5.1	9.98	59.6	29.8
EQ_3D_3axis_2	CNP 44%	9.7	10.56	7.7	10.00	52.3	35.1
EQ_3D_1axis_1	CNP 100%	4.1	6.63	3.8	8.89	36.6	53.8
EQ_3D_1axis_2	CNP 100%	16.3	10.00	19.8	6.00	37.1	44.3
EQ_3D_2axis_1	CNP 100%	16.6	6.00	18.5	10.01	38.7	43.5
EQ_3D_3axis_3	CNP 100%	16.6	6.00	18.7	10.01	38.7	43.9
EQ_3D_3axis_4	RRS 16%	6.4	3.18	9.2	4.59	36.5	52.7
EQ_3D_3axis_5	RRS 44%	11.8	4.09	16.0	3.90	34.8	49.7
EQ_3D_3axis_6	RRS 100%	18.2	2.57	23.5	2.58	1.6	1.3

Table L-16: A1-3D-SD-b model wall line base shear breakdown, nonlinear time history analysis

LONG		SOUTH			NORTH		
Load Case	**Ground Motion**	**Peak V_{bu} (kips)**	**SW V_{bu} (%)**	**GW V_{bu} (%)**	**Peak V_{bu} (kips)**	**SW V_{bu} (%)**	**GW V_{bu} (%)**
EQ_3D_3axis_1	CNP 16%	4.2	85.3	14.7	7.0	94.8	5.2
EQ_3D_3axis_2	CNP 44%	8.9	82.8	17.2	13.7	92.5	7.5
EQ_3D_1axis_1	CNP 100%	23.0	75.4	24.6	24.2	87.8	12.2
EQ_3D_1axis_2	CNP 100%	3.5	83.8	16.2	4.4	95.2	4.8
EQ_3D_2axis_1	CNP 100%	23.6	75.4	24.6	24.2	86.7	13.3
EQ_3D_3axis_3	CNP 100%	23.6	75.4	24.6	24.3	86.6	13.4
EQ_3D_3axis_4	RRS 16%	7.1	84.0	16.0	9.7	94.2	5.8
EQ_3D_3axis_5	RRS 44%	16.8	77.9	22.1	21.4	89.6	10.4
EQ_3D_3axis_6	RRS 100%	28.0	75.6	24.4	24.3	88.7	11.3
SHORT		**EAST**			**WEST**		
Load Case	**Ground Motion**	**Peak V_{bv} (kips)**	**SW V_{bv} (%)**	**GW V_{bu} (%)**	**Peak V_{bv} (kips)**	**SW V_{bv} (%)**	**GW V_{bv} (%)**
EQ_3D_3axis_1	CNP 16%	6.3	93.8	6.2	5.1	96.4	3.6
EQ_3D_3axis_2	CNP 44%	9.7	92.3	7.7	7.7	96.0	4.0
EQ_3D_1axis_1	CNP 100%	4.1	94.1	5.9	3.8	96.3	3.7
EQ_3D_1axis_2	CNP 100%	16.3	90.6	9.4	19.8	94.1	5.9
EQ_3D_2axis_1	CNP 100%	16.6	89.0	11.0	18.5	93.0	7.0
EQ_3D_3axis_3	CNP 100%	16.6	89.0	11.0	18.7	93.0	7.0
EQ_3D_3axis_4	RRS 16%	6.4	93.8	6.2	9.2	95.9	4.1
EQ_3D_3axis_5	RRS 44%	11.8	91.0	9.0	16.0	94.3	5.7
EQ_3D_3axis_6	RRS 100%	18.2	87.7	12.3	23.5	94.2	5.8

Table L-17: A1-3D-SD-b model peak hold down tensile force at certain locations, nonlinear time history analysis

		L1S1, LC5		L1S1, LC6		L1W1, LC7		L1W1, LC8	
Load Case	**Ground Motion**	**Peak F (kips)**	**t @ peak F (s)**	**Peak F (kips)**	**t @ peak F (s)**	**Peak F (kips)**	**t @ peak F (s)**	**Peak F (kips)**	**t @ peak F (s)**
EQ_3D_3axis_1	CNP 16%	-1.58	11.89	-0.18	9.99	-0.17	10.70	-0.44	10.16
EQ_3D_3axis_2	CNP 44%	-2.28	9.67	-0.64	10.36	-0.70	10.36	-0.75	3.91
EQ_3D_1axis_1	CNP 100%	-3.63	10.24	-1.12	9.99	-2.04	8.77	-1.03	8.75
EQ_3D_1axis_2	CNP 100%	-2.20	6.26	-1.80	10.01	-0.95	10.01	-2.27	6.01
EQ_3D_2axis_1	CNP 100%	-3.47	10.24	-3.15	10.00	-3.26	10.00	-1.99	6.00
EQ_3D_3axis_3	CNP 100%	-3.47	10.24	-3.17	10.00	-3.27	10.00	-2.01	6.01
EQ_3D_3axis_4	RRS 16%	-2.17	4.59	-0.35	3.39	-0.26	2.65	-0.99	4.77
EQ_3D_3axis_5	RRS 44%	-2.85	3.94	-0.94	2.70	-1.45	2.69	-1.60	4.13
EQ_3D_3axis_6	RRS 100%	-3.62	2.39	-1.69	6.10	-2.52	5.34	-2.82	2.60

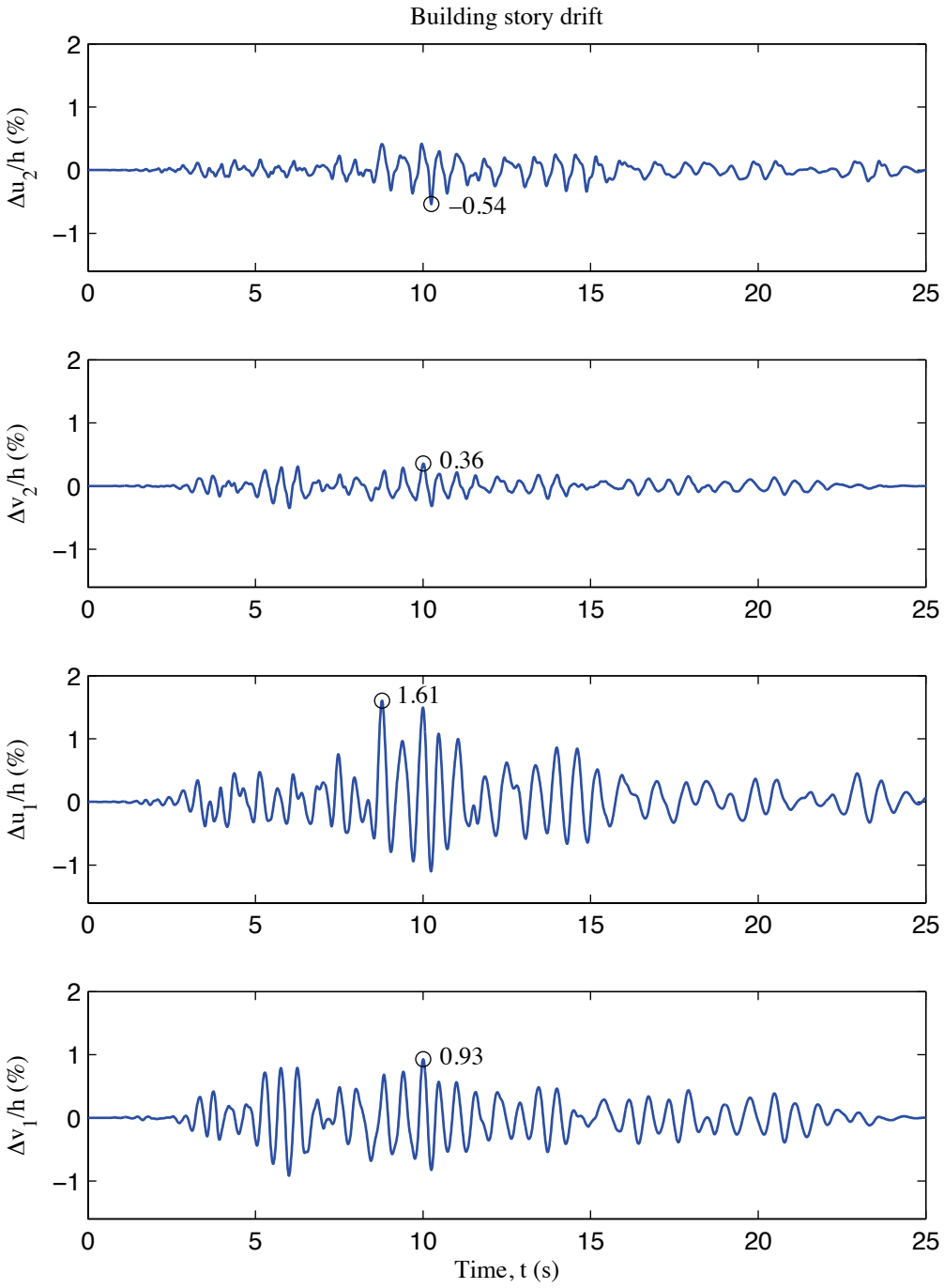

Figure L-6: A1-3D-SD-b model building story drift, 100 % Canoga Park, 3D nonlinear analysis

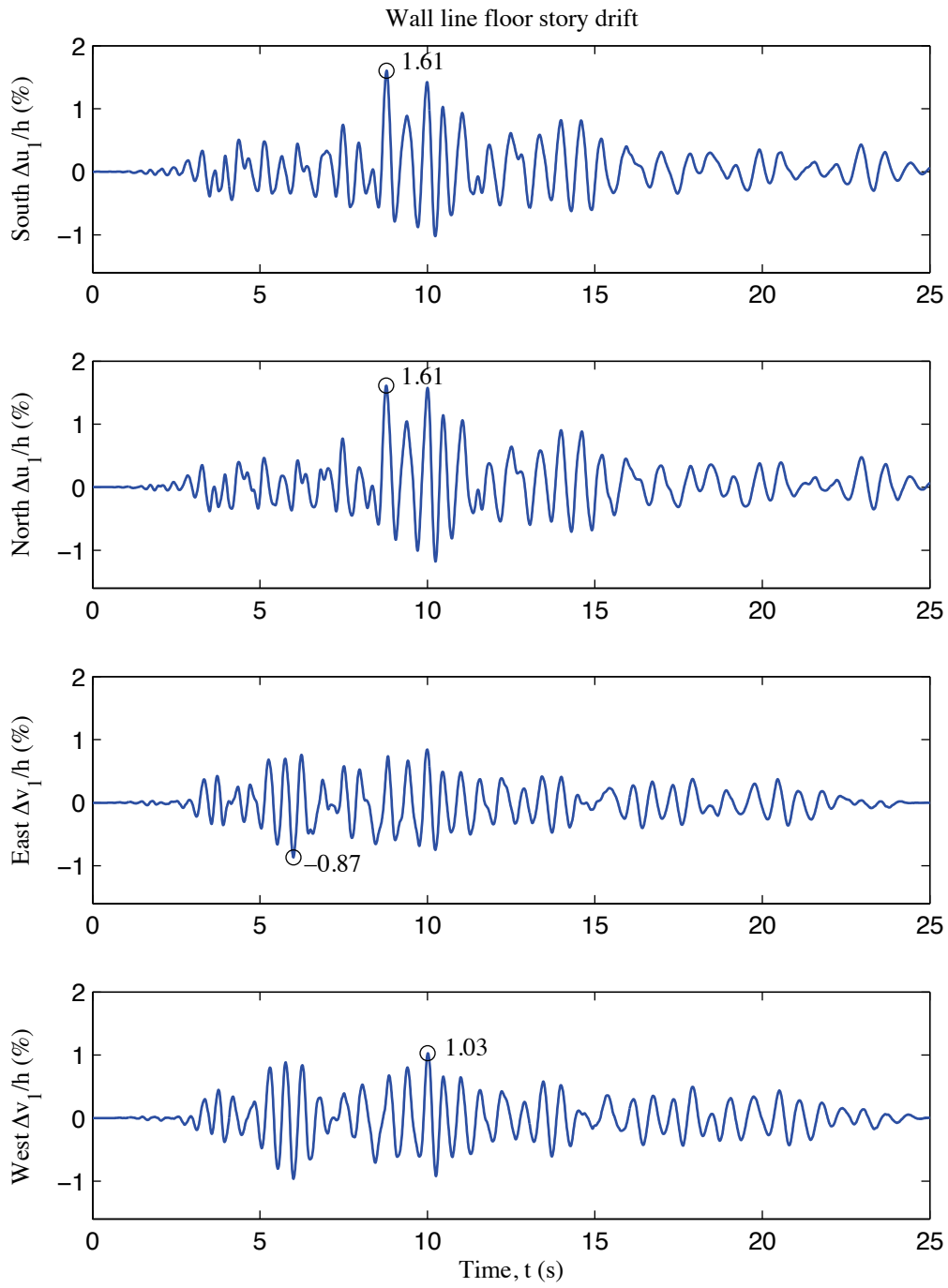

Figure L-7: A1-3D-SD-b model wall line floor story drift, 100 % Canoga Park, 3D nonlinear analysis

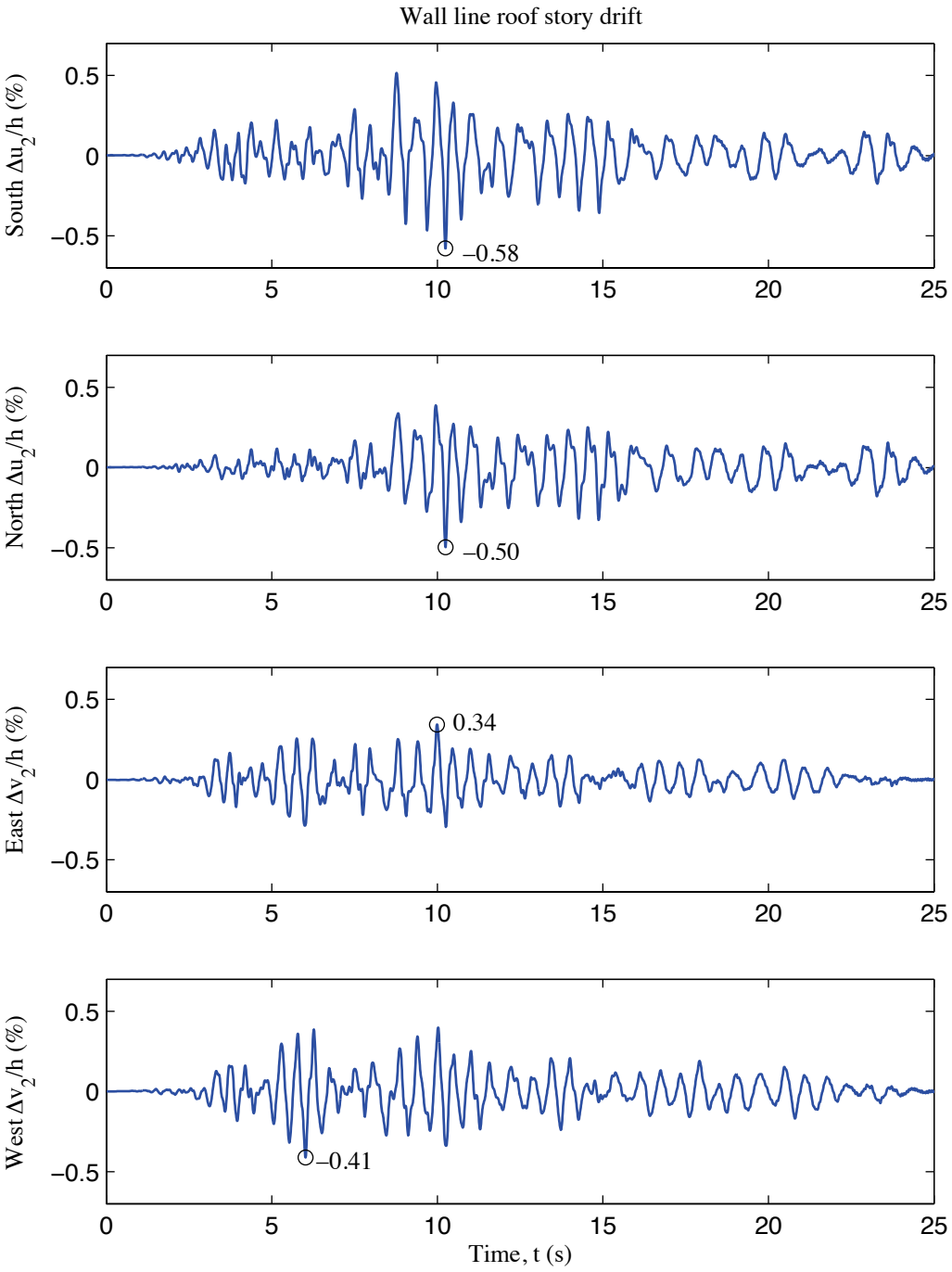

Figure L-8: A1-3D-SD-b model wall line roof story drift, 100 % Canoga Park, 3D nonlinear analysis

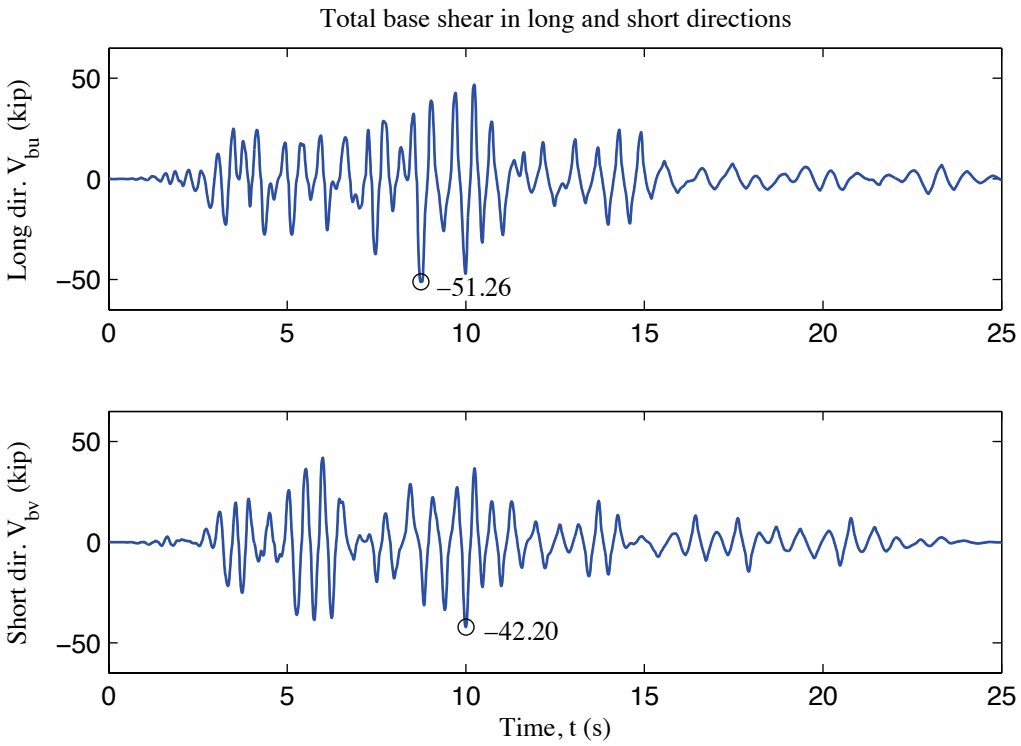

Figure L-9: A1-3D-SD-b model total building base shear, 100 % Canoga Park, 3D nonlinear analysis

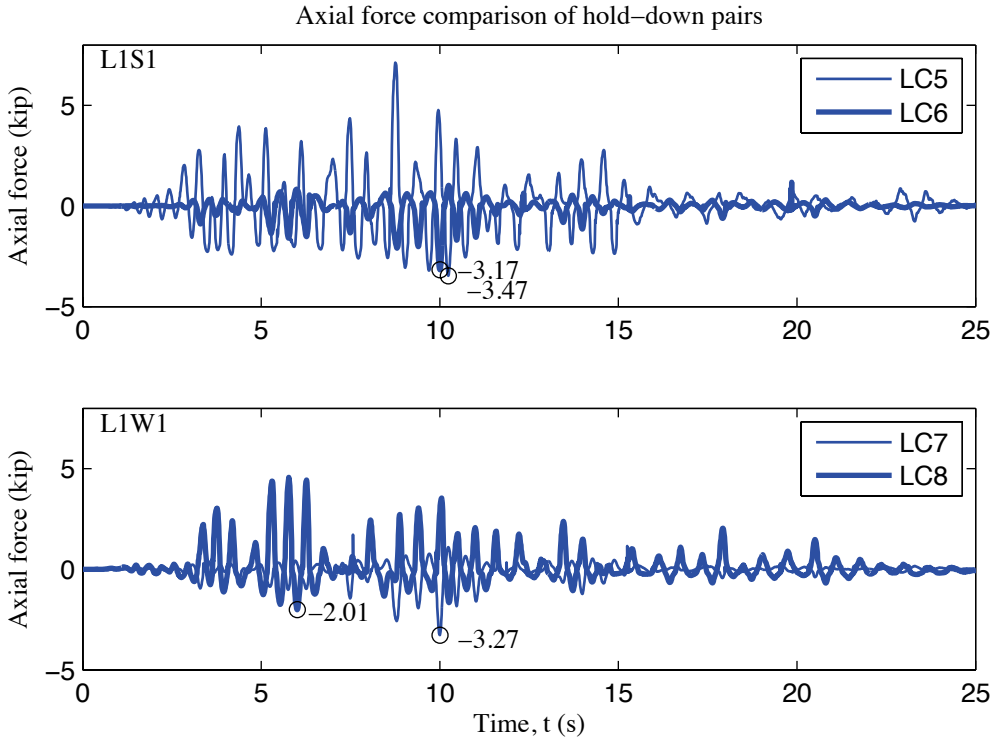

Figure L-10: A1-3D-SD-b model, load cell 5 to 8 axial forces, 100 % Canoga Park, 3D nonlinear analysis

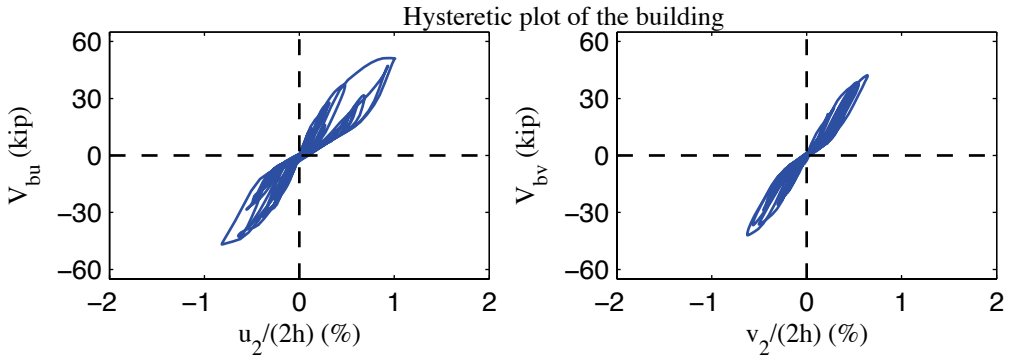

Figure L-11: A1-3D-SD-b model, hysteretic plot of the building, 100 % Canoga Park, 3D nonlinear analysis

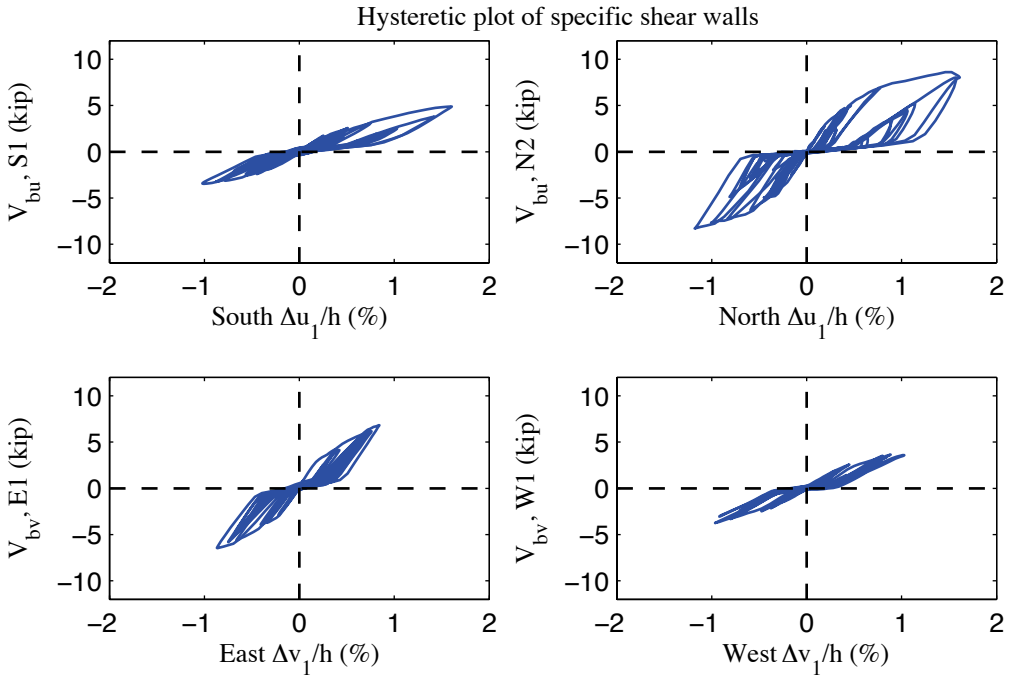

Figure L-12: A1-3D-SD-b model, hysteretic plot of shear walls at each elevation, 100 % Canoga Park, 3D nonlinear analysis

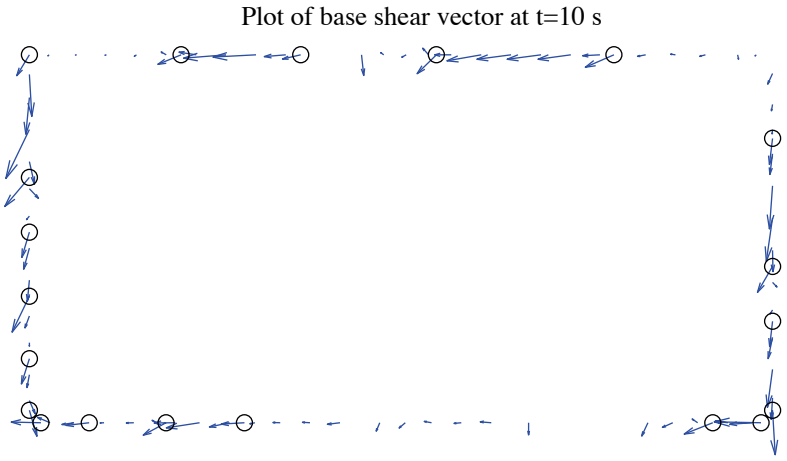

Figure L-13: A1-3D-SD-b model, field plot of peak total base shear, 100 % Canoga Park, 3D nonlinear analysis (maximum anchor/hold down base shear is 2.49 kips)

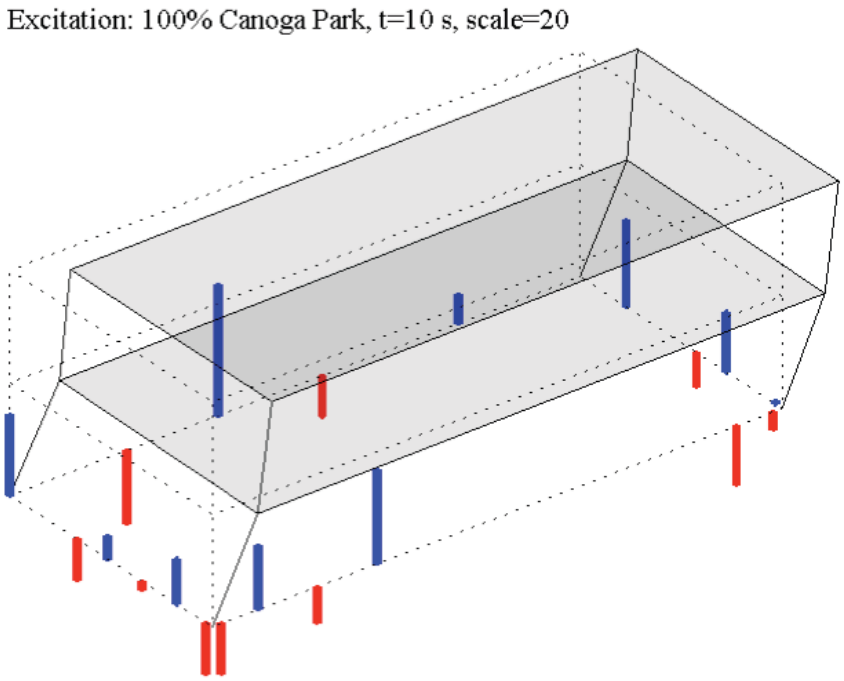

Figure L-14: A1-3D-SD-b model, simplified illustration of corner displacements with hold down forces from load cells,100 % Canoga Park, 3D nonlinear analysis (max hold down tensile force is -4.67 kips)

Appendix M: Analysis Results of State-of-the-art, Phase 2b, 2D, model a (A2b-2D-a)

M.1 Model description

This state-of-the-art 2D model features subpanel bracing models of shear walls and gravity walls, explicit models of hold downs, and rigid leaning columns. All walls are covered by OSB sheathing. Interplay between different elevations is not allowed in 2D models, representing the effect of flexible diaphragms. Seismic mass is lumped at leaning column nodes. The lateral displacement and shear wall capacity ($\delta(0.2V_{nA})$, $0.2V_{nA}$) from test is utilized to determine the stiffness of elastic material and the first point on the backbone curve of Pinching4 material of shear wall bracing. Figure M-1 (a) to (d) illustrate OpenSees models of South, North, East and West elevations. Simulation results are presented and discussed in later sections. Definitions of output physical quantities and explanation of post-process method can be found in Appendix E.

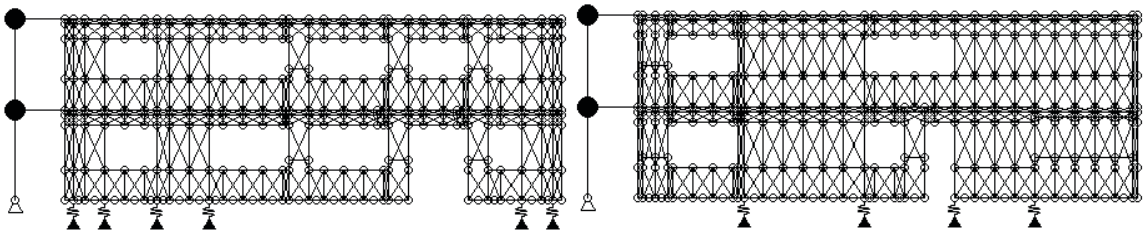

(a) South

(b) North

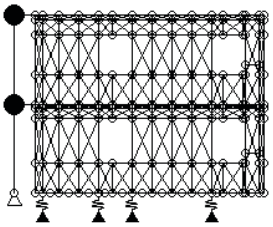

(c) East

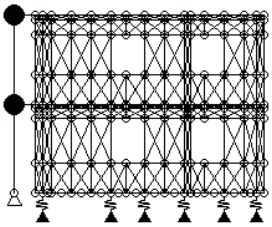

(d) West

Figure M-1: A2b-2D-a model

M.2 Free vibration analysis results

Free vibration analysis is performed for each elevation model. Values of first two natural periods are tabulated (Table M-1). Figure M-2 shows corresponding mode shapes.

Table M-1: Free vibration analysis results, A2b-2D-a model

Elevation	1st natural period (s)	2nd natural period (s)
South	0.287	0.128
North	0.201	0.102
East	0.303	0.121
West	0.317	0.128

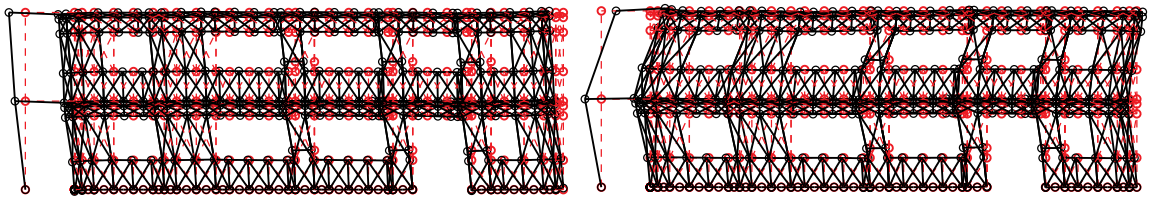

(a) South, mode 1, T_1=0.287 s (b) South, mode 2, T_2=0.128 s

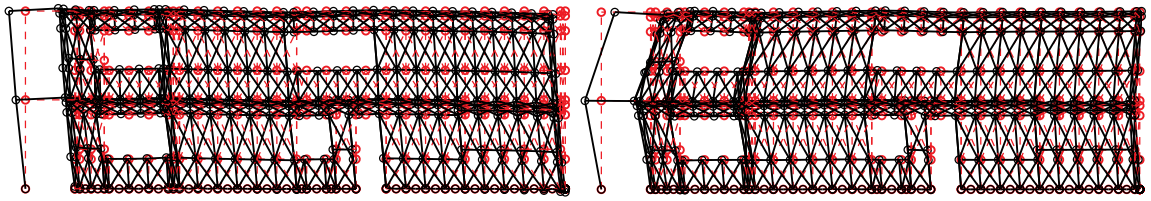

(c) North mode 1, T_1=0.201 s (d) North mode 2, T_2=0.102 s

(e) East mode 1, T_1=0.303 s (f) East mode 2, T_2=0.121 s

(g) West mode 1, T_1=0.317 s (h) West mode 2, T_2=0.128 s

Figure M-2: First two natural modes of A2b-2D-a model

M.3 Linear static analysis results

Linear static analysis is performed on each wall line. The total lateral load on that wall line is one half of the design base shear. The vertical distribution of lateral load follows the distribution of equivalent lateral load in the design narrative (Madsen et al. 2011).

Although each wall line is analyzed independently, to make a better summary and to make better comparisons with 3D models, results of individual wall lines are post-processed to reconstruct physical quantities of the whole building behavior, such as building displacements/drifts and total building base shear.

Table M-2 summarizes the breakdown of peak total base shear among four elevations. As shown in the table, each of two facing wall lines take 5.5 kips of base shear, and wall lines perpendicular to the loading direction take zero base shear as a natural result of 2D analysis.

Table M-3 shows peak building and wall line deflections. Practicing engineers can linearly upscale these data and develop an estimate of the building's performance at a certain lateral force level. In 2D analysis, only wall lines along the loading direction have displacements in the loading direction.

Table M-4 is an evaluation of the each wall line's lateral stiffness of long and short direction and its breakdown among shear walls (SW) and other systems. Covered by the same type of OSB sheathing with shear walls (even though the fastener spacing is

different), gravity walls make a comparable contribution to total lateral stiffness like shear walls. The percentage ranges from 14.3% (West) to as much as 49.7% (South). This also indicates that behaviors of individual wall lines can vary significantly since they have very different stiffness and breakdown of lateral force and gravity systems.

Table M-2: Breakdown of peak base shear, linear static analysis, A2b-2D-a model

Load direction	**LONG**				
Elevation	**South V_b**	**North V_b**	**East V_b**	**West V_b**	**Peak V_b**
kips	5.5	5.5	0.0	0.0	11.1
%	50.0	50.0	0.0	0.0	100.0
Load direction	**SHORT**				
Elevation	**South V_b**	**North V_b**	**East V_b**	**West V_b**	**Peak V_b**
kips	0.0	0.0	5.5	5.5	11.1
%	0.0	0.0	50.0	50.0	100.0

Table M-3: Peak building and wall line deflection, linear static analysis, A2b-2D-a model

Load direction	**LONG**							
Deflection (in.)	**u_1**	**u_2**	**v_1**	**v_2**	**Δu_1**	**Δu_2**	**Δv_1**	**Δv_2**
Building	0.065	0.109	0.000	0.000	0.065	0.043	0.000	0.000
South	0.092	0.149	0.000	0.000	0.092	0.057	0.000	0.000
North	0.039	0.068	0.000	0.000	0.039	0.029	0.000	0.000
East	-	-	-	-	-	-	-	-
West	-	-	-	-	-	-	-	-
Load direction	**SHORT**							
Deflection (in.)	**u_1**	**u_2**	**v_1**	**v_2**	**Δu_1**	**Δu_2**	**Δv_1**	**Δv_2**
Building	0.000	0.000	0.103	0.174	0.000	0.000	0.103	0.071
South	-	-	-	-	-	-	-	-
North	-	-	-	-	-	-	-	-
East	0.000	0.000	0.096	0.163	0.000	0.000	0.096	0.067
West	0.000	0.000	0.110	0.185	0.000	0.000	0.110	0.075

Table M-4: Breakdown of lateral stiffness, A2b-2D-a model

SOUTH			**NORTH**		
Shear wall k_u (%)	**Gravity wall k_u (%)**	**k_u (kip/in)**	**Shear wall k_v (%)**	**Gravity wall k_v (%)**	**k_v (kip/in)**
50.3	49.7	37.0	74.3	25.7	81.6
EAST			**WEST**		
Shear wall k_u (%)	**Gravity wall k_u (%)**	**k_u (kip/in)**	**Shear wall k_v (%)**	**Gravity wall k_v (%)**	**k_v (kip/in)**
84.7	15.3	34.0	85.7	14.3	29.9

M.4 Nonlinear static (pushover) analysis results

Table M-5 is created following the same logic with Table M-2, but the analysis type is nonlinear static (pushover). Pushover curves of the building and each wall line are presented in Figure M-3 and Figure M-4.

These tables and figures indicate that the wall lines do not reach their peak capacity at exactly the same drift level. Accordingly, total capacity of the building reconstructed using 2D results is no greater than the sum of wall line capacities in the load direction. This observation is more apparent in long direction. Total capacity of the wall line increases since the capacity of gravity walls is included. The trend is more significant in long direction given that North and South elevations are much wider and have larger areas covered by sheathed gravity walls. The missing of diaphragm stiffness and induced interplay of wall lines can make a significant difference between 2D analysis and real 3D analysis.

Table M-5: Breakdown of peak base shear, pushover analysis, A2b-2D-a model

Load direction	**LONG**				
Elevation	**South V_b**	**North V_b**	**East V_b**	**West V_b**	**Peak V_b**
kips	25.2	35.2	0.0	0.0	58.4
%	43.2	60.2	0.0	0.0	100.0
Load direction	**SHORT**				
Elevation	**South V_b**	**North V_b**	**East V_b**	**West V_b**	**Peak V_b**
kips	0.0	0.0	18.5	20.1	37.4
%	0.0	0.0	49.5	53.7	100.0

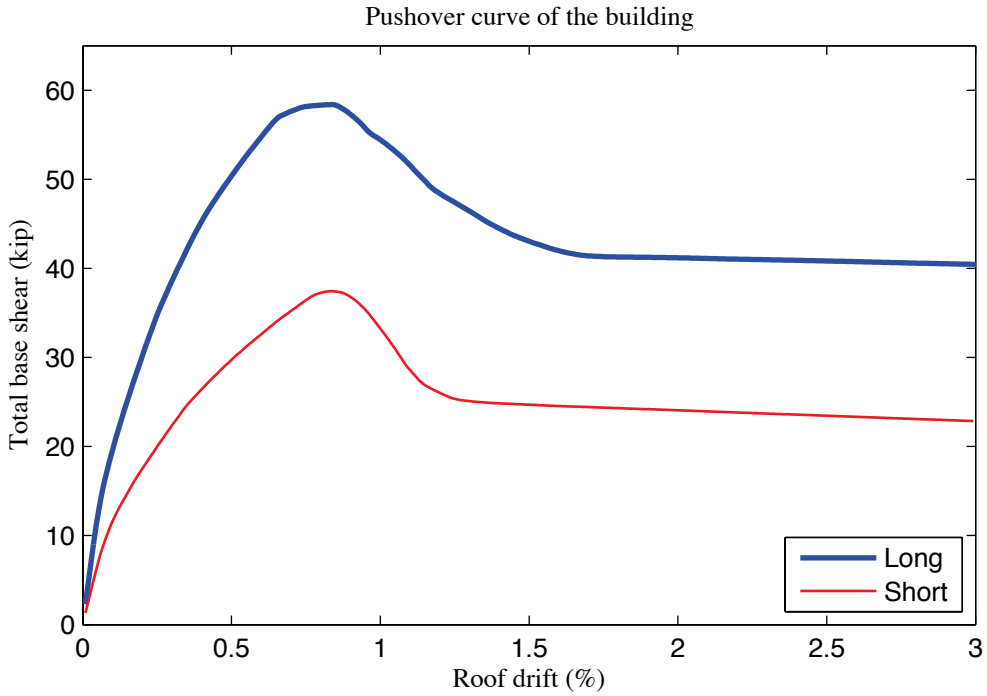

Figure M-3: Pushover curve of A2b-2D-a model

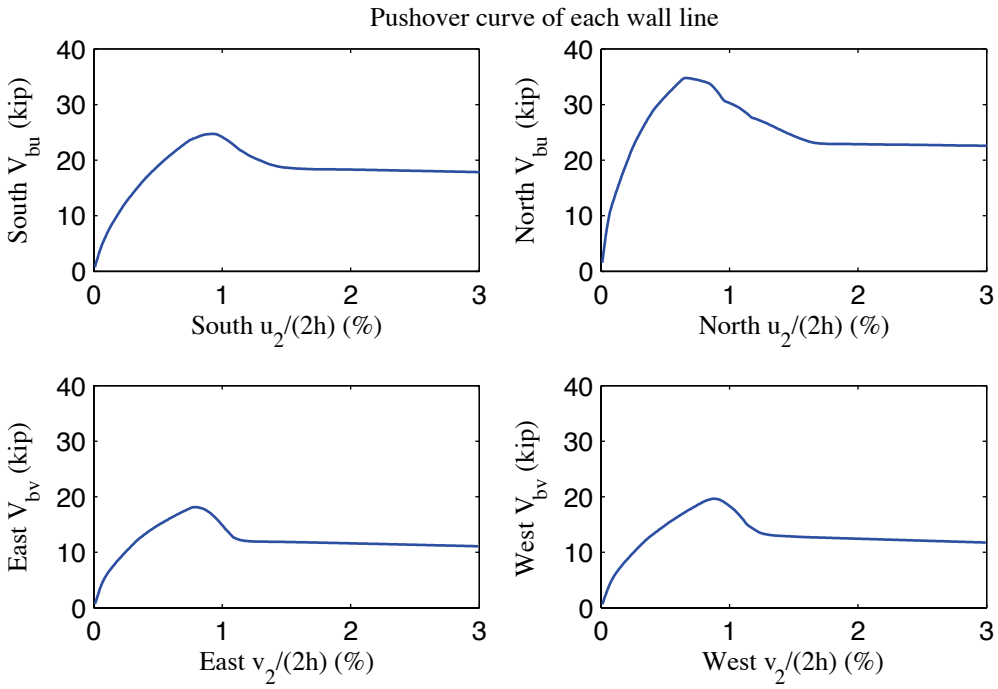

Figure M-4: Pushover curve of each wall line, A2b-2D-a model

M.5 Linear time history analysis results

Linear time history analysis is performed on 2D models under Canoga Park and Rinaldi ground motion records of Northridge earthquake in 1994. We considered three scale levels (16%, 44% and 100%) and single axis excitation is applied in the lateral direction of a single wall line.

Table M-6 to Table M-9 demonstrate the reconstructed linear elastic performance of the building under designated ground motions. Table M-6 shows peak story relative accelerations in the unit of g. Table M-7 and Table M-8 report peak roof drift and story drift of the building and the corresponding time step (t_*) and the base shear at that time. Note that the base shear at the time of peak roof drift may not be the peak total building base shear in that direction (see Table M-9).

The response of each wall line is available directly from 2D analysis results, so peak story drift and peak base shear of each wall line are listed in Table M-10 and Table M-11.

Wall lines behave linearly since peak drift and peak base shear appear at the same time when the ground motion is linearly scaled. Figure M-5 is a vector plot of the peak total resultant base shear of the building under 100% Canoga Park excitation. Since four dynamical analyses in 2D should be performed separately in order to create the plot, base shear vectors are always in-line with the wall. Comparison with nonlinear analysis results of the same excitation provides insightful observations on the building's response and requirements on modeling fidelity and analysis type.

Table M-6: A2b-2D-a model peak story relative acceleration in g, linear time history analysis

Load Case	Ground Motion	LONG			SHORT		
		a_g	Floor a	Roof a	a_g	Floor a	Roof a
EQ_2D_1axis_1	CNP 16%	0.067	0.076	0.113	0.057	0.120	0.192
EQ_2D_1axis_2	CNP 44%	0.185	0.201	0.306	0.157	0.341	0.578
EQ_2D_1axis_3	CNP 100%	0.420	0.456	0.700	0.356	0.776	1.315
EQ_2D_1axis_4	RRS 16%	0.132	0.125	0.188	0.078	0.239	0.377
EQ_2D_1axis_5	RRS 44%	0.363	0.342	0.526	0.214	0.657	1.035
EQ_2D_1axis_6	RRS 100%	0.825	0.785	1.167	0.486	1.493	2.353

Table M-7: A2b-2D-a model peak building roof drift and base shear, linear time history analysis

Load Case	Ground Motion	LONG			SHORT		
		$u_2/(2h)$ (%)	t_* (s)	V_b @ t_* (kips)	$v_2/(2h)$ (%)	t_* (s)	V_b @ t_* (kips)
EQ_2D_1axis_1	CNP 16%	0.035	8.69	8.3	0.087	9.94	12.5
EQ_2D_1axis_2	CNP 44%	0.096	8.69	22.8	0.239	9.94	34.5
EQ_2D_1axis_3	CNP 100%	0.217	8.69	51.9	0.543	9.94	78.3
EQ_2D_1axis_4	RRS 16%	0.075	2.59	16.7	-0.144	4.35	20.9
EQ_2D_1axis_5	RRS 44%	0.205	2.59	45.9	-0.395	4.35	57.4
EQ_2D_1axis_6	RRS 100%	0.467	2.59	104.3	-0.898	4.35	130.5

Table M-8: A2b-2D-a model peak building story drift, linear time history analysis

Load Case	Ground Motion	LONG				SHORT			
		$\Delta u_1/h$ (%)	t_* (s)	$\Delta u_2/h$ (%)	t_* (s)	$\Delta v_1/h$ (%)	t_* (s)	$\Delta v_2/h$ (%)	t_* (s)
EQ_2D_1 axis_1	CNP 16%	0.045	8.69	0.025	8.69	0.106	9.94	0.068	9.94
EQ_2D_1 axis_2	CNP 44%	0.123	8.69	0.068	8.69	0.292	9.94	0.186	9.94
EQ_2D_1 axis_3	CNP 100%	0.280	8.69	0.154	8.69	0.664	9.94	0.422	9.94
EQ_2D_1 axis_4	RRS 16%	0.097	2.59	0.052	2.59	-0.180	4.35	-0.115	4.66
EQ_2D_1 axis_5	RRS 44%	0.268	2.59	0.143	2.59	-0.496	4.35	-0.316	4.66
EQ_2D_1 axis_6	RRS 100%	0.609	2.59	0.325	2.59	-1.126	4.35	-0.718	4.66

Table M-9: A2b-2D-a model peak building base shear, linear time history analysis

		LONG		SHORT		RESULTANT	
Load Case	**Ground Motion**	**Peak V_{bu} (kip)**	**t @ peak V_{bu} (s)**	**Peak V_{bv} (kip)**	**t @ peak V_{bv} (s)**	**Peak V_b (kip)**	**t @ peak V_b (s)**
EQ_2D_1 axis_1	CNP 16%	8.3	8.69	12.5	9.94	12.9	9.94
EQ_2D_1 axis_2	CNP 44%	22.8	8.69	34.5	9.94	35.5	9.94
EQ_2D_1 axis_3	CNP 100%	51.9	8.69	78.3	9.94	80.6	9.94
EQ_2D_1 axis_4	RRS 16%	16.9	2.58	20.9	4.35	24.0	4.35
EQ_2D_1 axis_5	RRS 44%	46.6	2.58	57.4	4.35	65.9	4.35
EQ_2D_1 axis_6	RRS 100%	105.9	2.58	130.5	4.35	149.9	4.35

Table M-10: A2b-2D-a model peak wall line story drift, linear time history analysis

LONG		**SOUTH**				**NORTH**			
Load Case	**Ground Motion**	**$\Delta u_1/h$ (%)**	**t_* (s)**	**$\Delta u_2/h$ (%)**	**t_* (s)**	**$\Delta u_1/h$ (%)**	**t_* (s)**	**$\Delta u_2/h$ (%)**	**t_* (s)**
EQ_2D_1axis_1	CNP 16%	0.068	8.71	0.039	8.70	0.033	8.68	0.028	7.35
EQ_2D_1axis_2	CNP 44%	0.187	8.71	0.107	8.70	0.091	8.68	0.076	7.35
EQ_2D_1axis_3	CNP 100%	0.425	8.71	0.242	8.70	0.207	8.68	0.173	7.35
EQ_2D_1axis_4	RRS 16%	0.161	2.60	0.088	4.53	0.061	4.32	0.042	3.07
EQ_2D_1axis_5	RRS 44%	0.444	2.60	0.243	4.53	0.167	4.32	0.116	3.07
EQ_2D_1axis_6	RRS 100%	1.009	2.60	0.552	4.53	0.379	4.32	0.265	3.07
SHORT		**EAST**				**WEST**			
Load Case	**Ground Motion**	**$\Delta v_1/h$ (%)**	**t_* (s)**	**$\Delta v_2/h$ (%)**	**t_* (s)**	**$\Delta v_1/h$ (%)**	**t_* (s)**	**$\Delta v_2/h$ (%)**	**t_* (s)**
EQ_2D_1axis_1	CNP 16%	0.128	9.93	0.085	9.94	0.099	9.96	0.061	9.96
EQ_2D_1axis_2	CNP 44%	0.353	9.93	0.233	9.94	0.272	9.96	0.168	9.96
EQ_2D_1axis_3	CNP 100%	0.802	9.93	0.529	9.94	0.618	9.96	0.383	9.96
EQ_2D_1axis_4	RRS 16%	0.192	4.34	0.124	4.64	0.212	4.53	0.145	4.68
EQ_2D_1axis_5	RRS 44%	0.527	4.34	0.340	4.64	0.582	4.53	0.398	4.68
EQ_2D_1axis_6	RRS 100%	1.198	4.34	0.774	4.64	1.324	4.53	0.904	4.68

Table M-11: A2b-2D-a model peak wall line base shear, linear time history analysis

LONG		SOUTH		NORTH		% of Peak V_{bu}	
Load Case	**Ground Motion**	**Peak V_{bu} (kips)**	**t @ peak V_{bu} (s)**	**Peak V_{bu} (kips)**	**t @ peak V_{bu} (s)**	**South**	**North**
EQ_2D_1axis_1	CNP 16%	4.2	8.71	4.5	8.68	48.1	51.9
EQ_2D_1axis_2	CNP 44%	11.5	8.71	12.3	8.68	48.1	51.9
EQ_2D_1axis_3	CNP 100%	26.1	8.71	28.0	8.68	48.0	52.0
EQ_2D_1axis_4	RRS 16%	9.9	2.60	8.3	4.32	54.7	45.3
EQ_2D_1axis_5	RRS 44%	27.2	2.60	22.9	4.32	54.7	45.3
EQ_2D_1axis_6	RRS 100%	61.9	2.60	52.2	4.32	54.7	45.3
SHORT		**EAST**		**WEST**		**% of Peak V_{bv}**	
Load Case	**Ground Motion**	**Peak V_{bv} (kips)**	**t @ peak V_{bv} (s)**	**Peak V_{bv} (kips)**	**t @ peak V_{bv} (s)**	**East**	**West**
EQ_2D_1axis_1	CNP 16%	7.8	9.93	5.3	9.96	60.8	39.2
EQ_2D_1axis_2	CNP 44%	21.4	9.93	14.5	9.96	60.8	39.2
EQ_2D_1axis_3	CNP 100%	48.6	9.93	33.0	9.96	60.8	39.2
EQ_2D_1axis_4	RRS 16%	11.6	4.34	11.3	4.53	53.5	46.5
EQ_2D_1axis_5	RRS 44%	31.9	4.34	31.0	4.53	53.5	46.5
EQ_2D_1axis_6	RRS 100%	72.6	4.34	70.6	4.53	53.5	46.5

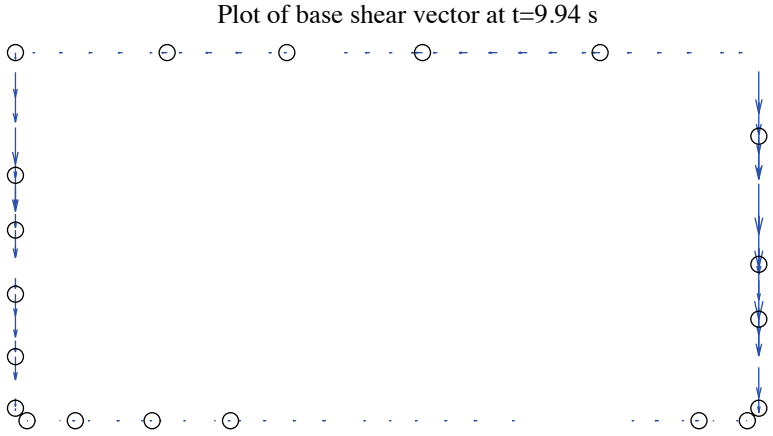

Figure M-5: A2b-2D-a model, base shear vector plot at the moment of peak total base shear, 100 % Canoga Park, 2D linear analysis (maximum anchor/hold down base shear is 5.24 kips)

M.6 Nonlinear time history analysis results

Same ground motions are applied to the model with material and geometrical nonlinearity. Table M-12 to Table M-17 are replicas of Table M-6 to Table M-11, but for nonlinear time history analyses. Since this analysis type is most complicated and closest to reality and experiments, behavior of wall lines and smeared hold downs are further studied. Table M-18 expands the breakdown of each wall line's peak base shear between shear walls, gravity walls and other systems. Table M-19 is peak value of hold down tensile force of two selected pairs. Hold down 5 and 6 are on shear wall L1S1, South elevation and hold down 7 and 8 are on shear wall L1W1, West elevation. These shear walls have lowest capacities compared with others on the same wall line and they meet at the southwest edge of the building.

Time history plots in this section include plots of story drifts of the building and each wall line (Figure M-6 to Figure M-8), total building base shear in long and short direction (Figure M-9) and axial forces of hold downs in (Figure M-10). Hysteretic plots in Figure M-11 and Figure M-12 are helpful for visual examination of nonlinear base shear-drift relationship of the building and the weakest shear wall on each wall line. In comparison with linear time history analysis, vector plot of peak total base shear is illustrated in Figure M-13. Figure M-14 presents a simplified deformed shape of the building (see (Peterman 2014) for details of the method) and axial force of all twenty hold downs at the moment of peak total base shear. The same sign convention with tests is adopted. Red bars indicate tensile (negative) force and blue ones are for compressive (positive) force.

Hysteretic behavior is seen in the building and typical shear walls under design-based earthquake (100% Canoga Park excitation in one axis, see Figure M-11 and Figure M-12). However, behaviors of individual wall lines differ significantly. South wall line reaches 1.4% peak floor story drift but peak story drifts of all other wall lines are less than 1.2% (Table M-16). The reconstructed peak building story drift is 0.86% in long direction, (Table M-14), still much less than the peak value of South wall line. The worst-case scenario from 2D analysis can greatly overestimate the nonlinear response of the whole building and yield conservative observation. Figure M-13 shows that peak resultant base shear is taken by both shear walls and gravity walls, and that base shear vectors in anchors and hold downs align with wall lines due to the limit of 2D modeling and analysis. Table M-19, Figure M-10 and Figure M-14 demonstrate that hold downs in a pair do not experience the same amount of force with opposite signs even in 2D analysis, an evidence that supports Type II shear wall behavior despite Type I design assumption.

The near-field Rinaldi record is much stronger in terms of peak ground acceleration, especially in the long direction. With the addition of sheathed gravity walls, the lateral resistance of wall lines increases significantly. Even when loaded with 100% Rinaldi record, peak story drifts of North, East and West wall lines are all below 1.7%. Only South wall line is believed to fail with peak story drift over 10%. The portion of base shear taken by gravity wall does not change much with scale factors considered so far in this research, as shown in Table M-18. Again, the table demonstrates that the base shear taken by anchors on bottom tracks of gravity walls can be quite large, sometimes even larger than half of the total base shear (e.g. South wall lines).

Table M-12: A2b-2D-a model peak story relative acceleration in g, nonlinear time history analysis

Load Case	Ground Motion	LONG			SHORT		
		a_g	Floor a	Roof a	a_g	Floor a	Roof a
EQ_2D_1axis_1	CNP 16%	0.067	0.101	0.175	0.057	0.141	0.198
EQ_2D_1axis_2	CNP 44%	0.185	0.547	0.636	0.157	0.377	0.547
EQ_2D_1axis_3	CNP 100%	0.420	1.047	1.087	0.356	0.675	0.926
EQ_2D_1axis_4	RRS 16%	0.132	0.298	0.329	0.078	0.344	0.280
EQ_2D_1axis_5	RRS 44%	0.363	1.388	1.149	0.214	0.791	0.978
EQ_2D_1axis_6	RRS 100%	0.825	1.691	1.221	0.486	0.738	1.078

Table M-13: A2b-2D-a model peak building roof drift and base shear, nonlinear time history analysis

Load Case	Ground Motion	LONG			SHORT		
		$u_2/(2h)$ (%)	t_* (s)	V_b @ t_* (kips)	$v_2/(2h)$ (%)	t_* (s)	V_b @ t_* (kips)
EQ_2D_1axis_1	CNP 16%	0.034	8.69	8.2	0.070	9.96	8.9
EQ_2D_1axis_2	CNP 44%	0.137	8.72	17.3	0.211	9.98	18.9
EQ_2D_1axis_3	CNP 100%	0.550	8.75	40.3	0.797	10.07	36.9
EQ_2D_1axis_4	RRS 16%	0.081	2.60	14.5	0.127	3.36	13.8
EQ_2D_1axis_5	RRS 44%	0.319	2.66	29.0	0.377	6.07	25.4
EQ_2D_1axis_6	RRS 100%	2.729	2.95	36.1	1.011	6.11	36.6

Table M-14: A2b-2D-a model peak building story drift, nonlinear time history analysis

Load Case	Ground Motion	LONG				SHORT			
		$\Delta u_1/h$ (%)	t_* (s)	$\Delta u_2/h$ (%)	t_* (s)	$\Delta v_1/h$ (%)	t_* (s)	$\Delta v_2/h$ (%)	t_* (s)
EQ_2D_1 axis_1	CNP 16%	0.044	8.68	0.024	8.69	0.091	9.97	0.051	9.39
EQ_2D_1 axis_2	CNP 44%	0.199	8.71	0.085	9.94	0.304	9.98	-0.125	8.46
EQ_2D_1 axis_3	CNP 100%	0.859	8.75	0.247	8.73	1.161	10.07	0.452	8.87
EQ_2D_1 axis_4	RRS 16%	0.114	2.61	0.050	2.59	0.182	3.36	-0.076	4.45
EQ_2D_1 axis_5	RRS 44%	0.500	2.67	0.141	2.65	0.510	6.06	0.275	3.95
EQ_2D_1 axis_6	RRS 100%	5.279	2.96	0.336	2.63	1.614	6.14	0.511	6.08

Table M-15: A2b-2D-a model peak building base shear, nonlinear time history analysis

		LONG		SHORT		RESULTANT	
Load Case	**Ground Motion**	**Peak V_{bu} (kip)**	**t @ peak V_{bu} (s)**	**Peak V_{bv} (kip)**	**t @ peak V_{bv} (s)**	**Peak V_b (kip)**	**t @ peak V_b (s)**
EQ_2D_1 axis_1	CNP 16%	8.2	8.68	9.1	9.97	9.6	10.47
EQ_2D_1 axis_2	CNP 44%	19.5	8.69	18.9	9.98	23.3	8.44
EQ_2D_1 axis_3	CNP 100%	56.2	8.71	40.1	10.05	56.2	8.71
EQ_2D_1 axis_4	RRS 16%	15.4	2.58	14.1	3.35	15.7	4.40
EQ_2D_1 axis_5	RRS 44%	38.2	2.61	25.7	6.06	40.0	2.59
EQ_2D_1 axis_6	RRS 100%	102.0	2.80	46.5	6.05	103.4	2.81

Table M-16: A2b-2D-a model peak wall line story drift, nonlinear time history analysis

LONG		**SOUTH**				**NORTH**			
Load Case	**Ground Motion**	**$\Delta u_1/h$ (%)**	**t_* (s)**	**$\Delta u_2/h$ (%)**	**t_* (s)**	**$\Delta u_1/h$ (%)**	**t_* (s)**	**$\Delta u_2/h$ (%)**	**t_* (s)**
EQ_2D_1axis_1	CNP 16%	0.061	10.48	0.039	4.05	0.035	8.68	0.030	7.35
EQ_2D_1axis_2	CNP 44%	0.392	10.55	0.182	10.39	0.125	11.83	0.060	8.45
EQ_2D_1axis_3	CNP 100%	1.429	8.77	0.394	10.26	0.463	8.71	0.203	8.70
EQ_2D_1axis_4	RRS 16%	0.221	4.41	0.097	4.56	0.060	2.57	0.042	3.07
EQ_2D_1axis_5	RRS 44%	0.851	2.68	0.259	4.01	0.347	4.37	0.124	6.73
EQ_2D_1axis_6	RRS 100%	10.091	2.98	0.417	2.64	1.437	2.69	0.334	3.11
SHORT		**EAST**				**WEST**			
Load Case	**Ground Motion**	**$\Delta v_1/h$ (%)**	**t_* (s)**	**$\Delta v_2/h$ (%)**	**t_* (s)**	**$\Delta v_1/h$ (%)**	**t_* (s)**	**$\Delta v_2/h$ (%)**	**t_* (s)**
EQ_2D_1axis_1	CNP 16%	0.111	9.95	0.065	9.95	0.094	7.45	0.063	7.60
EQ_2D_1axis_2	CNP 44%	0.313	9.98	0.139	9.97	0.305	9.98	0.151	8.44
EQ_2D_1axis_3	CNP 100%	1.127	10.07	0.463	8.88	1.215	10.07	0.482	9.45
EQ_2D_1axis_4	RRS 16%	0.167	3.34	0.076	3.36	0.214	3.37	0.112	4.45
EQ_2D_1axis_5	RRS 44%	0.513	6.06	0.295	3.95	0.525	6.07	0.290	3.95
EQ_2D_1axis_6	RRS 100%	1.675	6.14	0.534	6.08	1.592	6.13	0.525	6.08

Table M-17: A2b-2D-a model peak wall line base shear, nonlinear time history analysis

LONG		SOUTH		NORTH		% of Peak V_{bu}	
Load Case	**Ground Motion**	**Peak V_{bu} (kips)**	**t @ peak V_{bu} (s)**	**Peak V_{bu} (kips)**	**t @ peak V_{bu} (s)**	**South**	**North**
EQ_2D_1axis_1	CNP 16%	3.6	10.48	4.7	7.35	43.5	57.0
EQ_2D_1axis_2	CNP 44%	13.5	10.56	12.2	11.82	62.8	37.8
EQ_2D_1axis_3	CNP 100%	25.4	8.74	26.3	8.71	44.2	46.8
EQ_2D_1axis_4	RRS 16%	9.2	4.41	7.9	2.57	50.2	50.2
EQ_2D_1axis_5	RRS 44%	21.2	2.68	22.3	4.36	47.3	50.3
EQ_2D_1axis_6	RRS 100%	25.1	2.60	35.8	2.60	19.6	24.2
SHORT		**EAST**		**WEST**		**% of Peak V_{bv}**	
Load Case	**Ground Motion**	**Peak V_{bv} (kips)**	**t @ peak V_{bv} (s)**	**Peak V_{bv} (kips)**	**t @ peak V_{bv} (s)**	**East**	**West**
EQ_2D_1axis_1	CNP 16%	5.5	9.95	4.7	7.45	58.1	42.7
EQ_2D_1axis_2	CNP 44%	9.7	9.98	9.4	9.98	51.5	49.5
EQ_2D_1axis_3	CNP 100%	18.6	10.07	20.0	10.05	46.0	49.9
EQ_2D_1axis_4	RRS 16%	6.8	3.33	7.6	3.37	48.0	52.9
EQ_2D_1axis_5	RRS 44%	13.1	6.06	13.1	6.07	50.8	50.5
EQ_2D_1axis_6	RRS 100%	19.1	6.05	20.7	6.05	41.2	44.5

Table M-18: A2b-2D-a model wall line base shear breakdown, nonlinear time history analysis

LONG		SOUTH			NORTH		
Load Case	**Ground Motion**	**Peak V_{bu} (kips)**	**SW V_{bu} (%)**	**GW V_{bu} (%)**	**Peak V_{bu} (kips)**	**SW V_{bu} (%)**	**GW V_{bu} (%)**
EQ_2D_1axis_1	CNP 16%	3.6	31.5	68.5	4.7	63.4	36.6
EQ_2D_1axis_2	CNP 44%	13.5	38.1	61.9	12.2	61.8	38.2
EQ_2D_1axis_3	CNP 100%	25.4	36.4	63.6	26.3	55.9	44.1
EQ_2D_1axis_4	RRS 16%	9.2	38.1	61.9	7.9	63.4	36.6
EQ_2D_1axis_5	RRS 44%	21.2	36.2	63.8	22.3	57.3	42.7
EQ_2D_1axis_6	RRS 100%	25.1	36.5	63.5	35.8	55.5	44.5
SHORT		**EAST**			**WEST**		
Load Case	**Ground Motion**	**Peak V_{bv} (kips)**	**SW V_{bv} (%)**	**GW V_{bu} (%)**	**Peak V_{bv} (kips)**	**SW V_{bv} (%)**	**GW V_{bv} (%)**
EQ_2D_1axis_1	CNP 16%	5.5	75.5	24.5	4.7	82.3	17.7
EQ_2D_1axis_2	CNP 44%	9.7	73.2	26.8	9.4	82.3	17.7
EQ_2D_1axis_3	CNP 100%	18.6	74.2	25.8	20.0	82.3	17.7
EQ_2D_1axis_4	RRS 16%	6.8	75.7	24.3	7.6	82.9	17.1
EQ_2D_1axis_5	RRS 44%	13.1	71.6	28.4	13.1	80.6	19.4
EQ_2D_1axis_6	RRS 100%	19.1	74.1	25.9	20.7	82.1	17.9

Table M-19: A2b-2D-a model peak hold down tensile force at certain locations, nonlinear time history analysis

		L1S1, LC5		L1S1, LC6		L1W1, LC7		L1W1, LC8	
Load Case	**Ground Motion**	**Peak F (kips)**	**t @ peak F (s)**	**Peak F (kips)**	**t @ peak F (s)**	**Peak F (kips)**	**t @ peak F (s)**	**Peak F (kips)**	**t @ peak F (s)**
EQ_2D_1axis_1	CNP 16%	-0.11	10.48	-0.45	8.70	-0.64	9.41	-0.14	9.40
EQ_2D_1axis_2	CNP 44%	-0.65	10.56	-1.76	8.72	-1.48	9.98	-0.31	8.45
EQ_2D_1axis_3	CNP 100%	-1.19	10.25	-4.11	8.74	-4.11	10.07	-0.77	8.49
EQ_2D_1axis_4	RRS 16%	-0.36	4.58	-1.18	2.62	-1.17	3.38	-0.23	4.41
EQ_2D_1axis_5	RRS 44%	-0.74	3.12	-3.17	2.68	-2.34	6.08	-0.34	2.89
EQ_2D_1axis_6	RRS 100%	-1.13	2.45	-3.91	2.60	-4.51	6.08	-0.91	2.59

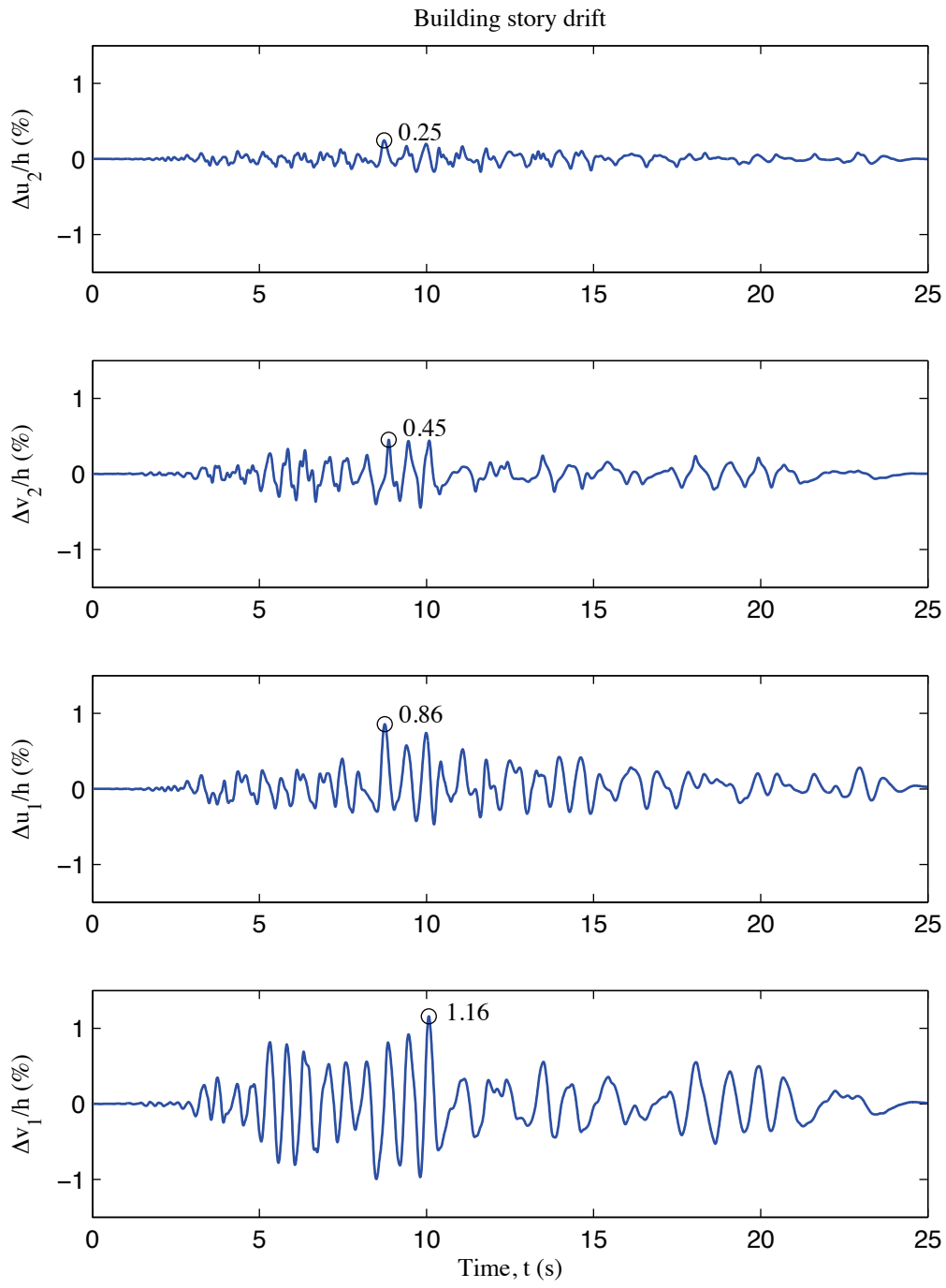

Figure M-6: A2b-2D-a model building story drift, 100 % Canoga Park, 2D nonlinear analysis

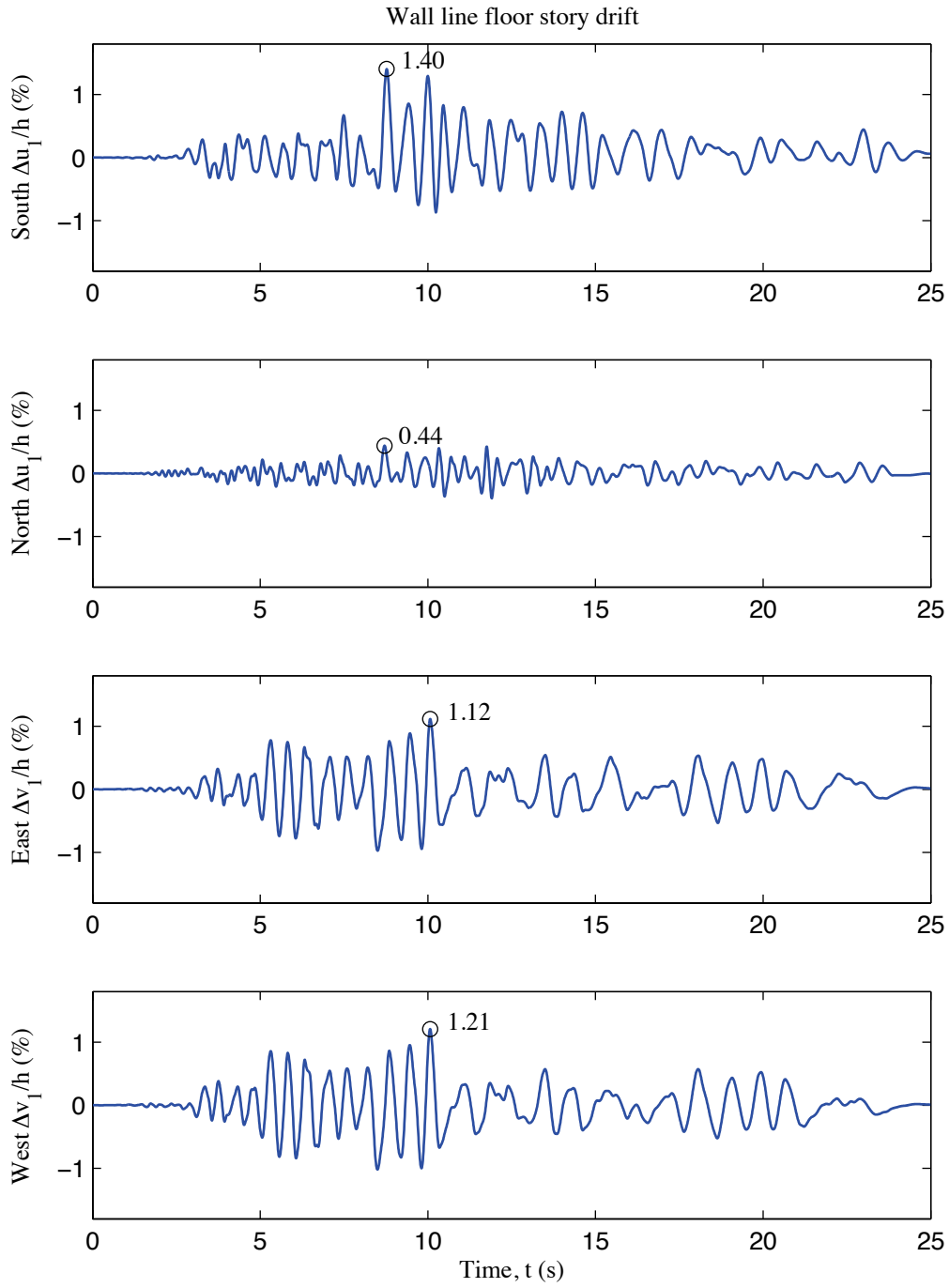

Figure M-7: A2b-2D-a model wall line floor story drift, 100 % Canoga Park, 2D nonlinear analysis

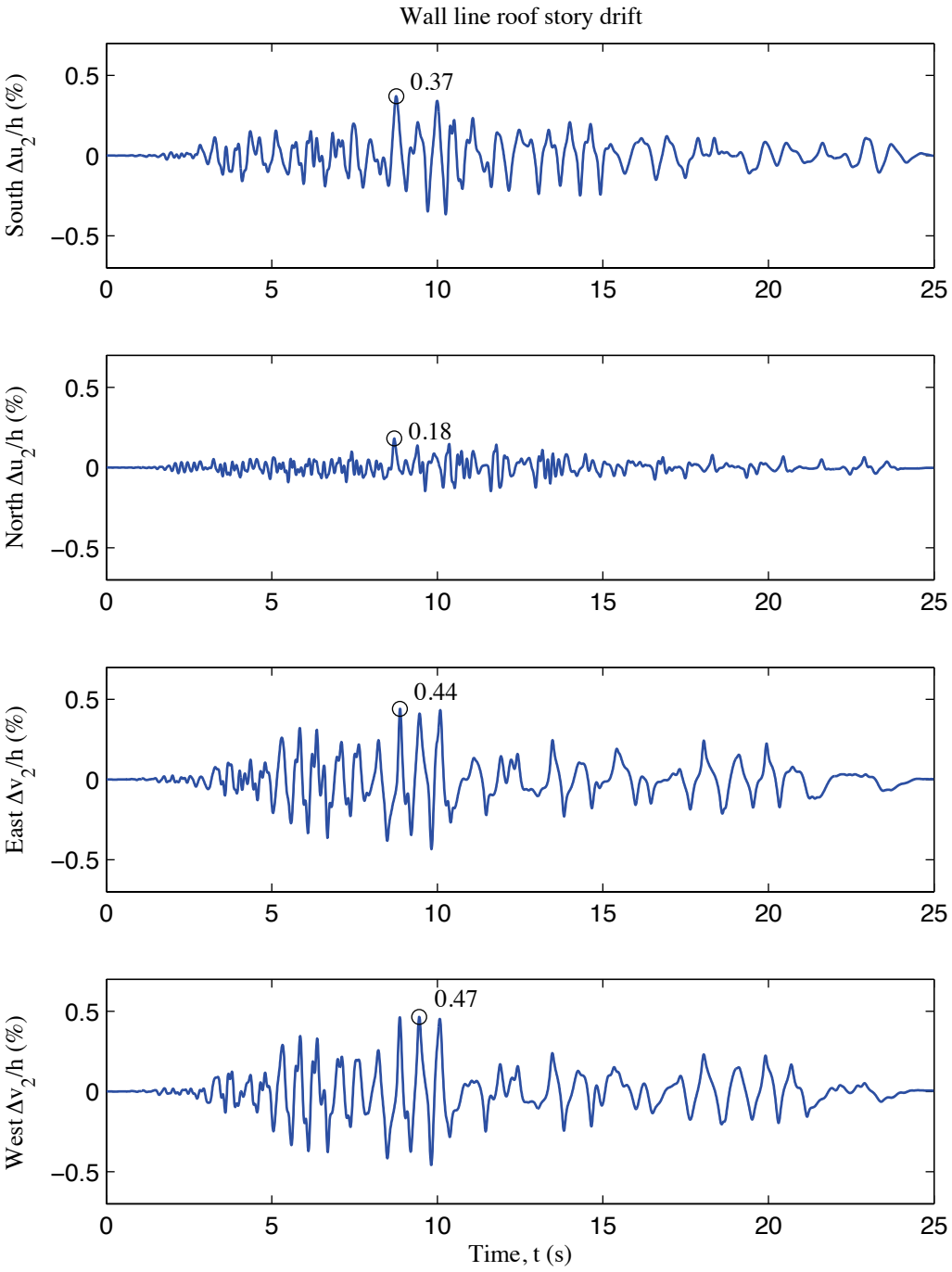

Figure M-8: A2b-2D-a model wall line roof story drift, 100 % Canoga Park, 2D nonlinear analysis

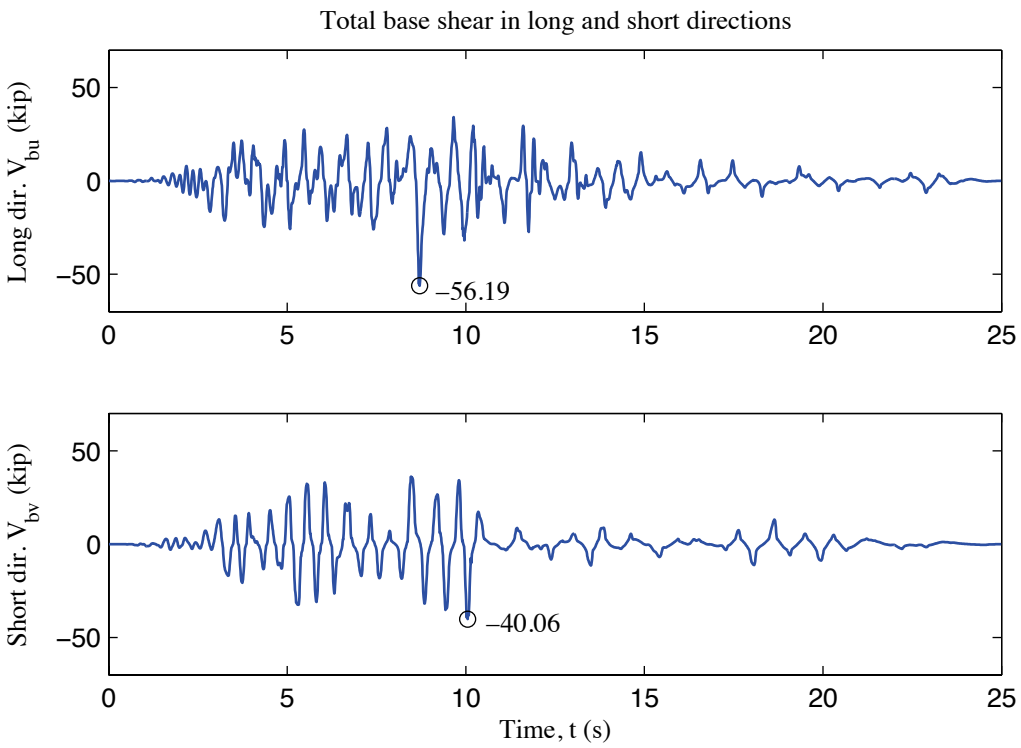

Figure M-9: A2b-2D-a model total building base shear, 100 % Canoga Park, 2D nonlinear analysis

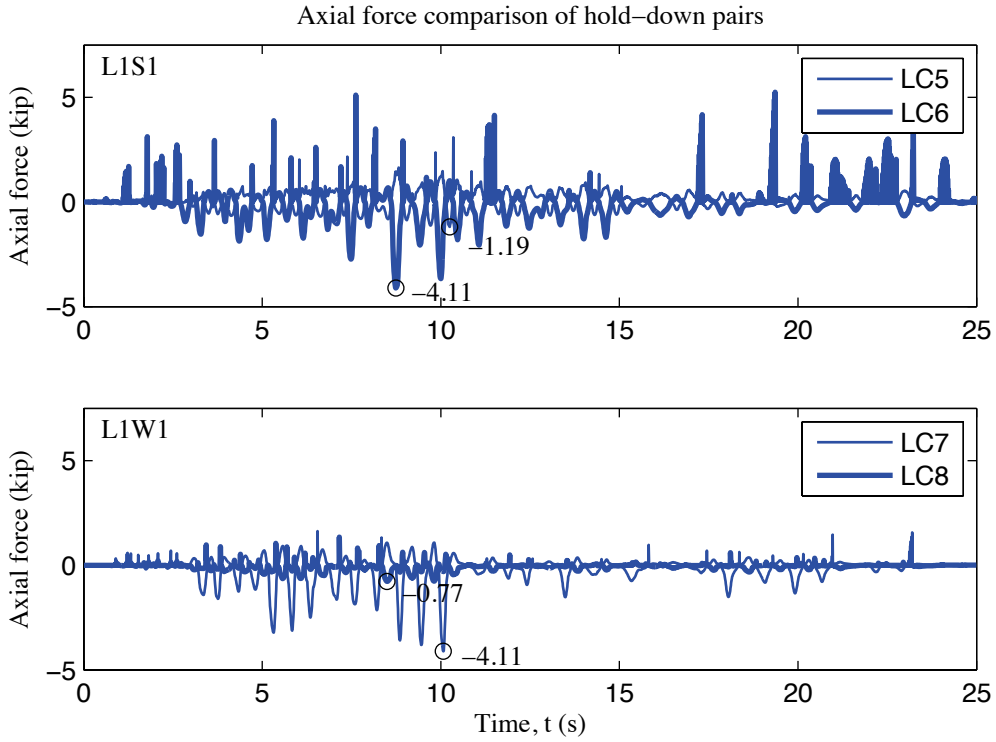

Figure M-10: A2b-2D-a model, load cell 5 to 8 axial forces, 100 % Canoga Park, 2D nonlinear analysis

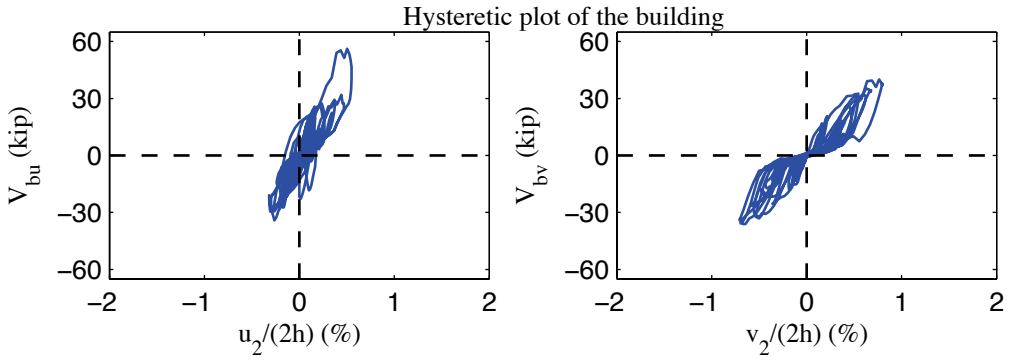

Figure M-11: A2b-2D-a model, hysteretic plot of the building, 100 % Canoga Park, 2D nonlinear analysis

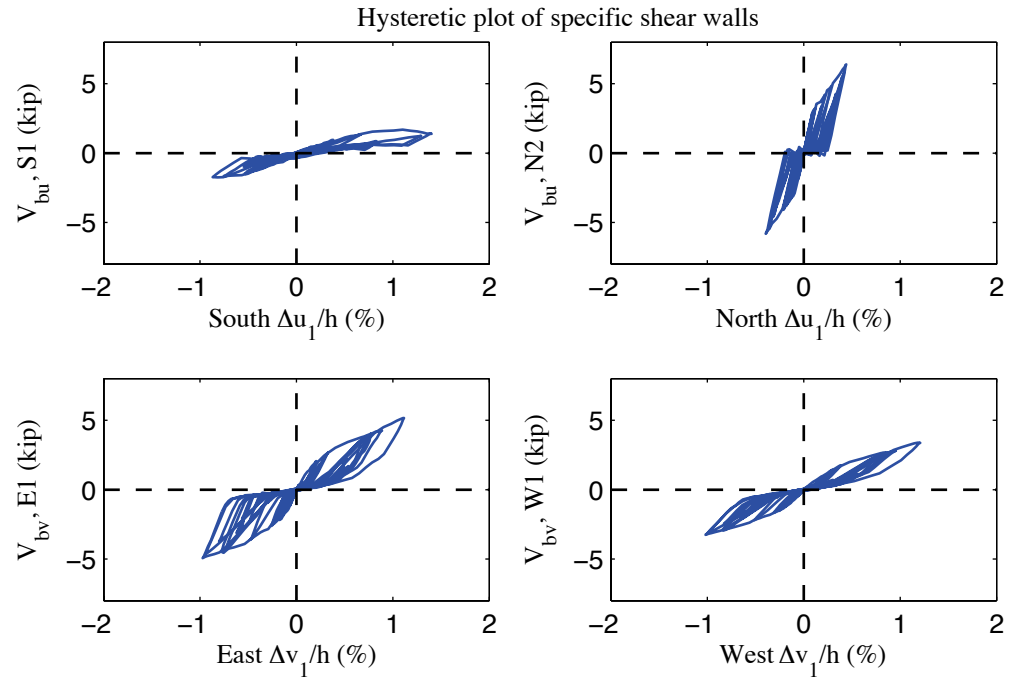

Figure M-12: A2b-2D-a model, hysteretic plot of shear walls at each elevation, 100 % Canoga Park, 2D nonlinear analysis

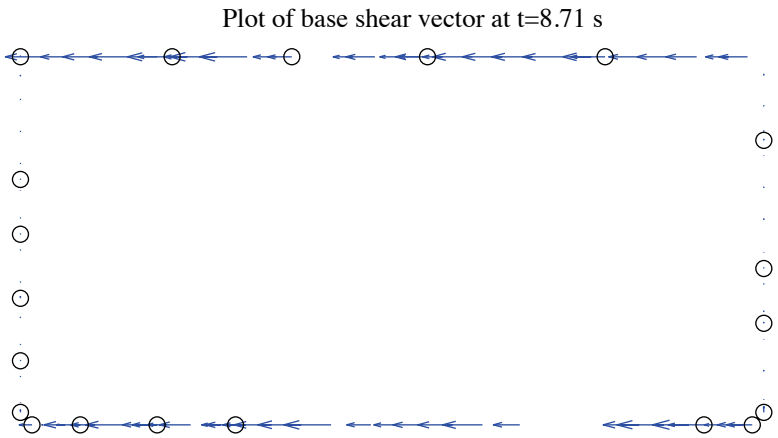

Figure M-13: A2b-2D-a model, field plot of peak total base shear, 100 % Canoga Park, 2D nonlinear analysis (maximum anchor/hold down base shear is 1.56 kips)

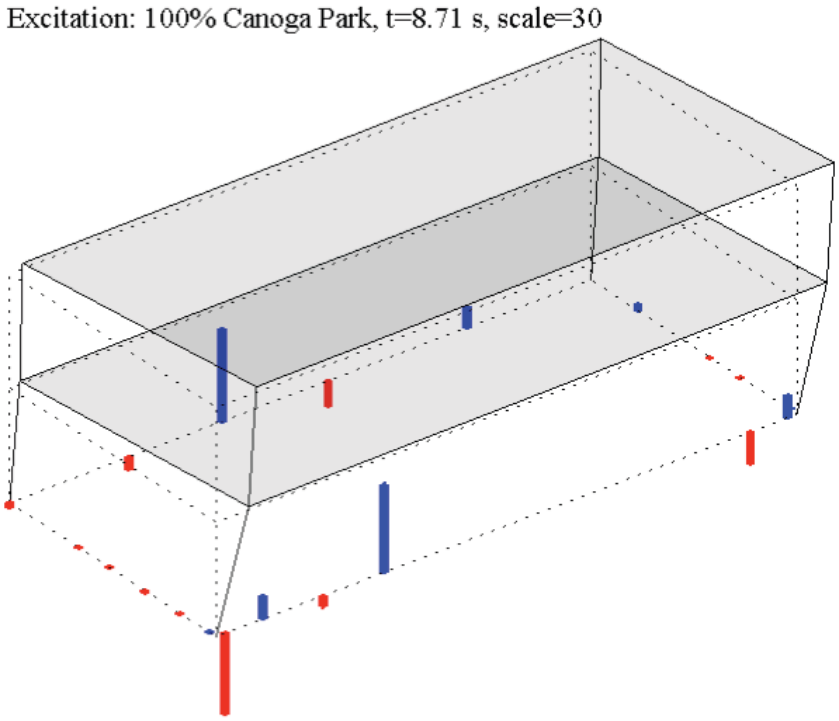

Figure M-14: A2b-2D-a model, simplified illustration of corner displacements with hold down forces from load cells,100 % Canoga Park, 2D nonlinear analysis (max hold down tensile force is -3.80 kips)

Appendix N: Analysis Results of State-of-the-art, Phase 2b, 3D, rigid-diaphragm, model a (A2b-3D-RD-a)

N.1 Model description

This state-of-the-art 3D model features subpanel bracing models of shear walls and gravity walls, explicit models of hold downs, and rigid diaphragms. All walls are covered by OSB sheathing. Seismic mass is distributed to corners and stud ends. The lateral displacement and shear wall capacity ($\delta(0.2V_{nA})$, $0.2V_{nA}$) from test is utilized to determine the stiffness of elastic material and the first point on the backbone curve of Pinching4 material of shear wall bracing. Figure N-1 is the 3D drawing of the building model with all members and diagonal bracings of sheathing panels. Definitions of output physical quantities and explanation of post-process method can be found in Appendix K.

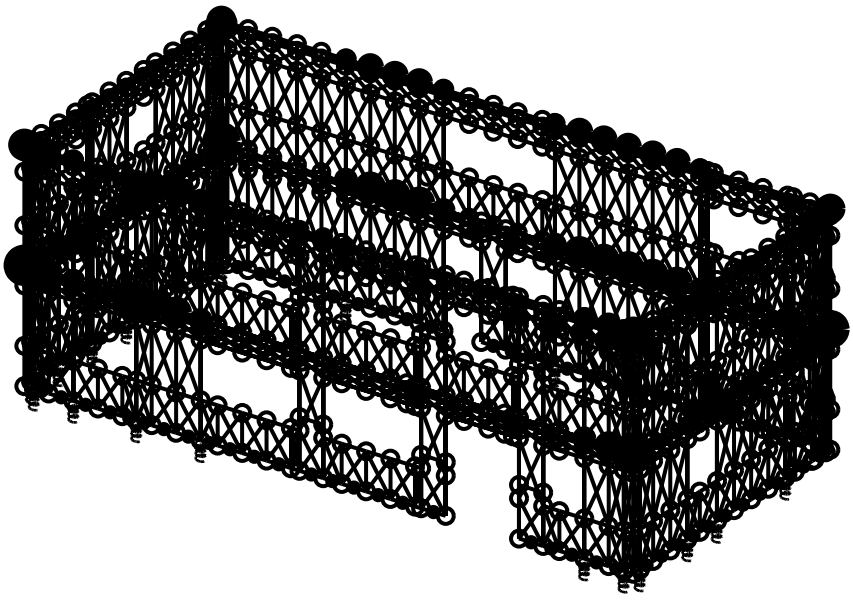

Figure N-1: A2b-3D-RD-a model

N.2 Free vibration analysis results

Free vibration analysis results are presented in Table N-1 and Figure N-2. Lateral stiffness in the short direction is smaller than lateral stiffness in the long direction and torsional stiffness is the largest. The observation holds for the first and the second mode, as indicated by Table N-1.

Table N-1: Free vibration analysis results, A2b-3D-RD-a model

Mode number	Natural period (s)	Mode description
1	0.283	Short, 1st
2	0.212	Long, 1st
3	0.183	Torsion, 1st
4	0.104	Short, 2nd
5	0.081	Long, 2nd
6	0.071	Torsion, 2nd

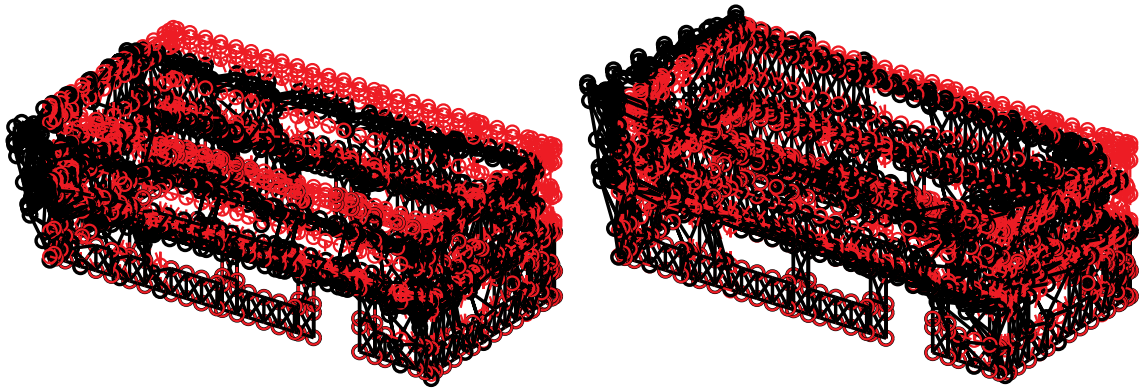

(a) Mode 1, T_1=0.283 s (b) Mode 2, T_2=0.212 s

Figure N-2: First two natural modes of A2b-3D-RD-a model

N.3 Linear static analysis results

Table N-2 to Table N-4 present linear static analysis results. The lateral load is the equivalent lateral force available from the design narrative (Madsen et al. 2011), applied equally at four corners. Two separate analyses were performed with the loading at long or short direction.

Table N-2 summarizes the breakdown of peak total base shear among four elevations. Due to the interplay of asymmetrical LFRS, wall lines perpendicular to the loading direction still take a very small portion of base shear.

Table N-3 shows peak building and wall line deflections. Practicing engineers can linearly upscale these data and develop an estimate of the building's performance at a certain lateral force level.

Table N-4 is an evaluation of the building's lateral stiffness of long and short direction and its breakdown among shear walls (SW) and other systems. Covered by the same type of OSB sheathing with shear walls (even though the fastener spacing is different), gravity walls make a comparable contribution to total lateral stiffness like shear walls. The effect is even more apparent in long direction, where wall lines are much wider and have larger areas covered by gravity walls. The stiffness of gravity walls can account for as much as 39% and 19% of total lateral stiffness in long and short direction.

Table N-2: Breakdown of peak base shear, linear static analysis, A2b-3D-RD-a model

Load direction	**LONG**				
Elevation	**South V_b**	**North V_b**	**East V_b**	**West V_b**	**Peak V_b**
kips	3.8	7.2	0.0	0.1	11.1
%	34.8	64.7	0.2	0.7	100.0
Load direction	**SHORT**				
Elevation	**South V_b**	**North V_b**	**East V_b**	**West V_b**	**Peak V_b**
kips	0.0	0.1	5.7	5.4	11.1
%	0.1	0.5	51.1	48.5	100.0

Table N-3: Peak building and wall line deflection, linear static analysis, A2b-3D-RD-a model

Load direction	**LONG**							
Deflection (in.)	**u_1**	**u_2**	**v_1**	**v_2**	**Δu_1**	**Δu_2**	**Δv_1**	**Δv_2**
Building	0.049	0.079	-0.004	-0.007	0.049	0.031	-0.004	-0.003
South	0.054	0.088	-0.004	-0.007	0.054	0.034	-0.004	-0.003
North	0.043	0.071	-0.004	-0.007	0.043	0.028	-0.004	-0.003
East	0.049	0.079	0.009	0.012	0.049	0.031	0.009	0.004
West	0.049	0.079	-0.016	-0.026	0.049	0.031	-0.016	-0.010
Load direction	**SHORT**							
Deflection (in.)	**u_1**	**u_2**	**v_1**	**v_2**	**Δu_1**	**Δu_2**	**Δv_1**	**Δv_2**
Building	-0.002	-0.003	0.085	0.141	-0.002	-0.001	0.085	0.056
South	-0.005	-0.008	0.085	0.141	-0.005	-0.003	0.085	0.056
North	0.002	0.003	0.085	0.141	0.002	0.001	0.085	0.056
East	-0.002	-0.003	0.079	0.130	-0.002	-0.001	0.079	0.051
West	-0.002	-0.003	0.092	0.153	-0.002	-0.001	0.092	0.061

Table N-4: Breakdown of lateral stiffness, A2b-3D-RD-a model

LONG			**SHORT**		
Shear wall k_u (%)	**Gravity wall k_u (%)**	**k_u (kip/in)**	**Shear wall k_v (%)**	**Gravity wall k_v (%)**	**k_v (kip/in)**
61.4	38.6	139.7	80.7	19.3	76.3

N.4 Nonlinear static (pushover) analysis results

Table N-5 is created following the same logic with Table N-2, but the analysis type is nonlinear static (pushover). Pushover curves of the building and each wall line are presented in Figure N-3 and Figure N-4.

Clearly, the interaction between wall lines is much more significant when material and geometrical nonlinearity is included. These tables and figures indicate that the wall lines do not reach their peak capacity at exactly the same drift level and wall lines perpendicular to the load can take a nontrivial amount of base shear. Total capacity of the wall line increases since the capacity of gravity walls is included. The boost is larger in long direction. Consequently, total capacity of the building in long direction is much larger than the short direction.

Table N-5: Breakdown of peak base shear, pushover analysis, A2b-3D-RD-a model

Load direction	**LONG**				
Elevation	**South V_b**	**North V_b**	**East V_b**	**West V_b**	**Peak V_b**
kips	36.6	40.7	3.2	5.4	73.3
%	50.0	55.6	4.3	7.3	100.0
Load direction	**SHORT**				
Elevation	**South V_b**	**North V_b**	**East V_b**	**West V_b**	**Peak V_b**
kips	6.5	3.5	25.9	26.6	52.2
%	12.4	6.6	49.6	51.0	100.0

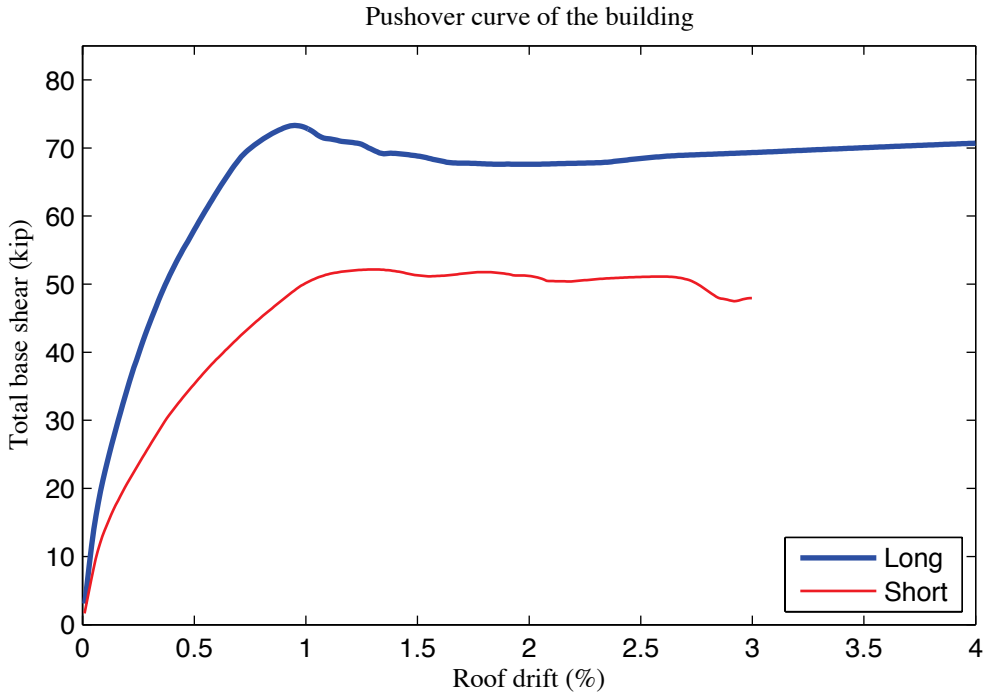

Figure N-3: Pushover curve of A2b-3D-RD-a model

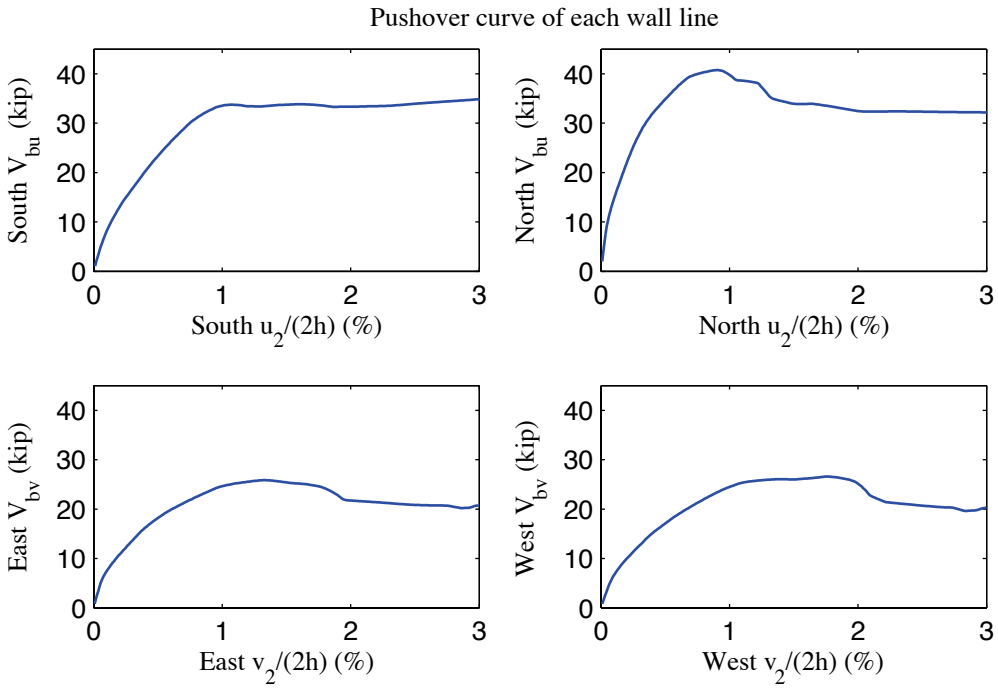

Figure N-4: Pushover curve of each wall line, A2b-3D-RD-a model

N.5 Linear time history analysis results

Linear time history analysis is performed on the model under Canoga Park and Rinaldi ground motion records of Northridge earthquake in 1994. We considered three scale levels (16%, 44% and 100%) and loadings in one, two and three axes.

Table N-6 to Table N-9 demonstrate the building's linear elastic performance under designated ground motions. Table N-6 shows peak story relative accelerations in the unit of g. Table N-7 and Table N-8 report peak roof drift and story drift of the building and the corresponding time step (t_*) and the base shear at that time. Note that the base shear at the time of peak roof drift may not be the peak total building base shear in that direction (see Table N-9).

The building behaves linearly since peak drift and peak base shear appear at the same time when the ground motion is linearly scaled. Figure N-5 is a vector plot of the peak total resultant base shear of the building under three axial, 100% Canoga Park excitation. The directions of arrows imply that base shear taken by shear walls and gravity systems does not necessarily follow the direction of wall lines due to the effect of 3D coupling. Comparison with nonlinear analysis results of the same excitation provides insightful observations on the building's response and requirements on modeling fidelity and analysis type.

Table N-6: A2b-3D-RD-a model peak story relative acceleration in g, linear time history analysis

		LONG			SHORT			UP		
Load Case	**Ground Motion**	**a_g**	**Floor a**	**Roof a**	**a_g**	**Floor a**	**Roof a**	**a_g**	**Floor a**	**Roof a**
EQ_3D_3axis_1	CNP 16%	0.067	0.080	0.122	0.057	0.153	0.239	0.078	0.095	0.091
EQ_3D_3axis_2	CNP 44%	0.185	0.215	0.342	0.157	0.430	0.699	0.215	0.582	0.517
EQ_3D_1axis_1	CNP 100%	0.420	0.526	0.783	0	0.132	0.206	0	0.309	0.287
EQ_3D_1axis_2	CNP 100%	0	0.179	0.270	0.356	1.027	1.667	0	1.100	1.003
EQ_3D_2axis_1	CNP 100%	0.420	0.496	0.798	0.356	1.017	1.669	0	0.658	0.584
EQ_3D_3axis_3	CNP 100%	0.420	0.496	0.798	0.356	1.017	1.669	0.489	0.658	0.584
EQ_3D_3axis_4	RRS 16%	0.132	0.152	0.251	0.078	0.193	0.314	0.133	0.147	0.125
EQ_3D_3axis_5	RRS 44%	0.363	0.418	0.684	0.214	0.575	0.944	0.367	0.559	0.516
EQ_3D_3axis_6	RRS 100%	0.825	0.962	1.553	0.486	1.391	2.306	0.834	1.747	1.605

Table N-7: A2b-3D-RD-a model peak building roof drift and base shear, linear time history analysis

		LONG			SHORT		
Load Case	**Ground Motion**	**$u_2/(2h)$ (%)**	**t_* (s)**	**V_b @ t_* (kips)**	**$v_2/(2h)$ (%)**	**t_* (s)**	**V_b @ t_* (kips)**
EQ_3D_3axis_1	CNP 16%	0.026	6.26	8.8	0.089	9.90	15.4
EQ_3D_3axis_2	CNP 44%	0.072	6.26	24.6	0.259	9.90	44.1
EQ_3D_1axis_1	CNP 100%	0.161	7.35	52.3	-0.039	8.22	7.6
EQ_3D_1axis_2	CNP 100%	-0.056	7.38	14.8	0.623	9.90	104.3
EQ_3D_2axis_1	CNP 100%	0.164	6.27	57.2	0.619	9.90	103.3
EQ_3D_3axis_3	CNP 100%	0.164	6.27	57.2	0.619	9.90	103.3
EQ_3D_3axis_4	RRS 16%	0.058	2.57	18.3	-0.116	4.31	18.5
EQ_3D_3axis_5	RRS 44%	0.160	2.58	50.1	-0.335	4.31	53.0
EQ_3D_3axis_6	RRS 100%	0.367	2.58	113.6	-0.793	4.31	124.6

Table N-8: A2b-3D-RD-a model peak building story drift, linear time history analysis

		LONG				SHORT			
Load Case	**Ground Motion**	**$\Delta u_1/h$ (%)**	**t_* (s)**	**$\Delta u_2/h$ (%)**	**t_* (s)**	**$\Delta v_1/h$ (%)**	**t_* (s)**	**$\Delta v_2/h$ (%)**	**t_* (s)**
EQ_3D_3axis_1	CNP 16%	0.034	6.26	0.018	6.26	0.113	9.89	0.065	9.90
EQ_3D_3axis_2	CNP 44%	0.094	6.26	0.050	6.26	0.326	9.90	0.192	9.90
EQ_3D_1axis_1	CNP 100%	0.207	7.35	0.114	7.35	-0.046	8.22	-0.032	8.22
EQ_3D_1axis_2	CNP 100%	-0.070	7.38	0.043	9.76	0.781	9.90	0.465	9.90
EQ_3D_2axis_1	CNP 100%	0.215	6.27	0.115	6.26	0.776	9.90	0.465	9.91
EQ_3D_3axis_3	CNP 100%	0.215	6.27	0.115	6.26	0.776	9.90	0.465	9.91
EQ_3D_3axis_4	RRS 16%	0.076	2.57	0.039	2.57	-0.142	4.31	-0.090	4.30
EQ_3D_3axis_5	RRS 44%	0.211	2.58	0.110	2.58	-0.412	4.31	-0.259	4.31
EQ_3D_3axis_6	RRS 100%	0.481	2.58	0.252	2.58	-0.975	4.32	-0.613	4.31

Table N-9: A2b-3D-RD-a model peak building base shear, linear time history analysis

		LONG		SHORT		RESULTANT	
Load Case	**Ground Motion**	**Peak V_{bu} (kip)**	**t @ peak V_{bu} (s)**	**Peak V_{bv} (kip)**	**t @ peak V_{bv} (s)**	**Peak V_b (kip)**	**t @ peak V_b (s)**
EQ_3D_3axis_1	CNP 16%	8.8	6.27	15.4	9.89	15.9	9.90
EQ_3D_3axis_2	CNP 44%	25.0	6.27	44.1	9.90	45.2	9.90
EQ_3D_1axis_1	CNP 100%	53.7	6.27	8.5	6.02	53.7	6.27
EQ_3D_1axis_2	CNP 100%	14.8	7.38	104.3	9.90	104.7	9.90
EQ_3D_2axis_1	CNP 100%	57.2	6.27	103.3	9.90	105.8	9.90
EQ_3D_3axis_3	CNP 100%	57.2	6.27	103.3	9.90	105.8	9.90
EQ_3D_3axis_4	RRS 16%	18.3	2.57	18.5	4.31	20.6	4.30
EQ_3D_3axis_5	RRS 44%	50.1	2.58	53.0	4.31	59.8	4.31
EQ_3D_3axis_6	RRS 100%	113.6	2.58	125.1	4.32	142.9	4.31

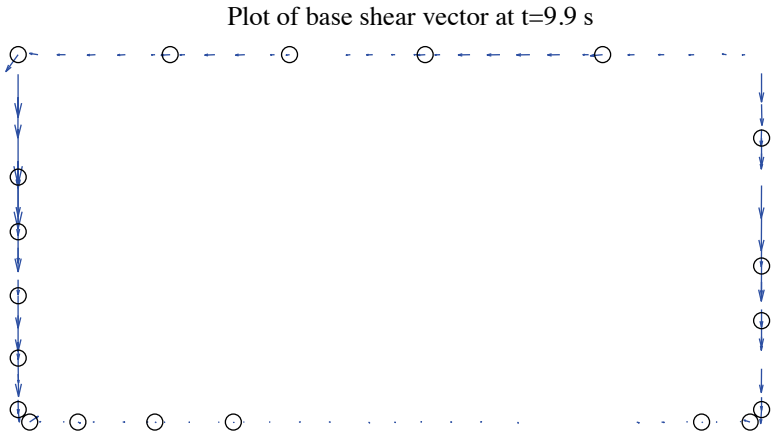

Figure N-5: A2b-3D-RD-a model, base shear vector plot at the moment of peak total base shear, 100 % Canoga Park, 3D linear analysis (maximum anchor/hold down base shear is 6.57 kips)

N.6 Nonlinear time history analysis results

Same ground motions are applied to the model with material and geometrical nonlinearity. Table N-10 to Table N-13 are replicas of Table N-6 to Table N-9, but for nonlinear time history analyses. Since this analysis type is most complicated and closest to reality and experiments, behavior of wall lines and hold downs are further studied. Table N-14 is the table of peak wall line story drifts and corresponding time steps. Table N-15 is designed for peak base shear of each wall line and the last two columns of the table are percentages of base shear of two facing wall lines in the same direction when the total base shear in that direction takes peak value. Table N-16 expands the breakdown of each wall line's peak base shear between shear walls, gravity walls and other systems. Table N-17 is peak value of hold down tensile force of two selected pairs. Hold down 5 and 6 are on shear wall L1S1, South elevation and hold down 7 and 8 are on shear wall L1W1, West elevation. These shear walls have lowest capacities compared with others on the same wall line and they meet at the southwest edge of the building, so interacted nonlinear behavior is expected to appear.

Time history plots in this section include plots of story drifts of the building and each wall line (Figure N-6 to Figure N-8), total building base shear in long and short direction (Figure N-9) and axial forces of hold downs in Table N-17 (Figure N-10). Hysteretic plots in Figure N-11 and Figure N-12 are helpful for visual examination of nonlinear base shear-drift relationship of the building and the weakest shear wall on each wall line. In comparison with linear time history analysis, vector plot of peak total base shear is illustrated in Figure N-13. Figure N-14 presents a simplified deformed shape of the

building (see (Peterman 2014) for details of the method) and axial force of all twenty hold downs at the moment of peak total base shear. The same sign convention with tests is adopted. Red bars indicate tensile (negative) force and blue ones are for compressive (positive) force.

Hysteretic behavior is seen in the building and typical shear walls under design-based earthquake (100% Canoga Park excitation in 3 axes, see Figure N-11 and Figure N-12). Even though post-peak response on the backbone curve is not initiated under this excitation level, wall lines behave differently. West wall line reaches 0.98% peak floor story drift but peak story drifts of all other wall lines are less than 0.68% (Table N-14). Given the significantly increased capacity and stiffness in long direction, peak story drift of long direction is less than short direction (0.57% vs. 0.81%, Table N-12). Figure N-13 clearly shows that base shear vectors in anchors and hold downs do not align with wall lines, a sign of coupled wall line behavior. Table N-17, Figure N-10 and Figure N-14 demonstrate that hold downs in a pair do not experience the same amount of force with opposite signs, an evidence that supports Type II shear wall behavior despite Type I design assumption.

The near-field Rinaldi record is much stronger in terms of peak ground acceleration, especially in the long direction. With the additional lateral force resistance provided by sheathed gravity walls, simulation results show that the building can survive even 100% Rinaldi ground motion, the maximum considered earthquake in this research. This time, long direction story drift is about 1.8%, close to threshold value of post-peak response

(arguably 2%) on the backbone curve and is larger than short direction value. The portion of base shear taken by gravity wall does not change much with scale factors considered so far in this research, as shown in Table N-16. Again, the table demonstrates that the base shear taken by anchors on bottom tracks of gravity walls can be quite large, sometimes even larger than half of the total base shear (e.g. South wall lines).

Table N-10: A2b-3D-RD-a model peak story relative acceleration in g, nonlinear time history analysis

		LONG			SHORT			UP		
Load Case	**Ground Motion**	**a_g**	**Floor a**	**Roof a**	**a_g**	**Floor a**	**Roof a**	**a_g**	**Floor a**	**Roof a**
EQ_3D_3axis_1	CNP 16%	0.067	0.172	0.180	0.057	0.203	0.242	0.078	0.094	0.093
EQ_3D_3axis_2	CNP 44%	0.185	0.345	0.407	0.157	0.223	0.324	0.215	0.086	0.089
EQ_3D_1axis_1	CNP 100%	0.420	0.620	0.952	0	0.053	0.071	0	0.161	0.139
EQ_3D_1axis_2	CNP 100%	0	0.152	0.144	0.356	0.578	0.821	0	0.227	0.203
EQ_3D_2axis_1	CNP 100%	0.420	0.685	0.999	0.356	0.621	0.767	0	1.400	1.272
EQ_3D_3axis_3	CNP 100%	0.420	0.685	0.999	0.356	0.621	0.767	0.489	1.400	1.272
EQ_3D_3axis_4	RRS 16%	0.132	0.195	0.223	0.078	0.259	0.323	0.133	0.151	0.146
EQ_3D_3axis_5	RRS 44%	0.363	0.508	0.699	0.214	0.457	0.621	0.367	0.178	0.157
EQ_3D_3axis_6	RRS 100%	0.825	1.180	1.613	0.486	0.708	1.114	0.834	0.969	0.902

Table N-11: A2b-3D-RD-a model peak building roof drift and base shear, nonlinear time history analysis

		LONG			SHORT		
Load Case	**Ground Motion**	**$u_2/(2h)$ (%)**	**t_* (s)**	**V_b @ t_* (kips)**	**$v_2/(2h)$ (%)**	**t_* (s)**	**V_b @ t_* (kips)**
EQ_3D_3axis_1	CNP 16%	0.028	6.28	8.8	0.088	9.95	13.2
EQ_3D_3axis_2	CNP 44%	0.108	8.66	24.0	-0.143	8.43	15.3
EQ_3D_1axis_1	CNP 100%	-0.349	10.52	48.3	-0.019	8.01	2.5
EQ_3D_1axis_2	CNP 100%	-0.030	10.01	0.9	0.606	10.00	37.7
EQ_3D_2axis_1	CNP 100%	-0.383	10.52	48.9	0.640	10.01	38.6
EQ_3D_3axis_3	CNP 100%	-0.383	10.52	48.9	0.640	10.01	38.6
EQ_3D_3axis_4	RRS 16%	0.057	2.80	14.9	-0.105	4.39	13.9
EQ_3D_3axis_5	RRS 44%	0.261	4.39	41.4	0.357	3.89	29.2
EQ_3D_3axis_6	RRS 100%	1.114	2.71	70.1	-0.780	2.59	42.4

Table N-12: A2b-3D-RD-a model peak building story drift, nonlinear linear time history analysis

		LONG				SHORT			
Load Case	**Ground Motion**	**$\Delta u_1/h$ (%)**	**t_* (s)**	**$\Delta u_2/h$ (%)**	**t_* (s)**	**$\Delta v_1/h$ (%)**	**t_* (s)**	**$\Delta v_2/h$ (%)**	**t_* (s)**
EQ_3D_3 axis_1	CNP 16%	0.039	5.01	-0.022	4.05	0.118	9.94	-0.062	10.47
EQ_3D_3 axis_2	CNP 44%	0.154	8.66	-0.062	11.87	-0.201	8.43	-0.086	10.18
EQ_3D_1 axis_1	CNP 100%	0.525	8.71	-0.229	10.51	-0.024	7.75	-0.018	8.30
EQ_3D_1 axis_2	CNP 100%	-0.041	10.04	-0.030	10.00	0.775	10.02	0.462	9.99
EQ_3D_2 axis_1	CNP 100%	0.570	8.71	-0.271	10.52	0.807	10.02	0.502	10.00
EQ_3D_3 axis_3	CNP 100%	0.570	8.71	-0.271	10.52	0.807	10.02	0.502	10.00
EQ_3D_3 axis_4	RRS 16%	0.079	2.58	0.038	2.79	-0.155	4.39	-0.072	4.74
EQ_3D_3 axis_5	RRS 44%	0.379	4.39	0.148	4.40	0.482	3.89	0.231	3.89
EQ_3D_3 axis_6	RRS 100%	1.849	2.70	-0.407	3.98	-1.010	2.60	-0.564	2.58

Table N-13: A2b-3D-RD-a model peak building base shear, nonlinear time history analysis

		LONG		SHORT		RESULTANT	
Load Case	**Ground Motion**	**Peak V_{bu} (kip)**	**t @ peak V_{bu} (s)**	**Peak V_{bv} (kip)**	**t @ peak V_{bv} (s)**	**Peak V_b (kip)**	**t @ peak V_b (s)**
EQ_3D_3axis_1	CNP 16%	9.8	5.01	13.2	9.94	13.8	9.94
EQ_3D_3axis_2	CNP 44%	24.1	8.65	17.1	9.95	24.1	8.65
EQ_3D_1axis_1	CNP 100%	51.4	8.71	3.4	7.75	51.4	8.71
EQ_3D_1axis_2	CNP 100%	3.9	9.87	38.4	10.01	38.4	10.01
EQ_3D_2axis_1	CNP 100%	53.2	8.71	38.6	10.01	53.2	8.71
EQ_3D_3axis_3	CNP 100%	53.2	8.71	38.6	10.01	53.2	8.71
EQ_3D_3axis_4	RRS 16%	16.2	2.58	15.1	4.54	16.9	4.22
EQ_3D_3axis_5	RRS 44%	42.6	4.38	29.2	3.89	42.7	4.38
EQ_3D_3axis_6	RRS 100%	73.6	2.62	42.4	2.59	82.0	2.60

Table N-14: A2b-3D-RD-a model peak wall line story drift, nonlinear time history analysis

LONG		SOUTH				NORTH			
Load Case	**Ground Motion**	**$\Delta u_1/h$ (%)**	**t_* (s)**	**$\Delta u_2/h$ (%)**	**t_* (s)**	**$\Delta u_1/h$ (%)**	**t_* (s)**	**$\Delta u_2/h$ (%)**	**t_* (s)**
EQ_3D_3axis_1	CNP 16%	0.044	6.26	0.028	11.82	0.040	5.00	0.026	4.92
EQ_3D_3axis_2	CNP 44%	0.168	8.67	0.072	11.87	0.147	8.64	0.061	8.65
EQ_3D_1axis_1	CNP 100%	0.529	8.71	0.237	10.51	0.522	8.71	0.221	10.51
EQ_3D_1axis_2	CNP 100%	0.108	10.04	0.068	10.00	0.027	10.03	0.021	24.29
EQ_3D_2axis_1	CNP 100%	0.598	8.71	0.290	10.52	0.543	8.71	0.253	10.52
EQ_3D_3axis_3	CNP 100%	0.598	8.71	0.290	10.52	0.543	8.71	0.253	10.52
EQ_3D_3axis_4	RRS 16%	0.096	2.58	0.049	2.79	0.067	4.32	0.034	7.22
EQ_3D_3axis_5	RRS 44%	0.407	4.40	0.152	4.57	0.370	4.38	0.145	4.40
EQ_3D_3axis_6	RRS 100%	1.936	2.70	0.466	3.98	1.779	2.73	0.349	3.98
SHORT		**EAST**				**WEST**			
Load Case	**Ground Motion**	**$\Delta v_1/h$ (%)**	**t_* (s)**	**$\Delta v_2/h$ (%)**	**t_* (s)**	**$\Delta v_1/h$ (%)**	**t_* (s)**	**$\Delta v_2/h$ (%)**	**t_* (s)**
EQ_3D_3axis_1	CNP 16%	0.084	9.95	0.062	10.48	0.153	9.94	0.073	9.95
EQ_3D_3axis_2	CNP 44%	0.141	7.19	0.081	5.95	0.295	8.42	0.125	9.96
EQ_3D_1axis_1	CNP 100%	0.060	2.61	0.038	7.55	0.052	7.45	0.037	7.44
EQ_3D_1axis_2	CNP 100%	0.650	10.00	0.379	9.99	0.910	10.02	0.545	9.99
EQ_3D_2axis_1	CNP 100%	0.678	10.00	0.392	9.99	0.982	10.04	0.617	10.00
EQ_3D_3axis_3	CNP 100%	0.678	10.00	0.392	9.99	0.982	10.04	0.617	10.00
EQ_3D_3axis_4	RRS 16%	0.128	3.15	0.061	4.57	0.204	4.39	0.089	4.74
EQ_3D_3axis_5	RRS 44%	0.407	6.07	0.186	6.04	0.591	3.43	0.291	4.45
EQ_3D_3axis_6	RRS 100%	0.854	2.58	0.470	4.38	1.299	6.10	0.694	2.58

Table N-15: A2b-3D-RD-a model peak wall line base shear, nonlinear time history analysis

LONG		SOUTH		NORTH		% of Peak V_{bu}	
Load Case	**Ground Motion**	**Peak V_{bu} (kips)**	**t @ peak V_{bu} (s)**	**Peak V_{bu} (kips)**	**t @ peak V_{bu} (s)**	**South**	**North**
EQ_3D_3axis_1	CNP 16%	3.3	6.26	6.9	5.01	29.4	70.1
EQ_3D_3axis_2	CNP 44%	9.4	8.67	15.1	8.65	37.0	62.7
EQ_3D_1axis_1	CNP 100%	20.0	8.71	31.4	8.71	38.8	61.0
EQ_3D_1axis_2	CNP 100%	6.6	10.04	4.9	10.03	110.5	8.1
EQ_3D_2axis_1	CNP 100%	21.3	8.72	31.8	8.71	40.1	59.8
EQ_3D_3axis_3	CNP 100%	21.3	8.72	31.8	8.71	40.1	59.8
EQ_3D_3axis_4	RRS 16%	6.5	2.58	10.1	4.32	39.8	60.0
EQ_3D_3axis_5	RRS 44%	16.7	4.40	26.6	4.38	37.1	62.5
EQ_3D_3axis_6	RRS 100%	33.1	2.62	40.6	2.62	45.0	55.1
SHORT		**EAST**		**WEST**		**% of Peak V_{bv}**	
Load Case	**Ground Motion**	**Peak V_{bv} (kips)**	**t @ peak V_{bv} (s)**	**Peak V_{bv} (kips)**	**t @ peak V_{bv} (s)**	**East**	**West**
EQ_3D_3axis_1	CNP 16%	5.9	9.94	7.3	9.95	44.6	55.1
EQ_3D_3axis_2	CNP 44%	7.5	7.19	10.3	8.42	41.2	58.5
EQ_3D_1axis_1	CNP 100%	4.3	2.51	3.0	7.56	112.4	10.9
EQ_3D_1axis_2	CNP 100%	18.1	10.01	20.5	10.02	47.2	52.6
EQ_3D_2axis_1	CNP 100%	18.5	10.00	21.1	10.04	47.7	52.7
EQ_3D_3axis_3	CNP 100%	18.5	10.00	21.1	10.04	47.7	52.7
EQ_3D_3axis_4	RRS 16%	7.0	3.15	8.5	4.55	43.0	56.3
EQ_3D_3axis_5	RRS 44%	13.9	6.07	16.3	3.43	45.7	53.6
EQ_3D_3axis_6	RRS 100%	20.3	6.04	24.1	6.10	45.7	52.5

Table N-16: A2b-3D-RD-a model wall line base shear breakdown, nonlinear time history analysis

LONG		SOUTH			NORTH		
Load Case	**Ground Motion**	**Peak V_{bu} (kips)**	**SW V_{bu} (%)**	**GW V_{bu} (%)**	**Peak V_{bu} (kips)**	**SW V_{bu} (%)**	**GW V_{bu} (%)**
EQ_3D_3axis_1	CNP 16%	3.3	37.6	62.4	6.9	63.8	36.2
EQ_3D_3axis_2	CNP 44%	9.4	41.7	58.3	15.1	60.4	39.6
EQ_3D_1axis_1	CNP 100%	20.0	40.3	59.7	31.4	55.5	44.5
EQ_3D_1axis_2	CNP 100%	6.6	38.5	61.5	4.9	64.5	35.5
EQ_3D_2axis_1	CNP 100%	21.3	39.1	60.9	31.8	55.7	44.3
EQ_3D_3axis_3	CNP 100%	21.3	39.1	60.9	31.8	55.7	44.3
EQ_3D_3axis_4	RRS 16%	6.5	39.7	60.3	10.1	62.5	37.5
EQ_3D_3axis_5	RRS 44%	16.7	41.0	59.0	26.6	55.7	44.3
EQ_3D_3axis_6	RRS 100%	33.1	40.9	59.1	40.6	55.8	44.2
SHORT		**EAST**			**WEST**		
Load Case	**Ground Motion**	**Peak V_{bv} (kips)**	**SW V_{bv} (%)**	**GW V_{bu} (%)**	**Peak V_{bv} (kips)**	**SW V_{bv} (%)**	**GW V_{bv} (%)**
EQ_3D_3axis_1	CNP 16%	5.9	77.8	22.2	7.3	84.1	15.9
EQ_3D_3axis_2	CNP 44%	7.5	76.9	23.1	10.3	83.0	17.0
EQ_3D_1axis_1	CNP 100%	4.3	75.9	24.1	3.0	80.8	19.2
EQ_3D_1axis_2	CNP 100%	18.1	73.5	26.5	20.5	83.1	16.9
EQ_3D_2axis_1	CNP 100%	18.5	73.7	26.3	21.1	83.3	16.7
EQ_3D_3axis_3	CNP 100%	18.5	73.7	26.3	21.1	83.3	16.7
EQ_3D_3axis_4	RRS 16%	7.0	77.5	22.5	8.5	84.0	16.0
EQ_3D_3axis_5	RRS 44%	13.9	72.4	27.6	16.3	81.4	18.6
EQ_3D_3axis_6	RRS 100%	20.3	73.8	26.2	24.1	83.8	16.2

Table N-17: A2b-3D-RD-a model peak hold down tensile force at certain locations, nonlinear time history analysis

		L1S1, LC5		L1S1, LC6		L1W1, LC7		L1W1, LC8	
Load Case	**Ground Motion**	**Peak F (kips)**	**t @ peak F (s)**	**Peak F (kips)**	**t @ peak F (s)**	**Peak F (kips)**	**t @ peak F (s)**	**Peak F (kips)**	**t @ peak F (s)**
EQ_3D_3axis_1	CNP 16%	-0.39	9.66	-0.20	9.94	-0.13	9.94	-0.51	9.80
EQ_3D_3axis_2	CNP 44%	-1.13	12.14	-0.33	9.96	-0.21	9.95	-0.63	8.41
EQ_3D_1axis_1	CNP 100%	-2.18	10.52	-0.28	8.69	-0.56	8.69	-0.43	10.35
EQ_3D_1axis_2	CNP 100%	-2.03	10.00	-1.11	10.00	-0.54	10.00	-1.01	5.99
EQ_3D_2axis_1	CNP 100%	-2.26	10.52	-1.67	10.01	-1.31	9.41	-1.10	10.29
EQ_3D_3axis_3	CNP 100%	-2.26	10.52	-1.67	10.01	-1.31	9.41	-1.10	10.29
EQ_3D_3axis_4	RRS 16%	-0.67	4.22	-0.21	4.55	-0.12	4.56	-0.58	4.38
EQ_3D_3axis_5	RRS 44%	-2.02	4.25	-0.60	3.90	-0.36	4.39	-0.85	4.10
EQ_3D_3axis_6	RRS 100%	-2.79	3.11	-1.10	6.07	-0.91	2.71	-1.66	2.61

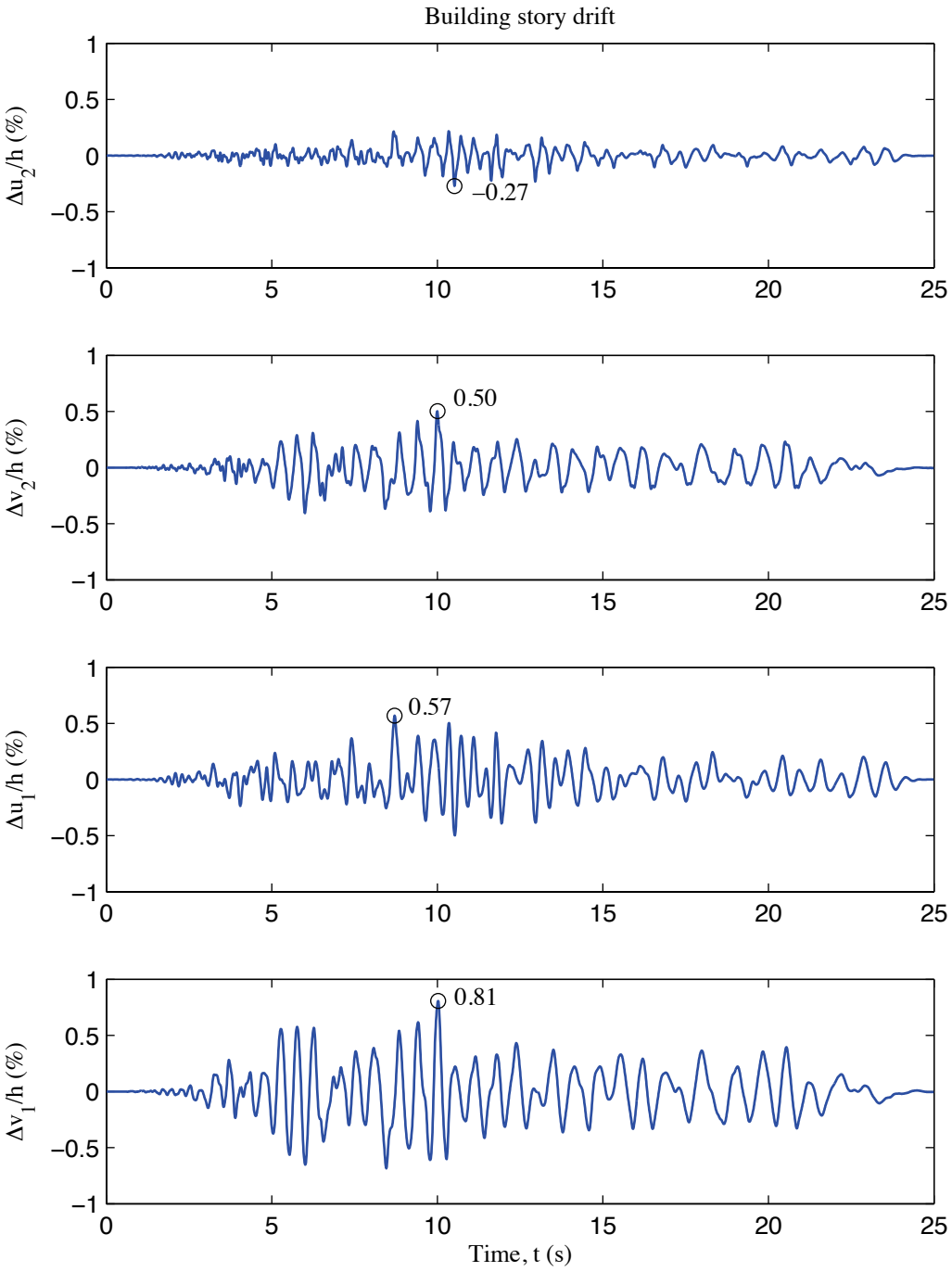

Figure N-6: A2b-3D-RD-a model building story drift, 100 % Canoga Park, 3D nonlinear analysis

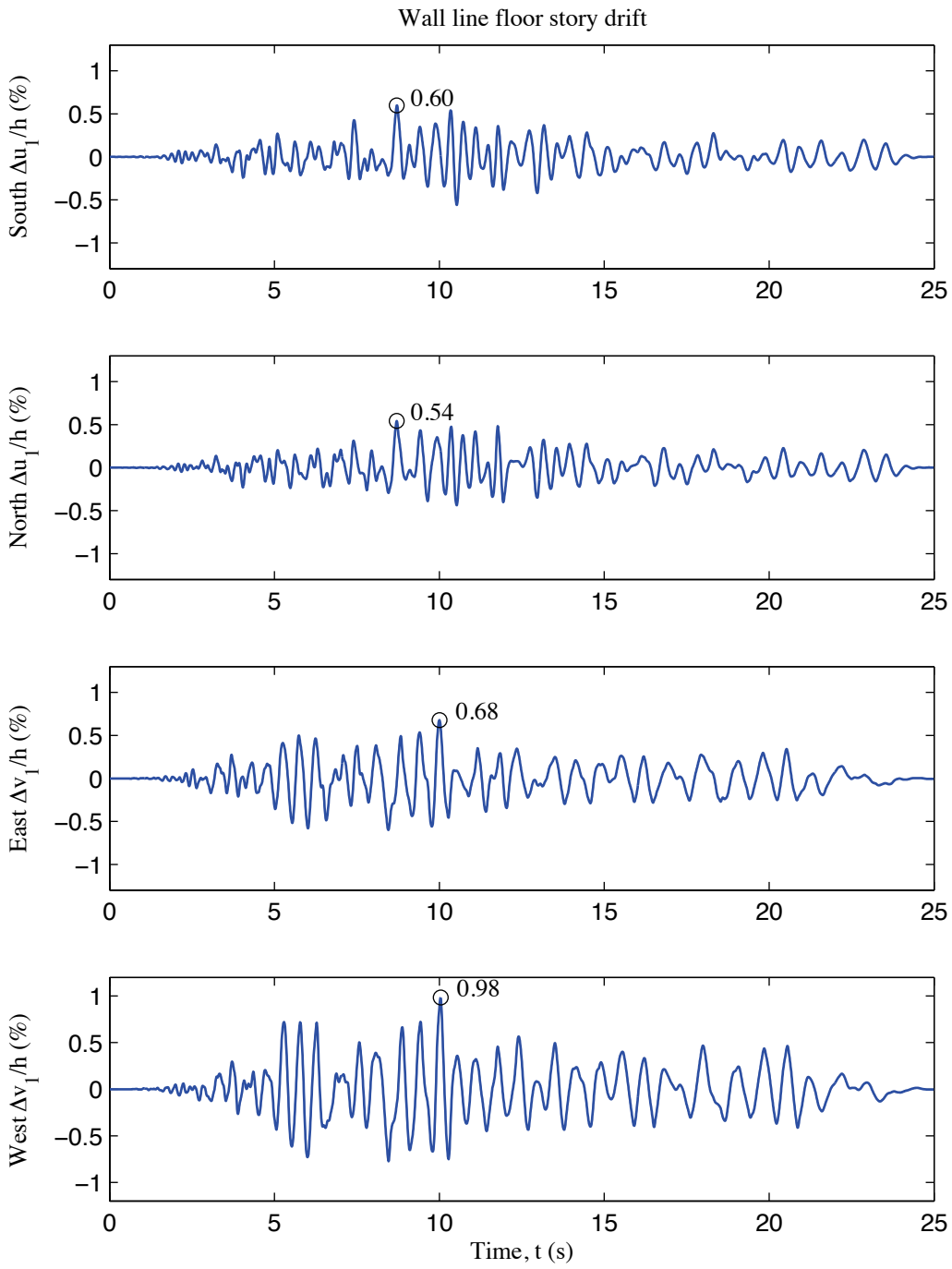

Figure N-7: A2b-3D-RD-a model wall line floor story drift, 100 % Canoga Park, 3D nonlinear analysis

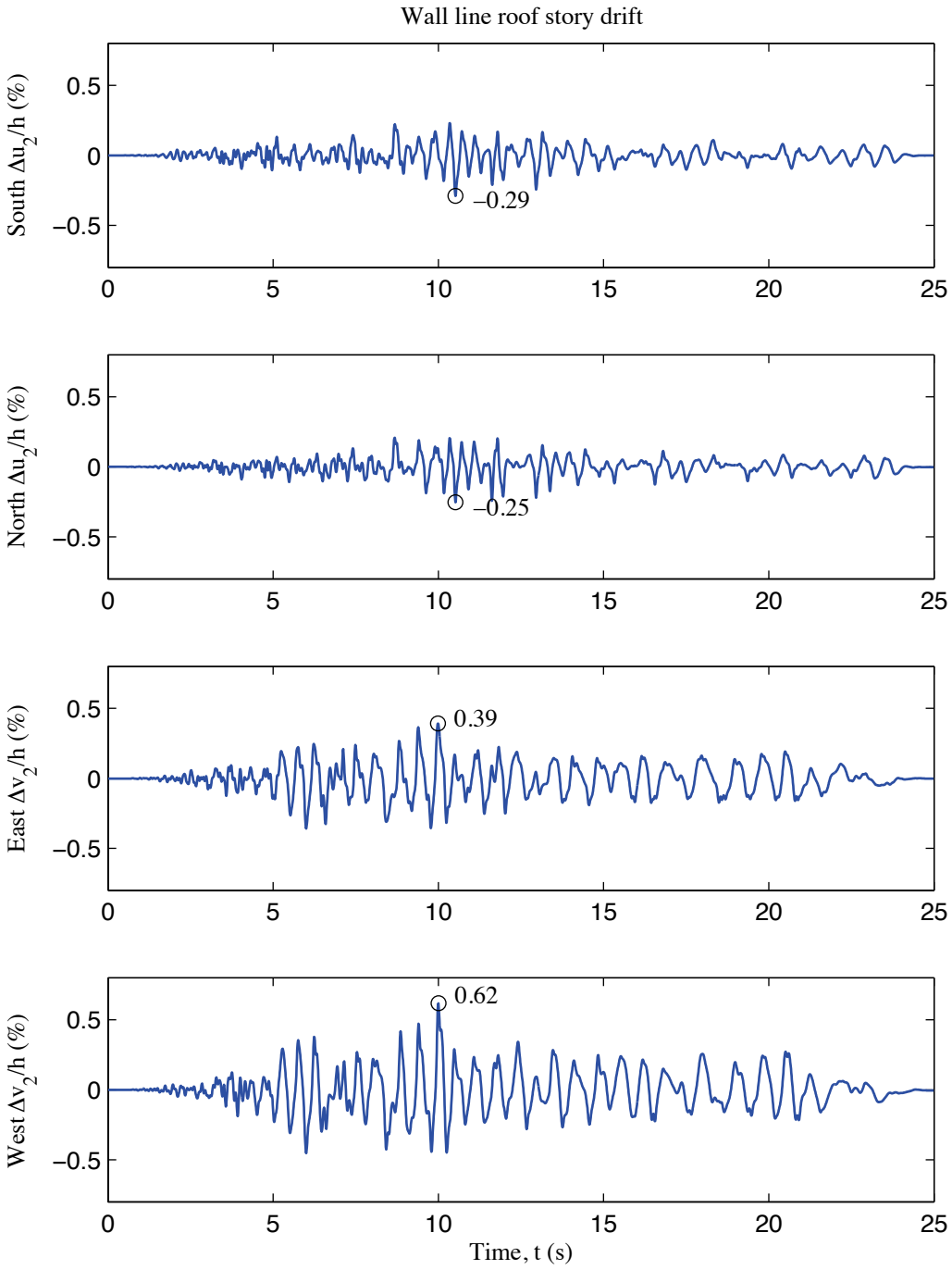

Figure N-8: A2b-3D-RD-a model wall line roof story drift, 100 % Canoga Park, 3D nonlinear analysis

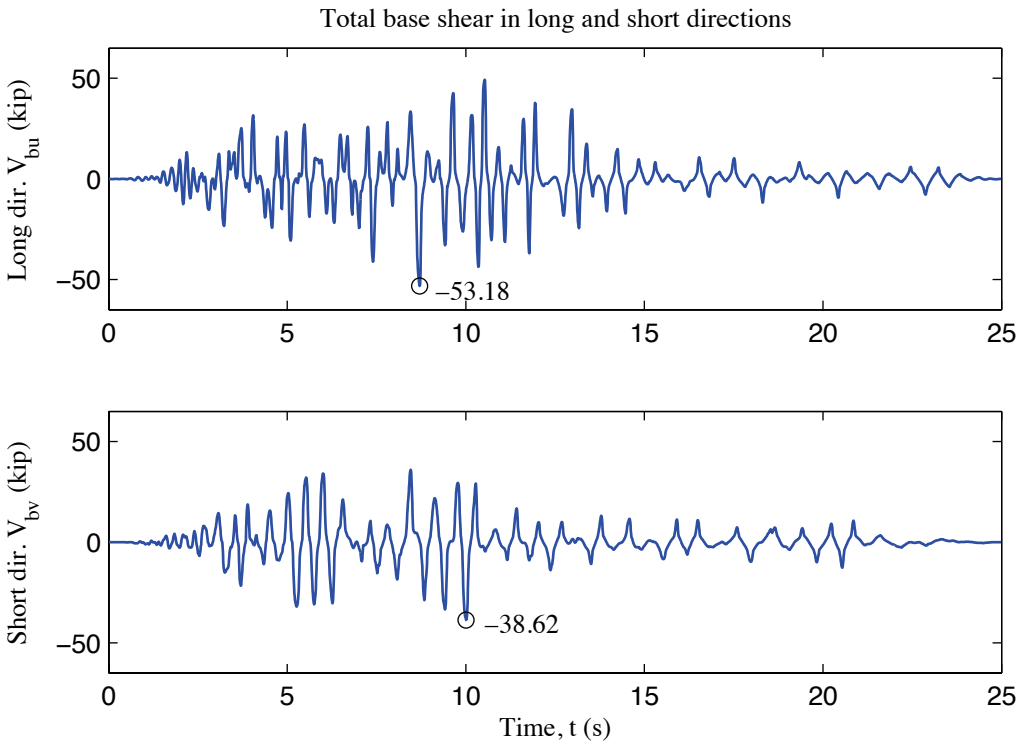

Figure N-9: A2b-3D-RD-a model total building base shear, 100 % Canoga Park, 3D nonlinear analysis

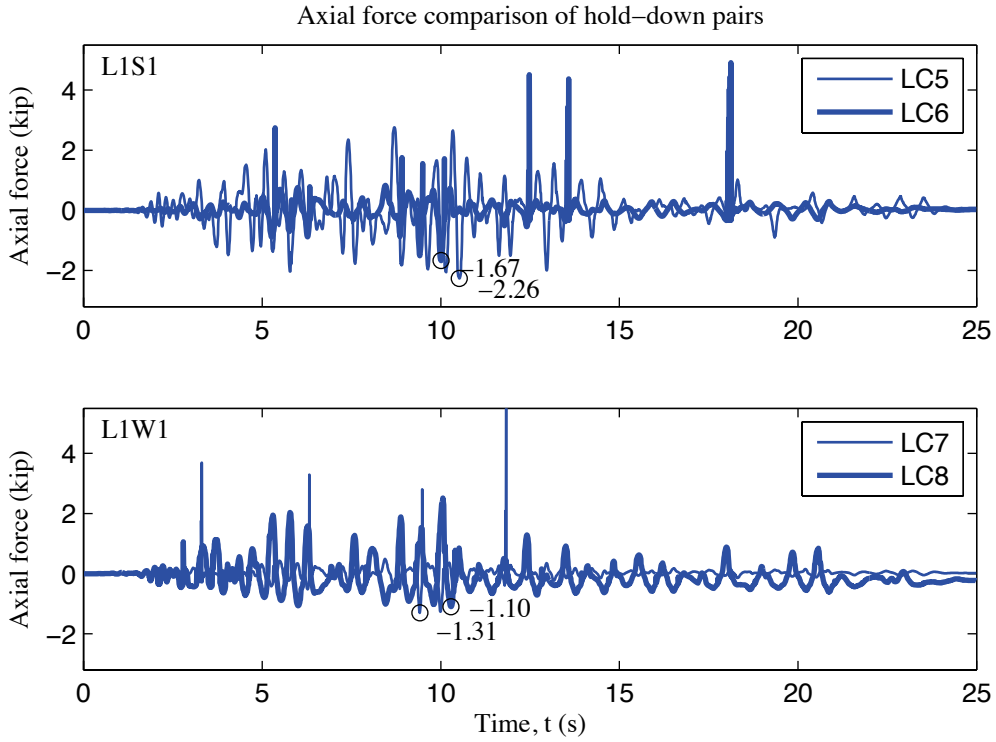

Figure N-10: A2b-3D-RD-a model, load cell 5 to 8 axial forces, 100 % Canoga Park, 3D nonlinear analysis

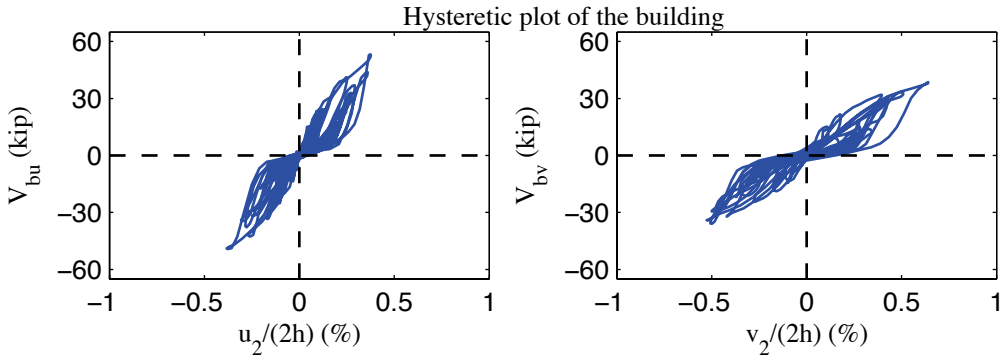

Figure N-11: A2b-3D-RD-a model, hysteretic plot of the building, 100 % Canoga Park, 3D nonlinear analysis

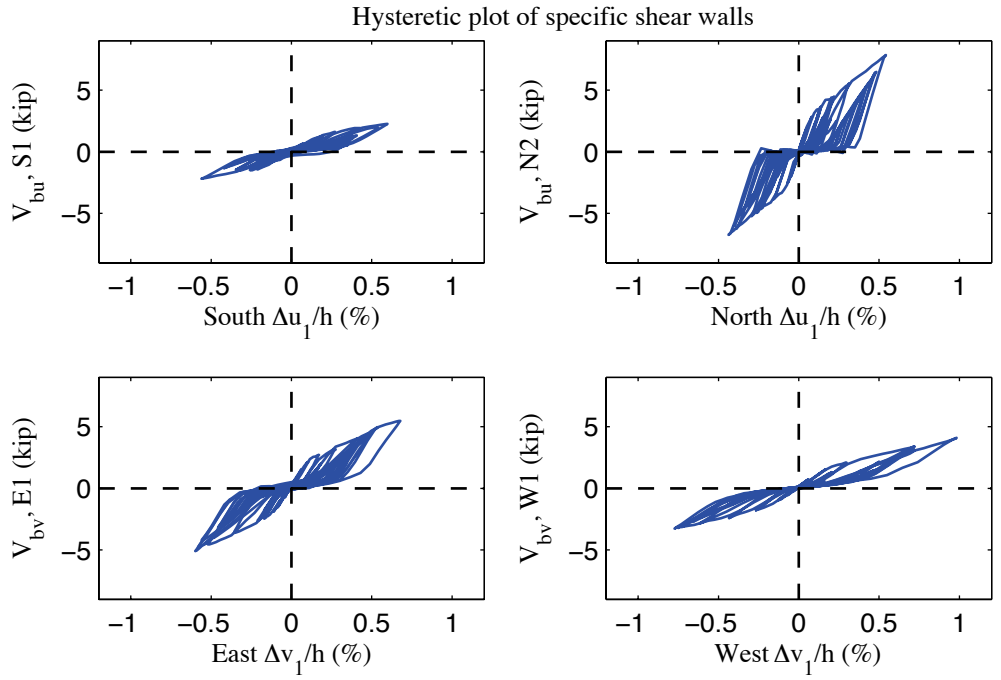

Figure N-12: A2b-3D-RD-a model, hysteretic plot of shear walls at each elevation, 100 % Canoga Park, 3D nonlinear analysis

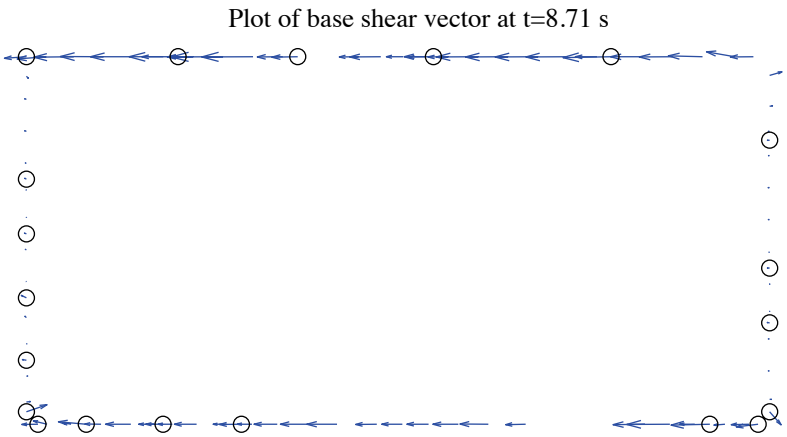

Figure N-13: A2b-3D-RD-a model, field plot of peak total base shear, 100 % Canoga Park, 3D nonlinear analysis (maximum anchor/hold down base shear is 1.76 kips)

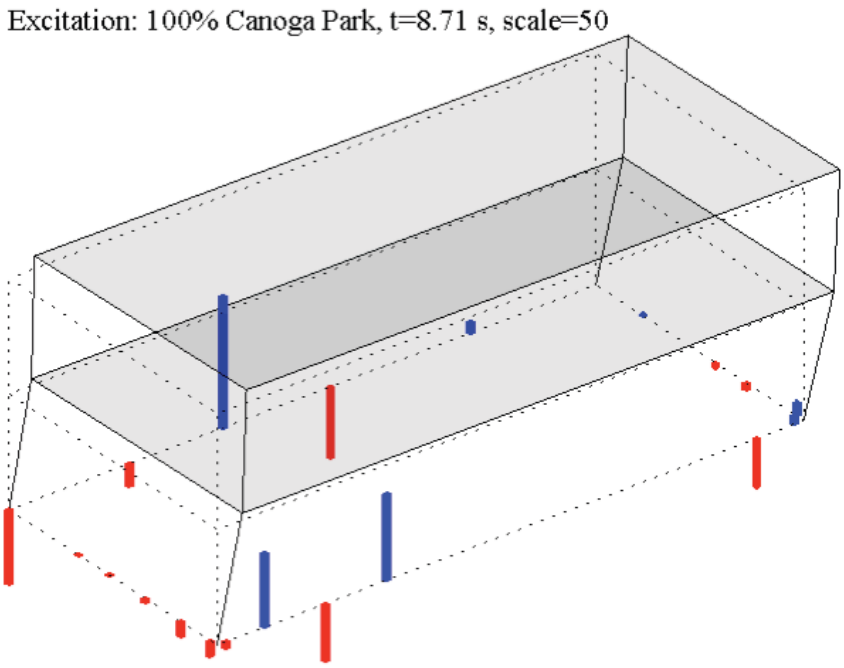

Figure N-14: A2b-3D-RD-a model, simplified illustration of corner displacements with hold down forces from load cells,100 % Canoga Park, 3D nonlinear analysis (max hold down tensile force is -2.76 kips)

Appendix O: Analysis Results of State-of-the-art, Phase 2b, 3D, semirigid-diaphragm, model a (A2b-3D-SD-a)

O.1 Model description

This state-of-the-art 3D model features subpanel bracing models of shear walls and gravity walls, explicit models of hold downs, and semi-rigid diaphragms modeled by subpanel bracings. All walls are covered by OSB sheathing. Seismic mass is distributed to corners and stud ends. The lateral displacement and shear wall capacity ($\delta(0.2V_{nA})$, $0.2V_{nA}$) from test is utilized to determine the stiffness of elastic material and the first point on the backbone curve of Pinching4 material of shear wall bracing. Figure O-1 is the 3D drawing of the building model with all members and diagonal bracings of sheathing panels. Definitions of output physical quantities and explanation of post-process method can be found in Appendix K.

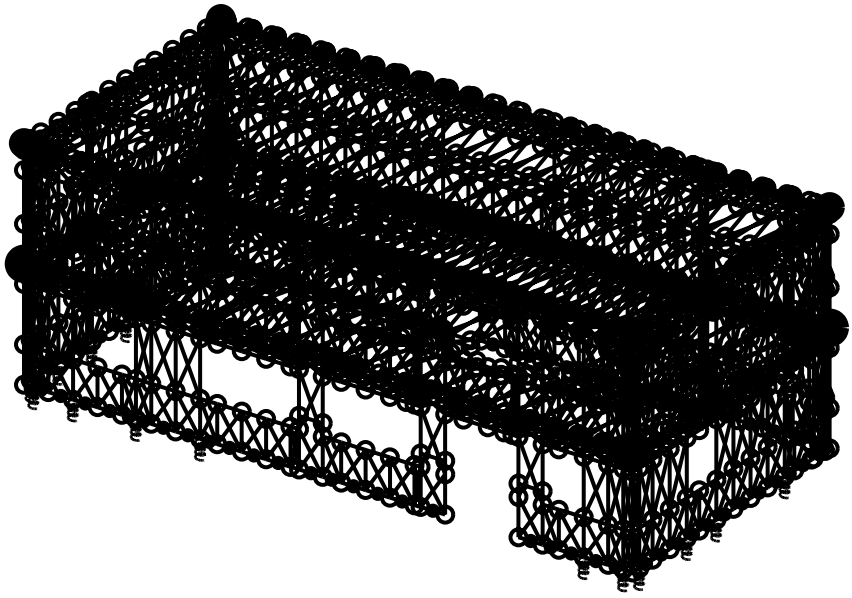

Figure O-1: A2b-3D-SD-a model

O.2 Free vibration analysis results

Free vibration analysis results are presented in Table O-1 and Figure O-2. Lateral stiffness in the short direction is smaller than lateral stiffness in the long direction and torsional stiffness is the largest. The observation holds for the first and the second mode, as indicated by Table O-1.

Table O-1: Free vibration analysis results, A2b-3D-SD-a model

Mode number	Natural period (s)	Mode description
1	0.282	Short, 1st
2	0.218	Long, 1st
3	0.173	Torsion, 1st
4	0.125	Short, 2nd
5	0.088	Long, 2nd
6	0.073	Torsion, 2nd

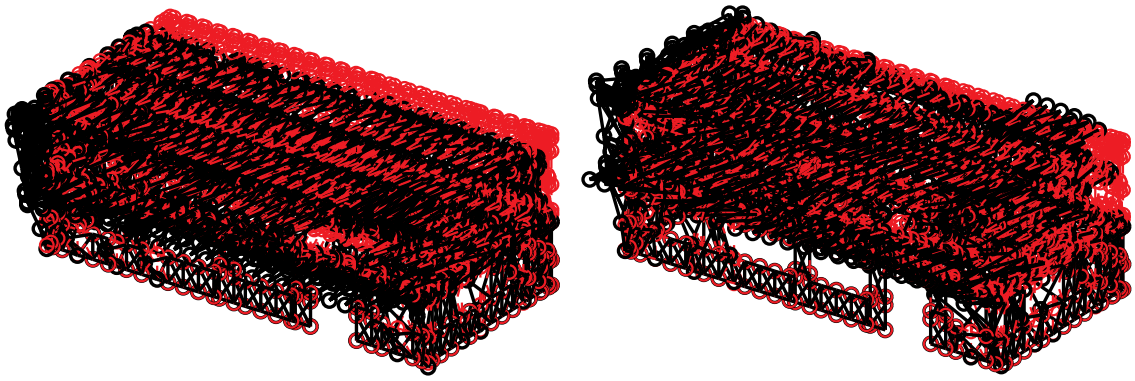

(a) Mode 1, T_1=0.282 s (b) Mode 2, T_2=0.218 s

Figure O-2: First two natural modes of A2b-3D-SD-a model

O.3 Linear static analysis results

Table O-2 to Table O-4 present linear static analysis results. The lateral load is the equivalent lateral force available from the design narrative (Madsen et al. 2011), applied equally at four corners. Two separate analyses were performed with the loading at long or short direction.

Table O-2 summarizes the breakdown of peak total base shear among four elevations. Due to the interplay of asymmetrical LFRS, wall lines perpendicular to the loading direction still take a very small portion of base shear.

Table O-3 shows peak building and wall line deflections. Practicing engineers can linearly upscale these data and develop an estimate of the building's performance at a certain lateral force level.

Table O-4 is an evaluation of the building's lateral stiffness of long and short direction and its breakdown among shear walls (SW) and other systems. Covered by the same type of OSB sheathing with shear walls (even though the fastener spacing is different), gravity walls make a comparable contribution to total lateral stiffness like shear walls. The effect is even more apparent in long direction, where wall lines are much wider and have larger areas covered by gravity walls. The stiffness of gravity walls can account for as much as 41% and 26% of total lateral stiffness in long and short direction.

Table O-2: Breakdown of peak base shear, linear static analysis, A2b-3D-SD-a model

Load direction	**LONG**				
Elevation	**South V_b**	**North V_b**	**East V_b**	**West V_b**	**Peak V_b**
kips	4.1	6.9	0.0	0.2	11.1
%	36.6	62.0	0.1	1.4	100.0
Load direction	**SHORT**				
Elevation	**South V_b**	**North V_b**	**East V_b**	**West V_b**	**Peak V_b**
kips	0.3	0.4	5.3	5.1	11.1
%	2.3	3.4	48.2	46.1	100.0

Table O-3: Peak building and wall line deflection, linear static analysis, A2b-3D-SD-a model

Load direction	**LONG**							
Deflection (in.)	**u_1**	**u_2**	**v_1**	**v_2**	**Δu_1**	**Δu_2**	**Δv_1**	**Δv_2**
Building	0.049	0.081	-0.002	-0.003	0.049	0.032	-0.002	-0.001
South	0.056	0.092	-0.002	-0.004	0.056	0.035	-0.002	-0.002
North	0.041	0.070	-0.001	-0.002	0.041	0.029	-0.001	0.001
East	0.049	0.081	0.008	0.013	0.049	0.031	0.008	0.005
West	0.048	0.081	-0.012	-0.019	0.048	0.033	-0.012	-0.007
Load direction	**SHORT**							
Deflection (in.)	**u_1**	**u_2**	**v_1**	**v_2**	**Δu_1**	**Δu_2**	**Δv_1**	**Δv_2**
Building	-0.001	-0.002	0.081	0.130	-0.001	-0.001	0.081	0.049
South	-0.004	-0.006	0.081	0.129	-0.004	-0.003	0.081	0.048
North	0.002	0.003	0.081	0.131	0.002	0.001	0.081	0.050
East	0.001	-0.002	0.074	0.117	0.001	-0.001	0.074	0.043
West	-0.001	-0.002	0.088	0.142	-0.001	0.001	0.088	0.055

Table O-4: Breakdown of lateral stiffness, A2b-3D-SD-a model

LONG			**SHORT**		
Shear wall k_u (%)	**Gravity wall k_u (%)**	**k_u (kip/in)**	**Shear wall k_v (%)**	**Gravity wall k_v (%)**	**k_v (kip/in)**
59.8	41.2	139.1	73.6	26.4	85.1

O.4 Nonlinear static (pushover) analysis results

Table O-5 is created following the same logic with Table O-2, but the analysis type is nonlinear static (pushover). Pushover curves of the building and each wall line are presented in Figure O-3 and Figure O-4.

Clearly, the interaction between wall lines is much more significant when material and geometrical nonlinearity is included. These tables and figures indicate that the wall lines do not reach their peak capacity at exactly the same drift level and wall lines perpendicular to the load can take a nontrivial amount of base shear. Total capacity of the wall line increases since the capacity of gravity walls is included. The boost is larger in long direction. Consequently, total capacity of the building in long direction is much larger than the short direction.

Table O-5: Breakdown of peak base shear, pushover analysis, A2b-3D-SD-a model

Load direction	**LONG**				
Elevation	**South V_b**	**North V_b**	**East V_b**	**West V_b**	**Peak V_b**
kips	35.7	41.0	1.8	8.1	76.9
%	46.4	53.3	2.4	10.5	100.0
Load direction	**SHORT**				
Elevation	**South V_b**	**North V_b**	**East V_b**	**West V_b**	**Peak V_b**
kips	12.0	9.8	26.3	27.2	66.3
%	18.1	14.8	39.7	41.0	100.0

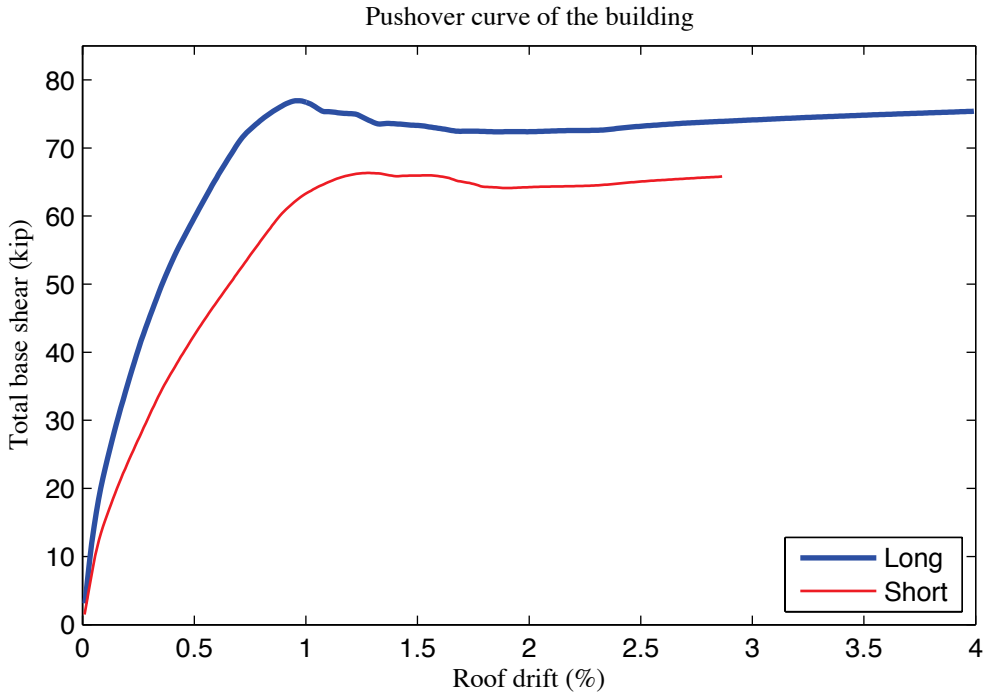

Figure O-3: Pushover curve of A2b-3D-SD-a model

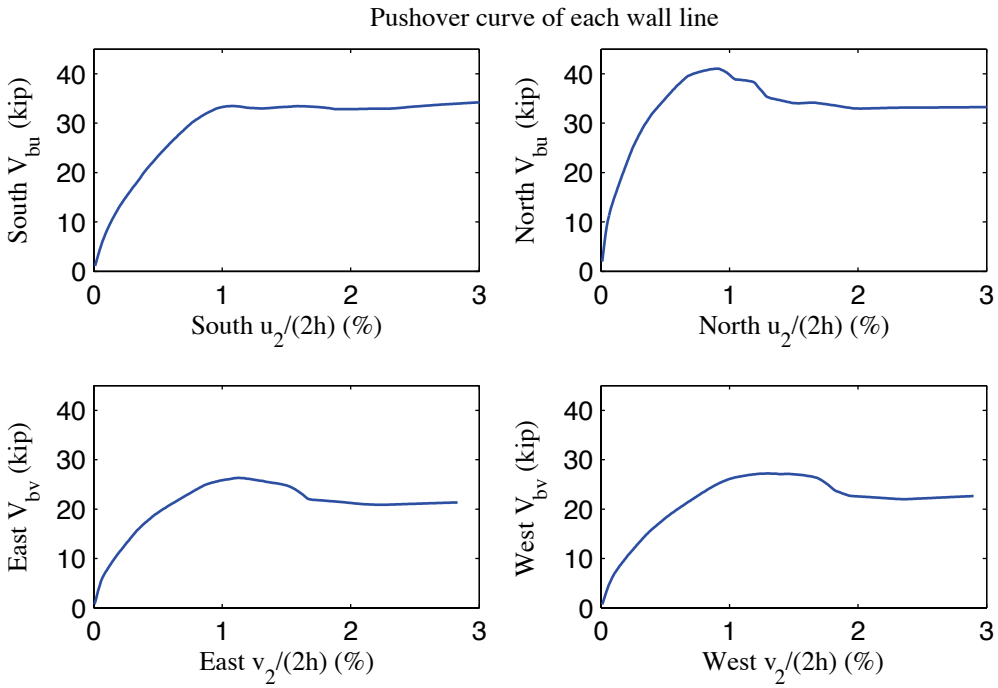

Figure O-4: Pushover curve of each wall line, A2b-3D-SD-a model

O.5 Linear time history analysis results

Linear time history analysis is performed on the model under Canoga Park and Rinaldi ground motion records of Northridge earthquake in 1994. We considered three scale levels (16%, 44% and 100%) and loadings in one, two and three axes.

Table O-6 to Table O-9 demonstrate the building's linear elastic performance under designated ground motions. Table O-6 shows peak story relative accelerations in the unit of g. Table O-7 and Table O-8 report peak roof drift and story drift of the building and the corresponding time step (t_*) and the base shear at that time. Note that the base shear at the time of peak roof drift may not be the peak total building base shear in that direction (see Table O-9).

The building behaves linearly since peak drift and peak base shear appear at the same time when the ground motion is linearly scaled. Figure O-5 is a vector plot of the peak total resultant base shear of the building under three axial, 100% Canoga Park excitation. The directions of arrows imply that base shear taken by shear walls and gravity systems does not necessarily follow the direction of wall lines due to the effect of 3D coupling. Comparison with nonlinear analysis results of the same excitation provides insightful observations on the building's response and requirements on modeling fidelity and analysis type.

Table O-6: A2b-3D-SD-a model peak story relative acceleration in g, linear time history analysis

		LONG			SHORT			UP		
Load Case	**Ground Motion**	**a_g**	**Floor a**	**Roof a**	**a_g**	**Floor a**	**Roof a**	**a_g**	**Floor a**	**Roof a**
EQ_3D_3axis_1	CNP 16%	0.067	0.086	0.137	0.057	0.148	0.218	0.078	0.105	0.087
EQ_3D_3axis_2	CNP 44%	0.185	0.238	0.375	0.157	0.432	0.627	0.215	0.283	0.241
EQ_3D_1axis_1	CNP 100%	0.420	0.543	0.869	0	0.094	0.137	0	0.254	0.210
EQ_3D_1axis_2	CNP 100%	0	0.119	0.186	0.356	1.006	1.475	0	1.148	1.043
EQ_3D_2axis_1	CNP 100%	0.420	0.549	0.873	0.356	1.016	1.464	0	0.861	0.768
EQ_3D_3axis_3	CNP 100%	0.420	0.550	0.874	0.356	1.023	1.477	0.489	0.945	0.840
EQ_3D_3axis_4	RRS 16%	0.132	0.127	0.212	0.078	0.207	0.279	0.133	0.122	0.102
EQ_3D_3axis_5	RRS 44%	0.363	0.365	0.563	0.214	0.605	0.816	0.367	0.503	0.444
EQ_3D_3axis_6	RRS 100%	0.825	0.831	1.286	0.486	1.410	1.942	0.834	1.141	1.059

Table O-7: A2b-3D-SD-a model peak building roof drift and base shear, linear time history analysis

		LONG			SHORT		
Load Case	**Ground Motion**	**$u_2/(2h)$ (%)**	**t_* (s)**	**V_b @ t_* (kips)**	**$v_2/(2h)$ (%)**	**t_* (s)**	**V_b @ t_* (kips)**
EQ_3D_3axis_1	CNP 16%	0.026	6.94	8.5	0.083	9.90	16.0
EQ_3D_3axis_2	CNP 44%	0.073	6.94	23.8	0.238	9.90	45.2
EQ_3D_1axis_1	CNP 100%	0.174	6.95	55.6	-0.037	12.02	8.5
EQ_3D_1axis_2	CNP 100%	0.050	10.05	9.0	0.562	9.90	106.0
EQ_3D_2axis_1	CNP 100%	0.172	6.94	55.1	0.558	9.90	105.0
EQ_3D_3axis_3	CNP 100%	0.172	6.94	55.1	0.562	9.90	105.5
EQ_3D_3axis_4	RRS 16%	0.055	2.58	17.1	-0.102	4.31	18.3
EQ_3D_3axis_5	RRS 44%	0.148	2.58	46.2	-0.298	4.31	52.6
EQ_3D_3axis_6	RRS 100%	0.341	4.31	93.2	-0.702	4.31	123.1

Table O-8: A2b-3D-SD-a model peak building story drift, linear time history analysis

		LONG				SHORT			
Load Case	**Ground Motion**	**$\Delta u_1/h$ (%)**	**t_* (s)**	**$\Delta u_2/h$ (%)**	**t_* (s)**	**$\Delta v_1/h$ (%)**	**t_* (s)**	**$\Delta v_2/h$ (%)**	**t_* (s)**
EQ_3D_3axis_1	CNP 16%	0.034	6.94	0.018	6.94	0.110	9.90	0.056	9.90
EQ_3D_3axis_2	CNP 44%	0.096	6.94	0.050	6.94	0.316	9.90	0.161	9.90
EQ_3D_1axis_1	CNP 100%	0.228	6.95	0.120	6.95	-0.050	12.02	0.025	12.14
EQ_3D_1axis_2	CNP 100%	0.062	10.05	0.038	10.05	0.743	9.90	0.381	9.90
EQ_3D_2axis_1	CNP 100%	0.225	6.94	0.118	6.94	0.738	9.90	0.378	9.90
EQ_3D_3axis_3	CNP 100%	0.226	6.94	0.119	6.94	0.743	9.90	0.381	9.90
EQ_3D_3axis_4	RRS 16%	0.074	2.58	0.036	4.31	-0.132	4.31	-0.072	4.31
EQ_3D_3axis_5	RRS 44%	0.200	2.58	0.103	4.31	-0.386	4.31	-0.210	4.31
EQ_3D_3axis_6	RRS 100%	0.449	2.58	0.238	4.31	-0.909	4.32	-0.497	4.31

Table O-9: A2b-3D-SD-a model peak building base shear, linear time history analysis

		LONG		SHORT		RESULTANT	
Load Case	**Ground Motion**	**Peak V_{bu} (kip)**	**t @ peak V_{bu} (s)**	**Peak V_{bv} (kip)**	**t @ peak V_{bv} (s)**	**Peak V_b (kip)**	**t @ peak V_b (s)**
EQ_3D_3axis_1	CNP 16%	9.0	4.88	16.0	9.90	16.2	9.90
EQ_3D_3axis_2	CNP 44%	24.7	4.88	45.2	9.90	45.7	9.90
EQ_3D_1axis_1	CNP 100%	56.3	4.88	8.6	12.03	56.3	4.88
EQ_3D_1axis_2	CNP 100%	10.4	6.89	106.0	9.90	106.1	9.90
EQ_3D_2axis_1	CNP 100%	56.7	4.88	105.0	9.90	106.3	9.90
EQ_3D_3axis_3	CNP 100%	56.8	4.88	105.5	9.90	106.8	9.90
EQ_3D_3axis_4	RRS 16%	17.1	2.58	18.3	4.31	23.1	4.31
EQ_3D_3axis_5	RRS 44%	46.2	2.58	52.6	4.31	66.3	4.31
EQ_3D_3axis_6	RRS 100%	103.7	2.58	123.4	4.32	154.4	4.31

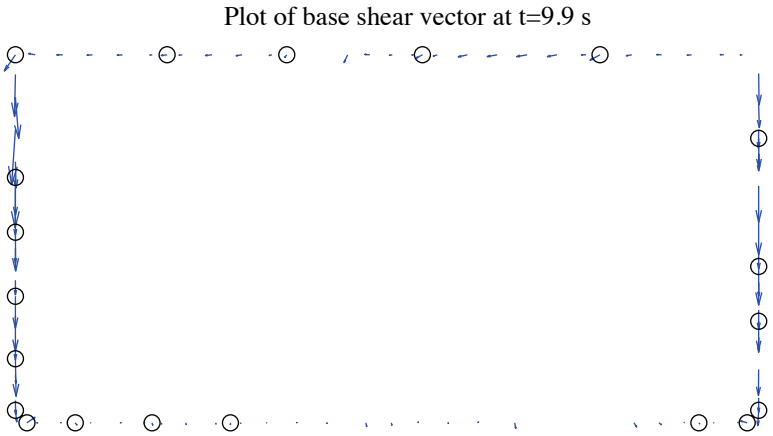

Figure O-5: A2b-3D-SD-a model, base shear vector plot at the moment of peak total base shear, 100 % Canoga Park, 3D linear analysis (maximum anchor/hold down base shear is 6.20 kips)

O.6 Nonlinear time history analysis results

Same ground motions are applied to the model with material and geometrical nonlinearity. Table O-10 to Table O-13 are replicas of Table O-6 to Table O-9, but for nonlinear time history analyses. Since this analysis type is most complicated and closest to reality and experiments, behavior of wall lines and hold downs are further studied. Table O-14 is the table of peak wall line story drifts and corresponding time steps. Table O-15 is designed for peak base shear of each wall line and the last two columns of the table are percentages of base shear of two facing wall lines in the same direction when the total base shear in that direction takes peak value. Table O-16 expands the breakdown of each wall line's peak base shear between shear walls, gravity walls and other systems. Table O-17 is peak value of hold down tensile force of two selected pairs. Hold down 5 and 6 are on shear wall L1S1, South elevation and hold down 7 and 8 are on shear wall L1W1, West elevation. These shear walls have lowest capacities compared with others on the same wall line and they meet at the southwest edge of the building, so interacted nonlinear behavior is expected to appear.

Time history plots in this section include plots of story drifts of the building and each wall line (Figure O-6 to Figure O-8), total building base shear in long and short direction (Figure O-9) and axial forces of hold downs in Table O-17 (Figure O-10). Hysteretic plots in Figure O-11 and Figure O-12 are helpful for visual examination of nonlinear base shear-drift relationship of the building and the weakest shear wall on each wall line. In comparison with linear time history analysis, vector plot of peak total base shear is illustrated in Figure O-13. Figure O-14 presents a simplified deformed shape of the

building (see (Peterman 2014) for details of the method) and axial force of all twenty hold downs at the moment of peak total base shear. The same sign convention with tests is adopted. Red bars indicate tensile (negative) force and blue ones are for compressive (positive) force.

Hysteretic behavior is seen in the building and typical shear walls under design-based earthquake (100% Canoga Park excitation in 3 axes, see Figure O-11 and Figure O-12). Even though post-peak response on the backbone curve is not initiated under this excitation level, wall lines behave differently. North wall line reaches 0.47% peak floor story drift but peak story drifts of all other wall lines are between 0.63% and 0.70% (Table O-14). Given the significantly increased capacity and stiffness in long direction, peak story drift of long direction is less than short direction (0.55% vs. 0.66%, Table O-12). Figure O-13 clearly shows that base shear vectors in anchors and hold downs do not align with wall lines, a sign of coupled wall line behavior. Table O-17, Figure O-10 and Figure O-13 demonstrate that hold downs in a pair do not experience the same amount of force with opposite signs, an evidence that supports Type II shear wall behavior despite Type I design assumption.

The near-field Rinaldi record is much stronger in terms of peak ground acceleration, especially in the long direction. With the additional lateral force resistance provided by sheathed gravity walls, simulation results show that the building can survive even 100% Rinaldi ground motion, the maximum considered earthquake in this research. This time, long direction story drift is about 1.6%, close to threshold value of post-peak response

(arguably 2%) on the backbone curve and is larger than short direction value. The portion of base shear taken by gravity wall does not change much with scale factors considered so far in this research, as shown in Table O-16. Again, the table demonstrates that the base shear taken by anchors on bottom tracks of gravity walls can be quite large, sometimes even larger than half of the total base shear (e.g. South wall lines).

Table O-10: A2b-3D-SD-a model peak story relative acceleration in g, nonlinear time history analysis

		LONG			SHORT			UP		
Load Case	**Ground Motion**	**a_g**	**Floor a**	**Roof a**	**a_g**	**Floor a**	**Roof a**	**a_g**	**Floor a**	**Roof a**
EQ_3D_3axis_1	CNP 16%	0.067	0.171	0.171	0.057	0.197	0.233	0.078	0.044	0.040
EQ_3D_3axis_2	CNP 44%	0.185	0.247	0.312	0.157	0.237	0.275	0.215	0.107	0.088
EQ_3D_1axis_1	CNP 100%	0.420	0.748	0.955	0	0.120	0.103	0	0.151	0.127
EQ_3D_1axis_2	CNP 100%	0	0.098	0.095	0.356	0.628	0.672	0	0.243	0.223
EQ_3D_2axis_1	CNP 100%	0.420	0.604	0.808	0.356	0.816	0.848	0	0.989	0.879
EQ_3D_3axis_3	CNP 100%	0.420	0.612	0.834	0.356	0.594	0.809	0.489	1.142	0.971
EQ_3D_3axis_4	RRS 16%	0.132	0.174	0.227	0.078	0.290	0.400	0.133	0.067	0.061
EQ_3D_3axis_5	RRS 44%	0.363	0.505	0.532	0.214	0.510	0.663	0.367	0.268	0.225
EQ_3D_3axis_6	RRS 100%	0.825	1.128	1.462	0.486	0.826	1.038	0.834	0.972	0.817

Table O-11: A2b-3D-SD-a model peak building roof drift and base shear, nonlinear time history analysis

		LONG			SHORT		
Load Case	**Ground Motion**	**$u_2/(2h)$ (%)**	**t_* (s)**	**V_b @ t_* (kips)**	**$v_2/(2h)$ (%)**	**t_* (s)**	**V_b @ t_* (kips)**
EQ_3D_3axis_1	CNP 16%	0.036	6.94	11.5	0.087	9.94	14.3
EQ_3D_3axis_2	CNP 44%	0.105	8.66	24.2	0.136	9.97	17.0
EQ_3D_1axis_1	CNP 100%	0.338	11.77	48.0	-0.025	12.15	4.1
EQ_3D_1axis_2	CNP 100%	-0.025	10.02	3.0	0.452	9.99	41.4
EQ_3D_2axis_1	CNP 100%	0.369	8.70	53.6	0.448	9.99	40.4
EQ_3D_3axis_3	CNP 100%	0.362	8.69	53.4	0.453	9.99	40.5
EQ_3D_3axis_4	RRS 16%	0.050	2.59	14.5	-0.119	4.38	16.6
EQ_3D_3axis_5	RRS 44%	0.231	4.39	38.2	0.343	6.01	33.6
EQ_3D_3axis_6	RRS 100%	0.969	2.69	76.5	0.783	6.07	53.5

Table O-12: A2b-3D-SD-a model peak building story drift, nonlinear linear time history analysis

		LONG				SHORT			
Load Case	**Ground Motion**	**$\Delta u_1/h$ (%)**	**t_* (s)**	**$\Delta u_2/h$ (%)**	**t_* (s)**	**$\Delta v_1/h$ (%)**	**t_* (s)**	**$\Delta v_2/h$ (%)**	**t_* (s)**
EQ_3D_3 axis_1	CNP 16%	0.048	6.95	0.024	6.94	0.121	9.94	0.053	9.93
EQ_3D_3 axis_2	CNP 44%	0.156	8.66	0.055	8.66	0.201	9.96	0.072	9.97
EQ_3D_1 axis_1	CNP 100%	0.517	8.71	-0.181	10.51	-0.042	12.14	0.015	11.99
EQ_3D_1 axis_2	CNP 100%	-0.034	10.04	-0.020	10.01	0.683	9.99	0.223	9.98
EQ_3D_2 axis_1	CNP 100%	0.557	8.70	-0.191	10.51	0.654	9.99	0.243	9.99
EQ_3D_3 axis_3	CNP 100%	0.554	8.70	-0.188	10.51	0.659	9.99	0.246	9.99
EQ_3D_3 axis_4	RRS 16%	0.071	2.59	-0.032	4.21	-0.184	4.38	0.061	4.54
EQ_3D_3 axis_5	RRS 44%	0.360	4.39	0.106	4.41	0.508	6.01	0.178	6.01
EQ_3D_3 axis_6	RRS 100%	1.641	2.69	0.331	2.63	1.198	6.07	0.376	6.05

Table O-13: A2b-3D-SD-a model peak building base shear, nonlinear time history analysis

		LONG		SHORT		RESULTANT	
Load Case	**Ground Motion**	**Peak V_{bu} (kip)**	**t @ peak V_{bu} (s)**	**Peak V_{bv} (kip)**	**t @ peak V_{bv} (s)**	**Peak V_b (kip)**	**t @ peak V_b (s)**
EQ_3D_3axis_1	CNP 16%	11.5	6.94	14.3	9.95	14.8	9.94
EQ_3D_3axis_2	CNP 44%	24.2	8.66	17.9	5.22	24.2	8.66
EQ_3D_1axis_1	CNP 100%	52.2	8.71	4.1	12.15	52.2	8.71
EQ_3D_1axis_2	CNP 100%	4.7	10.05	41.6	9.98	41.6	9.98
EQ_3D_2axis_1	CNP 100%	53.6	8.70	40.4	9.99	53.6	8.70
EQ_3D_3axis_3	CNP 100%	53.4	8.69	40.5	9.99	53.4	8.69
EQ_3D_3axis_4	RRS 16%	14.8	2.58	16.9	4.54	19.7	4.20
EQ_3D_3axis_5	RRS 44%	40.2	4.38	33.6	6.01	45.5	4.38
EQ_3D_3axis_6	RRS 100%	77.1	2.64	53.5	6.07	81.7	2.61

Table O-14: A2b-3D-SD-a model peak wall line story drift, nonlinear time history analysis

LONG		SOUTH				NORTH			
Load Case	**Ground Motion**	**$\Delta u_1/h$ (%)**	**t_* (s)**	**$\Delta u_2/h$ (%)**	**t_* (s)**	**$\Delta u_1/h$ (%)**	**t_* (s)**	**$\Delta u_2/h$ (%)**	**t_* (s)**
EQ_3D_3axis_1	CNP 16%	0.063	11.84	0.031	11.75	0.043	6.94	0.026	6.93
EQ_3D_3axis_2	CNP 44%	0.208	8.68	0.067	8.66	0.124	8.65	0.047	7.35
EQ_3D_1axis_1	CNP 100%	0.567	11.77	0.204	10.51	0.488	8.71	0.170	11.61
EQ_3D_1axis_2	CNP 100%	0.078	10.03	0.045	10.02	0.021	9.95	0.018	9.97
EQ_3D_2axis_1	CNP 100%	0.656	8.72	0.215	10.52	0.472	8.70	0.178	8.69
EQ_3D_3axis_3	CNP 100%	0.658	8.71	0.210	10.52	0.472	8.69	0.170	10.51
EQ_3D_3axis_4	RRS 16%	0.097	2.61	0.043	4.22	0.056	2.57	0.030	4.20
EQ_3D_3axis_5	RRS 44%	0.464	4.41	0.158	4.42	0.297	4.37	0.107	4.38
EQ_3D_3axis_6	RRS 100%	1.856	2.69	0.397	3.95	1.429	2.69	0.321	3.07
SHORT		**EAST**				**WEST**			
Load Case	**Ground Motion**	**$\Delta v_1/h$ (%)**	**t_* (s)**	**$\Delta v_2/h$ (%)**	**t_* (s)**	**$\Delta v_1/h$ (%)**	**t_* (s)**	**$\Delta v_2/h$ (%)**	**t_* (s)**
EQ_3D_3axis_1	CNP 16%	0.107	9.94	0.047	9.93	0.136	9.94	0.061	9.93
EQ_3D_3axis_2	CNP 44%	0.178	9.38	0.071	9.37	0.287	8.41	0.109	9.97
EQ_3D_1axis_1	CNP 100%	0.105	11.91	0.052	7.42	0.119	11.79	0.064	11.80
EQ_3D_1axis_2	CNP 100%	0.604	9.98	0.192	9.97	0.770	9.99	0.261	9.99
EQ_3D_2axis_1	CNP 100%	0.631	9.98	0.224	5.98	0.684	10.00	0.276	9.99
EQ_3D_3axis_3	CNP 100%	0.630	9.99	0.223	5.98	0.698	10.00	0.284	9.99
EQ_3D_3axis_4	RRS 16%	0.119	3.15	0.049	3.15	0.266	4.38	0.087	4.36
EQ_3D_3axis_5	RRS 44%	0.380	6.01	0.130	6.00	0.758	4.44	0.286	4.43
EQ_3D_3axis_6	RRS 100%	0.775	2.90	0.288	3.43	1.648	6.07	0.504	3.96

Table O-15: A2b-3D-SD-a model peak wall line base shear, nonlinear time history analysis

LONG		SOUTH		NORTH		% of Peak V_{bu}	
Load Case	**Ground Motion**	**Peak V_{bu} (kips)**	**t @ peak V_{bu} (s)**	**Peak V_{bu} (kips)**	**t @ peak V_{bu} (s)**	**South**	**North**
EQ_3D_3axis_1	CNP 16%	4.6	11.84	7.5	6.94	33.3	65.4
EQ_3D_3axis_2	CNP 44%	10.9	8.68	13.8	8.65	42.8	55.7
EQ_3D_1axis_1	CNP 100%	20.8	11.76	30.5	8.71	39.0	58.4
EQ_3D_1axis_2	CNP 100%	5.0	10.03	3.0	10.00	95.8	1.9
EQ_3D_2axis_1	CNP 100%	22.5	8.71	30.0	8.70	41.5	56.0
EQ_3D_3axis_3	CNP 100%	22.5	8.71	30.0	8.69	41.2	56.2
EQ_3D_3axis_4	RRS 16%	6.6	2.61	9.2	2.57	39.6	59.0
EQ_3D_3axis_5	RRS 44%	17.8	4.40	23.3	4.37	41.1	56.6
EQ_3D_3axis_6	RRS 100%	32.9	2.64	41.0	2.64	42.7	53.2
SHORT		**EAST**		**WEST**		**% of Peak V_{bv}**	
Load Case	**Ground Motion**	**Peak V_{bv} (kips)**	**t @ peak V_{bv} (s)**	**Peak V_{bv} (kips)**	**t @ peak V_{bv} (s)**	**East**	**West**
EQ_3D_3axis_1	CNP 16%	6.7	9.95	6.9	9.95	46.4	47.8
EQ_3D_3axis_2	CNP 44%	8.5	9.39	10.3	8.41	37.5	55.6
EQ_3D_1axis_1	CNP 100%	6.5	11.78	5.8	11.79	88.4	3.0
EQ_3D_1axis_2	CNP 100%	17.7	9.98	19.1	9.99	42.6	45.6
EQ_3D_2axis_1	CNP 100%	18.1	9.98	17.8	10.00	44.7	43.9
EQ_3D_3axis_3	CNP 100%	18.1	9.98	18.0	10.00	44.7	44.2
EQ_3D_3axis_4	RRS 16%	6.9	3.15	9.9	4.38	39.8	53.1
EQ_3D_3axis_5	RRS 44%	13.2	6.01	18.5	4.44	39.3	50.5
EQ_3D_3axis_6	RRS 100%	19.5	3.90	26.4	6.05	34.9	49.2

Table O-16: A2b-3D-SD-a model wall line base shear breakdown, nonlinear time history analysis

LONG		SOUTH			NORTH		
Load Case	**Ground Motion**	**Peak V_{bu} (kips)**	**SW V_{bu} (%)**	**GW V_{bu} (%)**	**Peak V_{bu} (kips)**	**SW V_{bu} (%)**	**GW V_{bu} (%)**
EQ_3D_3axis_1	CNP 16%	4.6	39.2	60.8	7.5	62.6	37.4
EQ_3D_3axis_2	CNP 44%	10.9	43.0	57.0	13.8	61.3	38.7
EQ_3D_1axis_1	CNP 100%	20.8	40.1	59.9	30.5	55.1	44.9
EQ_3D_1axis_2	CNP 100%	5.0	38.1	61.9	3.0	61.9	38.1
EQ_3D_2axis_1	CNP 100%	22.5	39.7	60.3	30.0	55.1	44.9
EQ_3D_3axis_3	CNP 100%	22.5	39.8	60.2	30.0	55.1	44.9
EQ_3D_3axis_4	RRS 16%	6.6	39.6	60.4	9.2	62.6	37.4
EQ_3D_3axis_5	RRS 44%	17.8	40.9	59.1	23.3	56.6	43.4
EQ_3D_3axis_6	RRS 100%	32.9	41.7	58.3	41.0	55.4	44.6
SHORT		**EAST**			**WEST**		
Load Case	**Ground Motion**	**Peak V_{bv} (kips)**	**SW V_{bv} (%)**	**GW V_{bu} (%)**	**Peak V_{bv} (kips)**	**SW V_{bv} (%)**	**GW V_{bv} (%)**
EQ_3D_3axis_1	CNP 16%	6.7	78.8	21.2	6.9	84.1	15.9
EQ_3D_3axis_2	CNP 44%	8.5	76.3	23.7	10.3	83.3	16.7
EQ_3D_1axis_1	CNP 100%	6.5	79.9	20.1	5.8	83.5	16.5
EQ_3D_1axis_2	CNP 100%	17.7	73.0	27.0	19.1	82.8	17.2
EQ_3D_2axis_1	CNP 100%	18.1	73.3	26.7	17.8	82.2	17.8
EQ_3D_3axis_3	CNP 100%	18.1	73.3	26.7	18.0	82.4	17.6
EQ_3D_3axis_4	RRS 16%	6.9	77.5	22.5	9.9	83.5	16.5
EQ_3D_3axis_5	RRS 44%	13.2	72.4	27.6	18.5	82.9	17.1
EQ_3D_3axis_6	RRS 100%	19.5	73.6	26.4	26.4	84.2	15.8

Table O-17: A2b-3D-SD-a model peak hold down tensile force at certain locations, nonlinear time history analysis

		L1S1, LC5		L1S1, LC6		L1W1, LC7		L1W1, LC8	
Load Case	**Ground Motion**	**Peak F (kips)**	**t @ peak F (s)**	**Peak F (kips)**	**t @ peak F (s)**	**Peak F (kips)**	**t @ peak F (s)**	**Peak F (kips)**	**t @ peak F (s)**
EQ_3D_3axis_1	CNP 16%	-0.44	11.84	-0.19	9.94	-0.13	9.94	-0.36	9.79
EQ_3D_3axis_2	CNP 44%	-1.01	8.26	-0.42	9.97	-0.30	9.96	-0.54	8.41
EQ_3D_1axis_1	CNP 100%	-1.96	10.51	-0.31	8.70	-0.62	8.70	-0.50	11.78
EQ_3D_1axis_2	CNP 100%	-1.76	9.99	-1.12	9.98	-0.61	9.97	-0.80	10.21
EQ_3D_2axis_1	CNP 100%	-1.99	10.52	-1.34	9.99	-1.09	9.98	-0.81	5.98
EQ_3D_3axis_3	CNP 100%	-1.99	10.52	-1.36	9.98	-1.10	9.98	-0.81	5.97
EQ_3D_3axis_4	RRS 16%	-0.75	4.21	-0.22	4.55	-0.12	3.30	-0.54	4.37
EQ_3D_3axis_5	RRS 44%	-1.93	4.25	-0.99	6.01	-0.58	6.01	-1.10	4.43
EQ_3D_3axis_6	RRS 100%	-2.74	3.96	-1.71	6.05	-1.11	2.69	-1.57	2.60

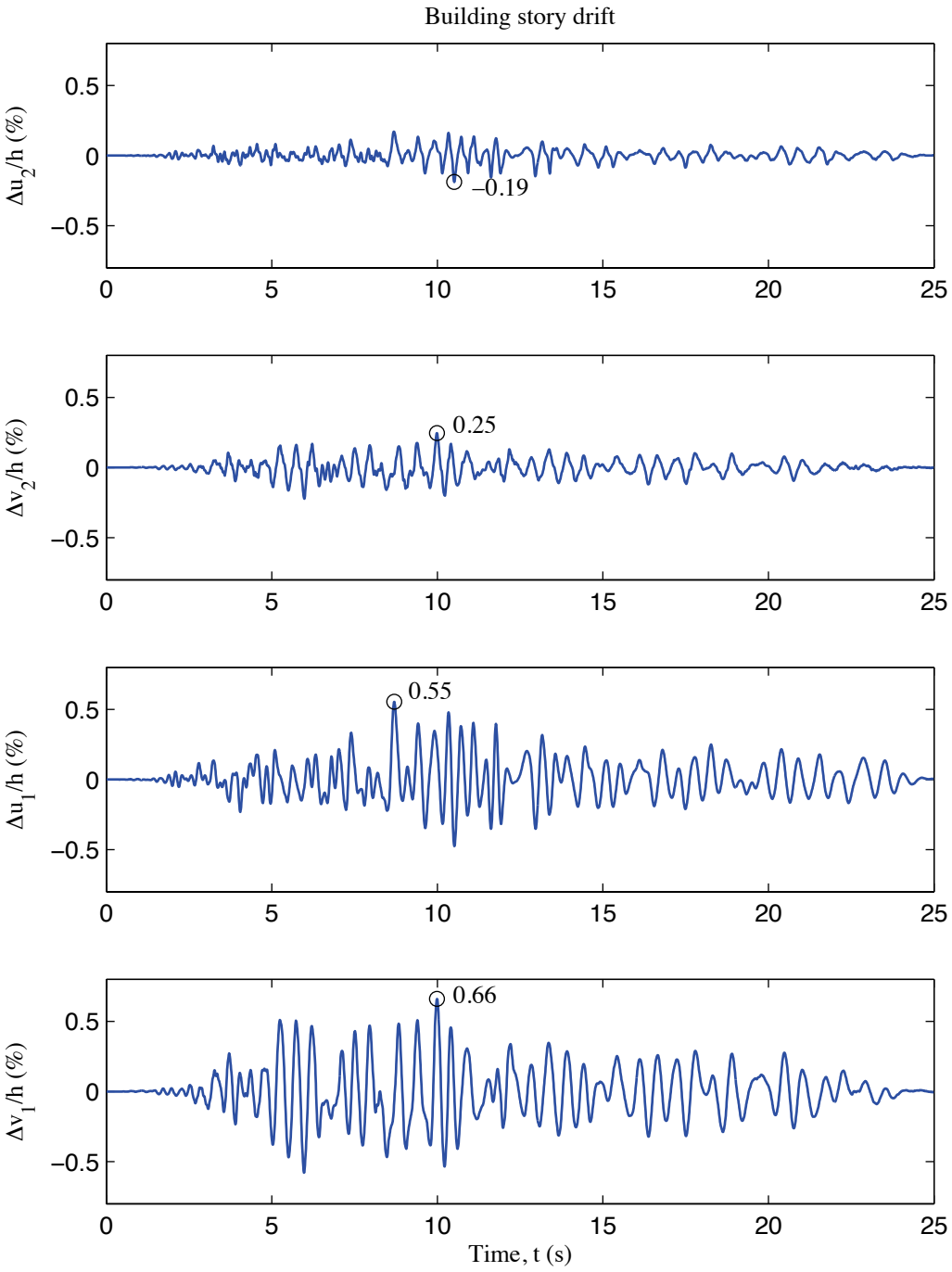

Figure O-6: A2b-3D-SD-a model building story drift, 100 % Canoga Park, 3D nonlinear analysis

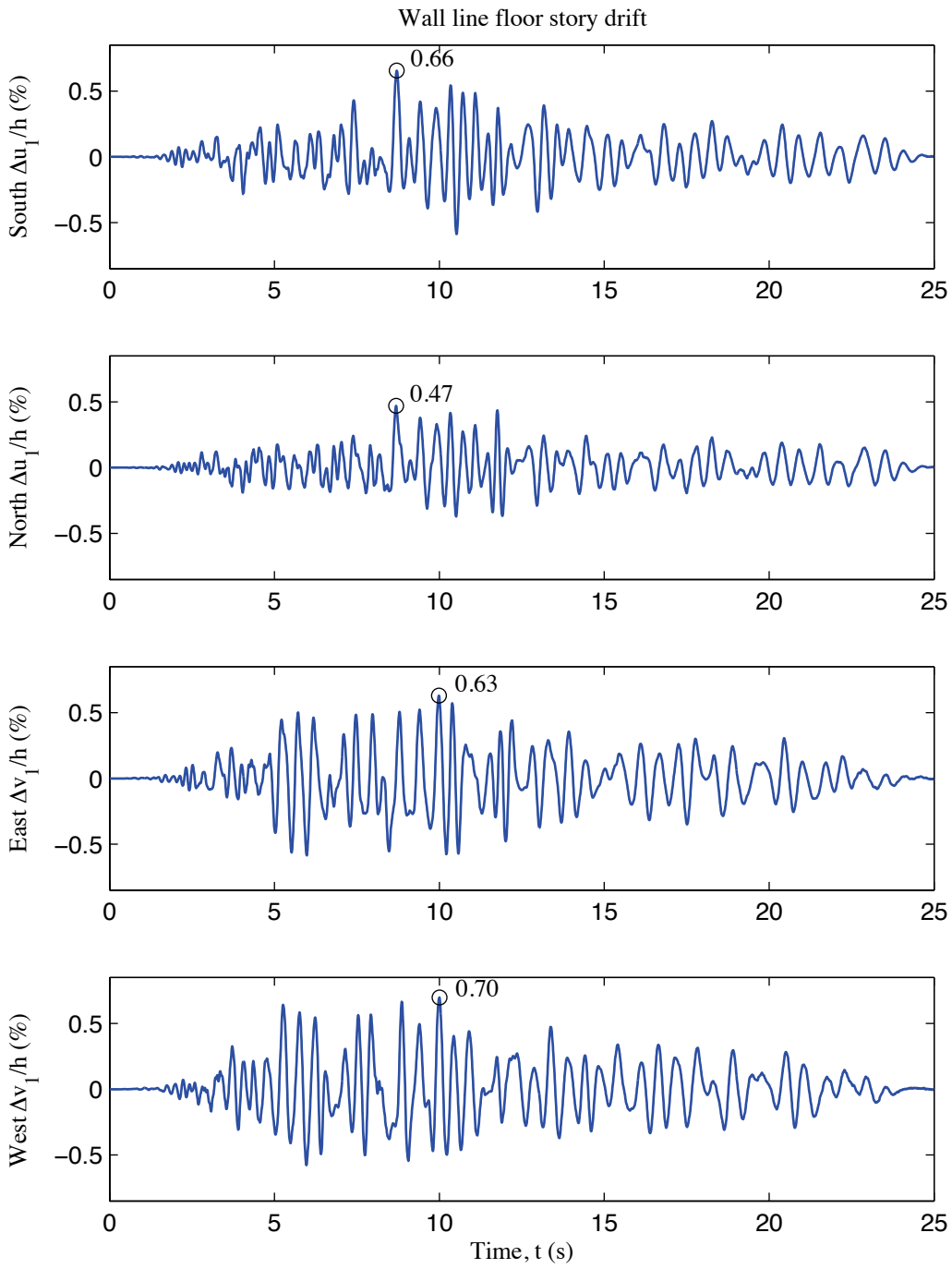

Figure O-7: A2b-3D-SD-a model wall line floor story drift, 100 % Canoga Park, 3D nonlinear analysis

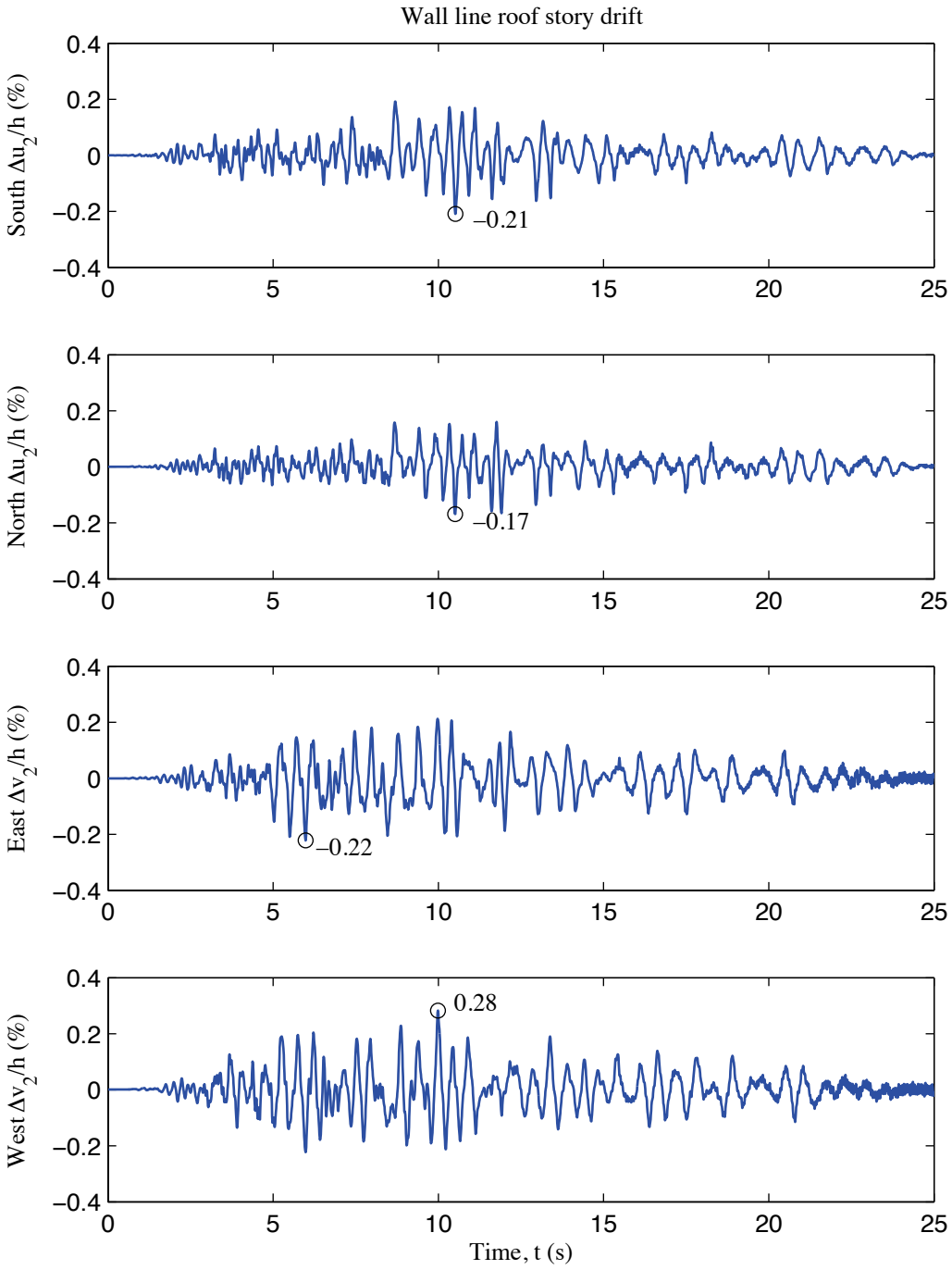

Figure O-8: A2b-3D-SD-a model wall line roof story drift, 100 % Canoga Park, 3D nonlinear analysis

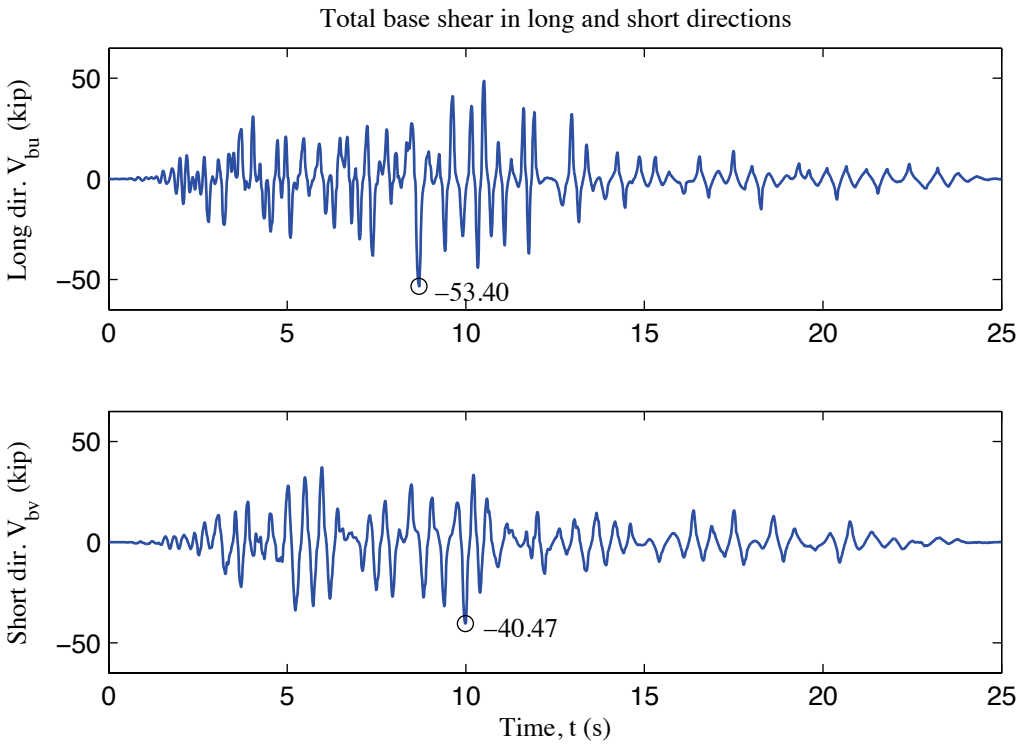

Figure O-9: A2b-3D-SD-a model total building base shear, 100 % Canoga Park, 3D nonlinear analysis

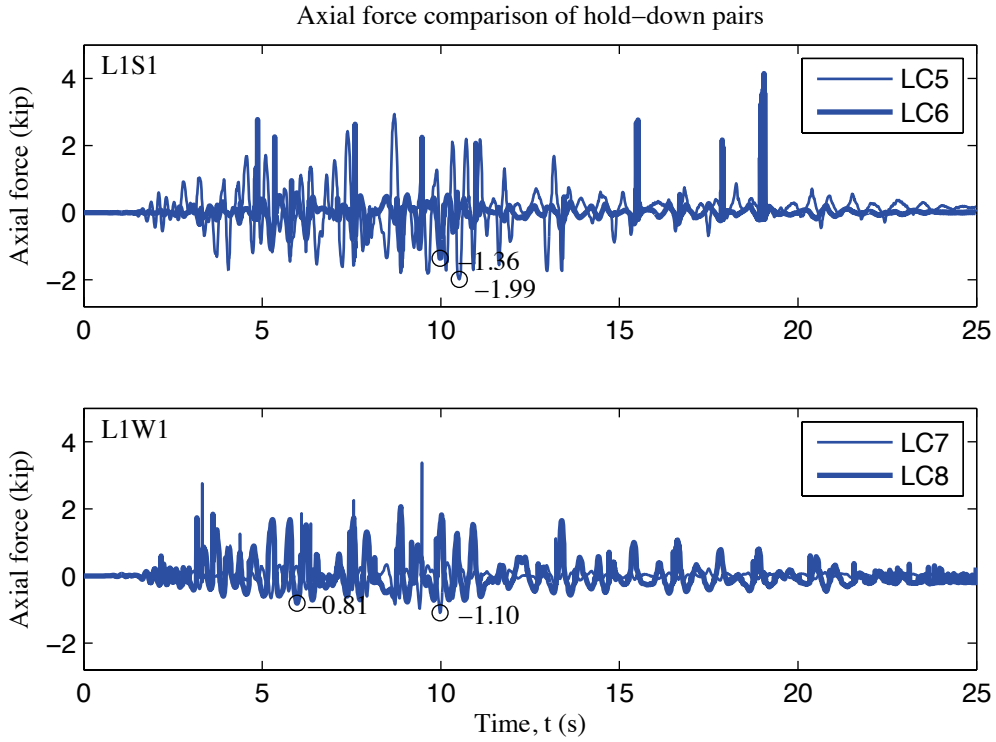

Figure O-10: A2b-3D-SD-a model, load cell 5 to 8 axial forces, 100 % Canoga Park, 3D nonlinear analysis

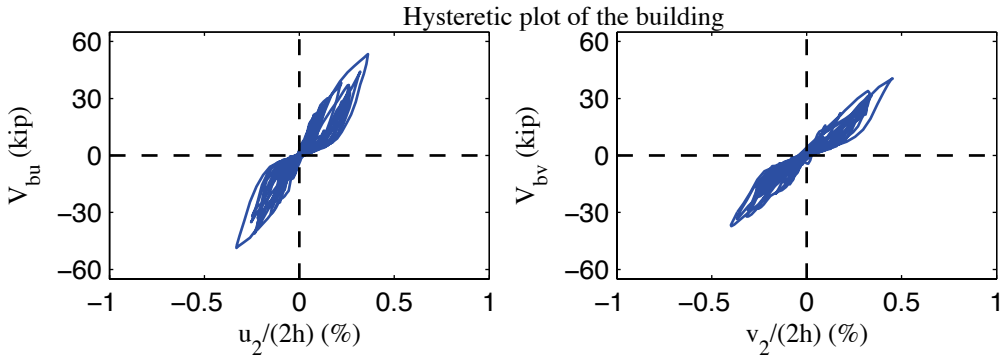

Figure O-11: A2b-3D-SD-a model, hysteretic plot of the building, 100 % Canoga Park, 3D nonlinear analysis

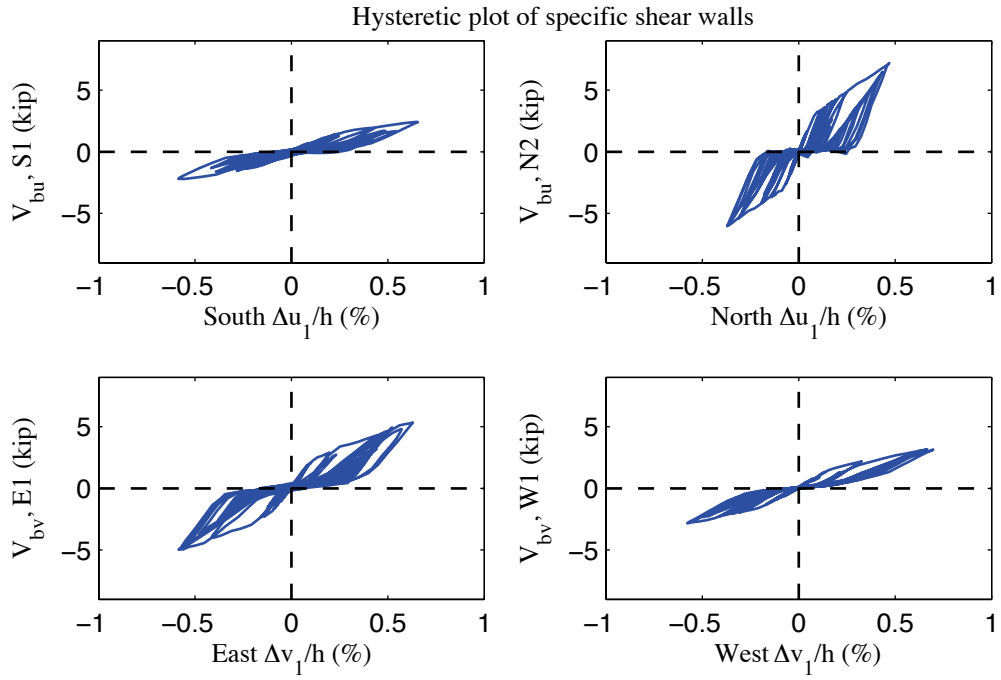

Figure O-12: A2b-3D-SD-a model, hysteretic plot of shear walls at each elevation, 100 % Canoga Park, 3D nonlinear analysis

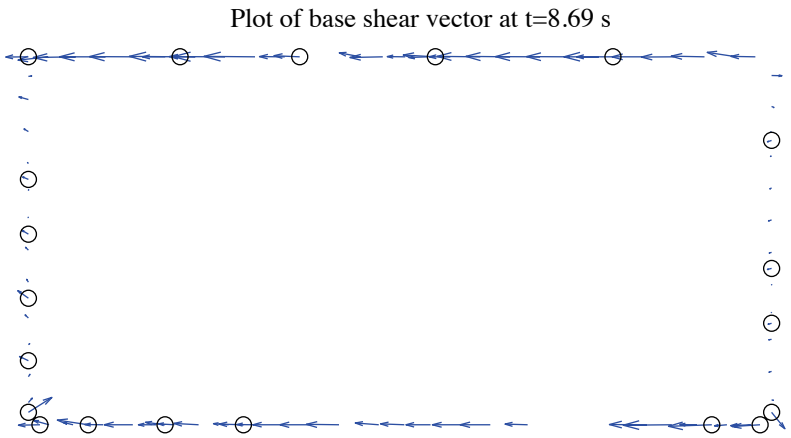

Figure O-13: A2b-3D-SD-a model, field plot of peak total base shear, 100 % Canoga Park, 3D nonlinear analysis (maximum anchor/hold down base shear is 1.61 kips)

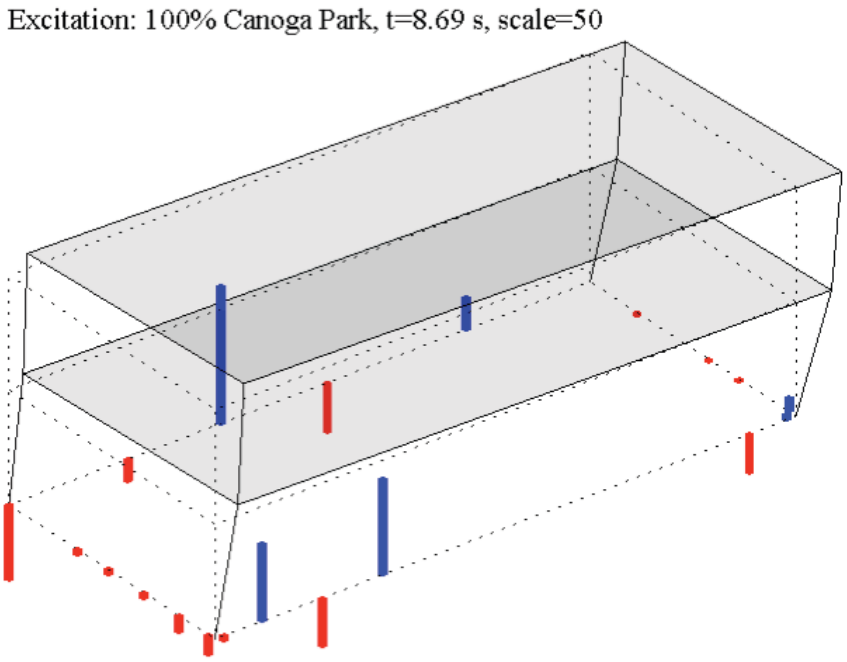

Figure O-14: A2b-3D-SD-a model, simplified illustration of corner displacements with hold down forces from load cells,100 % Canoga Park, 3D nonlinear analysis (max hold down tensile force is -2.81 kips)

Appendix P: Analysis Results of State-of-the-art, Phase 2c, 2D, model a (A2c-2D-a)

P.1 Model description

This state-of-the-art 2D model features subpanel bracing models of shear walls and gravity walls, explicit models of hold downs, and rigid leaning columns. All walls are covered by both OSB and gypsum sheathing. Interplay between different elevations is not allowed in 2D models, representing the effect of flexible diaphragms. Seismic mass is lumped at leaning column nodes. The lateral displacement and shear wall capacity ($\delta(0.2V_{nA})$, $0.2V_{nA}$) from test is utilized to determine the stiffness of elastic material and the first point on the backbone curve of Pinching4 material of shear wall bracing. Figure P-1 (a) to (d) illustrate OpenSees models of South, North, East and West elevations. Simulation results are presented and discussed in later sections. Definitions of output physical quantities and explanation of post-process method can be found in Appendix E.

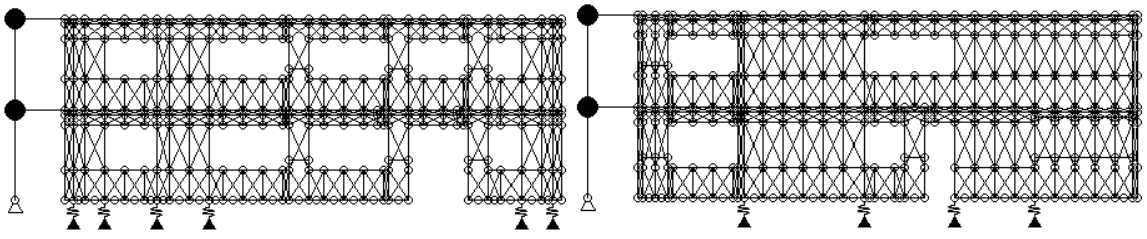

(a) South

(b) North

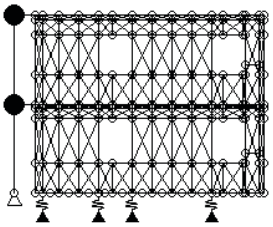

(c) East

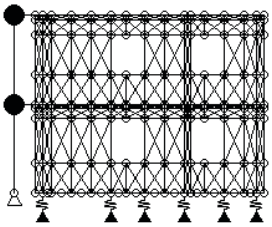

(d) West

Figure P-1: A2c-2D-a model

P.2 Free vibration analysis results

Free vibration analysis is performed for each elevation model. Values of first two natural periods are tabulated (Table P-1). Figure P-2 shows corresponding mode shapes.

Table P-1: Free vibration analysis results, A2c-2D-a model

Elevation	1st natural period (s)	2nd natural period (s)
South	0.232	0.107
North	0.176	0.093
East	0.257	0.103
West	0.255	0.105

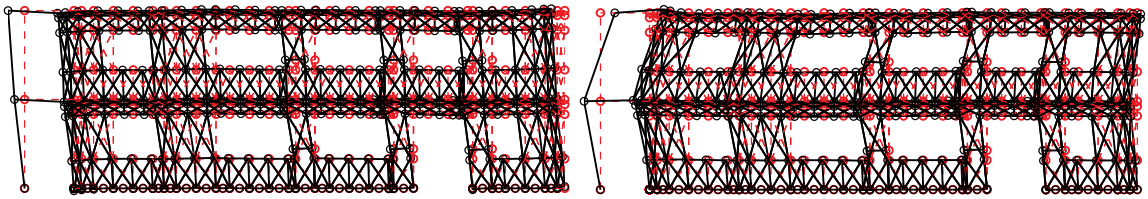

(a) South, mode 1, T_1=0.232 s (b) South, mode 2, T_2=0.107 s

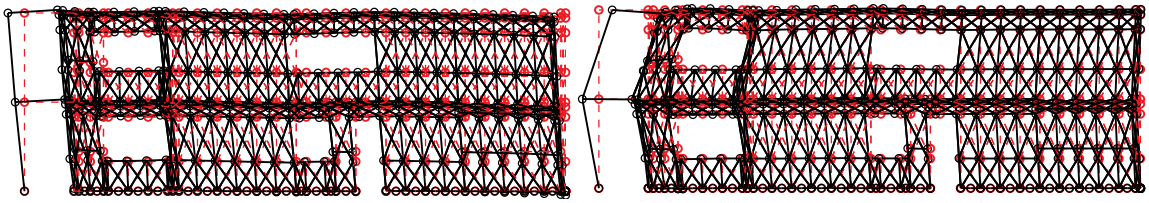

(c) North mode 1, T_1=0.176 s (d) North mode 2, T_2=0.093 s

(e) East mode 1, T_1=0.257 s (f) East mode 2, T_2=0.103 s

(g) West mode 1, T_1=0.255 s (h) West mode 2, T_2=0.105 s

Figure P-2: First two natural modes of A2c-2D-a model

P.3 Linear static analysis results

Linear static analysis is performed on each wall line. The total lateral load on that wall line is one half of the design base shear. The vertical distribution of lateral load follows the distribution of equivalent lateral load in the design narrative (Madsen et al. 2011).

Although each wall line is analyzed independently, to make a better summary and to make better comparisons with 3D models, results of individual wall lines are post-processed to reconstruct physical quantities of the whole building behavior, such as building displacements/drifts and total building base shear.

Table P-2 summarizes the breakdown of peak total base shear among four elevations. As shown in the table, each of two facing wall lines take 5.5 kips of base shear, and wall lines perpendicular to the loading direction take zero base shear as a natural result of 2D analysis.

Table P-3 shows peak building and wall line deflections. Practicing engineers can linearly upscale these data and develop an estimate of the building's performance at a certain lateral force level. In 2D analysis, only wall lines along the loading direction have displacements in the loading direction.

Table P-4 is an evaluation of the each wall line's lateral stiffness of long and short direction and its breakdown among shear walls (SW) and other systems. Covered by the same type of OSB sheathing with shear walls (even though the fastener spacing is

different), gravity walls make a comparable contribution to total lateral stiffness like shear walls. The percentage ranges from 11.0% (West) to as much as 45.1% (South). This also indicates that behaviors of individual wall lines can vary significantly since they have very different stiffness and breakdown of lateral force and gravity systems.

Table P-2: Breakdown of peak base shear, linear static analysis, A2c-2D-a model

Load direction	**LONG**				
Elevation	**South V_b**	**North V_b**	**East V_b**	**West V_b**	**Peak V_b**
kips	5.5	5.5	0.0	0.0	11.1
%	50.0	50.0	0.0	0.0	100.0
Load direction	**SHORT**				
Elevation	**South V_b**	**North V_b**	**East V_b**	**West V_b**	**Peak V_b**
kips	0.0	0.0	5.5	5.5	11.1
%	0.0	0.0	50.0	50.0	100.0

Table P-3: Peak building and wall line deflection, linear static analysis, A2c-2D-a model

Load direction	**LONG**							
Deflection (in.)	**u_1**	**u_2**	**v_1**	**v_2**	**Δu_1**	**Δu_2**	**Δv_1**	**Δv_2**
Building	0.043	0.072	0.000	0.000	0.043	0.030	0.000	0.000
South	0.057	0.094	0.000	0.000	0.057	0.037	0.000	0.000
North	0.028	0.050	0.000	0.000	0.028	0.022	0.000	0.000
East	-	-	-	-	-	-	-	-
West	-	-	-	-	-	-	-	-
Load direction	**SHORT**							
Deflection (in.)	**u_1**	**u_2**	**v_1**	**v_2**	**Δu_1**	**Δu_2**	**Δv_1**	**Δv_2**
Building	0.000	0.000	0.067	0.115	0.000	0.000	0.067	0.048
South	-	-	-	-	-	-	-	-
North	-	-	-	-	-	-	-	-
East	0.000	0.000	0.066	0.113	0.000	0.000	0.066	0.048
West	0.000	0.000	0.069	0.117	0.000	0.000	0.069	0.049

Table P-4: Breakdown of lateral stiffness, A2c-2D-a model

SOUTH			**NORTH**		
Shear wall k_u (%)	**Gravity wall k_u (%)**	**k_u (kip/in)**	**Shear wall k_v (%)**	**Gravity wall k_v (%)**	**k_v (kip/in)**
54.9	45.1	58.6	74.4	25.6	109.9
EAST			**WEST**		
Shear wall k_u (%)	**Gravity wall k_u (%)**	**k_u (kip/in)**	**Shear wall k_v (%)**	**Gravity wall k_v (%)**	**k_v (kip/in)**
86.9	13.1	48.8	89.0	11.0	47.1

P.4 Nonlinear static (pushover) analysis results

Table P-5 is created following the same logic with Table P-2, but the analysis type is nonlinear static (pushover). Pushover curves of the building and each wall line are presented in Figure P-3 and Figure P-4.

These tables and figures indicate that the wall lines do not reach their peak capacity at exactly the same drift level. Accordingly, total capacity of the building reconstructed using 2D results is no greater than the sum of wall line capacities in the load direction. This observation is more apparent in long direction. Total capacity of the wall line increases since the capacity of gravity walls is included. The trend is more significant in long direction given that North and South elevations are much wider and have larger areas covered by sheathed gravity walls. The missing of diaphragm stiffness and induced interplay of wall lines can make a significant difference between 2D analysis and real 3D analysis.

Table P-5: Breakdown of peak base shear, pushover analysis, A2c-2D-a model

Load direction	**LONG**				
Elevation	**South V_b**	**North V_b**	**East V_b**	**West V_b**	**Peak V_b**
kips	30.3	43.6	0.0	0.0	72.4
%	41.8	60.2	0.0	0.0	100.0
Load direction	**SHORT**				
Elevation	**South V_b**	**North V_b**	**East V_b**	**West V_b**	**Peak V_b**
kips	0.0	0.0	22.5	24.2	45.6
%	0.0	0.0	49.3	53.0	100.0

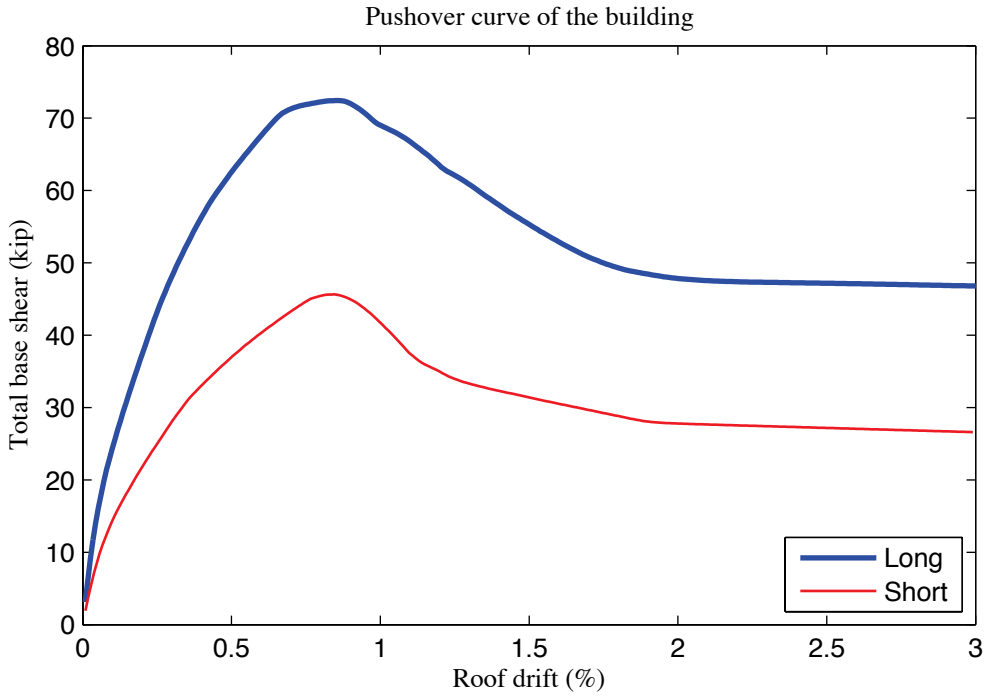

Figure P-3: Pushover curve of A2c-2D-a model

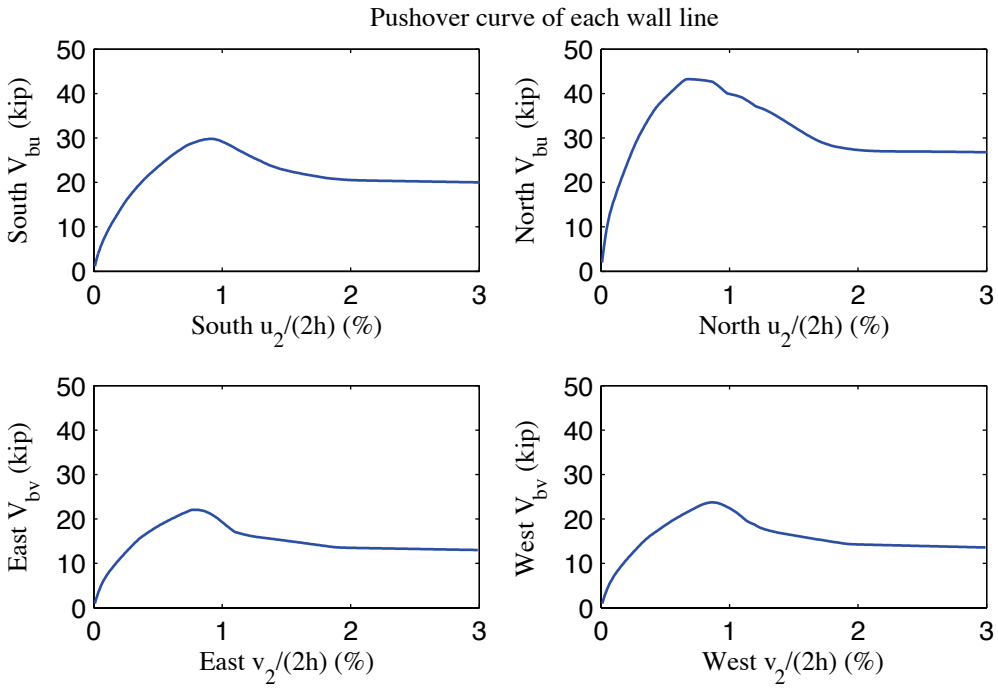

Figure P-4: Pushover curve of each wall line, A2c-2D-a model

P.5 Linear time history analysis results

Linear time history analysis is performed on 2D models under Canoga Park and Rinaldi ground motion records of Northridge earthquake in 1994. We considered three scale levels (16%, 44% and 100%) and single axis excitation is applied in the lateral direction of a single wall line.

Table P-6 to Table P-9 demonstrate the reconstructed linear elastic performance of the building under designated ground motions. Table P-6 shows peak story relative accelerations in the unit of g. Table P-7 and Table P-8 report peak roof drift and story drift of the building and the corresponding time step (t_*) and the base shear at that time. Note that the base shear at the time of peak roof drift may not be the peak total building base shear in that direction (see Table P-9).

The response of each wall line is available directly from 2D analysis results, so peak story drift and peak base shear of each wall line are listed in Table P-10 and Table P-11.

Wall lines behave linearly since peak drift and peak base shear appear at the same time when the ground motion is linearly scaled. Figure P-5 is a vector plot of the peak total resultant base shear of the building under 100% Canoga Park excitation. Since four dynamical analyses in 2D should be performed separately in order to create the plot, base shear vectors are always in-line with the wall. Comparison with nonlinear analysis results of the same excitation provides insightful observations on the building's response and requirements on modeling fidelity and analysis type.

Table P-6: A2c-2D-a model peak story relative acceleration in g, linear time history analysis

Load Case	Ground Motion	LONG			SHORT		
		a_g	Floor a	Roof a	a_g	Floor a	Roof a
EQ_2D_1axis_1	CNP 16%	0.067	0.080	0.164	0.057	0.094	0.142
EQ_2D_1axis_2	CNP 44%	0.185	0.190	0.368	0.157	0.230	0.391
EQ_2D_1axis_3	CNP 100%	0.420	0.436	0.833	0.356	0.523	0.882
EQ_2D_1axis_4	RRS 16%	0.132	0.092	0.161	0.078	0.197	0.336
EQ_2D_1axis_5	RRS 44%	0.363	0.247	0.439	0.214	0.554	0.934
EQ_2D_1axis_6	RRS 100%	0.825	0.560	0.991	0.486	1.260	2.124

Table P-7: A2c-2D-a model peak building roof drift and base shear, linear time history analysis

Load Case	Ground Motion	LONG			SHORT		
		$u_2/(2h)$ (%)	t_* (s)	V_b @ t_* (kips)	$v_2/(2h)$ (%)	t_* (s)	V_b @ t_* (kips)
EQ_2D_1axis_1	CNP 16%	-0.025	8.46	8.1	-0.038	9.71	8.7
EQ_2D_1axis_2	CNP 44%	-0.069	8.46	22.4	-0.106	9.71	23.9
EQ_2D_1axis_3	CNP 100%	-0.157	8.46	50.8	-0.240	9.71	54.4
EQ_2D_1axis_4	RRS 16%	0.035	2.56	13.2	-0.072	4.30	14.9
EQ_2D_1axis_5	RRS 44%	0.096	2.56	36.2	-0.197	4.30	40.9
EQ_2D_1axis_6	RRS 100%	0.219	2.56	82.3	-0.448	4.30	93.1

Table P-8: A2c-2D-a model peak building story drift, linear time history analysis

Load Case	Ground Motion	LONG				SHORT			
		$\Delta u_1/h$ (%)	t_* (s)	$\Delta u_2/h$ (%)	t_* (s)	$\Delta v_1/h$ (%)	t_* (s)	$\Delta v_2/h$ (%)	t_* (s)
EQ_2D_1 axis_1	CNP 16%	-0.032	8.46	-0.018	8.46	-0.049	9.71	-0.028	9.71
EQ_2D_1 axis_2	CNP 44%	-0.089	8.46	-0.049	8.46	-0.134	9.71	-0.078	9.71
EQ_2D_1 axis_3	CNP 100%	-0.203	8.46	-0.112	8.46	-0.304	9.71	-0.177	9.71
EQ_2D_1 axis_4	RRS 16%	0.045	2.56	0.025	2.56	-0.084	4.30	-0.059	4.30
EQ_2D_1 axis_5	RRS 44%	0.123	2.56	0.070	2.56	-0.231	4.30	-0.163	4.30
EQ_2D_1 axis_6	RRS 100%	0.279	2.56	0.158	2.56	-0.526	4.30	-0.371	4.30

Table P-9: A2c-2D-a model peak building base shear, linear time history analysis

		LONG		SHORT		RESULTANT	
Load Case	**Ground Motion**	**Peak V_{bu} (kip)**	**t @ peak V_{bu} (s)**	**Peak V_{bv} (kip)**	**t @ peak V_{bv} (s)**	**Peak V_b (kip)**	**t @ peak V_b (s)**
EQ_2D_1 axis_1	CNP 16%	8.1	8.46	8.7	9.71	8.8	9.71
EQ_2D_1 axis_2	CNP 44%	22.4	8.46	23.9	9.71	24.2	9.71
EQ_2D_1 axis_3	CNP 100%	50.8	8.46	54.4	9.71	55.0	9.71
EQ_2D_1 axis_4	RRS 16%	13.2	2.56	14.9	4.30	18.1	4.30
EQ_2D_1 axis_5	RRS 44%	36.2	2.56	40.9	4.30	49.7	4.30
EQ_2D_1 axis_6	RRS 100%	82.3	2.56	93.1	4.30	113.0	4.30

Table P-10: A2c-2D-a model peak wall line story drift, linear time history analysis

LONG		**SOUTH**				**NORTH**			
Load Case	**Ground Motion**	**$\Delta u_1/h$ (%)**	**t_* (s)**	**$\Delta u_2/h$ (%)**	**t_* (s)**	**$\Delta u_1/h$ (%)**	**t_* (s)**	**$\Delta u_2/h$ (%)**	**t_* (s)**
EQ_2D_1axis_1	CNP 16%	0.059	8.46	0.032	8.46	0.033	4.27	0.026	4.27
EQ_2D_1axis_2	CNP 44%	0.161	8.46	0.089	8.46	0.090	4.27	0.071	4.27
EQ_2D_1axis_3	CNP 100%	0.367	8.46	0.203	8.46	0.205	4.27	0.160	4.27
EQ_2D_1axis_4	RRS 16%	0.082	4.33	0.045	4.33	0.042	2.55	0.030	7.61
EQ_2D_1axis_5	RRS 44%	0.225	4.33	0.124	4.33	0.116	2.55	0.084	7.61
EQ_2D_1axis_6	RRS 100%	0.512	4.33	0.281	4.33	0.265	2.55	0.190	7.61
SHORT		**EAST**				**WEST**			
Load Case	**Ground Motion**	**$\Delta v_1/h$ (%)**	**t_* (s)**	**$\Delta v_2/h$ (%)**	**t_* (s)**	**$\Delta v_1/h$ (%)**	**t_* (s)**	**$\Delta v_2/h$ (%)**	**t_* (s)**
EQ_2D_1axis_1	CNP 16%	0.047	9.70	0.031	6.59	0.054	9.71	0.033	9.72
EQ_2D_1axis_2	CNP 44%	0.130	9.70	0.085	6.59	0.150	9.71	0.089	9.72
EQ_2D_1axis_3	CNP 100%	0.295	9.70	0.193	6.59	0.341	9.71	0.203	9.72
EQ_2D_1axis_4	RRS 16%	0.084	2.78	0.061	4.29	0.093	4.30	0.069	4.30
EQ_2D_1axis_5	RRS 44%	0.232	2.78	0.168	4.29	0.255	4.30	0.190	4.30
EQ_2D_1axis_6	RRS 100%	0.527	2.78	0.383	4.29	0.581	4.30	0.432	4.30

Table P-11: A2c-2D-a model peak wall line base shear, linear time history analysis

LONG		SOUTH		NORTH		% of Peak V_{bu}	
Load Case	**Ground Motion**	**Peak V_{bu} (kips)**	**t @ peak V_{bu} (s)**	**Peak V_{bu} (kips)**	**t @ peak V_{bu} (s)**	**South**	**North**
EQ_2D_1axis_1	CNP 16%	5.8	8.46	6.0	4.27	71.3	28.7
EQ_2D_1axis_2	CNP 44%	15.9	8.46	16.6	4.27	71.3	28.7
EQ_2D_1axis_3	CNP 100%	36.2	8.46	37.8	4.27	71.3	28.7
EQ_2D_1axis_4	RRS 16%	7.9	4.33	7.7	2.55	43.0	57.0
EQ_2D_1axis_5	RRS 44%	21.8	4.33	21.2	2.55	43.0	57.0
EQ_2D_1axis_6	RRS 100%	49.4	4.33	48.3	2.55	43.0	57.0
SHORT		**EAST**		**WEST**		**% of Peak V_{bv}**	
Load Case	**Ground Motion**	**Peak V_{bv} (kips)**	**t @ peak V_{bv} (s)**	**Peak V_{bv} (kips)**	**t @ peak V_{bv} (s)**	**East**	**West**
EQ_2D_1axis_1	CNP 16%	4.2	9.70	4.6	9.71	47.7	52.3
EQ_2D_1axis_2	CNP 44%	11.5	9.70	12.5	9.71	47.6	52.4
EQ_2D_1axis_3	CNP 100%	26.1	9.70	28.5	9.71	47.6	52.4
EQ_2D_1axis_4	RRS 16%	7.5	2.78	7.8	4.30	47.9	52.1
EQ_2D_1axis_5	RRS 44%	20.5	2.78	21.3	4.30	47.9	52.1
EQ_2D_1axis_6	RRS 100%	46.7	2.78	48.5	4.30	47.9	52.1

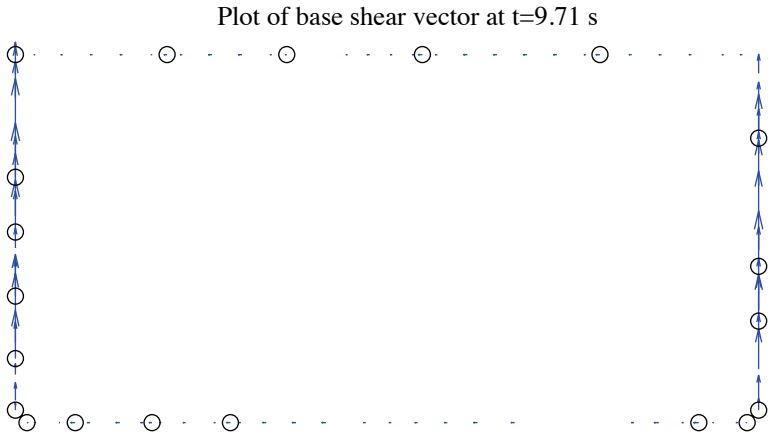

Figure P-5: A2c-2D-a model, base shear vector plot at the moment of peak total base shear, 100 % Canoga Park, 2D linear analysis (maximum anchor/hold down base shear is 2.86 kips)

P.6 Nonlinear time history analysis results

Same ground motions are applied to the model with material and geometrical nonlinearity. Table P-12 to Table P-17 are replicas of Table P-6 to Table P-11, but for nonlinear time history analyses. Since this analysis type is most complicated and closest to reality and experiments, behavior of wall lines and smeared hold downs are further studied. Table P-18 expands the breakdown of each wall line's peak base shear between shear walls, gravity walls and other systems. Table P-19 is peak value of hold down tensile force of two selected pairs. Hold down 5 and 6 are on shear wall L1S1, South elevation and hold down 7 and 8 are on shear wall L1W1, West elevation. These shear walls have lowest capacities compared with others on the same wall line and they meet at the southwest edge of the building.

Time history plots in this section include plots of story drifts of the building and each wall line (Figure P-6 to Figure P-8), total building base shear in long and short direction (Figure P-9) and axial forces of hold downs in (Figure P-10). Hysteretic plots in Figure P-11 and Figure P-12 are helpful for visual examination of nonlinear base shear-drift relationship of the building and the weakest shear wall on each wall line. In comparison with linear time history analysis, vector plot of peak total base shear is illustrated in Figure P-13. Figure P-14 presents a simplified deformed shape of the building (see (Peterman 2014) for details of the method) and axial force of all twenty hold downs at the moment of peak total base shear. The same sign convention with tests is adopted. Red bars indicate tensile (negative) force and blue ones are for compressive (positive) force.

Hysteretic behavior is seen in the building and typical shear walls under design-based earthquake (100% Canoga Park excitation in one axis, see Figure P-11 and Figure P-12). However, behaviors of individual wall lines differ significantly. South wall line reaches 0.93% peak floor story drift but peak story drifts of all other wall lines are less than 0.73% (Table P-16). The reconstructed peak building story drift is 0.36% in long direction, (Table P-14), still much less than the peak value of South wall line. The worst-case scenario from 2D analysis can greatly overestimate the nonlinear response of the whole building and yield conservative observation. Figure P-13 shows that peak resultant base shear is taken by both shear walls and gravity walls, and that base shear vectors in anchors and hold downs align with wall lines due to the limit of 2D modeling and analysis. Table P-19, Figure P-10 and Figure P-14 demonstrate that hold downs in a pair do not experience the same amount of force with opposite signs even in 2D analysis, an evidence that supports Type II shear wall behavior despite Type I design assumption.

The near-field Rinaldi record is much stronger in terms of peak ground acceleration, especially in the long direction. With the addition of sheathed gravity walls, the lateral resistance of wall lines increases significantly. Even when loaded with 100% Rinaldi record, peak story drifts of North, East and West wall lines are all below 1.2%. Only South wall line is believed to fail with peak story drift over 5.5%. The portion of base shear taken by gravity wall does not change much with scale factors considered so far in this research, as shown in Table P-18. Again, the table demonstrates that the base shear taken by anchors on bottom tracks of gravity walls can be quite large, sometimes even larger than half of the total base shear (e.g. South wall lines).

Table P-12: A2c-2D-a model peak story relative acceleration in g, nonlinear time history analysis

Load Case	Ground Motion	LONG			SHORT		
		a_g	Floor a	Roof a	a_g	Floor a	Roof a
EQ_2D_1axis_1	CNP 16%	0.067	0.136	0.213	0.057	0.164	0.220
EQ_2D_1axis_2	CNP 44%	0.185	0.588	0.608	0.157	0.514	0.429
EQ_2D_1axis_3	CNP 100%	0.420	1.577	0.999	0.356	0.692	0.924
EQ_2D_1axis_4	RRS 16%	0.132	0.255	0.284	0.078	0.365	0.330
EQ_2D_1axis_5	RRS 44%	0.363	1.221	0.986	0.214	0.641	0.839
EQ_2D_1axis_6	RRS 100%	0.825	2.492	1.286	0.486	1.088	1.159

Table P-13: A2c-2D-a model peak building roof drift and base shear, nonlinear time history analysis

Load Case	Ground Motion	LONG			SHORT		
		$u_2/(2h)$ (%)	t_* (s)	V_b @ t_* (kips)	$v_2/(2h)$ (%)	t_* (s)	V_b @ t_* (kips)
EQ_2D_1axis_1	CNP 16%	0.030	8.65	8.2	0.063	9.90	10.7
EQ_2D_1axis_2	CNP 44%	0.090	11.72	18.9	0.160	9.95	18.9
EQ_2D_1axis_3	CNP 100%	0.356	8.71	39.5	0.510	9.99	37.7
EQ_2D_1axis_4	RRS 16%	0.051	2.57	14.5	-0.112	4.36	16.2
EQ_2D_1axis_5	RRS 44%	0.222	2.63	30.2	0.326	6.04	29.0
EQ_2D_1axis_6	RRS 100%	1.547	2.86	27.3	0.762	6.06	45.5

Table P-14: A2c-2D-a model peak building story drift, nonlinear time history analysis

Load Case	Ground Motion	LONG				SHORT			
		$\Delta u_1/h$ (%)	t_* (s)	$\Delta u_2/h$ (%)	t_* (s)	$\Delta v_1/h$ (%)	t_* (s)	$\Delta v_2/h$ (%)	t_* (s)
EQ_2D_1 axis_1	CNP 16%	0.042	8.66	0.019	8.65	0.081	9.90	0.045	9.90
EQ_2D_1 axis_2	CNP 44%	0.132	11.72	0.052	8.67	0.213	9.94	0.108	9.96
EQ_2D_1 axis_3	CNP 100%	0.552	8.73	0.180	8.69	0.710	10.00	0.319	9.98
EQ_2D_1 axis_4	RRS 16%	0.070	2.57	0.033	2.57	-0.156	4.36	0.072	4.54
EQ_2D_1 axis_5	RRS 44%	0.335	2.63	0.110	2.63	0.448	3.40	0.244	3.90
EQ_2D_1 axis_6	RRS 100%	2.915	2.87	0.293	2.63	1.137	6.07	0.421	6.04

Table P-15: A2c-2D-a model peak building base shear, nonlinear time history analysis

		LONG		SHORT		RESULTANT	
Load Case	**Ground Motion**	**Peak V_{bu} (kip)**	**t @ peak V_{bu} (s)**	**Peak V_{bv} (kip)**	**t @ peak V_{bv} (s)**	**Peak V_b (kip)**	**t @ peak V_b (s)**
EQ_2D_1 axis_1	CNP 16%	8.2	8.65	11.0	9.89	11.4	9.89
EQ_2D_1 axis_2	CNP 44%	20.9	7.37	19.3	9.94	24.4	8.42
EQ_2D_1 axis_3	CNP 100%	50.5	8.66	37.7	9.99	50.5	8.66
EQ_2D_1 axis_4	RRS 16%	14.7	2.56	16.2	4.36	20.1	4.52
EQ_2D_1 axis_5	RRS 44%	37.4	2.59	30.7	3.39	39.6	2.58
EQ_2D_1 axis_6	RRS 100%	93.7	2.74	46.6	6.02	94.2	2.74

Table P-16: A2c-2D-a model peak wall line story drift, nonlinear time history analysis

LONG		**SOUTH**				**NORTH**			
Load Case	**Ground Motion**	**$\Delta u_1/h$ (%)**	**t_* (s)**	**$\Delta u_2/h$ (%)**	**t_* (s)**	**$\Delta u_1/h$ (%)**	**t_* (s)**	**$\Delta u_2/h$ (%)**	**t_* (s)**
EQ_2D_1axis_1	CNP 16%	0.077	8.66	0.035	8.66	0.033	4.28	0.026	4.27
EQ_2D_1axis_2	CNP 44%	0.247	11.89	0.098	8.67	0.101	7.36	0.059	4.21
EQ_2D_1axis_3	CNP 100%	0.931	8.74	0.283	8.71	0.325	8.65	0.152	8.67
EQ_2D_1axis_4	RRS 16%	0.134	4.37	0.060	4.38	0.044	2.55	0.032	7.62
EQ_2D_1axis_5	RRS 44%	0.569	2.64	0.244	6.84	0.227	4.33	0.078	4.52
EQ_2D_1axis_6	RRS 100%	5.541	2.91	0.388	2.63	0.927	4.40	0.302	6.79
SHORT		**EAST**				**WEST**			
Load Case	**Ground Motion**	**$\Delta v_1/h$ (%)**	**t_* (s)**	**$\Delta v_2/h$ (%)**	**t_* (s)**	**$\Delta v_1/h$ (%)**	**t_* (s)**	**$\Delta v_2/h$ (%)**	**t_* (s)**
EQ_2D_1axis_1	CNP 16%	0.072	9.88	0.040	9.89	0.103	9.91	0.057	9.91
EQ_2D_1axis_2	CNP 44%	0.216	9.94	0.112	9.96	0.220	9.95	0.120	9.96
EQ_2D_1axis_3	CNP 100%	0.707	10.00	0.345	9.98	0.731	10.00	0.324	9.98
EQ_2D_1axis_4	RRS 16%	0.164	4.35	0.078	4.54	0.162	4.52	0.081	4.36
EQ_2D_1axis_5	RRS 44%	0.447	3.40	0.268	3.90	0.470	3.41	0.258	3.90
EQ_2D_1axis_6	RRS 100%	1.172	6.07	0.468	6.04	1.131	6.07	0.410	6.04

Table P-17: A2c-2D-a model peak wall line base shear, nonlinear time history analysis

LONG		SOUTH		NORTH		% of Peak V_{bu}	
Load Case	**Ground Motion**	**Peak V_{bu} (kips)**	**t @ peak V_{bu} (s)**	**Peak V_{bu} (kips)**	**t @ peak V_{bu} (s)**	**South**	**North**
EQ_2D_1axis_1	CNP 16%	5.7	8.66	6.1	4.28	69.4	31.0
EQ_2D_1axis_2	CNP 44%	12.7	11.89	13.3	7.36	38.2	62.1
EQ_2D_1axis_3	CNP 100%	27.0	8.74	26.6	8.65	42.7	52.1
EQ_2D_1axis_4	RRS 16%	8.5	4.38	7.7	2.55	48.5	51.8
EQ_2D_1axis_5	RRS 44%	21.1	2.64	20.7	4.33	50.1	50.0
EQ_2D_1axis_6	RRS 100%	30.2	2.61	44.2	4.38	23.3	20.5
SHORT		**EAST**		**WEST**		**% of Peak V_{bv}**	
Load Case	**Ground Motion**	**Peak V_{bv} (kips)**	**t @ peak V_{bv} (s)**	**Peak V_{bv} (kips)**	**t @ peak V_{bv} (s)**	**East**	**West**
EQ_2D_1axis_1	CNP 16%	5.2	9.88	6.3	9.91	45.7	54.8
EQ_2D_1axis_2	CNP 44%	9.8	9.94	9.7	9.95	50.7	50.1
EQ_2D_1axis_3	CNP 100%	18.8	10.00	19.4	10.00	49.6	51.2
EQ_2D_1axis_4	RRS 16%	8.5	4.35	8.2	4.52	51.6	49.1
EQ_2D_1axis_5	RRS 44%	15.2	3.40	15.7	3.41	49.5	50.0
EQ_2D_1axis_6	RRS 100%	22.6	6.08	23.7	6.06	46.1	48.2

Table P-18: A2c-2D-a model wall line base shear breakdown, nonlinear time history analysis

LONG		SOUTH			NORTH		
Load Case	**Ground Motion**	**Peak V_{bu} (kips)**	**SW V_{bu} (%)**	**GW V_{bu} (%)**	**Peak V_{bu} (kips)**	**SW V_{bu} (%)**	**GW V_{bu} (%)**
EQ_2D_1axis_1	CNP 16%	5.7	34.0	66.0	6.1	60.2	39.8
EQ_2D_1axis_2	CNP 44%	12.7	36.1	63.9	13.3	61.1	38.9
EQ_2D_1axis_3	CNP 100%	27.0	36.4	63.6	26.6	56.1	43.9
EQ_2D_1axis_4	RRS 16%	8.5	34.5	65.5	7.7	60.5	39.5
EQ_2D_1axis_5	RRS 44%	21.1	37.0	63.0	20.7	57.9	42.1
EQ_2D_1axis_6	RRS 100%	30.2	35.7	64.3	44.2	53.8	46.2
SHORT		**EAST**			**WEST**		
Load Case	**Ground Motion**	**Peak V_{bv} (kips)**	**SW V_{bv} (%)**	**GW V_{bu} (%)**	**Peak V_{bv} (kips)**	**SW V_{bv} (%)**	**GW V_{bv} (%)**
EQ_2D_1axis_1	CNP 16%	5.2	71.2	28.8	6.3	81.1	18.9
EQ_2D_1axis_2	CNP 44%	9.8	73.2	26.8	9.7	81.6	18.4
EQ_2D_1axis_3	CNP 100%	18.8	70.7	29.3	19.4	80.2	19.8
EQ_2D_1axis_4	RRS 16%	8.5	78.2	21.8	8.2	81.9	18.1
EQ_2D_1axis_5	RRS 44%	15.2	71.5	28.5	15.7	80.7	19.3
EQ_2D_1axis_6	RRS 100%	22.6	73.8	26.2	23.7	81.7	18.3

Table P-19: A2c-2D-a model peak hold down tensile force at certain locations, nonlinear time history analysis

		L1S1, LC5		L1S1, LC6		L1W1, LC7		L1W1, LC8	
Load Case	**Ground Motion**	**Peak F (kips)**	**t @ peak F (s)**	**Peak F (kips)**	**t @ peak F (s)**	**Peak F (kips)**	**t @ peak F (s)**	**Peak F (kips)**	**t @ peak F (s)**
EQ_2D_1axis_1	CNP 16%	-0.11	12.91	-0.65	8.66	-0.89	9.91	-0.21	9.91
EQ_2D_1axis_2	CNP 44%	-0.48	11.89	-1.47	11.74	-1.62	9.95	-0.28	8.41
EQ_2D_1axis_3	CNP 100%	-1.15	10.59	-3.89	8.72	-3.64	9.99	-0.56	8.47
EQ_2D_1axis_4	RRS 16%	-0.30	4.52	-1.04	4.38	-1.23	4.53	-0.24	4.37
EQ_2D_1axis_5	RRS 44%	-0.86	4.63	-2.87	2.64	-2.54	6.05	-0.42	4.09
EQ_2D_1axis_6	RRS 100%	-1.02	2.45	-4.58	2.61	-4.56	6.05	-0.79	2.86

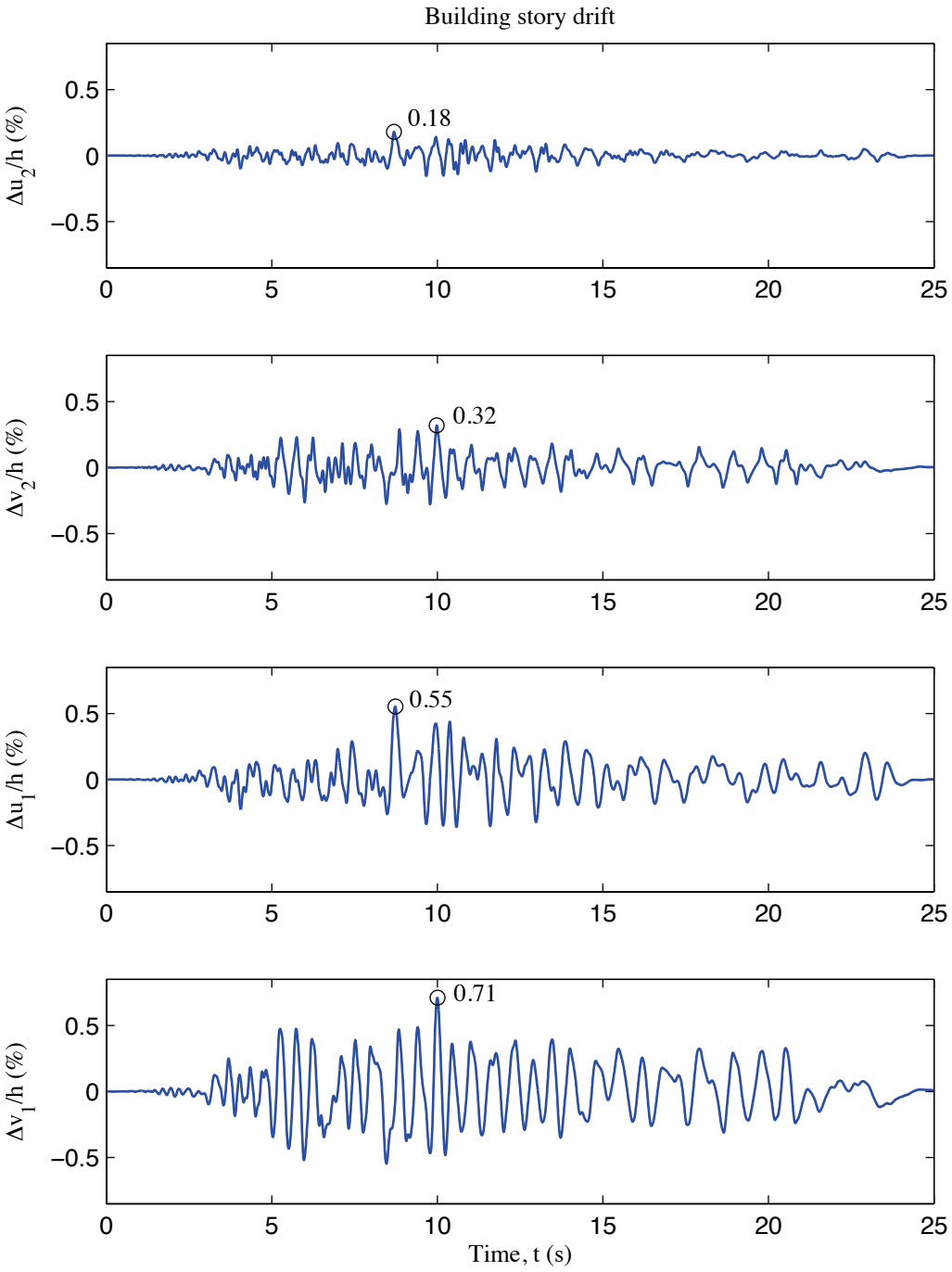

Figure P-6: A2c-2D-a model building story drift, 100 % Canoga Park, 2D nonlinear analysis

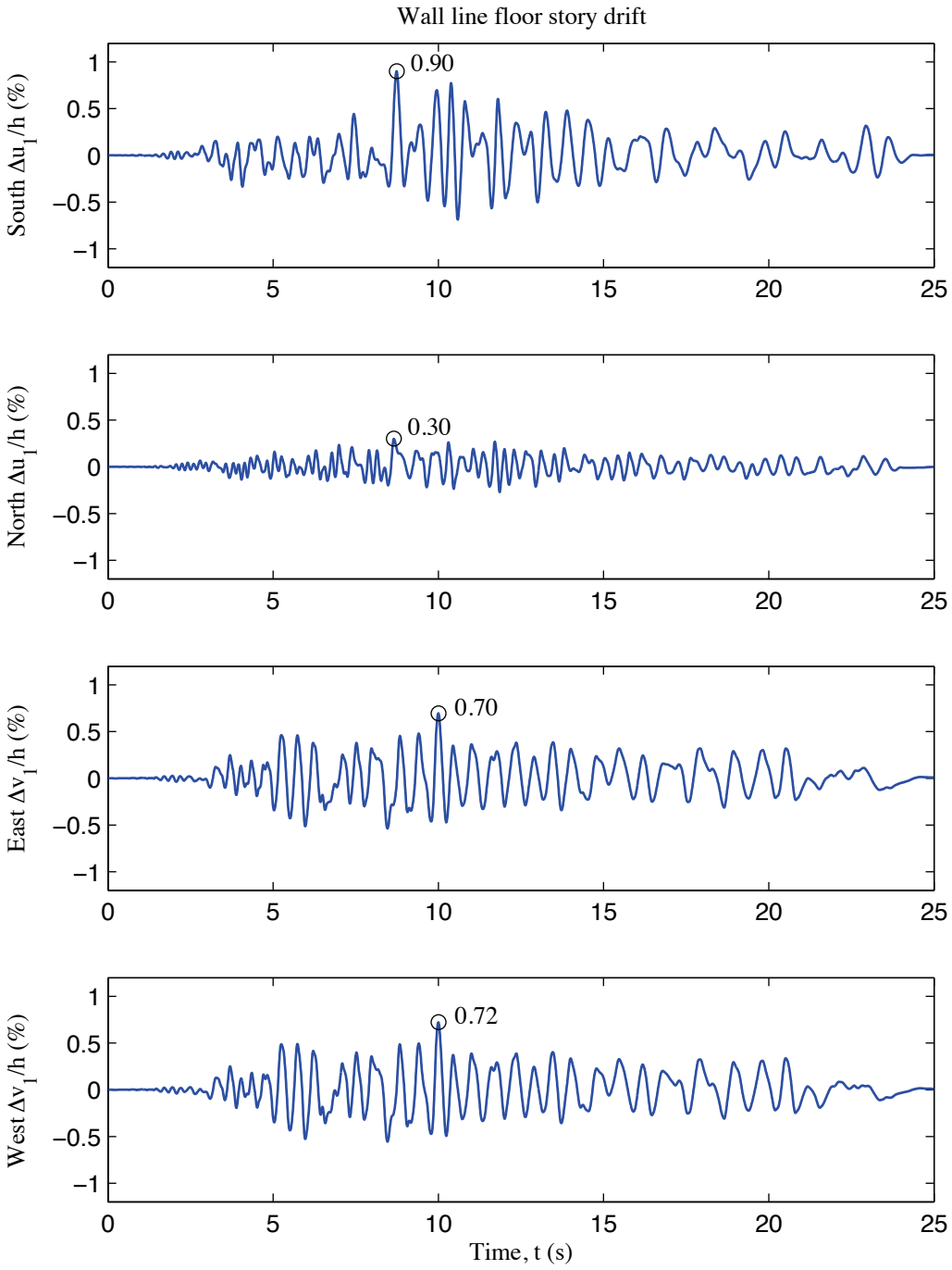

Figure P-7: A2c-2D-a model wall line floor story drift, 100 % Canoga Park, 2D nonlinear analysis

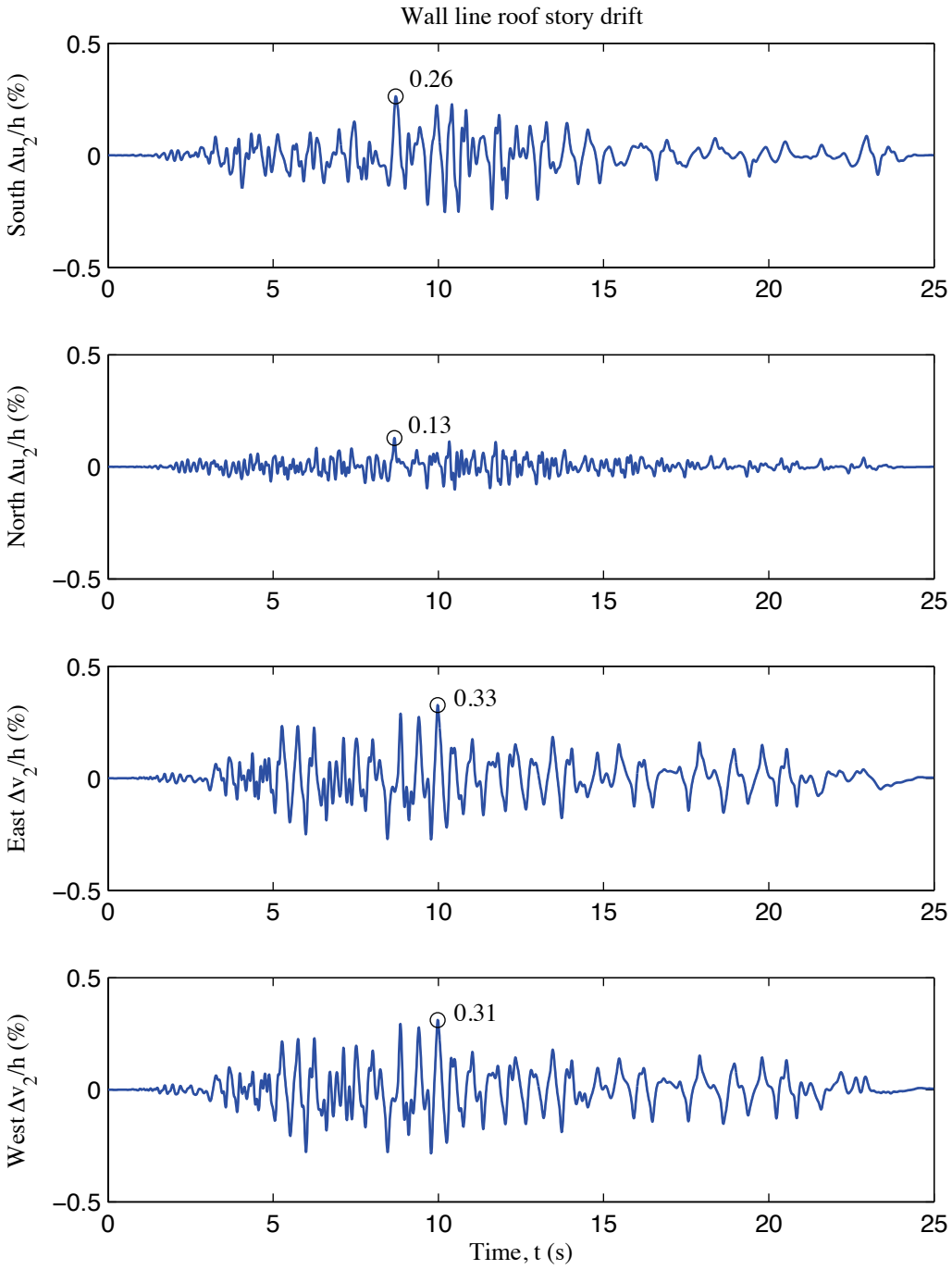

Figure P-8: A2c-2D-a model wall line roof story drift, 100 % Canoga Park, 2D nonlinear analysis

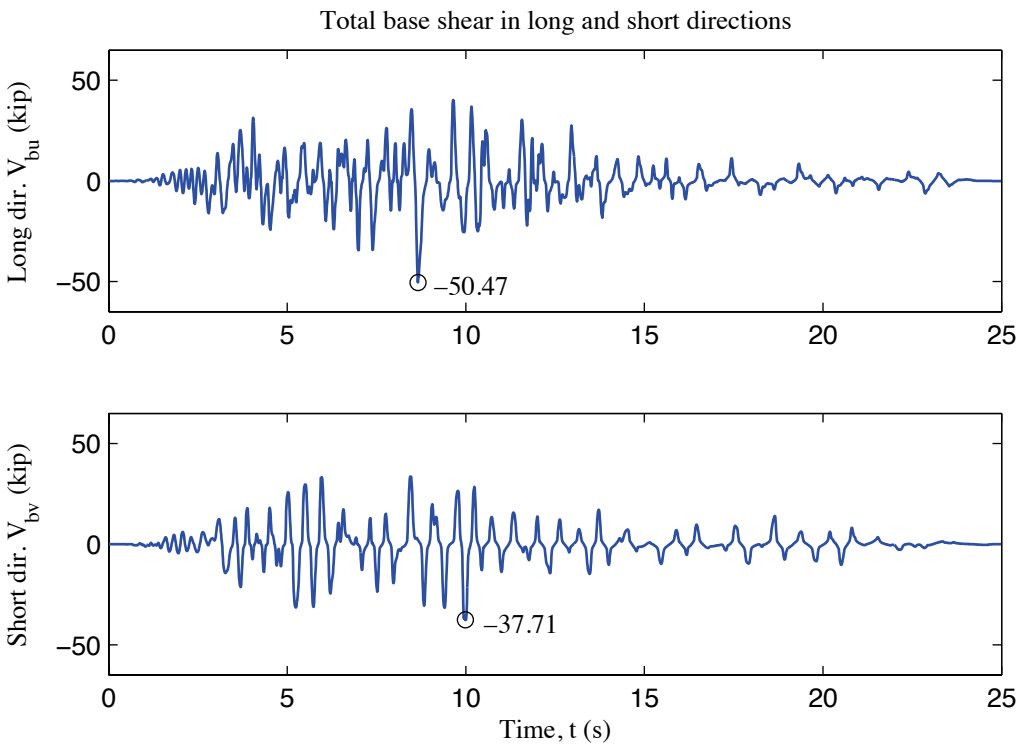

Figure P-9: A2c-2D-a model total building base shear, 100 % Canoga Park, 2D nonlinear analysis

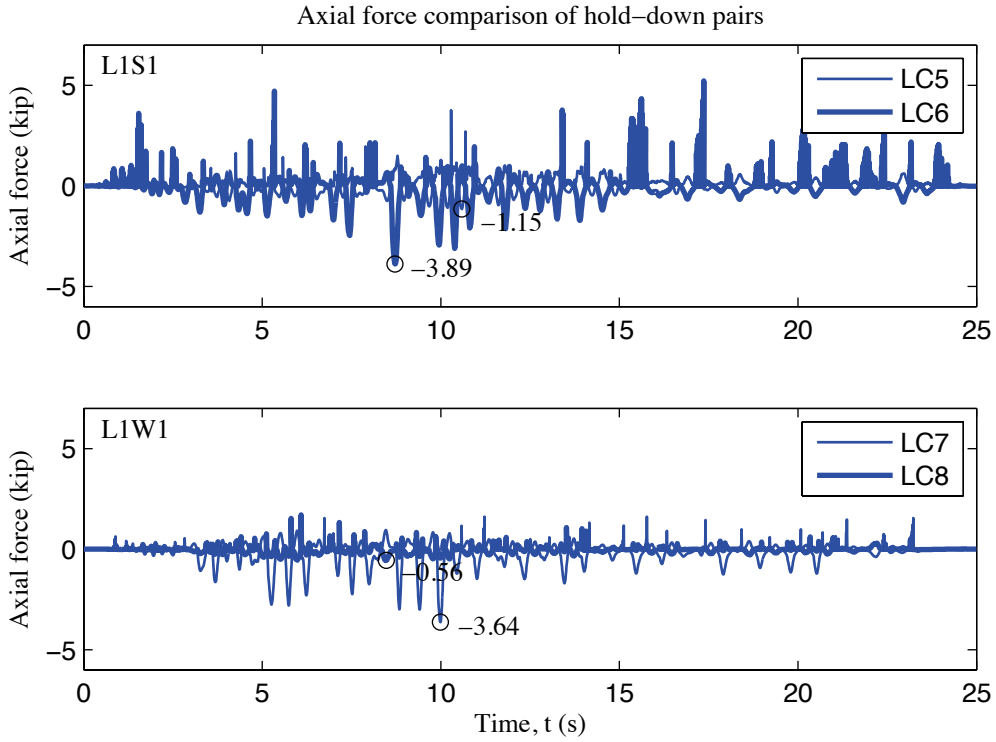

Figure P-10: A2c-2D-a model, load cell 5 to 8 axial forces, 100 % Canoga Park, 2D nonlinear analysis

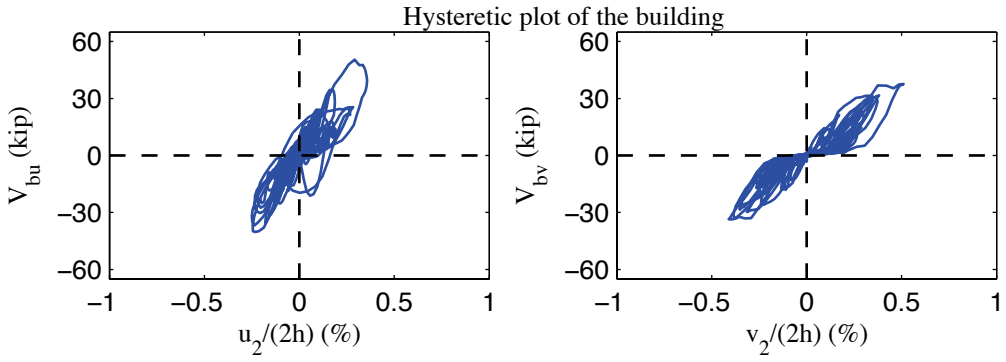

Figure P-11: A2c-2D-a model, hysteretic plot of the building, 100 % Canoga Park, 2D nonlinear analysis

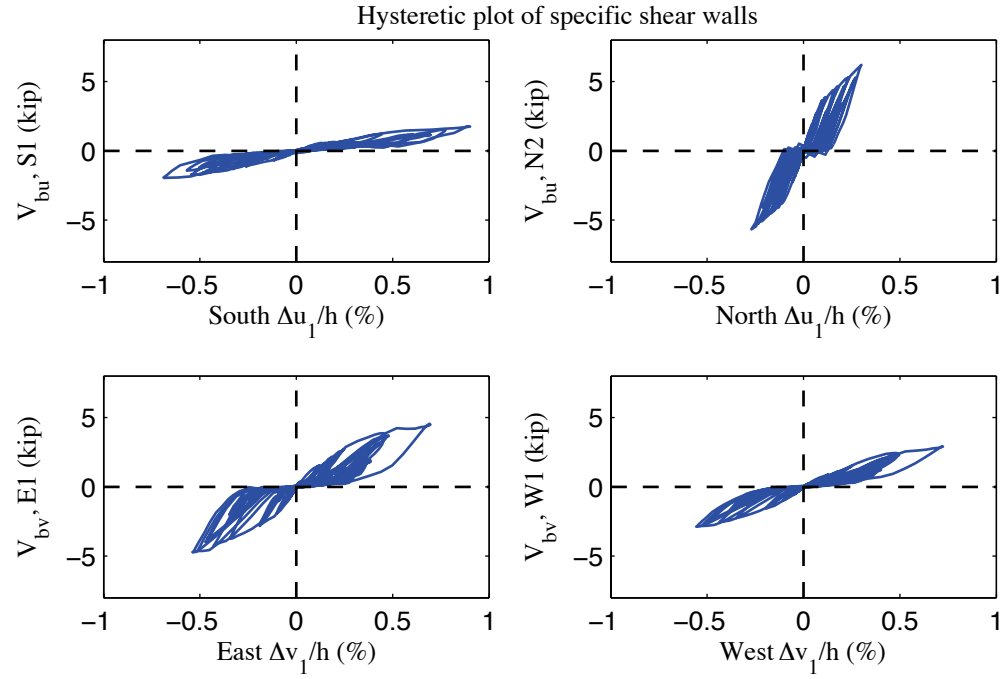

Figure P-12: A2c-2D-a model, hysteretic plot of shear walls at each elevation, 100 % Canoga Park, 2D nonlinear analysis

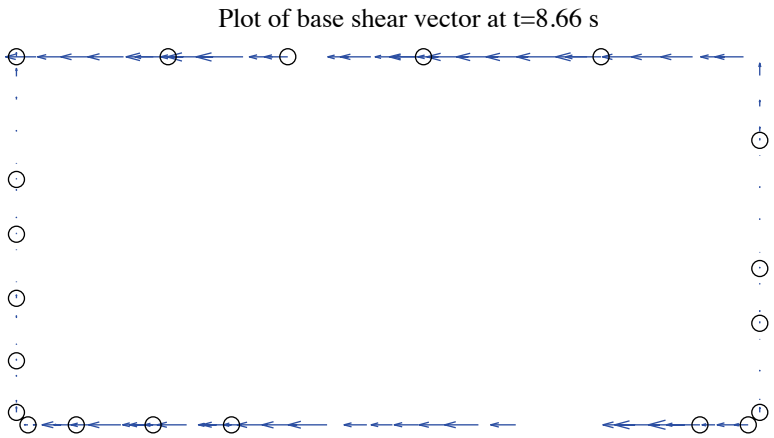

Figure P-13: A2c-2D-a model, field plot of peak total base shear, 100 % Canoga Park, 2D nonlinear analysis (maximum anchor/hold down base shear is 1.54 kips)

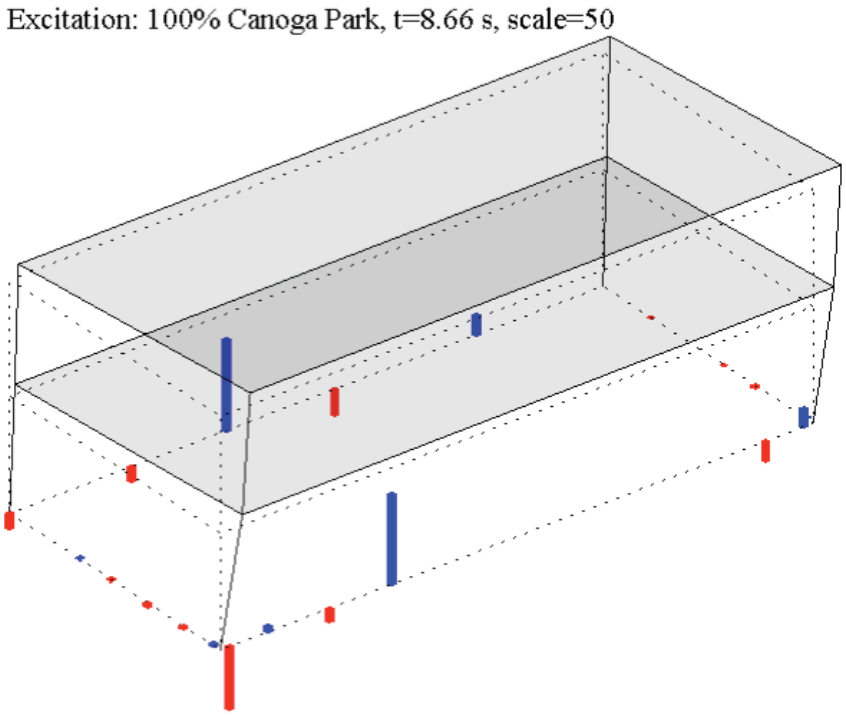

Figure P-14: A2c-2D-a model, simplified illustration of corner displacements with hold down forces from load cells,100 % Canoga Park, 2D nonlinear analysis (max hold down tensile force is -2.87 kips)

Appendix Q: Analysis Results of State-of-the-art, Phase 2c, 3D, rigid-diaphragm, model a (A2c-3D-RD-a)

Q.1 Model description

This state-of-the-art 3D model features subpanel bracing models of shear walls and gravity walls, explicit models of hold downs, and rigid diaphragms. All walls are covered by OSB and gypsum sheathing. Seismic mass is distributed to corners and stud ends. The lateral displacement and shear wall capacity ($\delta(0.2V_{nA})$, $0.2V_{nA}$) from test is utilized to determine the stiffness of elastic material and the first point on the backbone curve of Pinching4 material of shear wall bracing. Figure Q-1 is the 3D drawing of the building model with all members and diagonal bracings of sheathing panels. Definitions of output physical quantities and explanation of post-process method can be found in Appendix K.

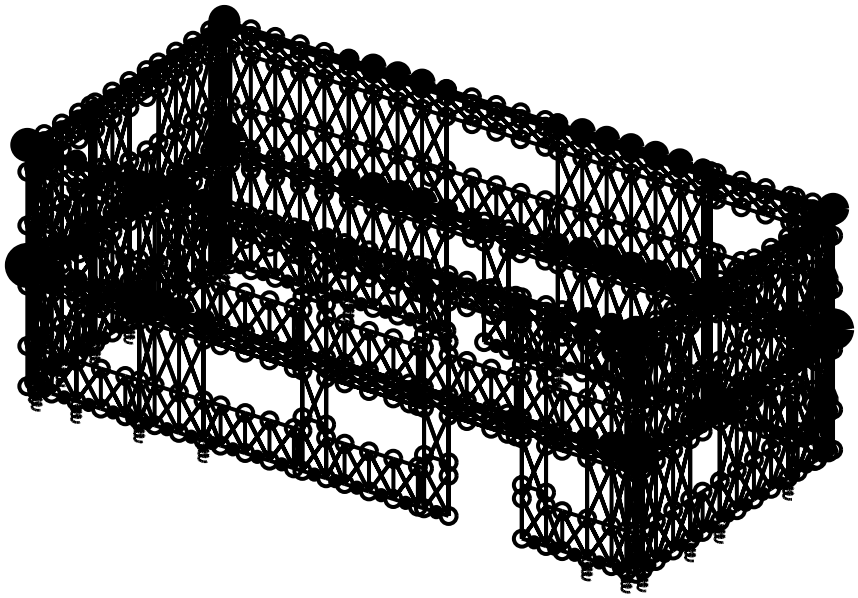

Figure Q-1: A2c-3D-RD-a model

Q.2 Free vibration analysis results

Free vibration analysis results are presented in Table Q-1 and Figure Q-2. Lateral stiffness in the short direction is smaller than lateral stiffness in the long direction and torsional stiffness is the largest. The observation holds for the first and the second mode, as indicated by Table Q-1.

Table Q-1: Free vibration analysis results, A2c-3D-RD-a model

Mode number	Natural period (s)	Mode description
1	0.226	Short, 1st
2	0.170	Long, 1st
3	0.150	Torsion, 1st
4	0.083	Short, 2nd
5	0.064	Long, 2nd
6	0.058	Torsion, 2nd

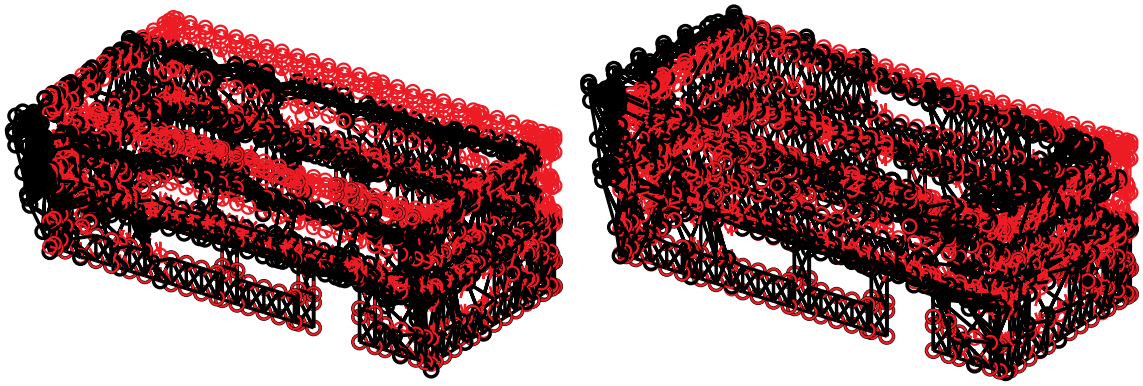

(a) Mode 1, T_1=0.226 s (b) Mode 2, T_2=0.170 s

Figure Q-2: First two natural modes of A2c-3D-RD-a model

Q.3 Linear static analysis results

Table Q-2 to Table Q-4 present linear static analysis results. The lateral load is the equivalent lateral force available from the design narrative (Madsen et al. 2011), applied equally at four corners. Two separate analyses were performed with the loading at long or short direction.

Table Q-2 summarizes the breakdown of peak total base shear among four elevations. Due to the interplay of asymmetrical LFRS, wall lines perpendicular to the loading direction still take a very small portion of base shear.

Table Q-3 shows peak building and wall line deflections. Practicing engineers can linearly upscale these data and develop an estimate of the building's performance at a certain lateral force level.

Table Q-4 is an evaluation of the building's lateral stiffness of long and short direction and its breakdown among shear walls (SW) and other systems. Covered by the same type of OSB and gypsum sheathing with shear walls (even though the fastener spacing is different), gravity walls make a comparable contribution to total lateral stiffness like shear walls. The effect is even more apparent in long direction, where wall lines are much wider and have larger areas covered by gravity walls. The stiffness of gravity walls can account for as much as 37% and 15% of total lateral stiffness in long and short direction.

Table Q-2: Breakdown of peak base shear, linear static analysis, A2c-3D-RD-a model

Load direction	**LONG**				
Elevation	**South V_b**	**North V_b**	**East V_b**	**West V_b**	**Peak V_b**
kips	4.1	6.9	0.0	0.1	11.1
%	36.7	62.5	0.1	0.8	100.0
Load direction	**SHORT**				
Elevation	**South V_b**	**North V_b**	**East V_b**	**West V_b**	**Peak V_b**
kips	0.0	0.0	5.6	5.4	11.1
%	0.1	0.4	50.8	48.9	100.0

Table Q-3: Peak building and wall line deflection, linear static analysis, A2c-3D-RD-a model

Load direction	**LONG**							
Deflection (in.)	**u_1**	**u_2**	**v_1**	**v_2**	**Δu_1**	**Δu_2**	**Δv_1**	**Δv_2**
Building	0.031	0.052	-0.002	-0.005	0.031	0.020	-0.002	-0.003
South	0.034	0.056	-0.002	-0.005	0.034	0.022	-0.002	-0.003
North	0.029	0.047	-0.002	-0.005	0.029	0.019	-0.002	-0.003
East	0.031	0.052	0.004	0.005	0.031	0.020	0.004	-0.002
West	0.031	0.052	-0.008	-0.015	0.031	0.020	-0.008	-0.006
Load direction	**SHORT**							
Deflection (in.)	**u_1**	**u_2**	**v_1**	**v_2**	**Δu_1**	**Δu_2**	**Δv_1**	**Δv_2**
Building	0.000	0.001	0.053	0.087	0.000	0.000	0.053	0.034
South	-0.002	-0.003	0.053	0.087	-0.002	-0.001	0.053	0.034
North	0.001	0.002	0.053	0.087	0.001	0.001	0.053	0.034
East	0.000	0.001	0.050	0.082	0.000	0.000	0.050	0.032
West	0.000	0.001	0.056	0.092	0.000	0.000	0.056	0.036

Table Q-4: Breakdown of lateral stiffness, A2c-3D-RD-a model

LONG			**SHORT**		
Shear wall k_u (%)	**Gravity wall k_u (%)**	**k_u (kip/in)**	**Shear wall k_v (%)**	**Gravity wall k_v (%)**	**k_v (kip/in)**
63.3	36.7	217.1	85.1	14.9	122.0

Q.4 Nonlinear static (pushover) analysis results

Table Q-5 is created following the same logic with Table Q-2, but the analysis type is nonlinear static (pushover). Pushover curves of the building and each wall line are presented in Figure Q-3 and Figure Q-4.

Clearly, the interaction between wall lines is much more significant when material and geometrical nonlinearity is included. These tables and figures indicate that the wall lines do not reach their peak capacity at exactly the same drift level and wall lines perpendicular to the load can take a nontrivial amount of base shear. Total capacity of the wall line increases since the capacity of gravity walls is included. The boost is larger in long direction. Consequently, total capacity of the building in long direction is much larger than the short direction.

Table Q-5: Breakdown of peak base shear, pushover analysis, A2c-3D-RD-a model

Load direction	**LONG**				
Elevation	**South V_b**	**North V_b**	**East V_b**	**West V_b**	**Peak V_b**
kips	39.9	49.8	3.8	5.3	87.9
%	45.4	56.6	4.3	6.1	100.0
Load direction	**SHORT**				
Elevation	**South V_b**	**North V_b**	**East V_b**	**West V_b**	**Peak V_b**
kips	7.1	3.8	30.8	32.3	62.4
%	11.4	6.2	49.4	51.9	100.0

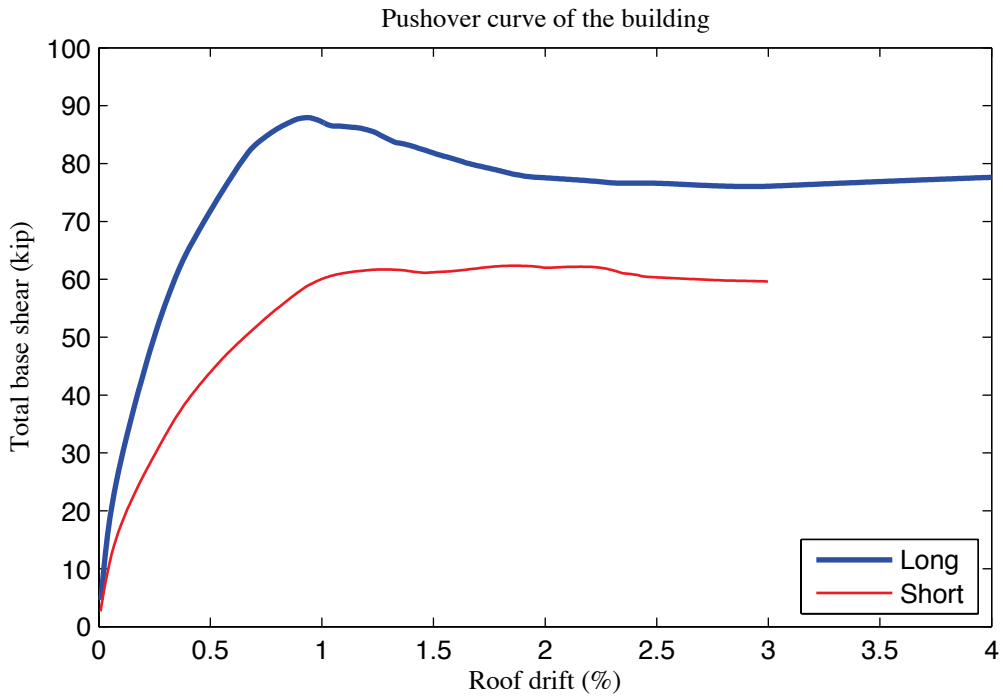

Figure Q-3: Pushover curve of A2c-3D-RD-a model

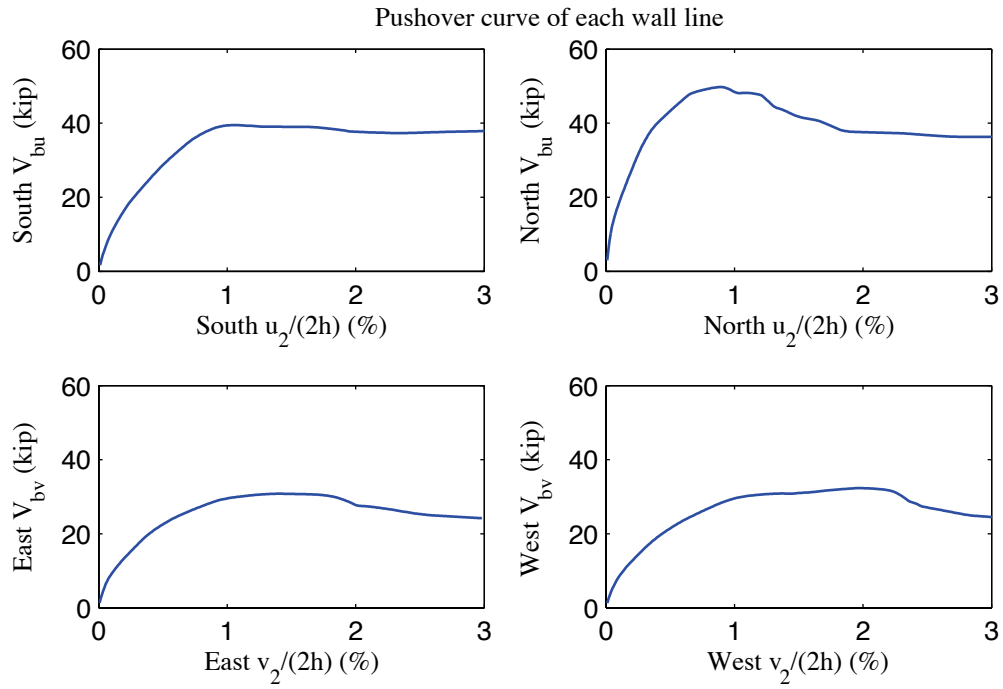

Figure Q-4: Pushover curve of each wall line, A2c-3D-RD-a model

Q.5 Linear time history analysis results

Linear time history analysis is performed on the model under Canoga Park and Rinaldi ground motion records of Northridge earthquake in 1994. We considered three scale levels (16%, 44% and 100%) and loadings in one, two and three axes.

Table Q-6 to Table Q-9 demonstrate the building's linear elastic performance under designated ground motions. Table Q-6 shows peak story relative accelerations in the unit of g. Table Q-7 and Table Q-8 report peak roof drift and story drift of the building and the corresponding time step (t_*) and the base shear at that time. Note that the base shear at the time of peak roof drift may not be the peak total building base shear in that direction (see Table Q-9).

The building behaves linearly since peak drift and peak base shear appear at the same time when the ground motion is linearly scaled. Figure Q-5 is a vector plot of the peak total resultant base shear of the building under three axial, 100% Canoga Park excitation. The directions of arrows imply that base shear taken by shear walls and gravity systems does not necessarily follow the direction of wall lines due to the effect of 3D coupling. Comparison with nonlinear analysis results of the same excitation provides insightful observations on the building's response and requirements on modeling fidelity and analysis type.

Table Q-6: A2c-3D-RD-a model peak story relative acceleration in g, linear time history analysis

		LONG			SHORT			UP		
Load Case	**Ground Motion**	**a_g**	**Floor a**	**Roof a**	**a_g**	**Floor a**	**Roof a**	**a_g**	**Floor a**	**Roof a**
EQ_3D_3axis_1	CNP 16%	0.067	0.124	0.197	0.057	0.143	0.221	0.078	0.048	0.048
EQ_3D_3axis_2	CNP 44%	0.185	0.342	0.538	0.157	0.385	0.600	0.215	0.309	0.252
EQ_3D_1axis_1	CNP 100%	0.420	0.764	1.202	0	0.128	0.203	0	0.521	0.480
EQ_3D_1axis_2	CNP 100%	0	0.163	0.270	0.356	0.772	1.207	0	0.940	0.800
EQ_3D_2axis_1	CNP 100%	0.420	0.783	1.215	0.356	0.853	1.312	0	1.309	1.168
EQ_3D_3axis_3	CNP 100%	0.420	0.783	1.215	0.356	0.853	1.312	0.489	1.309	1.168
EQ_3D_3axis_4	RRS 16%	0.132	0.128	0.206	0.078	0.152	0.263	0.133	0.105	0.089
EQ_3D_3axis_5	RRS 44%	0.363	0.363	0.585	0.214	0.425	0.725	0.367	0.532	0.492
EQ_3D_3axis_6	RRS 100%	0.825	0.836	1.368	0.486	0.957	1.649	0.834	1.084	1.048

Table Q-7: A2c-3D-RD-a model peak building roof drift and base shear, linear time history analysis

		LONG			SHORT		
Load Case	**Ground Motion**	**$u_2/(2h)$ (%)**	**t_* (s)**	**V_b @ t_* (kips)**	**$v_2/(2h)$ (%)**	**t_* (s)**	**V_b @ t_* (kips)**
EQ_3D_3axis_1	CNP 16%	0.026	4.26	12.2	-0.046	7.19	12.5
EQ_3D_3axis_2	CNP 44%	0.071	4.26	33.4	-0.122	7.19	32.8
EQ_3D_1axis_1	CNP 100%	0.159	4.26	75.4	-0.029	4.52	8.6
EQ_3D_1axis_2	CNP 100%	0.038	6.98	13.2	-0.247	6.57	62.4
EQ_3D_2axis_1	CNP 100%	0.163	4.26	75.7	-0.268	7.19	71.2
EQ_3D_3axis_3	CNP 100%	0.163	4.26	75.7	-0.268	7.19	71.2
EQ_3D_3axis_4	RRS 16%	0.030	2.54	14.8	-0.054	2.74	14.1
EQ_3D_3axis_5	RRS 44%	0.084	2.54	40.8	-0.148	2.74	38.0
EQ_3D_3axis_6	RRS 100%	0.191	2.54	92.4	-0.333	2.74	85.3

Table Q-8: A2c-3D-RD-a model peak building story drift, linear time history analysis

		LONG				SHORT			
Load Case	**Ground Motion**	**$\Delta u_1/h$ (%)**	**t_* (s)**	**$\Delta u_2/h$ (%)**	**t_* (s)**	**$\Delta v_1/h$ (%)**	**t_* (s)**	**$\Delta v_2/h$ (%)**	**t_* (s)**
EQ_3D_3axis_1	CNP 16%	0.033	4.26	0.019	4.26	-0.058	7.19	-0.035	7.18
EQ_3D_3axis_2	CNP 44%	0.091	4.26	0.051	4.26	-0.154	7.19	-0.090	7.19
EQ_3D_1axis_1	CNP 100%	0.203	4.26	0.115	4.26	-0.036	4.52	-0.023	4.53
EQ_3D_1axis_2	CNP 100%	0.047	6.98	0.029	6.98	-0.310	7.20	-0.193	6.57
EQ_3D_2axis_1	CNP 100%	0.208	4.26	0.118	4.26	-0.338	7.19	-0.198	7.19
EQ_3D_3axis_3	CNP 100%	0.208	4.26	0.118	4.26	-0.338	7.19	-0.198	7.19
EQ_3D_3axis_4	RRS 16%	0.040	2.54	-0.021	3.04	-0.068	2.74	-0.040	2.74
EQ_3D_3axis_5	RRS 44%	0.111	2.54	-0.058	3.04	-0.185	2.74	-0.110	2.74
EQ_3D_3axis_6	RRS 100%	0.253	2.54	-0.137	7.60	-0.418	2.74	0.253	7.39

Table Q-9: A2c-3D-RD-a model peak building base shear, linear time history analysis

		LONG		SHORT		RESULTANT	
Load Case	**Ground Motion**	**Peak V_{bu} (kip)**	**t @ peak V_{bu} (s)**	**Peak V_{bv} (kip)**	**t @ peak V_{bv} (s)**	**Peak V_b (kip)**	**t @ peak V_b (s)**
EQ_3D_3axis_1	CNP 16%	12.2	4.26	12.5	7.19	13.3	7.19
EQ_3D_3axis_2	CNP 44%	33.4	4.26	32.8	7.19	35.4	7.19
EQ_3D_1axis_1	CNP 100%	75.4	4.26	9.1	4.44	75.7	4.26
EQ_3D_1axis_2	CNP 100%	14.0	6.90	64.7	7.20	64.7	7.20
EQ_3D_2axis_1	CNP 100%	75.7	4.26	71.2	7.19	78.2	7.19
EQ_3D_3axis_3	CNP 100%	75.7	4.26	71.2	7.19	78.2	7.19
EQ_3D_3axis_4	RRS 16%	14.8	2.54	14.1	2.74	17.3	7.59
EQ_3D_3axis_5	RRS 44%	40.8	2.54	38.2	7.38	47.5	2.54
EQ_3D_3axis_6	RRS 100%	92.4	2.54	85.5	7.39	109.3	7.60

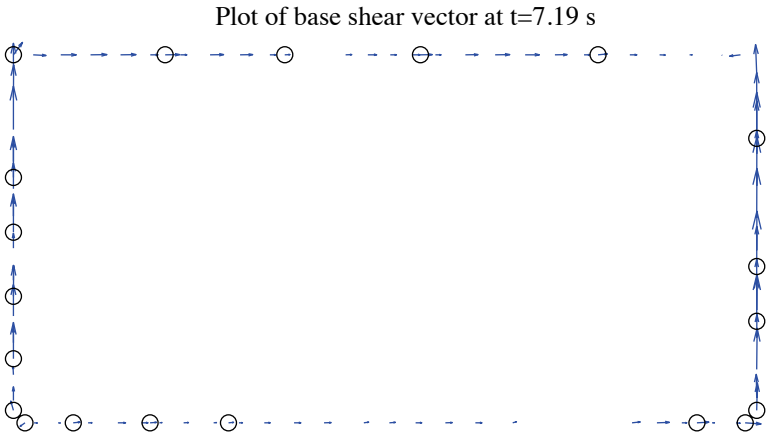

Figure Q-5: A2c-3D-RD-a model, base shear vector plot at the moment of peak total base shear, 100 % Canoga Park, 3D linear analysis (maximum anchor/hold down base shear is 3.95 kips)

Q.6 Nonlinear time history analysis results

Same ground motions are applied to the model with material and geometrical nonlinearity. Table Q-10 to Table Q-13 are replicas of Table Q-6 to Table Q-9, but for nonlinear time history analyses. Since this analysis type is most complicated and closest to reality and experiments, behavior of wall lines and hold downs are further studied. Table Q-14 is the table of peak wall line story drifts and corresponding time steps. Table Q-15 is designed for peak base shear of each wall line and the last two columns of the table are percentages of base shear of two facing wall lines in the same direction when the total base shear in that direction takes peak value. Table Q-16 expands the breakdown of each wall line's peak base shear between shear walls, gravity walls and other systems. Table Q-17 is peak value of hold down tensile force of two selected pairs. Hold down 5 and 6 are on shear wall L1S1, South elevation and hold down 7 and 8 are on shear wall L1W1, West elevation. These shear walls have lowest capacities compared with others on the same wall line and they meet at the southwest edge of the building, so interacted nonlinear behavior is expected to appear.

Time history plots in this section include plots of story drifts of the building and each wall line (Figure Q-6 to Figure Q-8), total building base shear in long and short direction (Figure Q-9) and axial forces of hold downs in Table Q-17 (Figure Q-10). Hysteretic plots in Figure Q-11 and Figure Q-12 are helpful for visual examination of nonlinear base shear-drift relationship of the building and the weakest shear wall on each wall line. In comparison with linear time history analysis, vector plot of peak total base shear is illustrated in Figure Q-13. Figure Q-14 presents a simplified deformed shape of the

building (see (Peterman 2014) for details of the method) and axial force of all twenty hold downs at the moment of peak total base shear. The same sign convention with tests is adopted. Red bars indicate tensile (negative) force and blue ones are for compressive (positive) force.

Hysteretic behavior is seen in the building and typical shear walls under design-based earthquake (100% Canoga Park excitation in 3 axes, see Figure Q-11 and Figure Q-12). Even though post-peak response on the backbone curve is not initiated under this excitation level, wall lines behave differently. West wall line reaches 0.67% peak floor story drift but peak story drifts of all other wall lines are less than 0.50% (Table Q-14). Given the significantly increased capacity and stiffness in long direction, peak story drift of long direction is less than short direction (0.39% vs. 0.57%, Table Q-12). Figure Q-13 clearly shows that base shear vectors in anchors and hold downs do not align with wall lines, a sign of coupled wall line behavior. Table Q-17, Figure Q-10 and Figure Q-14 demonstrate that hold downs in a pair do not experience the same amount of force with opposite signs, an evidence that supports Type II shear wall behavior despite Type I design assumption.

The near-field Rinaldi record is much stronger in terms of peak ground acceleration, especially in the long direction. With the additional lateral force resistance provided by sheathed gravity walls, simulation results show that the building can survive even 100% Rinaldi ground motion, the maximum considered earthquake in this research. This time, peak story drifts in both directions are about 1.06%, not even close to threshold value of

post-peak response (arguably 2%) on the backbone curve. The portion of base shear taken by gravity wall does not change much with scale factors considered so far in this research, as shown in Table Q-16. Again, the table demonstrates that the base shear taken by anchors on bottom tracks of gravity walls can be quite large, sometimes even larger than half of the total base shear (e.g. South wall lines).

Table Q-10: A2c-3D-RD-a model peak story relative acceleration in g, nonlinear time history analysis

		LONG			SHORT			UP		
Load Case	**Ground Motion**	**a_g**	**Floor a**	**Roof a**	**a_g**	**Floor a**	**Roof a**	**a_g**	**Floor a**	**Roof a**
EQ_3D_3axis_1	CNP 16%	0.067	0.166	0.173	0.057	0.145	0.154	0.078	0.047	0.050
EQ_3D_3axis_2	CNP 44%	0.185	0.286	0.339	0.157	0.332	0.386	0.215	0.110	0.097
EQ_3D_1axis_1	CNP 100%	0.420	0.583	0.822	0	0.077	0.089	0	0.154	0.161
EQ_3D_1axis_2	CNP 100%	0	0.087	0.104	0.356	0.432	0.863	0	0.278	0.258
EQ_3D_2axis_1	CNP 100%	0.420	0.622	0.820	0.356	0.509	0.791	0	0.957	0.952
EQ_3D_3axis_3	CNP 100%	0.420	0.622	0.820	0.356	0.509	0.791	0.489	0.957	0.952
EQ_3D_3axis_4	RRS 16%	0.132	0.146	0.231	0.078	0.181	0.225	0.133	0.099	0.093
EQ_3D_3axis_5	RRS 44%	0.363	0.376	0.579	0.214	0.501	0.629	0.367	0.186	0.166
EQ_3D_3axis_6	RRS 100%	0.825	1.098	1.786	0.486	0.851	1.412	0.834	0.650	0.672

Table Q-11: A2c-3D-RD-a model peak building roof drift and base shear, nonlinear time history analysis

		LONG			SHORT		
Load Case	**Ground Motion**	**$u_2/(2h)$ (%)**	**t_* (s)**	**V_b @ t_* (kips)**	**$v_2/(2h)$ (%)**	**t_* (s)**	**V_b @ t_* (kips)**
EQ_3D_3axis_1	CNP 16%	0.023	4.28	9.1	-0.038	9.70	9.5
EQ_3D_3axis_2	CNP 44%	0.061	8.66	21.6	0.155	9.95	22.4
EQ_3D_1axis_1	CNP 100%	0.238	8.67	52.2	-0.022	7.09	4.2
EQ_3D_1axis_2	CNP 100%	-0.017	9.96	1.8	0.426	9.96	38.8
EQ_3D_2axis_1	CNP 100%	0.258	8.68	54.4	0.443	9.97	39.4
EQ_3D_3axis_3	CNP 100%	0.258	8.68	54.4	0.443	9.97	39.4
EQ_3D_3axis_4	RRS 16%	-0.036	4.19	13.7	-0.071	4.31	12.8
EQ_3D_3axis_5	RRS 44%	0.163	4.35	38.2	-0.276	4.41	29.9
EQ_3D_3axis_6	RRS 100%	0.695	4.43	76.8	0.777	6.05	53.2

Table Q-12: A2c-3D-RD-a model peak building story drift, nonlinear linear time history analysis

		LONG				SHORT			
Load Case	**Ground Motion**	**$\Delta u_1/h$ (%)**	**t_* (s)**	**$\Delta u_2/h$ (%)**	**t_* (s)**	**$\Delta v_1/h$ (%)**	**t_* (s)**	**$\Delta v_2/h$ (%)**	**t_* (s)**
EQ_3D_3 axis_1	CNP 16%	-0.031	4.19	0.018	8.65	-0.054	9.70	-0.026	10.49
EQ_3D_3 axis_2	CNP 44%	0.087	8.66	0.039	11.70	0.212	9.95	0.097	9.95
EQ_3D_1 axis_1	CNP 100%	0.353	8.68	0.129	8.66	-0.028	7.10	-0.016	5.57
EQ_3D_1 axis_2	CNP 100%	-0.022	10.45	-0.017	9.96	0.539	9.97	0.321	9.96
EQ_3D_2 axis_1	CNP 100%	0.387	8.68	-0.147	11.56	0.566	9.98	0.325	9.97
EQ_3D_3 axis_3	CNP 100%	0.387	8.68	-0.147	11.56	0.566	9.98	0.325	9.97
EQ_3D_3 axis_4	RRS 16%	-0.047	4.19	-0.025	4.19	-0.095	4.31	-0.047	4.31
EQ_3D_3 axis_5	RRS 44%	0.240	4.35	0.087	4.35	-0.384	4.41	0.183	3.39
EQ_3D_3 axis_6	RRS 100%	1.066	4.43	-0.372	4.60	1.044	6.06	0.571	3.92

Table Q-13: A2c-3D-RD-a model peak building base shear, nonlinear time history analysis

		LONG		SHORT		RESULTANT	
Load Case	**Ground Motion**	**Peak V_{bu} (kip)**	**t @ peak V_{bu} (s)**	**Peak V_{bv} (kip)**	**t @ peak V_{bv} (s)**	**Peak V_b (kip)**	**t @ peak V_b (s)**
EQ_3D_3axis_1	CNP 16%	10.0	8.62	9.5	9.70	10.6	3.64
EQ_3D_3axis_2	CNP 44%	21.6	8.66	22.4	9.94	27.0	9.93
EQ_3D_1axis_1	CNP 100%	52.3	8.68	4.9	5.35	52.3	8.68
EQ_3D_1axis_2	CNP 100%	4.6	9.84	39.4	9.97	39.4	9.97
EQ_3D_2axis_1	CNP 100%	54.4	8.68	39.7	9.96	54.5	8.68
EQ_3D_3axis_3	CNP 100%	54.4	8.68	39.7	9.96	54.5	8.68
EQ_3D_3axis_4	RRS 16%	13.7	4.19	12.9	4.30	17.8	4.29
EQ_3D_3axis_5	RRS 44%	38.4	4.34	31.9	3.36	40.0	4.35
EQ_3D_3axis_6	RRS 100%	84.0	2.64	53.2	6.06	84.2	2.64

Table Q-14: A2c-3D-RD-a model peak wall line story drift, nonlinear time history analysis

LONG		SOUTH				NORTH			
Load Case	**Ground Motion**	**$\Delta u_1/h$ (%)**	**t_* (s)**	**$\Delta u_2/h$ (%)**	**t_* (s)**	**$\Delta u_1/h$ (%)**	**t_* (s)**	**$\Delta u_2/h$ (%)**	**t_* (s)**
EQ_3D_3axis_1	CNP 16%	0.042	4.28	0.021	4.28	0.027	8.62	0.018	8.65
EQ_3D_3axis_2	CNP 44%	0.092	8.66	0.042	11.70	0.085	7.35	0.037	11.81
EQ_3D_1axis_1	CNP 100%	0.358	8.68	0.135	11.87	0.349	8.67	0.124	8.66
EQ_3D_1axis_2	CNP 100%	0.049	9.99	0.038	9.96	0.019	10.00	0.011	10.00
EQ_3D_2axis_1	CNP 100%	0.415	8.69	0.149	8.67	0.369	8.68	0.149	11.55
EQ_3D_3axis_3	CNP 100%	0.415	8.69	0.149	8.67	0.369	8.68	0.149	11.55
EQ_3D_3axis_4	RRS 16%	0.063	4.29	0.032	4.19	0.034	2.56	0.020	3.05
EQ_3D_3axis_5	RRS 44%	0.275	4.37	0.097	4.36	0.227	4.34	0.079	4.35
EQ_3D_3axis_6	RRS 100%	1.114	2.64	0.371	6.99	1.100	4.42	0.402	4.60
SHORT		**EAST**				**WEST**			
Load Case	**Ground Motion**	**$\Delta v_1/h$ (%)**	**t_* (s)**	**$\Delta v_2/h$ (%)**	**t_* (s)**	**$\Delta v_1/h$ (%)**	**t_* (s)**	**$\Delta v_2/h$ (%)**	**t_* (s)**
EQ_3D_3axis_1	CNP 16%	0.054	9.70	0.034	5.47	0.059	9.56	0.035	9.53
EQ_3D_3axis_2	CNP 44%	0.176	9.95	0.080	9.95	0.249	9.94	0.115	9.95
EQ_3D_1axis_1	CNP 100%	0.058	4.43	0.029	4.51	0.056	5.07	0.036	5.08
EQ_3D_1axis_2	CNP 100%	0.475	9.97	0.276	9.96	0.608	9.98	0.367	9.96
EQ_3D_2axis_1	CNP 100%	0.501	9.95	0.263	9.96	0.667	9.99	0.389	9.97
EQ_3D_3axis_3	CNP 100%	0.501	9.95	0.263	9.96	0.667	9.99	0.389	9.97
EQ_3D_3axis_4	RRS 16%	0.067	4.59	0.037	5.21	0.138	4.31	0.065	4.31
EQ_3D_3axis_5	RRS 44%	0.285	3.36	0.126	5.97	0.525	4.41	0.243	3.38
EQ_3D_3axis_6	RRS 100%	0.853	6.05	0.480	3.93	1.268	6.07	0.677	6.03

Table Q-15: A2c-3D-RD-a model peak wall line base shear, nonlinear time history analysis

LONG		SOUTH		NORTH		% of Peak V_{bu}	
Load Case	**Ground Motion**	**Peak V_{bu} (kips)**	**t @ peak V_{bu} (s)**	**Peak V_{bu} (kips)**	**t @ peak V_{bu} (s)**	**South**	**North**
EQ_3D_3axis_1	CNP 16%	4.6	4.19	6.7	8.62	32.6	66.4
EQ_3D_3axis_2	CNP 44%	8.1	8.65	14.4	7.35	37.1	62.7
EQ_3D_1axis_1	CNP 100%	19.7	8.68	32.3	8.68	37.7	61.7
EQ_3D_1axis_2	CNP 100%	4.8	8.98	4.8	10.00	77.9	23.7
EQ_3D_2axis_1	CNP 100%	21.3	8.69	33.3	8.68	38.4	61.2
EQ_3D_3axis_3	CNP 100%	21.3	8.69	33.3	8.68	38.4	61.2
EQ_3D_3axis_4	RRS 16%	6.2	4.19	7.9	2.56	45.0	54.8
EQ_3D_3axis_5	RRS 44%	16.4	4.36	24.3	4.34	36.4	63.3
EQ_3D_3axis_6	RRS 100%	36.0	2.64	50.6	4.40	42.8	57.2
SHORT		**EAST**		**WEST**		**% of Peak V_{bv}**	
Load Case	**Ground Motion**	**Peak V_{bv} (kips)**	**t @ peak V_{bv} (s)**	**Peak V_{bv} (kips)**	**t @ peak V_{bv} (s)**	**East**	**West**
EQ_3D_3axis_1	CNP 16%	5.0	9.70	5.0	9.56	52.8	47.0
EQ_3D_3axis_2	CNP 44%	10.5	9.95	12.0	9.94	46.4	53.5
EQ_3D_1axis_1	CNP 100%	5.8	4.53	4.4	5.08	107.3	6.9
EQ_3D_1axis_2	CNP 100%	19.1	9.97	20.7	9.98	48.4	52.1
EQ_3D_2axis_1	CNP 100%	19.8	9.95	21.5	9.99	49.6	51.3
EQ_3D_3axis_3	CNP 100%	19.8	9.95	21.5	9.99	49.6	51.3
EQ_3D_3axis_4	RRS 16%	6.0	4.60	8.3	4.31	36.2	63.7
EQ_3D_3axis_5	RRS 44%	13.8	3.36	18.6	4.41	43.3	55.9
EQ_3D_3axis_6	RRS 100%	24.8	6.05	28.7	6.07	45.4	53.5

Table Q-16: A2c-3D-RD-a model wall line base shear breakdown, nonlinear time history analysis

LONG		SOUTH			NORTH		
Load Case	**Ground Motion**	**Peak V_{bu} (kips)**	**SW V_{bu} (%)**	**GW V_{bu} (%)**	**Peak V_{bu} (kips)**	**SW V_{bu} (%)**	**GW V_{bu} (%)**
EQ_3D_3axis_1	CNP 16%	4.6	39.4	60.6	6.7	59.6	40.4
EQ_3D_3axis_2	CNP 44%	8.1	39.4	60.6	14.4	60.1	39.9
EQ_3D_1axis_1	CNP 100%	19.7	42.1	57.9	32.3	54.9	45.1
EQ_3D_1axis_2	CNP 100%	4.8	38.1	61.9	4.8	60.6	39.4
EQ_3D_2axis_1	CNP 100%	21.3	41.2	58.8	33.3	55.0	45.0
EQ_3D_3axis_3	CNP 100%	21.3	41.2	58.8	33.3	55.0	45.0
EQ_3D_3axis_4	RRS 16%	6.2	39.6	60.4	7.9	60.1	39.9
EQ_3D_3axis_5	RRS 44%	16.4	42.0	58.0	24.3	56.7	43.3
EQ_3D_3axis_6	RRS 100%	36.0	40.1	59.9	50.6	53.9	46.1
SHORT		**EAST**			**WEST**		
Load Case	**Ground Motion**	**Peak V_{bv} (kips)**	**SW V_{bv} (%)**	**GW V_{bu} (%)**	**Peak V_{bv} (kips)**	**SW V_{bv} (%)**	**GW V_{bv} (%)**
EQ_3D_3axis_1	CNP 16%	5.0	71.1	28.9	5.0	81.2	18.8
EQ_3D_3axis_2	CNP 44%	10.5	75.9	24.1	12.0	82.7	17.3
EQ_3D_1axis_1	CNP 100%	5.8	76.3	23.7	4.4	81.1	18.9
EQ_3D_1axis_2	CNP 100%	19.1	71.9	28.1	20.7	81.3	18.7
EQ_3D_2axis_1	CNP 100%	19.8	72.4	27.6	21.5	81.7	18.3
EQ_3D_3axis_3	CNP 100%	19.8	72.4	27.6	21.5	81.7	18.3
EQ_3D_3axis_4	RRS 16%	6.0	72.3	27.7	8.3	83.3	16.7
EQ_3D_3axis_5	RRS 44%	13.8	73.1	26.9	18.6	81.0	19.0
EQ_3D_3axis_6	RRS 100%	24.8	73.8	26.2	28.7	83.3	16.7

Table Q-17: A2c-3D-RD-a model peak hold down tensile force at certain locations, nonlinear time history analysis

		L1S1, LC5		L1S1, LC6		L1W1, LC7		L1W1, LC8	
Load Case	**Ground Motion**	**Peak F (kips)**	**t @ peak F (s)**	**Peak F (kips)**	**t @ peak F (s)**	**Peak F (kips)**	**t @ peak F (s)**	**Peak F (kips)**	**t @ peak F (s)**
EQ_3D_3axis_1	CNP 16%	-0.47	4.18	-0.10	9.86	-0.08	9.86	-0.49	4.99
EQ_3D_3axis_2	CNP 44%	-0.91	4.21	-0.42	9.94	-0.27	9.95	-0.74	9.81
EQ_3D_1axis_1	CNP 100%	-2.06	11.86	-0.23	8.65	-0.43	8.66	-0.58	8.67
EQ_3D_1axis_2	CNP 100%	-1.89	9.96	-0.91	9.96	-0.48	9.96	-1.06	8.45
EQ_3D_2axis_1	CNP 100%	-2.08	10.48	-1.48	9.96	-1.23	9.96	-1.04	8.46
EQ_3D_3axis_3	CNP 100%	-2.08	10.48	-1.48	9.96	-1.23	9.96	-1.04	8.46
EQ_3D_3axis_4	RRS 16%	-0.73	4.19	-0.12	4.45	-0.08	4.45	-0.69	4.31
EQ_3D_3axis_5	RRS 44%	-1.95	4.23	-0.59	5.99	-0.34	5.99	-1.11	4.40
EQ_3D_3axis_6	RRS 100%	-2.63	3.06	-2.09	6.05	-1.36	6.80	-1.57	2.60

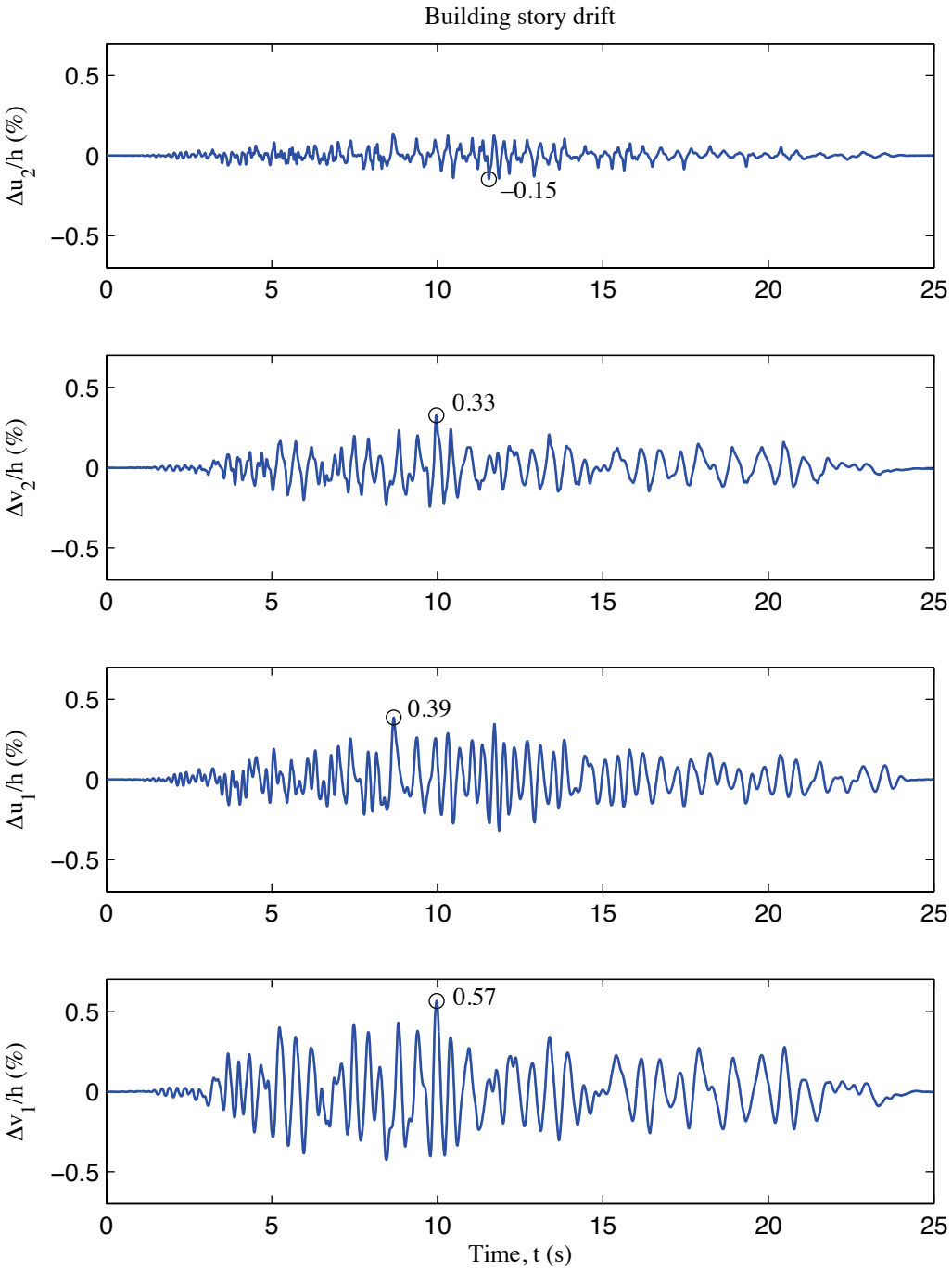

Figure Q-6: A2c-3D-RD-a model building story drift, 100 % Canoga Park, 3D nonlinear analysis

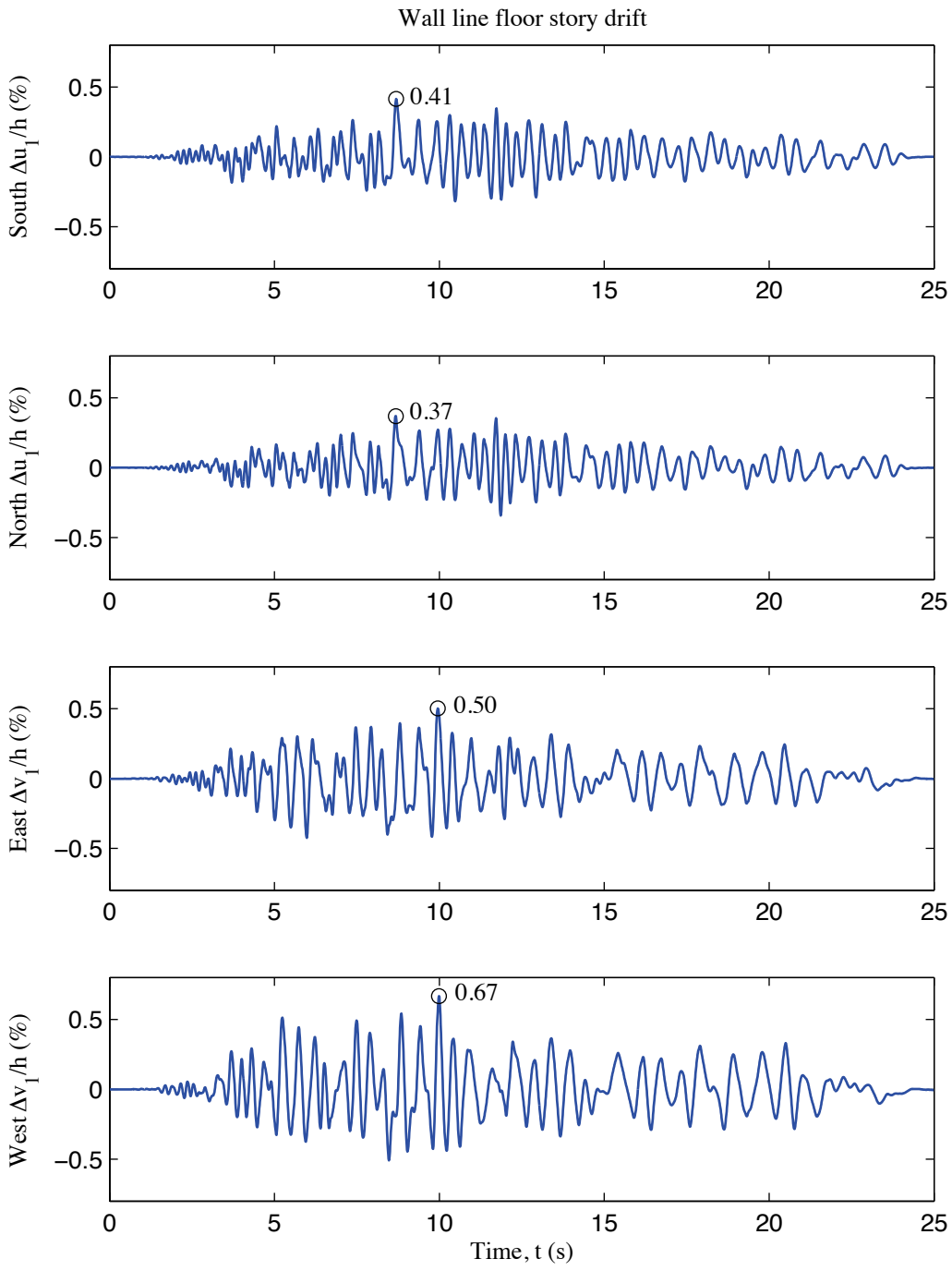

Figure Q-7: A2c-3D-RD-a model wall line floor story drift, 100 % Canoga Park, 3D nonlinear analysis

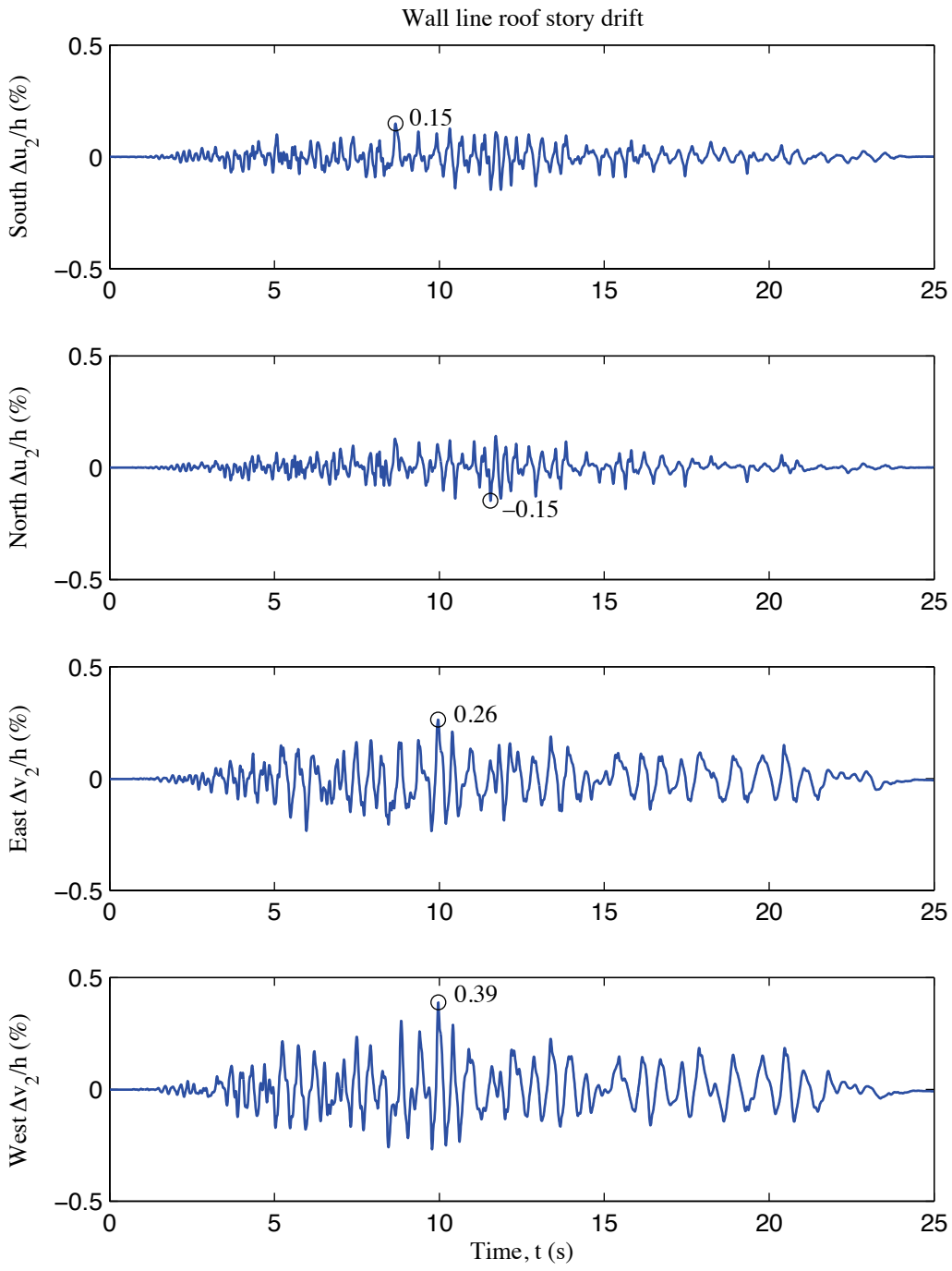

Figure Q-8: A2c-3D-RD-a model wall line roof story drift, 100 % Canoga Park, 3D nonlinear analysis

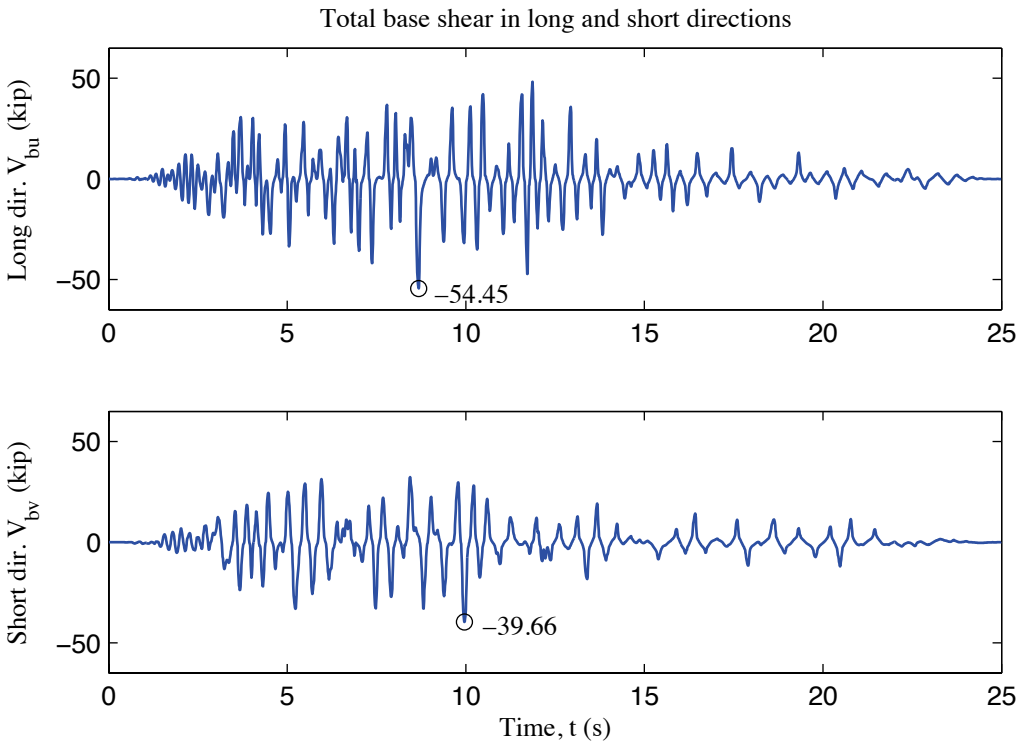

Figure Q-9: A2c-3D-RD-a model total building base shear, 100 % Canoga Park, 3D nonlinear analysis

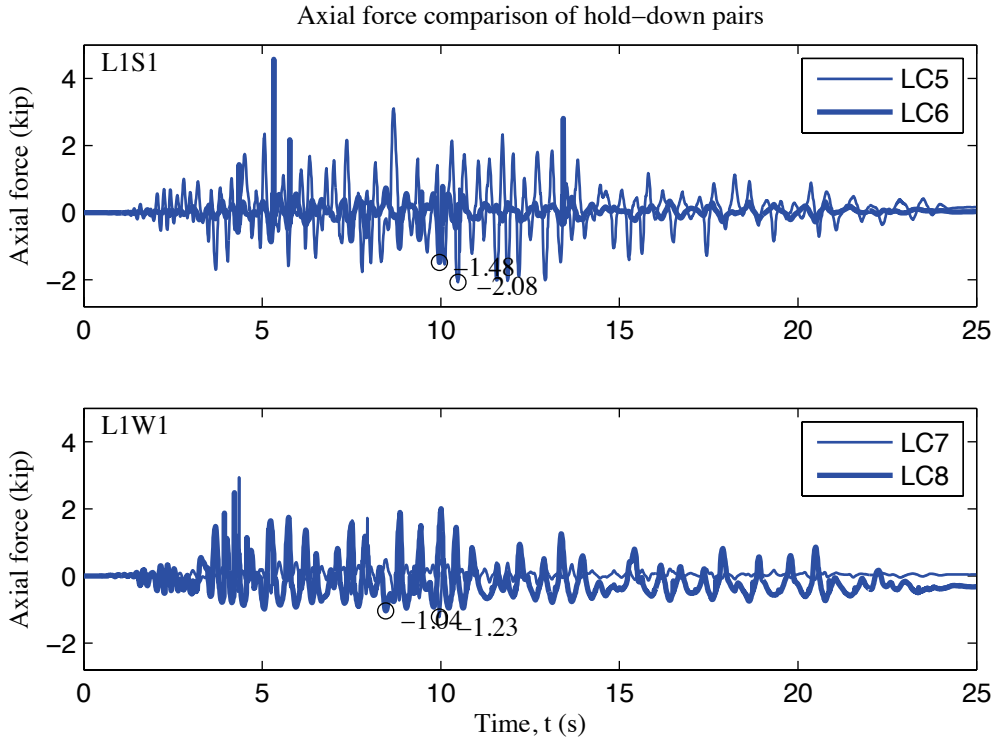

Figure Q-10: A2c-3D-RD-a model, load cell 5 to 8 axial forces, 100 % Canoga Park, 3D nonlinear analysis

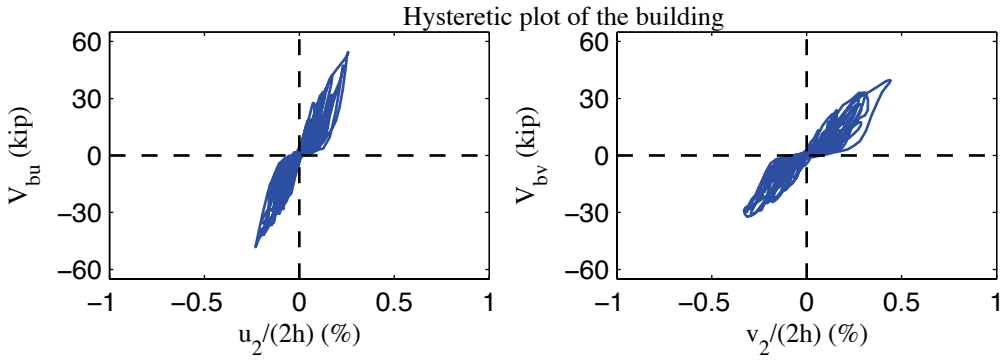

Figure Q-11: A2c-3D-RD-a model, hysteretic plot of the building, 100 % Canoga Park, 3D nonlinear analysis

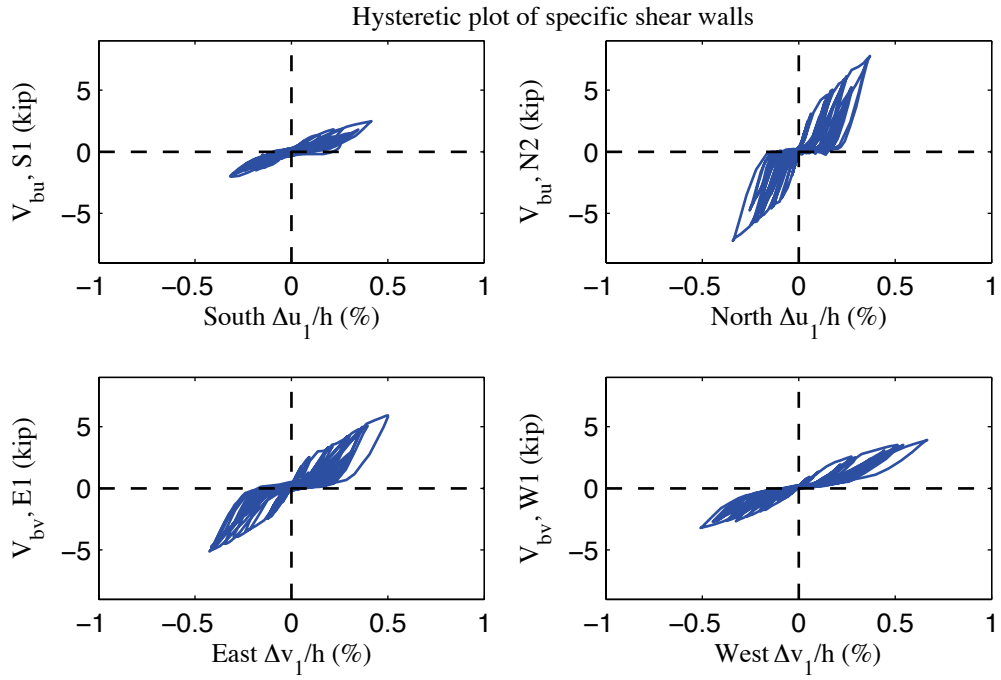

Figure Q-12: A2c-3D-RD-a model, hysteretic plot of shear walls at each elevation, 100 % Canoga Park, 3D nonlinear analysis

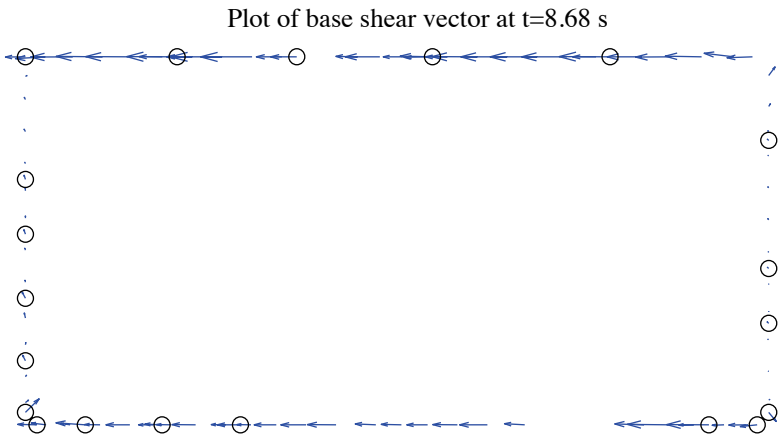

Figure Q-13: A2c-3D-RD-a model, field plot of peak total base shear, 100 % Canoga Park, 3D nonlinear analysis (maximum anchor/hold down base shear is 1.73 kips)

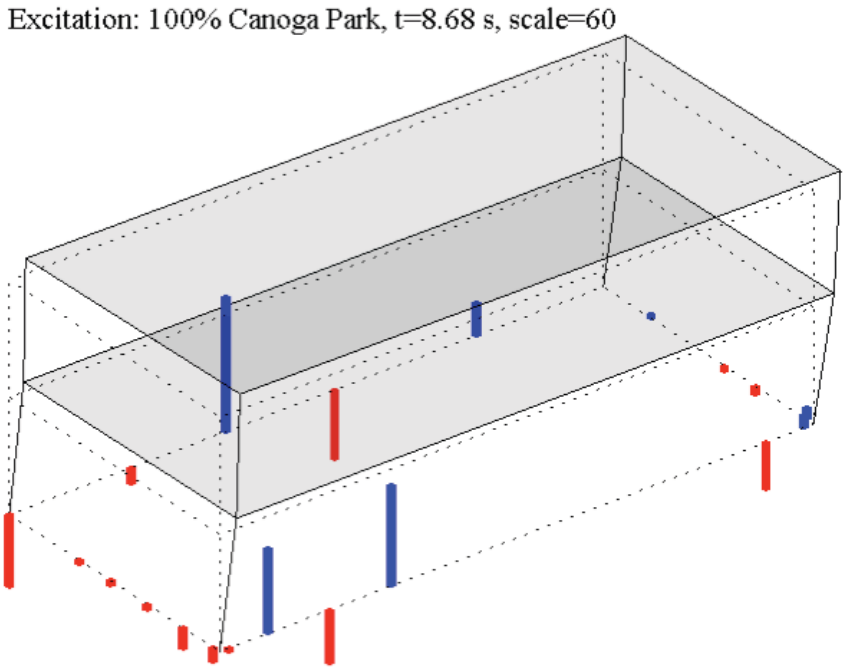

Figure Q-14: A2c-3D-RD-a model, simplified illustration of corner displacements with hold down forces from load cells,100 % Canoga Park, 3D nonlinear analysis (max hold down tensile force is -2.65 kips)

Appendix R: Analysis Results of State-of-the-art, Phase 2c, 3D, semirigid-diaphragm, model a (A2c-3D-SD-a)

R.1 Model description

This state-of-the-art 3D model features subpanel bracing models of shear walls and gravity walls, explicit models of hold downs, and semi-rigid diaphragms modeled by subpanel bracings. All walls are covered by OSB and gypsum sheathing. Seismic mass is distributed to corners and stud ends. The lateral displacement and shear wall capacity ($\delta(0.2V_{nA})$, $0.2V_{nA}$) from test is utilized to determine the stiffness of elastic material and the first point on the backbone curve of Pinching4 material of shear wall bracing. Figure R-1 is the 3D drawing of the building model with all members and diagonal bracings of sheathing panels. Definitions of output physical quantities and explanation of post-process method can be found in Appendix K.

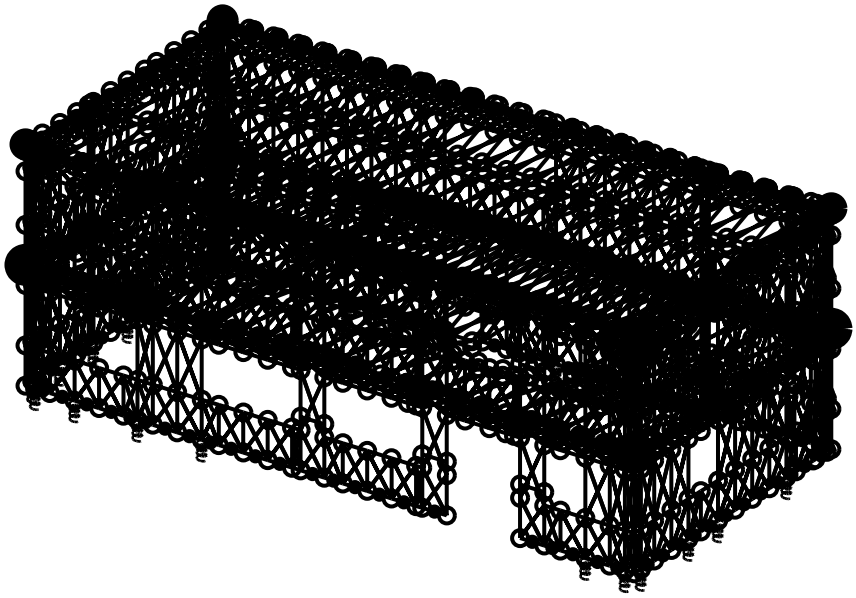

Figure R-1: A2c-3D-SD-a model

R.2 Free vibration analysis results

Free vibration analysis results are presented in Table R-1 and Figure R-2. Lateral stiffness in the short direction is smaller than lateral stiffness in the long direction and torsional stiffness is the largest. The observation holds for the first and the second mode, as indicated by Table R-1.

Table R-1: Free vibration analysis results, A2c-3D-SD-a model

Mode number	**Natural period (s)**	**Mode description**
1	0.234	Short, 1st
2	0.175	Long, 1st
3	0.143	Torsion, 1st
4	0.114	Short, 2nd
5	0.071	Long, 2nd
6	0.068	Torsion, 2nd

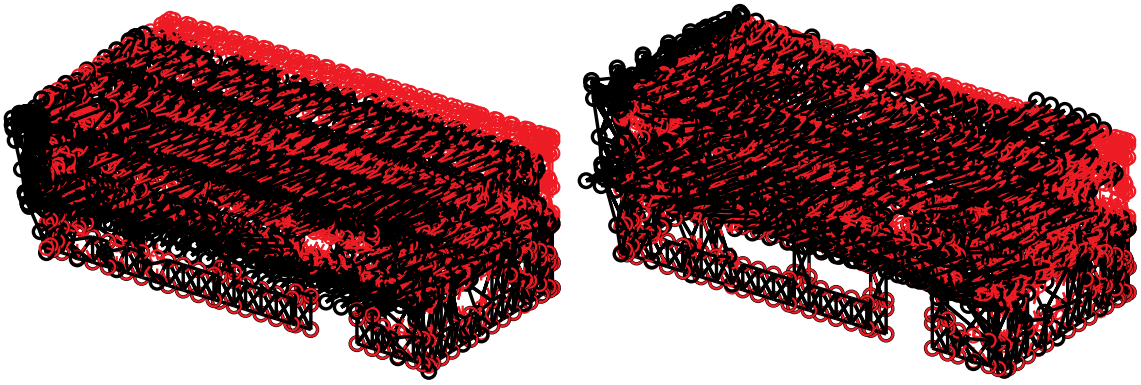

(a) Mode 1, T_1=0.234 s (b) Mode 2, T_2=0.175 s

Figure R-2: First two natural modes of A2c-3D-SD-a model

R.3 Linear static analysis results

Table R-2 to Table R-4 present linear static analysis results. The lateral load is the equivalent lateral force available from the design narrative (Madsen et al. 2011), applied equally at four corners. Two separate analyses were performed with the loading at long or short direction.

Table R-2 summarizes the breakdown of peak total base shear among four elevations. Due to the interplay of asymmetrical LFRS, wall lines perpendicular to the loading direction still take a very small portion of base shear.

Table R-3 shows peak building and wall line deflections. Practicing engineers can linearly upscale these data and develop an estimate of the building's performance at a certain lateral force level.

Table R-4 is an evaluation of the building's lateral stiffness of long and short direction and its breakdown among shear walls (SW) and other systems. Covered by the same type of OSB and gypsum sheathing with shear walls (even though the fastener spacing is different), gravity walls make a comparable contribution to total lateral stiffness like shear walls. The effect is even more apparent in long direction, where wall lines are much wider and have larger areas covered by gravity walls. The stiffness of gravity walls can account for as much as 39% and 24% of total lateral stiffness in long and short direction.

Table R-2: Breakdown of peak base shear, linear static analysis, A2c-3D-SD-a model

Load direction	**LONG**				
Elevation	**South V_b**	**North V_b**	**East V_b**	**West V_b**	**Peak V_b**
kips	4.4	6.6	0.0	0.1	11.1
%	39.3	59.4	0.1	1.3	100.0
Load direction	**SHORT**				
Elevation	**South V_b**	**North V_b**	**East V_b**	**West V_b**	**Peak V_b**
kips	0.2	0.3	5.4	5.1	11.1
%	1.9	2.9	48.7	46.5	100.0

Table R-3: Peak building and wall line deflection, linear static analysis, A2c-3D-SD-a model

Load direction	**LONG**							
Deflection (in.)	**u_1**	**u_2**	**v_1**	**v_2**	**Δu_1**	**Δu_2**	**Δv_1**	**Δv_2**
Building	0.032	0.053	-0.001	-0.002	0.032	0.021	-0.001	-0.001
South	0.036	0.059	-0.001	-0.003	0.036	0.023	-0.001	-0.001
North	0.027	0.046	-0.001	0.001	0.027	0.019	-0.001	0.001
East	0.032	0.053	0.004	0.006	0.032	0.021	0.004	0.002
West	0.031	0.053	-0.006	-0.009	0.031	0.022	-0.006	-0.004
Load direction	**SHORT**							
Deflection (in.)	**u_1**	**u_2**	**v_1**	**v_2**	**Δu_1**	**Δu_2**	**Δv_1**	**Δv_2**
Building	0.001	0.001	0.064	0.100	0.001	0.001	0.064	0.036
South	-0.002	-0.003	0.064	0.099	-0.002	-0.001	0.064	0.035
North	0.001	0.002	0.065	0.101	0.001	0.001	0.065	0.036
East	0.001	0.001	0.060	0.092	0.001	-0.001	0.060	0.032
West	-0.001	0.001	0.069	0.108	-0.001	0.001	0.069	0.040

Table R-4: Breakdown of lateral stiffness, A2c-3D-SD-a model

LONG			**SHORT**		
Shear wall k_u (%)	**Gravity wall k_u (%)**	**k_u (kip/in)**	**Shear wall k_v (%)**	**Gravity wall k_v (%)**	**k_v (kip/in)**
60.7	39.3	213.6	76.1	23.9	110.0

R.4 Nonlinear static (pushover) analysis results

Table R-5 is created following the same logic with Table R-2, but the analysis type is nonlinear static (pushover). Pushover curves of the building and each wall line are presented in Figure R-3 and Figure R-4.

Clearly, the interaction between wall lines is much more significant when material and geometrical nonlinearity is included. These tables and figures indicate that the wall lines do not reach their peak capacity at exactly the same drift level and wall lines perpendicular to the load can take a nontrivial amount of base shear. Total capacity of the wall line increases since the capacity of gravity walls is included. The boost is larger in long direction. Consequently, total capacity of the building in long direction is much larger than the short direction.

Table R-5: Breakdown of peak base shear, pushover analysis, A2c-3D-SD-a model

Load direction	**LONG**				
Elevation	**South V_b**	**North V_b**	**East V_b**	**West V_b**	**Peak V_b**
kips	39.2	50.1	2.7	8.9	91.6
%	42.8	54.7	2.9	9.7	100.0
Load direction	**SHORT**				
Elevation	**South V_b**	**North V_b**	**East V_b**	**West V_b**	**Peak V_b**
kips	11.6	9.4	31.3	32.5	76.5
%	15.1	12.3	40.9	42.5	100.0

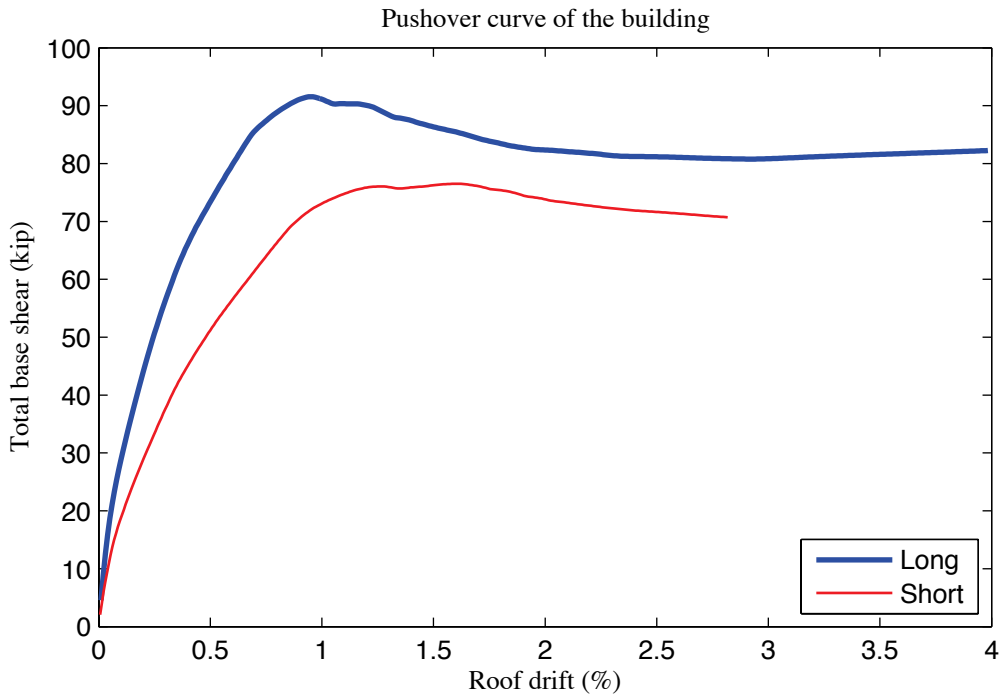

Figure R-3: Pushover curve of A2c-3D-SD-a model

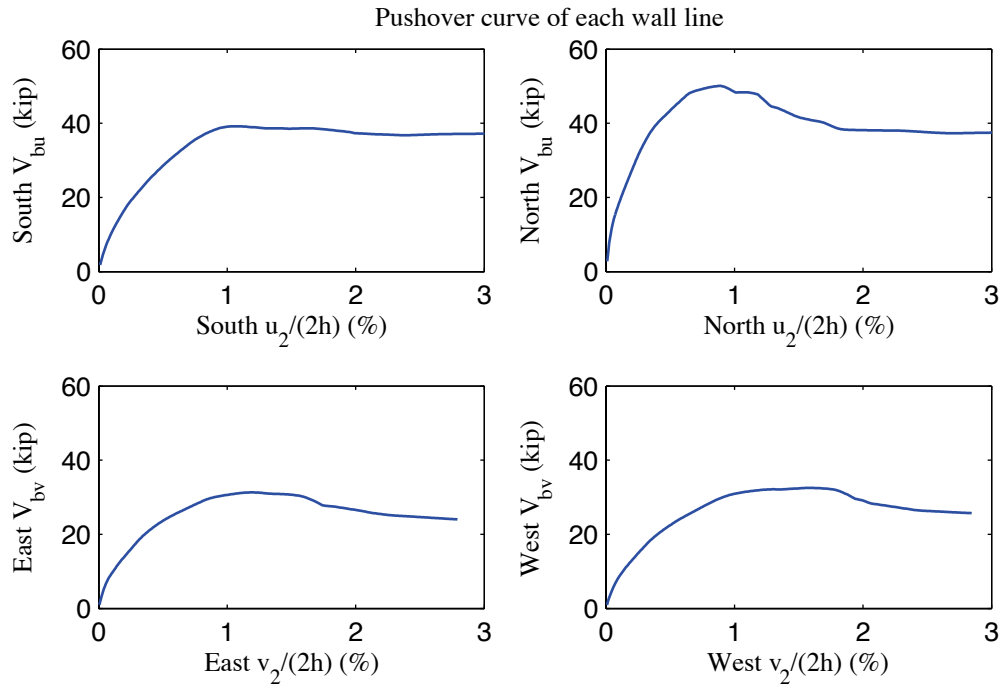

Figure R-4: Pushover curve of each wall line, A2c-3D-SD-a model

R.5 Linear time history analysis results

Linear time history analysis is performed on the model under Canoga Park and Rinaldi ground motion records of Northridge earthquake in 1994. We considered three scale levels (16%, 44% and 100%) and loadings in one, two and three axes.

Table R-6 to Table R-9 demonstrate the building's linear elastic performance under designated ground motions. Table R-6 shows peak story relative accelerations in the unit of g. Table R-7 and Table R-8 report peak roof drift and story drift of the building and the corresponding time step (t_*) and the base shear at that time. Note that the base shear at the time of peak roof drift may not be the peak total building base shear in that direction (see Table R-9).

The building behaves linearly since peak drift and peak base shear appear at the same time when the ground motion is linearly scaled. Figure R-5 is a vector plot of the peak total resultant base shear of the building under three axial, 100% Canoga Park excitation. The directions of arrows imply that base shear taken by shear walls and gravity systems does not necessarily follow the direction of wall lines due to the effect of 3D coupling. Comparison with nonlinear analysis results of the same excitation provides insightful observations on the building's response and requirements on modeling fidelity and analysis type.

Table R-6: A2c-3D-SD-a model peak story relative acceleration in g, linear time history analysis

		LONG			SHORT			UP		
Load Case	**Ground Motion**	**a_g**	**Floor a**	**Roof a**	**a_g**	**Floor a**	**Roof a**	**a_g**	**Floor a**	**Roof a**
EQ_3D_3axis_1	CNP 16%	0.067	0.127	0.193	0.057	0.109	0.165	0.078	0.028	0.023
EQ_3D_3axis_2	CNP 44%	0.185	0.342	0.526	0.157	0.301	0.459	0.215	0.242	0.213
EQ_3D_1axis_1	CNP 100%	0.420	0.759	1.171	0	0.112	0.154	0	0.432	0.375
EQ_3D_1axis_2	CNP 100%	0	0.108	0.142	0.356	0.678	1.078	0	0.628	0.554
EQ_3D_2axis_1	CNP 100%	0.420	0.765	1.182	0.356	0.682	1.061	0	0.979	0.871
EQ_3D_3axis_3	CNP 100%	0.420	0.765	1.182	0.356	0.682	1.062	0.489	0.945	0.837
EQ_3D_3axis_4	RRS 16%	0.132	0.150	0.236	0.078	0.158	0.246	0.133	0.063	0.048
EQ_3D_3axis_5	RRS 44%	0.363	0.430	0.668	0.214	0.446	0.702	0.367	0.460	0.413
EQ_3D_3axis_6	RRS 100%	0.825	0.993	1.551	0.486	1.044	1.633	0.834	0.841	0.758

Table R-7: A2c-3D-SD-a model peak building roof drift and base shear, linear time history analysis

		LONG			SHORT		
Load Case	**Ground Motion**	**u_2/(2h) (%)**	**t_* (s)**	**V_b @ t_* (kips)**	**v_2/(2h) (%)**	**t_* (s)**	**V_b @ t_* (kips)**
EQ_3D_3axis_1	CNP 16%	-0.025	4.87	12.5	-0.036	6.58	10.4
EQ_3D_3axis_2	CNP 44%	-0.070	4.87	33.8	-0.101	6.58	28.6
EQ_3D_1axis_1	CNP 100%	-0.159	4.87	74.9	-0.022	4.36	8.2
EQ_3D_1axis_2	CNP 100%	0.023	6.81	7.5	-0.233	6.58	65.1
EQ_3D_2axis_1	CNP 100%	-0.161	4.88	75.3	-0.233	6.58	64.7
EQ_3D_3axis_3	CNP 100%	-0.161	4.88	75.2	-0.233	6.58	64.7
EQ_3D_3axis_4	RRS 16%	0.031	7.51	13.5	0.051	7.39	15.0
EQ_3D_3axis_5	RRS 44%	0.087	7.51	37.3	0.143	7.39	41.0
EQ_3D_3axis_6	RRS 100%	-0.202	7.61	88.3	0.335	7.40	94.5

Table R-8: A2c-3D-SD-a model peak building story drift, linear time history analysis

		LONG				SHORT			
Load Case	**Ground Motion**	**$\Delta u_1/h$ (%)**	**t_* (s)**	**$\Delta u_2/h$ (%)**	**t_* (s)**	**$\Delta v_1/h$ (%)**	**t_* (s)**	**$\Delta v_2/h$ (%)**	**t_* (s)**
EQ_3D_3axis_1	CNP 16%	-0.033	4.87	-0.018	4.87	-0.046	6.58	-0.026	6.58
EQ_3D_3axis_2	CNP 44%	-0.092	4.87	-0.049	4.87	-0.129	6.58	-0.072	6.58
EQ_3D_1axis_1	CNP 100%	-0.207	4.87	-0.112	4.88	-0.028	4.36	-0.015	4.36
EQ_3D_1axis_2	CNP 100%	-0.028	6.91	0.018	6.82	-0.298	6.58	-0.168	6.58
EQ_3D_2axis_1	CNP 100%	-0.209	4.88	-0.113	4.88	-0.298	6.58	-0.167	6.58
EQ_3D_3axis_3	CNP 100%	-0.209	4.88	-0.113	4.88	-0.298	6.58	-0.168	6.58
EQ_3D_3axis_4	RRS 16%	0.040	2.54	0.023	7.51	0.066	7.39	0.036	7.39
EQ_3D_3axis_5	RRS 44%	0.113	2.54	0.063	7.51	0.184	7.39	0.102	7.39
EQ_3D_3axis_6	RRS 100%	0.269	2.54	0.147	7.52	0.429	7.39	0.243	7.40

Table R-9: A2c-3D-SD-a model peak building base shear, linear time history analysis

		LONG		SHORT		RESULTANT	
Load Case	**Ground Motion**	**Peak V_{bu} (kip)**	**t @ peak V_{bu} (s)**	**Peak V_{bv} (kip)**	**t @ peak V_{bv} (s)**	**Peak V_b (kip)**	**t @ peak V_b (s)**
EQ_3D_3axis_1	CNP 16%	12.5	4.87	10.4	6.58	12.5	4.87
EQ_3D_3axis_2	CNP 44%	33.8	4.87	28.6	6.58	34.0	4.87
EQ_3D_1axis_1	CNP 100%	74.9	4.87	8.7	4.45	75.0	4.87
EQ_3D_1axis_2	CNP 100%	8.6	6.91	65.1	6.58	65.1	6.58
EQ_3D_2axis_1	CNP 100%	75.3	4.88	64.7	6.58	75.4	4.88
EQ_3D_3axis_3	CNP 100%	75.2	4.88	64.7	6.58	75.4	4.88
EQ_3D_3axis_4	RRS 16%	14.7	2.54	15.0	7.39	18.3	7.51
EQ_3D_3axis_5	RRS 44%	40.5	2.54	41.0	7.39	50.7	7.51
EQ_3D_3axis_6	RRS 100%	95.9	2.54	94.9	7.39	114.9	7.51

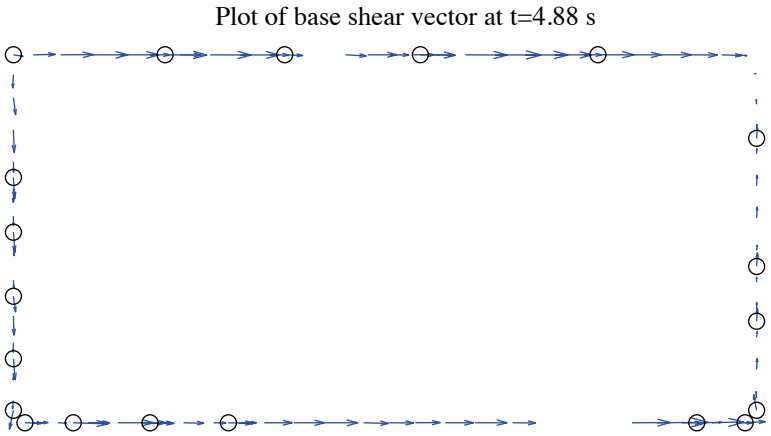

Figure R-5: A2c-3D-SD-a model, base shear vector plot at the moment of peak total base shear, 100 % Canoga Park, 3D linear analysis (maximum anchor/hold down base shear is 2.50 kips)

R.6 Nonlinear time history analysis results

Same ground motions are applied to the model with material and geometrical nonlinearity. Table R-10 to Table R-13 are replicas of Table R-6 to Table R-9, but for nonlinear time history analyses. Since this analysis type is most complicated and closest to reality and experiments, behavior of wall lines and hold downs are further studied. Table R-14 is the table of peak wall line story drifts and corresponding time steps. Table R-15 is designed for peak base shear of each wall line and the last two columns of the table are percentages of base shear of two facing wall lines in the same direction when the total base shear in that direction takes peak value. Table R-16 expands the breakdown of each wall line's peak base shear between shear walls, gravity walls and other systems. Table R-17 is peak value of hold down tensile force of two selected pairs. Hold down 5 and 6 are on shear wall L1S1, South elevation and hold down 7 and 8 are on shear wall L1W1, West elevation. These shear walls have lowest capacities compared with others on the same wall line and they meet at the southwest edge of the building, so interacted nonlinear behavior is expected to appear.

Time history plots in this section include plots of story drifts of the building and each wall line (Figure R-6 to Figure R-8), total building base shear in long and short direction (Figure R-9) and axial forces of hold downs in Table R-17 (Figure R-10). Hysteretic plots in Figure R-11 and Figure R-12 are helpful for visual examination of nonlinear base shear-drift relationship of the building and the weakest shear wall on each wall line. In comparison with linear time history analysis, vector plot of peak total base shear is illustrated in Figure R-13. Figure R-14 presents a simplified deformed shape of the

building (see (Peterman 2014) for details of the method) and axial force of all twenty hold downs at the moment of peak total base shear. The same sign convention with tests is adopted. Red bars indicate tensile (negative) force and blue ones are for compressive (positive) force.

Hysteretic behavior is seen in the building and typical shear walls under design-based earthquake (100% Canoga Park excitation in 3 axes, see Figure R-11 and Figure R-12). Even though post-peak response on the backbone curve is not initiated under this excitation level, wall lines behave differently. North wall line reaches 0.35% peak floor story drift but peak story drifts of all other wall lines are between 0.47% and 0.54% (Table R-14). Given the significantly increased capacity and stiffness in long direction, peak story drift of long direction is less than short direction (0.38% vs. 0.53%, Table R-12). Figure R-13 clearly shows that base shear vectors in anchors and hold downs do not align with wall lines, a sign of coupled wall line behavior. Table R-17, Figure R-10 and Figure R-14 demonstrate that hold downs in a pair do not experience the same amount of force with opposite signs, an evidence that supports Type II shear wall behavior despite Type I design assumption.

The near-field Rinaldi record is much stronger in terms of peak ground acceleration, especially in the long direction. With the additional lateral force resistance provided by sheathed gravity walls, simulation results show that the building can survive even 100% Rinaldi ground motion, the maximum considered earthquake in this research. This time, peak story drifts in both directions are between 1.0% and 1.2%, not even close to

threshold value of post-peak response (arguably 2%) on the backbone curve. The portion of base shear taken by gravity wall does not change much with scale factors considered so far in this research, as shown in Table R-16. Again, the table demonstrates that the base shear taken by anchors on bottom tracks of gravity walls can be quite large, sometimes even larger than half of the total base shear (e.g. South wall lines).

Table R-10: A2c-3D-SD-a model peak story relative acceleration in g, nonlinear time history analysis

		LONG			SHORT			UP		
Load Case	**Ground Motion**	**a_g**	**Floor a**	**Roof a**	**a_g**	**Floor a**	**Roof a**	**a_g**	**Floor a**	**Roof a**
EQ_3D_3axis_1	CNP 16%	0.067	0.155	0.183	0.057	0.167	0.207	0.078	0.055	0.051
EQ_3D_3axis_2	CNP 44%	0.185	0.204	0.271	0.157	0.334	0.426	0.215	0.132	0.107
EQ_3D_1axis_1	CNP 100%	0.420	0.553	0.774	0	0.135	0.169	0	0.105	0.096
EQ_3D_1axis_2	CNP 100%	0	0.094	0.107	0.356	0.679	0.847	0	0.191	0.202
EQ_3D_2axis_1	CNP 100%	0.420	0.600	0.698	0.356	0.635	0.703	0	1.056	0.925
EQ_3D_3axis_3	CNP 100%	0.420	0.600	0.673	0.356	0.674	0.728	0.489	1.081	0.990
EQ_3D_3axis_4	RRS 16%	0.132	0.130	0.231	0.078	0.177	0.205	0.133	0.104	0.104
EQ_3D_3axis_5	RRS 44%	0.363	0.416	0.457	0.214	0.573	0.603	0.367	0.232	0.228
EQ_3D_3axis_6	RRS 100%	0.825	1.001	1.535	0.486	1.048	1.365	0.834	3.358	3.170

Table R-11: A2c-3D-SD-a model peak building roof drift and base shear, nonlinear time history analysis

		LONG			SHORT		
Load Case	**Ground Motion**	**$u_2/(2h)$ (%)**	**t_* (s)**	**V_b @ t_* (kips)**	**$v_2/(2h)$ (%)**	**t_* (s)**	**V_b @ t_* (kips)**
EQ_3D_3axis_1	CNP 16%	-0.023	4.02	11.4	0.036	9.86	9.5
EQ_3D_3axis_2	CNP 44%	0.046	8.62	17.9	0.161	9.95	26.6
EQ_3D_1axis_1	CNP 100%	0.232	8.67	52.4	-0.021	8.73	3.9
EQ_3D_1axis_2	CNP 100%	-0.015	10.42	4.1	0.358	9.96	43.8
EQ_3D_2axis_1	CNP 100%	0.255	8.69	47.5	0.360	9.97	43.4
EQ_3D_3axis_3	CNP 100%	0.252	8.69	46.5	0.362	9.97	43.4
EQ_3D_3axis_4	RRS 16%	0.036	4.32	11.9	-0.074	4.31	14.3
EQ_3D_3axis_5	RRS 44%	0.139	4.35	36.3	0.241	3.36	34.7
EQ_3D_3axis_6	RRS 100%	0.624	2.63	85.1	0.752	6.05	63.7

Table R-12: A2c-3D-SD-a model peak building story drift, nonlinear linear time history analysis

		LONG				SHORT			
Load Case	**Ground Motion**	**$\Delta u_1/h$ (%)**	**t_* (s)**	**$\Delta u_2/h$ (%)**	**t_* (s)**	**$\Delta v_1/h$ (%)**	**t_* (s)**	**$\Delta v_2/h$ (%)**	**t_* (s)**
EQ_3D_3 axis_1	CNP 16%	-0.033	4.02	0.015	8.62	0.051	9.86	0.021	9.86
EQ_3D_3 axis_2	CNP 44%	0.064	8.62	0.027	8.61	0.248	9.95	0.077	9.93
EQ_3D_1 axis_1	CNP 100%	0.353	8.67	0.115	8.66	-0.029	8.72	-0.013	8.70
EQ_3D_1 axis_2	CNP 100%	-0.022	9.95	-0.012	10.42	0.532	9.96	0.185	9.96
EQ_3D_2 axis_1	CNP 100%	0.383	8.68	0.129	8.69	0.521	9.97	0.203	9.96
EQ_3D_3 axis_3	CNP 100%	0.381	8.68	0.125	8.69	0.525	9.98	0.203	9.96
EQ_3D_3 axis_4	RRS 16%	0.050	4.31	0.025	4.33	-0.105	4.32	-0.044	4.30
EQ_3D_3 axis_5	RRS 44%	0.220	4.35	0.061	4.36	0.375	3.36	-0.120	4.41
EQ_3D_3 axis_6	RRS 100%	1.011	2.64	0.248	2.62	1.158	6.05	0.365	6.04

Table R-13: A2c-3D-SD-a model peak building base shear, nonlinear time history analysis

		LONG		SHORT		RESULTANT	
Load Case	**Ground Motion**	**Peak V_{bu} (kip)**	**t @ peak V_{bu} (s)**	**Peak V_{bv} (kip)**	**t @ peak V_{bv} (s)**	**Peak V_b (kip)**	**t @ peak V_b (s)**
EQ_3D_3axis_1	CNP 16%	11.4	4.02	9.6	9.87	12.0	4.02
EQ_3D_3axis_2	CNP 44%	17.9	8.62	26.6	9.95	27.9	9.93
EQ_3D_1axis_1	CNP 100%	52.4	8.67	5.4	5.25	52.4	8.67
EQ_3D_1axis_2	CNP 100%	5.7	9.85	43.8	9.96	43.9	9.96
EQ_3D_2axis_1	CNP 100%	54.3	8.68	43.4	9.97	54.7	9.94
EQ_3D_3axis_3	CNP 100%	54.0	8.68	43.4	9.97	54.4	9.94
EQ_3D_3axis_4	RRS 16%	14.9	2.55	14.4	4.30	19.2	4.31
EQ_3D_3axis_5	RRS 44%	37.5	2.59	34.7	3.36	39.9	4.35
EQ_3D_3axis_6	RRS 100%	85.1	2.63	64.0	6.05	85.5	2.63

Table R-14: A2c-3D-SD-a model peak wall line story drift, nonlinear time history analysis

LONG		SOUTH				NORTH			
Load Case	**Ground Motion**	**$\Delta u_1/h$ (%)**	**t_* (s)**	**$\Delta u_2/h$ (%)**	**t_* (s)**	**$\Delta u_1/h$ (%)**	**t_* (s)**	**$\Delta u_2/h$ (%)**	**t_* (s)**
EQ_3D_3axis_1	CNP 16%	0.047	4.20	0.020	8.69	0.027	4.02	0.015	9.15
EQ_3D_3axis_2	CNP 44%	0.084	8.64	0.034	4.03	0.053	6.93	0.027	6.92
EQ_3D_1axis_1	CNP 100%	0.379	8.67	0.131	11.87	0.331	8.67	0.110	8.67
EQ_3D_1axis_2	CNP 100%	0.054	9.95	0.028	9.98	0.017	9.99	0.018	10.18
EQ_3D_2axis_1	CNP 100%	0.473	8.71	0.147	8.70	0.354	8.67	0.116	9.38
EQ_3D_3axis_3	CNP 100%	0.469	8.71	0.141	8.70	0.352	8.67	0.113	8.69
EQ_3D_3axis_4	RRS 16%	0.077	4.31	0.038	4.33	0.038	2.54	0.023	2.54
EQ_3D_3axis_5	RRS 44%	0.271	4.37	0.087	4.38	0.185	4.34	0.058	4.34
EQ_3D_3axis_6	RRS 100%	1.162	2.65	0.296	6.80	0.966	4.41	0.281	4.56
SHORT		**EAST**				**WEST**			
Load Case	**Ground Motion**	**$\Delta v_1/h$ (%)**	**t_* (s)**	**$\Delta v_2/h$ (%)**	**t_* (s)**	**$\Delta v_1/h$ (%)**	**t_* (s)**	**$\Delta v_2/h$ (%)**	**t_* (s)**
EQ_3D_3axis_1	CNP 16%	0.048	9.86	0.029	9.88	0.066	10.49	0.034	9.33
EQ_3D_3axis_2	CNP 44%	0.251	9.95	0.075	9.93	0.245	9.95	0.081	9.94
EQ_3D_1axis_1	CNP 100%	0.086	7.01	0.039	5.27	0.093	7.40	0.050	7.40
EQ_3D_1axis_2	CNP 100%	0.475	9.96	0.157	9.96	0.590	9.96	0.214	9.96
EQ_3D_2axis_1	CNP 100%	0.506	9.98	0.182	9.96	0.541	9.97	0.226	9.96
EQ_3D_3axis_3	CNP 100%	0.508	9.98	0.182	9.96	0.548	9.97	0.227	9.96
EQ_3D_3axis_4	RRS 16%	0.078	5.21	0.039	5.22	0.156	4.32	0.063	4.31
EQ_3D_3axis_5	RRS 44%	0.293	3.36	0.078	3.38	0.507	4.40	0.200	4.40
EQ_3D_3axis_6	RRS 100%	0.907	6.05	0.322	6.04	1.427	3.91	0.446	4.12

Table R-15: A2c-3D-SD-a model peak wall line base shear, nonlinear time history analysis

LONG		SOUTH		NORTH		% of Peak V_{bu}	
Load Case	**Ground Motion**	**Peak V_{bu} (kips)**	**t @ peak V_{bu} (s)**	**Peak V_{bu} (kips)**	**t @ peak V_{bu} (s)**	**South**	**North**
EQ_3D_3axis_1	CNP 16%	5.0	4.20	6.9	4.02	37.9	60.5
EQ_3D_3axis_2	CNP 44%	7.5	8.64	11.3	6.92	40.2	58.8
EQ_3D_1axis_1	CNP 100%	20.3	8.67	31.1	8.67	38.7	59.3
EQ_3D_1axis_2	CNP 100%	4.4	9.96	3.8	9.99	57.7	41.5
EQ_3D_2axis_1	CNP 100%	22.8	8.71	32.3	8.67	39.9	58.0
EQ_3D_3axis_3	CNP 100%	22.8	8.71	32.1	8.67	39.9	58.0
EQ_3D_3axis_4	RRS 16%	7.0	4.31	8.7	2.54	41.0	58.1
EQ_3D_3axis_5	RRS 44%	16.3	4.36	21.4	4.34	42.6	55.7
EQ_3D_3axis_6	RRS 100%	36.4	2.64	48.3	4.38	42.7	54.6
SHORT		**EAST**		**WEST**		**% of Peak V_{bv}**	
Load Case	**Ground Motion**	**Peak V_{bv} (kips)**	**t @ peak V_{bv} (s)**	**Peak V_{bv} (kips)**	**t @ peak V_{bv} (s)**	**East**	**West**
EQ_3D_3axis_1	CNP 16%	4.9	9.87	5.4	10.49	50.9	45.2
EQ_3D_3axis_2	CNP 44%	12.9	9.95	11.9	9.95	48.4	44.8
EQ_3D_1axis_1	CNP 100%	7.4	7.01	6.4	7.40	128.9	32.6
EQ_3D_1axis_2	CNP 100%	19.2	9.96	20.6	9.96	43.9	47.0
EQ_3D_2axis_1	CNP 100%	20.0	9.98	19.6	9.97	46.0	45.3
EQ_3D_3axis_3	CNP 100%	20.0	9.98	19.8	9.97	46.0	45.6
EQ_3D_3axis_4	RRS 16%	6.7	5.21	9.0	4.32	36.1	58.8
EQ_3D_3axis_5	RRS 44%	14.0	3.36	18.6	4.40	40.5	51.5
EQ_3D_3axis_6	RRS 100%	25.6	6.05	30.3	3.91	39.9	46.5

Table R-16: A2c-3D-SD-a model wall line base shear breakdown, nonlinear time history analysis

LONG		SOUTH			NORTH		
Load Case	**Ground Motion**	**Peak V_{bu} (kips)**	**SW V_{bu} (%)**	**GW V_{bu} (%)**	**Peak V_{bu} (kips)**	**SW V_{bu} (%)**	**GW V_{bu} (%)**
EQ_3D_3axis_1	CNP 16%	5.0	39.9	60.1	6.9	59.3	40.7
EQ_3D_3axis_2	CNP 44%	7.5	39.0	61.0	11.3	59.3	40.7
EQ_3D_1axis_1	CNP 100%	20.3	41.8	58.2	31.1	54.9	45.1
EQ_3D_1axis_2	CNP 100%	4.4	34.4	65.6	3.8	58.4	41.6
EQ_3D_2axis_1	CNP 100%	22.8	41.6	58.4	32.3	54.8	45.2
EQ_3D_3axis_3	CNP 100%	22.8	41.6	58.4	32.1	54.8	45.2
EQ_3D_3axis_4	RRS 16%	7.0	38.4	61.6	8.7	60.1	39.9
EQ_3D_3axis_5	RRS 44%	16.3	42.0	58.0	21.4	57.5	42.5
EQ_3D_3axis_6	RRS 100%	36.4	40.5	59.5	48.3	54.0	46.0
SHORT		**EAST**			**WEST**		
Load Case	**Ground Motion**	**Peak V_{bv} (kips)**	**SW V_{bv} (%)**	**GW V_{bu} (%)**	**Peak V_{bv} (kips)**	**SW V_{bv} (%)**	**GW V_{bv} (%)**
EQ_3D_3axis_1	CNP 16%	4.9	74.1	25.9	5.4	82.4	17.6
EQ_3D_3axis_2	CNP 44%	12.9	74.0	26.0	11.9	82.8	17.2
EQ_3D_1axis_1	CNP 100%	7.4	77.8	22.2	6.4	82.9	17.1
EQ_3D_1axis_2	CNP 100%	19.2	71.8	28.2	20.6	81.3	18.7
EQ_3D_2axis_1	CNP 100%	20.0	72.0	28.0	19.6	80.9	19.1
EQ_3D_3axis_3	CNP 100%	20.0	72.0	28.0	19.8	80.9	19.1
EQ_3D_3axis_4	RRS 16%	6.7	74.0	26.0	9.0	83.4	16.6
EQ_3D_3axis_5	RRS 44%	14.0	72.9	27.1	18.6	81.3	18.7
EQ_3D_3axis_6	RRS 100%	25.6	73.7	26.3	30.3	83.6	16.4

Table R-17: A2c-3D-SD-a model peak hold down tensile force at certain locations, nonlinear time history analysis

		L1S1, LC5		L1S1, LC6		L1W1, LC7		L1W1, LC8	
Load Case	**Ground Motion**	**Peak F (kips)**	**t @ peak F (s)**	**Peak F (kips)**	**t @ peak F (s)**	**Peak F (kips)**	**t @ peak F (s)**	**Peak F (kips)**	**t @ peak F (s)**
EQ_3D_3axis_1	CNP 16%	-0.54	4.20	-0.10	9.86	-0.08	9.86	-0.37	4.30
EQ_3D_3axis_2	CNP 44%	-0.89	4.21	-0.53	9.94	-0.40	9.93	-0.63	9.79
EQ_3D_1axis_1	CNP 100%	-1.83	11.86	-0.30	8.65	-0.52	8.65	-0.54	8.66
EQ_3D_1axis_2	CNP 100%	-1.66	9.96	-1.04	9.96	-0.60	9.96	-0.90	8.42
EQ_3D_2axis_1	CNP 100%	-1.79	12.94	-1.42	9.96	-1.23	9.95	-0.95	8.42
EQ_3D_3axis_3	CNP 100%	-1.81	12.94	-1.43	9.96	-1.23	9.96	-0.96	8.43
EQ_3D_3axis_4	RRS 16%	-0.68	4.20	-0.13	5.97	-0.10	2.96	-0.60	4.33
EQ_3D_3axis_5	RRS 44%	-1.68	4.54	-0.65	4.57	-0.34	5.98	-1.03	4.40
EQ_3D_3axis_6	RRS 100%	-2.59	3.90	-2.37	6.05	-1.37	6.05	-1.87	4.12

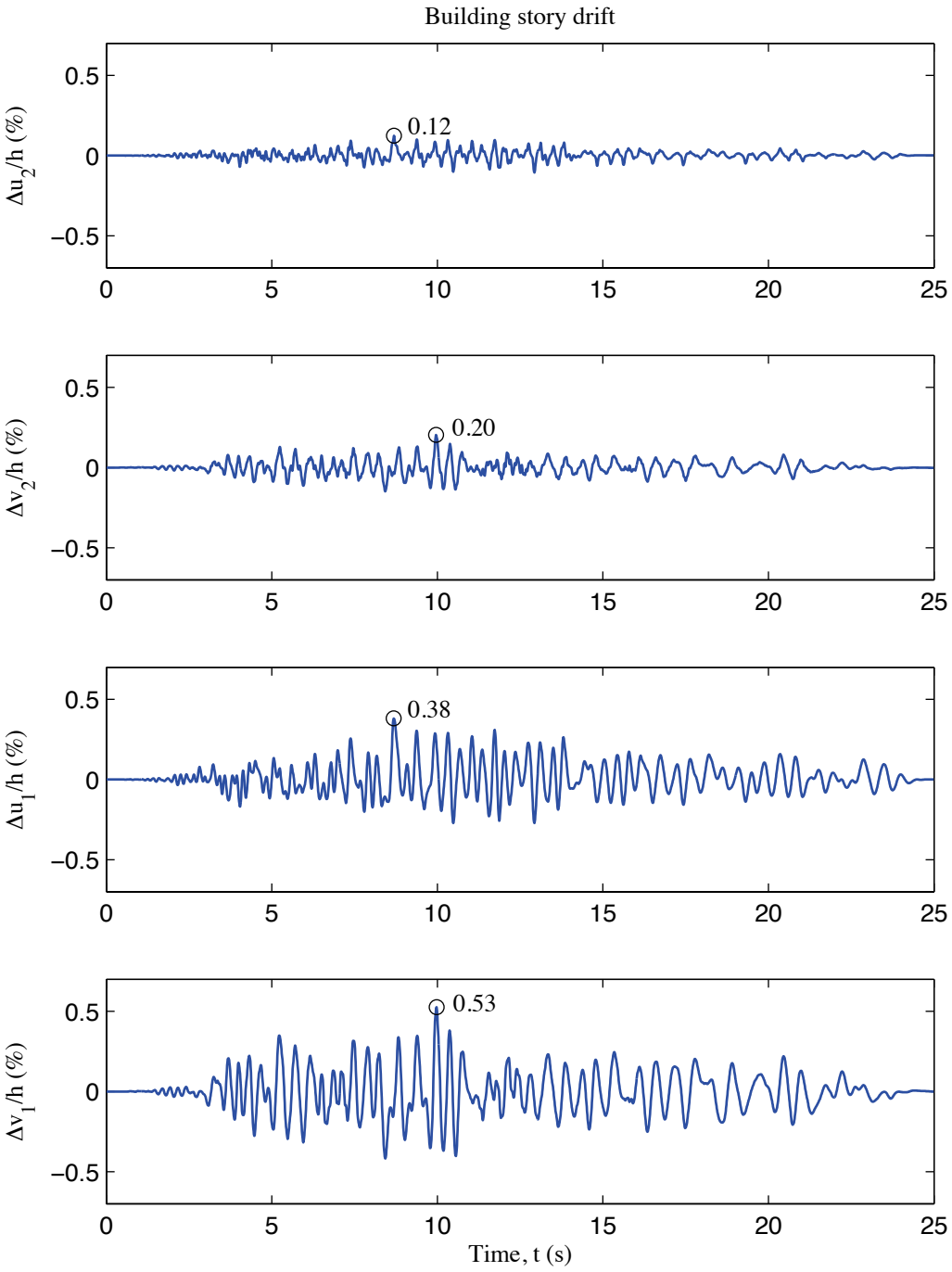

Figure R-6: A2c-3D-SD-a model building story drift, 100 % Canoga Park, 3D nonlinear analysis

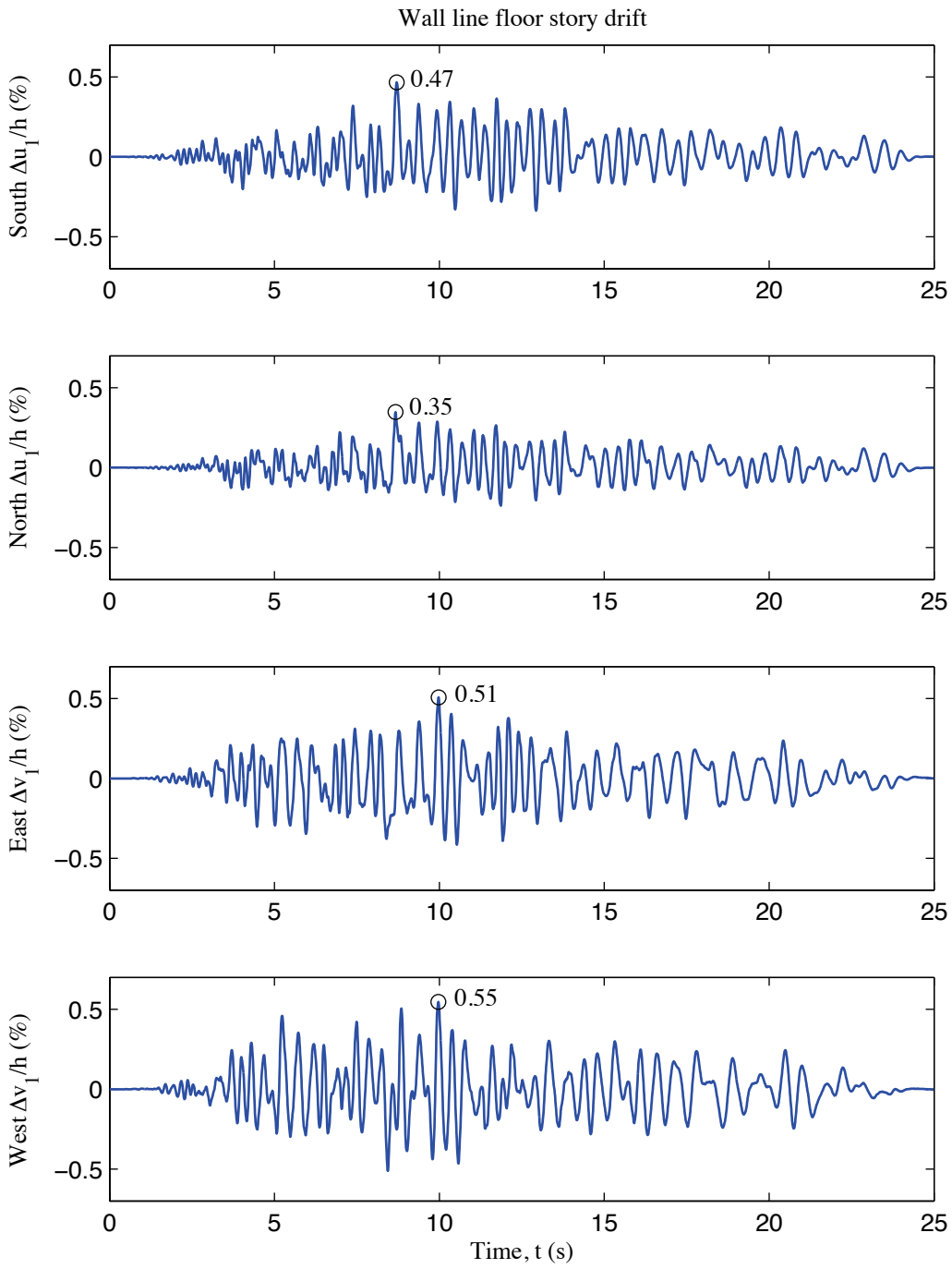

Figure R-7: A2c-3D-SD-a model wall line floor story drift, 100 % Canoga Park, 3D nonlinear analysis

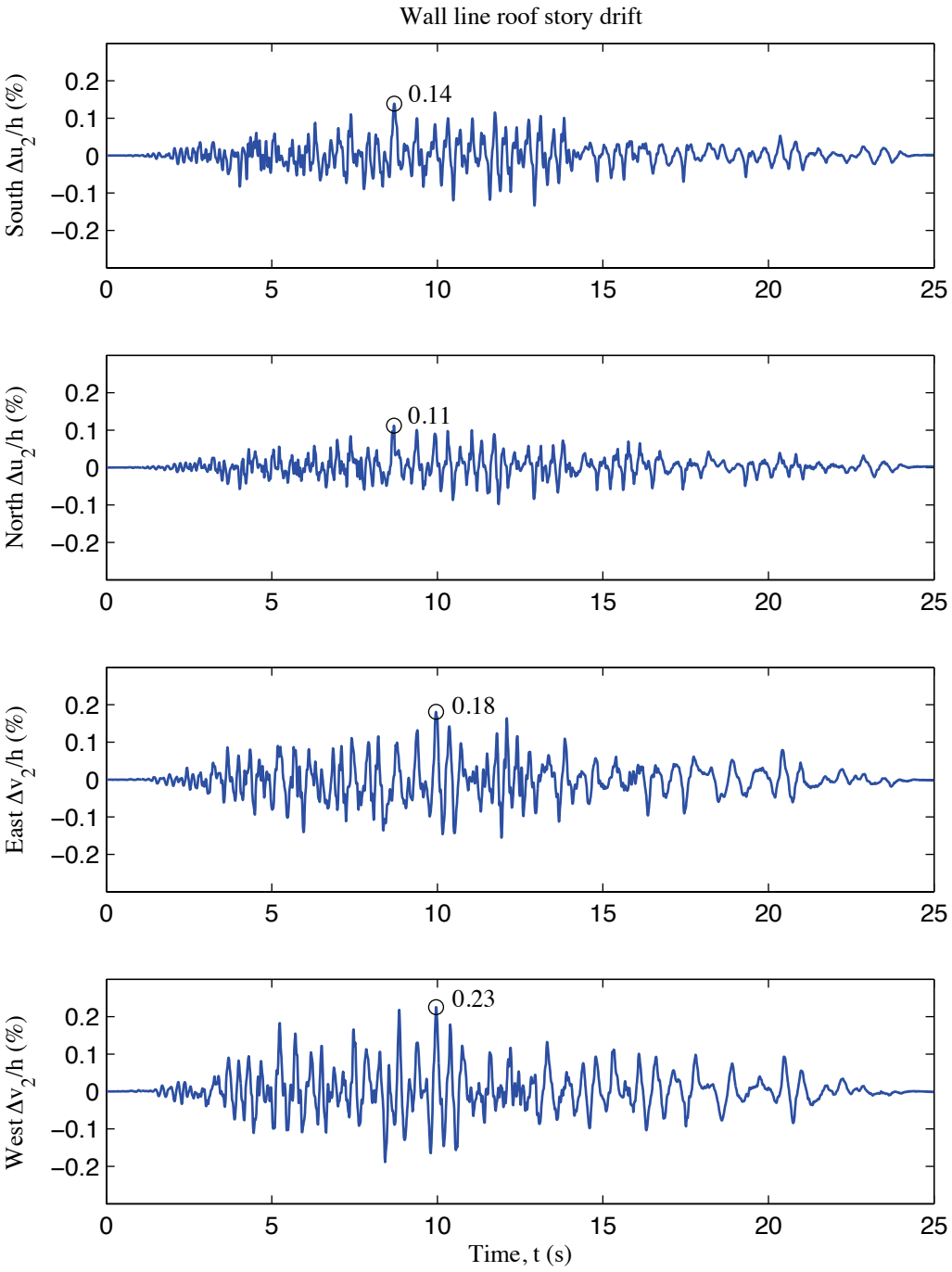

Figure R-8: A2c-3D-SD-a model wall line roof story drift, 100 % Canoga Park, 3D nonlinear analysis

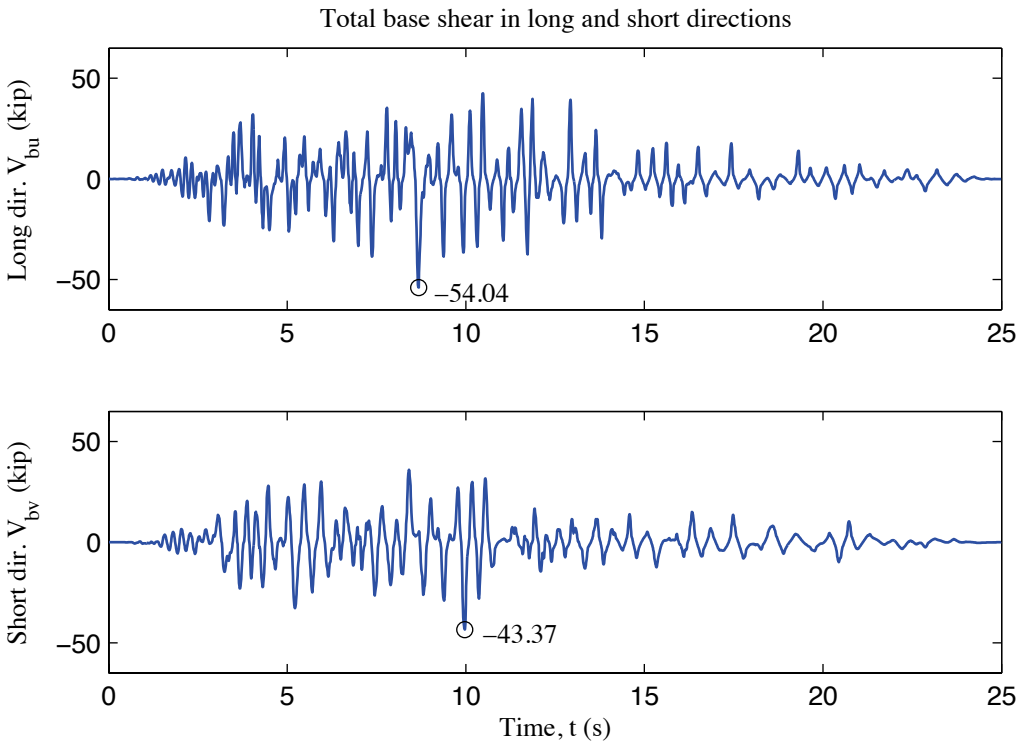

Figure R-9: A2c-3D-SD-a model total building base shear, 100 % Canoga Park, 3D nonlinear analysis

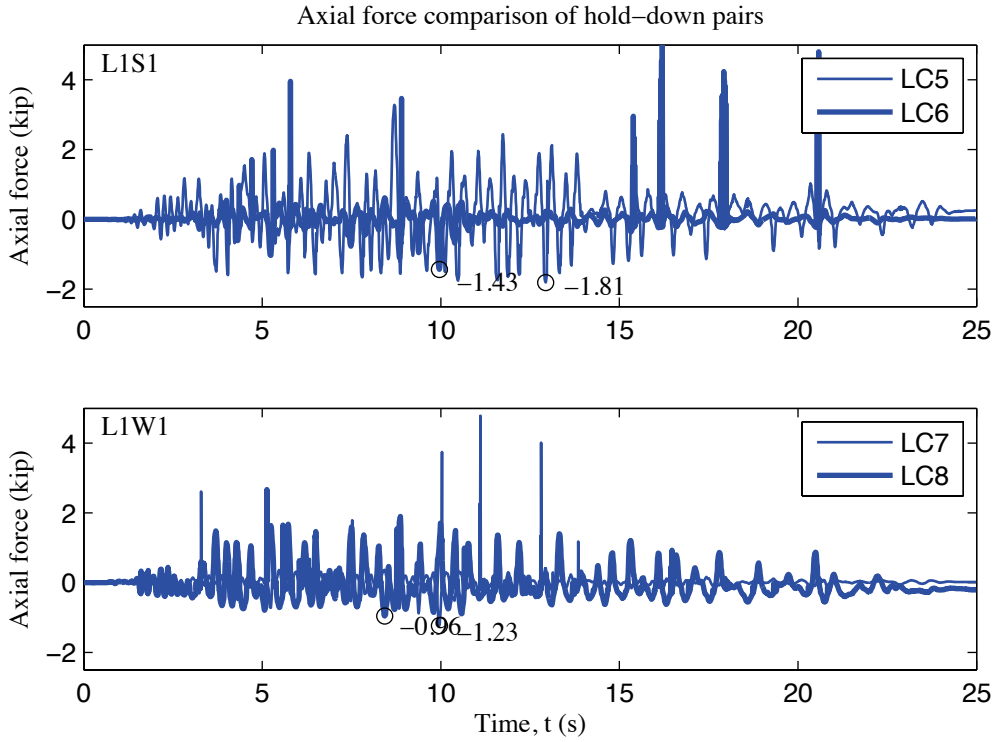

Figure R-10: A2c-3D-SD-a model, load cell 5 to 8 axial forces, 100 % Canoga Park, 3D nonlinear analysis

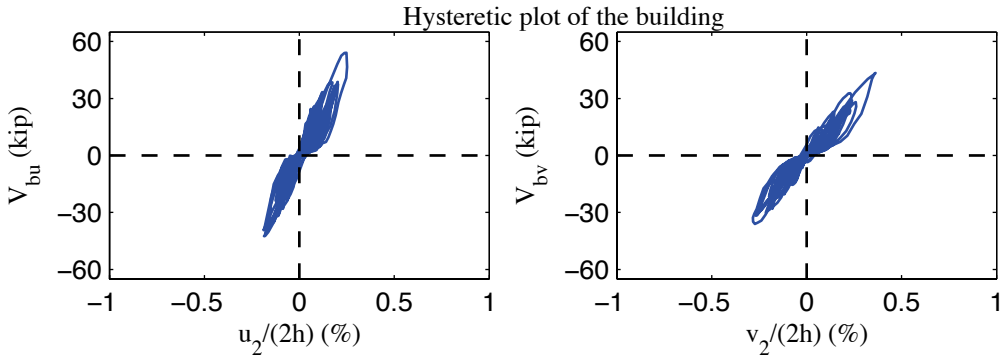

Figure R-11: A2c-3D-SD-a model, hysteretic plot of the building, 100 % Canoga Park, 3D nonlinear analysis

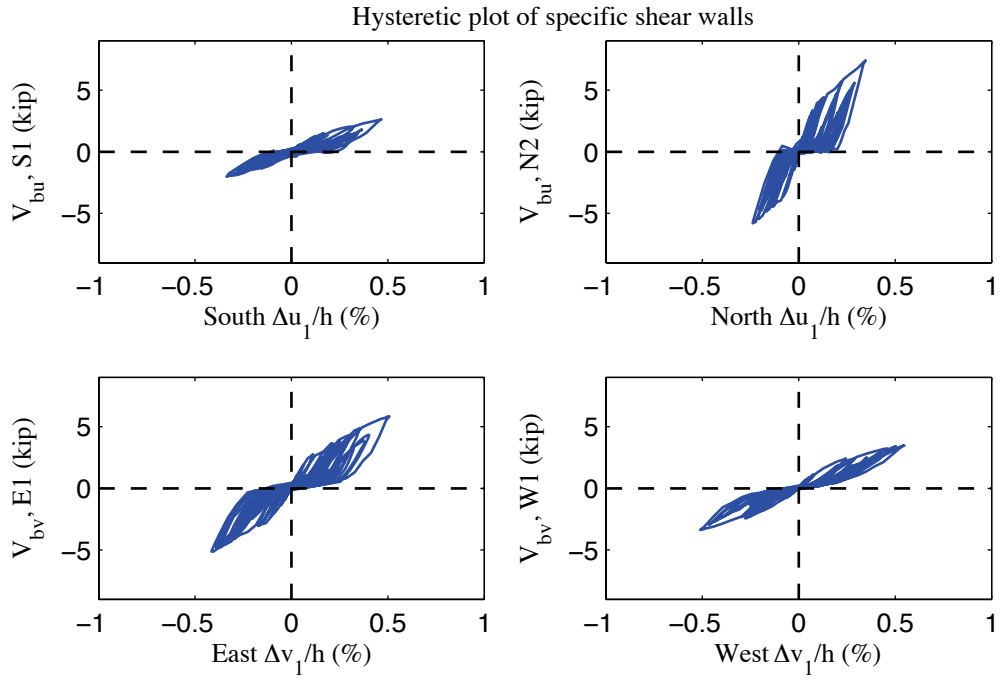

Figure R-12: A2c-3D-SD-a model, hysteretic plot of shear walls at each elevation, 100 % Canoga Park, 3D nonlinear analysis

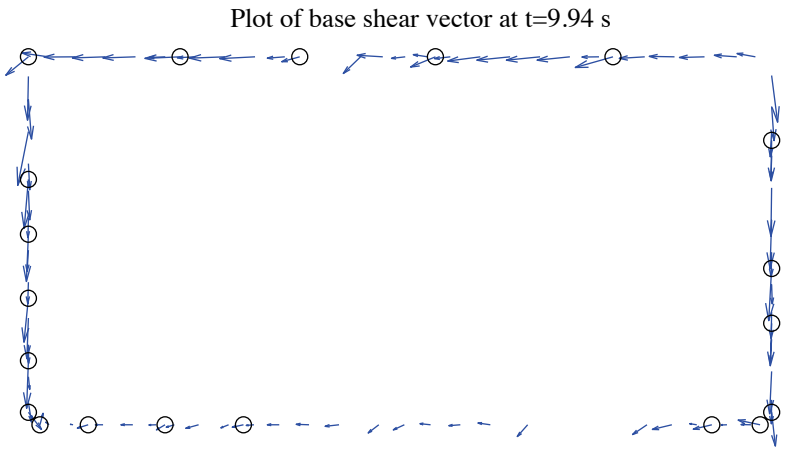

Figure R-13: A2c-3D-SD-a model, field plot of peak total base shear, 100 % Canoga Park, 3D nonlinear analysis (maximum anchor/hold down base shear is 1.80 kips)

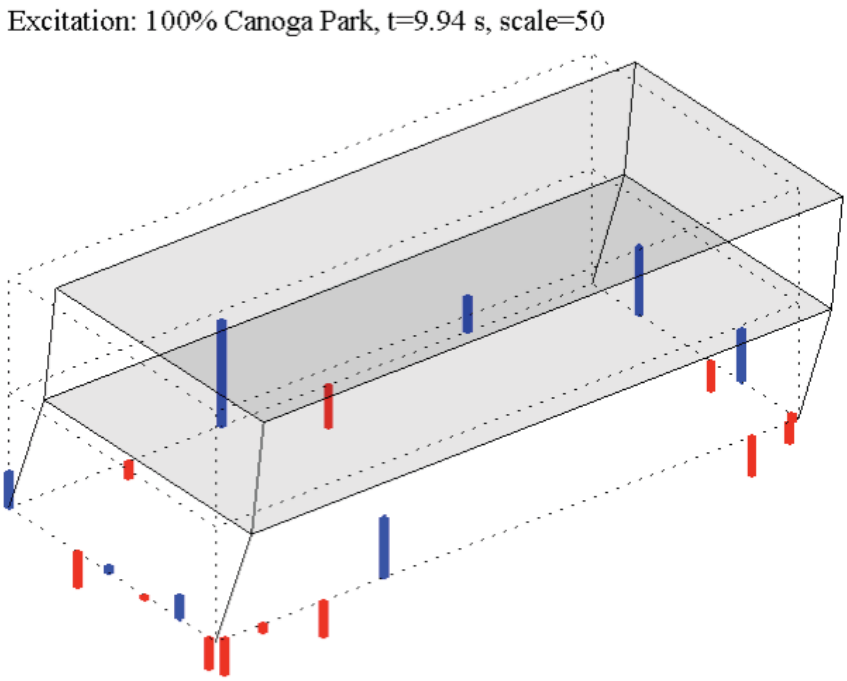

Figure R-14: A2c-3D-SD-a model, simplified illustration of corner displacements with hold down forces from load cells,100 % Canoga Park, 3D nonlinear analysis (max hold down tensile force is -1.59 kips)

Appendix S: Analysis Results of State-of-the-art, Phase 2d, 3D, rigid-diaphragm, model a (A2d-3D-RD-a)

S.1 Model description

This state-of-the-art 3D model features subpanel bracing models of shear walls and gravity walls, explicit models of hold downs, and rigid diaphragms. All walls are covered by OSB and gypsum sheathing. This model is also the only one that includes interior walls. One gypsum sheathed interior wall is modeled using two nonlinear diagonals. Seismic mass is distributed to corners and stud ends. The lateral displacement and shear wall capacity ($\delta(0.2V_{nA})$, $0.2V_{nA}$) from test is utilized to determine the stiffness of elastic material and the first point on the backbone curve of Pinching4 material of shear wall bracing. Figure S-1 is the 3D drawing of the building model with all members and diagonal bracings of sheathing panels. Definitions of output physical quantities and explanation of post-process method can be found in Appendix K.

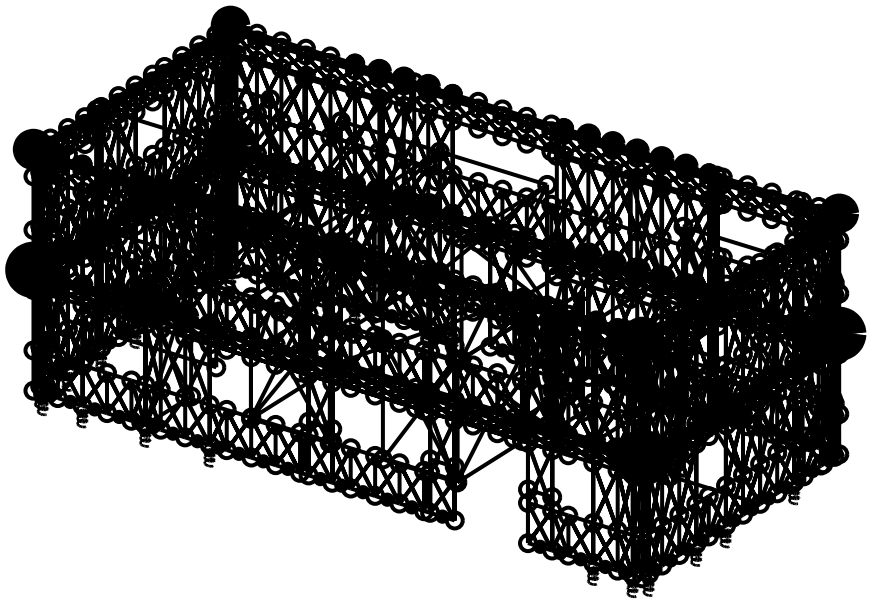

Figure S-1: A2d-3D-RD-a model

S.2 Free vibration analysis results

Free vibration analysis results are presented in Table S-1 and Figure S-2. Lateral stiffness in the short direction is smaller than lateral stiffness in the long direction and torsional stiffness is the largest. The observation holds for the first and the second mode, as indicated by Table S-1.

Table S-1: Free vibration analysis results, A2d-3D-RD-a model

Mode number	Natural period (s)	Mode description
1	0.215	Short, 1st
2	0.171	Long, 1st
3	0.151	Torsion, 1st
4	0.078	Short, 2nd
5	0.065	Long, 2nd
6	0.057	Torsion, 2nd

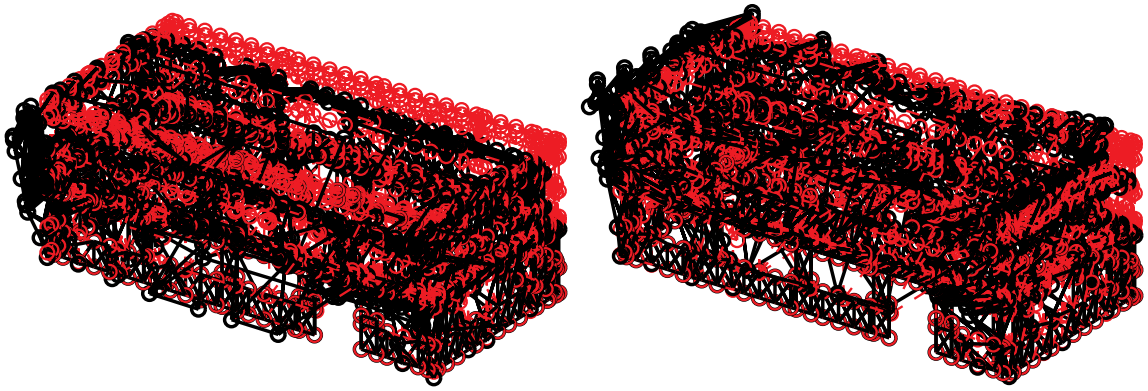

(a) Mode 1, T_1=0.215 s (b) Mode 2, T_2= 0.171s

Figure S-2: First two natural modes of A2d-3D-RD-a model

S.3 Linear static analysis results

Table S-2 to Table S-4 present linear static analysis results. The lateral load is the equivalent lateral force available from the design narrative (Peterman 2014), applied equally at four corners. Two separate analyses were performed with the loading at long or short direction.

Table S-2 summarizes the breakdown of peak total base shear among four elevations. Due to the interplay of asymmetrical LFRS, wall lines perpendicular to the loading direction still take a very small portion of base shear.

Table S-3 shows peak building and wall line deflections. Practicing engineers can linearly upscale these data and develop an estimate of the building's performance at a certain lateral force level.

Table S-4 is an evaluation of the building's lateral stiffness of long and short direction and its breakdown among shear walls (SW) and other systems. Covered by the same type of OSB and gypsum sheathing with shear walls (even though the fastener spacing is different), gravity walls make a comparable contribution to total lateral stiffness like shear walls. The effect is even more apparent in long direction, where wall lines are much wider and have larger areas covered by gravity walls. Regarded as nonstructural building components, interior walls actually provides additional supports in the middle of the building, and they also support shear walls and gravity walls that meet with them.

Accordingly, the stiffness of systems other than shear walls can account for as much as 43% and 37% of total lateral stiffness in long and short direction.

Table S-2: Breakdown of peak base shear, linear static analysis, A2d-3D-RD-a model

Load direction	**LONG**				
Elevation	**South V_b**	**North V_b**	**East V_b**	**West V_b**	**Peak V_b**
kips	3.6	6.0	0.2	1.2	11.1
%	32.8	54.4	2.0	10.9	100.0
Load direction	**SHORT**				
Elevation	**South V_b**	**North V_b**	**East V_b**	**West V_b**	**Peak V_b**
kips	0.0	0.0	5.6	5.4	11.1
%	0.1	0.4	50.8	48.9	100.0

Table S-3: Peak building and wall line deflection, linear static analysis, A2d-3D-RD-a model

Load direction	**LONG**							
Deflection (in.)	**u_1**	**u_2**	**v_1**	**v_2**	**Δu_1**	**Δu_2**	**Δv_1**	**Δv_2**
Building	0.028	0.046	-0.002	-0.003	0.028	0.018	-0.002	-0.002
South	0.030	0.050	-0.002	-0.003	0.030	0.020	-0.002	-0.002
North	0.025	0.041	-0.002	-0.003	0.025	0.017	-0.002	-0.002
East	0.028	0.046	0.004	0.006	0.028	0.018	0.004	0.002
West	0.028	0.046	-0.008	-0.013	0.028	0.018	-0.008	-0.005
Load direction	**SHORT**							
Deflection (in.)	**u_1**	**u_2**	**v_1**	**v_2**	**Δu_1**	**Δu_2**	**Δv_1**	**Δv_2**
Building	0.000	-0.001	0.046	0.075	0.000	-0.001	0.046	0.029
South	-0.001	-0.002	0.046	0.075	-0.001	-0.001	0.046	0.029
North	0.001	0.001	0.046	0.075	0.001	0.001	0.046	0.029
East	0.000	-0.001	0.044	0.072	0.000	-0.001	0.044	0.028
West	0.000	-0.001	0.048	0.079	0.000	-0.001	0.048	0.031

Table S-4: Breakdown of lateral stiffness, A2d-3D-RD-a model

LONG			**SHORT**		
Shear wall k_u (%)	**Gravity wall k_u (%)**	**k_u (kip/in)**	**Shear wall k_v (%)**	**Gravity wall k_v (%)**	**k_v (kip/in)**
56.7	43.3	244.5	62.9	37.1	143.3

S.4 Nonlinear static (pushover) analysis results

Table S-5 is created following the same logic with Table S-2, but the analysis type is nonlinear static (pushover). Pushover curves of the building and each wall line are presented in Figure S-3 and Figure S-4.

Clearly, the interaction between wall lines is much more significant when material and geometrical nonlinearity is included. These tables and figures indicate that the wall lines do not reach their peak capacity at exactly the same drift level and wall lines perpendicular to the load can take a nontrivial amount of base shear. Total capacity of the wall line increases since the capacity of gravity walls is included. The boost is larger in long direction. Consequently, total capacity of the building in long direction is much larger than the short direction. Interior wall also provides further increase of total capacity of the building in both directions.

Table S-5: Breakdown of peak base shear, pushover analysis, A2d-3D-RD-a model

Load direction	**LONG**				
Elevation	**South V_b**	**North V_b**	**East V_b**	**West V_b**	**Peak V_b**
kips	43.8	52.3	7.3	12.3	104.1
%	42.1	50.2	7.0	11.8	100.0
Load direction	**SHORT**				
Elevation	**South V_b**	**North V_b**	**East V_b**	**West V_b**	**Peak V_b**
kips	9.0	12.6	31.4	32.5	74.8
%	12.0	16.8	41.9	43.5	100.0

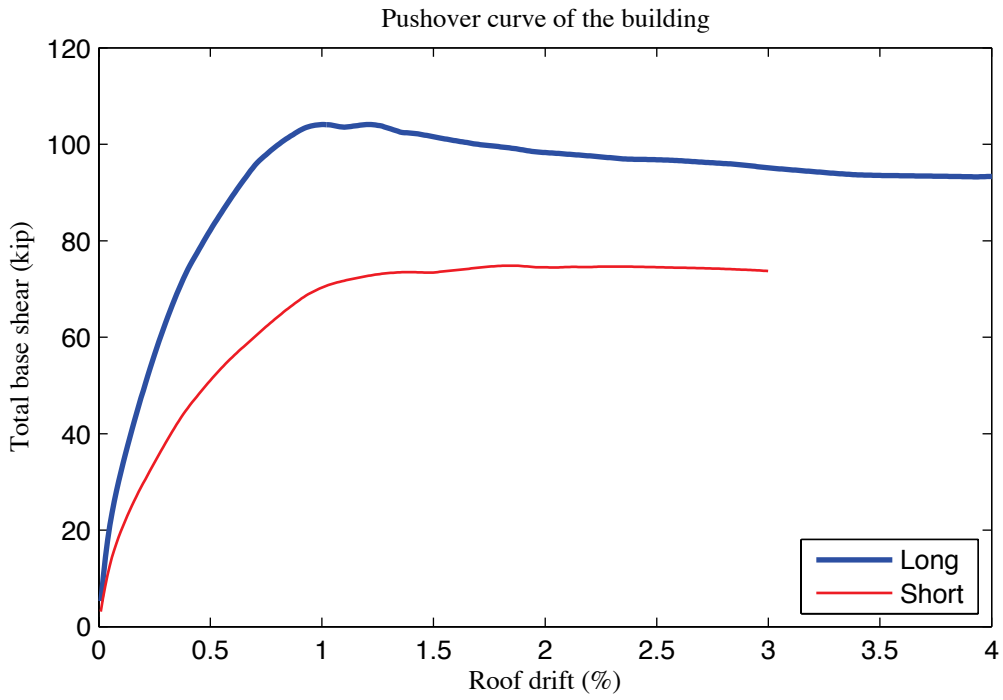

Figure S-3: Pushover curve of A2d-3D-RD-a model

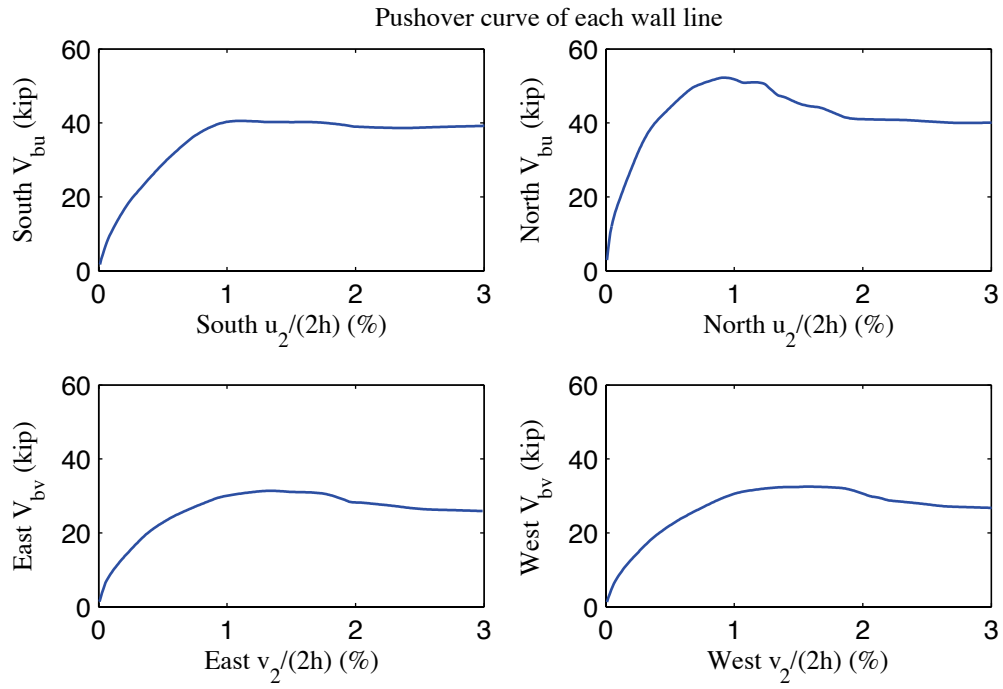

Figure S-4: Pushover curve of each wall line, A2d-3D-RD-a model

S.5 Linear time history analysis results

Linear time history analysis is performed on the model under Canoga Park and Rinaldi ground motion records of Northridge earthquake in 1994. We considered three scale levels (16%, 44% and 100%) and loadings in one, two and three axes.

Table S-6 to Table S-9 demonstrate the building's linear elastic performance under designated ground motions. Table S-6 shows peak story relative accelerations in the unit of g. Table S-7 and Table S-8 report peak roof drift and story drift of the building and the corresponding time step (t_*) and the base shear at that time. Note that the base shear at the time of peak roof drift may not be the peak total building base shear in that direction (see Table S-9).

The building behaves linearly since peak drift and peak base shear appear at the same time when the ground motion is linearly scaled. Figure S-5 is a vector plot of the peak total resultant base shear of the building under three axial, 100% Canoga Park excitation. The directions of arrows imply that base shear taken by shear walls and gravity systems does not necessarily follow the direction of wall lines due to the effect of 3D coupling. An interesting phenomenon is that concentrated base shear forces appear at locations where exterior and interior walls meet. Comparison with nonlinear analysis results of the same excitation provides insightful observations on the building's response and requirements on modeling fidelity and analysis type.

Table S-6: A2d-3D-RD-a model peak story relative acceleration in g, linear time history analysis

		LONG			SHORT			UP		
Load Case	**Ground Motion**	**a_g**	**Floor a**	**Roof a**	**a_g**	**Floor a**	**Roof a**	**a_g**	**Floor a**	**Roof a**
EQ_3D_3axis_1	CNP 16%	0.067	0.120	0.178	0.057	0.163	0.268	0.078	0.028	0.022
EQ_3D_3axis_2	CNP 44%	0.185	0.327	0.479	0.157	0.435	0.714	0.215	0.388	0.344
EQ_3D_1axis_1	CNP 100%	0.420	0.690	1.058	0	0.159	0.260	0	0.365	0.335
EQ_3D_1axis_2	CNP 100%	0	0.228	0.331	0.356	0.923	1.444	0	0.878	0.806
EQ_3D_2axis_1	CNP 100%	0.420	0.734	1.068	0.356	0.992	1.563	0	1.005	0.909
EQ_3D_3axis_3	CNP 100%	0.420	0.734	1.068	0.356	0.992	1.563	0.489	1.005	0.909
EQ_3D_3axis_4	RRS 16%	0.132	0.150	0.236	0.078	0.159	0.233	0.133	0.075	0.068
EQ_3D_3axis_5	RRS 44%	0.363	0.414	0.651	0.214	0.431	0.648	0.367	0.438	0.391
EQ_3D_3axis_6	RRS 100%	0.825	0.943	1.493	0.486	1.007	1.488	0.834	0.965	0.884

Table S-7: A2d-3D-RD-a model peak building roof drift and base shear, linear time history analysis

		LONG			SHORT		
Load Case	**Ground Motion**	**$u_2/(2h)$ (%)**	**t_* (s)**	**V_b @ t_* (kips)**	**$v_2/(2h)$ (%)**	**t_* (s)**	**V_b @ t_* (kips)**
EQ_3D_3axis_1	CNP 16%	-0.022	4.17	12.1	-0.051	7.16	15.8
EQ_3D_3axis_2	CNP 44%	-0.060	4.17	32.7	-0.136	7.16	41.3
EQ_3D_1axis_1	CNP 100%	-0.129	4.17	71.2	-0.033	4.52	11.1
EQ_3D_1axis_2	CNP 100%	0.051	6.97	15.8	-0.290	7.17	87.0
EQ_3D_2axis_1	CNP 100%	-0.136	4.17	72.3	-0.311	7.17	94.7
EQ_3D_3axis_3	CNP 100%	-0.136	4.17	72.3	-0.311	7.17	94.7
EQ_3D_3axis_4	RRS 16%	-0.030	3.03	17.3	-0.043	4.29	13.7
EQ_3D_3axis_5	RRS 44%	-0.084	3.03	47.0	0.115	7.37	36.7
EQ_3D_3axis_6	RRS 100%	-0.192	3.03	104.5	0.278	7.37	86.5

Table S-8: A2d-3D-RD-a model peak building story drift, linear time history analysis

		LONG				SHORT			
Load Case	**Ground Motion**	**$\Delta u_1/h$ (%)**	**t_* (s)**	**$\Delta u_2/h$ (%)**	**t_* (s)**	**$\Delta v_1/h$ (%)**	**t_* (s)**	**$\Delta v_2/h$ (%)**	**t_* (s)**
EQ_3D_3axis_1	CNP 16%	-0.029	4.17	0.016	4.25	-0.065	7.16	-0.037	7.16
EQ_3D_3axis_2	CNP 44%	-0.079	4.17	0.042	4.25	-0.173	7.16	-0.099	7.16
EQ_3D_1axis_1	CNP 100%	-0.168	4.17	0.093	4.25	-0.038	4.52	-0.027	4.52
EQ_3D_1axis_2	CNP 100%	-0.064	7.07	0.041	7.16	-0.370	7.17	-0.210	7.17
EQ_3D_2axis_1	CNP 100%	-0.177	4.17	0.098	4.26	-0.398	7.17	-0.225	7.17
EQ_3D_3axis_3	CNP 100%	-0.177	4.17	0.098	4.26	-0.398	7.17	-0.225	7.17
EQ_3D_3axis_4	RRS 16%	-0.039	3.03	-0.021	3.03	-0.056	4.29	-0.030	4.29
EQ_3D_3axis_5	RRS 44%	-0.109	3.03	-0.059	3.03	-0.146	7.26	0.085	7.37
EQ_3D_3axis_6	RRS 100%	-0.248	3.03	-0.138	3.04	0.349	7.37	0.207	7.37

Table S-9: A2d-3D-RD-a model peak building base shear, linear time history analysis

		LONG		SHORT		RESULTANT	
Load Case	**Ground Motion**	**Peak V_{bu} (kip)**	**t @ peak V_{bu} (s)**	**Peak V_{bv} (kip)**	**t @ peak V_{bv} (s)**	**Peak V_b (kip)**	**t @ peak V_b (s)**
EQ_3D_3axis_1	CNP 16%	12.1	4.17	15.8	7.16	15.9	7.16
EQ_3D_3axis_2	CNP 44%	32.7	4.17	41.9	7.17	42.3	7.17
EQ_3D_1axis_1	CNP 100%	71.2	4.17	11.4	4.43	71.6	4.17
EQ_3D_1axis_2	CNP 100%	17.7	7.07	87.0	7.17	88.0	7.17
EQ_3D_2axis_1	CNP 100%	72.3	4.17	94.7	7.17	95.3	7.17
EQ_3D_3axis_3	CNP 100%	72.3	4.17	94.7	7.17	95.3	7.17
EQ_3D_3axis_4	RRS 16%	17.3	3.03	13.7	4.29	18.2	3.03
EQ_3D_3axis_5	RRS 44%	47.0	3.03	36.7	7.37	49.5	3.03
EQ_3D_3axis_6	RRS 100%	104.5	3.03	86.5	7.37	110.6	3.03

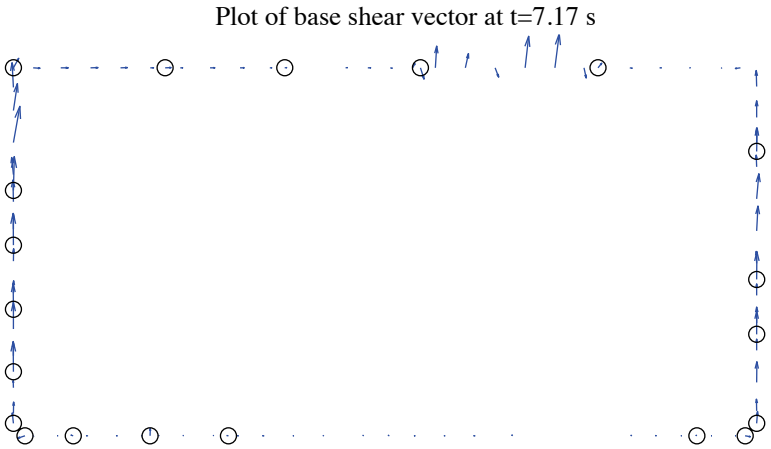

Figure S-5: A2d-3D-RD-a model, base shear vector plot at the moment of peak total base shear, 100 % Canoga Park, 3D linear analysis (maximum anchor/hold down base shear is 4.74 kips)

S.6 Nonlinear time history analysis results

Same ground motions are applied to the model with material and geometrical nonlinearity. Table S-10 to Table S-13 are replicas of Table S-6 to Table S-9, but for nonlinear time history analyses. Since this analysis type is most complicated and closest to reality and experiments, behavior of wall lines and hold downs are further studied. Table S-14 is the table of peak wall line story drifts and corresponding time steps. Table S-15 is designed for peak base shear of each wall line and the last two columns of the table are percentages of base shear of two facing wall lines in the same direction when the total base shear in that direction takes peak value. Table S-16 expands the breakdown of each wall line's peak base shear between shear walls, gravity walls and other systems. Table S-17 is peak value of hold down tensile force of two selected pairs. Hold down 5 and 6 are on shear wall L1S1, South elevation and hold down 7 and 8 are on shear wall L1W1, West elevation. These shear walls have lowest capacities compared with others on the same wall line and they meet at the southwest edge of the building, so interacted nonlinear behavior is expected to appear.

Time history plots in this section include plots of story drifts of the building and each wall line (Figure S-6 to Figure S-8), total building base shear in long and short direction (Figure S-9) and axial forces of hold downs in Table S-17 (Figure S-10). Hysteretic plots in Figure S-11 and Figure S-12 are helpful for visual examination of nonlinear base shear-drift relationship of the building and the weakest shear wall on each wall line. In comparison with linear time history analysis, vector plot of peak total base shear is illustrated in Figure S-13. Figure S-14 presents a simplified deformed shape of the

building (see (Peterman 2014) for details of the method) and axial force of all twenty hold downs at the moment of peak total base shear. The same sign convention with tests is adopted. Red bars indicate tensile (negative) force and blue ones are for compressive (positive) force.

Hysteretic behavior is seen in the building and typical shear walls under design-based earthquake (100% Canoga Park excitation in 3 axes, see Figure S-11 and Figure S-12). Even though post-peak response on the backbone curve is not initiated under this excitation level, wall lines behave differently. West wall line reaches 0.57% peak floor story drift but peak story drifts of all other wall lines are less than 0.46% (Table S-14). Given the significantly increased capacity and stiffness in long direction, peak story drift of long direction is less than short direction (0.33% vs. 0.51%, Table S-12). Figure S-13 clearly shows that base shear vectors in anchors and hold downs do not align with wall lines, a sign of coupled wall line behavior. Concentrated distribution of base shear is also seen in some exterior walls where they meet interior walls. Table S-17, Figure S-10 and Figure S-14 demonstrate that hold downs in a pair do not experience the same amount of force with opposite signs, an evidence that supports Type II shear wall behavior despite Type I design assumption. In Table S-10, peak story relative acceleration in vertical direction is very large. The happens only at a certain moment, and the time step is set as 0.005 seconds, 50% of the original ground motion to overcome convergence problems.

The near-field Rinaldi record is much stronger in terms of peak ground acceleration, especially in the long direction. With the additional lateral force resistance provided by

sheathed gravity walls, simulation results show that the building can survive even 100% Rinaldi ground motion, the maximum considered earthquake in this research. This time, long and short direction story drifts are about 0.84% and 0.99%, not even close to threshold value of post-peak response (arguably 2%) on the backbone curve. The portion of base shear taken by gravity wall does not change much with scale factors considered so far in this research, as shown in Table S-16. Again, the table demonstrates that the base shear taken by anchors on bottom tracks of gravity walls can be quite large, sometimes even larger than half of the total base shear (e.g. South wall lines).

Table S-10: A2d-3D-RD-a model peak story relative acceleration in g, nonlinear time history analysis

		LONG			SHORT			UP		
Load Case	**Ground Motion**	**a_g**	**Floor a**	**Roof a**	**a_g**	**Floor a**	**Roof a**	**a_g**	**Floor a**	**Roof a**
EQ_3D_3axis_1	CNP 16%	0.067	0.103	0.146	0.057	0.124	0.163	0.078	0.022	0.016
EQ_3D_3axis_2	CNP 44%	0.185	0.263	0.334	0.157	0.301	0.417	0.215	0.115	0.116
EQ_3D_1axis_1	CNP 100%	0.420	0.711	0.867	0	0.166	0.198	0	0.847	0.801
EQ_3D_1axis_2	CNP 100%	0	0.123	0.160	0.356	0.536	0.904	0	15.082	14.865
EQ_3D_2axis_1	CNP 100%	0.420	0.732	0.809	0.356	0.442	0.913	0	22.466	21.624
EQ_3D_3axis_3	CNP 100%	0.420	0.732	0.809	0.356	0.442	0.913	0.489	22.466	21.624
EQ_3D_3axis_4	RRS 16%	0.132	0.125	0.205	0.078	0.194	0.236	0.133	0.047	0.040
EQ_3D_3axis_5	RRS 44%	0.363	0.494	0.621	0.214	0.468	0.714	0.367	8.563	8.103
EQ_3D_3axis_6	RRS 100%	0.825	3.342	4.948	0.486	6.652	12.728	0.834	74.122	73.278

Table S-11: A2d-3D-RD-a model peak building roof drift and base shear, nonlinear time history analysis

Load Case	Ground Motion	LONG			SHORT		
		$u_2/(2h)$ (%)	t_* (s)	V_b @ t_* (kips)	$v_2/(2h)$ (%)	t_* (s)	V_b @ t_* (kips)
EQ_3D_3axis_1	CNP 16%	-0.019	4.17	9.8	-0.034	6.57	9.5
EQ_3D_3axis_2	CNP 44%	0.051	8.64	21.7	0.151	9.92	25.4
EQ_3D_1axis_1	CNP 100%	0.234	8.65	55.2	-0.027	8.69	5.2
EQ_3D_1axis_2	CNP 100%	-0.027	9.96	3.0	0.394	9.95	40.6
EQ_3D_2axis_1	CNP 100%	0.230	8.66	55.0	0.401	9.96	41.6
EQ_3D_3axis_3	CNP 100%	0.230	8.66	55.0	0.401	9.96	41.6
EQ_3D_3axis_4	RRS 16%	0.029	2.54	14.7	-0.058	7.30	14.0
EQ_3D_3axis_5	RRS 44%	0.118	2.58	36.5	0.240	3.35	32.4
EQ_3D_3axis_6	RRS 100%	0.577	4.42	74.3	0.735	6.04	59.6

Table S-12: A2d-3D-RD-a model peak building story drift, nonlinear linear time history analysis

Load Case	Ground Motion	LONG				SHORT			
		$\Delta u_1/h$ (%)	t_* (s)	$\Delta u_2/h$ (%)	t_* (s)	$\Delta v_1/h$ (%)	t_* (s)	$\Delta v_2/h$ (%)	t_* (s)
EQ_3D_3 axis_1	CNP 16%	-0.025	4.17	-0.012	4.17	-0.047	6.57	-0.022	6.56
EQ_3D_3 axis_2	CNP 44%	0.068	8.64	0.034	8.63	0.211	9.91	0.091	9.92
EQ_3D_1 axis_1	CNP 100%	0.328	8.66	0.143	8.65	-0.037	8.69	0.029	8.32
EQ_3D_1 axis_2	CNP 100%	-0.036	9.98	-0.024	9.96	0.493	9.96	0.301	9.95
EQ_3D_2 axis_1	CNP 100%	0.329	8.67	0.136	8.65	0.507	9.96	0.300	9.96
EQ_3D_3 axis_3	CNP 100%	0.329	8.67	0.136	8.65	0.507	9.96	0.300	9.96
EQ_3D_3 axis_4	RRS 16%	0.040	2.54	-0.019	3.05	-0.083	7.30	-0.033	7.31
EQ_3D_3 axis_5	RRS 44%	0.183	2.58	0.065	7.05	0.331	3.35	0.164	5.97
EQ_3D_3 axis_6	RRS 100%	0.840	4.42	-0.340	4.58	0.988	6.04	0.519	6.02

Table S-13: A2d-3D-RD-a model peak building base shear, nonlinear time history analysis

		LONG		SHORT		RESULTANT	
Load Case	**Ground Motion**	**Peak V_{bu} (kip)**	**t @ peak V_{bu} (s)**	**Peak V_{bv} (kip)**	**t @ peak V_{bv} (s)**	**Peak V_b (kip)**	**t @ peak V_b (s)**
EQ_3D_3axis_1	CNP 16%	9.8	4.17	9.5	6.57	10.6	4.17
EQ_3D_3axis_2	CNP 44%	21.7	8.64	25.5	9.91	28.8	9.91
EQ_3D_1axis_1	CNP 100%	55.7	8.66	5.2	8.69	55.9	8.66
EQ_3D_1axis_2	CNP 100%	5.8	9.87	40.7	9.96	40.8	9.96
EQ_3D_2axis_1	CNP 100%	55.0	8.66	43.2	9.94	55.4	8.66
EQ_3D_3axis_3	CNP 100%	55.0	8.66	43.2	9.94	55.4	8.66
EQ_3D_3axis_4	RRS 16%	14.7	2.54	14.0	7.30	16.4	2.53
EQ_3D_3axis_5	RRS 44%	36.5	2.58	33.1	3.35	38.4	2.57
EQ_3D_3axis_6	RRS 100%	86.8	4.42	61.9	6.04	91.9	4.42

Table S-14: A2d-3D-RD-a model peak wall line story drift, nonlinear time history analysis

LONG		SOUTH				NORTH			
Load Case	**Ground Motion**	**$\Delta u_1/h$ (%)**	**t_* (s)**	**$\Delta u_2/h$ (%)**	**t_* (s)**	**$\Delta u_1/h$ (%)**	**t_* (s)**	**$\Delta u_2/h$ (%)**	**t_* (s)**
EQ_3D_3axis_1	CNP 16%	0.032	4.18	0.016	4.18	0.021	4.17	0.011	4.24
EQ_3D_3axis_2	CNP 44%	0.072	9.61	0.034	8.64	0.066	8.64	0.033	8.63
EQ_3D_1axis_1	CNP 100%	0.339	8.66	0.150	8.65	0.318	8.66	0.136	8.65
EQ_3D_1axis_2	CNP 100%	0.088	9.98	0.049	9.96	0.018	9.79	0.014	8.24
EQ_3D_2axis_1	CNP 100%	0.356	8.69	0.156	8.66	0.319	8.66	0.121	8.65
EQ_3D_3axis_3	CNP 100%	0.356	8.69	0.156	8.66	0.319	8.66	0.121	8.65
EQ_3D_3axis_4	RRS 16%	0.052	4.29	0.026	4.19	0.033	2.54	0.017	2.53
EQ_3D_3axis_5	RRS 44%	0.230	2.58	0.084	4.38	0.180	4.33	0.068	4.33
EQ_3D_3axis_6	RRS 100%	0.944	4.42	0.379	4.42	0.737	4.42	0.323	4.58
SHORT		**EAST**				**WEST**			
Load Case	**Ground Motion**	**$\Delta v_1/h$ (%)**	**t_* (s)**	**$\Delta v_2/h$ (%)**	**t_* (s)**	**$\Delta v_1/h$ (%)**	**t_* (s)**	**$\Delta v_2/h$ (%)**	**t_* (s)**
EQ_3D_3axis_1	CNP 16%	0.040	6.56	0.022	6.56	0.060	6.78	0.028	7.09
EQ_3D_3axis_2	CNP 44%	0.174	9.91	0.069	9.92	0.248	9.91	0.114	9.93
EQ_3D_1axis_1	CNP 100%	0.082	4.54	0.046	8.29	0.063	7.02	0.047	8.18
EQ_3D_1axis_2	CNP 100%	0.414	9.95	0.259	9.94	0.589	9.97	0.351	9.95
EQ_3D_2axis_1	CNP 100%	0.461	9.95	0.258	9.95	0.568	9.97	0.344	9.96
EQ_3D_3axis_3	CNP 100%	0.461	9.95	0.258	9.95	0.568	9.97	0.344	9.96
EQ_3D_3axis_4	RRS 16%	0.071	7.30	0.033	7.30	0.113	4.30	0.048	4.30
EQ_3D_3axis_5	RRS 44%	0.233	3.15	0.126	5.96	0.524	4.40	0.224	4.57
EQ_3D_3axis_6	RRS 100%	0.776	6.04	0.466	6.01	1.199	6.04	0.576	6.03

Table S-15: A2d-3D-RD-a model peak wall line base shear, nonlinear time history analysis

LONG		SOUTH		NORTH		% of Peak V_{bu}	
Load Case	**Ground Motion**	**Peak V_{bu} (kips)**	**t @ peak V_{bu} (s)**	**Peak V_{bu} (kips)**	**t @ peak V_{bu} (s)**	**South**	**North**
EQ_3D_3axis_1	CNP 16%	3.7	4.18	5.3	4.17	33.9	54.4
EQ_3D_3axis_2	CNP 44%	6.9	9.61	12.8	8.64	30.3	59.1
EQ_3D_1axis_1	CNP 100%	19.1	8.66	30.8	8.66	34.2	55.2
EQ_3D_1axis_2	CNP 100%	7.1	9.98	4.3	9.79	76.2	17.5
EQ_3D_2axis_1	CNP 100%	19.7	8.69	30.7	8.66	34.3	55.2
EQ_3D_3axis_3	CNP 100%	19.7	8.69	30.7	8.66	34.3	55.2
EQ_3D_3axis_4	RRS 16%	5.4	4.29	8.1	2.54	32.8	55.2
EQ_3D_3axis_5	RRS 44%	14.8	2.58	21.4	4.33	40.6	49.7
EQ_3D_3axis_6	RRS 100%	33.0	4.42	43.7	4.42	38.1	50.4
SHORT		**EAST**		**WEST**		**% of Peak V_{bv}**	
Load Case	**Ground Motion**	**Peak V_{bv} (kips)**	**t @ peak V_{bv} (s)**	**Peak V_{bv} (kips)**	**t @ peak V_{bv} (s)**	**East**	**West**
EQ_3D_3axis_1	CNP 16%	3.9	6.56	5.1	6.78	38.9	49.6
EQ_3D_3axis_2	CNP 44%	10.4	9.91	12.1	9.91	40.8	47.6
EQ_3D_1axis_1	CNP 100%	7.2	4.54	5.1	8.52	34.4	52.0
EQ_3D_1axis_2	CNP 100%	17.2	9.95	20.7	9.97	41.7	50.0
EQ_3D_2axis_1	CNP 100%	18.8	9.94	20.3	9.97	43.5	43.5
EQ_3D_3axis_3	CNP 100%	18.8	9.94	20.3	9.97	43.5	43.5
EQ_3D_3axis_4	RRS 16%	6.2	7.30	7.5	4.30	44.6	43.6
EQ_3D_3axis_5	RRS 44%	12.1	3.15	19.1	4.40	36.0	52.6
EQ_3D_3axis_6	RRS 100%	24.3	6.04	29.3	6.04	39.2	47.3

Table S-16: A2d-3D-RD-a model wall line base shear breakdown, nonlinear time history analysis

LONG		SOUTH			NORTH		
Load Case	**Ground Motion**	**Peak V_{bu} (kips)**	**SW V_{bu} (%)**	**GW V_{bu} (%)**	**Peak V_{bu} (kips)**	**SW V_{bu} (%)**	**GW V_{bu} (%)**
EQ_3D_3axis_1	CNP 16%	3.7	39.2	60.8	5.3	57.5	42.5
EQ_3D_3axis_2	CNP 44%	6.9	39.2	60.8	12.8	60.6	39.4
EQ_3D_1axis_1	CNP 100%	19.1	42.3	57.7	30.8	55.4	44.6
EQ_3D_1axis_2	CNP 100%	7.1	48.4	51.6	4.3	56.8	43.2
EQ_3D_2axis_1	CNP 100%	19.7	41.4	58.6	30.7	55.6	44.4
EQ_3D_3axis_3	CNP 100%	19.7	41.4	58.6	30.7	55.6	44.4
EQ_3D_3axis_4	RRS 16%	5.4	38.8	61.2	8.1	60.1	39.9
EQ_3D_3axis_5	RRS 44%	14.8	42.6	57.4	21.4	57.5	42.5
EQ_3D_3axis_6	RRS 100%	33.0	41.0	59.0	43.7	54.0	46.0
SHORT		**EAST**			**WEST**		
Load Case	**Ground Motion**	**Peak V_{bv} (kips)**	**SW V_{bv} (%)**	**GW V_{bu} (%)**	**Peak V_{bv} (kips)**	**SW V_{bv} (%)**	**GW V_{bv} (%)**
EQ_3D_3axis_1	CNP 16%	3.9	69.5	30.5	5.1	82.1	17.9
EQ_3D_3axis_2	CNP 44%	10.4	76.2	23.8	12.1	82.7	17.3
EQ_3D_1axis_1	CNP 100%	7.2	77.4	22.6	5.1	81.3	18.7
EQ_3D_1axis_2	CNP 100%	17.2	73.2	26.8	20.7	81.3	18.7
EQ_3D_2axis_1	CNP 100%	18.8	72.9	27.1	20.3	81.2	18.8
EQ_3D_3axis_3	CNP 100%	18.8	72.9	27.1	20.3	81.2	18.8
EQ_3D_3axis_4	RRS 16%	6.2	72.9	27.1	7.5	83.6	16.4
EQ_3D_3axis_5	RRS 44%	12.1	73.9	26.1	19.1	81.2	18.8
EQ_3D_3axis_6	RRS 100%	24.3	74.1	25.9	29.3	83.2	16.8

Table S-17: A2d-3D-RD-a model peak hold down tensile force at certain locations, nonlinear time history analysis

		L1S1, LC5		L1S1, LC6		L1W1, LC7		L1W1, LC8	
Load Case	**Ground Motion**	**Peak F (kips)**	**t @ peak F (s)**	**Peak F (kips)**	**t @ peak F (s)**	**Peak F (kips)**	**t @ peak F (s)**	**Peak F (kips)**	**t @ peak F (s)**
EQ_3D_3axis_1	CNP 16%	-0.44	4.18	-0.09	7.09	-0.06	7.09	-0.50	6.78
EQ_3D_3axis_2	CNP 44%	-0.90	9.61	-0.36	9.91	-0.23	9.91	-0.88	9.76
EQ_3D_1axis_1	CNP 100%	-1.92	11.87	-0.22	6.98	-0.34	6.98	-0.69	8.65
EQ_3D_1axis_2	CNP 100%	-1.91	8.81	-0.70	9.95	-0.34	5.17	-1.08	8.42
EQ_3D_2axis_1	CNP 100%	-1.87	12.95	-1.20	9.96	-0.96	9.95	-1.08	8.42
EQ_3D_3axis_3	CNP 100%	-1.87	12.95	-1.20	9.96	-0.96	9.95	-1.08	8.42
EQ_3D_3axis_4	RRS 16%	-0.66	4.18	-0.11	7.19	-0.08	7.19	-0.71	4.30
EQ_3D_3axis_5	RRS 44%	-1.84	4.54	-0.47	4.57	-0.29	4.58	-1.18	4.39
EQ_3D_3axis_6	RRS 100%	-2.79	6.16	-2.36	6.16	-2.15	7.14	-2.24	4.42

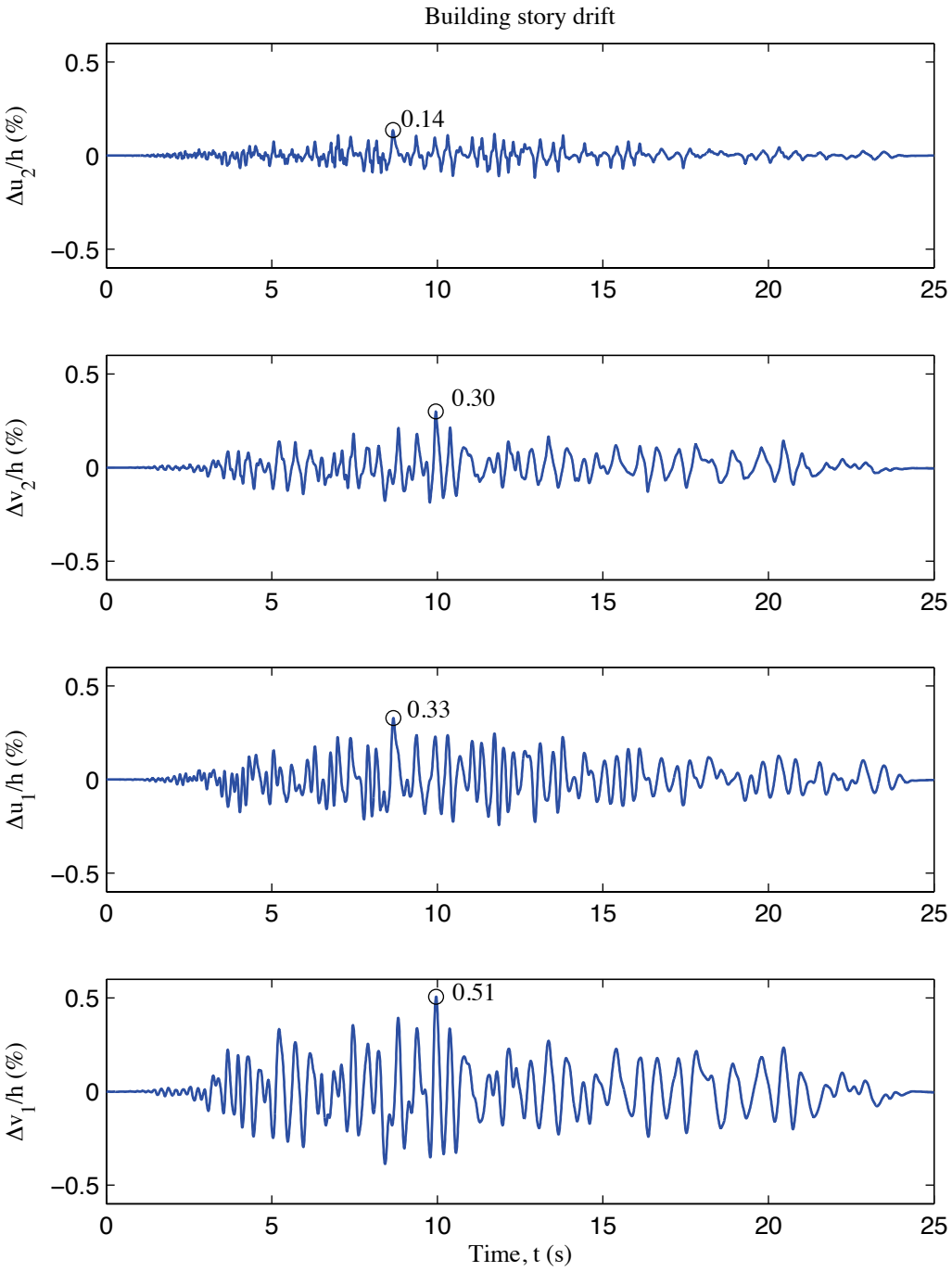

Figure S-6: A2d-3D-RD-a model building story drift, 100 % Canoga Park, 3D nonlinear analysis

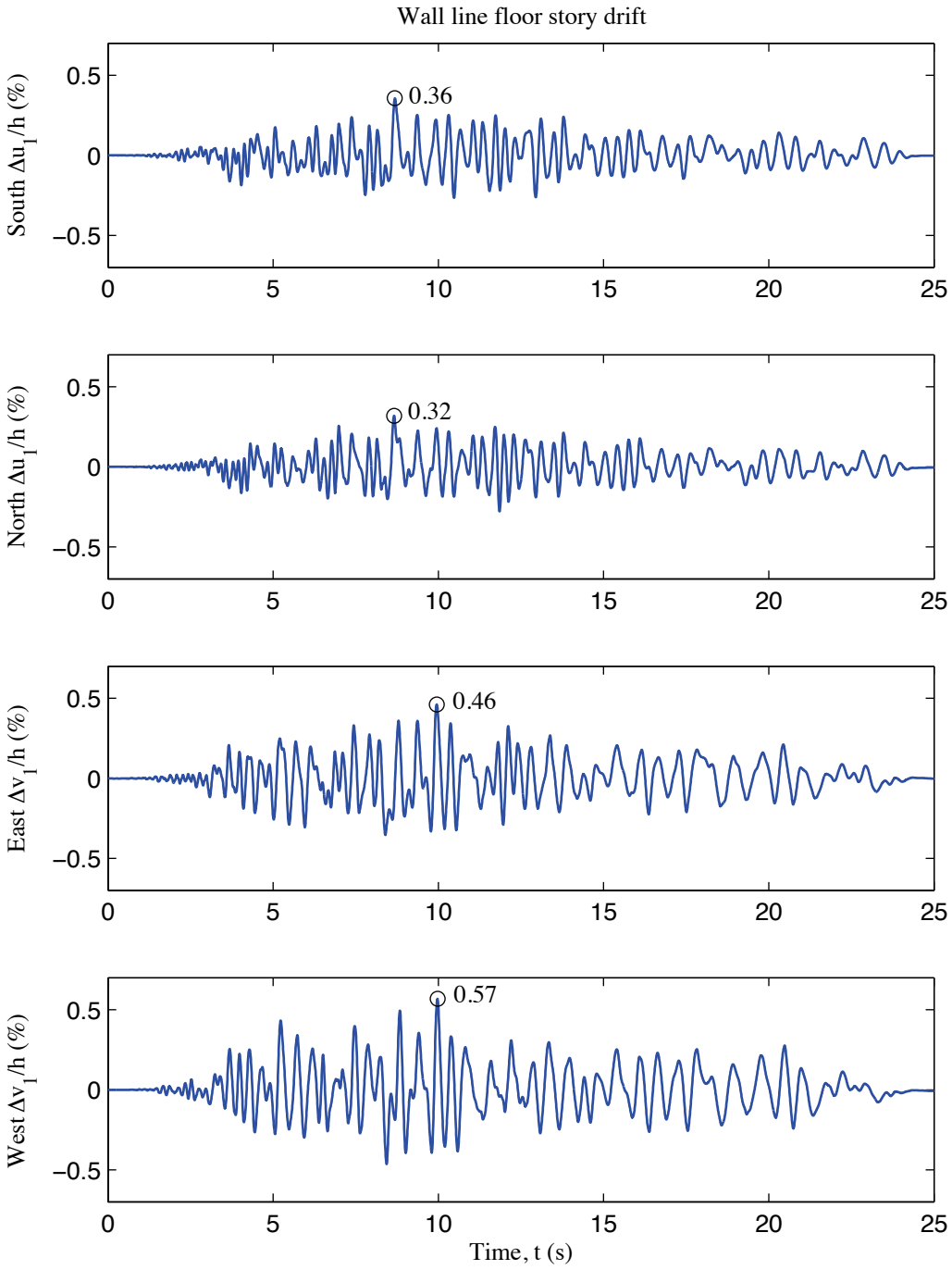

Figure S-7: A2d-3D-RD-a model wall line floor story drift, 100 % Canoga Park, 3D nonlinear analysis

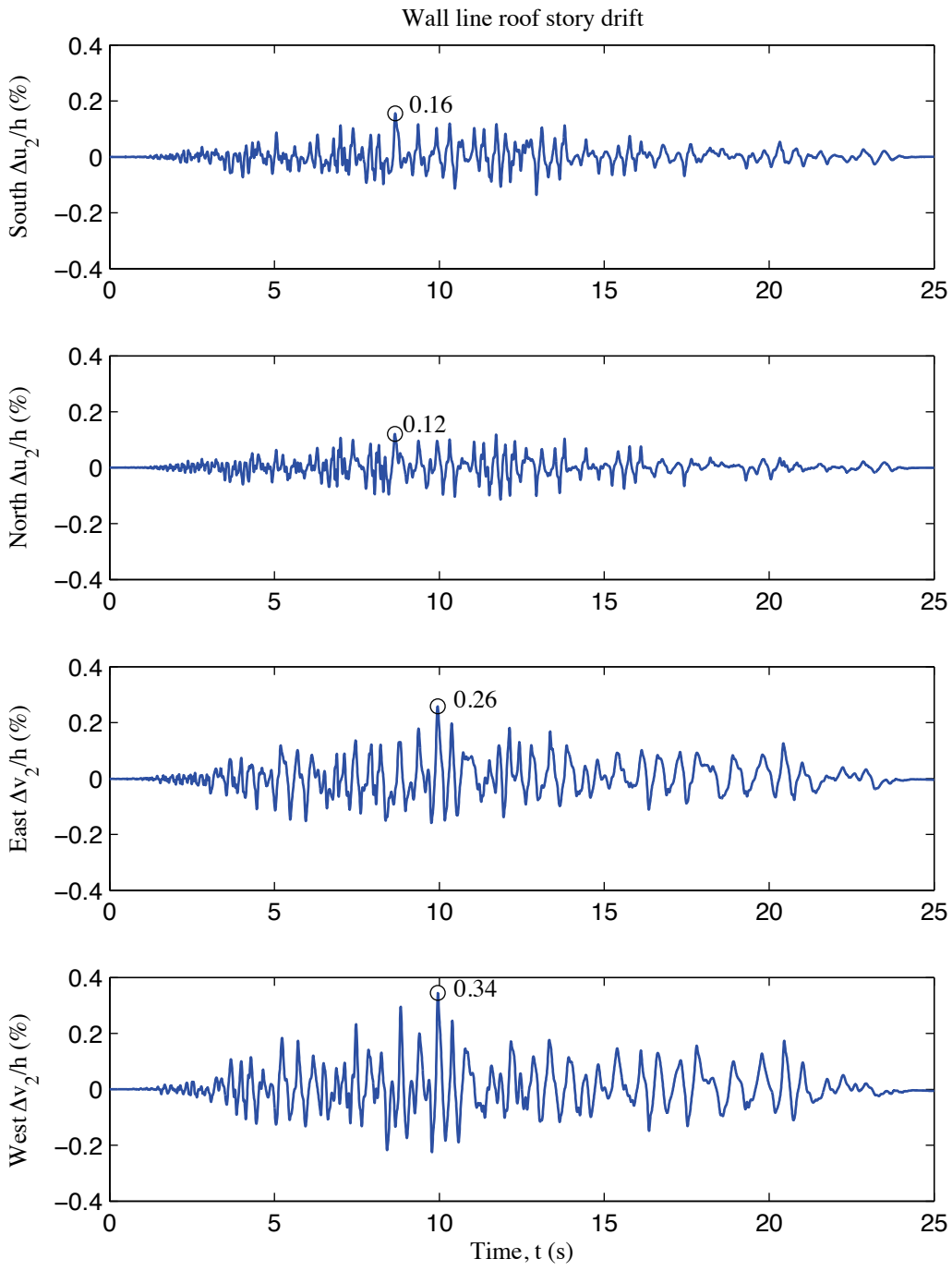

Figure S-8: A2d-3D-RD-a model wall line roof story drift, 100 % Canoga Park, 3D nonlinear analysis

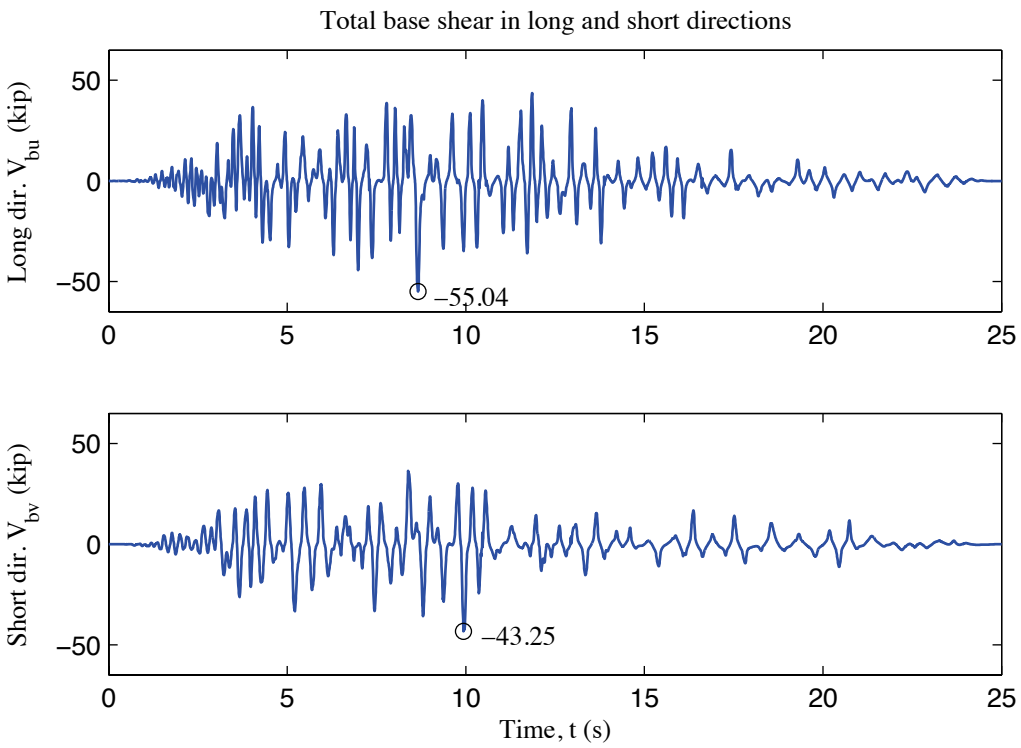

Figure S-9: A2d-3D-RD-a model total building base shear, 100 % Canoga Park, 3D nonlinear analysis

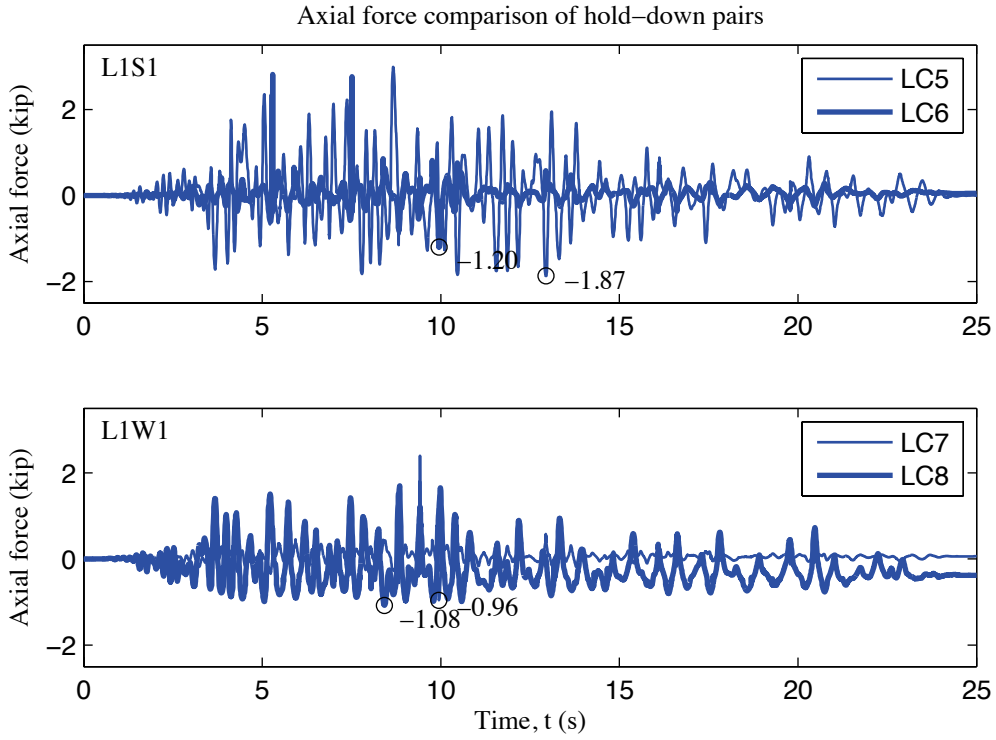

Figure S-10: A2d-3D-RD-a model, load cell 5 to 8 axial forces, 100 % Canoga Park, 3D nonlinear analysis

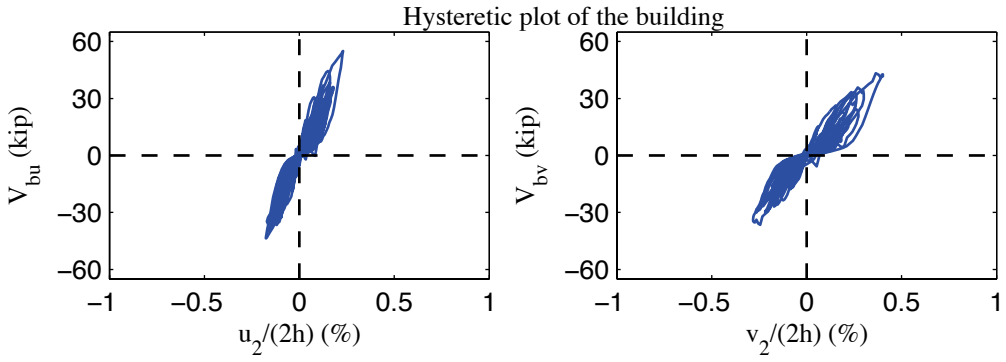

Figure S-11: A2d-3D-RD-a model, hysteretic plot of the building, 100 % Canoga Park, 3D nonlinear analysis

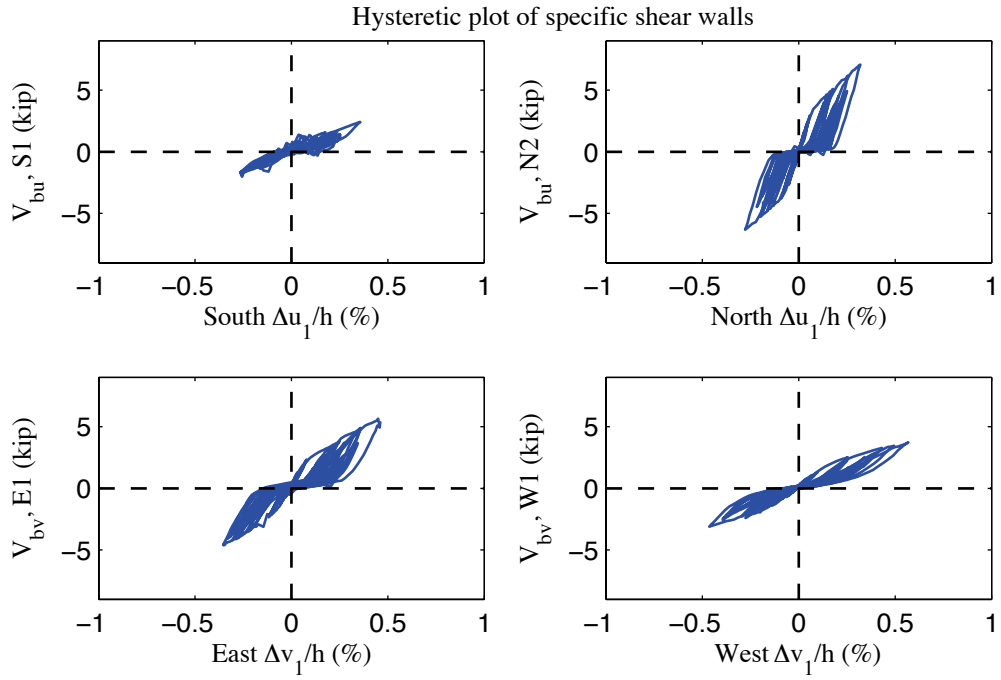

Figure S-12: A2d-3D-RD-a model, hysteretic plot of shear walls at each elevation, 100 % Canoga Park, 3D nonlinear analysis

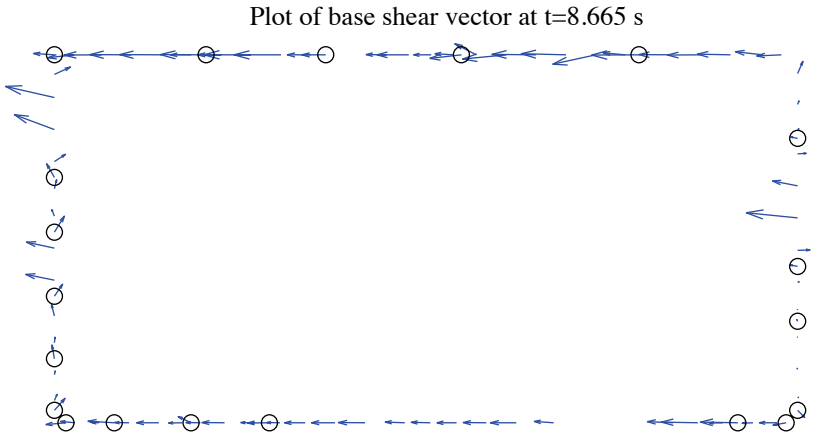

Figure S-13: A2d-3D-RD-a model, field plot of peak total base shear, 100 % Canoga Park, 3D nonlinear analysis (maximum anchor/hold down base shear is 1.71 kips)

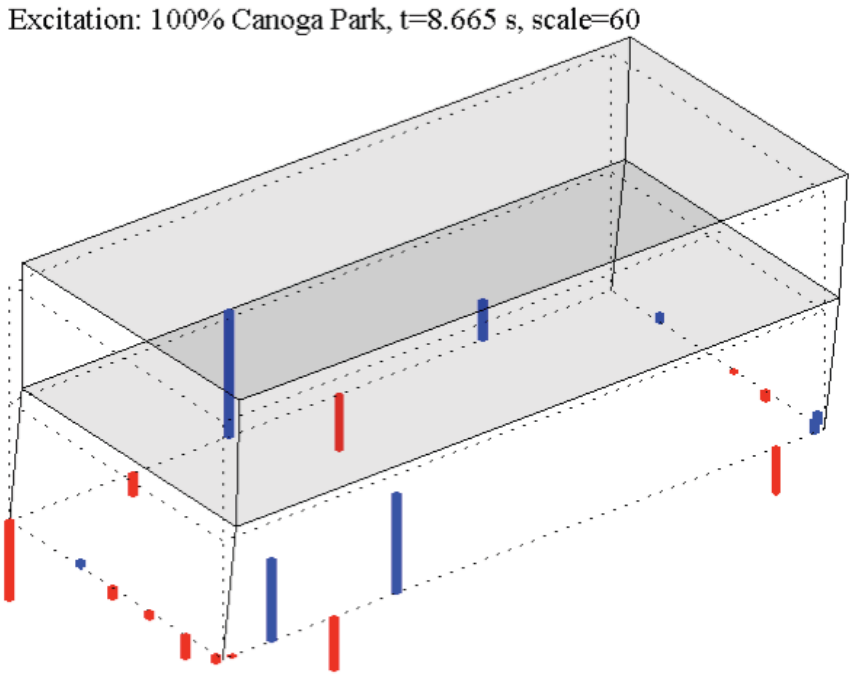

Figure S-14: A2d-3D-RD-a model, simplified illustration of corner displacements with hold down forces from load cells, 100 % Canoga Park, 3D nonlinear analysis (max hold down tensile force is -2.90 kips)

Appendix T: Details on Incremental Dynamic Analysis and Performance Evaluation of A1-3D-SD-a model

T.1 Incremental dynamic analysis results of A1-3D-SD-a model

The high-fidelity 3D, semi-rigid diaphragm model (A1-3D-SD-a) of the CFS-NEES building at construction Phase 1 with assumed structural components only is adopted for IDA. This structural-only model has all essential details of the tested building and its response provides a reasonable match with test data (see Chapter 3 for model description and Chapter 4 for model vs. test comparison). Twenty-two far-field ground motion record pairs in the set of FEMA P695 (Applied Technology Council 2009) are applied to excite the structural model. As suggested by FEMA P695, each record pair is applied twice to each model, once with the ground motion records oriented along one principal direction, and then again with the records rotated 90 degrees. Through the process of ground motion record scaling, individual records in each set are firstly "normalized" by their respective peak ground velocities (see Appendix A of FEMA P695 for details and normalization factors). This step is intended to remove unwarranted variability between records due to inherent differences in event magnitude, distance to source, source type and site conditions, without eliminating overall record-to-record variability (Applied Technology Council 2009).

In IDA of the A1-3D-SD-a model, about 1000 nonlinear 2-axis time history analyses have been performed. The peak story drift among floor and roof level is chosen as the damage measure and the spectral acceleration of the first natural period of the structure (S_a) is the intensity measure. These choices of DM and IM are popular options, as

suggested by pioneering researchers (Vamvatsikos and Cornell 2002). As further discussed by Baker and Cornell (Baker and Cornell 2006), for consistency with conventions in seismology, the S_a of the two axis excitation is defined as the geometrical average of the two S_a under excitation in x and y direction separately. Note that the S_a value does not change when the two earthquakes switch directions. The procedure of IDA has also been applied to A2b-3D-SD-a model corresponds to Phase 2b building with OSB sheathing of gravity walls and simplified P-3D-RD-b model.

Figure T-1 provides IDA analysis results in terms of peak story drift vs. first mode spectral acceleration. Record-to-record uncertainty is observed: some normalized ground motion records are scaled up to 5 times to ensure the peak drift is large enough to trigger failure in the building. The failure, or collapse, is detected by checking the peak story drift vs. a prescribed drift-limit. Sometimes, dynamic instability takes place, which implies the drift is so large and becomes unbounded at a certain excitation level, as shown by flat horizontal lines that extend (to infinity) in Figure T-1.

The determination of drift-limit for collapse plays a crucial role in the performance evaluation. Only after that limit is defined, can the post-processing proceed by checking S_a level for each ground motion at which structure fails. For wood structures, which boast similar seismic behavior to CFS structures, (Christovasilis et al. 2014) propose a drift-limit for collapse of 7%. Special steel moment frames may use drifts as high as 9-10% (Applied Technology Council 2009). For comparison the building's maximum allowable story drift using Table 12.12-1 in ASCE 7-10 (American Society of Civil Engineers

2010), i.e. the design drift, is 2.5%. As reported in Peterman's dissertation (Peterman 2014), the maximum drift experienced over all tests performed was 1.2% for the story and 1.4% for an individual wall line, occurring in the Phase 1 design basis earthquake ground motion. However, the archetype building never failed in shaking table tests and it went back to the upright configuration after the shake. Testing to collapse would be necessary to experimentally estimate the permissible seismic story drift. However, the force levels required and concerns about the large specimens damaging the lab precludes higher levels of testing. Shear wall tests utilizing the same details as the CFS-NEES shear walls took up to 4% before collapse and the drift at peak capacity was typically around 2% (Liu et al. 2012).

Since the backbone curve of the Pinching4 material used for the diagonal truss elements modeling the shear walls are characterized using isolated shear wall test results from Liu et al. (Liu et al. 2012), the building's peak capacity determined from pushover analysis (Figure T-2) typically coincides with ~2% story drift. However, even though the Pinching4 backbone curve of the shear wall elements has a post-peak drop of capacity close to 40%, the pushover curve of the building which allows for re-distribution drops little after the peak due to the interaction of other components with shear walls. Pushover analysis shows that the ductility of the A1-3D-SD-a model of even the structural-only Phase 1 building is not small, so the proposed drift limit for collapse is set as 4% (marked by the vertical dash line in Figure T-1) to avoid being too conservative.

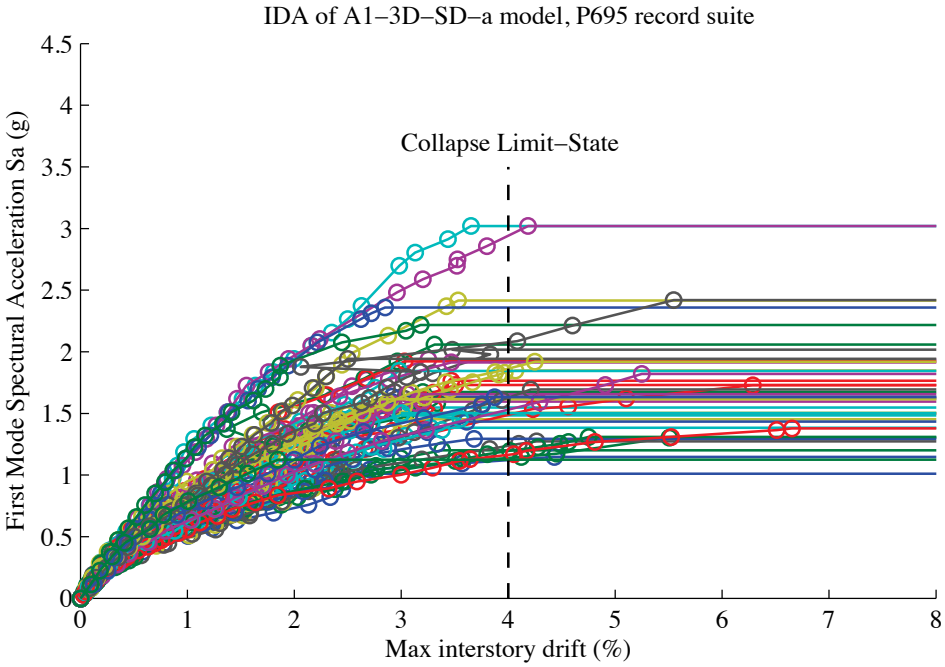

Figure T-1: IDA result of A1-3D-SD-a model

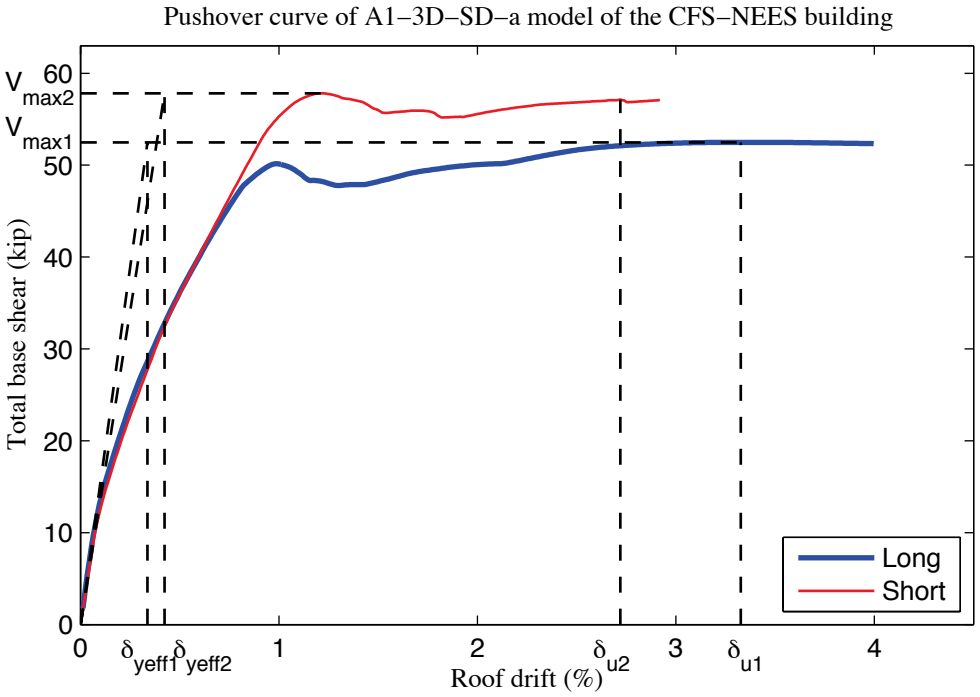

Figure T-2: Pushover curve of A1-3D-SD-a model

T.2 Post-processing of nonlinear analysis results

(a) Post-processing of pushover analysis results

Post-processing of the pushover analysis precedes IDA in that lateral capacity of the archetype building, archetype overstrength Ω, and period-based ductility μ_T should be determined first from pushover analysis. Archetype overstrength Ω is directly related to the evaluation of the system of overstrength factor Ω_O as discussed later in the section. Period-based ductility μ_T is used later in the quantification of uncertainties in accepted collapse margin ratios for evaluation of the response modification factor R.

As described in FEMA P695 (Applied Technology Council 2009), the overstrength factor for a given index archetype model, Ω, is defined as the ratio of the maximum base shear resistance, V_{max}, to the design base shear, V:

$$\Omega = V_{\max}/V \tag{T-1}$$

The period-based ductility for a given index archetype model, μ_T, is defined as the ratio of ultimate roof drift displacement, δ_u, (defined as shown in Figure T-2) to the effective yield roof drift displacement $\delta_{y,eff}$:

$$\mu_T = \delta_u/\delta_{y,eff} \tag{T-2}$$

In order to quantify δ_u, FEMA P695 mentioned that the lateral loads should be applied monotonically until a loss of 20% of the base shear capacity ($0.8V_{max}$) is achieved and is

the deflection at that post-peak base shear level. Furthermore, it provides a formula to calculate $\delta_{y,eff}$ rather than selecting it graphically from the pushover curve:

$$\delta_{y,eff} = C_0 \frac{V_{\max}}{W}\left[\frac{g}{4\pi^2}\right]\left(\max\left(T, T_1\right)\right)^2 \tag{T-3}$$

where C_0 relates the fundamental-mode (SDOF) displacement to roof displacement, V_{max}/W is the maximum base shear normalized by the building weight, g is the gravity constant, T is the fundamental period ($C_u T_a$, defined by Eqn. (5-5) in FEMA P695)

$$T = C_u T_a = C_u T_t h_n^x \geq 0.25 \text{seconds} \tag{T-4}$$

where h_n is the building height, the values of the coefficient, C_u, are given in Table 12.8-1 of ASCE/SEI 7-05 (American Society of Civil Engineers 2005), and values of period parameters C_t and x are given in Table 12.8-2 of ASCE/SEI 7-05.

As described in Eqn. C3-4 of ASCE/SEI 41-06 (ASCE/SEI Seismic Rehabilitation Standards Committee 2007), the coefficient C_0 in Eqn. (T-3) is given by

$$C_0 = \phi_{1,r} \frac{\sum_1^N m_x \phi_{1,x}}{\sum_1^N m_x \phi_{1,x}^2} \tag{T-5}$$

where m_x is the mass at level x; and $\phi_{1,x}$ ($\phi_{1,r}$) is the ordinate of the fundamental model at level x (roof), and N is the number of levels.

For three-dimensional analysis, FEMA P695 provides a special note at the end of its Section 6.3 (Applied Technology Council 2009), saying that "separate nonlinear static analyses should be performed to evaluate overstrength and ultimate roof drift displacement independently along the two principle axes of the index archetype model" and "resulting values for overstrength and ultimate roof drift displacement are then calculated by averaging the values from each of the principle loading directions."

Referring to our case study of the A1-3D-SD-a model, the definition of V_{max}, V, *and* δ_u, and $\delta_{y,eff}$ are illustrated in Figure T-2. In that figure, the pushover curves go flat eventually and never drop below $0.8V_{max}$ after reaching peak capacity. Therefore, the ultimate displacement δ_u is taken at the initiation point where the pushover curve flattens; an alternative would be to use 4%. However, δ_u determined in Figure T-2 correspond to roof drift less than 4% (full height of the building is 18 ft (5.49 m)) and are thus more conservative estimations. Other than this assumption, the calculation went strictly following the aforementioned procedure and results are tabulated in Table T-1.

Other numbers used in calculations, include the building's total weight W=77575 lb, story seismic weight w_1=41817 lb, w_2=29474 lb and design base shear $V=C_S W$=0.143×77585=11061 lb as can be found in the design narrative (Madsen et al. 2011). Also according to (Madsen et al. 2011), S_{D1}=0.5, so C_u=1.4 (Table 12.8-1 of ASCE/SEI 7-05) and T_a=0.175 s. Then $T=C_u T_a$=0.245 s, so T=0.25 s.

Table T-1: Summary of calculation of overstrength and period-based ductility, A1-3D-SD-a model

	Overstrength calculation		
	LONG	**SHORT**	**MEAN**
V_{max} (kips)	52.49	57.83	-
Ω	4.74	5.23	4.99
	Period-based ductility calculation		
	LONG	**SHORT**	**MEAN**
$\phi_{1,1}$ (in.)	0.192	0.483	-
$\phi_{1,2}$ ($\phi_{1,r}$) (in.)	0.284	0.852	-
C_0	1.188	1.239	-
V_{max}/W	0.68	0.75	-
δ_u (in.)	7.19	5.87	
$\delta_{y,eff}^*$ (in.)	0.81	0.93	-
μ_T	8.87	6.31	7.59

*: $\delta_{y,eff}$ from pushover curves are 0.73 in. and 0.92 in.

(b) Post-processing of IDA results

With the specified collapse drift limit (4% herein), the collapse data from IDA results are utilized first to determine a set of S_a values associated with the onset of collapse for each ground motion, as illustrated in Figure T-3 with discrete dots (also referred to as an empirical cumulative distribution function). The probability of collapse at a given S_a level, x, can then be estimated as the fraction of records for which collapse occurs at a level lower than x (Baker 2015). Furthermore, a cumulative distribution function (CDF) is generated by fitting a lognormal distribution through the collapse data points of the empirical cumulative distribution function (solid curves in Figure T-3).

Once the CDF is determined, the median collapse capacity ($\hat{S}_{CT}$ in Figure T-3) corresponding to 50% probability of collapse is determined. The collapse margin ratio, *CMR*, as the primary parameter in the characterization of the collapse performance evaluation is given by

$$CMR = \frac{\hat{S}_{CT}}{S_{MT}} \tag{T-6}$$

Where the MCE intensity is obtained from the response spectrum of MCE ground motions at the fundamental period, T (Applied Technology Council 2009).

According to Section 6.4.5 of FEMA P695 (Applied Technology Council 2009), "because ground motions records are applied in pairs in three-dimensional nonlinear dynamic analyses, collapse behavior of each index archetype model resulting from each ground motion component is coupled." Background studies have shown that the median collapse intensity resulting from three-dimensional analyses is on average about 20% less than the median collapse intensity resulting from two-dimensional analyses. To achieve parity with the two-dimensional analyses, the *CMR* calculated based on median collapse intensity, $\hat{S}_{CT}$, obtained from three-dimensional analyses should be multiplied by a factor of 1.2.

The fitting of lognormal CDF to the empirical CDF of the IDA collapse results is equivalent to the estimation of two parameters of the lognormal distribution:

$$P\left(C \mid IM = x\right) = \Phi\left(\frac{\ln x - \mu}{\sigma}\right) \tag{T-7}$$

where $P(C \mid IM = x)$ is the probability that a ground motion with $IM = x$ will cause the structure to collapse, $\Phi(\ )$ is the standard normal cumulative distribution function (CDF), $\exp(\mu)$ is the median of the fragility function (the *IM* level with 50% probability of

collapse) and σ is the standard deviation of ln*IM* (sometimes referred to as the dispersion of *IM*) (Baker 2015).

Various methods have been proposed for this parameter estimation problem. For example, the method derived by Baker (Baker 2015) is a maximum-likelihood estimation and it is more efficient when fewer nonlinear history analyses are performed. In this research, the more classical method of moments estimator developed by Ibarra and Krawinkler (Ibarra and Krawinkler 2005) is adopted. The estimation of μ and σ are given below

$$\hat{\mu} = \frac{1}{n}\sum_{i=1}^{n} \ln IM_i \tag{T-8}$$

$$\hat{\sigma} = \sqrt{\frac{1}{n-1}\sum_{i=1}^{n} \left(\ln IM_i - \hat{\mu}\right)^2} \tag{T-9}$$

where *n* is the number of ground motions considered, and *IMi* is the *IM* value associated with onset of collapse of the *i*th ground motion.

If the collapse drift limit is taken as 4%, the estimated μ and σ using points on the empirical cumulative distribution function are 0.478 and 0.226. The fitted analytical fragility curve is plotted in Figure T-3(a). The median collapse capacity ($\hat{S}_{CT} = 1.61g$ in the figure) corresponds to 50% probability of collapse.

The design narrative (Madsen et al. 2011) says the MCE spectral response acceleration for short periods S_{MS}=1.39 g for the CFS-NEES building. As per Table 6-1 of FEMA P695 (Applied Technology Council 2009) the transition period T_S is 0.6 s for the archetype building with site class D. Then Eqn. (6-2) of FEMA P695 determines that for short-period archetypes ($T \leq T_S$), $S_{MT}=S_{MS}$. So S_{MT} is also 1.39 g for our archetype. Taking the modification of 3D analysis into account, the *CMR* of Phase 1 archetype building represented by A1-3D-SD-a model is

$$CMR = 1.2 \times \frac{1.61}{1.39} = 1.39$$

In comparison with the fragility curve based on 4% collapse drift limit, the procedure is repeated for the case of 2% collapse drift limit and the resulted fragility curve is illustrated in Figure T-3(b). However, the median collapse capacity is smaller than S_{MT} indicating *CMR* is less than 1 for that case. This is a conservative prediction of the building's robustness under seismic load, but illustrates the sensitivity of the drift limit selection.

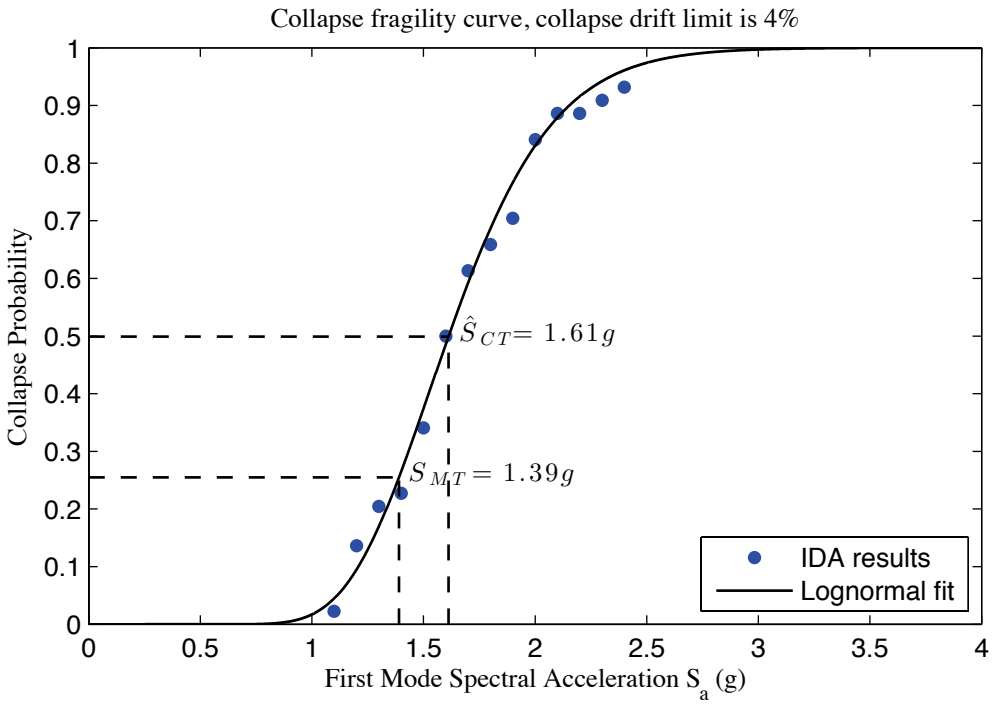

(a) Collapse fragility curve, proposed collapse drift limits for a 4% drift limit

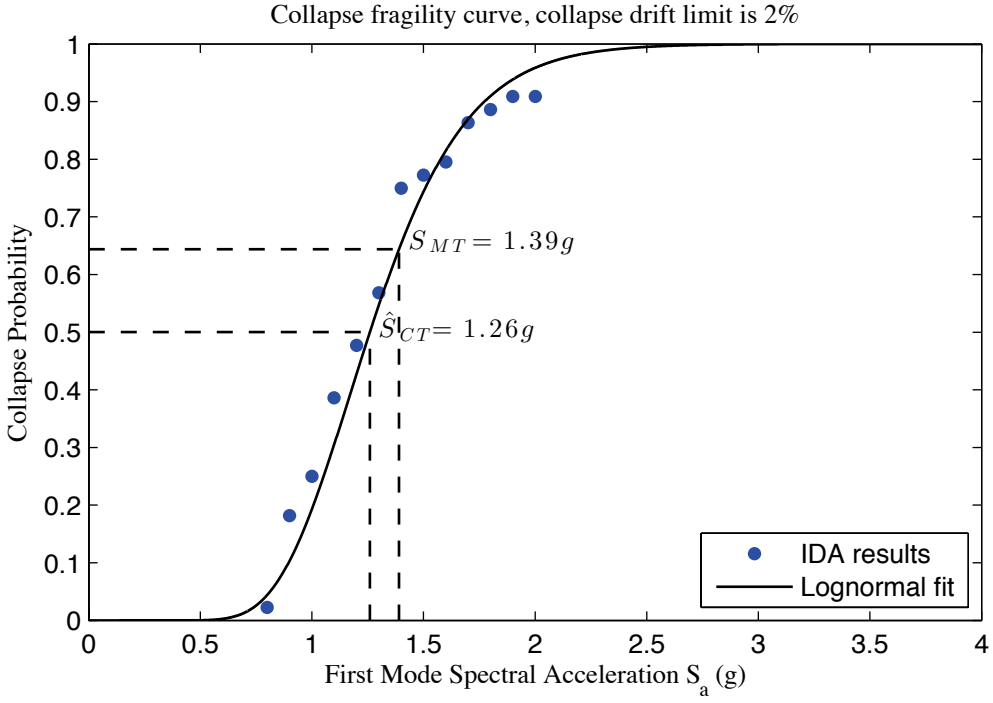

(b) Collapse fragility curve, proposed collapse drift limits for a 2% drift limit

Figure T-3: Collapse fragility curve with two proposed collapse drift limits

T.3 Performance evaluation of the archetype building using FEMA P695 Procedure

The complete performance evaluation is elaborated in Chapter 7 of FEMA P695 (Applied Technology Council 2009). The process utilizes results from pushover analyses to determine an appropriate value of the system overstrength factor, Ω_O, and results from nonlinear static and time history analyses to evaluate the acceptability of a trial value of the response modification coefficient, R. The deflection amplification factor, C_d, is derived from an acceptable value of R, with consideration of the effective damping of the system of interest.

The trial value of the response modification coefficient, R, used to design index archetypes (R=6.5 in our design), is evaluated in terms of the acceptability of the collapse margin ratio. The evaluation is fulfilled by comparing the adjusted collapse margin ratio (*ACMR*) to the accepted collapse margin ratio. *ACMR* is the collapse margin ratio after adjustment for the effects of spectral shape, while accepted collapse margin ratio is dependent on the quality of the information used to define the system, total system uncertainty, and established limits on collapse probability.

Post-processing of pushover analysis results is presented in Section 6.3.1. Period-based ductility, μ_T from pushover analysis is used in the calculation of the adjusted collapse margin ratio for each archetype using the spectral shape factor, *SSF*, which is also dependent on the fundamental period, T. For each index archetype i, *ACMR* is given by

$$ACMR_i = SSF_i \times CMR_i \tag{T-10}$$

Currently in this research, only one archetype model A1-3D-SD-a is studied, so i is one.

As discussed in Section 7.2.1 of FEMA P695 (Applied Technology Council 2009), rare ground motions in the Western United States have a distinctive spectral shape that is peaked at the period of interest, and drops off more rapidly (and has less energy) at periods that are longer or shorter than the period of interest. Spectral shape of this type may cause rare records to be less damaging than would otherwise be expected based on the shape of the standard design spectrum. To remove this conservative bias, simplified spectral shape factors, *SSF*, which depend on fundamental period and period-based ductility, are used to adjust the collapse margin ratios. Table 7-1a and Table 7-1b in of FEMA P695 provide values of *SSF* with respect to T, μ_T and Seismic Design Categories. For our archetype building with $T \leq 0.5$ s and $\mu_T \geq 8$ and site class D, *SSF* is 1.33 as per Table 7-1b.

The determination of accepted collapse margin ratio on the right hand side of the evaluation check requires characterization of uncertainties including Record-to-Record Uncertainty (*RTR*), Design Requirements Uncertainty (*DR*), Test Data Uncertainty (*TD*) and Modeling Uncertainty (*MDL*).

According to Section 7.3 of FEMA P695 (Applied Technology Council 2009), a fixed value of Record-to-Record Uncertainty $\beta_{RTR} = 0.40$ is assumed in the performance evaluation of systems with significant period elongation (i.e., period-based ductility, $\mu_T \geq$

3). Most systems, even those with limited ductile capacity, have significant period elongation before collapse, and are appropriately evaluated using this value.

The rating of *DR*, *TD* and *MDL* are specifically discussed in Chapter 3 and Chapter 5 of FEMA P695. These uncertainties are rated among four levels from most deterministic to most uncertain: superior, good, fair, and poor. If four component random variables (*RTR*, *DR*, *TD*, and *MDL*) are assumed to be statistically independent, the lognormal standard deviation parameter, β_{TOT}, describing the total collapse uncertainty, is given by Eqn. (7-5) in FEMA P695 (Applied Technology Council 2009)

$$\beta_{TOT} = \sqrt{\beta_{RTR}^2 + \beta_{DR}^2 + \beta_{TD}^2 + \beta_{MDL}^2} \tag{T-11}$$

For β_{RTR} = 0.40, the value of total system collapse uncertainty β_{TOT} is tabulated in Table 7-2a to Table 7-2d in FEMA P695 (Applied Technology Council 2009) with respect to *DR*, *TD*, and *MDL*.

The rating of uncertainties is inevitably subjective; to reduce bias in the decision making process, three cases are considered herein. The design requirement is regarded as 'Good' according to Chapter 3 of FEMA P695, since it provides safeguards against unanticipated failure modes and addressed important design concerns but our test and simulation results suggest it is conservative. From the perspective of testing, close attention have been paid to design, construction and loading details at every construction phase. In terms of modeling, A1-3D-SD-a model try to include all structural components and characterize their stiffness, capacity and hysteretic behavior; the resulted model's predicted response

matches reasonably well with test data but non-structural components are not included. Consequently, the uncertainties in test data and modeling are rated as 'Good' or even 'Superior' if we tend to be more optimistic. The resulted total system collapse uncertainty β_{TOT} from tables in FEMA P695 is included in Table T-2.

Finally, the evaluation of the Response Modification Coefficient R, is performed by checking adjusted collapse margin ratio against accepted collapse margin ratio. As per FEMA P695 (Applied Technology Council 2009), acceptable performance is achieved when, for each performance group, adjusted collapse margin ratios, $ACMR$, for each index archetype meet the following two criteria:

1. The average value of adjusted collapse margin ratio for each performance group exceeds $ACMR_{10\%}$

$$\overline{ACMR_i} \geq ACMR_{10\%} \tag{T-12}$$

2. Individual values of adjusted collapse margin ratio for each index archetype within a performance group exceeds

$$ACMR_i \geq ACMR_{20\%} \tag{T-13}$$

where $ACMR_{10\%}$ and $ACMR_{20\%}$ are tabulated in Table 7-3 of FEMA P695 (Applied Technology Council 2009) as a function of β_{TOT}.

Note that we are evaluating only one archetype model, so *i* is just one and there is no difference between individual and the average values. It can be seen that even the archetype building at Phase 1 represented by A1-3D-SD-a model pass the evaluation of *R*, with a small margin of *ACMR* over accepted *CMR*.

Table T-2: Modeling options of the CFS-NEES archetype building in performance comparison (the case finally used is in bold type)

Quality of DR	Quality of TD	Quality of MDL	β_{TOT}	*ACMR*	$ACMR_{10\%}$	$ACMR_{20\%}$	Pass/Fail
Good	Superior	Superior	0.475	1.85	1.84	1.49	Pass
Good	Good	Superior	0.500	1.85	1.90	1.52	Pass
Good	**Good**	**Good**	**0.525**	**1.85**	**1.96**	**1.56**	**Pass**

The evaluation of the overstrength Factor Ω_O, is much simpler. The average value of archetype overstrength, Ω calculated for each performance group should be compared to the system overstrength factor Ω_O used in design. As mentioned in Section 7.6 of FEMA P695, "Ω_O should not be taken as less than the largest average value of calculated archetype overstrength, Ω, from any performance group." Also Ω_O need not exceed 1.5 times the response modification coefficient, *R*. A practical limit on the value of Ω_O is about 3.0.

For our archetype model, the average Ω from pushover analysis is 4.99, 66% larger than Ω_O = 3.0 taken in design process. However, FEMA P695 also points out that "example applications show that values of archetype overstrength, Ω, can be as large as Ω = 6.0 for certain configurations, and are highly variable." As a result, caution and scrutiny is needed before drawing any deterministic conclusion from the evaluation of Ω_O.

Appendix U: Details on Incremental Dynamic Analysis and Performance Evaluation of A2b-3D-SD-a model

U.1 Incremental dynamic analysis results of A2b-3D-SD-a model

The high-fidelity 3D, semi-rigid diaphragm model (A2b-3D-SD-a) of the CFS-NEES building at construction Phase 2b with assumed structural components and OSB sheathing of gravity walls is adopted for IDA. This model has all essential details of the tested building and its response provides a reasonable match with test data (see Chapter 3 for model description and Chapter 4 for model vs. test comparison). Twenty-two far-field ground motion record pairs in the set of FEMA P695 (Applied Technology Council 2009) are applied to excite the structural model. As suggested by FEMA P695, each record pair is applied twice to each model, once with the ground motion records oriented along one principal direction, and then again with the records rotated 90 degrees. Through the process of ground motion record scaling, individual records in each set are firstly "normalized" by their respective peak ground velocities.

In IDA of the A2b-3D-SD-a model, about 1000 nonlinear 2-axis time history analyses have been performed. The peak story drift among floor and roof level is chosen as the damage measure and the spectral acceleration of the first natural period of the structure (S_a) is the intensity measure. For consistency with conventions in seismology, the S_a of the two axis excitation is defined as the geometrical average of the two S_a under excitation in x and y direction separately.

Figure U-1 provides IDA analysis results in terms of peak story drift vs. first mode spectral acceleration. Record-to-record uncertainty is observed: some normalized ground motion records are scaled up to 6 times to ensure the peak drift is large enough to trigger failure in the building. The failure, or collapse, is detected by checking the peak story drift vs. a prescribed drift-limit. Sometimes, dynamic instability takes place, which implies the drift is so large and becomes unbounded at a certain excitation level, as shown by flat horizontal lines that extend (to infinity) in Figure U-1. As discussed in Appendix T, the proposed drift limit for collapse is set as 4% (marked by the vertical dash line in Figure U-1).

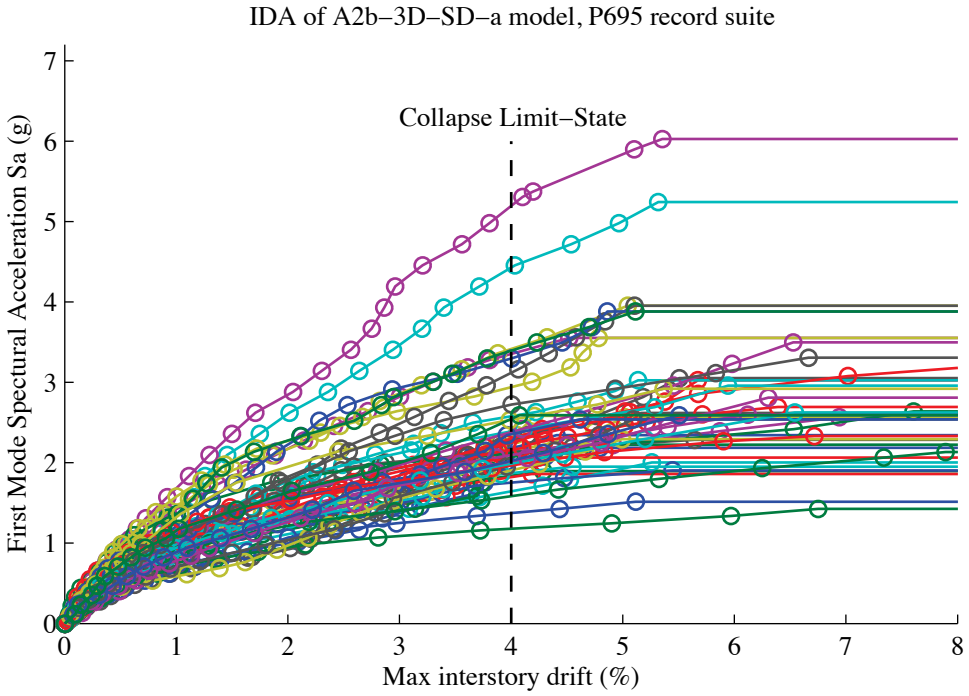

Figure U-1: IDA result of A2b-3D-SD-a model

U.2 Post-processing of nonlinear analysis results

(a) Post-processing of pushover analysis results

Post-processing of the pushover analysis precedes IDA in that lateral capacity of the archetype building, archetype overstrength Ω, and period-based ductility μ_T should be determined first from pushover analysis. Archetype overstrength Ω is directly related to the evaluation of the system of overstrength factor Ω_O as discussed later in the section. Period-based ductility μ_T is used later in the quantification of uncertainties in accepted collapse margin ratios for evaluation of the response modification factor R.

As described in FEMA P695 (Applied Technology Council 2009), the overstrength factor for a given index archetype model, Ω, is defined as the ratio of the maximum base shear resistance, V_{max}, to the design base shear, V:

$$\Omega = V_{\max} / V \tag{U-1}$$

The period-based ductility for a given index archetype model, μ_T, is defined as the ratio of ultimate roof drift displacement, δ_u, (defined as shown in Figure U-2) to the effective yield roof drift displacement $\delta_{y,eff}$:

$$\mu_T = \delta_u / \delta_{y,eff} \tag{U-2}$$

In order to quantify δ_u, FEMA P695 mentioned that the lateral loads should be applied monotonically until a loss of 20% of the base shear capacity ($0.8V_{max}$) is achieved and is the deflection at that post-peak base shear level.

Referring to our case study of the A2b3D-SD-a model, the definition of V_{max}, V, *and* δ_u, and $\delta_{y,eff}$ are illustrated in Figure U-2. In that figure, the pushover curves go flat eventually and never drop below $0.8V_{max}$ after reaching peak capacity. Therefore, the ultimate displacement δ_u is taken at the initiation point where the pushover curve flattens; an alternative would be to use 4%. However, δ_u determined in Figure U-2 correspond to roof drift less than 4% (full height of the building is 18 ft (5.49 m)) and are thus more conservative estimations. Other than this assumption, the calculation went strictly following the procedure described in Appendix T and results are tabulated in Table U-1.

Other numbers used in calculations, include the building's total weight W=77575 lb, story seismic weight w_1=41817 lb, w_2=29474 lb and design base shear $V=C_S W$=0.143×77585=11061 lb as can be found in the design narrative (Madsen et al. 2011).

Table U-1: Summary of calculation of overstrength and period-based ductility, A2b-3D-SD-a model

	Overstrength calculation		
	LONG	**SHORT**	**MEAN**
V_{max} (kips)	77.59	66.32	-
Ω	6.96	6.00	6.48
	Period-based ductility calculation		
	LONG	**SHORT**	**MEAN**
$\phi_{1,1}$ (in.)	0.221	1.614	-
$\phi_{1,2}$ ($\phi_{1,r}$) (in.)	0.362	2.729	-
C_0	1.220	1.229	-
V_{max}/W	0.99	0.85	-
δ_u (in.)	8.62	6.19	
$\delta_{y,eff}^*$ (in.)	0.93	0.80	-
μ_T	9.30	7.72	8.51

*: $\delta_{y,eff}$ from pushover curves are 0.55 in. and 0.77 in.

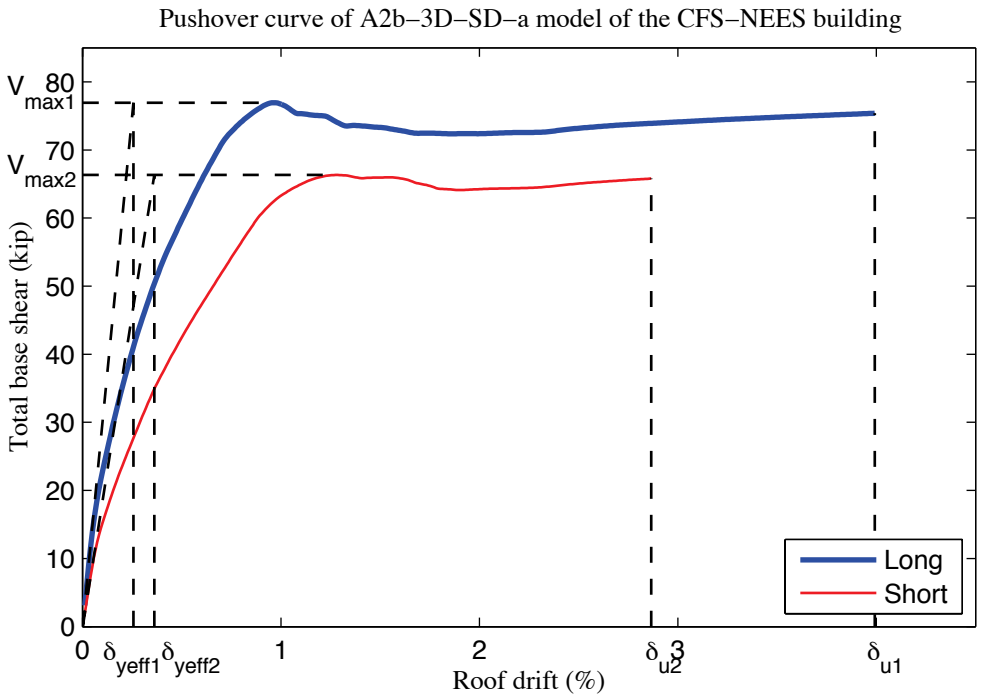

Figure U-2: Pushover curve of A2b-3D-SD-a model

(b) Post-processing of IDA results

With the specified collapse drift limit (4% herein), the collapse data from IDA results are utilized first to determine a set of S_a values associated with the onset of collapse for each ground motion, as illustrated in Figure U-3 with discrete dots (also referred to as an empirical cumulative distribution function). The probability of collapse at a given S_a level, x, can then be estimated as the fraction of records for which collapse occurs at a level lower than x (Baker 2015). Furthermore, a cumulative distribution function (CDF) is generated by fitting a lognormal distribution through the collapse data points of the empirical cumulative distribution function (solid curves in Figure U-3).

Once the CDF is determined, the median collapse capacity ($\hat{S}_{CT}$ in Figure U-3) corresponding to 50% probability of collapse is determined. The collapse margin ratio,

CMR, as the primary parameter in the characterization of the collapse performance evaluation is given by

$$CMR = \frac{\hat{S}_{CT}}{S_{MT}} \tag{U-3}$$

Where the MCE intensity is obtained from the response spectrum of MCE ground motions at the fundamental period, *T* (Applied Technology Council 2009). According to Section 6.4.5 of FEMA P695 (Applied Technology Council 2009), the *CMR* calculated based on median collapse intensity, $\hat{S}_{CT}$, obtained from three-dimensional analyses should be multiplied by a factor of 1.2. Detailed explanation on this amplification is provided in Appendix T.

The fitting of lognormal CDF to the empirical CDF of the IDA collapse results is equivalent to the estimation of two parameters of the lognormal distribution:

$$P\left(C \mid IM = x\right) = \Phi\left(\frac{\ln x - \mu}{\sigma}\right) \tag{U-4}$$

where $P(C \mid IM = x)$ is the probability that a ground motion with $IM = x$ will cause the structure to collapse, $\Phi(\ )$ is the standard normal cumulative distribution function (CDF), $\exp(\mu)$ is the median of the fragility function (the *IM* level with 50% probability of collapse) and σ is the standard deviation of $\ln IM$ (sometimes referred to as the dispersion of *IM*) (Baker 2015). In this research, the more classical method of moments estimator

developed by Ibarra and Krawinkler (Ibarra and Krawinkler 2005) is adopted to estimate μ and σ (see Appendix T for formulae of estimation).

If the collapse drift limit is taken as 4%, the estimated μ and σ using points on the empirical cumulative distribution function are 0.848 and 0.244. The fitted analytical fragility curve is plotted in Figure U-3. The median collapse capacity ($\hat{S}_{CT} = 2.33g$ in the figure) corresponds to 50% probability of collapse.

The design narrative (Madsen et al. 2011) says the MCE spectral response acceleration for short periods S_{MS}=1.39 g for the CFS-NEES building. As per Table 6-1 of FEMA P695 (Applied Technology Council 2009) the transition period T_S is 0.6 s for the archetype building with site class D. Then Eqn. (6-2) of FEMA P695 determines that for short-period archetypes ($T \leq T_S$), $S_{MT}=S_{MS}$. So S_{MT} is also 1.39 g for our archetype. Taking the modification of 3D analysis into account, the *CMR* of Phase 2b archetype building represented by A2b-3D-SD-a model is

$$CMR = 1.2 \times \frac{2.33}{1.39} = 2.01$$

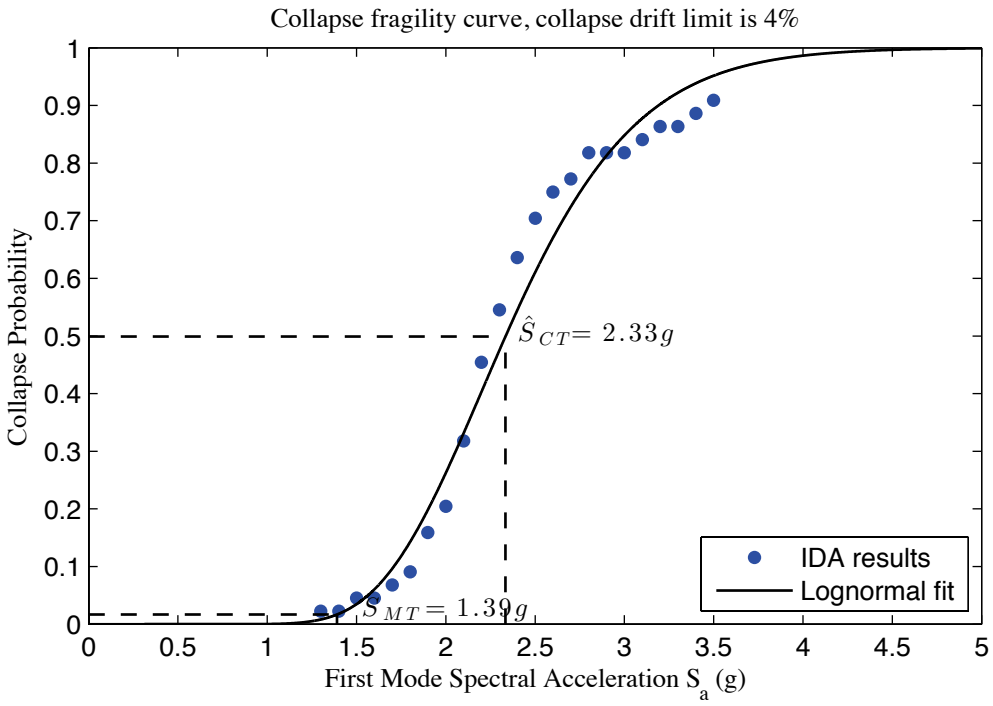

Figure U-3: Collapse fragility curve with proposed collapse drift limits for a 4% drift limit

U.3 Performance evaluation of the archetype building using FEMA P695 Procedure

The complete performance evaluation is elaborated in Chapter 7 of FEMA P695 (Applied Technology Council 2009). The process utilizes results from pushover analyses to determine an appropriate value of the system overstrength factor, Ω_O, and results from nonlinear static and time history analyses to evaluate the acceptability of a trial value of the response modification coefficient, R. The deflection amplification factor, C_d, is derived from an acceptable value of R, with consideration of the effective damping of the system of interest.

The trial value of the response modification coefficient, R, used to design index archetypes (R=6.5 in our design), is evaluated in terms of the acceptability of the collapse margin ratio. The evaluation is fulfilled by comparing the adjusted collapse margin ratio

(*ACMR*) to the accepted collapse margin ratio. *ACMR* is the collapse margin ratio after adjustment for the effects of spectral shape, while accepted collapse margin ratio is dependent on the quality of the information used to define the system, total system uncertainty, and established limits on collapse probability.

Post-processing of pushover analysis results is presented in Section 6.3.1. Period-based ductility, μ_T from pushover analysis is used in the calculation of the adjusted collapse margin ratio for each archetype using the spectral shape factor, *SSF*, which is also dependent on the fundamental period, *T*. For each index archetype *i*, *ACMR* is given by

$$ACMR_i = SSF_i \times CMR_i \tag{U-5}$$

Currently in this research, only one archetype model A2b-3D-SD-a is studied, so *i* is one.

As discussed in Section 7.2.1 of FEMA P695 (Applied Technology Council 2009), simplified spectral shape factors, *SSF*, which depend on fundamental period and period-based ductility, are used to adjust the collapse margin ratios. Table 7-1a and Table 7-1b in of FEMA P695 provide values of *SSF* with respect to *T*, μ_T and Seismic Design Categories. For our archetype building with $T \leq 0.5$ s and $\mu_T \geq 8$ and site class D, *SSF* is 1.33 as per Table 7-1b.

The determination of accepted collapse margin ratio on the right hand side of the evaluation check requires characterization of uncertainties including Record-to-Record

Uncertainty (*RTR*), Design Requirements Uncertainty (*DR*), Test Data Uncertainty (*TD*) and Modeling Uncertainty (*MDL*).

According to Section 7.3 of FEMA P695 (Applied Technology Council 2009), a fixed value of Record-to-Record Uncertainty β_{RTR} = 0.40 is assumed in the performance evaluation of systems with significant period elongation (i.e., period-based ductility, $\mu_T \geq$ 3). Most systems, even those with limited ductile capacity, have significant period elongation before collapse, and are appropriately evaluated using this value.

The rating of *DR*, *TD* and *MDL* are specifically discussed in Chapter 3 and Chapter 5 of FEMA P695. These uncertainties are rated among four levels from most deterministic to most uncertain: superior, good, fair, and poor. If four component random variables (*RTR*, *DR*, *TD*, and *MDL*) are assumed to be statistically independent, the lognormal standard deviation parameter, β_{TOT}, describing the total collapse uncertainty, is given by Eqn. (7-5) in FEMA P695 (Applied Technology Council 2009)

$$\beta_{TOT} = \sqrt{\beta_{RTR}^2 + \beta_{DR}^2 + \beta_{TD}^2 + \beta_{MDL}^2} \tag{U-6}$$

For β_{RTR} = 0.40, the value of total system collapse uncertainty β_{TOT} is tabulated in Table 7-2a to Table 7-2d in FEMA P695 (Applied Technology Council 2009) with respect to *DR*, *TD*, and *MDL*.

The rating of uncertainties is inevitably subjective; to reduce bias in the decision making process, three cases are considered herein. The design requirement is regarded as 'Good' according to Chapter 3 of FEMA P695, since it provides safeguards against unanticipated failure modes and addressed important design concerns but our test and simulation results suggest it is conservative. From the perspective of testing, close attention have been paid to design, construction and loading details at every construction phase. In terms of modeling, A2b-3D-SD-a model try to include all structural components and OSB sheathing of gravity walls and characterize their stiffness, capacity and hysteretic behavior; the resulted model's predicted response matches reasonably well with test data. Consequently, the uncertainties in test data and modeling are rated as 'Good' or even 'Superior' if we tend to be more optimistic. The resulted total system collapse uncertainty β_{TOT} from tables in FEMA P695 is included in Table U-2.

Finally, the evaluation of the Response Modification Coefficient R, is performed by checking adjusted collapse margin ratio against accepted collapse margin ratio. As per FEMA P695 (Applied Technology Council 2009), acceptable performance is achieved when, for each performance group, adjusted collapse margin ratios, $ACMR$, for each index archetype meet the following two criteria:

1. The average value of adjusted collapse margin ratio for each performance group exceeds $ACMR_{10\%}$

$$\overline{ACMR_i} \geq ACMR_{10\%} \tag{U-7}$$

2. Individual values of adjusted collapse margin ratio for each index archetype within a performance group exceeds

$$ACMR_i \geq ACMR_{20\%} \tag{U-8}$$

where $ACMR_{10\%}$ and $ACMR_{20\%}$ are tabulated in Table 7-3 of FEMA P695 (Applied Technology Council 2009) as a function of β_{TOT}.

Note that we are evaluating only one archetype model, so *i* is just one and there is no difference between individual and the average values. It can be seen that the archetype building at Phase 2b represented by A2b-3D-SD-a model pass the evaluation of *R*, with a large margin of *ACMR* over accepted *CMR*.

Table U-2: Modeling options of the CFS-NEES archetype building in performance comparison (the case finally used is in bold type)

Quality of DR	Quality of TD	Quality of MDL	β_{TOT}	*ACMR*	$ACMR_{10\%}$	$ACMR_{20\%}$	Pass/Fail
Good	Superior	Superior	0.475	2.67	1.84	1.49	Pass
Good	**Good**	**Superior**	**0.500**	**2.67**	**1.90**	**1.52**	**Pass**
Good	Good	Good	0.525	2.67	1.96	1.56	Pass

The evaluation of the Overstrength Factor Ω_O, is much simpler. The average value of archetype overstrength, Ω calculated for each performance group should be compared to the system overstrength factor Ω_O used in design. As mentioned in Section 7.6 of FEMA P695, "Ω_O should not be taken as less than the largest average value of calculated archetype overstrength, Ω, from any performance group." Also Ω_O need not exceed 1.5

times the response modification coefficient, R. A practical limit on the value of Ω_O is about 3.0.

For our archetype model, the average Ω from pushover analysis is 6.48, 116% larger than Ω_O = 3.0 taken in design process. However, FEMA P695 also points out that "example applications show that values of archetype overstrength, Ω, can be as large as Ω = 6.0 for certain configurations, and are highly variable." As a result, caution and scrutiny is needed before drawing any deterministic conclusion from the evaluation of Ω_O.

Appendix V: Details on Incremental Dynamic Analysis and Performance Evaluation of P-3D-RD-b model

V.1 Incremental dynamic analysis results of P-3D-RD-b model

The state-of-the-practice 3D, rigid diaphragm model (P-3D-RD-b) of the CFS-NEES building with shear wall models based on AISI S213 specification (American Iron and Steel Institute 2009) is adopted for IDA. This structural-only low fidelity model employs shear walls as the only LFRS and it significantly underestimates the building's stiffness and capacity (see Chapter 3 for model description and Chapter 5 for comparisons of simulation results). Twenty-two far-field ground motion record pairs in the set of FEMA P695 (Applied Technology Council 2009) are applied to excite the structural model. As suggested by FEMA P695, each record pair is applied twice to each model, once with the ground motion records oriented along one principal direction, and then again with the records rotated 90 degrees. Through the process of ground motion record scaling, individual records in each set are firstly "normalized" by their respective peak ground velocities.

In IDA of the P-3D-RD-b model, about 1000 nonlinear 2-axis time history analyses have been performed. The peak story drift among floor and roof level is chosen as the damage measure and the spectral acceleration of the first natural period of the structure (S_a) is the intensity measure. For consistency with conventions in seismology, the S_a of the two axis excitation is defined as the geometrical average of the two S_a under excitation in x and y direction separately.

Figure V-1 provides IDA analysis results in terms of peak story drift vs. first mode spectral acceleration. Record-to-record uncertainty is observed, but most of forty-four excitation pairs can create a peak drift large enough to trigger failure in the building at a scale factor less than 2.0. The failure, or collapse, is detected by checking the peak story drift vs. a prescribed drift-limit. Sometimes, dynamic instability takes place, which implies the drift is so large and becomes unbounded at a certain excitation level, as shown by flat horizontal lines that extend (to infinity) in Figure V-1. As discussed in Appendix T, the proposed drift limit for collapse is set as 4% (marked by the vertical dash line in Figure V-1).

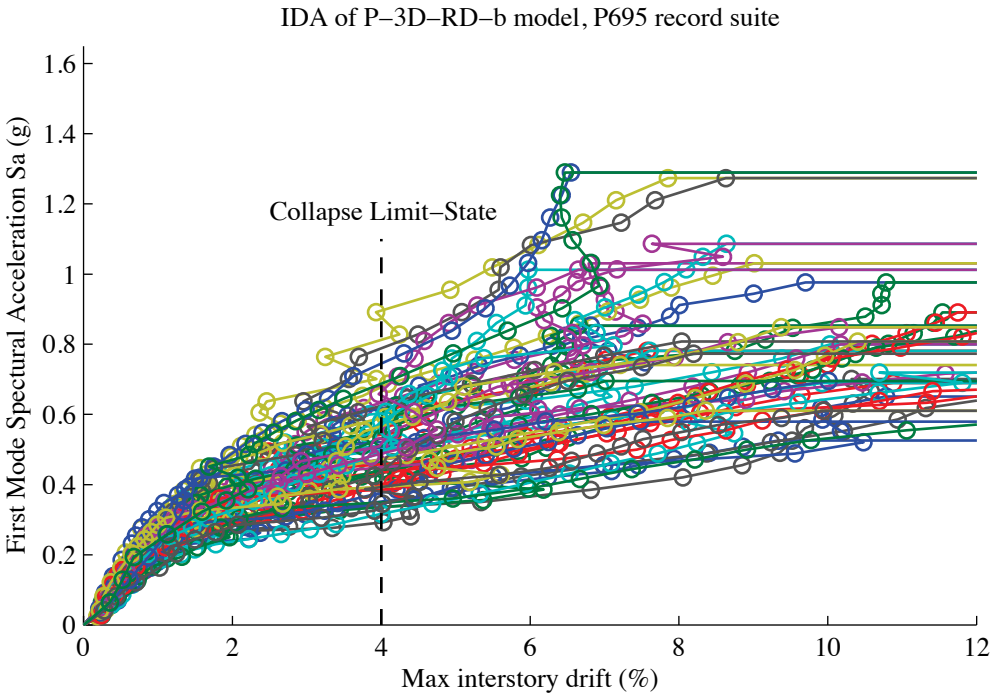

Figure V-1: IDA result of P-3D-RD-b model

V.2 Post-processing of nonlinear analysis results

(a) Post-processing of pushover analysis results

Post-processing of the pushover analysis precedes IDA in that lateral capacity of the archetype building, archetype overstrength Ω, and period-based ductility μ_T should be determined first from pushover analysis. Archetype overstrength Ω is directly related to the evaluation of the system of overstrength factor Ω_O as discussed later in the section. Period-based ductility μ_T is used later in the quantification of uncertainties in accepted collapse margin ratios for evaluation of the response modification factor R.

As described in FEMA P695 (Applied Technology Council 2009), the overstrength factor for a given index archetype model, Ω, is defined as the ratio of the maximum base shear resistance, V_{max}, to the design base shear, V:

$$\Omega = V_{\max} / V \tag{V-1}$$

The period-based ductility for a given index archetype model, μ_T, is defined as the ratio of ultimate roof drift displacement, δ_u, (defined as shown in Figure V-2) to the effective yield roof drift displacement $\delta_{y,eff}$:

$$\mu_T = \delta_u / \delta_{y,eff} \tag{V-2}$$

In order to quantify δ_u, FEMA P695 mentioned that the lateral loads should be applied monotonically until a loss of 20% of the base shear capacity ($0.8V_{max}$) is achieved and is the deflection at that post-peak base shear level.

Referring to our case study of the P-3D-RD-a model, the definition of V_{max}, V, *and* δ_u, and $\delta_{y,eff}$ are illustrated in Figure V-2. In that figure, the pushover curves drop sharply below $0.8V_{max}$ after reaching peak capacity. Therefore, the ultimate displacement δ_u is very close to $\delta_{y,eff}$ so the ductility predicted by this model is only slightly larger than 1.0. As montioned above, this model is an inadequate one, so its significant underestimation of the building's ductility cannot reflect reality. The calculation followed the procedure described in Appendix T and results are tabulated in Table V-1.

Other numbers used in calculations, include the building's total weight W=77575 lb, story seismic weight w_1=41817 lb, w_2=29474 lb and design base shear $V=C_S W$=0.143×77585=11061 lb as can be found in the design narrative (Madsen et al. 2011).

Table V-1: Summary of calculation of overstrength and period-based ductility, P-3D-RD-b model

	Overstrength calculation		
	LONG	**SHORT**	**MEAN**
V_{max} (kips)	21.47	17.84	-
Ω	1.94	1.61	1.78
	Period-based ductility calculation		
	LONG	**SHORT**	**MEAN**
$\phi_{1,1}$ (in.)	0.454	1.000	-
$\phi_{1,2}$ ($\phi_{1,r}$) (in.)	0.861	1.922	-
C_0	1.236	1.256	-
V_{max}/W	0.28	0.23	-
δ_u (in.)	1.81	2.19	
$\delta_{y,eff}^{*}$ (in.)	2.12	1.76	-
μ_T^{**}	1.0	1.24	1.17

*: $\delta_{y,eff}$ from pushover curves are 1.15 in. and 1.62 in.
**: μ_T caluated from equation value of $\delta_{y,eff}$ is less than 1.0 for long direction, so use 1.0

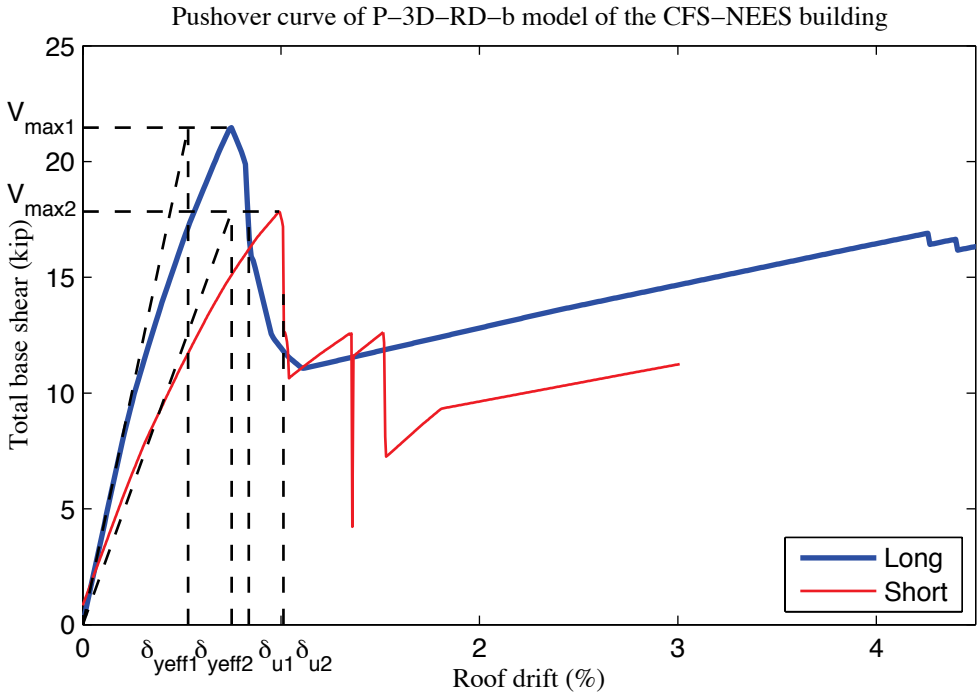

Figure V-2: Pushover curve of P-3D-RD-b model

(b) Post-processing of IDA results

With the specified collapse drift limit (4% herein), the collapse data from IDA results are utilized first to determine a set of S_a values associated with the onset of collapse for each ground motion, as illustrated in Figure V-3 with discrete dots (also referred to as an empirical cumulative distribution function). The probability of collapse at a given S_a level, x, can then be estimated as the fraction of records for which collapse occurs at a level lower than x (Baker 2015). Furthermore, a cumulative distribution function (CDF) is generated by fitting a lognormal distribution through the collapse data points of the empirical cumulative distribution function (solid curves in Figure V-3).

Once the CDF is determined, the median collapse capacity ($\hat{S}_{CT}$ in Figure V-3) corresponding to 50% probability of collapse is determined. The collapse margin ratio,

CMR, as the primary parameter in the characterization of the collapse performance evaluation is given by

$$CMR = \frac{\hat{S}_{CT}}{S_{MT}} \tag{V-3}$$

Where the MCE intensity is obtained from the response spectrum of MCE ground motions at the fundamental period, *T* (Applied Technology Council 2009). According to Section 6.4.5 of FEMA P695 (Applied Technology Council 2009), the *CMR* calculated based on median collapse intensity, $\hat{S}_{CT}$, obtained from three-dimensional analyses should be multiplied by a factor of 1.2. Detailed explanation on this amplification is provided in Appendix T.

The fitting of lognormal CDF to the empirical CDF of the IDA collapse results is equivalent to the estimation of two parameters of the lognormal distribution:

$$P\left(C \mid IM = x\right) = \Phi\left(\frac{\ln x - \mu}{\sigma}\right) \tag{V-4}$$

where $P(C \mid IM = x)$ is the probability that a ground motion with $IM = x$ will cause the structure to collapse, $\Phi(\ )$ is the standard normal cumulative distribution function (CDF), $\exp(\mu)$ is the median of the fragility function (the *IM* level with 50% probability of collapse) and σ is the standard deviation of $\ln IM$ (sometimes referred to as the dispersion of *IM*) (Baker 2015). In this research, the more classical method of moments estimator

developed by Ibarra and Krawinkler (Ibarra and Krawinkler 2005) is adopted to estimate μ and σ (see Appendix T for formulae of estimation).

If the collapse drift limit is taken as 4%, the estimated μ and σ using points on the empirical cumulative distribution function are -0.736 and 0.335. The fitted analytical fragility curve is plotted in Figure V-3. The median collapse capacity ($\hat{S}_{CT} = 0.48g$ in the figure) corresponds to 50% probability of collapse.

The design narrative (Madsen et al. 2011) says the MCE spectral response acceleration for short periods S_{MS}=1.39 g for the CFS-NEES building. As per Table 6-1 of FEMA P695 (Applied Technology Council 2009) the transition period T_S is 0.6 s for the archetype building with site class D. Then Eqn. (6-2) of FEMA P695 determines that for short-period archetypes ($T \leq T_S$), $S_{MT}=S_{MS}$. So S_{MT} is also 1.39 g for our archetype. Taking the modification of 3D analysis into account, the *CMR* of Phase 1 archetype building represented by P-3D-RD-b model is

$$CMR = 1.2 \times \frac{0.48}{1.39} = 0.41$$

Clearly, such a low value (much less than 1.0) of CMR suggests the building's seismic design is not safe. However, our test and high-fidelity model results show that the complete building can even survive the MCE. Again, the results in this appendix only demonstrate the inadequacy of this model.

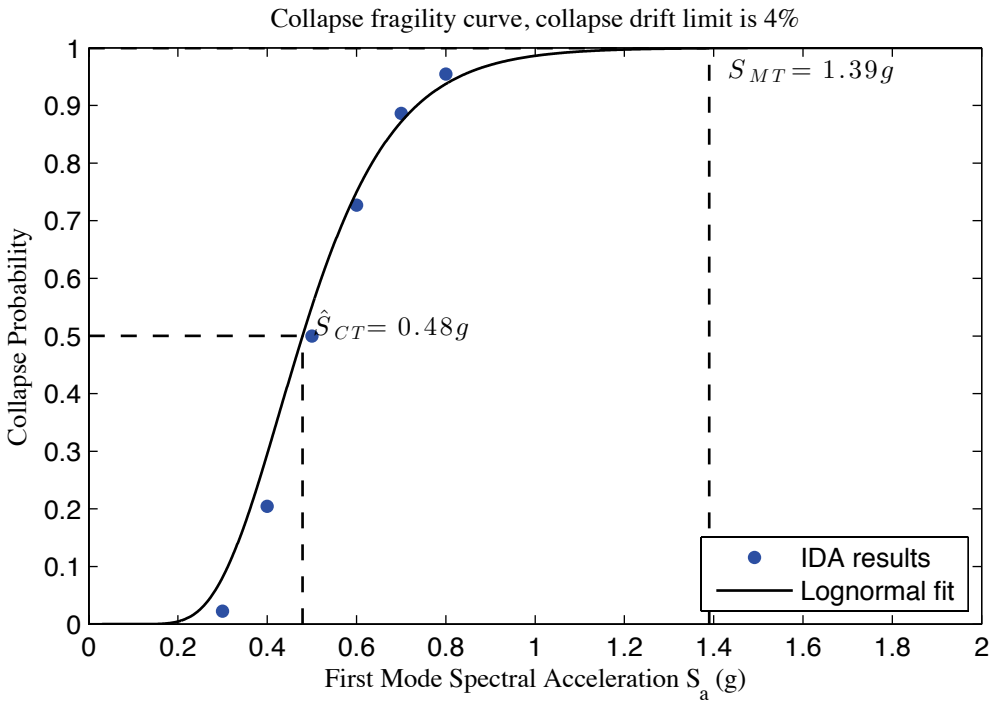

Figure V-3: Collapse fragility curve with proposed collapse drift limits for a 4% drift limit

V.3 Performance evaluation of the archetype building using FEMA P695 Procedure

The complete performance evaluation is elaborated in Chapter 7 of FEMA P695 (Applied Technology Council 2009). The process utilizes results from pushover analyses to determine an appropriate value of the system overstrength factor, Ω_O, and results from nonlinear static and time history analyses to evaluate the acceptability of a trial value of the response modification coefficient, R. The deflection amplification factor, C_d, is derived from an acceptable value of R, with consideration of the effective damping of the system of interest.

The trial value of the response modification coefficient, R, used to design index archetypes (R=6.5 in our design), is evaluated in terms of the acceptability of the collapse margin ratio. The evaluation is fulfilled by comparing the adjusted collapse margin ratio

(*ACMR*) to the accepted collapse margin ratio. *ACMR* is the collapse margin ratio after adjustment for the effects of spectral shape, while accepted collapse margin ratio is dependent on the quality of the information used to define the system, total system uncertainty, and established limits on collapse probability.

Post-processing of pushover analysis results is presented in Section 6.3.1. Period-based ductility, μ_T from pushover analysis is used in the calculation of the adjusted collapse margin ratio for each archetype using the spectral shape factor, *SSF*, which is also dependent on the fundamental period, *T*. For each index archetype *i*, *ACMR* is given by

$$ACMR_i = SSF_i \times CMR_i \tag{V-5}$$

Currently in this research, only one archetype model P-3D-RD-b is studied, so *i* is one.

As discussed in Section 7.2.1 of FEMA P695 (Applied Technology Council 2009), simplified spectral shape factors, *SSF*, which depend on fundamental period and period-based ductility, are used to adjust the collapse margin ratios. Table 7-1a and Table 7-1b in of FEMA P695 provide values of *SSF* with respect to *T*, μ_T and Seismic Design Categories. For our archetype building with $T = 0.8$ s and $\mu_T = 1.2$ (as predicted by P-3D-RD-a model) and site class D, *SSF* is 1.06 as per Table 7-1b.

The determination of accepted collapse margin ratio on the right hand side of the evaluation check requires characterization of uncertainties including Record-to-Record

Uncertainty (*RTR*), Design Requirements Uncertainty (*DR*), Test Data Uncertainty (*TD*) and Modeling Uncertainty (*MDL*).

According to Section 7.3 of FEMA P695 (Applied Technology Council 2009), a fixed value of Record-to-Record Uncertainty β_{RTR} = 0.40 is assumed in the performance evaluation of systems with significant period elongation (i.e., period-based ductility, $\mu_T \geq$ 3). Most systems, even those with limited ductile capacity, have significant period elongation before collapse, and are appropriately evaluated using this value..

The rating of *DR*, *TD* and *MDL* are specifically discussed in Chapter 3 and Chapter 5 of FEMA P695. These uncertainties are rated among four levels from most deterministic to most uncertain: superior, good, fair, and poor. If four component random variables (*RTR*, *DR*, *TD*, and *MDL*) are assumed to be statistically independent, the lognormal standard deviation parameter, β_{TOT}, describing the total collapse uncertainty, is given by Eqn. (7-5) in FEMA P695 (Applied Technology Council 2009)

$$\beta_{TOT} = \sqrt{\beta_{RTR}^2 + \beta_{DR}^2 + \beta_{TD}^2 + \beta_{MDL}^2} \tag{V-6}$$

For β_{RTR} = 0.40, the value of total system collapse uncertainty β_{TOT} is tabulated in Table 7-2a to Table 7-2d in FEMA P695 (Applied Technology Council 2009) with respect to *DR*, *TD*, and *MDL*. As predicted by P-3D-RD-a model, μ_T is only 1.2 (see previous section). However, the model itself is far from reality and it greatly underestimates μ_T so

tabulated values for *DR*, *TD*, and *MDL* is still adopted here despite the premise that they are developed for $\mu_T \geq 3$.

The rating of uncertainties is inevitably subjective; to reduce bias in the decision making process, two cases are considered herein. The design requirement is regarded as 'Good' according to Chapter 3 of FEMA P695, since it provides safeguards against unanticipated failure modes and addressed important design concerns but our test and simulation results suggest it is conservative. From the perspective of testing, close attention have been paid to design, construction and loading details at every construction phase. The uncertainty is test data can be rated as 'Good' or even 'Superior' if we tend to be more optimistic. In terms of modeling, P-3D-RD-b model only models shear walls as the only LFRS with code-based capacity and rigid diaphragms; all other structural and nonstructural components are missing. The resulted model's predicted response deviates greatly from test data and high-fidelity models. Consequently, the uncertainties in modeling for P-3D-RD-b model can only be rated as 'poor'. The resulted total system collapse uncertainty β_{TOT} from tables in FEMA P695 is included in Table V-2.

Finally, the evaluation of the Response Modification Coefficient *R*, is performed by checking adjusted collapse margin ratio against accepted collapse margin ratio. As per FEMA P695 (Applied Technology Council 2009), acceptable performance is achieved when, for each performance group, adjusted collapse margin ratios, *ACMR*, for each index archetype meet the following two criteria:

1. The average value of adjusted collapse margin ratio for each performance group exceeds $ACMR_{10\%}$

$$\overline{ACMR_i} \geq ACMR_{10\%} \tag{V-7}$$

2. Individual values of adjusted collapse margin ratio for each index archetype within a performance group exceeds

$$ACMR_i \geq ACMR_{20\%} \tag{V-8}$$

where $ACMR_{10\%}$ and $ACMR_{20\%}$ are tabulated in Table 7-3 of FEMA P695 (Applied Technology Council 2009) as a function of β_{TOT}.

Note that we are evaluating only one archetype model, so i is just one and there is no difference between individual and the average values. It can be seen that the archetype building represented by P-3D-RD-b model fails the evaluation of R drastically. The building, as predicted by P-3D-RD-b model, has no chance of passing the evaluation even with the most optimistic estimation of uncertainties since its $ACMR$ is so low.

Table V-2: Modeling options of the CFS-NEES archetype building in performance comparison (the case finally used is in bold type)

Quality of DR	Quality of TD	Quality of MDL	β_{TOT}	$ACMR$	$ACMR_{10\%}$	$ACMR_{20\%}$	Pass/Fail
Good	Superior	Poor	0.675	0.43	2.38	1.76	Fail
Good	**Good**	**Poor**	**0.700**	**0.43**	**2.45**	**1.80**	**Fail**

The evaluation of the Overstrength Factor Ω_O, is much simpler. The average value of archetype overstrength, Ω calculated for each performance group should be compared to the system overstrength factor Ω_O used in design. As mentioned in Section 7.6 of FEMA P695, "Ω_O should not be taken as less than the largest average value of calculated archetype overstrength, Ω, from any performance group." Also Ω_O need not exceed 1.5 times the response modification coefficient, R. A practical limit on the value of Ω_O is about 3.0.

For our archetype model, the average Ω from pushover analysis is 1.17, 61% smaller than Ω_O = 3.0 taken in design process. However, this evaluation of Ω_O, along with the evaluation of R in this appendix, are not meaningful but only demonstrates that the most complicated state-of-the-practice P-3D-RD-b model (see Table 3-3 for comparison of modeling options) is a poor representation of the archetype building and its prediction of the building's behavior is unreliable.

Curriculum Vita

Jiazhen Leng was born on October 3, 1984 in Rushan, Shandong Province, China.

Grown up and educated in Beijing, the capital of China, Jiazhen attended Beijing No. 4 High School and graduated in 2002. He spent seven years at Beihang University (BUAA) as an undergraduate and graduate student majoring aerospace engineering. In 2009, he attended Johns Hopkins University in Baltimore, MD with a fellowship. Through his years at JHU, he received M.S. and Ph.D. in Civil Engineering and another M.S. in Mechanical Engineering. His dissertation is about modeling and simulation of multi-story cold-formed steel framed building.

Jiazhen's enthusiasm for structures originates from his hobby of making and collecting scale-model aircrafts since childhood. His research interests include modeling, analysis and design optimization of structures and computational mechanics. He will be continuing his research at McGill University in Montreal, Canada as a postdoctoral research fellow on simulation and optimization of aerospace structures.